EUV Lithography

SECOND EDITION

Downloaded From: https://www.spiedigitallibrary.org/ebooks/ on 09 Mar 2022
Terms of Use: https://www.spiedigitallibrary.org/terms-of-use

Downloaded From: https://www.spiedigitallibrary.org/ebooks/ on 09 Mar 2022
Terms of Use: https://www.spiedigitallibrary.org/terms-of-use

EUV Lithography

SECOND EDITION

Vivek Bakshi, *Editor*

SPIE PRESS
Bellingham, Washington USA

Downloaded From: https://www.spiedigitallibrary.org/ebooks/ on 09 Mar 2022
Terms of Use: https://www.spiedigitallibrary.org/terms-of-use

Library of Congress Cataloging-in-Publication Data

Names: Bakshi, Vivek, editor.
Title: EUV lithography / Vivek Bakshi, editor.
Description: Second edition. | Bellingham, Washington, USA : SPIE Press, [2018]
Identifiers: LCCN 2017051759 | ISBN 9781510616783 (hard cover) | ISBN 1510616780 (hard cover) | ISBN 9781510616790 (PDF) | ISBN 1510616799 (PDF) | ISBN 9781510616806 (ePub) | ISBN 1510616802 (ePub) | ISBN 9781510616813 (Kindle) | ISBN 1510616810 (Kindle)
Subjects: LCSH: Ultraviolet radiation–Industrial applications. | Photolithography. | Optical coatings.
Classification: LCC QC459 .E98 2018 | DDC 621.3815–dc23 LC record available at https://lccn.loc.gov/2017051759

Published by

SPIE
P.O. Box 10
Bellingham, Washington 98227-0010 USA
Phone: +1 360.676.3290
Fax: +1 360.647.1445
Email: books@spie.org
Web: http://spie.org

Chapters 1–5 and 6B–10:
Copyright © 2018 Society of Photo-Optical Instrumentation Engineers (SPIE)

All rights reserved. Chapters 1–5 and 6B–10 of this publication may not be reproduced or distributed in any form or by any means without written permission of the publisher.

Chapter 6A is a work of the U.S. Government and is not subject to copyright.

The content of this book reflects the work and thought of the authors and editor. Every effort has been made to publish reliable and accurate information herein, but the publisher is not responsible for the validity of the information or for any outcomes resulting from reliance thereon.

Cover image © 2017 ASML Netherlands B.V.

Printed in the United States of America.
First Printing.
For updates to this book, visit http://spie.org and type “PM283” in the search field.

Downloaded From: https://www.spiedigitallibrary.org/ebooks/ on 09 Mar 2022
Terms of Use: https://www.spiedigitallibrary.org/terms-of-use

To the technologists, suppliers, and chipmakers
who have made EUVL a reality

Downloaded From: https://www.spiedigitallibrary.org/ebooks/ on 09 Mar 2022
Terms of Use: https://www.spiedigitallibrary.org/terms-of-use

Downloaded From: https://www.spiedigitallibrary.org/ebooks/ on 09 Mar 2022
Terms of Use: https://www.spiedigitallibrary.org/terms-of-use

Contents

Foreword to the Second Edition *xvii*
Preface to the Second Edition *xix*
List of Contributors *xxv*
List of Acronyms and Abbreviations *xxvii*

1 EUV Lithography: An Historical Perspective **1**
Hiroo Kinoshita and Obert Wood
1.1 Introduction 1
1.2 The Early Stage of Development—1981 to 1992 3
1.3 The Second Stage of Development—1993 to 1996 11
1.3.1 Two-mirror imaging system development 13
1.3.2 Three-mirror imaging system development 16
1.3.3 MOS device demonstration using EUVL 17
1.4 Other Developments in Japan and Europe 19
1.5 The Development of Individual Technologies 21
1.5.1 Selection of the exposure wavelength 22
1.5.2 Design of reflective imaging systems 25
1.5.3 Fabrication and evaluation of aspherical mirrors 28
1.5.4 Multilayer coatings and reflection masks 32
1.5.5 EUV resist development 37
1.5.6 EUV light source development 38
1.6 EUVL Conferences 41
1.7 Summary 42
Acknowledgments 43
References 46

2 The EUV LLC: An Historical Perspective **57**
Stefan Wurm
2.1 Introduction 58
2.1.1 Background 59
2.1.2 Need for a revolutionary approach 60
2.2 Formation of the EUV LLC 60
2.2.1 Vision 60
2.2.2 Implementation 61

Downloaded From: https://www.spiedigitallibrary.org/ebooks/ on 09 Mar 2022
Terms of Use: https://www.spiedigitallibrary.org/terms-of-use

2.2.3 Organizational structure 64
2.3 Program Structure 69
2.3.1 Organization 69
2.3.2 Risk management 69
2.3.3 Reporting 71
2.3.4 Documentation 72
2.4 Program Results 74
2.4.1 Technical accomplishments 74
2.4.2 IP portfolio 77
2.4.3 Program statistics 83
2.4.4 Delays 83
2.5 Retrospective Observations 85
2.5.1 Improvements 85
2.5.2 External issues 88
2.5.3 Benefits 89
2.6 Status of EUV Development at the End of the EUV LLC 91
2.6.1 Risk reduction 91
2.7 Summary 92
Appendix 2A: Major Accomplishments of the EUV LLC Program 94
Appendix 2B: EUV LLC Program Patents 99
Acknowledgments 105
References 106

3A EUV Sources for High-Volume Manufacturing 109
Igor V. Fomenkov, David C. Brandt, Alexander I. Ershov, Alexander A. Schafgans, Yezheng Tao, Georgiy O. Vaschenko, and Bruno La Fontaine
3A.1 Introduction to EUV Light Sources 109
3A.2 EUV Source Requirements 114
3A.3 Laser-Produced Plasma Source System 119
3A.3.1 EUV power scaling 119
3A.3.2 Tin target delivery 130
3A.3.3 Pre-pulse technology 135
3A.3.4 EUV collector 136
3A.3.5 Debris mitigation 143
3A.3.6 Hydrogen as a buffer gas 147
3A.3.7 Tin management 150
3A.3.8 Controls 154
3A.4 Summary and Future Outlook 155
References 156

3B High-Power EUV Source by Gigaphoton for High-Volume Manufacturing 165
Hakaru Mizoguchi, Taku Yamazaki, Tatsuya Yanagida, Krzysztof M. Nowak, and Takashi Saito
3B.1 Introduction 165

Downloaded From: https://www.spiedigitallibrary.org/ebooks/ on 09 Mar 2022
Terms of Use: https://www.spiedigitallibrary.org/terms-of-use

3B.2 High-Power LPP EUV Light Source with Pre-pulse Technology 166
3B.2.1 System concept 166
3B.2.2 Tin droplet generation technology 166
3B.2.3 Pre-pulse technology and high-CE operation 167
3B.2.4 Superconducting magnet debris mitigation method (SM3) and the collector mirror 171
3B.2.5 Driver CO_2 laser system 173
3B.3 250-W HVM LPP-EUV Source 181
3B.3.1 Pilot #1 system construction 181
3B.3.2 CE measurements and improvement 182
3B.3.3 Latest data of the Pilot #1 system 183
3B.3.4 Change of collector mirror reflectance during operation 184
3B.4 Conclusion and Acknowledgment 185
References 186

4A The EQ-10 Electrodeless Z-Pinch™ Metrology Source 193
Stephen F. Horne, Matthew M. Besen, Paul A. Blackborow, Ron Collins, Deborah Gustafson, Matthew J. Partlow, and Donald K. Smith
4A.1 Operating Principles 193
4A.2 Diagnostics for the EQ-10 196
4A.3 Source Performance 197
4A.3.1 Power and brightness 198
4A.3.2 Spatial and temporal stability 200
4A.4 Typical Installations 202
4A.5 Conclusions 202
References 202

4B High-Brightness LDP Source for Mask Inspection 207
Yusuke Teramoto
4B.1 Introduction 207
4B.2 LDP System Configuration 209
4B.3 EUV Brightness and Power 212
4B.4 EUV Spectrum and Out-of-Band Radiation 214
4B.5 Stability and Reliability 215
4B.6 Source Cleanliness 217
4B.7 Summary 221
Acknowledgments 221
References 221

5 Optical Systems for EUVL 225
Sascha Migura, Winfried Kaiser, Jens Timo Neumann, Hartmut Enkisch, and Dirk Hellweg
5.1 Introduction 226
5.2 Optical Systems: Beginning and Present 228
5.2.1 Introduction 228

Downloaded From: https://www.spiedigitallibrary.org/ebooks/ on 09 Mar 2022
Terms of Use: https://www.spiedigitallibrary.org/terms-of-use

5.2.2 Beginning: collaborations and funding in Europe 229
5.2.3 Early optical systems: MET, HiNA, and SFET 230
5.2.4 Prototypes: Alpha Demo Tool and EUV1 232
5.2.5 Preproduction system: Starlith® 3100 235
5.2.6 HVM: Starlith® 3300/3400 family 237
5.3 The Future: High-NA 240
5.3.1 Introduction 240
5.3.2 Optical system for high-NA 241
5.3.3 Theoretical background 246
5.3.4 Conclusion on optical systems for EUVL 253
5.4 Optical Modules: Collector 254
5.4.1 Introduction 254
5.4.2 EUV collector types 254
5.4.3 Grazing-incidence collectors 255
5.4.4 Normal-incidence collectors 260
5.5 Optical Modules: Illuminator 263
5.5.1 Introduction 263
5.5.2 Key performance parameters 263
5.5.3 Realization options 265
5.5.4 Pupil tuning 269
5.5.5 Technical challenges 269
5.6 Optical Modules: Projection Optics 270
5.6.1 Introduction 270
5.6.2 Basic design specifications 271
5.6.3 Optics manufacturing: mirror surface 273
5.6.4 Modeling and simulating stray light and flare 279
5.6.5 Optics manufacturing: mirror coating 297
5.7 Mask Inspection: The ZEISS AIMS EUV 308
5.7.1 Introduction 308
5.7.2 Principle and application 308
5.7.3 System concept 311
5.7.4 Tool capabilities 312
5.7.5 Tool performance 314
5.7.6 Summary 316
Acknowledgments 316
References 317

6A Optics Contamination 335
Charles S. Tarrio, Shannon B. Hill, Robert F. Berg, and Saša Bajt
6A.1 Introduction 335
6A.1.1 Background 337
6A.1.2 The chemical processes 338
6A.2 Optics Contamination Research 339
6A.2.1 Carbonization and oxidation: photons or photoelectrons 339

Downloaded From: https://www.spiedigitallibrary.org/ebooks/ on 09 Mar 2022
Terms of Use: https://www.spiedigitallibrary.org/terms-of-use

6A.2.2 The elimination of oxidation as a problem: requirements for oxidation-resistant cap layers 340
6A.2.3 Development of contamination-resistant cap layers 341
6A.3 Optics Contamination Experiments 343
6A.3.1 Facilities 343
6A.3.2 Carbonization: admitted-gas studies 345
6A.4 Resist Outgas Testing 353
6A.4.1 Early measurements 353
6A.4.2 Witness-sample testing 355
6A.4.3 Witness-sample testing: nonconventional resists 356
6A.5 Cleaning and Contamination Control 357
6A.6 Summary and Future Outlook 358
References 358

6B Collector Contamination: Normal-Incidence (Multilayer) Collectors 369
Daniel T. Elg, Shailendra N. Srivastava, and David N. Ruzic
6B.1 Introduction 369
6B.2 Overview of Normal-Incidence Collector Mirrors 371
6B.3 Collector Performance 375
6B.3.1 Debris mitigation and contamination 375
6B.3.2 Atomic hydrogen cleaning 387
6B.3.3 Hydrogen plasma cleaning 393
6B.3.4 Compatibility of multilayer mirrors with H_2 plasma 398
6B.4 Summary 401
Acknowledgments 403
References 403

7 EUV Mask and EUV Mask Metrology 411
Jinho Ahn and Chan-Uk Jeon
7.1 Introduction 412
7.2 EUVL Mask Structure and Process Flow 413
7.3 Mask Substrate 414
7.3.1 Thermal expansion coefficient 414
7.3.2 Surface figure requirements 415
7.3.3 Defect requirements 417
7.4 Multilayer and Backside Conductive Coating 418
7.4.1 Multilayer deposition process 418
7.4.2 Multilayer characterization 421
7.4.3 Multilayer performance improvement techniques and defect mitigation 422
7.4.4 Capping layer 427
7.4.5 Backside conductive coating and mask handling 428
7.5 Absorber Stack and Pattern Fabrication 428
7.5.1 Absorber layer 429

Downloaded From: https://www.spiedigitallibrary.org/ebooks/ on 09 Mar 2022
Terms of Use: https://www.spiedigitallibrary.org/terms-of-use

7.5.2 Antireflection coating 430
7.5.3 E-beam patterning 431
7.5.4 Absorber stack etch 431
7.6 Mask Inspection, Metrology, and Repair 432
7.6.1 Multilayer defect inspection 432
7.6.2 Absorber pattern inspection 435
7.6.3 Multilayer defect repair 437
7.6.4 Multilayer defect compensation 440
7.6.5 Absorber defect repair 442
7.6.6 Next-generation repair 444
7.6.7 Aerial image metrology 447
7.7 Mask Contamination Protection and Cleaning 450
7.7.1 Pellicle 450
7.7.2 Mask cleaning 457
7.8 Advanced Mask Structure for Better Imaging 458
7.8.1 Shadowing effect 458
7.8.2 Bossung curve asymmetry and focus shift 460
7.8.3 Alternative mask structures 461
7.8.4 Etched ML binary mask 462
7.8.5 Attenuated phase shift mask 465
7.8.6 Alternating phase shift mask 470
7.8.7 Black border 472
7.8.8 Mask design for high-NA 473
7.9 Summary and Future Outlook 474
Acknowledgments 475
References 475

8 Photoresists for EUV Lithography 493
Robert L. Brainard, Mark Neisser, Gregg Gallatin, and Amrit Narasimhan
8.1 Introduction 494
8.2 Earliest EUV Resist Imaging 495
8.3 Absorption Coefficients of EUV Photoresists 500
8.3.1 Definitions of transmission and absorption 500
8.3.2 Early absorption goals 501
8.3.3 A change in absorption goals: from light to dark 502
8.3.4 Measuring absorption of actual resist films 503
8.4 Mechanisms of Resist Exposure to EUV Light 505
8.4.1 Introduction 505
8.4.2 The physics of EUV exposure mechanisms 506
8.4.3 The chemistry of EUV exposure mechanisms 508
8.4.4 Maximum quantum yield in chemically amplified photoresists 508
8.4.5 Total electron yield in EUV photoresists 509
8.4.6 Mechanisms of acid generation in CARs 510

Downloaded From: https://www.spiedigitallibrary.org/ebooks/ on 09 Mar 2022
Terms of Use: https://www.spiedigitallibrary.org/terms-of-use

8.4.7 Electron travel distance in photoresists 515
8.4.8 Conclusions 516
8.5 Organic Photoresists 518
8.5.1 Polymethylmethacrylate (PMMA) resists 518
8.5.2 Environmentally stable chemically amplified photoresists 518
8.5.3 Low-activation-energy acetal or ketal resists 520
8.5.4 Chain-scission resists 521
8.5.5 ArF polymer platforms 522
8.5.6 Sulfonium-based resists 522
8.5.7 High-fluorine resists 522
8.5.8 Non-polymer-based organic EUV resists 523
8.6 Characterization of Development Using AFM 524
8.7 Strategies for Improving Resist Sensitivity: Acid Amplifiers and Photosensitized CARs 526
8.7.1 Introduction to acid amplifiers 526
8.7.2 Lithographic capabilities of acid amplifiers in EUV photoresists 527
8.7.3 Fluorine-stabilized AAs and olefin triggers 529
8.7.4 Synthesis and preliminary lithographic performance of fluorine-stabilized polymers 531
8.7.5 Photosensitized chemically amplified resists (PSCAR) 531
8.7.6 Conclusions 534
8.8 Metal-Containing Resists 534
8.8.1 Metal oxide resists from Oregon State University and Inpria 535
8.8.2 Tin oxide cluster resists from CNSE 539
8.8.3 Mononuclear metal resists 542
8.9 LER and Modeling 548
8.9.1 Background: continuous and stochastic models 548
8.9.2 Modeling steps 550
8.9.3 Specific resist models 553
8.10 Benchmarking Studies: Tool Dependence and Resist Performance 561
8.10.1 Introduction 561
8.10.2 Interference lithography 562
8.10.3 MET imaging 563
8.10.4 Beta tool and production scanner imaging 565
8.10.5 Comparison to ArF 565
8.10.6 Comparison of organic and metal-based resists 565
8.11 Summary 566
8.11.1 Background 566
8.11.2 Mechanism of EUV exposure 566
8.11.3 Types of resists 567
8.11.4 Acid amplifiers and PSCAR 568

Downloaded From: https://www.spiedigitallibrary.org/ebooks/ on 09 Mar 2022
Terms of Use: https://www.spiedigitallibrary.org/terms-of-use

8.11.5 LER and modeling 569
8.11.6 Benchmarking of resists 570
Notes and References 570

9 Fundamentals of EUVL Scanners 593
Jan B. P. van Schoot and Johannes C. M. Jasper
9.1 Introduction 593
9.1.1 EUVL scanner outline 593
9.1.2 Business drivers 594
9.2 EUVL Projection Tool Overview: History and Future 605
9.2.1 Small-field tools 605
9.2.2 Full-field tools: past 0.25 NA 606
9.2.3 Full-field tools: current 0.33 NA 606
9.2.4 Full-field tools: future 0.55 NA 606
9.3 EUVL Scanner Architecture 619
9.3.1 Introduction: architecture overview 619
9.3.2 The optical system 620
9.3.3 Mechatronic architecture 626
9.3.4 Wafer and mask stage 627
9.3.5 Optics and contamination control 628
9.3.6 Metrology 630
9.3.7 Material handling systems and clamps 634
9.3.8 EUV pellicles 635
9.4 Outlook 636
9.4.1 Future prospects 638
Acknowledgments 640
References 640

10 EUVL System Patterning Performance 651
Patrick Naulleau and Gregg Gallatin
10.1 Introduction: The Benefits of EUV Imaging 651
10.2 Parameters Affecting EUV Patterning Performance 654
10.2.1 Partial coherence 654
10.2.2 Aberrations and contrast 654
10.2.3 Flare and contrast 655
10.2.4 Chromeless phase-shift-mask printing in the EUV range 656
10.3 EUV and Aerial Image Variability 659
10.3.1 LER transfer from the mask to the wafer 660
10.3.2 Mask roughness effects on LER 664
10.3.3 Mask roughness effects on printed contact size variations 672
10.4 Stochastics in Patterning 674
10.4.1 Introduction 674
10.4.2 Photon stochastics: an analytic description 675
10.4.3 A stochastic model 678

Downloaded From: https://www.spiedigitallibrary.org/ebooks/ on 09 Mar 2022
Terms of Use: https://www.spiedigitallibrary.org/terms-of-use

10.4.4 Photon and material effects 679
10.4.5 Contact CDU limits 681
References 683

Appendix: Reference Data for the EUV Spectral Region 689
Eric M. Gullikson and David Attwood
A.1 Introduction 689
References 707

Index 709

Downloaded From: https://www.spiedigitallibrary.org/ebooks/ on 09 Mar 2022
Terms of Use: https://www.spiedigitallibrary.org/terms-of-use

Downloaded From: https://www.spiedigitallibrary.org/ebooks/ on 09 Mar 2022
Terms of Use: https://www.spiedigitallibrary.org/terms-of-use

Foreword to the Second Edition

For more than five decades, the semiconductor industry has been following Moore's law, and optical lithography has been a key enabler of its continued extension. This has been done by a combination of reducing the wavelength of optical lithography roughly every decade, increasing the numerical aperture of the projection lens of the lithography scanner every few years, and relentlessly pursuing methods to push the capabilities of optical lithography to physical limits by reducing the value of k_1.

Since the pioneering work on extreme-ultraviolet lithography (EUVL) in the late 1980s by Bell Labs, Lawrence Livermore National Lab, and in Japan, it has been known that optical projection lithography would be possible in the extreme ultraviolet region. However, the obstacles to making it a cost-effective technology in the volume production of advanced integrated circuits were formidable. Most noticeably were the obstacles in the areas of optics, source, mask, and resist.

Since 1997, ASML has explored multiple technologies to extend lithography beyond 193-nm ArF optical lithography. These included EUVL, e-beam projection lithography, and ion-beam projection lithography. X-ray lithography was not considered because of the $1\times$ mask challenge, which puts severe limits on its potential extension. All three programs were executed through international collaboration—in the case of EUVL, via the EUCLIDES program in Europe and via collaboration with the Virtual National Lab in the USA. In early 2000, ASML decided that EUVL was the technology of choice to which to extend optical projection lithography. EUVL had the best cost-of-ownership potential as well as extendibility to smaller nodes. Two $NA = 0.25$ EUV "alpha-demo" tools were built and shipped by ASML in 2006—one to IMEC (Belgium) and one to CNSE (Albany, New York, USA). These tools were instrumental in further increasing the momentum of EUVL and helped develop the mask and resist infrastructure.

Meanwhile, optical projection lithography using a 193-nm ArF laser was extended beyond anybody's expectation by the introduction of immersion lithography (which extended the NA of the scanner to 1.35) and spacer technology. Today's 193-nm immersion lithography scanners with additional processing can mass produce features on integrated circuits that are a fraction

Downloaded From: https://www.spiedigitallibrary.org/ebooks/ on 09 Mar 2022
Terms of Use: https://www.spiedigitallibrary.org/terms-of-use

of the wavelength. However, spacer technology and related solutions lead to additional deposition and etch steps, increasing cost, complexity, and cycle time at every node. Therefore, the need for EUVL is greater than ever.

Today multiple 0.33-NA EUVL scanners have been shipped and are being used by leading semiconductor makers in all segments for process development and pre-production. The use of EUVL in volume manufacturing is imminent.

This book is a must read for anyone interested in the past, present, and future of EUVL. Industry experts explain in detail the challenges faced and how they were overcome. It gives an outlook to the future, when the NA of the EUVL scanner will be increased even further, thus extending Moore's law to the 2-nm node and beyond. The book is a tribute to all of the people who have worked hard for decades to make EUVL a reality in advanced IC production.

Jos Benschop, Ph.D.
Senior Vice President Technology ASML
SPIE Fellow

Downloaded From: https://www.spiedigitallibrary.org/ebooks/ on 09 Mar 2022
Terms of Use: https://www.spiedigitallibrary.org/terms-of-use

Preface to the Second Edition

I am delighted to share with readers this second edition of *EUV Lithography* (EUVL) from SPIE Press. EUVL is the next-generation lithography (NGL) currently finding its way into fabs for advanced computer chip making. This book is intended for people involved in one or more aspects of EUVL as well as for students, who will find this text equally valuable. This book covers the fundamental and latest status of all aspects of EUVL used in the field. It thoroughly covers currently used techniques and equipment plus related topics, including light sources, optics, masks, photoresists, contamination, imaging, and scanners. Each of these aspects of EUVL is an area of expertise in itself, but the implications of each area affect the applications of others. Hence, I recommend that those involved in one aspect of EUVL refer to this book's chapters on other topics to understand the full implications of each technology.

During the nine years since SPIE Press published the first edition of *EUV Lithography*, much progress been made in the development of EUVL as the choice technology for NGL. In 2008, EUVL was a prime contender to replace 193-nm-based optical lithography in leading-edge computer chip making, but not everyone was convinced of this at that point. Switching from 193-nm to 13.5-nm wavelengths was a much bigger jump than the industry had previously attempted. This step brought several difficult challenges in all areas of lithography—light source, scanner, mask, mask handling, optics, optics metrology, resist, computation, materials, and optics contamination. These challenges have been effectively resolved, and several leading-edge chipmakers have announced dates, starting in 2018, for inserting EUVL into high-volume manufacturing.

The development of scanners has been equally challenging. Although EUVL development started in the early 1980s, by 2008 only two alpha-level scanners were in the field, and beta-level scanners were still several years out. Today, more than 14 production- and pre-production-level EUVL scanners are in fabs. This year alone, six production-level EUVL scanners have been shipped to several leading-edge chipmakers, and the current backlog of orders for EUVL scanners is almost two dozen. After decades of intense development and investment, EUVL has now achieved technical and commercial success as the leading NGL technology. This book, strengthened by the insights of many

Downloaded From: https://www.spiedigitallibrary.org/ebooks/ on 09 Mar 2022
Terms of Use: https://www.spiedigitallibrary.org/terms-of-use

technologists whose work brought EUVL to this point, showcases the various technical components that have enabled its success.

EUVL technology has enabled the extension of Moore's law and is expected to take current chip manufacturing technology to the end of Moore's law. This means that we are not expecting another switch in wavelength for advanced lithography, and Moore's extension will come via further development of EUVL. Moore's law states that the number of transistors per square inch of computer chip will double approximately every two years. This requirement has resulted in the need for continued development and commercial deployment of new lithography techniques that can continue to print ever-smaller circuit elements. As new lithography technologies are expected to be used at multiple nodes of decreasing feature sizes, EUVL will need to continue to evolve to meet the challenges of the next nodes until the laws of physics force us to look for a new class of transistors and computers. This book provides an overview of the current status of EUVL, while shedding light on the challenges that EUVL technologists need to address in order to continue extending Moore's law.

In this edition, we address the same general technical areas as in the first edition. However, the second edition contains much new information not readily available to readers before. Although some of the authors also appear in the first edition, their chapters are either new or have been thoroughly rewritten to contain lots of new data.

This text contains 10 chapters and an Appendix of Reference Data for the EUV Spectral Region. Three of the chapters have been split into two parts, each written by different authors: Chapter 3 on high-power EUV sources, Chapter 4 on metrology sources, and Chapter 6 on optical contamination.

Chapter 1 on EUVL history is written by Hiroo Kinoshita and Obert Wood, two scientists who are widely recognized as the pioneers of EUVL; Prof. Kinoshita is credited with the earliest reported work on EUVL. This is the most comprehensive and authoritative history of EUVL development available today, and being an historical account, is the only chapter that remains unchanged from the first edition. Topics covered are early development of EUVL as well as development of individual components such as source, optics, metrology, and photoresists.

Chapter 2 on the EUV LLC has been thoroughly rewritten and provides useful information on the origins and achievements of that consortium. Topics covered are the history of the LLC, major accomplishments, patents issued, and retrospective observations.

Chapter 3 on high-power EUV sources for the EUVL scanner is divided into two subchapters. Subchapter 3A is by authors from Cymer, LLC, now part of ASML. Cymer is currently leading in the area of high-power, tin-based laser-produced plasma (Sn LPP) EUV source development, and its sources are those integrated into EUVL scanners in the field. The authors have written a

Downloaded From: https://www.spiedigitallibrary.org/ebooks/ on 09 Mar 2022
Terms of Use: https://www.spiedigitallibrary.org/terms-of-use

comprehensive review of EUV source technology, with lots of new information that readers will find valuable. Topics covered are EUV power scaling, tin target delivery, pre-pulse technology, collector, debris mitigation, use of hydrogen as a buffer gas, management of tin in the source, and the latest performance results for their light source.

Gigaphoton is a second supplier for high-power EUV sources, with important differences in the design of their high-power Sn LPP source. We have included their subchapter 3B to ensure complete coverage of the critical topic of high-power EUV sources. This subchapter covers the design of Gigaphoton's source as well as the topics of tin droplet generation technology, pre-pulse technology, the superconductive magnet debris mitigation method, the driver CO_2 laser system, and the latest data from their pilot operation.

Chapter 4 covers metrology sources used for actinic inspection of mask defects. These sources require only a few watts of power, while brightness and stability are the key parameters of interest. For this type of metrology source, the current workhorse is the electrodeless Z-Pinch™ source from Energetiq, which is covered in subchapter 4A. This subchapter covers operating principles, diagnostics, and data on source performance in terms of power, brightness, and spatial and temporal stability.

Chapter 4B is written by Yusuke Teramoto of BLV Licht- und Vakuumtechnik GmbH, whose technology is a laser-driven discharge-produced plasma (LDP) source. This technology was previously a contender for high-power sources for EUVL scanners and is currently being considered for metrology applications. This subchapter covers LDP system configuration, and data on brightness, power, stability, reliability, source cleanliness, and in-band and out-of-band radiation spectra.

There are several additional technologies for EUV metrology sources, some of which are covered in the book *EUV Sources for Lithography*, published by SPIE Press in 2006. I refer readers looking for additional information on high-power and metrology sources to that monograph.

Chapter 5 covers optics and optical systems for scanners, including illuminator and projection optics, a brief introduction to multilayer deposition, high-numerical-aperture (NA) optics, source collector optics, and the AIMS EUV tool. Since publication of the first edition, the focus of optics has moved from R&D to commercial production. The authors of this chapter are from Carl Zeiss, which now produces commercial optical components for EUVL scanners. This chapter is full of new information and contains an impressive coverage of fundamentals and the latest data on components that are now part of EUVL scanners in the field. For additional fundamental and historical information on EUV optics, readers are referred to subchapters 4A through 4D in the first edition of the book.

Chapter 6 is on optics contamination, which was deemed a leading challenge for EUVL early on, but later became a technical issue that is now

Downloaded From: https://www.spiedigitallibrary.org/ebooks/ on 09 Mar 2022
Terms of Use: https://www.spiedigitallibrary.org/terms-of-use

considered to be addressed. This chapter is divided into two subchapters. Subchapter 6A is written by NIST et al., with a focus on fundamentals of optics contamination and resist outgassing test, to quantify contamination from EUV photoresists. Chapter 6B by University of Illinois researchers et al. covers contamination of the normal-incidence source collector in the EUVL scanner and cleaning techniques for removal of tin.

Chapter 7 by Jinho Ahn of Hanyang University and Chan-Uk Jeon of Samsung covers EUV mask and EUV mask metrology. Topics include mask manufacturing, mask substrate, absorber stacks, pattern formation, mask inspection, metrology and repair, mask contamination, pellicles, and future designs for EUV masks.

Chapter 8 on EUV photoresists for EUVL is by Robert Brainard of SUNY Albany et al. EUV resist technology continues to develop, and lots of new information is provided in this chapter. The chapter covers absorption coefficients of EUV resists, the mechanism of resist exposure to EUV light, organic- and metal-containing resists, resist characterization, benchmarking, and strategies for improving resist performance and line edge roughness (LER).

Chapter 9 on EUVL scanners is written by ASML, the sole maker of these tools. This chapter covers scanners from 0.2-NA, current 0.33-NA, and future 0.55-NA designs. For current scanners, the chapter describes the optical system, mechatronic architecture, wafer and reticle stage, optics and contamination control, metrology, material handling systems, and EUV pellicles.

Chapter 10 by Patrick Naulleau of Lawrence Berkeley National Laboratory (LBNL) and Gregg Gallatin has been thoroughly rewritten, with lots of new coverage of EUV patterning development from the last ten years. This chapter illustrates the benefits of EUV imaging, parameters affecting EUV patterning performance, EUV and aerial image variability, and stochastics in patterning.

I would like to comment on the process of selecting topics and authors for this volume. As noted earlier, EUVL technology has made great progress since our first edition was published. This includes development of new scanners, optics, light sources, mask, resists, and contamination control, as well as addressing new challenges for patterning. Recent announcements by several chipmakers about plans to use EUVL in fabs, as well as the large number of orders for EUVL scanners, testify to that progress. At this point, options for technology components have been largely identified. Choices have been narrowed to one or two options in most areas, although for areas such as photoresist, potential choices remain much greater. Hence, while looking for authors and deciding on coverage for various topics, I focused on technology options that have been chosen by the industry for technical and business reasons. So this edition focuses more on giving technical information about technology that is now being used in the field for EUVL, while covering future options for further scaling of technology as much as possible.

Downloaded From: https://www.spiedigitallibrary.org/ebooks/ on 09 Mar 2022
Terms of Use: https://www.spiedigitallibrary.org/terms-of-use

I also should discuss what we decided to include from the first edition in terms of topics, chapters, and authors, and my reasons for making changes. (Please note the first edition had lots of very important technical information and will continue to be available on the SPIE Digital Library.)

The only portions from the first edition included in this volume are EUV Lithography: A Historical Perspective (Chapter 1) and the Appendix for fundamental constants. These were very well written, and little new information could be added to them, while the information provided is still fresh and relevant for readers today.

Two earlier chapters, for which we did not have new data and were of historical nature, were not included: a chapter on high-resolution EUV tools for resist exposure and aerial image monitoring, as it relates to a tool for early development of EUVL, and a chapter on lithography cost of ownership. However, these chapters are preserved for readers in the first edition.

Also, certain chapters from the first edition, although not included in this text, have technical and historical information that students of EUVL may find valuable. These include Chapter 4A Optics and Multilayer Coatings for EUVL Systems, Chapter 4B Projection Systems for EUVL, Chapter 4C Specification, Fabrication, Testing, and Mounting of EUVL Optical Substrates, Chapter 4D Multilayer Optical Coatings for EUVL, Chapter 5 EUVL Optical Testing, and Chapter 6B Grazing Angle Collector Contamination.

Readers also are encouraged to review the extensive database of SPIE's conference proceedings as well as refereed papers from the *Journal of Micro/Nano Lithography, MEMS, and MOEMS* (*JM3*) for detailed, current information about various aspects of EUVL. SPIE's Digital Library (www.spiedigitallibrary.org) remains the most extensive source of EUVL-related information. Additional information on EUV sources and EUVL in general is available from presentations by various source suppliers and researchers in the annual Source Workshop and EUVL Workshops. Readers can refer to these for the latest information on EUVL. Proceedings for these workshops are available at www.euvlitho.com. Both of these reference sources have been used extensively by authors in this book.

The primary strength of this edition is that the contributions come from leading suppliers or subject matter experts in each technical area. We have succeeded in compiling this second edition through the contributions, dedication, and hard work of our knowledgeable authors. As I said in the first edition, EUVL is a reality today due to the labor of hundreds of technologists around the world. I now acknowledge the financial investment and risk that was taken by suppliers and chipmakers who believed in this technology and worked very hard to achieve its current success. For these reasons, I have dedicated this book to the technologists, suppliers, and chipmakers who have made EUVL a reality.

I also would like to thank my family, whose influence, encouragement, and support have allowed me to undertake a project of this scope. First of all,

Downloaded From: https://www.spiedigitallibrary.org/ebooks/ on 09 Mar 2022
Terms of Use: https://www.spiedigitallibrary.org/terms-of-use

my father, Mr. Om Prakash Bakshi, M.A. set a very high standard for written communication and the pursuit of excellence, which to this day I can only strive to meet. My mother, Mrs. Pushpa Bakshi, M.A., a retired lecturer of the Punjabi language, always set an example of hard work and taught me a pragmatic approach toward solving everyday problems, which still guides me. Also, this book would not have been possible without the support of my family: my wife, Bethany, who often took care of more than her fair share of duties; and my kids, Emily and Taru, who did not always have my full attention as I struggled to find time to complete this project during my otherwise very full schedule.

Finally, I would like to thank SPIE Press Manager Timothy Lamkins and SPIE Senior Editor Dara Burrows. Dara's attention to detail and patience with numerous missed deadlines made project completion possible. I very much appreciate their support and hard work to make this book project a *reality*.

Vivek Bakshi, Ph.D.
President, EUV Litho, Inc.
December 2017
vivek.bakshi@euvlitho.com
http://www.euvlitho.com

Vivek Bakshi is founder and president of EUV Litho, Inc., an organization he formed in 2007 to promote EUV lithography via consulting, workshops, and education. He provides consulting services in the areas of EUV lithography and general lithography to investors, funding agencies, universities, national labs, and suppliers. He also organizes the annual International Workshop on EUV Lithography (EUVL Workshop) and the annual International Workshop on EUV and Soft X-ray Sources (Source Workshop). He teaches EUVL short courses around the world.

Dr. Bakshi is Adjunct Professor in the School of Physics, University College Dublin, Ireland. He is a member of the Editorial Board and Associate Editor of *JM3* (SPIE's *Journal of Micro/Nano Lithography, MEMS, and MOEMS*). He frequently blogs about EUVL for the magazine *Solid State Technology* (http://www.electroiq.com/euvl-focus/). He is widely quoted in trade media on EUVL-related topics and is an internationally recognized expert on EUV source technology and EUV lithography. Previously, he was a Senior Member of the Technical Staff in SEMATECH's Lithography Division.

Dr. Bakshi has authored/coauthored more than 125 technical publications, including book chapters, articles in peer-reviewed journals, technical reports, and trade publications. He has edited three books on EUVL: *EUV Sources for Lithography* (SPIE Press, 2006), *EUV Lithography* (SPIE Press, 2008), and *Extreme Ultraviolet Lithography* (SPIE Press, 2012) (co-edited with Anthony Yen). He holds three U.S. patents in the area of EUVL.

Downloaded From: https://www.spiedigitallibrary.org/ebooks/ on 09 Mar 2022
Terms of Use: https://www.spiedigitallibrary.org/terms-of-use

List of Contributors

Jinho Ahn
Hanyang University, South Korea

David Attwood
Lawrence Berkeley National Laboratory, USA

Saša Bajt
Deutsches Elektronen-Synchrotron, Germany

Vivek Bakshi
EUV Litho, Inc., USA

Jos Benschop
ASML Netherlands B.V., The Netherlands

Robert F. Berg
National Institute of Standards and Technology, USA

Matthew M. Besen
Energetiq Technology, Inc., USA

Paul A. Blackborow
Energetiq Technology, Inc., USA

Robert L. Brainard
University of Albany, USA

David C. Brandt
ASML US, USA

Ron Collins
Energetiq Technology, Inc., USA

Daniel T. Elg
University of California, Berkeley, USA

Hartmut Enkisch
Carl Zeiss SMT GmbH, Germany

Alexander I. Ershov
ASML US, USA

Igor V. Fomenkov
ASML US, USA

Gregg Gallatin
Applied Math Solutions, LLC, USA

Eric M. Gullikson
Lawrence Berkeley National Laboratory, USA

Deborah Gustafson
Energetiq Technology, Inc., USA

Dirk Hellweg
Carl Zeiss SMT GmbH, Germany

Shannon B. Hill
National Institute of Standards and Technology, USA

Stephen F. Horne
Energetiq Technology, Inc., USA

Downloaded From: https://www.spiedigitallibrary.org/ebooks/ on 09 Mar 2022
Terms of Use: https://www.spiedigitallibrary.org/terms-of-use

Johannes (Hans) C. M. Jasper
ASML Netherlands B.V.,
The Netherlands

Chan-Uk Jeon
Samsung Electronics, South Korea

Winfried Kaiser
Carl Zeiss SMT GmbH,
Germany

Hiroo Kinoshita
University of Hyogo, Japan

Bruno La Fontaine
Hermes Microvision Inc., an ASML company, USA

Sascha Migura
Carl Zeiss SMT GmbH,
Germany

Hakaru Mizoguchi
Gigaphoton Inc., Japan

Amrit Narasimhan
GLOBALFOUNDRIES Inc.,
USA

Patrick Naulleau
Lawrence Berkeley National Laboratory, USA

Mark Neisser
Kempur Microelectronics Inc.,
China

Jens Timo Neumann
Carl Zeiss SMT GmbH, Germany

Krysztof M. Nowak
Gigaphoton Inc., Japan

Matthew J. Partlow
Energetiq Technology, Inc.,
USA

David N. Ruzic
University of Illinois at Urbana-Champaign, USA

Takashi Saito
Gigaphoton Inc., Japan

Alexander A. Schafgans
ASML US, USA

Donald K. Smith
Energetiq Technology, Inc., USA

Shailendra N. Srivastava
University of Illinois at Urbana-Champaign, USA

Yezheng Tao
ASML US, USA

Charles S. Tarrio
National Institute of Standards and Technology, USA

Yusuke Teramoto
BLV Licht- und Vakuumtechnik GmbH, Germany

Jan B. P. van Schoot
ASML Netherlands B.V.,
The Netherlands

Georgiy O. Vaschenko
ASML US, USA

Obert Wood
GLOBALFOUNDRIES, USA

Stefan Wurm
ATICE, LLC, USA

Taku Yamazaki
Gigaphoton Inc., Japan

Tatsuya Yanagida
Gigaphoton Inc., Japan

Downloaded From: https://www.spiedigitallibrary.org/ebooks/ on 09 Mar 2022
Terms of Use: https://www.spiedigitallibrary.org/terms-of-use

Acronyms and Abbreviations

AA	acid amplifier
ABI	actinic blank inspection
ADT	Alpha Demo Tool
AFM	atomic force microscopy
AIMS	Aerial Image Measurement System (ZEISS)
ALS	Advanced Light Source (of LBNL)
APC	advanced process control
APMI	actinic patterned mask inspection
APSM	alternating phase shift mask
AR	antireflective
ARC	antireflective coating
ARS	angle-resolved scattering (function)
ASE	amplified spontaneous emission
ASET	Association for Super-Advanced Electronics Technologies
ATP	acceptance testing procedure
BESSY	Berlin Electron Storage Ring Society for Synchrotron Radiation
BNL	Brookhaven National Laboratory
BSDF	bidirectional scattering distribution function
BSE	backscattered primary electron
BTS	beam transport system
CA	chemically amplified
CAD	computer-aided design
CAR	chemically amplified resist
CCD	charge-coupled device
CCP	computer-controlled polishing
CCS	computer-controlled surfacing
CD	critical dimension
CDU	critical dimension uniformity
CE	conversion efficiency
CGH	computer-generated hologram
CNSE	College of Nanoscale Science and Engineering
CNT	carbon nanotube

Downloaded From: https://www.spiedigitallibrary.org/ebooks/ on 09 Mar 2022
Terms of Use: https://www.spiedigitallibrary.org/terms-of-use

CPMI	Center for Plasma-Material Interactions
CRADA	cooperative research and development agreement
CRA	chief ray angle
CRAA	chief ray azimuthal angle
CRAO	chief ray angle at object
CSM	coherent scattering microscopy
CTE	coefficient of thermal expansion
cw	continuous wave
CXRO	Center for X-Ray Optics, Lawrence Berkeley National Lab
DARPA	Defense Advanced Research Projects Agency
DC	direct current
DCO	dedicated chuck overlay
DDR&E	Director of Defense Research & Engineering
DGSS	droplet generator steering system
DLG	droplet generator
DOC	Department of Commerce
DOD	Department of Defense
DOE	Department of Energy
DOF	depth of focus
DPP	discharge-produced plasma
DRAM	dynamic random access memory
DSI	defect signal intensity
DUV	deep ultraviolet
EAL	effective attenuation length
EIDEC	Evolving nano-process Infrastructure Development Center
EIPB	Electron, Ion, and Photon Beams (international symposium)
EMI	EUV Mask Infrastructure (consortium)
EPE	edge placement error
EPL	electron-beam projection lithography
ESA	energy sector analyzer
ESCAP	environmentally stable chemically amplified photoresist
ESL	etch stop layer
ESPRIT	European Strategic Program on Research on Information Technology
ETS	Engineering Test Stand
EUCLIDES	Extreme UV Concept Lithography Development System (program)
EUV	extreme ultraviolet
EUV LLC	EUV Limited Liability Corporation
EUVA	Extreme Ultraviolet Lithography System Development Association
EUVL	extreme ultraviolet lithography

Downloaded From: https://www.spiedigitallibrary.org/ebooks/ on 09 Mar 2022
Terms of Use: https://www.spiedigitallibrary.org/terms-of-use

EXTATIC	Extreme UV Alpha Tools Integration Consortium (MEDEA+)
fab	fabrication facility
FAF	fast axial flow
FC	Faraday cup
FFTT	far-field test tool
FIB	focus ion beam
FOM	Fundamenteel Onderzoek der Materie Institute
FOUP	front-opening unified pod
FOV	field of view
FPR	fill pupil ratio
FQY	field quantum yield
FTE	full-time equivalent
FTF	fast transverse flow
FWHM	full width at half maximum
GC-MS	gas chromatograph with a mass spectrometer
GFIS	gas field ion source
HIT	Himeji Institute of Technology
hp, HP	half-pitch
HPDL	high-power drive laser
HPSS	high-power seed system
HSFR	high-spatial-frequency roughness
HSQ	hydrogen silsesquioxane
H-V	horizontal/vertical
HVM	high-volume manufacturing
IBD	ion-beam sputter deposition
IBF	ion-beam figuring
IC	integrated circuit
IF	intermediate focus
IL	interference lithography
ILT	Institute of Laser Technology (Fraunhofer)
IP	intellectual property
IPD	in-plane distortion
IPE	image placement error
IPL	ion-beam projection lithography
ITRS	International Technology Roadmap for Semiconductors
LANL	Los Alamos National Laboratory
LBNL	Lawrence Berkeley National Laboratory
LCDU	local critical dimension uniformity
LDD	low defect deposition
LER	line-edge roughness
LESiS	low-energy electron scattering in solids

Downloaded From: https://www.spiedigitallibrary.org/ebooks/ on 09 Mar 2022
Terms of Use: https://www.spiedigitallibrary.org/terms-of-use

LLNL	Lawrence Livermore National Laboratory
LMIS	liquid metal ion source
LPP	laser-produced plasma
L/S	line/space
LSC	laser shock-wave cleaning
LSFR	low-spatial-frequency roughness
LSM	layered synthetic microstructure
LTEM	low-thermal-expansion material
LTF	LER transfer function
LWR	linewidth roughness
MAG	magnification
MDA	ML defect avoidance
MEDEA+	Microelectronics Development for European Applications+
MET	micro-exposure tool
ML	multilayer
MLM	multilayer mirror
MMO	machine-to-machine overlay
MOPA	master oscillator power amplifier
MOS	metal–oxide semiconductor
MPPM	Multivariate Poisson Propagation Model
MSFR	mid-spatial-frequency roughness
MTF	modulation transfer function
NA	numerical aperture
NGL	next-generation lithography
NILS	normalized image log slope
NIST	National Institute of Standards and Technology
NMOS	n-type metal–oxide semiconductor
NOMO	no master oscillator
OoB	out-of-band
OPC	optical proximity correction
OPD	out-of-plane distortion
OPO	on-product overlay
OSA	Optical Society of America
PACE	plasma-assisted cleaning by electrostatics
PAG	photo-acid generator
PCM	pulse count modulation
PEB	post-exposure bake
PFBS	pentafluorobenzene-sulfonic acid
PFR	pupil fill ratio
PHS	poly-4-hydroxystyrene
PMI	phase-measuring interferometer
PMMA	poly(methyl methacrylate)
PMS	poly-4-methoxystyrene

Downloaded From: https://www.spiedigitallibrary.org/ebooks/ on 09 Mar 2022
Terms of Use: https://www.spiedigitallibrary.org/terms-of-use

POB	projection optics box
POL	polymerization olefin loading
PP	photosensitizer precursor
PS	photosensitizer
PSCAR™	photosensitized chemically amplified resist
PSD	power spectral density
PSF	point spread function
PSI	Paul Scherrer Institut
PSM	phase shift mask
PSPDI	phase-shifting point-diffraction interferometer
PSS	pulse-shaping switch
P/T	precision-to-tolerance ration
PTB	Physikalisch-Technische Bundesanstalt
PTO	Patent and Trademark Office (U.S.)
PV	peak to valley
QE	quantum efficiency
QCL	quantum cascade laser
QCM	quartz crystal microbalance
RDC	Research Development Center (of the VNL)
RF	radiofrequency
RGA	residual gas analyzer
RIE	reactive ion etching
RLS	resolution, LER, and sensitivity (tradeoff)
rms, RMS	root mean square
RMSD	RMS density
ROFR	right of first refusal
sccm	standard cubic centimeters per minute
SE	spectroscopic ellipsometry
SEM	scanning electron microscopy
SEMI	Semiconductor Equipment and Materials International
SERM	scanning EUV reflective microscope
SEVD	spherical equivalent volume diameter
SHC	supersonic hydrocleaning
SIA	Semiconductor Industry Association
SIMS	secondary-ion mass spectroscopy
SM3	superconducting magnet debris mitigation method
SMIF	standard mechanical interface
SMO	source mask optimization
SNL	Sandia National Laboratories
SOHO	Solar and Heliospheric Observatory
SPF	spectral purity filter
SPP	silicone-based positive photoresist
SR	synchrotron radiation

Downloaded From: https://www.spiedigitallibrary.org/ebooks/ on 09 Mar 2022
Terms of Use: https://www.spiedigitallibrary.org/terms-of-use

SRAM	static random-access memory
SRC	Semiconductor Research Corporation
SRIM	Stopping and Range of Ions in Matter (program)
SSL	solid-state laser
SVGL	Silicon Valley Group Lithography
SXPL	soft-x-ray projection lithography
TEM	transmission electron microscope
TEY	total electron yield
TIS	total integrated scatter
TISD	TIS density
ULE®	ultralow expansion (Corning glass)
USAL	United States Advanced Lithography
VNL	Virtual National Laboratory
wph	wafers per hour
XPL	x-ray proximity lithography
XPS	x-ray photoelectron spectroscopy
XRD	x-ray diffraction
YAG	yttrium aluminum garnet
ZCT	zero-crossing temperature

Downloaded From: https://www.spiedigitallibrary.org/ebooks/ on 09 Mar 2022
Terms of Use: https://www.spiedigitallibrary.org/terms-of-use

Chapter 1
EUV Lithography: An Historical Perspective*

Hiroo Kinoshita
University of Hyogo, Kobe City, Hyogo Prefecture, Japan

Obert Wood
Advanced Micro Devices, Sunnyvale, California, USA

1.1 Introduction
1.2 The Early Stage of Development—1981 to 1992
1.3 The Second Stage of Development—1993 to 1996
  1.3.1 Two-mirror imaging system development
  1.3.2 Three-mirror imaging system development
  1.3.3 MOS device demonstration using EUVL
1.4 Other Developments in Japan and Europe
1.5 The Development of Individual Technologies
  1.5.1 Selection of the exposure wavelength
  1.5.2 Design of reflective imaging systems
  1.5.3 Fabrication and evaluation of aspherical mirrors
  1.5.4 Multilayer coatings and reflection masks
  1.5.5 EUV resist development
  1.5.6 EUV light source development
1.6 EUVL Conferences
1.7 Summary
Acknowledgments
References

1.1 Introduction

For more than three decades, the number of transistors on a chip has grown exponentially, doubling on the average of every 18 months. With each new technology generation, the role of lithography has increased in importance not only because of the requirements for smaller feature sizes and tighter overlay, but also because of the increasing costs for lithography tools. Optical

*This chapter has not been updated from the first edition of this book (2009).

Downloaded From: https://www.spiedigitallibrary.org/ebooks/ on 09 Mar 2022
Terms of Use: https://www.spiedigitallibrary.org/terms-of-use

projection lithography and its extensions, e.g., water immersion, are expected to remain the lithographic technologies of choice until at least 2010. Extreme-ultraviolet lithography (EUVL) extends optical lithography to a higher resolution and provides a larger depth of focus because it utilizes a shorter imaging wavelength (13.5 nm versus 193–248 nm) and employs a smaller numerical aperture (NA) imaging system (0.25–0.45 NA versus 0.93–1.35 NA). This chapter recounts the early years of EUVL development, from the first imaging with normal-incidence multilayer (ML)-coated mirrors in 1981 to the beginning of EUVL commercialization efforts at the end of 1996.

Early concepts for EUVL emerged from research in Japan and the U.S. during the 1980s using soft x rays in the 4-nm to 40-nm wavelength range.[1–4] The results of the first demonstration of soft-x-ray reduction lithography using multilayer-coated Schwarzschild optics were made public in 1986.[1] The first demonstration of the technology's potential and of nearly diffraction-limited imaging took place in 1990.[5] Because of EUVL's potential to be utilized at ever-smaller feature sizes, a consortium of U.S. national laboratories, integrated device manufacturers, and private commercial companies combined to form the EUV Limited Liability Company (EUV LLC) in 1997 to guide and fund its commercialization. (For details, see Chapter 2 of this book.) Today, commercial EUV exposure tool development is underway at ASML, Canon, and Nikon, and EUVL infrastructure development is under active development worldwide at a number of universities, national laboratories, and semiconductor consortia.

Most of the basic concepts needed for EUVL were demonstrated, and most of the EUV-specific critical issues were identified during the early years. Sufficient progress was made on all of the critical issues during this time period that none thereafter were regarded as "show stoppers;" several critical issues were resolved entirely. Two early success stories were in the fabrication and metrology of aspheric surfaces and in the application and metrology of reflective ML coatings. In the beginning, aspheric surfaces were not much more than laboratory curiosities, but eventually they could be fabricated with a controlled spectrum of surface heights spanning spatial wavelengths from the clear aperture of the part down to $\sim$1 nm. Reflective ML coatings initially provided only marginally larger reflectances than a grazing-incidence mirror, but later could provide normal-incidence reflectances close to the theoretical maximum. The work done on ML coatings for EUVL has spawned important research on the processes by which a single atomic layer can be formed and on the quality of the interface between materials. While some EUV-specific critical issues still have not been completely resolved, the questions that remain tend to involve cost and reliability rather than technical issues.

The major historical developments that took place from 1981 to 1992 are summarized in Section 1.2 and from 1993 to 1996 in Section 1.3. Other relevant developments that took place in Japan and Europe are summarized in Section 1.4. The development of the most important components and

Downloaded From: https://www.spiedigitallibrary.org/ebooks/ on 09 Mar 2022
Terms of Use: https://www.spiedigitallibrary.org/terms-of-use

subsystems are described in Section 1.5, including the selection of the exposure wavelength, the design of reflective imaging systems, the fabrication and evaluation of aspherical mirrors, and the development of ML coatings and reflection masks, EUV resists, and EUV light sources. The most important EUVL conferences that took place during the early years, together with a list of the conference proceedings and technical journals that contain the majority of papers on EUVL from its beginning in the mid-1980s through 1996, are described in Section 1.6 and in Tables 1.1 and 1.2. A short summary of the current status of EUVL is presented in Section 1.7, followed by an extensive list of references.

1.2 The Early Stage of Development—1981 to 1992

The use of normal-incidence reflective optics for x-ray microscopes and x-ray telescopes was proposed in the early 1980s,[6–8] but the key enabling technology—efficient ML reflective coatings—was not sufficiently advanced at that time to be of much use. Nevertheless, in 1981, J. Henry, E. Spiller, and M. Weisskopf succeeded in measuring the imaging performance of a normal-incidence x-ray telescope at a wavelength of 6.76 nm.[6] The test was performed at a 1000-foot-long x-ray test and calibration facility at the Marshall Space Flight Center in Huntsville, Alabama. The primary mirror was 3 inches in diameter and 0.5 inch thick. The ZERODUR® mirror substrate was figured to better than $\lambda/100$ ($\lambda = 632.8$ nm) and smoothed to x-ray tolerances using a proprietary technique. A ML coating consisting of 124 alternating layers of a rhenium-tungsten (Re-W) alloy and carbon (C) was deposited directly on the ZERODUR substrate. The measured resolution was ~1 arcsec full width at half maximum (FWHM), and the integrated reflectivity at the half-power point was 2.8%.

Table 1.1 List of technical journals containing papers on early EUVL development.

Journal / Publisher	Volume (Issue)	Date/Year
Applied Optics / OSA	**32**(34)	Dec 1993
Journal of Vacuum Science and Technology B / AVS	**6**(6)	Nov/Dec 1989
Journal of Vacuum Science and Technology B / AVS	**7**(6)	Nov/Dec 1990
Journal of Vacuum Science and Technology B / AVS	**8**(6)	Nov/Dec 1991
Journal of Vacuum Science and Technology B / AVS	**9**(6)	Nov/Dec 1992
Journal of Vacuum Science and Technology B / AVS	**10**(6)	Nov/Dec 1993
Journal of Vacuum Science and Technology B / AVS	**11**(6)	Nov/Dec 1994
Journal of Vacuum Science and Technology B / AVS	**12**(6)	Nov/Dec 1995
Journal of Vacuum Science and Technology B / AVS	**13**(6)	Nov/Dec 1996
Journal of X-ray Science and Technology / IOS Press	**3**	1993
Microelectronic Engineering / Elsevier	**9**(1-4)	May 1989
Microelectronic Engineering / Elsevier	**13**(1-4)	March 1991
Microelectronic Engineering / Elsevier	**17**(1-4)	March 1992
Microelectronic Engineering / Elsevier	**23**(1-4)	Jan 1994
Microelectronic Engineering (MNE'94) / Elsevier	**27**(1-4)	Feb 1995
Microelectronic Engineering (MNE'95) / Elsevier	**30**(1-4)	Jan 1996

Downloaded From: https://www.spiedigitallibrary.org/ebooks/ on 09 Mar 2022
Terms of Use: https://www.spiedigitallibrary.org/terms-of-use

Table 1.2 List of conference proceedings containing papers on early EUVL development.

Conference Proceedings	Editor(s)	Vol.	Year
OSA Proc. on Soft-X-Ray Projection Lithography	J. Bokor	12	1991
OSA Proc. on Soft-X-Ray Projection Lithography Topical Meeting, Monterey, California, May 10–12, 1993	A. M. Hawryluk R. H. Stulen	18	1993
OSA Proc. on Extreme Ultraviolet Lithography Topical Meeting, Monterey, California, Sept. 19–21, 1994	F. Zernike D. T. Attwood	23	1994
OSA TOPS on Extreme Ultraviolet Lithography Topical Meeting, Boston, Massachussets, May 1–3, 1996	G. D. Kubiak D. Kania	4	1996
Proc. SPIE – Electron-Beam, X-Ray, and Ion-Beam Technology Submicrometer Lithographies IX	D. J. Resnick	1263	May 1990
Proc. SPIE – Electron-Beam, X-Ray, and Ion-Beam Technology Submicrometer Lithographies for Manufacturing	M. C. Peckerar	1465	Aug. 1991
Proc. SPIE – Electron-Beam, X-Ray, and Ion-Beam Technology Submicrometer Lithographies for Manufacturing II	M. C. Peckerar	1671	July 1992
Proc. SPIE – Electron-Beam, X-Ray, and Ion-Beam Technology Submicrometer Lithographies III	D. O. Patterson	1924	June 1993
Proc. SPIE – Applications of Laser Plasma Radiation	M. C. Richardson	2015	1994
Proc. SPIE – Electron-Beam, X-Ray, and Ion-Beam Technology Submicrometer Lithographies IV	D. O. Patterson	2194	May 1994
Proc. SPIE – Electron-Beam, X-Ray, and Ion-Beam Technology Submicrometer Lithographies V	J. M. Warlaumont	2437	May 1995
Proc. SPIE – X-Ray and Extreme Ultraviolet Optics	R. B. Hoover A. B. C. Walker, Jr.	2515	June 1995
Proc. SPIE – Electron-Beam, X-Ray, and Ion-Beam Technology Submicrometer Lithographies VI	D. E. Seeger	2723	May 1996
X-ray Microscopy II: Proceedings of the Second International Symposium on X-ray Microscopy, Springer-Verlag, Berlin, 1988	A. G. Michette G. R. Morrison C. J. Buckley		1988
X-ray Microscopy III: Proceedings on the Third International Symposium on X-ray Microscopy, London, September 3-7, 1990	D. Sayre, J. Kurz M. Howells H. Rarback		1992
X-ray Microscopy IV: Proceedings on the Fourth International Symposium on X-ray Microscopy, Chernogolovka, Russia, Sept 20–24, 1993	V. V. Aristov A. I. Erko		1994

In 1981, J. Underwood and T. Barbee, Jr. constructed a layered synthetic microstructure (LSM) that reflected the first-order K-band emissions of C ($\lambda = 4.48$ nm) at normal incidence, then used it to obtain images of a grid illuminated with a C target x-ray tube.[8] The LSM consisted of 76 layer pairs of W ($d_W = 7.65$ Å) and C ($d_C = 15.10$ Å) deposited on a 76.2-mm diameter, 0.38-mm-thick silicon (Si) wafer. The integrated reflectivity of the LSM-coated mirror was estimated to be about 6%. The mirror was set up on an optical bench in a vacuum chamber in the configuration shown in Fig. 1.1 and was illuminated using an x-ray tube with a colloidal graphite-coated target. The detector, a special fine-grained film sensitive to soft x rays (Eastman Kodak SO-212), was exposed for one hour; when developed, the film revealed a 5-line/mm pattern. This experiment is believed to be the first normal-incidence imaging using a ML-coated optic.

Downloaded From: https://www.spiedigitallibrary.org/ebooks/ on 09 Mar 2022
Terms of Use: https://www.spiedigitallibrary.org/terms-of-use

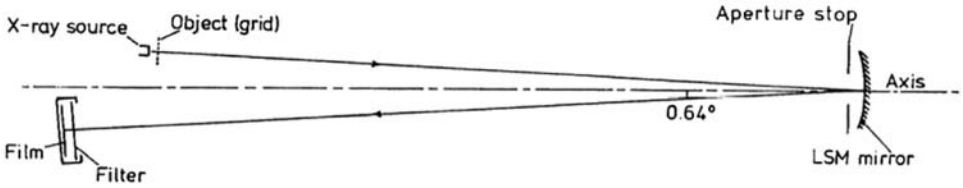

Figure 1.1 Experimental arrangement for normal-incidence imaging with carbon K x rays (reprinted from Ref. 8 with permission from Nature Publishing Group).

In 1982, when lithographic exposure tools illuminated with the g-line of mercury (Hg) were just becoming available, few lithographers were paying much attention to the possibility of x-ray reduction imaging. In fact, the leading alternative lithographic technology at that time was x-ray proximity lithography (XPL). The target resolution for XPL was 0.5 μm, a feature size that was difficult to print at that time using optical projection lithography. IBM in the U.S., NTT in Japan, and others were actively engaged in the development of XPL and were using it for the trial production of semiconductor devices. The performance of XPL steppers and x-ray resists seemed adequate, but there were too many manufacturing problems with the x-ray proximity masks.

In 1984, H. Kinoshita of NTT began to seriously consider x-ray reduction lithography as a viable alternative to XPL. Figure 1.2 shows the configuration of the first experimental setup for x-ray reduction lithography.[1] Since the first imaging system was designed to image a ring-shaped field, the mask and wafer stages were expected to move in sync to extend the exposed area. Initially, the mirrors consisted of a tungsten-carbon ML[9] deposited on a SiC blank, and the mask was a transparent Si stencil. Later, an imaging system designed to work near the absorption edge of Si was built at the High Energy Physics Laboratory in Tsukuba, Japan, and the initial experiments were carried out at that location. In the beginning, the alignment accuracy of the imaging system mirrors was very poor because the alignment was carried out with a visible microscope, and all of the replicated patterns were severely distorted. An image of a 4-μm line-and-space (L/S) pattern was finally produced in 1985 (see Fig. 1.3), and the results of the early experiments were first presented

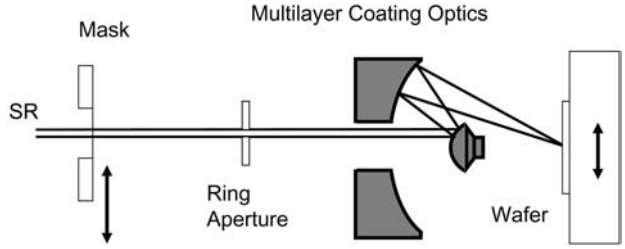

Figure 1.2 Experimental arrangement used by NTT for the first demonstration of soft-x-ray projection imaging (SR – synchrotron radiation).

Downloaded From: https://www.spiedigitallibrary.org/ebooks/ on 09 Mar 2022
Terms of Use: https://www.spiedigitallibrary.org/terms-of-use

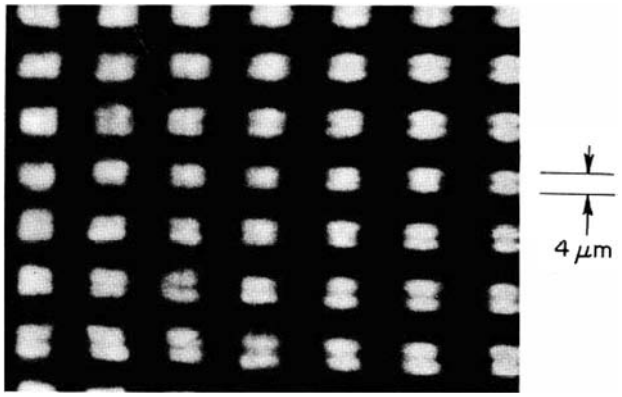

Figure 1.3 Photograph of a 4-μm pattern of dots in a PMMA resist produced by imaging with Schwarzschild optics in 1986.

at the annual meeting of the Japan Society of Applied Physics in 1986. Unfortunately, the response to the paper was rather negative; the audience seemed unwilling to believe that an image had actually been made by bending x rays.

In 1985, T. Barbee, Jr., S. Mrowka, and M. Hettrick reported the development of molybdenum-silicon (Mo-Si) ML coatings that yielded a high normal-incidence reflectivity at wavelengths around 20 nm.[10] This was the first report of a normal-incidence reflectivity beyond the theoretically predicted value that had ever been obtained experimentally (Fig. 1.4).

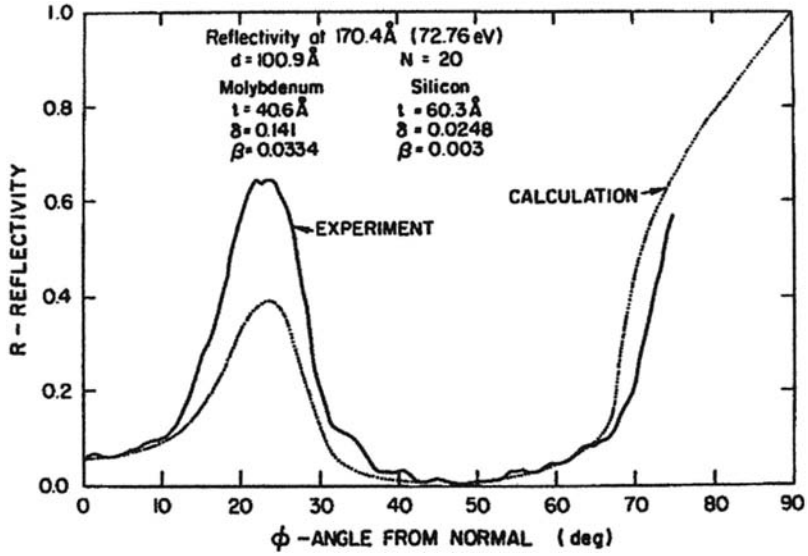

Figure 1.4 Reflectivity of a Mo-Si multilayer film at a wavelength of 170.4 Å (reprinted from Ref. 10 with permission from OSA).

Downloaded From: https://www.spiedigitallibrary.org/ebooks/ on 09 Mar 2022
Terms of Use: https://www.spiedigitallibrary.org/terms-of-use

In 1986, at the end of a presentation on photo-ionization pumping of short-wavelength lasers at the Short Wavelength Coherent Radiation: Generation and Applications Conference in Monterey, California, W. Silfvast and O. Wood of AT&T Bell Labs suggested to a representative of a U.S. government funding agency that "the development of soft-x-ray lasers when taken together with the possibility of multilayer reflectors in this spectral region could lead to a practical system for lithography."[3] The reviews of the subsequent funding proposal, entitled "Tenth micron lithography with a 10 Hz 37.2 nm sodium laser," were extremely negative. The reviewers maintained that "even if each of the components and subsystems could be fabricated, the complete lithography system would be so complex that its uptime would be negligible," and "the printing of 0.1-μm features might be of use for a few high-speed GaAs circuits, but would never be needed for Si integrated circuits." Because the authors remained convinced that the ideas put forward in their proposal were ones that needed to be explored, the technical parts of the proposal were submitted to a technical journal and subsequently appeared in the first issue of the 1988 volume of *Microelectronic Engineering*.[3]

In 1988, A. Hawryluk and L. Seppala of Lawrence Livermore National Laboratory (LLNL) proposed soft-x-ray projection lithography (SXPL) using a two-mirror imaging system at the 32nd International Symposium on Electron, Ion and Photon Beams (EIPB) in Ft. Lauderdale, Florida, in a paper entitled, "Soft x-ray projection lithography using an x-ray reduction camera."[4] The design of their 5× reduction camera, shown in Fig. 1.5, was based on an inverse Cassegrain. Taking into account the penetration depth of the resist materials, the exposure wavelength was set to the absorption edge of C (4.48 nm); a concave spherical mask was used to correct for the curvature of the image field.[4] In 1989, A. Hawryluk, N. Ceglio, and D. Gaines changed the

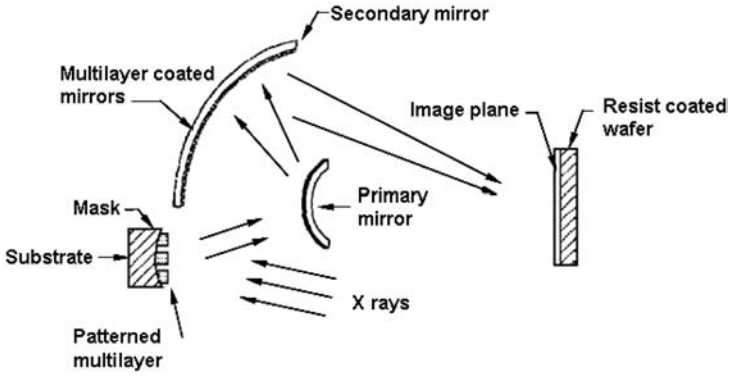

Figure 1.5 X-ray reduction camera with corrected field curvature and uniform illumination developed by LLNL (reprinted from Ref. 4 with permission from the American Vacuum Society).

Downloaded From: https://www.spiedigitallibrary.org/ebooks/ on 09 Mar 2022
Terms of Use: https://www.spiedigitallibrary.org/terms-of-use

design wavelength to 13 nm and proposed a system that employed a flat mask and a flat wafer in combination with a scanning stage for the mask and wafer so a larger area could be exposed.[11] The authors of these proposals, all members of the Advanced Diagnostics Group in the Laser Fusion Program at LLNL, were actively developing the components and techniques needed for soft-x-ray plasma diagnostics (e.g., grazing-incidence optics, ML-coated optics, Fresnel zone plates, transmission gratings, etc.); hence, they were able to make important contributions to the development of SXPL from the very start.

In 1989, H. Kinoshita et al. of NTT described early work in Japan at the 33rd International EIPB Symposium in Monterey, California, in a paper entitled, "Soft x-ray reduction lithography." The paper described the first replication of a 0.5-μm pattern with a Schwarzschild imaging system and a reflection-type mask (Fig. 1.6).[12] The paper also included suggestions on (1) the optimum exposure wavelength, (2) the structure and fabrication of reflective masks, and (3) the characteristics of a practical soft-x-ray resist. At the EIPB symposium banquet in the Monterey Aquarium, a Russian woman, Dr. Tania Jewell of AT&T, cornered Dr. Kinoshita and proceeded to deluge him with questions. The combination of poor Japanese English and poor Russian English made conversation extremely difficult, so the discussion continued for a long time with Obert Wood of AT&T acting as interpreter. The following year, AT&T announced the printing of a 0.05-μm pattern using SXPL. The authors of this chapter regard the discussion that night in Monterey in 1989 as having been "the dawn of EUVL".

In 1990, D. Berreman et al. of AT&T Bell Labs described the printing of 0.2-μm features using a 20:1 reduction iridium (Ir)-coated Schwarzschild optic at a wavelength of 36 nm (Fig. 1.7).[13] Later that year, J. Bjorkholm et al. of AT&T demonstrated diffraction-limited imaging at a 14-nm wavelength using a Mo-Si ML-coated Schwarzschild camera by printing features as small as 0.05 μm in photoresist,[5] as shown in Fig. 1.8. In 1991, A. MacDowell et al. of AT&T described an Ir-coated 1:1 Offner ring-field imaging system for use at a wavelength of 42 nm (Fig. 1.9).[14] Although the group at AT&T specialized in lasers and optical devices, they were also thinking about how to apply laser

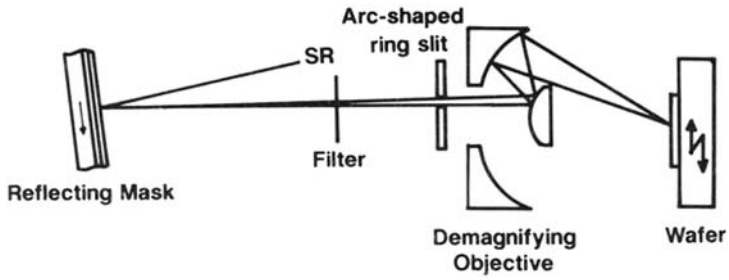

Figure 1.6 Schematic illustration of the experimental setup to evaluate the image-forming characteristics of Schwarzschild optics and a flat reflective mask (reprinted from Ref. 12 with permission from the American Vacuum Society).

Downloaded From: https://www.spiedigitallibrary.org/ebooks/ on 09 Mar 2022
Terms of Use: https://www.spiedigitallibrary.org/terms-of-use

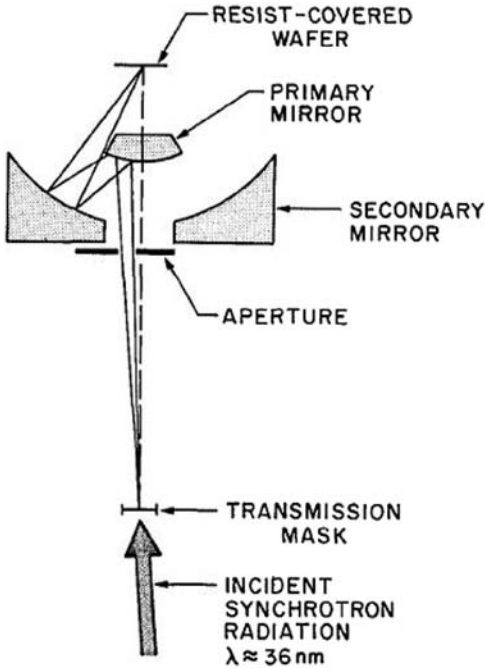

Figure 1.7 Schematic diagram of the experimental arrangement for soft-x-ray projection imaging with a Schwarzschild objective used by AT&T Bell Labs (reprinted from Ref. 13 with permission from OSA).

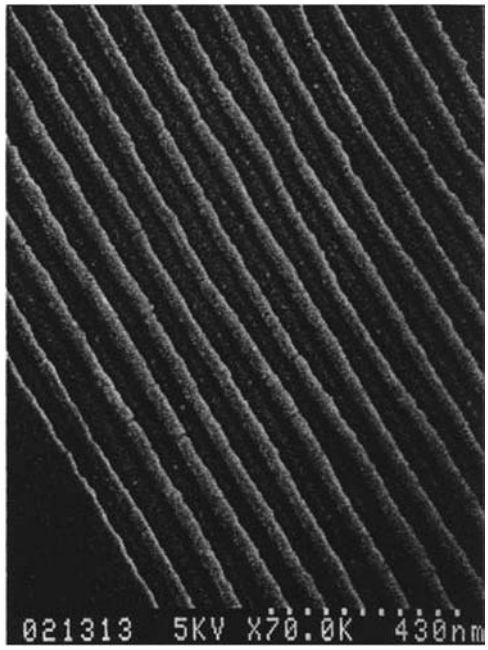

Figure 1.8 SEM image showing a closeup of 0.05-μm lines and spaces printed by AT&T Bell Labs using a Mo-Si ML-coated Schwarzschild optic (reprinted from Ref. 5 with permission from the American Vacuum Society).

Downloaded From: https://www.spiedigitallibrary.org/ebooks/ on 09 Mar 2022
Terms of Use: https://www.spiedigitallibrary.org/terms-of-use

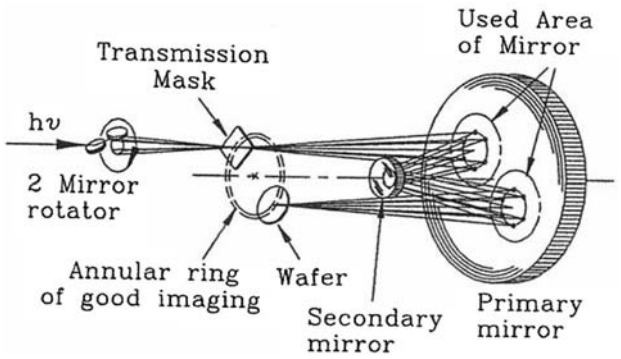

Figure 1.9 Experimental arrangement for soft-x-ray imaging utilizing a 1:1 Offner relay (reprinted from Ref. 75 with permission from OSA).

technology to lithography. Their main goal was to obtain proof of diffraction-limited imaging using an on-axis Schwarzschild camera without distortion. That goal was different from H. Kinoshita's initial goal of obtaining a large exposure field. Nevertheless, the demonstration of diffraction-limited imaging by AT&T helped pave the way for the development of reduction lithography at short wavelengths.

In 1991, the first Optical Society of America (OSA) Topical Meeting on Soft-X-ray Projection Lithography took place in Monterey, California. At this conference, a group from Sandia National Laboratories (SNL) and AT&T reported the first SXPL system with a laser plasma source (Fig. 1.10).[15] The laser plasma source consisted of a 1.25 J/pulse KrF excimer laser operating at repetition rates up to 100 Hz focused to a 150-μm diameter spot on a rotating gold-coated cylindrical target. At an intensity on the target of 7×10^{10} W/cm^2, the measured total conversion efficiency (CE) in a 4.5% spectral band centered at 13.9 nm was 0.5%. Images of a transmission mask were made in spin-cast films of poly(methyl methacrylate) (PMMA) 50- to 60-nm thick using a 0.08-NA Schwarzschild optic. An atomic force micrograph (AFM) of a portion of the resist image reproduced in Fig. 1.11 shows that 0.1- and 0.15-μm features were clearly resolved.

At the 1992 OSA Topical Meeting on Soft-X-ray Projection Lithography, NTT presented exposure results for a two-aspherical-mirror imaging system[16] (Fig. 1.12) designed by K. Kurihara, et al.[17] The experiment utilized a synchrotron source, a two-mirror illumination system, a C filter to eliminate wavelengths longer than 400 Å, a reflecting mask, a two-aspherical-mirror imaging system, and a resist-coated wafer. The illumination system, employing a Köhler design and consisting of two toroidal mirrors, illuminated a 100-mm-wide ring-shaped field on a reflecting mask. The incident angle on the optics was nearly normal (~2 deg), and the imaging system was telecentric with respect to the plane of the wafer. To expose a large square field on the wafer, the mask and

Downloaded From: https://www.spiedigitallibrary.org/ebooks/ on 09 Mar 2022
Terms of Use: https://www.spiedigitallibrary.org/terms-of-use

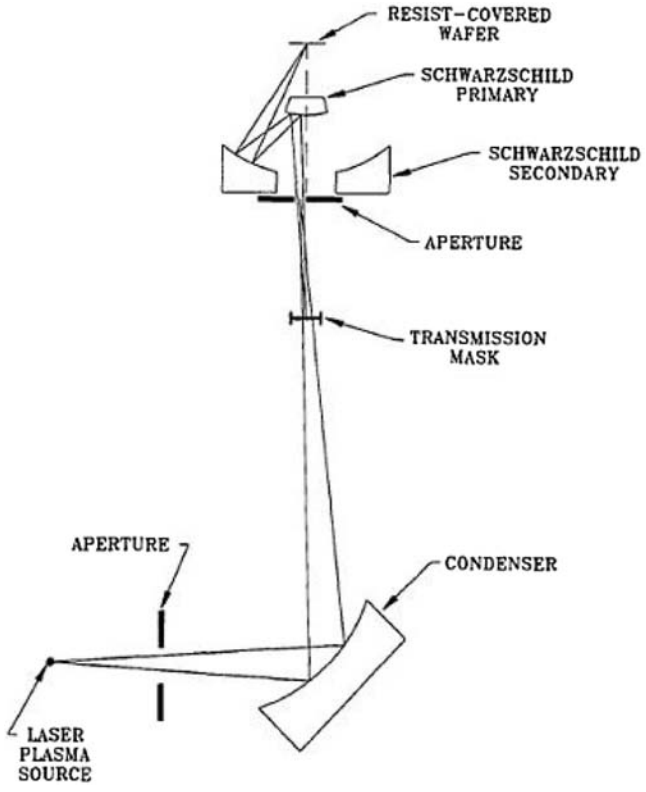

Figure 1.10 Soft-x-ray projection imaging system using Schwarzschild optics and a laser plasma source [reprinted from G. Kubiak et al., *J. Vac. Sci. & Tech. B* **9**, 3184 (1991) with permission from the American Vacuum Society].

wafer stages were made to move in sync. The optics for the first experiment were fabricated by Hidaka Kougaku of Japan, but the measurement of their performance with a Fizeau interferometer revealed that they did not meet the required specifications. Subsequently, NTT had more precise mirrors fabricated by Tinsley Laboratories (Fig. 1.13) and two years later succeeded in replicating patterns over a 10-mm^2 field using the improved optics.[18]

1.3 The Second Stage of Development—1993 to 1996

During the second stage of EUVL development from 1993 to 1996, the focus of R&D work worldwide shifted from demonstrations of EUV imaging to the development of EUV imaging systems that could provide larger image fields and smaller wavefront errors, and to EUVL system integration. The start of this second stage of development coincided with a change in the name of the technology from SXPL to EUVL. The name change was proposed in May 1993 at the OSA Topical Meeting on Soft-X-ray Projection Lithography in

Downloaded From: https://www.spiedigitallibrary.org/ebooks/ on 09 Mar 2022
Terms of Use: https://www.spiedigitallibrary.org/terms-of-use

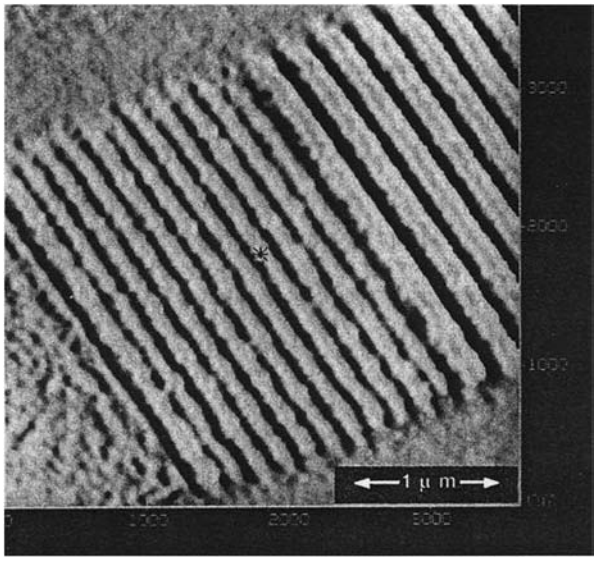

Figure 1.11 AFM of a soft-x-ray image in PMMA showing a high-contrast recording of features down to 0.1 μm and a low-contrast recording of 0.05-μm lines and spaces [reprinted from G. Kubiak et al., *J. Vac. Sci. & Tech. B* **9**, 3184 (1991) with permission from the American Vacuum Society].

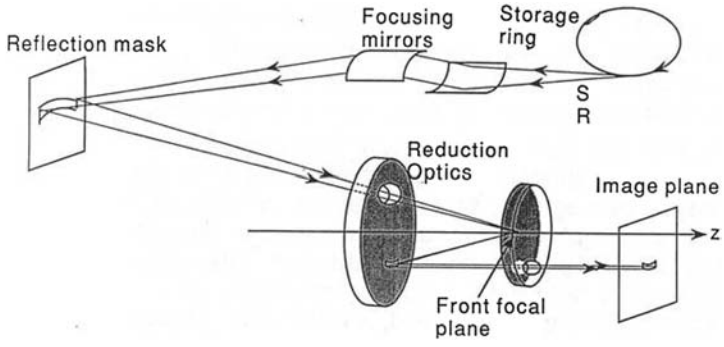

Figure 1.12 Schematic illustration of the two-aspherical-mirror imaging system developed by NTT (reprinted from Ref. 19 with permission from OSA).

Monterey by Richard Freeman of AT&T, ostensibly to avoid confusion with x-ray proximity lithography, which was also under development at that time. EUV lithography sounded like a natural extension of deep-ultraviolet (DUV) lithography, the type of optical lithography widely used commercially in 1993, and the new name was readily adopted. The end of the second stage of EUVL development was marked by the fabrication of the first metal–oxide semiconductor (MOS) devices using EUVL in 1996, and the beginning of EUVL commercialization efforts at the EUV LLC in early 1997.

Downloaded From: https://www.spiedigitallibrary.org/ebooks/ on 09 Mar 2022
Terms of Use: https://www.spiedigitallibrary.org/terms-of-use

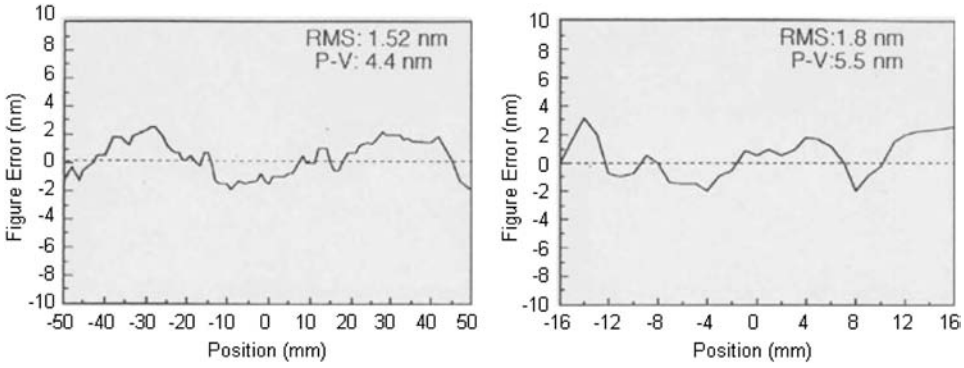

Figure 1.13 Measured figure error of aspherical mirrors fabricated by Tinsley Laboratory in 1993 (reprinted from Ref. 19 with permission from OSA).

1.3.1 Two-mirror imaging system development

In 1993, H. Kinoshita et al. of NTT fabricated and assembled a 5× reduction, 0.07-NA, two-aspherical-mirror imaging system with a 20×0.4 mm exposure area[19] based on a design described by K. Kurihara et al.[17] Unfortunately, the figure errors of the concave and convex mirrors, 8.8-nm and 2.0-nm rms, respectively, were out of specification for 0.1-μm imaging. Nevertheless, when the system was assembled and aligned, imaging of features as small as 0.25 μm was achieved over a 10×0.6 mm area, and imaging of 0.15-μm features was achieved over a portion of a 2×0.6 mm ring-shaped field, as shown in Fig. 1.14. In 1996, Haga et al. succeeded in expanding the exposure area of the two-aspherical-mirror imaging system to 20×25 mm by utilizing new critical-illumination optics to illuminate a ring-shaped field area of 20×0.6 mm and by synchronously scanning the mask and wafer stages.[20] The exposure time for a 10-mm square area at the NTT superconducting storage ring in Atsugi (Super ALIS) was about 16 minutes when the ring current was 500 mA.

In 1994, a U.S. National EUV Lithography Program made up of teams of researchers from LLNL, Lawrence Berkeley National Laboratories (LBNL), SNL, and AT&T Bell Labs was launched with financial support from the U.S. Department of Energy. The program was led by Dr. Frits Zernike, Jr., formerly of SVG Lithography, and its progress was monitored by a technical advisory group consisting of W. F. Brinkman (AT&T), D. O. Patterson [Defense Advanced Research Projects Agency (DARPA)], J. R. Carruthers (Intel), J. A. Glaze (JAMAR), K. H. Brown (SEMATECH), G. E. Fuller (Texas Instruments), D. A. Markle (Ultratech Stepper), and C. W. Fowler (U.S. Department of Energy). This program was the first attempt in the U.S. to pursue the development of EUVL in an organized way. Prior to this, EUVL projects between U.S. national laboratories and private corporations were carried out via a series of cooperative research and development agreements (CRADAs).

Downloaded From: https://www.spiedigitallibrary.org/ebooks/ on 09 Mar 2022
Terms of Use: https://www.spiedigitallibrary.org/terms-of-use

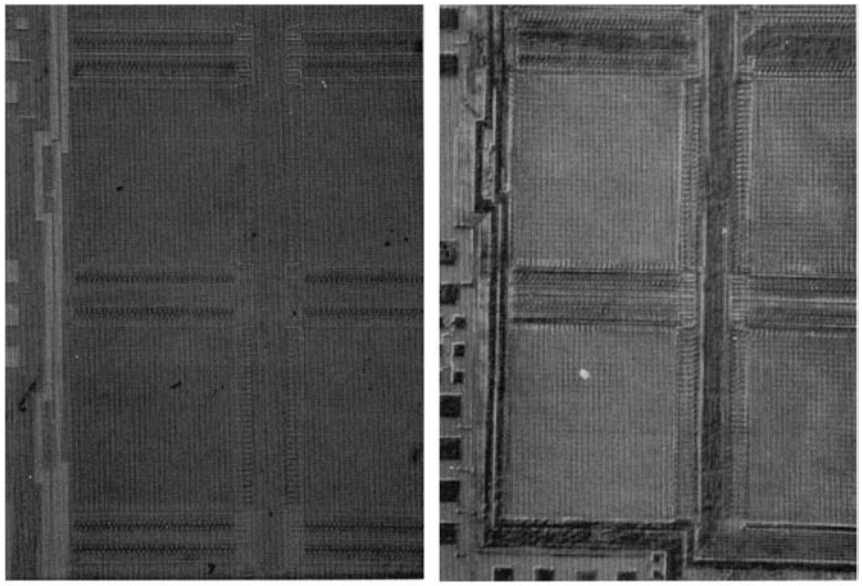

Figure 1.14 Photographs obtained with a two-aspherical-mirror imaging system developed by NTT of (a) reflection mask patterns and (b) replicated patterns (reprinted from Ref. 19 with permission from OSA).

In 1994, G. Sommargren of LLNL developed the 3.4× reduction, 0.06-NA, two-mirror, four-reflection ring-field imaging system shown in Fig. 1.15. This system was used in a testbed facility at LLNL to evaluate "front-end" issues such as high-repetition-rate laser drivers, CE of laser light to EUV radiation, and condenser systems with specific illumination and coherence requirements.[21] In 1996, B. La Fontaine et al. used this system to print features as small as 0.137 μm.[22] The imaging results were not as good as expected given the low measured imaging system wavefront error. The lower-than-expected image

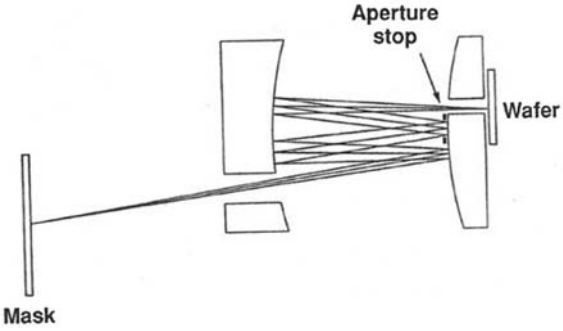

Figure 1.15 Optical layout for an all-spherical, two-mirror, four-reflection ring-field imaging system developed by LLNL (reprinted from Ref. 21 with permission from OSA).

Downloaded From: https://www.spiedigitallibrary.org/ebooks/ on 09 Mar 2022
Terms of Use: https://www.spiedigitallibrary.org/terms-of-use

contrast was attributed to the presence of scattered light in the image plane (flare). Thus, B. La Fontaine et al. were among the first to suggest that, in the future, the surface characteristics of imaging system optics needed to be specified more fully, i.e., beyond that needed to ensure a low system wavefront error and a high EUV reflectance.[22]

In 1995, D. A. Tichenor et al. of SNL began development work on the first EUVL laboratory tool capable of precise overlay.[23] This so-called 10X-II Schwarzschild was the first laboratory EUVL tool that combined a near-diffraction-limited imaging capability, accurate stages, and an integrated through-the-lens alignment system. The major components of the tool, shown in Fig. 1.16, included a 10× reduction, 0.08-NA Schwarzschild imaging system with 0.1-μm resolution (the measured wavefront error was ~1 nm rms), a debris-mitigated laser plasma source, a magnetically levitated wafer stage, an electrostatic wafer chuck, and a grazing-incidence optical system to maintain focus. Coarse mask-to-wafer alignment was carried out in a pre-alignment station equipped with a microscope and a micrometer stage. A manual wafer

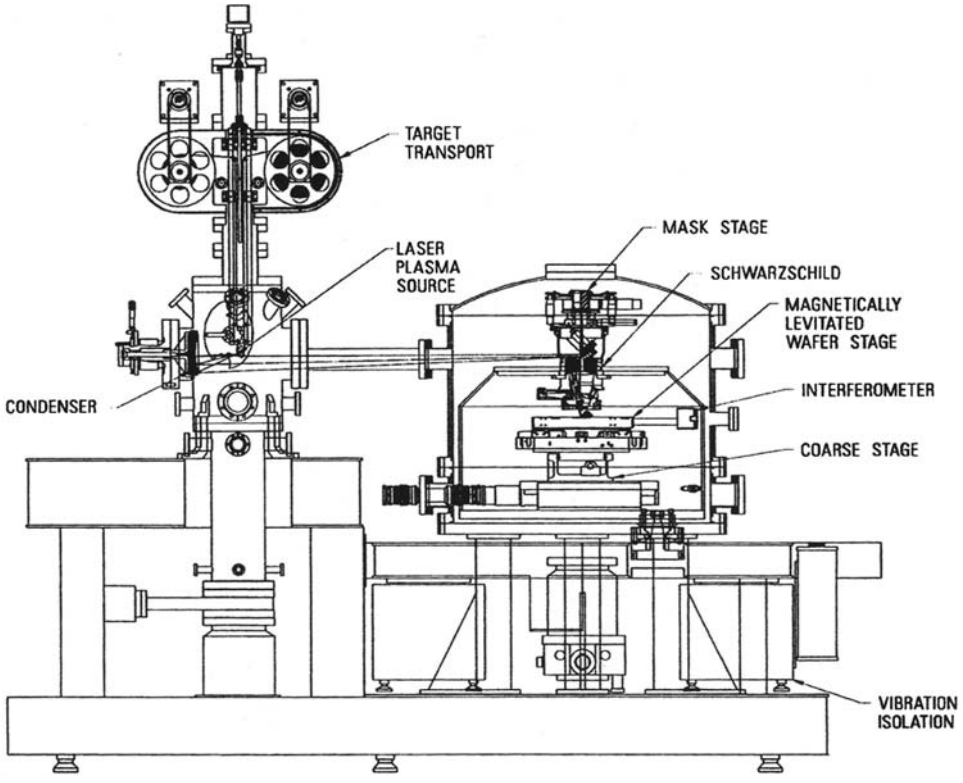

Figure 1.16 Sketch of a laboratory EUVL tool based on a laser plasma source, a 10x-reduction Schwarzschild camera, and a magnetically levitated fine stage developed at SNL (reprinted from Ref. 23).

Downloaded From: https://www.spiedigitallibrary.org/ebooks/ on 09 Mar 2022
Terms of Use: https://www.spiedigitallibrary.org/terms-of-use

transfer system was used to transfer wafers to the exposure chamber. Fine mask-to-wafer alignment was performed with a through-the-lens optical moiré alignment system.[24]

In 1996, A. A. MacDowell et al. of AT&T Bell Labs described the initial results from AT&T's second 1:1 Offner ring-field imaging system using a new mirror substrate fabricated by SVG Lithography Systems.[25] The imaging performance of the previous Offner system, fabricated in 1992, suggested that the imaging would improve significantly if the figure errors of the mirrors were improved. During the mirror fabrication process, emphasis was placed on reducing surface figure errors, but no attempt was made to define errors within the mid-spatial-frequency range. The resolution of the new Offner system was significantly improved, and the new imaging system was able to print 75-nm dense lines/spaces; however, the image modulation was not as high as expected based on the measured system wavefront, which suggested that small-angle scattering of light from mid-spatial-frequency surface roughness (flare) was dominating the imaging results. The disappointing imaging results from the new Offner imaging system provided additional evidence that the substrate surfaces in future EUV imaging systems needed to meet much tighter specifications for figure (~100–1 mm), mid-spatial-frequency roughness (~1000–1 μm), and nano-roughness (~1000–10 nm).

1.3.2 Three-mirror imaging system development

In 1996, D. A. Tichenor et al. of SNL described the fabrication and evaluation of the 5× reduction, 0.1-NA, three-aspherical-mirror ring-field imaging system[24] shown in Fig. 1.17. The system was based on a reflective triplet design developed in 1994 by J. H. Bruning et al. of Tropel Corporation[26] for AT&T Bell Labs. The system utilized low-departure aspheric reflectors, its wafer size was telecentric, and it had low-distortion (<0.2 waves at 13-nm

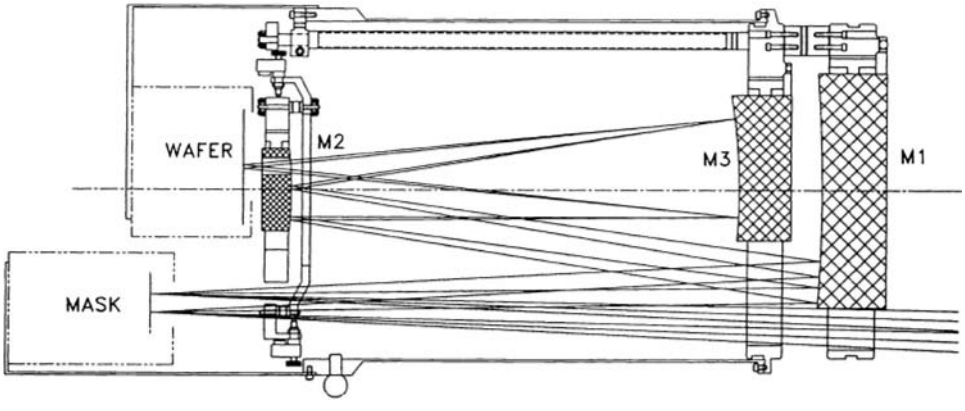

Figure 1.17 Three-aspherical-mirror imaging system developed by SNL, Tropel, and AT&T (reprinted from Ref. 23).

Downloaded From: https://www.spiedigitallibrary.org/ebooks/ on 09 Mar 2022
Terms of Use: https://www.spiedigitallibrary.org/terms-of-use

wavelengths over a 25×1 mm arc-shaped image field). It had two design limitations: the aperture stop was not accessible, and the three-mirror reflections required the mask and wafer planes to be placed on the same side of the imaging system, which resulted in mechanical interference that limited the scanning. Nevertheless, the design represented a major step in EUV camera development, beyond that of the spherical systems and two-mirror aspheric systems that had been built previously. The mirrors used in the imaging system were fabricated by Tinsley Laboratory using computer-controlled optical surfacing and computer-generated holographic nulls. All three mirrors were figured to a precision of 0.6 nm rms as measured interferometrically over a spatial scale from about 1 mm to the full clear aperture. At that time, the mirrors for this system were the most precisely figured set of aspheres in existence. Measurements of the mid-spatial-frequency surface errors and the high-spatial-frequency roughness using white-light interferometry and atomic force microscopy, respectively, showed that an additional five-fold reduction in surface errors over most of the spatial frequency spectrum would be necessary before these mirrors could be used in an EUVL manufacturing tool. Finite element analysis was used to design mounts that would assure a stress-free condition and preserve the precise figure of the mirrors. The wavefront error of the assembled and aligned system at various field points ranged from 1.0 nm to 1.7 nm rms.[24] These values were in agreement, to within the accuracy of the measurements, with simulations based on figure data from the individual mirrors. The measured wavefront error was better than that of most spherical EUV systems at that time. The results demonstrated that a small wavefront error could be realized in an advanced aspheric imaging system with a ring-field dimension comparable to that required in a practical EUVL camera design; they also provided the know-how needed to assemble the four-mirror EUV imaging system in the Engineering Test Stand (ETS) developed by the EUV LLC several years later.

1.3.3 MOS device demonstration using EUVL

In 1996, a team from SNL, AT&T, and the University of California, Berkeley fabricated the first demonstration MOS device using the 10X-II EUV Schwarzschild system described above.[27] The team fabricated n-type MOS (NMOS) transistors with gate lengths ranging from 0.075 μm to 2.0 μm using a modified NMOS process in which the active areas were defined by local-oxidation-of-silicon (LOCOS) isolation, as shown in Fig. 1.18. The gate oxide layers were grown by thermal oxidation and had thicknesses of 2.5 nm, 4 nm, and 5.5 nm. The gate was a 150-nm-thick *in situ* doped n^+-polysilicon deposited by low-pressure chemical vapor deposition (LPCVD). It used a blanket boron (B) punch-through stop (80 keV, $3 \times 10^{12}/cm^2$), and a lightly doped drain structure was formed with low-temperature oxide (LTO) spacers.

Downloaded From: https://www.spiedigitallibrary.org/ebooks/ on 09 Mar 2022
Terms of Use: https://www.spiedigitallibrary.org/terms-of-use

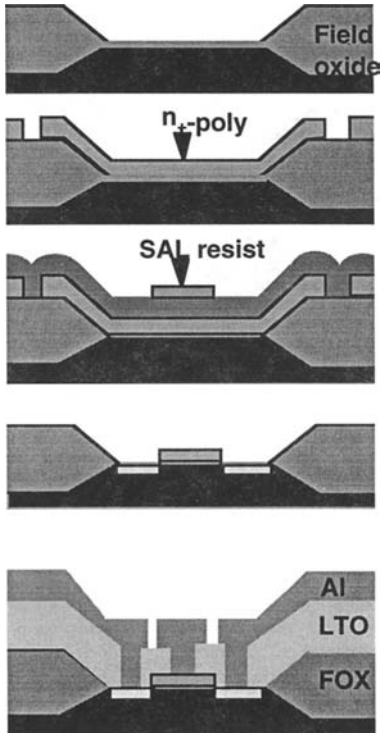

Figure 1.18 Schematic diagram of the NMOS process used to fabricate the first semiconductor devices using EUVL (Al – aluminum; LTO – low-temperature oxide; FOX – field oxide) (reprinted from Ref. 27 with permission from OSA).

Shallow junctions were created by low-energy arsenic (As) implantation (10 keV, $3 \times 10^{13}/\text{cm}^2$) and deep junctions by high-energy As implantation (50 keV, $2 \times 10^{15}/\text{cm}^2$). Five lithography steps were used to define the NMOS devices. The active area, EUV alignment marks, contacts, and metal layers were defined using I-line lithography. The EUV alignment marks were patterned directly into the polysilicon layer immediately before trilayer deposition to create marks with the highest possible fidelity. All of the process steps, except for ion implantation and EUV gate-level lithography, were carried out in the Microfabrication Facilities at the University of California, Berkeley. Figure 1.19 shows the I-V and subthreshold characteristics of one of the NMOS devices with a 0.1-μm long and 3-μm wide gate. The threshold voltage was 0.55 V, the transconductance was 200 mS/mm, the saturated drain current was 400 μA, and the subthreshold swing was 90 mV/decade.

The National EUV Lithography Program funded by the U.S. Department of Energy lasted for approximately three years, and when it ended most of the early EUVL research work in the U.S. also ended. The establishment of the EUV LLC in 1996–1997 marked the beginning of commercialization efforts in the U.S. Work at the EUV LLC contributed to all aspects of EUV

Downloaded From: https://www.spiedigitallibrary.org/ebooks/ on 09 Mar 2022
Terms of Use: https://www.spiedigitallibrary.org/terms-of-use

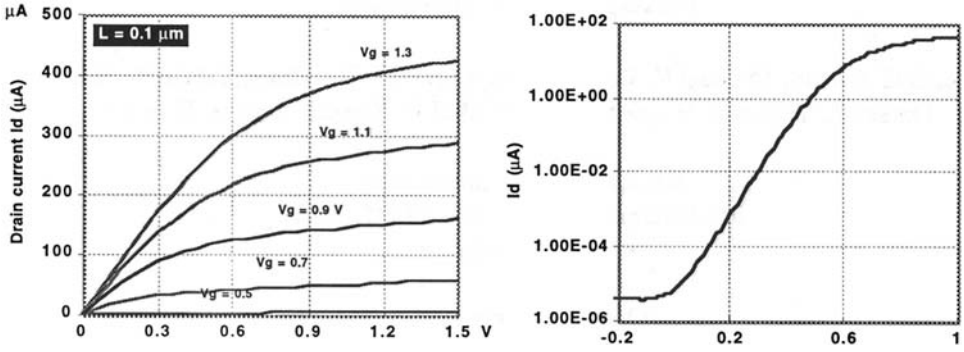

Figure 1.19 Characteristics of a 0.1-μm NMOS transistor with EUVL gate level patterning (3-μm gate width) (reprinted from Ref. 27 with permission from OSA).

development until November 2002 and brought EUVL significantly closer to the stage of practical use. Stepper-makers SVG Lithography and ASML participated directly in the program. Many specialists in the fields of optics, polishing, thin films, metrology, and laser plasmas worked together with the EUV LLC in a complicated organizational arrangement, while a consortium of integrated device manufacturers that included AMD, IBM, Infineon, Intel, Micron, and Motorola supplied funding and provided technical guidance to the program. The organization and accomplishments of the EUV LLC are described in detail in Chapter 2 of this book.

1.4 Other Developments in Japan and Europe

From 1984 to 1992, the development of EUVL technology in Japan was pursued mainly by NTT and focused on demonstrating the feasibility of replicating 0.1-μm patterns using ML-coated Schwarzschild optics. Starting in 1991, Hitachi and Nikon began to make advances in EUVL through experiments at SORTEC and at the High Energy Physics Laboratory in Tsukuba, respectively. In 1993, T. Namioka of Tohoku University organized a soft-x-ray optics meeting focused on ML coatings and EUV light-source development that intensified EUVL research activities in Japan. The early EUV work at Hitachi confirmed that 70-nm L/S patterns could be printed using 20× reduction Schwarzschild optics with either etched ML or absorber-over-layer reflection masks.[28] From 1992 to 1995, EUVL work in Japan focused on developing two-aspherical-mirror imaging systems that had an exposure field large enough for practical use.[20,29,30] By 1996, Hitachi had succeeded in designing, fabricating, and assembling such a system.[30] The mirrors for their two-aspherical-mirror imaging system were fabricated using a novel small-tool asphere generator. The figure accuracy for the convex asphere, measured with a Fizeau interferometer, was 18-nm peak to valley, and the surface roughness, measured with an AFM, was 0.16-nm rms. While

Downloaded From: https://www.spiedigitallibrary.org/ebooks/ on 09 Mar 2022
Terms of Use: https://www.spiedigitallibrary.org/terms-of-use

neither mirror achieved sufficient figure accuracy to support diffraction-limited imaging, when a narrow arc on the mask was illuminated with synchrotron radiation at the Photon Factory in Tsukuba, 0.12-μm-wide lines and spaces were delineated over portions of the ring field.[30] The early EUVL work at Nikon was focused on developing some of the basic technologies needed for EUVL, the fabrication of aspheric surfaces using a small-tool polishing machine, a Kohler critical-illumination system for use with a ring-field reflective imaging system, a debris-mitigated laser-plasma EUV source, and damage-free reflection-mask fabrication technology. In 1996, K. Murikami et al. of Nikon described the design of a three-aspherical-mirror ring-field imaging system.[31] After Dr. Kinoshita joined the Himeji Institute of Technology (HIT) in 1995, Nikon and Hitachi launched joint research projects with HIT, eventually resulting in the development of a three-aspherical-mirror EUVL imaging system for demonstration MOS device fabrication.[32]

By the autumn of 1998, the need for advanced EUVL equipment development became widely recognized in Japan, and the Association for Super-Advanced Electronics Technologies (ASET) was formed.[33] Soon thereafter, Intel and Samsung began cooperating with ASET on EUVL research, a move that helped accelerate the globalization of EUVL research and development. The ASET EUV program focused on mask fabrication and resist technologies using the EUV imaging system at HIT, and on EUV reflectometry and EUV imaging system wavefront metrology using beamlines at the New SUBARU synchrotron facility. In June 2002, a new government-funded organization—called the Extreme Ultraviolet Lithography System Development Association (EUVA)[34]—focused on the development of EUV light sources, and projection optics was established.

In Europe, early EUVL research was carried out by various branches of the Fundamenteel Onderzoek der Materie (FOM) Institute and was supported by the government of The Netherlands under the framework of EUREKA. In 1991, this work led to the design for an extended-field EUV imaging system that employed two spherical mirrors and a concave reflection mask,[35] as well as a novel coating system for EUV reflective multilayers that employed electron-beam deposition and interface smoothing by ion bombardment.[36] By 1993, the work in Europe had expanded to include development of a krypton-fluorine (KrF) laser-induced soft-x-ray source[37] and a liquid-droplet target system that produced much less debris.[38] In January 1994, a collaborative EUVL development program called EXULT involving ASM Lithography, the FOM Institute, SOPRA, Carl Zeiss Inc., Technical University Delft, and The Netherlands Center for Laser Research was launched to concentrate on high-power debris-free sources, precision optics fabrication and metrology, and defect-free masks.[39] In August 1998, a new European research program called the Extreme UV Concept Lithography Development System (EUCLIDES) was

Downloaded From: https://www.spiedigitallibrary.org/ebooks/ on 09 Mar 2022
Terms of Use: https://www.spiedigitallibrary.org/terms-of-use

launched by ASM Lithography, Carl Zeiss Inc., and Oxford Instruments.[40] By building on results from EUCLIDES and from the French national EUVL program called Programme Extreme UV (PREUVE), a larger collaborative program called Microelectronics Development for European Applications+ (MEDEA+) was launched in January 2001 and focused on the development of EUV exposure tools, light sources, imaging systems, and mask manufacturing.[41] The MEDEA+ Extreme UV Alpha Tools Integration Consortium (EXTATIC) project recently resulted in the development of two full-field EUV R&D exposure tools.

1.5 The Development of Individual Technologies

The most important advances in EUVL development that were made each year from 1985 to 1996 in Europe, Japan, and the U.S. were detailed in Sections 1.2, 1.3, and 1.4. A graphical record of these advances is illustrated in the fishbone diagram shown in Fig. 1.20, where one or more highlights from each year's technical progress have been recorded in the lower half of the figure. Four scientific and technological breakthroughs that occurred during this time period, without which EUVL would not have been possible, are also shown in Fig. 1.20 (in the upper half of the figure). These four major advances—the first demonstrations of normal-incidence imaging in the

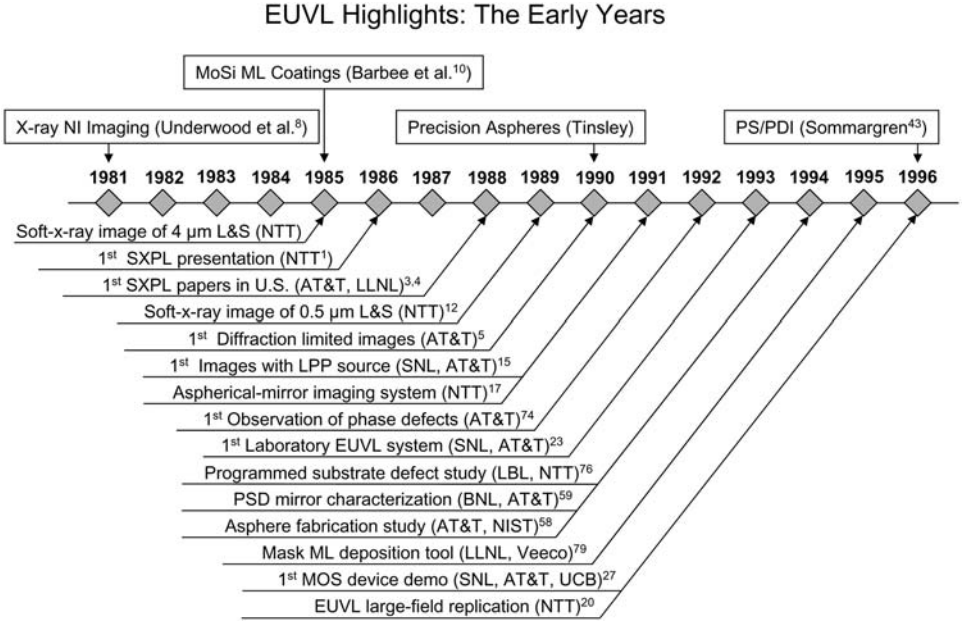

Figure 1.20 Fishbone diagram showing the yearly highlights of early EUVL development from 1981 through 1996 (NI – normal incidence).

Downloaded From: https://www.spiedigitallibrary.org/ebooks/ on 09 Mar 2022
Terms of Use: https://www.spiedigitallibrary.org/terms-of-use

soft-x-ray spectral region, the development of Mo-Si ML coatings, the fabrication of precision aspheres, and the invention of the phase-shifting point-diffraction interferometer (PSPDI)—not only enabled EUVL but also may have accelerated progress in other fields of science and technology that utilize reflective imaging systems, e.g., astronomy, microscopy, satellite surveillance, plasma diagnostics, spectroscopy, and medicine. More information on the first normal-incidence-imaging experiments can be found in Section 1.2. More information on the ML coating work of E. Spiller[42] and T. Barbee[10] can be found in Sections 1.5.1 and 1.5.4. More information on asphere development at Tinsley Laboratory and on the PSPDI developed by G. Sommargren[43] can be found in Section 1.5.3. The remainder of Section 1.5 focuses on the development of the individual components and subsystems needed for EUVL exposure tools (reflective imaging systems, aspherical mirrors, reflective ML coatings, and short-wavelength radiation sources) and for the supporting infrastructure (reflection masks and resists).

1.5.1 Selection of the exposure wavelength

One of the earliest and most important decisions made in the field of EUVL was the choice of exposure wavelength.[12] That choice influenced the design of the projection optics, set the peak reflectivity and bandwidth of the ML reflective coatings, and had a profound impact on the performance of EUV resist materials. Over the course of the early work, exposure wavelengths as short as 4 nm and as long as 85 nm were considered;[44] the lower limit for this wavelength range was determined by throughput considerations (the reflectivity of a ML decreases, and its bandwidth becomes smaller as the wavelength becomes shorter), and the upper limit was determined by imaging system requirements (resolution and depth of focus).

The primary motivation for EUVL was to develop an exposure tool capable of a higher resolution and a larger depth of focus than was possible with DUV or 193-nm lithography. The two fundamental relationships describing lithographic imaging system resolution R and depth of focus (DOF) are

$$R = \frac{k_1 \lambda}{NA}, \tag{1.1}$$

and

$$DOF = \pm \frac{k_2 \lambda}{(NA)^2}, \tag{1.2}$$

where λ is the wavelength of the imaging radiation, and NA is the numerical aperture of the imaging system. The parameters k_1 and k_2 are empirically determined and take on values that depend on the critical dimension (CD) tolerance and the size of an acceptable integrated-circuit (IC) manufacturing

Downloaded From: https://www.spiedigitallibrary.org/ebooks/ on 09 Mar 2022
Terms of Use: https://www.spiedigitallibrary.org/terms-of-use

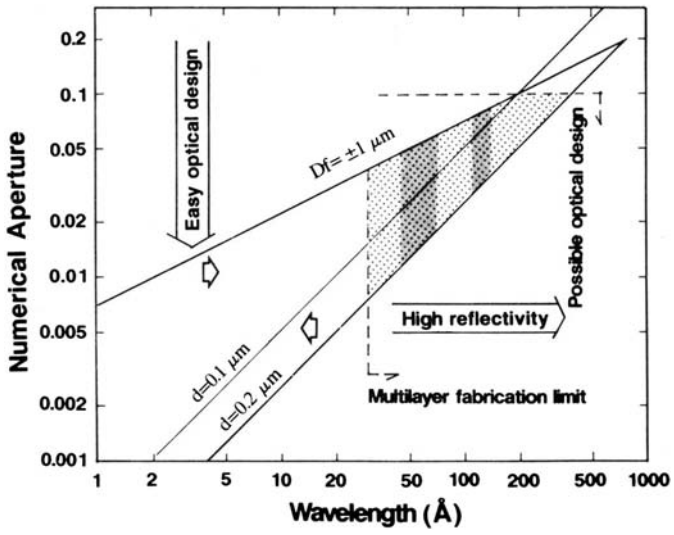

Figure 1.21 Plot of NA versus wavelength used by NTT to select the optimum exposure wavelength for SXPL (reprinted from Ref. 12 with permission from the American Vacuum Society).

process window. The NA and exposure wavelength required for a given resolution and DOF can be calculated using Eqs. (1.1) and (1.2) and are shown graphically in Fig. 1.21. The resolution and DOF targets in 1989 (resolution better than 0.1 μm and DOF larger than ±1 μm) could be met by imaging systems with a NA and exposure wavelength in the shaded area shown in Fig. 1.21 ($0.01 < NA < 0.1$ and $3 \text{ nm} < \lambda < 40 \text{ nm}$).

Multilayer coatings are efficient normal-incidence reflectors at EUV wavelengths from 4.5–30 nm.[45] A ML coating consists of alternating layers of high-Z and low-Z materials and functions like a quarter-wave stack, i.e., it provides enhanced reflectivity over a narrow wavelength band peaked at the Bragg wavelength, $\lambda = 2\Lambda\sin(\theta)$, where Λ is the ML period, and θ is the angle of incidence. Generally, the highest reflectivity occurs at wavelengths for which the absorption of the low-Z material in the ML is at a minimum and occurs in discrete bands near atomic absorption edges. The best low-Z materials for ML coatings are C (for wavelengths longer than 4.4 nm), B (for wavelengths longer than 6.7 nm), beryllium (Be) (for wavelengths longer than 11.3 nm), Si (for wavelengths longer than 12.5 nm), and lithium (Li) (for wavelengths longer than 23.9 nm).[44] For practical throughput, the ML must provide ~30% or more peak reflectivity and have a bandwidth of 0.3–0.4 nm so that the different angles of incidence on all of the mirrors in a multimirror projection optic can be matched.[12]

The sensitivity and absorption depth of an EUV resist depends almost entirely on its EUV absorption coefficient. Because PMMA resist is typical of many organic resist materials in the EUV, the absorption coefficient of

Downloaded From: https://www.spiedigitallibrary.org/ebooks/ on 09 Mar 2022
Terms of Use: https://www.spiedigitallibrary.org/terms-of-use

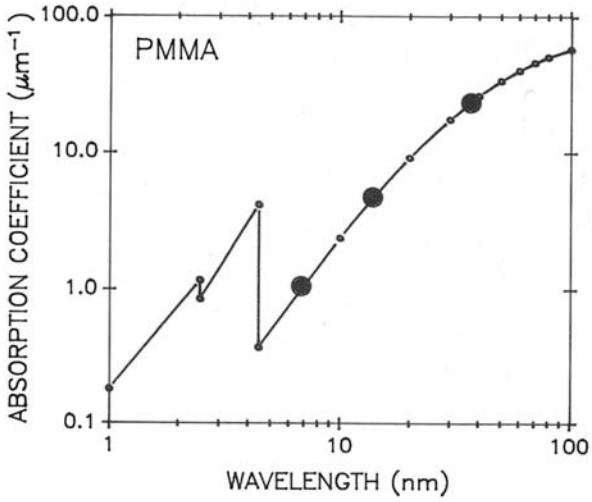

Figure 1.22 Absorption coefficient of PMMA versus wavelength in the EUV spectral region (reprinted from Ref. 46 with permission from OSA).

PMMA versus wavelength is shown in Fig. 1.22. The large discontinuity in absorption near 4.4 nm is due to the K-edge of C. If EUVL could be carried out at 4.4 nm, quite thick resist layers could be used. Unfortunately, C-based MLs—the only materials that give useful normal-incidence reflectance in this wavelength region—are characterized by low reflectance and have an exceedingly narrow reflectance bandwidth. Early experimental work by H. Kinoshita et al.[12] showed that the development depth of PMMA reached a limit at 0.08 μm at an 11.8-nm wavelength but is more than 0.3 μm at a 5-nm wavelength. They concluded that exposure wavelengths longer than ~10 nm would require either a bilayer resist process or a new resist material with a development depth of at least 0.3 μm.[12] Later experimental work by O. Wood et al. showed that the large absorption coefficient of carbon-based resist materials at 13.9 nm resulted in unsatisfactory sidewall profiles when the resist was employed in a single-layer process.[46] The resist sidewall profile is improved somewhat at a 11.3-nm wavelength, which is the reflectance maximum of Be-based MLs[47] and is improved dramatically at a 6.8-nm wavelength, which is the reflectance maximum of B-based MLs.[48] However, imaging at a 6.8-nm wavelength begins to be degraded by chromatic vignetting.[49]

Taking into account the required resolution and DOF, ML reflectance and bandwidth, and resist performance, the choice of exposure wavelength was narrowed in the earliest work[12] to two wavelength regions: from 4.5 to 7 nm and from 11.5 to 13 nm. In a slightly later work,[44] the choice was narrowed to discrete wavelength bands in the vicinity of 11.3, 13, 17, and 24 nm. Today, based on more practical considerations such as overall system

Downloaded From: https://www.spiedigitallibrary.org/ebooks/ on 09 Mar 2022
Terms of Use: https://www.spiedigitallibrary.org/terms-of-use

throughput and worker safety concerns over the use of Be-based MLs in a semiconductor fab, the choice of exposure wavelength has become a narrow band of wavelengths near 13.5 nm. In 1989, the imaging system requirements (resolution better than 100 nm and DOF larger than ± 1 μm) could be met with a 0.1-NA imaging system with three or four ML-coated mirrors. To meet today's targets for resolution and DOF (resolution better than 32 nm and DOF larger than ± 0.15 μm), Mo-Si ML-coated imaging systems with 0.25 NA and 6 to 8 aspheric mirrors are required.

1.5.2 Design of reflective imaging systems

The first EUVL imaging experiment employed Schwarzschild optics,[12] which are notable because they produce an aberration-free image on one axis even though both mirrors have spherical surfaces. However, with that design the blur caused by coma increases linearly with distance from the axis. Thus, the designer of a Schwarzschild system can, in practice, always balance to some extent the aberration and field size on one axis. In 1986, H. Kinoshita et al. proposed an off-axis Schwarzschild system with a scanning stage to enlarge the exposure field. A ray-tracing program was used to design the optics so that there would be little aberration at an off-axis position.[1,2] In 1988, A. Hawryluk et al. proposed an inverse Cassegrain design with a curved mask to compensate for the aberration of image curvature.[4] In 1989, O. Wood et al. showed that the 1:1 Offner annular-field system, which provides diffraction-limited imaging in a narrow ring-shaped field at one particular image height (where third- and fifth-order astigmatism are balanced), can be used in the EUV if restricted to NAs around 0.1.[50] Although these early spherical mirror designs were useful for principle verification, they are not suitable for the projection optics in an EUVL tool. The optical system in a lithographic exposure tool must satisfy the following three minimum requirements:

1. be telecentric on the image side (to prevent magnification change with image plane defocus);
2. provide a high resolution and a wide exposure field; and
3. employ an even number of mirrors (so that object and image are on opposite sides of the projection optics to allow unrestricted wafer travel).

In 1989, a two-aspherical-mirror imaging system satisfying these minimum requirements was developed by H. Kinoshita et al. of NTT.[19] In that design, the primary mirror was convex, the secondary mirror was concave, the radius of curvature of both was about 980 mm, and the separation between the mirrors was about 820 mm. The telecentric design made use of a ring-shaped field and aspherical mirrors to reduce aberrations. The mirrors had conic surfaces (i.e., had no higher-order aspheric terms) to make them easier to fabricate and had about the same radius of curvature so that the image plane would be flat. The reflection mask was planar; a curved reflection mask for aberration

Downloaded From: https://www.spiedigitallibrary.org/ebooks/ on 09 Mar 2022
Terms of Use: https://www.spiedigitallibrary.org/terms-of-use

correction was not employed to ensure a practical mask fabrication process. The incident angles on the mirrors and mask were set to approximately normal incidence to facilitate wavelength matching of the ML coatings. Since the ML periods were almost equal, the two mirrors and the reflection mask could be coated in a single deposition run. Moreover, the image degradation due to the phase shift that occurs at reflection could be neglected because of the use of near–normal incidence.

In 1990, T. Jewell et al. of AT&T devised a four-aspherical-mirror reflective imaging system with a ring field shown in Fig. 1.23 that satisfied all of the requirements for practical 0.1-μm EUV projection lithography.[51] This design was based on a reflective Cook triplet, with a fourth mirror added between the secondary and tertiary mirrors. It was a 4× reduction system with a NA of 0.1 and provided excellent image quality over a several-millimeter-wide ring. All of the mirrors were rotationally symmetric surfaces with low aspheric departure. The radius at the center of the ring field was 31.5 mm on wafer, which allowed the exposure of large chips by scanning. Adding the fourth mirror enabled several of the requirements of a practical lithography system to be met: (1) it brought the object and image to opposite sides of the projection system, thus allowing unlimited wafer travel; (2) it provided an accessible stop; (3) when power was added to the fourth mirror, it helped to provide a larger back clearance; and (4) it helped to achieve full astigmatic correction over a large field of view, thereby reducing alignment sensitivity. In ring-field systems, the width of the ring is usually limited by astigmatism. However, in the AT&T four-aspherical-mirror design, since the astigmatism was corrected over nearly

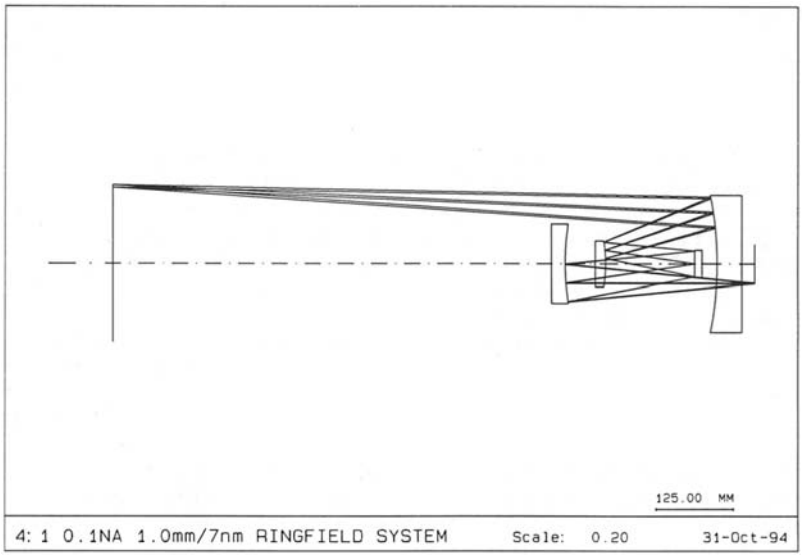

Figure 1.23 Layout of a four-mirror ring-field system designed by Tania Jewell of AT&T (reprinted from Ref. 104 with permission from OSA).

Downloaded From: https://www.spiedigitallibrary.org/ebooks/ on 09 Mar 2022
Terms of Use: https://www.spiedigitallibrary.org/terms-of-use

the entire image field, the width of the ring was limited by distortion. For example, for a 1.0-mm-wide ring, the amount of residual distortion was 7.0 nm in the scan direction and 3.5 nm in the cross-scan direction; for a 2.5-mm-wide ring, the values increase to 40.0 nm and 20 nm, respectively. An additional feature of this design was an optimum chief ray angle in the object space. During system optimization, the chief ray angle with respect to a line normal to the mask was constrained to a minimum of 2.5 deg to allow sufficient room to bring the illumination beam to the mask.

The search for an unobscured reflective imaging system design that would satisfy all of the requirements for the projection optics in an EUV exposure tool started with the two-spherical-mirror systems well known from astronomy and microscopy but quickly progressed to designs involving three or more aspheric reflectors.[26,52,53] Some of the lessons learned from the early EUV imaging system design work were:

1. The use of aspheres cannot be avoided.
2. Scanning ring-field designs are the simplest systems that can print a large field.
3. To avoid image smear in a scanning system, image distortion must be minimized, not only across the ring width in the radial direction but also all the way to the outer edges of the arc defined by the slit in the cross-scan direction.
4. A practical system must employ an even number of mirrors so that multiple chips on the same wafer can be exposed.
5. The design must incorporate an accessible stop so that diffraction orders from features at different places on the mask will not be passed or blocked by the limiting apertures in the system and result in a nonuniform image structure.

In 1996, O. Wood et al. began searching for a design for a larger-NA, all-reflective imaging system that would capitalize on recent advances in optical interferometry[43] and asphere fabrication.[54] The optical layout for one such design, a 5× reduction, 0.5-NA six-aspherical-mirror imaging system, is shown in Fig. 1.24.[55] Its image field was a 30-mm-wide by 1-mm-wide ring. It had an accessible aperture stop. All of its beam clearances were acceptable, and the magnitude of the largest aspheric departure was ~150 μm. Some of the lessons learned during the 1996 reflective imaging system design work were:

1. To minimize scan distortion and mirror substrate size, the design should be of the ring-field type.
2. Good designs will likely have a minimum of six aspheric mirrors.
3. The two mirrors closest to the image should probably utilize the Schwarzschild design form.
4. The complexity of reflective imaging system design is reduced considerably when the NA is kept at or below 0.5.

Downloaded From: https://www.spiedigitallibrary.org/ebooks/ on 09 Mar 2022
Terms of Use: https://www.spiedigitallibrary.org/terms-of-use

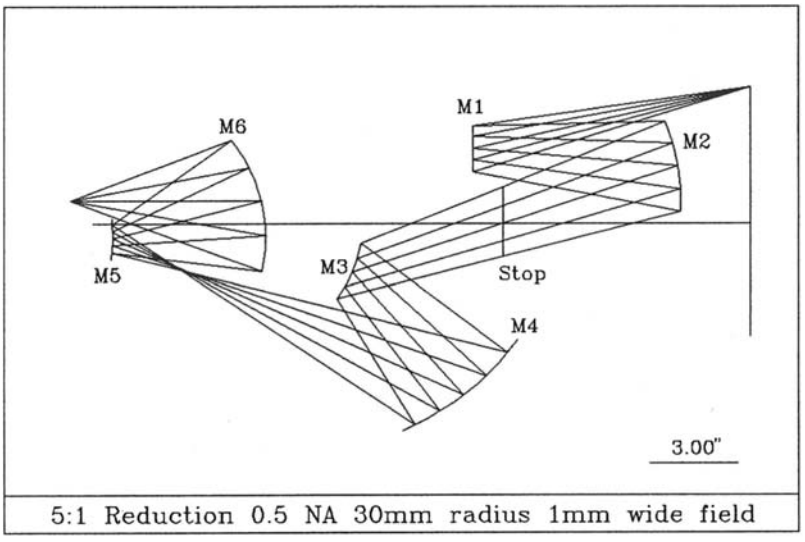

Figure 1.24 Layout for a six-mirror, 0.50-NA ring-field imaging system (reprinted from Ref. 55 with permission from OSA).

1.5.3 Fabrication and evaluation of aspherical mirrors

In the late 1980s, the surface figure and surface finish tolerances of the mirrors needed for EUV imaging systems were well beyond the capabilities of the optics industry. Since that time, a number of new and more accurate optical polishing and metrology techniques have been developed to support EUVL applications, many of which have found application in other areas of optics as well (astronomy, aerial reconnaissance, satellite communications, etc.).

Before 1990, commercial phase-measuring interferometers (PMIs) offered $\lambda/1000$ resolution and $\lambda/300$ repeatability. Absolute figure uncertainty was about $\lambda/20$ for flats up to 150 nm in diameter and no better than $\lambda/10$ or so for spheres, largely because of the quality of the reference surfaces that were available at that time. For aspheres, the absolute figure uncertainty was only about $\lambda/5$ or so, provided that the asphere could be compared to a reference sphere that had no more than a few waves of figure departure.[56] Around 1990, the highest precision obtainable for an aspherical surface was about 8 nm rms. At about that time, Tinsley Laboratories helped Ball Aerospace develop the COSTAR correction optics for the Hubble Space Telescope. This spectacular achievement increased confidence in the computer-controlled surfacing (CCS) technique that Tinsley had employed.[57] The first step in Tinsley's asphere fabrication process, illustrated in Fig. 1.25, involved precision machining with a diamond grinding wheel to produce an initial spherical surface accuracy of 1 to 2 μm, as measured with a contact-type profilometer. In the second process step, an aspherical surface meeting the required specifications was fabricated by an iterative process that employed subaperture polishing tools

Downloaded From: https://www.spiedigitallibrary.org/ebooks/ on 09 Mar 2022
Terms of Use: https://www.spiedigitallibrary.org/terms-of-use

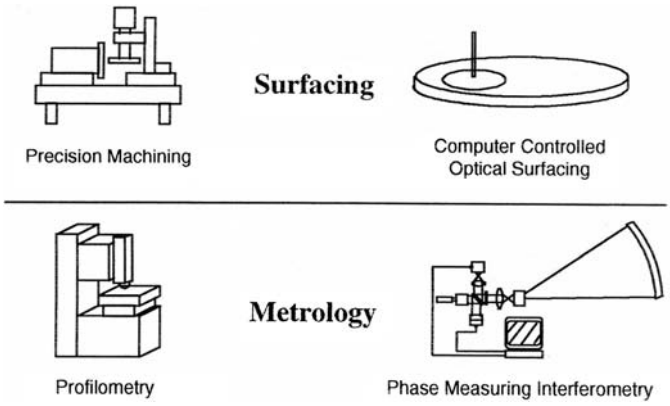

Figure 1.25 Aspheric fabrication process at Tinsley Laboratory using four core technologies (reprinted from a presentation by D. Bajuk and R. Kestner at the Second U.S.–Japan Workshop on Soft-X-Ray Optics: Technical Challenges, Lake Yamanaka, Japan, Nov. 12–14, 1996, with permission from D. Bajuk).

and a phase-measuring interferometer (PMI) to measure the shape. In 1993, Tinsley Laboratories fabricated two aspherical mirrors for a two-mirror, 0.07-NA EUV imaging system, but the accuracy was only 1.5 nm for the concave mirror and 1.8 nm for the convex one.[19] In 1995, NTT used these mirrors to replicate patterns less than 100 nm in size in an area over 10-mm square by employing a scanning mechanism for the mask and wafer.[20]

From 1991 to 1994, a precision optics fabrication study[58] was carried out by AT&T Bell Labs [with partial financial support from NIST's Acceptance Testing Procedure (ATP) program] to determine the current state of the art in aspheric fabrication and to identify promising approaches to further reduce surface figure errors. Four leading optics manufacturers were asked to fabricate an aspheric reflector substrate for an existing three-mirror EUV imaging system design. This element, called M2, was an on-axis asphere having an outside diameter of 92 mm, a clear aperture of 64 mm, and a maximum aspheric departure from the best-fit sphere of less than 2 μm. Various fabrication methods were used, including conventional artisan figuring, ion milling, and computer-controlled polishing. The metrology methods used in the fabrication and evaluation of the final part included the use of PMI with a refractive null, PMI with a computer-generated holographic (CGH) null, and a custom non-null Fizeau interferometer. The best reported measurement obtained from this study indicated that one manufacturer had achieved a figure error of ~0.6 nm rms after removal of tilt, power, and coma.[23] Subsequent advances in the fabrication and metrology of aspheres were made, and an accuracy of 0.3 nm was achieved in 2000. A record of the progress in the manufacture of aspherical mirrors at Tinsley Laboratories is shown in Fig. 1.26.

Visible-light PMI is the metrology most commonly used to provide the feedback needed for substrate figuring. Since PMI is a comparative technique,

Downloaded From: https://www.spiedigitallibrary.org/ebooks/ on 09 Mar 2022
Terms of Use: https://www.spiedigitallibrary.org/terms-of-use

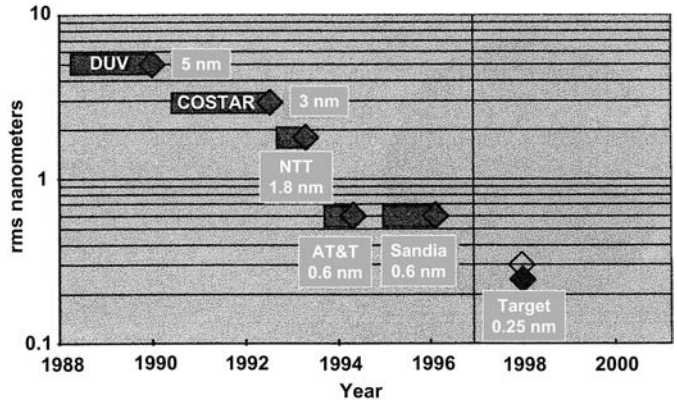

Figure 1.26 Advances in aspherical mirror fabrication at Tinsley Laboratories (reprinted from Ref. 57 with permission from D. Bajuk).

its accuracy is limited by the quality of the reference, whether it be an optical surface, a null lens, or a CGH. In the past, many methods were developed to increase the accuracy of PMI, including making a series of measurements with the reference in transposed positions, but no technique had demonstrated the accuracy needed for EUV optics development. In 1996, G. Sommargren of LLNL developed a new type of PMI that utilized a diffraction-based reference, the principle of which is illustrated in Fig. 1.27.[43] Light leaving the end of a single-mode optical fiber diffracts to form a spherical wavefront. Part of this wavefront is incident on the optic under test and is reflected back

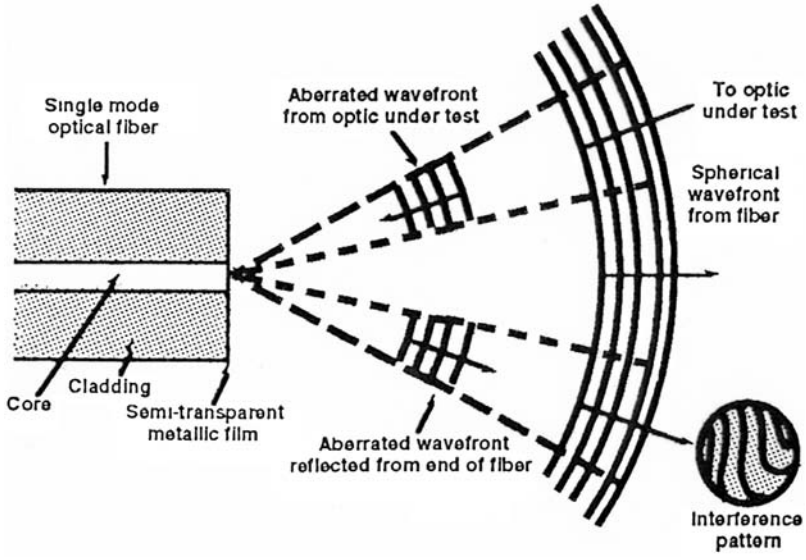

Figure 1.27 Principle of operation of the PSPDI developed by G. Sommargren (reprinted from Ref. 43 with permission from OSA).

Downloaded From: https://www.spiedigitallibrary.org/ebooks/ on 09 Mar 2022
Terms of Use: https://www.spiedigitallibrary.org/terms-of-use

toward the fiber. This aberrated wavefront reflects from a semitransparent metal film on the face of the fiber and interferes with part of the original spherical wavefront to produce an interference pattern on a CCD camera. Initial measurements of surface figure with such an interferometer showed that its measurement accuracy was better than 0.50 nm rms. Additional developments since that time have resulted in measurement accuracies approaching 0.10 nm rms.

The surface topography of mirrors for EUVL must be precisely controlled from spatial scales extending from the clear aperture of the part to the wavelength of the illumination. Surface figure data at low spatial frequencies obtained from visible light interferometry are needed to ensure diffraction-limited imaging. Surface finish data at mid- and high spatial frequencies obtained with a white-light interferometric microscope and an AFM are needed to predict the distribution of scattered radiation in the imaging system. These fine-scale fluctuations in the effective surface height are best described in statistical terms.[59] Eugene Church of the U.S. Army Armament Research, Development and Engineering Center was one of the first to point out that highly polished optical surfaces (such as x-ray mirror substrates) are frequently fractal-like,[60] with power spectra given by an inverse power law. Power spectral density (PSD) surface height data for an aspheric optic fabricated for an EUVL imaging system are shown in Fig. 1.28.[61] This aspheric substrate exhibits both a precise figure and minimal surface roughness at higher spatial frequencies. Power-law fits to the PSDs are also shown in Fig. 1.28. If most of the roughness power is concentrated at high-spatial-frequency roughness (HSFR), which is the case for highly polished optics, the scattered light will not reach the image plane; hence, it will not

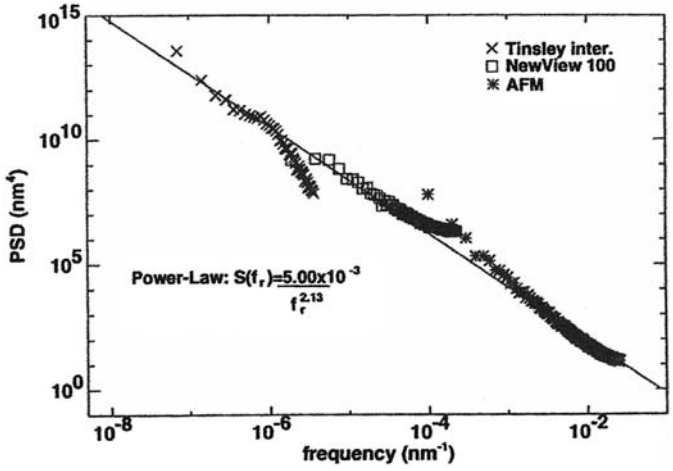

Figure 1.28 Plot of the 2D power spectral density description of the surface of a convex aspheric substrate (reprinted from Ref. 61 with permission from OSA).

Downloaded From: https://www.spiedigitallibrary.org/ebooks/ on 09 Mar 2022
Terms of Use: https://www.spiedigitallibrary.org/terms-of-use

contribute to contrast loss in the image plane, but instead will merely result in EUV reflectivity loss. On the other hand, mid-spatial-frequency roughness (MSFR) can scatter light into the image plane and will result in a corresponding loss in contrast. For this reason, MSFR and its concomitant image flare is a serious concern for EUVL, even today.

Progress in the fabrication and metrology of aspheres since the early 1990s is nothing short of miraculous. In the beginning, only low-departure aspheres could be fabricated, and these were found to be only marginally useful for two-mirror EUV imaging systems. Today, aspheres that meet the stringent requirements of a large-NA, six-mirror EUVL imaging system (<0.2 nm rms for figure, MSFR, and HSFR) are available commercially. As evidence for this, at the 5th International EUVL Symposium in Barcelona in October 2006, one aspheric mirror substrate with 0.05-nm rms figure, 0.15-nm rms MSFR, and 0.09-nm rms HSFR was reported by Carl Zeiss Inc.; another substrate with 0.18-nm rms figure, 0.135-nm rms MSFR, and 0.09-nm rms HSFR was reported by Nikon Corporation.

For high resolution, an imaging system must meet or exceed the classical diffraction limit: the total wavefront error must be less than 0.25 waves peak to valley (Rayleigh criterion) or 0.07 waves rms (Maréchal criterion). The total wavefront error in a lithographic imaging system must be smaller still (0.02 waves rms) to ensure that the residual aberrations will not result in a significant loss in DOF and CD control.[62] The total system wavefront error at each point in the image field of an EUV imaging system will depend on the surface profile and alignment of each mirror, and on the spatially varying properties of its ML reflective coating because EUV coatings behave completely differently at their design wavelength than they do in visible light. It was recognized very early on that undulator radiation would be an ideal source for EUV interferometry,[63] and several different EUV interferometers were developed.[64,65] The most accurate one was the PSPDI.[66,67] Foucault and Ronchi's testing of the alignment of EUV optics was also demonstrated using both synchrotron and laser-plasma light sources.[68,69] The early experimental work showed that functional testing at the operational wavelength, i.e., EUV interferometry, was particularly important when aligning and qualifying a new EUV imaging system.

1.5.4 Multilayer coatings and reflection masks

At normal incidence, no naturally occurring material provides more than about 1% reflectance in the EUV spectral region at wavelengths below 30 nm because the index of refraction of all materials in this region approaches unity. This fact is illustrated in the plots of the normal-incidence reflectance of Al and Ir versus wavelength[70] shown in Fig. 1.29(a). In 1972, E. Spiller of IBM showed that ML structures composed of thin layers of materials that have widely different EUV absorption values can lead to constructive interference

Downloaded From: https://www.spiedigitallibrary.org/ebooks/ on 09 Mar 2022
Terms of Use: https://www.spiedigitallibrary.org/terms-of-use

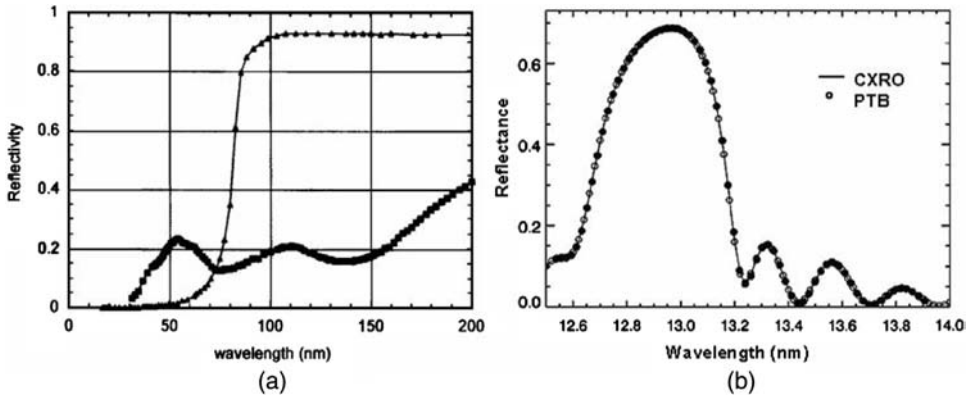

Figure 1.29 (a) Normal-incidence reflectances of clean Al (triangles) and Ir (squares) surfaces (reprinted from Ref. 70). (b) Normal-incidence reflectance of a Mo-Si ML with 40 bilayers measured at the Center for X-Ray Optics (CXRO) and at Physikalisch-Technische Bundesanstalt (PTB) (reprinted from Ref. 72).

and therefore enhanced reflection.[42] In 1981, J. Underwood and T. Barbee[8] demonstrated normal-incidence soft-x-ray imaging at a wavelength of 4.46 nm, and in 1988, A. Walker et al. obtained soft-x-ray images of the solar corona with a normal-incidence Cassegrain multilayer telescope.[71] This was the turning point for EUV optics—the point where it became clear than normal-incidence ML-coated optics offered clear advantages over the severe aberrations, small field of view, and difficulty of manufacturing grazing-incidence optics. A further key development occurred in 1985, when T. Barbee et al.[10] demonstrated that the ML combination of Mo and Si had an exceptionally high normal-incidence reflectivity at wavelengths just longer than the Si L_1 absorption edge at 12.4 nm. The normal-incidence reflectance of the best modern Mo-Si MLs now approaches 70% in a narrow band of wavelengths near 13 nm,[72] as shown in Fig. 1.29(b).

Depositing a ML film on a curved optical surface produced several practical problems. One was peeling due to the large stress in a ML film deposited on a spherical substrate with a small radius of curvature. Also, the ML was strongly affected by humidity; when it was left in air, exfoliation occurred. Moreover, the instant it was taken out of the sputtering equipment, the stress balance collapsed and pinholes formed. In addition, since initially the bottom layer was Si and the top layer was Mo, scattering occurred because of the roughening of the Mo surface due to oxidation, which reduced the contrast of replicated patterns. H. Takenaka and his colleagues at NTT solved these problems one by one; for example, they used C or Si as a capping layer to reduce scattering, and they finally managed to make a stable ML on a spherical surface. Each of the mirrors in an EUVL exposure tool must have the highest possible reflectivity at 13 nm (to maximize tool throughput), and more importantly, the central wavelength of the reflectivity must be controlled

Downloaded From: https://www.spiedigitallibrary.org/ebooks/ on 09 Mar 2022
Terms of Use: https://www.spiedigitallibrary.org/terms-of-use

to better than 0.01 nm (to maximize imaging performance). To provide diffraction-limited printing resolution, the mirror surfaces must have surface figure errors on the order of ~0.1 nm rms, and the ML coating deposition must not contribute more than 0.25 of this total error, a requirement that leads to strict requirements on the coating thickness over the entire optical surface.

Today, EUV mask blanks are similar to mask blanks for conventional optical lithography except that they are coated with 40 layer pairs of Mo (2.8-nm thick) and Si (4.1-nm thick) instead of a single layer of chrome. The 6-inch-square × 0.25-inch-thick mask substrate is a low-thermal-expansion material (LTEM) instead of quartz. A variety of technologies for patterning ML-coated reflective masks were evaluated early on, including patterned gold (Au)[11] and other absorbing overlayers,[73] reactive-ion-etched MLs,[12,73] and ion-damaged ML regions by ion implantation.[73] Among the three patterning techniques, the formation of buffer and absorber layers atop a Mo-Si ML-coated blank, like that shown in Fig. 1.30, is now preferred because it offers the most straightforward repair options. The buffer layer between the absorber and the ML reflector protects the ML from damage during absorber patterning and repair. Just as is done with chrome-on-quartz masks for optical lithography, the patterned absorber on an EUV mask can be inspected using a commercially available DUV mask inspection tool and can be repaired as needed using focused-ion or electron-beam techniques.[74] EUV masks are unlike masks for conventional optical lithography because a few hours of exposure to an EUV beam in vacuum can leave behind a carbon footprint on an EUV reflective mask, which is caused by cracking of residual hydrocarbons in the vacuum system (as shown in Fig. 1.31).[75] This suggests that an EUV mask must be able to withstand repeated cleanings.

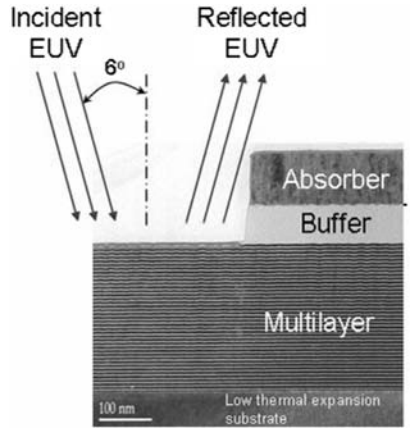

Figure 1.30 Cross-sectional transmission electron microscope (TEM) image showing EUV reflective mask architecture [reprinted from H. J. Levinson, *Principles of Lithography, 2nd Edition*, SPIE Press, Bellingham, Washington (2005)].

Downloaded From: https://www.spiedigitallibrary.org/ebooks/ on 09 Mar 2022
Terms of Use: https://www.spiedigitallibrary.org/terms-of-use

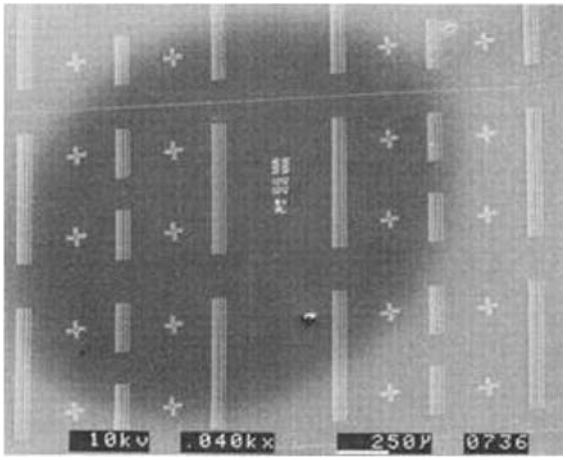

Figure 1.31 SEM image of a Mo-Si ML reflection mask after several hours of soft-x-ray irradiation. The rather poor vacuum (10^{-6} Torr) resulted in the cracking of residual hydrocarbons so that C is plated out on the mask (dark area) (reprinted from Ref. 75 with permission from OSA).

While the repair of defects that occur during the absorber patterning process is relatively straightforward, repair of defects in the ML coating or on the substrate below the reflective coating is more problematic. Examples of these phase defects were found during EUV printing experiments as early as 1992, in which a long diagonal feature was printed on the wafer using a mask that had no obvious corresponding absorber feature.[74] Subsequent examination of the mask revealed a 2.7-nm-deep, 8-μm-wide depression on the substrate beneath the ML coating. Since the depth of this depression was nearly the 0.25-nm wavelength depth needed for perfect cancellation of the reflected waves, its presence resulted in an unexpected, high-contrast feature in the aerial image. The fact that this feature was not noticed prior to resist printing pointed to the need for at-wavelength inspection to qualify EUV blanks. The first systematic observation of the effect of substrate defects in EUVL masks on resist images was carried out by K. Nguyen et al.[76–78] in 1993. That study employed a 5:1 reduction reflection mask with programmed substrate defects of various shapes and sizes. The defects, patterned using e-beam lithography and lift-off, were 20-nm high, and their widths on the mask ranged from 2 to 0.2 μm. The reflective ML coating consisted of 30 Mo-Si bilayers with a d spacing of 7.25 nm; the reflection peak was at a 14.0-nm wavelength. The absorber patterns consisted of a repeating series of 10-, 5-, 2-, and 1-μm lines and spaces in evaporated Au that was 150-nm thick. An optical phase contrast microscope image of the mask, showing the 150-nm-thick absorber lines in the foreground and the 20-nm-thick programmed defects in the background, is shown in Fig. 1.32(a). A scanning electron microscopy (SEM) image of the programmed defect mask in PMMA

Downloaded From: https://www.spiedigitallibrary.org/ebooks/ on 09 Mar 2022
Terms of Use: https://www.spiedigitallibrary.org/terms-of-use

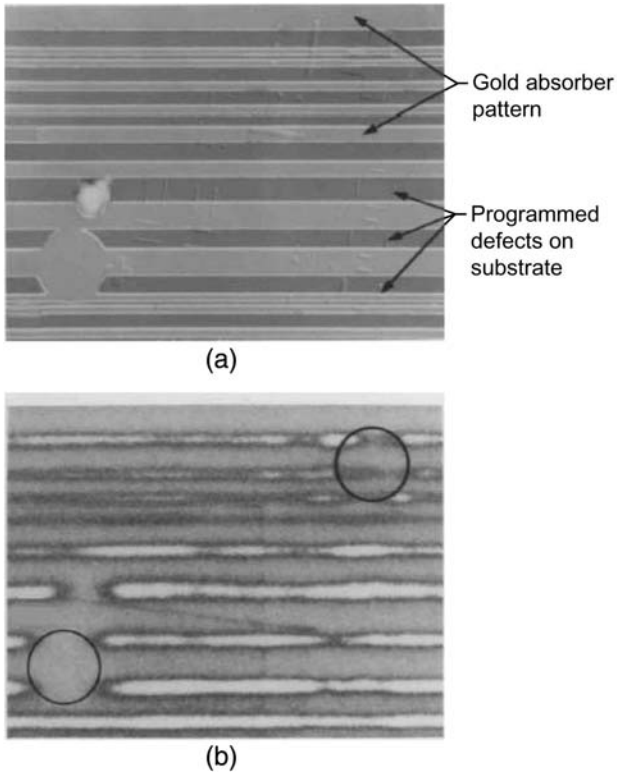

Figure 1.32 (a) Optical phase contrast microscope image of a programmed defect mask. (b) PMMA resist SEM image of the programmed defect mask exposed using the two-mirror EUV aspheric system at the Photon Factory in Tsukuba, Japan (reprinted from Ref. 76 with permission from OSA).

resist exposed using the two-mirror EUV imaging system (resolution: 0.15 μm) at the Photon Factory in Tsukuba, Japan is shown in Fig. 1.32(b). The circled areas show the effects of two gross defects, one in the absorber layer and the other on the substrate, that were used as markers for the location and observation of the smaller programmed defects. Because defects in and under the ML reflective coating were found to be such a serious issue, a project was launched in 1995 to design and build a deposition system specifically to produce low-defect EUV blanks. The system utilized an ion-beam sputter-deposition technique to deposit complete, 81-layer-high Mo-Si MLs on 150-mm diameter (100)-oriented Si substrates.[79] This deposition system was subsequently shown to produce MLs with five orders of magnitude fewer particle defects than typical ML coatings, with the best samples achieving defect densities of $2 \times 10^{-2}/\text{cm}^2$.

The early work on EUV ML coatings resulted in the selection of Mo-Si as the reflective coating of choice as well as the development of several different deposition techniques to control the ML coating thickness on curved mirror

Downloaded From: https://www.spiedigitallibrary.org/ebooks/ on 09 Mar 2022
Terms of Use: https://www.spiedigitallibrary.org/terms-of-use

substrates. The early work on EUV reflection masks identified the mask architecture that has become standard today, recognized the importance of carbon contamination on an EUV mask, observed and systematically studied blank substrate phase defects, suggested that at-wavelength inspection of EUV mask blanks might be needed, and developed an ion-beam-sputter deposition system to deposit low-defect-density Mo-Si MLs on Si wafers—the forerunner to the Veeco low-defect-deposition ML tool in use today at International SEMATECH's Mask Blank Development Center in Albany, New York and at other mask shops in Japan and Europe.

1.5.5 EUV resist development

In 1989, in some of the earliest work on candidate soft-x-ray resist materials, G. Kubiak et al. of SNL characterized the near-edge x-ray absorption fine-structure spectra, exposure sensitivity, contrast, and post-exposure processing of selected polysilane resists exposed at photon energies close to the Si $L_{2,3}$ absorption edge (100 eV).[80] They found sensitivities in the range of 600 to 3000 mJ/cm^2 and contrasts in the range from 0.5 to 1.4, depending on the polysilane side chain. In 1990, D. Berreman et al. of AT&T reported on the soft-x-ray sensitivity and contrast of three e-beam resists: polybutene-1 sulfone (PBS), 2,2,2-trifluoroethyl α-chloro-acrylate (EBR-9), and PMMA.[81] By incorporating thin imaging layers of these materials into a trilayer resist scheme, D. Berreman et al. succeeded in exposing, developing, and transferring features as small as 0.2 μm into Si using undulator radiation at a $\sim$36-nm wavelength. In 1990, G. Taylor et al. of AT&T pointed out that the absorption of resist materials is substantially higher (10 to 100$\times$ higher) in the soft-x-ray region than in the visible and DUV regions because soft-x-ray absorption results from the atomic nature of the excitation rather than from the making or breaking of molecular bonds.[82] G. Taylor et al. published the absorption parameters for 10 polymers, representative of well-known resist materials, derived from the atomic scattering factors given in the Henke tables.[83] In 1991, W. Mansfield et al. of AT&T studied the performance of PMMA at 37.5- and 14-nm exposure wavelengths, and presented measurements of thickness removed versus exposure dose, lithographic sensitivity, and the exposure-independent absorption coefficient; they found with both simulation and experiment that the smaller absorption coefficient in PMMA at 14 nm caused the profile of the minimum features to be of significantly higher quality.[84] W. Mansfield et al. also concluded that the absorption coefficient of PMMA is the primary determinant of sensitivity and contrast in the soft-x-ray region. In 1993, A. MacDowell et al. of AT&T attempted to circumvent the resist absorption problem by using a surface-imaging resist process with an organosilane monolayer film that was first exposed to soft-x-ray radiation, then selectively metalized using lithium salt of ethylenediamine (LiEDA) grafting chemistry, and finally nickel (Ni) plated.[85]

Downloaded From: https://www.spiedigitallibrary.org/ebooks/ on 09 Mar 2022
Terms of Use: https://www.spiedigitallibrary.org/terms-of-use

Using this process, A. MacDowell et al. managed to demonstrate resolution ≤ 0.25 μm at an exposure dose of 50-mJ/cm^2 but found that the printed features were exceedingly grainy, probably because of a nonoptimal Ni-plating process. In 1994, O. Wood et al. showed, via resist printing experiments in positive-tone PMMA and in negative-tone AZ PN114 at three different exposure wavelengths, that high resist absorption leads to unsatisfactory sidewall profiles except at the shortest wavelength (19 deg at 37.5 nm, 65 deg at 13.9 nm, and 83 deg at 6.8 nm).[46] O. Wood et al. were concerned that sloping sidewalls would result in poor CD control and pointed out that using an illumination wavelength between 6.8 nm and 13.9 nm would be advantageous.

In 1996, D. Wheeler et al. of SNL reviewed the sensitivity, resolution, optical density, and etch selectivity of the four most promising EUV resist schemes that had been studied up to that time: trilayer resists (a thin imaging layer on top of a pattern transfer layer on top of planarizing and processing layers), bilayer resists (solution-developed resists containing inorganic materials to enhance their etch resistance), plasma-deposited organo-metallic resists, and silylated resists.[86] They concluded that none of the candidate resist schemes would be able to meet the requirements of the first pilot production exposure tools: resolution better than 40 nm, sidewall angle > 88 deg, linearity between ±5% and 10%, line-edge roughness (LER) and CD control no greater than 5 nm, and sensitivity better than 5 mJ/cm^2. Given the cost and complexity of developing a new resist and using history as a guide, it is not surprising that, even after 10 additional years of development, the availability of an EUV resist that can simultaneously meet the resolution, LER, and sensitivity requirements of an EUVL pilot production tool continues to remain near the top of the EUV critical issue list.

1.5.6 EUV light source development

Although the development of EUVL light sources has been covered in depth in a recently published technical volume,[87] the light sources employed in the early years of EUVL development—synchrotron radiation from electron storage rings and laser-produced plasmas (LPPs)—are briefly described in this section. The key issues with EUV sources, during the early years and today, were their low conversion efficiency and requirement for extensive debris mitigation.

In 1993, J. Murphy et al. of Brookhaven National Laboratory (BNL) discussed the design requirements for a compact 600-MeV electron storage ring that could be used as a source for EUVL and deliver in excess of 1 W of 13-nm light in a 2% bandwidth.[88] Based on the assumptions (unrealistic given today's reality) that an EUVL exposure tool would employ a three-mirror imaging system and would only be required to print 15 6-inch-diameter wafers per hour (wph) using a resist with a sensitivity of ~5 mJ/cm^2, it was shown that a compact synchrotron source would be able to supply the flux needed for

Downloaded From: https://www.spiedigitallibrary.org/ebooks/ on 09 Mar 2022
Terms of Use: https://www.spiedigitallibrary.org/terms-of-use

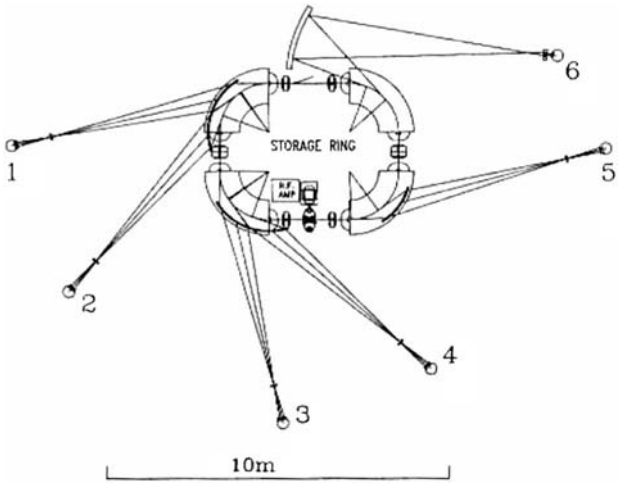

Figure 1.33 Schematic plan view of a 600-MeV storage ring designed at BNL together with six EUVL cameras (reprinted from Ref. 88 with permission from OSA).

six EUVL exposure tools. The floor plan of a small 600-MeV storage ring that can supply flux to six EUV exposure tools is shown in Fig. 1.33; the figure does not show the 100-MeV electron linear accelerator that serves as the electron source because it is assumed to be located in a subfab. While it is now generally agreed that a synchrotron light source cannot provide the average power needed for a modern commercial EUVL exposure tool, synchrotron light sources continue to play an important role in actinic defect inspection of EUV reticle blanks, actinic wavefront metrology of EUV imaging systems, advanced EUV resist screening, and accelerated life testing of oxidation-resistant coatings for EUV optics.

In the early 1990s, a number of experimental and theoretical studies showed that LPP sources could achieve CEs from laser energy to EUV energy in a ~2% bandwidth near a 13-nm wavelength of ~1% to 2%, depending on target material, laser intensity, laser pulse width, and laser wavelength.[89–91] For example, Fig. 1.34 shows the EUV CE for an LPP source that employed a frequency-doubled Nd:YAG (532 nm) laser as a function of the atomic number of the target material, from a paper by R. Kauffman et al. of LLNL.[91] The CE is highest for tin (Sn) and antimony (Sb) targets and is also high for high-Z targets such as Au and lead (Pb). With a Sn target, a CE using 0.53-μm laser light was found to increase rapidly with laser intensity until it peaked at $\sim 2 \times 10^{11}$ W/cm^2 and then fell off slowly at higher intensities.

In 1991, the first EUV imaging system at SNL utilized a LPP source that employed a KrF (248-nm) laser and a Au-drum target.[15] It was immediately apparent that debris ejected from the source posed a major threat to the lifetime of nearby condenser mirrors due to (1) deposition of debris (particulates) from the source hardware, (2) deposition of atomic vapor from

Downloaded From: https://www.spiedigitallibrary.org/ebooks/ on 09 Mar 2022
Terms of Use: https://www.spiedigitallibrary.org/terms-of-use

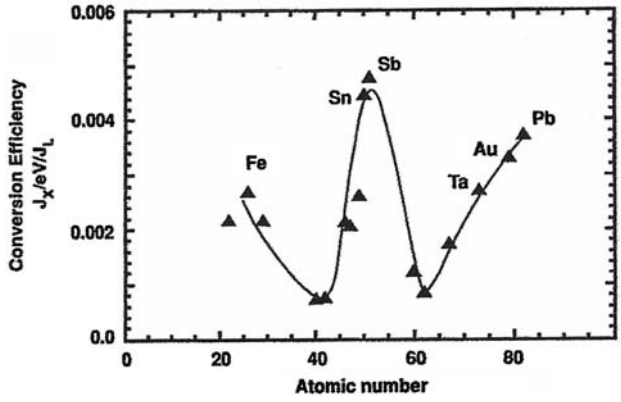

Figure 1.34 Dependence of the LPP CE at 13 nm on the atomic number of the target material (reprinted from Ref. 91 with permission from OSA).

the source plasma, and (3) erosion by high-energy ions. Since that time, a great deal of effort has been put into designing and testing a variety of debris-mitigation schemes, including placing a low-pressure inert gas in the source vacuum chamber to decelerate particles from the source,[92] positioning a gas jet in front of the components to be protected,[93] using a fast mechanical shutter or rotating mechanical chopper to block debris that arrives long after the EUV radiation,[94] and utilizing an electrostatic repeller field.[95] The deceleration of source particles using a gas jet [typically of argon (Ar) and helium (He)] and a repeller field is such that the average fast-particle energy can be decreased from keV levels to near 100 eV. Unfortunately, even this lower-energy debris must be eliminated, especially if it is an atomic vapor such as Sn, since a ~1-nm-thick coating of Sn on the collector optics results in a 1% drop in EUV reflectance, so it must be removed periodically using an *in situ* cleaning process. The use of a gas flow and a rotating mechanical chopper was found to reduce the rate of debris deposition from a metal target by a factor of about 1000; however, no known combination of debris-mitigation techniques was identified that could provide the degree of cleanliness needed for a commercial system, and today the effectiveness of the debris-mitigation system still places an upper limit on the collector life.

The only alternative to debris mitigation is to minimize debris production using a so-called mass-limited target.[96] The basic idea behind a mass-limited target is to supply only the amount of target material that is needed for efficient production of EUV radiation. When a mass-limited target is exposed to the high-intensity central part of a beam from a pulsed laser, a very large fraction of the target atoms are highly ionized and emit EUV radiation, the net effect being a significant reduction in the number of ejected atoms, ions, and particles. The most promising method of producing a mass-limited target is to introduce a stream of tiny droplets into the laser focus.[97] A number of mass-limited target ideas have been tested experimentally, including thin

Downloaded From: https://www.spiedigitallibrary.org/ebooks/ on 09 Mar 2022
Terms of Use: https://www.spiedigitallibrary.org/terms-of-use

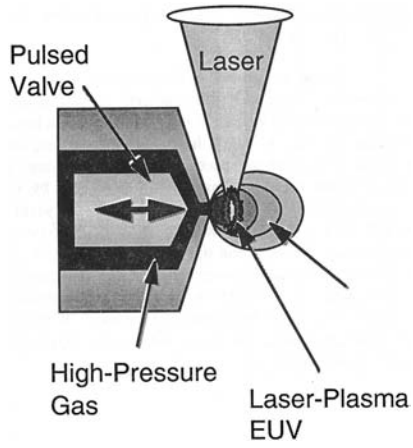

Figure 1.35 Configuration of a laser plasma EUV source at SNL based on a supersonic Xe cluster jet target (reprinted from Ref. 102 with permission from OSA).

metal films on Mylar tape,[98] gas puff targets,[99] liquid droplet targets,[100] cryogenic pellet targets,[101] and supersonic gas cluster targets.[102] In 1996, G. Kubiak et al. of SNL developed a system that employed a target consisting of high-density gas clusters.[102] A schematic diagram of a supersonic xenon (Xe) cluster source is shown in Fig. 1.35. Early CE measurements showed that an LPP source based on the Xe cluster jet was approximately 58% as efficient at 13.5 nm as sources based on a solid Au target; they were also very close to the values for solid copper (Cu), Mo, and W targets. Furthermore, when a Xe jet is irradiated, it produces no solid debris; and because Xe has a high vapor pressure at room temperature, it does not condense on nearby mirrors. The reflectance of ML-coated condenser mirrors placed near the Xe jet EUV source was found to be reduced by only 14% after 1.4×10^8 plasma pulses, an improvement of more than 100,000 fold over the first solid Au target EUV source. A progress record of the condenser mirror lifetimes for LPP EUV sources between 1991 and 1999 is shown in Fig. 1.36.[103] The lifetime of EUV source collector optics is rated today as one of the most worrisome EUV critical issues.

1.6 EUVL Conferences

As noted in Section 1.2, the first conference on Soft-X-Ray Projection Lithography was held in Monterey, California, on April 10–12, 1991. Jeff Bokor of AT&T Bell Labs and John Bruning of GCA Tropel helped organize the meeting, which was sponsored by the OSA and supported by the U.S. Air Force Office of Scientific Research. Two additional OSA topical meetings with the same name were held in the same city in 1992 and 1993. Two OSA Topical Meetings on Extreme Ultraviolet Lithography were held again in

Downloaded From: https://www.spiedigitallibrary.org/ebooks/ on 09 Mar 2022
Terms of Use: https://www.spiedigitallibrary.org/terms-of-use

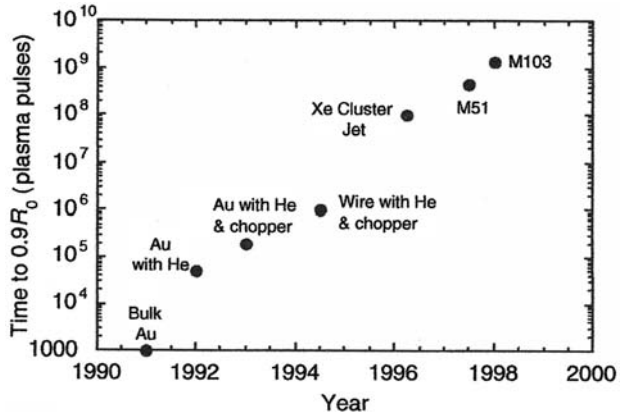

Figure 1.36 Progress on EUVL condenser mirror lifetime, expressed as the number of plasma pulses required to reduce the original mirror reflectivity by 10% (reprinted from Ref. 103).

Monterey in 1994, and in Boston, in 1996. A Workshop on At-Wavelength Testing of Soft-X-ray Projection Optics was held in Gaithersburg, Massachusetts, on June 22, 1992. John Bjorkholm and Mark Himel of AT&T and Tom Lucatorto of the National Institute of Standards and Technology (NIST) organized the workshop, which was sponsored by NIST and AT&T Bell Labs and supported by the U.S. Department of Commerce Advanced Technology Program and the U.S. DARPA Microelectronics Technology Office. A joint U.S.–Japan Workshop on Soft-X-ray Projection Lithography, organized by Prof. Takesi Namioka of Tohoku University, was held in Lake Yamanaka, Japan on October 27–29, 1993. An International Workshop on EUV Lithography was held in Oberkochen, Germany on November 14–15, 1995, where the presentations were collected and distributed to the participants but not published. A second U.S.–Japan Workshop on Soft-X-ray Optics: Technical Challenges was held in Lake Yamanaka, Japan on November 12–14, 1996. This meeting was chaired by M. Ginter of the University of Maryland, M. Peckerar of the U.S. Naval Research Laboratory, H. Kinoshita of Himeji Institute of Technology, and M. Yamamoto of Tohoku University, and it was sponsored by the ONR Asian Office and the Japan Society for Precision Engineering (JSPE). Tables 1.1 and 1.2 feature a selection of technical journals and conference proceedings that contain the majority of papers describing the developments in EUV (SXPL) lithography from the beginning through 1996.

1.7 Summary

According to the latest *International Technology Roadmap for Semiconductors* (ITRS), EUVL will be used to fabricate large-scale integrations (LSIs) at the 32-nm half-pitch device node starting in 2011. To achieve that goal, the trial

Downloaded From: https://www.spiedigitallibrary.org/ebooks/ on 09 Mar 2022
Terms of Use: https://www.spiedigitallibrary.org/terms-of-use

production of 32-nm LSIs using an EUVL beta-level exposure tool must be accomplished by 2009. Several EUVL exposure tools with 0.3-NA imaging systems and exposure areas less than 1 mm in diameter are currently available. These tools provide a resolution of 30 nm or better in resist materials, although a better than 20-nm resolution should be possible based on the performance of the optics. The most-important critical issue at the present time is the development of an EUV light source that can support a 100 wafer/hour throughput. Since the specification of the EUV imaging system has already been decided, the problem is determining how to boost the intensity of an EUV light source from ~6 W (the maximum power today) to 115 W (the power required for 100 wafer/hour throughput, assuming 5-mJ/cm^2 resist sensitivity) without a concomitant increase in debris production. Another critical issue is the development of a resist with a LER of 2 nm or less because LER influences the width of an exposed pattern. For resists, there appears to be a tradeoff between LER and sensitivity; it is important to find a material with a small LER that requires a small exposure dose. Unlike a conventional optical imaging system, an EUVL imaging system operates in reflection, so increasing the number of mirrors in the system rapidly decreases its throughput. All possibilities for improving the exposure tool, light source, and resist must be investigated with the goal of mitigating the severity of the specifications so that a practical EUVL exposure tool can be realized as quickly as possible.

In conclusion, EUVL research and development over the past 20 years has led to a number of significant breakthroughs. The drive to develop a practical EUVL technology spread to both hemispheres in the latter half of the 1980s; we can now look back at the history of the early development work with a wonderful sense of accomplishment. Many lithographic technologies have been developed and screened during the last 20 years. Several critical problems still remain, including light-source power and reliability; mask defectivity and flatness; and resist resolution, sensitivity, and LER. However, it now appears that solutions can be found because the two biggest obstacles—the fabrication of aspherical mirrors and of reflective MLs—have been overcome.

The first international conference with "EUVL" in the title was held near Mt. Fuji in 1993. In his opening address at that conference, Dr. Kinoshita said, "As long as we do not lose the desire that has sprung from within us, technology will steadily advance from the micro to the nano to the pico." The many improvements that have been made during the course of EUVL development, particularly in the fabrication of aspherical mirrors and reflective MLs, have already validated Dr. Kinoshita's 1993 prediction.

Acknowledgments

So many scientists and engineers were involved in early EUVL development that an all-inclusive listing of their names and institutions is probably not

Downloaded From: https://www.spiedigitallibrary.org/ebooks/ on 09 Mar 2022
Terms of Use: https://www.spiedigitallibrary.org/terms-of-use

possible. Even so, the authors gratefully acknowledge Eberhard Spiller (IBM) and Troy Barbee (Stanford University) for the development of reflective ML coatings, Dan Bajuk and Bob Kestner (Tinsley Laboratories) for the development of precision aspheric surfaces, and Gary Sommargren (LLNL) for the development of the PSPDI. Without these seminal contributions, EUVL would not be possible. The authors would also like to acknowledge the contributions of the more than 300 individuals listed below.

In Japan, important contributions were made by the following:
ETL: Kouichi Hoh and N. Tanino.
Hitachi: Masaaki Ito, Souichi Katagiri, Shigeo Moriyama, Taro Ogawa, Hiroaki Oizumi, Eiichi Seya, Tsuneo Terasawa, and Hiromasa Yamanashi.
Nikon: Noriaki Kandaka, Hiroyuki Kondo, Kiyoto Mashima, Katsuhiko Murakami, Hiroshi Nagata, Masayuki Ohtani, Tetsuya Oshino, Sumito Shimizu, K. Ilzuka, and Shoichiro Yishida.
NTT: Tsuneyuki Haga, Yoshikazu Ishii, Kenji Kurihara, Tomoaki Kawamura, Hiroo Kinoshita, Tsutomu Mizota, Hisataka Takenaka.
Osaka University: Hiroaki Aritome, Hiroyuki Diado, M. Kado, K. A. Tanaka, and K. Yamashita.
SORTEC: Nobufumi Atoda, Yukihiko Maejima, Tushihiko Tanaka, Takeo Watanabe, and Yoshio Yamashita.
Tohoku University: Takeshi Namioka, Masaki Yamamoto, and Mihiro Yanagihara.
Others: Yasuaki Fukuda (Canon), Shigetaro Ogura (Kobe Design University), Kiyoshi Fujii (NEC), Izumi Kaytaoka (JAE), and Souichi Inoue (Toshiba).

In the U.S., important contributions were made by the following:
AT&T: Dwight Berreman, John Bjorkholm, Jeff Bokor, Craig Boyce, Bill Brinkman, Kevin Dreyer, Raissa D'Souza, Kathy Early, Lou Eichner, Linus Fetter, Rick Freeman, Joe Griffith, Lloyd Harriott, Marc Himel, R. Hull, Rich Hutton, D. Y. Jeon, Tanya Jewell, Bruno La Fontaine, Alex Liddle, Alastair MacDowell, Bill Mansfield, Peter Mulgrew, Megan O'Malley, John Pastalan, Eric Raab, Joe Russo, Chuck Shank, Z. Shen, Bill Silfvast, Steve Spector, Susan Stein, Leo Szeto, Zhengquan Tan, Don Taylor, Garry Taylor, Greg Timp, Don Tennant, Sheila Vaidya, Warren Waskiewicz, Don White, David Windt, and Obert Wood.
Grumman: Vincent Calia, A. Grillo, Robert Gutowski, Jayaram Krishnaswamy, Ira Lehrman, and Alan Todd.
IBM: Norman Bobroff, Doug Goodman, Alan Rosenbluth, and Eberhard Spiller.
Los Alamos National Laboratory (LANL): J. Abdallah, B. Carlsten, R. D. Fulton, J. C. Goldstein, M. E. Jones, D. P. Kilcrease, J. M. Kinross-Wright, S. H. Kong, Brian Newnam, D. C. Nguyen, D. M. Oro, D. S. Prono, J. K. Studebaker, R. Sturgess, and Vriddhachalam Viswanathan.

Downloaded From: https://www.spiedigitallibrary.org/ebooks/ on 09 Mar 2022
Terms of Use: https://www.spiedigitallibrary.org/terms-of-use

LBNL: Erik Anderson, Dave Attwood, Raul Beguiristain, Daniel Chen, Paul Denham, Ken Goldberg, Ronald Gronsky, Eric Gullikson, Malcolm Howells, Keith Jackson, Chantal Khan-Malek, Masato Koike, Jeff Kortright, Hector Medecki, Tai Nguyen, Regina Soufli, Jim Underwood, and Max Wei.
LLNL: Craig Alford, Sherry Baker, Troy Barbee, Ray Beach, Rich Bionta, M. J. Carey, Nat Ceglio, D. Celliers, Charles Cerjan, Henry Chapman, Dino Ciarlo, Simon Cohen, T. P. Daly, Brent Dane, Louis DaSilva, K. W. DeLong, B. L. Fix, Dave Gaines, Jim Glaze, Lloyd Hackel, H. W. Hauschildt, Andy Hawryluk, Mark Hermann, John Honig, Ralph Hostetler, Don Kania, Robert Kauffman, Pat Kearney, Rick Levesque, Dan Makowiecki, Claud Montcalm, T. Orzechowski, Don Phillion, Robert Rosen, Lynn Seppala, Ken Skulina, Gary Sommargren, James Spallas, Ronnie Spitzer, Dan Stearns, A. Stith, Don Sweeney, John Taylor, Pat Troccolo, Steve Vernon, F. W. Weber, and Luis Zapata.
NIST: Charles Clark, Dave Ederer, Tyler Estler, Chris Evans, J. Fu, Tom Lucatorto, T. McWaid, Bob Parks, Charlie Tarrio, Ted Vorburger, and Rich Watts.
Ovonics: Georgy Gutman, John Keem, Kevin Parker, and Jim Wood.
SNL: Richard Arling, Kurt Berger, Luis Bernardez, S. R. Birtola, L. A. Brown, Greg Cardinale, Weng Chow, Bruce Draper, Archie Farnsworth, Denis Grady, Robert Gutowski, R. S. Goeke, Steve Haney, Craig Henderson, Tom Hunter, Robert Hwang, Paul Jin, A. A. Jojola, P. N. Keifer, Ron Kensek, Eric Kneedler, Stewart Kohler, Kevin Krenz, Glenn Kubiak, Paul Mahl, Mike Malinowski, C. C. Neumann, Rod Nissen, Rick Olson, Duane Outka, Phillip Paul, Yon Perras, Avi Ray-Chaudhuri, Paul Resnick, Paul Rockett, Randal Schmitt, Michelle Schulberg, Rich Shagam, Tony Smith, Rick Stulen, Bill Sweatt, Dan Tichenor, Tim Trucano, Ruben Urenda, Mial Warren, R. D. Watson, J. W. Weed, L. I. Weingarten, J. R. Wendt, Dave Wheeler, G. A. Wilkerson, and John Wronosky.
University of California, Berkeley: Charlie Fields, H. Fujioka, Ken Gustafson, Chenming Hu, Derek Lee, Bernice Lum, Andy Neureuther, David Newmark, Khanh Nguyen, Bill Oldham, Edita Tejnil, and Alfred Wong.
University of Central Florida/CREOL: Kenneth Beck, Howard Bender, C. DePriest, Ann Marie Eligon, Kai Gabel, Art Hanzo, Jim Harvey, Fing Jin, M. A. Klosner, Donna O'Connell, Martin Richardson, G. Shimkaveg, Bill Silfvast, Jerry Thorpe, D. Torres, and Victor Yanovsky.
Veeco Instruments: B. Druz, A. V. Hayes, H. Hedge, E. Osten, and R. Rajan.

Contributions were also made by Bill Arnold (**AMD**), George Lawrence (**Applied Optics Research**), Yuanda Cheng (**Arizona State University**), Jim Murphy and Peter Takacs (**BNL**), M. Isaacson (**Cornell University**), John Bruning and Chunsheng Huang (**GCA Tropel**), John Carruthers and Patrick Troccolo (**Intel**), Michael Powers and Harry Shields (**JAMAR**), Nick Economou

Downloaded From: https://www.spiedigitallibrary.org/ebooks/ on 09 Mar 2022
Terms of Use: https://www.spiedigitallibrary.org/terms-of-use

and Diane Stewart (**Micrion**), Jeff Calvert and Tim Koloski (**NRL**), Paul Fisher and Michael Gouge (**Oak Ridge National Laboratory**), Mike Rodgers and Kevin Thompson (**Optical Research Associates**), Michael Kassner and Michael Viliardos (**Oregon State University**), Stan Mrowka (**Oxford Research Group**), Malcolm McGeoch (**PLEX**), Mitch Ruda (**Ruda Associates**), Karen Brown and Gil Shelden (**SEMATECH**), Dave Shafer (**Shafer Optical Design**), R. Browning and Fabian Pease (**Stanford University**), Dave Williamson and Frits Zernike (**SVG Lithography**), Dan Bajuk and Bob Kestner (**Tinsley Laboratories**), David Shealy and Cheng Wang (**University of Alabama**), Rajiv Singh (**University of Florida**), Dave Markle (**Ultratech**), Gene Church (**U.S. ARDEC**), Franco Cerrina and Waiman Ng (**University of Wisconsin-Madison**).

In Europe, important contributions were made by the following:
DIMES, Delft: Nigel Duddles, J. Romijn, B. A. C. Rousseeuw, and E. W. J. van der Drift.
FOM: Fred Bijkerk, Eric Louis, Alexander Mitrofanov, Eric Puik, R. Schlatmann, Leonid Shmaenok, Marnix van der Wiel, A. van Honk, Gert van Dorssen, Y. Y. Platonova, A. P. Shevelko, Jan Verhoeven, Harm-Jan Voorma, and H. Zeijelmaker.
Lambda Physik: R. Desor, Helmut Frowein, Bernard Nikolaus, and Frank Voss.
Lund Institute of Technology: Hans Hertz, Lars Malmqvist, and Lars Rymell.
Philips: Joseph Braat.
PTB-Berlin: Detlef Fuchs, Michael Krumrey, Frank Scholze, and Gehard Ulm.

References

1. H. Kinoshita, T. Kaneko, H. Takei, N. Takeuchi, and S. Ishihara, "Study on x-ray reduction projection lithography," presented at the 47th Autumn Meeting of the Japan Society of Applied Physics, Paper No. 28-ZF-15 (1986).
2. T. Namioka, "Current research activities in the field of multilayers for soft x-rays in Japan," *Revue Phys. Appl.* **23**, 1711–1726 (1988).
3. W. T. Silfvast and O. R. Wood, II, "Tenth micron lithography with a 10 Hz 37.2 nm sodium laser," *Microelectron. Eng.* **8**, 3–11 (1988).
4. A. M. Hawryluk and L. G. Seppala, "Soft x-ray projection lithography using an x-ray reduction camera," *J. Vac. Sci. Technol. B* **6**, 2162–2166 (1988).
5. J. Bjorkholm, J. Bokor, L. Eichner, R. R. Freeman, J. Gregus, T. E. Jewell, W. M. Mansfield, A. A. MacDowell, E. L. Raab, W. T. Silfvast, L. H. Szeto, D. M. Tennant, W. K. Waskiewicz, D. L. White, D. L. Windt, O. R. Wood, II, and J. H. Bruning, "Reduction imaging using

Downloaded From: https://www.spiedigitallibrary.org/ebooks/ on 09 Mar 2022
Terms of Use: https://www.spiedigitallibrary.org/terms-of-use

multilayer coated optics: printing of features smaller than 0.1 microns," *J. Vac. Sci. Technol. B* **8**, 1509–1513 (1990).
6. J. Henry, E. Spiller, and M. Weisskopf, "Imaging performance of a normal incidence x-ray telescope measured at 0.18 KeV," *Proc. SPIE* **316**, 166–168 (1981) [doi: 10.1117/12.933150].
7. I. Lovas, W. Stanty, E. Spiller, R. Tibbetts, and J. Wilczynski, "Design and assembly of a high resolution Schwarzschild microscope for soft-x-rays," *Proc. SPIE* **316**, 90–97 (1981) [doi: 10.1117/12.933138].
8. J. H. Underwood and T. W. Barbee, Jr., "Soft x-ray imaging with a normal incidence mirror," *Nature* **294**, 429–431 (1981).
9. K. Takei and Y. Maeda, "Preparation of multi-layered tungsten-carbon films by ion beam sputtering," *Jpn. J. Appl. Phys.* **24**, 1366–1367 (1985).
10. T. W. Barbee, Jr., S. Mrowka, and M. Hettrick, "Molybedenum-silicon multilayer mirrors for the extreme ultraviolet," *Appl. Opt.* **24**, 883–886 (1985).
11. A. Hawryluk, N. Ceglio, and D. Gaines, "Reflection mask technologies for x-ray projection lithography," *J. Vac. Sci. Technol. B* **7**, 1702–1704 (1989).
12. H. Kinoshita, K. Kurihara, Y. Ishii, and Y. Torii, "Soft-x-ray reduction lithography using multilayer mirrors," *J. Vac. Sci. Technol. B* **7**, 1648–1651 (1989).
13. D. W. Berreman, J. E. Bjorkholm, L. Eichner, R. R. Freeman, T. E. Jewell, W. M. Mansfield, A. A. MacDowell, M. L. O'Malley, E. L. Raab, W. T. Silfvast, L. H. Szeto, D. M. Tennant, W. K. Waskiewicz, D. L. White, D. L. Windt, O. R. Wood, II, and J. H. Bruning, "Soft-x-ray projection lithograph: printing of 0.20-μm features using 20:1 reduction," *Opt. Lett.* **15**, 529–531 (1990).
14. A. MacDowell, J. E. Bjorkholm, J. Bokor, L. Eichner, R. R. Freeman, W. M. Mansfield, J. Pastalan, L. H. Szeto, D. M. Tennant, O. R. Wood, II, T. E. Jewell, W. K. Waskiewicz, D. L. White, D. L. Windt, W. T. Silfvast, and F. Zernike, "Soft x-ray projection lithography using a 1:1 ring field optical system," *J. Vac. Sci. Technol. B* **9**, 3193–3197 (1991).
15. G. D. Kubiak, D. A. Tichenor, M. E. Malinowski, R. H. Stulen, S. J. Haney, K. W. Berger, L. A. Brown, J. E. Bjorkholm, R. R. Freeman, W. M. Mansfield, D. M. Tennant, O. R. Wood, II, J. Bokor, T. E. Jewell, D. L. White, D. L. Windt, and W. K. Waskiewicz, "Diffraction-limited soft-X-ray projection lithography with a laser plasma source," *J. Vac. Sci. Technol. B* **9**, 3184–3188 (1991).
16. H. Kinoshita, K. Kurihara, T. Mizota, T. Haga, H. Takenaka, and Y. Ishii, "Soft-x-ray reduction lithography using a reflection mask," in *OSA Proceedings on Soft-X-Ray Projection Lithography 1991*, Vol. **12**, pp. 11–15 (1991).

Downloaded From: https://www.spiedigitallibrary.org/ebooks/ on 09 Mar 2022
Terms of Use: https://www.spiedigitallibrary.org/terms-of-use

17. K. Kurihara, H. Kinoshita, T. Mizota, T. Haga, and Y. Torii, "Two-mirror telecentric optics for soft x-ray reduction lithography," *J. Vac. Sci. Technol. B* **9**, 3189–3192 (1991).
18. H. Kinoshita, "SXPL in Japan," in *OSA Proc. on Soft X-ray Projection Lithography 1993*, Vol. **18**, pp. 74–78 (1993).
19. H. Kinoshita, K. Kurihara, T. Mizota, T. Haga, H. Takenaka, and Y. Torii, "Large-area, high-resolution pattern replication by the use of a two-aspherical-mirror system," *Appl. Opt.* **32**, 7079–7083 (1993).
20. T. Haga, M. Tinone, H. Takenaka, and H. Kinoshita, "Large-field ($>20 \times 25$ mm^2) replication by EUV lithography," *Microelectron. Eng.* **30**, 179–182 (1996).
21. G. E. Sommargren, "Performance of a two mirror, four reflection, ring field imaging system," *OSA Proc. on Extreme Ultraviolet Lithography 1994*, Vol. **23**, pp. 103–108 (1995).
22. B. La Fontaine, D. P. Gaines, D. R. Kania, G. E. Sommargren, S. L. Baker, and D. Ciarlo, "Performance of a two-mirror, four-reflection ring-field optical system operating at $\lambda = 13$ nm," *OSA Trends Opt. Photon.* **4**, 186–191 (1996).
23. D. A. Tichenor, G. D. Kubiak, S. J. Haney, R. P. Nissen, K. W. Berger, R. W. Arling, A. K. Ray-Chaudhuri, K. B. Nguyen, R. H. Stulen, J. B. Wronosky, J. D. Jordan, T. G. Smith, J. R. Darnold, P. M. Kahle, A. A. Jojola, S. M. Kohler, R. S. Urenda, D. R. Wheeler, J. E. Bjorkholm, O. R. Wood, II, G. N. Taylor, and R. S. Hutton, "Recent results in the development of an integrated EUVL laboratory tool," *Proc. SPIE* **2437**, 292–307 (1995) [doi: 10.1117/12.209167].
24. D. A. Tichenor, A. K. Ray-Chaudhuri, G. D. Kubiak, K. B. Nguyen, S. J. Haney, K. W. Berger, R. P. Nissen, Y. E. Perras, P. S. Jin, L. I. Weingarten, P. N. Keifer, R. H. Stulen, R. N. Shagam, W. C. Sweatt, T. G. Smith, O. R. Wood, II, A. A. MacDowell, J. E. Bjorkholm, T. E. Jewell, F. Zernike, B. L. Fix, and H. W. Hauschildt, "Progress in the development of EUV imaging systems," *OSA Trends Opt. Photon.* **4**, 2–8 (1996).
25. A. A. MacDowell, Z. Shen, K. Fujii, J. E. Bjorkholm, R. R. Freeman, L. Fetter, D.W. Taylor, D. M. Tennant, L. Eichner, W. K. Waskiewicz, D. L. White, D. L. Windt, O.R. Wood, II, S. Haney, and T. Jewell, "Extreme ultraviolet 1:1 ring-field lithography machine," *OSA Trends Opt. Photon.* **4**, 192–198 (1996).
26. J. H. Bruning, A. R. Phillips, Jr., D. R. Shafer, and A. D. White, "Lens system for x-ray projection lithography camera," U.S. Patent No. 5,353,322 (October 4, 1994).
27. K. B. Nguyen, G. F. Cardinale, D. A. Tichenor, G. D. Kubiak, K. Berger, A. K. Ray-Chaudhuri, Y. Perras, S. J. Haney, R. Nissen, K. Krenz, R. H. Stulen, H. Fujioka, C. Hu, J. Bokor, D. M. Tennant, and

Downloaded From: https://www.spiedigitallibrary.org/ebooks/ on 09 Mar 2022
Terms of Use: https://www.spiedigitallibrary.org/terms-of-use

L. A. Fetter, "Fabrication of MOS devices with extreme ultraviolet lithography," *OSA Trends Opt. Photon.* **4**, 208–211 (1996).
28. M. Ito, H. Oizumi, T. Soga, H. Yamanashi, T. Ogawa, S. Katagiri, E. Sega, and E. Takeda, "Soft x-ray projection imaging with multilayer reflection masks," *Microelectron. Eng.* **27**, 285–290 (1995).
29. M. Ito, S. Katagiri, H. Yamanashi, E. Seya, T. Ozawa, H. Oizumi, and T. Terasawa, "Optical technology for EUV lithography," *OSA Trends Opt. Photon.* **4**, 9–12 (1996).
30. S. Katagiri, M. Ito, H. Yananashi, E. Seya, and T. Terasawa, "Optical system for high-throughput EUV lithography," *Proc. SPIE* **2723**, 34–45 (1996) [doi: 10.1117/12.240487].
31. K. Murakami, T. Oshino, S. Shimizu, W. Wasa, H. Kondo, M. Ohtani, N. Kandaka, K. Mashima, and K. Nomura, "Basic technologies for extreme ultraviolet lithography," *OSA Trends Opt. Photon.* **4**, 16–20 (1996).
32. H. Kinoshita, T. Watanabe, M. Niibe, M. Ito, H. Oizumi, H. Yamanashi, K. Murakami, T. Oshino, Y. Platonov, and N. Grupido, "Three-aspherical-mirror system for EUV lithography," *Proc. SPIE* **3331**, 20–31 (1998) [doi: 10.1117/12.309580].
33. S. Okazaki, "EUV lithography research program at ASET," *Proc. SPIE* **3676**, 238–245 (1999) [doi: 10.1117/12.351095].
34. Extreme Ultraviolet Lithography System Development Association (EUVA), Japan.
35. F. Bijkerk, H.-J. Voorma, E. J. Puik, E. Louis, G. E. van Dorssen, M. J. van der Wiel, J. Verhoeven, E. W. J. M. van der Drift, J. Romijn, and B. A. C. Rousseeuw, "Design of an extended image field soft-x-ray projection system," in *OSA Proc. on Soft-X-Ray Projection Lithography 1991*, Vol. **12**, pp. 51–53 (1991).
36. E. Puik, M. J. van der Wiel, H. Zeijlemaker, and J. Verhoeven, "Ion bombardment of x-ray multilayer coatings: comparison of ion etching and ion assisted deposition," *Appl. Surf. Sci.* **47**, 251–260 (1991).
37. F. Bijkerk, E. Louis, L. Shmaenok, H.-J. Voorma, M. J. van der Wiel, R. Schlatmann, J. Verhoeven, F. Voss, R. Desor, and B. Nikolaus, "Enhanced performance of KrF laser-induced x-ray sources and multilayer mirrors for SXPL," in *OSA Proc. on Soft X-Ray Projection Lithography 1993*, Vol. **18**, pp. 114–116 (1993).
38. L. Rymell and H. M. Hertz, "Droplet target for low-debris laser-plasma soft x-ray generation," *Opt. Commun.* **103**, 105–110 (1993).
39. F. Bijkerk, "Development of extreme ultraviolet lithography along the European route," *OSA Trends Opt. Photon.* **4**, 13–15 (1996).
40. J. P. H. Benschop, W. M. Kaiser, and D. C. Ockwell, "EUCLIDES: the European EUVL program," *Proc. SPIE* **3676**, 246–252 (1999) [doi: 10.1117/12.351165].

Downloaded From: https://www.spiedigitallibrary.org/ebooks/ on 09 Mar 2022
Terms of Use: https://www.spiedigitallibrary.org/terms-of-use

41. Microelectronics Development for European Applications+ (MEDEA+), France, http://www.medeaplus.org.
42. E. Spiller, "Multilayer optics for x-rays," in *Physics, Fabrication and Applications of Multilayer Structures*, P. Dhez and C. Weisbuch, Eds., pp. 271–309, Plenum, New York (1987).
43. G. Sommargren, "Phase shifting diffraction interferometry for measuring extreme ultraviolet optics," *OSA Trends Opt. Photon.* **4**, 108–112 (1996).
44. A. M. Hawryluk and N. M. Ceglio, "Wavelength considerations in soft-x-ray projection lithography," *Appl. Opt.* **32**, 7062–7067 (1993).
45. D. G. Stearns, R. S. Rosen, and S. P. Vernon, "Multilayer mirror technology for soft-x-ray projection lithography," *Appl. Opt.* **32**, 6952–6960 (1993).
46. O. R. WoodII, J. E. Bjorkholm, K. F. Dreyer, L. Fetter, M. D. Himel, R. R. Freeman, D. M. Tennant, J. E. Griffith, G. N. Taylor, W. K. Waskiewicz, D. L. White, D. L. Windt, A. A. MacDowell, B. LaFontaine, B. M. Lum, A. R. Neureuther, J. B. Kortright, E. M. Gullikson, and K. B. Nguyen, "Experiments and simulations of EUV lithographic resist patterning at wavelengths from 7 to 40 nm," in *OSA Proc. on Extreme Ultraviolet Lithography 1994*, Vol. **23**, pp. 83–88 (1995).
47. K. Skulina, C. Alford, R. Bionta, D. Makowiecki, E. M. Gullikson, R. Soufli, J. B. Kortright, and J. H. Underwood, "Beryllium based multilayers for normal incidence EUV reflectance," in *OSA Proc. on Extreme Ultraviolet Lithography 1994*, Vol. **23**, pp. 52–55 (1995).
48. J. B. Kortright, E. M. Gullikson, and P. E. Denham, "Masked deposition techniques for achieving multilayer period variations required for short-wavelength (68-A) soft-x-ray imaging optics," *Appl. Opt.* **32**, 6961–6968 (1993).
49. D. W. Berreman, "Multilayer reflecting x-ray optical systems: chromatic vignetting by narrow reflection bands," *Appl. Opt.* **30**, 1741–1745 (1991).
50. O. R. Wood, II, T. E. Jewell, and W. T. Silfvast, "Short-wavelength annular-field optical system for imaging tenth-micron features," *J. Vac. Sci. Technol. B* **6**, 1613–1615 (1989).
51. T. Jewell, J. Rodgers, and K. Thompson, "Reflective systems design study for soft x-ray projection lithography," *J. Vac. Sci. Technol. B* **8**, 1519–1523 (1990).
52. K. Murakami, T. Oshino, S. Shimizu, W. Wasa, H. Knodo, M. Ohtani, N. Kandaka, K. Mashima, and K. Nomura, "Basic technologies for extreme ultraviolet lithography," *OSA Trends Opt. Photon.* **4**, 16–20 (1996).
53. W. C. Sweatt, "Ring-field EUVL camera with large étendu," *OSA Trends Opt. Photon.* **4**, 178–180 (1996).
54. R. Kestner, "Precision asphere fabrication and metrology to tolerances <1 nm rms," *Extreme Ultraviolet Lithography OSA Technical Digest* **77**, Optical Society of America, Washington, D.C. (1996).

Downloaded From: https://www.spiedigitallibrary.org/ebooks/ on 09 Mar 2022
Terms of Use: https://www.spiedigitallibrary.org/terms-of-use

55. O. R. Wood, II, J. E. Bjorkholm, A. A. MacDowell, S. Vaidaya, and D. R. Shafer, "Projection lithography with all-reflecting optics," *OSA Trends Opt. Photon.* **4**, 181–184 (1996).
56. W. T. Estler and C. J. Evans, "Surface figure metrology for x-ray optics," in *OSA Proc. on Soft-X-Ray Projection Lithography 1991*, Vol. **12**, pp. 145–146 (1991).
57. D. Bajuk and R. Kestner, The Japan Society for Precision Engineering (JSPE) *Proc. of the Second U.S.-Japan Workshop on Soft X-ray Optics: Technical Challenges*, Mt. Fuji, Japan, Nov. 12–14, 1996.
58. J. E. Bjorkholm, "Fabrication and testing of precision optics for soft x-ray projection lithography," NIST ATP Program (1991) http://www.atp.nist.gov. Search the ATP Funded Project Database for AT&T.
59. D. L. Windt, W. K. Waskiewicz, and J. E. Griffith, "Surface finish requirements for soft x-ray mirrors," *Appl. Opt.* **33**, 2025–2031 (1994).
60. E. L. Church, "Fractal surface finish," *Appl. Opt.* **27**, 1518–1526 (1988).
61. D. P. Gaines, D. W. Sweeney, K. W. DeLong, S. P. Vernon, S. L. Baker, D. A. Tichenor, and R. Kestner, "Surface characterization of optics for EUV lithography," *OSA Trends Opt. Photon.* **4**, 103–106 (1996).
62. D. M. Williamson, "The elusive diffraction limit," in *OSA Proc. on Extreme Ultraviolet Lithography 1994*, Vol. **23**, pp. 94–97 (1994).
63. D. T. Attwood, G. Sommargren, R. Beguiristain, K. Nguyen, J. Bokor, N. Ceglio, K. Jackson, M. Koike, and J. Underwood, "Undulator radiation for at-wavelength interferometry of optics for extreme-ultraviolet lithography," *Appl. Opt.* **32**, 7022–7031 (1993).
64. K. A. Goldberg, R. Beguiristain, J. Bokor, H. Medecki, K. Jackson, D. T. Attwood, G. E. Sommargren, J. P. Spallas, and R. Hostetler, "Point diffraction interferometry at EUV wavelengths," in *OSA Proc. on Extreme Ultraviolet Lithography 1994*, Vol. **32**, pp. 134–141 (1995).
65. J. E. Bjorkholm, A. A. MacDowell, O. R. Wood, II, Z. Tan, B. LaFontaine, and D. M. Tennant, "Phase-measuring interferometry using extreme ultraviolet radiation," *J. Vac. Sci. Technol. B* **13**, 2919–2922 (1995).
66. E. Tejnil, K. A. Goldberg, H. Medecki, R. Beguiristain, J. Bokor, and D. T. Attwood, "Phase-shifting point diffraction interferometry for at wavelength testing of lithographic optics," *OSA Trends Opt. Photon.* **4**, 118–122 (1996).
67. H. Medecki, E. Tejnil, K. A. Goldberg, and J. Bokor, "Phase-shifting point diffraction interferometer," *Opt. Lett.* **21**, 1526–1528 (1996).
68. Z. Tan, A. A. MacDowell, B. LaFontaine, J. Russo, J. E. Bjorkholm, D. Tennant, D. Taylor, M. Himel, O. R. Wood, II, R. R. Freeman, W. K. Waskiewicz, D. L. Windt, D. L. White, S. Spector, A. K. Ray-Chaudhuri, and R. H. Stulen, "At wavelength metrology of EUV cameras using lateral-shearing interferometry," in *OSA Proc. on Extreme Ultraviolet Lithography 1994*, Vol. **32**, pp. 151–160 (1995).

Downloaded From: https://www.spiedigitallibrary.org/ebooks/ on 09 Mar 2022
Terms of Use: https://www.spiedigitallibrary.org/terms-of-use

69. A. K. Ray-Chaudhuri, R. H. Stulen, W. Ng, F. Cerrian, S. Spector, Z. Tan, J. Bjorkholm, and D. Tennant, "EUV metrology of multilayer optics," in *OSA Proc. on Extreme Ultraviolet Lithography 1994*, Vol. **32**, pp. 161–165 (1995).
70. C. Tarrio, R. E. Vest, and S. Grantham, "Absolute extreme-ultraviolet metrology," *Proc. SPIE* **4450**, 94–107 (2001) [doi: 10.1117/12.431244].
71. A. B. C. Walker, T. W. Barbee, R. B. Hoover, and J. F. Lundblom, "Soft x-ray images of the solar corona with a normal incidence Cassegrain multilayer telescope," *Science* **241**, 1781 (1988).
72. F. Scholze, J. Tummler, E. Gullikson, and A. Aquilla, "Comparison of extreme ultraviolet reflectance measurements," *J. Microlithography, Microfabrication & Microsystems* **2**, 233–235 (2003) [doi: 10.1117/1.1583735].
73. D. M. Tennant, J. E. Bjorkholm, R. M. D'Souza, L. Eichner, R. R. Freeman, J. Z. Pastalan, L. H. Szeto, O. R. Wood, II, T. E. Jewell, W. M. Mansfield, W. K. Waskiewicz, D. L. White, D. L. Windt, and A. A. MacDowell, "Reflective mask technologies and imaging results in soft x-ray projection lithography" *J. Vac. Sci. Technol. B* **9**, 3176–3183 (1991).
74. D. M. Tennant, L. A. Fetter, L. R. Harriott, A. A. MacDowell, P. P. Mulgrew, W. K. Waskiewicz, D.L. Windt, and O.R. Wood, II, "Defect repair for soft x-ray projection lithography masks," *J. Vac. Sci. Technol. B* **10**, 3134–3140 (1992).
75. A. A. MacDowell, J. E. Bjorkholm, K. Early, R. R. Freeman, M. D. Himel, P. P. Mulgrew, L. H. Szeto, D. W. Taylor, D. M. Tennant, O. R. Wood, II, J. Bokor, L. Eichner, T. E. Jewell, W. K. Waskiewicz, D. L. White, D. L. Windt, R. M. D'Souza, W. T. Silfvast, and F. Zernike, "Soft-ray projection imaging with a 1:1 ring-field optic," *Appl. Opt.* **32**, 7072–7078 (1993).
76. K. Nguyen, D. Attwood, T. Mizota, T. Haga, and H. Kinoshita, "Imaging of EUV lithographic masks with programmed substrate defects," in *OSA Proc. on Extreme Ultraviolet Lithography 1994*, Vol. **23**, pp. 193–203 (1994).
77. K. B. Nguyen, T. Mizota, T. Haga, H. Kinoshita, and D. T. Attwood, "Imaging of extreme ultraviolet lithographic masks with programmed substrate defects," *J. Vac. Sci. Technol. B* **12**, 3833–3840 (1994).
78. K. B. Nguyen, A. K. Ray-Chaudhuri, R. H. Stulen, K. Krenz, L. A. Fetter, D. M. Tennant, and D. L. Windt, "Printability of substrate and absorber defects on extreme ultraviolet lithographic masks," *J. Vac. Sci. Technol. B* **13**, 3082–3088 (1995).
79. S. P. Vernon, D. R. Kania, P. A. Kearney, R. A. Levesque, A. V. Hayes, B. Druz, E. Osten, R. Rajan, and H. Hedge, "Reticle blanks for extreme ultraviolet lithography: ion beam sputter deposition of low defect density Mo/Si multilayers," *OSA Trends Opt. Photon.* **4**, 44–48 (1996).
80. G. D. Kubiak, D. A. Outka, and J. M. Zeigler, "Soft x-ray resist characterization: Studies with a laser plasma x-ray source," *Proc. SPIE* **1263**, 272–281 (1990) [doi: 10.1117/12.20148].

Downloaded From: https://www.spiedigitallibrary.org/ebooks/ on 09 Mar 2022
Terms of Use: https://www.spiedigitallibrary.org/terms-of-use

81. D. W. Berreman, J. E. Bjorkholm, M. Becker, L. Eichner, R. R. Freeman, T. E. Jewell, W. M. Mansfield, A. A. MacDowell, M. L. O'Malley, E. L. Raab, W. T. Silfvast, L. H. Szeto, D. M. Tennant, W. K. Waskiewicz, D. L. White, D. L. Windt, and O. R. Wood, II, "Use of trilevel resists for high-resolution soft-x-ray projection lithography," *Appl. Phys. Lett.* **56**, 2180–2182 (1990).
82. G. N. Taylor, R. S. Hutton, D. L. Windt, and W. M. Mansfield, "Resist schemes for soft x-ray lithography," *Proc. SPIE* **1343**, 258–273 (1990) [doi: 10.1117/12.23198].
83. B. L. Henke, P. Lee, T. J. Tanaka, R. L. Shirnabukuro, and B. K. Fujikawa, *Atomic Data and Nuclear Data Tables* **27**, 1 (1982).
84. W. M. Mansfield, J. E. Bjorkholm, A. A. MacDowell, R. R. Freeman, L. H. Szeto, G. N. Taylor, D. M. Tennant, W. K. Waskiewicz, D. L. Windt, D. L. White, O. R. Wood, II, R. M. D'Souza, and A. R. Neureuther, "Effects of absorption on resist performance in soft-x-ray projection lithography," in *OSA Proc. on Soft-X-Ray Projection Lithography 1991*, Vol. **12**, pp. 129–131 (1991).
85. A. A. MacDowell, J. M. Calvert, T. S. Koloski, and O. R. Wood, II, "New surface imaging resist technology for SXPL," in *OSA Proc. on Soft-X-Ray Projection Lithography 1993*, Vol. **18**, pp. 87–93 (1993).
86. D. R. Wheeler, G. Kubiak, A. Ray-Chaudhuri, and C. Henderson, "Basic issues associated with four potential EUV resist schemes," *OSA Trends Opt. Photon.* **4**, 33–38 (1996).
87. V. Bakshi, Ed., *EUV Sources for Lithography*, SPIE Press, Bellingham, Washington (2005).
88. J. B. Murphy, D. L. White, A. A. MacDowell, and O. R. Wood, II, "Synchrotron radiation sources and condensers for projection x-ray lithography," *Appl. Opt.* **32**, 6920–6929 (1993).
89. P. D. Rockett, J. A. Hunter, R. Kensek, R. E. Olson, G. D. Kubiak, and K. W. Berger, "XUV conversion efficiency in a low-intensity KrF laser plasma for projection lithography," in *OSA Proc. on Soft X-Ray Projection Lithography*, Vol. **12**, pp. 76–79 (1991).
90. R. C. Spitzer, R. L. Kauffman, T. Orzechowski, D. W. Phillion, and C. Cerjan, "Soft x-ray production from laser produced plasmas for lithography applications," *J. Vac. Sci. Technol B* **11**, 2986–6900 (1993).
91. R. L. Kauffman, D. W. Phillion, and R. C. Spitzer, "X-ray production ~13 nm from laser-produced plasmas for projection x-ray lithography applications," *Appl. Opt.* **32**, 6897–6900 (1993).
92. M. L. Ginter and T. J. McIlrath, "Debris and VUV emission from a laser-produced plasma operating at 150 Hz using a krypton fluoride laser," *Appl. Opt.* **27**, 885–889 (1988).
93. L. Rymell and H. M. Hertz, "Debris elimination in a droplet-target laser-plasma soft x-ray source," *Rev. Sci. Instru.* **66**, 4916–4920 (1995).

Downloaded From: https://www.spiedigitallibrary.org/ebooks/ on 09 Mar 2022
Terms of Use: https://www.spiedigitallibrary.org/terms-of-use

94. M. Richardson, W. T. Silfvast, H. A. Bender, A. Hanzo, V. P. Yanovsky, F. Jin, and J. Thorpe, "Characterization and control of laser plasma flux parameters for soft-x-ray projection lithography," *Appl. Opt.* **32**, 6901–6910 (1993).
95. F. Jin and M. Richardson, "New laser plasma source for extreme ultraviolet lithography," *Appl. Opt.* **34**, 5750–5760 (1995).
96. M. Richardson, K. Gabel, F. Jin, and W. Silfvast, "Cryogenic targets for laser-plasma x-ray lithography sources," in *OSA Proc. on Soft X-Ray Projection Lithography 1993*, Vol. **18**, pp. 156–162 (1993).
97. E. Noda, S. Suzuki, and O. Morimiya, "Droplet target delivery method for high pulse-rate laser-plasma extreme ultraviolet light source," *U.S. Patent No. 4*, **723**, 262 (1988).
98. S. J. Haney, K. W. Berger, G. D. Kubiak, P. D. Rockett, and J. Hunter, "Prototype high-speed tape target transport for a laser plasma soft-x-ray projection lithography source," *Appl. Opt.* **32**, 6934–6937 (1993).
99. H. Fiedorowicz, A. Bartnik, Z. Patron, and P. Parys, "X-ray emission from laser-irradiated gas puff targets," *Appl. Phys. Lett.* **62**, 2778–2780 (1993).
100. L. Rymell and H. M. Hertz, "Droplet target for low-debris laser-plasma soft x-ray generation," *Opt. Commun.* **103**, 105–110 (1993).
101. G. D. Kubiak, K. Krenz, P. D. Rocket, J. A. Hunter, M. J. Gouge, and P. Fisher, "Cryogenic pellet laser plasma source targets," in *OSA Proc. on Extreme Ultraviolet Lithography 1994*, Vol. **23**, pp. 248–254 (1995).
102. G. D. Kubiak, L. J. Bernardez, K. D. Krenz, D. J. O'Connell, R. Gutowski, and A. M. M. Todd, "Debris-free EUVL sources based on gas jets," *OSA Trends Opt. Photon.* **4**, 66–71 (1996).
103. J. E. M. Goldsmith, G. D. Kubiak, and W. P. Ballard, "LPP source development and operation in the Engineering Test Stand," *EUV Sources for Lithography*, V. Bakshi, Ed., pp. 649–667, SPIE Press, Bellingham, Washington (2005).
104. T. E. Jewell, "Four-mirror ring-field system for EUV projection lithography," in *OSA Proc. on Extreme Ultraviolet Lithography 1994*, Vol. **23**, pp. 98–102 (1994).

Hiroo Kinoshita is an expert with over 30 years of experience in lithography. He worked for NTT, where he developed the step-and-repeat x-ray lithography system and an EUVL experimental system. He moved to Himeji Institute of Technology (now the University of Hyogo) in 1995, and since then he has been responsible for the industrial application of synchrotron radiation. He has authored over 100 technical papers on EUVL.

Downloaded From: https://www.spiedigitallibrary.org/ebooks/ on 09 Mar 2022
Terms of Use: https://www.spiedigitallibrary.org/terms-of-use

Obert Wood is a principal member of the technical staff in the Strategic Lithography Technology Department at Advanced Micro Devices. He was a member of the technical staff at Bell Labs for 34 years and has extensive experience in EUVL, ultrahigh-intensity lasers, and laser surgery. He received his B.S., M.S., and Ph.D. degrees in electrical engineering from the University of California, Berkeley in 1964, 1965, and 1969, respectively. He is the author or coauthor of 215 technical papers, and the inventor or co-inventor of 20 patents. He is a Fellow of the OSA, a senior member of IEEE, and a member of the AAAS, the American Physical Society, the American Vacuum Society, and SPIE.

Downloaded From: https://www.spiedigitallibrary.org/ebooks/ on 09 Mar 2022
Terms of Use: https://www.spiedigitallibrary.org/terms-of-use

Chapter 2
The EUV LLC: An Historical Perspective

Stefan Wurm
ATICE LLC, Albany, New York, USA

2.1 Introduction
- 2.1.1 Background
- 2.1.2 Need for a revolutionary approach

2.2 Formation of the EUV LLC
- 2.2.1 Vision
- 2.2.2 Implementation
- 2.2.3 Organizational structure

2.3 Program Structure
- 2.3.1 Organization
- 2.3.2 Risk management
- 2.3.3 Reporting
- 2.3.4 Documentation

2.4 Program Results
- 2.4.1 Technical accomplishments
- 2.4.2 IP portfolio
- 2.4.3 Program statistics
- 2.4.4 Delays

2.5 Retrospective Observations
- 2.5.1 Improvements
- 2.5.2 External issues
- 2.5.3 Benefits

2.6 Status of EUV Development at the End of the EUV LLC
- 2.6.1 Risk reduction

2.7 Summary
Appendix 2A: Major Accomplishments of the EUV LLC Program
Appendix 2B: EUV LLC Program Patents
Acknowledgments
References

Downloaded From: https://www.spiedigitallibrary.org/ebooks/ on 09 Mar 2022
Terms of Use: https://www.spiedigitallibrary.org/terms-of-use

2.1 Introduction

The Extreme Ultraviolet Limited Liability Company (EUV LLC) was formed in 1997 to advance the R&D on EUV lithography (EUVL). The company contracted with the Department of Energy (DOE) Virtual National Laboratory, consisting of Lawrence Berkeley, Lawrence Livermore, and Sandia National Laboratories, to accelerate EUV technology development and to reduce the risks associated with developing manufacturing tools and transferring the technology to industry for commercialization. The program started as a three-year program and later was extended to six years.

It can be stated with a significant level of confidence that the EUV technology as applied to lithography would not be a future contender for IC manufacturing if it had not been for the formation and pursuit of the technology by the EUV LLC. EUVL research would have stopped within the U.S. in the 1997 time frame, and the technology would not have provided a future manufacturing option.

The EUV LLC program demonstrated the viability of EUV lithography, reduced the commercialization risks for EUVL to an acceptable level, and enabled the following key accomplishments:

- design and fabrication of a complete, integrated, full-field (24 mm $\times$ 32.5 mm), scanning, alpha class lithography tool denoted as the Engineering Test Stand (ETS);
- development and integration of computer-aided design methods to support thermal, dynamic, and vibration design and analysis of individual components, subsystems, and complete system operation;
- development of a reflective EUV mask technology including multilayer (ML)-coated, low-thermal-expansion-material (LTEM) mask blanks complete with metrology, ML defect repair methods, patterning inspection, and repair processes;
- implementation of EUV optics fabrication projects with industry to demonstrate continuous optics fabrication technology improvement and development of engineered ML with capping layers to provide good reflectivity and stability;
- demonstration of extensive EUV lithographic printing using extended DUV resists; and
- collection of over 150 domestic and foreign patents and numerous technical/trade secrets.

A decade has passed since this chapter was first written.[1] The summary of the initial EUV LLC program vision, history, successes, delays, and issues as well as the comments regarding changes that could have been made during the early phases of the program to improve technological success and commercial implementation stand as they are (some of them even more relevant today than a decade ago). However, given the pioneering role that the EUV LLC

Downloaded From: https://www.spiedigitallibrary.org/ebooks/ on 09 Mar 2022
Terms of Use: https://www.spiedigitallibrary.org/terms-of-use

played in enabling key EUV technologies, this chapter will take a closer look at the intellectual property (IP) portfolio developed by the EUV LLC and, specifically, its reception by the industry commercializing the technology since the EUV LLC program ended in 2003.

2.1.1 Background

During the late 1990s, the semiconductor industry was rapidly growing, and companies were implementing aggressive plans to maintain or accelerate the technology for integrated circuits (IC) following Moore's law, e.g., doubling the number of transistors on an IC device every 18 months. Although extensions of conventional optical lithography methods using deep ultraviolet (DUV) light were expected to continue for printing dimensions below 100 nm, manufacturing projections indicated that a new lithography technology would be needed to print features <70 nm without manufacturing throughput loss. Several technologies were pursued, including proximity x-ray, projection electron and ion beams, and shorter DUV wavelengths. EUV lithography (EUVL) using 13- to 14-nm EUV light was considered a promising technology, although many challenges had to be addressed before it could be considered mature enough to be used in commercial lithography tools for manufacturing. These challenges included demonstrating a complete EUV tool with an illumination system consisting of a radiation source and condenser system, a reduction camera with precision ML-coated mirrors, defect-free reflective masks, an EUV-sensitive resist, metrology to support manufacturing and inspection of reticles, and non-EUV-specific subsystems consisting of the focus and overlay systems, scanning mask and wafer stages, optics housing, wafer- and reticle-handling interfaces, robotics, and issues related to operating in the vacuum environment required for an EUVL tool.

As noted in Chapter 1,[2] in 1988 imaging using x-ray wavelength light had been proposed by Hawryluk and Seppala[3] at the Lawrence Livermore National Laboratory (LLNL) and by Silfvast and Wood[4] at AT&T; in 1989, the first imaging was demonstrated by Kinoshita, et al. at NTT.[5,6] Continued work was pursued by AT&T and the U.S. national laboratories during the early 1990s, and many of the basic imaging concepts were demonstrated. During the mid-1990s, several industrial companies, including Intel, AMD, Ultratech, Tropel, JMAR, and others, partnered with the U.S. Department of Energy (DOE) national laboratories through cooperative research and development agreements (CRADAs) to study the semiconductor industry's possible use of 13-nm EUV light in lithography.

While the IC industry was expanding at a rapid rate during the mid-1990s, the DOE faced substantial budget reductions when the U.S. Congress eliminated programs it deemed unnecessary, especially R&D projects at the national laboratories that were not directly tied to weapons or defense

Downloaded From: https://www.spiedigitallibrary.org/ebooks/ on 09 Mar 2022
Terms of Use: https://www.spiedigitallibrary.org/terms-of-use

programs. In addition, the national laboratories had gone through several voluntary reductions in work force. In 1996, the DOE decided to stop all work on the EUV program, including the projects that had been co-funded during the mid-1990s through CRADAs with the industrial companies. However, based on early lithographic demonstrations using EUV wavelengths at the DOE labs and in Japan, Intel decided that EUVL had sufficient potential to warrant continued R&D work. Since the DOE was discontinuing the program and personnel would be immediately assigned to other programs, there was an urgency to keep the R&D team together to maintain momentum. Therefore, in late 1996, Intel provided bridge funding to maintain the EUV research while a more extensive program was developed and CRADAs were signed with these three national laboratories: LLNL,[7] Lawrence Berkeley National Laboratory (LBNL),[8] and Sandia National Laboratory (SNL).[9]

2.1.2 Need for a revolutionary approach

The R&D necessary to successfully demonstrate EUVL was projected to be very expensive, much greater than any of the individual lithography equipment manufacturers could afford. This was especially true if the technology were to be made available by 2005, when a new lithography would be required to support IC manufacturing at the smaller feature sizes predicted by the *International Technology Roadmap for Semiconductors* (ITRS).[10] Early estimates by Intel and the national laboratories indicated that a funding level of approximately US $60M per year would be needed to maintain and accelerate the R&D program at the three national laboratories.

Although a new startup company could conceivably have been established to perform EUV R&D, the time to organize a company, acquire a facility, obtain and install equipment, and recruit experienced staff would have caused substantial delays. In addition, the urgency required an immediate decision and prevented a lengthy study of alternative methods of development. As a result, an Intel committee led by Gerry Parker (Intel Senior Vice President), John Carruthers (Director of Components Research at Intel), and Jack Salvador (Intel Legal Counsel) recommended the formation of a "virtual" company using the resources available at the national laboratories to continue the development of EUV technology.

2.2 Formation of the EUV LLC

2.2.1 Vision

Intel's initial vision for EUVL development, with input from each of the three DOE laboratories, involved establishing a virtual company called the EUV Limited Liability Company (EUV LLC) that would consist of a consortium of IC companies. The vision included obtaining funding for the company by

Downloaded From: https://www.spiedigitallibrary.org/ebooks/ on 09 Mar 2022
Terms of Use: https://www.spiedigitallibrary.org/terms-of-use

selling shares of stock to IC companies that would manage the company and would share in the technology achievements. The EUV LLC would contract with the DOE laboratories, which were to be combined to form the Virtual National Laboratory (VNL), for a majority of the R&D related to demonstrating EUVL technology. In addition, the EUV LLC would develop partnerships to transfer the technology and IP to the semiconductor equipment manufacturers to manufacture beta and production tools. In return for early access to the technology and IP licenses, the manufacturers would provide right of first refusal (ROFR) to the EUV LLC member companies for beta and production EUVL tools and would pay royalties to the EUV LLC for tools sold to non-LLC member companies. The EUV LLC would also establish joint development programs (JDPs) with other commercial companies to produce major components or subsystems for the lithography tools and the infrastructure for masks, resists, metrology tools, etc., to support EUVL in commercial IC manufacturing.

The EUV LLC would be responsible for obtaining funding and managing the program. Detailed goals and objectives would be established to accelerate the technology development and to reduce risks associated with developing manufacturing tools. The success of the virtual company in cooperatively funding an expensive project and accelerating the technology development and transfer to industry could provide a new paradigm for the future development of enabling technologies for high-technology industries.

Since one of the major technical objectives of the program was to accelerate the technology development and transfer the results to industry for commercialization, the initial planning indicated a three-year development program beginning in 1997, with the transfer of the technology to commercialization in 2000–2001.

2.2.2 Implementation

The EUV LLC, under Intel leadership, was incorporated in late 1996; in April 1997, it signed a three-year CRADA with the VNL. Motorola and AMD joined the LLC as founding members. Subsequently, Micron, Infineon, and IBM joined the virtual company. Although the investment levels by the members varied, the organization achieved a major goal of providing broad IC industry support for EUVL.

The EUV LLC / VNL CRADA had at least three unique characteristics. First, a single CRADA with the VNL incorporated the resources of each of the three laboratories. Second, the CRADA was completely funded by private industry and did not contain any matching funds from the DOE. Third, the provisions of the CRADA gave the EUV LLC complete ownership of the IP developed within the program and the right to patent the IP. The DOE retained the right to use the technology, royalty-free, for use in defense applications.

Downloaded From: https://www.spiedigitallibrary.org/ebooks/ on 09 Mar 2022
Terms of Use: https://www.spiedigitallibrary.org/terms-of-use

2.2.2.1 Business model

The business model involved four organizational components—the EUV LLC, the VNL, semiconductor equipment manufacturers, and suppliers—as shown in Fig. 2.1. The basic model involved the VNL providing research, development, and engineering through funding and the EUV LLC providing program direction. In return for funding the technology development, IP was harvested from the VNL in the form of knowledge, U.S. and foreign patents, and other IP such as trade secrets consisting of technology learning. The IP and licenses were transferred to the semiconductor equipment manufacturers and suppliers in return for early access to beta and production lithography tools and components, and royalty payments obtained from sales to nonmember companies. In addition to providing program funding, the EUV LLC provided program direction to the VNL and suppliers. Mask patterning technology was developed through separate agreements with the suppliers.

Funding was to be obtained by the sale of EUV LLC shares to the member companies at US $5M per share. Each share provided access to a beta or production lithography tool through a ROFR in the order that the shares were purchased. If a company did not exercise its ROFR, the right to purchase a tool was transferred to the next member in the priority sequence until the members' tool needs were satisfied. After the member companies had their development and manufacturing tools, the semiconductor equipment manufacturer could sell tools to nonmembers and transfer the royalties to the EUV LLC. The EUV LLC business model provided infrastructure suppliers

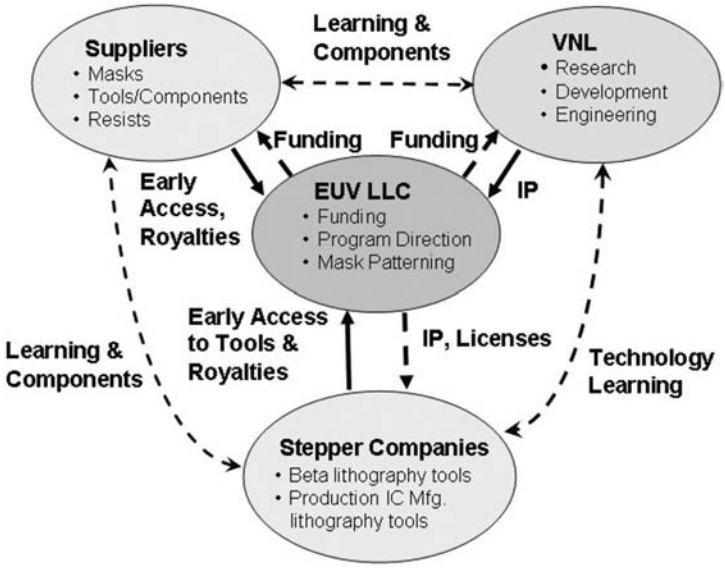

Figure 2.1 EUV LLC business model showing the four major entities.

Downloaded From: https://www.spiedigitallibrary.org/ebooks/ on 09 Mar 2022
Terms of Use: https://www.spiedigitallibrary.org/terms-of-use

with access to the technology and a use license with low upfront costs, small royalties based on sales, and ROFRs for EUV LLC member companies.

In late 1997, an agreement was signed with the first semiconductor equipment manufacturer, Silicon Valley Group Lithography (SVGL), which was acquired in 2002 by ASML of The Netherlands, to participate in the program with the objective of developing beta and production tools to the EUV LLC members that were subject to ROFR assignments. In 1998, similar agreements were signed with ASML and United States Advanced Lithography (USAL).

The legal structure of the EUV LLC was flexible and allowed a corporate structure that was attractive to the various participants. When necessary, the structure was modified to accommodate changing issues and circumstances. The number and variety of EUV LLC members provided critical support to demonstrate the value of the program to the industrial community and to the U.S. government.

2.2.2.2 Goals and objectives

The EUV LLC program goals included the following:

- to facilitate research, development, and engineering and enable semiconductor equipment manufacturers to provide beta and early production exposure tools to support IC manufacturing by 2005;
- to design and fabricate an integrated scanning alpha exposure tool to provide EUV learning and early process development;
- to assist in the development of the supplier and process infrastructure to assure the availability of masks, optics, coatings, photoresists, EUV sources, and metrology for successful technology implementation in manufacturing.

A major underlying objective throughout the program was to reduce the risks associated with implementing a new lithography technology into manufacturing.

2.2.2.3 Resources

To the extent allowed by funding, the EUV LLC had access to almost unlimited resources through the VNL in a number of fields of expertise, including optics design, at-wavelength and visible wavelength metrology, ML engineering and deposition, vacuum engineering, precision engineering design and component fabrication, magnetic levitation stage design and fabrication, control software, and associated support technologies.

The decision to use the R&D resources at the DOE laboratories provided an optimum way to establish a virtual company with access to world-class talent in a very short period of time. The team that was assembled provided extensive background knowledge for EUV research, materials analysis,

Downloaded From: https://www.spiedigitallibrary.org/ebooks/ on 09 Mar 2022
Terms of Use: https://www.spiedigitallibrary.org/terms-of-use

environmental issues, and metrology. In addition, the physical laboratories were already established for most of the initial work. If a new company had been formed, extensive delays would have been encountered in recruiting the required talent, locating and facilitating the laboratories, and establishing the management and support infrastructure. In addition, laboratory personnel were anxious to participate in a "new" nonconventional, industry-led R&D program.

In addition to the VNL, each member company selected specific projects for advanced internal work to enable the technology and to gain advanced development experience. Much of the work was envisioned to provide a working knowledge of the technology within the company and therefore to accelerate the transfer of EUV technology into manufacturing at the appropriate time.

The unique combination of expertise at the national laboratories could not have been found anywhere else, specifically in technology areas where semiconductor equipment manufacturers had little or no experience. The industry expertise of the EUV LLC members provided the critical mass to succeed in demonstrating the complex, challenging EUV technology. This is most evident by comparing the EUV technology effort with competing next-generation lithography (NGL) technologies, which lacked resources in science, engineering, and manpower to achieve the required critical investment.

2.2.3 Organizational structure

The EUV LLC organization consisted of a central business office, a management board, an advisory board, a number of coordinating committees and working groups, representatives from the semiconductor equipment manufacturers and component and subsystem suppliers, and the VNL, as shown in Fig. 2.2. Although some of the key personnel changed during the five-year program, the figure includes the responsible personnel in the various positions at the end of the program in early 2003.

2.2.3.1 Management board

The management board, consisting of high-level representatives from each of the member companies and chaired by Intel Senior Vice President Sunlin Chou, was responsible for funding and overseeing the operation of the EUV LLC. The management board provided overall guidance for program objectives, budget, and spending plans, and evaluated the technical progress of the program. Formal meetings were held monthly in Santa Clara, California, where technical progress was reviewed and business and supplier issues were discussed. Detailed reports were presented by the finance, technology, and IP committees.

Downloaded From: https://www.spiedigitallibrary.org/ebooks/ on 09 Mar 2022
Terms of Use: https://www.spiedigitallibrary.org/terms-of-use

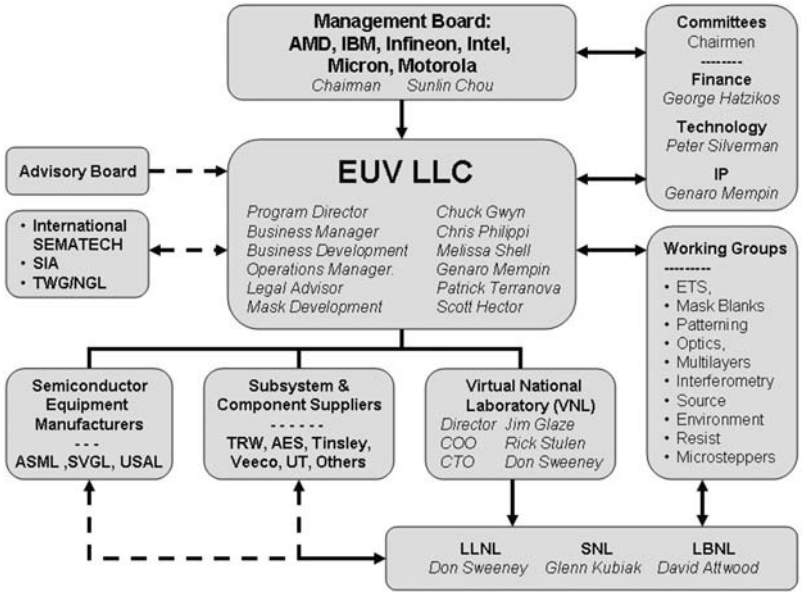

Figure 2.2 EUV LLC organizational structure with the committee chairpersons and staff positions at the end of the main program in early 2003. During the program extension, John Taylor (LLNL), John Goldsmith (SNL), and Erik Anderson (LBNL) provided management for the VNL.

2.2.3.2 The EUV LLC office

The EUV LLC office was responsible for providing program direction, funding, resist evaluation, mask pattering, and process development. This office ran the daily operations using personnel from the member companies consisting of a program director, business manager, business development manager, operations manager, legal advisor, and mask development manager. The office held weekly project status meetings and scheduled and organized workshops, review meetings, and press meetings as required. The office director reported to the management board and provided all interfaces between the EUV LLC representatives and the VNL.

The EUV LLC member company assignees provided onsite management and support. EUV LLC team representatives participated in all working group meetings, assisted in technical analysis and design projects, and served as an industry sounding board for the laboratory staff.

2.2.3.3 Committees

The key committees consisted of the finance, technology, and IP committees with the following responsibilities:

Finance: Tracked expenditures by the VNL, industrial subcontractors, and the EUV LLC operations office; reviewed proposed budgets; and solicited the sale of additional shares in the EUV LLC to meet budget requirements.

Downloaded From: https://www.spiedigitallibrary.org/ebooks/ on 09 Mar 2022
Terms of Use: https://www.spiedigitallibrary.org/terms-of-use

Business: Developed a business plan to meet the EUV LLC funding needs, negotiated joint development agreements, solicited new membership in the EUV LLC, and marketed additional EUV LLC shares to meet funding requirements.

Technology: Identified technical goals and objectives, reviewed technical progress, allocated funding, and identified risks for each of the technical projects.

Intellectual Property: Reviewed invention and technical advances by each of the VNL laboratories, and classified the invention disclosure items for patent applications (either domestic or foreign or both) or as a trade secret.

Each committee contained one or more members from each of the EUV LLC member companies. The committees met monthly to discuss progress, status, and critical issues, and to develop a set of action requirements (ARs) directed to the EUV LLC office or management board for follow up.

2.2.3.4 Working groups

Working groups were established in all of the key technology areas:

- Engineering Test Stand (ETS)
- mask blanks
- mask patterning
- optics design and fabrication
- ML coatings
- interferometry (visible and at-wavelength)
- EUV source development
- operational environment
- photoresist development and evaluation
- microsteppers

Additional working groups or subgroups were formed as needed to address other key issues and were dissolved when the problems were solved.

2.2.3.5 Virtual National Laboratory

The Virtual National Laboratory (VNL) consisted of the combined activities of the three DOE laboratories plus an overall management team consisting of a director, chief operations officer, and chief technical officer. This team was responsible for oversight of the work at the three laboratories and for directing the work through the program managers at each of the laboratories. The VNL team was responsible for developing detailed program plans, including schedules and the work breakdown structure, to accomplish the program objectives established by the EUV LLC. Each of the laboratories

Downloaded From: https://www.spiedigitallibrary.org/ebooks/ on 09 Mar 2022
Terms of Use: https://www.spiedigitallibrary.org/terms-of-use

and the VNL management team held regular weekly and monthly program management meetings. The VNL team was also responsible for planning, organizing, and preparing the quarterly, full-day program review meetings. Although interlaboratory teams worked on some projects, R&D was divided among the three laboratories as follows: LBNL was responsible for EUV interferometry of individual optics and projection optics boxes (POBs) for micro-exposure tools (METs) and ETS POBs, defect inspection and analysis, and EUV scattering; LLNL was responsible for optics design, ML coatings, mask blanks, visible light metrology of optics and POBs, POB engineering, and condenser design; and SNL was responsible for systems engineering, environmental controls, source development, 10×-reduction microstepper experiments, modeling, and resist development.

2.2.3.6 External advisory group coordination

In addition to guidance provided by the member companies, the EUV LLC sought advice from external organizations on program directions, political issues, and management input.

2.2.3.6.1 Advisory board

The advisory board consisted of key representatives from industrial and government agencies. The advisory board membership consisted of representatives from the following:

- the six EUV LLC member companies: AMD, IBM, Infineon, Intel, Micron, and Motorola;
- nonmember IC companies: Texas Instruments and Lucent;
- six U.S. government agencies: the DOE, the Department of Defense (DOD),[11] the Defense Advanced Research Projects Agency (DARPA),[12] the Office of the Director of Defense Research & Engineering (DDR&E),[13] the Department of Commerce (DOC),[14] and the National Institute for Standards and Technology (NIST);[15]
- the VNL;
- the industry consortium SEMATECH;[16]
- the Semiconductor Industry Association (SIA);[17] and
- the Semiconductor Research Corporation (SRC).[18]

The purpose of the advisory board was to critique the broad technical progress and objectives of the EUV LLC and to provide feedback to the EUV LLC on its assessment of overall program progress, schedules, potential political issues and interactions, and possible conflicts that should be addressed. Voluntary help was also solicited from specific members of the advisory board to help mitigate potential issues within various government agencies.

Downloaded From: https://www.spiedigitallibrary.org/ebooks/ on 09 Mar 2022
Terms of Use: https://www.spiedigitallibrary.org/terms-of-use

2.2.3.6.2 SEMATECH/SIA coordination

The SEMATECH and SIA organizations held semiannual NGL review meetings that were attended by industry, university, and government personnel. Their objective was to evaluate the progress toward developing several potential advanced lithography technologies to be used by the IC industry and to select the NGL technology at the appropriate time. The potential lithography technologies included proximity x-ray, electron-beam projection lithography (EPL), ion-beam projection lithography (IPL), 157 nm, and EUVL. Each of these technologies faced a number of potential showstoppers and issues that needed to be resolved before the industry could implement the technology into a manufacturing tool. The technologies were competing for funding and against a timeline to become the technology of choice by the industry, and SEMATECH provided the evaluation forum. In addition, SEMATECH provided funding support for critical industrial and university projects.

2.2.3.7 Suppliers

The initial semiconductor equipment manufacturers consisted of SVGL, ASML, and USAL. Although invited to participate in design reviews and working groups, Nikon and Canon were not invited to join as official EUV LLC-sponsored semiconductor equipment manufacturers because of U.S. government restrictions on foreign participation. The semiconductor equipment manufacturers were responsible for developing beta and production lithography tools using R&D from the EUV LLC program.

Joint development agreements (JDAs) and contracts were established with several companies, including TRW, Tinsley, Veeco, AES, Ultratech, and others to develop EUV sources, optics, and ML coating tools. Initial agreements involved the development of a 1.5-kW laser by TRW, advanced ML coating tools by Veeco, advanced optics polishing and manufacture by Tinsley, source hardware by AES, and magnetic stage components by Ultratech. These companies were involved in specific working groups and participated in the quarterly reviews.

The rigid restrictions imposed by CRADA Article XXII caused problems for foreign suppliers because they were required to demonstrate a U.S. benefit. This requirement tended to discourage normal commercial interactions between these suppliers and the VNL. The early failure to recognize that the U.S. government would prevent the EUV LLC from licensing lithography suppliers in Japan prevented the development of a robust competitive environment for the development of EUVL. Addressing this issue early in the program is one area in which the EUV LLC could have been more successful.

Downloaded From: https://www.spiedigitallibrary.org/ebooks/ on 09 Mar 2022
Terms of Use: https://www.spiedigitallibrary.org/terms-of-use

2.3 Program Structure

The initial EUV LLC overall program objective was to develop enabling EUVL technology to increase knowledge and reduce the risks for suppliers who were developing beta stepper/scanners in 2004 and production tools in 2006. This objective focused on three areas: (1) technology development for a laser-produced plasma (LPP) source, precision ML-coated optics, defect-free mask blanks, and supporting metrology; (2) design and fabrication of the ETS to demonstrate full-field imaging using a 0.1-NA, 4× magnification system with the equivalent EUV flux for a 10-wafer/hour throughput (200-mm wafers); and (3) development of supporting technologies for mask patterning, resist development/evaluation, and microstepper experiments.

2.3.1 Organization

The technical program was divided into seven major tasks with subtasks to support the overall program objectives (see Table 2.1). Each of the tasks was assigned to program managers at specific laboratories within the VNL, and a detailed work breakdown structure was developed that described the schedule, resources, and activities to be performed. Microsoft Project software was used for planning and documentation.

2.3.2 Risk management

Formal risk management was imposed early in the program for all technical and business areas. A rank-ordered list of technical and interaction risks that could delay or prevent completion of the R&D and timely commercialization of the technology was developed for each major technology area. The R&D risks were associated with technical issues or problems that needed to be solved. The interaction risks included intermeshing the individual technical accomplishments by the different teams into a composite schedule and specific team interface issues that needed to be addressed early in the development schedule to assure simultaneous completion of critical elements of the program. Interaction risks also included issues that needed to be addressed with the industry partners associated with the technology commercialization.

The formal risk-reduction process involved five distinct steps: (1) identifying the technical or implementation risks for each task both from a top-down and bottom-up approach by the teams involved; (2) scoring each risk according to scores listed in Table 2.2 and prioritizing the issues; (3) developing action plans to reduce each risk; (4) tracking and reporting progress in reducing the risks; and (5) repeating the process by refining the risk list through modification, elimination, or addition of a new risk.

Each of the risks was listed on a "score card" by each of the working groups and scored on a three-point system according to solution status or

Downloaded From: https://www.spiedigitallibrary.org/ebooks/ on 09 Mar 2022
Terms of Use: https://www.spiedigitallibrary.org/terms-of-use

Table 2.1 EUV LLC program tasks.

Major Task		Subtasks	
1	EUV Optics	1.1	EUV optic design
		1.2	Projection optics substrates
		1.3	Mounted projection optics
		1.4	POB
		1.5	Condenser optics substrates
2	ML Coating	2.1	ML coatings reflective improvement
		2.2	ML stress and substrate effects
		2.3	Uniform graded coatings
		2.4	ETS coatings samples evaluation
		2.5	Mo_2C/Si coatings
		2.6	Mo/Be reflectivity optimization
		2.7	Deposition equipment upgrades and controls
		2.8	Projection optics coating facilities
		2.9	Condenser coating facilities
		2.10	Other optics coatings
3	Metrology	3.1	100-pm phase-shifting point diffraction interferometer (PSPDI)
		3.2	Reflectometry and scattering
		3.3	At-wavelength interferometry
		3.4	At-wavelength defect inspection
4	Masks	4.1	150-mm reflection mask substrates
		4.2	Low-defect-deposition tool facility
		4.3	150-mm mask blanks with < 0.1 defects/cm^2
		4.4	Defect reduction in EUVL mask blanks
		4.5	Defect smoothing and repair for EUVL mask blanks
5	EUV Source	5.1	Advanced source for ETS illuminator
		5.2	Discharge source
		5.3	ETS illuminator
6	Resist	6.1	10× microsteppers
		6.2	Resist imaging and processing
7	ETS	7.1	POB integration
		7.2	ETS illuminator
		7.3	ETS system, body, and robotics
		7.4	ETS environment
		7.5	Stage subsystem
		7.6	Control subsystem
		7.7	System modeling
		7.8	System design environment

Table 2.2 EUV LLC risk-level definitions.

Risk Level	Designation
1.0	Problem defined (no solution identified)
1.5	Possible solution identified, R&D being performed
2.0	Basic solution in development
2.5	Solution demonstrated
3.0	Proven solution or supplier engaged for commercialization

Downloaded From: https://www.spiedigitallibrary.org/ebooks/ on 09 Mar 2022
Terms of Use: https://www.spiedigitallibrary.org/terms-of-use

schedule impact. Later in the program, half-point scoring was incorporated to recognize progress in reducing the risks, as shown in Table 2.2.

The individual working group lists were combined into a high-level list of risks to designate the top 15 to 20 risks. These lists were reviewed and updated at the quarterly reviews. The entire risk list for subprojects frequently contained several hundred items at the lowest level of the hierarchy.

During the formal quarterly reviews, a risk scorecard was presented for each project. The scorecard listed each specific risk and briefly described the issues and progress associated with that risk. Numerical scores were summarized for each risk. During each review, the current scores were compared with the previous review scores to measure the level of progress, and a target date was established to indicate when the risk needed to be resolved. Color coding was used to emphasize any lack of progress and the severity of the risk within the program.

2.3.3 Reporting

Aggressive program management methods and oversight were provided by the industrial partners. In addition to developing a detailed work breakdown structure for all aspects of the program, the VNL set detailed milestones and deliverable schedules. Auxiliary goals were established to coincide with technical presentations at conferences to highlight EUV progress and to increase industry awareness and interest in the technology. Once the decision was made to report on EUVL advances and to directly compete with the other NGL technologies at the SEMATECH/SIA NGL meetings, additional milestones were established to demonstrate the technology advances at those NGL meetings and to demonstrate progress toward resolving the critical issues defined by the NGL task force.

The high level of program visibility provided at technical conferences, leadership by Intel, and program progress generated good press coverage in the technical journals and general news publications. Over 100 press and news articles enabled various interest groups within the political and industrial communities to identify with the program and support it for their own success.

2.3.3.1 Weekly meetings

Status-update meetings for the program managers and EUV LLC representatives were held weekly in the EUV LLC office at SNL in Livermore, California. Call-in options were available for the EUV LCC members who could not attend the meeting and for managers who were traveling. Key technical and business highlights were discussed, and appropriate actions were identified to address problem areas. Five- to ten-page written reports summarizing activities in the EUV LLC office, technical highlights within the VNL, plans, and required actions were published weekly and distributed to approximately sixty EUV LLC representatives and VNL program managers.

Downloaded From: https://www.spiedigitallibrary.org/ebooks/ on 09 Mar 2022
Terms of Use: https://www.spiedigitallibrary.org/terms-of-use

2.3.3.2 Monthly and quarterly reviews

Formal reviews were presented each month to the technology committee. In addition to providing updates on critical issues, specific topic presentations were provided by key technical personnel on an as-requested basis. Also, business and IP issues were discussed at the regular monthly committee meetings.

Formal eight-hour quarterly reviews were held at an off-site hotel in Pleasanton, California. These reviews were attended by approximately 80 representatives from member companies, suppliers, and VNL personnel. In addition to reviews at each meeting of general technical progress in key areas such as the ETS design and fabrication, other topics were reviewed at alternating meetings to ensure in-depth coverage of all aspects of the program. During each review, attendees identified action items for attention during the next quarter. Copies of all foils used in the presentations were provided to the attendees.

2.3.3.3 NGL Review

Annual technology status reports were presented at the SEMATECH NGL technology reviews. Critical issues and potential showstopper problems were identified by the attendees for action by the EUV LLC / VNL.

2.3.3.4 International meetings

The EUV LLC, working with SEMATECH and ASET,[19] established an Annual International EUV Workshop that was held each autumn.[20] The first workshop took place on October 13, 1999 in Monterey, California, with succeeding workshops rotating among the U.S., Europe, and Japan. Progress in developing the EUV technology was reported worldwide; separate international coordinating meetings and workshops were held for various topics in conjunction with the workshop.

2.3.4 Documentation

A variety of reporting mechanisms were used to document the program results, including monthly committee meetings and weekly status meetings. Minutes were written for all meetings and distributed to the EUV LLC members and interested EUV LLC managers.

2.3.4.1 White papers

In response to SEMATECH requests, several white papers were published during the early phases of the program to summarize the technology status and challenges.[21] These 200-page reports introduced the technology; outlined the program organization; and documented the technical progress, remaining problems, cost of ownership model, and plans for resolving the remaining technical issues.

Downloaded From: https://www.spiedigitallibrary.org/ebooks/ on 09 Mar 2022
Terms of Use: https://www.spiedigitallibrary.org/terms-of-use

2.3.4.2 Quarterly reports

Formal quarterly reports were prepared by the VNL program and project managers. These reports discussed the technical projects in detail, including problem areas, and disclosed possible inventions to be considered for patents or trade-secret classification.

2.3.4.3 Conference presentations and journal publications

The program supported the presentation of technical results at national and international conferences and the publication of articles in technical periodicals. This motivated laboratory research personnel and generated good public relations for the program. A formal process was used to review proposed presentations and publications. During the 6-year EUV LLC program, the review committees examined 590 abstracts and papers, as shown in Fig. 2.3, and provided feedback to the authors to improve the quality of material recommended for presentation or publication. A large majority of the proposals was recommended for publication.

2.3.4.4 Website

Midway through the program, a password-controlled website was established for the EUV LLC member companies and VNL personnel. The site contained copies of the foils presented at the quarterly reviews, minutes from the working groups, selected abstracts and written versions of published papers, calendars, and personnel listings with contact information. It also provided access to reference material, and in many instances the foils and illustrations from the site were used by the EUV LLC member company personnel to prepare presentations at their facilities.

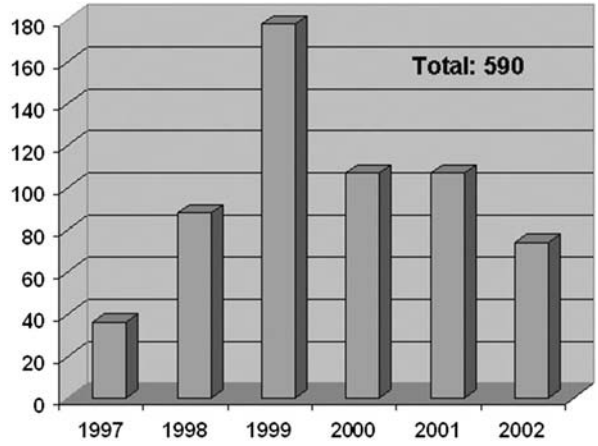

Figure 2.3 Abstracts and papers reviewed by the EUV LLC review committee.

Downloaded From: https://www.spiedigitallibrary.org/ebooks/ on 09 Mar 2022
Terms of Use: https://www.spiedigitallibrary.org/terms-of-use

2.4 Program Results

2.4.1 Technical accomplishments

By most measures, the program accomplished every technical goal established by the EUV LLC by providing excellent technology advances and an enormous amount of technical information.

One major goal was to design and fabricate an integrated full-field (24×32.5 mm) 0.1-NA scanning lithography tool that demonstrated all aspects of EUV technology, including the EUV source, optical collection and focusing system, synchronized scanning stages, environmental control system, and computer control complete with low-defect reflective masks. This lithography system, the ETS, is shown in Figs. 2.4 through 2.8 along with representative images in Fig. 2.9.

One highly significant measure of the success of the EUV LLC program is that no major new technical surprises have been uncovered during the commercialization of EUV technology. This is in strong contrast to the experience of other NGL technologies in which major showstoppers were uncovered. For example, the development of 157-nm lithography failed because of the late discovery of CaF_2 birefringence.

A detailed description of the EUVL technology development status in 2003, reflecting the signature contributions made by the EUV LLC / VNL, is provided in Ref. 22. Most of the technical program accomplishments are summarized in Appendix 2A. Highlights of the program include the following:

- designed and fabricated a complete, integrated, full-field (24 mm $\times$ 32.5 mm), scanning alpha class lithography tool, the ETS, complete with a computer-controlled system;

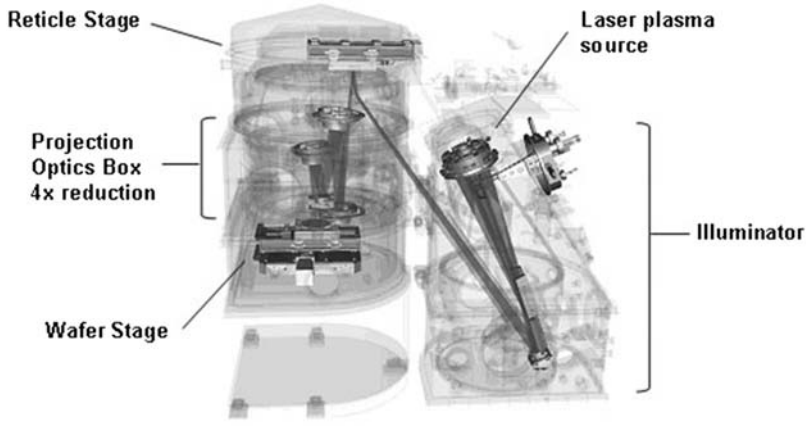

Figure 2.4 Schematic drawing of the optics path in the ETS identifying major system components (reprinted with permission from Intel).

Downloaded From: https://www.spiedigitallibrary.org/ebooks/ on 09 Mar 2022
Terms of Use: https://www.spiedigitallibrary.org/terms-of-use

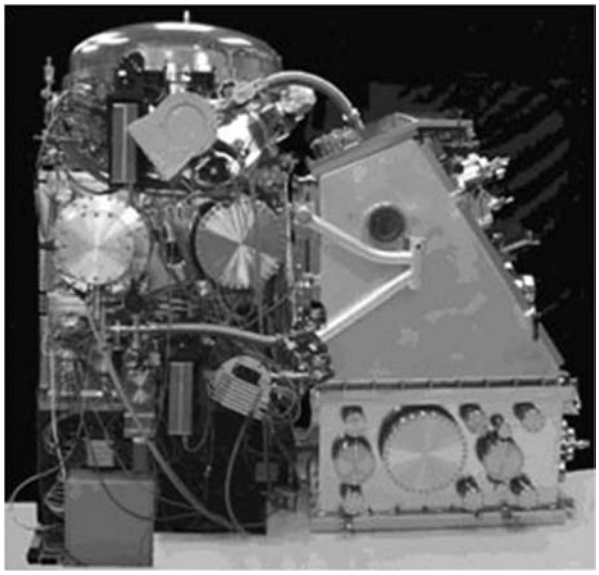

Figure 2.5 Initial assembly of the ETS illuminator and wafer exposure chambers (reprinted with permission from Intel).

Figure 2.6 Right-side view of the fully assembled ETS showing the source chamber and wafer exposure chambers with associated control and utility connections (reprinted with permission from Intel).

- pioneered the development of both LPP sources and electrical discharge-produced plasma (DPP) sources;
- developed and integrated computer-aided design methods to support thermal, dynamic, and vibration design and analysis of individual components, subsystems, and complete system operation;

Downloaded From: https://www.spiedigitallibrary.org/ebooks/ on 09 Mar 2022
Terms of Use: https://www.spiedigitallibrary.org/terms-of-use

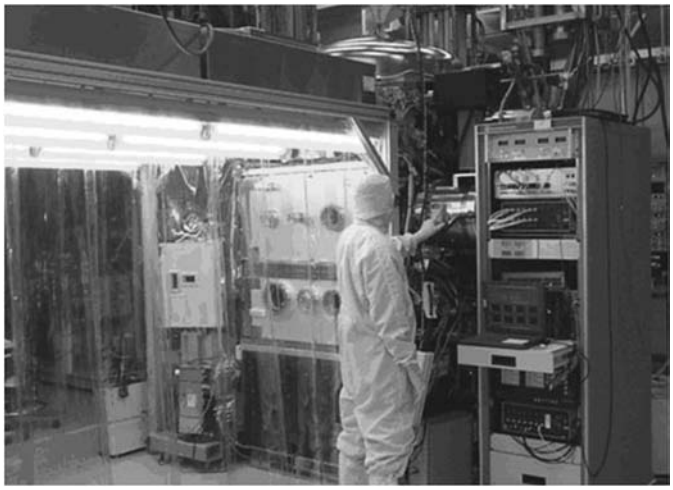

Figure 2.7 Front view of the completed ETS showing the wafer exposure chamber (reprinted with permission from Intel).

Figure 2.8 Control console for the ETS with graphic displays to control the wafer exposure and monitor the status of the LPP source, condenser, and projection optics flux systems (reprinted with permission from Intel).

Downloaded From: https://www.spiedigitallibrary.org/ebooks/ on 09 Mar 2022
Terms of Use: https://www.spiedigitallibrary.org/terms-of-use

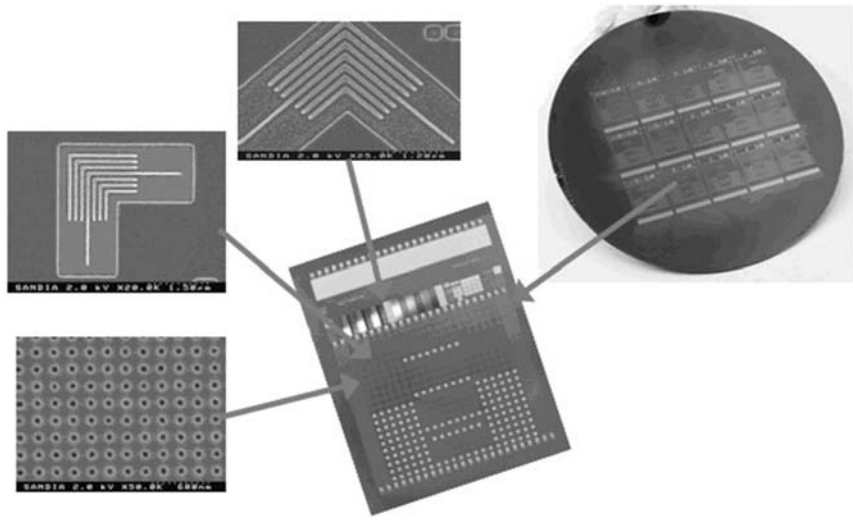

Figure 2.9 Representative printed test patterns and wafer obtained using the ETS (reprinted with permission from Intel).

- developed reflective EUV mask technology, including ML-coated LTEM mask blanks complete with metrology, ML defect repair methods, patterning inspection, and repair processes;
- implemented EUV optics fabrication projects with the industry to demonstrate continuous improvement in optics fabrication technology;
- developed and engineered MLs with capping layers to provide good reflectivity and stability;
- pioneered environmental mitigation techniques to maintain POB optics in pristine conditions, and pioneered optics cleaning technologies to remove carbon and oxide from optics surfaces;
- demonstrated extensive EUVL printing using extended DUV resists;
- obtained SEMATECH support for the infrastructure technology;
- provided formal program management and reporting; and
- reviewed and collected over 300 IP items, including ~150 awarded or pending patents and numerous technical/trade secrets.

2.4.2 IP portfolio

2.4.2.1 EUV LLC U.S. patent portfolio

During the development of the initial EUV LLC concept, a key decision was to capture an extensive IP portfolio from the work at the VNL and the member companies. This goal did two things: (1) it supported assembling a large patent portfolio for use by suppliers, and (2) it minimized the possibility that a single development organization would capture blocking IP that could inhibit or prevent efficient implementation of the technology. Individual VNL

Downloaded From: https://www.spiedigitallibrary.org/ebooks/ on 09 Mar 2022
Terms of Use: https://www.spiedigitallibrary.org/terms-of-use

researchers were encouraged to disclose new ideas, and a formal VNL team of consultants was established to process the disclosures and develop the formal patent applications. The disclosure review resulted in patent filings, classification as copyright material, classification as CRADA-protected material, or classification as trade secrets. A detailed listing of the EUV LLC U.S. patents based on the U.S. Patent and Trademark Office (PTO) database status as of April 2016 is included in Appendix 2B.

As can be seen in Fig. 2.10, the EUV LLC continued to file U.S. patents well beyond the end of the technical program, which was completed at the end of December 2002. According to data retrieved from the U.S. PTO public database through the first quarter of 2016, the last EUV LLC patent was filed in 2006, and EUV LLC patents were granted as late as 2011. Figure 2.10 also shows a patent that pre-dated the EUV LLC. This patent, filed in 1994, belongs to a group of EUV source patents filed by the University of Central Florida and seems to have been acquired by the EUV LLC. Of the 151 EUV LLC patent disclosures filed with the U.S. PTO, 144 resulted in granted patents. However, not all of these 144 patents were maintained by the EUV LLC (see Fig. 2.11). The U.S. PTO patent status of those 144 patents shows that 125 of them were active as of April 2016.

Given the many years of EUV technology development and commercialization after the EUV LLC technical program ended (15 years as of 2017), the 19 U.S. patents the EUV LLC choose not to maintain represent a surprisingly small fraction (~13%) of the total number of EUV LLC patents issued. This indicates that the EUV LLC achieved its goal in this area, i.e., developing a strong patent portfolio to safeguard the continued development and commercialization of EUV technology and infrastructure. It is no surprise that the relative number of discontinued U.S. patents (40%) is highest for EUV source, as the technology in this area had evolved farther from the

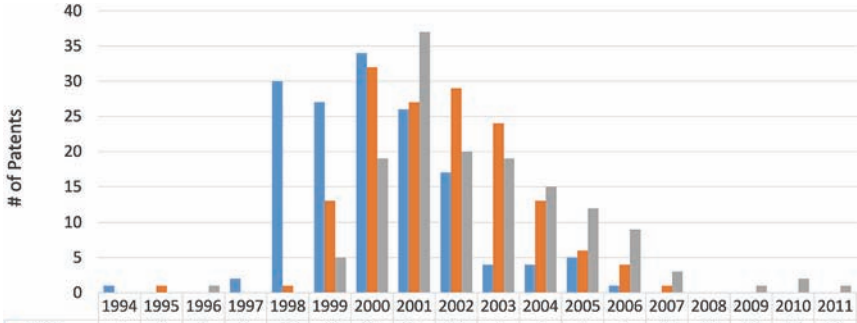

	1994	1995	1996	1997	1998	1999	2000	2001	2002	2003	2004	2005	2006	2007	2008	2009	2010	2011
Filed	1	0	0	2	30	27	34	26	17	4	4	5	1	0	0	0	0	0
Published	0	1	0	0	1	13	32	27	29	24	13	6	4	1	0	0	0	0
Granted	0	0	1	0	0	5	19	37	20	19	15	12	9	3	0	1	2	1

Figure 2.10 EUV LLC U.S. patents filed, published, and granted based on U.S. Patent and Trademark Office data from April 2016.

Downloaded From: https://www.spiedigitallibrary.org/ebooks/ on 09 Mar 2022
Terms of Use: https://www.spiedigitallibrary.org/terms-of-use

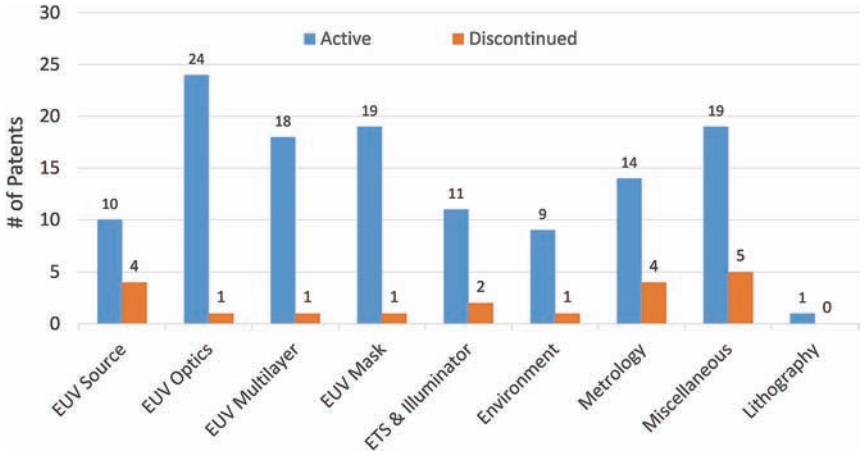

Figure 2.11 EUV LLC active (125) and discontinued (19) U.S. patents based on U.S. PTO data as of April 2016.

development status at the end of 2002 than, e.g., EUV optics and mask technology; all of the four discontinued EUV source patents covered capillary-discharge source IP, which is not the technology pursued for high-volume manufacturing (HVM) exposure tools. The second highest percentage (~29%) of discontinued EUV LLC patents is found in the metrology area. However, a closer look at this part of the portfolio shows that the EUV LLC chose to discontinue only those patents whose areas were covered by multiple filings or, in a single case, where the technology was more of the ancillary type than core EUV IP. In this case, the technology would be considered background IP for anybody either practicing EUV or building EUV tools or materials. Similar considerations may have applied to the discontinuation of EUV LLC patents in the "Miscellaneous" patent group (~26%) representing ancillary-type EUV exposure tool patents or patents where new developments went beyond what the EUV LLC patent covered.

It certainly took much longer (than what was expected at the end of the EUV LLC technical program in December 2002) to commercialize and mature EUV technology and infrastructure to a level that seems almost ready to support HVM.

However, as shown in Fig. 2.12, the remaining lifetime of EUV LLC U.S. patents seems to still cover the likely introduction of EUV into HVM in the next 2–3 years, and then one—or maybe even two—more generations of EUV tools and materials after that.

2.4.2.2 Industry reception of the EUV LLC patent portfolio

The EUV LLC patent-filing strategy was driven by the need to ensure that no single company could disrupt the commercialization of EUV lithography combined with the technical goal of demonstrating all key elements of the

Downloaded From: https://www.spiedigitallibrary.org/ebooks/ on 09 Mar 2022
Terms of Use: https://www.spiedigitallibrary.org/terms-of-use

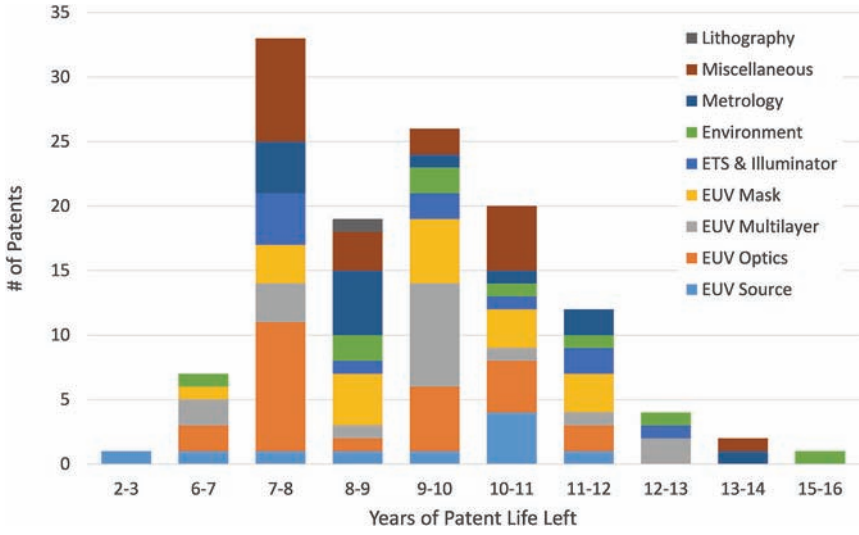

Figure 2.12 Remaining patent life of active EUV U.S. patents (125) based on a 25-year patent life, starting at the filing date.

technology. This strategy should have resulted in the EUV LLC IP portfolio becoming critical background IP for any company that set out to participate in the EUV marketplace, either as a user of the technology or as a provider of tools and materials required to practice EUV lithography. While it is difficult to assess if this really happened because IP licensing deals are usually not made public, one can infer the perceived relevance of the EUV LLC IP portfolio by looking at how it is referenced in the U.S. patent database.

Excluding EUV LLC U.S. patent self-references, a search on the U.S. PTO website shows that as of April 2016, 2,131 U.S. patents reference the 144 EUV LLC patents. Looking at the 125 still-active EUV patents (Fig. 2.13), this number goes down to 1,685 EUV LLC patent references coming from roughly 185 companies (the number is a good estimate as 53 of patent assignees could not be identified). However, the bulk of the references (~1,300 references) to the active EUV LLC patent portfolio comes from about 20 companies.

Not surprisingly, the bulk of the references to the active EUV LLC patent portfolio comes from tool/optics manufacturers and semiconductor manufacturers and equipment suppliers (~2/3). As can also be seen from Fig. 2.13, EUV remained a fertile research area for universities, national laboratories, and other research institutions that are not directly tied to manufacturing. Somewhat surprising is the relatively smaller representation of the equipment and materials suppliers. The category for lithography mask includes all merchant mask shops as well as EUV mask blank suppliers (captive mask shops are included in the chip manufacturer category). One reason for this could be that companies in this category choose to protect their developments

Downloaded From: https://www.spiedigitallibrary.org/ebooks/ on 09 Mar 2022
Terms of Use: https://www.spiedigitallibrary.org/terms-of-use

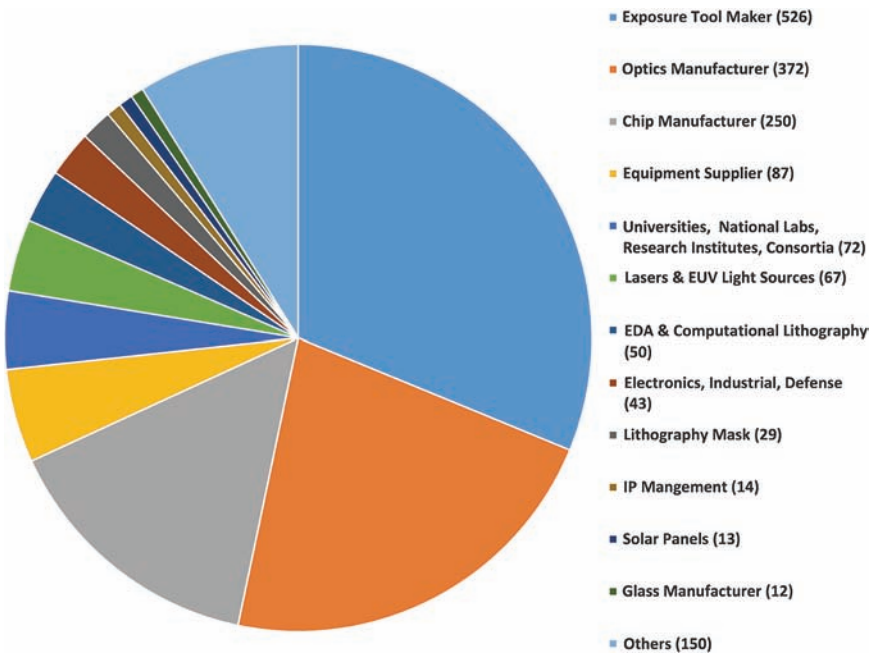

Figure 2.13 U.S. patent references to the 125 active U.S. patents broken down by company or organization type.

as trade secrets rather than to let competitors know their capabilities by filing patents.

One would expect that the relative semiconductor market size in the larger geographical regions would be a good reflection on how relevant EUV technology is to a given region. Restricting this comparison to the chip manufacturers, one can see from Fig. 2.14 that the relative global market size of chip manufacturers in each of the major regions is indeed a good reflection of how important EUV technology is for this region. For the purposes of this comparison, a U.S. patent filed by a given chip manufacturer was included if it referenced EUV in the claims section.

Figure 2.15 shows a comparison of EUV-relevant U.S. patent filings (again as measured by "EUV" being mentioned in the patent claims section) between EUV LLC members and nonmembers among chip manufacturers. While both groups filed about the same number of EUV-relevant U.S. patents, there is a clear difference in how the EUV LLC patent portfolio has been referenced. The pie chart in Fig. 2.15 likely underestimates the magnitude of this difference in perception regarding the EUV LLC IP. This is because only few of the original EUV LLC members are still among the leading-edge chip manufacturers, so the relative weight of the nonmembers pursuing EUV is now greater than it was when the EUV LLC completed its technical program in 2002. The industry landscape is different today from

Downloaded From: https://www.spiedigitallibrary.org/ebooks/ on 09 Mar 2022
Terms of Use: https://www.spiedigitallibrary.org/terms-of-use

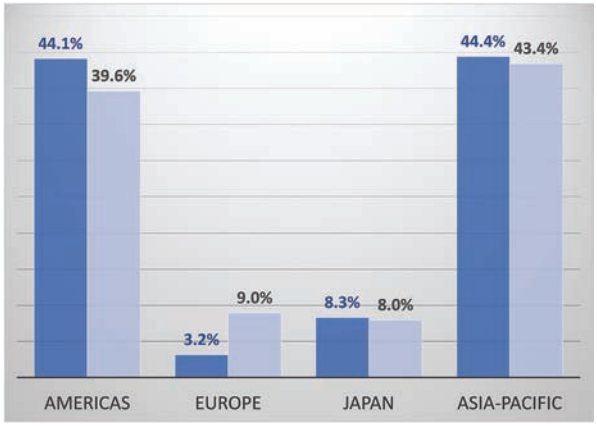

Figure 2.14 Relative market size (dark-gray bars) of chip manufacturers (based on World Semiconductor Trade Statistics data from August 2015) in major geographical regions compared to relative percentage (light-gray bars) of EUV-related U.S. patent filings.

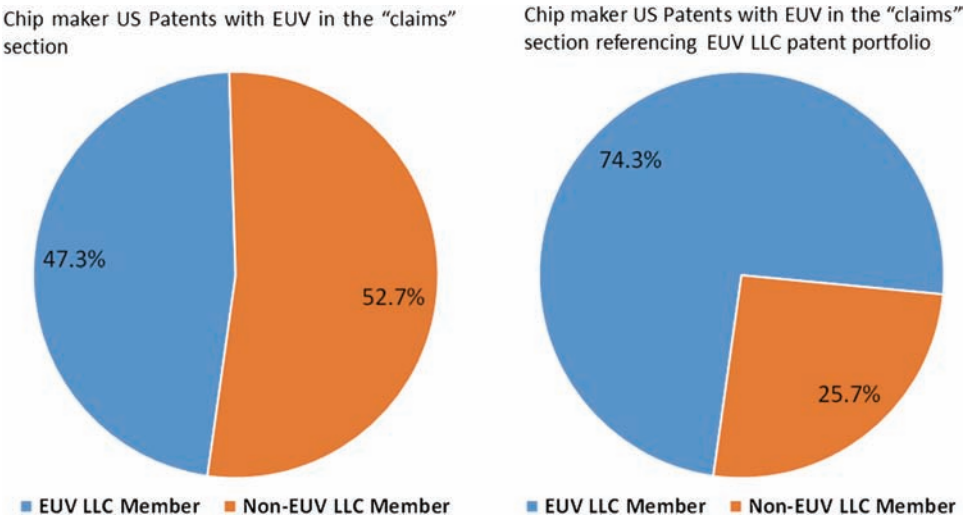

Figure 2.15 Comparison of U.S. patent filings of EUV LLC members versus nonmembers.

what it looked like in the early 2000s; among the top 3–4 chipmakers that may be using EUV, only one EUV LLC member remains. The EUV LLC patent portfolio was created to enable EUV commercialization for the industry. However, this industry now has a much smaller number of leading-edge chipmakers and an increasingly consolidated equipment- and material-supplier base that becomes increasingly dependent on those few remaining leading-edge chipmakers. The result is a much more competitive landscape, and it remains to be seen if—once EUV is finally used in HVM—this will lead to a different perception of the EUV LLC portfolio among companies in the EUV market, technology users, and providers.

Downloaded From: https://www.spiedigitallibrary.org/ebooks/ on 09 Mar 2022
Terms of Use: https://www.spiedigitallibrary.org/terms-of-use

2.4.3 Program statistics

During the six-year program, the EUV LLC's funding and manpower investment was responsible for substantial EUVL technical progress. The external investment by the EUV LLC in VNL and supplier-sponsored projects was well over US $270M, including technical and management support. The full-time equivalent (FTE) personnel assigned to the program each year by the VNL are shown in Fig. 2.16. Some of the program statistics are summarized in Table 2.3.

2.4.4 Delays

In spite of the attractiveness of EUV technology and EUV LLC support, the technology encountered several implementation delays. Because of technology

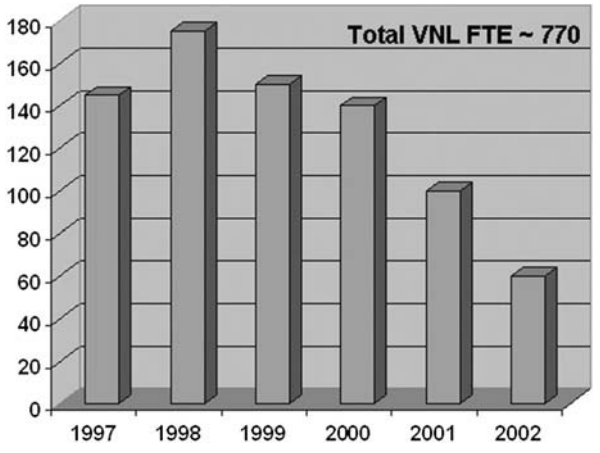

Figure 2.16 VNL personnel working on the EUV LLC program.

Table 2.3 Key program statistics.

Agreement	Three-year CRADA signed in 1997; extended twice for a total of six years
Financial investment	Over US $270M invested by the EUV LLC (~$250M with the VNL)
Personnel	Total personnel included 387 at VNL and 160 at member companies
Risk issues	>400 risk issues tracked
Publications and presentations	600 publications and presentations (>38 meetings/publications)
Quarterly reviews	24 quarterly reviews
Meetings	~250 weekly status update meetings; hundreds of working group meetings
Critical reviews	10 SEMATECH NGL critical reviews
Facility tours	~100 facility and laboratory tours and company reviews
Press	>100 press articles
Documentation	three white papers
	24 quarterly reports
	280 EUV LLC weekly reports (1400 pages)
	850 VNL weekly highlights
	~10,000 viewgraphs

Downloaded From: https://www.spiedigitallibrary.org/ebooks/ on 09 Mar 2022
Terms of Use: https://www.spiedigitallibrary.org/terms-of-use

extensions, program delays, and the value of additional R&D to support EUVL, the CRADA with the VNL was extended initially for two additional years and then subsequently for another three years (this later extension was terminated after 1½ years). These extensions provided a mechanism to continue the technology development as well as documentation and collection of IP. Some of the main reasons for the delays are discussed below.

2.4.4.1 Extension of DUV

One reason for the delay was a change in expectations for DUV technology: the expectations for existing DUV technologies were extended far beyond those of the mid-1990s, when EUVL was first proposed. Even though EUVL was first proposed for introduction at the 100-nm node, it was not ready as planned in the middle of the last decade, and DUV became the main technology at 45 nm half-pitch using water-based immersion technologies.[23,24] Because the DUV extensions from 248 nm to 193 nm and 157 nm and then to immersion were viewed as simple extensions of the existing optical lithography, there was a widespread industry reluctance to divert resources to a new technology like EUVL. It has been estimated that the diversion caused by 157-nm technology, which was later proven unsatisfactory, caused at least a two-year delay in EUVL development. It is worth noting that the extensions of 248 nm and 193 nm were largely enabled by optical polishing and metrology technology, which was initially developed for EUV optics.

With the 193-nm single-patterning immersion technology reaching its limits and EUV not ready for HVM at 32 nm, the industry had no choice but to move to adopt 193-nm immersion double patterning and is currently in the process of extending this technology to quadruple patterning for the 10-nm technology node. The increasing complexity and cost of multiple patterning as well as the concurrent maturation of EUV technology are now likely to lead to a co-existence of EUV lithography and 193-nm multiple-patterning lithography. As of early 2017, several companies are running or ramping up EUV pilot lines, and it could be that at the 7-nm node selected critical layers will be printed with EUV, while 5 nm seems to be the real target for EUV HVM introduction in a mix/match with 193-nm multiple patterning.

2.4.4.2 Competitive technologies

In addition to the 193-nm, 157-nm, and potentially 126-nm optical technologies,[25] alternative IPL, EPL, and proximity x-ray lithography also had industry support as NGL technologies in the late 1990s and into the early 2000s. Various alliances were established to support a specific technology—IBM and AT&T sponsored EPL, the Europeans focused on IPL, the EUV LLC championed EUVL, and Japan and separately IBM focused on proximity x-ray lithography. There was some disparity in the level of research and reporting for each of the technologies. The EUVL program reported technology challenges

Downloaded From: https://www.spiedigitallibrary.org/ebooks/ on 09 Mar 2022
Terms of Use: https://www.spiedigitallibrary.org/terms-of-use

and risks in addition to technical progress, which gave EUV technology issues much higher visibility than problems with other technologies; consequently, risks for EUVL were often perceived as more severe. At various points during the program, EUVL issues such as optics finishing accuracy, the possibility of mask phase defects, critical dimension (CD) control, defect-free masks and mask costs, high source power, and high cost of ownership were considered EUV technology showstoppers.

2.4.4.3 Economic downturn

Although the development of EUVL and other NGL technologies began in the mid-1990s when industry and technology advancement interest was high, the subsequent economic downturn caused many companies to delay investments in advanced lithography technologies. Economic fluctuations caused oscillations in the technology interest, the expected manufacturing insertion date, and development schedule, which also tended to increase costs. In addition, the projected high tool cost, on the order of US $25M, discouraged company commitments. Even though the cost was high by I-line and DUV standards, the projected cost was well in line with SEMATECH's predictions for an NGL technology based on the increasing cost trends associated with decreasing technology node dimensions and time lines.

2.4.4.4 Industry indecision

The lack of strong industry support for a specific NGL technology provided mixed messages for the manufacturing tool suppliers. Even though each technology had a strong sponsor, the levels of industry commitment varied. The semiconductor manufacturers' vacillation in making investments and the apparent lack of consensus for NGL technology caused the equipment development companies and their suppliers to delay the advanced investment required to establish the infrastructure, which led to additional cascading delays.

2.5 Retrospective Observations

Even though by most measures the EUV LLC program was very successful, activities could have been done differently in several areas.

2.5.1 Improvements

2.5.1.1 Additional planning and slower ramp

Because of the time pressures to implement the EUVL program, both to retain laboratory support and enthusiasm and to obtain industry support for the technology rather than other potential NGL technologies, the VNL program was scaled up during the first year from the minimal DOE investment to a higher level. As a result, various projects competed for personnel, and some

Downloaded From: https://www.spiedigitallibrary.org/ebooks/ on 09 Mar 2022
Terms of Use: https://www.spiedigitallibrary.org/terms-of-use

projects were started prematurely. Later oscillations in funding resulted in personnel cutbacks with the accompanying reduction in morale. If more suppliers had been engaged before the program scaled up, and if a more uniform funding rate could have been supported, the funding could have been used more efficiently.

2.5.1.2 Additional member company involvement

Even though Intel deserves the major credit for starting and maintaining the program, an earlier, stronger marketing effort to enlist EUV LLC members could have had tremendous benefit. If all six members had been members of the EUV LLC before signing the CRADA, their influence could have been used with the government to modify the terms of the CRADA. In addition, a more unified investment by all members may have resulted in a stronger buy-in from the companies with more ownership for problems and solutions. The early requirement for minimum percentage ownership in the EUV LLC, which was later removed, should have remained in effect in an attempt to provide more active participation. Although a decision was made at the beginning of the program to not count members' "in-kind" investments in the EUV LLC, perhaps an alternative in-kind investment with a specified number of onsite assignees could have helped ensure more active participation.

2.5.1.3 Additional semiconductor equipment manufacturer involvement

In retrospect, an ideal program could have been implemented differently. For example, a large investment was made to produce the ETS. A better investment would have been to develop the alpha tool for one of the stepper companies using VNL resources. For instance, a partnership could have been developed with a single semiconductor equipment manufacturer to use the VNL modeling, simulation, and design resources to develop its alpha tool. This would have involved a joint design by the semiconductor equipment manufacturer and VNL engineers using VNL design tools. The alpha tool could have been assembled in offsite leased laboratory space in the Livermore area, which could have become a branch development center. Congruent with the alpha tool development, the semiconductor equipment manufacturer could have refined the design (with SNL assistance) to build the beta or preproduction tool. Although a single semiconductor equipment manufacturer is used as an example, with adequate planning, several companies could have bid on the alpha tool development, and the company offering the best support, business plan, and investment could have been awarded the VNL's support. In addition, since the total ETS investment was on the order of US $100M, some funding assistance could have been provided to the semiconductor equipment manufacturer in return for its active participation and assignment of onsite personnel. This approach also would have provided

Downloaded From: https://www.spiedigitallibrary.org/ebooks/ on 09 Mar 2022
Terms of Use: https://www.spiedigitallibrary.org/terms-of-use

a good transition to ensure complete industry use and ownership of the tool after the VNL's formal program was completed.

The EUV LLC could have required more direct involvement by TRW/CEO to develop the LPP source at the VNL instead of in its facilities. In light of TRW/CEO's acquisition by Northrop Grumman in early 2003 and the subsequent decision to stop EUV source development work, this action would have protected some of the knowledge base for reapplication.

2.5.1.4 Supplier involvement

Suppliers were not as involved in the program as they could have been, resulting in less technology transfer and commercialization than planned. Varying levels of IC company interest discouraged suppliers from investing more aggressively. If suppliers had been more actively involved from the beginning and had assigned personnel on site at the VNL to be responsible for technology transfer and for providing inputs to the program on a continuing basis, more effort could have been directed toward solving the suppliers' specific problems.

2.5.1.5 DOE support

The laboratories' management always supported the program; however, the levels of support varied substantially during the six-year program. Initially, the program had the attention of management at all levels, but the interest of new managers varied. In addition, several personnel were promoted during the program. Some of the replacement personnel were more experienced than others, and the program results often reflected those experience levels. During the later phases of the program, the DOE received substantial government support for homeland security. At this point, there was a lower level of interest in the EUV LLC contributions, and because of the internal competition for personnel within the laboratories and decreased funding from the EUV LLC, many of the pioneering EUV personnel left the program, creating gaps in the program expertise.

2.5.1.6 Program termination

The program termination could have been handled differently. Although the intent was to leave the EUVL research operations intact with an operating ETS for use by the VNL Resource Development Center (RDC), the transition did not go as smoothly as desired. First, even though SEMATECH funded a number of projects, the level of funding and difficulty in establishing formal projects resulted in smaller projects than the laboratories needed to maintain a critical resource base and support the technology development. Second, even though the VNL started a marketing program, the high VNL costs and the industry's ever-changing target for commercial implementation of EUVL discouraged suppliers from investing in VNL projects. Third, even though the

Downloaded From: https://www.spiedigitallibrary.org/ebooks/ on 09 Mar 2022
Terms of Use: https://www.spiedigitallibrary.org/terms-of-use

EUV LLC companies purchased ETS usage shifts for their proprietary experiments, the shift subscriptions were not sufficient to guarantee the necessary support for the ETS for a full year. Instead, a compromise was made to operate the ETS for a partial year at a reduced level of support. This decision, coupled with the loss of key operating and engineering personnel, had a disastrous effect in early 2003 that resulted in operational errors and technical problems with EUV sources that could not be adequately solved. This experience with the ETS user facility was disappointing to the EUV LLC companies; most of them received fewer good operational shifts than purchased, and the imaging results were distorted by lack of experimental control. The net result was that the system was completely shut down at the end of June 2003 because of a lack of continuing demand by the EUV LLC members.

2.5.1.7 Missed opportunities

The VNL RDC user facility did not meet its objective because the EUV LLC overestimated the technical readiness of the ETS to support a pilot line exposure service, and because the VNL underestimated the resources required to provide exposure to the ETS that could have retained current users and attracted potential new users. Many of the RDC problems were not EUV-specific and could have been avoided if, for example, the processing capabilities essential for the user facility had been integrated in a pilot line fashion. However, this would have required EUV LLC members to provide the personnel and material resources to run the RDC by themselves.

Another aspect of the RDC may have provided an even greater benefit than delivering exposed wafers to RDC customers: EUV technology learning. Although EUV is an optical lithography technology, many of its subsystem technologies are different from those used in current 193-nm lithography tools. Significant learning could have been captured by running the ETS for customer use and by capturing and understanding all of the EUV-specific problems in a systematic way. This may have been possible within a year, and semiconductor equipment manufacturers and EUV system subcomponent suppliers could have greatly benefited from this learning.

2.5.2 External issues

2.5.2.1 Washington, D.C. involvement

During the early phases of the program, the project generated conflicting interest within the Washington, D.C. government agency community. The DOE supported the program as a demonstration of a large industry partnership and a continued focus on technology. The DOC interpreted the program as a way for foreign companies to gain access to leading U.S. technology from the national laboratories. This latter view was further emphasized by private company personnel visits to the Washington, D.C. offices.

Downloaded From: https://www.spiedigitallibrary.org/ebooks/ on 09 Mar 2022
Terms of Use: https://www.spiedigitallibrary.org/terms-of-use

2.5.2.2 CRADA negotiations

Before the formal beginning of the program, additional time should have been spent to resolve CRADA issues. The IP patenting issue was resolved to the benefit of the EUV LLC in that the EUV LLC owns the titles to all patents, with certain use rights outside of lithography reserved by the DOE. This was a monumental accomplishment because CRADA participants generally obtain only a nonexclusive license. The issue of "net U.S. benefit" also should have been addressed more thoroughly before the CRADA was signed. Since a large amount of political effort was invested to deal with some industry representatives and the DOC after signing the CRADA, the time required to make a case for foreign involvement initially could have been a good investment. Perhaps a more complex partnership between the EUV LLC and Japan than with SVGL could have been proposed that would have provided a "net U.S. benefit" and supported competitive development.

Although time was urgent, in 1997 the EUV LLC was negotiating from a position of strength with a very anxious DOE in regard to implementing the program. Even though the DOE desired for this to be an industry-owned and supported program, the DOE may have been willing to provide some complementary or matching investment in related technologies (like metrology) to provide additional leverage for the EUV LLC funding. Although the DOE provided some overhead tax relief for capital purchases, they might have been willing to reduce other overhead rate charges or reduce the laboratory tax to extend the leverage of EUV LLC funding.

2.5.3 Benefits

2.5.3.1 VNL

The VNL obtained substantial benefit from the EUV LLC program. The program provided interesting research for its engineers and scientists and thus continued to build the knowledge base for the laboratories. It provided personnel with the opportunity to present and publish more than 500 papers and to gain professional recognition, thus providing a good motivator for innovative research. The program exposed the laboratory personnel to industry management methods, cost controls, and daily environmental changes. It also gave the laboratories visibility within political, press, and industrial environments. The DOE highlighted the program as one of the most successful leading-edge technology development industry projects, and in 2003 the VNL received an R&D 100 award for the design and fabrication of the ETS.

2.5.3.2 Industry

The EUV LLC program benefited industry in the form of proof-of-concept for EUVL system design and the fundamental engineering associated with using EUV for imaging. The semiconductor equipment manufacturers

Downloaded From: https://www.spiedigitallibrary.org/ebooks/ on 09 Mar 2022
Terms of Use: https://www.spiedigitallibrary.org/terms-of-use

benefited from the learning associated with optics fabrication and metrology by Tinsley and ZEISS, the vacuum materials qualification by VNL experiments, the environmental and contamination control methods (protection, mitigation, and thermophoresis) that were demonstrated, and the sensor development in such areas as dose control, thermal management, and optics alignment, which can be used in numerous areas of system design and fabrication. Basic development has also been done for specialized components such as spectral purity filters, sensors for various metrology applications, and standards for component performance and metrology. In addition, the basic development and value of modeling software for application, visualization, and analysis has been demonstrated as applied to system, subsystem, and component design.

For subsystem design, both the LPP and DPP sources have been characterized, and the scalability of each has been evaluated; POB design, engineering, and fabrication have been demonstrated, and thermal management and alignment methods have been developed. Precision ML-coated optics have been fabricated by several suppliers. In other infrastructure areas such as mask blank fabrication with defect-free absorbers and buffer layers, and patterning with defect repair and inspection, the commercialization risks have been reduced.

Finally, for IC manufacturers, the proof-of-concept ETS demonstrated both small-field and scanned images, thus reducing the engineering risk associated with developing complete alpha and beta tools. The ETS provided imaging experiences that can be used to project the level of difficulty in adapting EUVL to a manufacturing environment. In addition, basic mask manufacturing methods were demonstrated along with the necessary metrology for inspecting the reticles. The extension of DUV resists was evaluated, and the importance of line-edge roughness (LER) and sensitivity has been highlighted and categorized for small images. In summary, many of the system engineering risks and the issues associated with implementing EUVL into manufacturing have been reduced.

The technology proof-of-concept, the EUV LLC business model that targeted enabling suppliers, and the SEMATECH / EUV LLC relationship enabled SEMATECH in 2003 to ramp up its effort to drive infrastructure readiness at a scale that was beyond the EUV LLC / VNL scope. A significant portion of the critical infrastructure efforts that enable EUV commercialization can trace their beginnings back to technology developed by the EUV LLC / VNL or through collaboration with suppliers and SEMATECH. Prominent among those are the SEMATECH Mask Blank Development Center[26] and the SEMATECH EUV Resist Test Center,[27] both in Albany, New York; the SEMATECH micro-exposure tool (MET)[28] and actinic inspection tool[29] in Berkeley, California; EUV exposure and mask tools at IC manufacturers and captive[30] and merchant mask shops;[31] and much of the EUV-specific metrology that has been adopted by companies and consortia around the world.

Downloaded From: https://www.spiedigitallibrary.org/ebooks/ on 09 Mar 2022
Terms of Use: https://www.spiedigitallibrary.org/terms-of-use

Last of all, the written reports and conference presentations and papers generated during the EUV LLC program captured the discoveries for use by all development organizations. In addition, the patents provide adequate protection for companies continuing to pursue EUVL R&D.

2.6 Status of EUV Development at the End of the EUV LLC

2.6.1 Risk reduction

As another method for describing the technical accomplishments of the EUV LLC program, several important technology risks and potential showstoppers for technology implementation were eliminated. Early answers to specific questions about system engineering and commercialization were resolved. Some of the risks and resolved showstoppers included the following:

- The manufacture of production-quality EUV optics with controlled figure and finish was demonstrated in at least three laboratories.
- Precision, low-stress, graded ML optical coatings were fabricated.
- Visible and at-wavelength metrologies were developed for optical fabrication and alignment.
- Low-defect reticle blanks were fabricated.
- The repair of reticle defects was demonstrated.
- Stable EUVL LPP and DPP sources were demonstrated.
- Extended DUV photoresists were developed, screened, and evaluated for LER and sensitivity.
- An EUVL alpha tool was fabricated and its operation demonstrated.
- POBs were fabricated, and optics were fabricated, coated, and aligned.
- A system assembled with thermal control of all critical surfaces and imaging was demonstrated.
- Systems engineering risk reduction was demonstrated with module partitioning and characterization.
- Environment and contamination control was demonstrated with thermophoresis protection and mitigation.
- Dose, thermal, and alignment sensors were developed, evaluated, and characterized.
- Mask blanks were fabricated.
- Mask patterning processes (including absorbers, buffer layers, repair, and inspection) were demonstrated.
- Thermal management (methods and materials) was demonstrated in all system areas.
- Extensive modeling software for engineering, visualization, and analysis was developed.
- A library of materials and components was vacuum tested and qualified.
- A vacuum system was designed.

Downloaded From: https://www.spiedigitallibrary.org/ebooks/ on 09 Mar 2022
Terms of Use: https://www.spiedigitallibrary.org/terms-of-use

- Wafer and reticle chucking (heat transfer, deformation, clamping) was demonstrated.
- Spectral purity filters were developed.
- Standards (for reticles, MLs, etc.) were developed.

With EUV LLC and VNL support focused on solid technology progress, including reducing technology risks and eliminating technology showstoppers, EUVL technology was selected at the fifth and final SEMATECH NGL workshop in August 2001 as the technology of choice on the NGL roadmap for the 45-nm half-pitch and below.

2.6.1.1 Industry involvement

Before the involvement of the EUV LLC, the emphasis and work on EUV R&D had been limited to the DOE laboratories, AT&T, and a few universities. During the EUV LLC program, the level of interest and work expanded to a large number of companies, laboratories, and universities world-wide, largely in the U.S., Europe, and Japan. Most of the active participating organizations at the end of the EUV LLC technical program are listed in Table 2.4.

2.7 Summary

Although expensive, the EUV LLC program by most measures was very successful in terms of technical accomplishments, the unique management of a large program, the speed of implementation, the teamwork achieved between the VNL and industry representatives, and the consolidation of IP. If the program had not been initiated by Intel, it is very likely that all EUVL research would have been stopped, first at the DOE laboratories and later at AT&T, the only industrial organizations in the U.S. working on EUVL in 1997 and 1998. It is likely that the advanced lithography work in Japan would have continued to focus on proximity x-ray lithography, and work in Europe would have continued on IPL. Both Japan and Europe would have gradually discontinued the small amount of work on EUVL, and major EUV programs within ASET and MEDEA+ would not have been started. In 1997, the SEMATECH NGL task force relegated EUVL to fourth place behind x-ray, EPL, and IPL technologies, so without the EUV LLC program, there would have been no resurgence of interest in EUVL.

Given that both a focused EUVL program and private investment were needed, the path chosen to implement a virtual company using the national laboratories was an efficient and cost-effective approach. Although the VNL personnel and associated overhead costs were high, creating a new company or subsidiary with adequate facilities, equipment, and expert staff would have taken much longer and been far more expensive.

Downloaded From: https://www.spiedigitallibrary.org/ebooks/ on 09 Mar 2022
Terms of Use: https://www.spiedigitallibrary.org/terms-of-use

Table 2.4 Worldwide EUV interest at the end of 2003.

Companies	IC Companies	Laboratories and Universities	Consortia
ADE	AMD	Argonne National Laboratory	United States
AERONEX	IBM	LBNL	EUV LLC
ASML	Infineon	LLNL	SEMATECH
ASML Optics	Intel	MIT[32]	SRC
CEO	Micron	NIST	VNL RDC
Conexant	Motorola	NRL[33]	Europe
Corning Inc.		SNL	IMEC[34]
Corning Tropel Corp		Colorado State University	LETI[35]
Cymer		University of California-Berkeley	MEDEA+[36]
DuPont Photomask		University of Illinois	PREUVE[37]
Etec		University of Maryland	Japan
EUV Technology		University of Nevada	ASET
Invax		University of Texas	EUVA[38]
Janos Tech.		University of Wisconsin	AIST[39]
JMAR			
KLA-Tencor			
Luxel			
Opimax			
ORA			
Osmic			
Paragon Optics			
Photronics			
Plex LLC			
QED			
REO			
Rohwedder			
RTC LLC			
Schott-Lithotech			
Shipley			
Thermacore			
TRW			
Veeco			
Wave Optics			
ORA			

Finally, the technical accomplishments demonstrated EUVL with a full-field scanning prototype tool, resolved all major technology problems that had been identified at that time, and reduced the technology commercialization risks to an acceptable level. However, as we now know, some of the scaling challenges between where the EUV LLC left off and what was required for an HVM tool have been underestimated. Particularly so in the EUV source and EUV mask blank areas from a technical stand point and in creating much of the EUV mask tool infrastructure on the commercialization side. It took much longer and a much greater effort than what was believed in 2003 to achieve mask blanks with no printable defects and to develop an EUV source with the productivity and reliability to support HVM. Even though the commercial implementation of the technology has taken longer than initially

Downloaded From: https://www.spiedigitallibrary.org/ebooks/ on 09 Mar 2022
Terms of Use: https://www.spiedigitallibrary.org/terms-of-use

postulated, alpha EUVL tools have been fabricated by companies in Europe and Japan, and two alpha tools were delivered in 2006. With the maturing of the EUVL infrastructure and the delivery of the first alpha tools by the semiconductor equipment manufacturers, lithography experts expected EUVL to be the HVM technology for the 32-nm half-pitch and below.[40] However, this turned out not to be the case. It took almost a decade longer into early 2017 for companies to pronounce that they can make defect-free masks and for EUV exposure tools to come close to meeting chip-manufacturer HVM requirements for introduction. The EUV alpha tools were followed up by six preproduction systems (NXE:3100) from ASML in 2011–2013. As of the writing of this update, there are 14 EUV exposure systems in the field: 8 NXE3300B and 6 NXE:3350B systems. According to the tool manufacturer, all of those will be field upgradeable to support their use for HVM. As of early 2017, the first HVM type tool—an ASML NXE:3400B system—is being shipped to a customer, and the NXE:3400B series is expected to provide the backbone for EUV HVM at the 5-nm node.[41]

The accomplishments of the exposure tool, EUV optics, and EUV source manufacturers were complemented by a comparable number of achievements by material suppliers and equipment suppliers to provide the materials and mask equipment tool infrastructure required to support HVM ramp-up in the 2018–2020 time frame.

In retrospect, with the benefit of six years' worth of experience, the program could have been improved by

- performing additional upfront planning and enlistment of IC company and suppliers support;
- ramping up the initial program more slowly; and
- obtaining more supplier industry involvement and buy-in early in the program.

The success of the virtual company in cooperatively funding an expensive project and accelerating the technology development with transfer to the industry could provide a new paradigm for the future development of enabling technologies for high-technology industries.

Appendix 2A: Major Accomplishments of the EUV LLC Program

Essentially all of the initial EUV LLC program objectives were met, and the EUVL technology was demonstrated, including the module development and system integration. Extensive learning was obtained during the program. Some of the many program accomplishments are detailed below:

- **Designed and fabricated a complete, integrated, full-field (24 × 32.5 mm), scanning, alpha-class lithography tool denoted as the Engineering Test Stand (ETS)**

Downloaded From: https://www.spiedigitallibrary.org/ebooks/ on 09 Mar 2022
Terms of Use: https://www.spiedigitallibrary.org/terms-of-use

  - low-jitter, full-speed scanning maglev reticle and wafer stages for use in a vacuum environment;
  - complete control system incorporating 15 controllers and over 430 components;
  - environmentally engineered vacuum system to control the buildup of hydrocarbons and to control oxidation within the illuminator, POB, and wafer and reticle zones;
  - thermally and dynamically stable mechanical structure commensurate with the small tolerances needed to support sub-100-nm lithography;
  - Active cooling for optics and components in the illuminator to maintain thermal stability during system operation;
  - illuminator with a high-brightness laser, a variety of Xe target nozzles, a diffuser for unused target material recovery, debris mitigation, beam-shaping optics, thermal management, a spectral purity filter, and dose control. The diffuser was developed by Northrop Grumman Corp. but was not used in the ETS.
  - POB alignment using a two-step process with coordinate measuring machine optics positioning and a visible light interferometric measurement of the wavefront aberrations using an array of pinholes to guide fine adjustments of the mirrors for optimum alignment;
  - Integrated exposure chamber with vibration isolation, a POB, metrology trays, a focus system, reticle and wafer handlers, and reticle and wafer stage framework;
  - reticle and wafer-handling system including electrostatic chucking, mechanical fixturing, and thermal control;
  - summary of typical facility requirements consistent with power, cooling, and environmental requirements, and analysis extensions for manufacturing use;
  - two interchangeable super-Invar POBs with exact-constraint optics mounting and active alignment, complete with an environmentally controlled shipping container;
  - precise system instrumentation with >120 sensors for temperature, flux, imaging, alignment, and dose;
  - passive thermophoretic protection method for protecting masks from particulate contamination; and
  - system and component operating vacuum environmental requirements with methods for selecting acceptable materials and components, including testing and qualification.

- **Pioneered the development of two types of plasma sources**
  - LPP source with a variety of gas, cluster, liquid, and solid Xe targets with diffuser collectors;
  - high-power (1500 W, 5000 Hz) laser with TRW;

Downloaded From: https://www.spiedigitallibrary.org/ebooks/ on 09 Mar 2022
Terms of Use: https://www.spiedigitallibrary.org/terms-of-use

  - capillary discharge source tube with debris mitigation and thermal management; and
  - high-current pulse power supply for discharge source.

- **Developed and integrated computer-aided design methods to support thermal, dynamic, and vibrational design and analysis of individual components, subsystems, and complete system operation**
  - design aids used to support module and subsystem partitioning and analysis to optimize system interfaces;
  - finite element analysis with extensive dynamical, thermal, and lithography modeling and simulation;
  - validated design methods with experimental confirmation of system and component operation; and
  - extensive visualization techniques applied to optimize the design process and minimize design errors.

- **Developed reflective EUV mask technology including ML-coated, LTEM mask blanks complete with metrology, ML defect-repair methods, patterning inspection, and repair processes**
  - ML repair methods for phase and amplitude defects with Monte Carlo analysis predicting mask blank yield as a function of defect type and location;
  - metrology for quantifying mask blank flatness;
  - defect smoothing methods for covering up to 70-nm substrate defects, thus minimizing metrology and defect-removal requirements;
  - optimization of a reflective ML stack with absorber and buffer layers;
  - evaluation of a number of absorbers, including Ti, TiN, AlCu, Cr, TaSiN, TaSi, Ta, and TaN, with selection of Cr and TaN providing the best characteristics; and
  - provision of framework for EUVL Semiconductor Equipment and Materials International (SEMI) standards, including wavelength, mask materials and format, reticle handling, chucking and clamping, allowable thermal and deformation tolerances, etc.

- **Implemented EUV optics fabrication project with industry to demonstrate continuous improvement in the fabrication technology**
  - development of a process for production-quality figure, mid-spatial-frequency roughness (MSFR), and high-spatial-frequency roughness (HSFR) polishing with Tinsley using flat and spherical samples;
  - fabrication of two sets of ETS mirrors, three sets of 0.1-NA, 10× microstepper optics, and two sets of 0.3-NA, 5× MET optics with demonstrated continuous improvement;

Downloaded From: https://www.spiedigitallibrary.org/ebooks/ on 09 Mar 2022
Terms of Use: https://www.spiedigitallibrary.org/terms-of-use

  - precision visible-light PSPDI metrology system with initial accuracy <0.25-nm rms, with extension to a lensless system having 0.1-nm rms accuracy to support optics fabrication; and
  - successful championing and fabrication of only the clear aperture of large aspheric optics to reduce tool size and optic blank manufacturing requirements.

- **Developed engineered MLs with capping layers to provide good reflectivity and stability**
  - development of two-ion-beam and one-magnetron ML deposition systems with Veeco;
  - fundamental Mo-Si and Mo-Be ML data to support decision to not use Be because of toxicity and to focus on Mo-Si for worldwide use;
  - ML coating process to obtain a sample mask blank with a record low of 0.008 defects/cm^2 @ 60-nm defect size;
  - achieved 70% reflectivity with six month stability using stable capping layers.
  - Mo-Si with up to 70% reflectivity and less than 1% reflectivity loss with aging;
  - Ru capping layer to provide optimum ML stability by preventing oxidation;
  - evaluation of accelerated aging methods to simulate EUV flux with an electron beam to provide the equivalent secondary electron density at the surface;
  - processes for depositing precision uniform and graded coatings for flat and aspheric surfaces;
  - reflectometer using synchrotron radiation to characterize ML reflectivity as a function of wavelength with benchmarking by Japan and Europe;
  - implementation of at-wavelength interferometry, alignment, and defect inspection;
  - achievement of at-wavelength ML-coating uniformity measured to 0.05-nm rms; and
  - precision control of ML deposition processes to permit accurate ML matching for mirrors and mask coated at different times.

- **Demonstrated EUVL printing**
  - application of extended DUV resists;
  - evaluation of various optimized ML and absorber stack structures;
  - characterization of EUVL flare and development of methods to control flare;
  - characterization of horizontal/vertical printing bias caused by asymmetry of ETS illumination; and

Downloaded From: https://www.spiedigitallibrary.org/ebooks/ on 09 Mar 2022
Terms of Use: https://www.spiedigitallibrary.org/terms-of-use

  - achievement of extensive static imaging using the ETS POB and synchrotron imaging system with variable illumination configurations (variable coherence disk, dipole, rotated dipole, off axis, and annular).

- **Demonstrated extended DUV resists**
  - application of ultrathin, pinhole-free resist process as a replacement for top-surface-imaged resists.
  - evaluation of tradeoffs between LER, sensitivity, and resolution;
  - evaluation of >100 resist formulations;
  - attainment of the benchmark of a 6-nm LER 3σ @ 2 mJ/cm^2 resist;
  - establishment of a standard method for measuring LER;
  - performance of shot-noise print analysis that indicated shot noise is not a problem below 32-nm half-pitch; and
  - development of support for EUV resist testing using the MET at LBNL.

- **Obtained SEMATECH support for infrastructure technologies**
  - reduction of risks and demonstration of sufficient development progress to gain acceptance of EUVL by the SEMATECH/SIA NGL Task Force as the lithography of choice for 45-nm half-pitch manufacturing;
  - provision of technology transfer to support the SEMATECH Mask Blank Development Center (MBDC); and
  - assistance with development of statements of work (SOWs) with deliverables for infrastructure and SEMATECH MBDC projects.

- **Implemented formal program management**
  - detailed work breakdown with over 50 major project elements;
  - technology and interaction risk identification, scoring, and reporting; and
  - formal working groups for each project with regular reporting.

- **Program reporting**
  - Twenty-four eight-hour quarterly reviews over six years with approximately eighty attendees present at each review from LLC companies, VNL, and suppliers;
  - quarterly reports written to summarize technical accomplishments, issues, and plans;
  - review of more than 590 articles and abstracts for conference presentations and publications (over 40 different conferences and periodicals);
  - more than 100 press articles in a variety of technical publications, newspapers, and world-wide journals;
  - participation in 10 SEMATECH NGL critical reviews;

Downloaded From: https://www.spiedigitallibrary.org/ebooks/ on 09 Mar 2022
Terms of Use: https://www.spiedigitallibrary.org/terms-of-use

  - numerous onsite laboratory tours and company reviews;
  - 280 EUV LLC-written weekly reports (~1400 pages) with 850 weekly highlights;
  - more than 10,000 viewgraphs presented;
  - more than 400 risk issues tracked; and
  - approximately 250 weekly status update meetings.

- **Reviewed and collected program intellectual property**
  - IP committee quarterly meetings and review of over 300 items;
  - IP committee decisions: obtain patents for 146 items, classify 116 items as CRADA-protected (processes and trade secrets), and copyright 17 items; and
  - as of December 31, 2003, 98 patents awarded and 51 pending; several patent applications resulted in multiple patents, and 16 were abandoned for various reasons.

- **Personnel participation**
  - more than 770 FTE personnel years with a peak of 170 FTEs in 1998 and a minimum of 58 FTEs in 2002.
  - program participation by approximately 250 different personnel at the VNL; and
  - program participation by more than 160 different personnel at member companies.

- **Intangible program strengths demonstrated**
  - technical breadth and teamwork across VNL laboratories;
  - superb VNL team quality (technical expertise and innovation, ownership of problems and issues, dedication to completing milestones, and leadership by managers);
  - accelerated EUVL progress as a result of the competition provided by other NGL technologies;
  - optimum blending of commercial and laboratory cultures; and
  - growth of EUVL development from work by a few laboratories in 1997 to a worldwide effort involving more than 100 industrial companies, universities, and laboratories in 2003.

Appendix 2B: EUV LLC Program Patents

The EUV LLC program developed numerous IP items that were classified as patentable in the U.S. The following tables summarize the EUV LLC U.S. patent filings as of April 2016 and include the patent title, the U.S. patent or application number, the patent status, and the patent lifetime, if applicable.

Downloaded From: https://www.spiedigitallibrary.org/ebooks/ on 09 Mar 2022
Terms of Use: https://www.spiedigitallibrary.org/terms-of-use

Table B.1 Metrology patents.

Patent Title / Patent Application Title	U.S. Patent / Application No.	Patent Status	Remaining Patent Life (Years)
Dual-domain point diffraction interferometer	6,100,978	Active	7.9
Null test Fourier domain alignment technique for phase-shifting point diffraction interferometer	6,111,646	Active	7.7
In Situ alignment system for phase-shifting point-diffraction interferometry	6,118,535	Active	8.1
Monolithic pattern-sensitive detector	6,130,431	Active	7.1
Phase-shifting point diffraction interferometer focus-aid enhanced mask	6,151,115	Active	8.2
Phase-shifting point diffraction interferometer grating designs	6,195,169	Active	7.4
Fourier-transform and global contrast interferometer alignment methods	6,239,878	Active	8.4
Phase-shifting point diffraction interferometer phase grating designs	6,266,147	Active	8.4
Phase-shifting point diffraction interferometer mask designs	6,307,635	Discontinued	N/A
Miniature self-contained vacuum compatible electronic imaging microscope	6,327,102	Discontinued	N/A
System for interferometric distortion measurements that define an optical path	6,559,952	Active	9.0
Dual-domain lateral shearing interferometer	6,707,560	Active	9.3
EUV mirror based absolute incident flux detector	6,710,351	Active	10.3
Universal EUV inband intensity detector	6,781,135	Active	11.5
Method and apparatus for detecting the presence and thickness of carbon and oxide layers on EUV reflective surfaces	6,847,463	Active	11.1
Reticle stage based linear dosimeter	6,906,781	Discontinued	N/A
Extended surface parallel coating inspection method	7,016,030	Discontinued	N/A
Reticle stage based linear dosimeter	7,196,771	Active	13.8
Reticle stage based linear dosimeter	20050206870	N/A	N/A

Table B.2 Optics patents.

Patent Title / Patent Application Title	U.S. Patent / Application No.	Patent Status	Remaining Patent Life (Years)
Cleaning process for EUV optical substrates	5,958,143	Active	6.9
Reflective optical imaging system with balanced distortion	5,973,826	Active	6.8
Deformable mirror for short wavelength applications	5,986,795	Active	7.1
Embedded fiducials in optical surfaces	6,014,264	Active	7.4
High numerical aperture ring field projection system for extreme ultraviolet lithography	6,033,079	Active	7.8
High numerical aperture projection system for extreme ultraviolet projection lithography	6,072,852	Active	7.1
Projection optics box	6,147,818	Active	7.6
High numerical aperture ring field projection system for extreme ultraviolet lithography	6,183,095	Active	8.6
High numerical aperture ring field projection system for extreme ultraviolet lithography	6,188,513	Active	7.8

(*continued*)

Downloaded From: https://www.spiedigitallibrary.org/ebooks/ on 09 Mar 2022
Terms of Use: https://www.spiedigitallibrary.org/terms-of-use

Table B.2 (*Continued*)

Patent Title / Patent Application Title	U.S. Patent / Application No.	Patent Status	Remaining Patent Life (Years)
Surface figure control for coated optics	6,206,528	Active	7.3
Pedestal substrate for coated optics	6,206,966	Active	7.3
Reflective optical imaging systems with balanced distortion	6,226,346	Active	7.1
Interferometric at-wavelength flare characterization of EUV optical systems	6,233,056	Active	9.2
High numerical aperture ring field projection system for extreme ultraviolet lithography	6,262,836	Active	9.4
High numerical aperture ring field projection system for extreme ultraviolet lithography	6,318,869	Discontinued	N/A
Method of fabricating reflection-mode EUV diffraction elements	6,392,792	Active	9.6
Compact multi-bounce projection system for extreme ultraviolet projection lithography	6,426,506	Active	8.0
Low-cost method for producing extreme ultraviolet lithography optics	6,634,760	Active	10.3
Apparatus for generating partially coherent radiation	6,798,494	Active	10.3
Correction of localized shape errors on optical surfaces by altering the localized density of surface or near-surface layers	6,844,272	Active	10.8
Fabrication of precision optics using an imbedded reference surface	6,849,859	Active	9.8
Apparatus for generating partially coherent radiation	6,859,263	Active	11.8
Method of fabricating reflection-mode EUV diffusers	6,861,273	Active	9.9
Diffractive optical element for extreme ultraviolet wavefront control	7,027,226	Active	10.3
Figure correction of multilayer coated optics	7,662,263	Active	11.3
Correcting surface contour of a non-rigid object through control of surface residual stress	20040100638	N/A	N/A

Table B.3 Multilayer patents.

Patent Title / Patent Application Title	U.S. Patent / Application No.	Patent Status	Remaining Patent Life (Years)
Method to adjust multilayer film stress induced deformation of optics	6,011,646	Active	6.8
High reflectance-low stress Mo-Si multilayer reflective coatings	6,110,607	Active	6.8
Method to adjust multilayer film stress induced deformation of optics	6,134,049	Active	7.3
MoRu/Be multilayers for extreme ultraviolet applications	6,228,512	Active	8.0
High reflectance and low stress Mo_2C/Be multilayers	6,229,652	Active	7.5
Process for fabricating high reflectance-low stress Mo–Si multilayer reflective coatings	6,309,705	Discontinued	N/A
Coatings on reflective mask substrates	6,352,803	Active	9.1
Multilayer films with sharp, stable interfaces for use in EUV and soft X-ray application	6,396,900	Active	10.0

(*continued*)

Downloaded From: https://www.spiedigitallibrary.org/ebooks/ on 09 Mar 2022
Terms of Use: https://www.spiedigitallibrary.org/terms-of-use

Table B.3 (*Continued*)

Patent Title / Patent Application Title	U.S. Patent / Application No.	Patent Status	Remaining Patent Life (Years)
Method and system using power modulation for maskless vapor deposition of spatially graded thin film and multilayer coatings with atomic-level precision and accuracy	6,425,988	Active	9.5
Electrostatic particle trap for ion beam sputter deposition	6,451,176	Active	9.5
Ion beam collimating grid to reduce added defects	6,521,897	Active	9.5
Method and system for producing sputtered thin films with sub-angstrom thickness uniformity or custom thickness gradients	6,524,449	Active	8.6
Method for measuring and controlling beam current in ion beam processing	6,554,968	Active	9.3
Method and system using power modulation and velocity modulation producing sputtered thin films with sub-angstrom thickness uniformity or custom thickness gradients	6,668,207	Active	9.5
Optimized capping layers for EUV multilayers	6,780,496	Active	10.8
Growth of multi-component alloy films with controlled graded chemical composition on sub-nanometer scale	6,867,149	Active	11.3
EUV lithography reticles fabricated without the use of a patterned absorber	7,049,033	Active	12.2
Dynamic mask for producing uniform or graded-thickness thin films	7,062,348	Active	9.2
Method for in-situ cleaning of carbon contaminated surfaces	7,147,722	Active	13.0
Use of ion beams for protecting substrates from particulate defect contamination in ultra-low-defect coating processes	20040055871	N/A	N/A

Table B.4 Environment patents.

Patent Title / Patent Application Title	U.S. Patent / Application No.	Patent Status	Remaining Patent Life (Years)
Protection of lithographic components from particle contamination	6,153,044	Active	6.9
Process for producing radiation-induced self-terminating protective coatings on a substrate	6,231,930	Active	8.6
Method for protection of lithographic components from particle contamination	6,253,464	Active	9.3
Mitigation of radiation induced surface contamination	6,533,952	Active	8.6
Self-cleaning optic for extreme ultraviolet lithography	6,664,554	Active	9.7
Apparatus for in situ cleaning of carbon contaminated surfaces	6,772,776	Active	10.3
Method and apparatus for debris mitigation for an electrical discharge source	6,989,629	Discontinued	N/A
Condenser optic with sacrificial reflective surface	7,239,443	Active	15.1
Adhesive particle shielding	7,473,301	Active	11.3
Method for the protection of extreme ultraviolet lithography optics	7,740,916	Active	12.9
Method for reducing carbon contamination of multilayer mirrors	20030064161	N/A	N/A
Apparatus for in-situ cleaning of carbon contaminated surfaces	20040211448	N/A	N/A

Downloaded From: https://www.spiedigitallibrary.org/ebooks/ on 09 Mar 2022
Terms of Use: https://www.spiedigitallibrary.org/terms-of-use

Table B.5 Mask patents.

Patent Title / Patent Application Title	U.S. Patent / Application No.	Patent Status	Remaining Patent Life (Years)
Mask fabrication process	6,015,640	Active	6.8
Method for mask repair using defect compensation	6,235,434	Active	7.6
Low thermal distortion extreme-UV lithography reticle	6,316,150	Active	7.3
Mitigation of substrate defects in reticles using multilayer buffer layers	6,319,635	Active	8.6
Method for fabricating an ultra-low expansion mask blank having a crystalline silicon layer	6,368,942	Active	8.8
Low thermal distortion Extreme-UV lithography reticle and method	6,395,455	Active	10.2
Low thermal distortion extreme-UV lithography reticle	6,441,885	Active	10.2
Multi-level scanning method for defect inspection	6,484,306	Active	8.6
Mitigation of substrate defects in reflective reticles using sequential coating and annealing	6,489,066	Active	9.8
Removable pellicle for lithographic mask protection and handling	6,492,067	Active	8.6
Method and apparatus for inspecting reflection masks for defects	6,555,828	Active	7.5
Hybrid shearing and phase-shifting point diffraction interferometer	6,573,997	Active	9.2
Method for fabricating reticles for EUV lithography without the use of a patterned absorber	6,635,391	Active	9.6
Compensation of flare-induced CD changes EUVL	6,815,129	Active	9.3
Repair of localized defects in multilayer-coated reticle blanks for extreme ultraviolet lithography	6,821,682	Active	9.3
Compliant layer chucking surface	6,835,415	Active	11.7
Etched-multilayer phase shifting masks for EUV lithography	6,875,543	Active	11.3
Method and apparatus for inspecting an EUV mask blank	6,963,395	Discontinued	N/A
Method to repair localized amplitude defects in an EUV lithography mask blank	6,967,168	Active	10.1
Method for the manufacture of phase shifting masks for EUV lithography	7,022,435	Active	11.3
Ion-assisted deposition techniques for the planarization of topological defects	20030164998	N/A	N/A

Table B.6 ETS and illuminator patents.

Patent Title / Patent Application Title	U.S. Patent / Application No.	Patent Status	Remaining Patent Life (Years)
Diffractive element in extreme-UV lithography condenser	6,118,577	Active	7.3
Condenser for ring-field deep-ultraviolet and extreme-ultraviolet lithography	6,186,632	Active	7.6
Extreme-UV lithography condenser	6,210,865	Active	7.8
Diffractive element in extreme-UV lithography condenser	6,285,497	Discontinued	N/A
Condenser for extreme-UV lithography with discharge source	6,285,737	Discontinued	N/A
Illumination system having a plurality of movable sources	6,396,068	Active	9.4
Condenser for ring-field deep ultraviolet and extreme ultraviolet lithography	6,398,374	Active	8.8

(*continued*)

Downloaded From: https://www.spiedigitallibrary.org/ebooks/ on 09 Mar 2022
Terms of Use: https://www.spiedigitallibrary.org/terms-of-use

Table B.6 (*Continued*)

Patent Title / Patent Application Title	U.S. Patent / Application No.	Patent Status	Remaining Patent Life (Years)
Constant volume gas cell optical phase-shifter	6,421,130	Active	7.8
Diffraction spectral filter for use in extreme-UV lithography condenser	6,469,827	Active	9.3
Condenser for photolithography system	6,700,644	Active	11.1
Synchrotron-based EUV lithography illuminator simulator	6,768,567	Active	11.1
Holographic illuminator for synchrotron-based projection lithography systems	6,927,887	Active	10.4
Condenser optic with sacrificial reflective surface	7,081,992	Active	12.7
Vacuum compatible, high-speed, 2-D mirror tilt stage	7,273,289	N/A	N/A

Table B.7 Source patents.

Patent Title / Patent Application Title	U.S. Patent / Application No.	Patent Status	Remaining Patent Life (Years)
Efficient narrow spectral width soft-X-ray discharge sources	5,499,282	Active	3.0
Configurations, materials and wavelengths for EUV lithium plasma discharge lamps	5,963,616	Discontinued	N/A
Erosion resistant nozzles for laser plasma extreme ultraviolet (EUV) sources	6,011,267	Active	6.8
Capillary discharge extreme ultraviolet lamp source for EUV microlithography and other related applications	6,031,241	Discontinued	N/A
Discharge lamp sources apparatus and methods	6,188,076	Discontinued	N/A
Debris blocker/collector and emission enhancer for discharge sources	6,232,613	Active	7.3
Extreme-UV electrical discharge source	6,356,618	Discontinued	N/A
Electrode configuration for extreme-UV electrical discharge source	6,498,832	Active	9.8
Radiation source with shaped emission	6,563,907	Active	10.6
Adjustable bore capillary discharge	6,576,917	Active	8.7
Capillary discharge source	6,654,446	Active	10.3
Discharge source with gas curtain for protecting optics from particles	6,714,624	Active	10.3
Method and apparatus for debris mitigation for an electrical discharge source	6,888,297	Active	11.6
Fluid jet electric discharge source	7,034,322	N/A	N/A

Table B.8 Lithography patents.

Patent Title / Patent Application Title	U.S. Patent / Application No.	Patent Status	Remaining Patent Life [Years]
Thin layer imaging process for microlithography using radiation at strongly attenuated wavelengths	6,673,525	Active	8.8

Downloaded From: https://www.spiedigitallibrary.org/ebooks/ on 09 Mar 2022
Terms of Use: https://www.spiedigitallibrary.org/terms-of-use

Table B.9 Miscellaneous patents.

Patent Title / Patent Application Title	U.S. Patent / Application No.	Patent Status	Remaining Patent Life (Years)
Precision tip-tilt-piston actuator that provides exact constraint	5,986,827	Active	7.1
Extreme-ultraviolet lithography machine	6,031,598	Active	7.3
Thermophoretic vacuum wand	6,072,157	Active	7.6
Electrostatically screened, voltage-controlled electrostatic chuck	6,169,652	Active	7.8
Light weight high-stiffness stage platen	6,188,150	Active	8.1
Apparatus and method for in-situ cleaning of resist outgassing windows	6,192,897	Active	7.7
Wafer chamber having a gas curtain for extreme-UV lithography	6,198,792	Active	7.5
Extreme-UV lithography system	6,225,027	Active	8.0
Projection lithography with distortion compensation using reticle chuck contouring	6,229,871	Active	8.2
Thermophoretic vacuum wand	6,232,578	Active	8.8
Liquid zone seal	6,279,601	Discontinued	N/A
Highly damped kinematic coupling for precision instruments	6,325,351	Discontinued	N/A
Motorized support jack	6,328,282	Discontinued	N/A
Extreme-UV lithography vacuum chamber zone seal	6,333,775	Active	7.7
Graphical user interface for image acquisition and processing	6,341,183	Discontinued	N/A
Extreme-UV scanning wafer and reticle stages	6,353,271	Discontinued	N/A
Extreme-UV lithography vacuum chamber zone seal (vacuum apparatus)	6,545,745	Active	10.5
Extreme-UV lithography vacuum chamber zone seal (photolithography system)	6,549,264	Active	10.5
Motorized support jack	6,561,486	Active	10.4
Mask-to-wafer alignment system	6,642,995	Active	10.5
Photo-imageable composition	6,645,696	Active	10.5
Portable outgas detection apparatus	6,734,422	Active	9.8
In-vacuum exposure shutter	6,744,493	Active	9.2
Vacuum compatible, high-speed, 2-D mirror tilt stage	7,273,289	Active	14.0

Acknowledgments

The first version of this chapter in the original edition of this book was coauthored with Chuck Gwyn, the General Manager of the EUV LLC from 1997 to 2003. His contributions provided much of the substance and color to this EUV LLC history—even after this revision. I am grateful that I had the experience of working with him back then at the EUV LLC and that I had the privilege of coauthoring the original book chapter with him. I hope this updated version does justice to the high standards to which Chuck held himself and his colleagues. Anything short of that and/or any added errors are my sole responsibility.

The EUVL program was supported by a large number of dedicated scientists, engineers, and managers at the VNL and the EUV LLC. A list of over 500 personnel involved within these two organizations can be found in

Downloaded From: https://www.spiedigitallibrary.org/ebooks/ on 09 Mar 2022
Terms of Use: https://www.spiedigitallibrary.org/terms-of-use

the acknowledgment section in this chapter in the first edition of this book. In addition, many individual contributors at a number of component, subsystem, and exposure tool suppliers, SEMATECH, U.S. and foreign universities, and foreign associations provided invaluable contributions to the EUV LLC program and have not been listed. The EUV LLC is indebted to all and acknowledges their contributions.

References

1. C. W. Gwyn and S. Wurm, "EUV LLC: An Historical Perspective," Chapter 2 in *EUV Lithography*, V. Bakshi, Ed., SPIE Press, Bellingham, Washington (2009) [doi: 10.1117/3.769214.ch2.]
2. H. Kinoshita and O. Wood, "EUV Lithography: An Historical Perspective," Chapter 1 in *EUV Lithography*, V. Bakshi, Ed., SPIE Press, Bellingham, Washington, USA (2009) [doi: 10.1117/3.769214.ch1].
3. A. M. Hawryluk and L. G. Seppala, "Soft x-ray projection lithography using an x-ray reduction camera," *J. Vac. Sci. Technol. B* **6**, 2162–2166 (1988).
4. W. T. Silfvast and O. R. Wood, II, "Tenth micron lithography with a 10 Hz 37.2 nm sodium laser," *Microelec. Eng.* **8**, 3–11 (1988).
5. H. Kinoshita, K. Kurihara, and H. Takenaka, "Soft x-ray reduction lithography using multilayer mirrors," *J. Vac. Sci. Tech. B* **7**, 1648–1651 (1989).
6. H. Kinoshita, *Extreme Ultraviolet Lithography: Principles and Basic Technologies*, Lambert Academic Publishing, Saarbruecken, Germany (2016).
7. Lawrence Livermore National Laboratory (LBNL), USA, http://www.llnl.gov.
8. Lawrence Berkeley National Laboratory (LLNL), USA, http://www.lbl.gov.
9. Sandia National Laboratory (SNL), USA, http://www.sandia.gov.
10. *International Technology Roadmap for Semiconductors* (ITRS), http://public.itrs.net.
11. United States Department of Defense (DOD), http://www.defenselink.mil.
12. United States Defense Advanced Research Projects Agency (DARPA), http://www.darpa.mil.
13. United Stated Director of Defense Research & Engineering (DDR&E), http://www.dod.gov/ddre.
14. United States Department of Commerce (DOC), http://www.commerce.gov.
15. National Institute for Standards and Technology (NIST), USA, http://www.nist.gov.
16. SEMATECH, http://www.sematech.org.
17. Semiconductor Industry Association (SIA), USA, http://www.sia-online.org.

Downloaded From: https://www.spiedigitallibrary.org/ebooks/ on 09 Mar 2022
Terms of Use: https://www.spiedigitallibrary.org/terms-of-use

18. Semiconductor Research Corporation (SRC), USA, http://www.src.org.
19. Association of Super-Advanced Electronics Technologies (ASET), Japan, http://www.aset.or.jp.
20. All EUV Workshop material can be found at http://www.sematech.org/meetings/archives.htm.
21. C. W. Gwyn, "Extreme Ultraviolet Lithography," EUV LLC Program Report, November 1999.
22. S. Wurm and C. W. Gwyn, "EUV Lithography," Chapter 8 in *Microlithography: Science and Technology*, Second Edition, K. Suzuki, Ed., CRC Press/Taylor & Francis Information Group, Boca Raton, Florida (2007).
23. P. J. Silverman, "Extreme ultraviolet lithography: overview and development status," *J. Micro/Nanolith. MEMS MOEMS* **4**(1), 011006 (2005) [doi: 10.1117/1.1862647].
24. J. Mulkens, D. Flagello, B. Streefkerk, and P. Graeupner, "Benefits and limitations of immersion lithography," *J. Micro/Nanolith. MEMS MOEMS.* **3**(1), 104–114 (2004) [doi: 10.1117/1.1636768].
25. H. Kang, A. Bourov, and B. W. Smith, "Optical lithography at a 126-nm wavelength," *Proc. SPIE* **4343**, 797–801 (2001) [doi: 10.1117/12.436707].
26. A. Ma, P. Kearney, D. Krick, R. Randive, I. Reiss, P. Mirkarimi, and E. Spiller, "Progress towards the development of a commercial tool and process for EUVL mask blanks," *Proc. SPIE* **5751**, 168–177 (2005) [doi: 10.1117/12/599936].
27. K. Lowack, A. Rudack, K. Dean, M. Malloy, and M. Lercel, "The EUV resist test center at SEMATECH-North" *Proc. SPIE* **6151**, 61512U (2006) [doi: 10.1117/12.657683].
28. P. Naulleau, C. Rammeloo, J. P. Cain, K. Dean, P. Denham, K. A. Goldberg, B. Hoef, B. La Fontaine, A. R. Pawlowski, C. Larson, and G. Wallraff, "Investigation of the current resolution limits of advanced extreme ultraviolet (EUV) resists" *Proc. SPIE* **6151**, 61510Y (2006) [doi: 10.1117/12.657005].
29. K. A. Goldberg et al., "Actinic inspection of EUV programmed multilayer defects and cross-correlation measurements," presented at the 50th International Conference on Electron, Ion, and Photon Beams and Nanolithography (EIPBN), Baltimore, Maryland, May 31–June 2, 2006.
30. A. Hand, "Infrastructure steps closer to EUV lithography," Semiconductor International, 38–42 (Sept. 2005).
31. F. Letzkus, J. Butschke, M. Irmscher, H. Sailer, U. Dersch, and C. Holfeld, "EUVL mask manufacturing: technologies and results," *Proc. SPIE* **5992**, 59922A (2005) [doi : 10.1117/12.628957].
32. Massachusetts Institute of Technology (MIT), USA, http://web.mit.edu.
33. United States Naval Research Laboratory (NRL), http://www.nrl.navy.mil.
34. Interuniversity MicroElectronics Center (IMEC), Belgium, http://www.imec.be.

Downloaded From: https://www.spiedigitallibrary.org/ebooks/ on 09 Mar 2022
Terms of Use: https://www.spiedigitallibrary.org/terms-of-use

35. Commissariat à l'Energie Atomique (CEA)/Laboratoire d'Electronique de Technologie de l'Information (LETI), France, http://www-leti.cea.fr.
36. Microelectronics Development for European Applications+ (MEDEA+), France, http://www.medeaplus.org.
37. PRogramme Extrême UV (PREUVE) is the French national EUVL program. Its participants include national research laboratories, universities, and leading companies in optics, precision engineering, and semiconductor manufacturing.
38. Extreme UltraViolet Lithography System Development Association (EUVA), Japan, http://www.euva.or.jp.
39. National Institute of Advanced Industrial Science and Technology (AIST), Japan, http://www.aist.go.jp.
40. 2006 SEMATECH Litho Forum, Vancouver, British Columbia, May 23–24 (2006).
41. Most recent updates from EUV stakeholders are available from the material presented: at the Conference 10143 "Extreme Ultraviolet Lithography VIII" at the annual SPIE Advanced Lithography Meeting, 26 February–2 March, 2017; and at the International EUV Symposium held in Hiroshima, Japan, 24–26 October, 2016.

Stefan Wurm received his physics diploma and his doctorate in physics from the Technische Universität München, Germany. He is currently the owner of ATICE LLC, a technology strategy consulting company he founded in 2016. His 20+ year career in the semiconductor industry before that includes engineering-, management- and executive-level positons in technology development at Siemens Semiconductors, Infineon, Qimonda, SEMATECH, AMD, and GLOBALFOUNDRIES.

Dr. Wurm is recognized for his decade-long industry leadership that helped enable EUV infrastructure through developing and sustaining alliances in leading-edge technology collaborations with worldwide consortia, research institutions, and industry. He has been on assignment to the International 300 mm Initiative (I300I), International SEMATECH, the EUV LLC, and SEMATECH.

Downloaded From: https://www.spiedigitallibrary.org/ebooks/ on 09 Mar 2022
Terms of Use: https://www.spiedigitallibrary.org/terms-of-use

Chapter 3A
EUV Sources for High-Volume Manufacturing

Igor V. Fomenkov, David C. Brandt, Alexander I. Ershov, Alexander A. Schafgans, Yezheng Tao, and Georgiy O. Vaschenko
ASML US, San Diego, California, USA

Bruno La Fontaine
Hermes Microvision Inc., an ASML company, San Jose, California, USA

3A.1 Introduction to EUV Light Sources
3A.2 EUV Source Requirements
3A.3 Laser-Produced Plasma Source System
- 3A.3.1 EUV power scaling
- 3A.3.2 Tin target delivery
- 3A.3.3 Pre-pulse technology
- 3A.3.4 EUV collector
- 3A.3.5 Debris mitigation
- 3A.3.6 Hydrogen as a buffer gas
- 3A.3.7 Tin management
- 3A.3.8 Controls

3A.4 Summary and Future Outlook
References

3A.1 Introduction to EUV Light Sources

This chapter describes the development of a laser-produced-plasma (LPP) EUV source for advanced lithography applications in high-volume manufacturing (HVM) of semiconductor devices. EUVL is expected to succeed 193-nm immersion multipatterning technology for sub-10-nm critical-layer patterning. The most recent results from high-power systems targeted at the 250-W configuration are described to date. The requirements and technical challenges related to successful implementation of these technologies are outlined for the reader. Development of second-generation LPP light sources for ASML's NXE:3300B, NXE:3350B, and NXE:3400B (Fig. 3A.1) EUV scanners is complete, with approximately 15 units installed and

Downloaded From: https://www.spiedigitallibrary.org/ebooks/ on 09 Mar 2022
Terms of Use: https://www.spiedigitallibrary.org/terms-of-use

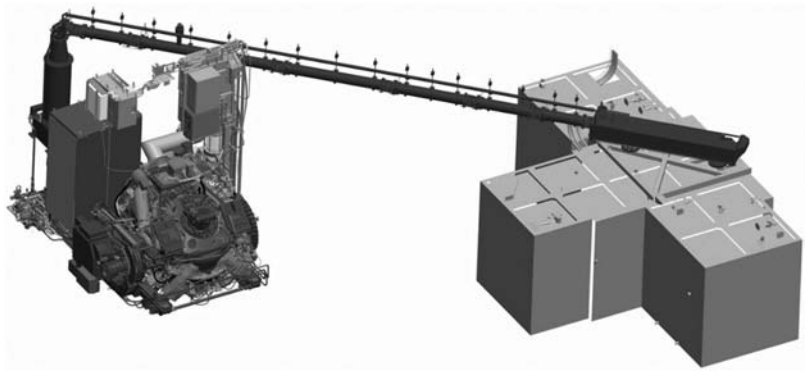

Figure 3A.1 Drawing of a LPP source for ASML's NXE:3300B, shown with a four-amplifier drive laser 'T' configuration [radiofrequency (RF) generators and heat exchangers not shown]. The beam delivery begins at the top of the last amplifier (center position of the long axis) and extends to the input of the vessel. The vessel contains the collector and droplet generator and a suit of sensors and diagnostics such as EUV monitors as well as cameras to view droplets and plasma, and to measure pressure and gas flow (adapted from Ref. 40).

operational at chipmaker customers. Different aspects and performance characteristics of the sources as well as related research and development progress at our facilities were already described in detail in several earlier publications.[1–5] We have described initial dose stability results, power scaling and availability data for ASML's NXE:3100 first-generation sources,[6,7] and have reported on several new development results.[8–10] Ten first-generation NXE:3100 sources (Fig. 3A.2) have been operational for over five years; five systems were deployed to customers for use in process development at early adopters of EUVL technology. Key features of the NXE platform as well as scanner performance during the system introduction have already been reviewed in detail.[11] In this chapter, we report on the characterization of source components that are critical to achieve the higher power required for the second-generation light sources to support EUV scanners at chipmaker production facilities. The NXE:3300B source drive laser uses a master oscillator power amplifier (MOPA) laser architecture with a pre-pulse mode of operation.[39,45] The pre-pulse conditions the target from a liquid tin (Sn) droplet to a lower-density target at the focal plane of the laser focusing optics. A main (high-energy) pulse from the drive laser is then focused onto the pre-pulse-conditioned target, creating a highly ionized plasma that emits EUV radiation at wavelengths around 13.5 nm.

An early prototype version of an EUV system built by Sandia National Labs was called the Engineering Test Stand (ETS), as shown in Fig. 3A.3. This system became operational in 2002 and was used as proof of principle that the technology could be developed with industry backing.[12]

Downloaded From: https://www.spiedigitallibrary.org/ebooks/ on 09 Mar 2022
Terms of Use: https://www.spiedigitallibrary.org/terms-of-use

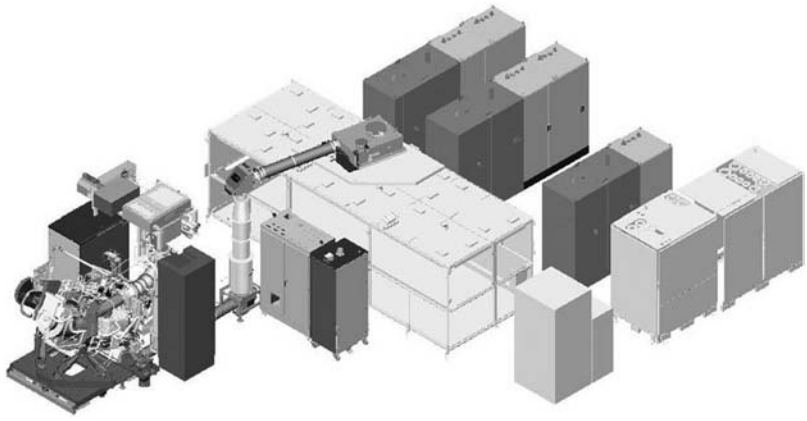

Figure 3A.2 Drawing of a LPP source for the ASML NXE:3100. The large rectangular structure in the center is the CO_2 drive laser, with its RF generators and water-cooled heat exchangers shown to the right. A beam delivery tube sits on top of the drive laser on one end and brings the beam to a focusing system just under the vacuum vessel (shown on the left). The vessel contains the collector and droplet generator as well as a host of other sensors and diagnostics (reprinted from Ref. 39).

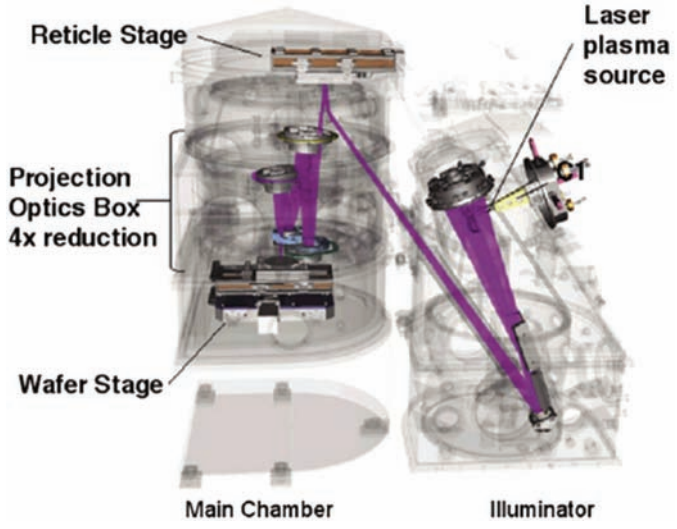

Figure 3A.3 EUV system built at Sandia National Labs (EUV LLC) in Livermore, California (reprinted from Ref. 12).

For use in a lithography system, an EUV source is more than a light-emitting plasma. The EUV light needs to be collected and directed toward the lithography exposure tool using reflective collector optics as efficiently as possible. LPP sources use a normal-incidence collector that can collect EUV light from the plasma over a solid angle of approximately 5 sr.[5] The light

Downloaded From: https://www.spiedigitallibrary.org/ebooks/ on 09 Mar 2022
Terms of Use: https://www.spiedigitallibrary.org/terms-of-use

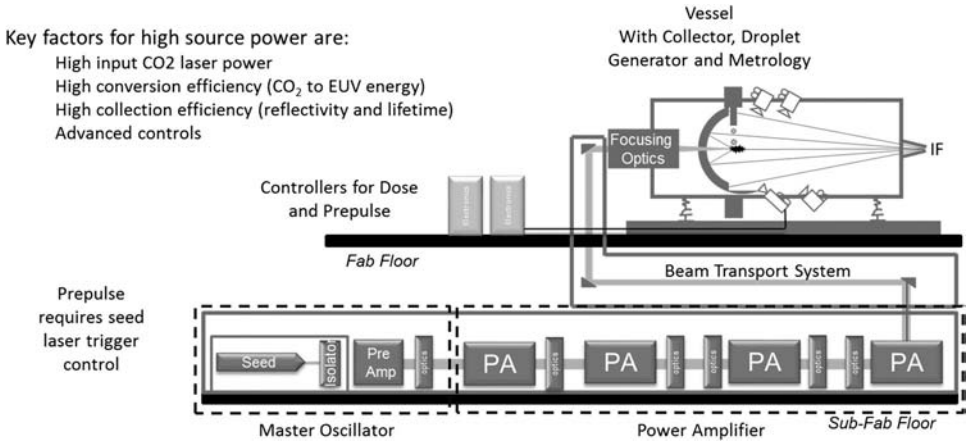

Figure 3A.4 Schematic of the LPP source system (adapted from Ref. 51).

entering the EUV scanner also needs to have certain characteristics, which are specified at the image point of the plasma source, called the intermediate focus (IF), as shown in Fig. 3A.4.

To be used in EUVL, the source needs to meet specifications for the following five parameters: power, spectral content, étendue, dose stability, and lifetime. These parameters are closely coupled and should be carefully considered when engineering the source. Source power is arguably the most important requirement. The power specification has evolved over the years and is driven by the need of lithography systems to print at a higher resolution and an ever-increasing productivity.

The leading-edge manufacturers of integrated semiconductor electronics have continued to make tremendous progress in packing more devices onto their chips using 193-nm immersion lithography by introducing double- and quadruple-patterning techniques. Device manufacturers currently project that EUV lithography will be used in HVM at the 7-nm node and beyond. In the meantime, the throughput required from lithography exposure tools has continued to climb, leading to EUV source power requirements of >200 W at introduction to HVM.[13]

Another important factor in defining the power requirement is the resist sensitivity. As the critical dimensions (CDs) of features to print in resist become smaller, the dose required to print these features tends to increase. This is due to two main factors. (1) The aerial image of smaller features produced by the projection optics usually has a lower contrast, which requires a larger dose to print. (2) With smaller CDs, stochastic effects tend to cause higher line-edge roughness (LER) unless a higher-dose resist, up to 20–40 mJ/cm^2, is used.[13] During the 1990s, the assumption for the resist dose was 5 mJ/cm^2.[14]

Downloaded From: https://www.spiedigitallibrary.org/ebooks/ on 09 Mar 2022
Terms of Use: https://www.spiedigitallibrary.org/terms-of-use

Main types of EUV sources

Two main types of EUV sources have been developed for lithography over the past 25 years: the discharge-produced plasma (DPP) sources and the LPP sources. Both are incoherent sources of EUV light pumped through collisional processes and emit over a large solid angle.[15] Only LPP sources are currently being pursued commercially for higher-power applications for EUVL scanners. In this chapter, we restrict our attention to LPP sources for lithography scanners. The representative geometries of both first- and second-generation LPP source vessels are shown in Fig. 3A.5.

LPP sources

There are two major differences between LPP and DPP sources. (1) The light-emitting plasma in LPP sources is smaller and created much farther away from any surface compared to most DPP designs.[15] This allows collection of EUV light over a larger solid angle while still meeting the étendue requirement. (2) Although the overall wall-plug-to-EUV-power efficiency may be lower in LPP than DPP, the conversion efficiency from laser to EUV light is higher (up to ~5% or greater[16,17]). Therefore, less power is deposited into the source chamber, making thermal management less of an issue. At the core of the LPP source is a target material that is radiated with a high-energy laser pulse. As the plasma reaches critical density, the dielectric function becomes negative; laser light is reflected by the critical surface and cannot propagate further. For CO_2 laser irradiance values on the order of 10^{10} to 10^{11} W/cm^2, Sn can be ionized multiple times (Sn^{+7} to Sn^{+13}), and the electron

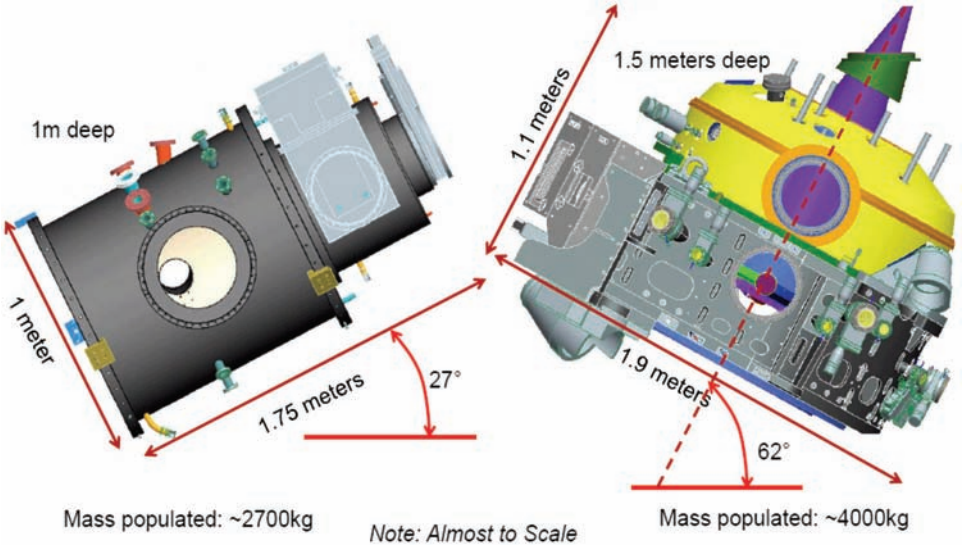

Figure 3A.5 (left) NXE:3100 source vessel and (right) NXE:3300B source vessel (reprinted from Ref. 46).

Downloaded From: https://www.spiedigitallibrary.org/ebooks/ on 09 Mar 2022
Terms of Use: https://www.spiedigitallibrary.org/terms-of-use

temperature of the plasma can reach the desired range of $T_e \sim 30$ eV, leading to efficient EUV emission around 13.5 nm.

Concept of mass-limited targets

Controlling source debris is also an extremely important aspect of the LPP source design. Early in the development of LPP sources for lithography, it was realized that the total mass of target material used during the laser–plasma interaction would need to be minimized to avoid generation of debris in the form of target fragments and clusters of neutrals that don't contribute to the EUV emission. Several designs aiming to limit the mass of the target exposed to the high-irradiance laser pulse have been conceived and tested over the years. Starting with a solid surface (e.g., a rotating cylindrical target to provide a fresh surface for every laser pulse), then using thin target tapes, spray jets, liquid filaments, and finally small droplets, the amount of fuel material that could be ablated by the laser pulse and would end up as debris was reduced dramatically.[15] The main breakthrough came with the advent of liquid tin droplet generation for the target material.[18] Even today, considerable effort is being made to reduce the size of the droplet, control the precise spatial and temporal characteristics of the target, and increase the target material supply to ensure that lifetime (or runtime) is not a limiting component in the overall availability of the EUV scanner.

Main components of LPP sources

The LPP source comprises five main components: (1) A high-power CO_2 laser consisting of a MOPA, (2) a beam transport system (BTS), including the focusing and beam position control, (3) a vacuum vessel to house the laser–plasma interaction that generates EUV light, (4) a droplet generator, providing the target to be irradiated by the laser beam, and (5) a normal-incidence collector. Figure 3A.6 provides a concept drawing of the Cymer LPP EUV source vessel.

The CO_2 laser light is focused onto a Sn droplet delivered by the droplet generator. The laser–plasma interaction takes place at the primary focus of the ellipsoidal collector mirror. The laser–droplet alignment is measured and carefully adjusted with optical metrology modules and sensors, providing feedback to maintain synchronization and optimal performance. An ellipsoidal collector transmits EUV light collected from the plasma and redirects it through the IF aperture into the illumination optics of the scanner.[8–10]

3A.2 EUV Source Requirements

The key challenge of EUVL is achieving sufficiently high wafer throughput, as shown in Fig. 3A.7. EUV mirrors typically have a reflectivity of less than 70%,

Downloaded From: https://www.spiedigitallibrary.org/ebooks/ on 09 Mar 2022
Terms of Use: https://www.spiedigitallibrary.org/terms-of-use

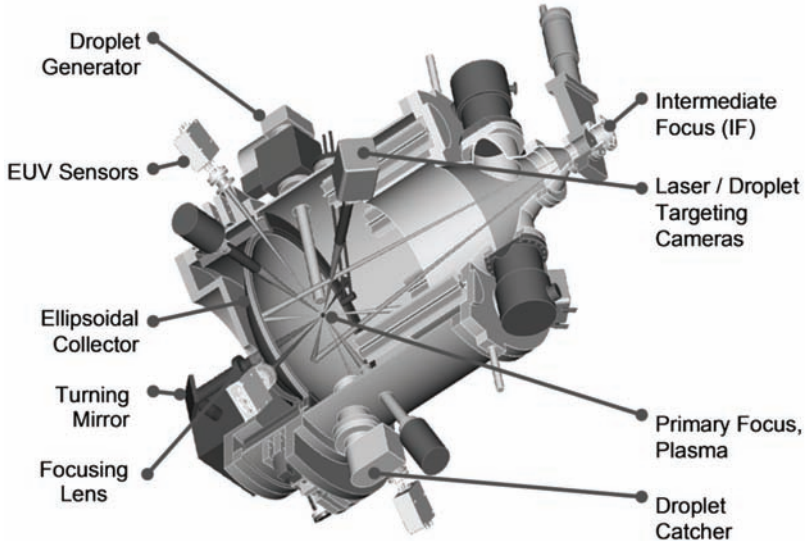

Figure 3A.6 Concept drawing of a Cymer LPP source vessel (reprinted from Ref. 4).

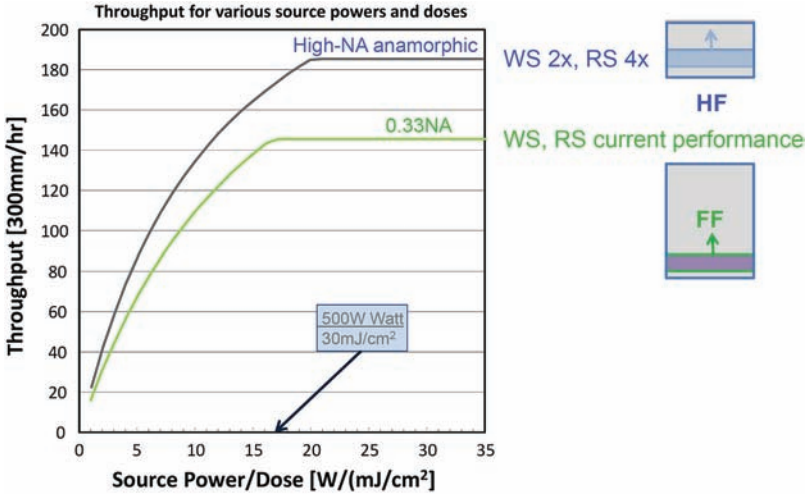

Figure 3A.7 Typical wafer throughput model used to estimate source power requirements (reprinted from Ref. 29).

which leads to very strict requirements for the power of the EUV light source to overcome the high losses. The illumination and projection optical system require multiple mirrors to provide high-quality images over the full lithography field. After the additional mask reflection and the finite transmission of background gases in the exposure system, transmission of the light from the source intermediate focus to the wafer is less than 1%. The use of pellicles to protect the reflective mask (reticle) is expected to further

Downloaded From: https://www.spiedigitallibrary.org/ebooks/ on 09 Mar 2022
Terms of Use: https://www.spiedigitallibrary.org/terms-of-use

reduce photon transmission through the scanner by ~10 to 20%.[19] Approximately 16 J is required to expose a 300-mm wafer, assuming a resist sensitivity of 20 mJ/cm^2. To achieve a throughput of 100 wafers per hour (wph) at a typical scanner duty cycle of 60%, the power at the wafer should be greater than about 550 mW, which means that the EUV source power provided to the exposure tool at IF should be greater than 250 W, as shown in Table. 3A.1.[29] For comparison, current 193-nm light sources for lithography have power levels of 90 W to support a throughput of 200 wph.[20]

To produce this level of EUV power for the scanner, plasma is produced using a high-power laser beam focused on Sn droplets with an average conversion efficiency from laser pulse energy to EUV pulse energy of approximately 5%.[16] After the loss due to the efficiency of collecting the plasma light (collection solid angle) and the transmission of the background gas within the source, more than 20 kW of laser power is needed to produce 200 W of EUV power at the IF. Consequently, ~98% of the laser power coming into the source vessel can lead to thermal loads that need to be managed. Managing the thermal loads would be even worse in a DPP source because of the lower conversion and collection efficiency.[15] LPP sources have a more open geometry, where the plasma is located a safe distance from any critical surface within the source vessel. This stand-off distance is up to 100 times larger in a LPP source compared to a DPP source, leading to mechanical heat loads on hardware components inside the vacuum vessel that are orders of magnitude lower and significantly more manageable. Still, thermal management of the source is a significant challenge when operating at varying duty cycles to accommodate scanner firing patterns.

As EUVL is introduced in HVM, it should also offer extendibility to future lithography nodes. Historically, extendibility has been achieved

Table 3A.1 Requirements for EUV sources as of 2017.

Source Characteristics	Requirements
Wavelength	13.5 nm
EUV power (inband)	250 W*@ 20 mJ/cm^2
Repetition frequency	>50 kHz***
	There is no upper limit.
Integrated energy stability	±0.5%, 3σ through 2-mm slit
Source cleanliness	Reflectivity degradation ≤10% (relative) after 1 terapulse**
Etendue of source output	max 3.3 mm^2 sr***
Max. solid angle input to illuminator (sr)	0.03–0.2 [sr]***
Spectral purity:	
130–400 nm (DUV/UV) (%)	<1% at wafer, values at IF-design dependent
>400 nm (IR/visible) at wafer (%)	<10–100% at wafer, values at IF-design dependent

*At IF
**After IF
**Design dependent

Downloaded From: https://www.spiedigitallibrary.org/ebooks/ on 09 Mar 2022
Terms of Use: https://www.spiedigitallibrary.org/terms-of-use

through techniques such as off-axis illumination.[21] Currently, the most advanced lithography scanners have illumination systems that can produce illumination with a pupil fill ratio smaller than 0.2. Therefore, any point on the mask is illuminated with a range of angles of incidence that is less than 20% of the numerical aperture of the lens. This translates into a smaller étendue or source size requirement through the fixed optical system. A LPP, being considerably smaller than a DPP, satisfies this tighter étendue requirement.

Spectral content

The EUV scanner uses many reflective surfaces utilizing Mo/Si multilayer films. For this reason, the source spectrum needs to be centered at 13.5 nm within a bandwidth of 2%, as shown in Fig. 3A.8.[2,3] For example, for 10 reflections from IF to the wafer and peak mirror reflectivity of 67%, this specification ensures that about 2% of the light is transmitted. It is interesting to note here that, unlike previous generations of lithography, the wavelength used for EUVL was not defined first by the source capability. Rather, it was defined by the availability of mirrors with adequate reflectivity in this spectral domain. As such, the spectral requirement is the most stringent requirement for EUV sources.[15]

The EUV source also has to be spectrally pure, limiting the amount of light in the DUV–UV range (130 to 400 nm) to less than 7%. This is because the Mo/Si coatings are highly reflective in that band, as shown in Fig. 3A.9, and the resists are sensitive to DUV wavelengths. In addition, transmission of

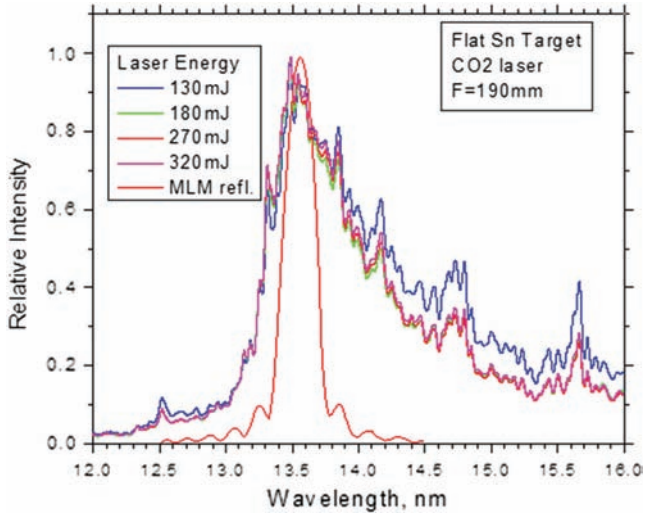

Figure 3A.8 The inband EUV spectrum is well matched to the Mo/Si multilayer-mirror reflectivity (reprinted from Ref. 43).

Downloaded From: https://www.spiedigitallibrary.org/ebooks/ on 09 Mar 2022
Terms of Use: https://www.spiedigitallibrary.org/terms-of-use

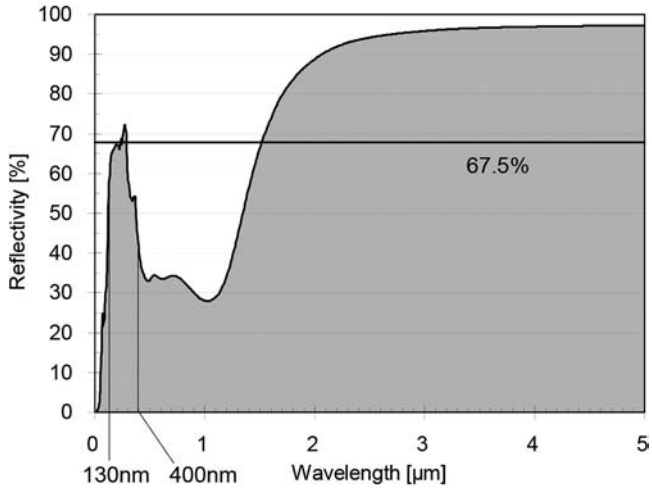

Figure 3A.9 Mo/Si mirror reflectivity in the DUV through IR range. K. Ota, Nikon, Y. Watanabe Canon, H. Franken and V. Banine, ASML Joint Specification (reprinted from Ref. 44).

the infrared (IR) radiation from the drive laser through IF should be minimized to avoid excessive heating of the wafer and projection optics.

Etendue

It is important that the source étendue matches the EUV scanner. Etendue is defined as the product of the area of the EUV-emitting plasma and the solid angle subtended by the collector optics. This specification is generally accepted to be less than 1–3.3 mm^2 sr and depends on the optical design of the illuminator and projection optics.[15] If the étendue of the source is too large, not all of the light can be coupled to the optical system of the scanner.

Dose stability and control

Process control in lithography relies on the ability to control the energy delivered to the wafer to expose the resist. For critical features, the exposure latitude is on the order of only a few percent. To achieve sufficient control, the source itself should contribute a fraction of a percent of the dose error. In a pulsed-source operation, this stability can be achieved with a high repetition rate and pulse-to-pulse energy control. Current LPP sources operate at a repetition rate of 50 kHz and are capable of $<0.5\%$ dose error.[35]

Lifetime

Another very important characteristic of the EUV source is its lifetime, which is critical in terms of cost-of-ownership and for the economic viability of EUV lithography. Early on, a target of 30,000 hours was set for the source. For LPP sources, the collector is arguably the most critical component in terms of

Downloaded From: https://www.spiedigitallibrary.org/ebooks/ on 09 Mar 2022
Terms of Use: https://www.spiedigitallibrary.org/terms-of-use

lifetime due to the harsh environment in which it resides and the cost of a large, curved, hyper-smooth, multilayer-coated EUV optic. Tin debris, high-energy ions, and neutrals from the plasma can interact with the collector surface and have the potential to degrade its reflectivity over time.

3A.3 Laser-Produced Plasma Source System

The system architecture typically includes the following major subsystems (shown in Fig. 3A.4): the drive laser, the BTS, and the source vacuum vessel. The drive laser is, e.g., a CO_2 laser with multiple stages of amplification to reach the required power level of >20 kW. It may be operated in pulsed mode at ~50 kHz with RF pumping from generators operating in the megahertz range. The laser is typically installed in the sub-fab along with its RF generators and water-to-water heat exchangers. The source controller may turn on/off bursts of pulses for exposing a 26 × 33 mm field size using 20mJ/cm^2 resist. The ratio of the time when the burst is on to the burst period defines the duty cycle. As the source power is increased, the time to scan a full field decreases, making the overhead time to step between fields a more significant part of the overall throughput budget. The beam may be expanded as it leaves the drive laser to maintain the energy density on the BTS mirrors within a certain operating range. Turning mirrors may be used to allow the beam to travel from the sub-fab to the fab through the waffle-slab floor with the needed flexibility for positioning the laser with respect to the source vessel (and scanner) on the floor above. The laser and BTS are typically completely enclosed and interlocked to meet laser class-1 requirements. The BTS delivers the beam to a focusing optical system where the 10.6-μm wavelength light is focused to a minimum spot size. The focused beam propagates through a central aperture in the collector and strikes the droplet at the primary focus of the ellipsoidal collector mirror inside the vacuum space of the source vessel chamber. The droplet generator delivers liquid tin droplets of, e.g., ~30-μm diameter to the same position at a 50-kHz repetition rate; both laser pulse and droplets are steered and timed to ensure proper targeting. The laser pulse vaporizes and heats the tin into a plasma cloud. The EUV light emitted by the plasma may be collected and transmitted with a multilayer-coated ellipsoidal mirror to an IF where it passes through a small aperture into the scanner volume that houses the illumination optics. Other modules on the source vessel may include some metrology modules for measuring EUV energy and for imaging of droplets and plasma.

3A.3.1 EUV power scaling

With the advent of MOPA pre-pulse technology, significant progress has been made to produce higher EUV power levels required for HVM. EUV power at IF on the order of ~250 W has been demonstrated.[13] The development of

Downloaded From: https://www.spiedigitallibrary.org/ebooks/ on 09 Mar 2022
Terms of Use: https://www.spiedigitallibrary.org/terms-of-use

higher-power CO_2 lasers, together with higher conversion efficiency achieved through improved laser–plasma energy coupling, have resulted in an order-of-magnitude increase in EUV power at IF over the past few years. Here, we describe some recent developments as well as provide some insight into the motivation behind historical architectural changes and future improvements.

In general, EUV source architectural changes have been made to address specific limitations to EUV power scaling, thereby enabling higher EUV power to be achieved as the source architecture evolves. The EUV power at IF is determined by several contributions for an LPP-based source:

$$\text{EUV power at IF (W)} = \text{laser power (W)} * \text{CE} * [1 - \text{overhead}\,] * f, \quad \text{(3A.1)}$$

where laser power is the average laser power used to generate the plasma, CE is the conversion efficiency of the laser power into EUV power radiated into 2π sr within 2% bandwidth around the central wavelength of 13.5 nm, overhead is the amount of EUV power required to deliver the specified dose stability, and f includes all of the physical factors in the plasma-containing vessel that impact EUV transmission from the primary focus where plasma is generated to the IF. (Examples of such factors include the reflectivity of the collector and its solid angle, transmission of the background gas, etc.) Importantly, for a pulsed EUV light source, Eq. (3A.1) can also be formulated on a per-pulse basis, describing the energy per pulse of both the laser and EUV in mJ. This last concept is important when we discuss technology development activities and various demonstrations of EUV pulse energy capabilities. By understanding the technology requirements to deliver high EUV pulse energy, one can determine many of the performance requirements for full-repetition-rate operation (typically $\sim$50 kHz for the architectures discussed here).

The architecture of a high-power CO_2 laser is understandably of great importance for successfully scaling the EUV power emitted by the LPP. We will discuss laser seed systems later in this section; here we focus on the details of laser amplifiers, which provide the majority of the >20-kW CO_2 laser power achieved in EUV light sources today. There are two types of commercially available high-power CO_2 laser amplifiers that can be used in EUV light sources. Trumpf (Germany) manufactures the TruFlow series of fast-axial flow, RF pumped, CO_2 laser amplifiers, which meet the stringent reliability requirements demanded of equipment utilized for HVM. The gas mix can be customized and typically includes CO_2, N_2, and He, and the amplifiers typically operate at or near $1/10^{th}$ atmospheric pressure. The gas is forced axially (along the direction of laser propagation) through the RF discharge region, thereby reducing the RF-induced heating of the gas, which can be problematic in short-pulsed CO_2 laser systems.[22] In the EUV source architectures discussed here, three or four fast-axial flow CO_2 amplifiers may

Downloaded From: https://www.spiedigitallibrary.org/ebooks/ on 09 Mar 2022
Terms of Use: https://www.spiedigitallibrary.org/terms-of-use

be serially arranged to provide much greater amplification than a single amplifier. Finally, the gas mix, pressure, and applied RF power are fine-tuned to match the optimal amplification settings as the laser pulse propagates through the amplifiers. This combination of amplifiers is referred to as a drive laser in EUV sources. Figure 3A.10 shows the current generation of the Trumpf TruFlow series laser amplifiers.

A similar drive-laser arrangement can be achieved using an alternative laser system under development by Mitsubishi, in Japan, and these amplifiers employ fast transverse flow of CO_2 gas. The advantage of transverse flow is that the transit time of the gas through the discharge region can be very short, in principle, thereby allowing for excellent laser gain performance.[23] Regardless of the amplifier architecture, the maturity of high-power CO_2 laser systems that can provide the power, stability, beam quality, and reliability required for HVM have enabled the successful scaling of EUV light sources to the >250-W power levels now being achieved.

In general, the ability to scale-up EUV power is based on hardware improvements that have increased the laser power and insight into the plasma physics relevant for LPPs, which has led to enhanced CE. Understanding of key parameters for EUV power scaling has enabled identification of the necessary architectural changes to be embodied in the next-generation EUV light sources. LPP EUV source architecture has undergone several important changes, following a progression in the fundamental laser technique for producing plasma. In particular, three methods for producing plasma are: no master oscillator (NOMO), MOPA, and MOPA with pre-pulse. NOMO is a technique for producing plasma whereby a grating or a mirror is placed on the backside of the laser gain medium.[39] As the tin droplet travels through the

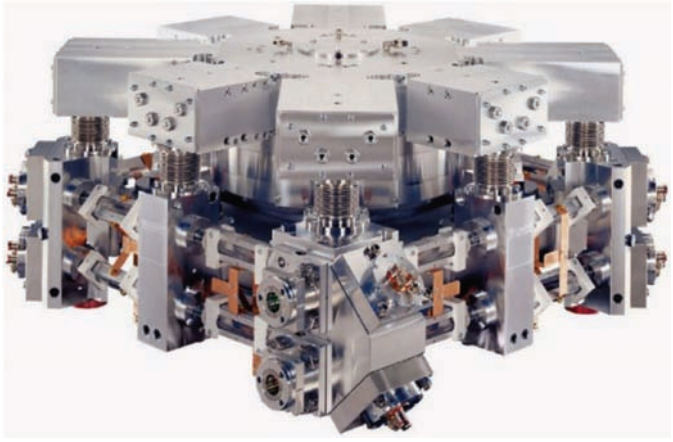

Figure 3A.10 Trumpf TruFlow series laser amplifier (reprinted from www.trumpf.com/en_US/products/lasers/co2-lasers/truflow/).

Downloaded From: https://www.spiedigitallibrary.org/ebooks/ on 09 Mar 2022
Terms of Use: https://www.spiedigitallibrary.org/terms-of-use

focal region, it serves as a mirror to complete the laser cavity. Ideally, the total stored laser energy is delivered only after the droplet has entered the focusing volume. Advantages of this architecture include precise laser-to-droplet timing without any droplet detection or control because it is an inherently self-timed and stable system. This was the principle of operation for NXE:3100 light sources installed at customer sites starting in late 2010 (Fig. 3A.11).[39] These light sources produced up to 10 W of dose-controlled EUV power at multiple customer sites by 2011.[6,7] In this configuration, the lasers produced roughly 8 kW of power on-droplet (laser energy intercepted by the tin droplets that can be converted into EUV) with an average CE of ~0.8% and dose overhead near 45%.

When considering how to scale EUV power from 10 W, looking at Eq. (3A.1), it is clear that both laser power and CE must be greatly increased from the NXE:3100 NOMO values. There are several drawbacks with the NOMO architecture for EUV power scaling. First, the amount of stored energy in the laser is limited by parasitic reflections, which result in amplified spontaneous emission, thereby depleting the gain available for making plasma, and limiting the total laser power. Second, since the NOMO laser pulse is dependent on stochastic processes between the droplet and the laser gain medium, the precise laser pulse shape cannot be controlled, placing limits on CE.[39] Finally, lacking the ability to actively transform the tin droplet into a lower-density target optimized for laser absorption, the NOMO technique is additionally limited to low CE compared with other LPP techniques. Therefore, NOMO has EUV scaling limitations that must be overcome with architectural solutions.

Following the development of the NOMO technique, the architecture transitioned to seeded laser amplifier techniques, namely MOPA and MOPA with pre-pulse (Fig. 3A.12). Both techniques involve a master oscillator that generates a laser pulse that seeds the power amplifiers for single-pass gain extraction. The seed pulse is temporally triggered by the tin droplet such that the laser pulse and the tin droplet arrive at primary focus at precisely the same instant. The MOPA pulse generation and shaping componentry are all included in the seed system module, which was first mated with the NXE:3100 three-stage power amplifier system for R&D throughout 2011 and 2012. By

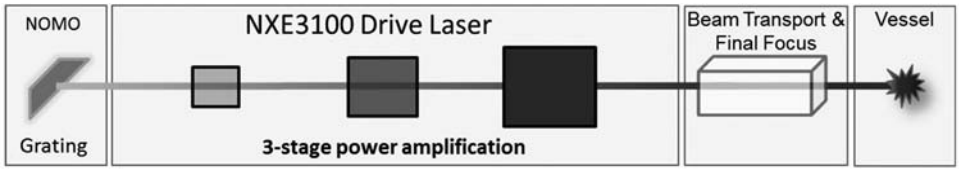

Figure 3A.11 Schematic of the NOMO technique, where a grating is mated with three-stage power amplifier system. As the Sn droplet crosses through the laser focus, the laser gain is rapidly dumped, resulting in plasma formation (reprinted from Ref. 39).

Downloaded From: https://www.spiedigitallibrary.org/ebooks/ on 09 Mar 2022
Terms of Use: https://www.spiedigitallibrary.org/terms-of-use

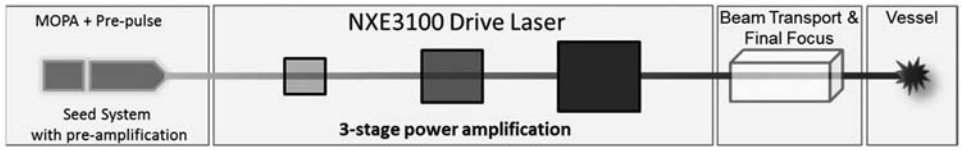

Figure 3A.12 Schematic of the NXE:3100 MOPA pre-pulse architecture (reprinted from Ref. 39).

pairing the laser power amplifiers with the MOPA architecture, it was possible to greatly increase the laser power and demonstrate 30-W EUV meeting dose specifications. Yet, without the ability to reduce the Sn density for enhanced laser absorption utilizing a pre-pulse, the NXE:3100 MOPA architecture is limited to a relatively low CE of ~1%.[39]

With the addition of pre-pulse technology to the MOPA architecture, CE can be significantly increased. The pre-pulse is a laser pulse that impacts the tin droplet prior to the main pulse, transforming the droplet into an improved target for enhanced plasma formation. The pre-pulse modifies the initial droplet into a larger target. This results in increased surface area and more favorable density, demonstrating the importance of precisely controlling the material distribution for better laser energy coupling. Figure 3A.13 illustrates that pre-pulse is one of the key EUV-power-scaling approaches employed to date, showing the relationship between CE and target size as generated by the pre-pulse.

By 2013, the NXE:3100 MOPA pre-pulse systems under development were capable of 50-W EUV power while meeting dose specifications with ~30% overhead.[39] With the architectural improvements over the NOMO technique, the drive laser was capable of ~12-kW on-droplet power with

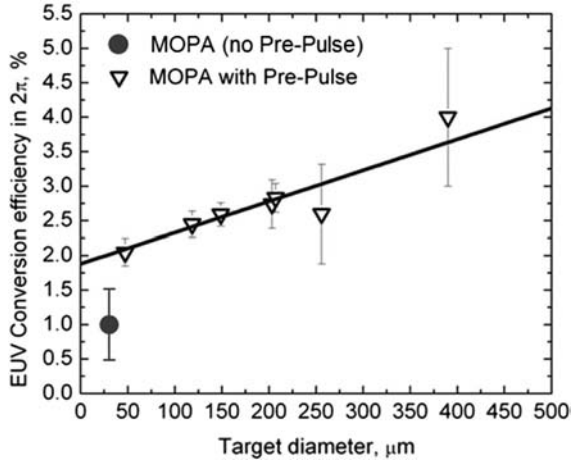

Figure 3A.13 Conversion efficiency as a function of target diameter formed by the pre-pulse. All data were collected on an NXE:3100 MOPA pre-pulse stand-alone source. Vertical bars show standard deviation of 1500 sequential pulses (reprinted from Ref. 39).

Downloaded From: https://www.spiedigitallibrary.org/ebooks/ on 09 Mar 2022
Terms of Use: https://www.spiedigitallibrary.org/terms-of-use

~2.5% CE. However, there were two issues with the NXE:3100 MOPA pre-pulse development systems for EUV power scaling; sub-optimal thermal performance of transmissive focusing optics at higher laser powers, and insufficient available laser power in the three-stage power amplification chain. In order to address these drawbacks and deliver higher EUV power to customers, the NXE:3300B MOPA pre-pulse architecture was developed.

Due to the MOPA pre-pulse R&D activities on the NXE:3100 platform, three significant architectural improvements were introduced with the NXE:3300B light source. Beyond the pre-pulse capability, another power amplification stage was added, thereby increasing the available laser power, and the focusing optics were changed to an all-reflective design to enable better thermal performance.

The first NXE:3300B systems were operational by mid-2014 and produced >40-W dose-controlled EUV power with the MOPA pre-pulse technique.[39] However, 40-W EUV performance was below expectations because the actual CE was lower than anticipated. Leveraging our understanding of the key parameters for generating high-conversion-efficiency plasma, we identified that the primary reason for the low CE performance was one aspect of the non-ideal temporal delivery of the main pulse energy, which we refer to as pedestal energy.

The main laser pulse is temporally shaped within the seed system prior to pre-amplification using a pulse-shaping switch (PSS). Pedestal energy is formed by leakage of light through the PSS due to insufficient contrast (extinction ratio) between the open states and the closed states. This leakage energy is then amplified, resulting in temporal deformation of the laser pulse. Three examples of pedestal energy and the dependence of CE on pedestal energy are shown in Fig. 3A.14. Of importance is the relationship between the

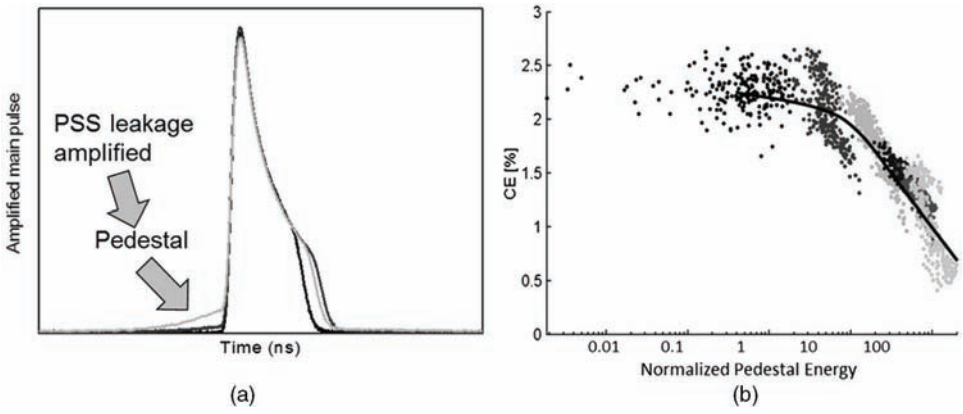

Figure 3A.14 (a) Three examples of differing pedestal energy levels on the fully amplified main pulse at the exit of the drive laser and (b) the dependence of CE on pedestal energy (reprinted from Ref. 39).

Downloaded From: https://www.spiedigitallibrary.org/ebooks/ on 09 Mar 2022
Terms of Use: https://www.spiedigitallibrary.org/terms-of-use

pedestal energy and CE, which indicates that pedestal energy must be minimized below a certain threshold energy level, otherwise it will negatively impact CE.

The mechanism by which the pedestal energy reduces CE is visualized in Fig. 3A.15. For a main pulse with minimal pedestal energy, the target material distribution shows no signs of spatial deformations (image A). However, when moderate pedestal energy is present at the leading edge of the main pulse, the target material distribution becomes deformed, as characterized by tendrils of material moving in the direction of the incident laser energy (image B). This deformation of material by the pedestal energy works counter to the precise target formation enabled by the pre-pulse, thereby lowering CE.

Reducing the pedestal energy allows for increased CE and for the total laser power to be increased to the architecturally defined operating point. The EUV power of NXE:3300B systems increased significantly, resulting first in 80-W dose-controlled EUV power and, in quick succession, 100-W[39] dose-controlled EUV power at multiple locations including customer sites (see Figs. 3A.16 and 3A.17). These performance examples indicate improvements to all parameters related to EUV power scaling: laser power, CE, and overhead.

Figure 3A.17 shows a timeline of dose-controlled EUV power achieved with the various LPP EUV light source architectures discussed. The rate of increasing EUV power of the NXE:3100 platform is slower than that of the NXE:3300B platform. This difference can be understood as a maturing in our physical understanding of the complex plasma physics involved in LPP EUV generation and of the engineering required to realize high EUV power. EUV increased 10× from the fielded NOMO systems to the fielded MOPA pre-pulse systems in 2014.

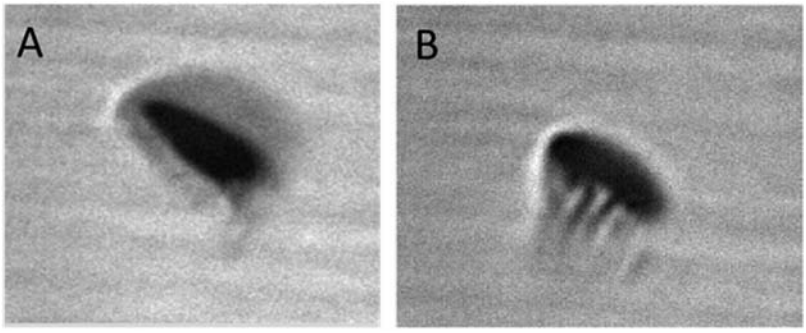

Figure 3A.15 Sn targets (edge-on) within the first few nanoseconds of the arrival of the main pulse. The main pulse is incident from the top of the images. (a) A normal target for a main pulse with minimal pedestal energy. (b) A deformed target caused by a main pulse with moderate pedestal energy (reprinted from Ref. 39).

Downloaded From: https://www.spiedigitallibrary.org/ebooks/ on 09 Mar 2022
Terms of Use: https://www.spiedigitallibrary.org/terms-of-use

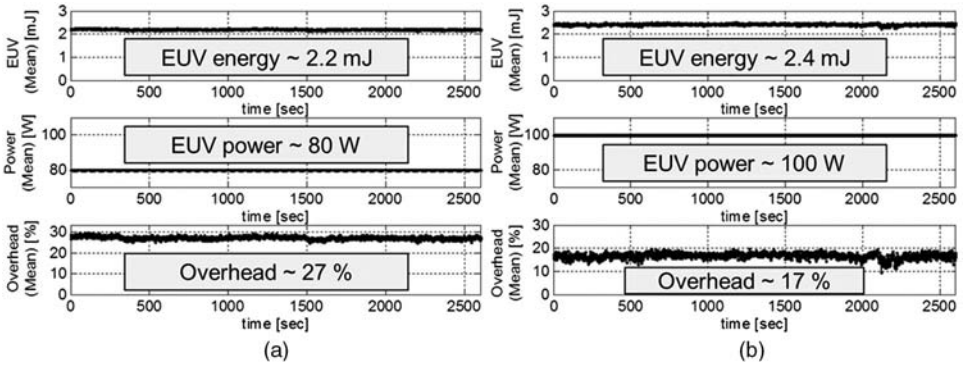

Figure 3A.16 (a) 80-W dose-controlled EUV power with 27% overhead demonstrated on a stand-alone NXE:3300B light source in San Diego. (b) 100-W dose-controlled EUV power with 17% overhead at a customer site. In both cases, CE was ~3.5% (reprinted from Ref. 39).

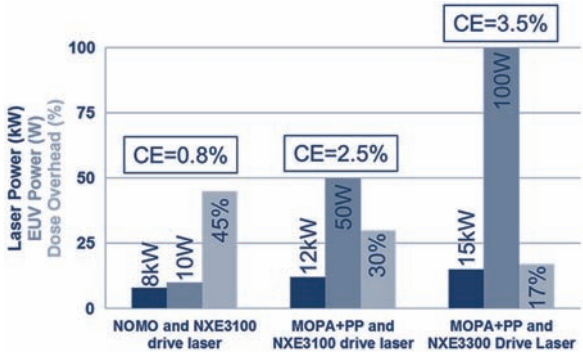

Figure 3A.17 Trends in the LPP EUV light source performance from 2009 to the end of 2014. All EUV power values are dose controlled and meet dose specifications, and are representative of three LPP architectures (NOMO, MOPA+PP on the NXE:3100 drive laser, and MOPA+PP on the NXE:3300B drive laser). (Reprinted from Ref. 39.)

To scale beyond 100 W, continuing improvement to the laser power capability and CE was required. The development of a high-power seed system (HPSS) and high-power drive laser (HPDL) were initiated. The HPSS architecture needs to provide better pulse shaping capability, greater pre-amplification, and improved isolation from parasitic effects. As part of the development activities, and to clearly assess the performance enhancements offered by the HPSS, a breadboard HPSS was mated with a standard NXE:3100 three-stage amplification chain. Because the HPSS has greater pre-amplification, it can more deeply saturate the power amplifiers, which results in many benefits. One of these benefits is an increase in the peak instantaneous power of the laser pulse at the exit of the amplification chain. Indeed,

Downloaded From: https://www.spiedigitallibrary.org/ebooks/ on 09 Mar 2022
Terms of Use: https://www.spiedigitallibrary.org/terms-of-use

the HPSS delivered ~4% CE in this configuration.[39] Therefore, not only does the HPSS enable the laser power to be increased, it also provides an increase to CE.

Similar to the breadboard development approach employed with the HPSS, the first HPDLs were built utilizing four-stage power amplifiers. The HPDL also uses more powerful amplifiers that, in factory acceptance tests qualifying the new architecture, achieved ~30 kW (~25% increase over the standard NXE:3300B drive laser under the same conditions).[39]

During 2015, performance of a HPSS fully integrated with a HPDL was successfully demonstrated on in-house research platforms operating at typical customer conditions. With regards to the instantaneous laser power, the HPDL together with a HPSS produces laser pulses that are roughly 3× higher peak instantaneous power than those of an NXE:3300B laser system combined with precise control of laser pedestal energy. Such improvements in the main pulse characteristics, in addition to target formation developments, have enabled access to even more favorable plasma conditions, leading to a mean CE in excess of 5.5%.[42] By late 2015 and early 2016, a modified NXE:3300B source with HPSS and HPDL had demonstrated one-hour dose-controlled EUV power at 210 W, illustrating the ability for LPP EUV source technology to meet HVM needs. These results are shown in Fig. 3A.18.

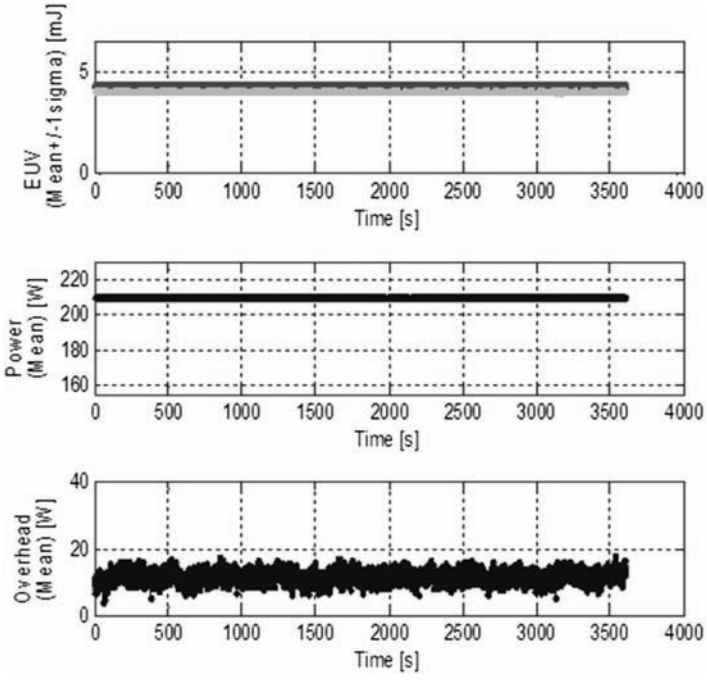

Figure 3A.18 Stable operation of the ASML-Cymer LPP source at 210 W for 1 hour (reprinted from Ref. 45).

Downloaded From: https://www.spiedigitallibrary.org/ebooks/ on 09 Mar 2022
Terms of Use: https://www.spiedigitallibrary.org/terms-of-use

The demonstration of >205-W dose-controlled EUV power on a research platform represents a significant milestone for the EUVL industry. The commonly understood entry point for HVM is >125 wph, which, with the optical throughput of the NXE:3400B scanner, results in a required source power of >205 W at IF. Based on learning from the >205-W demonstration on a research platform at the beginning of 2016, progress in EUV power scaling in 2016 and 2017 focused on securing the performance of the shipping configuration of 125 wph with an integrated 205-W EUV source and NXE:3400B scanner. This result was achieved in July 2017, where scanner throughput of >126 wph was demonstrated on a complete NXE:3400B scanner with the EUV source operating at ~207 W.

Additionally, focus in 2017 was to demonstrate >250-W EUV power on a stand-alone source in the shipping configuration. The main significance of 250-W EUV power is two-fold: (1) to ensure that lifetime performance of the EUV source always enables >125 wph at customer sites and (2) to give customers flexibility in configuration of the NXE:3400B to include pellicles or membranes designed to significantly improve mask and wafer defectivity, but which reduce optical throughput.

In the second quarter of 2017, 250 W was achieved in the shipping configuration EUV source to be paired with the NXE:3400B scanner. This required the complete integration of years of R&D, illustrating that all of the key elements for laser—plasma interaction are well controlled and generally well understood. Figure 3A.19 shows the 250-W demonstration, which meets

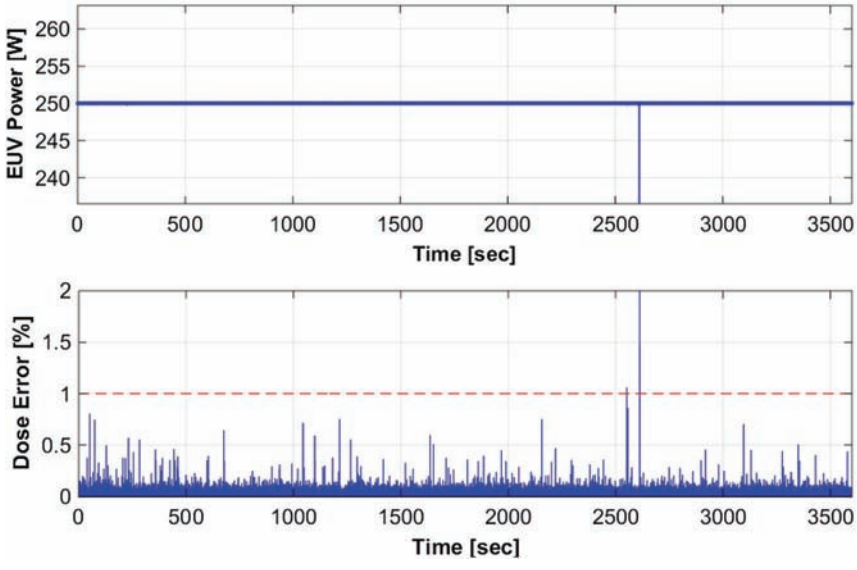

Figure 3A.19 Stand-alone stable operation of the ASML-Cymer LPP source in the shipping configuration at 250 W for one hour, meeting all dose specifications for power stability at the wafer level (reprinted from Ref. 13 with permission from M. Lercel).

Downloaded From: https://www.spiedigitallibrary.org/ebooks/ on 09 Mar 2022
Terms of Use: https://www.spiedigitallibrary.org/terms-of-use

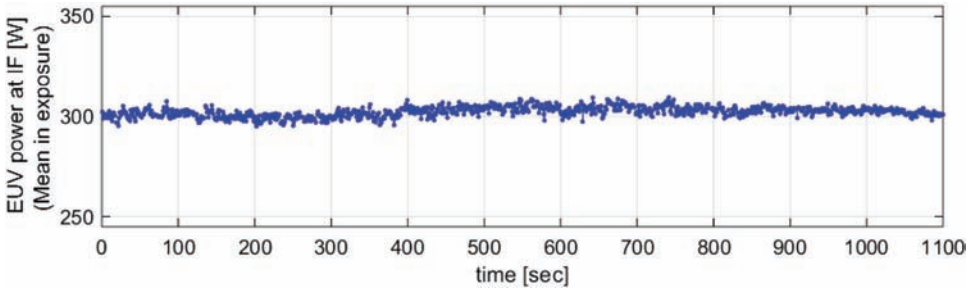

Figure 3A.20 Demonstration of the open-loop power capability of an EUV source, showing stable 300-W operation with typical customer exposure settings. The power difference between the open-loop power, shown here, and 250-W closed-loop power represents the power overhead, indicating significant power overhead for stable power delivery at 250 W (reprinted from Ref. 13 with permission from M. Lercel).

all requirements on EUV power stability for dose specifications at the wafer level. Additionally, Fig. 3A.20 shows the open-loop 300-W average EUV power at IF, demonstrating very good power overhead at the 250-W operating point.

With improvements to the EUV source discussed, the power targets for HVM have been achieved for the first time on a product-configuration EUV source. This progress in EUV power scaling continues the rapid trend established over the past several years, shown in Fig. 3A.21.

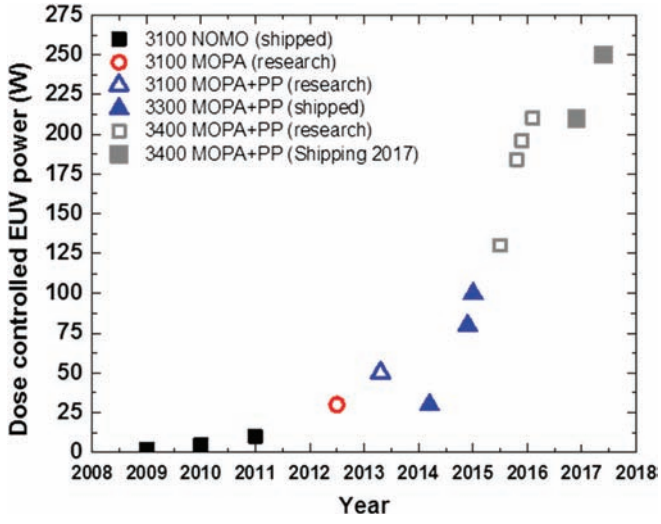

Figure 3A.21 Historical EUV power-scaling trend using LPP sources. All data points show the delivered, dose-controlled EUV power at IF and must meet dose specifications for energy stability at the wafer level for at least one hour to qualify for representation on this plot (reprinted from Ref. 13 with permission from M. Lercel).

Downloaded From: https://www.spiedigitallibrary.org/ebooks/ on 09 Mar 2022
Terms of Use: https://www.spiedigitallibrary.org/terms-of-use

The previous sections outlined just some of the performance improvements that have been leveraged for EUV power scaling. The EUV power-scaling trajectory has fundamentally relied on improvements to laser-to-plasma energy coupling and has been, in this way, just as much about scaling CE, leading to many simultaneous benefits for source operation. As the energy balance within the plasma shifts ever more toward EUV radiation, there remains less energy for Sn debris kinetics, providing the potential for significant improvement to the lifetime of plasma-facing surfaces.

3A.3.2 Tin target delivery

One of the key technologies of an EUV LPP source consists of the generation of extremely small and stable tin (Sn) droplets at high frequency that are used as the fuel for producing the plasma and EUV light. The droplet generator provides a constant stream of liquid tin droplets to the focal point of the collector where the CO_2 laser pulse is used to create the light-emitting plasma. The main requirement for the droplet generator is to deliver small droplet targets of identical size and spacing at the repetition rate of the laser pulses. These droplets are typically <30 μm in diameter and are generated at a speed of roughly 70 to 100 m/s with inter-droplet timing stability better than 0.2% of the period. When irradiated by a CO_2 laser, each tin droplet is evaporated, ionized, and heated to the optimal temperature at which the plasma produces EUV photons most efficiently. Droplets with high temporal and spatial stability have been consistently produced over a month of operation time.[13] Continuous improvement of the performance of droplet generators in terms of reliability and availability, and continuing the reduction of the droplet size are both paramount in supporting the future requirements of EUV sources. Sn droplets may be generated at a repetition rate of 50 kHz without interruption, which is the same repetition rate as the laser. The droplets themselves may be generated with a reservoir where tin is heated above its melting temperature (231.9 °C) and is then pushed through a filter and a nozzle by a pressurized gas, as depicted in Fig. 3A.22. The pressure applied and the size of the nozzle determine the size and velocity of the droplets. A modulator on the nozzle of the droplet generator tunes the delivery rate of the droplets.

One of the key advantages of the LPP EUV technology is that there is no direct contact of EUV plasma with materials, which makes thermal management of the source more practical than in other EUV source configurations. This advantage is achieved mainly through the use of mass-limited targets for generation of light-emitting plasma, namely, tin droplets.

The main function of the droplet generator is to deliver droplets of molten tin of a required size at a repetition rate of ~50 kHz to the focal spot of the EUV collecting optic, where the droplets are irradiated by the drive laser pulses. In order to enable stable operation of the EUV source, droplets should have exactly the same size and should arrive consistently in the same location

Downloaded From: https://www.spiedigitallibrary.org/ebooks/ on 09 Mar 2022
Terms of Use: https://www.spiedigitallibrary.org/terms-of-use

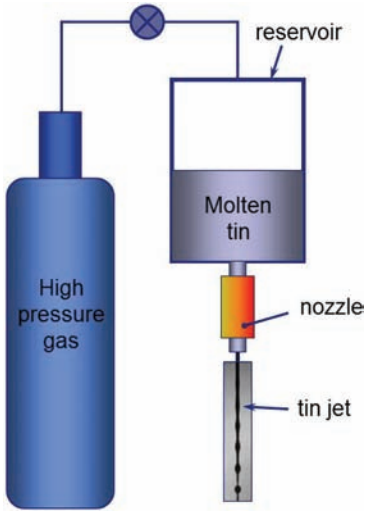

Figure 3A.22 Schematic diagram of a droplet generator (reprinted from Ref. 49).

with positional errors significantly smaller than the droplet size. In addition, the time interval between the droplets should be highly reproducible, within a fraction of a percent. Lastly, droplets should have sufficient distance between them and momentum to minimize the pushout effect of plasma generation on the approaching next target. Typical parameters achieved[41] by current droplet generation systems are summarized in Table 3A.2.

Figure 3A.22 depicts the principle of operation of the droplet generator. The key components of this device are the tin reservoir and the nozzle. The reservoir is heated to above the melting point of tin so that it stays in liquid state. A gas line is connected to the reservoir and is pressurized to a level depending on the desired droplet parameters. This high pressure is required to accelerate tin as it is passed through the nozzle having a small orifice. As tin exits the nozzle, initially, a continuous jet is formed that is later broken up into small droplets due to the forces of surface tension. The droplet breakup process is controlled by an actuator that imposes mechanical vibrations on the nozzle, thus setting the required frequency of the droplets. Droplet velocity produced in such a configuration is related to applied gas

Table 3A.2 Typical droplet generator parameters.

Parameter	Typical values
Droplet diameter	10–30 μm
Droplet frequency	40–100 kHz
Transverse stability (3σ)	<2 μm
Longitudinal stability (3σ)	<2 μm
Droplet velocity	60–120 m/s

Downloaded From: https://www.spiedigitallibrary.org/ebooks/ on 09 Mar 2022
Terms of Use: https://www.spiedigitallibrary.org/terms-of-use

pressure. Once released from the nozzle, the tin jet undergoes a breakup process, as the cylindrical shape of the jet is less stable than the same volume of tin formed in small spheres. The theory of this process was put forward by Lord Rayleigh.[24] By observing the breakup of liquid jets, it was realized that, although there is a fairly broad range of droplet sizes and droplet-to-droplet distances, there is a maximum in this distribution where droplets naturally tend to break up. For a typical liquid tin jet, this frequency is in the range of 4–6 MHz. The frequency of the drive laser on EUV sources is typically ~40–100 kHz. Experimental observations of tin jets are shown in Fig. 3A.23. As can be seen in this experiment, a continuous tin jet that is stretched too far becomes unstable and tends to form pinch points between the intended nodes. This observation is indeed in agreement with Rayleigh theory of the jet breakup.

One of the early ideas that was developed mainly in the relation to ink-jet technology is the charge-and-deflect concept.[25–27] This concept has been proposed for EUV application as well.[28] According to this concept, the droplets produced at high frequency by applying a sine wave waveform to a nozzle modulation element are charged electrostatically and then passed between deflection plates. Most of the droplets are deflected, but periodically one droplet is allowed to stay on the straight trajectory (Fig. 3A.24). Thus, droplets at a lower frequency and with large droplet-to-droplet spacing can be produced. This method, even though conceptually elegant, has multiple practical shortcomings when considered in EUV droplet generation. First, most of the material that is jetted through the nozzle is not used and must be collected in a way that does not contribute to debris generation. For significant dividing ratios, handling unused droplets can be a major problem. Also, the large electrostatic fields required for this method can be screened out by the charged particles produced in EUV source plasma. Accurate control of droplet charge can be complicated by the spontaneous charging of the droplets via an electro-kinetic effect or other mechanisms.

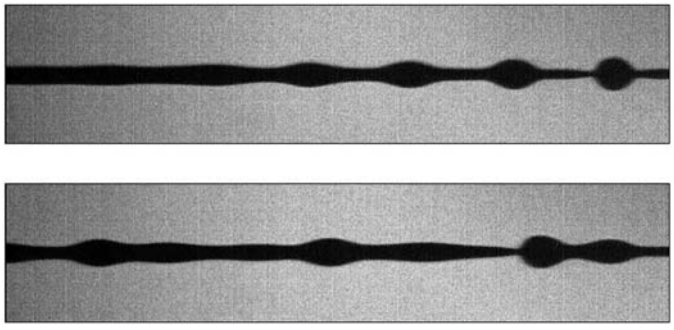

Figure 3A.23 Tin jet breakup due to harmonic modulation (reprinted from Ref. 25 with permission from AIP Publishing).

Downloaded From: https://www.spiedigitallibrary.org/ebooks/ on 09 Mar 2022
Terms of Use: https://www.spiedigitallibrary.org/terms-of-use

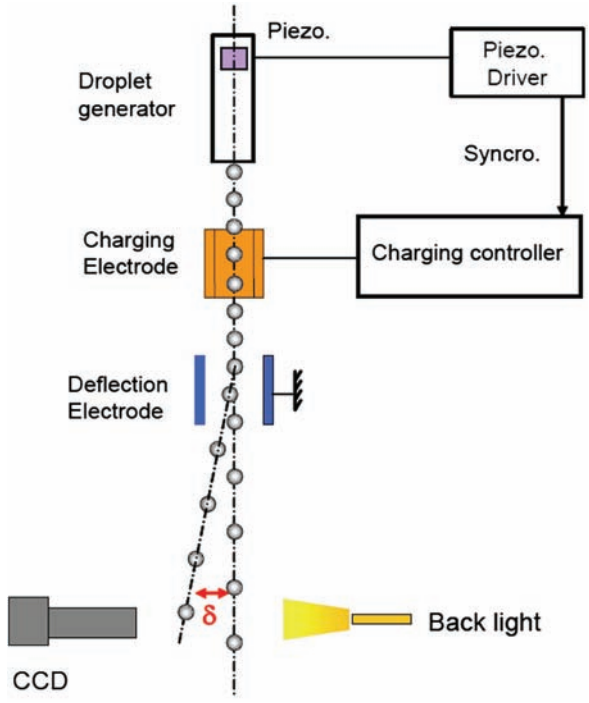

Figure 3A.24 Schematic diagram demonstrating the charge-and-deflect concept for reducing the frequency of droplets produced through the Rayleigh breakup mechanism (reprinted from Ref. 50).

A breakthrough in droplet generator technology came in a form of the realization that instead of producing droplets with the desired low frequency directly through the Rayleigh breakup process, one can form such droplets by combining several Rayleigh droplets through a coalescence process at a relatively short distance from the nozzle. This can be accomplished through simultaneously controlling the Rayleigh breakup process and by modulating the velocities of the individual droplets in such a way that favors fast coalescence of the Rayleigh droplets into droplets of a larger size and lower frequency. Many waveforms can be used to achieve the same result with varied extents of efficiency, i.e., with the different coalescence distance of the droplets. For example, this can be achieved with frequency modulated, phase modulated, rectangular pulse, saw tooth, delta pulse, and other waveforms.[32–34] Each of these waveforms contains the fundamental frequency that is desired for the coalesced droplets (such as 50 kHz) and at least one higher-frequency harmonic in the Rayleigh breakup range that is required to control the breakup process. Figure 3A.25 shows a typical pattern of the small droplets that form immediately as they break up from the continuous jet and the droplets formed through the coalescence process at some distance. Approximately 100 small droplets at an average frequency of 5 MHz

Downloaded From: https://www.spiedigitallibrary.org/ebooks/ on 09 Mar 2022
Terms of Use: https://www.spiedigitallibrary.org/terms-of-use

Figure 3A.25 Modulated droplets as they break up from a continuous jet (top) and fully coalesced (formed) droplets at some distance from the nozzle (bottom).

were used in this example to produce 50-kHz droplets with a 1.5-mm droplet-to-droplet spacing. In addition to an efficient use of tin, this method also offers an advantage of averaging out positional and timing fluctuations between a large number of droplets breaking off from the jet, thus making the resulting coalesced droplets significantly more stable than droplets produced with Rayleigh breakup.

Scaling the droplet generator performance to enable higher source power requires increasing the drive gas pressure to increase the separation distance from droplet to droplet (Fig. 3A.26). This is needed to counter the forces on droplets originating from the plasma event. The shock wave, or so-called 'ion wind,' can significantly distort the next droplet such that energy stability control is reduced; however, higher-speed droplets with increased momentum and greater separation enable power scaling to continue. Droplet spacing is shown to increase with higher gas pressure.

Since the desired performance of the droplet generator has been realized, lifetime and overall reliability of the droplet generators on EUV sources have become the focus of development efforts. Most important breakthroughs have been on the materials science side of the technology. Additionally, recent significant advances in protecting tin from contamination have paved the way for radical transformations of the droplet generation system architecture with emphasis on preventing tin supply from limiting the operational runtime of the droplet generator.

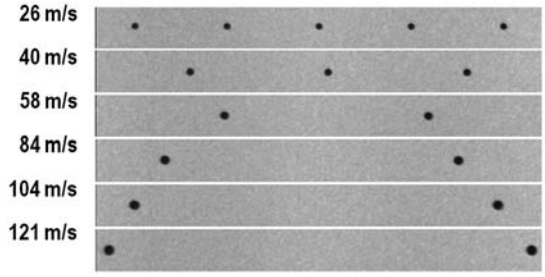

Figure 3A.26 Higher-velocity droplets arrive at the target location with greater spacing (reprinted from Ref. 49).

Downloaded From: https://www.spiedigitallibrary.org/ebooks/ on 09 Mar 2022
Terms of Use: https://www.spiedigitallibrary.org/terms-of-use

3A.3.3 Pre-pulse technology

The typical size of a Sn droplet is significantly smaller than the laser beam diameter at its focal position. For this reason, further conditioning of the target needs to take place once the droplets have left the droplet generator. This is achieved by the use of a pre-pulse, as shown in Fig. 3A.27.

The size and material distribution of formed targets using pre-pulse are critical for CE and EUV power scaling. In addition to these parameters, target density and its profile, and volume distribution of the target material are crucial for further improvement of CE and EUV power scaling. Coupling of the main pulse with an optimized target leads to higher CE, manageable debris, and improved EUV power scaling. Figure 3A.28(a) is a shadowgraph of a typical low-density target generated with pre-pulse technologies. For comparison, Fig. 3A.28(b) shows a disk target. An optimized tin target has

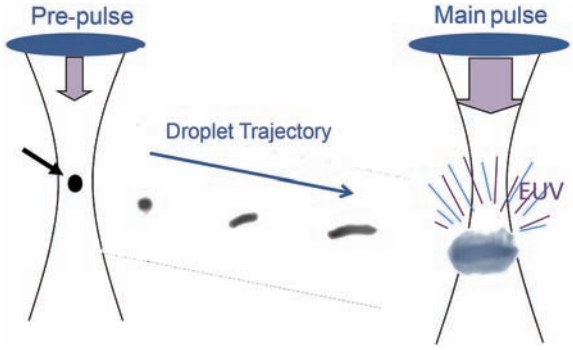

Figure 3A.27 Pre-pulse concept illustration showing expansion of the Sn droplet to match the main-pulse beam waist diameter and lower density of the target material (reprinted from Ref. 45).

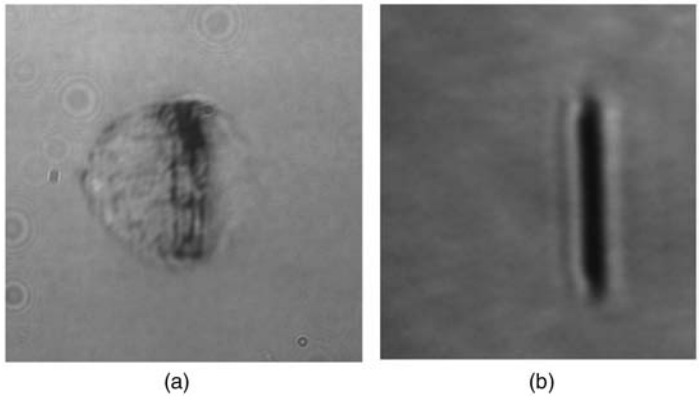

Figure 3A.28 (a) Shadowgraph of 3D spherical target preformed and (b) the disk target (reprinted from Ref. 40).

Downloaded From: https://www.spiedigitallibrary.org/ebooks/ on 09 Mar 2022
Terms of Use: https://www.spiedigitallibrary.org/terms-of-use

lower density than a liquid target, and when irradiated by the main drive laser pulse, a plasma without a steep density gradient is created.

More efficient use of target material and more efficient laser absorption are obtained by creating distributed laser absorption instead of localized laser absorption. More Sn ions are involved to emit EUV, leading to higher conversion efficiency. With lower density targets, higher CE and EUV power was demonstrated, as shown in Fig. 3A.29.[42] A conversion efficiency of 6% and 350-W in-burst EUV power at low duty cycle has been demonstrated on test sources in development laboratories,[42] as shown in Fig. 3A.30.

Uniform low-density tin targets without steep gradients not only enhance EUV generation but also reduce the kinetic energy of ions. During the plasma expansion, a static electric field is formed due to the separation of fast electrons and slower ions. This electric field accelerates ions from its plasma temperature, i.e., several 10 eV, up to several keV, depending on the plasma density profile. The electric field can be described as inversely proportional to the plasma density gradient, which means that a more gentle plasma density gradient leads to longer plasma scale length, resulting in a lower electric field and reduced kinetic energy of ions. Therefore, a low-density target also helps Sn debris mitigation and optics lifetime.

3A.3.4 EUV collector

An advantage of LPP sources is the isolated nature of the plasma, with open access to the EUV emission pattern over the full 4π sr; however, typically, only the 2π hemisphere is used to collect EUV light. A normal-incidence design with a solid angle of up to 5.5 sr provides approximately $2\times$ more collection than the DPP collectors. A sample photograph of such a collector is shown in Fig. 3A.31. The challenge is to achieve high reflectance over the full

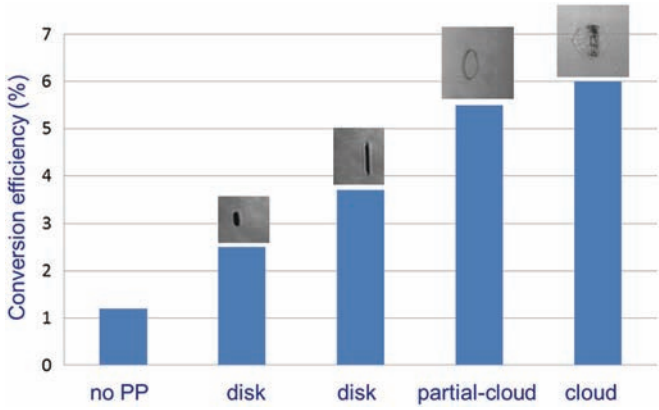

Figure 3A.29 Conversion efficiency with various target shapes and densities (reprinted from Ref. 40).

Downloaded From: https://www.spiedigitallibrary.org/ebooks/ on 09 Mar 2022
Terms of Use: https://www.spiedigitallibrary.org/terms-of-use

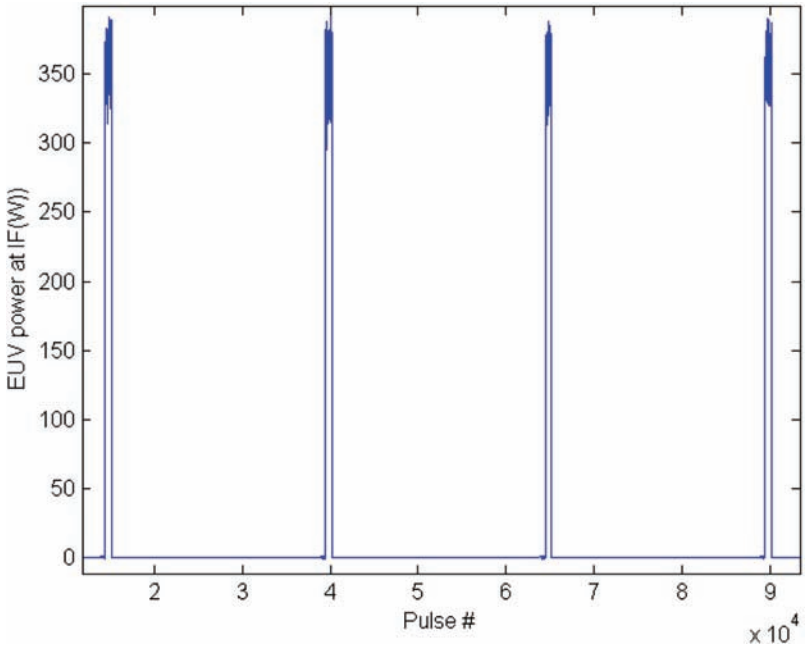

Figure 3A.30 350-W in-burst EUV power obtained with a low-density target.

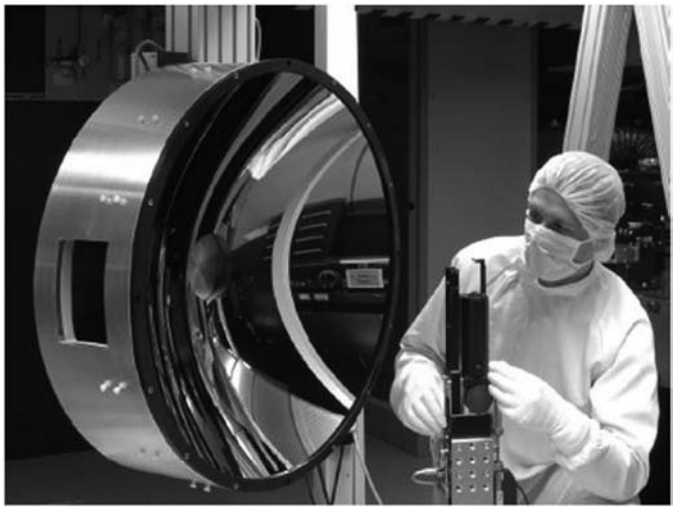

Figure 3A.31 Photograph of a normal-incidence EUV collector used in the ASML NXE:3100 source (reprinted from Ref. 52 with permission from OSA).

surface of the collector, accepting the fact that when the angle of incidence approaches 45 deg, only the s-polarized light is reflected.

A multilayer coating may be used to achieve high EUV reflectance, but tradeoffs need to be considered because the maximum reflectivity of such

Downloaded From: https://www.spiedigitallibrary.org/ebooks/ on 09 Mar 2022
Terms of Use: https://www.spiedigitallibrary.org/terms-of-use

multilayer films depends on the quality of the mirror surface in terms of nano-roughness. The smoother the surface the higher the EUV reflectivity. The EUV collector may be a normal-incidence, multilayer-coated, graded ellipsoidal collector mirror, covering approximately 5 sr solid angle. Photons are collected from the emitting plasma and transmitted to the intermediate focus (IF) where they can be used by the lithography exposure tool (Fig. 3A.32).

In addition, the infrastructure for manufacturing large-size normal-incidence collector mirrors is already in place. A large number of full-size collectors with ~5-sr collecting angle have been fabricated for NXE sources.

Collectors may be characterized in the sources by acquiring images of the EUV light reflected by the collector past the IF point. Far-field EUV images can be obtained that show a convolution of the EUV light emitted by the plasma and the collector reflectivity for unpolarized light. A far-field test tool (FFTT) (Figs. 3A.33 and 3A.34) can be used not only to record EUV images but also to characterize any deterioration of the collector reflectivity over time and to analyze the spectral content of the light past IF.

Out-of-band (OoB) radiation can be measured in MOPA pre-pulse mode of operation using a grating spectrometer. Figure 3A.35 presents the absolute intensities of the measured emission features in J/nm (into 2π solid angle) versus wavelength in nanometers for the spectral range of 130–600 nm. The exponential extrapolation of the measured spectral densities into the

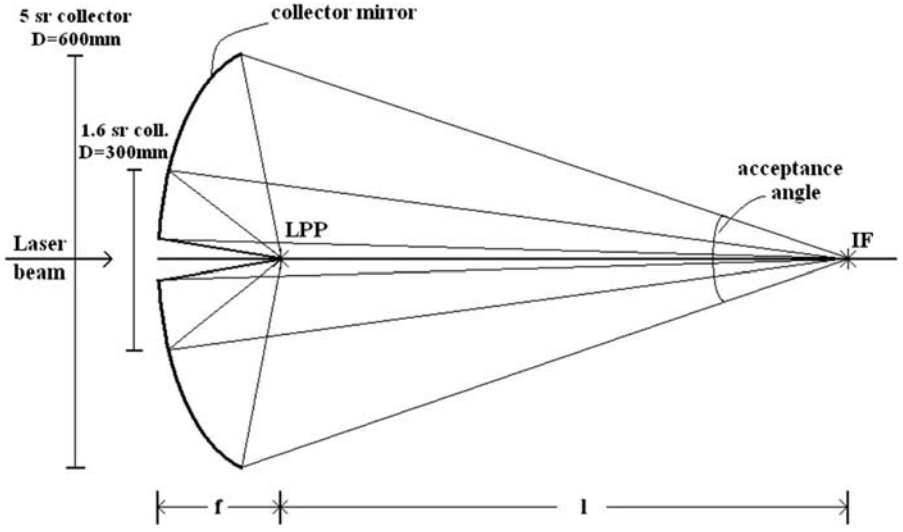

Figure 3A.32 Schematics of light-collection geometry with an ellipsoidal collector and refocused image at IF. Examples of a 5-sr collector (650-mm diameter) and a 1.6-sr subaperture (half-size) configuration are shown in comparison (reprinted from Ref. 8).

Downloaded From: https://www.spiedigitallibrary.org/ebooks/ on 09 Mar 2022
Terms of Use: https://www.spiedigitallibrary.org/terms-of-use

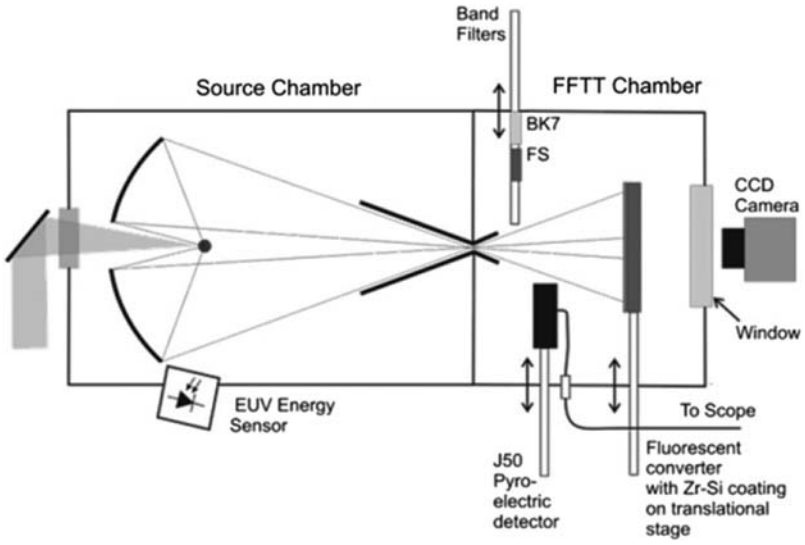

Figure 3A.33 Schematic of the source vessel attached to a FFTT (reprinted from Ref. 16).

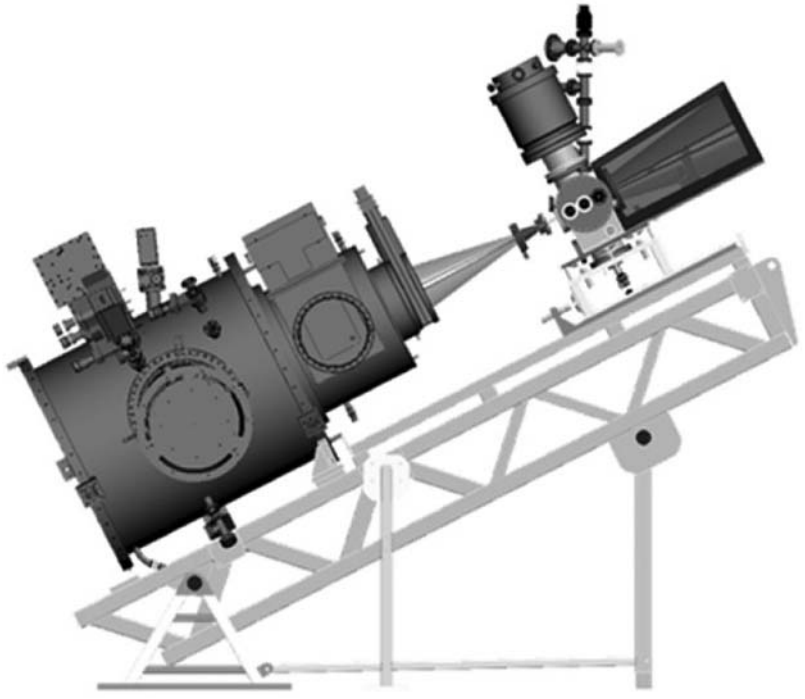

Figure 3A.34 NXE:3100 vessel with a FFTT attached behind IF (reprinted from Ref. 16).

Downloaded From: https://www.spiedigitallibrary.org/ebooks/ on 09 Mar 2022
Terms of Use: https://www.spiedigitallibrary.org/terms-of-use

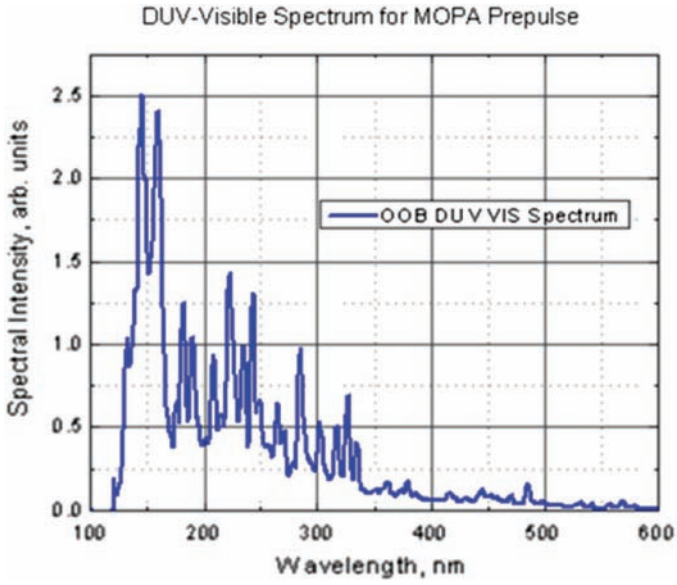

Figure 3A.35 DUV spectrum of plasma with optimized alignment and correction for second-order diffraction (average of 90 readouts). (Reprinted from Ref. 16.)

short- and long-wavelength ranges enables us to estimate the OoB radiation for the bands from 130 nm to 350 nm and from 1 μm to 5 μm, which are most critical, as these wavelengths could potentially expose the photoresist and blur the image.

The OoB measurements were taken on a 3100 source operating in MOPA pre-pulse mode at an open-loop raw power level of ~100 W in the burst, or 4.5 mJ per pulse into 2π sr. The DUV content was measured to be approximately 0.3% of the EUV energy content when at optimal focus, as shown in Fig. 3A.35.[16] Additionally, the OoB radiation was measured when the plasma was outside of the optimal focus position of the CO_2 drive laser. The DUV OoB energy content is reduced when the plasma is out of focus, as shown in Fig. 3A.36.[16]

The inband spectrum of a MOPA pre-pulse Sn CO_2 plasma is shown in Fig. 3A.37. There is a strong line at 13.5 nm. As the laser focus is moved through the plasma position ($\pm z$), the peak intensity is reduced.[31] The reflectivity of the multilayer is well matched with the emission of the plasma and produces a spectral filtering effect of the near-inband emission. When the multilayer from, e.g., 10 reflections is convolved to emulate the total transmission to the wafer, only a 2% band from the plasma emission is used to expose the photoresist; hence, power in a 2% bandwidth around 13.5 nm is required.

Figure 3A.38 shows one series of corresponding reflectivity curves as a function of wavelength. The lateral multilayer thickness gradient was

Downloaded From: https://www.spiedigitallibrary.org/ebooks/ on 09 Mar 2022
Terms of Use: https://www.spiedigitallibrary.org/terms-of-use

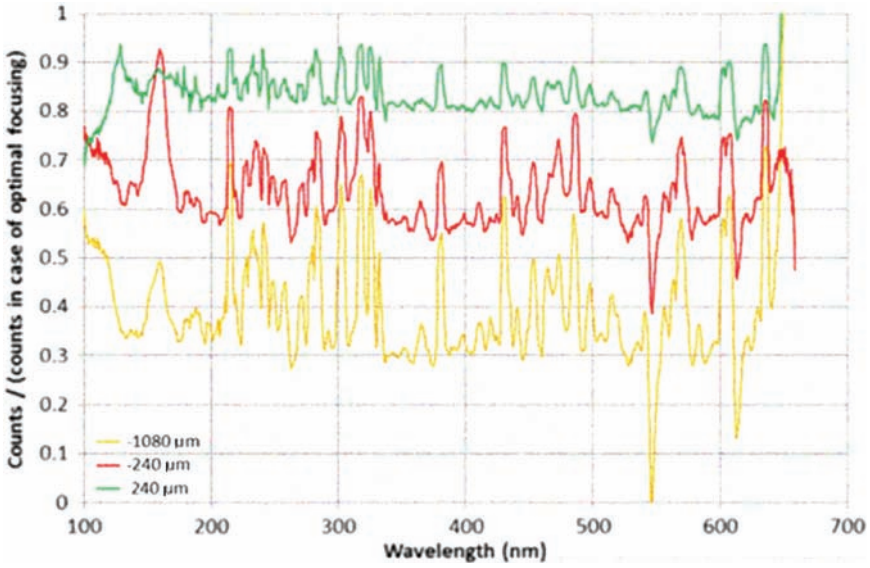

Figure 3A.36 Ratios of spectra at several focus (z) positions to the spectrum at the optimal position (average of >60 readouts per position). (Reprinted from Ref. 16.)

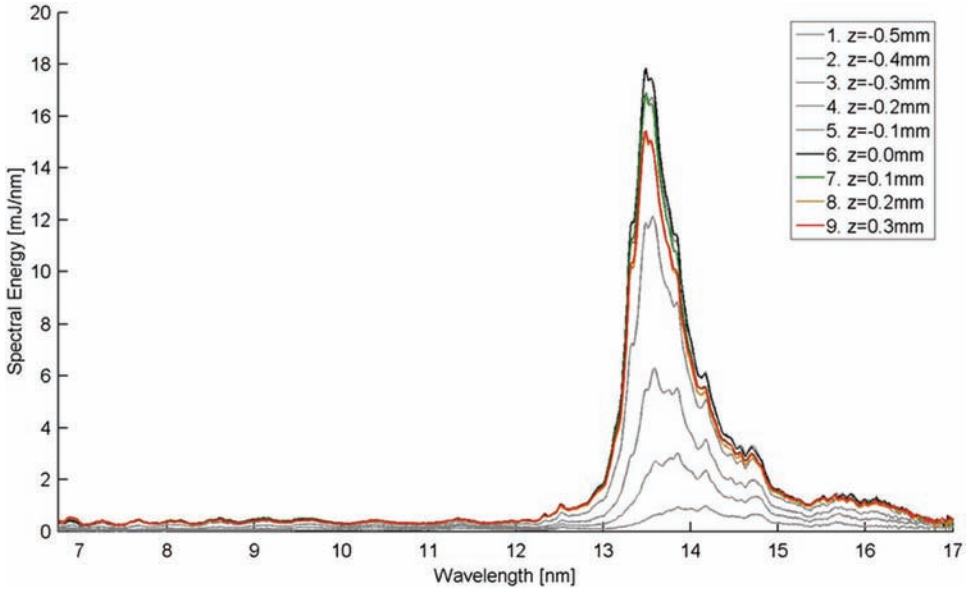

Figure 3A.37 Inband spectrum of Sn CO_2 LPP as the focal plane of the laser moves in and out of focus (reprinted from Ref. 31).

optimized using test samples prior to collector coating in order to meet the specified center wavelength of 13.50 nm. The FWHM of the reflectivity curves is typically >0.48 nm.

Downloaded From: https://www.spiedigitallibrary.org/ebooks/ on 09 Mar 2022
Terms of Use: https://www.spiedigitallibrary.org/terms-of-use

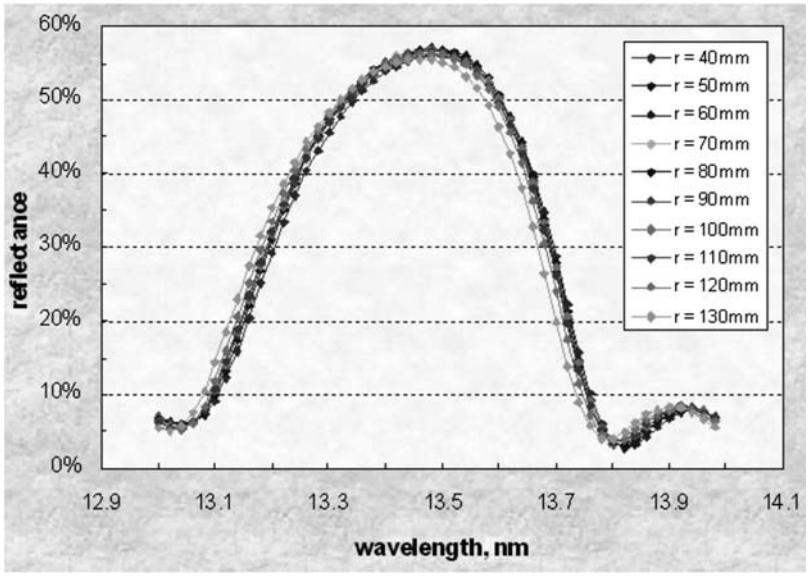

Figure 3A.38 Reflectivity curves at different mirror radii as a function of wavelength (adapted from Ref. 30 with permission from T. Feigl).

Achieving long collector lifetime is one of the most, if not *the* most, difficult challenges for the introduction of EUVL into HVM. The source environment within the vacuum vessel needs to be taken into account as high-energy ions and neutrals from the plasma could strike the collector surface and cause irreversible damage. As a protection to the multilayer reflective coating, hydrogen buffer gas can be used within the vacuum chamber to slow down the high-energy ions, along with special collector capping layers.

Improvements in the efficacy of the debris mitigation techniques implemented in the LPP source resulted in longer lifetime achieved in actual sources operating in the field, as can be seen in Fig. 3A.39, which shows up to 120 billion pulses for the best-performing NXE:3100 collectors.[40] The relative reflectivity of one of the collectors used for over a year in a NXE:3100 sources, operating at a power level of 10 W, stayed above ~50% for more than 10^{11} pulses. As the source power is increased, collector protection needed to be adapted to increase the lifetime of EUV collectors. A tin cleaning technique using hydrogen radicals was developed to enhance the rate of tin removal from the collector. A photograph of an NXE:3100 collector covered with a significant amount of Sn is shown in Fig. 3A.40. After exposure to the hydrogen radicals, the collector has been cleaned of the Sn that was covering its surface (Fig. 3A.41). The combination of continued improvements in Sn management inside the EUV source vessel and assisted tin cleaning provide a path toward the lifetime requirement of 30,000 hours mentioned earlier.

Downloaded From: https://www.spiedigitallibrary.org/ebooks/ on 09 Mar 2022
Terms of Use: https://www.spiedigitallibrary.org/terms-of-use

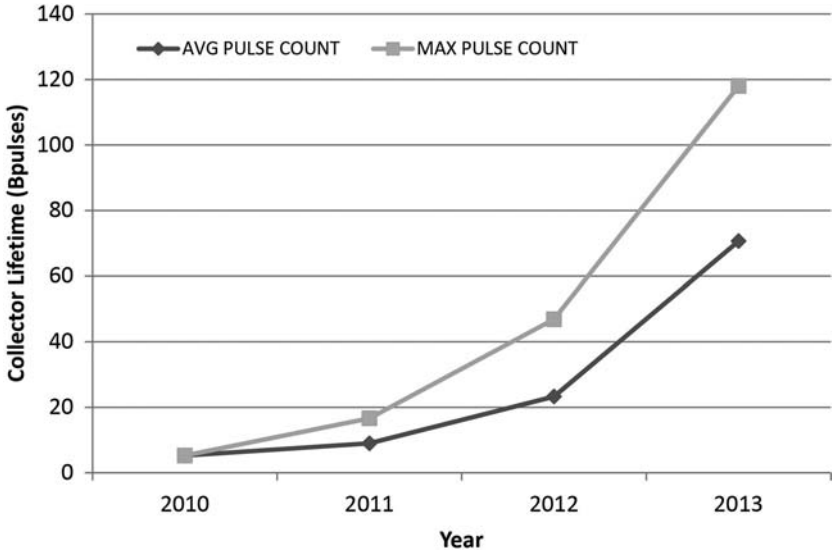

Figure 3A.39 Improvements of NXE:3100 collector lifetime in terms of total number of pulses. The black line shows the typical average lifetime in the field, and the gray line shows the maximum lifetimes achieved in the field (reprinted from Ref. 40).

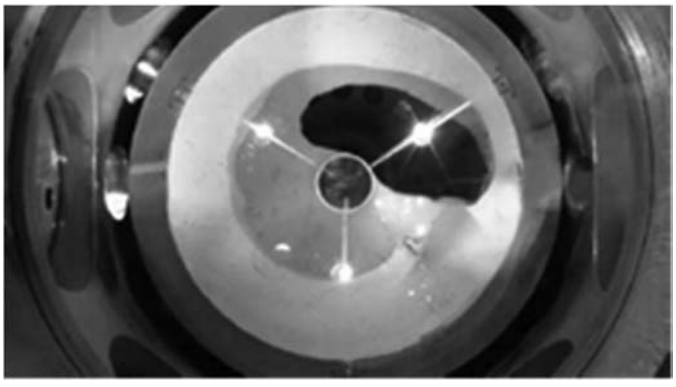

Figure 3A.40 Sample NXE:3100 collector after use, showing Sn accumulation (light gray) (reprinted from Ref. 40).

3A.3.5 Debris mitigation

Debris mitigation technology consisting of a hydrogen gas barrier can be incorporated into the source vessel to protect the multilayer coating on the collector from etching or implantation due to plasma ions, both of which would result in a rapid reflectivity loss and ultimately reduce CE and power output in a matter of minutes. Hydrogen gas pressure determines the Sn-ion stopping power (Fig. 3A.42).[47] As the buffer gas pressure is increased, both

Downloaded From: https://www.spiedigitallibrary.org/ebooks/ on 09 Mar 2022
Terms of Use: https://www.spiedigitallibrary.org/terms-of-use

Figure 3A.41 Same NXE:3100 collector as in Fig. 3A.40, after hydrogen radical cleaning (reprinted from Ref. 40).

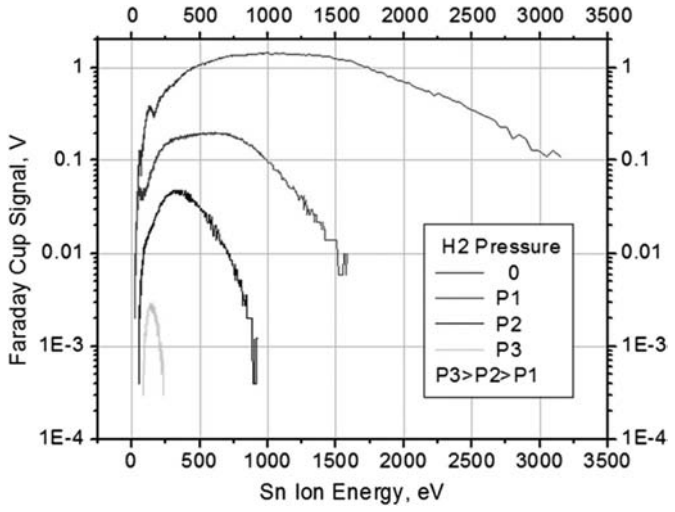

Figure 3A.42 Hydrogen buffer gas pressure versus ion energy and flux at the location of the collector surface (reprinted from Ref. 47).

the ion energy and the ion flux reaching the surface of the collector are significantly reduced.

Hydrogen gas provides a second benefit for debris mitigation as H_2 gas cracks into elemental hydrogen in the presences of the high-energy plasma. Elemental hydrogen reacts with tin to form stannane (SnH_4), which is gaseous and is pumped out of the vessel. The reaction of H radicals with Sn to form SnH_4 is

$$\mathrm{Sn\,(s) + 4H\,(g) \rightarrow SnH_4\,(g).} \tag{3A.2}$$

Additionally, since hydrogen is the lightest element, it is the least absorptive of EUV radiation.

Downloaded From: https://www.spiedigitallibrary.org/ebooks/ on 09 Mar 2022
Terms of Use: https://www.spiedigitallibrary.org/terms-of-use

To provide consistently high EUV source availability, reflectivity of all optical surfaces inside the source should remain at high levels without degradation and the optical path should remain clear of obscurations as the source continues to operate. Optical surfaces in the source can be divided into three groups: EUV collector mirror, CO_2 beam delivery optics, and metrology optics, which might include visible and near-IR optics as well as EUV energy sensors. Of these three groups, protection of collector mirror reflectivity from degradation is the most challenging task. With an exception of the last mirror, the in-vacuum CO_2 beam delivery does not have a direct line of sight to the plasma. Metrology optics are quite remote from the plasma and normally are protected by counter gas flows and geometry. In this chapter, we primarily focus on protection of the EUV collector mirror.

Sn ions are good EUV emitters but, unfortunately, Sn atoms are strong EUV absorbers. Choosing liquid Sn as the EUV target material means that Sn will be unavoidably accumulated inside the vessel. At the same time, Sn should be prevented from accumulating on the optical surfaces and building up into the optical path. To illustrate how strongly Sn atoms absorb EUV radiation, Fig. 3A.43 shows EUV absorption of a 10-nm layer of Sn as a function of wavelength near the EUV band. The calculation was done using the CXRO database.[36]

Because of this high absorption of Sn for 13.5-nm light, it does not take a lot to cause significant degradation of collector reflectivity. For example, Fig. 3A.44 shows the calculated source operation time (before collector reflectivity is reduced by 10%) as a function of droplet size. In this example, it is assumed that all Sn contained in the droplets hit by the laser beam is spread uniformly across the collector surface. One can see from the figure that collector lifetime is really very small and only a very tiny fraction (on the order of 10^{-8} of all the Sn material that was hit by the laser) can be allowed to accumulate on the collector surface to provide the required minimum collector lifetime of 1 year.

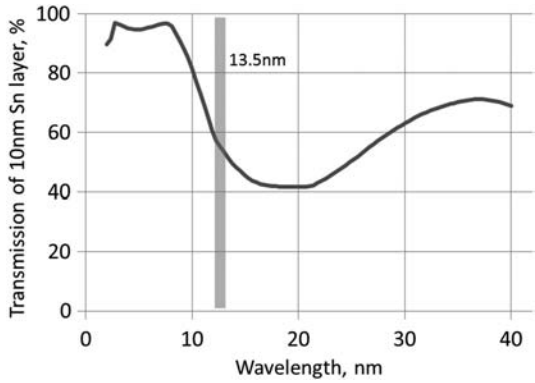

Figure 3A.43 Transmission of 10-nm-thick Sn layer as a function of wavelength.

Downloaded From: https://www.spiedigitallibrary.org/ebooks/ on 09 Mar 2022
Terms of Use: https://www.spiedigitallibrary.org/terms-of-use

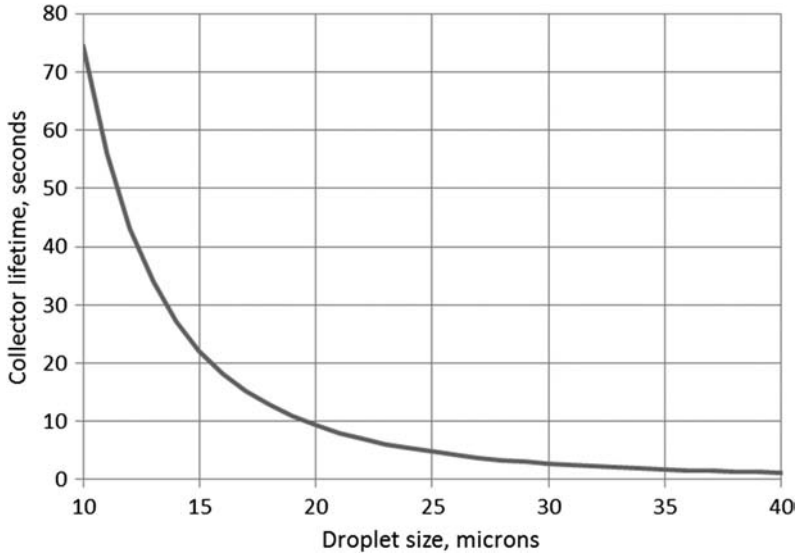

Figure 3A.44 Collector lifetime (at 10% reflectivity degradation) as a function of droplet size, assuming that all Sn contained in droplets hit by the laser beam is spread uniformly over the collector surface. 50-kHz operation with 80% utilization and 20% dose margin is assumed.

All of the debris that needs to be taken care of in the source can be divided into two large categories: primary and secondary debris. Primary debris comes directly from the plasma before collision with any surface or before being trapped by the gas flows in the source. The presence of buffer gas (H_2) reduces the kinetic energy of fast ions through collisions, and has been shown to eliminate any potential damage to the collector surface by primary debris. This debris does not directly lead to collector reflectivity degradation, but it affects the debris mitigation performance by heating up the gas and decreasing its density in the volume between the plasma and the collector surface. To reduce this effect, fresh cold gas has to flow constantly into the vessel at high flow rates.

Secondary debris consists of all debris that undergoes collision with a surface such as the vessel walls. This includes Sn micro-particles that scatter or are otherwise transported back to the collector surface. Secondary debris also includes Sn material accumulating inside the vessel. Sn accumulation can lead to Sn debris protruding into the EUV or CO_2 optical path. Sn debris impedes the vacuum exhaust path and thus changes the gas flow in the vessel, as does accumulated Sn falling or dripping onto the collector surface since it is facing up against gravity in the EUV source. Sn accumulation in liquid form (e.g., due to heat from the plasma) leads to another type of debris: the ejection of liquid Sn material under H-radical flux. This effect is caused by H-radicals diffusing through liquid Sn and recombining into H_2 molecules, thus causing

Downloaded From: https://www.spiedigitallibrary.org/ebooks/ on 09 Mar 2022
Terms of Use: https://www.spiedigitallibrary.org/terms-of-use

accumulation of H_2 gas inside the liquid Sn. This accumulation of H_2 gas leads to formation of H_2 bubbles that diffuse to the surface of liquid Sn and burst at the surface. As a result, a number of small droplets are generated. These droplets are typically up to 50 μm in diameter (but can reach a size of 1 mm) and have a velocity of few meters per second. They can also end up on the collector surface, after having been carried there by gravity, gas flow, or their initial momentum.

3A.3.6 Hydrogen as a buffer gas

There are several requirements for the buffer gas in the EUV source. It must efficiently cool the region near the plasma and efficiently stop fast Sn ions, and it should be able to efficiently etch Sn from the collector surface. It has to do all these three functions without imposing excessively high EUV absorption. Typically, maximum EUV absorption by the buffer gas of 20–30% is acceptable in the EUV power budget. Last, but not least, the buffer gas has to be economical in the quantities required for the source operation.

There are several alternatives for the buffer gas, which we will evaluate against these requirements. In order to cool the plasma, high heat capacity and high heat conductivity of the gas is required. Figure 3A.45 shows heat capacity for several buffer gas alternatives. We can see that hydrogen and nitrogen, as diatomic gases, show higher specific heat capacity of the group. Figure 3A.46 shows thermal conductivity for the buffer gas alternatives. Here again, hydrogen is the gas with the highest thermal conductivity. The last, but not least, parameter is the ability to stop fast ions. In general, any gas can stop fast ions if its density is high enough. The task is to find the gas that can do the job and still have reasonable EUV transmission. Figure 3A.47 shows, by way

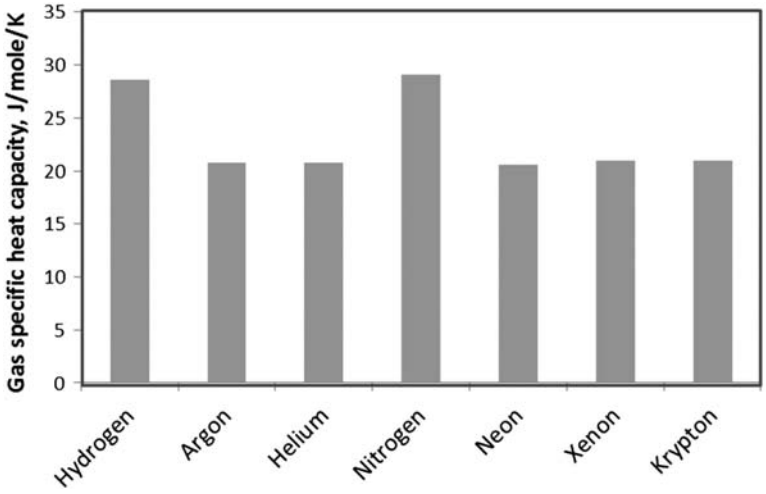

Figure 3A.45 Specific heat capacity for buffer gas alternatives (reprinted from Ref. 48).

Downloaded From: https://www.spiedigitallibrary.org/ebooks/ on 09 Mar 2022
Terms of Use: https://www.spiedigitallibrary.org/terms-of-use

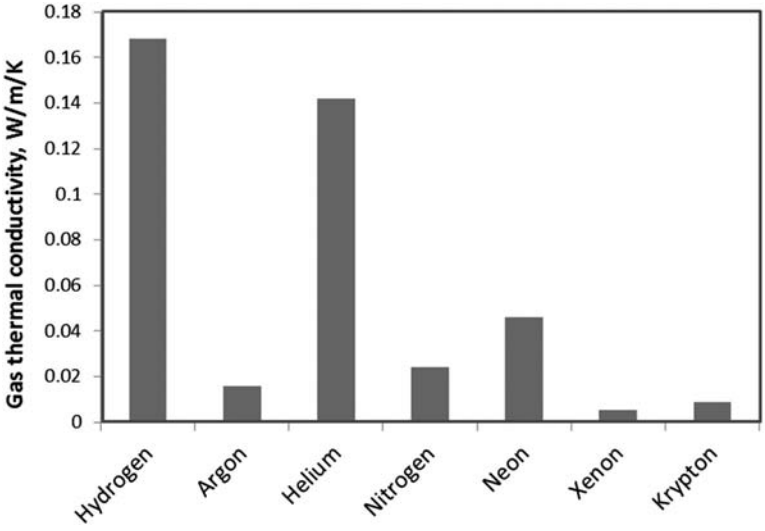

Figure 3A.46 Heat conductivity comparison for buffer gas alternatives (reprinted from Ref. 48).

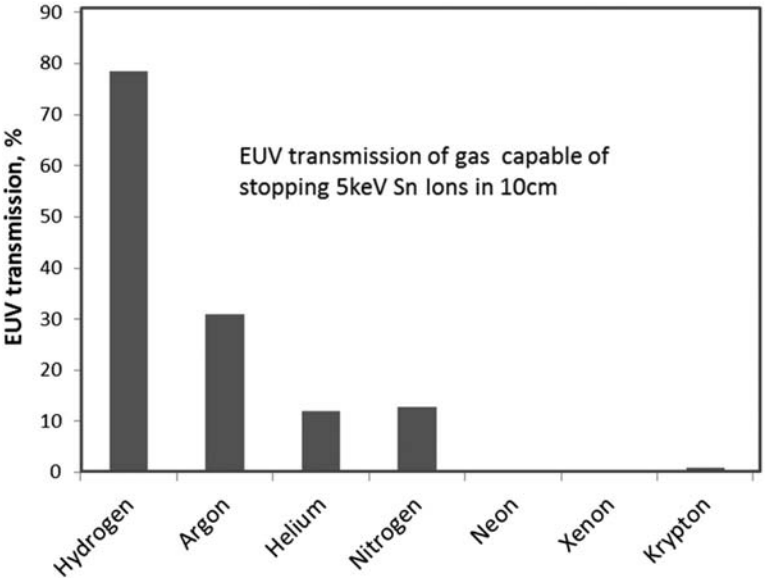

Figure 3A.47 EUV transmission comparison for buffer gas alternatives (reprinted from Ref. 48).

of example, EUV transmission of a gas column 1.5-m long (the typical distance that EUV photons travel inside the source vessel) with a gas density sufficient to stop 5-keV Sn ions over a distance of 10 cm.

In addition to being the best gas in terms of thermal properties and for stopping ions, hydrogen also happens to be a good etchant for Sn. This is

Downloaded From: https://www.spiedigitallibrary.org/ebooks/ on 09 Mar 2022
Terms of Use: https://www.spiedigitallibrary.org/terms-of-use

quite fortunate because it allows for the use of pure hydrogen (without any additives) in the source to etch Sn. Sn etching with hydrogen is described by the following reaction:

$$\mathrm{Sn} + 4 \cdot \mathrm{H} \rightarrow \mathrm{SnH_4}. \tag{3A.3}$$

Hydrogen radicals ·H are produced in the source by dissociation of molecular hydrogen:

$$\mathrm{H_2} \rightarrow \cdot\mathrm{H} + \cdot\mathrm{H}. \tag{3A.4}$$

Dissociation of molecular hydrogen occurs by several mechanisms in the source: dissociation in the plasma region, photo-dissociation by plasma radiation, and dissociation by photoelectrons.

Once SnH_4 (stannane) is formed, it can be pumped away since it is gas under the source conditions. However, competing mechanisms are photo-dissociation of stannane and catalytic dissociation on Sn-covered surfaces. These mechanisms tend to bring Sn back to collector surfaces, thus reducing the cleaning rate. The goal of debris mitigation is to minimize the residence time of stannane in the vessel and to reduce the number of wall collisions of stannane molecules, thus reducing the effects of Sn re-deposition due to stannane dissociation. The total Sn cleaning rate is thus

$$K_{\mathrm{net}} = K_{\mathrm{SnH4_formation}} \cdot (1 - K_{\mathrm{Sn_redep}}), \tag{3A.5}$$

where K_{net} is the net etch rate of Sn, $K_{\mathrm{SnH4_formation}}$ is the rate of SnH_4 formation, and $K_{\mathrm{Sn_redep}}$ is the rate of Sn redeposition.

Another application that hydrogen is used for is protection of the scanner volume (illumination optics) from debris generated in the source. The scanner has many optical surfaces that are very expensive to replace and are very sensitive to contamination. Primary micro-particles generated at the plasma location are usually blocked by a small obscuration in the direct line of sight from the plasma to the IF. This way, virtually 100% of all primary debris can be blocked from traveling into the scanner volume. There is, however, still a risk of secondary debris penetrating the scanner. This risk is minimized by careful design of the internal hardware of the source vessel. As can be seen, hydrogen as a buffer gas provides several functions for Sn management, the most important being reduction of Sn flux to the collector, etching Sn from the collector, cooling the plasma region, and carrying debris out of the vessel. It is clear that hydrogen is the leader by a large margin for the all three functions; thus, hydrogen is the best gas to use in the LPP source.

An alternative method to reduce the Sn flux moving toward the collector can be achieved using magnetic confinement. Gigaphoton developed the concept of magnetic debris mitigation. The idea of this concept is to trap Sn ions with a strong magnetic field and direct them into a designated Sn trap, as

Downloaded From: https://www.spiedigitallibrary.org/ebooks/ on 09 Mar 2022
Terms of Use: https://www.spiedigitallibrary.org/terms-of-use

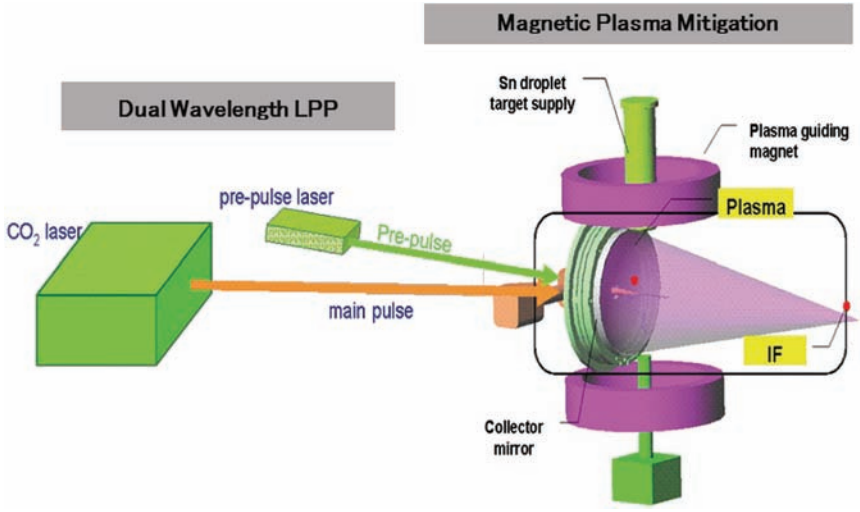

Figure 3A.48 Diagram showing the concept of an EUV source with magnetic debris mitigation (reprinted from Ref. 37).

shown in Fig. 3A.48.[37] A fairly high magnetic field (exceeding 1T) is required, thus necessitating use of superconducting magnets. Also, in order for this concept to be efficient, reduced background gas pressure is required; otherwise, collision of Sn ions with gas molecules will reduce the efficiency of the magnetic field trapping.

Figure 3A.49 shows a plot of the reported debris deposition onto the collector with magnetic debris mitigation.[38] Sn flux is quite small for most of the collector surface, but in two locations it reaches about 2 nm per MPulse, which is near the location of the traps. This is a very high flux that cannot be easily cleaned and will likely mean quick loss of EUV reflectivity in these areas. Overall, magnetic debris mitigation can be considered as an alternative or addition to the baseline debris mitigation with hydrogen gas.

3A.3.7 Tin management

Besides keeping the collector free from debris, another important issue is properly managing tin accumulation in the vessel. The problem is very challenging due to the volume of Sn used by the source. A simple calculation assuming 50-kHz operation of the source with a 20% dose margin and 80% pulse utilization shows tin usage by the source verses droplet size over the 7-year lifetime of a vessel (Fig. 3A.50). Only the droplets that were hit by the laser are used to calculate the total Sn consumption in this graph, as the unused droplets are trapped in the droplet catcher and removed periodically. The source consumes on the order of 100 L or more over its lifetime, at the current droplet size of ~30-μm diameter. The Sn has to be properly captured and removed from the vessel while minimizing the chances that this Sn will

Downloaded From: https://www.spiedigitallibrary.org/ebooks/ on 09 Mar 2022
Terms of Use: https://www.spiedigitallibrary.org/terms-of-use

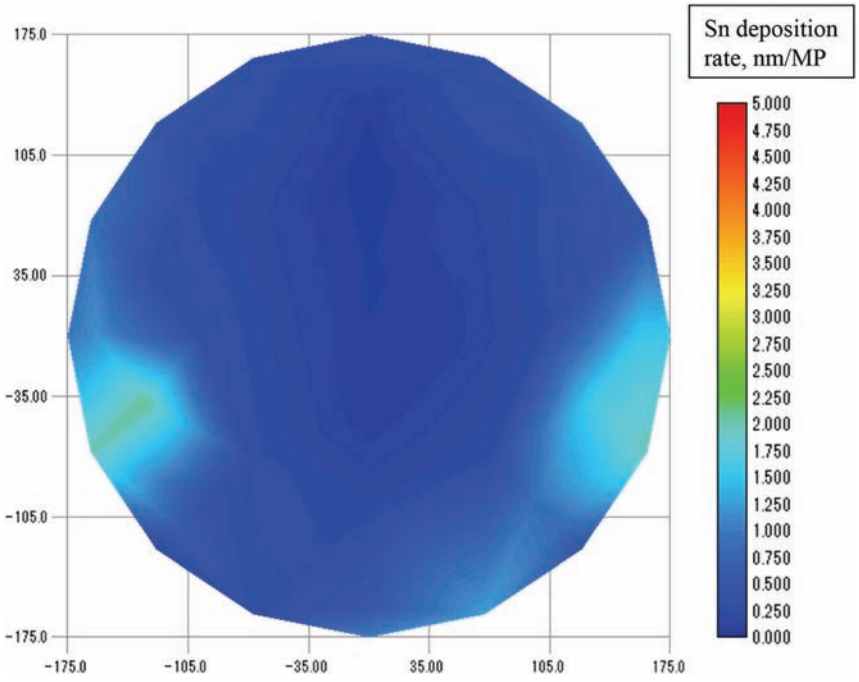

Figure 3A.49 Debris deposition onto the collector with magnetic debris mitigation (reprinted from Ref. 38).

end up on the collector before it is removed from the vessel. Another important function of debris mitigation is to prevent any Sn from entering the scanner volume. Because there are no materials that transmit EUV photons with material thickness over 1 μm, the source and the scanner are connected through an open aperture, which means that if proper care is not taken, Sn can flow from the source into the scanner volume.

Tin management inside the vessel

Figure 3A.50 shows that the Sn management function of the vessel should be able to handle somewhere in the neighborhood of 100 L of Sn over the source lifetime for a 30-μm droplet. Mitigation of primary debris relies on buffer gas that stops fast Sn ions generated by the laser–target interaction, cools the plasma region, and absorbs momentum and heat generated by the plasma. The counterflow of buffer gas also creates protection against Sn diffusion toward the collector. Another goal is to create the gas flow pattern in the source in such a way that tin vapor is trapped by this flow and carried out of the vessel before it has a chance to deposit on the vessel internal hardware and walls. It is practically impossible to completely eliminate vapor Sn deposition inside the vessel, but it can be minimized, which, among other things, is driven by minimizing the gas residence time in the vessel. Both cooling the plasma

Downloaded From: https://www.spiedigitallibrary.org/ebooks/ on 09 Mar 2022
Terms of Use: https://www.spiedigitallibrary.org/terms-of-use

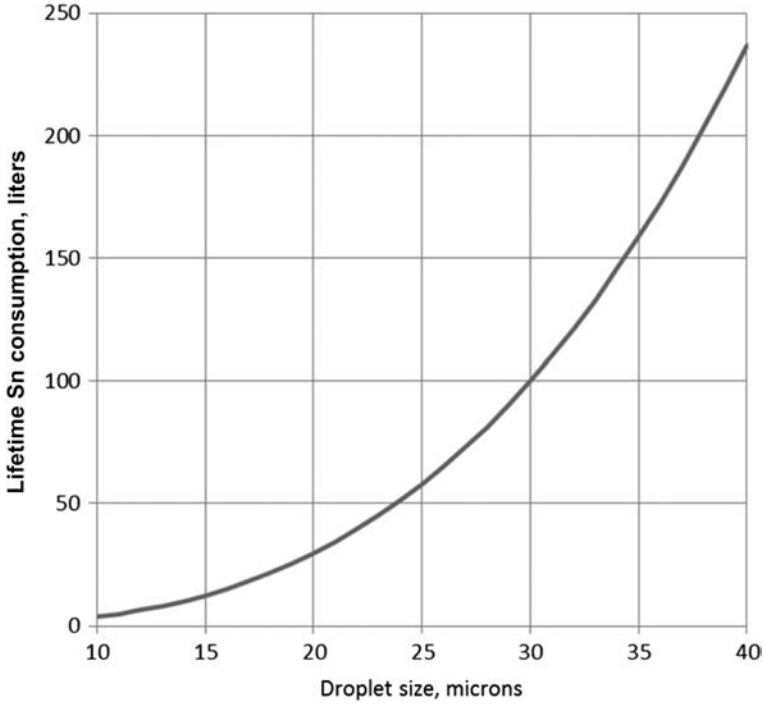

Figure 3A.50 Source Sn consumption over a 7-year lifetime versus droplet size. 50-kHz droplet frequency, 20% dose margin, and 80% pulse utilization is assumed.

and minimizing tin deposition lead to increased flows of buffer gas. The probability of Sn vapor sticking to the solid surface is close to one; therefore, some fraction of Sn vapor gets deposited to the walls before it is pumped away. Fast micro-droplets are not affected by the gas flow and travel on the line of sight. Most of these micro-droplets have their initial velocity vectors away from the collector surface, so they mainly deposit on the vessel walls.

Managing the secondary debris is another function of debris mitigation. In order to minimize backscattering of micro-droplets, which can lead to Sn deposition on the collector surface, the vessel may have vanes that minimize specular reflection of Sn particles toward the collector. Several types and geometries of vanes are used in EUV sources, but they are all designed to trap Sn particles via the multiple bounces they undergo on the vanes.

Tin removal from the vessel

Sn removal is a very important function of Sn mitigation, since most of the Sn (ideally, more than 95%) needs to be removed. Technically, Sn removal can be done either online or offline with EUV production. Online Sn removal is much preferred since it does not lead to interruptions in the source operation, while offline Sn removal is a service action and thus reduces source

Downloaded From: https://www.spiedigitallibrary.org/ebooks/ on 09 Mar 2022
Terms of Use: https://www.spiedigitallibrary.org/terms-of-use

availability. Removal of vapor phase debris is done with the gas flow of hydrogen, as already discussed. Once the Sn vapor is removed from the main volume of the vessel and is outside of the optical path, it is very desirable to separate this Sn vapor debris from the rest of the hydrogen exhaust flow so that it does not clog the gas pump lines.

We found that keeping surfaces cold leads to Sn accumulation in a fluffy, low-density form. This type of accumulation should be avoided since, in this form, Sn quickly fills a significant volume, which leads to blockage of gas flows and pumping paths, and protrusion of Sn into the EUV optical path. Tin deposition on hot surfaces leads to formation of dense Sn that occupies the minimum volume possible for the given mass. Also, Sn above its melting point can flow under gravity; therefore, can be made to flow into a dedicated collection location. The main problem here is associated with the source geometry and collector facing upward such that a wall is needed directly above the collector (see Fig. 3A.5).

Another problem with molten Sn is that, when hydrogen radicals are present, small Sn droplets can be ejected into the gas above the molten Sn surface. These Sn droplets present a real challenge to the Sn management system in the source since many of them cannot be controlled with gas flow or require unacceptably large amounts of gas flow. Therefore, the molten Sn should only be allowed to accumulate in the vessel for a limited time.

Source–scanner interface

The EUV collector may have an ellipsoidal shape that collects EUV light emitted from plasma and transmits it into its second focus, commonly referred to as its intermediate focus (IF). This focus is a logical interface between the source and the scanner. As was previously mentioned, the interface between the source and the scanner is an open aperture. To minimize gas phase diffusion from the source to the scanner, a gas dynamic lock approach can be used, where a buffer gas flows through the opening in the direction from the scanner to the source. While gas phase diffusion can be effectively suppressed by this dynamic gas lock, some fast or large micro-particles can still possibly penetrate it. These micro-particles moving directly from the plasma to the IF can be blocked by a small obscuration bar. Because the diameter of the IF aperture is generally quite small, the size of this obscuration can also be quite small so it does not block much ($\sim$5%) EUV light. Attention also needs to be given to micro-droplets that can reach the IF aperture after bouncing from vessel walls and other internal hardware. This is usually minimized by choosing geometrical shapes that eliminate the specular path taken by the particles toward the IF, requiring them to bounce multiple times before they reach the IF aperture. Since the fraction of these particles that can continue to move after each bounce reduces exponentially, several bounces is usually enough to reduce the flux of these particles below an acceptable level.

Downloaded From: https://www.spiedigitallibrary.org/ebooks/ on 09 Mar 2022
Terms of Use: https://www.spiedigitallibrary.org/terms-of-use

3A.3.8 Controls

Droplet steering

A droplet generator steering system (DGSS) can use two-stage actuation and metrology feedback to maintain alignment of the stream of tin droplets generated by the droplet generator through the primary focus of the EUV source collector. Large-scale motion can be achieved with servo-motors, while piezo-technology is used in series to create fast and precise motions.

Three components can be used for positional feedback to the steering system control loop, e.g., a line laser module, a fine-droplet steering camera, and a coarse-droplet steering camera. The purpose of the line laser module is to illuminate the droplets so that they are visible to both cameras. The coarse-droplet steering camera provides the zoomed-out view of the droplet needed for initial position feedback toward the primary focus, while the fine-droplet steering camera provides more-precise and higher-rate feedback for the fine motion of the piezo-stage steering the droplet generator. Using this combination of motion, control algorithms, and metrology feedback, the DGSS ensures that the droplet generator can be steered quickly and accurately, in turn, ensuring optimized EUV performance.

In order to minimize the risk of hitting the collector or other structures in the source vessel during startup, the droplet generator may, e.g., be purposely steered away from the collector during droplet generator pressurization and (because droplets are produced rapidly) be readjusted to make the droplet stream pass back to the collector focal point.

Laser-to-droplet timing

The source CO_2 timing controller is responsible for specifying the delay time from a droplet detection event to the firing of the pre-pulse (PP) and main pulse (MP) lasers, as shown in Fig. 3A.51. The source contains metrology that allows it to detect when a droplet passes a defined location in space, nominally a few

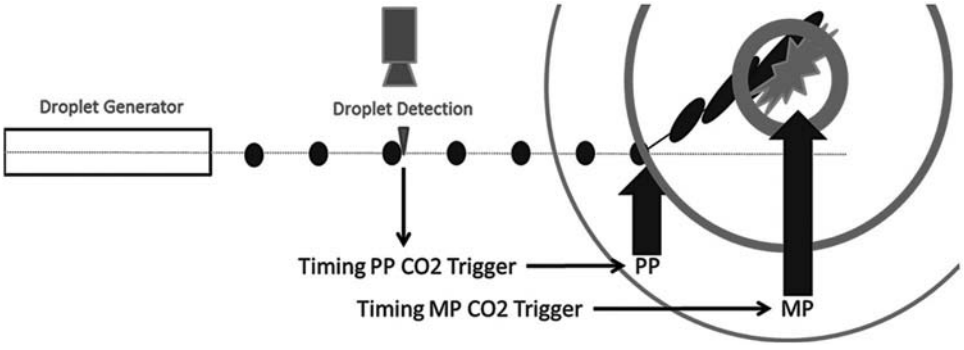

Figure 3A.51 Illustration of laser-to-droplet targeting dynamics.

Downloaded From: https://www.spiedigitallibrary.org/ebooks/ on 09 Mar 2022
Terms of Use: https://www.spiedigitallibrary.org/terms-of-use

millimeters from where the plasma is to be created. Critical to this metrology is its ability to not be blinded by preceding plasma events (false triggers).

Laser-to-droplet targeting

The source CO_2 position controller is responsible for steering the CO_2 pre-pulse and main pulse lasers to intersect the droplet position. The source may contain metrology that allows it to detect pointing errors in the forward-going CO_2 beam as well as errors detected from the intersection with the droplet position from the reflected return beam.

EUV dose control

In order to generate uniform field exposures, it is important that every point on the field see the same total integrated EUV energy. The best way to do this is to generate 100% stable EUV pulses of the desired energy given the photoresist sensitivity and scan speed. Unfortunately, the current state-of-the-art does not always not allow that to occur. Field exposure differences are caused by CO_2 pulse-to-pulse energy variations, droplet velocity differences, and CO_2-to-droplet alignment variations. A technique called pulse count modulation (PCM) can be used to address these variations. The control mechanism is then a modulation of the firing time of the drive laser so that the droplet is either inside or outside the beam path. This works throughout an exposure because the scanner moves the wafer beneath the illuminating slit until the entire die has been illuminated. Every point on an exposure field is exposed to EUV light for an amount of time equal to the time required to move that point through the slit, which can be as short as 5 ms (or 250 shots). The amount of EUV light received by each point on the field is given by a (weighted) moving average of the pulse-to-pulse EUV energy, also known as the dose. Thus, PCM is able to regulate the average EUV energy during wafer exposure so that every die on the wafer is exposed with the same amount of EUV energy. This technique requires that the source be capable of generating an average EUV energy per pulse larger than the desired target energy by 20–30%. This energy overhead is required so that all packets can achieve their average energy target. Pulse count modulation is capable of generating a stable EUV dose on the order of 0.2%.[16]

3A.4 Summary and Future Outlook

With scalability to meet requirements of ASML scanners, laser-produced plasma sources have been shown to be the leading technology and provide a path toward the higher power needed by lithography tools as they evolve over their life cycle. Five NXE:3100, eight NXE:3300B, four NXE:3350B, and two NXE:3400B BLPP sources have been used by leading-edge chipmaker R&D sites around the world, accumulating the necessary knowledge and know-how

Downloaded From: https://www.spiedigitallibrary.org/ebooks/ on 09 Mar 2022
Terms of Use: https://www.spiedigitallibrary.org/terms-of-use

to eventually move into the HVM environment. MOPA pre-pulse technology has been validated as the path to higher power output, and stabilized power of 250 W at intermediate focus has been demonstrated, using advanced control technology to meet the dose stability target of $<\pm 0.5\%$ 3σ with reduced dose margin. Normal-incidence collector mirrors with >5-sr light collection and high average reflectivity are being produced in volume and are showing increasingly long lifetimes in the field. Enhanced collector protection and *in situ* cleaning technologies are both expected to further increase lifetime. Several more NXE:3400B sources are currently being built and are planned to be shipped to customers in 2017.

References

1. R. Peeters, S. Lok, E. van Alphen, N. Harned, P. Kuerz, M. Lowisch, H. Meijer, D. Ockwell, E. van Setten, G. Schifflers, J.-W. van der Horst, J. Stoeldraijer, R. Kazinczi, R. Droste, H. Meiling, and R. Kool, "ASML's NXE platform performance and volume introduction," *Proc. SPIE* **8679**, 86791F (2013) [doi: 10.1117/12.2010932].
2. D. C. Brandt, I. V. Fomenkov, A. I. Ershov, W. N. Partlo, D. W. Myers, N. R. Böwering, N. R. Farrar, G. O. Vaschenko, O. V. Khodykin, A. N. Bykanov, J. R. Hoffman, C. P. Chrobak, S. N. Srivastava, I. Ahmad, C. Rajyaguru, D. J. Golich, D. A. Vidusek, S. De Dea, and R. R. Hou, "LPP source system development for HVM," *Proc. SPIE* **7271**, 727103 (2009) [doi: 10.1117/12.814228].
3. I. V. Fomenkov, D. C. Brandt, A. N. Bykanov, A. I. Ershov, W. N. Partlo, D. W. Myers, N. R. Böwering, N. R. Farrar, G. O. Vaschenko, O. V. Khodykin, J. R. Hoffman, C. P. Chrobak, S. N. Srivastava, D. J. Golich, D. A. Vidusek, S. De Dea, and R. R. Hou, "Laser-produced plasma light source for EUVL," *Proc. SPIE* **7271**, 727138 (2009) [doi: 10.1117/12.814272].
4. N. R. Böwering, I. V. Fomenkov, D. C. Brandt, A. N. Bykanov, A. I. Ershov, W. N. Partlo, D. W. Myers, N. R. Farrar, G. O. Vaschenko, O. V. Khodykin, J. R. Hoffman, C. P. Chrobak, S. N. Srivastava, I. Ahmad, C. Rajyaguru, J. D. Golich, D. A. Vidusek, S. De Dea, and R. R. Hou, "Performance results of laser-produced plasma test and prototype light sources for EUV lithography," *J. Micro/Nanolith. MEMS MOEMS* **8**(4), 041504 (2009) [doi: 10.1117/12.1.3224942].
5. D. C. Brandt, I. V. Fomenkov, A. I. Ershov, W. N. Partlo, D. W. Myers, R. L. Sandstrom, B. M. La Fontaine, M. J. Lercel, A. N. Bykanov, N. R. Böwering, G. O. Vaschenko, O. V. Khodykin, S. N. Srivastava, I. Ahmad, C. Rajyaguru, P. Das, V. B. Fleurov, K. Zhang, D. J. Golich, S. De Dea, R. R. Hou, W. J. Dunstan, C. J. Wittak, P. Baumgart, T. Ishihara, R. D. Simmons, R. N. Jacques, and R. A. Bergstedt, "LPP

Downloaded From: https://www.spiedigitallibrary.org/ebooks/ on 09 Mar 2022
Terms of Use: https://www.spiedigitallibrary.org/terms-of-use

source system for HVM," *Proc. SPIE* **7969**, 79691H (2011) [doi: 10.1117/12.882208].
6. D. C. Brandt, I. V. Fomenkov, M. J. Lercel, B. M. La Fontaine, D. W. Myers, D. J. Brown, A. I. Ershov, R. L. Sandstrom, A. N. Bykanov, G. O. Vaschenko, N. R. Böwering, P. Das, V. B. Fleurov, K. Zhang, S. N. Srivastava, I. Ahmad, C. Rajyaguru, S. De Dea, W. J. Dunstan, P. Baumgart, T. Ishihara, R. D. Simmons, R. N. Jacques, R. A. Bergstedt, P. I. Porshnev, C. J. Wittak, M. R. Woolston, R. J. Rafac, J. Grava, A. A. Schafgans, and Y. Tao, "Laser produced plasma EUV sources for device development and HVM," *Proc. SPIE* **8322**, 83221I (2012) [doi: 10.1117/12.916521].
7. I. V. Fomenkov, N. R. Böwering, D. C. Brandt, D. J. Brown, A. N. Bykanov, A. I. Ershov, B. La Fontaine, M. J. Lercel, and D. W. Myers, "Laser produced plasma light source development for HVM," *Proc. SPIE* **8322**, 83222N (2012) [doi: 10.1117/12.2048195].
8. T. Feigl, S. Yulin, M. Perske, H. Pauer, M. Schürmann, N. Kaiser, N. R. Böwering, O. V. Khodykin, I. V. Fomenkov, and D. C. Brandt, "Enhanced reflectivity and stability of high-temperature LPP collector mirrors," *Proc. SPIE* **7077**, 70771W (2008) [doi: 10.1117/12.802322].
9. I. V. Fomenkov, B. A. M. Hansson, N. R. Böwering, A. I. Ershov, W. N. Partlo, V. B. Fleurov, O. V. Khodykin, A. N. Bykanov, C. L. Rettig, J. R. Hoffman, E. L. Vargas, J. A. Chavez, W. F. Marx, and D. C. Brandt, "High-power low cost drive laser for LPP source," *Proc. SPIE* **6151**, 61513X (2006) [doi: 10.1117/12.655733].
10. I. V. Fomenkov, D. C. Brandt, A. N. Bykanov, A. I. Ershov, W. N. Partlo, D. W. Myers, N. R. Böwering, G. O. Vaschenko, O. V. Khodykin, J. R. Hoffman, E. L. Vargas, R. D. Simmons, J. A. Chavez, and C. P. Chrobak, "Laser-produced plasma source system development," *Proc. SPIE* **6517**, 65173J (2007) [doi: 10.1117/12.713454].
11. I. V. Fomenkov, A. I. Ershov, W. N. Partlo, D. W. Myers, D. Brown, R. L. Sandstrom, B. M. La Fontaine, A. N. Bykanov, G. O. Vaschenko, O. V. Khodykin, N. R. Böwering, P. Das, V. B. Fleurov, K. Zhang, S. N. Srivastava, I. Ahmad, C. Rajyaguru, S. De Dea, R. R. Hou, W. J. Dunstan, P. Baumgart, T. Ishihara, R. D. Simmons, R. N. Jacques, R. A. Bergstedt, and D. C. Brandt, "Laser produced plasma light source for EUVL," *Proc. SPIE* **7969**, 796933 (2011) [doi: 10.1117/12.882210].
12. D. A. Tichenor, G. D. Kubiak, W. C. Replogle, L. E. Klebanoff, J. B. Wronosky, L. C. Hale, H. N. Chapman, J. S. Taylor, J. A. Folta, C. Montcalm, and R. M. Hudyma, "EUV engineering test stand," *Proc. SPIE* **3997**, 48 (2000) [doi: 10.1117/12.390083].
13. M. Lercel, "EUV for affordable volume production," presented at SEMICON West 2017, San Francisco, California.

Downloaded From: https://www.spiedigitallibrary.org/ebooks/ on 09 Mar 2022
Terms of Use: https://www.spiedigitallibrary.org/terms-of-use

14. P. J. Silverman, "Insertion of EUVL into high-volume manufacturing," *Proc. SPIE* **4343**, 12–18 (2001) [doi: 10.1117/12.436631].
15. V. Bakshi, ed., *EUV Sources for Lithography*, SPIE Press, Bellingham, Washington (2006) [doi: 10.1117/3.613774].
16. I. V. Fomenkov, D. C. Brandt, N. R. Farrar, B. La Fontaine, D. W. Myers, D. J. Brown, A. I. Ershov, N. R. Bowering, D. J. Riggs, R. J. Rafac, S. De Dea, M. Purvis, R. Peeters, H. Meiling, N. Harned, D. Smith, R. Kazinczi, and A. Pirati, "Laser produced plasma light source for HVM," *Proc. SPIE* **9048**, 904835 (2014) [doi: 10.1117/12.2048195].
17. H. Mizoguchi, H. Nakarai, T. Abe, K. M. Nowak, Y. Kawasuji, H. Tanaka, Y. Watanabe, T. Hori, T. Kodama, Y. Shiraishi, T. Yanagida, T. Yamada, T. Yamazaki, S. Okazaki, and T. Saitou, "Performance of new high-power HVM LPP-EUV source," *Proc. SPIE* **9776**, 97760J (2016) [doi: 10.1117/12.2218405].
18. J. M. Algots, O. Hemberg, and A. Bykanov, "Liquid metal micro-droplet generator for laser produced plasma target delivery used in an extreme ultra-violet source," *Proc. SPIE* **5751** (2005) [doi: 10.1117/12.601045].
19. D. Brouns, A. Bendiksen, P. Broman, E. Casimiri, P. Colsters, P. Delmastro, D. de Graaf, P. Janssen, M. van de Kerkhof, R. Kramer, M. Kruizinga, H. Kunzel, F. van der Meulen, D. Ockwell, M. Peter, D. Smith, B. Verbrugge, D. van de Weg, J. Wiley, N. Wojewoda, C. Zoldesi, and P. van Zwol, "NXE pellicle: offering an EUV pellicle solution to the industry," *Proc. SPIE* **9776**, 97761Y (2016) [doi: 10.1117/12.2221909].
20. R. Burdt, T. Duffey, J. Thornes, T. Bibby, R. Rokitsky, E. Mason, J. Melchior, T. Aggarwal, D. Haran, J. Wang, G. Rechtsteiner, M. Haviland, and D. Brown, "Flexible power 90W to 120W ArF immersion light source for future semiconductor lithography," *Proc. SPIE* **9052**, 90522K (2014) [doi: 10.1117/12.2048082].
21. H. J. Levinson, Ed., *Principles of Lithography*, Third Edition, SPIE Press, Bellingham, Washington (2011) [doi: 10.1117/3.865363].
22. C. Hertzler and R. Wollermann-Windgasse, "High-power CO_2-lasers above 10 kW," *Proc. SPIE* **2206** (1994) [doi: 10.1117/12.184579].
23. Y. Tanino, J. Nishimae, T. Yamamoto, T. Tamida, K. Funaoka, and S. Fujikawa, "Highly efficient high-power polsed CO_2 laser characterized by transverse-flow laser amplifiers," *Proc. SPIE* **9048**, 90480E (2014) [doi: 10.1117/12.2045566].
24. J. W. Strutt, Lord Rayleigh, "On the instability of jets," *Proc. London Math. Society* **10**, 4–13 (1878).
25. J. M. Schneider and C. D. Hendricks, "Source of uniform-sized liquid droplets," *Rev. Sci. Instrum.* **35**(10), 1349–1350 (1964).
26. R. G. Sweet, "High frequency recording with electrostatically deflected ink jets," *Rev. Sci. Instrum.* **36**(2), 131–136 (1965).

Downloaded From: https://www.spiedigitallibrary.org/ebooks/ on 09 Mar 2022
Terms of Use: https://www.spiedigitallibrary.org/terms-of-use

27. G. L. Fillmore, W. L. Buehner, and D. L. West, "Drop charging and deflection in an electrostatic ink jet printer," *IBM J. Res. Dev.* **1**, 37–47 (1972).
28. A. Endo, T. Abe, H. Hoshino, Y. Ueno, M. Nakano, T. Asayama, H. Komori, G. Soumagne, H. Mizoguchi, A. Sumitani, and K. Toyoda, "CO_2 laser-produced Sn plasma as the solution for high-volume manufacturing EUV lithography," *Proc. SPIE* **6703**, 670309 (2007) [doi: 10.1117/12.732254].
29. J. van Schoot, K. Troost, F. Bornebroek, R. van Ballegoij, S. Lok, P. Krabbendam, J. Stoeldraijer, E. Loopstra, J. Benschop, J. Finders, H. Meiling, E. van Setten, B. Kneer, P. Kuerz, W. Kaiser, T. Heil, S. Migura, and J. T. Neumann, "High-NA EUV lithography enabling Moore's law in the next decade," *Proc. SPIE* **10450**, 104500U (2017) [doi: 10.1117/12.2280592].
30. S. Schröder, M. Trost, T. Feigl, J. E. Harvey, and A. Duparré, "Efficient specification and characterization of surface roughness for extreme ultraviolet optics," *Proc. SPIE* **7969**, 79692C (2011) [doi: 10.1117/12.89120]
31. I. Fomenkov, D. Brandt, D. Brown, D. Evans, A. Ershov, D. Riggs, R. Rafac, A. LaForge, J. Stewart, D. Myers, M. Purvis, M. Vargas, S. De Dea, K. Hoffman, A. Schafgans, Y. Tao, G. Vaschenko, S. Rokitski, and A. Pirati, *2015 Proc. EUVL Symposium*, October 2015, Maastricht, The Netherlands, euvlsymposium.lbl.gov/pdf/2015.
32. M. Orme and E. P. Muntz, "New technique for producing highly uniform droplet streams over an extended range of disturbance wavenumbers," *Rev. Sci. Instrum.* **58**(2), 279–284 (1987).
33. M. Orme and E. P. Muntz, "The manipulation of capillary stream breakup using amplitude-modulated disturbances: A pictorial and quantitative representation," *Physics of Fluids A: Fluid Dynamics (1989–1993)*, **2**(7), 1124–1140 (1990).
34. G. O. Vaschenko, "Laser produced plasma EUV light source," U.S. Patent No. 8,530,871, 10 Sep. 2013.
35. I. Fomenkov, B. La Fontaine, D. Brown, I. Ahmad, P. Baumgart, N. Bowering, D. Brandt, A. Bykanov, S. De Dea, A. Ershov, N. Farrar, D. Golich, M. Lercel, D. Myers, C. Rajyaguru, S. Srivastava, Y. Tao, and B. Vaschenko, "Development of stable extreme-ultraviolet sources for use in lithography exposure systems," *J. Micro/Nanolith., MEMS MOEMS* **11**(2), 021110 (2012) [doi: 10.1117/1.JMM.11.2.02110].
36. B. L. Henke, E. M. Gullikson, and J. C. Davis. "X-ray interactions: photoabsorption, scattering, transmission, and reflection at E = 50-30000 eV, Z = 1-92," *Atomic Data and Nuclear Data Tables* **54**(2), 181–342 (July 1993), CXRO X-ray database, LBNL, Berkeley, California.

Downloaded From: https://www.spiedigitallibrary.org/ebooks/ on 09 Mar 2022
Terms of Use: https://www.spiedigitallibrary.org/terms-of-use

37. H. Mizoguchi, H. Nakarai, T. Abe, K. M. Nowak, Y. Kawasuji, H. Tanaka, Y. Watanabe, T. Hori, T. Kodama, Y. Shiraishi, T. Yanagida, G. Soumagne, T. Yamada, T. Yamazaki, S. Okazaki, and T. Saitou, "Performance of one hundred watt HVM LPP-EUV source," *Proc. SPIE* **9422**, 94220C (2015) [doi: 10.1117/12.2086347].
38. H. Mizoguchi, T. Yamazaki, and T. Saitoh, "Development of 250W EUV light source for HVM lithography," 2016 International Workshop on EUV Lithography, Berkeley, California; H. Mizoguchi, H. Nakarai, and T. Abe, et al. "Development of 250W EUV light source for HVM lithography," *Proc. SPIE* **10097**, 1009702 (2017) [doi: 10.1117/12.2261075].
39. A. A. Schafgans, D. Brown, I. Fomenkov, R. Sandstrom, A. Ershov, G. Vaschenko, R. Rafac, M. Purvis, S. Rokitski, Y. Tao, D. Riggs, W. Dunstan, M. Graham, N. Farrar, D. Brandt, N. Bowering, A. Pirati, N. Harned, C. Wagner, H. Meiling, and R. Kool, "Performance optimization of MOPA pre-pulse LPP light source," *Proc. SPIE* **9422**, 94220B (2015) [doi: 10.1117/12.2087421].
40. D. C. Brandt, I. V. Fomenkov, N. R. Farrar, B. La Fontaine, D. W. Myers, D. J. Brown, A. I. Ershov, N. R. Bowering, D. J. Riggs, R. J. Rafac, S. De Dea, R. Peeters, H. Meiling, N. Harned, D. Smith, and A. Pirati, and R. Kazinczi, "LPP EUV source readiness for NXE 3300B," *Proc. SPIE* **9048**, 90480C (2014) [doi: 10.1117/12.2048184].
41. I. V. Fomenkov, A. I. Ershov, W. N. Partlo, D. W. Myers, R. L. Sandstrom, N. R. Bowering, G. O. Vaschenko, O. V. Khodykin, A. N. Bykanov, S. N. Srivastava, I. Ahmad, C. Rajyaguru, D. J. Golich, S. De Dea, R. R. Hou, K. M. O'Brien, W. J. Dunstan, and D. C. Brandt, "Laser-produced plasma light source for EUVL," *Proc. SPIE* **7636**, 763639 (2010) [doi: 10.1117/12.848408].
42. I. Fomenkov, "Status and outlook of LPP light sources for HVM EUVL," *Proc. 2015 International Workshop on EUV Lithography*, 15–19 June, Maui, Hawaii, p. 3 (2015).
43. D. C. Brandt, I. V. Fomenkov, A. I. Ershov, W. N. Partlo, D. W. Myers, N. R. Böwering, N. R. Farrar, G. O. Vaschenko, O. V. Khodykin, A. N. Bykanov, J. R. Hoffman, C. P. Chrobak, S. N. Srivastava, I. Ahmad, C. Rajyaguru, D. J. Golich, D. A. Vidusek, S. De Dea, and R. R. Hou, "LLP source system development for HVM," *Proc. SPIE* **7271**, 727103 (2009) [doi: 10.1117/12.814228].
44. K. Ota, Y. Watanabe, V. Banine, and H. Franken, "EUV source requirements for EUV lithography," Chapter 2 in *EUV Sources for Lithography*, V. Bakshi, Ed., SPIE Press, Bellingham, Washington, pp. 27–43 (2005) [doi: 10.1117/3.613774.ch2].
45. M. A. Purvis, A. Schafgans, D. J. W. Brown, I. Fomenkov, R. Rafac, J. Brown, Y. Tao, S. Rokitski, M. Abraham, M. Vargas, S. Rich, T. Taylor,

Downloaded From: https://www.spiedigitallibrary.org/ebooks/ on 09 Mar 2022
Terms of Use: https://www.spiedigitallibrary.org/terms-of-use

and D. Brandt, "Advancements in predictive plasma formation modeling," *Proc. SPIE* **9776**, 97760K (2016) [doi: 10.1117/12.2221991].
46. D. C. Brandt, I. V. Fomenkov, N. R. Farrar, B. La Fontaine, D. W. Myers, D. J. Brown, A. I. Ershov, R. L. Sandstrom, G. O. Vaschenko, N. R. Böwering, P. Das, V. Fleurov, K. Zhang, S. N. Srivastava, I. Ahmad, C. Rajyaguru, S. De Dea, W. J. Dunstan, P. Baumgart, T. Ishihara, R. Simmons, R. Jacques, R. Bergstedt, P. Porshnev, C. Wittak, R. Rafac, J. Grava, A. Schafgans, Y. Tao, K. Hoffman, T. Ishikawa, D. Evans, and S. Rich, "CO_2/Sn LPP EUV sources for device development and HVM, *Proc. SPIE* **8679**, 86791G (2013) [doi: 10.1117/12.2011212].
47. D. C. Brandt, I. V. Fomenkov, A. I. Ershov, W. N. Partlo, D. W. Myers, R. L. Sandstrom, N. R. Böwering, A. N. Bykanov, G. O. Vaschenko, O. V. Khodykin, S. N. Srivastava, I. Ahmad, C. Rajyaguru, D. J. Golich, S. De Dea, R. R. Hou, K. O'Brian, and W. J. Dunsten "LPP source system development for HVM," *Proc. SPIE* **7636**, 76361I (2010) [doi: 10.1117/12.848404]
48. I. V. Fomenkov "EUV Lithography: Progress in LPP source power scaling and availability," EUVL Workshop 2017, 15 June 2017, Berkeley, California.
49. I. V. Fomenkov "EUVL exposure tools for HVM: Status and outlook," EUVL Workshop 2016, 16 June 2016, Berkeley, California.
50. M. Nakano, T. Yabu, H. Someya, T. Abe, G. Soumagne, A. Endo, and A. Sumitani, "Sn droplet target development for laser produced plasma EUV light source," *Proc. SPIE* **6921**, 692140 (2008) [doi: 10.1117/12.771820].
51. I. Fomenkov, D. Brandt, A. Ershov, A. Schafgans, Y. Tao, G. Vaschenko, S. Rokitski, M. Kats, M. Vargas, M. Purvis, R. Rafac, B. La Fontaine, S. De Dea, A. LaForge, J. Stewart, S. Chang, M. Graham, D. Riggs, T. Taylor, M. Abraham, and D. Brown, "Light sources for high-volume manufacturintg EUV lithography: technology, performance, and power scaling," *Advanced Optical Technologies* **6**(3–4), 173–186 (2017).
52. M. Trost, S. Schröder, T. Feigl, A. Duparré, and A. Tünnermann, "Influence of the substrate finish and thin film roughness on the optical performance of Mo/Si multilayers," *Appl. Opt.* **50**, C148–C153 (2011).

Downloaded From: https://www.spiedigitallibrary.org/ebooks/ on 09 Mar 2022
Terms of Use: https://www.spiedigitallibrary.org/terms-of-use

Igor V. Fomenkov is an ASML Fellow in the Technology Development Group in San Diego, California. After completing a Ph.D. in physics and mathematics at Moscow Institute of Physics and Technology (MPTI) in 1986, he joined the General Physics Institute as a senior scientist, where he worked in the field of interaction of high-intensity laser radiation with matter, and diagnostics of LPP. He joined Cymer in 1992 and worked on the development of high-power, high-reliability KrF and ArF excimer lasers for DUV (at 248 nm and 193 nm) microlithography. Since 1997, he has been conducting R&D on sources for EUV lithography at 13.5 nm. His research on EUV light generation based on DPP and LPP included defining the source architecture, namely, the LPP EUV source using a high-power, high-repetition-rate CO_2 laser and tin droplets as a source target material and development of the source for HVM. He became a Cymer Fellow in 2003 and an ASML Fellow in 2014. He has authored more 50 technical papers in the field of LPP, DUV lasers, and sources for EUV lithography, and holds over 100 patents in the areas of DUV and EUV light sources.

David C. Brandt received a B.S. in mechanical engineering from California Polytechnic State University, San Luis Obispo, in 1988, and attended the graduate program in electrical engineering at Santa Clara University from 1989 to 1991. From 1989 through 1996 he managed engineering development activities of chemical vapor deposition systems for Watkins-Johnson. In 1996 he joined Cymer (now ASML). He managed the international subsidiary startups in Taiwan, Korea, and Singapore in 1997 during the production launch of DUV lithography. From 1998 through 2004, he led Cymer's Product Marketing group, where he worked with ASML, Canon, and Nikon to define new requirements of future excimer lasers for 248-nm and 193-nm lithography. In 2004, he joined the EUV Development group to lead the Product Marketing activities with lithography tool manufacturers and early adopter chipmakers. He has been the speaker/coauthor of 17 SPIE Advanced Lithography and EUVL Symposium talks on EUV source technology.

Alexander I. Ershov received his Ph.D. in physics from Moscow General Physics Institute in 1990. His areas of research include laser physics, laser materials interactions, and plasma physics. Since 1997 he has been working on developing light sources for lithography, first at Cymer, then at ASML. He holds more than 100 patents in the field of excimer lasers and EUV light sources.

Downloaded From: https://www.spiedigitallibrary.org/ebooks/ on 09 Mar 2022
Terms of Use: https://www.spiedigitallibrary.org/terms-of-use

Alexander A. Schafgans is a principal scientist at Cymer, ASML, the global leader in developing light sources used by the semiconductor industry to pattern advanced logic and memory. In his role at Cymer, Schafgans' work has focused on leading EUV power-scaling activities from 10 W through 500 W. During his Ph.D. in physics, Schafgans focused on the infrared and optical properties of correlated electron materials and graduated from University of California, San Diego in 2011.

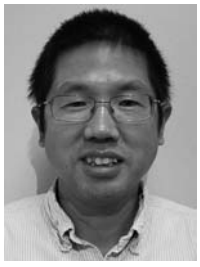

Yezheng Tao obtained his Ph.D in plasma physics from China Institute of Atomic Energy, Beijing in 2001. His previous research was in high-intensity lasers and their application in laser fusion. Since 2003, his focus has been on the laser-produced-Sn-plasma EUV source at ILE, Osaka University, Japan and University of California, San Diego. He joined ASML in 2011 and is currently a principal scientist working on an efficient, clean, and reliable EUV lithography source for high-volume production.

Georgiy O. Vaschenko received his Ph.D. in electrical engineering from Colorado State University in 2002. His research interests include ultrafast optical metrology, light-emitting semiconductor devices and materials, and EUV light technology. In 2006 he joined Cymer (now ASML) to focus on development of EUV light sources for semiconductor lithography. He is currently a Principal Scientist with ASML, working on a target delivery system for EUV sources.

Bruno La Fontaine is a SPIE Fellow. He received his Ph.D. in physics for the characterization of LPPs using Thomson scattering in 1992, from Institut National de la Recherche Scientifique and The National Research Council of Canada. He currently leads the development of a novel integrated e-beam metrology and software product (PFM), offering large improvement in throughput over traditional e-beam defect inspection techniques. Prior to his current engagement at HMI, he led the development of clean EUV sources at Cymer from 2010 to 2015. Between 2000 and 2010, he led the overall development of EUV lithography at Advanced Micro Devices and was recognized as AMD Fellow.

Downloaded From: https://www.spiedigitallibrary.org/ebooks/ on 09 Mar 2022
Terms of Use: https://www.spiedigitallibrary.org/terms-of-use

Chapter 3B
High-Power EUV Source by Gigaphoton for High-Volume Manufacturing

Hakaru Mizoguchi, Taku Yamazaki, Tatsuya Yanagida, Krzysztof M. Nowak, and Takashi Saito
Gigaphoton Inc., Kanagawa, Japan

3B.1 Introduction
3B.2 High-Power LPP EUV Light Source with Pre-pulse Technology
3B.2.1 System concept
3B.2.2 Tin droplet generation technology
3B.2.3 Pre-pulse technology and high CE operation
3B.2.4 Superconducting magnet debris mitigation method (SM3) and the collector mirror
3B.2.5 Driver CO_2 laser system
3B.3 250-W HVM LPP-EUV Source
3B.3.1 Pilot #1 system construction
3B.3.2 CE measurements and improvement
3B.3.3 Latest data of the Pilot #1 system
3B.3.4 Change of collector mirror reflectance during operation
3B.4 Conclusion and Acknowledgment
References

3B.1 Introduction

Extreme ultraviolet (EUV) light sources have been developed together with scanning exposure tools. A 10-W EUV light source tool was shipped by ASML as an α-demo tool in 2007[1] and by Nikon as EUV-1 in 2008.[2] ASML then developed a β-tool: the NXE-3100 at the beginning of 2011 with a 100-W EUV light source.[3,4] Requirements of the EUV exposure tool are now represented by the γ-tool: the NXE3300 [for high-volume manufacturing (HVM)].[5] Several machines have been already shipped since 2013. The required EUV power is 250 W of clean power [after purifying infrared (IR) and deep-ultraviolet (DUV) spectra] at intermediate focus (IF) for the current

Downloaded From: https://www.spiedigitallibrary.org/ebooks/ on 09 Mar 2022
Terms of Use: https://www.spiedigitallibrary.org/terms-of-use

generation of EUVL scanners, and this requirement is expected to rise to 500 W for the next generation of EUVL scanners.[6] The current demonstrated power level is 250 W.[7]

In this chapter, we present the latest results of EUV sources having more than 100-W EUV power, as well as the design of a 250-W EUV source produced by Gigaphoton and the progress in its development for semiconductor HVM.

3B.2. High-Power LPP EUV Light Source with Pre-pulse Technology

3B.2.1 System concept

Since 2002, Gigaphoton has been developing the carbon dioxide (CO_2) laser-produced tin (Sn) plasma (CO_2-Sn-LPP) EUV light source, which is the most promising solution to a 13.5-nm high-power (>200 W) light source for HVM EUV lithography (EUVL). We have chosen the CO_2-Sn-LPP method because of its high conversion efficiency, high power scalability, and its spatial freedom around the plasma. We have proposed three unique, original technologies: (1) pre-pulse technology, (2) magnetic debris mitigation technology, and (3) high-efficiency CO_2 laser technology.[8,9] Theoretical[10] and experimental[11] data clearly demonstrate the advantage of the combination of a CO_2 laser and a Sn plasma in order to realize high conversion efficiency (CE) from the drive laser.

The conceptual layout of Gigaphoton's HVM EUV light source is shown in Fig. 3B.1, and the process of the Sn debris mitigation with the magnetic field is shown in Fig. 3B.2. First, the Sn droplet target is irradiated with the pre-pulse laser, and the Sn droplet is crushed into a submicron mist that expands over time. Secondly, after a certain time delay, the expanded mist cloud is heated by the pulsed CO_2 laser beam; i.e., the cloud is converted to a high-temperature plasma with highly excited Sn ions (ions with a highly charged state). During the recombination processes, the Sn plasma emits 13.5-nm EUV light. Most of the Sn ions can be trapped by the magnetic field via Larmor movement and be guided away. Plasma residues after EUV light emission are eventually scattered inside the vessel and are removed from the collector by gas etching. To enhance the EUV energy and to maximize the Sn debris mitigation, the number of Sn ions generated during the laser heating process should be maximized.

3B.2.2 Tin droplet generation technology

The generation of small Sn droplets is essential to Sn debris mitigation; i.e., the mass of the Sn droplet should be minimized for generating a given number of EUV photons. The liquid Sn droplets are generated by the droplet generator (DLG), and the droplet diameter is around 20 μm. The Sn supply tank is heated above the melting temperature of Sn (>231.93 °C). Photographs of droplet generation with 60 m/s (at 100 kHz), 90 m/s (at 100 kHz), and 90 m/s (at 50 kHz) are shown in Fig. 3B.3.

Downloaded From: https://www.spiedigitallibrary.org/ebooks/ on 09 Mar 2022
Terms of Use: https://www.spiedigitallibrary.org/terms-of-use

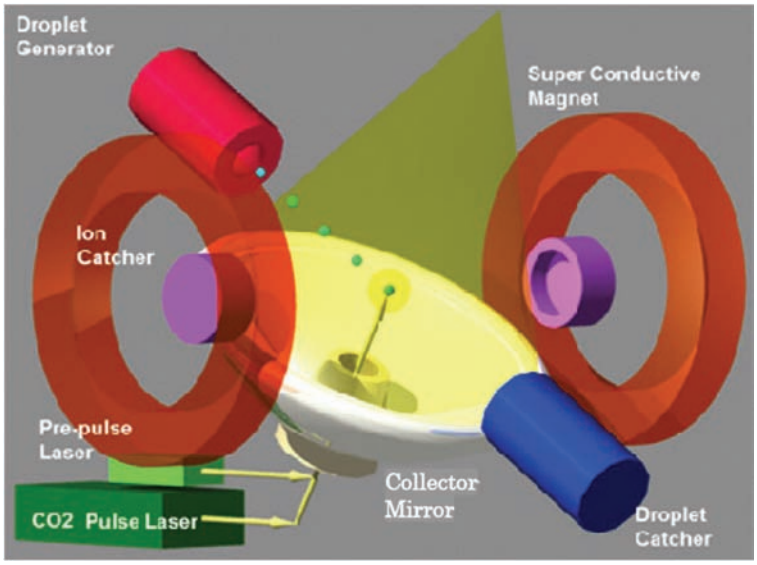

Figure 3B.1 The concept of the Gigaphoton HVM EUV light source (source: Gigaphoton Inc.).

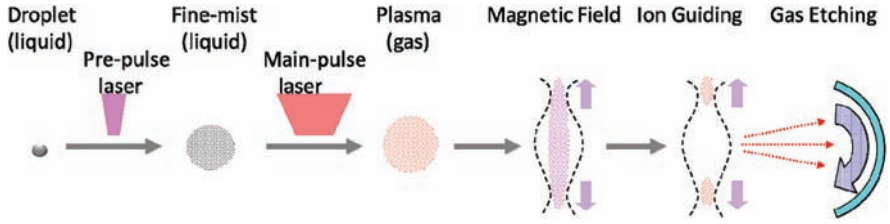

Figure 3B.2 EUV emission and Sn mitigation process concept (source: Gigaphoton Inc.).

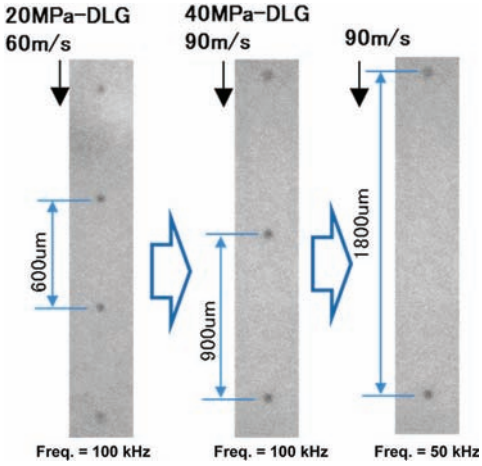

Figure 3B.3 Droplet generator (DLG) (source: Gigaphoton Inc.).

Downloaded From: https://www.spiedigitallibrary.org/ebooks/ on 09 Mar 2022
Terms of Use: https://www.spiedigitallibrary.org/terms-of-use

The long-term positional stability of the droplets guarantees long-term EUV power stability at IF. The droplet position is measured by a CCD camera, and its value is fed back to the DLG stage. This is one of the key steps because the droplet position determines the EUV source position. In addition, the pre-pulse laser and the CO_2 laser shooting positions are monitored in order to obtain a stable CE, a stable EUV source position, and stable debris mitigation, which are all essential for industrial usage. Figure 3B.4 is a schematic of the droplet position sensing and control system, and the pre-pulse laser and CO_2 laser position control system, which stabilize the plasma position and the EUV pulse energy, respectively.

3B.2.3 Pre-pulse technology and high-CE operation

A pre-pulse laser, which irradiates the Sn droplet before the CO_2 laser, plays an important role in LPP EUV generation. The CE of EUV emission is improved by forming an optimum target distribution with a pre-pulse laser, especially with a picosecond solid-state laser (SSL). In 2011, Yanagida et al. reported a CE of 4.7% with a 20-μm diameter droplet, which has been demonstrated by optimizing the pre-pulse laser conditions, as shown in Fig. 3B.5 (top curve with squares), with a small experimental device.[12] Different droplet expansion mechanisms for nanosecond and picosecond pre-pulses explain the major difference in CE. In addition, CE is almost constant with heating CO_2 laser energy. These basic studies have contributed to the development of the high-power production machine and to the basic design for further EUV power scaling together with theoretical calculations. This high-CE technology enables a 250-W EUV source with a 20-kW CO_2 laser.

CE can be improved by expanding the droplet target with a pre-pulse laser. The primary reason for the improvement is an increased overlapping

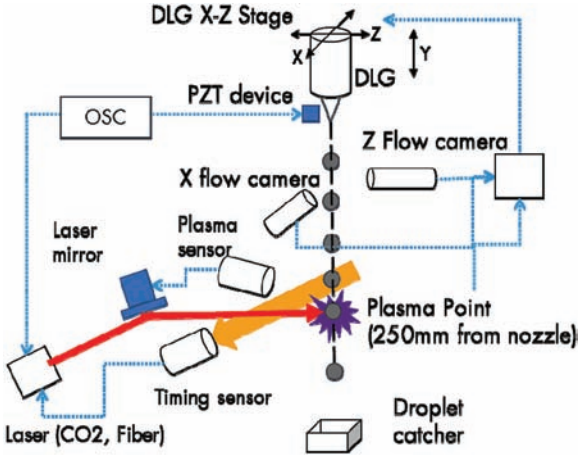

Figure 3B.4 Schematic of the DLG system (source: Gigaphoton Inc.).

Downloaded From: https://www.spiedigitallibrary.org/ebooks/ on 09 Mar 2022
Terms of Use: https://www.spiedigitallibrary.org/terms-of-use

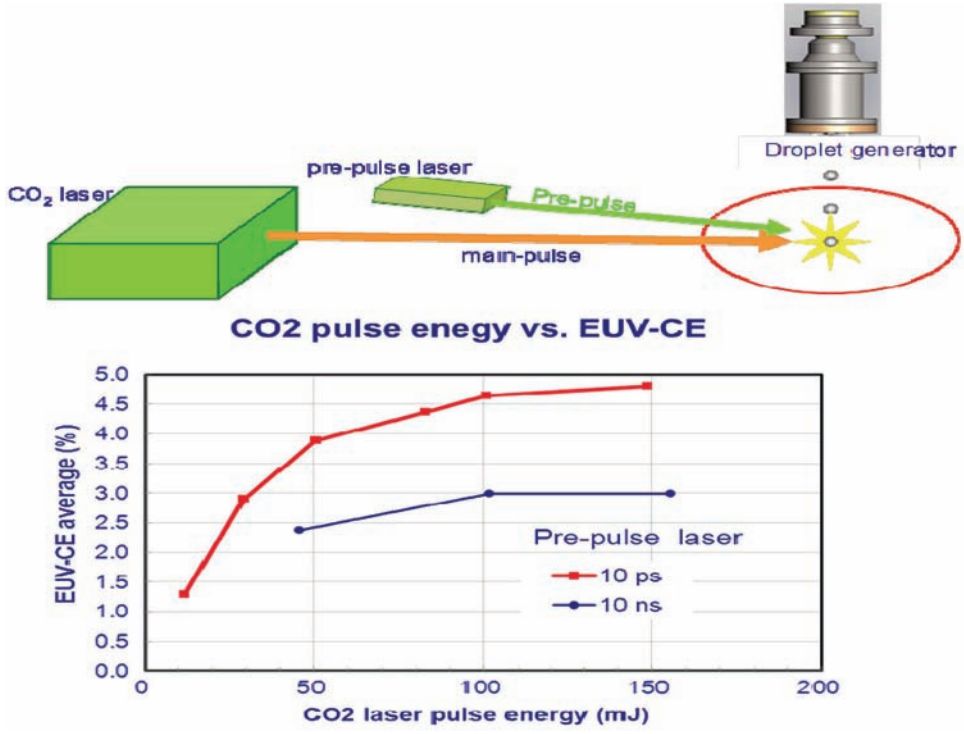

Figure 3B.5 (Top) Schematic of the experimental device used to optimize the pre-pulse laser conditions and (bottom) CE versus CO_2 laser energy (source: Gigaphoton Inc.).

area between the target and the CO_2 laser beam. The beam diameter of the CO_2 laser at the target position is generally a few hundreds of microns. The overlap ratio against a 20-μm droplet is too small. Therefore, a large amount of the laser energy passes the target without interaction. Another reason for the improvement is the reduction of target density by expansion. It is known that the optimum ion density of a Sn plasma for highly efficient 13.5-nm EUV emission is around 10^{17} to 10^{19} cm^{-3}.[13] Based on a simple estimation, an initial target should be expanded to a few hundreds of microns in diameter in order to provide such a low density target. A SSL, which typically has a wavelength of 1 μm, is suitable for a pre-pulse laser. Since a SSL has excellent spatial beam quality, it is easy to focus the beam to the range of the droplet diameter. The ideal spatial profile with high positional stability leads to highly stable droplet–laser interaction. Furthermore, a SSL can generate an ultrashort pulse without technical difficulty because of its inherent broad spectrum. Gigaphoton employs a SSL with a picosecond pulse width as a pre-pulse laser, achieving a maximum CE. 100-W average EUV power has been demonstrated with a CE of 5% in the pilot source at Gigaphoton. A CE of 5.5% has been recorded from a low-repetition-rate experimental apparatus (Fig. 3B.6).[14]

Downloaded From: https://www.spiedigitallibrary.org/ebooks/ on 09 Mar 2022
Terms of Use: https://www.spiedigitallibrary.org/terms-of-use

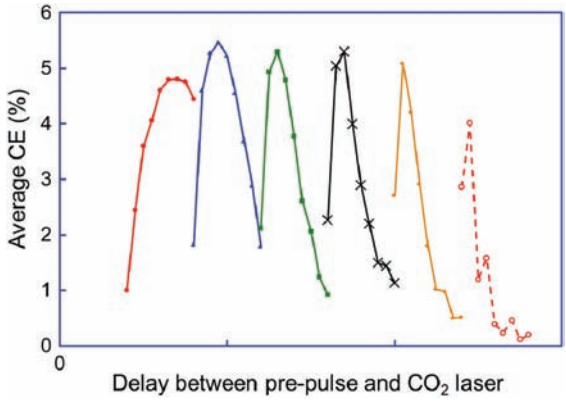

Figure 3B.6 CE of 5.5% has been recorded from Gigaphoton's experimental apparatus (source: Gigaphoton Inc.).

A distinctive target distribution was formed by picosecond pre-pulse laser irradiation. Figure 3B.7 shows shadowgraphs of target distributions after irradiation with pre-pulse lasers of different pulse widths. A disk shape is formed with a nanosecond pre-pulse laser. The diameter of the target is sufficiently large. However, the target still has a high density. The CE for the disk target is limited to 3–4%. In the case of the picosecond pre-pulse, a more isotropic distribution—like a dome—is observed. The density of the dome

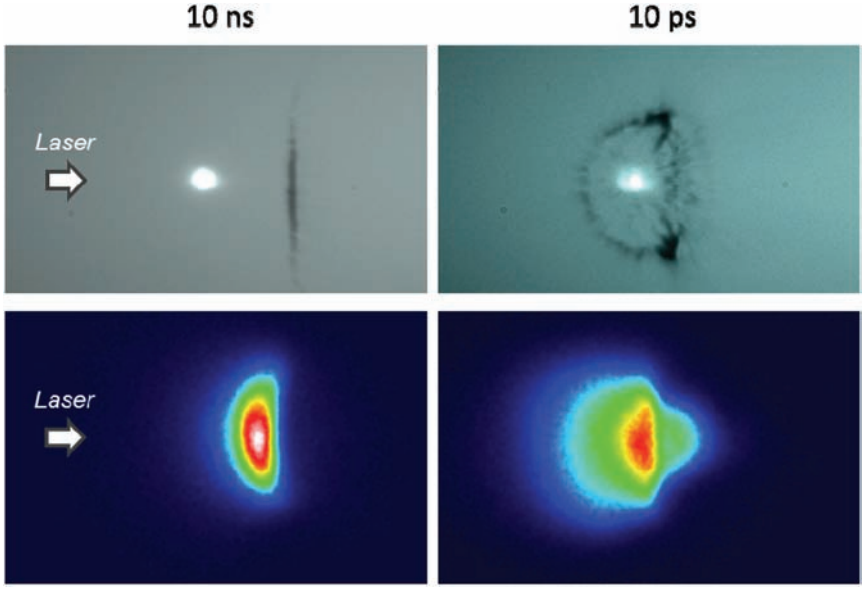

Figure 3B.7 (Top) Shadowgraphs of targets after pre-pulse irradiation with 10-ns pulse width and 10-ps pulse width. (Bottom) EUV emission after interaction with the main pulse (source: Gigaphoton Inc.).

Downloaded From: https://www.spiedigitallibrary.org/ebooks/ on 09 Mar 2022
Terms of Use: https://www.spiedigitallibrary.org/terms-of-use

target is almost certainly low compared to the disk target. This clear difference between the target distributions due to the difference in pulse width has been theoretically well explained by radiation hydrodynamics simulation.[15]

The dome target enables large-volume EUV emission because of its optimum density profile. EUV emission images for the disk and the dome targets are shown at the bottom of Fig. 3B.7. The emission profiles reflect the original target distributions well. In the dome target, the EUV emission volume increased along the laser axis compared to that in the disk target; thus, the CE improved. The plasma parameter profiles (such as electron density, electron temperature, and ion average charge state) on the laser axis during CO_2 laser irradiation were measured for the dome target with collective Thomson scattering (Fig. 3B.8).[16–18] The electron density of the EUV emission area was on the order of 10^{18} cm^{-3} with a gentle gradient. The area was heated to more than 25 eV, which was suitable for EUV emission, over the whole range. We believe that the target distribution with the gentle density gradient enabled efficient laser absorption and large-volume EUV emission.

3B.2.4 Superconducting magnet debris mitigation method (SM3) and the collector mirror

Our Sn debris mitigation concept using the magnetic field is simple. As EUV light is emitted from the Sn plasma, which is mainly composed of Sn ions and

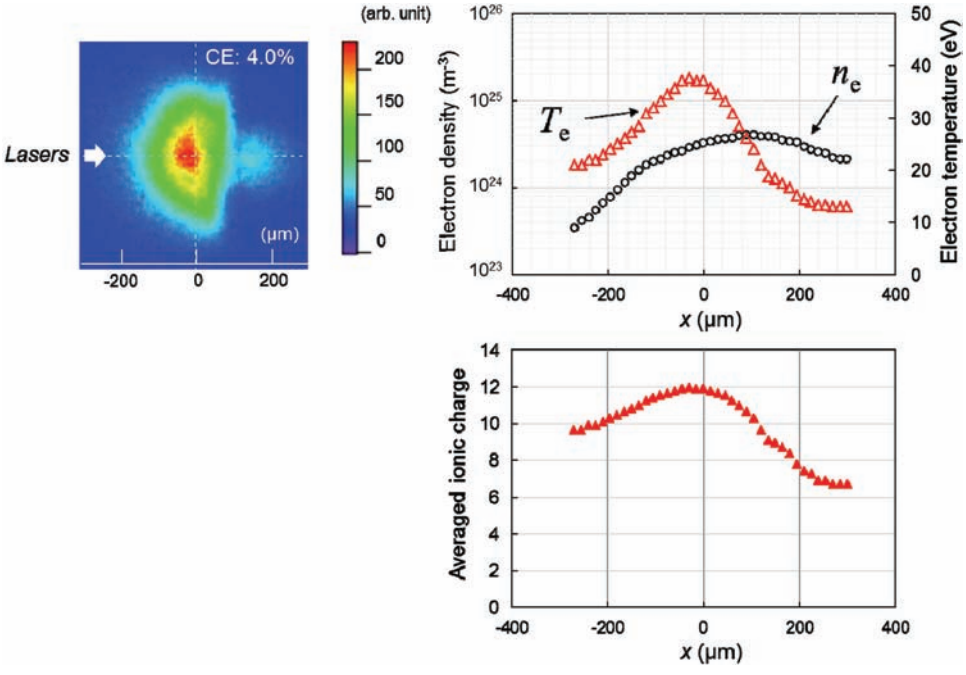

Figure 3B.8 Plasma profiles measured with collective Thomson scattering (source: Gigaphoton Inc.).

Downloaded From: https://www.spiedigitallibrary.org/ebooks/ on 09 Mar 2022
Terms of Use: https://www.spiedigitallibrary.org/terms-of-use

electrons, almost all of the Sn ions can be trapped in the strong magnetic field. Also, some neutral atoms can be guided and trapped by charge exchange with ions. In reality, however, not all of the Sn atoms and ions can be trapped in the magnetic field (Fig. 3B.9).[19] We have investigated system behavior under various conditions in order to optimize Sn debris mitigation parameters.

The picosecond pre-pulse scheme is also effective in debris mitigation. Sn debris from plasma is composed of ions, neutral atoms, and fragments with diameters of several tens of nanometers to several microns. In order to effectively trap and mitigate Sn debris by a magnetic field, the degree of Sn ionization needs to be increased. Initially, a droplet is divided into many fragments by the pre-pulse laser. These fragments are vaporized and ionized by the CO_2 laser irradiation. Especially with a picosecond pre-pulse laser, fragment sizes become smaller than those with a nanosecond pre-pulse laser. Generally, the smaller the fragments the more readily those are vaporized and ionized by a CO_2 laser irradiation. The number of fragments after CO_2 laser irradiation was measured with Mie scattering. The fragments were vaporized to a negligible level, as shown in Fig. 3B.10.

The degree of ionization of the vaporized Sn gas was measured using the laser-induced fluorescence method. It was estimated that approximately 100% of the debris was ionized in the case with a picosecond pre-pulse laser, as shown in Fig. 3B.11.[19] Therefore, most of the Sn debris from the plasma can be controlled by a magnetic field. The debris mitigation scheme with a magnetic field works ideally in combination with the picosecond pre-pulse technique.

After the EUV plasma is created, the EUV light is collected by a multilayer mirror. However, the EUV plasma emits not only EUV light, but

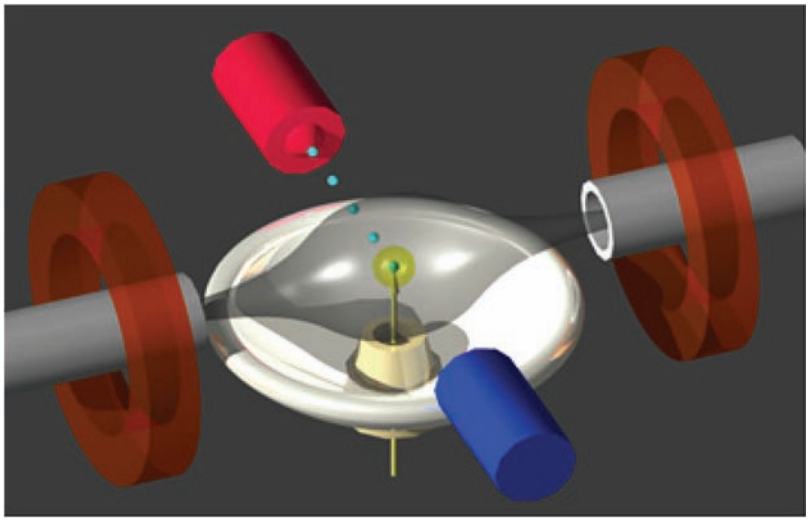

Figure 3B.9 Collector mirror and mitigation system (source: Gigaphoton Inc.).

Downloaded From: https://www.spiedigitallibrary.org/ebooks/ on 09 Mar 2022
Terms of Use: https://www.spiedigitallibrary.org/terms-of-use

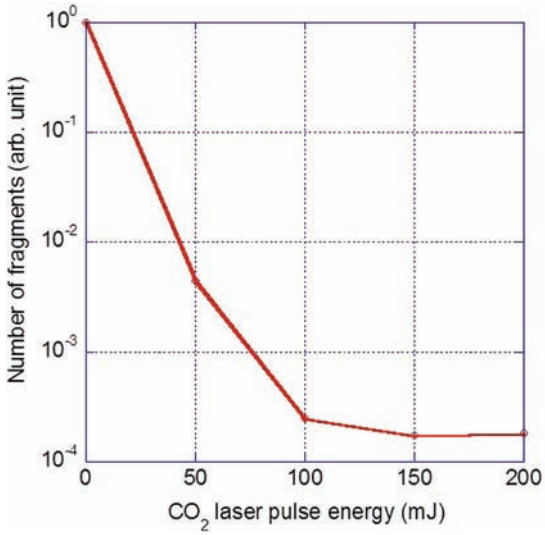

Figure 3B.10 Number of fragments after CO_2 laser irradiation (source: Gigaphoton Inc.).

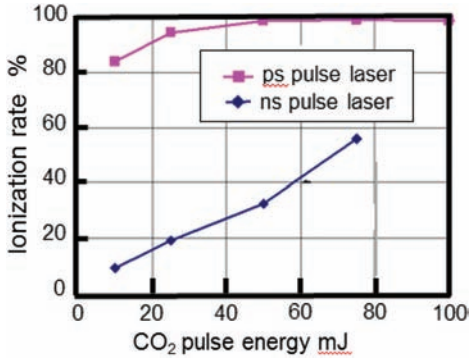

Figure 3B.11 Ionization rate of Sn from plasma after CO_2 laser irradiation (source: Gigaphoton Inc.).

also UV light, visible light, and IR light. These light components are called out-of-band (OoB) light (Fig. 3B.12). Reflected IR light from the structured multilayer generates an interference pattern at the focal plane, and only IR light is absorbed by an aperture stop. Figure 3B.13 shows the schematic of this new filter.[20]

3B.2.5 Driver CO_2 laser system

An EUV power level of 115 W at IF was initially drawn as the minimum value required to enable HVM-worthy productivity of 100 wph.[21] Once all sources of EUV photon loss located between the plasma and the IF are accounted for, the HVM productivity target requires ~500 W of EUV power

Downloaded From: https://www.spiedigitallibrary.org/ebooks/ on 09 Mar 2022
Terms of Use: https://www.spiedigitallibrary.org/terms-of-use

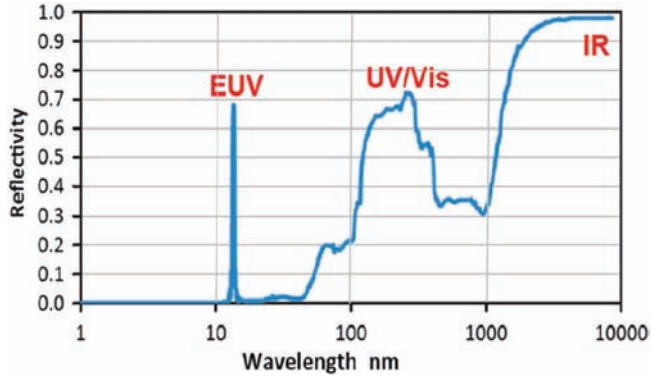

Figure 3B.12 OoB spectrum emitted from EUV plasma (source: Gigaphoton Inc.).

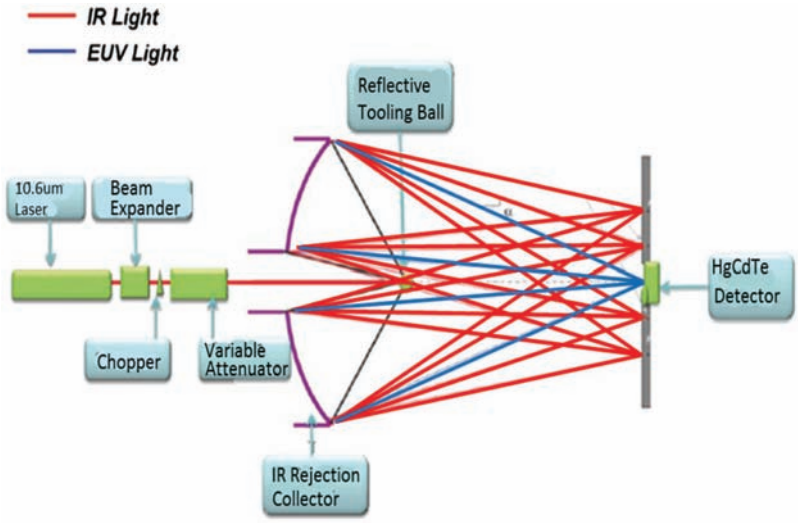

Figure 3B.13 Schematic of a new type of filter (source: Gigaphoton Inc.).

at the plasma point.[6] Such an EUV power level at plasma, in turn, requires at least 18 kW on average, with the drive-laser power delivered in stable pulses of repetition rates in excess of 50 kHz. More recent estimates indicate that >250 W at IF is needed; therefore, there is continuing pressure to develop a more powerful laser driver.[9]

Theoretical and experimental studies[22–25] have shown that the ~10-μm wavelength generated by CO_2 lasers is favorable for a LPP EUV source over the ~1-μm wavelength delivered by solid-state lasers in terms of higher CE and reduced production of debris.[26,27] An optimal timescale for energy coupling from the laser field to the plasma was found to be around 10 ns for the CO_2 lasers.[28] Traditionally, the pulsed operation was achieved either by gain switching, intracavity Q-switching, passive or active mode-locking, or

Downloaded From: https://www.spiedigitallibrary.org/ebooks/ on 09 Mar 2022
Terms of Use: https://www.spiedigitallibrary.org/terms-of-use

extracavity modulation. However, only electro-optical modulation methods provide the required pulse format and sufficient control to facilitate synchronization with the Sn droplet target. The first account of the electro-optically modulated, cavity-dumped, Q-switching technique is believed to have been reported in 1963,[29] and an application to CO_2 lasers was reported not very long after that.[30] This configuration, depicted in Fig. 3B.14, combined with cw-like RF pumping, can realize the required pulse repetition rates and a pulse duration of 10–20 ns, delivered in a relatively good temporal shape, as shown in Fig. 3B.15. This kind of master oscillator, employing a sealed-off, RF-discharge-excited, waveguide laser was used previously in LPP EUV source development.[31–33] However, the output power level was limited in this kind of master oscillator to <20 W; therefore, a post-amplification was required to reach multi-kilowatt powers, forming the configuration of a so-called master oscillator power amplifier (MOPA) system.

The simplicity of the Q-switched, cavity-dumped oscillator gives rise to a number of limitations. A small leakage of the Q-switch in the closed state manifests as a so-called pedestal preceding the main pulse, visible in Fig. 3B.15. The exponential-like rising pedestal is undesired because it gets amplified preferentially and leads to an undesired pulse width broadening. The pedestal, however, can be suppressed relatively easily by another electro-optical modulator. Another issue that cannot be solved so easily is a large susceptibility to a parasitic seeding caused by a considerable level of

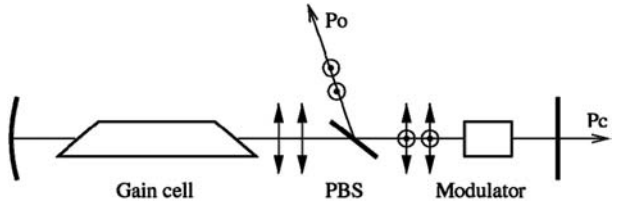

Figure 3B.14 Schematic of a conventional Q-switched, cavity-dumped, pulsed laser (adapted from Ref. 34).

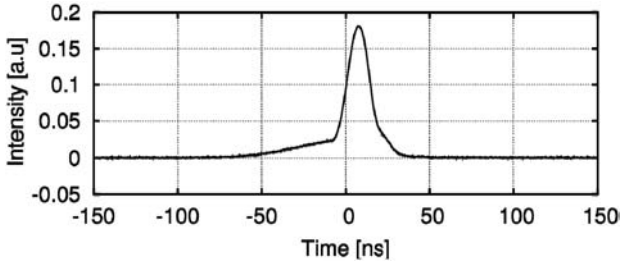

Figure 3B.15 A typical output pulse shape generated by a commercial cavity-dumped Q-switched CO_2 laser (source: Gigaphoton Inc.).

Downloaded From: https://www.spiedigitallibrary.org/ebooks/ on 09 Mar 2022
Terms of Use: https://www.spiedigitallibrary.org/terms-of-use

back-propagating, amplified spontaneous emission (ASE). This parasitic optical flux is a result of the high gain-length product of >6 of the MOPA amplifier chain employed in the LPP source. This is quite a challenge because the optical flux in such an oscillator builds from spontaneous emission power levels, and these are rather low in the case of a long (10.6 μm) wavelength, effectively much lower than micro-watts. A small amount of ASE back-propagating in the amplifier system can therefore easily injection-lock the operation of the oscillator, leading to spectral and temporal instabilities of the oscillator output. As a consequence, a large isolation factor counted in many tens of decibels is required to render the oscillator resistant to ASE, which is at least troublesome. Last but not least, a conventional Q-switched laser does not lend itself easily to a multiline operation, the benefits of which are briefly mentioned below.

The limitations of the previously described techniques were elegantly circumvented by an application of mid-IR-emitting semiconductor quantum cascade lasers (QCLs) as the seeders. QCLs emerged in the mid-1990s[35] and very quickly revolutionized the area of gas sensing and spectroscopy. Their interesting spectro-temporal output properties were investigated for the first time at Gigaphoton in 2008 from the perspective of seeding a master oscillator, resulting in an excellent match to the requirements of LPP.[36,37] The pulses generated by the QCLs were naturally down-chirped in frequency due to the electrical power dissipation in the active region and the associated detuning of the optical feedback. The magnitude of the chirp was found to closely match[36] the typical bandwidth of CO_2-medium laser lines, resulting in the possibility of a robust generation of ultra-stable pulses with adjustable durations of approximately 10–35 ns in a novel CO_2 oscillator,[38] as depicted schematically in Fig. 3B.16. Figure 3B.17 shows typical pulse shapes obtained from the oscillator shown in Fig. 3B.16 seeded with the P20 or P18 line of the regular band. These single-shot traces were obtained using a fast (<1 ns) rise-time photovoltaic sensor: PV-10.6 by VIGO S.A.

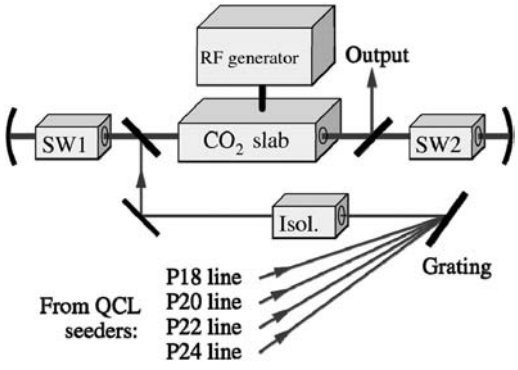

Figure 3B.16 Schematic of a novel multiline, short-pulse oscillator featuring four seed QCLs developed especially for LPP EUV application (source: Gigaphoton Inc.).

Downloaded From: https://www.spiedigitallibrary.org/ebooks/ on 09 Mar 2022
Terms of Use: https://www.spiedigitallibrary.org/terms-of-use

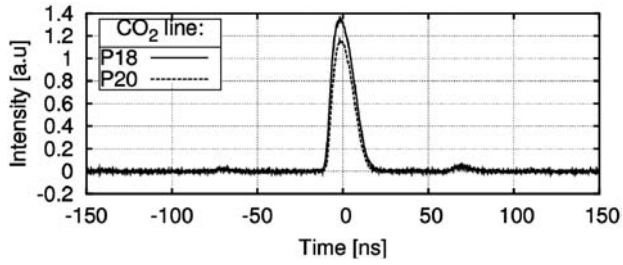

Figure 3B.17 Typical pulse shapes obtained from the oscillator shown in Fig. 3B.16 seeded with the P20 or P18 line of the regular band. These single-shot traces were obtained using a fast (<1 ns) rise-time photovoltaic sensor: PV-10.6 by VIGO S.A (source: Gigaphoton Inc.).

This oscillator was invented at Gigaphoton and built especially for the purpose of exploiting the attractive features of QCLs. The first results demonstrating the simultaneous operation on two lines (P20 and P18) of the regular band were made public in 2010,[39] and the electronic pulse envelope adjustment was reported first in 2011.[40] This technique has a number of interesting features that distinguish it from the other methods of multiline short-pulse generation mentioned earlier. The pulse duration is determined only by the chirp rate of the QCL seeder and the gain bandwidth of the laser transition addressed. The seed wavelength is determined only by the QCL chip design and its operational parameters, facilitating very precise electronic tuning. An ultra-stable pulse is a consequence of intentional suppression of the eigenmodes of the oscillator cavity. Multiple modes are almost always present in conventional designs, resulting in a modulation of the pulse envelope due to transverse or longitudinal mode beating. High resistance to ASE (>40 dB) is achieved due to the sufficiently high peak power of currently available QCLs; the multiline operation is achieved by combining multiple QCL sources. The timing and intensity of each QCL seeder pulse is individually controllable, allowing for easy online pulse duration adjustment (Fig. 3B.18),[41] as well as

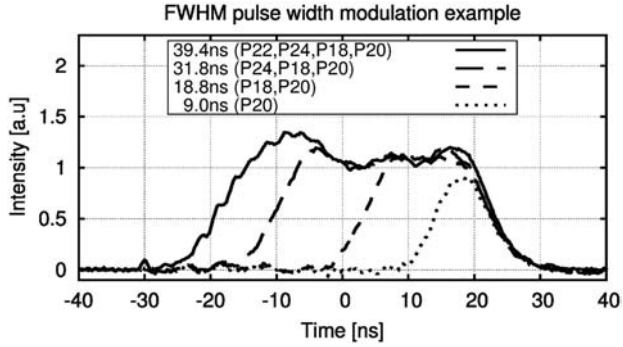

Figure 3B.18 Experimental confirmation of the electronic pulse duration adjustment capability of the QCL-seeded master oscillator (source: Gigaphoton Inc.).

Downloaded From: https://www.spiedigitallibrary.org/ebooks/ on 09 Mar 2022
Terms of Use: https://www.spiedigitallibrary.org/terms-of-use

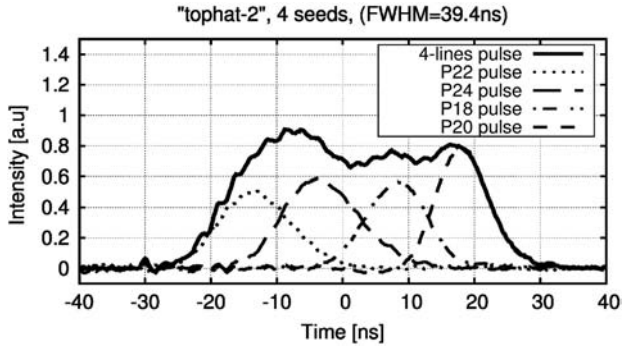

Figure 3B.19 Example of pulse waveform synthesis by means of adjustment of seed pulse timing and amplitude (source: Gigaphoton Inc.).

pulse envelope shaping and spectral line timing adjustments (Fig. 3B.19).[41] The oscillator can operate asynchronously in a wide range of pulse frequencies (0–100 kHz), facilitating synchronization with a droplet target. The output power level of this master oscillator is similar to that of a conventional Q-switched laser. Therefore, a train of two small, multipass amplifiers based on slab-waveguide laser technology has been developed to boost the power up to a level sufficient for effective driving of the power preamplifier, ~100 W. Electro-optical isolation between these components was implemented to suppress parasitic oscillations. All of the components of these oscillator systems have been internally developed by Gigaphoton and form the proprietary oscillator system.[41]

The advent of the use of a RF-discharge excitation technique in the mid-1960s[42] enabled the development of CO_2 lasers that combine improved efficiency and output power from compact packages. A new class of CO_2 lasers based on a slab-waveguide, diffusion-cooled geometry was invented as a consequence. The RF-discharge excitation technique has also supplanted the DC-discharge excitation of multi-kilowatt, fast-flow CO_2 lasers. Nowadays, these most powerful lasers exist commercially in two designs: the fast-axial-flow (FAF)[43] and the fast-transverse-flow (FTF) configurations.[43] The forced rapid flow of laser gas allows for an increased RF power input without an adverse overheating of the gas medium, resulting in higher output power levels compared to their diffusion-cooled counterpart, but at the expense of increased system complexity (blowers, heat exchangers, etc.).[44] These systems are of interest for the LPP driver because they can be utilized as power amplifiers.[33–35] A record output power of 20 kW (cw) from a small package has been achieved by Trumpf GmbH with its TruFlow FAF laser series.[43]

It is well known that the energy extraction efficiency from CO_2 media by short pulses of a duration comparable to rotational relaxation times can be as little as 30% compared to cw operation. It is also known that this situation can be mitigated to some extent[46] if the pulses contain frequencies of multiple laser

Downloaded From: https://www.spiedigitallibrary.org/ebooks/ on 09 Mar 2022
Terms of Use: https://www.spiedigitallibrary.org/terms-of-use

transitions of a rotational manifold. About 20% extraction improvement was theoretically predicted at the Institute of Laser Physics in St. Petersburg for 4-line 20-ns pulses compared to single-line amplification in commercial FAF amplifiers.[47] This seemingly small improvement can however translate into additional kilowatts of power in a >20-kW laser system; therefore, multiline operation of the master oscillator was also targeted in our application. The multi-kilowatt amplifier stages of the MOPA system require input power levels of some kilowatts for reasonably large energy extraction; therefore, pre-amplification must be implemented to maximize efficiency. A multipass amplifier arrangement is required to obtain the high power gain necessary to boost the low (<100-W) power level of the master oscillator to that required by the FAF or FTF power amplifier stages. Such arrangements with FAF amplifiers were quite impractical due to their low Fresnel number. A multipass configuration based on the largest slab-waveguide, diffusion-cooled laser available on the market was successfully developed[48] in collaboration with Rofin GmbH. However, its overall power gain was found to be somewhat insufficient, in spite of achieving record efficiencies. The FTF amplifiers, characterized by a large cross-sectional area, lent themselves to multipassing much more easily than their FAF counterparts.[45] Due to a nearly 2× larger value of the small-signal gain, the FTF configuration allowed for a simpler multipass optical arrangement and >2× more output power compared to the slab-waveguide-laser-based configuration. For these reasons, Gigaphoton started a collaboration with Mitsubishi Electric with the aim of developing FTF laser chambers for application in LPP EUV sources.

We have constructed three prototype EUV LPP systems to date, called Proto #1, Proto #2, and Pilot #1. The main difference between these systems is CO_2 laser power, while the other specifications remain practically the same. The work on Proto #1 commenced in 2011,[49] and this device served as a development platform for system technology integration and component testing. The Proto #1 system featured a CO_2 laser driver comprising Gigaphoton's master oscillator described briefly above, a slab-waveguide-laser-based preamplifier, and a chain of two FAF power amplifiers. The construction of Proto #2 started in the second half of 2013. Proto #2 benefited from the laser technology developed in co-operation with Mitsubishi Electric under the auspices and support of the New Energy and Industrial Technology Development Organization (NEDO), Japan.[50,51] This system employed a newly designed, FTF-based multipass preamplifier and a train of three FAF-based power amplifiers, as illustrated in Fig. 3B.20.

The Proto #2 system became operational in the beginning of 2014, and in 2015 we succeeded in demonstrating a reliable 20-kW output power.[52] We are currently in the process of completing the construction of the Pilot #1 system, which is intended to integrate all of the technologies developed at Gigaphoton to date.

Downloaded From: https://www.spiedigitallibrary.org/ebooks/ on 09 Mar 2022
Terms of Use: https://www.spiedigitallibrary.org/terms-of-use

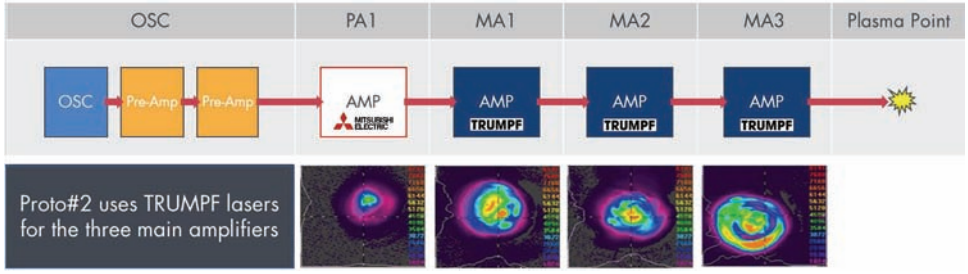

Figure 3B.20 Schematic of the 20-kW-class CO_2 laser driver system, Proto #2, and some of its output beam profiles (source: Gigaphoton Inc.).

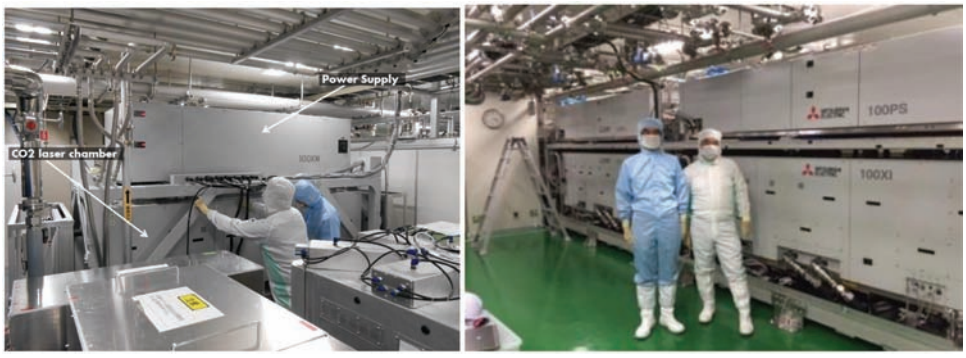

Figure 3B.21 Construction of the Pilot #1 CO_2 laser system (source: Gigaphoton Inc.).

The CO_2 laser driver, shown in Fig. 3B.21 in its early stage of assembly, is similar to that of Proto #2 with the difference that the FAF amplifiers were replaced with Mitsubishi's FTF units, as illustrated in Fig. 3B.22.[53] This system has the potential to produce more CO_2 laser power in a beam that is of higher quality than that of the Proto #2 system, allowing for the reliable production of a 250-W power target. The laser driver in this system is currently undergoing diagnostics and operation testing.

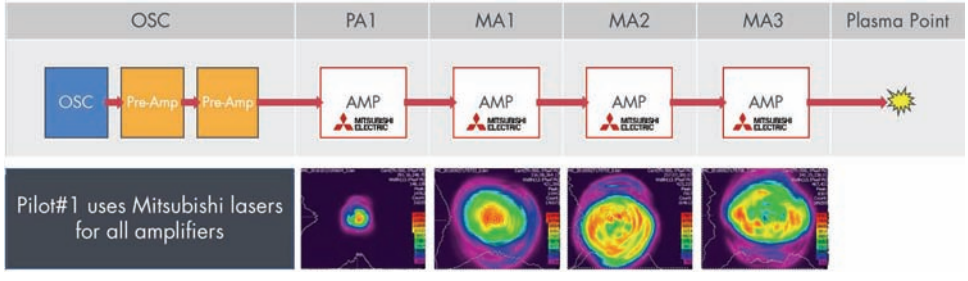

Figure 3B.22 Schematic of the 27-kW-class CO_2 laser driver system Pilot #1 and some of its output beam profiles (source: Gigaphoton Inc.).

Downloaded From: https://www.spiedigitallibrary.org/ebooks/ on 09 Mar 2022
Terms of Use: https://www.spiedigitallibrary.org/terms-of-use

3B.3 250-W HVM LPP-EUV Source[14,54]

3B.3.1 Pilot #1 system construction

The Pilot #1 HVM EUV light source layout is shown in Fig. 3B.23. This system consists of a drive laser system, a beam transfer system, and an EUV chamber system. We are planning to use four laser amplifiers that are produced by Mitsubishi Electric. The Pilot #1 system is currently being constructed; a schematic of the system is shown in Fig. 3B.24. Table 3B.1 shows the target specifications of Gigaphoton's EUV source.

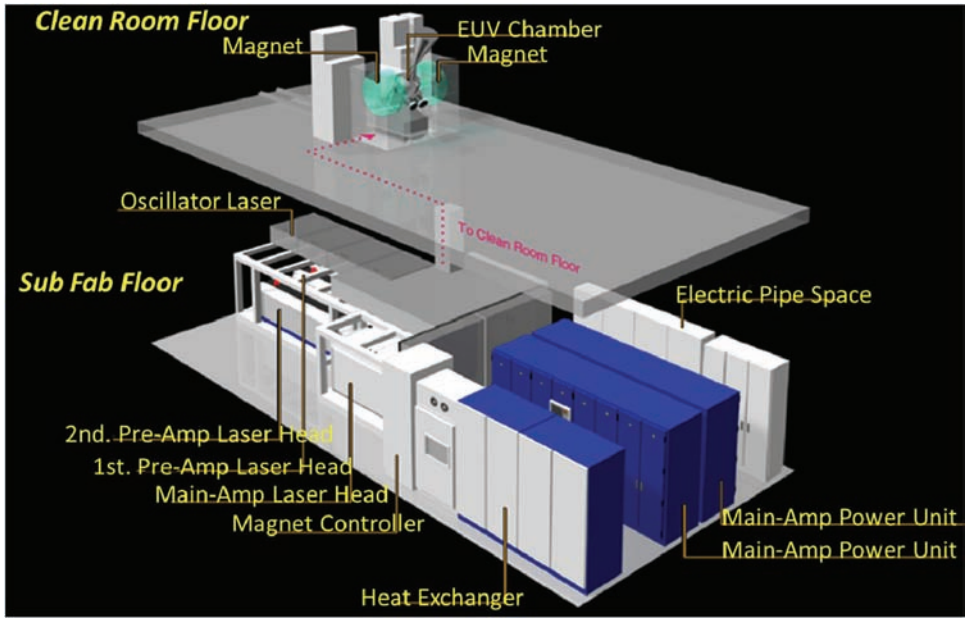

Figure 3B.23 GL200E-Pilot #1 (source: Gigaphoton Inc.).

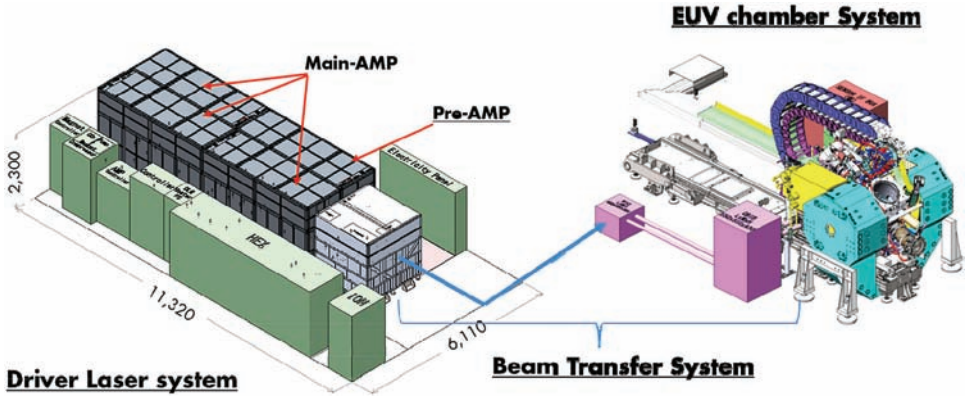

Figure 3B.24 Schematic of the Pilot #1 system construction (source: Gigaphoton Inc.).

Downloaded From: https://www.spiedigitallibrary.org/ebooks/ on 09 Mar 2022
Terms of Use: https://www.spiedigitallibrary.org/terms-of-use

Table 3B.1 Target specifications of Gigaphoton's EUV sources.

		Proto#1 Proof of Concept	Proto#2 Key Technology	Pilot#1 HVM Ready
Target Performance	EUV Power	25W	>100W	250W
	CE	3 %	4.0 %	5.0 %
	Pulse Rate	100kHz	100kHz	100kHz
	Output Angle	Horizontal	62°upper	62°upper
	Availability	~1 week	~1 week	>75%
Technology	Droplet Generator	20 - 25μm	< 20μm	< 20μm
	CO_2 Laser	5kW	20kW	27kW
	Pre-pulse Laser	picosecond	picosecond	picosecond
	Collector Mirror Lifetime	Used as development platform	10 days	> 3 months

3B.3.2 CE measurements and improvement

Differences between the CO_2 driver laser beam profiles of the focus point of Proto #2 and Pilot #1 are shown in Fig. 3B.25. The beam profile of the Pilot #1 system is much more symmetrical and homogeneous, which improves the CE. The Pilot #1 system therefore achieved a significant increase in CE to between 5.0% and 5.5%. The improved homogeneity is due to the different excitation scheme of the CO_2 laser making the beam profile at the focus point of the CO_2 laser system.

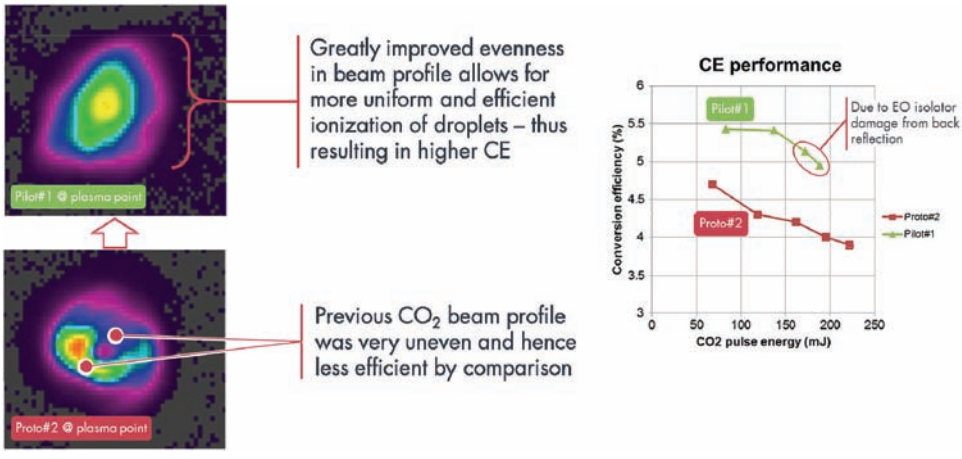

Figure 3B.25 Driver laser beam profiles and CE performance of Proto #2 and Pilot #1 (source: Gigaphoton Inc.).

Downloaded From: https://www.spiedigitallibrary.org/ebooks/ on 09 Mar 2022
Terms of Use: https://www.spiedigitallibrary.org/terms-of-use

3B.3.3 Latest data of the Pilot #1 system

Operation of the Pilot #1 system started in September 2016; an example of the operational data of this system is shown in Fig. 3B.26. The EUV inband power is 117 W, with 95% duty cycle, 50 kHz (111-W average power), and an operation time of 22 hours. The CO_2 laser power is only 9.5 kW because of the 5% high-CE operation. The dose stability data (taken during 22 hours) is shown in Fig. 3B.27. This data shows very good stability and corresponds to 92.3% die yield.

The tin mitigation simulation of the collector mirror of the Pilot #1 system also shows significant improvement in cleanness compared to the

	Performance
Conversion Efficiency	4.9%
Power (average at IF)	111W
Duty Cycle	95%
Power (In band)	117W
Operation Pulse Number	3.8Bpls
Operation Time	22hrs
Dose Margin	25%
CO_2 Power	9.5kW
Pulse Rate	50kHz
Pulse Duration	~10ns
Availability (4 week average)	17%

Note

Although CE and average power show relatively good results, availability continues to be a gating issue. The biggest cause of this problem is the back reflection in the CO_2 laser.

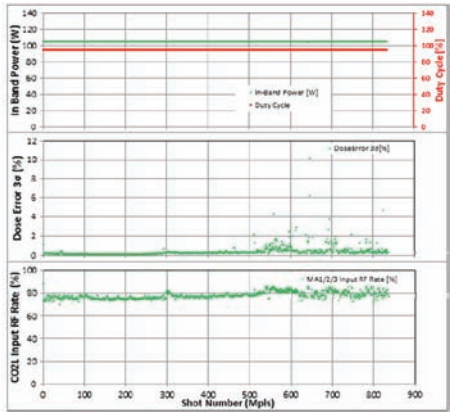

Figure 3B.26 EUV emission data (source: Gigaphoton Inc.).

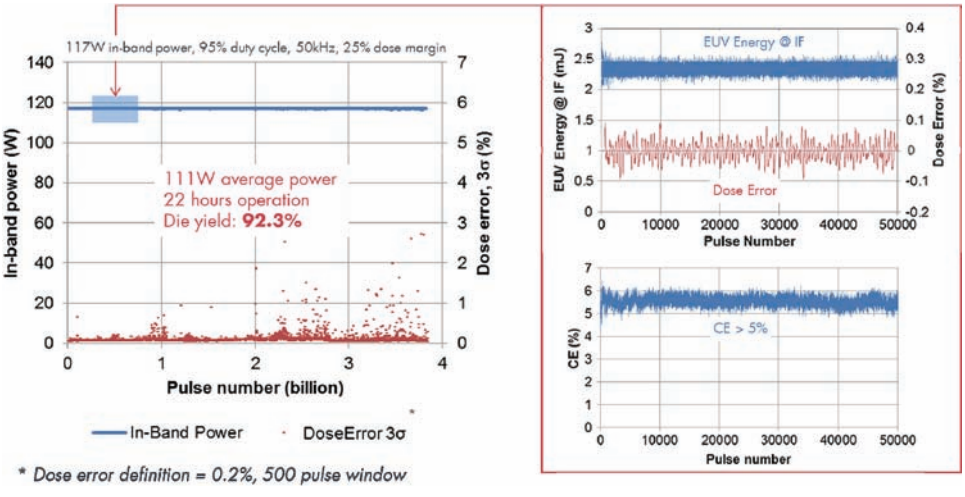

Figure 3B.27 Dose stability data (source: Gigaphoton Inc.).

Downloaded From: https://www.spiedigitallibrary.org/ebooks/ on 09 Mar 2022
Terms of Use: https://www.spiedigitallibrary.org/terms-of-use

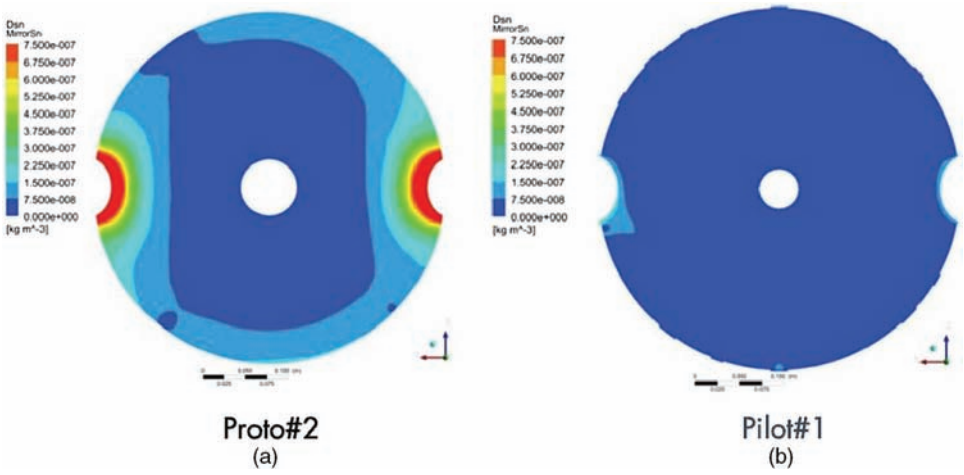

Figure 3B.28 Simulation of tin deposition rate on the collector mirrors of (a) Proto #2 and (b) Pilot #1 (source: Gigaphoton Inc.).

Proto #2 system (Fig. 3B.28) due to optimization of the hydrogen gas flow on the collector mirror. This data promises an increased lifetime of the collector mirror of the Pilot #1 system.

3B.3.4 Change of collector mirror reflectance during operation

As a latest result, we mounted a collector mirror on the Proto #2 system and recently tested the performance of the SM3 system. Figure 3B.29 shows the reflectance change during 25B pulses of operation. At the first and second trials, the reflectance decreased 10% per GPulse. However, after optimization of the

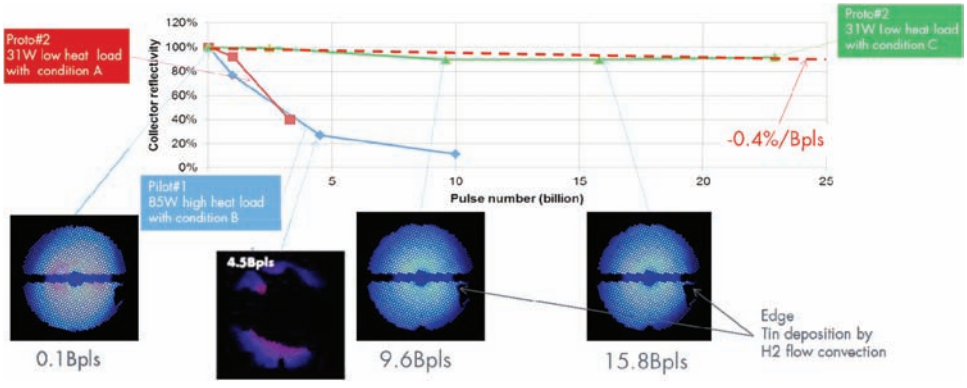

Figure 3B.29 Reflectance change of the collector mirror under the SM3 (source: Gigaphoton Inc.).

Downloaded From: https://www.spiedigitallibrary.org/ebooks/ on 09 Mar 2022
Terms of Use: https://www.spiedigitallibrary.org/terms-of-use

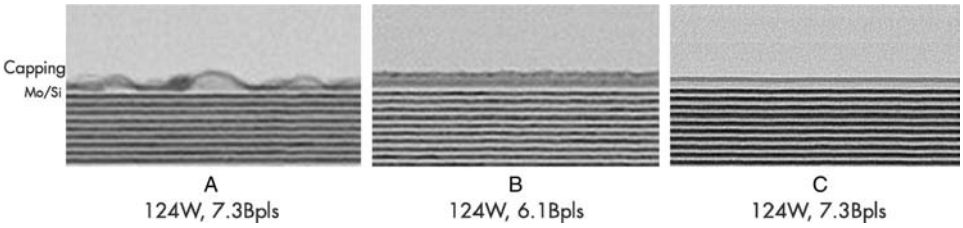

Figure 3B.30 Differences in the surfaces of the three capping layer materials: A, B, and C (source: Gigaphoton Inc.).

SM3, the reflectance decreased 0.4% per GPulse. This means that one month of operation is possible with SM3. We are now starting a >100-GPulse test with the SM3 system.[55] We also took data using several different capping layer materials during operation. Figure 3B.30 shows the difference between the capping layer materials. Material A shows blistering due to hydrogen penetration, material B shows deposition of tin, and material C shows a clean surface.[55] These phenomenon have not yet been explained and will be the focus of an important study in the near future.

3B.4 Conclusion and Acknowledgment

Gigaphoton has developed the Pilot #1 system for HVM EUV lithography. This system demonstrates 117-W EUV power (IF clean power in burst), 50 kHz, with 22 hours of stable operation. Pilot #1 uses a 27-kW CO_2 laser amplifier system that consists of one pre-amplifier and three main amplifiers made by Mitsubishi Electric from Japan. This Pilot system will be available soon to the EUV lithography market to support 10-nm node semiconductor mass manufacturing.

This work was partially supported by the New Energy and Industrial Technology Development Organization (NEDO), Japan. We acknowledge their continuous support. We also acknowledge the following researchers and organizations. Plasma simulation was supported by Dr. Atsushi Sunahara at Osaka University. Plasma diagnostics was supported by Dr. Kentaro Tomita, Prof. Kiichiro Uchino, and others at Kyushu University. Laser engineering was supported by Dr. Akira Endo in HiLase Project (Prague). Collector mirror development—especially RIT and CO_2 laser amplifier development—was supported by the Mitsubishi Electric CO_2 laser amplifier development team: Dr. Yoichi Tanino, Dr. Junichi Nishimae, Dr. Shuichi Fujikawa, and others. The authors truly miss Dr. Yoichi Tanino of Mitsubishi Electric and are saddened by his sudden death on 1 February 2014. We appreciate his excellent achievement of CO_2 amplifier development in a very short time period. Finally, the authors are grateful for the contributions to this chapter made by Dr. George Soumagne.

Downloaded From: https://www.spiedigitallibrary.org/ebooks/ on 09 Mar 2022
Terms of Use: https://www.spiedigitallibrary.org/terms-of-use

References

1. N. Harned, M. Goethals, R. Groeneveld, P. Kuerz, M. Lowisch, H. Meijer, H. Meiling, K. Ronse, J. Ryan, M. Tittnich, H.-J. Voorma, J. Zimmerman, U. Mickan, and S. Lok, "EUV lithography with the Alpha Demo Tools: status and challenges," *Proc. SPIE* **6517**, 651706 (2007) [doi: 10.1117/12.712065].
2. T. Miura, K. Murakami, K. Suzuki, Y. Kohama, K. Morita, K. Hada, Y. Ohkubo, and H. Kawai "Nikon EUVL development progress update," *Proc. SPIE* **6921**, 69210M (2008) [doi: 10.1117/12.772444].
3. C. Wagner, N. Harned, P. Kuerz, M. Lowisch, H. Meiling, D. Ockwell, R. Peeters, K. van Ingen-Schenau, E. van Setten, J. Stoeldraijer, and B. Thuering, "EUV into production with ASML's NXE platform," *Proc. SPIE* **7636**, 76361H (2010) [doi: 10.1117/12.845700].
4. R. Peeters, S. Lok, E. van Alphen, N. Harned, P. Kuerz, M. Lowisch, H. Meijer, D. Ockwell, E. van Setten, G. Schiffelers, J.-W. van der Horst, J. Stoeldraijer, R. Kazinczi, R. Droste, H. Meiling, and R. Kool, "ASML's NXE platform performance and volume introduction," *Proc. SPIE* **8679**, 86791F (2013) [doi: 10.1117/12.2010932].
5. B. Turkot, "EUV lithography for HVM," Keynote Presentation at 2017 International Workshop on EUV Lithography, CXRO, LBNL, Berkeley, California, 12–15 June 2017.
6. J. van Schoot, K. Troost, A. Pirati, R. van Ballegoij, P. Krabbendam, J. Stoeldraijer, E. Loopstra, J. Benschop, J. Finders, H. Meiling, E. van Setten, B. Kneer, B. Thuering, W. Kaiser, T. Heil, and S. Migura, "The Future of EUV lithography: Enabling Moore's law in the next decade," Invited Paper at 2017 International Workshop on EUV Lithography, CXRO, LBNL, Berkeley, California, 12–15 June 2017.
7. I. Fomenkov, "EUV Lithography: Progress in LPP source power scaling and availability," Keynote Presentation at 2017 International Workshop on EUV Lithography, CXRO, LBNL, Berkeley, California, 12–15 June 2017.
8. A. Endo, H. Hoshino, T. Suganuma, M. Moriya, T. Ariga, Y. Ueno, M. Nakano, T. Asayama, T. Abe, H. Komori, G. Soumagne, H. Mizoguchi, A. Sumitani, and K. Toyoda, "Laser-produced EUV light source development for HVM," *Proc. SPIE* **6517**, 65170O (2007) [doi: 10.1117/12.711097].
9. H. Mizoguchi, T. Yamazaki, and T. Saitou, "High power HVM LPP-EUV source with long collector mirror lifetime," Keynote Presentation at 2017 International Workshop on EUV Lithography, CXRO, LBNL, Berkeley, California, 12–15 June 2017.
10. K. Nishihara, A. Sasaki, A. Sunahara, and T. Nishikawa, "Conversion Efficiency of LPP Sources," Chapter 11 in *EUV Sources for Lithography*,

Downloaded From: https://www.spiedigitallibrary.org/ebooks/ on 09 Mar 2022
Terms of Use: https://www.spiedigitallibrary.org/terms-of-use

V. Bakshi, Ed., SPIE Press, Bellingham, Washington, pp. 339–370 (2006) [doi: 10.1117/3.613774.ch11].
11. H. Tanaka, A. Matsumoto, K. Akinaga, A. Takahashi, and T. Okada, "Comparative study on emission characteristics of extreme ultraviolet radiation from CO_2 and Nd:YAG laser-produced tin plasmas," *Appl. Phys. Lett.* **87**, 041503 (2005).
12. T. Yanagida, H. Nagano, Y. Wada, T. Yabu, S. Nagai, G. Soumagne, T. Hori, K. Kakizaki, A. Sumitani, J. Fujimoto, H. Mizoguchi, and A. Endo, "Characterization and optimization of tin particle mitigation and EUV conversion efficiency in a laser produced plasma EUV light source," *Proc. SPIE* **7969**, 79692T (2011) [doi: 10.1117/12.879189].
13. V. Bakshi, Ed., *EUV Sources for Lithography*, SPIE Press, Bellingham, Washington (2006) [doi: 10.1117/3.613774].
14. H. Mizoguchi "Development of 250W EUV light source for HVM lithography," 2016 EUVL Symposium, 24–26 Oct. 2016, Hiroshima, Japan.
15. V. V. Medvedev, V. G. Novikov, V. V. Ivanov et al., "Advances in computer simulation tools for plasma-based sources of EUV radiation," *presented at International Workshop on EUV Lithography*, Hawaii, 23–27 June 2014.
16. K. Tomita, Y. Sato, K. Nishikawa, K. Uchino, T. Yanagida, H. Tomura, Y. Wada, M. Kunishima, T. Kodama, H. Mizoguchi, and A. Sunahara, "Development of a collective Thomson scattering system for laser-produced tin plasmas for extreme-ultraviolet light sources," *Appl. Phys. Express* **8**(12) (2015).
17. K. Tomita, K. Nakayama, K. Inoue, A. Sunahara, and K. Uchino, "A collective laser Thomson scattering system for diagnostics of laser-produced plasmas for extreme ultraviolet light sources," *Appl. Phys. Express* **6**(7) (2013).
18. Y. Sato, K. Tomita, S. Tsukiyama, T. Eguchi, K. Uchino, K. Kouge, H. Tomoru, T. Yanagida, Y. Wada, M. Kunishima, T. Komada, and H. Mizoguchi, "Spatial profiles of electron density, electron temperature, average ionic charge, and EUV emission of laser-produced Sn plasmas for EUV lithography," *Japanese. J. Appl. Phys.* **56**(3) (2017).
19. J. Fujimoto, T. Ohta, K. M. Nowak, T. Suganuma, H. Kameda, M. Moriya, T. Yokoduka, K. Fujitaka, A. Sumitani, and H. Mizoguchi, "Development of the reliable 20 kW class pulsed carbon dioxide laser system for LPP EUV light source," *Proc. SPIE* **7969**, 79692S (2011) [doi: 10.1117/12.879181].
20. Rigaku Corp. technical display: IR Rejection Collector Optic Manufacturing Process, *Proc. International Symposium on Extreme Ultraviolet Lithography 2013*, 6–10 Oct. 2013, Toyama).

Downloaded From: https://www.spiedigitallibrary.org/ebooks/ on 09 Mar 2022
Terms of Use: https://www.spiedigitallibrary.org/terms-of-use

21. V. Bakshi, Ed., *EUV Lithography*, SPIE Press, Bellingham, Washington (2009) [doi: 10.1117/3.769214].
22. R. Spitzer, T. Orzechowski, D. Phillion, R. Kauffman, and C. Cerjan, "Conversion efficiencies from laser-produced plasmas in the extreme ultraviolet regime," *J. Appl. Phys.* **79**, 2251–2258 (1996).
23. J. White, P. Dunne, P. Hayden, F. O'Reilly, and G. O'sullivan, "Optimizing 13.5 nm laser-produced tin plasma emission as a function of laser wavelength," *Appl. Phys. Lett.* **90**, 181502 (2007).
24. A. Hassanein, V. Sizyuk, S. Harilal, and T. Sizyuk, "Analysis, simulation, and experimental studies of Nd:YAG and CO_2 laser-produced plasma for EUV lithography sources," *Proc. SPIE* **7636**, 76360A (2010) [doi: 10.1117/12.848222].
25. S. Harilal, T. Sizyuk, A. Hassanein, D. Campos, P. Hough, and V. Sizyuk, "The effect of excitation wavelength on dynamics of laser-produced tin plasma," *J. Appl. Phys.* **109**, 063306 (2011).
26. Y. Ueno, H. Hoshino, T. Ariga, T. Miura, M. Nakano, H. Komori, G. Soumagne, A. Endo, H. Mizoguchi, A. Sumitani, and K. Toyoda, "Characterization of various Sn targets with respect to debris and fast ion generation," *Proc. SPIE* **6517**, 65173B (2007) [doi: 10.1117/12.711226].
27. A. Takahashi, D. Nakamura, K. Tamaru, T. Akiyama, and T. Okada, "Emission characteristics of debris from CO_2 and Nd:YAG laser produced tin plasmas for extreme ultraviolet lithography light source," *Appl. Phys. B: Lasers and Opt.* **92**, 73–77 (2008).
28. A. Hassanein, V. Sizyuk, S. Harilal, and T. Sizyuk, "Analysis, simulation, and experimental studies of Nd:YAG and CO_2 laser-produced plasma for EUV lithography sources," *Proc. SPIE* **7636**, 76360A (2010) [doi: 10.1117/12.848222].
29. K. Gurs and R. Muller, "Internal modulation of optical masers," *Proc. Symposium on Optical Masers, Polytechnic Institute of Brooklyn Symposia Series* XIII: Optical Masers, New York, pp. 243–252 (1963).
30. T. Bridges and P. Cheo, "Spontaneous self-pulsing and cavity dumping in a CO_2 laser with electro-optic Q-switching," *Appl. Phys. Lett.* **14**, 262–264 (1969).
31. T. Ariga, H. Hoshino, T. Miura, and A. Endo, "High-power pulsed CO_2 laser for EUV lithography," *Proc. SPIE* **6151**, 61513M (2006) [doi: 10.1117/12.656804].
32. I. Fomenkov, B. Hansson, N. Böwering, A. Ershov, W. Partlo, V. Fleurov, V. Khodykin, A. Bykanov, C. Rettig, J. Hoffman, E. Vargas, J. Chavez, W. Marx, and D. Brandt, "High-power low cost drive laser for LPP source," *Proc. SPIE* **6151**, 61513X (2006) [doi: 10.1117/12.655733].
33. H. Hoshino, T. Suganuma, T. Asayama, K. M. Nowak, M. Moriya, T. Abe, A. Endo, and A. Sumitani, "LPP EUV light source employing

Downloaded From: https://www.spiedigitallibrary.org/ebooks/ on 09 Mar 2022
Terms of Use: https://www.spiedigitallibrary.org/terms-of-use

high-power CO_2 laser," *Proc. SPIE* **6921**, 692131 (2008) [doi: 10.1117/12.771847].
34. J. Kiefer, T. Nussmeier, and F. Goodwin, "Intracavity CdTe modulators for CO_2 lasers," *IEEE J. Quant. Electron.* **8**, 173–179 (1972).
35. J. Faist, F. Capasso, D. Sivco, C. Sirtori, A. Hutchinson, and A. Cho, "Quantum cascade laser," *Science* **264**, 553 (1994).
36. K. M. Nowak, T. Ohta, T. Suganuma, T. Yokotsuka, J. Fujimoto, H. Mizoguchi, and A. Endo, "Spectral characteristics of quantum-cascade laser operating at 10.6mm wavelength for a seed application in laser-produced-plasma extreme UV source," *Opt. Lett.* **37**, 4765–4767 (2012).
37. K. M. Nowak, T. Ohta, T. Suganuma, T. Yokotsuka, J. Fujimoto, and H. Mizoguchi, "Wavefront measurement of single-mode quantum cascade laser beam for seed application in laser-produced plasma extreme ultraviolet system," *Opt. Lett.* **37**, 4886–4888 (2012).
38. K. M. Nowak, T. Ohta, T. Suganuma, J. Fujimoto, and H. Mizoguchi, "A novel multi-line short-pulse solid-state seeded carbon-dioxide laser for extreme ultraviolet employing multi-pass radio-frequency excited slab amplifier," *Opt. Lett.* **38**, 881–883 (2013).
39. K. M. Nowak, T. Suganuma, H. Hoshino, M. Moriya, T. Ohta, A. Sumitani, and A. Endo, "Improving efficiency of CO_2 laser system for LPP Sn EUV source," presented at *EUVL Workshop*, Maui, Hawaii, 11 June 2010.
40. K. M. Nowak, T. Ohta, J. Fujimoto, H. Mizoguchi, and A. Endo, "Towards 20kW CO_2 laser system for Sn LPP EUV source - a review of developments at Gigaphoton," presented at *EUVL Workshop*, UCD Dublin, Ireland, 8 November 2011.
41. K. M. Nowak, Y. Kurosawa, T. Suganuma, Y. Kawasuji, H. Nakarai, T. Saito, J. Fujimoto, and H. Mizoguchi, "Synthesis of arbitrary pulse waveforms in QCL-seeded ns-pulse CO_2 laser for optimization of LPP EUV source," *Opt. Lett.* **41**, 3118–3121 (2016).
42. C. K. N. Patel, "Selective excitation through vibrational energy transfer and optical maser action in CO_2," *Phys. Rev. Lett.* **13**, 617–619 (1964).
43. R. Beck, "Fast-axial-flow CO_2 laser with integrated turbo-blower," *Appl. Phys. B: Lasers and Optics* **42**, 233–236 (1987).
44. D. C. Brandt, I. V. Fomenkov, A. I. Ershov, W. N. Partlo, D. W. Myers, N. R. Böwering, N. R. Farrar, G. O. Vaschenko, O. V. Khodykin, A. N. Bykanov, J. R. Hoffman, C. P. Chrobak, S. N. Srivastava, I. Ahmad, C. Rajyaguru, D. J. Golich, D. A. Vidusek, and S. De Dea, "LPP source system development for HVM," *Proc. SPIE* **7271**, 727103 (2009) [doi: 10.1117/12.814228].

Downloaded From: https://www.spiedigitallibrary.org/ebooks/ on 09 Mar 2022
Terms of Use: https://www.spiedigitallibrary.org/terms-of-use

45. Y. Tanino, T. Yamamoto, J. Nishimae, and S. Fujikawa, "Efficient pulse amplification using a transverse-flow CO_2 laser for extreme ultraviolet light source," *Opt. Lett.* **37**, 3300–3302 (2012).
46. W. Witteman, *The CO_2 Laser*, Springer-Verlag, Berlin (1987).
47. A. Endo, "High power CO_2 laser," *presented at EUV Source Workshop*, Baltimore, Maryland, 6 May 2007.
48. K. M. Nowak, T. Ohta, T. Suganuma, J. Fujimoto, H. Mizoguchi, A. Sumitani, and A. Endo, "Efficient multi-line nanosecond pulse amplification in planar waveguide CO_2 amplifier for extreme UV laser-produced-plasma source," *Opt. Lett.* **39**(7), 1953–1956 (2014).
49. J. Fujimoto, T. Ohta, K. M. Nowak, T. Suganuma, H. Kameda, M. Moriya, T. Yokoduka, K. Fujitaka, A. Sumitani, and H. Mizoguchi, *"Development of the reliable 20 kW class pulsed carbon dioxide laser system for LPP EUV light source*, Proc. SPIE **7969** 79692S (2011) [doi: 10.1117/12.879181].
50. Y. Tanino, "A proposal for an EUV light source using transverse flow CO_2 lasers," *Proc. International Symposium on Extreme Ultraviolet Lithography 2012*, 1–4 Oct. 2012, Brussels, p. 1016 (2012).
51. K. M. Nowak, Y. Kawasuji, T. Ohta, and J. Nishimae, "EUV driver CO_2 laser system using multi-line nano-second pulse high-stability master oscillator for Gigaphoton's EUV LPP system," *Proc. International Symposium on Extreme Ultraviolet Lithography 2013*, 6–10 Oct. 2013, Toyama, Japan.
52. H. Mizoguchi, "Update on one hundred watt HVM LPP-EUV source performance" 2015 EUVL Symposium, 5–7 October 2015, Maastricht, The Netherlands.
53. K. Yasui, N. Nakamura, J. Nishimae, M. Naruse, K. Sugihara, and M. Matsubara, "Stable and scalable CO2 laser drivers for high-volume-manufacturing extreme ultraviolet lithography applications" 2016 EUVL Symposium, 24–26 Oct. 2016, Hiroshima, Japan.
54. H. Mizoguchi, H. Nakarai, T. Abe, K. M. Nowak, Y. Kawasuji, H. Tanaka, Y. Watanabe, T. Hori, T. Kodama, Y. Shiraishi, T. Yanagida, T. Yamada, T. Yamazaki, S. Okazaki, and T. Saitou, "Performance of new high-power HVM LPP-EUV source," *Proc. SPIE* **9776**, 97760J (2016) [doi: 10.1117/12.2218405].
55. H. Mizoguchi, H. Nakarai, T. Abe, K. M. Nowak, Y. Kawasuji, H. Tanaka, Y. Watanabe, T. Hori, T. Kodama, Y. Shiraishi, T. Yanagida, G. Soumagne, T. Yamada, T. Yamazaki, and T. Saitou, "High power LPP-EUV source with long collector mirror lifetime for high volume semiconductor manufacturing," 2017 EUVL Symposium, 11–14 Oct. 2017, Monterey, California.

Downloaded From: https://www.spiedigitallibrary.org/ebooks/ on 09 Mar 2022
Terms of Use: https://www.spiedigitallibrary.org/terms-of-use

Hakaru Mizoguchi is the Executive Vice President and CTO of Gigaphoton Inc. He was previously General Manager of the research division in Komatsu Ltd until 1999. He obtained a Doctoral degree in high-power excimer laser fields from Kyushu University in 1994. In 2000 he cofounded Gigaphoton Inc. From 2002 to 2010 he organized the EUV research group in the EUVA program. He is currently promoting EUV light source product development.

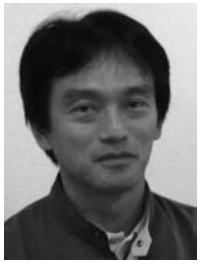

Taku Yamazaki has been the Deputy General Manager, EUV development division, Gigaphoton Inc. since 2012 and dedicates his efforts to current development. He received a Master's degree in mechanical engineering from Tokyo Institute Technology in 1984 and joined Komatsu Ltd. After working for several years in the research and development of robotics and laser applications, he joined Gigaphoton in 2000 to commercialize the excimer laser apparatus.

Tatsuya Yanagida is Chief Engineering Manager in the EUV development division of Gigaphoton Inc. He received a Dr. Eng. degree from Kyushu University, Japan in 2007. He joined Komatsu Ltd in 2007. Since 2007 he has been involved in the research and development of the LPP EUV light source.

Krzysztof M. Nowak received a M.Sc. degree (Hons) from Wrocław University of Technology, Poland in 1999. He received a Ph.D. degree from Heriot-Watt University in 2003 for his successful work demonstrating a direct-write, rapid prototyping of refractive micro-optics using pulsed CO_2 lasers. He cofounded the Scottish spinoff company PowerPhotonic, which commercialized this unique technology. Since 2007, he has been involved in the research and development of various aspects of design and computer modeling of a high-power CO_2 laser system for the EUV light source at Gigaphoton Inc. His achievements include a world-first demonstration of a new type of hybrid, solid-state-seeded pulsed CO_2 laser of unique output characteristics ideal for precision laser material processing applications. He recently moved to TeraDiode Inc. to work on the development of the disruptive technology of high-beam-quality direct-diode laser sources for material processing applications.

Downloaded From: https://www.spiedigitallibrary.org/ebooks/ on 09 Mar 2022
Terms of Use: https://www.spiedigitallibrary.org/terms-of-use

Takashi Saito received his M.S. and Ph.D. degrees in engineering from Tokyo Institute of Technology in 1988 and 2010, respectively. He joined NEC Corporation in 1988 where he worked on excimer laser research. He moved to Ushio Inc. in 1997 and joined Gigaphoton Inc. in 2000, working on excimer laser development for lithography. Since 2012, he has been working on EUV light source development for lithography. Currently, he is Director, Senior Executive Officer, and General Manager of the EUV development division at Gigaphoton.

Downloaded From: https://www.spiedigitallibrary.org/ebooks/ on 09 Mar 2022
Terms of Use: https://www.spiedigitallibrary.org/terms-of-use

Chapter 4A
The EQ-10 Electrodeless Z-Pinch™ Metrology Source

Stephen F. Horne, Matthew M. Besen, Paul A. Blackborow, Ron Collins, Deborah Gustafson, Matthew J. Partlow, and Donald K. Smith
Energetiq Technology, Inc., Woburn, Massachusetts, USA

4A.1 Operating Principles
4A.2 Diagnostics for the EQ-10
4A.3 Source Performance
4A.3.1 Power and brightness
4A.3.2 Spatial and temporal stability
4A.4 Typical Installations
4A.5 Conclusions
References

4A.1 Operating Principles

The EQ-10[1–3] is a discharge-produced plasma Z-pinch source operating in xenon, which relies on induction via a transformer core rather than conduction via electrodes to generate the Z-pinch current. In the basic design, the transformer primary circuit consists of two copper plates connected by a conductive tube at the center. The primary current flows radially in on one plate, axially through the central connection, and radially outward through the second plate. The induced secondary currents flow in a plasma through three electrically parallel paths that pierce the primary structure in three places (the plasma return holes), and then combine in the central bore. Figure 4.1 shows this geometry.

Sandwiched between the plates are two magnetic cores. The inner core, closely surrounding the central bore, provides the magnetic flux linkage between the primary current path through the copper and the three parallel secondary currents flowing in the plasma, which combine in the bore to generate the magnetic Z-pinch. The second core is near the outer radius of the device and surrounds the three plasma return holes. This core functions as a magnetic switch with a specific volt-second capacity matched to the

Downloaded From: https://www.spiedigitallibrary.org/ebooks/ on 09 Mar 2022
Terms of Use: https://www.spiedigitallibrary.org/terms-of-use

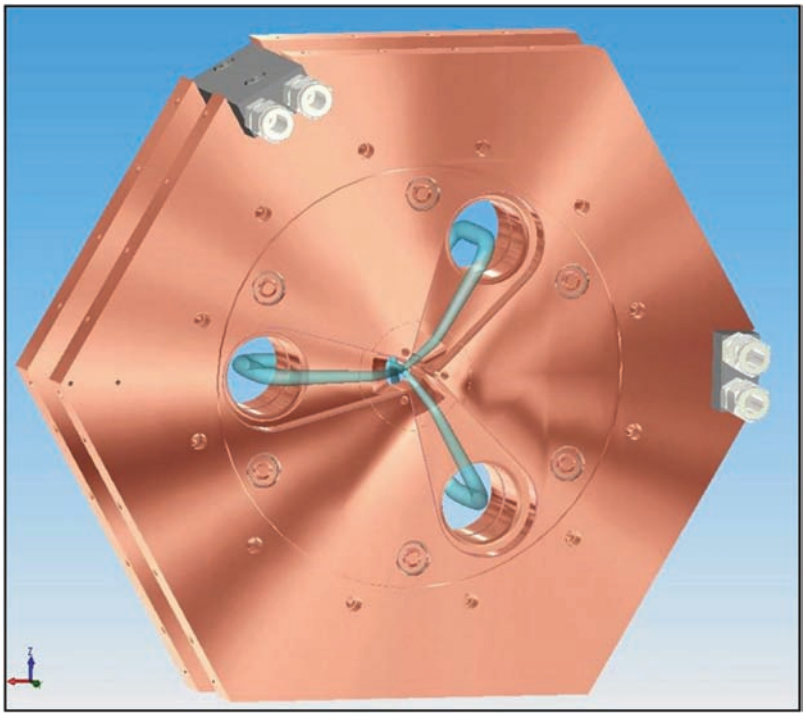

Figure 4A.1 Source and plasma geometry (reprinted from Ref. 2).

capacitance and charging system described below. Figure A4.2 shows a cross-section of the structure.

In operation, a capacitor bank (not shown) is connected across the copper plates symmetrically, with connections to each of the six facets of the copper plates. A fast electrical pulse (derived from a pulse-forming system—not shown) is applied to the plates, causing the capacitors to begin to charge. In parallel, current flows through the copper structure radially into one plate, through the bore, out the other plate. The magnetic switch acts as a high

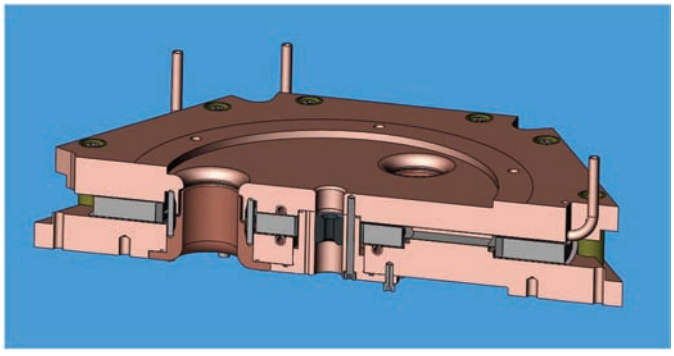

Figure 4A.2 Cross-section details (reprinted from Ref. 5).

Downloaded From: https://www.spiedigitallibrary.org/ebooks/ on 09 Mar 2022
Terms of Use: https://www.spiedigitallibrary.org/terms-of-use

impedance in series with the copper short circuit (effectively, a series inductance) during this charging process, allowing only a small leakage current to flow—until the switch core saturates. At this point, the core becomes essentially zero inductance, allowing the now charged capacitor bank to appear across the inner induction core. The current and magnetic field in the core ramps, generating an EMF that drives current in the plasma through the bore and plasma return holes. The plasma current flowing through the bore of the device generates its own local magnetic field, which acts to compress the plasma current channel. When this field becomes intense enough, a dynamic Z-pinch occurs, which collapses the current channel to less than 1-mm diameter in a few tens of nanoseconds—thus compressing and heating the plasma to the point where EUV emission occurs. Figure A4.3 shows a simplified schematic of the power system.

A point to note about the power circuit is that it is the electrical analogue of a driven nonlinear coupled oscillator. That mechanical system is often used as a model for exploration of chaotic behavior. We will return to this point in the discussion of temporal stability.[4]

Since the plasma current flows in closed loops and does not terminate in metal electrodes, no electrode debris is produced. The magnetic confinement of the plasma loops away from source surfaces results in greater spatial stability and further reduces debris. The bore region, which is exposed to the fierce sputtering environment produced by the xenon plasma, is designed to be easily replaceable.

The plasma size and shape are controllable primarily via the bore geometry. In an inspection or illumination application, detailed specifications for source size, uniformity, collection angle, length, and angular uniformity of

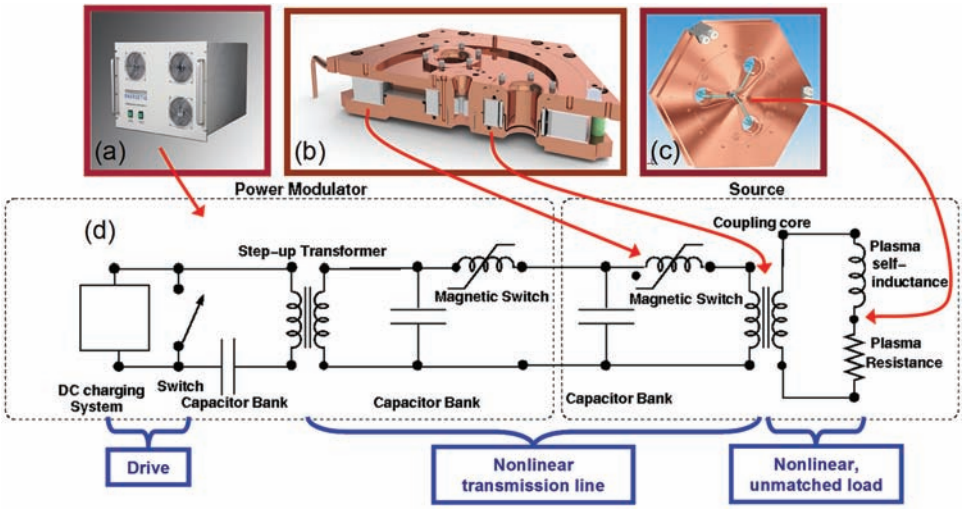

Figure 4A.3 (a)–(c) Illustrations and (d) schematic illustrating the key structures of the electrodeless Z-pinch EUV light source (reprinted from Ref. 13).

Downloaded From: https://www.spiedigitallibrary.org/ebooks/ on 09 Mar 2022
Terms of Use: https://www.spiedigitallibrary.org/terms-of-use

emission depend delicately on the specific design envisioned for the illumination optics. The plasma length for operating conditions and bore geometry reported here is ~8–10 mm FWHM by ~400 μm radially, and the available collection half angle is typically 8 deg. Other bore geometries have been developed to meet other étendue requirements, and specialized sources for specific applications have also been delivered.[5]

The commercial system is relatively simple to operate, with the user controlling source-operating parameters through a touch screen interface. Minimal routine maintenance is required (bore replacement every ~billion pulses, or 6 days of 24/7 operation). Figure A4.4 shows the three major components of the system.

4A.2 Diagnostics for the EQ-10

Developing the diagnostic capability for consistent and reliable EUV power/brightness metrology is a task as challenging as source development itself. Figure A4.5 shows the layout of our combined power/imaging diagnostic—the "dual diagnostic." Features to note are the use of multiple zirconium foils

Figure 4A.4 The EQ-10 source head, modulator, and control rack (source: Energetiq product literature, used by permission).

Downloaded From: https://www.spiedigitallibrary.org/ebooks/ on 09 Mar 2022
Terms of Use: https://www.spiedigitallibrary.org/terms-of-use

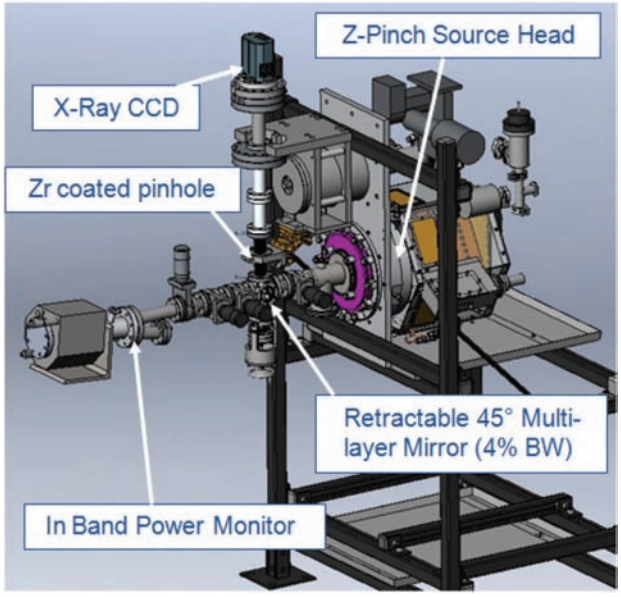

Figure 4A.5 The dual diagnostic, combining inband power and imaging capability (reprinted from Ref. 14).

mounted on retractable valves; this allows independent measurement and calibration of foil transmission. An insertable glass filter allows verification of foil integrity. Xenon pressure in the diagnostic beamline is monitored to correct for gas transmission. In addition, the beamline is heavily pumped to reduce uncertainty due to gas temperature. The power diagnostic itself uses a custom near-normal multilayer mirror designed and produced for us by the CXRO group at Berkeley; the mirror response is very close to ±1% bandwidth, which reduces errors due to assumptions about the source natural spectral bandwidth. The diagnostic (mirror+photodiode) is routinely recalibrated by the Synchrotron Ultraviolet Radiation Facility (SURF) at NIST, Gaithersburg, Maryland.

Size, position, and positional stability are measured using an x-ray pinhole camera incorporating a retractable 45-deg multilayer mirror and zirconium-coated pinhole to provide an inband image.

The dual diagnostic design allows near-simultaneous acquisition of power and imaging information, which together are analyzed to produce source brightness profiles. Mechanically, the diagnostic is anchored very rigidly to the source itself, to minimize errors due to mechanical drift.

4A.3 Source Performance

The requirements for the three main metrology tools (as of 2011)[6] are shown in Table 4A.1. While the EQ-10 source does not meet the brightness

Downloaded From: https://www.spiedigitallibrary.org/ebooks/ on 09 Mar 2022
Terms of Use: https://www.spiedigitallibrary.org/terms-of-use

Table 4A.1 Metrology source requirements as determined by toolmakers in 2011.

Application	Brightness W/mm^2/Sr	Etendue mm^2-Sr
AIMS EUV	100	5.00E-04
Pattern mask Inspection	40	1.50E-02
EUV Mask Blank Inspection	80	4.00E-03

requirements, nevertheless, it has been used successfully in both the AIMS and mask blank inspection roles.

4A.3.1 Power and brightness

The high-power version of the EQ-10 operates with 7-kW power input to the modulator. Given that the modulator is measured to be about 60% efficient, we estimate a conversion efficiency of about 0.5% at optimal performance, typical of a xenon Z-pinch source. We observe a variation of power (Fig. 4A.6) with chamber xenon pressure due to various physics tradeoffs.

Inband brightness is calculated by using only the spatial profile obtained by the camera, and by determining what overall scaling must be applied to that profile to match the power measurement at the same condition. This approach avoids potential errors due to invoking a model brightness profile (such as Gaussian) and also errors due to lack of absolute calibration of the

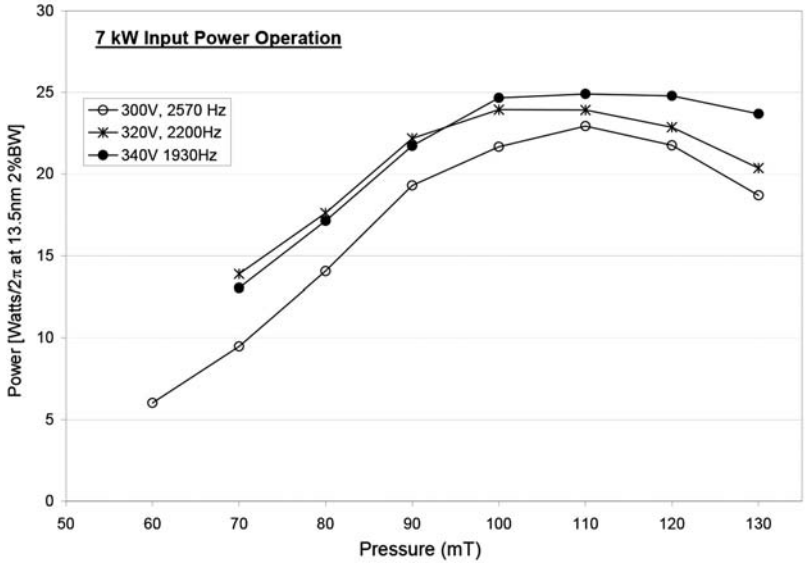

Figure 4A.6 Power optimizes at slightly different pressures, depending on source operating point (source: Energetiq product literature, used by permission).

Downloaded From: https://www.spiedigitallibrary.org/ebooks/ on 09 Mar 2022
Terms of Use: https://www.spiedigitallibrary.org/terms-of-use

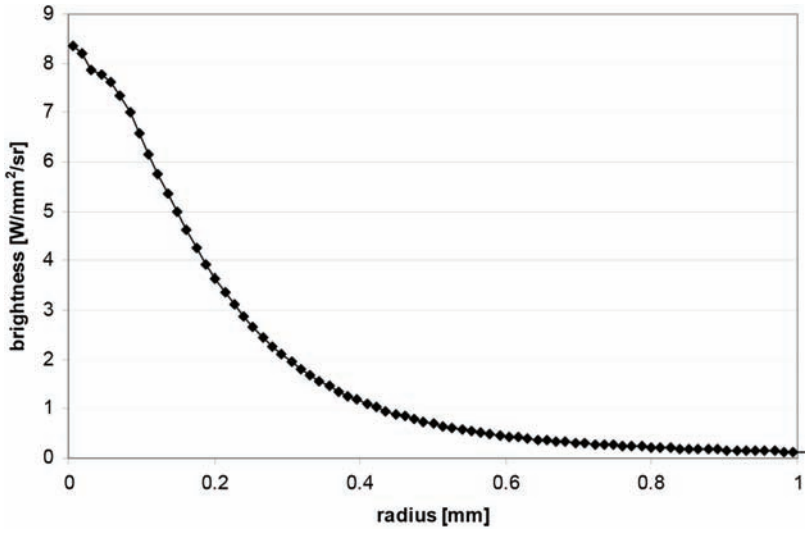

Figure 4A.7 Local brightness at a given distance *r* from the center of the pinch, for the redesigned EQ-10 source, for operating conditions 300 V, 2570 Hz, and 120 mT (source: Energetiq product literature, used by permission).

x-ray imaging diagnostic. A typical brightness profile is shown in Fig. 4A.7. As Fig. 4A.8 shows, the maximum brightness is obtained at somewhat higher pressure than the maximum power, as the plasma size and power optimize somewhat independently.

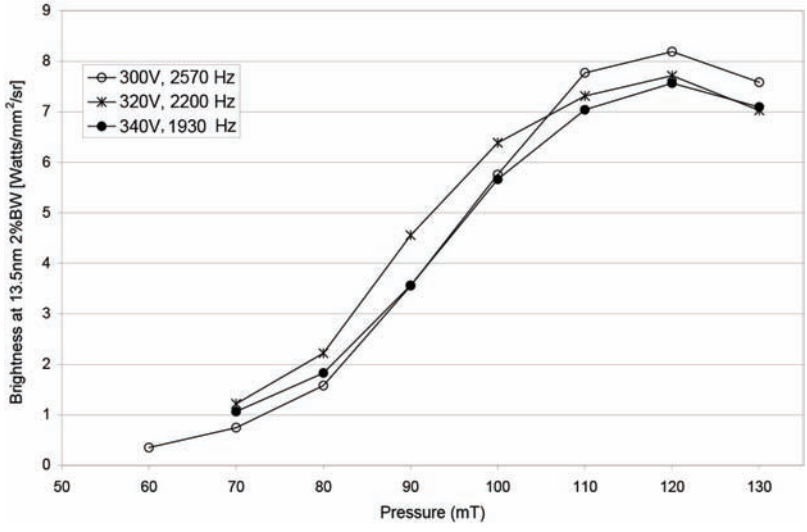

Figure 4A.8 Inband EUV peak brightness for the 7-kW DC input operating conditions (source: Energetiq product literature, used by permission).

Downloaded From: https://www.spiedigitallibrary.org/ebooks/ on 09 Mar 2022
Terms of Use: https://www.spiedigitallibrary.org/terms-of-use

4A.3.2 Spatial and temporal stability

Spatial and temporal stability are key metrics for a metrology source, especially in an inspection application. The electrodeless design of the EQ-10 leads to unusually good spatial stability characteristics because the boundary conditions at the beginning of the pinch phase are set by macroscopic variables that are either naturally symmetric or engineered to be so (such as the electric field topology impressed by the coupling core and massive copper conducting structures), not by details of the electrode–plasma interaction as in a conventional pinch. Figure 4A.9 shows one measure of stability, based on capturing the positional variation of the centroid of the x-ray camera image. The centroid RMS variation is about 5 μm RMS in each direction, as compared to the ~400-μm plasma FWHM. We suspect that this variation is due in large part to thermal drift of the diagnostic system.

Temporal stability of the source has been studied in detail, since in a metrology application depending on dose, variation in pulse energy may masquerade as, or hide, a defect. Single-pulse data is obtained by using a box-car integrator connected to the power monitor (Fig. 4A.5) to capture and integrate every pulse; the resulting time series is then analyzed in various ways.

One can imagine two separate sources of temporal instability that are independent to zero order. One source is due to the plasma physics of the source itself; for instance, if the gas density in the pinch region varies pulse to pulse for some reason, this will affect the resulting pinched density and therefore the EUV output. An independent source of instability is the power system itself—if the electrical power to the pinch varies pulse by pulse, then so will the EUV output. Since the modulator circuit contains both capacitive and

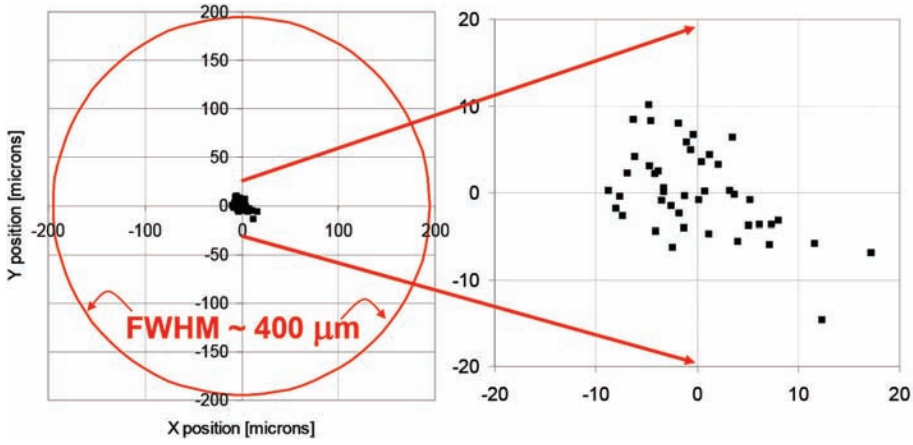

Figure 4A.9 Scatter plot showing source position over 44 hours of continuous operation (~300 million pulses). The source FWHM is shown in the left plot at ~400 μm. At the right is a blow up showing data points in detail. This measurement is limited by the stability of the mechanical alignment of the diagnostic beamline (reprinted from Ref. 15).

Downloaded From: https://www.spiedigitallibrary.org/ebooks/ on 09 Mar 2022
Terms of Use: https://www.spiedigitallibrary.org/terms-of-use

magnetic elements whose initial states might vary in uncontrolled ways (reflected power from the unmatched load can leave charge on the capacitors, for instance), we incorporated modifications to the power circuitry to reduce this effect.

The results for four interesting cases are show in Fig. 4A.10. Cases A(C) and B(D) are identical plasma conditions, with/without the modulator modification.

Table 4A.2 lists the results of several conditions, giving the DC voltage, pulse rate, and chamber pressure in millitorr. It is interesting to observe that, without the modulator modification, the best stability (least standard deviation in the pulse train) occurred at the lowest pressures; the worst, at the highest pressures. With the new modulator, this trend is reversed. Comparing similar conditions, the new modulator has better stability—nine times better at high pressure, but only a marginal improvement at the lowest pressure. The implication is that with the old modulator, the high-pressure instability was caused by the mismatched load; at low pressure, the load was better matched, and the remaining instability was due to plasma effects. The modifications substantially improved stability due to load mismatch, without

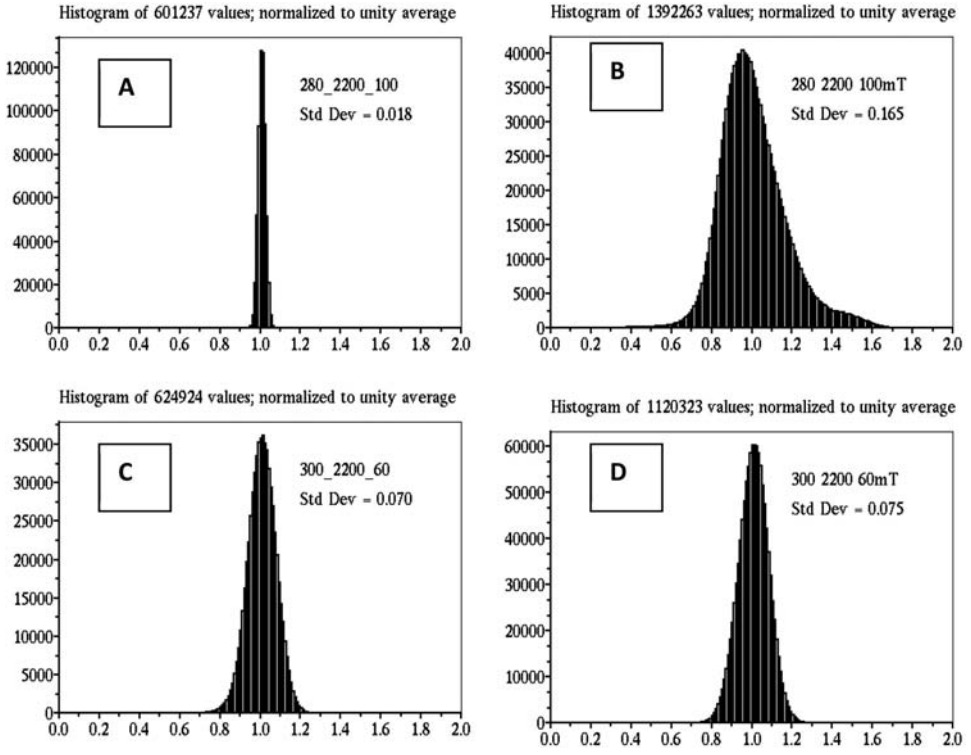

Figure 4A.10 Histograms showing statistics of consecutive pulses under different conditions (Left side – with upgraded modulator; right – without) (reprinted from Ref. 13).

Downloaded From: https://www.spiedigitallibrary.org/ebooks/ on 09 Mar 2022
Terms of Use: https://www.spiedigitallibrary.org/terms-of-use

Table 4A.2 Pulse statistics for various conditions. Statistics for the four cases (A, B, C, D) displayed as histograms in Fig. 4A.9 appear in the top and bottom row (reprinted from Ref. 13).

Conditions:	Standard Deviation:		Ratio:
V_Hz_mT	New	Old	Old/New
280_2200_100	A 0.0179	B 0.1651	9.20
280_1900_90	0.0190	0.0756	3.97
280_1900_70	0.0215	0.0804	3.74
280_1900_110	0.0223	0.1221	5.47
280_2200_80	0.0268	0.1009	3.76
300_2200_80	0.0359	0.0534	1.49
320_1900_100	0.0371	0.0773	2.08
320_1900_80	0.0402	0.0568	1.41
320_1900_60	0.0667	0.0876	1.31
300_2200_60	C 0.0705	D 0.0752	1.07

significantly affecting the low-pressure plasma effects. The improved performance observed with the upgraded modulator is significant since the optimum conditions for high brightness are at higher pressure. Typical single-pulse data under normal operating conditions have a relative standard deviation of 2% or less.

4A.4 Typical Installations

The EQ-10 has been commercially available since 2005,[7,8] and since then there have been approximately 20 sources installed worldwide. The applications vary among resist development,[9] resist outgassing,[10,11] mask blank inspection,[12] and various proprietary applications, including optics development and testing.

4A.5 Conclusions

The physics behind the electrodeless Z-pinch conspires to produce a simple and extremely stable EUV source, both temporally and spatially. As the industry moves towards HVM production levels, we expect further applications to appear as the industry knowledge base expands.

References

1. D. K. Smith, S. F. Horne, M. M. Besen, and P. A. Blackborow, "Inductively driven plasma light source," U.S. Patent No. 7,307,375 B2 (2007).
2. S. F. Horne, M. M. Besen, D. K. Smith, P. A. Blackborow, and R. D'Agostino, "Application of a high-brightness electrodeless Z-pinch EUV

Downloaded From: https://www.spiedigitallibrary.org/ebooks/ on 09 Mar 2022
Terms of Use: https://www.spiedigitallibrary.org/terms-of-use

source for metrology, inspection, and resist development," *Proc. SPIE*, **6151**, 61510P (2006) [doi: 10.1117/12.655696].
3. M. J. Partlow, M. M. Besen, P. A. Blackborow, R. Collins, D. Gustafson, S. F. Horne, and D. K. Smith, "Extreme-ultraviolet light source development to enable pre-production mask inspection," *J. Micro/Nanolitho. MEMS MOEMS* **11**(2), 021105 (2012) [doi: 10.1117/1.JMM.11.2.021105].
4. R. Wood, "Chaos: a real phenomenon in power electronics," *Proc. Fourth Annual IEEE Applied Power Electronics Conference and Exposition*, 13–17 March 1989, pp. 115–124 (1989).
5. S. F. Horne, F. M. Niell, M. J. Partlow, M. M. Besen, D. K. Smith, P. A. Blackborow, and D. Gustafson, "Development of a high-pulse-rate EUV source," *Proc. SPIE* **7271**, 72713A (2009) [doi: 10.1117/12.813765].
6. D. Gustfson, D. K. Smith, P. A. Blackborow, M. M. Besen, M. J. Patlow, and S. Horne, "Electrodeless Z-Pinch^{TM} EUV source for metrology applications," https://www.euvlitho.com/2013/P15.pdf.
7. G. Denbeaux, R. Garg, J. Waterman, C. Mbanaso, J. Netten, R. Brainard, Y.-J. Fan, L. Yankulin, A. Antohe, K. DeMarco, M. Jaffe, M. Waldron, and K. Dean, "Quantitative measurement of EUV resist outgassing," *Proc. SPIE* **6533**, 653318 (2007) [doi: 10.1117/12.737192].
8. G. Denbeaux, P. Naulleau, R. Garg, S. Horne, and M. Besen, "First use of the Energetiq 10W electrodeless EUV plasma source," 2005 International EUVL Symposium, 7–9 Oct., San Diego, California.
9. H. Yamamoto, T. Kozawa, S. Tagawa, H. B. Cao, H. Deng, and M. J. Leeson, "Polymer-structure dependence of acid generation in chemically amplified extreme ultraviolet resists," *Japanese J. Applied Physics*, **46**(2L), L142 (2007).
10. A. O. Antohe, C. Mbanaso, Y.-J. Fan, L. Yankulin, R. Garg, P. Thomas, G. Denbeaux, E. C. Piscani, and A. F. Wuest, "EUV resist outgassing: scaling to HVM intensity," *Proc. SPIE* **7271**, 727126 (2009) [doi: 10.1117/12.816555].
11. H. Oizumi, K. Matsumaro, S. Nomura, J. J. Santillan, T. Itani, T. Watanabe, N. Matsuda, T. Harada, and H. Kinoshita, "Relationships between EUV resist outgassing and contamination deposition at SELETE," *Proc. SPIE* **7969**, 796921 (2011) [doi: 10.1117/12.878571].
12. T. Kamo, T. Terasawa, T. Yamane, H. Shigemura, N. Takagi, T. Amano, K. Tawarayama, M. Nozoe, T. Tanaka, O. Suga, and I. Mori, "Evaluation of EUV mask defect using blank inspection, patterned mask inspection, and wafer inspection," *Proc. SPIE* **7969**, 79690J (2011) [doi:10.1117/12.879551].
13. S. F. Horne, "Improvements in pulse-to-pulse stability to the EQ-10 Electrodeless Z-Pinch EUV Source," *Proceedings of the SEMATECH*

Downloaded From: https://www.spiedigitallibrary.org/ebooks/ on 09 Mar 2022
Terms of Use: https://www.spiedigitallibrary.org/terms-of-use

Extreme Ultraviolet (EUV) Lithography Symposium, 17–20 Oct., Kobe, Japan (2010).
14. S. F. Horne, P. Blackborow, M. M. Besen, M. J. Partlow, D. Gustafson, and M. Goldstein, "Metrology sources for EUV lithography," CLEO: Science and Innovations 2013, *OSA Technical Digest* (online), paper JW1D.3 (2013).
15. S. F. Horne, M. J. Partlow, D. S. Gustafson, M. M. Besen, D. K. Smith, and P. A. Blackborow, "High brightness electrodeless Z-Pinch EUV source for mask inspection tools," *Proc. SPIE* **8322**, 83222M (2012) [doi: 10.1117/12.916476].

Stephen F. Horne has been the Senior Scientist at Energetiq Technology, Inc. since it was founded in 2004. He received his Ph.D. in plasma physics from the University of Wisconsin.

Matthew M. Besen is President and CTO of Energetiq Technology, a technical light source company. He holds B.S. and M.S. degrees in mechanical engineering from the Massachusetts Institute of Technology.

Paul A. Blackborow is Co-Chair of Energetiq Technology, Inc., a high-tech equipment company. He holds an M.A. degree in engineering from Cambridge University.

Downloaded From: https://www.spiedigitallibrary.org/ebooks/ on 09 Mar 2022
Terms of Use: https://www.spiedigitallibrary.org/terms-of-use

Ron Collins is the Director of Engineering at Energetiq Technology, Inc., a high-tech equipment company. He holds an A.S.M.E. degree in engineering from The University of Massachusetts at Lowell.

Debbie Gustafson is the Chief Executive Officer of Energetiq Technology, Inc., a high-tech equipment company. She holds a B.S. in mechanical engineering from Southeastern Massachusetts University (UMass Dartmouth) and an M.B.A. in management from Bentley University. Debbie also serves on the board of directors at WEST and the North American Advisory Board at SEMI.

Matthew J. Partlow is the Principal Scientist of Energetiq Technology, Inc., a high-tech equipment company. He holds a Ph.D. in physics from Stony Brook University.

Donald K. Smith is Co-Chair of Energetiq Technology, Inc., a company he co-founded in 2004. Dr. Smith has been a founder of three technology companies, including ASTeX (now a division of MKS) and Compact Instruments (also acquired by MKS). He served as Senior Vice President at ASTeX, President of Compact Instruments, and Vice President and CTO at MKS, before becoming President and Chairperson of Energetiq in 2004. Dr. Smith is an electrical engineer and plasma physicist, and an inventor of 46 U.S. patents. Before entering the semiconductor equipment industry, he was a Research Scientist in fusion-related plasma physics at MIT. He holds a B.S. in physics from Davidson College and a Ph.D. in electrical engineering from the University of Wisconsin.

Downloaded From: https://www.spiedigitallibrary.org/ebooks/ on 09 Mar 2022
Terms of Use: https://www.spiedigitallibrary.org/terms-of-use

Chapter 4B
High-Brightness LDP Source for Mask Inspection

Yusuke Teramoto
BLV Licht- und Vakuumtechnik GmbH, Aachen, Germany

4B.1 Introduction
4B.2 LDP System Configuration
4B.3 EUV Brightness and Power
4B.4 EUV Spectrum and Out-of-Band Radiation
4B.5 Stability and Reliability
4B.6 Source Cleanliness
4B.7 Summary
Acknowledgments
References

4B.1 Introduction

A laser-assisted discharge-produced plasma (LDP) source is being developed as an EUV source in mask inspection tool at BLV Licht- und Vakuumtechnik GmbH, Germany in cooperation with Fraunhofer Institute for Laser Technology (ILT), Germany, under the management of Ushio Inc., Japan. This unique system, in which a small laser is used to create the plasma that is then heated by a high-current discharge to obtain the EUV-emitting plasma, is based on the technology developed for the alpha- and beta-level EUV source for EUV lithography scanners.[1] However, the changes made to the system architecture and operational parameters turned this technology into a high-brightness EUV source for mask inspection.

In LDP, both the laser beam and the electrical discharge are used to create the EUV-emitting plasma. The LDP source consists of several modules, such as the source head module, the tin circulation module, the capacitor module, the laser module, the high-voltage power supply, and the debris shield and source control module.[2] The most important module is the so-called source head module where EUV light generation takes place. In the source head module [Fig. 4B.1(a)], two disk-shaped electrodes rotate through the liquid tin

Downloaded From: https://www.spiedigitallibrary.org/ebooks/ on 09 Mar 2022
Terms of Use: https://www.spiedigitallibrary.org/terms-of-use

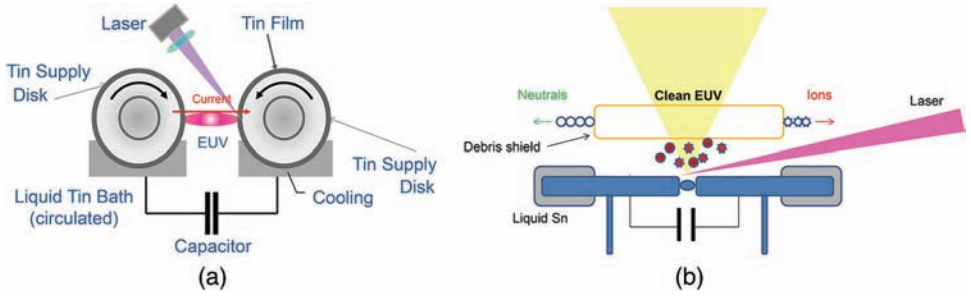

Figure 4B.1 Conceptual diagrams of a LDP source configuration: (a) front view and (b) top view (reprinted from Ref. 22).

(Sn) baths, which are connected to the energy storage capacitors. While the electrodes rotate through the Sn baths, the surfaces of the electrodes are covered by liquid Sn. The capacitors are charged to a specified voltage prior to the discharge. A combined laser beam provided by two Nd:YAG lasers[3,4] then irradiates the cathode to create a weak Sn plasma. The Sn plasma bridges the anode and cathode, and consequently ignites the discharge. A pulsed current of approximately 15 kA in peak and a few hundreds of nanoseconds in pulse duration flows into the plasma, causing the plasma density and temperature increase, and the EUV emission to occur. The EUV emission volume depends on how the laser and discharge parameters are tuned: a relatively large volume is used to gain radiation energy (mJ, for lithography purposes) and a small volume is used to enhance brightness (mJ/mm^2/sr, for mask inspection purposes). Pulse repetition rate is usually between a few kHz and a few tens of kHz. Some reports have shown the capability of operation at ~40–100 kHz.[5]

As mentioned above, the surfaces of the electrodes are always covered by liquid Sn. Such a feature eliminates the need for complex spatial and timing synchronization between the target and laser irradiation, as a Sn-covered electrode acts as an unlimited fuel supply, making a LDP source a highly robust and stable system.

As is commonly known,[6] Sn is the most efficient material for radiation having a wavelength of 13.5 nm. The conversion efficiency from the input energy to the output energy is much higher than that for xenon (up to 1%[7]).

Liquid Sn also works as the electrical conductor. Electrical power is applied to the electrodes through liquid Sn. Therefore, despite the rotating electrodes, there is no moving mechanical conductor in the LDP source, which potentially leads to the short lifetime.

Liquid Sn in the Sn baths is always circulating. Liquid Sn is supplied to the source head module from the Sn circulation modules, which are independently connected to the anode and cathode. The Sn circulation module consists of a reservoir that contains molten Sn, pumps that circulate liquid Sn, heaters that melt Sn in the initial state, and a cooling system that

Downloaded From: https://www.spiedigitallibrary.org/ebooks/ on 09 Mar 2022
Terms of Use: https://www.spiedigitallibrary.org/terms-of-use

cools the temperature of liquid Sn. The thermal conductivity of liquid Sn is 26 W/mK at 300 °C and much higher than that of water (0.6 W/mK at 20 °C). Part of the heat (almost 50%) created by the discharge operation is absorbed by liquid Sn and transferred to the Sn circulation modules. By activating the cooling, the liquid Sn temperature is kept constant in the reservoir.

Debris mitigation is a subject of high importance on all Sn-fueled EUV sources since particles and metal vapors are emitted from the discharge region and can cause degradation of the optical elements by deposition. Ions are also emitted from the discharge region and can sputter optical elements as well. In order to provide debris-free EUV photons, the LDP source employs a very efficient debris mitigation system or debris shield. A conceptual diagram of the debris shield is shown in Fig. 4B.1(b). The debris shield captures all of the particles and vapors, and captures or slows down most of the ions. Several components are used in the debris shield. One of them is Ar gas. The local pressure inside the debris shield is maintained higher than in the other region to provide high overall optical transmission and to maximize debris mitigation performance.

4B.2 LDP System Configuration

The LDP system comes with several cabinets, as shown in Fig. 4B.2. The main cabinet (shown in the middle) is installed in the clean room and is directly integrated to the inspection metrology tool; the sub-cabinets, such as power distributor, control module, and chiller are installed in the sub-fab or gray room. The total footprint depends on the cabinet layout. When the L-shaped layout is employed (as in Fig. 4B.2), the footprint is $7.4 \times 4.4\ m^2$. The LDP

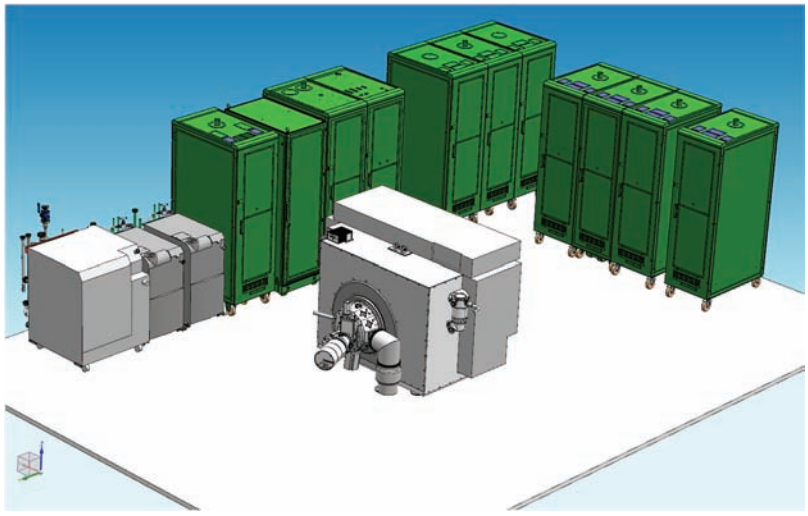

Figure 4B.2 Overall cabinet layout example of a LDP system.

Downloaded From: https://www.spiedigitallibrary.org/ebooks/ on 09 Mar 2022
Terms of Use: https://www.spiedigitallibrary.org/terms-of-use

system is designed for up to 10-kHz steady-state operation and requires peak electrical power up to 75 kVA. The number of sub-cabinets will be decreased in the future by combining several functions that are currently distributed in several cabinets into one cabinet.

Figure 4B.3 shows the main cabinet. The main body of the cabinet contains high-voltage components, such as the source head module, capacitor module, and Sn circulation module. All of the modules can be easily replaced at the time of maintenance. The vacuum chamber placed in front of the main cabinet is the interface to the inspection tool. The main cabinet has the size of $2.4 \times 2.0 \times 2.0$ m^3.

Figure 4B.4 shows the metrology setup used to evaluate the system's performance in terms of brightness and EUV power. In order to calculate brightness, a calibrated inband EUV energy monitor measures inband EUV radiation energy, and an inband EUV camera captures and analyzes the emission image. The monitor is placed after the debris shield to measure the debris-free EUV power, whereas the camera is placed in front of the debris shield (plasma side).

The EUV energy monitor can be replaced with the other metrology tools, such as an EUV spectrometer, an EUV beam analyzer, or an out-of-band (OoB) energy monitor. This energy monitor consists of a Zr-coated Si photodiode, a Mo/Si multilayer mirror, and a solid-angle-limited aperture. It is calibrated on the Xe-source-based calibration test bench with an energy monitor calibrated at the Physikalisch-Technische Bundesanstalt (PTB) synchrotron facility.[7]

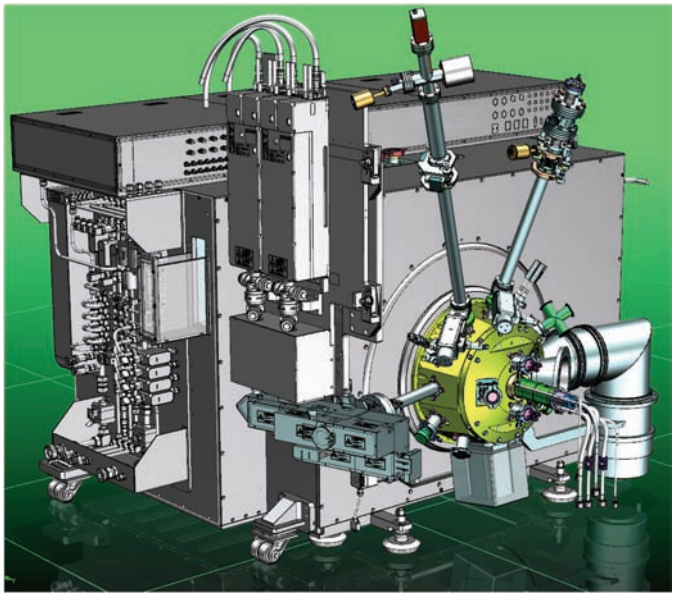

Figure 4B.3 Illustration of the main cabinet of LDP source (reprinted from Ref. 21).

Downloaded From: https://www.spiedigitallibrary.org/ebooks/ on 09 Mar 2022
Terms of Use: https://www.spiedigitallibrary.org/terms-of-use

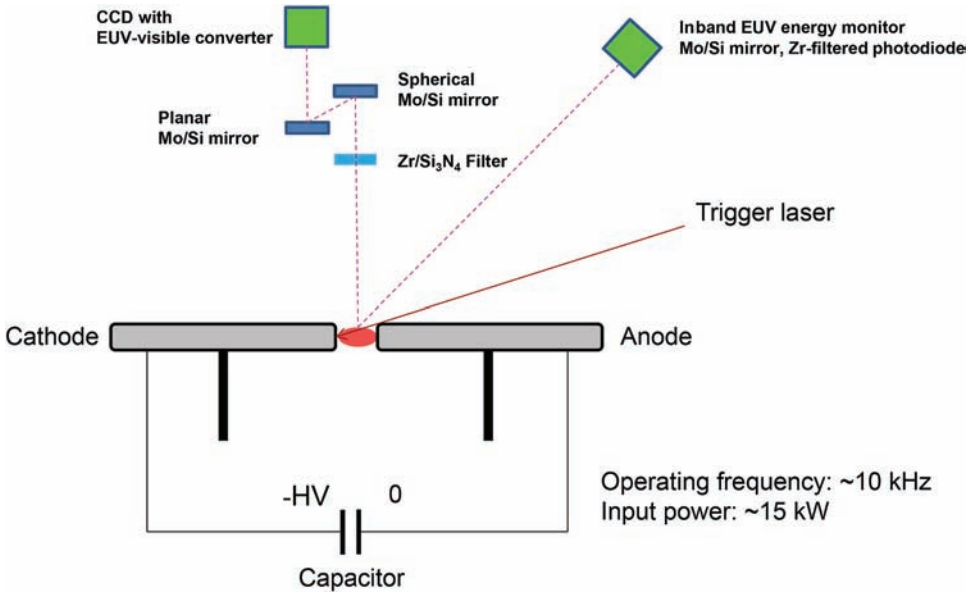

Figure 4B.4 Arrangement of the brightness measurement tools (reprinted from Ref. 22).

The EUV camera consists of a CCD sensor coated with an EUV-visible scintillator, a planar Mo/Si multilayer mirror, a spherical Mo/Si multilayer mirror, a Zr/Si_3N_4 filter, and an aperture. Its magnification is determined by the ratio of the optical length between the spherical mirror and CCD to the optical length between the spherical mirror and the plasma.

The EUV spectrometer consists of an entrance slit, a flat-field grating (Hitachi, 1200 lines/mm), and a back-illuminated CCD sensor (Roper Scientific, Model NTE/CCD-1340/400-EMB). The EUV beam analyzer is a structure that allows one to observe the expanding EUV beam, which is seen after the debris shield. It consists of a CCD camera and Zr-coated YAG crystal that converts EUV light into visible light. The OoB monitor consists of a set of bandpass filters and a water-cooled calorimeter. By selecting the filter, radiation power in the specific wavelength range can be measured.

There are three types of mask inspection in the EUVL processes that utilize 13.5-nm-wavelength radiation: actinic blank inspection (ABI), actinic patterned mask inspection (APMI), and the actinic Aerial Image Measurement System (AIMS).[8] Since EUV light is utilized in a different way in these inspections, the requirements to the EUV source are all slightly different. However, what is common in these inspections is that they require source brightness (in $W/mm^2/sr$) instead of power (W or W/sr) as is required in the lithography source. The requirements for ABI, APMI, and AIMS as provided by inspection tool makers are summarized in Table 4B.1. The development of LDP source technology aims to fulfill all of these requirements.

Downloaded From: https://www.spiedigitallibrary.org/ebooks/ on 09 Mar 2022
Terms of Use: https://www.spiedigitallibrary.org/terms-of-use

Table 4B.1 Source requirements for ABI, APMI and AIMS.[9–11]

	ABI	APMI	AIMS
Etendue (mm^2sr)	~0.02	0.01	
Brightness ($W/mm^2/sr$)	>30	>20	>30 (minimum) >100 (target)
Energy stability	<1% for >1 hour (10-ms integrated energy)		<3.5% (3σ, pulse-to-pulse)
Pulse repetition rate (kHz)		>10	
Duty cycle		>95% (minimum burst >15 s)	
Availability	14 days without maintenance	>95%	

4B.3 EUV Brightness and Power

A typical image of inband EUV emission (λ = 13.5 nm, bandwidth 2%) and its vertical and horizontal profiles are shown in Fig. 4B.5. This image was taken at 10 kHz in continuous operation mode. A typical plasma diameter is about 200 μm, and its length is 450 μm, both in FWHM. The cathode is on the right-hand side in this image. Since LDP is triggered by the laser beams, its diameter is much smaller than that of a typical Xe-discharge plasma.[12] And because there is no dielectric structure between the electrodes and around the plasma, the plasma can be observed from the angle perpendicular to the plasma axis, a capability that is unique to the LDP source. Although the point of peak brightness is located

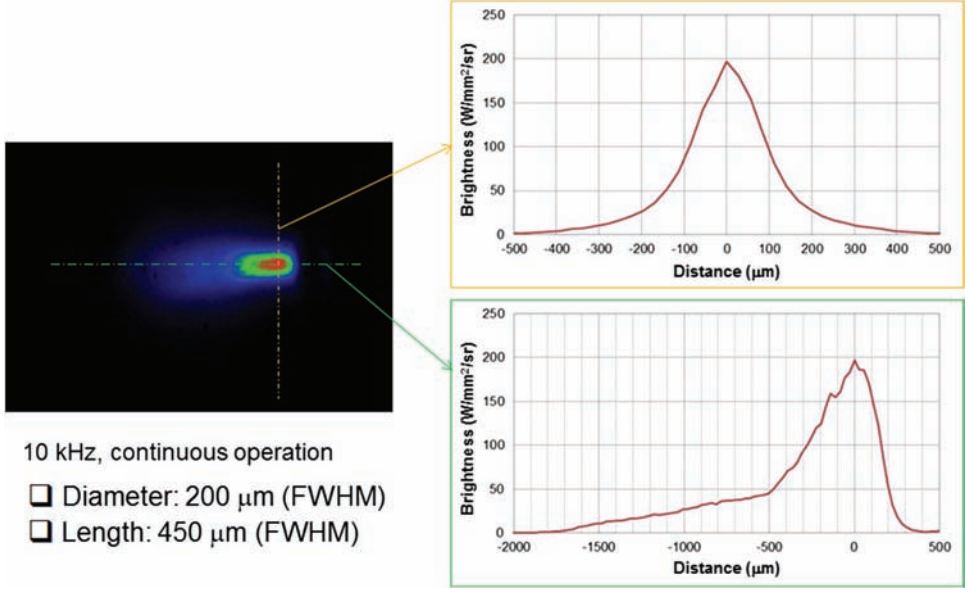

Figure 4B.5 Inband EUV plasma and its vertical (top) and horizontal (bottom) brightness profiles, under continuous operation at 10 kHz (reprinted from Ref. 22).

Downloaded From: https://www.spiedigitallibrary.org/ebooks/ on 09 Mar 2022
Terms of Use: https://www.spiedigitallibrary.org/terms-of-use

near the cathode surface, it is still a few hundreds of microns away from the surface. Therefore, the radiation emitted from the plasma can be utilized by the inspection tool at a large collection angle without obscuration by the electrodes. Note that the shape of the plasma varies depending on the condition of the lasers. By tuning the laser parameters, the system can be tuned to maximize the brightness, or to maximize the power by enlarging the plasma volume.

Inband EUV brightness in W/mm^2/sr is calculated by calibrating the inband EUV image with the inband EUV energy measured by the monitor. Figure 4B.6 shows the area-averaged brightness obtained after the debris shield as a function of discharge repetition rate. Each data point shows average data in time and area (200 μm in diameter), showing a linear increase of brightness with pulse repetition rate up to 9.5 kHz. The highest debris-free brightness obtained after the debris shield was 145 W/mm^2/sr, which corresponds to 225 W/mm^2/sr of peak brightness at the plasma. The brightness shown in Fig. 4B.6 is 64% of the peak brightness at the plasma. This reduction is caused by the attenuation of the debris shield (transmission is 73%, see Section 4B.6) and the aerial averaging of the brightness within the circle of 200 μm in diameter.

Although the LDP source is usually tuned to maximize the brightness (W/mm^2/sr), the inband EUV output power (W/2πsr) is also high compared to that of other source technologies.[13,14] Typical inband EUV output power obtained after the debris shield is ~60–70 W/2πsr at 3000 Hz. Output power linearly increases with increasing discharge repetition rate and reaches approximately 200 W/2πsr at 9000 Hz, as shown in Fig. 4B.7. Inband EUV output power at the plasma is ~260–300 W/2πsr, taking the transmission of the debris shield into account. The conversion efficiency (CE), calculated by

$$\mathrm{CE} = \frac{\text{In} - \text{band EUV power [W/2}\pi\text{sr]}}{\text{Discharge energy } \left[\frac{\text{J}}{\text{pulse}}\right] \times \text{ pulse repetition frequency [Hz]}} \times 100\ [\%] \tag{4B.1}$$

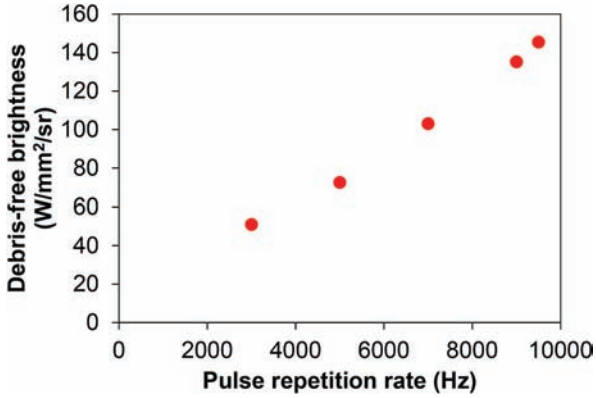

Figure 4B.6 Brightness after the debris shield versus pulse repetition rate (reprinted from Ref. 21).

Downloaded From: https://www.spiedigitallibrary.org/ebooks/ on 09 Mar 2022
Terms of Use: https://www.spiedigitallibrary.org/terms-of-use

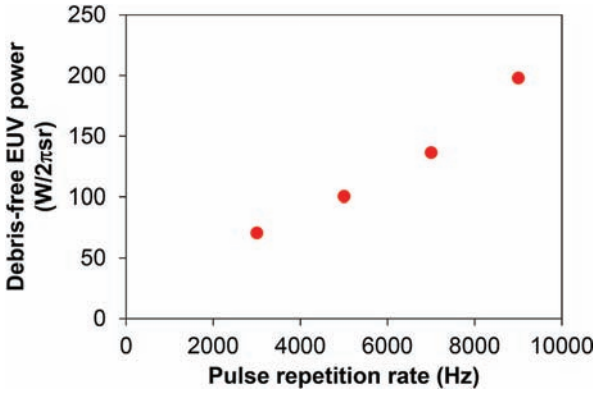

Figure 4B.7 Output power after the debris shield versus pulse repetition rate.

at the plasma, is therefore ~1.8–2.0%. The current CE is somewhat lower than that of the lithography source, which was reportedly as high as 2.5%.[2] Since the inspection source does not require power but instead requires brightness, the parameters are tuned in order to maximize the brightness. Therefore, the plasma density is made higher than that of the lithography source, and the resultant CE becomes somewhat lower.

4B.4 EUV Spectrum and Out-of-Band Radiation

A typical EUV spectrum measured after the debris shield is shown in Fig. 4B.8. Since the LDP plasma is still a discharge-produced plasma, where the major plasma heating is done by electrical discharge, the ion density of the plasma is considered to be as low as the gas-discharge-produced plasma.[15,16] Therefore, the LDP spectrum is very similar to that of the CO_2-laser-driven laser-produced plasma (LPP),[17] of which ion density is much lower than the YAG-laser-driven LPP.

The OoB radiation is an important consideration as some wavelength regions might influence the performance of the inspection tool. The OoB radiation power measurements were carried out using a variety of bandpass filters. Figure 4B.9 is a summary of the OoB radiation power measurements,

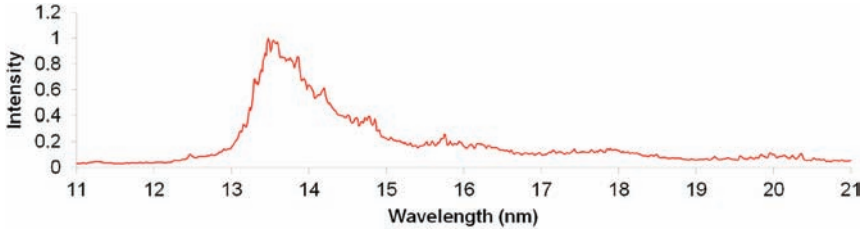

Figure 4B.8 EUV spectrum of the LDP source measured after debris shield (reprinted from Ref. 19).

Downloaded From: https://www.spiedigitallibrary.org/ebooks/ on 09 Mar 2022
Terms of Use: https://www.spiedigitallibrary.org/terms-of-use

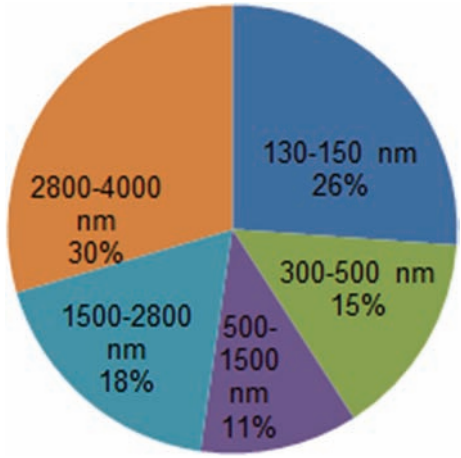

Figure 4B.9 Results of OoB radiation power measurements after the debris shield.

including the relative radiation power in each wavelength region with respect to inband EUV (2% bandwidth around 13.5 nm). Note that the power in $\lambda \sim 150$–300 nm was not well resolved in the experiment. Since this measurement was taken after the debris shield, the first collector optics received this radiation. However, according to the previous report,[18] most of the OoB radiation is not focused by the collector optics (only 5% with respect to inband EUV measured after intermediate focus, $\lambda \sim 130$–500 nm) and therefore is not transferred to the optical column of the inspection tool.

4B.5 Stability and Reliability

One of the unique features of the LDP source is dose energy stabilization control. EUV energy and capacitor voltage are monitored and controlled on a pulse-to-pulse basis. Figure 4B.10 shows the variations in pulse energy and dose energy stabilities with discharge repetition rate. The dose energy here is defined as the moving average of 40 pulses. Pulse energy stability remains at approximately 10% with increasing discharge repetition rate; there is no significant difference in when feedback control is activated versus when it is not. On the other hand, dose energy stability has a significant improvement when feedback control is on—close to 0.1% (1σ)—whereas, when feedback control is not activated, it increases to approximately 2% (1σ). Increasing discharge pulse repetition rate does not negatively influence dose energy stability as it remains constant throughout a wide range of pulse repetition rates.

Figure 4B.11 shows the relative displacement (in microns) of the emission center of gravity during 5 min. measured at 3 kHz. In this experiment, a second inband EUV camera was placed on the optical axis, after the debris shield, with 5-ms exposure time in order to study the position stability of EUV

Downloaded From: https://www.spiedigitallibrary.org/ebooks/ on 09 Mar 2022
Terms of Use: https://www.spiedigitallibrary.org/terms-of-use

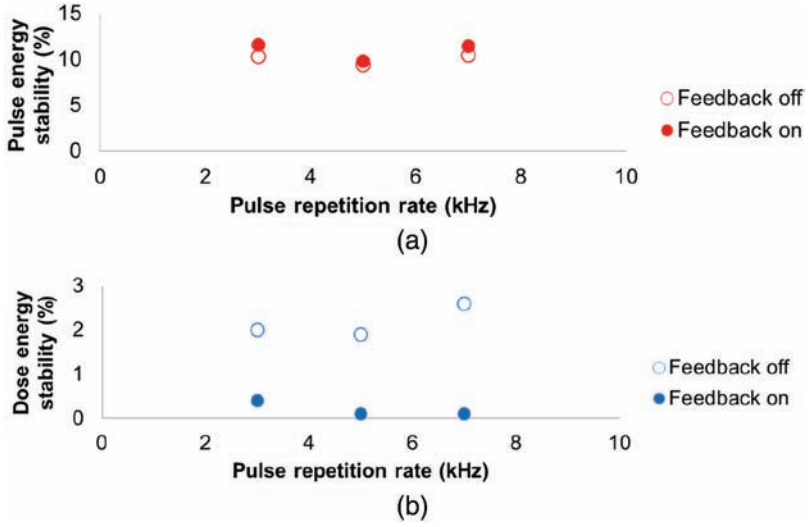

Figure 4B.10 Variation of (a) pulse EUV energy stability and (b) dose EUV energy stability with discharge pulse repetition rate (reprinted from Ref. 23).

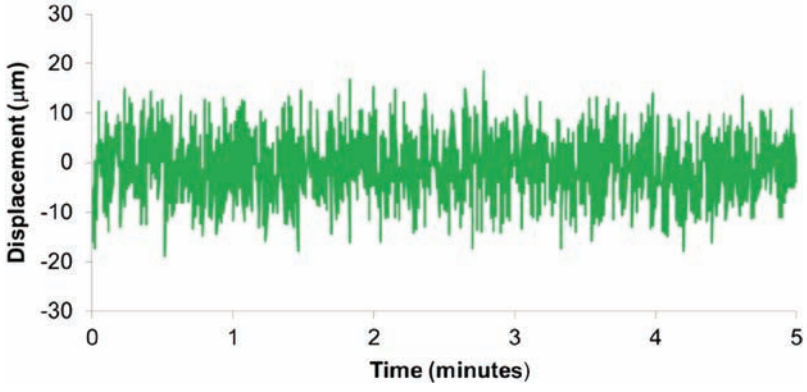

Figure 4B.11 Position stability of EUV emission (reprinted from Ref. 23).

emission. The result shows a standard deviation of 6 μm, representing 3% of the plasma's diameter (200 μm).

Long-term stability is as important as the other requirements. When it comes to insertion into the lithography process, the system must operate for a sufficiently long time period in a stable manner. Although it is difficult to evaluate such long-term stability only via the laboratory activities, many demonstrations at various power levels were made to evaluate the long-term source stability. Figure 4B.12 shows a summary of the long-term demonstrations made up until the time of writing this chapter, including one short-term demonstration at very high brightness.

Downloaded From: https://www.spiedigitallibrary.org/ebooks/ on 09 Mar 2022
Terms of Use: https://www.spiedigitallibrary.org/terms-of-use

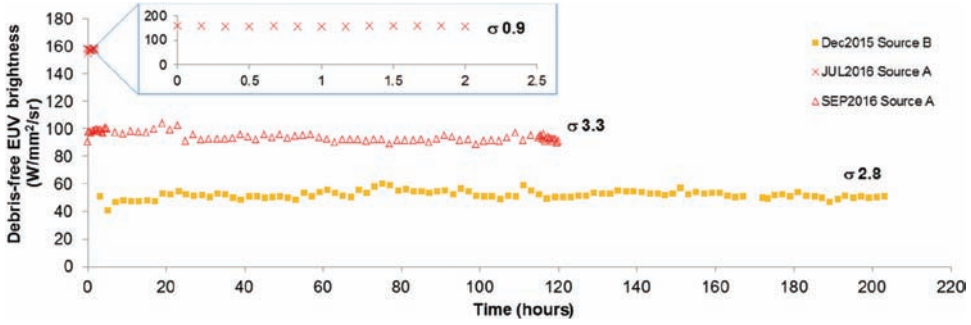

Figure 4B.12 Results of long-term reliability tests (adapted from Ref. 21).

Because it is very important to study and improve the reliability, two machines were used to obtain the basic performance stability as well as system-level performance stability. Source A in Fig. 4B.12 refers to the laboratory-grade source, and Source B is the semi-product-level source. On Source A, a non-interrupted operation was demonstrated for 120 hours at the brightness level of 95 W/mm^2/sr. In addition, in order to study the reliability at higher brightness levels and to show the future scalability, a demonstration was done for 2 hours at the brightness level of approximately 160 W/mm^2/sr. Although the system was operated at an input power of approximately 15 kW, the brightness was constant over time, and a very stable system operation was confirmed. On Source B, a non-interrupted operation was demonstrated for 210 hours (approximately 9 days) at a brightness level of approximately 50 W/mm^2/sr. Although the brightness was not as high as that of Source A, there is a straightforward way to increase the output brightness on Source B, mainly by increasing the efficiency and discharge repetition rate.

4B.6 Source Cleanliness

The effectiveness of the debris shield in the LDP source was previously proven in the beta-level EUV source used in the EUV scanner. The mask-inspection LDP source employs a technology that is similar to the previous version but modified. The debris shield must mitigate debris, but also must allow only minimal loss of the EUV light. The debris shield is usually customized to this requirement. In this section, examples of the optical transmission and debris mitigation performance of the currently used debris shield on the laboratory-grade LDP source are provided.

The optical transmission of the shield was measured by capturing the entire EUV beam after the debris shield using the EUV beam analyzer mentioned in Section 4B.4. The image example obtained with the shield is shown in Fig. 4B.13. It was found from the analysis that the shield has optical transmission of 73%. There is a structure like a bundle of thin blades inside the

Downloaded From: https://www.spiedigitallibrary.org/ebooks/ on 09 Mar 2022
Terms of Use: https://www.spiedigitallibrary.org/terms-of-use

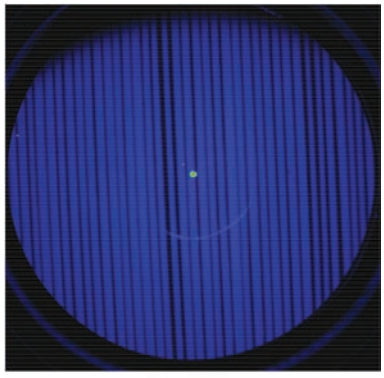

Figure 4B.13 EUV emission image observed after the debris shield (reprinted from Ref. 24).

debris shield. As seen in Fig. 4B.13, some blades are not straight and therefore shadow the EUV beam. Optical transmission can be further improved by improving the flatness of the blades.

In order to evaluate the cleanliness of the LDP source, several ruthenium (Ru) mirror samples were exposed under different conditions. The intention was to study how Sn deposition and Ru sputtering caused by ions would evolve with exposing times (more accumulated pulses).

Figure 4B.14 shows the schematics of the experimental setup. Ru samples were placed 631 mm away from the plasma, downstream from the debris shield, and perpendicular to the optical axis. After the exposure, the samples were analyzed by x-ray fluorescence (PANalytical, model Axios) in order to measure Sn deposition and Ru sputtering.

The Ru mirror samples were exposed at 7 kHz for the different numbers of pulses in order to study how Sn deposition and Ru sputter would evolve. Figure 4B.15 shows the evolution of Ru and Sn thicknesses over time. The Ru layer was sputtered at a constant rate of ~3–5 nm/GPulse at this frequency (7 kHz), while the Sn layer did not grow over time and remained <0.05 nm. Note that the Ru sputter rate has a weak relationship to discharge frequency and is normally ~1–3 nm/GPulse.[19]

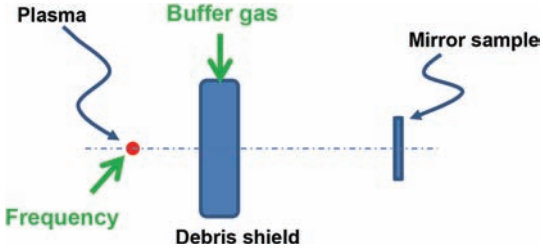

Figure 4B.14 Schematics of experimental setup for mirror sample exposure (reprinted from Ref. 25).

Downloaded From: https://www.spiedigitallibrary.org/ebooks/ on 09 Mar 2022
Terms of Use: https://www.spiedigitallibrary.org/terms-of-use

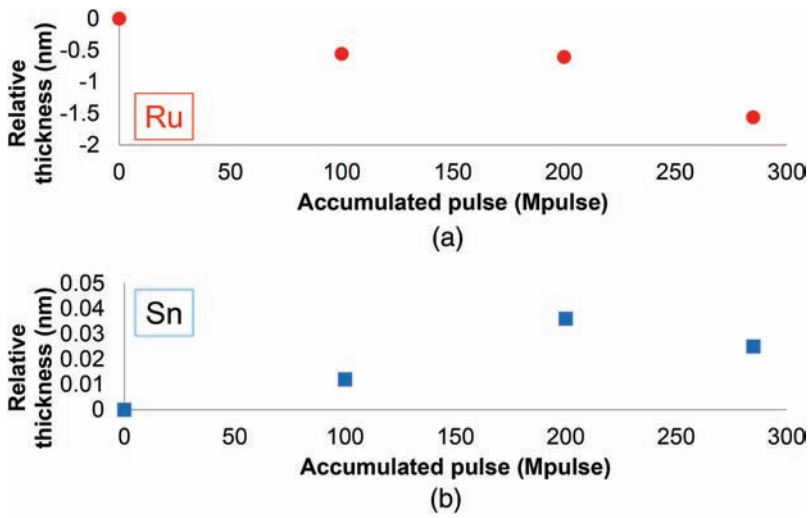

Figure 4B.15 Variation of (a) Ru and (b) Sn relative thickness with accumulated pulses (reprinted from Ref. 23).

Although the collector optics are not part of the LDP source at the moment, the previously obtained experimental data on the collector lifetime assessment shows that the collector lifetime is more than 3.5 months at 16.2B pulses.[2] Figure 4B.16 shows the trend of inband EUV power measured after the intermediate focus (IF) obtained at a beta-level LDP source integrated with the lithography scanner, where a very similar debris mitigation principle was employed. A nested grazing-incidence Ru collector was used in the source. After 3.5 months of use, in which 1500 hours were used in wafer production, the collector reflectivity dropped by 15%, as was derived from the power measured after the IF.

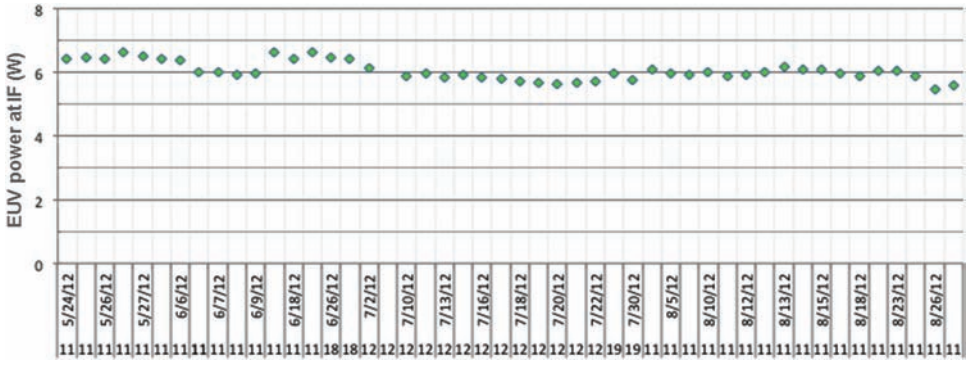

Figure 4B.16 Lifetime of a grazing-incidence Ru collector obtained in a lithography source (reprinted from Ref. 2 with permission).

Downloaded From: https://www.spiedigitallibrary.org/ebooks/ on 09 Mar 2022
Terms of Use: https://www.spiedigitallibrary.org/terms-of-use

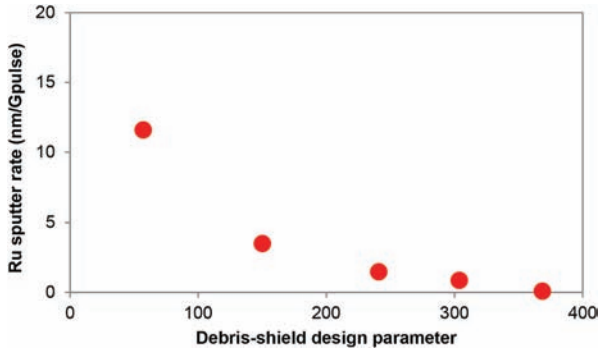

Figure 4B.17 Ru sputter rate as a function of a parameter change within the debris shield (reprinted from Ref. 21).

According to the dedicated study, it was confirmed that the Ru sputter rate can be further decreased to less than 1 nm/GPulse, as shown in Fig. 4B.17. This figure shows that the Ru sputter rate improved by a factor of 13 due to the design change of the debris shield from 11.6 nm/GPulse to 0.9 nm/GPulse.

Not only a grazing-incidence Ru mirror, but also a Mo/Si multilayer mirror can be used in the mask inspection tool. In order to assess the damage to the Mo/Si mirror, a sample was placed after the debris shield and exposed for 518M pulses at 6 kHz. Figure 4B.18 shows TEM images of the unexposed and the exposed areas of the Mo/Si mirror sample. From the analysis, it was

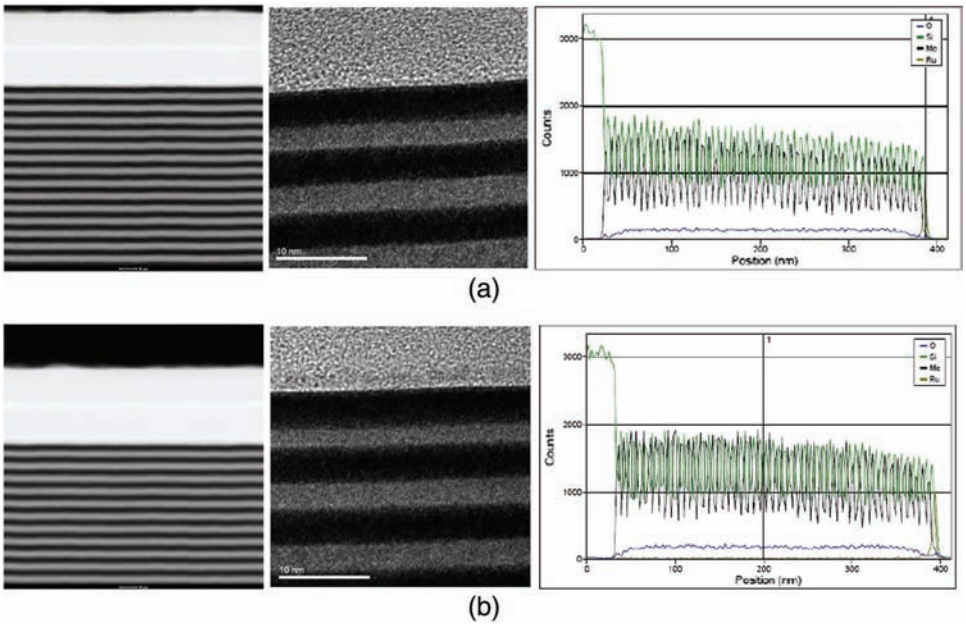

Figure 4B.18 TEM images of (a) the unexposed area and (b) the exposed area of the Mo/Si mirror sample (reprinted from Ref. 21).

Downloaded From: https://www.spiedigitallibrary.org/ebooks/ on 09 Mar 2022
Terms of Use: https://www.spiedigitallibrary.org/terms-of-use

concluded that both sputtering of the top layer and deposition of Sn were negligible. In addition, it was clear that individual Mo/Si layers were clearly identified with clear interlayer borders. This means that interlayer diffusion did not occur after an exposure of one day.

4B.7 Summary

The LDP source developed by BLV Licht- und Vakuumtechnik GmbH has shown sufficiently high brightness for use in actinic mask inspection tools. The peak brightness was as high as 225 W/mm^2/sr at the plasma level, and the area-averaged, debris-free brightness obtained after the debris shield was 145 W/mm^2/sr. Since the output power is also high due to Sn being the radiating material (the most efficient material for $\lambda = 13.5$ nm radiation), and the plasma volume is relatively large, the LDP source can be also used in the other applications such as an exposure beam line.[20] Dose energy stability of better than 0.1% (1σ) was achieved when the feedback control was activated. Position stability was confirmed to be 6 μm (1σ) at 3 kHz with the exposure time of 5 ms. Cleanliness has also been proven by the sample exposures using both Ru single-layer and Mo/Si multilayer mirror samples. Long-term demonstrations up to 9 days were carried out without interruption.

The important development items for this mask inspection source are system reliability, component lifetime, brightness stability, and system footprint. BLV is continuing their work on each development item to satisfy the future demands of mask inspection tools.

Acknowledgments

The author would like to thank the development team at BLV Licht- und Vakuumtechnik GmbH in Aachen, Germany (Bárbara Santos, Guido Mertens, Margarete Kops, and Ralf Kops), the development team at Ushio Inc., Japan (Hironobu Yabuta, Akihisa Nagano, Yuta Taniguchi, Noritaka Ashizawa, Takahiro Shirai, and Kunihiko Kasama) for the technical contributions to the data shown in this article. In addition, the author would like to thank Klaus Bergmann and Alexander von Wezyk at Fraunhofer ILT in Aachen, Germany for the development cooperation.

References

1. M. Yoshioka, Y. Teramoto, J. Jonkers, M. Schürmann, R. Apetz, V. Kilian, and M. Corthout, "Tin DPP source collector module (SoCoMo) ready for integration into Beta scanner," *Proc. SPIE* **7969**, 79691G (2011) [doi: 10.1117/12.879386].
2. M. Yoshioka, "Progress on laser assisted discharge produced plasma (LDP) EUV light source technology," 2012 International Symposium on

Downloaded From: https://www.spiedigitallibrary.org/ebooks/ on 09 Mar 2022
Terms of Use: https://www.spiedigitallibrary.org/terms-of-use

Extreme Ultraviolet Lithography, Sep. 30 to Oct. 4, 2012, Brussels, Belgium.
3. Y. Teramoto, B. Santos, G. Mertens, R. Kops, M. Kops, A. von Wezyk, K. Bergmann, H. Yabuta, A. Nagano, N. Ashizawa, Y. Taniguchi, T. Shirai, and K. Kasama, "Sn-fueled high-brightness compact EUV light source," in *High-Brightness Sources and Light-Driven Interactions*, OSA Technical Digest (online), Optical Society of America, paper ES4A.1 (2016).
4. F. Küpper, J. Vieker, K. Bergmann, Y. Teramoto, and J. Jonkers, "Power scaling of the Xtreme LDP EUV Source," 2012 International Symposium on Extreme Ultraviolet Lithography, Sep. 30 to Oct. 4, 2012, Brussels, Belgium.
5. E. Wagenaars, F. Küpper, J. Klein, W. Neff, M. Damen, P. Wel, D. Vaudrevange, and J. Jonkers, "Power scaling of an extreme ultraviolet light source for future lithography," *Applied Physics Letters* **92**, 181501 (2008).
6. G. O'sullivan, T. Cummins, C. O'Gorman, T. Donnelly, P. Dunne, P. Hayden, D. Kos, O. Maguire, F. O'Reilly, and E. Sokel, "Conversion efficiency of laser-produced plasmas at 13.5 nm and colliding plasmas as EUV sources," 2016 International Workshop on EUV and Soft X-Ray Sources, November 7–9, 2016, Amsterdam, The Netherlands.
7. *EUV Sources for Lithography*, V. Bakshi, Ed., SPIE Press, Bellingham, Washington (2006) [doi: 10.1117/3.613774].
8. S. Huh, P. Kearney, S. Wurm, F. Goodwin, H. Han, K. Goldberg, I. Mochi, and E. Gullikson, "EUV actinic defect inspection and defect printability at sub-32 nm half-pitch," *Proc. SPIE* **7470**, 74700Y (2009) [doi: 10.1117/12.835196].
9. O. Khodykin, "Actinic patterned mask inspection," 2014 International Workshop on EUV and Soft X-ray Sources, Dublin, Ireland, November 3–6, 2014.
10. H. Feldmann, J. Ruoff, U. Dinger, and A. Garetto, "Source requirements for next generation AIMS EUV mask metrology tool," 2014 International Workshop on EUV and Soft X-ray Sources, Dublin, Ireland, November 3–6, 2014.
11. S. F. Horne, "Metrology source requirements for actinic mask blank inspection," 2014 International Workshop on EUV and Soft X-ray Sources, Dublin, Ireland, November 3–6, 2014.
12. K. Bergmann, J. Vieker, and A. Wezyk, "Compact EUV source for metrology and inspection," 2015 International Workshop on EUV and Soft X-ray Sources, Dublin, Ireland, November 9–11, 2015.
13. R. Abhari, M. Brandstaetter, D. Hudgins, A. Sanders, M. Weber, and D. Boehringer, "Droplet-based high brightness LPP light sources for high volume metrology and inspection applications," 2016 International Workshop on EUV and Soft X-ray Sources, Amsterdam, The Netherlands, November 7–9, 2016.

Downloaded From: https://www.spiedigitallibrary.org/ebooks/ on 09 Mar 2022
Terms of Use: https://www.spiedigitallibrary.org/terms-of-use

14. K. Bergmann, J. Vieker, and A. Wezyk, "Scaling of discharge based XUV sources for metrology applications," 2016 International Workshop on EUV and Soft X-ray Sources, Amsterdam, The Netherlands, November 7–9, 2016.
15. K. Nishihara, A. Sunahara, A. Sasaki, H. Komori, A. Sumitani, K. Uchino, Y. Teamoto, K. Hotta, and E. Hotta, "Optimum plasma conditions for LPP- and LA-DPP-EUV sources," 2009 International Symposium on Extreme Ultraviolet Lithography, Oct. 18–21, 2009, Prague, Czech Republic.
16. K. Nishihara, A. Sunahara, A. Sasaki, K. Uchino, Y. Teramoto, and K. Hotta, "Optimization of LPP- and LA-DPP-EUV Light Sources," 2010 International Symposium on Extreme Ultraviolet Lithography, Oct. 17–20, 2010, Kobe, Japan.
17. A. Endo, H. Hoshino, T. Suganuma, M. Moriya, T. Ariga, Y. Ueno, M. Nakano, T. Asayama, T. Abe, H. Komori, G. Soumagne, H. Mizoguchi, A. Sumitani, and K. Toyoda, "Laser produced EUV light source development for HVM," *Proc. SPIE* **6517**, 65170O (2007) [doi: 10.1117/12.711097].
18. M. Corthout, "EUV light source – the path to HVM," 2011 International Symposium on Extreme Ultraviolet Lithography, Oct. 17–19, 2011, Miami, Florida, USA.
19. Y. Teramoto, B. Santos, G. Mertens, R. Kops, M. Kops, F. Küpper, A. von Wezyk, H. Yabuta, A. Nagano, T. Shirai, N. Ashizawa, K. Nakamura, and K. Kasama, "High-radiance LDP source for mask-inspection application," *Proc. SPIE* **9422**, 94220F (2015) [doi: 10.1117/12.2086606].
20. N. Koster, E. Sligte, F. Molkenboer, A. Deutz, P. Walle, P. Muilwijk, W. Mulckhuyse, B. Oostdijck, C. Hollemans, B. Nijland, P. Kerkhof, M. Putten, and J. Westerhout, "First light at EBL2," *Proc. SPIE* **10143**, 101431N (2017) [doi: 10.1117/12.2257997].
21. Y. Teramoto, B. Santos, G. Mertens, R. Kops, M. Kops, A. Wezyk, K. Bergmann, H. Yabuta, A. Nagano, N. Ashizawa, Y. Taniguchi, D. Yamatani, T. Shirai, K. Aoki, H. Yatsuyama, and K. Kasama, "High-radiance LDP source: clean, reliable and stable EUV source for mask inspection," 2016 International Symposium on Extreme Ultraviolet Lithography, Hiroshima, Japan, October 24–26, 2016.
22. Y. Teramoto, B. Santos, R. Kops, M. Kops, F. Küpper, A. von Wezyk, T. Yokoyama, G. Niimi, H. Yabuta, A. Nagano, M. Yoshioka, T. Shirai, N. Ashizawa, H. Sato, K. Nakamura, and K. Kasama, "High-radiance LDP source for mask-inspection application," 2013 International Symposium on Extreme Ultraviolet Lithography, Toyama, Japan, October 6–10, 2013.
23. Y. Teramoto, B. Santos, G. Mertens, R. Kops, M. Kops, H. Yabuta, A. Nagano, N. Ashizawa, T. Shirai, K. Nakamura, H. Katsuyama, and

Downloaded From: https://www.spiedigitallibrary.org/ebooks/ on 09 Mar 2022
Terms of Use: https://www.spiedigitallibrary.org/terms-of-use

K. Kasama, "High-radiance LDP source for mask inspection," 2015 International Symposium on Extreme Ultraviolet Lithography, Maastricht, the Netherlands, October 4–7, 2015.
24. Y. Teramoto, B. Santos, G. Mertens, R. Kops, M. Kops, A. Wezyk, K. Bergmann, H. Yabuta, A. Nagano, N. Ashizawa, Y. Taniguchi, T. Shirai, K. Nakamura, K. Aoki, and K. Kasama, "High-radiance LDP source: clean, reliable, and stable EUV source for mask inspection," *Proc. SPIE* **9776**, 97760L (2016) [doi: 10.1117/12.2219219].
25. Y. Teramoto, B. Santos, G. Mertens, R. Kops, M. Kops, F. Küpper, A. Wezyk, G. Niimi, H. Yabuta, A. Nagano, K. Nakamura, and K. Kasama, "High-radiance LDP source for mask inspection," 2014 International Symposium on Extreme Ultraviolet Lithography, Washington, D.C., USA, October 27–29, 2014.

Yusuke Teramoto received a Ph.D. degree in 2002 from Kumamoto University, Japan. He joined Ushio Inc. in April 2002 and started research and development of Xe- and Sn-fueled discharge EUV sources. In 2008, he moved to Aachen, Germany to participate the co-development program between Ushio, XTREME, Philips, and Fraunhofer ILT. He engaged in source development for NXE3100, working especially on power scaling. Now he works for BLV Licht- und Vakuumtechnik GmbH, an Ushio group company. He is currently the leader of R&D Unit 1 of the EUV Business Project managed by Ushio Inc. and working on EUV and x-ray metrology source research and development.

Downloaded From: https://www.spiedigitallibrary.org/ebooks/ on 09 Mar 2022
Terms of Use: https://www.spiedigitallibrary.org/terms-of-use

Chapter 5
Optical Systems for EUVL

Sascha Migura, Winfried Kaiser, Jens Timo Neumann, Hartmut Enkisch, and Dirk Hellweg*
Carl Zeiss SMT GmbH, Oberkochen, Germany

5.1 Introduction
5.2 Optical Systems: Beginning and Present
- 5.2.1 Introduction
- 5.2.2 Beginning: collaborations and funding in Europe
- 5.2.3 Early optical systems: MET, HiNA, and SFET
- 5.2.4 Prototypes: Alpha Demo Tool and EUV1
- 5.2.5 Preproduction system: Starlith® 3100
- 5.2.6 HVM: Starlith® 3300/3400 family

5.3 The Future: High-NA
- 5.3.1 Introduction
- 5.3.2 Optical system for high-NA
- 5.3.3 Theoretical background
- 5.3.4 Conclusion on optical systems for EUVL

5.4 Optical Modules: Collector
- 5.4.1 Introduction
- 5.4.2 EUV collector types
- 5.4.3 Grazing-incidence collectors
- 5.4.4 Normal-incidence collectors

5.5 Optical Modules: Illuminator
- 5.5.1 Introduction
- 5.5.2 Key performance parameters
- 5.5.3 Realization options
- 5.5.4 Pupil tuning
- 5.5.5 Technical challenges

5.6 Optical Modules: Projection Optics
- 5.6.1 Introduction
- 5.6.2 Basic design specifications
- 5.6.3 Optics manufacturing: mirror surface
- 5.6.4 Modeling and simulating stray light and flare
- 5.6.5 Optics manufacturing: mirror coating

*Contributions to this chapter have also been made by Holger Kierey, Bernhard Kneer, Udo Dinger, Thure Böhm, Bernd Dörband, and Ulrich Löring.

Downloaded From: https://www.spiedigitallibrary.org/ebooks/ on 09 Mar 2022
Terms of Use: https://www.spiedigitallibrary.org/terms-of-use

5.7 Mask Inspection: The ZEISS AIMS EUV
5.7.1 Introduction
5.7.2 Principle and application
5.7.3 System concept
5.7.4 Tool capabilities
5.7.5 Tool performance
5.7.6 Summary
Acknowledgments
References

5.1 Introduction

Optical technologies play an enabling role in the continuation of Moore's law.[1] The smallest achievable structure on a chip is linked to the resolution limit of the optical system used in the lithographic process. The underlying theory of optical imaging was investigated in 1873 by Ernst Abbe. His theory originally expressed the resolution limit of a microscope as

$$d = \frac{\lambda}{2n \sin \alpha} = \frac{1}{2}\frac{\lambda}{NA}, \tag{5.1}$$

where d is the minimum resolvable distance of two lines of a periodic diffraction grating, λ is the operating wavelength, n is the refractive index below the last lens element, α is the half of the opening angle on the object side, and NA is the numerical aperture.[2] Today, Abbe's formula is used in optical lithography in the form[3]

$$\text{Resolution} = k_1 \frac{\lambda}{NA}, \tag{5.2}$$

introducing the process parameter k_1 as a measure for the capability of the manufacturing process. Aiming at a low k_1 improves the resolution when λ and NA are given, but it will typically increase the general process complexity. Accordingly, there are three options to continue Moore's law. The first option is to increase the NA of the optical system. This appears to be the preferred option, since resolution can be significantly improved with limited impact on process complexity and illumination settings can be kept roughly the same, just scaled to the increased NA. The second option is to reduce k_1. While the NA is clearly defined by the optics, k_1 is an effective parameter that subsumes the capabilities and setup of the optics, the pattern to be printed, and the process methods involved. In recent years, most notably, multiple patterning has matured into an important process technique that allows one to push k_1 below the optical limit of 0.25. The optics supports a low k_1 by providing aggressive off-axis illumination with a low pupil fill ratio and a large freedom to generate customized illumination shapes. By introducing additional design rules for the chip and increasing complexity and cost, reducing k_1 postpones a change in the exposure

Downloaded From: https://www.spiedigitallibrary.org/ebooks/ on 09 Mar 2022
Terms of Use: https://www.spiedigitallibrary.org/terms-of-use

wavelength and hence postpones the development of a fundamentally new resist and processing technology. Finally, the third option is to reduce the exposure wavelength λ. This option requires the most effort in terms of changes to the infrastructure and development of new patterning materials and processes.

During the last decades, a new exposure wavelength λ has been introduced multiple times.[4] After the step to the next wavelength, the NA was increased and k_1 was lowered. At the time of writing in 2017, the semiconductor industry is in a transition phase to a reduced exposure wavelength. EUV lithography with $\lambda_{EUV} = 13.5$ nm is expected to replace immersion technology with $\lambda_{DUV} = 193$ nm for high-volume manufacturing (HVM) of the most critical layers of upcoming nodes. The smaller exposure wavelength offers huge resolution potential. Accordingly, EUV lithography promises the return to single exposure or simpler patterning processes and a significantly improved pattern fidelity of complex structures. Regarding the optical system, the short wavelength of $\lambda = 13.5$ nm imposes several new boundary conditions. Firstly, EUV light is strongly absorbed by all materials and gases; therefore, the whole system must be operated under vacuum. This implies that that all optical elements, including the mask, must be mirrors. Secondly, the refractive index of all materials at $\lambda = 13.5$ nm is very close to 1, so stacks of multilayers as Bragg reflectors have been found as a solution for mirror coatings. The optical constants of appropriate coating materials limit the mirror reflectivity to a theoretical maximum of ~74%. Practical values are close to ~70%. Hence, the design of a high-transmission EUV optical system must minimize the number of mirrors, achieved most effectively by using aspheres, which is particularly challenging in terms of optics technology. These boundary conditions lead to a layout for the optical train that is schematically shown in Fig. 5.1. For the purposes of this chapter, an EUV optical system consists of the following optical modules: collector, illuminator, mask (reticle), and projection optics.

This chapter reviews the progress of EUV optics over the years, the current status, and the steps toward the next generation. Different generations of EUV optical systems have been developed and built by different companies.[5–9] Regarding the details, this chapter mainly focuses on the optical systems and modules produced by ZEISS. A more application-oriented historical overview can be found in Ref. 10. Section 5.2 provides in chronological order an overview of the EUV optical systems that have already been realized. Section 5.3 gives an outlook on future EUV optical systems designed to continue Moore's law by opening a new phase of EUV lithography with printing capabilities below a resolution of 8 nm. Sections 5.4–5.6 discuss the most relevant technology challenges related to the design and manufacturing of the optical modules. Section 5.7 explains the Aerial Image Measurement System for EUV, or ZEISS AIMS EUV, which is an actinic tool for the printability analysis of EUV mask defects to ensure defect-free mask manufacturing, allowing cost-effective HVM.

Downloaded From: https://www.spiedigitallibrary.org/ebooks/ on 09 Mar 2022
Terms of Use: https://www.spiedigitallibrary.org/terms-of-use

Figure 5.1 Schematic drawing of an optical train for an EUVL scanner. The EUV light generated by a plasma source is collected and focused by a collector onto the entrance of the illuminator, the so-called intermediate focus (IF). The illuminator then forms the light such that the mask is illuminated very homogeneously from well-defined beam directions. The mask is a critical optical element in itself. The structures on the mask generate a complex diffraction pattern containing the circuit information. The projection optics catches and combines this diffraction pattern, finally imaging the mask structure onto the wafer.

5.2 Optical Systems: Beginning and Present

5.2.1 Introduction

After Hiroo Kinoshita proposed soft x-ray lithography (later called EUVL) in 1985,[11] the first efforts toward realization were initiated in Japan, the USA, and the Netherlands. During the following years, several optical systems with low NAs of up to 0.1 were designed and realized. Developed by Lawrence Livermore National Lab (LLNL) and Lawrence Berkeley National Laboratories (LBNL),[12] two micro-exposure tools (METs) with a NA of 0.3 were shipped—one to Berkeley and one to Exitech in 2004. The MET features an image field of 200 μm $\times$ 600 μm, intended for resist tests, mask studies, and research. Nikon Corp. and Canon Inc. also developed and produced optics with small fields. The next step was to provide full-field tools, featuring a 26 mm $\times$ 33 mm field size at the wafer (after scanning). Two prototypes for a full-field wafer scanner were delivered by ASML with ZEISS optics inside, the so-called Alpha Demo Tool (ADT), featuring a NA of 0.25. One ADT was shipped to SEMATECH (Albany, SUNY, USA) and the other to the Interuniversity Microelectronics Centre (IMEC, Leuven, Belgium). Another full-field tool was the EUV1 by Nikon. The ADT was followed by a number of NXE:3100 scanners that were installed directly at the chipmaker sites. The NXE:3100 is equipped with the Starlith® 3100, which is an enhanced version of the ADT optics with the same NA of 0.25, improved aberration control, a more advanced illuminator with a larger partial coherence factor σ, and the

Downloaded From: https://www.spiedigitallibrary.org/ebooks/ on 09 Mar 2022
Terms of Use: https://www.spiedigitallibrary.org/terms-of-use

possibility to use off-axis settings. [See Section 5.5.1 for the definition of the partial coherence factor σ and the pupil fill ratio (PFR)]. Delivered to customers for the first time in 2013, the Starlith® 3300 optical system followed. The Starlith® 3300 possesses a NA of 0.33, allows illumination setting changes without light loss, and is integrated into the NXE:3300B scanner by ASML. Based on the NXE:3300B, two systems have been developed, the NXE:3350B and the NXE:3400B. The NXE:3350B is an upgrade with improved aberrations, especially distortion for smaller overlay, and allows for customized illumination settings. The NXE:3400B features a highly flexible, freeform illumination as a new solution and further aberration improvements. At the time of writing, the NXE:3300B/3400B family is being rolled out for HVM in the semiconductor market[13–15] and is already being produced in significant numbers.

5.2.2 Beginning: collaborations and funding in Europe

The optical system is an essential part of the scanner. The development of the optical system from ZEISS is taking place in close collaboration with ASML. This collaboration dates back to 1983 when ZEISS began supplying lithography optics for Philips. These first optics operated at a wavelength of 436 nm, the so-called g-line of a mercury lamp. Since 1997, ASML and ZEISS have been working together in a strategic partnership. EUVL development at ZEISS started in mid-1990. Under the frame of the EXULT project, which was the beginning of the European EUV program, the first EUV workshop organized by ZEISS was held November 13th–14th, 1995 at the location of the ZEISS headquarters in Oberkochen, Germany. With participants from the EU and the US, this workshop started the feasibility study for the development and production of EUV optics at ZEISS and partners. EXULT is an acronym for "Extreme ultraviolet technology using power excimer laser." The EXULT project operated from January 1994 to March 1999 and was funded by the EUREKA organization, which is an intergovernmental network launched in 1985.[16] The Extreme UV Concept Lithography Development System program (EUCLIDES) was the first European research project to make EUVL a production technology.[17,18] The program operated from 1998 to 2000 as part of the European Strategic Program on Research in Information Technology (ESPRIT) and was financed by the European Commission. EUCLIDES was led by ASML and partnered by ZEISS and Oxford Instruments. Oxford Instruments studied the feasibility of a synchrotron as an EUV source. On the part of ZEISS, the results of EUCLIDES included optical design studies for the projection optics and the illuminator in order to derive technological requirements. The technology also included the manufacturing and the metrology of aspheric surfaces. Substantial progress was reached in 1999 with the fabrication of mirror ELT M2 for a projection optics designed by Corning Tropel Corp. for AT&T Bell Labs.[19] As an object for technology comparison, a residual rms surface error of 0.14 nm and a

Downloaded From: https://www.spiedigitallibrary.org/ebooks/ on 09 Mar 2022
Terms of Use: https://www.spiedigitallibrary.org/terms-of-use

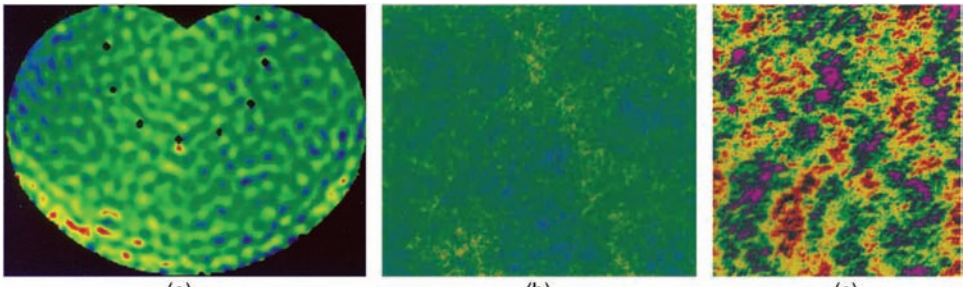

Figure 5.2 (a) Figure quality of a 0.14-nm rms surface error on a 1.8-μm aspheric ZERODUR® substrate measured with an in-house interferometer. (b) MSFR quality of 0.12-nm rms surface error on a spherical ZERODUR® substrate with a field of 300 μm × 300 μm measured with optical profilometer Micromap 512. (c) HSFR quality of 0.12-nm rms surface error on a spherical ZERODUR® substrate with a field 1 μm × 1 μm measured with AFM DI 5000.

roughness of 0.2 nm was achieved (Fig. 5.2) and appreciated as a major breakthrough in optics manufacturing. In search of the next-generation lithography (NGL), SEMATECH's NGL Task Force still listed "full field optical design" as the "Critical Issue #1 for EUV" in December 1998.[20] Although optical designs were available on paper, it was unclear if the requirements, especially regarding flare, could be met during manufacturing. Over a period of only three and a half years, from November 1997 to August 2001, the topic "Optics" matured from the status "potential showstopper" to "solution anticipated" in SEMATECH's NGL workshop survey.[21]

5.2.3 Early optical systems: MET, HiNA, and SFET

In mid-1999, ZEISS started to build the optics for the MET in cooperation with LLNL and LBNL. The MET is a small field tool with a rectangular field size at the wafer of 200 μm × 600 μm, a magnification (MAG) of 5×, a NA of 0.3, and an annular illumination with σ ranging from 0.36 to 0.55. The projection optics features a central obscuration in the exit pupil. A two-mirror design based on the concept of nearly equal radii of curvature provides good aberration control over the small field.[22] The optical surface quality of these two mirrors plays a crucial role in the imaging quality of the MET. In the beginning, ZEISS fabricated the aspheric optical surfaces for two systems. By applying a surface interferometry and polishing with a repeatability of ~60 pm, mirror figure and roughness values of 0.2–0.3 nm were achieved at the end of 2000. In mid-2001, the coating of the mirrors and assembly of the first MET were completed at LLNL. This MET was subsequently delivered to ZEISS for further testing of the aerial images and resist prints at the Berlin Electron Storage Ring Society for Synchrotron Radiation (BESSY). A beamline was set up specifically for research purposes at EUV wavelengths

Downloaded From: https://www.spiedigitallibrary.org/ebooks/ on 09 Mar 2022
Terms of Use: https://www.spiedigitallibrary.org/terms-of-use

using a synchrotron light source. Aerial image metrology qualified the final performance of the optical system and was based on the detection of 3D intensity distributions of imaged mask patterns. One of the first images printed with the MET at the EUV wavelength was taken at BESSY in November 2001 and is depicted in Fig. 5.3. The photographs show structures consisting of single lines and grouped lines arranged in different orientations. Going through focus, astigmatism, coma, and spherical aberration could be determined.

In addition to the aerial image measurement, an interferometer-based metrology machine was installed at BESSY in 2001. Its purpose was to show to what extent the DUV-proven shearing interferometer principle could also be applied to EUV. Figure 5.4 shows one of the first interferograms at EUV wavelengths, imaged in November 2002. A structured transmission mask was used, where a diffraction grating divides the incoming waves. Their superposition generates interference patterns that are registered by a detector

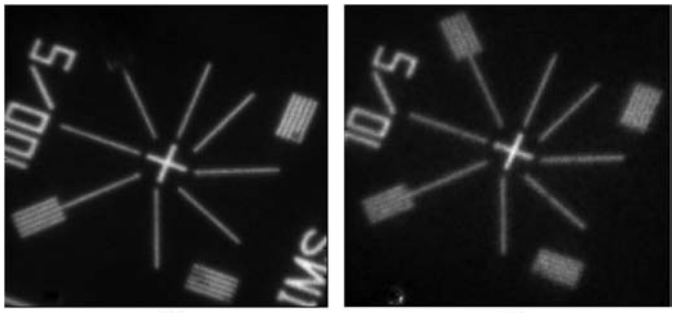

Figure 5.3 Aerial image metrology of patterns of single and grouped lines for a resolution test. (a) Test structures with 100-nm linewidth. The grouped lines are blurred but still resolved. (b) The pattern with 70-nm linewidth cannot be resolved.

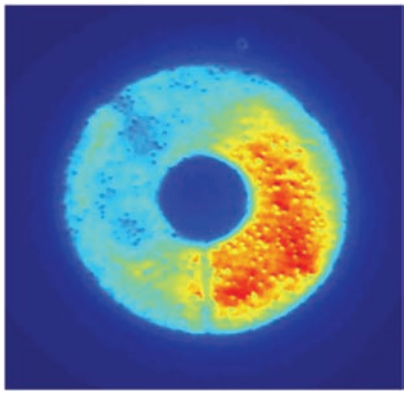

Figure 5.4 One of the first interferograms taken at EUV wavelengths. The grainy substructure is due to the setup of the detector system.

Downloaded From: https://www.spiedigitallibrary.org/ebooks/ on 09 Mar 2022
Terms of Use: https://www.spiedigitallibrary.org/terms-of-use

system. Recording several interference images with different positions of the diffraction grating, the topography of the wavefront can be calculated and thus the aberrations determined. Some series had been taken in various focus positions, finally proving the feasibility of the principle.

In 2003, Exitech Ltd transformed the production of the MET into a commercial endeavor, this time with ZEISS producing the complete projection optics and illuminator for several systems. Exitech Ltd shipped its first microstepper in 2004. The imaging performance of this microstepper allowed 45-nm half-pitch resolution for dense lines and 30-nm isolated lines. From 2001 to 2004, Nikon Corp. presented three sets of small-field tools featuring a field size of 300 μm $\times$ 500 μm, a NA of 0.3, and a selectable σ of up to 0.8. The so-called HiNA projection optics consists of two aspherical mirrors and served as a path finder for their full-field tool EUV1.[23] In 2006, Canon Inc. installed their small-field exposure tool (SFET), also with a NA of 0.3, at the Japanese consortium SELETE and started system design for a full-field system based on the experience gathered with SFET.[8] In 2010 microstepper tools were upgraded with the possibility to tune settings up to $\sigma = 0.9$. SEMATECH reported in November 2010 that after this upgrade the MET "routinely supports new materials screening down to 24-nm" half-pitch and in fact has an ultimate resolution below 20-nm half-pitch.[24] A MET redesign with a NA of 0.5, called MET5, was set up at a customer site in 2015. An ultimate resolution of <12-nm half-pitch is envisioned.[24] Zygo Corp. is producing the projection optics for the MET5, and ZEISS is fabricating its illuminator and the reticle metrology.[25–27] EIDEC has also developed a high-NA small-field exposure tool.[28]

5.2.4 Prototypes: Alpha Demo Tool and EUV1

The MET has mainly been used for photoresist and mask testing and did not allow for a systematic study of field-dependent imaging effects such as flare or chief ray angle rotation. Therefore, ASML and ZEISS continued their EUV development with the introduction of the first full-field R&D EUV system, which was capable of exposing a 26 mm $\times$ 33 mm full field at the wafer (after scanning) and featured a NA of 0.25 and a partial coherence factor of $\sigma = 0.5$. The ADT provided an opportunity to gather first experiences with EUV lithography processes in an open, pre-competitive R&D environment. Two optic sets for ADTs were produced and shipped.

The system metrology for the projection optics is a key building block in the manufacturing process. Its purpose is twofold: Firstly, the system metrology is used for final system qualification. Secondly, it is used for feedback loops in system adjustments during system integration. A key point is the selection of the operating wavelength of the system metrology. The simulation of the ADT projection optics and the alignment processes predicted that a metrology at $\lambda = 13.5$ nm was not mandatory. The expected differences to the established

Downloaded From: https://www.spiedigitallibrary.org/ebooks/ on 09 Mar 2022
Terms of Use: https://www.spiedigitallibrary.org/terms-of-use

Figure 5.5 The ADT metrology stand includes an interferometer and aerial image metrology, both at 248-nm wavelength and open for some manual interventions during the pre-alignment of the projection optics. The stand is additionally equipped with an air flow unit to reduce local air heating effects as well as for the nonactinic system metrology of the Starlith® 3100 projection optics. The term nonactinic means that the measurements are not performed at the exposure wavelength.

metrology at $\lambda = 248$ nm were correctable within the scanner. Essential challenges were the modifications to the proven machine setup and merging of aerial and interferometric metrology within a single machine unit (Fig. 5.5).

The IMEC ADT passed its site acceptance test in 2008. The EUV imaging analysis started by printing 32-nm dense and isolated lines and 50- to 55-nm contacts holes, corresponding to a 32-nm static random-access memory (SRAM) cell,[29] and dense lines and spaces with half-pitches ranging from 30 nm to 35 nm were printed.[30] The imaging analysis on the ADT at IMEC was also performed for a 22-nm SRAM cell with contact sizes of ~45 nm. At IMEC as well as at SUNY, the ADT was part of an integrated process line. The first functional devices were produced at SUNY in 2008 with the SRAM cell of an AMD Typhoon full-chip layout being printed.[31] A 22-nm SRAM cell was demonstrated by IMEC in 2009.[32] These results proved that EUV patterning can indeed be integrated into a semiconductor production flow. A monitoring of CD stability in 2010 based on 27-nm lines and spaces showed

Downloaded From: https://www.spiedigitallibrary.org/ebooks/ on 09 Mar 2022
Terms of Use: https://www.spiedigitallibrary.org/terms-of-use

critical dimension uniformity (CDU) values of 2.3 nm (3σ) for vertical features and 2.0 nm for horizontal features. In 2008, Nikon Corp. reported on their full-field tool, EUV1, which features a NA of 0.25 and a partial coherence factor of 0.8, and which was able to resolve 32-nm elbow patterns over the full field.[5]

The ADT was an opportunity to gain significant knowledge on EUV patterning. For instance, shadowing effects and their full-field dependency were studied.[33] As EUV lithography uses a reflective mask, the mask is illuminated from an oblique incidence angle. Otherwise, the light would simply be reflected back into the illuminator instead of proceeding into the projection optics. Due to this oblique incidence of light onto the mask, the imaging properties depend on the orientation of the mask features relative to the direction of the incident light; at field center, vertical lines are parallel to the incidence plane of the chief ray, and horizontal lines are orthogonal to the incidence plane. Consequently, horizontal lines cast a shadow and appear to be broader than vertical lines of the same physical width at the mask. This effect is called horizontal/vertical (H-V) bias. As the chief ray rotates over the field, this H-V bias becomes a field-dependent effect. An additional effect is related to flare. Since the mask shows brighter and darker regions, the resulting flare at the wafer will be field dependent, inducing field-dependent imaging effects. As a systematic effect, this can be compensated for based on the flare distribution of the optics.[34] In addition, flare can overframe the image field, thereby adding a dose offset at the edge of the adjacent field.

It was proven experimentally[33] that all three effects (shadowing, effective flare variations due to variations of the reticle brightness, and flare from adjacent exposures) can be compensated for by optical proximity correction (OPC). Initially, OPC referred to the correction of optical proximity errors: The image of a certain mask feature depends not only on the feature itself but also on its vicinity. The same mask feature in different vicinities will yield different images at the wafer. This effect is fundamental to a diffraction-limited system and can be computed. Nowadays, OPC means to add modifications and additions to the mask feature that compensate for the optical proximity error. Printing results on both ADTs showed in 2008 an almost 4-nm difference between horizontal and vertical lines of 35-nm half-pitch due to shadowing (wafer CD = 31.7 nm vertical, 35.5 nm horizontal). Correcting the shadowing by OPC, 30-nm isolated (1:6) lines could be printed with no directional dependence (28.0 nm vertical, 28.3 nm horizontal).[32] IMEC showed that for a wide range of pitches, field-dependent shadowing correction can be approximated by a relatively simple model.[35] The ADT was also used for studies to optimize the mask absorber.[36] Regarding the flare impact on imaging, IMEC measured on the ADT a CD variation of 1.2 nm between the bright and dark regions. In 2010, the difference could be reduced to 0.2 nm, after correcting for flare effects.[37] Thus, it was with the ADT that the feasibility of field-dependent OPC for shadowing and flare correction was

Downloaded From: https://www.spiedigitallibrary.org/ebooks/ on 09 Mar 2022
Terms of Use: https://www.spiedigitallibrary.org/terms-of-use

proven for the first time. The ADT at IMEC remained active until 2011, at which time it was replaced by the NXE:3100. See Ref. 38 for a brief review of OPC and other resolution enhancements technologies.

In addition to the shadowing effect, the oblique incident of light at the mask has another consequence: Moving the mask in the focus direction will change the apparent feature position as seen from the wafer. As placement specifications grow increasingly tight, requirements for the mask position as well as the mask flatness also tighten. Since it is challenging to meet these flatness requirements, an accurate measurement of the nonflatness has been proposed, followed by a correction of the predicted placement errors in the mask writing process.[39] This strategy has been implemented by NuFlare Technology, Inc. and has been successfully demonstrated on the ADT in a joint effort by NuFlare and SEMATECH.[40,41] A recent and rather detailed elaboration of this approach discriminates between the different spatial frequencies of mask nonflatness.[42] With its tight requirements, the mask is found to be a crucial element of the EUV lithography system, and the status of the mask infrastructure has been subject to frequent reviews.[43,44]

5.2.5 Preproduction system: Starlith® 3100

Learning from the prototype tools was essential for improving core optics technologies such as mirror polishing. These improvements were realized in the successor of the ADT optics, the Starlith® 3100 [Fig. 5.6(b)]. The layout for the projection optics remained the same; consequently, the NA of 0.25, the MAG of 4× and the full-field size remained unchanged. Following the ADT,

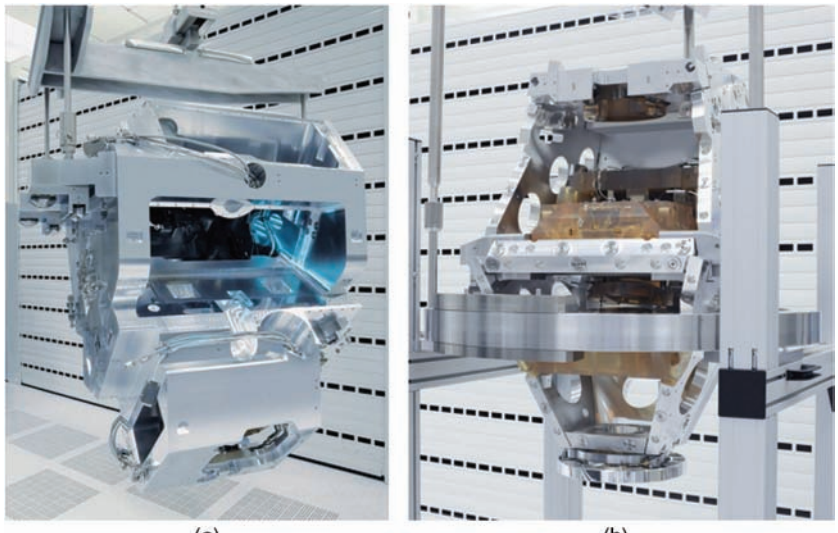

Figure 5.6 Optical modules for Starlith® 3100: (a) illuminator and (b) projection optics.

Downloaded From: https://www.spiedigitallibrary.org/ebooks/ on 09 Mar 2022
Terms of Use: https://www.spiedigitallibrary.org/terms-of-use

ASML built a high-volume, serial-production platform for EUV named NXE. The first shipment of the scanner NXE:3100 was in 2010. As mentioned in Section 5.2.2, flare was originally rated as the most critical issue for EUV optics. The source of flare is the scattering of EUV light from the roughness of the mirror surfaces. The amount of this stray light increases in proportion to the reciprocal of the squared wavelength λ, making it significantly more challenging for EUV compared to DUV to achieve satisfying roughness levels. The ADT exhibited a flare level of 16%. This high flare level together with the aberrations led to concerns regarding the image contrast. Therefore, a general target for flare of <8% was set. The Starlith® 3100 generation with flare values <6%—clearly below the original flare target—was shipped to chipmakers and research organizations. Thus, a reduction of flare by a factor of three was achieved between 2004 and 2008. In addition, reflectivity losses caused by Mo/Si interface roughness were reduced, increasing the transmission of the Starlith® 3100 by 50%. In order to keep the OPC effort within reasonable limits, currently, a flare target of <4% is required and was indeed achieved for the Starlith® 3300/3400 family.

Compared to the ADT with one conventional illumination setting at $\sigma = 0.5$, the illuminator for the Starlith® 3100 [Fig. 5.6(a)] offers two basic enhancements: a maximum partial coherence factor of $\sigma = 0.8$ is achievable, and an illumination setting change is possible by the utilization of diaphragms. The diaphragm is placed close to the pupil plane, creating a specific setting by blocking the unwanted light directly in the pupil. The disadvantage of this mechanism is that the light of the blocked pupil facets is lost, decreasing the throughput of the whole scanner. Only the use of the large conventional setting with $\sigma = 0.8$ gives the full transmission. Several standard off-axis settings are available by default. In addition, customized annular settings and polar settings are offered. These illumination settings can indeed be used to improve the resolution. For instance, 27-nm lines and spaces can be printed with the large conventional setting, 25-nm lines and spaces with the annular setting, and 22-nm lines and spaces with the dipole setting.[45]

While the ADT was delivered without actinic system metrology, actinic metrology was essential for the accuracy of the final adjustments of the Starlith® 3100 projection optics. In 2008, machines for both EUV and the nonactinic metrology were completed and ready for the first measurements. The stability of the metrology setup and the measurement procedures were proven by repeated measurements. The aberrations are described by Zernike polynomials.[46,47] Zernike polynomials form an orthogonal base and have the convenient property that they can be linked very directly to the imaging properties of the projection optics.[48] A set of Zernike coefficients is then used to describe the aberration. For the projection optics of the Starlith® 3100, all Zernike coefficients were specified with a repeatability of below 0.25 nm. In the nonactinic setup, this criterion was met for the higher coefficients,

Downloaded From: https://www.spiedigitallibrary.org/ebooks/ on 09 Mar 2022
Terms of Use: https://www.spiedigitallibrary.org/terms-of-use

equivalent to high-order aberrations, but not for the low-order aberrations. The repeatability of the lower coefficients is highly dependent on the stability of the setup, the light source, and the environment. For the actinic interferometer, the requirements for the low-order aberrations were within specification. Higher-order aberrations were measured with a repeatability of less than 0.03 nm.

5.2.6 HVM: Starlith® 3300/3400 family

The Starlith® 3300 is the first EUV lithography optics to be developed for HVM. Compared to the Starlith® 3100, the Starlith® 3300 is a completely new set of optics for the projection, for the illuminator, and for the collector (Fig. 5.7). The NA of the projection optics has been increased by more than 30%—from 0.25 to 0.33—keeping the MAG of 4× and the full-field size of 26 mm × 33 mm (after scanning). The first scanner featuring the optics of the Starlith® 3300 was shipped by ASML in 2013. Meanwhile, the Starlith® 3300/3400 family is being produced in significant numbers. The basic illumination setting of the Starlith® 3300 is a large conventional pupil filling up to $\sigma = 0.9$, which is sufficient for 22-nm resolution. In order to enable 18-nm resolution, annular, dipole, and quadrupole base settings are provided (Fig. 5.8), thus allowing enough process flexibility for a serial production tool. A flexible illuminator concept has been introduced for the Starlith® 3300, allowing setting changes without losing transmission. The idea behind this concept is explained in Section 5.5. In the NXE:3350B, the flexible illuminator concept with a PFR of 40% not only allows setting changes without light loss, it also enables customized illumination settings for specific patterns that are found by source mask optimization (SMO) for 16-nm resolution. SMO aims at maximizing the

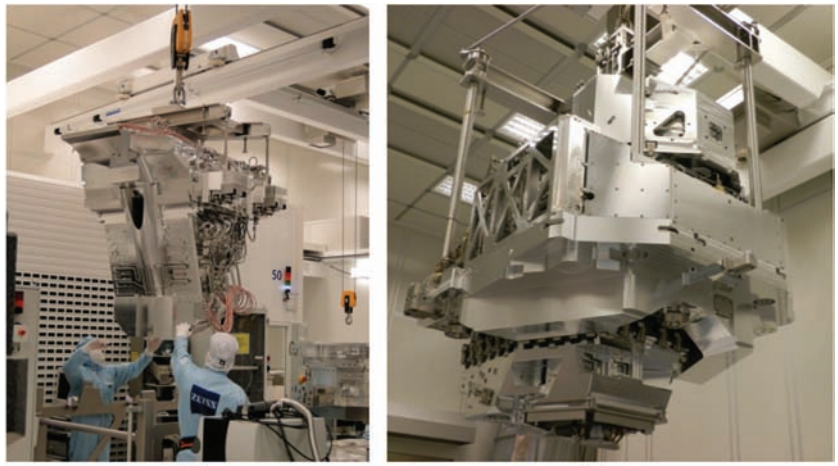

Figure 5.7 Optical modules for Starlith® 3300: (a) illuminator and (b) projection optics.

Downloaded From: https://www.spiedigitallibrary.org/ebooks/ on 09 Mar 2022
Terms of Use: https://www.spiedigitallibrary.org/terms-of-use

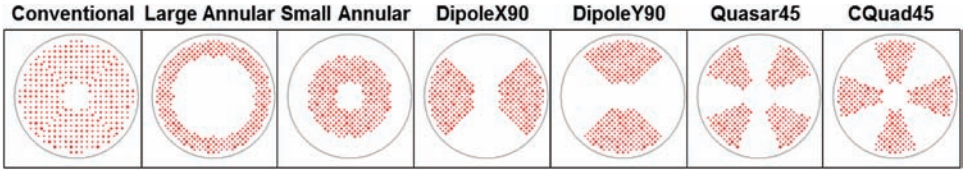

Figure 5.8 Standard illuminator settings of the NXE:3300B.

process window, simultaneously optimizing the pattern on the mask and the angular distribution of the illumination settings.[49] SMO capabilities are even enhanced in the NXE:3400B, which features a highly flexible illuminator, offering customers the opportunity to apply additional illumination settings with a maximum $\sigma = 1.0$, lower PFR of 20%, and rotated dipole settings for 13-nm resolution. Figure 5.9 shows these additional settings.

For the Starlith® 3300 system metrology, the actinic and nonactinic metrology are transferred into vacuum and merged into a single machine. In addition, the interferometer has a setup that allows parallel full-field measurements for the nonactinic part (i.e., obtaining all data over the full field simultaneously) and sequential full-field measurements for the actinic part. Figure 5.10 shows the wavefronts of the nonactinic setup. The interferograms are recorded simultaneously by a camera chip. By the simultaneous measurement of the field points in their fixed spatial relation, the relative tilts of the wavefronts can be measured and distortion can be calculated. Another advantage of parallelization is the substantial avoidance of error contributions due to time drift. Starting with the principle attempt to produce an interferogram at EUV wavelengths for the MET, a standard system metrology fit for serial production has finally been achieved.

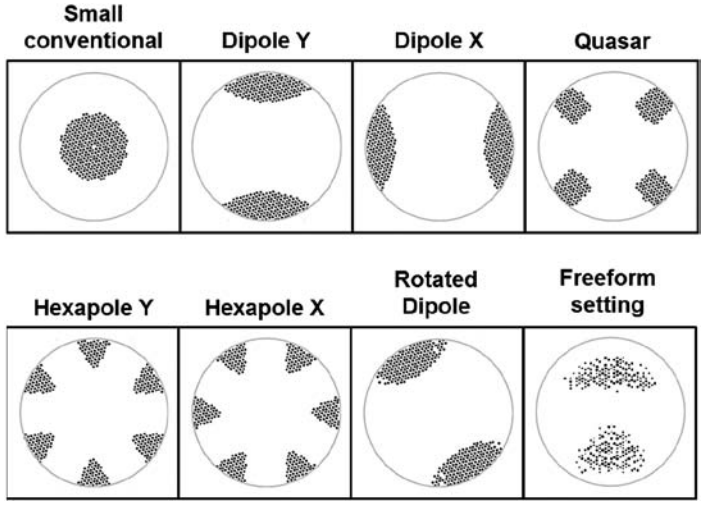

Figure 5.9 Examples of additional illuminator settings of the NXE:3400B.

Downloaded From: https://www.spiedigitallibrary.org/ebooks/ on 09 Mar 2022
Terms of Use: https://www.spiedigitallibrary.org/terms-of-use

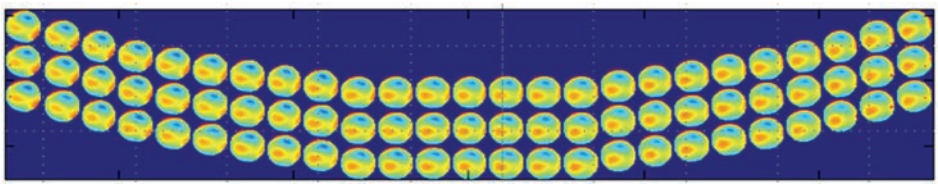

Figure 5.10 One of the first Starlith® 3300 wavefronts measured with the nonactinic, parallel, full-field interferometer in 2013 (focus is subtracted). Shown is the arrangement of the field points to be measured in the annular field.

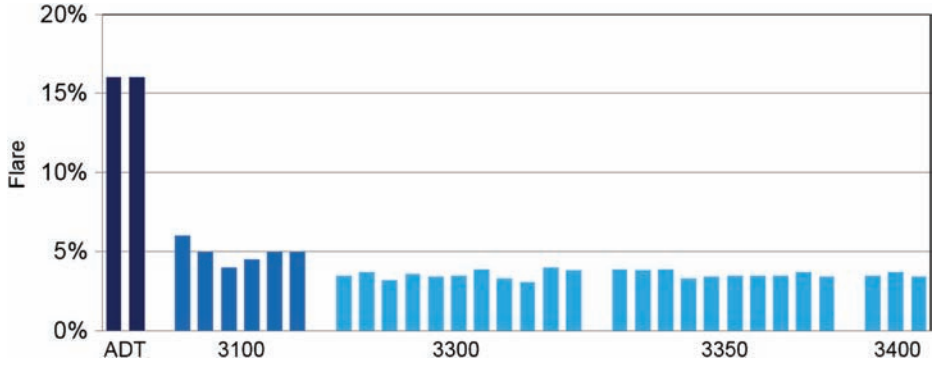

Figure 5.11 Flare of the optical system for individual units of the ADT, the Starlith® 3100, and the Starlith® 3300/3400 family. The Starlith® 3300/3400 family consistently meets the < 4% target.

Figure 5.11 shows the flare performance for individual units of the ADT optics, the Starlith® 3100 and the Starlith® 3300/3400 family. Figure 5.12 shows the corresponding wavefront rms of these shipped units.

ASML presented wafer data of the NXE:3300B at the SPIE Advanced Lithography Symposium in 2013.[50] Dense lines of 16 nm were printed with

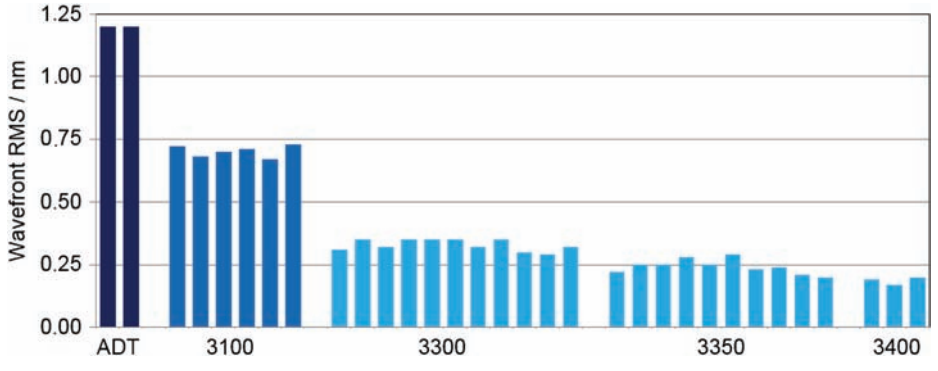

Figure 5.12 Wavefront rms (in nanometers) of the optical system for individual units of the ADT, the Starlith® 3100, and the Starlith® 3300/3400 family. The improvements over time are clearly visible.

Downloaded From: https://www.spiedigitallibrary.org/ebooks/ on 09 Mar 2022
Terms of Use: https://www.spiedigitallibrary.org/terms-of-use

significant process margins. Dose tolerance, or exposure latitude, was larger than 15%, proving that the increased contrast due to the reduced flare level of ~4% indeed enables a robust imaging process. Depth of focus (DOF) was shown to be larger than 120 nm. Other examples of the superior resolution capabilities of the NXE:3300B include 24-nm contact holes (sufficient to support 1× DRAM node), logic metal1 patterns with a minimum half-pitch of 23 nm and even 13-nm dense lines and spaces, showing the extendibility of the NXE:3300B. Not only the resolution, but also the imaging performance—and in particular the overlay performance—of the NXE:3300B met the expectations and noticeably exceeded those of the NXE:3100. Printing 22-nm lines over the full wafer with CDU ≤ 1.5 nm (3σ) was shown. The overlay to a reference layer printed with immersion lithography was measured to be better than 3.5 nm. At the time of this writing, the NXE:3300B has been under thorough qualification by major chipmakers for quite some time. At the Photomask Japan 2015 Symposium, Intel observed significant progress, claiming that the introduction of EUV into HVM is "a matter of when, not if."[51] At the SPIE Advanced Lithography 2016 Symposium, Intel, TSMC, and Samsung reported their findings in three keynote presentations, all of which provided consistent results. Quite comprehensive reviews of the status of EUV lithography were presented at this symposium.[52] The NXE:3300B and NXE:3350B have been tested in real fab environments and processes. CD and overlay performance were found to be stable over several months. In particular, the NXE machines could be combined with existing immersion scanners without any overlay penalty as compared to the traditional immersion–immersion mix. Chips containing layers printed with NXE showed electrical performance comparable to the immersion-only manufactured chips. In other words, resolution, CDU, and overlay performance meet the requirements of chipmakers. Tool availability and source power remain key issues to be solved for HVM. Nevertheless, TSMC announced that the NXE will be used for production at the N5 node,[13–15] and, as announced later, at a shrink version of the N7 node. Samsung announced in May 2016 the intention to use the NXE for volume production already in their L7 technology.[53] Today, EUVL optical systems support the requirements of HVM in terms of specifications and anticipated production volume. Figure 5.13 gives a concise overview of the product specifications for the discussed optical systems.

5.3 The Future: High-NA

5.3.1 Introduction

EUVL has always been considered a multi-node technology. In order to continue the roadmap of the semiconductor industry using EUVL, the NA of the optical system has to be increased significantly beyond the present value of 0.33. An increase of NA beyond 0.5 enables a resolution below 8 nm with

Downloaded From: https://www.spiedigitallibrary.org/ebooks/ on 09 Mar 2022
Terms of Use: https://www.spiedigitallibrary.org/terms-of-use

	Intended Use	Tool @site	Field size @image	MAG	NA	σ	Illumination	Resolution
MET	Research	2002	0.6 x 0.2mm²	5x	0.30	0.0-1.0	flexible	13nm
HiNA		2001	0.5 x 0.3mm²			0.8	selectable	30nm
SFET		2006	0.6 x 0.2mm²			0.3-0.7	annular	26nm
MET5		2015	0.03 x 0.15mm²		0.50	0.0-1.0	flexible	8nm
ADT		2006	26 x 33mm²	4x	0.25	0.5	fixed	32nm
EUV1		2008				0.8	conventional	32nm
Starlith® 3100	pre-production	2010				0.3-0.8	diaphragms	27nm
Starlith® 3300	HVM	2013			0.33	0.2-0.9	flexible	18nm
Starlith® 3350		2015				0.2-0.9	flexible	16nm
Starlith® 3400		2017				0.06-1.0	highly flexible	13nm

Figure 5.13 Overview of the product specifications for EUVL optical systems.

single exposure (Fig. 5.14). This section discusses specific effects that pose a challenge to high-NA: Firstly, the mask is becoming more important due to shadowing effects. Secondly, the angular spectrum on the second-to-last mirror increases significantly, such that the EUV coating on this mirror cannot reflect the light with sufficient intensity. As will be shown, these two effects necessitate new optics and force changes in the applied optical concepts when compared to the present optical systems. After discussing a potential solution on the level of the optical system, this section examines in more detail the theoretical background of the imaging effects induced by mask shadowing and central obscuration.

5.3.2 Optical system for high-NA

Figure 5.15(a) illustrates how the light cones and optical fields at the mask and wafer are defined in the NXE:3300B. Each field point at the mask is illuminated by an incoming light cone. The light cone is reflected into the projection optics. The openings of these cones are determined by the NA and the MAG. The numerical aperture at the mask NA_{mask} is given by the quotient NA/MAG and holds for the NXE:3300B:

$$NA_{mask} = \frac{NA}{MAG} = \frac{0.33}{4x} = 0.0825. \tag{5.3}$$

The incoming and outgoing light cones are separated by a chief ray angle at object (CRAO) of 6 deg. Looking at the middle of the optical field, the CRAO is defined at the mask as the angle measured against the surface normal of the central ray of the incoming light cone. An object field of $104\ \text{mm} \times 132\ \text{mm}$ at the mask is imaged onto an image field of

Downloaded From: https://www.spiedigitallibrary.org/ebooks/ on 09 Mar 2022
Terms of Use: https://www.spiedigitallibrary.org/terms-of-use

NA	0.25	0.33	0.45	0.50	0.55
Resolution @k1=0.3 single exposure / nm	16.2	12.3	9.0	8.1	7.4

Figure 5.14 Resolution of an EUVL optical system depending on NA.

26 mm × 33 mm at the wafer (after scanning). Figure 5.15(b) shows that this combination of MAG and CRAO cannot be used in a system with higher NA, as the light cones overlap. Overlapping of these cones means a physical obscuration at the edge of the pupil, effectively reducing the NA and hence the resolution capability of the system. A separation of the light cones is thus mandatory. Increasing the CRAO is a straightforward way to separate the light cones again [Fig. 5.15(c)]. For a moderate increase in NA from 0.33 to 0.45, an increase in CRAO from 6 deg to 9 deg is needed. As explained in more detail in Section 5.3.3, shadowing effects induced by the mask occur. Another way to reduce the angular spread at the mask while keeping the CRAO of 6 deg is to increase the MAG of the projection optics [Fig. 5.15(d)]. Increasing the MAG from 4× to 8× results in a sufficient reduction of the angular spread at the mask. This approach indeed restores excellent imaging performance together with high mask reflectivity.[54,55] A change in MAG implies a change in field size. Keeping the object field at the mask at the size of 104 mm × 132 mm, a MAG of 8× leads to a 13 mm × 16.5 mm quarter field at the wafer. If the chip design requires an odd number of dies, four quarter fields must be stitched together, resulting in four times more masks and four stitching lines. In addition, the scanner needs to step four times as much. Doubling the MAG from 4× to 8× but keeping the 26 mm × 33 mm full field at the wafer again achieves sufficient imaging performance together with high productivity, but requires a mask size of 12 inches instead of the currently used 6 inches.[56]

A further option is to squeeze the incoming and reflected light cones at the mask in only one direction[57,58] [Fig. 5.15(e)], enabling a CRAO of 6 deg and separating the cones. Since this is the folding direction of the optical train, i.e., the direction in which the CRAO is tilted away from normal incidence, it is also the direction in which effects induced by the mask matter the most. The MAG only has to be increased from 4× to 8× in the y direction, while the MAG of 4× can be maintained in the x direction. The MAGs in x and y become different, and thus the MAG becomes direction dependent, a concept called anamorphic projection. The angular spread at the mask also decreases in the relevant y direction, sufficiently reducing shadowing effects and hence enabling good imaging performance using a standard multilayer coating and absorber at the mask.[59] Note that the cones stay circular at the wafer. The anamorphic optics projects a stretched mask pattern into the desired isogonic

Downloaded From: https://www.spiedigitallibrary.org/ebooks/ on 09 Mar 2022
Terms of Use: https://www.spiedigitallibrary.org/terms-of-use

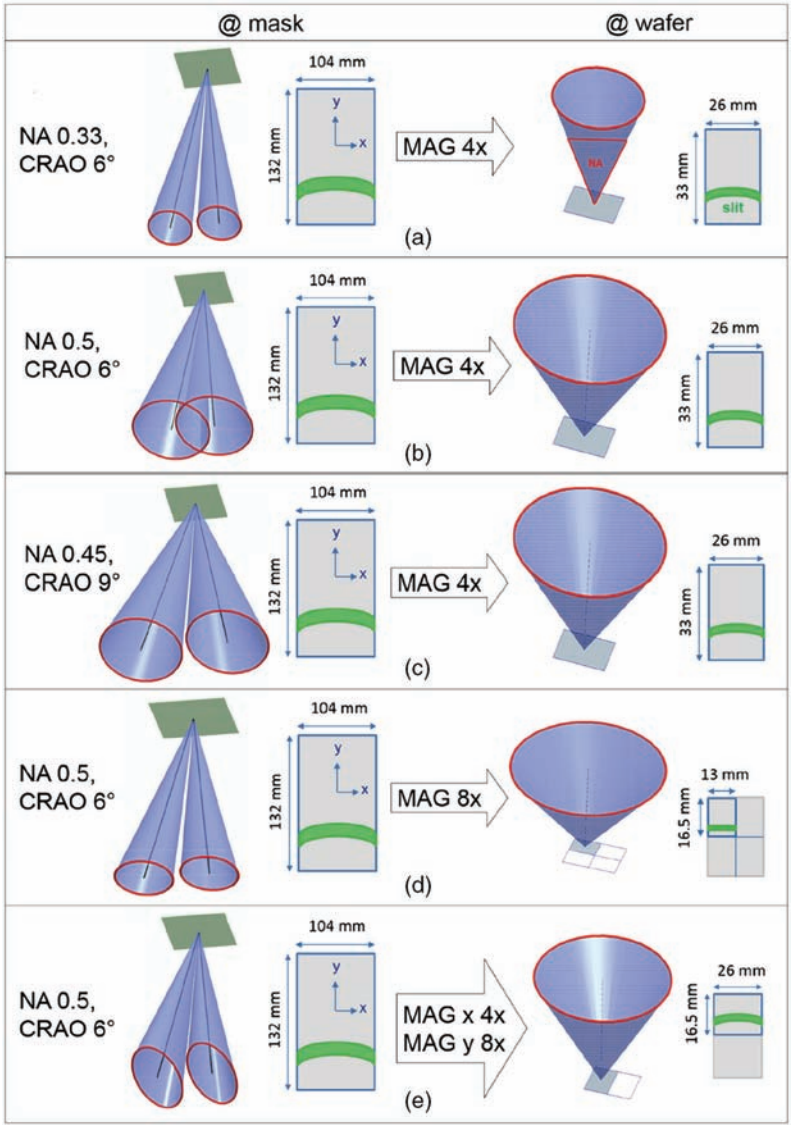

Figure 5.15 (a) As EUV uses reflective masks, oblique incidence at the mask is used to separate the incoming light cone (from the illuminator) from the outgoing light cone (toward the projection optics). (b) Enlarging the NA at the wafer while maintaining the MAG and the chief ray angle at object (CRAO) increases the NA at the mask. This causes the light cones to overlap. (c) Increasing the CRAO separates the light cones again but leads to significant shadowing issues. (d) Changing the MAG from 4× to 8× reduces angles at the mask to an acceptable level. But keeping the mask size at 6 inches reduces the image field at the wafer to a quarter field, yielding unacceptable productivity loss. (e) Changing the MAG to 8× only in the scanning direction of the lithography system reduces the critical incidence angles at the mask, enabling good imaging performance. Using a standard 6-inch mask, a half field can be exposed at the wafer.

Downloaded From: https://www.spiedigitallibrary.org/ebooks/ on 09 Mar 2022
Terms of Use: https://www.spiedigitallibrary.org/terms-of-use

patterns at the wafer. Applying this concept, a standard object field of a 6-inch mask can be imaged onto a half field of size 26 mm × 16.5 mm (after scanning) at the wafer. If the circuit design requires the full field, the configuration implies one stitching line. However, the half field concept has the potential to enable a high throughput of ≥150 wph for the scanner.[60]

Large angular loads occur not only at the mask. A higher NA leads to higher incidence angles within the projection optics as well. Figure 5.16 illustrates another challenge of a high-NA system, specifically relevant for the last two mirrors of the projection optics closest to the wafer. Light comes from the top right, hits the second-to-last mirror, is reflected to the last mirror, and is finally reflected onto the wafer, which is depicted at the bottom of the sketch. Since the second-to-last mirror must not block the light path from the last mirror to the wafer, this mirror is tilted outward to the right. Increasing the NA means that the depicted geometry, including the mirrors and light cones, is stretched horizontally. Thus, both the average angle of incidence and the angular range at each point on the second-to-last mirror increase for high-NA. Multilayer coatings set limits for the bandwidth for a given average angle, and standard EUV coatings are not able to reflect the combination of large angles and large angular spreads with high reflectivity. With increasing

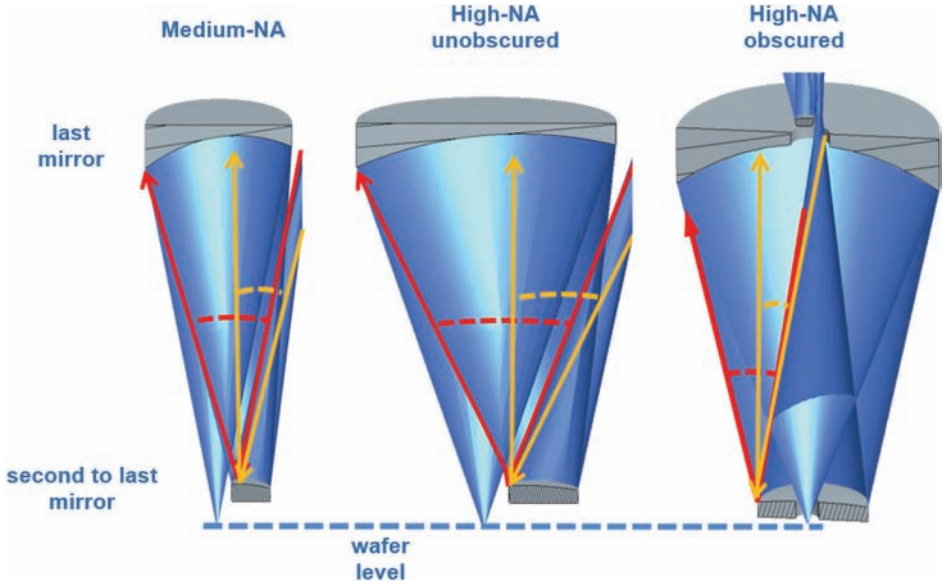

Figure 5.16 Last and second-to-last mirrors of the projection optics. (Left): Standard layout. The second-to-last mirror is tilted outward so as to not block the light path. (Middle): For a high-NA, mirror sizes increase, and hence the second-to-last mirror needs to be pushed out even farther. This leads to unacceptably large angles and angular ranges on this mirror. (Right): New layout. The second-to-last mirror is placed within the light path and holes are drilled in the mirrors so that incidence angles can be kept small.

Downloaded From: https://www.spiedigitallibrary.org/ebooks/ on 09 Mar 2022
Terms of Use: https://www.spiedigitallibrary.org/terms-of-use

NA, the operating points of an EUV coating will not match the angular load in a mirror point, and parts of the mirror will become black. The solution to this challenge is simple:[61] the second-to-last mirror is pushed back to the left again and holes are drilled into the mirrors through which the light can travel from the rest of the projection optics to the last two mirrors and finally to the wafer. This way, the angular load on the second-to-last mirror can be reduced. The angular load on the coatings is reduced so much that a significant transmission increase becomes possible.

The holes drilled in the mirrors have a specific effect on imaging. The center of the projection optics exit pupil is effectively blocked (Fig. 5.17). When exposing arbitrary patterns, typically, some part of the diffracted light is blocked by the central obscuration and is no longer available for image formation. The corresponding zeroth order misses an interference partner, and consequently some contrast is lost. One example is shown in Fig. 5.18, where vertical line-and-space (L/S) patterns through pitch are exposed with a relatively wide dipole. Assuming that the 9-nm lines (core) and 18-nm lines (periphery) are printed simultaneously, both are printed at various pitches. Here, the image quality is characterized by the normalized image log slope (NILS), which is defined by

$$NILS = CD\left[\frac{\partial \ln I}{\partial x}\right]_{I=I_{thr}}; \tag{5.4}$$

see Ref. 38 for a more detailed explanation. A large NILS means that the image intensity I has a steep slope close to the resist threshold I_{thr}, making the

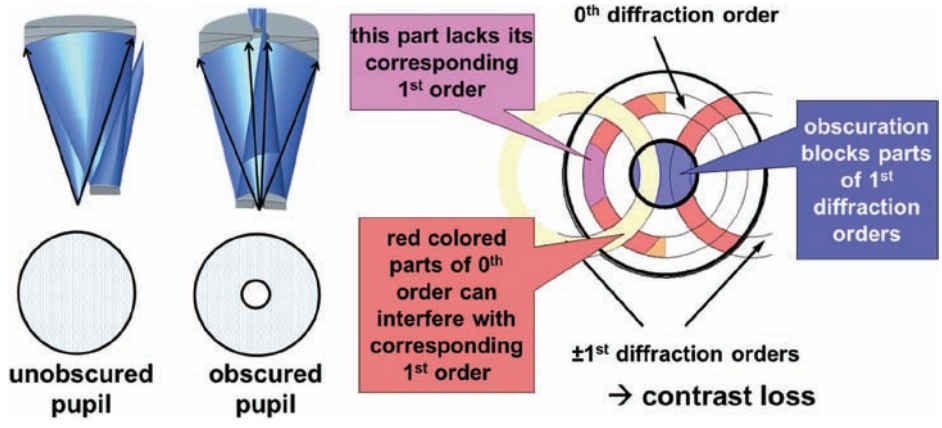

Figure 5.17 The modified design for the second-to-last mirror creates a central obscuration in the exit pupil of the projection optics (left). Although the illumination can be chosen such that the actual illumination (zeroth diffraction order) does not hit the obscuration, light is diffracted at the mask. Depending on the mask structures, some diffraction orders can hit the obscuration and can be blocked. As the blocked light is no longer available for image formation at the wafer, some contrast will be lost.

Downloaded From: https://www.spiedigitallibrary.org/ebooks/ on 09 Mar 2022
Terms of Use: https://www.spiedigitallibrary.org/terms-of-use

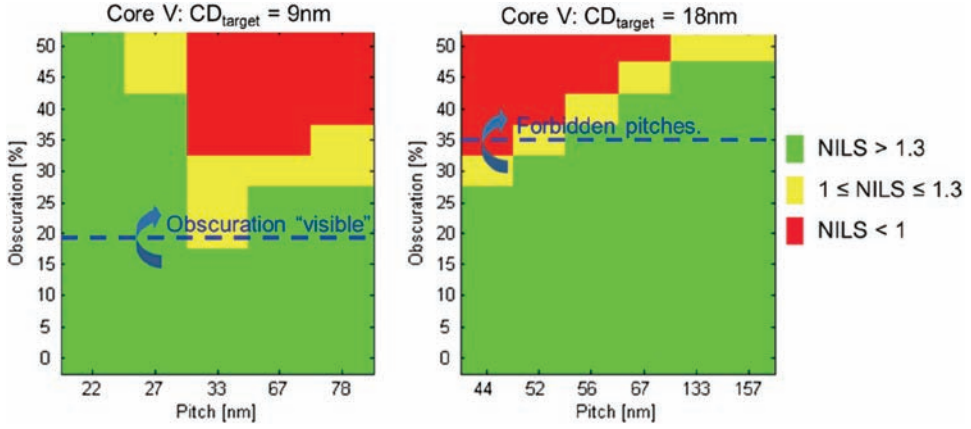

Figure 5.18 Obscuration impact on imaging. Part of the diffracted light is blocked by the obscuration, leading to some loss of contrast at the wafer. The NILS (as a measure for contrast) for spaces through pitch is shown, exposed with a dipole setting, as a function of the obscuration size. For obscuration radii <20% of the pupil radius, contrast loss is hardly noticeable. For obscuration radii between 20% and 35%, contrast loss becomes visible. For obscuration radii larger than 35% of the pupil radius, contrast loss for some pitches is so significant that it will no longer be possible to print these forbidden pitches with reasonable process margins.

process rather tolerant against dose variations. Using a simple threshold model for the resist, the contrast loss within the resist is modeled by convoluting the aerial image with a Gaussian kernel of standard deviation $\sigma = CD/3 = 3$ nm. As a rule of thumb, a process needs $NILS \geq 1$ to print with sufficient margins (displayed in yellow in Fig. 5.18). The process has large margins with $NILS \geq 1.3$ (displayed in green). With an increasing size of the central obscuration, the NILS degenerates and the obscuration becomes visible for some pitches at an obscuration radius of ~20% to ~25% of the clear aperture. Further increasing the obscuration radius to ~35%, the obscuration induces so-called forbidden pitches, which cannot be printed with sufficient process margins. Evaluating a variety of use cases, it turns out that this result is rather universal: A central obscuration is not critical as long as it covers less than ~4% to ~6% of the pupil area.

5.3.3 Theoretical background

The preceding section pointed at two locations with high angular load (the mask and the second-to-last mirror in the projection optics) and sketched the solutions for the challenges associated with these high angular loads. This section will take a closer look at these locations. In order to understand the mask effects on high-NA imaging, it is crucial to note that in addition to the CRAO, a whole range of incident angles appears on the mask. These angles are centered around the nonzero CRAO. The example sketched on the right

Downloaded From: https://www.spiedigitallibrary.org/ebooks/ on 09 Mar 2022
Terms of Use: https://www.spiedigitallibrary.org/terms-of-use

side of Fig. 5.19 illustrates that one pole of a dipole belongs to small angles of incidence, while the other pole belongs to large angles of incidence located at the opposite side of the illuminator pupil. The pattern on the mask is formed by an absorber located on top of the reflective multilayer. This absorber casts a shadow due to its thickness and the oblique incidence of light. Since light is not reflected from the top of the multilayer but from within, the shadowing effect is more significant than one would guess from only the geometrical height of the absorber.

Making the absorber thinner, or even reducing absorber thickness to zero, will reduce but not fully eliminate the shadowing effect. The shadowing depends on the angle of the incident light, as can be seen in the sketches of Fig. 5.19. Light with a rather shallow angle (left) sees rather strong shadowing and hence sees a relatively wide effective linewidth, whereas light with a steeper angle sees a much less severe shadowing and consequently sees a much smaller effective linewidth. Since one side of the illumination pupil consists of small angles and the other side of large angles, the two sides of the illumination pupil experience different absorber shadowing and consequently different effective linewidths. These angle-dependent effective linewidths lead to imbalances between the illumination poles as well as between the diffraction orders of the individual poles. However, this geometric picture is a strong simplification, as it neglects diffraction effects. Furthermore, the light is not reflected from one clearly defined plane within the multilayer but from within the bulk of the multilayer due to constructive interference. The multilayer behavior can in general be angle dependent and is able to reinforce or (partially) compensate absorber shadowing. Also, this simple geometric

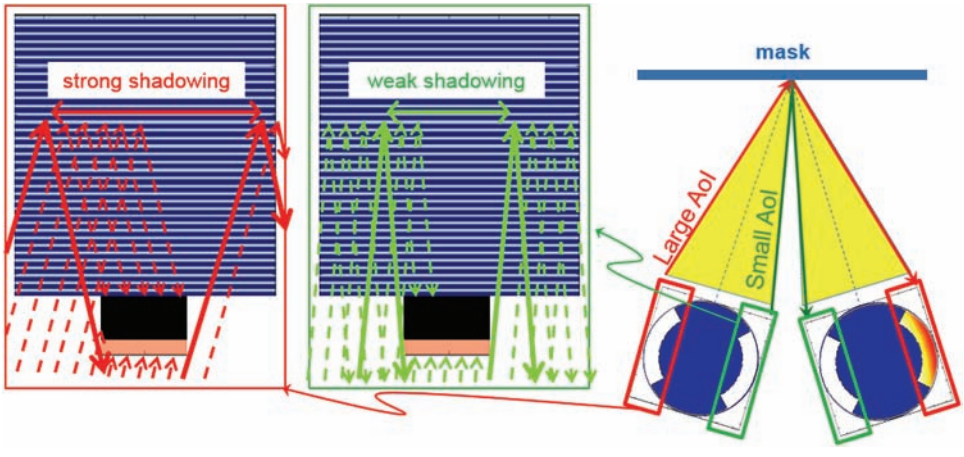

Figure 5.19 Simplified geometric sketch of absorber shadowing. In addition to the CRAO, a full range of angles are incident on the mask. Due to oblique illumination, the angles of incidence are not distributed symmetrically around zero but instead around the nonzero CRAO. In consequence, the two poles see different effective linewidths.

Downloaded From: https://www.spiedigitallibrary.org/ebooks/ on 09 Mar 2022
Terms of Use: https://www.spiedigitallibrary.org/terms-of-use

picture neglects the effects of the phase that the diffracted light may pick up due to rigorous mask effects. These phases will also depend on the angle of incidence. This picture also neglects the fact that the absorber is not perfectly dark. The absorber-covered area of the mask still reflects roughly 2% of the incident light.[62]

All of these effects are accounted for in rigorous simulations. Results from such rigorous simulations turn out to qualitatively agree with this simplified geometric picture.[54] Figure 5.20 shows simulated diffraction patterns for $NA = 0.33$ (CRAO = 6 deg) and $NA = 0.45$ (CRAO = 9 deg). The upper patterns were obtained for simulated open frame exposures, i.e., with no absorber pattern present on the mask. Consequently, the diffraction pattern as it would appear in the pupil plane of the projection optics contains only the zeroth order, namely, only the illumination dipole as it is reflected from the mask. Considering the two leftmost columns, a well-balanced pattern for the $NA = 0.33$ case can be found, while the $NA = 0.45$ case yields a noticeable intensity difference between the upper pole (small incidence angles) and the lower pole (large incidence angles). The large angles are attenuated by the multilayer stack as the reflectivity of the standard mask coatings drops for incidence angles ≥11 deg. The lower diffraction patterns were obtained for

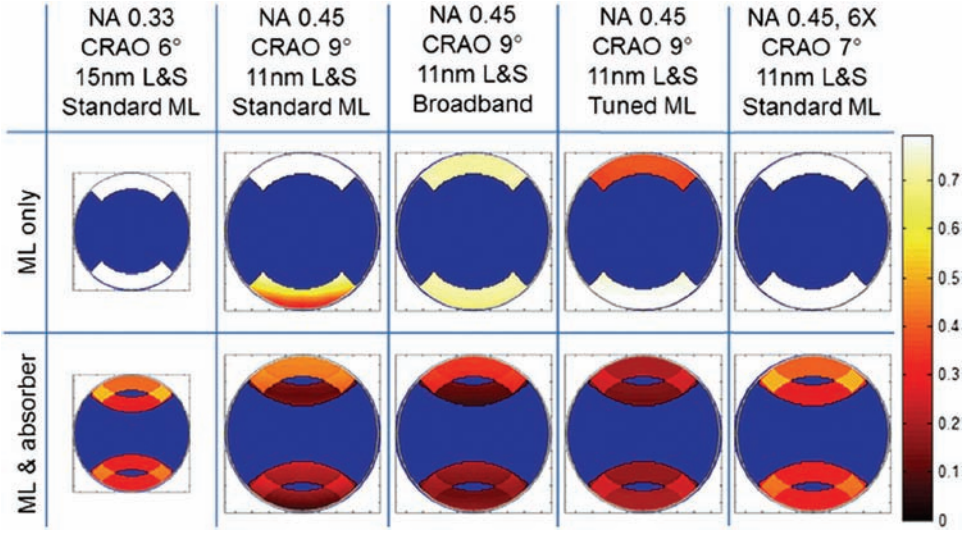

Figure 5.20 Diffraction patterns simulated for open frame exposure (pure multilayer reflection) and for lines-and-spaces with a half-pitch of 15 nm for $NA = 0.33$, 11 nm for $NA = 0.45$, i.e., $NA \times hp/\lambda = \text{const.} = 0.37$ in all cases. The upper pole corresponds to steep incidence on the mask (represented by the green frame in Fig. 5.19). The lower pole corresponds to shallow incidence on the mask (the red frame in Fig. 5.19). The upper row (open frame exposure) shows how the multilayer reflectivity changes according to the incidence angles and the ML stack layout. The lower row (with a L/S pattern on the mask) represents the additional contribution of absorber shadowing.

Downloaded From: https://www.spiedigitallibrary.org/ebooks/ on 09 Mar 2022
Terms of Use: https://www.spiedigitallibrary.org/terms-of-use

simulated L/S exposures, with a half-pitch (hp) of 15 nm in the $NA = 0.33$ case and 11 nm in the $NA = 0.45$ case; i.e., $NA \times hp/\lambda = \text{const.} = 0.37$ in all cases. There is absorber shadowing even in the diffraction pattern of the case with $NA = 0.33$. The zeroth order of the lower pole (large incidence angles) is slightly attenuated compared to the upper pole. This shadowing effect is tolerable for $NA = 0.33$. For the $NA = 0.45$ case, however, the imbalance between the two poles of the dipole is much more severe. As expected from the simple geometric consideration presented in the preceding section, the absorber induces significant shadowing on the lower pole (large incidence angles) and far less shadowing on the upper pole. Compared to the case of $NA = 0.33$, the lower pole is much more attenuated than the upper pole. The drop in multilayer reflectivity, which also attenuates the lower pole, reinforces this effect. This asymmetry of zeroth orders will lead to noticeable telecentricity effects[63,64] and can be partially compensated for by means of illumination tuning.[54] Apart from this imbalance of zeroth orders, the first diffraction order of the upper pole is also much weaker than the zeroth order. This first order is diffracted into a large angle of exit from the mask and hence is shadowed by the absorber. Such an intensity imbalance between the zeroth and first orders will lead to significant contrast loss in the aerial image.[65] In order to validate the simulations of mask effects for high-NA imaging, diffractometric experiments were performed at LBNL[66] using a mask manufactured by Samsung. The results of these measurements confirm the simulations.[55,66] The potential of anamorphic imaging to significantly reduce angle-related effects at the mask has been verified experimentally by, e.g., the SHARP microscope.[67]

Solving these imbalances in the diffraction patterns by tuning the multilayer does not provide satisfying results.[54,55] Instead, the MAG of the projection optics must be changed. Three possible strategies to cope with the mask effects at high-NA imaging are considered in the remaining columns of Fig. 5.20. The first two options correspond to two different optimizations of the multilayer stack. One multilayer is optimized for broadband reflectivity, as can be seen in the open frame pattern (upper row) of the third column. With this multilayer stack, both poles are reflected with the same efficiency in spite of their different angles of incidence. The full diffraction pattern including absorber still yields a noticeable asymmetry (lower row), since the absorber attenuates the large angles of incidence. The second option uses a multilayer stack optimized for the specific-use case at hand, and the resulting diffraction patterns can be seen in the fourth column. While the open frame reflectivity (upper row) shows a significant imbalance due to an attenuation of the upper pole (small angles of incidence), the full diffraction pattern with absorber (lower row) is well balanced. The absorber attenuates the large angles of incidence—in exact opposition to the multilayer behavior. This mutual attenuation of small and large incidence angles by multilayer and

Downloaded From: https://www.spiedigitallibrary.org/ebooks/ on 09 Mar 2022
Terms of Use: https://www.spiedigitallibrary.org/terms-of-use

absorber comes at the loss of mask reflectivity. The third option is different from the first two, as it still uses the standard mask stack. Instead of tuning the mask, the MAG of the projection optics is used to accommodate for the high-NA. As can be seen in the last column in Fig. 5.20, the diffraction pattern, both open frame and with absorber, looks very much like that in the $NA = 0.33$ case, but now at a finer resolution of 11-nm half-pitch instead of 15 nm. The figure indicates the wide radius of the diffraction pattern due to the high-NA at the wafer. By means of the increased MAG, the NA at the mask can be reduced to a value even below the $NA = 0.33$ case. In the $NA = 0.33$ case it is $NA_{mask} = 0.33/4 = 0.0825$, and in the $NA = 0.45$ case with a MAG of $6\times$ it is $NA_{mask} = 0.45/6 = 0.075$. All mask effects are reduced compared to the $NA = 0.33$ case in spite of the increased NA at the wafer. This allows for fine resolution at the wafer without suffering from mask effects.

Figure 5.21 shows the image quality results represented by image contrast and relative mask reflectivity. The blue bars represent the contrast of the aerial image, and the red bars represent the mask reflectivity normalized to the reflectivity obtained for the $NA = 0.33$ case. Using the standard multilayer, image contrast and mask reflectivity drop for the $NA = 0.45$ case, although the half-pitch has been scaled such that in both cases $k_1 = 0.37$ holds, naively suggesting a similar performance. The difference between these two cases is given by the large incidence angles at the mask in the $NA = 0.45$ case. A broadband multilayer, ensuring a uniform reflectivity of the multilayer throughout the whole range of incidence angles, helps to improve contrast as

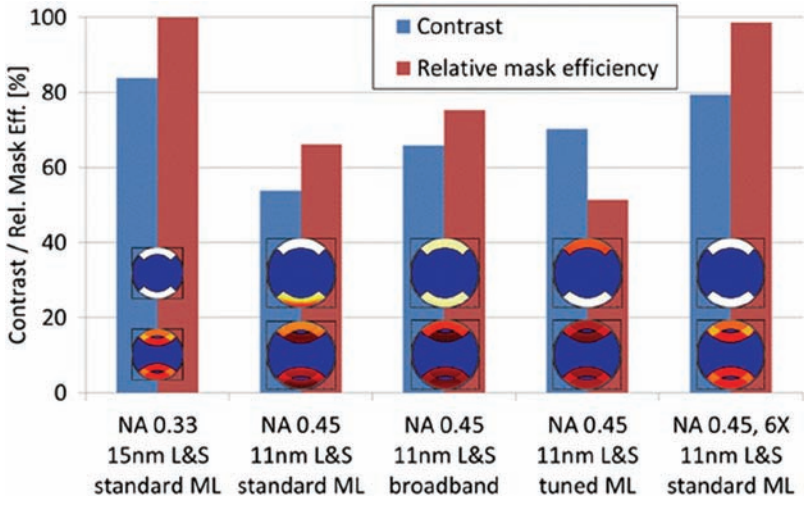

Figure 5.21 Image quality (represented by image contrast and mask efficiency) normalized to the *NA* = 0.33 reference case for various options at *NA* = 0.45. For all high-NA cases, only the one with the adjusted MAG (rightmost bars) roughly reproduces the performance of the *NA* = 0.33 reference case, but at improved resolution.

Downloaded From: https://www.spiedigitallibrary.org/ebooks/ on 09 Mar 2022
Terms of Use: https://www.spiedigitallibrary.org/terms-of-use

well as mask efficiency. But it still stays short of the performance of the $NA = 0.33$ reference case. The tuned multilayer compensates for the angle-dependent absorber shadowing by attenuating the small incidence angles and indeed helps to further improve the image contrast. But this gain in contrast comes at the loss of mask efficiency. Since EUV light is a rather expensive resource, this is clearly not an attractive option. The increased MAG, however, regains the performance of the $NA = 0.33$ reference case in both image contrast and mask efficiency at a resolution of 11-nm half-pitch compared to 15-nm half-pitch in the $NA = 0.33$ case. Keeping the MAG at $4\times$, mask effects have significant impact on the mask performance in terms of image quality and mask efficiency. Adopting the MAG enables a high-NA at the wafer.

For the sake of simplicity in this explanation of fundamental effects, anamorphic imaging is not yet employed and MAG is changed simultaneously in all orientations. The anamorphic performance is verified at the end of this section, including the obscuration and proving that this system indeed yields good imaging performance. Note that only the standard mask stack with a Ta-based absorber on top of a Mo/Si-based multilayer is presented, together with minor modifications. Alternatives to this mask technology have been discussed in the literature that utilize either new absorber materials allowing for thinner absorbers,[68] new materials for the multilayer stack reducing the penetration depth of EUV light within the multilayer,[69] or completely new mask architectures.[70–72] All of these concepts have the potential to mitigate mask-induced effects to some degree, although none of them fundamentally solves the issues. Furthermore, none of these concepts is even close to maturity.

In order to confirm the imaging feasibility of an anamorphic projection optics with a central obscuration, in the following an optical configuration is assumed with a NA of 0.55 and a central obscuration with radius 20% of the pupil radius, corresponding to an obscured area of 4% of the total pupil area. The high-NA system is compared to a Starlith® 3300 with a NA of 0.33 and an unobscured exit pupil. As a first example, we consider horizontal and vertical spaces through pitch, which are exposed simultaneously with a small annular setting. For the high-NA system, the half-pitch starts at 12 nm; for the system with $NA = 0.33$, the half-pitch starts at 20 nm. Since the illumination is located rather close to the center of the pupil, this use case will not be very sensitive to angle-related effects. However, when going through pitch, the diffraction orders will hit the obscuration. Comparing the high-NA system to the reference system, the imaging impact of the central obscuration can be studied. Simulated process windows for both cases are shown in Fig. 5.22. The focus axis is scaled accordingly to $1/(NA)^2$, and acknowledging that the depth of focus scales with this factor, a high-NA system hence exhibits a lower depth of focus.[73] This is an immediate consequence of a high-NA at the wafer side

Downloaded From: https://www.spiedigitallibrary.org/ebooks/ on 09 Mar 2022
Terms of Use: https://www.spiedigitallibrary.org/terms-of-use

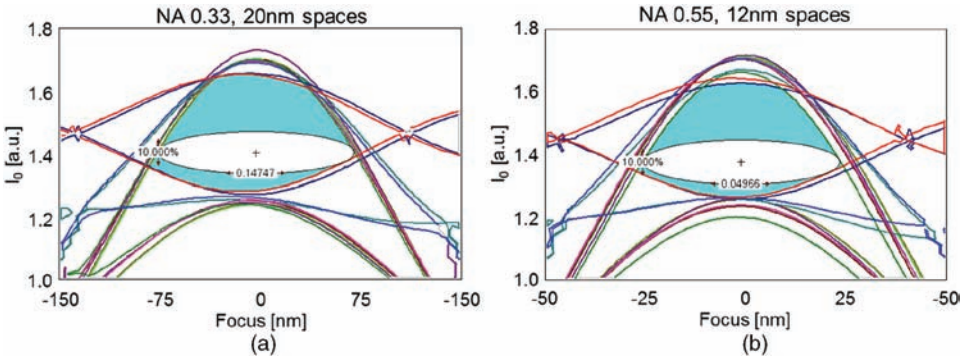

Figure 5.22 Process window for horizontal and vertical spaces through pitch, exposed with an annular setting. (a) 20-nm spaces with $NA = 0.33$ (isomorphic, no obscuration). (b) 12-nm spaces with $NA = 0.55$ (anamorphic, central obscuration with radius 20% of the pupil radius). DOF scales by $1/(NA)^2$, as expected. The anamorphic optics with central obscuration reproduces the imaging performance of the $NA = 0.33$ reference system but at an improved resolution, which will enable two more nodes.

and a side effect of high resolution. As has been the case with every NA step in the history of semiconductor lithography, the design of both scanner and optics needs to take care of this reduced depth of focus by a tight focus control. Apart from this expected difference, the simulated process windows look very similar. This means that the obscuration does not noticeably hurt the imaging performance.

Another example involves printing a two-bar trench pattern with a varying long pitch, using a quasar illumination setting, again simultaneously for horizontal and vertical orientation (Fig. 5.23). The widths of the trenches are 12 nm for the high-NA system and 20 nm for the system with $NA = 0.33$. This use case will not be affected at all by the central obscuration. Printing only horizontal and vertical features, diffraction orders will never hit the obscuration. Utilizing the edge of the pupil in the illumination, i.e., the edge of

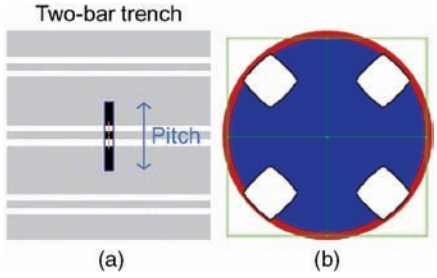

Figure 5.23 (a) Two-bar trench pattern exposed with (b) a quasar setting for the process window analysis shown in Fig. 5.24. The width of the trenches is 20 nm for $NA = 0.33$ and 12 nm for $NA = 0.55$. The center-to-center distance between the trenches is twice the trench width, and the distance between the adjacent two trench features is varied between 120 nm and 200 nm ($NA = 0.33$) and 72 nm and 120 nm ($NA = 0.55$).

Downloaded From: https://www.spiedigitallibrary.org/ebooks/ on 09 Mar 2022
Terms of Use: https://www.spiedigitallibrary.org/terms-of-use

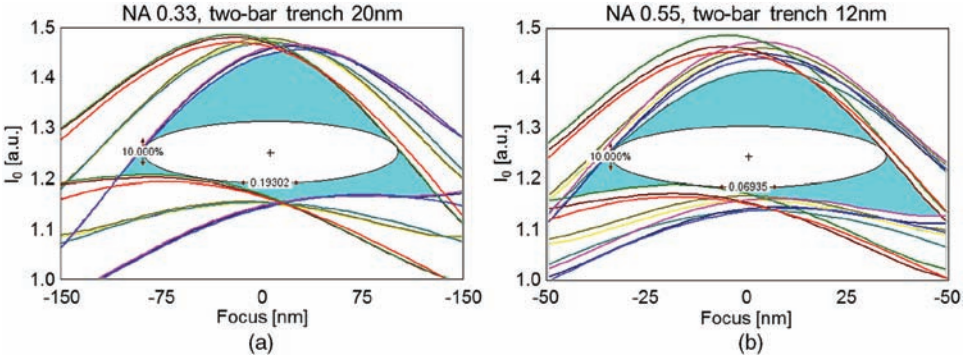

Figure 5.24 Process window for horizontal and vertical two-trench patterns through pitch, exposed with a quasar setting. (a) 20-nm spaces with $NA = 0.33$ (isomorphic, no obscuration). (b) 12-nm spaces with $NA = 0.55$ (anamorphic, central obscuration with radius 20% of the pupil radius).

the illumination light cone, this use case tests the angular effects of the anamorphic system. Simulated process windows are shown in Fig. 5.24. Again, the focus axis is scaled according to $1/(NA)^2$, and the process windows are very similar apart from the expected DOF difference. The anamorphic imaging concept works well, and the high-NA system extends the imaging performance of the $NA = 0.33$ reference system by roughly two more nodes. Restricting the examples to one probing the central obscuration and one probing angular effects, more results regarding the imaging behavior of an anamorphic high-NA system with central obscuration can be found in the literature.[59,74]

5.3.4 Conclusion on optical systems for EUVL

Optical systems for EUVL have undergone a tremendous evolution since the late eighties. In the subsequent years, research efforts were undertaken with low-NA and/or small-field optics. Full-field systems with increased NA were introduced as additional prototypes and research tools, produced and shipped in small series. For ASML and ZEISS, the ADT and NXE:3100 established a learning curve that enabled the successful development, production, and shipment of the NXE:3300B, the first EUV optics for HVM. Shipment of the NXE:3300B/3400B family started in 2013, securing progress in the semiconductor market for at least the entire coming decade. The ZEISS AIMS EUV is critical for ensuring HVM (see Section 5.7). Excellent performance data was demonstrated for all of these products. Over the years, ASML and ZEISS have undergone a successful learning and development process concerning the basic technologies that make these optical systems possible. The resolution capabilities of the optics were continuously improved. And extending the boundaries of what is technically feasible will not stop; high-NA optics will

Downloaded From: https://www.spiedigitallibrary.org/ebooks/ on 09 Mar 2022
Terms of Use: https://www.spiedigitallibrary.org/terms-of-use

have the potential for a resolution limit below 8 nm in a single exposure. Currently, ASML and ZEISS are working on a challenging R&D project to realize a high-NA tool featuring a NA of 0.55 with a half field and a central obscuration of ~20%. For the moment, these EUVL optics will be the summit in the quest for the ultimate lowest-cost-per-pixel printing machine, while continuing to extend Moore's law.

5.4 Optical Modules: Collector

5.4.1 Introduction

EUV scanners make use of plasma sources to generate the EUV light. The plasma is typically generated from heating Sn, either by electrical discharge on a Sn electrode (discharge-produced plasma, DPP) or by irradiating a small Sn droplet with an infrared laser beam (laser-produced plasma, LPP).[75] For EUVL applications, a high-power light source with > 200 W of usable EUV power is necessary to enable acceptable cost of ownership. LPP sources based on Sn target material with a pre-pulsed CO_2 laser operation recently have proven to be able to produce the required power of 100 to 250 W of narrowband EUV light at $\lambda = 13.5$ nm.[76,77] While the plasma of the EUV source radiates its light into all directions, the optical system can only utilize light in a defined narrow cone of its input NA. Therefore a stage of collection optics is necessary in the source to collect the emission from the plasma, suppress undesired wavelengths, and supply the radiation to the illuminator. The collection optics unit consists mainly of a collector and sometimes a spectral purity filter, which can also be unified into one optical element. Special requirements of the environmental conditions—such as high-radiation loads ranging from the IR to soft x ray—and exposure to strongly degrading particles and ions render the collection optics unit quite unique. In this section, basic design concepts for the collector will be discussed, and practical realization aspects for the ADT and the NXE:3100 will be explained in more detail.

5.4.2 EUV collector types

The surface of a collector mirror in the source is bombarded with ions and fragments of the Sn fuel, eroding the reflection coating away from the mirror or contaminating the surface with nonreflecting Sn particles; strong electromagnetic radiation in all wavelength ranges between infrared and x-ray impinges the surface, and high thermal loads have to be carried away by the collector mirror. At the same time, the illuminator needs a precisely determined and constant plasma image at its entrance at the intermediate focus (IF) to fulfill its functionality. Both grazing and normal-incidence EUV mirrors can be used to build suitable collection optics around the source plasma. But the different types of EUV sources each require different

Downloaded From: https://www.spiedigitallibrary.org/ebooks/ on 09 Mar 2022
Terms of Use: https://www.spiedigitallibrary.org/terms-of-use

properties of the optics. For example, compared to LPP sources, DPP sources exhibit a higher Sn contamination load onto the collector. Although debris mitigation techniques such as foil traps are installed, the amount of Sn used in this source type vessel is much higher. Another reason for the increased contamination load is the geometry of the liquid Sn electrodes for DPP. LPP sources work with only a microscopic portion of Sn-per-plasma pulse but need a very powerful mid-IR wavelength laser. The laser light is also reflected from the plasma to some extent, heats up the collector, and enters the illuminator if no filtering is applied. Also, the plasma and thus the light source characteristics are different. In an LPP source, the laser hits a microscopic Sn target that forms a relatively small plasma cloud with high peak irradiance. The small dimension of the plasma is beneficial for the illuminator because it enables a small étendue and a small pupil fill ratio. The plasma light source properties are transported via the optical imaging quality of the collector into a small and sharp plasma image on the IF. The DPP source has a much larger plasma volume and thus requires a collector capable to image a larger object field into a sharp image on the IF. A DPP source has a large electrode system on one side of the plasma that would make a mirror for light collection on that side useless. The plasma in the LPP source is generated in free space where the Sn droplets cross the beam of the IR laser.

Grazing-incidence collectors are a natural choice for the DPP source because they are better adapted to the geometry and plasma size restrictions of this source type, as well as to the higher Sn and debris load. The Wolter-type grazing-incidence collector offers the necessary large object field for DPP due to its nearly aplanatic design with two consecutive reflections, as will be shown in the next paragraph. Normal-incidence collectors can easily surround the LPP plasma, collect more light, and deliver less distortion of the imaging quality under high thermal loads. That makes them better suited for the high-power LPP sources. This can be achieved with simple ellipsoid collector mirror designs, as the plasma of LPP sources is small, even though such designs with only one reflection of the light at the collector surface are not aplanatic and exhibit varying magnification over their free aperture. In the following subsections, both kinds of collectors will be discussed individually together with application examples: the grazing-incidence collector of the ADT and the normal-incidence collector for most of the NXE:3100 tools.

5.4.3 Grazing-incidence collectors

A grazing-incidence EUV collector is typically realized as a Wolter collector. Hans Wolter proposed three types of x-ray imaging optics systems utilizing only grazing mirrors in 1952.[78] His main idea was to always use two sequential grazing reflections at different curved optical surfaces for imaging of objects with x rays, to keep the grazing angles small and thus reflectivity high, while at the same time mostly eliminating imaging errors from the

Downloaded From: https://www.spiedigitallibrary.org/ebooks/ on 09 Mar 2022
Terms of Use: https://www.spiedigitallibrary.org/terms-of-use

optics. Mainly relevant for collector application is the Wolter-type 1 system, which consists of a hyperboloid reflector followed by a paraboloid mirror for imaging a point radiator into infinity (or vice versa), or an ellipsoid mirror for finite lengths, as shown in Fig. 5.25. Its basic design principle follows the design of a Cassegrain reflector but using grazing optics. Both the hyperboloid and the ellipsoid/paraboloid surface share one common virtual focus point *F*. The scheme with the paraboloid reflector is extensively used for application in x-ray astronomy, where astronomical objects are imaged onto a detector in the near focus plane. With an ellipsoid reflector as the second mirror, the Wolter-type 1 is suitable for collecting the light of a plasma point in the near focus F′ of the system into a plasma image of the far focus F″.

The Wolter design with an exact hyperboloid and ellipsoid already corrects the spherical aberration of the imaging system but is not fully aplanatic as coma is not completely suppressed. Still it offers already a relatively large object field that can be imaged into a sharp image in the secondary focus of the ellipsoid. So large-sized plasmas benefit more from imaging with a Wolter collector compared to the simpler ellipsoid collectors. The Wolter-type 1 design can even be improved by a so called Wolter–Schwarzschild design, where both reflecting surfaces are changed slightly and become hyperbolas,[79] correcting spherical and coma aberrations. For practical applications though, the improvement in performance of the more complicated Wolter–Schwarzschild designs often is overruled by limiting manufacturing tolerances.[80] The hyperbolic section of the Wolter collector typically faces the plasma point of the source. In this way, the acceptance angle of the hyperbolic section can be high. Radiation is collected up to high angles, while the local grazing-incidence angles are kept small to achieve high reflectivity, as can be seen in Fig. 5.25. The outgoing light cone pointing toward the illuminator can be chosen to be small so that the input NA of the illuminator is not overfilled and no light is lost in the illuminator.

One disadvantage of this Wolter-type scheme is that only radiation in a narrow ring shape is collected from the plasma, and the resulting ring field in

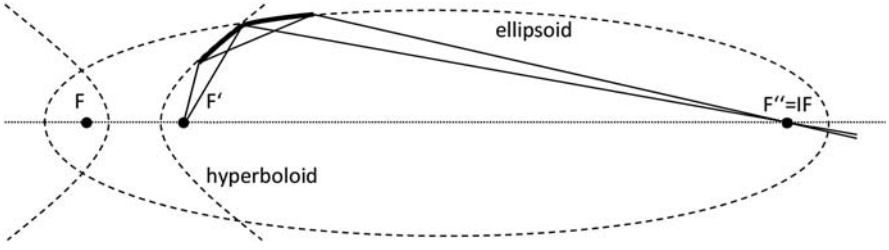

Figure 5.25 Wolter-type 1 scheme for imaging a plasma source in F′ with a high acceptance angle onto a point F″ = IF in finite distance. Only the bold, dark lines are physically realized; the dashed lines indicate the ellipsoid and hyperboloid. The thin, straight lines show individual light rays.

Downloaded From: https://www.spiedigitallibrary.org/ebooks/ on 09 Mar 2022
Terms of Use: https://www.spiedigitallibrary.org/terms-of-use

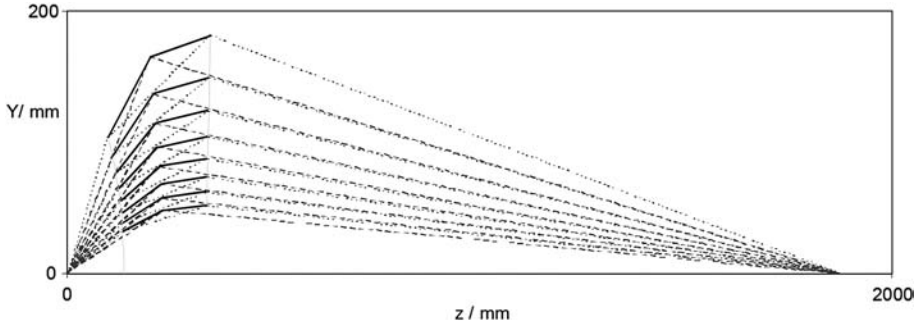

Figure 5.26 Schematic eight-mirror-shell-collector optical design (reprinted from Ref. 81).

the illuminator has a central shadow. It is possible to overcome this problem to some extent if the mirrors used for the reflection are thin circular shells and many of them are nested individually into each other. Figure 5.26 shows such a design with eight nested mirror shells for application as a collector for the ADT. But even with a higher number of shells, light in the central part of the field close to the optical axis cannot be reflected; due to the geometric conditions for the superposition of the ellipsoid and the hyperboloid, the collection angle of the shells becomes smaller and smaller when the shells are positioned closer to the optical axis. So an infinite number of shells would be necessary to completely fill the central obscuration. Practically, the limit where the additional light throughput gain of the collector is small compared to the cost for an additional shell is reached after about 8 to 15 shells for EUV collectors at $\lambda = 13.5$ nm. For hard x-ray telescopes in space applications, on the other hand, the grazing-incidence angles onto the mirror shells are even smaller, so that hundreds of nested shells are necessary to gain sufficient light. The shells have to be thin, as the thickness of each shell is a lost area where no light is reflected so that the associated region in the far field behind the secondary focus is dark.

Practically, the limit of the thickness is on the order of less than one to a few millimeters, since also a reliable cooling of the shells in vacuum at high source operation power needs to be secured. To avoid shadowing of neighboring reflecting surfaces and blind areas between the shells, only a small part at the outside of each shell is usable to mount the structure and feed a cooling system to the shells. The dimensional stability and accuracy of such thin wall metal structures under high thermal loads in vacuum typically is limiting the achievable imaging optical quality of Wolter-type collectors, both for the plasma image in the secondary focus of the ellipsoid section, as well as the far-field quality far behind the secondary focus. Since high throughput EUV illuminators depend highly on the far-field homogeneity and stability, this is a problem for the practical usage of grazing-incidence collectors in EUV systems at higher power.

Downloaded From: https://www.spiedigitallibrary.org/ebooks/ on 09 Mar 2022
Terms of Use: https://www.spiedigitallibrary.org/terms-of-use

The shells for grazing-incidence nested Wolter-type collectors are usually made via a high-precision metal replica process on so-called mandrels. The mandrel exhibits the original shape of the mirror shell and can be produced, for instance, via single-point diamond turning into an aluminum alloy, or by grinding and polishing from low-thermal expansion ceramics material (Fig. 5.27). The surface of the mandrel must be polished to the roughness levels that are needed later on for the high reflectivity of the mirror shell in the EUV spectral range. A complete set of mandrels is necessary to produce all of the different sized shells for a nested collector. When a mandrel is manufactured, a layer of metal is grown electrochemically on its outer surface, then this metal shell is separated from the mandrel, e.g., via the difference in the thermal expansion coefficient between the shell and the mandrel material. The mandrels can be used several times for production of more collectors. After separation, the optical shape accuracy and roughness of the mirror shell have to be measured. Figure 5.27 shows a single hyperbolic–elliptic mirror shell on an optical test setup where the deviation of shape and optical focusing capability is determined. After testing, the inner reflective surface can be coated with EUV-specific reflection coatings. Ruthenium, rhodium, or palladium are coating materials of choice with high reflectivity at grazing incidence for $\lambda = 13.5$ nm.

The set of shells needs to be assembled into a complete nested EUV collector. Figure 5.28 shows the process for a test collector with eight shells. Four of the mirror shells are already integrated into the mounting structure. The mounting of the individual shells is done on a test setup that optically controls the positioning of the collector subparts. The shells can be glued with high-temperature glue, clamped, welded, or brazed to the mounting structure.

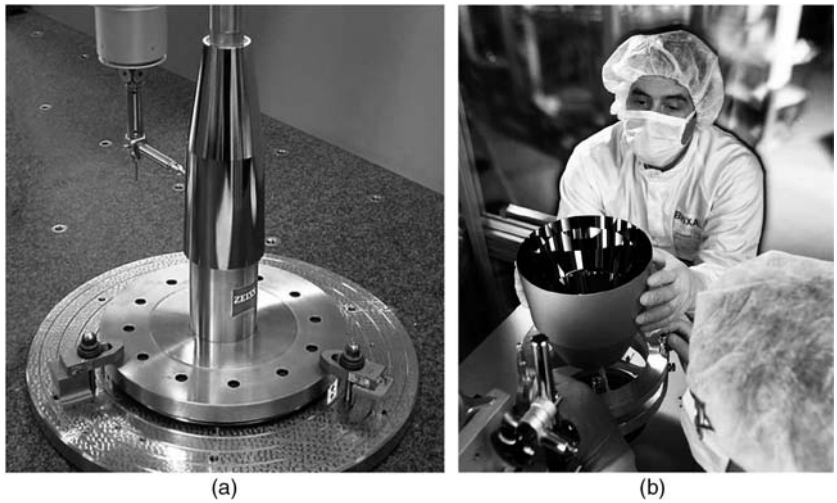

Figure 5.27 (a) An EUV collector mandrel during metrology. (b) A replicated mirror shell on the optical test stand (reprinted from Ref. 81).

Downloaded From: https://www.spiedigitallibrary.org/ebooks/ on 09 Mar 2022
Terms of Use: https://www.spiedigitallibrary.org/terms-of-use

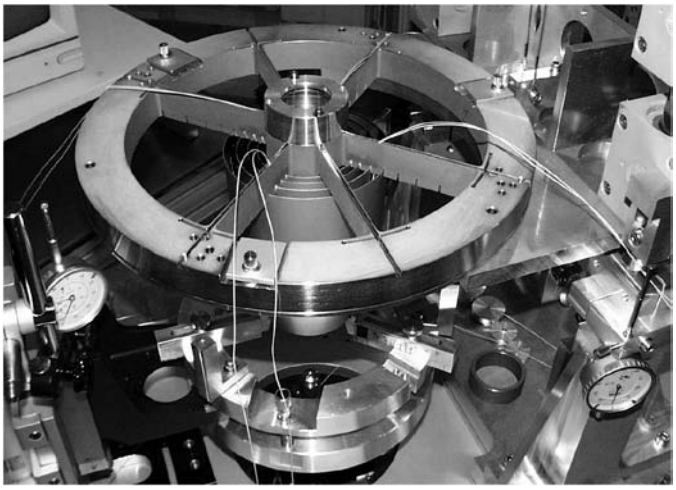

Figure 5.28 A four-shell-collector on the integration stand (reprinted from Ref. 81).

The six-fold mounting wheel provides temperature sensors, cooling, and strain relief structures to the nested collector shells.[81]

The fabrication processes for nested, thin walled, electroformed Wolter telescopes were developed mainly during the realization of ESA's XMM-Newton x-ray observatory.[82] Based on the experience of the fabrication of the German x-ray telescope ROSAT, ZEISS supplied the mandrels required for replication to this program in the early 1990s. Dedicated electroforming processes were implemented at ZEISS especially for the ABRIXAS mission[83] and were later adapted for the production of EUVL collectors.[84] The EUV source for the ADT was a DPP source. So Wolter-type 1 grazing-incidence collectors with eight nested mirror shells were designed and built for its operation. A ZEISS source-collector optical module for the ADT was shipped to ASML (Fig. 5.29). Media Lario Technologies developed and manufactured grazing-incidence collectors for the ADT and subsequent systems.[86–89]

The source-collector optical module provided space after the collector for a dedicated spectral purity grating filter. In case spectral filtering was not needed, the filter could be exchanged for a plane, grazing-incidence reflection mirror. The spectral purity filter (SPF) was designed and built as a blazed-grating filter with very shallow blaze angles at the ZEISS grating lab.[90] Figure 5.30 shows the working principle. The grating consisted of plane grating segments with individually varying line spacings and blaze angles, and formed a polygonal shape. The diffraction function was optimized to focus the EUV light with wavelength $\lambda = 13.5$ nm into the incidence aperture of the illuminator. Wavelengths much longer than the desired EUV light were directed into the zeroth orders of the gratings and blocked, whereas undesired near-EUV wavelengths were dispersed over the separating aperture and thus

Downloaded From: https://www.spiedigitallibrary.org/ebooks/ on 09 Mar 2022
Terms of Use: https://www.spiedigitallibrary.org/terms-of-use

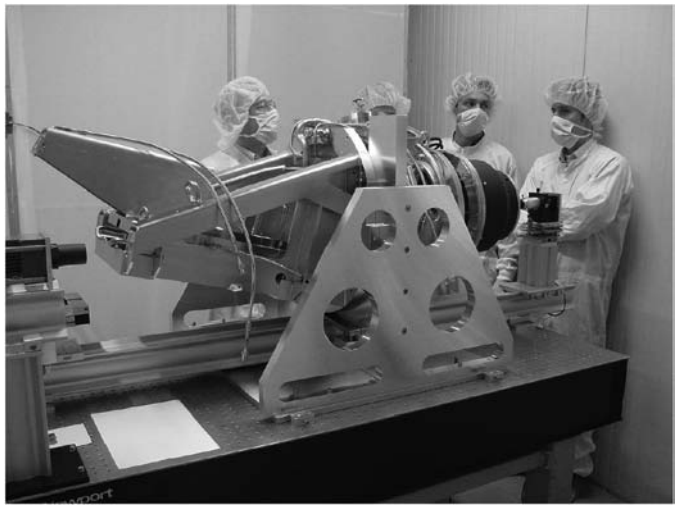

Figure 5.29 A ZEISS source collector module for the ADT was shipped to ASML (reprinted from Ref. 85 with permission from ZEISS).

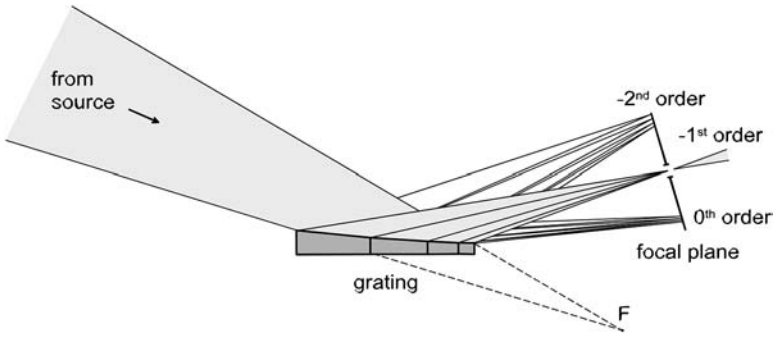

Figure 5.30 System layout for the EUV spectral purity filter of the ADT (reprinted from Ref. 90).

filtered away. Figure 5.31 shows one of the smaller segments before integration into the SPF in the clean room. The complete SPF was mounted and tested on an optical test bench with visible light.

5.4.4 Normal-incidence collectors

The simplest normal-incidence EUV collector scheme is the ellipsoid collector. Figure 5.32 shows the working principle. A rotational ellipsoid mirror surrounds the plasma in its first focus point F. Where the light from F hits the surface of the mirror, it is reflected into the direction of the ellipsoid's second focus point F′, as this is one of the mathematical properties of the ellipse. Thus, the ellipsoid can collect the emitted radiation from F over a very large solid

Downloaded From: https://www.spiedigitallibrary.org/ebooks/ on 09 Mar 2022
Terms of Use: https://www.spiedigitallibrary.org/terms-of-use

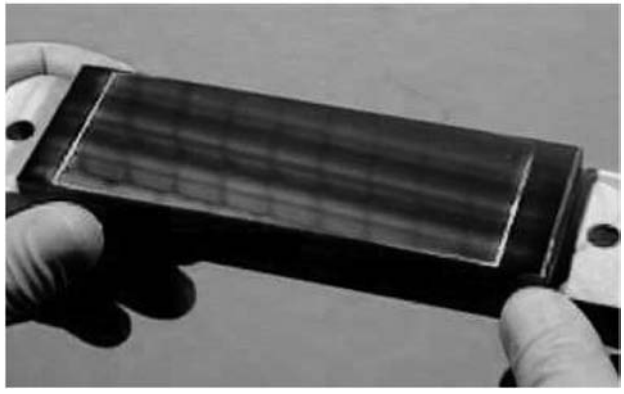

Figure 5.31 Final grating segment on the metallic substrate (reprinted from Ref. 90).

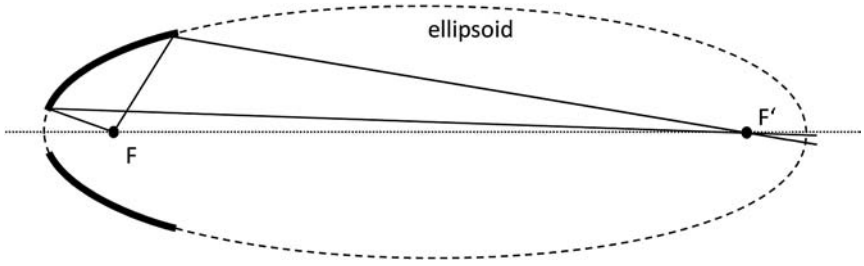

Figure 5.32 Working principle of a simple, normal-incidence ellipsoid collector.

angle. However, as the imaging through a simple ellipsoid is not aplanatic, the usable object/image size is very small. The beams used for imaging of the plasma encounter different magnifications over different optical heights of the collector so that rays imaging plasma components outside of the optical axis do not converge into one point in the image plane anymore. If the collector is used for small plasma sizes only, as is typical for LPP sources, and is adjusted precisely toward the light source, the imaging behavior can be still very good.

The optical surface of the ellipsoid collector is coated with a normal-incidence multilayer coating to reflect the incoming EUV radiation. A Mo/Si multilayer coating stack works perfectly close to the optical axis where the radiation arrives at the collector surface at a very steep angle. Toward the edge of the mirror, the reflectivity specified for the p-polarized light decreases rapidly on normal-incidence mirrors. Also, the distance of the mirror surface from the plasma point steadily grows toward the edge of the mirror so that a differential surface element of the collector has less and less solid-angle participation of the plasma emission. This results in a typical far-field shape of the ellipsoid collector with a strong maximum close to the optical axis and an intensity drop toward the edge of the mirror.[91] On the other hand, the far field behind the secondary focus is mostly free from shadows of obstructions

Downloaded From: https://www.spiedigitallibrary.org/ebooks/ on 09 Mar 2022
Terms of Use: https://www.spiedigitallibrary.org/terms-of-use

compared to the grazing-incidence Wolter collector. This helps the illuminator to efficiently use the light.

The normal-incidence collector delivers good imaging behavior even under the highest thermal loads if the mirror substrate is actively cooled. The substrate material has to be suitable for high thermal conductivity and low thermal expansion. Silicon, silicon carbide, aluminum/silicon alloys, and copper or copper/tungsten alloys are common materials for such normal-incidence collector mirror substrates. The cooling system has to be optimized to not disturb the far-field properties of the collector. The multilayer coating of the normal-incidence collector is sensitive and must be strongly protected against the debris and ions of the plasma. All EUV source manufacturers using normal-incidence collectors have developed debris mitigation schemes to keep the collector coating alive and free of Sn debris and damage. Normal-incidence EUV collectors were first used in an industrial setting for the ASML NXE:3100. In contrast to the ADT, the NXE:3100 was designed from the beginning to run at much higher source power of >100 W EUV in the IF and under production-compatible and high-volume operation conditions. As sources, DPP and LPP systems were regarded as possible solutions. However, LPP was used as a baseline source due to its lower debris-generation capability, smaller EUV plasma image, and better far-field quality. The NXE:3100 normal-incidence collectors are large ellipsoidal mirrors that surround the plasma with a nearly complete half sphere and collect the plasma EUV radiation into a cone that is acceptable for the illuminator (Fig. 5.33). The materials used are chosen to have a high thermal conductivity and to maintain the optical quality under the high thermal load in the LPP EUV source.

The plasma in an LPP source is driven by a strong IR drive laser, which typically hits the Sn target through the central hole of the collector. During

Figure 5.33 NXE:3100 collector. Clearly visible is the hole in the middle for the IR drive laser beam.

Downloaded From: https://www.spiedigitallibrary.org/ebooks/ on 09 Mar 2022
Terms of Use: https://www.spiedigitallibrary.org/terms-of-use

Figure 5.34 A collector with mounting mechanics on a coordinate measurement machine.

plasma generation, the IR laser light is not completely absorbed by the Sn droplet; it is also partly reflected by the space charge of the plasma and thus reaches the collector surface together with the EUV radiation. Typical Mo/Si coatings on the collector reflect well in the mid-IR region, and the reflectivity of the coating is about 80% around the 10.6-μm wavelength of the CO_2 drive laser. So the IR radiation of the laser would be transmitted via the collector into the scanner optical system, increasing mirror and wafer heating. A SPF can help to counter these effects. Figure 5.34 shows a collector that today has an average reflectivity of >40%.

5.5 Optical Modules: Illuminator

5.5.1 Introduction

The illuminator forms the light such that the mask is illuminated very homogeneously from well-defined irradiation angles. As described in the previous section, the collector collects the light of the plasma source into the IF. A direct illumination of the reticle by the IF is insufficient with respect to the desired performance. Instead, at the IF the light enters into the illuminator, which then produces a light distribution of high quality at the reticle. The key performance parameters of the illuminator are: uniform illumination of the object field, shaping of the light distribution in the pupil, and transmission.

5.5.2 Key performance parameters

One aspect of the desired quality is the intensity uniformity of the illumination over the complete optical field at the mask. This uniformity of the intensity

Downloaded From: https://www.spiedigitallibrary.org/ebooks/ on 09 Mar 2022
Terms of Use: https://www.spiedigitallibrary.org/terms-of-use

$\Delta I/I$ directly relates to the imaging performance; i.e., its impact on the uniformity of the CD is given by

$$\frac{\Delta CD}{CD} = \frac{2}{\text{NILS}} \frac{\Delta I}{I}. \tag{5.5}$$

Considering a CD control requirement of 10% and a NILS of 1, the allowable uniformity of the intensity is below 1%, as nonuniformity is one of many contributors.[92] Excellent uniformity can be achieved, especially if the illuminator decouples power fluctuations within the source from the object field.

Another task of the illuminator is the preparation of the desired angular distribution of the light toward the optical field at the mask. A description of the angular distribution is given by the partial coherence factor σ, which is defined as the relative radius of the illuminated part of the NA[93] (Fig. 5.35). Originally, this description was applied to on-axis illumination. In the context of off-axis illumination, the definition has to be broadened; e.g., for an annular setting, two quantities are defined by σ_{in} and σ_{out}, describing the inner and outer boundary lines of the illuminated part of the NA. With optimum off-axis illumination, the resolution can be improved by a factor ~2 compared to pure on-axis illumination.[2] For non–rotationally symmetric off-axis illumination settings, it is convenient to introduce the pupil fill ratio,

$$PFR = \frac{1}{\pi \max_{\sigma_x,\sigma_y} I(\sigma_x,\sigma_y)} \iint_{\sigma_x^2+\sigma_y^2 \le 1} I(\sigma_x,\sigma_y) d\sigma_x d\sigma_y, \tag{5.6}$$

where $I(\sigma_x, \sigma_y)$ denotes the position-dependent intensity within the illumination pupil. In general, it is beneficial when an illuminator enables a small PFR. A small PFR allows more aggressive off-axis illumination, improving the imaging resolution. It also offers more freedom to enhance contrast and hence the process window through SMO.[94] With less pupil area needed to be

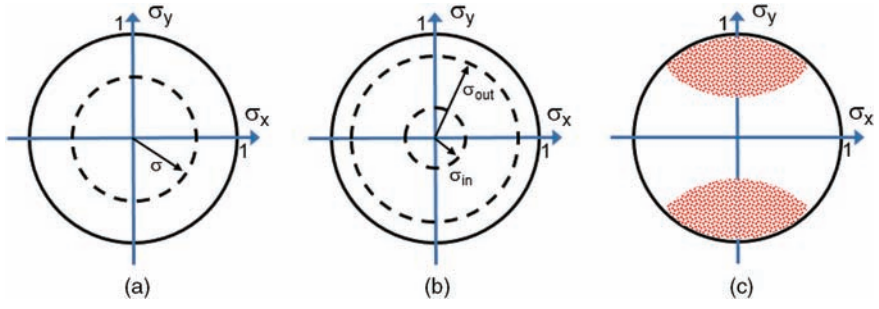

Figure 5.35 Definition of the partial coherence factor σ and PFR. σ_x and σ_y label the relative coordinates within the illumination pupil in the *x* and *y* directions for (a) a conventional setting, (b) an annular setting, and (c) non–rotationally symmetric off-axis settings.

Downloaded From: https://www.spiedigitallibrary.org/ebooks/ on 09 Mar 2022
Terms of Use: https://www.spiedigitallibrary.org/terms-of-use

filled with light, there is more freedom to choose how to distribute the light. An important measure for imperfections with regard to an ideal illumination pupil is the telecentricity error. A telecentricity error results in a pattern shift and therefore introduces overlay errors in the lithography process.[92]

The third quality metric of the illuminator is its transmission. The reflectivity for a high-reflection mirror coating at the EUV wavelength of $\lambda = 13.5$ nm is restricted to $\sim$70%. The number of reflections as well as the losses due to the finite size of the mirror elements have to be restricted to a minimum, especially because source power is a critical parameter in EUV.

5.5.3 Realization options

There are two types of illumination for EUV lithography: critical illumination and Köhler illumination.[95] Critical illumination projects the source onto the mask, whereas Köhler illumination projects the source into the pupil of the projection optics. Figures 5.36 and 5.41 illustrate these two concepts. In this chapter, illuminators for plasma sources with a large optical étendue are described. Illuminators for a low-étendue source, e.g., a synchrotron undulator beamline, need a different concept due to the high coherence.[96]

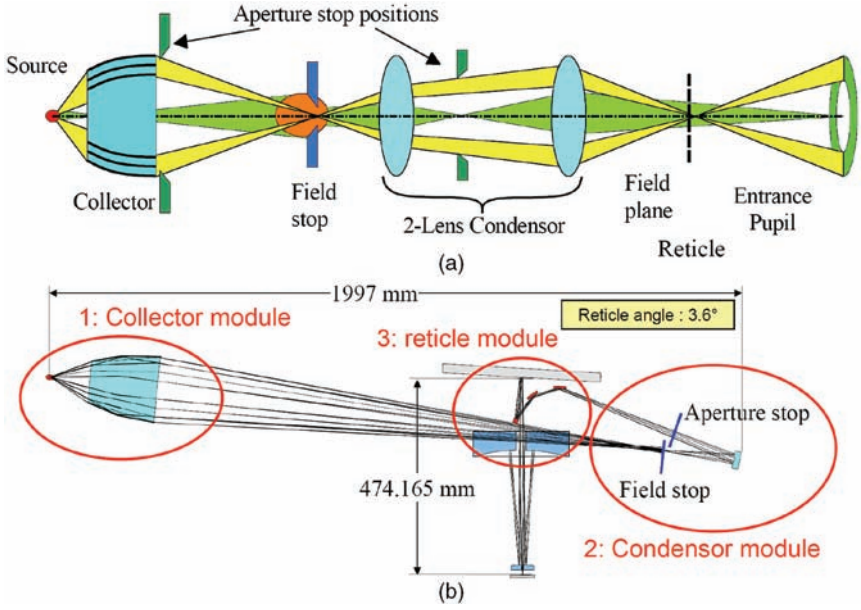

Figure 5.36 (a) Scheme for quasi-critical illumination of the MET. The yellow rays form the path for the so-called field rays with a small defocus at the field plane. The green rays form the path for the so-called pupil rays that focus in the pupil planes. The scheme is drawn as a transmitting lens; in reality, the two condenser lenses must be mirrors, and the system must be folded to avoid obscuration.[97] (b) The real design includes two additional folding mirrors (Figures reprinted from Ref. 98 with permission from ZEISS).

Downloaded From: https://www.spiedigitallibrary.org/ebooks/ on 09 Mar 2022
Terms of Use: https://www.spiedigitallibrary.org/terms-of-use

For the MET, a so-called quasi-critical illumination is used, where the source is imaged into the field plane with a defocus (Fig. 5.36). The critical illumination is efficient and offers sufficient quality for the small field. The angular distribution at the mask is already formed in the collector with the use of several spherical shells and an aperture stop. Therefore, the illumination pupil consists of several rings [Fig. 5.37(a)], achieving $\sigma_{in} = 0.36$ and $\sigma_{out} = 0.55$. A field stop is positioned at the IF and is imaged by a condenser with two mirrors onto the mask with a defocus. Between these two mirrors, a pupil plane conjugate to the pupil plane of the projection optics is formed, where apertures can be placed that can form different illumination settings like dipole or quadrupole. An illumination uniformity of ±2.5% at the field plane is achieved [Fig. 5.37(b)].

For critical illumination, intensity fluctuations of a plasma source directly affect the illumination uniformity at the mask. This behavior is acceptable for small-field systems used in resist testing or metrology; e.g., the ZEISS AIMS EUV uses critical illumination. However, full-field systems for printing patterns with EUV[99,100] are more suited to Köhler-type illumination because intensity fluctuations of a plasma source do not affect the uniformity at the mask but affect the light distribution in the pupil plane. This light distribution in the pupil plane is also relevant for the imaging behavior but is generally less sensitive than the uniformity at the mask. The concept of a Köhler-type illuminator with a fly's eye integrator unit[101] is sketched in Fig. 5.38. The highest benefit of such a design concept is excellent uniformity in the reticle (field) plane. The fly's eye integrator is composed of two mirrors consisting of reflecting facets. The first mirror is located at a distance from the IF so that an extended illuminated region is formed that is called the far field of the source. Each facet of the first mirror images the IF onto one facet of the second mirror. Each facet of the second mirror together with the condenser mirror

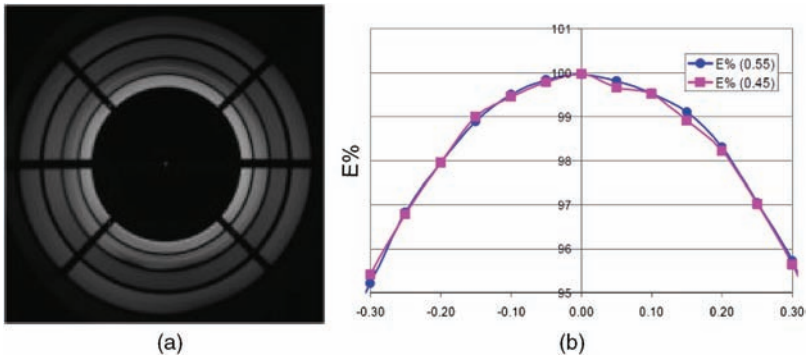

Figure 5.37 Performance of the MET. (a) Intensity distribution over the pupil. The rings result from the shells of the nested Wolter collector, and the stripes result from the mount for the shells. (b) Achieved illumination uniformity of ±2.5% for σ_{out} values of 0.45 and 0.55 (Figures reprinted from Ref. 98 with permission from ZEISS).

Downloaded From: https://www.spiedigitallibrary.org/ebooks/ on 09 Mar 2022
Terms of Use: https://www.spiedigitallibrary.org/terms-of-use

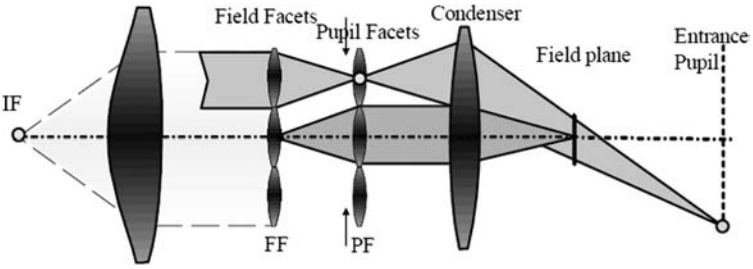

Figure 5.38 Schematic illustration of Köhler-type illumination for full-field illumination systems. The general design concept is shown for simplicity in lens representation. The dark gray rays show the path of field rays focused in field planes, whereas the light-gray rays show the path of pupil rays focused in pupil planes. The arrows close to the pupil facets indicate the position of a diaphragm that allows for pupil setting changes (reprinted from Ref. 102).

then images the corresponding facet of the first mirror onto the mask. Furthermore, the condenser mirror images the facets of the second mirror into the entrance pupil of the projection optics. Therefore, the second mirror is located at a plane conjugate to the pupil plane of the projection optics, and the facets are called pupil facets. The first mirror is located in a plane conjugate to a field plane of the projection optics, and the facets are called field facets. The highest efficiency can be achieved if the field facets have the shape of the required object field. By superpositioning hundreds of field facets at the mask, excellent uniformity of the illumination field is achieved. A uniformity of ±1% is achieved with the illuminator of the Starlith® 3100 (see Fig. 5.39). The light distribution at the mask is decoupled from spatial fluctuations within the plasma.

As a consequence, the pupil is composed of hundreds of light spots. This results in discrete exit pupils at the wafer (Figs. 5.8 and 5.9). This pupil discretization has no impact on the process window if taken into account in the layout of the structures on the mask, i.e., in the OPC process.[104] The impact of systematic or random fluctuations of pupil spots can be simulated, and appropriate tolerance specifications can be derived, ensuring that fluctuations do not deteriorate imaging.[92] Note that when calculating the PFR in the case of discrete pupils, connected envelopes around the pupil spots must be constructed.

An individual field facet paired with its corresponding pupil facet is called an illumination channel. A smart assignment of the illumination cannels minimizes the uniformity of the intensity over the pupil. Placing an exchangeable diaphragm into a plane close to the pupil facets allows the illumination settings to be changed for off-axis illumination of the mask. This kind of illuminator is used for the Starlith® 3100. The setting variation is enabled by blocking light directly in the pupil. One drawback is that the light

Downloaded From: https://www.spiedigitallibrary.org/ebooks/ on 09 Mar 2022
Terms of Use: https://www.spiedigitallibrary.org/terms-of-use

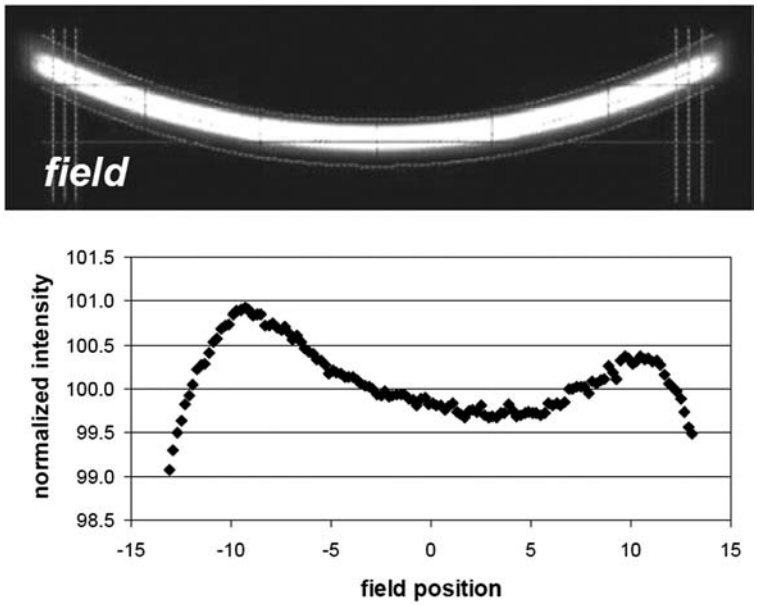

Figure 5.39 A uniformity of ±1% is achieved with the illuminator of the Starlith® 3100 (reprinted from Ref. 103).

of the blocked channels is lost. This light loss effectively changes the transmission of the Starlith® 3100 illuminator for a customized setting by

$$T_{eff} \approx \frac{A_{customized}}{A_{\sigma=0.8}}, \tag{5.7}$$

where $A_{customized}$ is the pupil area of the customized setting, and $A_{\sigma=0.8}$ is the pupil area of the setting with $\sigma = 0.8$ (Fig. 5.40). Thus, only a large conventional setting allows for full efficiency.

The efficiency loss in the Starlith® 3100 illuminator is no longer acceptable when operating the system for HVM. Therefore, the Starlith® 3300 offers illumination setting changes without transmission loss.[99] A flexible illuminator has been realized with the use of switchable field facets with limited degrees of freedom. Each field facet is grouped with several pupil facets (Fig. 5.41).

Figure 5.40 Schematic showing the results of changing the efficiency of the illuminator by changing settings for Starlith® 3100 (reprinted from Ref. 103).

Downloaded From: https://www.spiedigitallibrary.org/ebooks/ on 09 Mar 2022
Terms of Use: https://www.spiedigitallibrary.org/terms-of-use

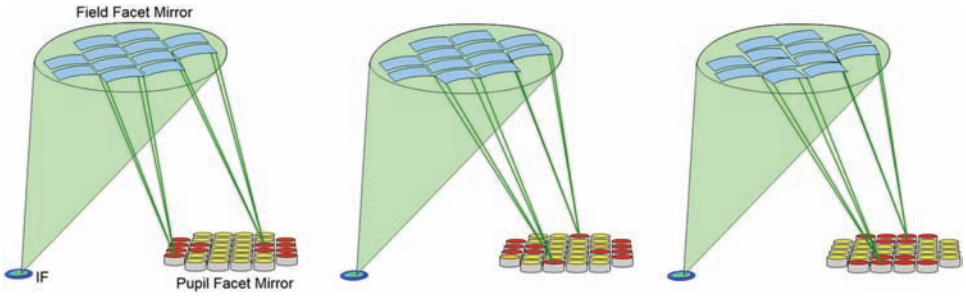

Figure 5.41 By switching each field facet from a first pupil facet to a second pupil facet, the illumination setting is changed from one dipole into a 90-deg-rotated dipole without loss of transmission (reprinted from Ref. 61).

The number of pupil facets per field facet is related to the minimum PFR. For the Starlith® 3300, each individual field facet is grouped with two pupil facets. This additional flexibility requires twice as many facets on the pupil mirror compared to the number required on an inflexible illuminator. With $\sigma = 0.2 \ldots 0.9$, the minimum PFR is 40%. The maximum PFR of 80% can be obtained by addressing every other pupil facet across the full pupil. The number of pupil facets was increased for the Starlith® 3400. As a consequence, several pupil facets can be grouped to each field facet. This results in greater flexibility for the settings with $\sigma = 0.0 \ldots 1.0$ and $PFR = 20\%$; e.g., rotated dipole settings can be realized (see Fig. 5.9).

5.5.4 Pupil tuning

Tuning of the illuminator pupil is a powerful means of image optimization.[105] Recently, SMO has further enhanced the imaging capabilities,[106] including discrete pupils,[107] and has been extended to EUV.[50,108,109] Customized settings, e.g., freeform pupils, are available in addition to the standard settings. Figure 5.42 shows how freeform pupils increase the process window. In particular, a small PFR of 20% significantly enhances the performance. A PFR smaller than 40% can be achieved by switching off certain field facets implying light loss. With the highly flexible illuminator of the NXE:3400B, a PFR of 20% can be achieved without light loss.

5.5.5 Technical challenges

The main technical challenges are of thermal nature. Over 30% of the EUV light is absorbed on each mirror. The first mirrors in the system especially suffer additionally from out-of-band EUV light. These mirrors have to handle about 1 kW of absorbed energy for a source providing 250-W power with "clean" EUV photons at IF. There is a specific challenge for the field facet mirror because the heat conduction in the hinges of the actuated facets has to be optimized, durable materials have to be chosen, and an appropriate cooler

Downloaded From: https://www.spiedigitallibrary.org/ebooks/ on 09 Mar 2022
Terms of Use: https://www.spiedigitallibrary.org/terms-of-use

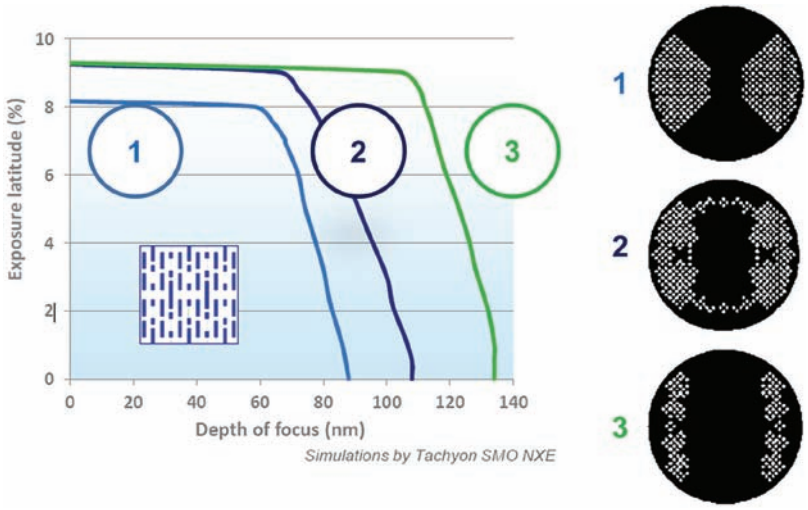

Figure 5.42 Simulated process windows for the wafer pattern depicted in the inlet with standard dipole setting (1), freeform setting with 40% PFR (2), and freeform setting with 20% PFR (3). The freedom in setting choice translates into a gain of process window (reprinted from Ref. 50).

has to be installed. Nevertheless, EUV multilayer coatings have to withstand a temperature of about 100 °C. The field facets focus the EUV light onto the pupil facets, and the absorbed power density on the order of $\sim$1 W/mm^2 is a major challenge. Thus, durable multilayer coatings and clean manufacturing processes are critical to guarantee the lifetime of the optics.

5.6 Optical Modules: Projection Optics

5.6.1 Introduction

This section describes key technologies of the projection optics in more detail and provides a concise outline of the fundamentals of (1) manufacturing mirror surfaces, (2) mirror metrology, and (3) multilayer coatings. After discussing basic design elements of the optical module, requirements for the surface figure and the roughness are derived. Due to the continuous learning and improvements in polishing technology, it is currently possible to yield exceptionally smooth surfaces, reducing the flare numbers to satisfying levels. The relationship between stray light and the roughness of the mirror surfaces is key to understanding how to derive the necessary surface roughness requirements. This aspect of EUV technology development is described in more detail. Owing to the importance of flare in EUV history, flare is taken as an example for a more comprehensive exposition. In particular, an alternative representation of the power spectral density (PSD) of the surface is

Downloaded From: https://www.spiedigitallibrary.org/ebooks/ on 09 Mar 2022
Terms of Use: https://www.spiedigitallibrary.org/terms-of-use

introduced, where the direct link between surface roughness and flare impact becomes more transparent. Multilayer coatings for normal-incidence mirrors are described with emphasis on their angular and spectral response. Finally, we explain how EUV reflectivity is measured and how coatings contribute to surface figure.

5.6.2 Basic design specifications

For optical lithography, the standardized shape of the field to be exposed at the wafer is a rectangle of 26 mm × 33 mm (after scanning). The MAG is set at 4×, which results in an object field of 104 mm × 132 mm. This configuration is chosen so that the object field just fits onto a 6-inch mask. During scan, a slit with full width of 26 mm at the wafer but significantly reduced length in the perpendicular direction is imaged by the projection optics. These properties were introduced for DUV lithography and, for compatibility reasons, are also applied to EUV. In particular for EUV, the optical field is specified to be rotationally symmetric and off-axis, which means that the center point of symmetry of the optics is outside of the field. In total, a rotationally symmetric part of an annulus (or ring field) with a width of 26 mm and a short height is defined as the image field (see Fig. 5.43). The ring field eases the aberration control for the projection optics. By choosing off-axis rotationally symmetric fields and a rotationally symmetric design, automatically off-axis segments of rotationally symmetric surfaces are generated as the optically active mirror surfaces for the projection optics. Furthermore, for a rotationally symmetric projection optics, the CRAO is constant at field points with a constant distance to the center point of symmetry with regard to the surface normal.

The wavefront aberrations of the projection optics cause overlay and CDU errors. Therefore, wavefront specification is crucial during the design process of the projection optics, and, typically, a satisfactory imaging performance requires a system wavefront deviation that is smaller than λ/50. Wavefront aberrations are related to the so-called figure of the mirror

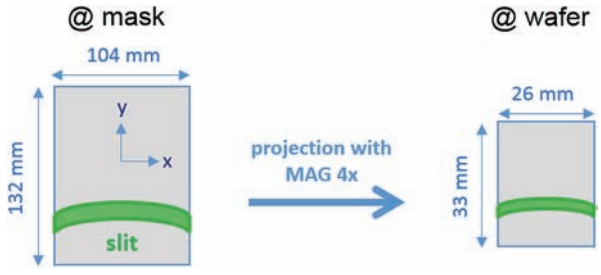

Figure 5.43 Left: 104 mm × 132 mm object field (after scanning) at the mask. The projection optics images a slit with a width of 104 mm onto the wafer. Right: A projection with a MAG of 4× results in a slit with a width of 26 mm at the wafer.

Downloaded From: https://www.spiedigitallibrary.org/ebooks/ on 09 Mar 2022
Terms of Use: https://www.spiedigitallibrary.org/terms-of-use

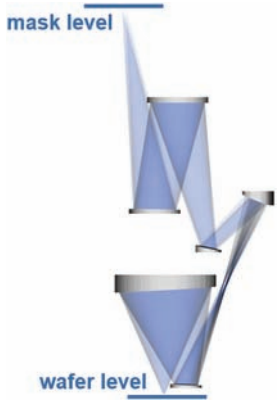

Figure 5.44 Design example of a six-mirror optical design for a projection optics.

surfaces themselves, where figure is the longwave deviation of a mirror surface from the nominal form. It turns out that optical designs with 6 mirrors are needed to correct the full field at NAs of 0.25 to 0.33; see Fig. 5.44 for a design example. The six-mirror configuration has been developed for the ADT, Starlith® 3100, and the Starlith® 3300/3400 family. Due to the NA, the mirror diameters can increase to sizes up to ~0.5 m. The required wavefront performance increases the necessity of steep aspheres. The position accuracy of the mirrors to be achieved and maintained during wafer exposure is in a range of less than a nanometer and a nanoradian. This is comparable to the pointing accuracy needed to hit a 20-cm-diameter target on the moon from the earth! However, mechanical parts can be manufactured and measured on the order of micrometers, which is 1000× larger than needed. Therefore, an adjustable-mirror-mounting technology has been developed. In combination with a stiff structure, the desired accuracy and stability can be achieved.

The basic product specifications for a projection optics include the size and shape of the object field, the CRAO, the MAG, the transmission, and the bounding box of the complete projection optics, including mechanics. Several remarks on these specifications are as follows: (a) The object field of the projection optics is at the mask, and the image field is at the wafer. (b) When the object field and the MAG are given, the image field is determined. (c) The CRAO is often indicated by just a single number. The CRAO was already set to 6 deg as a standard; this was used for the ADT, the NXE:3100 and the NXE:3300B/3400B family to separate the incoming and outgoing light cones at the mask. In the context of specifying the optical train, however, the angle distribution over the complete object field is needed. In particular, a varying projection of the CRAO in the x or y direction leads to field-dependent imaging effects. (d) Historically, it is called magnification, although following the path of the light, it is actually a demagnification.

Downloaded From: https://www.spiedigitallibrary.org/ebooks/ on 09 Mar 2022
Terms of Use: https://www.spiedigitallibrary.org/terms-of-use

5.6.3 Optics manufacturing: mirror surface

5.6.3.1 Closing the loop for figure control: manufacturing and metrology

An essential challenge for the projection optics is the manufacturing of the mirrors. The preparation of the surfaces of the mirror substrates is the first high-precision step for the later wavefront and, in particular, the flare performance. During these processes it is crucial to reach the specification for figure, mid-spatial-frequency roughness (MSFR) and high-spatial-frequency roughness (HSFR) simultaneously. The increase in resolution due to the short EUV wavelength is accompanied by extremely challenging requirements for the surface tolerances of the mirrors and will be discussed based on a rule of thumb. For surfaces exposed on one side to air or vacuum, topography errors Δh translate to wavefront errors $(n-1)\times\Delta h$ of the transmitted or reflected light bundle. Here, the refractive index is $n\approx 1.5$ for non-immersion lens surfaces, and for mirrors, the factor $n-1$ is replaced by the factor –2. Thus, mirror surfaces are generally four times more sensitive to surface errors than lens surfaces. In addition to the increased sensitivity of mirrors as compared to lens surfaces, the short wavelength itself also enhances the importance of the surface topography; aberration-driven wavefront errors are usually specified in units of the wavelength λ:

$$\Delta WFE_{single} = (n-1)\frac{\Delta h}{\lambda} \qquad [\text{in units}\,\lambda]. \tag{5.8}$$

For many imaging effects, it is actually this ratio between absolute wavefront error and wavelength that matters. Obviously, the short EUV wavelength of $\lambda_{EUV}=13.5$ nm significantly increases the impact of topography errors Δh as compared to DUV (ArF) with wavelength $\lambda_{DUV}=193$ nm. The total wavefront error rms resulting from figure errors is approximately

$$\Delta WFE_{total} = \sqrt{N}\,\Delta WFE_{single}, \tag{5.9}$$

where N is the number of optical surfaces. For an EUV system with 6 mirrors having the same wavefront quality as a DUV system with 60 surfaces, the surface quality requirements scale as

$$\frac{\Delta h(\text{mirror surface @ } \lambda = 13.5\text{ nm})}{\Delta h(\text{lens surface @ } \lambda = 193\text{ nm})} = \sqrt{\frac{60}{6}}\times\frac{1}{4}\times\frac{13.5}{193}\approx 0.05; \tag{5.10}$$

i.e., the requirements on low-frequency figure errors are 20× tighter for EUV surfaces. Furthermore, the off-axis geometry of the mirrors prohibits the compensation of low-frequency errors by rotating averaging. Astigmatic errors of the EUV mirrors have to be fully included in the figure budgets. Figure errors cover the frequency band between the clear aperture of the mirrors down to approximately 1 mm. These errors are attributed to

Downloaded From: https://www.spiedigitallibrary.org/ebooks/ on 09 Mar 2022
Terms of Use: https://www.spiedigitallibrary.org/terms-of-use

aberrations that deteriorate the fidelity of the imaging (CD and overlay). A system wavefront deviation of $RMS < \lambda/50$ is required, translating to a rms figure error of approximately $13.5\ \text{nm}/50/2/\sqrt{6} = 55$ pm rms on a single mirror surface. This number has to be met within the optical footprint belonging to one field point. The full mirror specification may be somewhat relaxed but typically will still remain below 100 pm rms.

The first step in the optics production is generating the basic shape of the mirror. Depending on the material, grinding or milling tools are used. Roughness reduction is achieved by polishing with comparatively large tools. Choosing appropriate polishing slurries and polishing pads is crucial for reaching the 100-pm range. Computer-controlled figuring technologies are used for figure correction; based on the error maps from the full-aperture interferometers, they shape the surface locally. Various technologies, such as, e.g., computer-controlled polishing (CCP), ion beam figuring (IBF), or magnetorheological figuring (MRF) can be used here.[110,111] Early work within the EUV LLC is summarized in Ref. 112. Additional contributions of third parties are reviewed in Refs. 8, and 113–115. The real challenge is to control figure quality simultaneously with the MSFR (spatial wavelengths typically in the domain of $\approx$1 mm ... 1 μm) and the HSFR (spatial wavelengths typically in the domain of $\approx$1 μm ... 10 nm). Figure correction processes tend to degrade the roughness, e.g., by residual tool tracks (mainly MSFR) or etching effects (mainly HSFR), whereas large-tool finishing degrades the aspheric figure due to the mismatch between the tool surface and the mirror surface. In order to converge to a sufficiently smooth surface over the figure (with MSFR and HSFR regimes meeting all system requirements), a careful balancing of finishing and correction steps in an iterative process is necessary. Related to figure quality, a reduction in the system wavefront was achieved, starting with <1.25 nm rms in the ADT, improving to <0.75 nm rms in the Starlith® 3100, and achieving <0.25 nm rms in the Starlith® 3300.

The achievable precision in a fabrication process is limited by the accuracy of the metrology tools used. The metrology for the production of EUVL mirrors has to cover the complete spatial frequency band, reaching from clear aperture down to 10 nm with accuracies and precision on atomic scales without leaving any frequency gaps. Figure is assessed by full-aperture interferometers equipped with dedicated compensation optics to deal with the aspheric shape of the surfaces. These instruments yield 2D surface topography maps. This information is the input for the computer-controlled figuring process. In order to enable a converging figuring process down to 100-pm surfaces, a repeatability significantly below 100 pm is necessary. Absolute accuracy must also be significantly below 100 pm. Since the required measurement accuracy is only a small fraction of a nanometer, the appropriate method to measure those surfaces is interferometry. MSFR is measured by micro-interferometers. Correct removal of the aspheric shape,

Downloaded From: https://www.spiedigitallibrary.org/ebooks/ on 09 Mar 2022
Terms of Use: https://www.spiedigitallibrary.org/terms-of-use

proper calibration of systematic interferometer errors, and the mitigation of vibrations are key to accurate and repeatable measurement results. HSFR usually is covered by scanning AFM. Special care must be taken for artifacts introduced by the scanning procedure or vibrations. Data of all three metrology tools (full-aperture interferometer, micro-interferometer, and AFM) is then merged and digested into a continuous PSD of the surface, covering the complete relevant frequency range without any gaps.

As argued above, a full mirror specification will typically be below 100 pm rms. This error contribution represents the total effect on the system wavefront caused by a single mirror. But the total error budget of the component consists of contributions from surface metrology, surface machining, inhomogeneities of the multilayer coating, coating tension, deformations induced by assembly, and thermal and aging effects. Furthermore, convergent machining of a surface only works if the reproducibility of the measurement covers only parts of the specification of the uncoated surface deviation. In total, a requirement for the repeatability of the measurement on the order of 10 pm is needed. The required absolute accuracy of the measurement is about 20 pm. Strictly speaking, this specification is only valid for error contributions that cannot be aligned in the system wavefront by means of rigid body movements of the mirrors relative to each other. Longwave surface figure errors such as, e.g., tilt, focus, and astigmatism are comparably well correctable, whereas the correction factors become distinctly smaller with decreasing spatial wavelength of the surface deviations.

Apart from tightly controlling the surface figure in manufacturing, very low values of the coefficient of thermal expansion (CTE) are important for EUVL mirror substrates. As will be shown in Section 5.6.5, only ~70% of the incoming EUV intensity is reflected, while ~30% is absorbed in the mirror material and transformed into heat. Since the whole EUVL system is built up in a vacuum chamber, the heat transfer from the mirrors to the outside is very limited. During operation, a temperature rise of a few Kelvin is not unusual for EUVL mirrors. For most materials, this temperature change will result in a surface deformation that is much bigger than the abovementioned specification. This mirror heating makes zero-expansion materials mandatory in EUVL projection optics. There are two classes of materials: glass ceramics (e.g., ZERODUR® or CLEARCERAM®) or amorphous-titanium–doped fused silica (e.g., ULE®). The CTE can be tailored to zero at a specific zero-crossing temperature (ZCT). To ensure system performance under operational conditions, the value of the ZCT, the CTE slope, and the spatial variation of the CTE have to be controlled at extremely tight levels.[116,117] Both material classes have certain disadvantages. In glass ceramics, certain figuring and finishing processes that have different removal rates for the ceramic and glassy components of glass may etch out the microcrystallites, thereby increasing the HSFR. Titanium-doped fused-silica blanks often show so-called striae, i.e., a

Downloaded From: https://www.spiedigitallibrary.org/ebooks/ on 09 Mar 2022
Terms of Use: https://www.spiedigitallibrary.org/terms-of-use

vertically stratified structure of slightly different material composition. This can translate into locally varying removal rates when the aspheric surface cuts through this structure. The striae usually contribute to the MSFR. Properly controlled figuring and finishing processes can avoid the buildup of striae on the surface. It can be advantageous to select the material class based on the mirror position in the system.[118]

5.6.3.2 Figure metrology: requirements, interferometer setups, and reproducibility

Metrology is an integral part in the fabrication process of the mirrors. While the polishing process is based on relative deviations in which material has to be removed in each polishing step, metrology has to provide absolute deviations from the required shape. The equipment must ensure a certain reproducibility of the measurement process as well as a tolerable deviation from the ideal shape. The Maréchal criterion can be applied to understand the required tolerances for figure metrology. Formally, it states that a wavefront can be regarded as diffraction limited if its rms phase error is $\sim 14\times$ less than its wavelength. In EUV lithography, even a factor of ~ 50 is required. The wavefront of the EUV lens must not exceed a deviation of ~ 270 pm rms; therefore, the deviation of a single mirror in a six mirror lens must then be smaller than ~ 55 pm rms. Taking into account the fact that parts of the figure errors can be compensated by system alignment, an overall tolerance on the order of ~ 100 pm rms can be assumed. This tolerance must be ensured for the sum over all deviation causes, such as fabrication errors, gravity bending, mounting effects, residual design deviations, coating effects, mirror heating, and others. Thus, the fabrication tolerance is only a fraction of the total tolerance. The required reproducibility $\sigma_{overall}$ of the measurement process is defined by the precision-to-tolerance ratio (P/T) according to

$$P/T = \frac{2\sigma}{\Delta F}. \tag{5.11}$$

Assuming a fabrication tolerance of $\Delta F = 100$ pm and an acceptable limit for P/T of 0.3, the measurement process must not exceed $\sigma = 15$ pm for a 1σ process. The question arises whether a surface metrology can be provided that resolves 1/15 of a diameter of a silicon atom. Considering a CCD camera looking at the total mirror surface, a camera pixel usually covers $\approx 10^{12}$ atoms simultaneously. In this way, the statistical effect leads to a mean deformation result of a fraction of an atom being sufficiently stable. Visualizing this extremely challenging requirement, an EUV mirror can be imagined to be inflated to the size of Germany with an area of about 360,000 km^2. Assuming a pixel size of 0.25 mm $\times$ 0.25 mm and an accuracy of ~ 15 pm rms, a pixel would then cover an area of 0.33 km $\times$ 0.33 km, and the average height would be measured with an accuracy of ~ 20 μm rms.

Downloaded From: https://www.spiedigitallibrary.org/ebooks/ on 09 Mar 2022
Terms of Use: https://www.spiedigitallibrary.org/terms-of-use

Currently, interferometry is the only suitable technique to provide the required accuracy on a full-size EUV mirror. Usually a visual laser wavelength is used, i.e., a HeNe laser with $\lambda = 632.8$ nm or $\lambda = 543$ nm. Metrology must then resolve $\approx \lambda/40{,}000$, an immense challenge for the detection process. Choosing a smaller wavelength does not really help unless x-ray or EUV wavelengths are used. The measurement equipment and process would have to be suitable to vacuum and would be restricted to using reflecting interferometer components. The interferometer basis used in most setups is the so-called Fizeau interferometer (see Ref. 199), in which the divergent laser light transmits a beamsplitter and is made parallel by a collimator. One portion of the light is reflected at the reference surface of a transmission flat, while the transmitted portion hits the mirror under test. After reflection, both portions are reflected by the beamsplitter, pass a beam stop, transmit an eye piece, and finally interfere on the CCD camera to form an interferogram. The interferogram shows the deviation of the test mirror from the reference surface. EUV mirrors have the shape of aspheric surfaces. Thus, the implemented reference must represent the appropriate aspherical shape to match the test surface. In many cases, a so-called null corrector or compensating system is inserted between the flat reference surface and the test piece. The null corrector provides the aspheric wavefront carrying the shape of the ideal asphere. See Ref. 120 for further details on the testing of aspherical elements.

The accuracy of the measurement is dependent on the qualification of the reference surface or null system. The reproducibility of the measurement depends on the ambient disturbances of the setup as well as the handling process of the test surface. Disturbances can be mechanical vibrations, radiation from heat sources, air turbulences, heat conduction, and heat convection. While there are facilities, tools, and processes to minimize the ambient disturbances, qualification of the absolute deviation is a much more difficult task. Since no suitable reference exists in the world, qualification methods and techniques have to be developed to estimate the overall absolute deviation of the null corrector from the ideal shape to better than 15 pm rms. A typical figure control test tower facility is shown in Fig. 5.45. EUV mirror and calibration equipment is being supplied by use of a robot. The interferometric setup is held by a granite housing that keeps mechanical and thermal disturbances to a minimum. A reproducibility of 12 pm rms of the measurement process can be achieved on an EUV mirror surface (Fig. 5.46). This performance is sufficient to guarantee a converging fabrication process and to deliver a quality suitable for mounting into the system.

5.6.3.3 Roughness improvements for flare reduction

Figure 5.47 summarizes some key performance improvements (figure, MSFR, and HSFR) on mirror level for the different ZEISS EUVL tool generations:

Downloaded From: https://www.spiedigitallibrary.org/ebooks/ on 09 Mar 2022
Terms of Use: https://www.spiedigitallibrary.org/terms-of-use

Figure 5.45 Test tower for interferometric figure control of EUV mirrors.

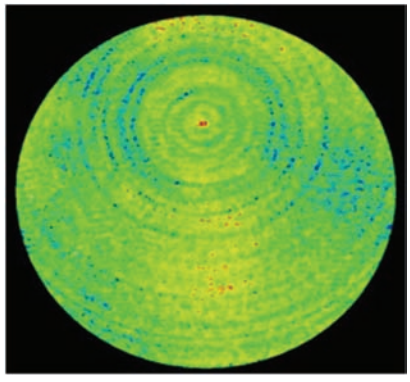

Figure 5.46 Interferometer performance demonstrating 12 pm rms reproducibility on a 200-mm-diameter circular fraction of an aspheric off-axis mirror. The pixel size is 0.3 mm.

MET, ADT, Starlith® 3100, and Starlith® 3300. The sizes of the mirrors have become significantly larger from tool generation to tool generation. At the same time, the surface performance requirements have continuously been tightened with each EUVL tool generation in order to comply with challenging imaging and throughput specifications. The MSFR roughness (rms) has improved by a factor of more than 3, and the figure performance (rms) by nearly a factor 4.5 from the MET to the Starlith® 3300/3400 family.

In more detail, Fig. 5.48 shows the reduction in flare-relevant MSFR over the years, which has been achieved on single mirrors integrated into the different full-field EUV optics ADT, Starlith® 3100, and Starlith® 3300/3400 family. In order to illustrate the significant progress in EUV mirror

Downloaded From: https://www.spiedigitallibrary.org/ebooks/ on 09 Mar 2022
Terms of Use: https://www.spiedigitallibrary.org/terms-of-use

Optics	MET	ADT	3100	3300 / 3400
Photos show relative mirror size		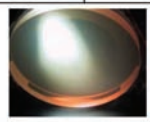		
Figure [pm rms] → aberrations	350	250	140	< 75
MSFR [pm rms] → flare	250	200	130	< 80
HSFR [pm rms] → light loss	300	250	150	< 100

Figure 5.47 Key performance improvements (figure, MSFR, and HSFR) to mirror level for the different EUV tool generations. The photos indicate the relative mirror sizes.

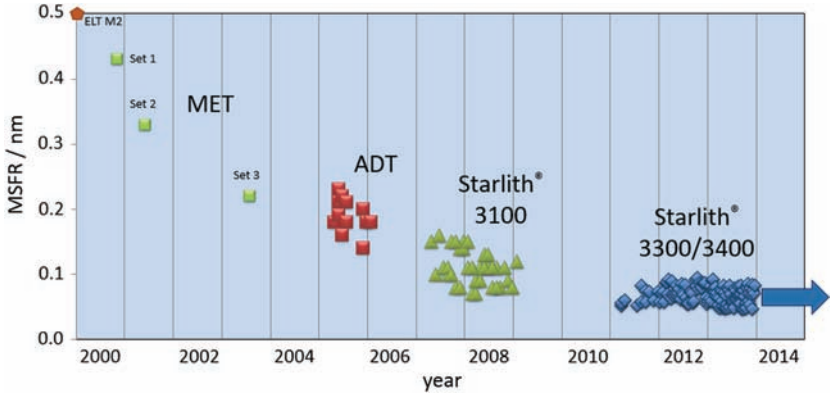

Figure 5.48 Improvements in MSFR achieved on single mirrors integrated in optical systems of different EUV tool generations: MET, ADT, Starlith® 3100, and Starlith® 3300. Data for the ELT M2 are also given. All MSFR values are based on the same definition.

fabrication since the year 1999, the MSFR levels of the early MET sets are also shown for a comprehensive comparison. It is demonstrated that the manufacturing of EUV mirrors has been successfully industrialized and a series production of EUV mirrors has been established since 2012.

5.6.4 Modeling and simulating stray light and flare

5.6.4.1 Significance of micro-roughness and flare in EUV systems

In the previous section the achievements in reducing mirror surface roughness and flare over several EUV tool generations were presented. A fundamental understanding of the sources of flare is particularly important in making these improvements. Therefore, a comprehensive overview of the basic theoretical background required for a precise estimation of flare will be given in the

Downloaded From: https://www.spiedigitallibrary.org/ebooks/ on 09 Mar 2022
Terms of Use: https://www.spiedigitallibrary.org/terms-of-use

following sections. The provided relations between the surface roughness of the individual components and their corresponding contributions to flare at the wafer constitute the basis for deriving the component roughness specification from the product flare specification and allow, *vice versa*, a precise flare prediction for each individual EUV projection system from the roughness measurements of the individual mirror surfaces.

The progress of optical lithography toward EUV entails increasing demands on the roughness of the optical surfaces. The reason is that, due to the total integrated scatter (TIS) (see Ref. 121),

$$TIS_{normal\ incidence} = \left(\frac{2\pi\ \Delta n}{\lambda}\right)^2 \cdot RMS^2, \tag{5.12}$$

the amount of stray light increases in proportion to the reciprocal of the squared wavelength λ. Comparing the EUV wavelength $\lambda_{EUV} = 13.5$ nm with the DUV wavelength $\lambda_{DUV} = 193$ nm yields a factor of $14.3^2 \approx 204$; i.e., the amount of stray light of an EUV mirror surface is more than 200× larger than the stray light of a DUV mirror with the same surface rms (rms of the roughness). While in DUV projection optics most of the optical elements are lens elements, all optical surfaces in EUV systems are mirrors. The amount of stray light is also proportional to the square of the factor Δn, which in the case of a lens element surface (refraction) is the difference between the refractive index n of the lens material and 1 ($\Delta n \approx 0.56$ for SiO_2 @ $\lambda_{DUV} = 193$ nm). In the case of a mirror surface (reflection), it is $\Delta n = 2$; i.e., for a DUV optical system, the stray light of a mirror is a factor $(2/0.56)^2 \approx 13$ times larger than the stray light of a lens element surface with the same surface roughness. In summary, an EUV mirror surface would induce a factor ~2600 more stray light compared to a DUV lens element surface with the same roughness.

On the one hand, surface scattering reduces the intensity of the specular reflection and consequently reduces transmission and throughput. On the other hand, (small-angle) scattered light may still propagate via the optical path to the wafer, thus contributing as flare to image blur and contrast loss. While large-angle scattering by roughness in the HSFR mainly contributes to transmission loss, because this stray light leaves the optical path somewhere in the projection optics and is vignetted by obscuring boundaries (e.g., mechanics, mirror contours, stops, apertures, etc.), flare is predominantly determined by the MSFR and the random high-frequency part of the low-spatial-frequency roughness (LSFR, spatial wavelengths in the domain of $> \ldots 1$ mm). The subsequent mid- and lower-frequency components of the LSFR corresponding to figure errors describe the floating transition from statistical flare to deterministic wavefront aberrations, which are usually described in terms of Zernike polynomials. Of course, this subdivision of

Downloaded From: https://www.spiedigitallibrary.org/ebooks/ on 09 Mar 2022
Terms of Use: https://www.spiedigitallibrary.org/terms-of-use

spatial frequencies into classes of LSFR, MSFR, and HSFR and their association to aberrations, flare, and transmission loss, respectively, is only a rough characterization of the mirror surface roughness and its stray light impact. This simplified consideration does not take into account the optical and mechanical design of the EUV projection optics: For each individual mirror surface in a specific design, lower and upper limits for spatial frequencies contributing to flare can be derived, and these limits usually are not sharp cutoffs. The transition from aberrations to flare and from flare to obscured stray light (contribution to transmission loss) varies from mirror to mirror and depends on the mirror's individual position in the optomechanical design. This point will be discussed in more detail later in this section.

The imaging impact of flare is significant. Stray light reaching the wafer as flare reduces the image contrast and the process window in the lithographic imaging process. In particular, it has a significant impact on the CD and the CDU of the printed features. The sensitivity of CD to dose errors becomes larger due to the reduced contrast; flare leads to proximity effects that depend on the local mask transmission and reduces the overlap of process windows due to dose offsets. In particular, isolated features on bright-field masks show the largest impact on flare. In the following sections, a comprehensive overview of the basic theoretical background required for a precise estimation of flare is presented.

5.6.4.2 Surface PSD and bidirectional scattering distribution function

In this section, the relations between the roughness of the optical surfaces of mirrors and the induced stray light characteristics (angular distribution of scattering) is briefly summarized. If the roughness of a mirror surface is small enough, scattering can be described by perturbation theory as first-order diffraction on the roughness acting as a Fourier decomposition of phase gratings with different spatial frequencies and phase amplitudes. In this sense, the scattering distribution is the superposition of the corresponding first-order-diffracted intensities. The underlying scattering theory in this so-called smooth-surface limit is the Rayleigh–Rice vector perturbation theory.[122–124] This theory describes the relationship between the roughness of a single surface represented by the PSD and the angle-resolved scattering (ARS) function, which represents the power dP_s scattered into the solid angle $d\Omega_s$ normalized to the incoming power P_i and the solid angle $d\Omega_s$ (see Ref. 121):

$$ARS(\theta_i, \phi_i; \theta_s, \phi_s) := \lim_{d\Omega_s \to 0} \frac{dP_s}{P_i \cdot d\Omega_s} = \frac{16\pi^2}{\lambda^4} \cdot Q(\theta_i, \phi_i; \theta_s, \phi_s) \cdot \cos\theta_i \cdot \cos^2\theta_s \cdot PSD_{2D}[\vec{f}(\vec{c}_i, \vec{c}_s)]. \tag{5.13}$$

Downloaded From: https://www.spiedigitallibrary.org/ebooks/ on 09 Mar 2022
Terms of Use: https://www.spiedigitallibrary.org/terms-of-use

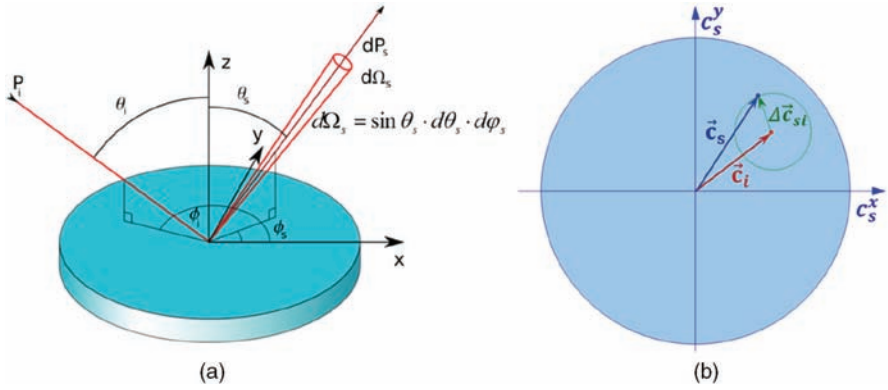

Figure 5.49 Definition of scattering variables for (a) ARS and (b) bidirectional scattering distribution function (BSDF).

The ARS is a function of θ_i, ϕ_i and of θ_s, ϕ_s, denoting the polar and azimuthal angles of incidence of the incoming plane wave, and the polar and azimuthal angles of scattering, respectively. See also Fig. 5.49(a) for the definition of these variables; notice that the polar angles θ_i and θ_s are defined with respect to the (local) surface normal. λ denotes the wavelength of light (i.e., $\lambda = 13.5$ nm for EUV). Q is the so-called polarization or reflectivity factor,[121] which can be considered as a generalization of the Fresnel reflectivity of a single surface for off-specular surface scattering. PSD_{2D} denotes (in general) the 2D PSD of the surface topography $h(x, y)$ and constitutes the powers of different roughness Fourier components in terms of the 2D spatial frequencies $\vec{f} = (f_x, f_y)$:

$$PSD_{2D}(\vec{f}) := \lim_{L\to\infty} \frac{1}{L^2} \left| \int_0^L \int_0^L d^2x \; h(\vec{x}) \; e^{-i\,2\pi\,\vec{f}\cdot\vec{x}} \right|^2. \tag{5.14}$$

The relation between the spatial frequencies $\vec{f}$ (the argument of the PSD) and the scattering angles $(\theta_i, \phi_i; \theta_s, \phi_s)$ or the corresponding direction cosines,

$$\vec{c}_i = \sin\theta_i \cdot \begin{pmatrix} \cos\phi_i \\ \sin\phi_i \end{pmatrix}, \qquad \vec{c}_s = \sin\theta_s \cdot \begin{pmatrix} \cos\phi_s \\ \sin\phi_s \end{pmatrix}, \tag{5.15}$$

respectively, is given by the grating equation:

$$\vec{f}(\vec{c}_i, \vec{c}_s) = \frac{\vec{c}_s - \vec{c}_i}{\lambda} = \frac{\Delta\vec{c}_{si}}{\lambda} \quad \text{with} \quad \Delta\vec{c}_{si} := \vec{c}_s - \vec{c}_i. \tag{5.16}$$

Due to this relation, it is often more convenient to describe the scattering characteristics equivalently as a function of the direction cosines $\vec{c}_i$ and $\vec{c}_s$

Downloaded From: https://www.spiedigitallibrary.org/ebooks/ on 09 Mar 2022
Terms of Use: https://www.spiedigitallibrary.org/terms-of-use

[see Fig. 5.49(b)] by the so-called bidirectional scattering distribution function (BSDF):

$$BSDF(\vec{c}_i, \vec{c}_s) := \frac{ARS(\theta_i, \phi_i; \theta_s, \phi_s)}{\cos\theta_s} = \frac{16\pi^2}{\lambda^4} \cdot Q'(\vec{c}_i, \vec{c}_s) \cdot \sqrt{1 - |\vec{c}_i|^2} \cdot \sqrt{1 - |\vec{c}_s|^2} \cdot PSD_{2D}\left(\frac{\Delta\vec{c}_{si}}{\lambda}\right). \quad (5.17)$$

Notice that in the definition of the BSDF the renormalization of the ARS by the factor $1/\cos\theta_s$ is attributed to the condition that $ARS(\theta_i, \phi_i; \theta_s, \phi_s) \cdot d\Omega_s \equiv BSDF(\vec{c}_i, \vec{c}_s) \cdot d^2c_s$ when integrating the ARS or the BSDF over the scattering variables θ_s, ϕ_s or direction cosines c_s^x, c_s^y, respectively.

Regarding the mid- and high-spatial frequency topography of the optical mirror surface, polishing and coating are predominantly statistical processes. Therefore, these surfaces reveal (in very good approximation) an isotropic roughness corresponding to a rotationally symmetric 2D PSD over several decades of spatial frequencies (at least in the mid- and high-spatial-frequency ranges MSFR and HSFR):

$$PSD_{2D}(\vec{f}) = PSD_{2Diso}(f); \quad (5.18)$$

i.e., the 2D PSD is a function of $f = \sqrt{f_x^2 + f_y^2}$ or the corresponding spatial wavelength $\Lambda = 1/f$, only. In this case, an isotropic roughness with a distinguished spatial wavelength Λ (or spatial frequency $f = 1/\Lambda$) induces a BSDF with scattered light in the direction cosines $\vec{c}_s$ on the circle around the specular direction $\vec{c}_i$ [the green circle in Fig. 5.50(b)]:

$$|\vec{c}_s - \vec{c}_i| = |\Delta\vec{c}_{si}| = \frac{\lambda}{\Lambda} = \lambda \cdot f. \quad (5.19)$$

To fulfill the tight flare specification for EUV imaging, the EUV mirror surfaces of the optical projection optics must inevitably be within the smooth surface limit such that the Rayleigh–Rice perturbation theory can indeed be applied to calculate the stray light from the micro-roughness of the mirror surfaces. The relevant quantity of the surface is the (isotropic 2D) surface PSD. This quantity determines the amount of stray light and its characteristics.

The isotropic 2D PSD of the EUV mirror surface roughness is determined by full-aperture visible-light interferometry in the LSFR range, by microscopic interferometry in the MSFR range, and by AFM in the HSFR range. These measurement data cover more than five or six decades of spatial frequencies. Typically, the roughness of the surfaces in the different spatial frequency ranges is characterized by several rms values that cover certain intervals $[\Lambda_1, \Lambda_2]$ of spatial wavelengths (typically decades or the ranges corresponding to LSFR, MSFR, and HSFR). The (squared) rms of the

Downloaded From: https://www.spiedigitallibrary.org/ebooks/ on 09 Mar 2022
Terms of Use: https://www.spiedigitallibrary.org/terms-of-use

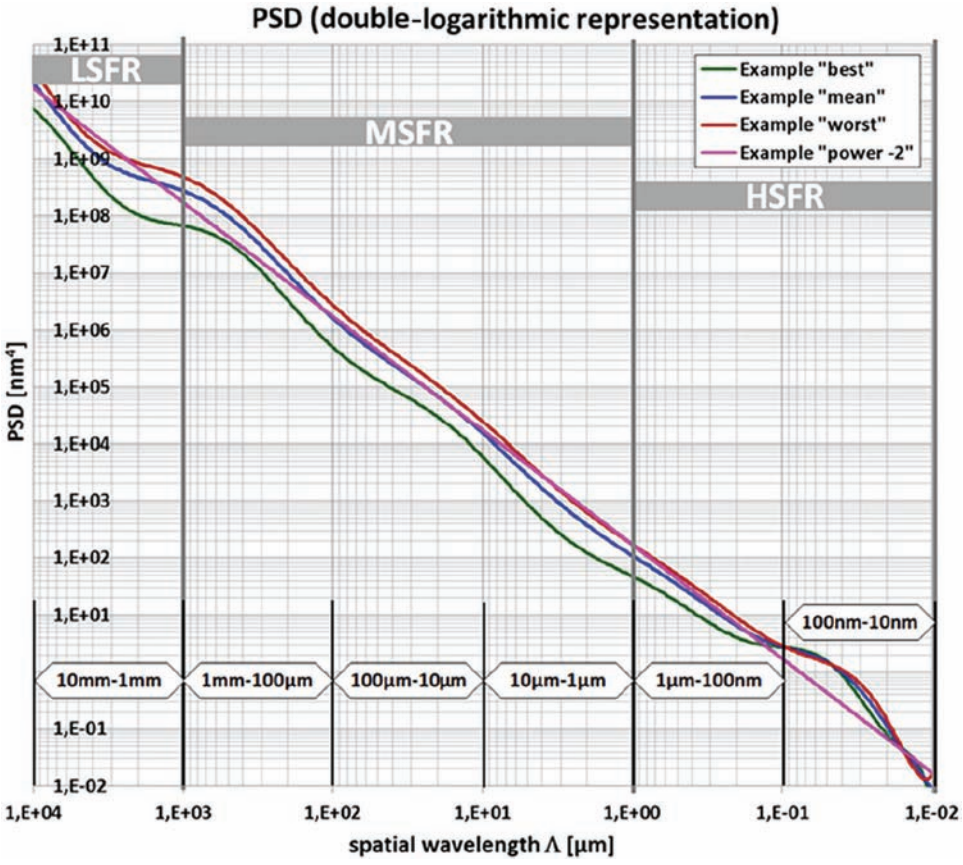

Figure 5.50 Examples of hypothetical surface PSDs in double-logarithmic representation. RMS values are given in Fig. 5.53.

roughness in a spatial wavelength interval $[\Lambda_1, \Lambda_2]$ can be calculated as integral of the PSD:

$$RMS^2([\Lambda_1, \Lambda_2]) = 2\pi \int_{f_1=1/\Lambda_1}^{f_2=1/\Lambda_2} df f \cdot PSD_{2\mathrm{D}iso}(f). \tag{5.20}$$

For direction cosines $\vec{c}_s$ of the scattered light with $|\vec{c}_s - \vec{c}_i| = |\Delta\vec{c}_{si}| = \lambda/\Lambda = \lambda \cdot f \ll 1$ (which complies very well to the MSFR regime), the integration of the BSDF over $\vec{c}_s$ within an annulus circular ring around the specular direction $\vec{c}_i$, i.e.,

$$\lambda/\Lambda_1 = \lambda \cdot f_1 \leq |\vec{c}_s - \vec{c}_i| \leq \lambda/\Lambda_2 = \lambda \cdot f_2, \tag{5.21}$$

gives the fraction of stray light in this annulus circular ring as an expression of the squared rms over the interval $[\Lambda_1, \Lambda_2]$ of spatial wavelengths ($\cos\theta_s \cong \cos\theta_i$):

Downloaded From: https://www.spiedigitallibrary.org/ebooks/ on 09 Mar 2022
Terms of Use: https://www.spiedigitallibrary.org/terms-of-use

$$TIS_{\theta_i}([\Lambda_1, \Lambda_2]) \cong \cos^2\theta_i \cdot \left(\frac{2\pi \cdot 2}{\lambda}\right)^2 \cdot RMS^2([\Lambda_1, \Lambda_2]). \tag{5.22}$$

This is the well-known TIS formula. In the special case of normal incidence ($\theta_i = 0$), the grating equation further simplifies to $\sin\theta_s = \lambda/\Lambda = \lambda \cdot f$ such that in this case the TIS formula describes the TIS within a circular cone $\theta_1 \leq \theta_s \leq \theta_2$ with $\sin\theta_1 = \lambda/\Lambda_1$ and $\sin\theta_2 = \lambda/\Lambda_2$.

Some remarks about the impact of the reflective multilayer coating on the surface PSD and on the BSDF should be made. Firstly, the coating changes the roughness properties of the optical surface. The thin-film growth of the multilayer replicates or smoothes the HSFR of the substrate and the underlying layers, and introduces an additional intrinsic HSFR roughness. Usually the net effect is an increased HSFR of the coated surface compared to the substrate surface. However, this depends on the coating process. HSFR can also be decreased if an appropriate smoothening process is applied (see Section 5.6.5.4). The MSFR essentially remains unchanged by the coating because for spatial wavelengths >1 μm the coating merely replicates the roughness of the substrate and does not introduce a significant intrinsic roughness. The modification of the surface roughness by thin-film growth can be described by roughness evolution models, e.g., by the linear growth model described in Refs. 125–127. Secondly, light scattering from a multilayer is much more sophisticated than the scattering from a single surface. Multilayer stray light models must be applied to describe scattering from the roughness of the interfaces of the multilayers as a resonance property of the coating, similar to the specular reflectance (see Refs. 127–131). In these models the scattered field is a coherent superposition of the fields scattered by each of the interfaces. Using the 2D isotropic top-surface PSD of the coated mirror and replacing the reflectivity factor Q in the single-surface BSDF/ARS by an expression of the unpolarized specular reflectivity R of the coated surface,

$$Q(\theta_i, \phi_i; \theta_s, \phi_s) \rightarrow \sqrt{R(\theta_i)} \cdot \sqrt{R(\theta_s)}, \tag{5.23}$$

this single-surface approximation gives a fairly good estimate of flare simulations of the EUV projection optics. This could be confirmed by comparing the BSDFs obtained with this simplified phenomenological model to the corresponding results of a full multilayer stray light simulation. See also the discussion in Ref. 132, where the same ansatz was used.

5.6.4.3 Decadic RMS density and TIS density: the better way to represent the isotropic surface PSD

As mentioned in the previous section, the relevant quantity that determines the amount of stray light and its characteristics is the isotropic 2D PSD of the EUV mirror surface. Usually this function is represented graphically by a

Downloaded From: https://www.spiedigitallibrary.org/ebooks/ on 09 Mar 2022
Terms of Use: https://www.spiedigitallibrary.org/terms-of-use

double-logarithmic plot of the PSD versus the spatial frequency f (or the spatial wavelength Λ). The problem with this representation is that one cannot really recognize the quality of the surface roughness over the various spatial wavelengths. Figure 5.50 shows some examples of hypothetical PSD curves: The green curve (Example "best") is the PSD with the smallest roughness in terms of rms, and the red curve (Example "worst") is the PSD with the largest roughness in terms of rms. The blue curve (Example "mean") describes a PSD somewhere between best and worse. Typically, optically finished surfaces often exhibit a PSD curve close to the square of the spatial wavelength ($PSD_{2\mathrm{D}iso} \sim f^{-2} \sim \Lambda^2$); such an idealized PSD of a so-called fractal surface[121,133–135] is given by the magenta curve (Example "power –2").

The double-logarithmic representation of the different examples of PSDs indicates differences in the roughness of the surfaces represented by these PSDs. However, it is in fact impossible to quantify (or even guess) the roughnesses and, correspondingly, the different stray light implications. Only when the rms values from the various PSDs are evaluated for different intervals of spatial wavelengths—covering, in total, the entire relevant spatial wavelength range—is the real surface roughness quality manifested in a quantifiable manner. Typically, one chooses decades of spatial wavelengths for these intervals such that a finite discrete number of rms values for these single decades (in total five to six decades) characterizes the progression of roughness over the (decades of) spatial wavelengths due to the progression of the PSD. The table at the top of Fig. 5.53 summarizes those decadic RMS values for the exemplary PSDs shown in Fig. 5.50. Notice that the fractal PSD (Example "power –2") exhibits a constant RMS value for all decades. To characterize the progression of the stray light impact over the (decades of) spatial wavelengths accordingly, the decadic TIS values can be calculated from the decadic RMS values via the TIS formula.

A better way to represent the isotropic 2D surface PSD is to introduce the concept of the so-called decadic RMS density (RMSD) or decadic TIS density (TISD). In contrast to the double-logarithmic PSD curve, these alternative representations of the PSD allow one to recognize—at first glance, and even quantitatively—the quality of the surface roughness over the various spatial wavelengths. The fancy but trivial trick is based on the fact that the discrete characterization of the mirror surface PSD via a finite number of decadic rms or decadic TIS values can be generalized to a continuous function of the continuous decadic number α, which is the decadic logarithm of the spatial frequency f:

$$f \;\rightarrow \alpha(f) = \log_{10}(f \cdot 1\ \mu\mathrm{m}) = -\log_{10}\left(\frac{\Lambda}{1\ \mu\mathrm{m}}\right),$$

$$\text{i.e.,}\quad f(\alpha) = \frac{1}{\Lambda(\alpha)} = \frac{10^{\alpha}}{1\ \mu\mathrm{m}}. \qquad (5.24)$$

Downloaded From: https://www.spiedigitallibrary.org/ebooks/ on 09 Mar 2022
Terms of Use: https://www.spiedigitallibrary.org/terms-of-use

In the integral of the 2D isotropic surface PSD used to calculate the squared rms, the spatial frequency f is substituted by the decadic number α:

$$df = \frac{d}{d\alpha} f(\alpha)\ d\alpha = \ln 10 \cdot f(\alpha)\ d\alpha \tag{5.25}$$

such that

$$\begin{aligned} RMS^2([\Lambda_1,\ \Lambda_2]) &= 2\pi \int_{f_1=1/\Lambda_1}^{f_2=1/\Lambda_2} df\ f \cdot PSD_{2\mathrm{D}iso}(f) \\ &= \int_{\alpha(f_1)}^{\alpha(f_2)} d\alpha\ 2\pi \cdot \ln 10 \cdot f^2(\alpha) \cdot PSD_{2\mathrm{D}iso}[f(\alpha)]. \end{aligned} \tag{5.26}$$

The new integrand defines the squared decadic rms density as function of the decadic number α as

$$RMSD^2(\alpha) \coloneqq 2\pi \cdot \ln 10 \cdot f^2(\alpha) \cdot PSD_{2\mathrm{D}iso}[f(\alpha)], \tag{5.27}$$

and the (squared) rms is given by the integral of the (squared) decadic RMSD over the decadic number α:

$$\begin{aligned} RMS^2([\Lambda_1, \Lambda_2]) = \int_{\alpha_1}^{\alpha_2} d\alpha\ RMSD^2(\alpha) \text{ with } \alpha_1 = \log_{10}\left(\frac{1\ \mu\mathrm{m}}{\Lambda_1}\right) \text{ and} \\ \alpha_2 = \log_{10}\left(\frac{1\ \mu\mathrm{m}}{\Lambda_2}\right). \end{aligned} \tag{5.28}$$

By analogy to the TIS formula, giving the relation between the surface rms and the TIS, the decadic TISD (for normal incidence $\theta_i = 0$) is defined from the decadic RMSD as function of the decadic number α as

$$TISD(\alpha) \coloneqq \left(\frac{2\pi \cdot 2}{\lambda}\right)^2 \cdot RMSD^2(\alpha), \tag{5.29}$$

and the TIS (for normal incidence $\theta_i = 0$) is calculated by the integral of the decadic TISD over the decadic number α:

$$\begin{aligned} TIS_{\theta_i=0}([\Lambda_1, \Lambda_2]) = \int_{\alpha_1}^{\alpha_2} d\alpha\ TISD(\alpha) \text{ with } \alpha_1 = \log_{10}\left(\frac{1\ \mu\mathrm{m}}{\Lambda_1}\right) \text{ and} \\ \alpha_2 = \log_{10}\left(\frac{1\ \mu\mathrm{m}}{\Lambda_2}\right). \end{aligned} \tag{5.30}$$

Figures 5.51 and 5.52 show these alternative representations of the exemplary surface PSDs shown in the double-logarithmic plot of Fig. 5.50. Notice that the fractal PSD $PSD_{2\mathrm{D}iso} \sim f^{-2}$ (Example "power –2") as a special case is characterized by constant decadic RMS and TIS densities. The advantages of this alternative representation of the isotropic PSD are evident:

Downloaded From: https://www.spiedigitallibrary.org/ebooks/ on 09 Mar 2022
Terms of Use: https://www.spiedigitallibrary.org/terms-of-use

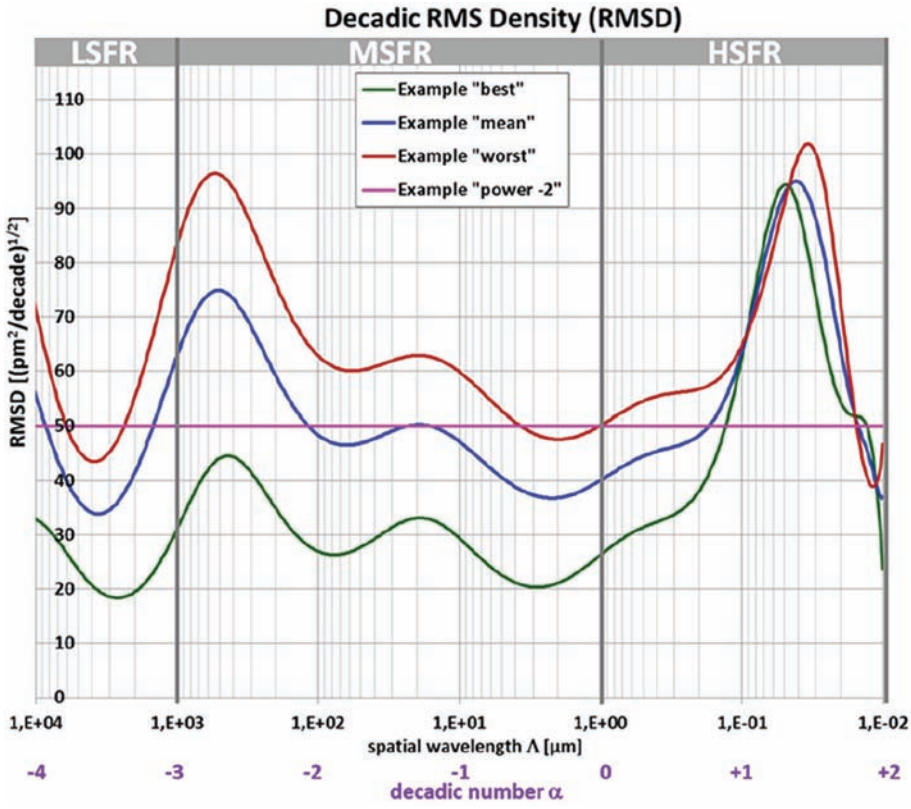

Figure 5.51 Isotropic 2D PSDs in Fig. 5.50 represented as decadic RMSD. RMS values are given in Fig. 5.53.

One can compare the different PSDs continuously over all spatial frequencies in a quantifiable manner on a linear scale in terms of TIS per decade or RMS per decade. One can even quantitatively guess the band RMS or band TIS values for the different decadic intervals of spatial wavelengths.

5.6.4.4 The stray light point spread function: the link between the surface PSD and the flare distribution at the wafer

In the foregoing sections, the relationships between the mirror surface roughness (PSD, RMS, and decadic RMSD) and the amount and characteristics of the light scattered off the mirror surface (BSDF, TIS, and decadic TISD) were discussed. Now we describe how this stray light is then distributed in the image plane at the wafer level. Therefore, the imaging of a perfect point source is being considered. This image is the so-called point spread function (PSF). The PSF of an ideal projection optics without any aberrations and without stray light is determined by the diffraction of light on

Downloaded From: https://www.spiedigitallibrary.org/ebooks/ on 09 Mar 2022
Terms of Use: https://www.spiedigitallibrary.org/terms-of-use

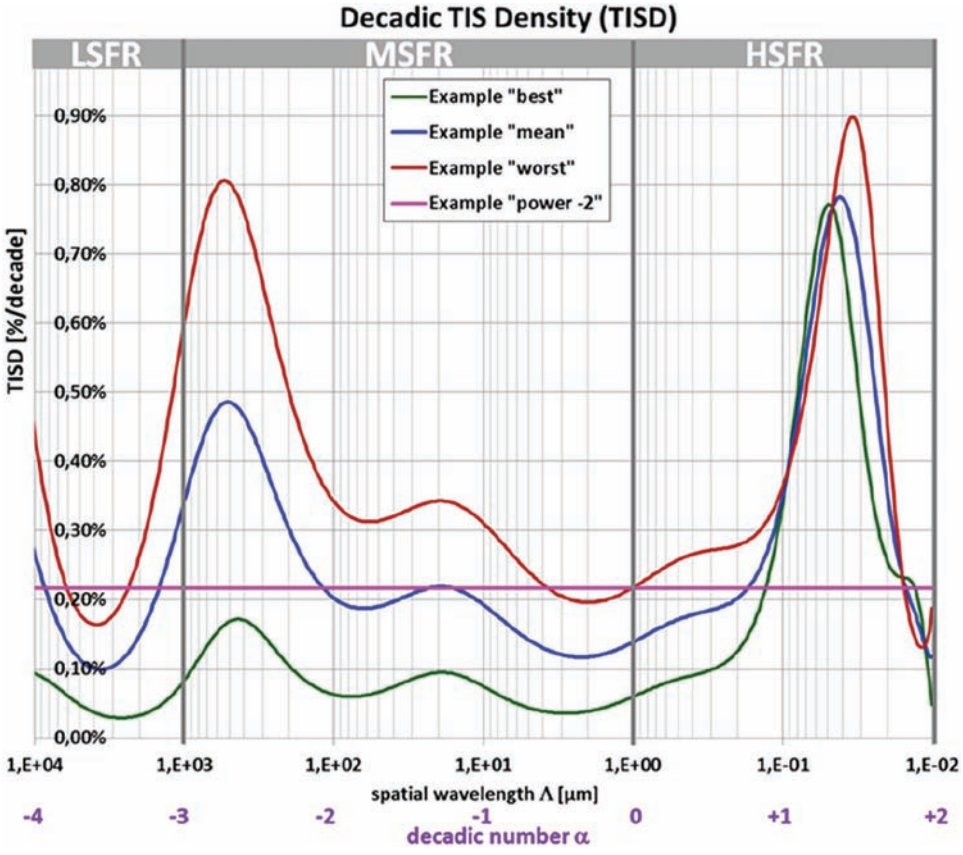

Figure 5.52 Isotropic 2D PSDs in Fig. 5.50 represented as decadic TISD. TIS values are given in Fig. 5.53.

the aperture stop that defines the NA of the projection optics. In this case, the PSF is the well-known Airy function $PSF_0(r)$ (see Ref. 136):

$$PSF_0(r) = \frac{\pi \cdot NA^2}{\lambda^2} \cdot \left[\frac{2 \cdot J_1\left(\frac{2\pi}{\lambda} \cdot NA \cdot r\right)}{\frac{2\pi}{\lambda} \cdot NA \cdot r} \right]^2 \tag{5.31}$$

where J_1 is the Bessel function of the first kind. The diameter of this Airy disk, which is defined by the radial distance of the first zero of the Airy function, is determined by the NA:

$$D_{Airy} = 1.22 \cdot \lambda / NA. \tag{5.32}$$

Any aberration in the wavefront of the exit pupil causes a redistribution of light within or outside of the Airy disk; low-pupil-frequency aberrations due to figure errors of mirrors cause a coherent redistribution of light within the

Downloaded From: https://www.spiedigitallibrary.org/ebooks/ on 09 Mar 2022
Terms of Use: https://www.spiedigitallibrary.org/terms-of-use

		10mm-1mm	1mm-100µm	100µm-10µm	10µm-1µm	1µm-100nm	100nm-10nm
RMS [pm]	Example "best"	24	38	30	23	38	71
	Example "mean"	44	65	48	40	48	75
	Example "worst"	57	84	61	51	56	78
	Example "power -2"	50	50	50	50	50	50
$TIS_{\vec{p}\vec{i}=\vec{0}}$ [%]	Example "best"	0,05%	0,12%	0,08%	0,05%	0,12%	0,44%
	Example "mean"	0,17%	0,37%	0,20%	0,14%	0,20%	0,49%
	Example "worst"	0,28%	0,61%	0,33%	0,23%	0,27%	0,53%
	Example "power -2"	0,22%	0,22%	0,22%	0,22%	0,22%	0,22%

Figure 5.53 RMS and TIS values of the various PSDs in Figs. 5.50–5.52 for six different intervals of spatial wavelengths, each representing one decade.

Airy disk ($<D_{Airy}$), whereas higher-pupil-frequency aberrations due to statistical surface errors of the mirrors with spatial frequencies beyond the figure errors cause an incoherent redistribution of light outside of the Airy disk ($>D_{Airy}$) (Fig. 5.54).

This discussion already indicates that flare cannot only be considered as light that is scattered from the surface roughness of a mirror and then propagates to the wafer, but also as the redistribution of light out of the

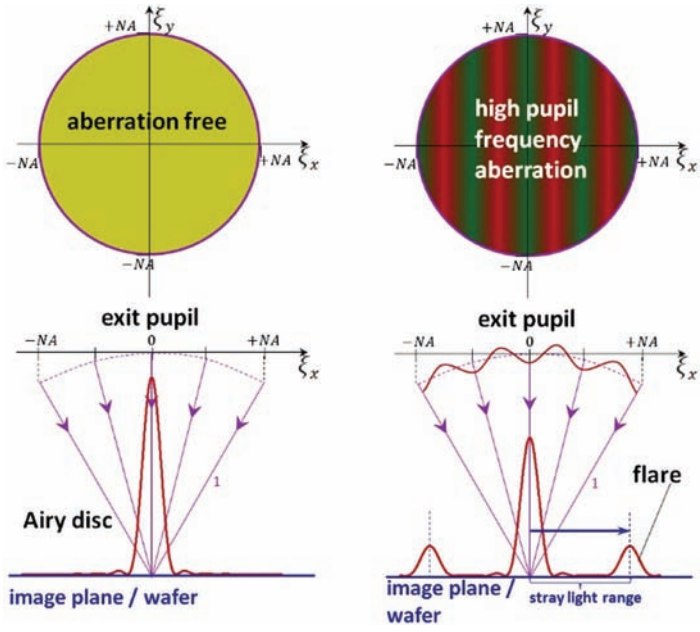

Figure 5.54 Redistribution of light out of the ideal PSF (Airy disk) due to higher-pupil-frequency aberrations.

Downloaded From: https://www.spiedigitallibrary.org/ebooks/ on 09 Mar 2022
Terms of Use: https://www.spiedigitallibrary.org/terms-of-use

Airy disk due to the high-pupil-frequency aberration in the wavefront of the exit pupil. In this conception of flare, the high-pupil-frequency aberration in the wavefront of the exit pupil is induced as phase error by the topography of the surface roughness in the subaperture on the mirror surface. In this context, the subaperture is the footprint of the light bundle belonging to the specific field point at the wafer, looking at the PSF. Figure 5.55 illustrates this alternative consideration of flare in a simplified 4*f* optical system.

For the sake of simplicity, optical designs are now assumed for which the subapertures of a single mirror surface have circular shape with radius R_{SA} and the mapping of the exit pupil [pupil coordinates $\vec{\xi} = (\xi_x, \xi_y)$] to the subaperture [subaperture coordinates $\vec{x} = (x, y)$] is simply a linear scaling:

$$\vec{x} \rightarrow \vec{\xi} = \frac{NA}{R_{SA}} \cdot \vec{x}. \tag{5.33}$$

Then a periodic surface error with spatial wavelength Λ (spatial frequency $f = 1/\Lambda$) in the subaperture is transformed into a periodic wavefront aberration having pupil wavelength Λ_p (pupil frequency $f_p = 1/\Lambda_p$) with

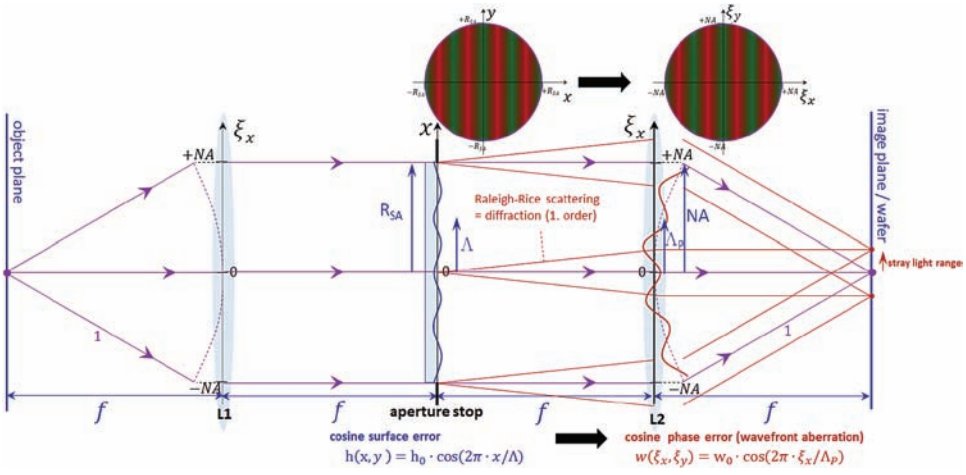

Figure 5.55 Simplified illustration of an alternative consideration of flare in a 4*f* optical system. The "roughness" with spatial wavelength Λ of a plane-parallel component induces stray light due to the Rayligh–Rice scattering theory. This stray light propagates to the wafer and hits (as flare) the image plane at a distance *r* from the center of the Airy disk. Alternative conception: The roughness topography with spatial wavelength Λ within the circular subaperture of radius R_{SA} induces a phase error with pupil wavelength Λ_p in the exit pupil. This aberration with pupil wavelength Λ_p induces a redistribution of a fraction of the light of the PSF at a distance *r*.

Downloaded From: https://www.spiedigitallibrary.org/ebooks/ on 09 Mar 2022
Terms of Use: https://www.spiedigitallibrary.org/terms-of-use

$$\Lambda \to \Lambda_P = \frac{NA}{R_{SA}} \cdot \Lambda, \qquad f \to f_p = \frac{R_{SA}}{NA} \cdot f. \tag{5.34}$$

The surface topography h within the subaperture of the mirror surface transforms by a scaling with a factor of $2 \cdot \langle \cos \theta_i \rangle$ to a wavefront aberration w (phase error $\phi = 2\pi/\lambda \cdot w$) in the exit pupil (assuming that the variation of $\cos \theta_i$ over the subaperture is small and can (for all rays) be represented by the average value $\langle \cos \theta_i \rangle$):

$$h(\vec{x}) \to w(\vec{\xi}) \cong 2 \cdot \langle \cos \theta_i \rangle \cdot h\left(\frac{R_{SA}}{NA} \cdot \vec{\xi}\right). \tag{5.35}$$

Analogous to the 2D surface PSD, the 2D pupil PSD PSD_{pupil} over the exit pupil as function of the pupil frequencies $\vec{f}_p$ can be defined as

$$PSD_{2\mathrm{D}pupil}(\vec{f}_p) = \frac{1}{\pi \cdot NA^2} \cdot \left| \int_{|\vec{\xi}| \le NA} d^2\xi \;\; w(\vec{\xi}) \cdot e^{-i\, 2\pi\, \vec{f}_p \cdot \vec{\xi}} \right|^2. \tag{5.36}$$

A simple calculation then gives the following relation of the 2D surface PSD over the subaperture with the 2D pupil PSD over the exit pupil:

$$PSD_{2\mathrm{D}pupil}(\vec{f}_p) \cong 4 \cdot \langle \cos\, \theta_i \rangle^2 \cdot \left(\frac{NA}{R_{SA}}\right)^2 \cdot PSD_{2\mathrm{D}}\left(\frac{NA}{R_{SA}} \cdot \vec{f}_p\right). \tag{5.37}$$

For any wavefront distortion w in the exit pupil (scalar phase error $\phi = 2\pi/\lambda \cdot w$) the modified PSF, $PSF_0(|\vec{x}_r|) \to PSF(\vec{x}_r)$, can be calculated from the absolute value of the Fourier transformation ($\vec{x}_r$ is the relative image coordinate at the wafer with $\vec{x}_r = \vec{0}$ at the center of the Airy disk):

$$PSF(\vec{x}_r) \propto \left| \int_{|\vec{\xi}| \le NA} d^2\xi \quad e^{i\, \frac{2\pi}{\lambda} \cdot w(\vec{\xi})} \cdot e^{-i\, \frac{2\pi}{\lambda}\, \vec{\xi} \cdot \vec{x}_r} \right|^2. \tag{5.38}$$

In the smooth wavefront limit, i.e., $\phi = 2\pi/\lambda \cdot w \ll 1$, and under the assumption that the Fourier components of w have only sufficiently large pupil frequencies f_p (e.g., $2NA \cdot f_p \ge 5$), the PSF of an exit pupil with higher-pupil-frequency aberrations is given as

$$PSF(\vec{x}_r) \cong (1 - TIS) \cdot PSF_0(|\vec{x}_r|) + PSF_{\mathrm{flare}}(\vec{x}_r). \tag{5.39}$$

Here, the stray light PSF PSF_{flare} describes the redistributed light outside of the Airy disk (in the case of sufficiently large pupil frequencies), and TIS is the total integrated scatter of this light attenuating the intensity of the unperturbed PSF by the factor (1-TIS). The stray light PSF is related to the 2D pupil PSD by

Downloaded From: https://www.spiedigitallibrary.org/ebooks/ on 09 Mar 2022
Terms of Use: https://www.spiedigitallibrary.org/terms-of-use

$$PSF_{\text{flare}}(\vec{x}_r) = \frac{4\pi^2}{\lambda^4} \cdot PSD_{2\text{D } pupil}\left(\frac{\vec{x}_r}{\lambda}\right). \tag{5.40}$$

In particular, this equation gives an important relation between the scatter range $\vec{x}_r$ and the pupil frequency $\vec{f}_p$:

$$\vec{x}_r = \lambda \cdot \vec{f}_p, \qquad r = |\vec{x}_r| = \lambda \cdot f_p = \frac{\lambda}{\Lambda_p}. \tag{5.41}$$

This is the right place to pick up the discussion about the borderline between aberrations and statistical flare. While low-pupil-frequency aberrations due to figure errors cause a coherent redistribution of light within the Airy disk ($r \leq D_{Airy}$) or slightly beyond, incoherent redistributions with ranges $r \geq r_{min} > D_{Airy}$ would be associated to statistical flare. Typically, one choses a minimum flare range r_{min} of two times the diameter of the Airy disk, i.e.,

$$r_{\min} := 2 \cdot D_{Airy} = 2 \cdot 1.22\ \lambda/NA \cong 5/(2\ NA) \cdot \lambda. \tag{5.42}$$

This corresponds to the pupil wavelengths:

$$\Lambda_p \leq \Lambda_p^{max} := \lambda/r_{min} \cong 2\ NA/5, \tag{5.43}$$

i.e., wavefront distortions with more than five periods over the total diameter of the exit pupil, or

$$\Lambda \leq \Lambda_{max} = 2R_{SA}/5 = D_{SA}/5, \tag{5.44}$$

i.e., more than five periods of a periodic surface error over the supaperture diameter $D_{SA} = 2R_{SA}$. This defines a somewhat arbitrary distinction between aberrations and flare. In fact, the transition from aberrations to statistical flare is not sharp.

Finally, using the relation [Eq. (5.40)] between the stray light PSF PSF_{flare} and the 2D pupil PSD $PSD_{2\text{D}pupil}$, and the connection [Eq. (5.37)] between the 2D surface PSD $PSD_{2\text{D}}$ and the 2D pupil PSD $PSD_{2\text{D}pupil}$, one obtains the ultimate link between the surface PSD of a single mirror (the n^{th} mirror M_n in the projection optics) and its incoherent contribution to the stray light PSF:

$$PSF_{flare}^{(n)}(r) \cong \frac{16\ \pi^2}{\lambda^4} \cdot \left(\frac{NA}{R_{SA}^{(n)}}\right)^2 \cdot \langle \cos\theta_i^{(n)} \rangle^2 \cdot PSD_{2\text{D}iso}\left(\frac{NA}{R_{SA}^{(n)} \cdot \lambda} \cdot r\right). \tag{5.45}$$

Here, an isotropic roughness of the mirror surface characterized by an isotropic 2D PSD $PSD_{2\text{D}iso}$ is assumed such that, with the linear mapping between the exit pupil and the subaperture on the mirror surface, this contribution to the stray light PSF $PSF_{flare}^{(n)}$ is rotationally symmetric. Moreover, this relation between the isotropic surface PSD and the

Downloaded From: https://www.spiedigitallibrary.org/ebooks/ on 09 Mar 2022
Terms of Use: https://www.spiedigitallibrary.org/terms-of-use

rotationally symmetric stray light PSF gives an important one-to-one correspondence between the spatial wavelength Λ and the scatter radius $r^{(n)}$ for each mirror surface:

$$r^{(n)} = r^{(n)}(\Lambda) = \frac{R_{SA}^{(n)}}{NA} \cdot \frac{\lambda}{\Lambda}. \tag{5.46}$$

The single stray light contributions of each individual n^{th} mirror add up linearly such that the total stray light PSF of the system with all N mirror surfaces is given by

$$PSF_{\text{flare}}(r) = \sum_{n=1}^{N} PSF_{flare}^{(n)}(r) \ . \tag{5.47}$$

5.6.4.5 Flare and vignetted stray light: flare-efficiency functions

The considerations of the previous section did not take into account any obscuration effects on stray light. For very small spatial wavelengths Λ (typically somewhere in the transitional area between MSFR and HSFR), when the scatter radii $r^{(n)}$ (or equivalently scatter angles represented by the difference $|\vec{c}_s - \vec{c}_i|$ of the direction cosines) become large, the scattered light may leave the optical path somewhere in the projection optics. This light is completely or partially vignetted by the obscuring boundaries of the mechanical design, e.g., at mechanical parts, mirror contours, stops, apertures, etc., and will not reach the wafer as flare. As long as the scatter radius $r^{(n)}$ lies inside the image field of the projection optics, the stray light PSF $PSF_{flare}^{(n)}$ derived in the previous section correctly accounts for the flare distribution. However, stray light with putative scatter radii $r^{(n)}$ that does not or does not completely intersect the image field might be completely or partially obscured. The question is, which spatial wavelengths of the mirror surface PSD, or equivalently, which decadic numbers α of the decadic RMS and TIS densities really contribute to flare at the wafer. Therefore, the concept of flare-efficiency functions is introduced. To this end, a decadic (normal incidence) TISD that is δ-peaked at a distinguished decadic number $\alpha_\nu = \log_{10}(\nu \cdot 1\ \mu\text{m})$ is considered:

$$TISD(\alpha, \alpha_\nu) := TIS \cdot \delta(\alpha - \alpha_\nu). \tag{5.48}$$

This decadic TISD represents an isotropic surface roughness with distinguished spatial frequency ν and corresponds to the following δ-peaked isotropic 2D PSD of the surface:

$$PSD_{2\text{D}iso}(f, \nu) = \frac{RMS^2}{2\pi \cdot \nu} \cdot \delta^{(1)}(f - \nu), \qquad RMS = \frac{\lambda \cdot \sqrt{TIS}}{2\pi \cdot 2}. \tag{5.49}$$

Downloaded From: https://www.spiedigitallibrary.org/ebooks/ on 09 Mar 2022
Terms of Use: https://www.spiedigitallibrary.org/terms-of-use

This δ-peaked decadic TISD is defined for the surface of each mirror M_n in the optomechanical design. The scanner integrated flare $flare^{(n)}(\alpha_v)$ is calculated by a ray-tracing simulation at a given field position and for a given feature size CD as a function of the decadic number α_v. The ratio of the calculated scanner integrated flare to the (normal incidence) TIS defines the (scanner integrated) flare efficiency function $FE^{(n)}(\alpha_v)$ of the n^{th} mirror surface for a given feature size and field position:

$$FE^{(n)}(\alpha_v) := \frac{flare^{(n)}(\alpha_v)}{TIS} \cdot \tag{5.50}$$

These functions describe for each mirror M_n which fraction of any (normal incidence) decadic TISD at any decadic number $\alpha = \log_{10}(f \cdot 1\ \mu\text{m})$ contributes to flare. They encompass several properties of the optomechanical design, the geometry and intensity distribution of the illuminated field, the geometry of the feature to measure flare, as well as the cos θ_i and cos θ_s dependencies in the BSDF of the Rayleigh–Rice perturbation theory; finally, the reflectivity and extinction effects of the multilayer coatings can also be factored in. Figure 5.56 shows an example of the flare efficiency functions for two different mirrors M_k (solid curve) and M_l (dashed curve) ($k < l$) at the field center for a dark circular pad with $CD = 2$ μm, testing for minimal flare ranges $r_{min} = CD/2 = 1$ μm.

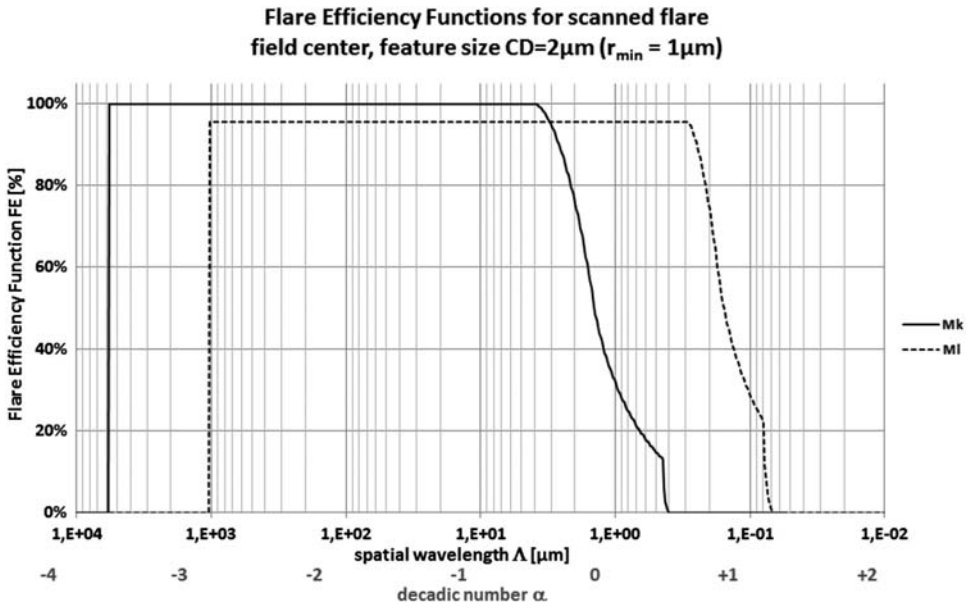

Figure 5.56 Flare efficiency functions for two different mirrors M_k (solid curve, $R_{SA} =$ 140 mm, $\theta_i \sim 0$ deg) and M_l (dashed curve, $R_{SA} = 25$ mm, $\theta_i \sim 12$ deg), where $k < l$, in an exemplary EUV projection system with $NA = 0.33$.

Downloaded From: https://www.spiedigitallibrary.org/ebooks/ on 09 Mar 2022
Terms of Use: https://www.spiedigitallibrary.org/terms-of-use

Coming straight to the point, the flare efficiency functions $FE^{(n)}$ define the flare-relevant portion of the (normal incidence) decadic TISD: For any given surface PSD $PSD_{2Diso}^{(n)}$ of the n^{th} mirror, the product of the corresponding decadic TISD $TISD^{(n)}$ and the individual flare efficiency function $FE^{(n)}$ can be calculated. This new function of the decadic number α is denoted as the decadic flare density $FD^{(n)}$:

$$FD^{(n)}(\alpha) := FE^{(n)}(\alpha) \cdot TISD^{(n)}(\alpha). \tag{5.51}$$

Figure 5.57 is a graphical presentation of decadic flare densities calculated from the four hypothetical decadic TIS densities shown in Fig. 5.52. For this example, the flare efficiency function of M_k was used, which is represented as the solid curve in Fig. 5.56.

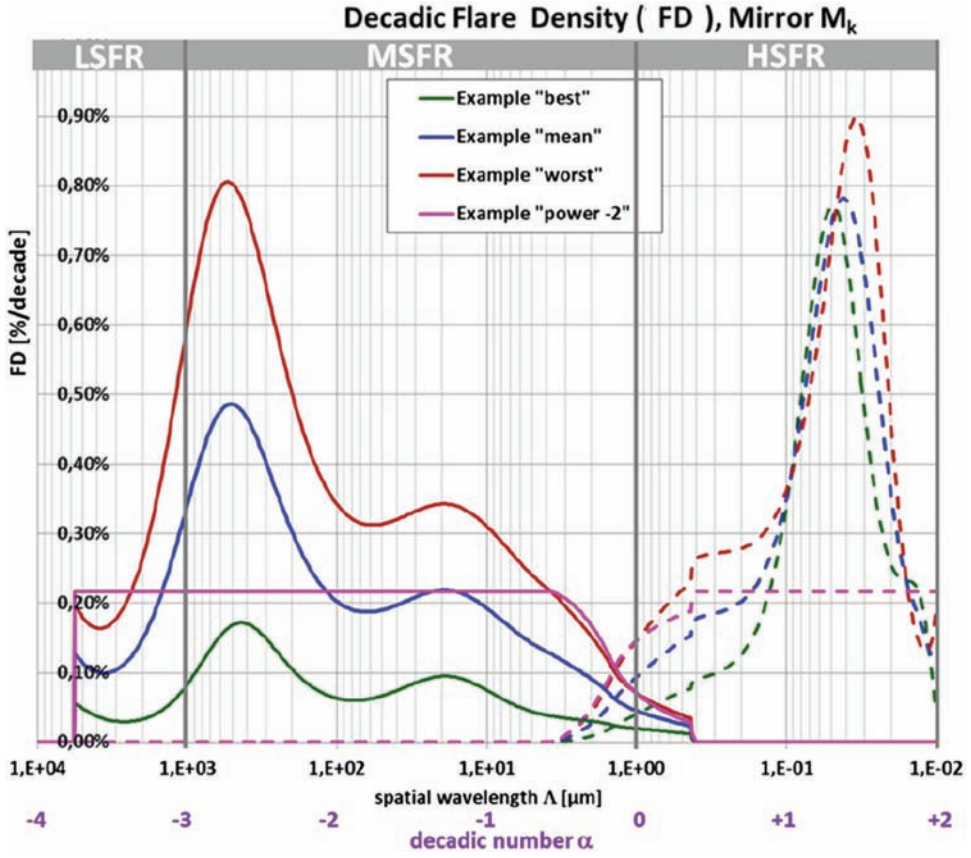

Figure 5.57 The solid curves show the decadic flare densities calculated from the four hypothetical decadic TIS densities of Fig. 5.52. Here, the flare efficiency function of M_k (represented as the solid curve in Fig. 5.56) is used as an example. The dashed curves represent the obscured part of the decadic TIS densities, which do not contribute to flare but to transmission loss.

Downloaded From: https://www.spiedigitallibrary.org/ebooks/ on 09 Mar 2022
Terms of Use: https://www.spiedigitallibrary.org/terms-of-use

The total flare contribution $flare^{(n)}$ of the n^{th} mirror M_n with this specific surface PSD $PSD_{2Diso}^{(n)}$ is then (for the given field position and feature size)

$$flare^{(n)} = \int d\alpha\ FD^{(n)}(\alpha) = \int d\alpha\ FE^{(n)}(\alpha) \cdot TISD^{(n)}(\alpha). \tag{5.52}$$

The integral covers the full range of the decadic number α of the spatial frequencies where the flare efficiency function $FE^{(n)}$ is nonzero.

The single flare contributions of each individual n^{th} mirror M_n add up linearly such that, finally, the total flare of the system with all N mirrors (for the given field position and feature size) is given by

$$flare = \sum_{n=1}^{N} flare^{(n)}. \tag{5.53}$$

With this equation, the basic theoretical framework for a precise estimation of flare in an optical EUV projection optics is complete. This framework constitutes the basis to derive roughness specifications of individual mirror surfaces within a projection optics from the underlying product flare specification. Moreover, it is applied for a precise flare prediction of any individual EUV projection system based on roughness measurements of the individual mirror surfaces integrated in the system.

5.6.5 Optics manufacturing: mirror coating

5.6.5.1 The difference between coatings for DUV and EUV lithography systems

The transition from DUV to EUV wavelengths in lithography applications, i.e., switching from $\lambda_{DUV} = 193$ nm to $\lambda_{EUV} = 13.5$ nm, calls for all-reflective systems since there are no sufficiently transparent materials for the latter wavelength that could be used to make transmissive optics. In this transition, the importance of coatings for the optical performance increases dramatically. Considering an uncoated lens element, about 92% of the incident DUV light is transmitted, while the remaining 8% is reflected at the front and back surfaces (Fig. 5.58). By means of antireflectance coatings on both surfaces, making use of destructive interference, the losses due to reflectance can practically be reduced to zero; this is, however, at the expense of some absorption in these coatings. Still, the transmission can be increased roughly from 92% to 99%.

In contrast to this, both the transmission and reflectance of an EUV beam incident on an arbitrary uncoated lens element or mirror substrate are zero. The EUV radiation is completely absorbed within the first micrometer of the material. Only if the substrate is coated with an artificial Bragg reflector—a multilayer coating consisting of alternating layers having high and low indices of refraction—a considerable portion of the incoming light is reflected. For

Downloaded From: https://www.spiedigitallibrary.org/ebooks/ on 09 Mar 2022
Terms of Use: https://www.spiedigitallibrary.org/terms-of-use

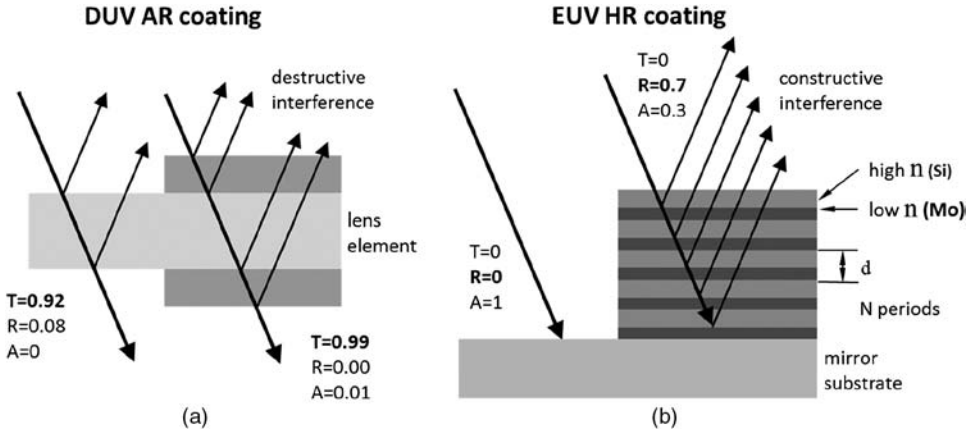

Figure 5.58 (a) Antireflective (AR) coatings compared to (b) EUV highly reflective (HR) coatings. DUV optics make use of transparent lens elements, and the AR coating increases the system transmission. EUV highly reflective coatings are the enabler of any EUV system but also limit the tool transmission.

the wavelength $\lambda = 13.5$ nm, multilayers based on molybdenum (Mo) and silicon (Si) have proven to yield the highest peak reflectance. The theoretical maximum for this is 75%, while in practice the reflectance can be higher than 70%. The reflectivity loss, as compared to the theoretical maximum, is mostly due to interface roughness and interdiffusion layers, i.e., layers of molybdenum silicide between the "clean" Mo and Si layers. In this sense, the EUV reflectance coatings are the true optical elements. Without them, no light will pass the optical train; however, due to their low reflectance, they also limit the optical performance of the system.

The next sections describe how the optical properties of coatings for EUV wavelengths can be measured and how the multilayer stack is optimized for high reflectance, low scattering, and high thermal stability. They further discuss how the coating interacts with the surface figure of the substrate it is deposited on. At the end of this section, estimations for the manufacturing accuracies required to obtain a working EUV lithography system are given.

5.6.5.2 Measuring the optical properties of coatings at EUV wavelengths

The optical properties of the coatings are essential for EUV lithography applications. Therefore, accurate and reliable measurement of both the specular reflectance and the off-specular stray light is needed. The lowest signal-to-noise ratio of those measurements can be reached at the intense and brilliant synchrotron-based light sources, e.g., the Advanced Light Source in of LBNL[137] in Berkeley and the Physikalisch-Technische Bundesanstalt (PTB) at BESSYII in Berlin.[138,139] At the ALS, the samples are limited in size to about twice the dimensions of a mask blank, whereas at the PTB, full-size EUV optics such as normal-incidence collectors can be accommodated in the

Downloaded From: https://www.spiedigitallibrary.org/ebooks/ on 09 Mar 2022
Terms of Use: https://www.spiedigitallibrary.org/terms-of-use

goniometer chamber. At both facilities, specular and nonspecular reflectivities can be measured. Recently, the PTB installed an EUV polarimeter that enables measurement of the full polarization properties of coatings.[140]

For an effective production process, in-house reflectometry at the production site is also needed. Lab-based reflectometers have been developed for this purpose. These generate the EUV light in either plasma or x-ray sources. This limits the available power and therefore leads to higher noise level of the measurements. Some of these lab-based reflectometers are designed for full-scale optics,[141,142] while others are optimized for mask blank characterization[143] or measurement of the angle-resolved scattering.[144]

5.6.5.3 The limits of peak reflectance at $\lambda = 13.5$ nm

The optical performance of EUV tools is limited by the optical constants of the coating material. This starts with the theoretical maximum peak reflectance. In order to obtain a high reflectance in an artificial Bragg crystal, the difference (i.e., the contrast) in refractive index between the two materials must be large, while the absorption should be as small as possible. However, looking at the optical constants of Mo and Si at $\lambda = 13.5$ nm (see Fig. 5.59), the difference in the refractive index is small ($\Delta n = 0.08$), while the average absorption is large ($k_{mean} = 0.004$). Due to the large absorption of the molybdenum, the highest peak reflectance is not obtained for a quarter-wave stack (i.e., each single layer of Mo and Si has a thickness of $\lambda/4$) but rather for a stack with a reduced Mo fraction. The Mo fraction is often called Γ, defined as the thickness of the Mo layer d_{Mo} devided by the total period legth $d_{\mathrm{Mo}} + d_{\mathrm{Si}}$. Still, Bragg's law [$\lambda = 2\, n\, d \sin(AOI)$] has to be obeyed, making the

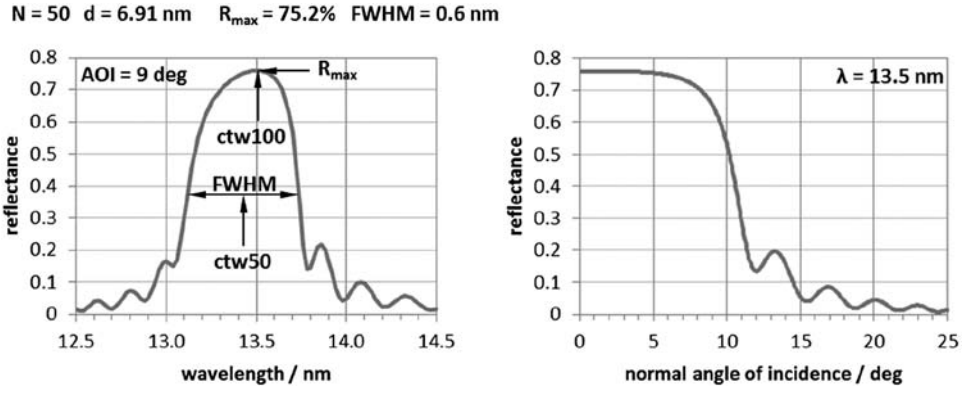

Figure 5.59 Definitions of the characteristic quantities of a $R(\lambda)$ spectrum: peak reflectance (R_{max}), centroid wavelength at 100% of the peak reflectance (ctw100), centroid wavelength at 50% of the peak reflectance (ctw50), and FWHM, a measure for the spectral acceptance of the coating. The optical constants of Mo and Si at $\lambda = 13.5$ nm are nMo = 0.921, kMo = 6.4E–3, nSi = 0.999, and kSi = 1.7E–3. Calculation of an ideal multilayer stack yields $R_{max} = 75.2\%$ and FWHM = 0.6 nm.

Downloaded From: https://www.spiedigitallibrary.org/ebooks/ on 09 Mar 2022
Terms of Use: https://www.spiedigitallibrary.org/terms-of-use

multilayer a half-wave stack with a period length of roughly 7 nm. With these parameters, the peak reflectance increases with the number of periods, saturating with ~50 periods at about 75%.

Besides the peak reflectance, the FWHM of the Bragg peak is also limited by the small contrast of the refractive index. As shown in Fig. 5.59, this holds true not only for the spectral response but also for the angular response of the multilayer, limiting the optical performance of EUV tools in two different ways. On one hand, the 0.6-nm FWHM of an ideal Mo/Si multilayer is smaller than the spectrum typically emitted by EUV plasma sources. Therefore, it is desirable to have coatings with high FWHM in order to obtain high system transmission. On the other hand, there could be mirrors in an EUV lithography tool that need to accept an angular range of incident rays that is larger than the angular bandwidth (about 10 deg) offered by an ideal Mo/Si coating. For both problems, a-periodic, sometimes called depth-graded, multilayer coatings provide a solution. The concept of so-called supermirrors, known for neutron deflection and for hard x-ray grazing-incidence mirrors with large spectral bandwidth,[145] was applied to normal-incidence EUV coatings.[146,147] It was found that stochastic designs (for which the layer thicknesses vary virtually randomly into the depth of the coating) can provide—either in the angular space or in the spectral space—a constant reflectance over a large range. This is obtained, however, at a much lower level regarding the peak reflectance.[148] Additionally, a stack with three periodic sub-stacks, all having different period lengths, gives a broader angular acceptance, the remaining oscillations being larger compared to the stochastic design. This is also true for measured reflectance curves of the actually deposited stacks, shown in Fig. 5.60.

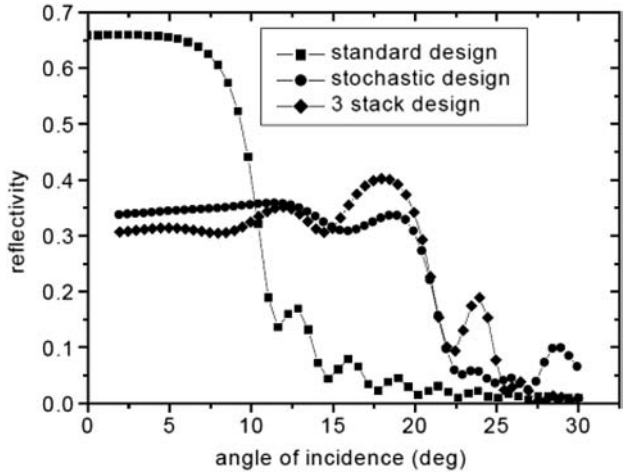

Figure 5.60 Measured EUV reflectivity of two different broadband mirrors in comparison to a standard multilayer mirror (reprinted from Ref. 148).

Downloaded From: https://www.spiedigitallibrary.org/ebooks/ on 09 Mar 2022
Terms of Use: https://www.spiedigitallibrary.org/terms-of-use

Although the deposited and measured broadband designs clearly show an increased acceptance as desired, they exhibit significant differences compared to the designed reflectance curves. The differences derive from deviations (caused by instabilities in the coating process) of the actually deposited thicknesses of the individual layers from the design values. In addition, the model used for optimization of the design is limited; e.g., the barrier layers and intermixing zones, which will be discussed later in this section, are not correctly accounted for.[147,149] Broadband coatings have also been developed for metrology applications, e.g., for EUV phase retarders and polarization analyzers.[150]

Real coatings have lower reflectance and spectral and angular acceptance values than the ideal multilayer shown in Fig. 5.59. Figure 5.61 shows a TEM cross-section of a Mo/Si multilayer. The interfaces between the Mo and Si layers are not ideally sharp but exhibit a transition zone in which the concentration of the two materials gradually changes. This is partly caused by intermixing due to kinetic energy of the deposited particles hitting the surface during the deposition process and partly by the chemical forces favoring the formation of molybdenum silicides. Another cause for low reflectance is the crystallinity of the Mo films, which leads to a certain HSFR of the interface, giving rise to large-angle scattering as discussed in Section 5.6.4.2. Moreover, interdiffusion and roughness effectively reduce the contrast of the refractive index, causing a further reduction in the peak reflectance and the FWHM of the Bragg peak. Therefore, in practice, the peak reflectance is limited to about 70%,[151–153] even if significant effort is made to minimize the index contrast loss.

One of the means to increase the index contrast at the interfaces between the high- and low-index materials is the introduction of thin barrier layers.[152] Such barrier layers consist of elements with low EUV absorption, such as

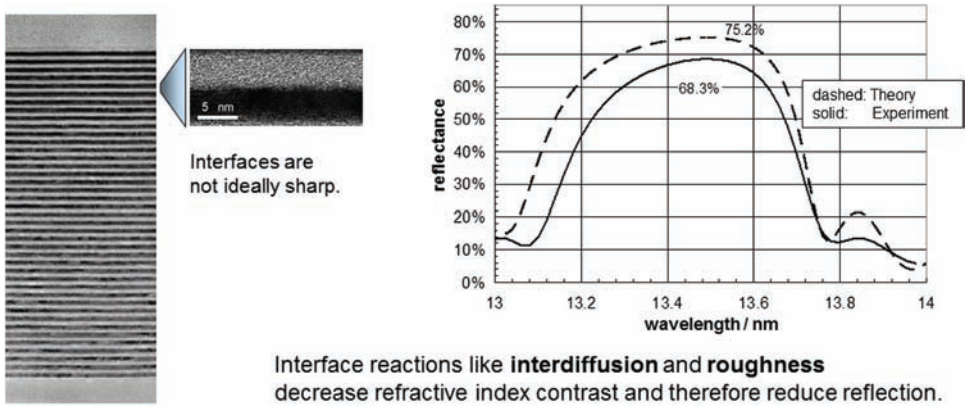

Figure 5.61 A TEM cross-section of a Mo/Si multilayer revealing interdiffusion and interface roughness. These cause a contrast loss at the interfaces, leading to a loss in both peak reflectance and spectral bandwidth of the coating.

Downloaded From: https://www.spiedigitallibrary.org/ebooks/ on 09 Mar 2022
Terms of Use: https://www.spiedigitallibrary.org/terms-of-use

boron, carbon, silicon, and compounds of these.[154–156] The gain in reflectance depends critically on the thickness of the barrier. If no barrier is present, the natural diffusion of Mo and Si leads to a mixture zone with a certain thickness, which results in a certain index contrast loss. In the case of a barrier that is thinner than the natural mixture zone, the index contrast is improved. If the barrier layer is made thicker, the index contrast is reduced again since the optical constants of, e.g., boron carbide (B_4C) or carbon (C) are similar to those of molybdenum silicides. Additionally, the absorption in the stack increases since the imaginary part of the refractive index is larger for these barrier materials when compared to Si and molybdenum silicides. In the case of 1-nm carbon barriers, the reflectance is ~7% smaller on both interfaces when compared to a pure Mo/Si stack without interdiffusion zones. This loss is caused by contrast loss and by enhanced absorption to about equal amounts. The loss due to reduced contrast is about the same for each of the two interfaces. The intensity of the standing wave has its maximum on the Si-on-Mo interface. Therefore, the loss due to absorption is much higher than on the Mo-on-Si interface (which is close to the minimum of the standing wave).

It turns out that there is a narrow regime of barrier layer thicknesses where the contrast is best. Effectively barrier layers can enhance the peak reflectance by 1 to 2%. An experimental example for this is given in Fig. 5.62. In addition, barrier layers can also enhance the thermal stability of EUV multilayers. At elevated temperatures of 100–275 °C, the diffusion of Mo and Si into the other material and the subsequent formation of a silicide is increased according to the Arrhenius law.[157] Apart from the contrast loss caused by the diffusion, the

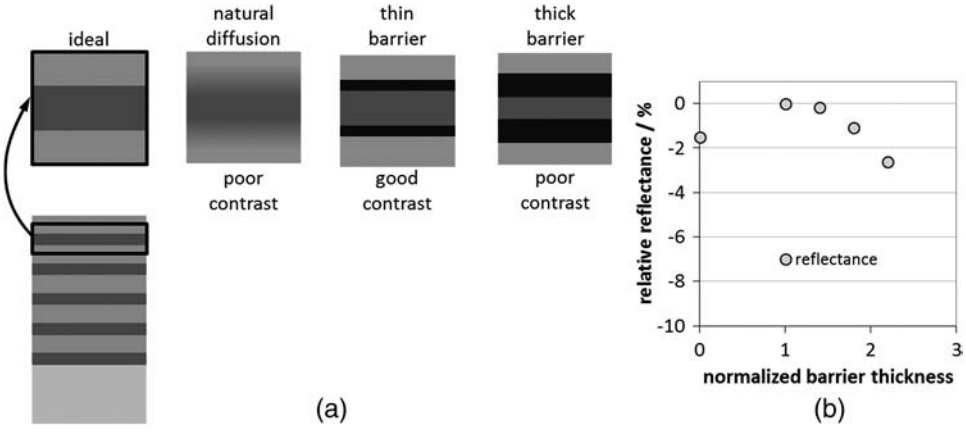

Figure 5.62 (a) Schematic of a multilayer with and without barrier layers. The contrast of refractive index is reduced by natural diffusion of the high- and low-index materials into each other. Thin barrier layers preventing diffusion can partially reduce this contrast loss, while thick barriers intrinsically reduce the contrast. (b) Experimental example of the peak reflectance depending on the barrier layer thickness. For each material system there is another optimum barrier layer thickness.

Downloaded From: https://www.spiedigitallibrary.org/ebooks/ on 09 Mar 2022
Terms of Use: https://www.spiedigitallibrary.org/terms-of-use

period also changes. The density of molybdenum silicide is larger than the average density of Mo and Si alone; therefore, at elevated temperatures, the period length of a multilayer reduces typically by several 100 pm within hours.

Barrier layers can suppress the diffusion more effectively than the naturally formed molybdenum silicide, thereby reducing the change in period length at elevated temperatures.[158–160] The thicker the barrier the less interdiffusion takes place and the smaller is the remaining period change, as shown in Fig. 5.63. Figure 5.63(b) compares the normalized period change during annealing at elevated temperatures (depending on the barrier layer thickness) to the relative reflectance before annealing for these coatings. The selection of material and thickness of the barrier is a compromise between thermal stability and peak reflectance. Generally, this choice must be made for each and every mirror in an optical system. The acceptable period change over lifetime is fixed and determines the barrier layers that are needed. In this way, stability of the coatings over the lifetime can be ensured.

Apart from diffusion, the roughness at the interfaces of the multilayer stack also leads to reduced reflectance. Making use of the TIS formula (see Section 5.6.4.2),

$$TIS_{normal\ incidence} = 1 - e^{-\left(\frac{2\pi\cdot 2}{\lambda}\cdot RMS\right)^2} \approx \left(\frac{2\pi\cdot 2}{\lambda}\right)^2 \cdot RMS^2, \qquad (5.54)$$

it can be estimated that a roughness of 0.5 nm leads to ~20% intensity loss due to scattering. There are two reasons for this roughness: Firstly, the substrate

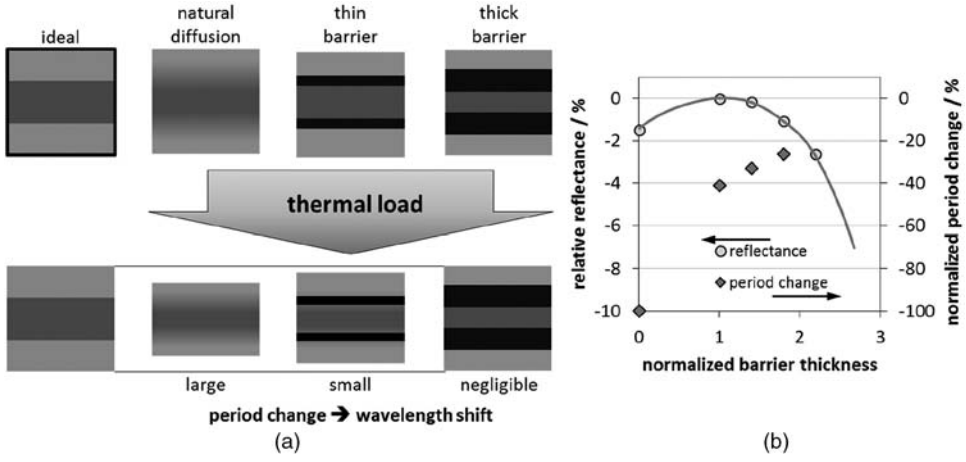

Figure 5.63 (a) Schematic of a multilayer under thermal load. High temperature enhances the diffusion. Diffusion leads to reduced period length, which results in a wavelength shift to smaller values. The thicker the barrier layers the smaller the diffusion. (b) Experimental example showing how the period change is reduced with larger barrier thickness and how the reflectance changes at the same time. The optimum choice of the barrier thickness depends on the application.

Downloaded From: https://www.spiedigitallibrary.org/ebooks/ on 09 Mar 2022
Terms of Use: https://www.spiedigitallibrary.org/terms-of-use

(on which the multilayer is coated) has some surface roughness, which is replicated by the multilayer coating. Secondly, the multilayer itself also has some intrinsic roughness.[144] To reduce the surface roughness of the substrate, either the polishing can be improved or the rough substrate can be coated with a smoothing layer.[161–166] To mitigate the roughness that usually builds up during the growth of an EUV multilayer, one can integrate into the coating process some means to enhance the mobility of atoms on the growing surface, supporting the effort to find a position that is energetically favorable (Fig. 5.64). This can be done by adding ion-beam polishing or heating of the substrate during the deposition process.[161,167,168] Standard methods to deposit multilayer coatings for EUV applications are magnetron sputtering,[169] ion-beam sputtering,[170] and electron-beam evaporation;[171] pulsed-laser deposition has also been reported.[172]

Even if operated under high-vacuum conditions, the residual gas contains sufficient amounts of water and hydrocarbons to degrade the reflectance of the multilayer coatings. These contaminants adsorb onto the mirror surfaces and are dissociated by the energetic EUV radiation, thereby, creating reactive ions and radicals created on the surface. The oxygen originating from the water causes oxidation of the outermost layer of the reflective multilayer coatings, while the remnants of the hydrocarbons cause the growth of carbon on the outermost layer.[173,174] The carbon layer can be removed by either oxygen or hydrogen radicals. Oxidation of the top layer has proved to be irreversible, causing a permanent reflectance loss. Initially, silicon was used as a top layer. In ambient conditions, silicon forms only a few nanometers of native oxide, in contrast to molybdenum, which exhibits a complete oxidation. At the cost of reflectance, mitigation schemes have been proposed

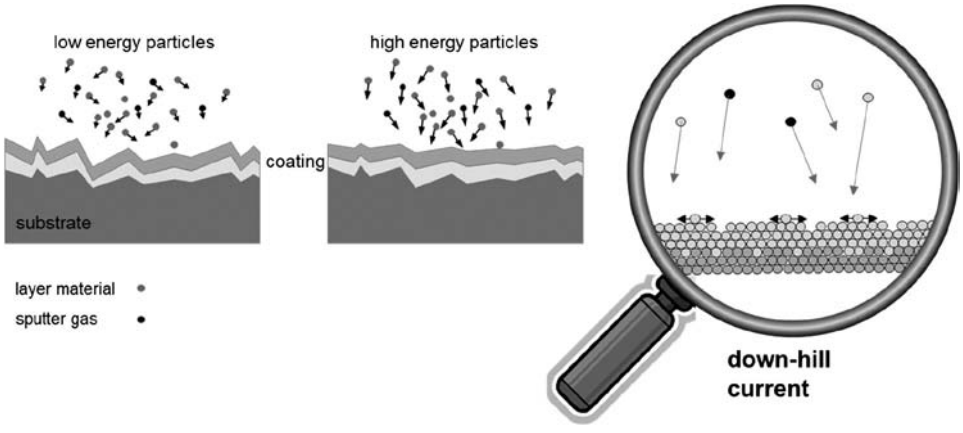

Figure 5.64 Roughening and smoothening of a growing layer. If the energy of particles on the surface is low, the lateral mobility is also low and the layer tends to roughen. With higher particle energies, mobility increases and particles are more likely to travel in a down-hill current into a valley, thereby creating a smoother surface.

Downloaded From: https://www.spiedigitallibrary.org/ebooks/ on 09 Mar 2022
Terms of Use: https://www.spiedigitallibrary.org/terms-of-use

to suppress the oxidation by letting a protective carbon layer grow from hydrocarbons such as ethanol. Capping layers that are not prone to oxidation (e.g., ruthenium) have been proposed and studied,[152] revealing good optical properties, high resistance to oxidation, and reducibility with hydrogen.[175–177] Many other cap materials have been suggested; Sasa Bajt and coworkers carried out a comprehensive survey[178] that favors ruthenium, rhodium, titanium dioxide and zirconium dioxide. Ruthenium oxide[179] and niobium oxide[180] have been investigated as well.

5.6.5.4 The coating changes the properties of the optical surface

Sections 5.6.3 and 5.6.4 explain that the surface of a mirror in an EUV lithography tool must meet stringent demands in all three spatial frequency domains, namely, figure, MSFR, and HSFR. The EUV reflective multilayer coating changes these properties (Fig. 5.65). Depending on the coating process, the HSFR is usually increased, but it also can be decreased if an appropriate smoothening process is applied. No such means exist for the MSFR. Here, the coating merely replicates the roughness of the substrate. The figure of the mirror is changed by the coating via both the layer stress and the lateral layer thickness gradient.

To illustrate the importance of the layer stress, once again the influence of the barrier layer thickness is considered. The presence of barrier layers makes a large difference in stress. But a variation in the barrier layer thickness can also easily change the layer stress by several tens of megapascals (Fig. 5.66). For a substrate with elastic modulus E, Poisson number $1/\nu$, and with a substrate thickness t_s coated with a layer of thickness t_f, the Stoney equation[181] relates the layer stress to the change in curvature. The change in curvature is the difference

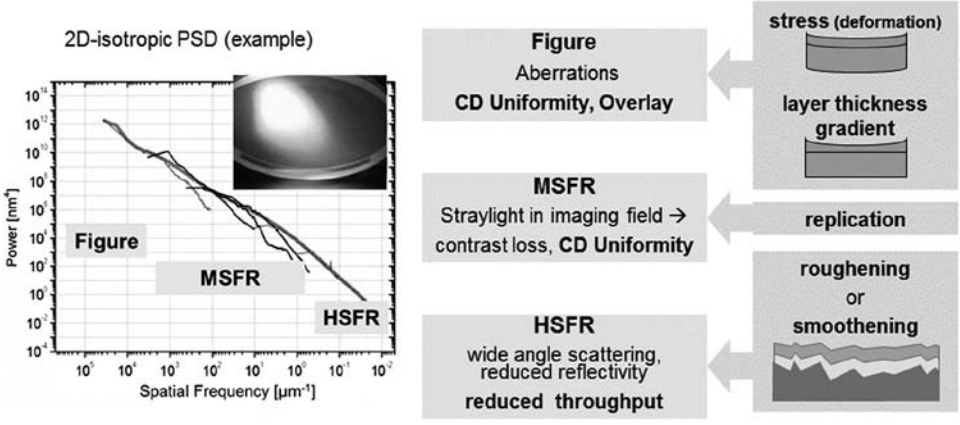

Figure 5.65 Influence of the coating on the PSD of the mirror. The PSD of the MSFR is largely replicated by the coating, while the HSFR is subject to roughening or smoothening, depending on the coating process parameters. Long-range figure errors are induced by the coating via the layer stress and the lateral layer thickness gradient.

Downloaded From: https://www.spiedigitallibrary.org/ebooks/ on 09 Mar 2022
Terms of Use: https://www.spiedigitallibrary.org/terms-of-use

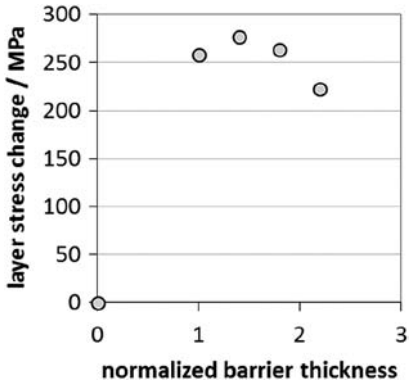

Figure 5.66 Layer stress depending on the barrier layer thickness. Stress changes strongly if barrier layers are introduced. The thickness of the barrier layers also plays a role.

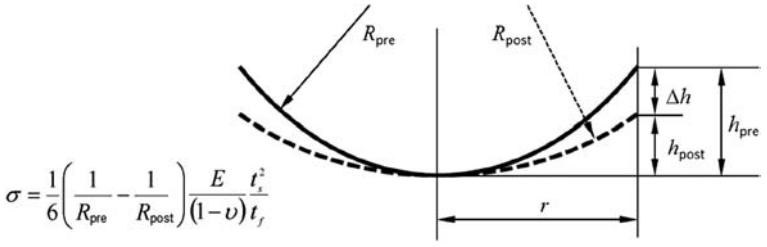

Figure 5.67 The Stoney equation with an illustration of how a change in the radius of curvature relates to the resulting figure change Δh.

between the inverses of the radii before R_{pre} and after R_{post} the deposition of the layer. The Stoney equation can be used to estimate the influence of the layer stress on the optical performance (Fig. 5.67).

Assuming a concave substrate (with a thickness of 100 mm and a radius of curvature of 700 mm made of silicon) and placing a film (with –100 MPa layer stress and of 0.5-μm thickness) onto the substrate, the radius of curvature increases by 0.06 μm. Moreover, assuming that the optical surface has a circular border with a radius of 250 mm, the substrate height at the border changes from h_{pre} to h_{post} by Δh of 16 nm. This is more than the wavelength of the EUV radiation. But as long as the deformation is strictly spherical, it can largely be compensated by means of alignment of the mirrors to each other. However, if the mirror substrate is not circular, additionally, the deformation of the optical surface due to the layer stress will be no longer rotationally symmetric, and compensation is very difficult. Assuming that only 1% of the figure change cannot be compensated for, the figure is degraded by 160 pm peak to valley (PV). Compared to the specs for the surface figure (100 pm rms) stated in Section 5.6.3.1, this is a significant contribution, and since the budget of 100 pm rms has to cover all contributions, 160 nm PV of the stress is indeed too much.

Downloaded From: https://www.spiedigitallibrary.org/ebooks/ on 09 Mar 2022
Terms of Use: https://www.spiedigitallibrary.org/terms-of-use

The Stoney equation hints at how to solve this problem. One option is to make the mirror substrate thicker, which is a very effective means since the substrate thickness contributes quadratically to the curvature. Other options make the substrate stiffer or the coating thinner, thereby reducing the bending force as well as the surface deformation. Finally, the stress of the coatings can be optimized by changing the composition of the optical stack, e.g., the Mo-to-Si ratio and the barrier layer thickness. Process parameters can be tuned, post-deposition treatments applied, or a stress-compensation layer added between the substrate and the optically effective multilayer.[182–185] By these means, the layer stress can be maintained in an acceptable range and the surface figure of the mirrors is preserved.

Another contribution of the coating to the figure error of the mirrors is the lateral thickness profile, as illustrated in Fig. 5.68. A mirror is assumed for which a multilayer of ∼50 periods with a constant period length of about 7 nm for the whole optical surface is required, and due to limitations of the coating process, the period length has a long range variation of ±0.1% over the mirror surface. This might imply that the minimum period length is 7 nm, while the maximum period length is 7.014 nm. Over the ∼50 periods, this difference of 14 pm in period length accumulates to a total change in figure of 600 pm, which again is large compared to the above-mentioned figure specification. Fortunately, part of this figure error (e.g., 50%) can also be compensated, which leaves a noncorrectable figure error of 300 pm PV. Recalling that the rms of a sinoidal oscillation equals about one-third of the PV, a noncorrectable figure error of 100 pm rms results. Since the budget of 100 pm rms has to cover all contributions, the acceptable variation of the period length is effectively smaller than ±0.1%. The same argument holds for a mirror that requires a specific lateral gradient of the period length. This is due to the small angular acceptance of the multilayer coating and the variation in the angle of incidence

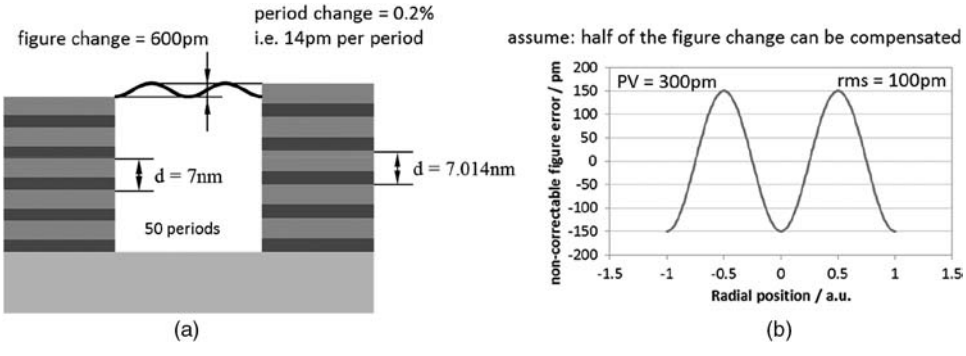

Figure 5.68 Relation between period change and figure change. (a) A difference in period length of 0.2% causes a PV in figure of 600 pm. (b) If 50% of a long-range figure change can be compensated in the tool, a figure error of 300 pm PV remains. This corresponds to a figure error of 100 pm rms.

Downloaded From: https://www.spiedigitallibrary.org/ebooks/ on 09 Mar 2022
Terms of Use: https://www.spiedigitallibrary.org/terms-of-use

over the optical surface. In this case, it is just the difference in the design gradient that must stay within the above-stated limits. For the four-mirror Engineering Test Stand system, examples for the normalized film thicknesses and for the noncompensatable thickness errors can be found in Ref. 186. In practice, thickness errors down to ±1 pm per bilayer on a substrate radius of more than 200 mm are indeed achievable today.

In conclusion, the properties of an EUV mirror are influenced to a large extent (surface figure) or even dominated (reflectance and large-angle stray light) by the multilayer coating. Apart from the peak reflectance, other properties of the coating, such as thermal stability and layer stress, also have a significant influence on the optical performance of a mirror. All properties of the coatings used in optical systems for EUV lithography are balanced to ensure optimal system performance.

5.7 Mask Inspection: The ZEISS AIMS EUV

5.7.1 Introduction

In optical lithography as used in current chip manufacturing, the mask pattern is imaged onto the wafer. This process is repeated many times for each wafer (on the order of 100 dies per wafer), and many wafers are exposed with each mask (at a rate of more than 100 wph). This means that the mask is extremely important for this process because it defines the chip structure and is replicated many times. However, if there were printing defects on the mask, these defects would be replicated on all wafers as well. Therefore, the production of masks free of printing defects is crucial. In 2009, the EUV mask infrastructure was analyzed by SEMATECH-driven working groups, and significant gaps in the mask metrology infrastructure were seen.[187] In particular, the need for an actinic aerial image measurement system was identified: "There is no viable HVM tooling scenario without an AIMS tool."[187] To close these gaps in the mask infrastructure, the EUV Mask Infrastructure (EMI) consortium was founded, and, in collaboration with ZEISS, the development and commercialization of the AIMS™ for EUV masks began. This tool is required for ensuring that masks are free of printing defects and therefore is seen as an enabling technology for HVM.

5.7.2 Principle and application

During the process of mask making, inspection tools usually find deviations of the real mask from its design or from other nominally identical structures on the mask. Furthermore, scanning electron microscopy (SEM) or other tools will likely be able to identify differences in repaired sites compared to sites without repair. How to decide which deviations need repair and how to verify the success of repairs? To answer these kind of questions it is important to understand the following two points: (1) What really matters is not the

Downloaded From: https://www.spiedigitallibrary.org/ebooks/ on 09 Mar 2022
Terms of Use: https://www.spiedigitallibrary.org/terms-of-use

physical deviation of the mask from its design structure but the effect on the printed wafer structure. (2) The mask imperfection is transferred to the wafer by imaging with the wafer fab scanner exposure system. The transfer of mask defects to the wafer is not just a demagnification factor but heavily depends on the imaging conditions, e.g., NA, illumination setting, imaging wavelength, and defocus. Since neither a mask inspection tool nor a mask review SEM has imaging conditions even close to the actual imaging conditions in the scanner, they cannot always reliably judge the printability of a discovered defect.

The AIMS approach to this is conceptually simple: It takes images of the structure to be investigated (e.g., imperfections found by patterned mask inspection or blank inspection) under the same imaging conditions as will be present in the scanner exposure system. This is called scanner emulation and explains the close link of the optical properties of the scanner exposure tool to those of the AIMS tool. Figure 5.69 illustrates this approach. The AIMS generates a magnified version of the aerial image of the scanner system by using the same mask-side imaging conditions. Due to its magnification, the AIMS has a lower wafer-side NA compared to the scanner system. Neglecting the vector nature of the electrical field, i.e., treating the electrical field as a scalar, the image is not changed apart from magnification. The differences resulting from the electrical field vector orientation at the wafer side are small for the NAs of current EUV systems. The high-NA DUV ZEISS AIMS tool is equipped with scanner mode emulation, allowing one to measure these vector

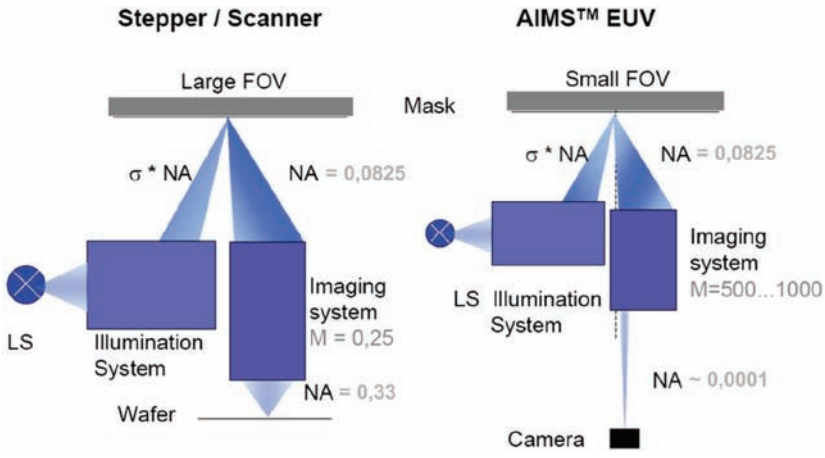

Figure 5.69 Schematic comparison of the stepper/scanner optical train and the AIMS. The AIMS uses the same imaging conditions on the reticle side as the stepper/scanner. In particular, it uses the same wavelength, the same mask-side NA, and the same illumination setting σ. The AIMS uses a camera system to detect the aerial image instead of exposing a photoresist. Therefore, it generates a magnified image of a small field of view (FOV) of the mask structure instead of a demagnified image of the full scanner slit. Magnification *M* and NA values given in the figure correspond to the ASML NXE:3300B system and its emulation by the ZEISS AIMS EUV (reprinted from Ref. 189).

Downloaded From: https://www.spiedigitallibrary.org/ebooks/ on 09 Mar 2022
Terms of Use: https://www.spiedigitallibrary.org/terms-of-use

effects. This tool does not need to simulate the effect of potential defects with all of the uncertainties about the real mask stack properties and thus does not need to know the mask stack parameters. It measures the effect of the potential defect on the scanner aerial image. With this approach, the ZEISS AIMS has become the established industry standard and the tool of reference for the review of potential defects.

Figure 5.70 shows how the AIMS is typically used in the mask-manufacturing process. This generic flow is similar for UV and EUV masks. However, there are significant differences between UV and EUV masks. Whereas UV masks are used in transmission, EUV masks are used in reflectance; therefore, their substrate is coated with a reflective multilayer beneath an absorber. The absorber defines the mask pattern. This more complex structure of EUV masks leads to additional classes of defects, as explained in Fig. 5.71. Defects on the substrate and within the multilayer generate bumps and pits that penetrate the multilayer. These defects change the phase of the reflected light, in contrast to absorber defects, which predominantly change the amplitude of the reflected light. The impact of these phase defects is highly dependent on the wavelength. Thus, it is particularly important for the review of EUV masks to use the EUV wavelength, i.e., an AIMS EUV needs to be actinic. Furthermore, the ability to measure the impact of defects on the process window and, in particular, on the through focus behavior, is required. It has been shown that for topological or phase defects, despite the small CD variation in the nominal focus plane, a defect may be significant when the reticle or wafer is slightly defocused.[188] From an application point of view, the ZEISS AIMS EUV is the natural extension of the established AIMS tools into the EUV.

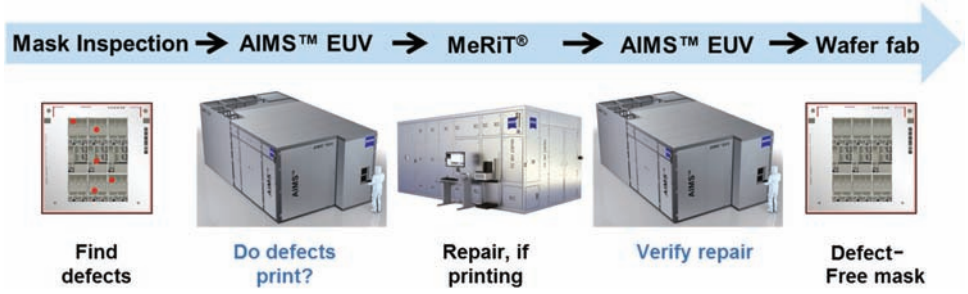

Figure 5.70 Typical use of the AIMS in the mask-manufacturing process. The AIMS receives the coordinates of potential defect sites from inspection tools. Based on a review of these sites with the AIMS, the impact on wafer printing is determined and the printing defects are repaired with a repair tool, such as, e.g., the ZEISS MeRiT. The success of the repairs can be verified using the AIMS such that the customer receives a mask free of printing defects. This figure shows only those process steps relevant to understanding the use of the AIMS; a complete mask-manufacturing process flow includes many more steps (reprinted from Ref. 190).

Downloaded From: https://www.spiedigitallibrary.org/ebooks/ on 09 Mar 2022
Terms of Use: https://www.spiedigitallibrary.org/terms-of-use

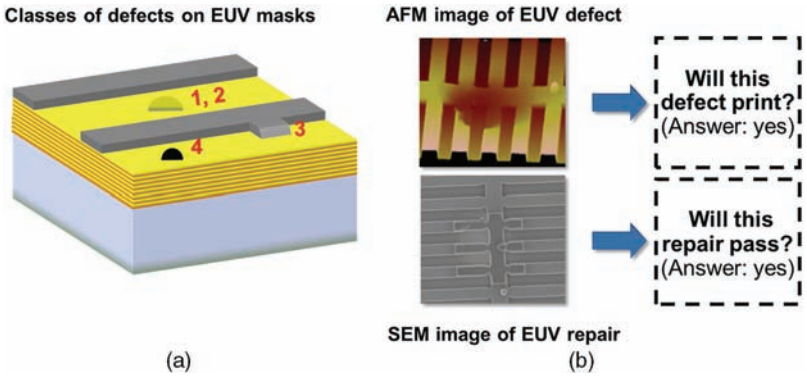

Figure 5.71 Defects on EUV masks. (a) In addition to the pattern transfer defects (3) and particles/residues (4) already known from UV masks, there are additional kinds of defects on EUV masks: substrate defects (1) and multilayer defects (2). These defects generate pits and bumps that penetrate the multilayer and therefore change the amplitude and phase of the reflected EUV light. (For more information on EUV mask defectivity see Refs. 193 and 194). (b) AFM image of a defect penetrating the multilayer and SEM image of a repaired pattern defect on an EUV mask. The answers to the mask production questions can be provided by the ZEISS AIMS EUV in the mask shop, i.e., long before wafer printing [part (a) reprinted from Ref. 191, and part (b) from Ref. 192].

5.7.3 System concept

Possible implementations of an aerial image microscope were investigated many years ago by a SEMATECH study[195] and have been analyzed in a ZEISS feasibility study prior to the main development program of the AIMS EUV tool.[196] To allow for an electronic recording of the mask aerial image, a high magnification on the order of 1000× is required. Four different concepts to realize this were investigated. Two of the concepts use a preliminary magnification step by an EUV optics followed by a secondary magnification. In the first concept, the EUV light is imaged on a scintillator plate, converting EUV photons to visible light, which is imaged by a visible light microscope on an electronic detector. This concept was realized by Exitech Ltd for a $NA = 0.25$ system.[197] In the second concept, a photocathode is used to convert EUV photons into photoelectrons, and an electron microscope is employed to image these electrons. The other two investigated concepts realize all of the magnification with EUV light. One of the all-EUV concepts uses a zone plate approach, and the other uses reflective EUV mirrors. The benefit of the concepts using secondary magnification is that a relatively easy Schwarzschild EUV optics with a magnification on the order of 10 can be employed and combined with commercially available microscope technology. However, an important drawback is that these concepts are less photon efficient because of the conversion step and require an order of magnitude higher source brightness to reach the same level of photon noise for a given exposure time compared to the all-EUV concepts. The zone plate approach is conceptually

Downloaded From: https://www.spiedigitallibrary.org/ebooks/ on 09 Mar 2022
Terms of Use: https://www.spiedigitallibrary.org/terms-of-use

elegant because it can image the mask onto a detector such as a CCD by only one optical element. However, because of chromatic aberrations intrinsic to this concept, the zone plate approach requires a narrow-bandwidth source, such as a synchrotron. Such a concept has been realized by, e.g., the SHARP research tool at the ALS synchrotron.[198] The reflective-mirror-based approach uses imaging conditions that are the closest to the scanner imaging conditions. This all-EUV approach requires challenging optics manufacturing capabilities. The progress driven by EUV scanner optics development and production enabled ZEISS to reach the required optics quality and to select this concept for the AIMS EUV tool. This approach enables a standalone tool that uses existing metrology-scale EUV plasma source technology with the best photon efficiency and close emulation of the scanner imaging conditions.

Whereas, for the productivity of EUV scanner tools, the source power is a key factor, for small-field metrology tools such as the AIMS EUV, the source brightness (i.e., the emitted power per area and solid angle) is more relevant. The AIMS EUV has a much smaller field size. Accordingly, its étendue is orders of magnitude smaller than that of an EUV scanner. Typical EUV plasma sources radiating in the full solid angle of 4π with plasma sizes of several tens to hundreds of a micrometer would massively "overfill" the étendue of the AIMS EUV system. This means that only the central region of the source plasma and a small solid angle can be used; i.e., only the power in this area and the solid angle contributes to the measurement.

Even though ZEISS' unique experience with the EUV scanner optics was crucial for the success of the AIMS EUV, the latter system is a complete EUV tool platform that by far exceeds the scope of an optical system alone. The technological differences between an AIMS EUV and the established AIMS tools for DUV lithography are enormous: A wavelength of $\lambda_{EUV} = 13.5$ nm is used instead of $\lambda_{DUV} = 193$ nm, an EUV plasma source is used instead of a laser source, reflective mirror optics are used instead of refractive lens optics, and ultraclean vacuum conditions are required instead of atmospheric pressure environments. As a result, a completely new platform needed to be developed for the AIMS EUV. Figure 5.72 shows a computer-aided design (CAD) view and a photograph of the tool.

5.7.4 Tool capabilities

The ZEISS AIMS EUV provides full scanner emulation; i.e., it uses the same mask illumination conditions and the same imaging conditions as the EUV scanners. To account for the various NAs of these tools and the various illumination conditions, the AIMS EUV is equipped with a mechanism to change the NA and the illumination setting. As illustrated in Fig. 5.73(a), the chief ray angle of the EUV scanner tool is rotated depending on the position within the scanner slit. As a consequence, the printed CD of structures that are identical on the mask will vary with their positions in the scanner slit due to

Downloaded From: https://www.spiedigitallibrary.org/ebooks/ on 09 Mar 2022
Terms of Use: https://www.spiedigitallibrary.org/terms-of-use

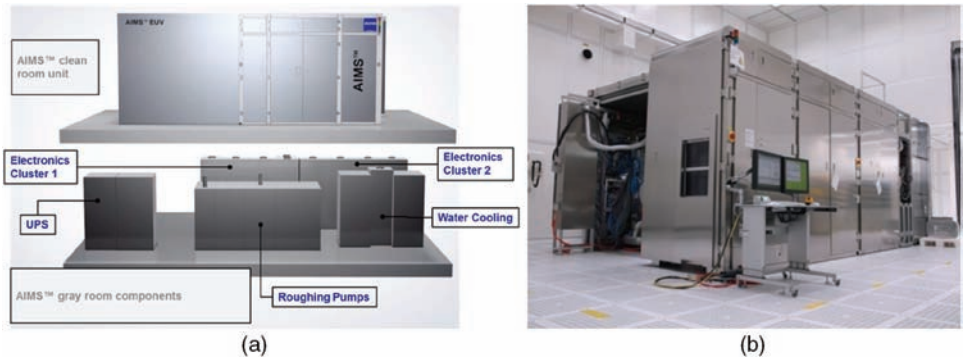

Figure 5.72 (a) CAD view of the ZEISS AIMS EUV tool. The tool consists of a cleanroom unit and a cluster of supply components to be installed in the subfab/gray room. With a length of about 7 m for the cleanroom unit, the AIMS EUV is one of the larger mask shop tools. (b) Photograph of an AIMS EUV tool (clean room unit) in the final integration phase (reprinted from Ref. 199).

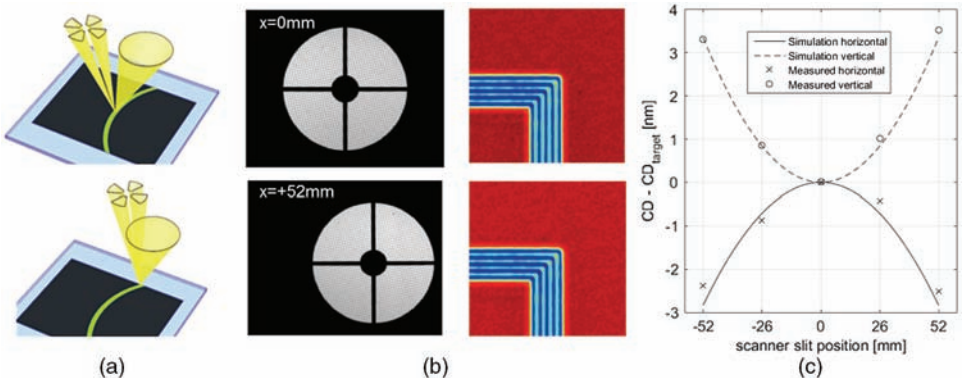

Figure 5.73 Emulation of the EUV scanner ring field. (a) Scanner ring field. The chief ray angle of the scanner is rotated depending on the position within the scanner slit. (b) Pupil images and corresponding field images taken with the AIMS EUV. The emulation of the chief ray angle can be seen as a shift of the pupil for the various positions within the scanner slit. This figure shows the center ($x = 0$ mm) and edge ($x = 52$ mm) of the scanner slit. In this example a 5-bar dense elbow structure of CD = 64 nm was imaged with a quasi-conventional illumination $\sigma = 0.2$–0.9 at a NA of 0.33/4 with the chief ray angles of the ASML NXE:3300B scanner tool. (CD and NA values as well as x coordinates are given for mask level). (c) Measured CD variation over the scanner slit compared to simulation (reprinted or adapted from Ref. 199).

the variation in the 3D shadowing effect. This effect of the scanner ring field is automatically emulated by the AIMS EUV; i.e., the chief ray is automatically adjusted such that it is at the same angle as is used in the scanner tool for this mask position. Figure 5.73(b) shows exemplary pupil images and corresponding field images taken with the AIMS EUV. Even though hardly

Downloaded From: https://www.spiedigitallibrary.org/ebooks/ on 09 Mar 2022
Terms of Use: https://www.spiedigitallibrary.org/terms-of-use

any difference is visible in the field images, a quantitative CD analysis [Fig. 5.73(c)] reveals a significant dependence of the CD on the scanner slit position. In this example, the H-V difference changes by more than 5 nm (in mask coordinates) over the scanner slit. This shows that the impact of the chief ray angle rotation is indeed significant and therefore is a necessary feature for scanner emulation. Moreover, these results show the capability of the AIMS EUV to study and quantify 3D EUV mask effects.

The AIMS EUV is able to automatically load, align and unload masks from reticle standard-mechanical-interface (SMIF) pods and EUV dual pods. Also the measurement sequences are automated which involve positioning the sites to be reviewed in the center of the AIMS field of view, focusing of the mask, acquiring focus stacks, setting of the chief ray angle and system calibrations. The evaluation software allows for quantitative analysis of e.g., CD, Bossung plots, and process window.

5.7.5 Tool performance

Performance data obtained from the AIMS EUV tool have been shown in detail in the context of technical conferences, and further updates will be given in future. In particular, high image quality and the ability to resolve target node features have been shown.[190,200] A key application of the AIMS EUV is the review of defects. Verduijn et al. used customer access slots on the prototype tool to analyze several classes of native defects, and compare AIMS EUV results with those of wafer prints obtained from an EUV scanner system.[201] The authors concluded that the AIMS EUV is able to detect all defects. In a recent measurement campaign done in the framework of a SEMATECH milestone, the tool performance status with respect to its key specifications was tested using final acceptance test procedures. It has been shown that the AIMS EUV fulfills its core specifications.[199] In this section some examples of performance measurements are provided. More details can be found in the publications cited in this section.

The AIMS EUV optics performance is qualified with an *in situ* metrology. An excellent flare level of below 1% has been demonstrated,[200] along with aberration performance at the scanner optics quality level, and illumination pupil performance reaching pole-balance and ellipticity specification.[199] Figure 5.74 shows images acquired with the AIMS EUV. Due to its excellent optical quality and photon-efficient design, the AIMS EUV delivers images with low noise and high contrast. The AIMS EUV is equipped with a high-performance stage, and a positioning performance below 100 nm has been shown.[199] Accordingly, the system can position each review site directly in the center region of the AIMS image. Furthermore, promising performance in terms of particle adders was demonstrated, and a productivity quantified in terms of run rate was measured with 45 sites/hour with 7 focus levels per site.[199]

Downloaded From: https://www.spiedigitallibrary.org/ebooks/ on 09 Mar 2022
Terms of Use: https://www.spiedigitallibrary.org/terms-of-use

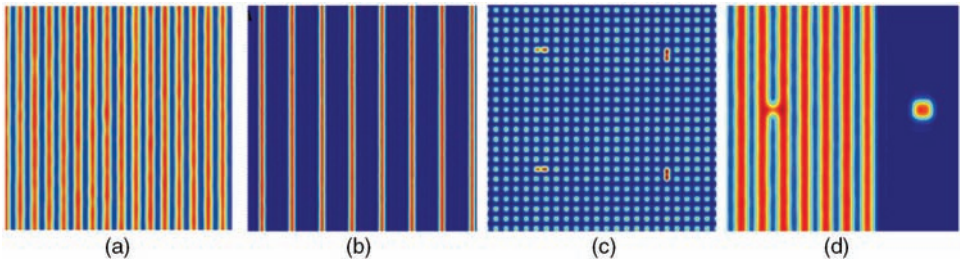

Figure 5.74 Exemplary images acquired with the AIMS EUV. All AIMS EUV images have a FOV of 8 μm × 8 μm; for better readability, this figure shows more detail. (a) 64-nm dense lines and spaces, dipole *x*, σ = 0.2–0.9, 2-μm detail shown. (b) CD = 88-nm lines and spaces with a pitch of 528 nm, quasi-conventional σ = 0.2–0.9, 4-μm detail shown. (c) 88-nm dense contacts with programmed defects, quasi-conventional σ = 0.2–0.9, 4-μm detail shown. (d) 96-nm dense lines and spaces with programmed defect, dipole *x*, σ = 0.2–0.9, 2-μm detail shown. All nanometer values are given on mask level, a NA of 0.33/4 (mask level) was used.

A key specification for the measurement performance is the CD reproducibility, which will be discussed in some detail. A defect is typically characterized by its CD change, i.e., by the structure size error it introduces. The tolerance with respect to such CD changes depends on the layer and the process. As rule of a thumb, CD changes of 10% or greater are regarded as defects. In repeated measurements of the same structure, ideally, the same structure size is always measured. The reproducibility of the measurement result is crucial for the quality of the AIMS EUV measurement and is characterized by the CD reproducibility. The test procedure is such that focus stacks with 3 levels (best focus, ±990-nm defocus at reticle level, corresponding to about ±60-nm defocus at wafer level) are acquired at three positions on the mask (left, center, and right). The underlying idea of the procedure is that the CD reproducibility is tested through a typical focus range of a Rayleigh unit of defocus of $0.5 * \lambda/(NA)^2 = 992$ nm and for the extreme positions of the exposure tool scanner slit of ±52 mm, i.e., for the extreme chief-ray angle rotations. The AIMS EUV was used in the ASML NXE:3300B emulation mode; i.e., NA = 0.33/4 (reticle-level coordinates), and the chief ray angle rotation of that exposure tool was used. In the described sequence, the measurement position on the mask is changed from left to center to right. The 3-step position change is repeated 10 times, resulting in 10 repeated measurements at each position with stage- and chief-ray angle movements between each measurement. This test was performed with a vertical dense line structure of $CD = 64$ nm with a dipole *x*, σ = 0.2–0.9 illumination and a dense contact pattern with $CD = 80$ nm and quasar σ = 0.2–0.9 illumination. All CD values refer to mask level; i.e., the structure size on the wafer will be smaller by a factor of four. For each feature and each reticle position, the first measurement was used to determine the threshold that yields the target CD.

Downloaded From: https://www.spiedigitallibrary.org/ebooks/ on 09 Mar 2022
Terms of Use: https://www.spiedigitallibrary.org/terms-of-use

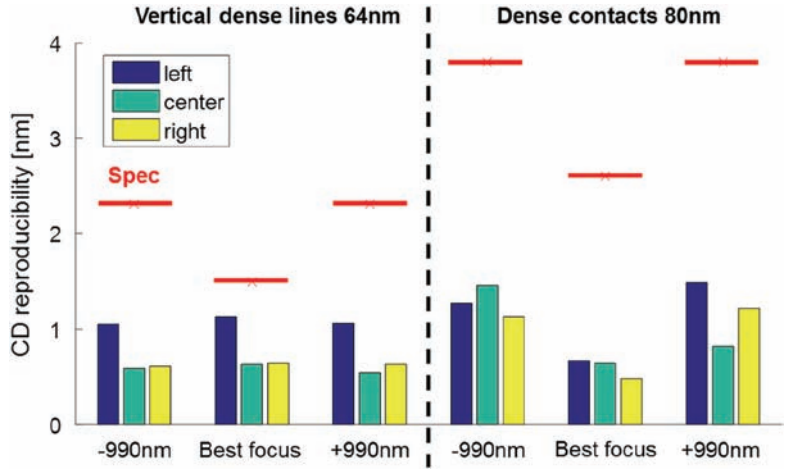

Figure 5.75 Measured CD reproducibility compared to specification. All values are 3× the standard deviation at mask level (reprinted from Ref. 199).

The same threshold was used for the subsequent measurements in the CD evaluation. The CD reproducibility is specified as 3× the standard deviation of the 10 repetitions. Figure 5.75 shows the result of this CD reproducibility test and compares it to the specification. CD reproducibility values on the order of 1 nm on mask level are reached with all values fulfilling this key specification of the AIMS EUV. Thus, the printability of defects can be predicted with a high confidence level.

5.7.6 Summary

The AIMS EUV is required for the volume manufacturing of EUV masks free of printing defects and is at the time of writing in its final integration phase. It images potential defect sites under the same imaging conditions as in the scanner exposure tool, thereby allowing one to determine whether a potential defect is printing. The AIMS EUV reaches its main acceptance testing procedure (ATP) specifications in terms of imaging, optics, positioning accuracy, CD reproducibility, productivity of the most relevant settings, and particles, and thus closes a gap in the infrastructure for HVM.

Acknowledgments

The authors gratefully thank the Federal Ministry of Education and Research of Germany and the DG Connect of the European Commission for continuous financial support over many years. The authors also thank Tilmann Heil, Martin Lowisch, Ulrich Wegmann, Martin Endres, Johannes Ruoff, Stefan Schulte, and Vladimir Kamenov for helpful discussions, expertise, and review of the manuscript.

Downloaded From: https://www.spiedigitallibrary.org/ebooks/ on 09 Mar 2022
Terms of Use: https://www.spiedigitallibrary.org/terms-of-use

References

1. G. E. Moore, "Cramming more components on electronic circuits," *Electronics* **38**(8), 114 (1965).
2. E. Abbe, "Beiträge zur Theorie des Mikroskops und der mikroskopischen Wahrnehmung," *Archiv für mikroskopische Anatomie* **9**(1), 413–468 (1873).
3. B. J. Lin, "Where is the lost resolution?" *Proc. SPIE* **0633**, 44–50 (1986) [doi: 10.1117/12.963701].
4. C. Wagner and N. Harned, "EUV lithography: Lithography gets extreme," *Nat. Photonics* **4**, 24–26 (2010).
5. K. Murakami, T. Oshino, H. Kondo, H. Chiba, K. Nomura, H. Kawai, Y. Kohama, K. Morita, K. Hada, Y. Ohkubo, and T. Miura, "Development of EUV lithography tools at Nikon," *Proc. SPIE* **7140**, 71401C (2008) [doi: 10.1117/12.804706].
6. K. Murakami, T. Oshino, H. Kondo, H. Chiba, K. Nomura, H. Kawai, Y. Kohama, K. Morita, K. Hada, and Y. Ohkubo, "Development of EUV lithography tools at Nikon," *Proc. SPIE* **7969**, 79690P (2011) [doi: 10.1117/12.879305].
7. K. Murakami, T. Oshino, H. Kondo, H. Chiba, K. Nomura, Y. Kawabe, T. Ono, N. Kandaka, A. Yamazaki, T. Yamaguchi, R. Shibata, and M. Shiraishi, "Development of EUV lithography tool technologies at Nikon," *Proc. SPIE* **8322**, 832215 (2012) [doi: 10.1117/12.917676].
8. S. Uzawa, H. Kubo, Y. Miwa, T. Tsuji, H. Morishima, K. Kajiyama, and T. Hasegawa, "Canon's development status of EUV technologies," *Proc. SPIE* **6921**, 69210N (2008) [doi: 10.1117/12.769894].
9. T. Hasegawa, S. Uzawa, T. Honda, Y. Higaki, A. Miyake, and H. Morishima, "Development status of Canon's full-field EUVL tool," *Proc. SPIE* **7271**, 72711Y (2009) [doi: 10.1117/12.813465].
10. A. Yen, "EUV lithography: from the very beginning to the eve of manufacturing," *Proc. SPIE* **9776**, 977632 (2016) [doi: 10.1117/12.2236044].
11. H. Kinoshita, *Extreme Ultraviolet Lithography: Principles and Basic Technologies*, Lambert Academic Publishing, Saarbrücken, Germany (2016).
12. P. Naulleau, K. A. Goldberg, E. H. Anderson, K. Bradley, R. Delano, P. Denham, B. Gunion, B. Harteneck, B. Hoef, H. Huang, K. Jackson, G. Jones, D. Kemp, J. A. Liddle, R. Oort, A. Rawlins, S. Rekawa, F. Salmassi, R. Tackaberry, C. Chung, L. Hale, D. Phillion, G. Sommargren, and J. Taylor, "Status of EUV micro-exposure capabilities at the ALS using the 0.3-NA MET optic," *Proc. SPIE* **5374**, 881 (2004) [doi: 10.1117/12.556538].
13. B. Turkot, "EUV progress toward HVM readiness," *Proc. SPIE* **9776**, 976602 (2016) [doi: 10.1117/12.2225014].

Downloaded From: https://www.spiedigitallibrary.org/ebooks/ on 09 Mar 2022
Terms of Use: https://www.spiedigitallibrary.org/terms-of-use

14. S.-S. Kim, "EUV lithography: progress and perspective," Keynote Presentation at SPIE's Extreme Ultraviolet Lithography VII conference, 22 Feb. 2016, San Jose, California.
15. A. Yen, "EUV for sub-10nm logic," Keynote Presentation at SPIE's Extreme Ultraviolet Lithography VII conference, 22 Feb. 2016, San Jose, California.
16. http://www.eurekanetwork.org/project/id/1182
17. J. P. H. Benschop, U. Dinger, and D. C. Ockwell, "EUCLIDES, first phase completed!" *Proc. SPIE* **3997** (2000) [doi: 10.1117/12.390073].
18. J. P. H. Benschop, W. M. Kaiser, and D. C. Ockwell, "EUCLIDES, the European EUVL program," *Proc. SPIE* **3676** (1999) [doi: 10.1117/12 .351165].
19. D. A. Tichenor, G. D. Kubiak, S. J. Haney, R. P. Nissen, K. W. Berger, R. W. Arling, A. K. Ray-Chaudhuri, K. B. Nguyen, R. H. Stulen, J. B. Wronsky, J. D. Jordan, T. G. Smith, J. R. Darnold, P. M. Kahle, A. A. Jojola, S. M. Kohler, R. S. Urenda, D. R. Wheeler, J. E. Gjorkholm, O. R. Wood, G. N. Taylor, and R. S. Hutton, "Recent results on the development of an integrated EUVL lithography tool," *Proc. SPIE* **2437**, 292 (1995) [doi: 10.1117/12.209167].
20. Dec. 1998 Next-Generation Lithography (NGL) Task Force (1998).
21. International SEMATECH, Final Report, September 21, 2001, 5th Next Generation Lithography (NGL) Workshop, 29–30 August 2001, Pasadena, California.
22. R. Soufli, R. M. Hudyma, E. Spiller, E. M. Gullikson, M. A. Schmidt, J. C. Robinson, S. L. Baker, C. C. Walton, and J. S. Taylor, "Sub-diffraction-limited multilayer coatings for the 0.3 numerical aperture micro-exposure tool for extreme ultraviolet lithography," *Appl. Opt.* **46** (18), 3736–3746 (2007).
23. T. Asami, "EUV exposure system development plan in Nikon," EUVL Symposium 2004, 1–4 November, Miyazaki, Japan.
24. D. Ashworth, J. Georger, Jr., K. Petrillo, K. Y. Cho, W. Montgomery, S. Wright, and E. Sohmen, "Sub-22nm EUV imaging on SEMATECH Albany Micro Exposure Tool," SEMATECH report, November 2, 2010.
25. H. Glatzel, D. Ashworth, M. Bremer, R. Chin, K. Cummings, L. Girard, M. Goldstein, E. Gullikson, R. Hudyma, J. Kennon, B. Kestner, L. Marchetti, P. Naulleau, R. Soufli, and E. Spiller, "Projection optics for extreme ultraviolet lithography (EUVL) micro-field exposure Tools (METs) with a numerical aperture of 0.5," *Proc. SPIE* **8679**, 867917 (2013) [doi: 10.1117/12.2012698].
26. K. Cummings, D. Ashworth, M. Bremer, R. Chin, Y.-J. Fan, L. Girard, H. Gatzel, M. Goldstein, E. Gullikson, J. Kennon, B. Kestner, L. Marchetti, R. Miyakawa, P. Naulleau, R. Soufli, X. Zhou, Y. Kandel, D. Bajuk, and S. Wurm, "The first 0.5 NA projection optic for extreme

Downloaded From: https://www.spiedigitallibrary.org/ebooks/ on 09 Mar 2022
Terms of Use: https://www.spiedigitallibrary.org/terms-of-use

ultraviolet lithography (EUVL) microfield exposure tool ('MET5')," EUVL Symposium 2013, 610 Oct., Toyama, Japan.
27. R. Soufli, J. C. Robinson, M. Fernández-Perea, E. Spiller, N. F. Brejnholt, M.-A. Descalle, M. J. Pivovaroff, and E. M. Gullikson, "Recent advances in reflective optics for EUV/x-ray laser sources," *X-Ray Lasers 2014: Proc. 14th International Conference on X Ray Lasers* **169**, J. Rocca, C. Menoni, and M. Marconi, Eds. Springer, p. 331 (2015).
28. S. Tanaka, S. Magoshi, H. Kawai, S. Inoue, W. Rosenthal, L. Girard, L. Marchetti, B. Kestner, and J. Kincade, "Current development status of HSFET (high NA small field exposure tool) in EIDEC," *Proc. SPIE* **9776**, 97761N (2016) [doi: 10.1117/12.2219368].
29. G. F. Lorusso, J. Hermans, A. M. Goethals, B. Baudemprez, F. Van Roey, A. M. Myers, I. Kim, B. S. Kim, R. M. Jonckheere, A. Niroomand, S. Lok, A. Van Dijk, J.-F. de Marneffe, S. Demuynck, D. Goossens, and K. Ronse, "Imaging performance of the EUV alpha demo tool at IMEC," *Proc. SPIE* **6921**, 69210O (2008) [doi: 10.1117/12.771983].
30. A.-M. Goethals, E. Hendrickx, R. Jonckheere, G. F. Lorusso, B. Baudemprez, J. Hermans, D. Laidler, A. Niroomand, F. Van Roey, A. Van Dijk, L. Romijn, N. Stepanenko, V. Timoshkov, F. Iwamoto, A. Myers, Y. Hyun, C. Lim, I. Pollentier, M. Leeson, J.-F. de Marneffe, S. Demuynck, and K. Ronse, "Implementing full field EUV lithography using the ADT," EUVL Symposium 2008, 28 Sept. to 1 Oct., Lake Tahoe, California.
31. H. Meiling, S. Lok, B. Hultermans, E. van Setten, B. Pierson, K. Cummings, C. Wagner, and N. Harned, "EUV alpha demo tool – stepping stones towards volume production," EUVL Symposium 2008, 28 Sept. to 1 Oct., Lake Tahoe, California.
32. H. Meiling, N. Buzing, K. Cummings, N. Harned, B. Hultermans, R. De Jonge, B. Kessels, P. Kürz, S. Lok, M. Lowisch, J. Mallman, B. Pierson, C. Wagner, A Van Dijk, E. Van Setten, J. Zimmerman, P. Cheang, and A. Chen, "EUVL: towards implementation in production," *Proc. SPIE* **7520**, 752008 (2009) [doi: 10.1117/12.845781].
33. G. F. Lorusso, E. Hendrickx, G. L. Fenger, and A. Niroomand, "Full chip correction of EUV design," *Proc. SPIE* **7636**, 763615 (2010) [doi: 10.1117/12.846966].
34. I. Kim, H. Kang, C. Park, J.-O. Park, J. Lee, J. Park, D. Goo, J. Yeo, S.-W. Choi, and W. Han, "Methodology of flare modeling and compensation in EUVL," *Proc. SPIE* **7140**, 714009 (2008) [doi: 10.1117/12.804673].
35. V. Philipsen and P. de Bisschop, "EUV mask shadowing effects and correction strategies," IMEC Partner Technical Week Review, April (2010).

Downloaded From: https://www.spiedigitallibrary.org/ebooks/ on 09 Mar 2022
Terms of Use: https://www.spiedigitallibrary.org/terms-of-use

36. H.-S. Seo, D.-G. Lee, B.-S. Ahn, C.-W. Koh, I.-Y. Kang, T. G. Kim, H. Kim, D. Kim, S.-S. Kim, and H.-K. Cho, "Absorber stack optimization in EUVL masks: lithographic performances in alpha demo tool and other issues," *Proc. SPIE* **7636**, 76360X (2010) [doi: 10.1117/12.847955].
37. G. F. Lorusso, E. Hendrickx, and A. Niroomand "Design correction in EUV," IMEC Partner Technical Week Review, April (2010).
38. C. A. Mack, *Field Guide to Optical Lithography*, SPIE Press, Bellingham, Washington (2006) [doi: 10.1117/3.665802].
39. S. Yoshitake, S. Tamamushi, T. Takigawa, S. Mitsui, M. Ogasawara, M. Ferber, K.-D. Röth, D. Adam, J. Butschke, and M. Irmscher, "Investigations on pattern placement accuracy of EUV mask," EUVL Symposium 2005, 7–9 Oct., San Diego, California.
40. S. Yoshitake, S. Yoshitake, S. Tamamushi, and M. Ogawawara, "Desired IP control methodology for EUV mask in current mask process," *24th European Mask and Lithography Conference* (EMCL) 21–24 Jan. 2008, Dresden, Germany (2008).
41. K. Orvek, J. Sohn, J. Choi, R. Engelstad, S. Raqunathan, J. Zimmerman, T. Laursen, Y. Shusuke, and T. Shoki, "Evaluation of an e-beam correction strategy for compensation of EUVL mask non-flatness," *Proc. SPIE* **7379**, 73790Q (2009) [doi: 10.1117/12.824267].
42. K. Ballman, C. Lee, T. Dunn, and A. Bean, "Error analysis of overlay compensation methodologies and proposed functional tolerances for EUV photomask flatness," *Proc. SPIE* **9984**, 99840S (2016) [doi: 10.1117/12.224228].
43. Harry J. Levinson, "Lithography and mask challenges at the leading edge," *Proc. SPIE* **9635**, 963502 (2015) [doi: 10.1117/12.2203117].
44. T. Liang, J. Magana, K. Chakravorty, E. Panning, and G. Zhang, "EUV mask infrastructure readiness and gaps for TD and HVM," *Proc. SPIE* **9635**, 963502 (2015) [doi: 10.1117/12.2203117].
45. E. Hendrickx, J. Hermans, G. Lorusso, V. Philipsen, P. Roubert, I. Pollentier, M. Goethals, R. Jonckheere, G. Vandenberghe, and K. Ronse, "From ASML Alpha Demo Tool to ASML NXE:3100 at IMEC," EUVL Symposium 2011, 17–19 Oct., Miami, Florida.
46. F. Zernike, "Beugungstheorie des Schneidenverfahrens und seiner verbesserten Form, der Phasenkontrastmethode," *Physica* **1**, 689–704 (1934).
47. M. Born and E. Wolf, *Principles of Optics: Electromagnetic Theory of Propagation, Interference and Diffraction of Light, Seventh Edition*, Cambridge University Press, Cambridge, p. 986 (1999).
48. P. Gräupner et al., "Impact of wavefront errors on low k_1 processes at extremely high NA," *Proc. SPIE* **5040** (2003) [doi: 10.1117/12.482694].
49. R. Socha, X. Shi, and D. LeHoty, "Simultaneous source mask optimization (SMO)," *Proc. SPIE* **5853**, 180–193 (2005) [doi: 10.1117/12.617431].

Downloaded From: https://www.spiedigitallibrary.org/ebooks/ on 09 Mar 2022
Terms of Use: https://www.spiedigitallibrary.org/terms-of-use

50. R. Peeters, S. Lok, E. van Alpen, N. Harned, P. Kuerz, M. Lowisch, H. Meijer, D. Ockwell, E. van Setten, G. Schiffelers, J.-W. van der Horst, J. Stoeldraijer, R. Kazinczi, R. Droste, H. Meiling, and R. Kool, "ASML's NXE platform performance and volume introduction," *Proc. SPIE* **8679**, 86791F (2013) [doi: 10.1117/12.2010932].
51. M. Phillips, "Mask challenges in complementary EUV/193i patterning," presented at Photomask Japan 2015, Yokohama, Japan.
52. N. Felix, D. Corliss, and K. Petrillo et al, "EUV patterning successes and frontiers," *Proc. SPIE* **9776**, 97761O (2016) [doi: 10.1117/12.2219894].
53. G. Lee, "Samsung to introduce EUV process to semiconductor foundries," iPnomic–IP Tech Trend Report, ETRC-KGTLAB, Seoul, 9 May 2016.
54. J. T. Neumann, P. Gräupner, W. Kaiser, R. Garreis, and B. Geh, "Interaction of 3D mask effects and NA in EUV lithography," *Proc. SPIE* **8522**, 852211 (2012) [doi: 10.1117/12.2009117].
55. J. T. Neumann, P. Gräupner, W. Kaiser, R. Garreis, and B. Geh, "Mask effects for high-NA EUV: impact of NA, chief-ray-angle, and reduction ratio," *Proc. SPIE* **8679**, 867915 (2013) [doi: 10.1117/12.2011455].
56. P. A. Kearney, O. Wood, E. Hendrickx, G. McIntyre, S. Inoue, F. Goodwin, S. Wurm, J. van Schoot, and W. Kaiser, "Driving the industry towards a consensus on high numerical aperture (high-NA) extreme ultraviolet (EUV)," *Proc. SPIE* **9048**, 90481O (2014) [doi: 10.1117/12.2048397].
57. S. Migura, B. Kneer, J. T. Neumann, W. Kaiser, and J. van Schoot, "EUV lithography optics for sub 9 nm resolution," EUVL Symposium 2014, Oct 27–29, Washington, D.C.
58. Carl Zeiss SMT GmbH, International Publication Number WO 2012/034995 A2 (Priority Date 15.9.2010).
59. J. T. Neumann, M. Rösch, P. Gräupner, S. Migura, B. Kneer, W. Kaiser, and K. van Ingen Schenau, "Imaging performance of EUV lithography optics configuration for sub-9nm resolution," *Proc. SPIE* **9422**, 94221H (2015) [doi: 10.1117/12.21755658].
60. J. van Schoot, K. van Ingen Schenau, C. Valentin, and S. Migura, "EUV lithography scanner for sub-8nm resolution," *Proc. SPIE* **9422**, 94221F (2015) [doi: 10.1117/12.2087502].
61. B. Kneer, S. Migura, W. Kaiser, J. T. Neumann, and J. van Schoot, "EUV lithography optics for sub-9nm resolution," *Proc. SPIE* **9422**, 94221G (2015) [doi: 10.1117/12.2175488].
62. N. Davydova, E. van Setten, R. de Kruif, D. Oorschot, M. Dusa, C. Wagner, J. Jiang, W. Liu, H. Kang, H. Liu, P. Spies, N. Wiese, and M. Waiblinger, "Imaging performance improvements by EUV mask tack optimization," *Proc. SPIE* **7985**, 79850X (2011) [doi: 10.1117/12.884504].

Downloaded From: https://www.spiedigitallibrary.org/ebooks/ on 09 Mar 2022
Terms of Use: https://www.spiedigitallibrary.org/terms-of-use

63. J. Ruoff, "Impact of mask topography and multilayer stack on high NA imaging of EUV masks," *Proc. SPIE* **7823**, 78231N (2010) [doi: 10.1117/12.864120].
64. V. Philipsen, E. Hendrickx, R. Jonckheere, G. Vandenberge, N. Dadydova, T. Fliervoet, and J. T. Neumann, "Impact of mask stack on high NA EUV imaging," EUVL Symposium 2012, 30 Sept. to 1 Oct., Brussels, Belgium.
65. H.-K Cho, "EUV readiness and EUV PPT performance," 2011 International Symposia on Extreme Ultraviolet Lithography and Lithography Extensions, Miami, Florida.
66. R. Chao, P. Graeupner, E. Gullikson, S.-S. Kim, J.-T. Neumann, R. Miyakawa, H.-S. Seo, A. Neureuther, and P. Naulleau, "Experimental verification of EUV mask limitations at high numerical apertures," *Proc. SPIE* **8679**, 86791M (2013) [doi: 10.1117/12.2013209].
67. M. P. Benk, A. Wojdyla, W. Chao, F. Salmassi, S. Oh, Y.-G. Wang, R. H. Miyakawa, P. P. Naulleau, and K. A. Goldberg, "Emulation of anamorphic imaging on the SHARP extreme ultraviolet mask microscope," *J. Micro/Nanolith. MEMS MOEMS* **15**, 033501 (2016) [doi: 10.1117/1.JMM.15.3.033501].
68. V. Philipsen et al., "Mask stacks for EUV imaging at high NA," IMEC Partner Technical Week Review, October (2012).
69. O. Wood, K. Wong, V. Parks, P. Kearney, J. Meyer-Ilse, V. Luong, V. Phillipsen, M. Faheem, Y. Liang, A. Kumar, E. Chen, C. Bennett, B. Fu, M. Gribelyuk, W. Zhao, P. Mangat, and P. Van der Heide, "Improved Ru/Si multilayer reflective coatings for advanced extreme ultraviolet lithography photomasks," *Proc. SPIE* **9776**, 977619 (2016) [doi: 10.1117/12.2219215].
70. A. Erdmann, T. Fühner, P. Evanschitzky, J. T. Neumann, J. Ruoff, and P. Gräupner, "Modeling studies on alternative EUV mask concepts for higher NA," *Proc. SPIE* **8679**, 86791Q (2013) [doi: 10.1117/12.2011432].
71. K. Takai, K. Motokawa, K. Murano, T. Kamo, and N. Hayashi, "Patterning of EUVL binary etched multilayer mask," *Proc. SPIE* **8880**, 88802M (2013) [doi: 10.1117/12.2033453].
72. L. van Look, V. Phillipsen, E. Hendrickx, G. Vandenberge, N. Davydova, F. Wittebrood, R. de Kruif, A. van Oosten, J. Miyazaki, T. Fliervoet, J. van Schoot, and J. T. Neumann, "Alternative EUV mask technology to compensate for mask 3D effects," *Proc. SPIE* **9658**, 96580I (2015) [doi: 10.1117/12.2197213].
73. P. Gräupner, R. B. Garreis, A. Goehnermeier, T. Heil, M. Lowisch, and D. G. Flagello, "Impact of wavefront errors on low k_1 processes at extremely high NA," *Proc. SPIE* **5040**, 119 (2003) [doi: 10.1117/12.482694].

Downloaded From: https://www.spiedigitallibrary.org/ebooks/ on 09 Mar 2022
Terms of Use: https://www.spiedigitallibrary.org/terms-of-use

74. K. van Ingen Schenau, G. Bottiglieri, J. van Schoot, J.-T. Neumann, and M. Roesch, "Imaging performance of the EUV high NA anamorphic system," *Proc. SPIE* **9661**, 96610S (2015) [doi: 10.1117/12.2195476].
75. N. R. Böwering, I. V. Fomenkov, D. C. Brandt, A. N. Bykanov, A. I. Erschv, W. N. Partlo, D. W. Myers, N. R. Farrar, G. O. Vaschenko, O. V. Khodykin, J. R. Hoffman, C. P. Chrobak, S. N. Srivastava, I. Ahmad, C. Rajyaguru, D. J. Golich, D. A. Vidisek, S. De Dea, and R. R. Hou, "Performance results of laser produced plasma test and prototype light sources for EUV lithography," *J. Micro/Nanolith. MEMS MOEMS* **8**(4), 041504 (2009) [doi: 10.1117/1/3224942].
76. W. van der Zande, Performance Overview and Outlook of EUV Lithography Systems (S2), Keynote Presentation at the 2015 International Workshop on EUV and Soft X-Ray Sources, 9–11 Nov., Dublin, Ireland.
77. A. Pirati, R. Peeters, and D. Smith et al. "EUV lithography performance for manufacturing: status and outlook," *Proc. SPIE* **9776**, 97760A (2016) [doi: 10.1117/12.2220423].
78. H. Wolter, "Spiegelsysteme streifenden Einfalls als abbildende Optiken für Röntgenstrahlen," *Annalen der Physik*. **445**(1), 94–114 (1952).
79. H. Wolter, "Verallgemeinerte Schwarzschildsche Spiegelsysteme streifender Reflexion als Optiken für Röntgenstrahlen," *Annalen der Physik*. **445** (4–5), 286–295 (1952).
80. P. L. Thompson and J. E. Harvey, "Systems engineering analysis of aplanatic Wolter type I x-ray telescopes," *Opt. Eng.* **39**(6), 1677–1691 (2000) [doi: 10.1117/1.602545].
81. W. J. Egle, W. Hafner, A. Matthes, E. Erzin, B. Gaenswein, H. Schwarz, P. Marczuk, M. Antoni, W. Singer, F. Melzer, and J. Hainz, "EUV collectors: design, development, fabrication, and testing," *Proc. SPIE* **5193**, 39 (2004) [doi: 10.1117/12.507736].
82. O. Citterio, P. Conconi, M Ghigo, F. Mazzoleni, H. W. Braeuninger, W. Burkert, N. Schulz, P. Gondoin, K. can Katwijk, and R. J. Laurance, "Results of X-Ray measurements on electroformed mirror shells for the XMM project," *Proc. SPIE* **1742**, 256 (1992) [doi: 10.1117/12.140559].
83. J. Altmann, W. J. Egle, U. Bingel, W. Hafner, B. Gaenswein, H. Schwarz, and A. Neugschwender, "Mirror system for the German x-ray satellite ABRIXAS: 1. Flight mirrors fabrication, integration and testing," *Proc. SPIE* **3444**, 350–360 (1998) [doi: 10.1117/12.331249].
84. P. Marczuk and W. Egle, "Grazing Incidence EUV Collectors," Chapter 33 in *EUV Sources for Lithography*, V. Bakshi, Ed., SPIE Press, Bellingham, Washington, pp. 873–892 (2006) [doi: 10.1117/3.613774].
85. P. Kürz, W. Bollinger, M. Dahl, M. Lowisch, C. Münster, F. Rohmund, T. Stein, T. Neidhardt, and P. Marczuk, "The EUV alpha demo tool

Downloaded From: https://www.spiedigitallibrary.org/ebooks/ on 09 Mar 2022
Terms of Use: https://www.spiedigitallibrary.org/terms-of-use

program at Carl Zeiss SMT AG," EUVL Symposium 2004, 1–4 Nov., Miyazaki, Japan.
86. G. Bianucci, G. L. Cassol, N. M. Ceglio, G. Valsecchi, and F. Zocchi, "Low CoO grazing incidence collectors for EUVL HVM," *Proc. SPIE* **8322**, 832216 (2012) [doi: 10.1117/12.916157].
87. G. Bianucci, A. Bragheri, G. L. Cassol, R. Mazzoleni, and F. E. Zocchi, "Enabling the 22nm node via grazing incidence collectors integrated into the DPP source for EUVL HVM," *Proc. SPIE* **7969**, 79690B (2011) [doi: 10.1117/12.879396].
88. J. Pankert, R. Apetz, and K. Bergmann et al., "EUV sources for the alpha-tools," *Proc. SPIE* **6151**, 61510Q (2006) [doi: 10.1117/12.657066].
89. M. Corthout, R. Apetz, and J. Brudermann et al., "Sn DPP source-collector modules: status of alpha resources, beta developments, and the scalability to HVM," *Proc. SPIE* **6921**, 69210V (2008) [doi: 10.1117/12.77633].
90. H. Kierey, K. Heidemann, B. Kleemann, R. Winters, W. Egle, W. Singer, F. Melzer, R. Wevers, and M. Antoni, "EUV spectral purity filter: optical and mechanical design, grating fabrication, and testing," *Proc. SPIE* **5193**, 70 (2004) [doi: 10.1117/12.507741].
91. I. V. Fomenkov, D. C. Brandt, and A. N. Bykanov et al., "Laser-produced plasma light source for EUVL," *Proc. SPIE* **7271**, 727138 (2009) [doi: 10.1117/12.814272].
92. M. Bienert, A. Göhnermeier, O. Natt, M. Lowissch, P. Gräupner, T. Heil, R. B. Garreis, K. van Ingen Schenau, and S. G. Hansen, "Imaging budgets for extreme ultraviolet optics: ready for 22-nm node and beyond," *J. Micro/Nanolith.* **8**(4), 041509 (2009) [doi: 10.1117/1.3238543].
93. H. H. Hopkins and P. M. Barham, "The influence of the condenser on microscopic resolution," *Proc. Phys. Soc.* **63**(10), 737 (1950).
94. J. Finders, S. Wuister, T. Last, G. Rispens, E. Psari, J. Lubkoll, E. van Setten, and F. Wittebrood, "Contrast optimization for 0.33NA EUV lithography," *Proc. SPIE* **9776**, 97761P (2016) [doi: 10.1117/12.2220036].
95. B. W. Smith, "The saga of sigma: influences of illumination throughout optical generations," *Proc. SPIE* **9052**, 905204 (2014) [doi: 10.1117/12.2048827].
96. P. P. Naulleau, K. A. Goldberg, P. Batson, J. Bokor, P. Denham, and S. Rekawa, "Fourier synthesis custom coherence illuminator for extreme ultraviolet microfield lithography," *Appl. Opt.* **42**(5), 820–826 (2003).
97. A. Brunton, J. Cashmore, P. Elbourn, G. Elliner, M. C. Gower, P. Grunewald, M. Harman, S. Hough, N. McEntee, S. Mundair, D. Rees, P. Richards, V. Truffert, I. Wallhead, and M. Whitfield, "High-resolution EUV microstepper tool for resist testing and technology evaluation," *Proc. SPIE* **5374**, 869 (2004) [doi: 10.1117/12.548343].

Downloaded From: https://www.spiedigitallibrary.org/ebooks/ on 09 Mar 2022
Terms of Use: https://www.spiedigitallibrary.org/terms-of-use

98. E. Sohmen, "Optical System for EUV microstepper," EUVL Symposium 2004, 1–4 Nov., Miyazaki, Japan.
99. M. Lowisch, P. Kuerz, O. Conradi, G. Wittich, W. Seitz, and W. Kaiser, "Optics for ASML's NXE:3300B platform," *Proc. SPIE* **8679**, 86791H (2013) [doi: 10.1117/12.2012158].
100. K. Murakami, T. Oshino, H. Kondo, H. Chiba, H. Komatusda, K. Noumura, and H. Iwata, "Development status of projection optics and illumination optics for EUV1," *Proc. SPIE* **6921**, 69210Q (2008) [doi: 10.1117/12.772435].
101. H. Komatsuda, "Novel illumination system for EUVL," *Proc. SPIE* **3997**, 765–776 (2000) [doi: 10.1117/12.390117].
102. M. Antoni, W. Singer, J. Schultz, J. Wangler, I. Escudero-Sanz, and B. Kruizinga, "Illumination optics design for EUV lithography," *Proc. SPIE* **4146**, 25 (2000) [doi: 10.1117/12.406673].
103. M. Lowisch, P. Kuerz, H.-J. Mann, O. Natt, and B. Thuering, "Optics for EUV production," *Proc. SPIE* **7636**, 763603 (2010) [doi: 10.1117/12.848624].
104. F. A. J. Driessen, N. Davydova, J. Jiang, H. Kang, V. Vaenkatesan, D. Oorschot, I. S. Kim, S. N. Kang, Y. Lee, J. Yeo, K. Gronlund, H. Y. Liu, K. van Ingen-Schenau, R. Peeters, C. Wagner, J. Zimmermann, and O. Schumann, "Holistic lithography for EUV: NXE:3100 characterization of first printed wafers using an advanced scanner model and scatterometry," *Proc. SPIE* **8166** (2011) [doi: 10.1117/12.898955].
105. C. A. Mack, "Optimum stepper performance through image manipulation," Proc. KTI Microelectronics Seminar, pp. 209–215 (1989).
106. A. E. Rosenbluth, S. J. Bukofsky, C. A. Fonesca, M. S. Hibbs, K. Lai, A. F. Molless, R. N. Singh, and A. K. K. Wong, "Optimum mask and source patterns to print a given shape," *J. Micro./Nanolith. MEMS MEOMS* **1**(1), 13–30 (2002) [doi: 10.1117/1.1448500].
107. K. Lai, A. E. Rosenbluth, S. Bagheri, J. Hoffnagle, K. Tian, D. Melville, J. Tirapu-Azpiroz, M. Fakhry, Y. Kim, S. Halle, G. McIntyre, A. Wagner, G. Burr, M. Burkhardt, D. Corliss, E. Gallagher, T. Faure, M. Hibbs, D. Flagello, J. Zimmermann, B. Kneer, F. Rohmund, F. Hartung, C. Hennerkes, M. Maul, R. Kazinczi, A. Engelen, R. Carpaij, R. Groenendijk, J. Hageman, and C. Russ, "Experimental result and simulation analysis for the use of pixelated illumination from source mask optimization for 22nm logic lithography process," *Proc. SPIE* **7274**, 72740A (2009) [doi: 10.1117/12.814680].
108. X. Liu, R. Howell, S. Hsu, K. Yang, K. Gronlund, F. Driessen, H.-Y. Liu, S. Hansen, K. van Ingen Schenau, T. Hollink, P. van Adrichem, K. Troost, J. Zimmermann, O. Schumann, C. Hennerkes, and P. Gräupner, "EUV source-mask optimization for 7nm node and beyond," *Proc. SPIE* **9048**, 90480Q (2014) [doi: 10.1117/12.2047585].

Downloaded From: https://www.spiedigitallibrary.org/ebooks/ on 09 Mar 2022
Terms of Use: https://www.spiedigitallibrary.org/terms-of-use

109. S. Hsu, R. Howell, J. Jia, H.-Y. Liu, K. Gronlund, S. Hansen, and J. Zimmermann, "EUV resolution enhancement techniques (RETs) for k_1 0.4 and below," *Proc. SPIE* **9422**, 94221I (2015) [doi: 10..1117/12.2086074].
110. U. Dinger, G. Seitz, S. Schulte, F. Eisert, C. Muenster, S. Burkart, S. Stacklies, C. Bustaus, H. Hoefer, M. Mayer, B. Fellner, O. Hocky, M. Rupp, K. Riedelsheimer, and P. Kuerz, "Fabrication and metrology of diffraction limited soft x-ray optics for the EUV microlithography," *Proc. SPIE* **5193**, 18–28 (2003) [doi: 10.1117/12.511489].
111. U. Dinger, F. Eisert, H. Lasser, M. Mayer, A. Seifert, G. Seitz, S. Stacklies, F.-J. Stickel, and M. Weiser, "Mirror substrates for EUV lithography: progress in metrology and optical fabrication technology," *Proc. SPIE* **4146**, 35–46 (2000) [doi: 10.1117/12.406674].
112. R. Soufli and J. S. Taylor, "Specification, Fabrication, Testing and Mounting of EUV Optical Substrates," Chapter 4c in *EUV Lithography*, V. Bakshi, Ed., SPIE Press, Bellingham, Washington, pp. 161–185 (2009) [doi: 10.1117/3.769215ch4c].
113. L. A. Marchetti, "Fabrication and metrology of 10X Schwarzschild optics for EUV imaging," *Proc. SPIE* **5193**, 1–10 (2003) [doi: 10.1117/12.510318].
114. T. Miura, K. Murakami, H. Kawai, Y. Kohama, K. Morita, K. Hada, and Y. Ohkubo, "Nikon EUVL development progress update," *Proc. SPIE* **7636**, 76361G (2010) [doi: 10.1117/12.846459].
115. H. Glatzel, D. Ashworth, M. Bremer, R. Chin, K. Cummings, L. Girard, M. Goldstein, E. Gullikson, R. Hudyma, J. Kennon, B. Kestner, L. Marchetti, P. Naulleau, R. Soufli, and E. Spiller, "Projection optics for extreme ultraviolet lithography (EUV) micro-field exposure tools (METs) with a numerical aperture of 0.5," *Proc. SPIE* **8679**, 867917 (2013) [doi: 10.1117/12.2012698].
116. I. Mitra, J. Alkemper, U. Nolte, A. Engel, R. Mueller, S. Ritter, H. Hack, K. Megges, H. Kohlmann, W. Pannhorst, M. J. Davis, L. Aschke, and K. Knapp, "Improved materials meeting the demands for EUV substrates," *Proc. SPIE* **5037**, 219–226 (2003) [doi: 10.1117/12.484728].
117. K. E. Hrdina, B. G. Ackerman, A. W. Fanning, C. E. Heckle, D. C. Jenne, and W. D. Navan, "Measuring and tailoring CTE within ULE glass," *Proc. SPIE* **5037**, 227–235 (2003) [doi: 10.1117/12.484925].
118. U. Dinger, F. Eisert, S. Koehler, A. Ochse, J. Zellner, M. Lowisch, and T. Laufer, "Projection objective," U.S. Patent 7557902 B2 (2009).
119. B. Dörband, H. Müller, and H. Gross, Handbook of Optical Systems, Vol. **5**, *Metrology of Optical Components and Systems*. Wiley-VCH Verlag, Weinheim, Germany (2012).

Downloaded From: https://www.spiedigitallibrary.org/ebooks/ on 09 Mar 2022
Terms of Use: https://www.spiedigitallibrary.org/terms-of-use

120. B. Braunecker, R. Hentschel, and H. J. Tiziani, Eds., *Advanced Optics Using Aspherical Elements*, SPIE Press, Bellingham, Washington (2008) [doi: 10.1117/3.741689].
121. J. C. Stover, *Optical Scattering: Measurement and Analysis*, 3rd ed., SPIE Press, Bellingham, Washington (2012) [doi: 10.1117/3.975276].
122. Lord Rayleigh, "On the dynamical theory of gratings," *Proc. Roy. Soc. A* **79**, 399–416 (1907).
123. S. O. Rice, "Reflection of electromagnetic waves from slightly rough surfaces," *Commun. Pure. Appl. Math.* **4**, 351–378 (1951).
124. E. L. Church and J. M. Zavada, "Residual surface roughness of diamond-turned optics," *Appl. Opt.* **14**, 1788–1795 (1975).
125. D. G. Stearns, "X-ray scattering from interfacial roughness in multilayer structures," *J. Appl. Phys.* **71**, 4286–4298 (1992).
126. D. G. Stearns, "Stochastic model for thin film growth and erosion," *Appl. Phys. Lett.* **62**, 1745–1747 (1993).
127. D. G. Stearns, D. P. Gaines, D. W. Sweeney, and E. M. Gullikson: "Nonspecular x-ray scattering in a multilayer-coated imaging system," *J. Appl. Phys.* **84**, 1003–1028 (1998).
128. J. M. Elson, "Multilayer-coated optics: guided-wave coupling and scattering by means of interface random roughness," *J. Opt. Soc. Am. A* **12**, 729–742 (1995).
129. P. Bousquet, F. Flory, and P. Roche, "Scattering from multilayer thin films: theory and experiment," *J. Opt. Soc. Am.* **71**, 1115–1123 (1981).
130. S. Schröder, "Light scattering of optical components at 193 nm and 13.5 nm," Ph.D. thesis Friedrich-Schiller-Universtät Jena (2008).
131. A. Haase, V. Soltwisch, C. Laubis, and F. Scholze, "Role of dynamic effects in the characterization of multilayers by means of power spectral density," *Appl. Optics* **53**(14), 3019–3027 (2014).
132. E. Spiller, *Soft X-Ray Optics*, SPIE Press, Bellingham, Washington (1994) [doi: 10.1117/3.176482].
133. E. L. Church, H. A. Jenkinson, and J. M. Zavada, "Relationship between surface scattering and microtopographic features," *Opt. Eng*. **18** (2), 125–136 [doi: 10.1117/12.7972337].
134. E. L. Church, "The statistical description of optical inhomogeneities," *National Bureau of Standards Special Publication* **574**, 51–54 (1980).
135. E. L. Church, "Fractal surface finish," *Appl. Opt.* **27**(8), 1518–1526 (1988).
136. M. Born and E. Wolf, *Principles of Optics*, Seventh Edition, Cambridge University Press, Cambridge (1999).
137. E. M. Gullikson, S. Mrowka, and B. B. Kaufmann, "Recent developments in EUV reflectometry at the Advanced Light Source," *Proc. SPIE* **4343** (2001) [doi: 10.1117/12.436712].
138. J. Tümmler, H. Blume, G. Brandt, J. Eden, B. Meyer, H. Scherr, F. Scholz, F. Scholze, and G. Ulm, "Characterization of the PTB EUV

Downloaded From: https://www.spiedigitallibrary.org/ebooks/ on 09 Mar 2022
Terms of Use: https://www.spiedigitallibrary.org/terms-of-use

reflectometry facility for large EUVL optical components," *Proc. SPIE* **5037** (2003) [doi: 10.1117/12.482668].
139. C. Laubis, A. Barboutis, M. Biel, C. Buchholz, B. Dubrau, A. Fischer, A. Hesse, J. Puls, C. Stadelhoff, V. Soltwisch, and F. Scholze, "Status of EUV reflectometry at PTB," *Proc. SPIE* **8679**, 867921 (2013) [doi: 10.1117/12.598728].
140. V. Soltwisch, A. Fischer, C. Laubis, C. Stadelhoff, F. Scholze, and A. Ullrich, "Polarization resolved measurements with the new EUV ellipsometer of PTB," *Proc. SPIE* **9422**, 942213 (2015) [doi: 10.1117/12.2085798].
141. L. van Loyen, T. Böttger, S. Schädlich, S. Braun, T. Foltyn, A. Leson, F. Scholze, and S. Müllender, "Laboratory LPP EUV reflectometer working with non-polarized radiation," *Appl. Surf. Sci.* **252**, 57–60 (2005).
142. A. Miyake, T. Miyachi, M. Amemiya, T. Hasegawa, N. Ogushi, T. Yamamoto, F. Masaki, and Y. Watanabe, "LPP-based reflectometer for characterization of EUV lithography systems," *Proc. SPIE* **5037** (2003) [doi: 10.1117/12.12.484969].
143. A. Farahzadi, C. Wies, and R. Lebert, "The task of EUV-reflectometry for HVM of EUV masks: first steps," *Proc. SPIE* **7470**, 74700E (2009) [doi: 10.1117/12.835176].
144. S. Schröder, T. Feigl, A. Duparré, and A. Tünnermann, "EUV reflectance and scattering of Mo/Si multilayers on differently polished substrates," *Optics Express* **15**(21), 13997–14012 (2007).
145. I. Kozhevnikov, I. Bukreeva, and E. Ziegler, "Design of x-ray supermirrors," *Nuclear Instruments and Methods A* **460**, 424–443 (2001).
146. S. P. Vernon, D. G. Stearns, and R. S. Rosen, "Chirped multilayer coatings for increased x-ray throughput," *Optics Letters* **18**(9), 672–674 (1992).
147. P. van Loevezijn, R. Schlatmann, J. Verhoeven, B. van Tiggelen, and E. Gullikson, "Numerical and experimental study of disordered multilayers for broadband x-ray reflection," *Applied Optics* **35**(19), 3614–3619 (1996).
148. T. Kuhlmann, S. A. Yulin, T. Feigl, N. Kaiser, H. Bernitzki, and H. Lauth, "Design and fabrication of broadband EUV multilayer mirrors," *Proc. SPIE* **4688** (2002) [doi: 10.1117/12.472327].
149. A. E. Yakshin, I. V. Kozhevnikov, E. Zoethout, E. Louis, and F. Bijkerk, "Properties of broadband depth-graded multilayer mirrors for EUV optical systems," *Optics Express* **18**(7), 6957–6971 (2010).
150. Z. Wang, H. Wang, J. Zhu, Z. Zhang, F. Wang, Y. Xu, S. Zhang, W. Wu, L. Chen, A. G. Michette, S. J. Pfauntsch, A. K. Powell, F. Schäfers, A. Gaupp, M. Cui, L. Sun, and M. MacDonald "Complete polarization

Downloaded From: https://www.spiedigitallibrary.org/ebooks/ on 09 Mar 2022
Terms of Use: https://www.spiedigitallibrary.org/terms-of-use

analysis of extreme ultraviolet radiation with a broadband phase retarder and analyzer," *Applied Physics Letters* **90**, 081910 (2007).
151. A. E. Yakshin, R. W. E. van de Kruijs, I. Nedelcu, E. Zoethout, E. Louis, F. Bijkerk, H. Enkisch, and S. Müllender "Enhanced reflectance of interface engineered Mo/Si multilayers produced by thermal particle deposition," *Proc. SPIE* **6517**, 65170I (2007) [doi: 10.1117/12.711796].
152. S. Bajt, J. B. Alameda, T. W. Barbee, Jr., W. M. Clift, J. A. Folta, B. B. Kaufmann, and E. A. Spiller, "Improved reflectance and stability of Mo/Si multilayers," *Optical Engineering* **41**(8), 1797–1804 (2002) [doi: 10.1117/12.1489426].
153. S. Braun, P. Gawlitza, A. Kubec, C. Gruhne, M. Menzel, and A. Leson "Nanometer multilayers for x-ray mirrors and lenses," 2nd Swedish-German Workshop on X-Ray Optics, HZB Berlin-Adlershof, April 28–30, 2015.
154. S. Braun, H. Mai, M. Moss, R. Scholz, and A. Leson, "Mo/Si multilayers with different barrier layers for applications as EUV mirrors," *Japanese J. Applied Physics* **41**(1), 4074–4081 (2002).
155. S. Braun, H. Mai, M. Moss, and R. Scholz, "Microstructure of Mo/Si multilayers with barrier layers," *Proc. SPIE* **4782**, 185–195 (2002) [doi: 10.1117/12.453818].
156. V. I. T. A. de Rooij-Lohmann, L. W. Veldhuizen, E. Zoethout, A. E. Yakshin, R. W. E. van de Kruijs, B. J. Thijsse, M. Gorgoi, F. Schäfers, and F. Bijkerk "Chemical interaction of B4C, B, and C with Mo/Si layered structures," *J. Applied Physics* **108**, 094314 (2010).
157. S. Bruijn, R. W. E. van de Kruijs, A. E. Yakshin, and F. Bijkerk, "In-situ study of the diffusion reaction mechanism in Mo/Si multilayered films," *Applied Surface Science* **257**, 2707–2711 (2011).
158. H. Takenaka, H. Ito, T. Haga, and T. Kawamura, "Design and fabrication of highly heat resistant Mo/Si multilayer soft x-ray mirrors with interleaved barrier layers," *J. Synchrotron Radiation* **5**, 708–710 (1998).
159. T. Feigl, H. Lauth, S. Yulin, and N. Kaiser, "Heat resistance of EUV multilayer mirrors for long-time applications," *Microelectronic Engineering* **57**, 3–8 (2001).
160. T. Böttger, D. Meyer, P. Paufler, S. Braun, M. Moss, H. Mai, and E. Beyer "Thermal stability of Mo/Si multilayers with boron carbide interlayers," *Thin Solid Films* **444**, 165–173 (2003).
161. U. Kleineberg, T. Westerwalbesloh, W. Hachmann, U. Heinzmann, J. Tümmler, F. Scholze, G. Ulm, and S. Müllender, "Effect of substrate roughness on Mo/Si multilayer optics for EUVL produced by UHV-e-beam evaporation and ion polishing," *Thin Solid Films* **433**, 230–236 (2003).

Downloaded From: https://www.spiedigitallibrary.org/ebooks/ on 09 Mar 2022
Terms of Use: https://www.spiedigitallibrary.org/terms-of-use

162. E. A. Spiller, S. L. Baker, E. Parra, and C. Tarrio, "Smoothing of mirror substrates by thin-film deposition," *Proc. SPIE* **3767**, 143–153 (1999) [doi: 10.1117/12.371112].
163. R. Soufli, E. A. Spiller, M. A. Schmidt, J. C. Robinson, S. L. Baker, S. Rati, M. A. Johnson, and E. M. Gullikson, "Smoothing of diamond-turned substrates for extreme ultraviolet illuminators," *Opt. Eng.* **43**(12), 3089–3095 (2004) [doi: 10.1117/1.1815005].
164. F. Salmassi, P. Naulleau, and E. Gullikson, "Spin-on-glass coatings for the generation of superpolished substrates for use in the extreme-ultraviolet region," *Applied Optics* **45**, 2404–2408 (2006).
165. S. Braun, B. Bendjus, T. Foltyn, M. Menzel, J. Schreiber, and D. Weißbach, "Carbon buffer layers for smoothing substrates of EUV and X-ray multilayer mirrors," *Proc. SPIE* **5392** (2004) [doi: 10.1117/12.541365].
166. P. Mirkarimi, E. Spiller, S. Baker, D. Stearns, J. Robinson, D. Olynick, F. Salmassi, J. Liddle, T. Liang, and A. Stivers, "A silicon-based, sequential coat-and-etch process to fabricate nearly perfect substrate surfaces," *J. Nanoscience and Nanotechnology* **6**(1), 28–35 (2006).
167. E. Louis, H.-J. Voorma, N. B. Koster, L. Shmaenok, F. Bijkerk, R. Schlatmann, J. Verhoeven, Yu. Ya. Platonov, G. E. van Dorssen, and H. A. Padmore, "Enhancement of reflectivity of multilayer mirrors for soft x-ray projection lithography by temperature optimization and ion bombardment," *Microelectronic Engineering* **23**(1–4), 215–218 (1994).
168. I. Nedelcu, R. v. d. Kruijs, A. Yakshin, F. Tichelaar, E. Zoethout, E. Louis, H. Enkisch, S. Müllender, and F. Bijkerk, "Interface roughness in Mo/Si multilayers," *Thin Solid Films* **515**, 434–438 (2006).
169. T. Barbee, Jr. and T. W. Barbee, III, "Molybdenum-silicon multilayer monochromator for the extreme ultraviolet," *Applied Physics Letters* **50** (25), 1841–1841 (1987).
170. K. Murakami and M. Shiraishi, "Stress control of Mo/Si-based multilayer coatings deposited by ion-beam sputtering," *Proc. SPIE* **4506**, 56–64 (2001) [doi: 10.1117/12.450945].
171. E. Louis, H.-J. Voorma, N. B. Shmaenok, F. Bijerk, R. Schlatmann, J. Verhoeven, Yu. Ya. Platanov, G. E. van Dorssen, and H. A. Padmore, "Enhancement of reflectivity of multilayer mirros for soft x-ray projection lithography by temperature optimization and ion bombardement," *Microelectronic Engineering* **23**(1–4), 215–218 (1994).
172. S. Braun, R. Dietsch, M. Haidl, T. Holz, H. Mai, S. Müllender, and R. Scholz, "Mo/Si multilayers for EUV applications prepared by pulsed laser deposition (PLD)," *Microelectronic Engineering* **57–58**, 9–15 (2001).
173. M. Wedowski, S. Bajt, J. A. Folta, E. M. Gullikson, U. Kleineberg, L. E. Klebanoff, M. E. Malinowski, and W. M. Clift, Lifetime studies of

Downloaded From: https://www.spiedigitallibrary.org/ebooks/ on 09 Mar 2022
Terms of Use: https://www.spiedigitallibrary.org/terms-of-use

Mo/Si and Mo/Be multilayer coatings for extreme ultraviolet lithography, *Proc. SPIE* **3767**, 217–224 (1999) [doi: 10.1117/12.371120].
174. H. Meiling, B. Mertens, F. Stietz, M. Wedowski, E. Klein, R. Kurt, E. Louis, and A. E. Yakshin, "Prevention of MoSi multilayer reflection loss in EUVL tools," *Proc. SPIE* **4506**, 93–104 (2001) [doi: 10.1117/12.450949].
175. I. Nishiyama, H. Oizumi, K. Motai, A. Izumi, T. Ueno, H. Akiyama, and A. Namiki, "Reduction of oxide layer on Ru surface by atomic-hydrogen treatment," *J. Vacuum Science and Technology B* **23**(6), 3129–3131 (2005).
176. S. Bajt, Z. R. Dai, E. J. Nelson, M. A. Wall, J. B. Alameda, N. Q. Nguyen, S. L. Baker, J. C. Robinson, J. S. Taylor, M. Clift, A. L. Aquila, E. M. Gullikson, and N. V. G. Edwards, "Oxidation resistance of Ru-capped EUV multilayers," *Proc. SPIE* **5751**, 118–127 (2005) [doi: 10.1117/12.597443].
177. Y. He, A. Goriachko, C. Korte, A. Farkas, G. Mellau, P. Dudin, L. Gregoratti, A. Barinov, M. Kiskinova, A. Stierle, N. Kaspar, S. Bajt, and H. Over, "Oxidation and reduction of ultrathin nanocrystalline Ru films on silicon: model system for Ru-capped extreme ultraviolet lithography optics," *J. Physical Chemistry C* **111**, 10988–10992 (2007).
178. S. Bajt, N. V. Edwards, and T. E. Madey, "Properties of ultrathin films appropriate for optics capping layers exposed to high energy photon irradiation," *Surface Science Reports* **63**(2), 73–99 (2008).
179. S. Yulin, N. Benoit, T. Feigl, N. Kaiser, M. Fang, and M. Chandhok, "Mo/Si multilayers with enhanced TiO_2- and RuO_2-capping layers," *Proc. SPIE* **6921**, 692118 (2008) [doi: 10.1117/12.772653].
180. M. Schürmann, S. Yulin, V. Nesterenko, T. Feigl, N. Kaiser, B. Tkachenko, and M. B. Schürmann, "Multi-technique study of carbon contamination and cleaning of Mo/Si mirrors exposed to pulsed EUV radiation," *Proc. SPIE* **7636**, 76361 (2010) [doi: 10.1117/12.848197].
181. G. Stoney, "The tension of metallic films deposited by electrolysis," *Proc. R. Soc. Lond. A* **82**, 172–175 (1909).
182. P. B. Mirkarimi, "Stress, reflectance, and temporal stability of sputter-deposited Mo/Si and Mo/Be multilayer films for extreme ultraviolet lithography," *Opt. Eng.* **38**(7), 1246–1259 (1999) [doi: 10.1117/1.602170].
183. D. Windt, W. Brown, C. Volkert, and W. Waskiewicz, "Variation in stress with background pressure in sputtered Mo/Si multilayer films," *J. Applied Physics* **78**(4), 2423–2430 (1995).
184. M. Moss, T. Böttger, S. Braun, T. Foltyn, and A. Leson, "Stress compensation of a Mo/Si/C highly reflective multilayer by means of an optimized buffer layer and heat treatment," *Thin Solid Films* **468**, 322–331 (2004).

Downloaded From: https://www.spiedigitallibrary.org/ebooks/ on 09 Mar 2022
Terms of Use: https://www.spiedigitallibrary.org/terms-of-use

185. K. Murakami and M. Shiraishi, "Stress control of Mo/Si-based multilayer coatings deposited by ion beam sputtering," *Proc. SPIE* **4506**, 56–64 (2001) [doi: 10.1117/12.450945].
186. R. Soufli, E. A. Spiller, M. A. Schmidt, C. Davidson, R. F. Grabner, E. M. Gullikson, B. B. Kaufmann, S. Mrowka, S. L. Baker, H. N. Chapman, R. M. Hudyma, J. S. Taylor, C. C. Walton, C. Montcalm, and J. A. Folta, "Multilayer optics for an extreme ultraviolet lithography tool with 70 nm resolution," *Proc. SPIE* **4343** (2001) [doi: 10.1117/12.436695].
187. B. Rice, "The EUV mask metrology gap," EUVL Symposium 2009, 18–21 Oct., Prague, Czech Republic.
188. C. H. Clifford, T. T. Chan, A. R. Neureuther, K. A. Goldberg, I. Mochi, and T. Liang, "Investigation of buried EUV mask defect printability using actinic inspection and fast simulation," *Proc. SPIE* **7488**, 74882H (2009) doi: [10.1117/12.829716].
189. U. Strößner, H. Seitz, R. Birkner, R. Richter, and T. Scherübl, "AIMS and resist simulation," *Proc. SPIE* **7122**, 71221D (2008) [doi: 10.1117/12.801226].
190. M. Weiss, D. Hellweg, J. H. Peters, A. Garetto, and M. Goldstein, "Actinic review of EUV masks: First results from the AIMS EUV system integration," *Proc. SPIE* **9048**, 90480X (2014) [doi: 10.1117/12.2046302].
191. A. Garetto, J. H. Peters, S. Perlitz, U. Matejka, D. Hellweg, and M. Weissal, "Status of the AIMS EUV Project," *Proc. SPIE* **8522**, 852222 (2012) [doi: 10.1117/12.981345].
192. M. Waiblinger, K. Kornilov, T. Hofmann, and K. Edinger, "E-beam induced EUV photomask repair: a perfect match," Presented at Eureapean Mask and Lithography Conference 2010, 18 Jan., Grenoble, France.
193. A. Rastegar and V. Jindal, "EUV mask defects and their removal," *Proc. SPIE* **8352**, 83520W (2012) [doi: 10.1117/12.923882].
194. R. Teki, A. John-Kadaksham, A. Ma, F. Goodwin, T. Yatsui, M Ohtsu, A. Hariprasad, U. Lagudu, S. Babu, P. Dumas, and R. Jenkins. "Material- and polishing induced defectivity on EUV mask substrates," EUVL Symposium 2012, 30 Sept. to 4 Oct., Brussels, Belgium.
195. A. Barty, J. S. Taylor, R. Hudyma, and E. Spiller, "Design and evaluation of system configurations for an EUV mask inspection microscope," Tech. Rep. UCRL-CR-149774 Lawrence Livermore National Laboratory, Livermore, California (2002).
196. H. Feldmann, J. Ruoff, W. Hamisch, and W. Kaiser, "Actinic review of EUV masks," *Proc. SPIE* **7636**, 76361C (2010) [doi: 10.1117/12.848380].

Downloaded From: https://www.spiedigitallibrary.org/ebooks/ on 09 Mar 2022
Terms of Use: https://www.spiedigitallibrary.org/terms-of-use

197. M. Booth, A. Brunton, J. Cashmore, P. Elbourn, G. Elliner, M. Gower, J. Greuters, J. Hirsch, L. Kling, N. McEntee, P. Richards, V. Truffert, I. Wallhead, M. Whitfield, and R. Hudyma "RIM-13: A high-resolution imaging tool for aerial image monitoring of EUV reticles," *Proc. SPIE* **5992**, 59922C (2005) [doi: 10.1117/12.629562].
198. K. A. Goldberg, I. Mochi, and M. Benk et al., "Commissioning an EUV mask microscope for lithography generations reaching 8 nm," *Proc. SPIE* **8679**, 867919 (2013) [doi: 10.1117/12.2011688].
199. D. Hellweg, S. Perlitz, K. Magnusson, R. Capelli, M. Koch, and M. Malloy, "Actinic review of EUV masks: performance data and status of the AIMS EUV System," *Proc. SPIE* **9776**, 97761A (2016) [doi: 10.1117/12.2219247].
200. M. R. Weiss, D. Hellweg, M. Koch, J. H. Peters, S. Perlitz, A. Garetto, K. Magnusson, R. Capelli, and V. Jindal, "Actinic review of EUV masks: Status and recent results of the AIMS EUV system," *Proc. SPIE* **9422**, 942219 (2015) [doi: 10.1117/12.2086265].
201. E. Verduijn, "Assessment of AIMS EUV and SHARP actinic wavelength mask defect review tools for the evaluation of blank defect printability," EUVL Symposium 2015, 5–7 October, Maastricht, The Netherlands.

Sascha Migura has been employed by Carl Zeiss SMT GmbH since finishing his Ph.D. in physics in 2006 at the University of Bonn. He has mainly worked on EUV lithography optics and was responsible for the optical designs of the Starlith® 3100 and Starlith® 3300. He was also Lead System Engineer for the pre-development of the high-NA EUV lithography optics.

Winfried Kaiser studied physics and technical optics at the Universities of Tübingen and Stuttgart and received his diploma in 1982. He joined ZEISS in 1982 as a scientist and has since held several management positions. He is currently Senior Vice President of Product Strategy at Carl Zeiss SMT GmbH. In 1995, he initiated the cooperation of European companies and institutes in EUV lithography development. Winfried Kaiser is a recipient of the 2006 European SEMI Award and was promoted to Carl Zeiss Fellow in 2007. In 2008, he was named a Fellow of SPIE was and inducted into the Chip Making Industry Hall of Fame. He received the SEMI Bob Graham SME Excellence Award in 2014.

Downloaded From: https://www.spiedigitallibrary.org/ebooks/ on 09 Mar 2022
Terms of Use: https://www.spiedigitallibrary.org/terms-of-use

Jens Timo Neumann works as Staff Scientist in the Imaging and Applications group of Carl Zeiss SMT GmbH. He joined the group in 2007 and since then has authored and coauthored numerous papers on various aspects of lithographic imaging. Since 2012, a focus of his work has been high-NA EUV lithography with a special interest in mask-related effects and optical concepts. He holds a Ph.D. in physics from the University of Göttingen.

Hartmut Enkisch received his Ph.D. in solid states physics from the Technical University of Dortmund in 2001. He joined the department for coating development at Carl Zeiss SMT GmbH in 2002 and was nominated Principal Scientist in 2015. He has been engaged in the coating processes of all EUV lithography tools developed by SMT and is inventor or co-inventor of more than 30 patents.

Dirk Hellweg received his Ph.D. in physics at the Institute of Quantum Optics at the Leibniz University of Hannover in 2003. He started his professional career at the Advanced Mask Technology Center in Dresden, where he worked on e-beam lithography. He joined Carl Zeiss SMT GmbH in 2005. He was a Lead System Engineer for DUV optical systems and is now working as Lead System Engineer for the ZEISS AIMS EUV.

Downloaded From: https://www.spiedigitallibrary.org/ebooks/ on 09 Mar 2022
Terms of Use: https://www.spiedigitallibrary.org/terms-of-use

Chapter 6A
Optics Contamination

Charles S. Tarrio, Shannon B. Hill, and Robert F. Berg
National Institute of Standards and Technology, Gaithersburg, Maryland, USA

Saša Bajt
Deutsches Elektronen-Synchrotron, Hamburg, Germany

6A.1 Introduction
- 6A.1.1 Background
- 6A.1.2 The chemical processes

6A.2 Optics Contamination Research
- 6A.2.1 Carbonization and oxidation: photons or photoelectrons
- 6A.2.2 The elimination of oxidation as a problem: requirements for oxidation-resistant cap layers
- 6A.2.3 Development of contamination-resistant-cap layers

6A.3 Optics Contamination Experiments
- 6A.3.1 Facilities
- 6A.3.2 Carbonization: admitted-gas studies

6A.4 Resist Outgas Testing
- 6A.4.1 Early measurements
- 6A.4.2 Witness-sample testing
- 6A.4.3 Witness-sample testing: nonconventional resists

6A.5 Cleaning and Contamination Control

6A.6 Summary and Future Outlook

References

6A.1 Introduction

The performance of EUV scanners in the field testifies that formidable obstacles to high-volume EUVL manufacturing have been overcome. A key element in this progress has been the virtual elimination of optics contamination as a major hurdle, a development involving several efforts worldwide and stretching over more than a decade. We will describe the chemical processes that lead to contamination, some of the research efforts directed at understanding them, and the resulting mitigation techniques that were developed.

Downloaded From: https://www.spiedigitallibrary.org/ebooks/ on 09 Mar 2022
Terms of Use: https://www.spiedigitallibrary.org/terms-of-use

Ionizing radiation creates chemical reactions that contaminate optical surfaces in an atmosphere with trace amounts of water vapor or organic molecules. Organic molecules adsorbed on the optical surface can be cracked by both the energetic radiation and the secondary electrons it produces, creating a contaminating carbon film. Adsorbed water molecules can be activated to generate strong oxidizers that attack the optical surface itself. However, these two processes can counteract each other, and in the presence of a significant partial pressure of organic molecules or a carbon overlayer, the oxidation by radicals from the water vapor can be reduced, or the carbon overlayer can be etched.

The problems of carbonization and oxidation of optics by ionizing radiation had been observed much earlier in satellite instruments exposed to UV radiation from the sun and in experiments at synchrotron facilities. Contamination was also a concern for lithography using UV radiation (e.g., 193 nm and 248 nm). EUVL was particularly sensitive to this issue due to the expense of EUV photon production and the many optical surfaces between the source and wafer. Even a 1% loss on each optic would reduce the total transmission below the threshold of economic viability. The problem was compounded by the fact that the optics, which consist of precisely figured, ultra-smooth mirrors coated by 40 or more molybdenum/silicon bilayers, could be irreversibly damaged by oxidation or many carbon-removal methods.

The elimination of optics contamination benefitted from experience gathered in the preproduction tools. The first major advance came from the development of an oxidation-resistant cap layer that protected the underlying, less-oxygen-resistant molybdenum and silicon. The next advance was dealing with the carbonization caused by the unavoidable organics coming from resist outgassing and some parts of the unbaked vacuum system. Cleaning of that carbonization by atomic hydrogen was shown to work without damaging the optics.[1] In 2006, ASML directed the development of a resist outgas test. The goal was to eliminate resists with excessive contamination that would require too-frequent cleaning of the projection optics and those resists that had elements that were thought to be not cleanable with atomic hydrogen (e.g., F, Cl, I, Br, P, and S). However, over the next seven years, users of the scanners in the field found that the carbon deposition rates were low enough that they could be managed without significant reduction in productivity for all reasonable chemically amplified resists. Current scanners operate in an atmosphere of low-pressure hydrogen, and the interaction of EUV radiation and hydrogen gas produces hydrogen radicals,[2] which significantly reduces the carbon deposition rate. In addition, these scanners have well-designed dynamic gas curtains[3] that act to reduce the amount of resist outgassing impinging on the optics. The only remaining concern is that one or more of the elements used in the newer metal-containing resists might produce contamination that cannot be cleaned by hydrogen radicals. Since development of novel resists is largely in the proprietary phase, we will not discuss that source of contamination here.

Downloaded From: https://www.spiedigitallibrary.org/ebooks/ on 09 Mar 2022
Terms of Use: https://www.spiedigitallibrary.org/terms-of-use

6A.1.1 Background

The problem of contamination resulting from ionizing radiation has long been known. Berthelot and Gaudenchon first observed the polymerization of organic molecules under ultraviolet illumination in 1910.[4] Contaminating films cause widespread problems in electron microscopy, including both charging of electron optics[5] and changes in specimens after long-term illumination.[6] Hillier[7] reviewed existing evidence in 1948 and correctly noted that the growth is due to electron-beam-induced deposition of carbon from organic molecules present in the vacuum system.

In 1983, Boller et al.[8] investigated the carbon contamination associated with synchrotron radiation. In their model, the interaction between energetic photons and a mirror surface creates secondary electrons that have sufficient energy to break the bonds of adsorbed organic molecules, eventually forming a solid carbonaceous layer or bonding with the surface of the mirror. The growth of carbon often led to an unacceptable decrease in reflectivity and a need to clean the carbon from the mirror.

The problem was also known to astrophysicists using spacecraft to observe the sun. The first long-term observation of this effect was on the Solar and Heliospheric Observatory (SOHO),[9] which was launched in 1995. SOHO instruments exhibited various degrees of degradation, summarized in Ref. 10. The environment of SOHO has some similarity to that of an EUVL tool in that water and organics outgassed from the spacecraft can interact with solar EUV photons. However, the gas pressures are lower, and the incident spectrum is considerably different: the solar spectrum is broader, the intensity is lower, and the radiation is continuous-wave (cw) rather than being delivered in nanosecond-duration pulses.

We shall focus on the EUVL projection optics, which are near-normal-incidence mirrors consisting of precisely figured substrates coated with alternating layers of Mo and Si (see Fig. 6A.1). Such multilayer coatings, first developed by Spiller,[11] enable high reflectivity and wavelength selectivity of EUV mirrors. In addition to the contamination problems observed on all optics exposed to ionizing radiation, there was an initial concern about the stability of the multilayers against interdiffusion. An early study reported that

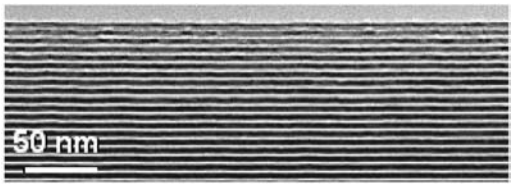

Figure 6A.1 Cross-sectional TEM image of the top part of a typical EUV multilayer. The multilayer mirror usually consists of 40 Mo/Si pairs. Silicon (low Z) is less absorbing and shown here as bright layers, while Mo (high Z) layers are dark (reprinted from Ref. 15).

Downloaded From: https://www.spiedigitallibrary.org/ebooks/ on 09 Mar 2022
Terms of Use: https://www.spiedigitallibrary.org/terms-of-use

Mo/Si multilayer mirrors (MLMs) have long-term stability at room temperature.[12] In this study, a MoSi mirror with a 1-nm C capping layer was measured, stored in air for 20 months, and re-measured, with no observable decrease in the reflectivity. On the other hand, Mo-terminated multilayers were shown to degrade to about 75% of their original reflectivity when stored in air due to oxidation of the Mo top layer.[13] In a study of radiation hardness versus interdiffusion, a Mo/Si multilayer was exposed to monochromatic undulator radiation and found not to degrade.[14] The exposed dose to the mirrors was equivalent to a 1.2-year EUV exposure in the low-throughput lithography system considered at that time. The predicted optics lifetime was based on a 9-hour exposure with an average intensity of 0.75 W/cm^2 and vacuum pressure $<5 \times 10^{-8}$ mbar (1 mbar = 100 Pa). These results thus overestimated the optics lifetime because they were performed in high vacuum and not in a realistic environment typical of an EUV exposure tool, with remnants of water vapor and other contaminants. Other lifetime studies performed on Si-capped MLMs exposed the optics to EUV radiation doses equivalent to several months of lithographic conditions (assuming a higher than 10 wph throughput).[16] It was observed that the surface carbon deposition was dependent on the residual gas concentration in the vacuum chamber. However, no structural damage was observed within the bulk of the MLMs. In addition, the reflectivity was fully recovered with ozone cleaning, although ozone overexposure can lead to damage via surface-layer oxidation.

6A.1.2 The chemical processes

Figures 6A.2 and 6A.3 schematically show the processes that lead to carbonization and oxidation, respectively. Several pathways are available

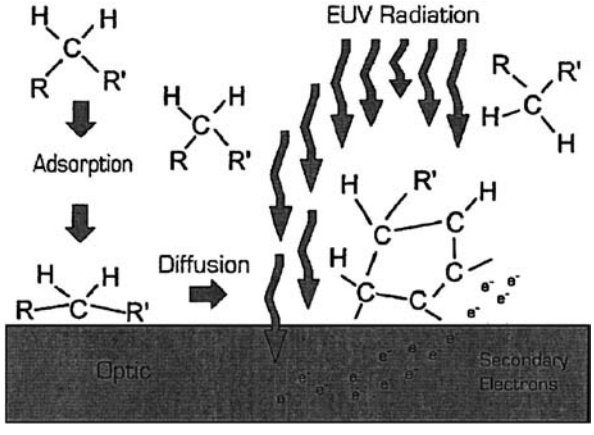

Figure 6A.2 Simple model showing the main radiation-induced processes related to carbon contamination (reprinted from Ref. 17 with permission from the American Vacuum Society).

Downloaded From: https://www.spiedigitallibrary.org/ebooks/ on 09 Mar 2022
Terms of Use: https://www.spiedigitallibrary.org/terms-of-use

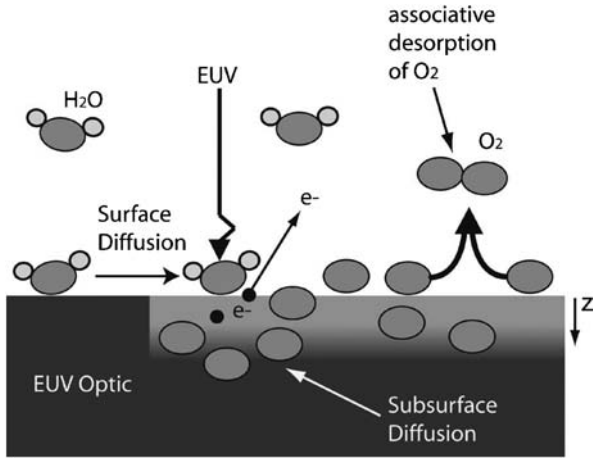

Figure 6A.3 Simple model showing the radiation-induced processes leading to oxidation of the optics surface (reprinted from Ref. 18 with permission from the American Vacuum Society).

after molecules adsorb onto the surface. The molecules may diffuse along the surface or thermally desorb. A photon may directly break a bond or stimulate desorption of the molecule, or it may do either of these indirectly via secondary-electron emission from the mirror. If an organic molecule is fragmented, this will lead to carbon deposition on the surface. If a water molecule is fragmented, the oxygen may diffuse into the mirror surface and create or increase the oxide layer.

6A.2 Optics Contamination Research

6A.2.1 Carbonization and oxidation: photons or photoelectrons

In high-volume manufacturing, the repeated introduction and EUV exposure of photoresist-coated wafers in the scanner means that the scanner's atmosphere will always contain levels of water and organics that are higher than in a research tool. The resulting combination of oxidation and carbonization depends on the balance between the two species and their activation by the EUV photons. The literature, however, is not clear as to whether the activation is predominantly done by the EUV radiation itself or by the secondary electrons generated by the EUV photons.

Boller et al.[8] carried out measurements of carbon growth using an undispersed synchrotron beam at different background pressures, doses, and temperatures. They constructed a semi-quantitative model based on incident molecular flux, cracking, and desorption. They observed a rapid growth of carbon for the first 5 nm, then a less rapid growth. A similar pattern was observed in the secondary-electron yield, which was consistent with the

Downloaded From: https://www.spiedigitallibrary.org/ebooks/ on 09 Mar 2022
Terms of Use: https://www.spiedigitallibrary.org/terms-of-use

smaller electron yield of carbon, leading to their model of secondary electrons as the predominant agent. The growth rate was weakly dependent on pressure because the pressure was governed only by a pumpdown time so that the pressure of water vapor, a mitigating gas, was considerably higher than any hydrocarbons. The authors observed a much higher growth at room temperature than at elevated temperatures, which is expected due to the lower adsorbate coverage at higher temperatures.

Hillier[7] investigated carbon growth in an electron microscope. He found that growth was very slow when the beam was illuminating only the thin-film sample being investigated, but much faster if part of the beam was hitting the support grid. This also seems to indicate the mechanism is initiated by secondary electrons.

Hollenshead and Klebanoff,[17,18] on the other hand, found via a combination of simulations and experiments that photo-absorption in the adsorbate is the primary mechanism driving carbon growth and oxidation. They calculated similar cross-sections for photons and secondary electrons, and since the measured total electron yield was just a few percent, they concluded that the vast majority of damage was due to photons. Their models also predicted reduced contamination at higher temperatures. Liu et al.[19] carried out measurements of desorption and dissociation of water on Ru(0001) surfaces. They found that the secondary electron cross-section was only about 20% to 25% as great as the photon cross-section.

Leontowich and Hitchcock[20,21] bear out the work of Boller et al.[8] They used an EUV microscope to focus the radiation down into a tunable monochromatic beam that irradiated a surface in an atmosphere of organic contaminants. They found that the rate of carbon growth varied strongly with the photon-absorption cross-section of the deposited carbon and not with that of the precursor molecules. With the reasonable assumption that the secondary electron emission of the deposited carbon varies with the carbon cross-section, one can conclude that the secondary emission is much more effective than the impinging photon flux in cracking the organic species. This is the most direct evidence that the primary growth mechanism is due to secondary electrons.

6A.2.2 The elimination of oxidation as a problem: requirements for oxidation-resistant cap layers

The EUVL community recognized the need for an oxidation-resistant cap layer.[22] Early experience with Si-capped Mo/Si MLMs revealed that Si was not very resistant to EUV-irradiation-induced oxidation. (Mo oxidizes more readily than Si and was never used as a terminal or cap layer.)

An ideal capping layer must satisfy many requirements, starting with its optical properties.[23] The reflectivity loss of the mirror at 13.5 nm due to absorption by the capping layer should be minimized. Initial screening of

Downloaded From: https://www.spiedigitallibrary.org/ebooks/ on 09 Mar 2022
Terms of Use: https://www.spiedigitallibrary.org/terms-of-use

various materials can be done using appropriate software and optical constants data;[24,25] however, given the need to maintain the highest possible reflectivity, one must actually test each of the initial candidate materials to eliminate any uncertainties.

The structure of the capping layer is also important. It must be smooth (on the order of 0.1-nm rms high-spatial-frequency roughness) and continuous, even though the layer is only 1–3 nm thick. These characteristics apply not only to the surface, but also to the interaction of the cap layer with the underlying layer of Mo or Si. Deposition must be done at temperatures below 100 °C to avoid intermixing in the underlying MLM stack, and it must generate minimal stresses in the film stack. The nanostructure of the capping layer, which plays a crucial role in surface chemistry, needs to be well-known and controllable. The capping layer should be impermeable to carbon and oxygen diffusion, either into or out of the MLM. If the capping layer is polycrystalline, this might require a specific crystallographic texture. Likewise, if the capping layer is amorphous, it should have no mobile vacancies.

Surface chemistry must also be considered. The capping-layer materials must be chemically inert with respect to air, the background gases (H_2, H_2O, CO, CO_2, hydrocarbons), and the stack materials. Different materials will also respond in different ways to mitigation and removal methods. Unfortunately, most of the existing surface science data are derived from well-characterized single-crystal sample surfaces. In practice, the capping layers are amorphous or polycrystalline, likely with high concentrations of defects and vacancies, so properties based on ideal single-crystal surfaces might be quite different from the properties of realistic capping-layer surfaces. Tsarfati et al.[26] studied a range of thin evaporated transition-metal thin films on Si/Mo bilayers. Of particular note, they found that 1.5 nm of Ru oxidized only upon exposure to atomic O. This exposure also removed all carbonaceous contaminants, while atomic H effectively reversed all of the oxidation.

Capping-layer materials must be thermally stable and stable against EUV-radiation-induced processes. Finally, the capping layer should be cost-effective and in accordance with environmental, health, and safety regulations during its manufacture and use.

6A.2.3 Development of contamination-resistant cap layers

Because of the proprietary nature of some of the materials being tested as capping layers, most of this section will be limited to the development of ruthenium capping layers, which were chosen by SEMATECH as a standard benchmark capping layer, and for which the results have been made public.

Figure 6A.4 shows a cross-section of the surface region of a Ru-capped MLM. Ru capping layers prepared with variations of voltage, current, sputtering gas, and target material were tested for their oxidation and thermal stability. The best capping layer was prepared using Ar sputtering gas and a

Downloaded From: https://www.spiedigitallibrary.org/ebooks/ on 09 Mar 2022
Terms of Use: https://www.spiedigitallibrary.org/terms-of-use

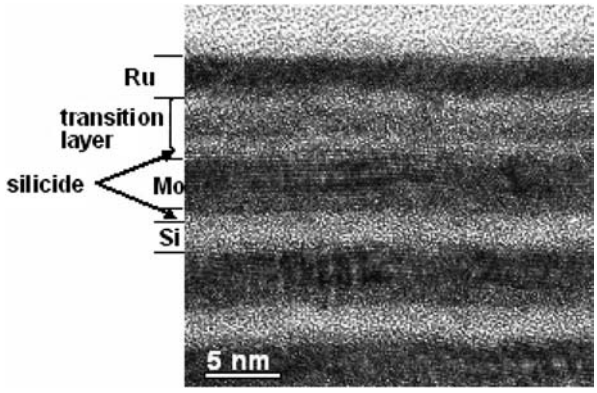

Figure 6A.4 Cross-sectional TEM image of an EUV multilayer showing the microstructure of the surface layers. The top dark layer is polycrystalline Ru deposited on top of the transition layer. Polycrystalline molybdenum and amorphous silicon layers are separated by thin, amorphous silicide layers (reprinted from Ref. 15).

metallic Ru target. TEM analysis of its microstructure[27] showed that it was the only one with preferentially oriented grains. In particular, Ru was polycrystalline with an average grain size of about 3.5 nm and a preferential growth orientation with Ru(0001) crystal planes parallel to the specimen surface. Based on limited TEM data, it appears that the Ru capping layers of other preparations had smaller, randomly oriented, and mostly oxidized grains.

As part of a SEMATECH-funded project, Lawrence Livermore National Laboratory (LLNL) also fabricated and tested five more capping-layer candidates. In descending order of reflectivity, measured as well as calculated, the candidate materials were SiC, yttria-stabilized zirconia, $MoSi_2$, PdAu, and Pd.[28] Due to limited funding, the capping-layer deposition processes were not optimized, and the capping layers had different deficiencies. For example, the Pd and PdAu capping layers showed island growth. These metals were also observed to diffuse into the underlying multilayer, which could possibly have been mitigated with a diffusion-boundary layer. The other materials appeared to allow oxidation of a few lower layers. None of these materials outperformed Ru.

After Ru, the most widely used capping layer is TiO_2, which has favorable optical and surface-reactivity properties. Adding a 2-nm-thick TiO_2 capping layer reduces the reflectivity by only 0.8%. This material belongs to the class of semiconductors with a relatively wide bandgap in the near UV. Exposing TiO_2 to photons with energy greater than the bandgap produces charge carriers, which cause oxidation-reduction reactions to occur on the TiO_2 surface. A TiO_2 thin film has strong oxidizing power and high photocatalytic activity for hydrocarbon oxidation,[29] suggesting that a TiO_2 capping layer could be self-cleaning. Work by Kim et al.[30] indicates that reactive magnetron

Downloaded From: https://www.spiedigitallibrary.org/ebooks/ on 09 Mar 2022
Terms of Use: https://www.spiedigitallibrary.org/terms-of-use

sputtering allows for control of the structure, composition, and properties of TiO_2 films. Studies at LLNL found that reactive RF sputtering of a TiO_2 target with $Ar:O_2$ sputtering gas produced a TiO_2 capping layer with good properties: the MLM had a reflectivity that was greater than 66%, and its lifetime under exposure to H_2O vapor was longer than for a Ru-capped MLM.[31] TEM studies show that the TiO_2 capping layer was amorphous, continuous, and fully covered the multilayer. Furthermore, the TiO_2 layer formed a sharp interface with Si so that no diffusion barrier was necessary. However, x-ray photoelectron spectroscopy (XPS) and scanning transmission electron microscopy (STEM) analysis indicate that Ar gas was incorporated into the TiO_2 capping layer. Yulin et al.[32] optimized deposition processes for MoSi multilayers with TiO_2 and RuO_2 cap layers, both with engineered interfaces.

Work on other alternative cap layers, many of which were discussed theoretically in Ref. 22, continues. Kriese et al.[33] recently investigated SiO_2 and ZrO_2 as potential cap layers. Unfortunately, the lack of a fundamental understanding of the surface chemistry in realistic environments makes it difficult to optimize the capping layer. For the present, ruthenium appears to be adequately resistant to damage caused by oxidation and hydrogen cleaning.

Industry eventually made the development of capping layers confidential, in part because the environmental conditions in the scanner (residual gas pressures and species) were confidential. Also, while depositing Ru can be done in DC mode, depositing oxides can require RF mode or pulsed laser deposition, elevated temperatures, and a sputter gas mixture of inert gas and oxygen—methods that are more complicated and riskier. This was the primary reason for SEMATECH's decision to use Ru as a standard benchmark capping layer for optics lifetime tests.

6A.3 Optics Contamination Experiments

6A.3.1 Facilities

The majority of early optics lifetime tests were performed both with electron (see Fig. 6A.5) and synchrotron EUV beams (see Fig. 6A.6) in specially built test chambers. The contamination test chambers, which could accommodate high gas pressures (up to 10^{-2} mbar), were typically separated from the upstream components through differential pumping or by a thin-film filter. The use of electron-beam irradiation was justified by initial evidence that irradiation with keV-energy electrons and 13.5-nm EUV photons resulted in similar oxidation rates on Si-capped MLs, with 1 μA of electron-beam current roughly equivalent to 1 mW of EUV power.[34] However, the apparent equivalence of the two methods was short-lived; results on Ru-capped MLs[35] showed differences due to the different surface chemistry and damage mechanisms.

Downloaded From: https://www.spiedigitallibrary.org/ebooks/ on 09 Mar 2022
Terms of Use: https://www.spiedigitallibrary.org/terms-of-use

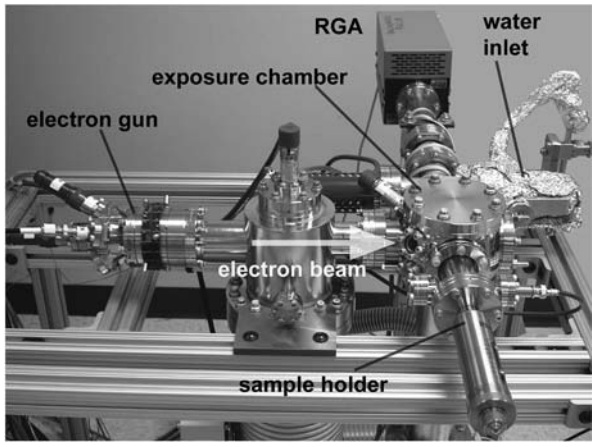

Figure 6A.5 Initial lifetime experiments were performed with electron beams. This photograph shows a setup at Sandia National Laboratories (SNL) (reprinted from Ref. 15).

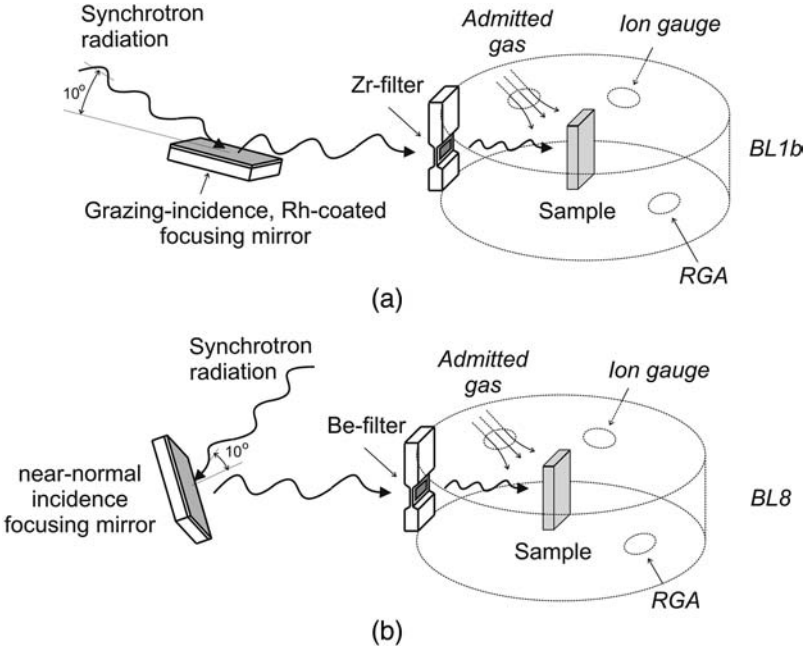

Figure 6A.6 Schematics of the end stations on (a) beamline 1b (BL1b) and (b) beamline 8 (BL8) at the NIST Synchrotron Ultraviolet Radiation Facility used for EUV-optics lifetime studies. Both end stations have a residual gas analyzer (RGA) to monitor the cleanliness and composition of the vacuum (reprinted from Ref. 43).

In recent years, most lifetime testing has been done with EUV photons. After initial work[33,35] at LBNL's Advanced Light Source (ALS), most of the testing of optics lifetimes proceeded on dedicated EUV sources. The Japanese

Downloaded From: https://www.spiedigitallibrary.org/ebooks/ on 09 Mar 2022
Terms of Use: https://www.spiedigitallibrary.org/terms-of-use

efforts are centered at the BL-3 beamline in the NewSUBARU synchrotron facility.[36] The research guided by ASML is being performed at several locations: at the ASML and the TNO laboratories with hollow-cathode-triggered pulsed sources;[37] and at the PTB Radiometry Laboratory, BESSY II, in Germany,[38] initially on the U180 undulator beamline[39] and later on the DLW 20 dipole bending magnet beamline.[40] Work in the U.S. has centered at two beamlines (BL1b and BL8) at the NIST Synchrotron Ultraviolet Radiation Facility (SURF III).[41,42] Comparison of results among the different facilities requires careful consideration of the exposure bandwidth, intensity, time structure (i.e., pulsed duty factor and peak versus average intensity), temperature, sample type, and vacuum environment, including the calibration of partial pressure measurements.

6A.3.2 Carbonization: admitted-gas studies

Although the initial contamination tests focused on the oxidation resistance of MLMs, lifetime testing performed under "real" tool conditions showed that ambient hydrocarbons play an important role in reducing oxidation of Ru capping layers.[44] In accelerated experiments where water vapor pressures were high ($>5 \times 10^{-7}$ mbar), the EUV-irradiation-induced damage on Ru capped MLMs decreased with increasing levels of water.[45] These results are explained by the presence of low-mass carbon-containing species in the chamber[45,46] as follows. A residual gas analysis made prior to the admission of the water showed low levels of low-mass carbon species. Subsequent measurements also could not detect these species coming from the water source. Hence, they were most likely displaced from the vacuum-chamber walls by the admitted water vapor.

These early observations coupled with the observation of the carbonization of optics and masks in the early test tools led to more extensive admitted-gas tests with organic molecules. Experiments were carried out in the facilities described in section 6A.3.2.1. Admitted gases have been selected to include resist outgas products[47] and other molecules observed in scanners,[48] and covering a wide range of vapor pressures. In order to make an informed guess as to the contamination rates from atmospheres containing organics, both the contaminant partial pressure and EUV intensity had to be varied over significant ranges.

6A.3.2.1 Intensity dependence

Intensity dependence falls between two limiting regimes referred to here as "photon-limited" and "mass-limited." At low intensities, the photon-limited contamination rate scales linearly with intensity and is determined by the equilibrium surface coverage of precursor molecules resulting from the balance of impingement from the gas phase and thermal desorption from the surface. At sufficiently high intensities, every adsorbed molecule will undergo an EUV-stimulated reaction before thermally desorbing, resulting in a mass-limited contamination rate that is independent of intensity. The distinction

Downloaded From: https://www.spiedigitallibrary.org/ebooks/ on 09 Mar 2022
Terms of Use: https://www.spiedigitallibrary.org/terms-of-use

between these two regimes can be complicated by the temporal characteristics of the source. Synchrotron sources used at some of the testing facilities that have pulse repetition rates in the MHz or tens of MHz range can be considered quasi-cw. The pulsed sources used at other experimental facilities have pulsed source with repetition rates between 0.1 kHz and 10 kHz. One expects that most pulsed sources used in these facilities have relatively small duty factors so that at an average intensity that would be in the low intensity region for a cw or quasi-cw source, the instantaneous intensity in the pulse is actually in the intensity saturated regime where the amount of contamination per photon is less than in the linear regime. Thus, for a given partial pressure of a contaminant species, we would expect the same or less contamination per unit dose for a pulsed source relative to a cw source operating at same average intensity, a difference that has actually been observed by Wolschrijn et al.[49]

Exposing a sample at several pressures, and each pressure at several EUV intensities, would be time consuming. To avoid this issue, Hill et al.[50] took advantage of the inherently quasi-Gaussian intensity distribution of their synchrotron beam at NIST, which could be accurately characterized with high spatial resolution. Thickness maps of the resulting carbon spots were then measured using both XPS and spectroscopic ellipsometry (SE) with sufficient spatial resolution that each map location could be correlated with a known EUV intensity. With this technique, the intensity dependence at a given pressure could be measured over a wide range of intensities with a single exposure.

Figure 6A.7 shows the results of such measurements using the high-intensity, broadband-EUV exposure facility on BL1b at NIST.[43] In order to eliminate effects due to standing-wave resonances in MLMs, these and subsequent measurements were made with trilayer samples consisting of the final three layers of a multilayer. The contamination rate scales linearly with intensity for highly contaminating species, such as toluene, tetradecane, and diethylbenzene, at partial pressures above 10^{-7} mbar. At lower pressures, however, the contamination rate begins to saturate with increasing intensity for these species, while benzene shows signs of saturation even at the elevated pressures. This behavior is consistent with two regimes of carbon growth for intensities significantly above (mass-limited) or below (photon-limited) a certain threshold, or saturation intensity I_{sat}. For intensities below I_{sat}, the rate at which adsorbed gas molecules are converted to deposited C is much smaller than the rate of thermal desorption. Hence, the C growth rate is proportional to the coverage of adsorbed precursor molecules on the surface in equilibrium with the ambient partial pressure. Since this steady-state coverage is not significantly affected by the EUV-irradiation-induced cracking, the contamination rate is photon-limited and scales linearly with intensity. For intensities much above I_{sat}, the situation is reversed; every molecule that adsorbs on the surface is likely to undergo a photon-stimulated reaction and adds to the

Downloaded From: https://www.spiedigitallibrary.org/ebooks/ on 09 Mar 2022
Terms of Use: https://www.spiedigitallibrary.org/terms-of-use

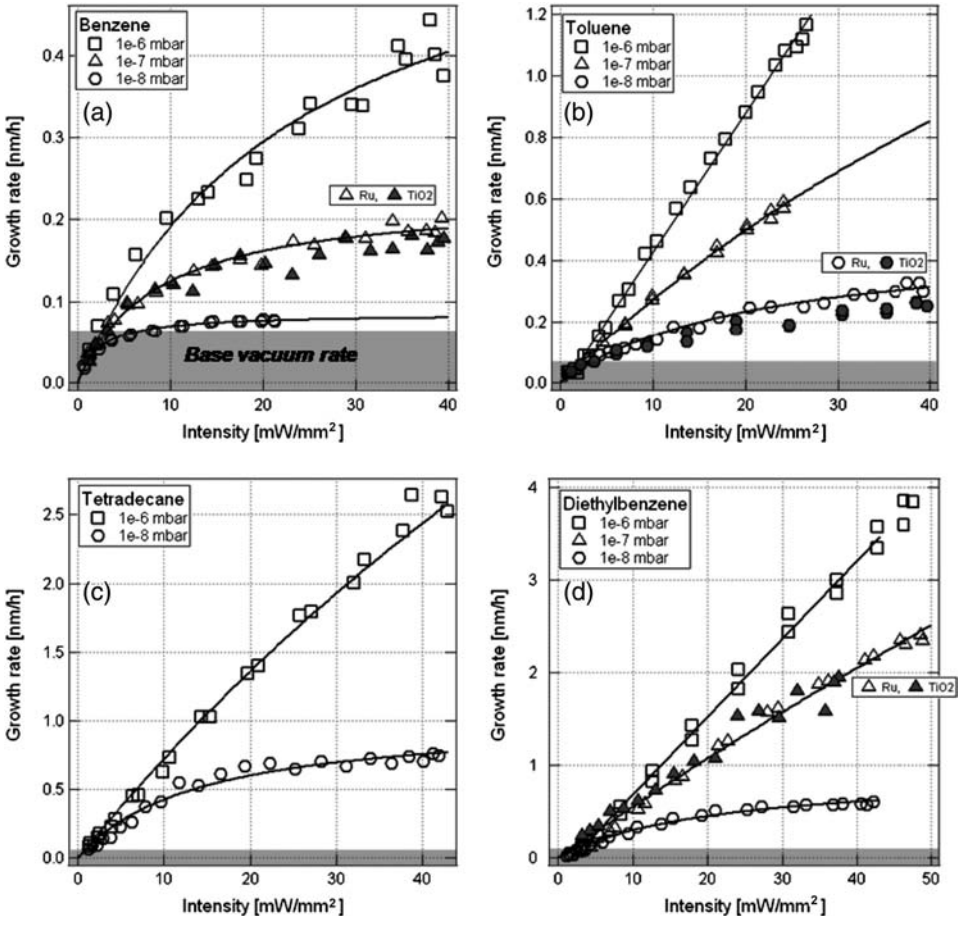

Figure 6A.7 Contamination rates for Ru-capped (outlined symbols) and TiO_2-capped (solid symbols) multilayer samples exposed to broadband EUV radiation on BL1b at the NIST synchrotron over a range of partial pressures of (a) benzene, (b) toluene, (c) tetradecane, and (d) diethylbenzene. The rates are determined by dividing the XPS-measured thickness by the exposure time. Partial pressures are reported without correction for ionization gauge sensitivity factors. Gray horizontal bands represent the intensity-independent background contamination rate of $\approx$ 0.07 nm/h with no admitted gas (reprinted from Ref. 43).

growing carbon layer before it thermally desorbs. In this mass-limited regime, the contamination rate will be independent of intensity and proportional to the rate at which molecules arrive at the surface, i.e., proportional to pressure.

6A.3.2.2 Pressure dependence

The linear pressure scaling in the mass-limited regime is indicated by the data in Fig. 6A.7(a). After subtraction of the background contamination rate (indicated by the gray horizontal bands), the asymptotic mass-limited rates for

Downloaded From: https://www.spiedigitallibrary.org/ebooks/ on 09 Mar 2022
Terms of Use: https://www.spiedigitallibrary.org/terms-of-use

$I \gg I_{sat}$ increases by roughly an order of magnitude for each decade of pressure rise from 10^{-8} mbar to 10^{-6} mbar.

For intensities below I_{sat}, in the photon-limited regime, the time rate of carbon growth (nanometers per hour) scales linearly with intensity, and the deposition is best characterized by the dose rate of carbon growth [nm/(mJ/mm^2)], which is given by the constant slope of the linear portions of the plots in Fig. 6A.7, for $I \ll I_{sat}$. It is clear from casual inspection that the slopes of the lines for 10^{-6} mbar curves in Figs. 6A.7 (b) and (d) are not 10 times larger than those for the 10^{-7} mbar data. This suggests that the pressure scaling of the dose rate of carbon growth in the photon-limited regime is highly sublinear. Indeed, a more extensive set of exposures on the lower-intensity, narrowband BL8 at NIST found the quasi-logarithmic dependence on pressure shown in Fig. 6A.8 for several species. Here the dose rate of C growth has been converted to a time rate of growth by reporting values at a specific intensity of 1 mW/mm^2.

The highly sublinear pressure dependence can be understood by considering that the surface density (coverage) of adsorbed molecules in the absence of EUV irradiation is determined by the equilibrium established between the impingement rate (and sticking coefficient) of molecules on the surface and the rate at which they are thermally desorbed. Direct measurements made by Yakshinskiy et al. of equilibrium coverages have demonstrated that the desorption rate increases with increasing coverage.[51,52]

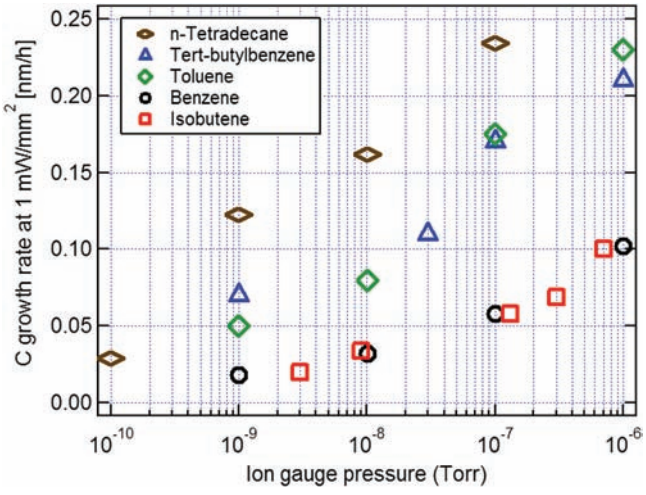

Figure 6A.8 Carbon growth rate on TiO_2-capped trilayer samples exposed to 1 mW/mm^2 of 13.5-nm radiation on BL8 of the NIST synchrotron in the presence of various pressures of five contaminant gases. Absolute partial pressures are accurate to within a factor of ±3 due to uncertainties in ionization gauge sensitivity and calibration for each gas. Relative uncertainties between pressures of a given gas are ±20%. Molecules are: n-tetradecane, $C_{14}H_{30}$; tert-butylbenzene, $C_{10}H_{14}$; toluene, C_7H_8; benzene, C_6H_6; and isobutene, C_4H_8.

Downloaded From: https://www.spiedigitallibrary.org/ebooks/ on 09 Mar 2022
Terms of Use: https://www.spiedigitallibrary.org/terms-of-use

The linear increase of impingement rate with pressure must compete with a simultaneous increase in desorption rate as the coverage grows with pressure. This results in the observed sublinear, quasi-logarithmic pressure scaling of equilibrium coverage and hence contamination rates. One possible reason for the coverage-dependent thermal desorption rate is that surface defects lead to a distribution of adsorption sites and energies. This model is often referred to as a Temkin-like isotherm,[53] as opposed to the more commonly employed Langmuir isotherm,[54] which assumes a constant, uniform adsorption energy.

The fact that carbon growth rates in the photon-limited regime seem to have a strongly sublinear dependence on pressure over many decades creates difficulties in extrapolating the results of some admitted gas tests to extremely low pressures. As illustrated in Fig. 6A.9, if a single measurement is made at high pressure in the photon-limited regime and linearly extrapolated to zero pressure, the lowest curve is obtained. A Langmuir extrapolation using the top three points gives something intermediate, while using all of the points and assuming a power-law dependence gives a result four orders of magnitude higher than the linear extrapolation. In order to extrapolate using a linear pressure dependence, the intensity must be high enough that the contamination occurs entirely in the mass-limited regime for both the measurements and the projected operating conditions.

The carbon growth rate obviously depends also on the type of molecule. The heavier organics have more carbon atoms and are generally stickier, so one would assume that the contamination rate would increase—possibly faster than linearly—with mass. However, the growth rates for a given pressure have a more complicated dependence on mass. As shown in

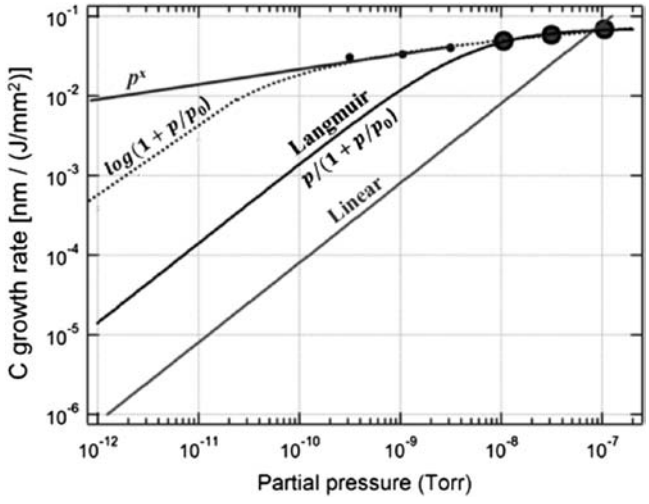

Figure 6A.9 Dose rate of contamination growth as a function of the partial pressure of tert-butylbenzene with four potential extrapolations of measured data to very low pressures.

Downloaded From: https://www.spiedigitallibrary.org/ebooks/ on 09 Mar 2022
Terms of Use: https://www.spiedigitallibrary.org/terms-of-use

Fig. 6A.8, the growth rate from toluene, with seven carbons, is almost twice that of benzene with six carbons, while that of isobutene, with four carbons, is roughly equal to that of benzene.[55] The vapor pressure of isobutene is also much higher than that of benzene, which should lead to a lower coverage of the former. Nevertheless, the rates observed for benzene and isobutene are similar.

6A.3.2.2 Wavelength dependence

The carbon growth rates were measured for three different species under identical conditions when irradiated by different bandwidths of EUV/UV light. Three different filters were used on BL8 at NIST to achieve the different irradiance spectra shown in Fig. 6A.10(b). Also included is the broadband output of BL1b. Figure 6A.10(a) plots the contamination rate per unit dose for each bandwidth in the photon-limited regime. The rates are normalized to those measured for the inband configuration of BL8 with a Be filter. The dramatic increase in contamination rate with wavelength from 10 nm to

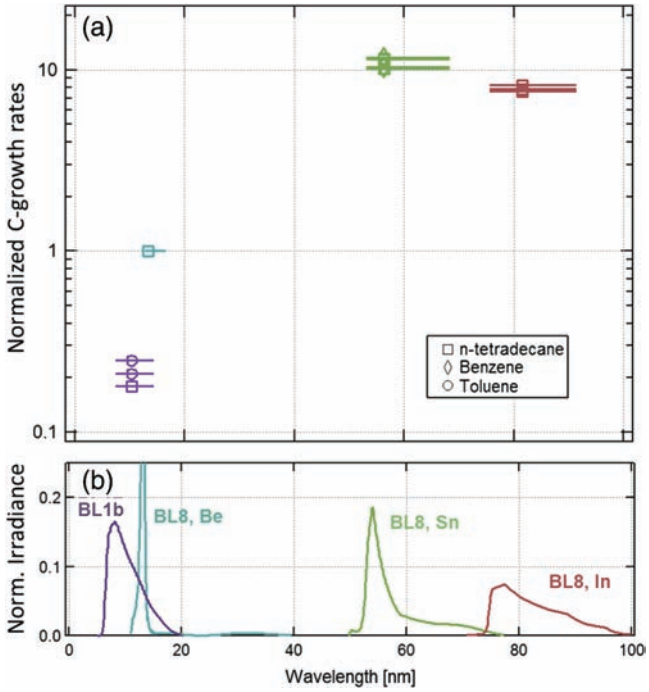

Figure 6A.10 (a) Carbon growth rate for several wavelength bands. Horizontal bars contain 80% of power for each configuration. (b) Calculated exposure spectra for the two NIST beamlines, BL1b and BL8, shown schematically in Fig. 6A.6. A Zr filter was used on BL1b, while Be, Sn, and In filters were used on BL8, as indicated. The plotted irradiance of each configuration was normalized to the area (total power) of the inband spectra for BL8 with a Be filter.

Downloaded From: https://www.spiedigitallibrary.org/ebooks/ on 09 Mar 2022
Terms of Use: https://www.spiedigitallibrary.org/terms-of-use

60 nm suggests that even low-intensity, out-of-band radiation could pose a contamination risk to lithographic systems.

The general trend of increasing contamination rate with wavelength in the range of 10 to 80 nm has been observed experimentally[56] and predicted by models.[16] A likely explanation of this behavior is that both the (gas phase) photo-absorption cross-section and the secondary electron yield for C increase to a maximum around 70 nm and drop rapidly at shorter wavelengths down to the C 1s absorption edge at 4.4 nm.

It should be noted that the samples exposed on BL8 were TiO_2-capped multilayers, while those on BL1b were Ru-capped; however, the rates were very similar for both capping materials in all cases where growth rates were measured on both substrates. [Compare open and filled symbols in panels (a), (b), and (d) of Fig. 6A.7.]

6A.3.2.3 Metrology of EUV-irradiation-induced carbon contamination

The thickness of the carbon (or oxide) deposited during contamination experiments such as those discussed above was typically measured using XPS and/or SE. The latter technique has many practical advantages over the former. SE is more widely available than XPS, it can be performed in air rather than vacuum, and it can typically measure small contamination spots with higher spatial resolution in much less time than XPS. SE also has precision well below a nanometer with equivalent accuracy when used to measure films of known composition and optical properties (e.g., SiO_2 or films deposited by a well-characterized industrial process). Unfortunately, the structure, morphology, and resulting optical properties of the carbon deposited by EUV-induced cracking are not well known and may vary significantly depending on the exposure conditions (as we will demonstrate below). Although it is possible to fit a reasonable optical model to a uniform, relatively thick ($\gg$10 nm) carbonaceous film of unknown structure and simultaneously determine its thickness using SE, this procedure is not reliable for a typical EUV-contamination deposit with a distribution of thicknesses $<$3 nm. Instead, an assumed optical model with fixed parameters must be applied, even though the structure may vary across the deposit.

Since the absolute thickness determined by SE depends critically on the optical model used to fit the data, XPS is a more reliable method for comparing carbon thicknesses deposited under varying conditions. The most common method for determining thickness using XPS is to measure the attenuation of the substrate signal (e.g., the Ru 3d or 3p peaks for Ru-capped MLMs or the Ti 2p peak for TiO_2-capped MLMs) caused by the overlayer of C. To use this technique, one must assume a practical effective attenuation length (EAL) for the photoelectrons originating in the substrate as they pass through the carbon film. The resulting C thickness will be proportional to the assumed EAL. A range of calculated and measured EALs is reported in the

Downloaded From: https://www.spiedigitallibrary.org/ebooks/ on 09 Mar 2022
Terms of Use: https://www.spiedigitallibrary.org/terms-of-use

literature,[43] and the results presented here use 2.08 nm for Ti 2p and Ru 3p substrates, as measured by Lesiak at al. for graphite with density 2.2 g/cm^3.[57]

Although there is not a universally accepted value for the EAL of EUV-deposited C, this quantity is much less sensitive to variations in the morphology and composition of carbon than the optical properties, and hence thicknesses, reported by SE. As reported by Hill et al., Fig. 6A.11 demonstrates this difference by overlaying a collection of thickness profiles from XPS and SE maps of several EUV-induced carbon deposition spots.[43] Also shown are the EUV dose profiles used to make the deposited carbon. The exposures were made at a variety of pressures; thus, there is not a common correlation between dose and thickness for all the profiles. The measurements show a dose-dependent discrepancy between thicknesses determined by XPS and SE that becomes quite pronounced for exposures with the largest peak doses in the center of the spots. In all cases, however, there is a good agreement in the wings of the C distributions where the local dose decreases to zero. One possible explanation of this dose-dependent

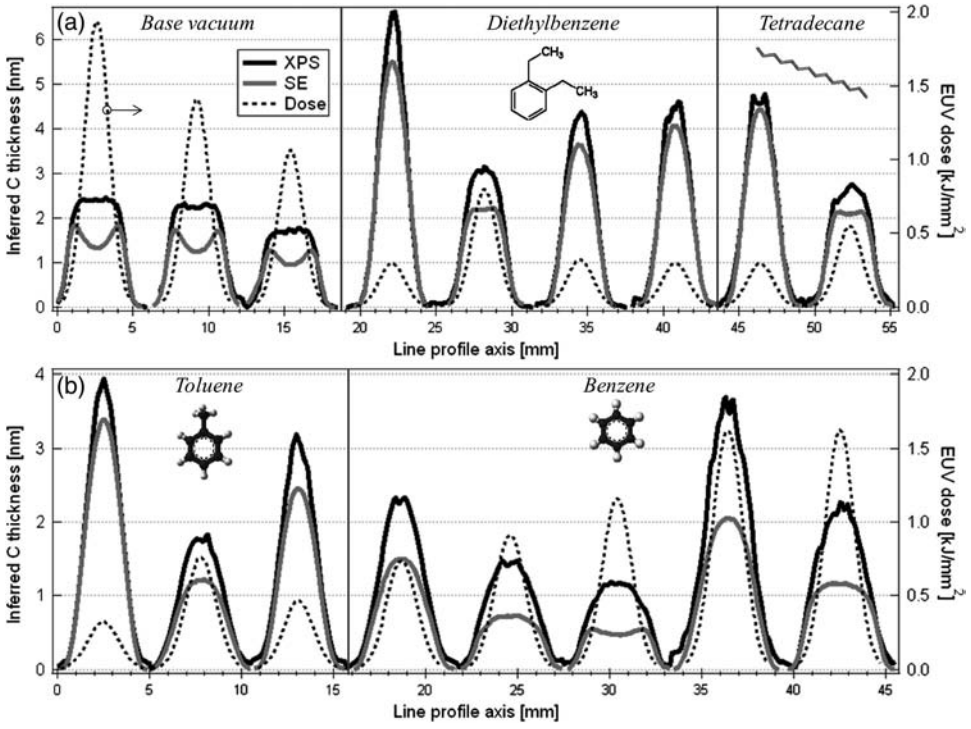

Figure 6A.11 Collected profiles of C thickness inferred from XPS and SE along lines through the centers of contamination spots created by EUV exposure in the base vacuum and various partial pressures of admitted (a) diethylbenzene and tetradecane. (b) toluene and benzene. The EUV dose distributions across the exposure spots are also plotted (dashed lines, right axis) (reprinted from Ref. 43).

Downloaded From: https://www.spiedigitallibrary.org/ebooks/ on 09 Mar 2022
Terms of Use: https://www.spiedigitallibrary.org/terms-of-use

correlation between XPS and SE is that the composition of the carbonaceous contamination is altered by subsequent EUV irradiation after its initial deposition. This hypothesis is supported by two previous studies. Matsuura et al.[58] reported that irradiation of amorphous chemical-vapor-deposited C by broadband synchrotron radiation resulted in a monotonic decrease of H content and increase in density with radiation dose. Nishiyama et al.[59] examined EUV-deposited C with several different metrologies, showing that the H content of EUV-deposited films was significantly lower in the deepest layers of the deposit that received the highest cumulative EUV dose. Both of these independent studies suggest that EUV irradiation will reduce the H content and increase the density of EUV-induced C deposits. Such variations in composition will skew the thickness reported by SE since a fixed optical model must be assumed across the entire spot. These findings are consistent with the NIST results shown in Fig. 6A.11.

6A.4 Resist Outgas Testing

6A.4.1 Early measurements

If sufficient care is taken in constructing a tool, the most probable cause of optics contamination would be the outgassing of the photoresist during EUV exposure. In order to gauge the contamination potential of this outgassing, a method was sought to qualify the photoresist before its use. Many groups worked on this problem, initially using three techniques.

The simplest method developed was to measure outgassing by a pressure-rise method.[60] This method involves measuring the pressure rise while irradiating a wafer with EUV. Using a calibrated gauge and knowing the pumping speed, the rate and total outgassing can be calculated. These tools have often been equipped with RGAs for partial chemical analysis. This method has the advantage of being reasonably simple, but little is learned about the actual complicated molecular components of the outgassing because of the difficulty in interpreting the RGA spectra.

A second method employed an RGA pointed directly at the illuminated spot.[61,62] Knowing the intercepted solid angle of the RGA and its absolute efficiency for detecting different molecules, the partial pressure, and thus outgassing rate, can be calculated for the different molecular fragments. Among the disadvantages is, again, the limited capability to interpret the RGA spectra. Additional complexities include fragmentation patterns that may be tool-specific and differences in conduction speeds among fragments of different mass. Careful calibration of each RGA over a wide mass range would also be required to compare results from different instruments.

A third method involved exposing the resist in an initially evacuated, unpumped chamber. After the exposure is complete, the chamber is filled with helium, which flows through the chamber and through a thermal desorption

Downloaded From: https://www.spiedigitallibrary.org/ebooks/ on 09 Mar 2022
Terms of Use: https://www.spiedigitallibrary.org/terms-of-use

tube.[63,64] Organics stick to the desorption medium. The tube is subsequently removed from the chamber and analyzed by a gas chromatograph with a mass spectrometer (GC-MS) detector. Helium is again flowed through the tube while it is heated, and the organics become volatilized and are subsequently deposited into a small cold region at the head of the GC column (cryofocus). Releasing the sample into the chromatography column separates species depending on their mobility, thus enabling a more specific analysis of the mass spectra than the RGA method, in which all outgas products (as well as background gases) are present all the time. However, the desorption tubes have sticking coefficients that are less than unity and vary with species and thus skew the chemical analysis.

SEMATECH conducted a round-robin with eight labs employing the three techniques described above.[47] The results for total outgassing differed by four orders of magnitude among the labs; however, if the highest and the lowest results are not used, the results are within a factor of 30. The labs using the desorption-tube method had the two lowest results, but there was no pattern among the labs using the total-pressure-rise method and the RGA method.

The large disparities observed in the SEMATECH round-robin motivated the development of a fourth method with less uncertainty. This method combined the total pressure rise with a subsequent chemical analysis.[65] Before the EUV illumination was turned on, all pumping of a very small chamber was valved off, and the pressure rate-of-rise was measured with a calibrated gauge. The pressure rise was monitored during and after EUV illumination, and the difference between the final pressure and that expected based on the background outgassing was the total rise due to the photoresist outgassing during illumination. The outgas products were then collected by cooling a trap to liquid-nitrogen temperature, and the collected products were subsequently analyzed in a GC-MS with cryofocusing. The trap collected all outgas products heavier than CO. Also, the very small volume of the chamber led to significant pressure rises that were easily measured by a calibrated capacitance-diaphragm gauge, which is species-independent. However, the heaviest, least-volatile outgas products were likely deposited onto the chamber walls and thus were not counted in the pressure rise nor trapped in the cryotrap.

In a subsequent intercomparison among three of the eight labs involved in the round-robin, NIST, IMEC, and CNSE found agreement within 30% for the total outgassing and identification of the same species.[66]

Contemporaneous with the photoresist outgas testing activity was a measurement to determine the relative contributions of the outgassing from photoresist and from the tool itself. The measurement, which was a modified version of the fourth outgassing method, was employed on one of the first preproduction micro-exposure tools at Intel.[67] In this case, a large liquid-nitrogen-cooled trap was employed and opened to the tool for several hours. Subsequent GC-MS analysis of the collected material found ketones and

Downloaded From: https://www.spiedigitallibrary.org/ebooks/ on 09 Mar 2022
Terms of Use: https://www.spiedigitallibrary.org/terms-of-use

aldehydes, likely from partial oxidation of hydrocarbon contaminants, as well as silicones, likely introduced from the ambient air in the clean room either during servicing or during the use of the loadlock. Subsequent EUVL tools were operated and maintained with more attention to cleanliness and did not suffer from these sorts of contamination.

6A.4.2 Witness-sample testing

The intercomparison difficulties described above caused ASML and others in the EUVL community to conclude that not only were there difficulties in the standardization of intercomparisons, but there was also no reliable method to predict the optics contamination from the available measurements, including chemical analyses of the photoresist outgas. For this reason, ASML proposed witness-sample testing in 2006 (see Ref. 68).

The witness-sample test consists of irradiating a witness sample in the same vacuum environment as a simultaneously irradiated photoresist. The thickness of the carbon contamination on the witness sample produced by the resist outgassing was subsequently measured using SE with an optical model specified by ASML. The carbon was then removed with hot-filament-generated atomic hydrogen, and the witness sample was analyzed using XPS to check for non-cleanable trace elements. During the exposure portion of the test, the dose to the resist must be the dose-to-clear E_0 as measured on that tool, and the witness sample must have a Ru surface so that its behavior mimics that of a Ru-capped multilayer. The illumination of the resist and witness sample may be EUV photons or electrons, but the irradiation of the witness sample must have sufficient intensity or current to lead to mass-limited growth. With mass-limited growth, test depends more on the characteristics of the resist than on the exposure tool.

Witness-sample testing is time-consuming and expensive, so many attempts have been made to develop alternative tests through simpler means. Many of the witness-sample-testing tools are fitted with RGAs capable of measuring low outgassing levels, and the resulting RGA spectra obtained during exposure can be correlated with the results of contamination-growth tests. Pollentier et al.[69] found that the contamination growth correlates well with a weighted integral over the mass spectrum, where the integrand is the product of the RGA signal with the mass raised to an empirically determined power. This correlation is likely due to the availability of an increasing number of carbon atoms, plus the lower volatility of species with greater masses. Unfortunately, the correlation, while useful, is not well understood because it appears to depend on whether the exposure was performed by EUV photons or electrons, and it varies with electron-beam energy.

Another correlation effort at the Evolving nano-process Infrastructure Development Center (EIDEC) focused on the grouping of resists into families whose composition (polymer backbone, photo-acid generator (PAG) and

Downloaded From: https://www.spiedigitallibrary.org/ebooks/ on 09 Mar 2022
Terms of Use: https://www.spiedigitallibrary.org/terms-of-use

quencher loading) was identical.[70] This study found that if the resist components are the same, the contamination growth increases with both PAG and quencher loading. Thus, the maximum contamination growth from this resist family would be that from a formulation having the highest expected PAG and quencher loading. A similar study found that the higher loading led to a greater contamination at the same dose, but that the E_0 value of the resist can be reduced enough that the contamination growth at E_0 is actually lower.[71] Later work at SEMATECH investigated different resist families with known PAG concentrations. When the concentrations of protecting unit and quencher were fixed, the carbon growth was linearly correlated with value of E_0, with the resist having the largest PAG concentration being the least contaminating.[72]

ASML's original specification for the witness-sample test required—for the exposure of one 300-mm wafer equivalent—less than 3 nm of contamination growth on the witness sample and, after hydrogen cleaning, less than a 0.23% reflectivity decrease caused by non-cleanable contamination (0.16% for second-generation tools).[73] In 2014, the unexpectedly good performance of in-tool mitigation[3] allowed the contamination growth to be relaxed to 10 nm,[74] and in February 2015, the test requirement of all conventional chemically amplified resists was suspended for the rest of the year.[75] The suspension was made permanent later that year at the IEUVI Resist TWG at the EUVL Symposium (5–7 October 2015, Maastricht, The Netherlands). During 2011–2015, the witness-sample test was key to the EUVL industry's cautious approach to avoiding contamination from photoresist outgassing. That caution provided a margin of safety that allowed users to gain experience with preproduction scanners and demonstrate the effectiveness of hydrogen-based in-tool mitigation techniques.

6A.4.3 Witness-sample testing: nonconventional resists

The requirements for resist outgas testing were re-examined with the advent of novel resists such as nanoparticle-containing hybrids,[76] metal-oxide-based resists,[77] and organometallic resists.[78] Previous outgassing studies were performed entirely on organic materials with a limited number of constituent elements. The presence of outgas components containing metallic elements such as Sn, Hf, Bi, etc., in a hydrogen atmosphere created new concerns about the cleanability of various reaction products. The outgassing of some of these resists has been measured and found to be low, but until recently, this was done with a standard witness-sample test, which is conducted in vacuum without the presence of hydrogen. Since the atmosphere in an EUVL scanner may contain hydrogen at pressures of up to 1 mbar,[79–81] and many metals form volatile hydrides or other hydrogen-containing compounds that may not be cleanable, ASML promoted the development of resist testing in a hydrogen atmosphere that mimics the scanner environment in which the pulsed EUV

Downloaded From: https://www.spiedigitallibrary.org/ebooks/ on 09 Mar 2022
Terms of Use: https://www.spiedigitallibrary.org/terms-of-use

intensity is high enough to generate hydrogen radicals.[82] EIDEC responded to ASML's need by developing the High Power EUV Irradiation Tool,[83] which has been used as a witness-sample testing facility to qualify nonconventional resists since Q3 2015. The tool was also used to demonstrate that the irradiation of a model material, such as SnO_2, in a hydrogen atmosphere can create a non-cleanable deposit on a Ru-capped witness sample. The need for such qualification tests in the future is, however, uncertain since ASML announced its intention to install a membrane in the dynamic gas lock to prevent any resist outgas from reaching any of the optics.[84] Although resist outgassing may no longer impact optics lifetimes, it may damage the dynamic-gas-lock membrane, so testing may still be necessary.

6A.5 Cleaning and Contamination Control

Carbon deposition on surfaces can be of several different forms. The EUV-deposited carbon on the projection optics is in a hydrogenated, polymeric form,[85] while that deposited in the environment of the source has a predominant diamond-like nature,[86] with the former version having a much faster cleaning rate than the latter.[85,87] Activated oxygen, such as ozone or atomic oxygen, has been commonly used to clean synchrotron optics and was demonstrated to be effective at removing EUV-deposited carbon from a TiO_2-capped multilayer.[88] If overused, however, these gases can irreversibly oxidize the optical surface, especially a non-oxide cap layer material such as ruthenium. Nishiyama et al. have achieved some success in reversing oxidation in ruthenium-capped multilayers with atomic hydrogen,[89] but there is concern that repeated cleanings using activated oxygen might create a stoichiometric version that cannot be reversed. Atomic hydrogen for stand-alone systems can be created efficiently using a hot filament,[90] and such a system was used to demonstrate efficient and nondamaging removal of EUV-deposited polymeric carbon.[91]

Controlling contamination in an actual tool requires a three-pronged strategy. First, measures are taken to reduce the transport of the resist outgas from the wafer to the optical surfaces; second, a mitigating gas, which can provide real-time cleaning action is introduced; and third, periodic *in situ* or *ex situ* cleaning cycles may be provided. A significant advance of the first prong was described in 2000 by Mertens et al.:[92] a dynamic gas lock reduced the conductance of heavy organics by five orders of magnitude while reducing EUV transmission by only 5%. More recently, ASML has advanced this approach as reported in its patents for gas locks and curtains.[78–80] The atmosphere within the scanner is proprietary, but it most likely includes hydrogen as a mitigating gas, which interacts with high-intensity EUV radiation to produce atomic and ionic hydrogen. ASML and its collaborating laboratories have studied this phenomenon[93] and its capability to remove

Downloaded From: https://www.spiedigitallibrary.org/ebooks/ on 09 Mar 2022
Terms of Use: https://www.spiedigitallibrary.org/terms-of-use

carbon.[2] Finally, research in generating plasmas for both *in situ* and *ex situ* cleaning operations is being conducted by ASML and its collaborating laboratories[2,94] in the event that the real-time mitigation is inadequate.

6A.6 Summary and Future Outlook

The study of optics contamination was a critical component of the research and development effort for EUVL from the very beginning of that enterprise. Through the work of several laboratories worldwide, the two major mechanisms for degradation of the projection optics, EUV-induced oxidation and EUV-induced carbonization, are now better understood and under control. Degradation of the optics by oxidation in the tool environment was reduced to a negligible level by the use of a 2-nm cap layer of Ru. Carbonization was eliminated as a problem by the use of hydrogen both (1) to form gas curtains that limit the exposure of the optics to the outgassing from resists and other organic materials in the tool and, (2) most likely, to provide hydrogen radicals that inhibit carbon deposition during operation. Atomic hydrogen can also be used in cleaning cycles to remove any accumulated carbon deposits resulting from extended operation.

A new generation of metal-containing resists is showing promise for very high-resolution patterning. There is now concern that some metal ions that can be liberated by hydrogen might not be cleaned from optical surfaces once deposited. Further study of this emerging field is necessary.

Attention has now turned to providing contamination mitigation and cleaning to the condenser optics, which are exposed to the debris from a very hot tin plasma. Here the degradation is caused by the deposition of Sn and the possible sputtering due to fast ions.[95] Hydrogen radicals are also effective for removing Sn because they form SnH_4, which is volatile at the operating temperature of the optics.[96] However, redeposition due to the decomposition of SnH_4 and possible benefits from cap layers other than Ru are currently an active field of research.[97,98]

References

1. H. Oizumi, H. Yamanashi, I. Nishiyama, K. Hashimoto, S. Ohsono, A. Masuda, A. Izumi, and H. Matsumura, "Contamination removal from EUV multilayer using atomic hydrogen generated by heated catalyzer," *Proc. SPIE* **5751**, 1147–1154 (2005) [doi: 10.1117/12.601136].
2. A. Dolgov, D. Lopaev, T. Rachimova, A. Kovalev, A. Vasil'eva, C. J. Lee, V. M. Krivtsun, O. Yakushev, and F. Bijkerk, "Comparison of H2 and He carbon cleaning mechanisms in extreme ultraviolet-induced and surface wave discharge plasmas," *J. Phys. D: Appl. Phys.* **47**(6), 065205 (2014).

Downloaded From: https://www.spiedigitallibrary.org/ebooks/ on 09 Mar 2022
Terms of Use: https://www.spiedigitallibrary.org/terms-of-use

3. P. W. H. De Jager, H. G. C. Werij, and P. van Zuylen, "Lithographic device," U.S. Patent 6459472 B1 (2002).
4. D. Berthelot and H. Gaudenchon, "The chemical effects of ultraviolet rays on gaseous bodies—the effects of polymerisation," *Comptes Rendus Hebdomadaires des Séances de l'Academie des Sciences* **150**, 1169–1172 (1910).
5. R. Lariviere Stewart, "Insulating films formed under electron and ion bombardment," *Phys. Rev.* **45**, 488–490 (1934).
6. J. H. L. Watson, "An effect of electron bombardment upon carbon black," *J. Appl. Phys.* **18**, 153–161 (1947).
7. J. Hillier, "On the investigation of specimen contamination in the electron microscope," *J. Appl. Phys.* **19**, 226 (1948).
8. K. Boller, R. P. Haelbich, H. Hogrefe, W. Jerk, and C. Kunz, "Investigation of carbon contamination of mirror surfaces exposed to synchrotron radiation," *Nucl. Instrum. Method.* **208**, 273–279 (1983).
9. V. Domingo, B. Fleck, and A. Poland, "The SOHO mission: An overview," *Solar Phys.* **162**, 1–37 (1995).
10. A. BenMoussa, S. Gissot, U. Schühle et al., "On-orbit degradation of solar instruments," *Solar Phys.* **288**, 389–434 (2013).
11. E. Spiller, "Low-loss reflectivity coatings using absorbing materials," *Appl. Phys. Lett.* **20**, 365–367 (1972).
12. T. W. Barbee, Jr., J. C. Rife, W. R. Hunter, M. P. Kowalski, R. G. Cruddace, and J. F. Seely, "Long-term stability of a Mo/Si multilayer structure," *Appl. Opt.* **32**, 4852–4854 (1993).
13. J. H. Underwood, E. M. Gullikson, and K. Nguyen, "Tarnishing of Mo/Si multilayer mirrors," *Appl. Opt.* **32**, 6985–6990 (1993).
14. D. Gaines, R. C. Spitzer, N. M. Ceglio, M. Krurey, and G. Ulm, "Radiation hardness of molybdenum silicon multilayers designed for use in a soft x-ray projection lithography system," *Appl. Opt.* **32**, 6991–6998 (1993).
15. S. Bajt, "Optics Contamination," Chapter 6A in *EUV Lithography*, V. Bakshi, Ed., SPIE Press, Bellingham, Washington, pp. 227–259 (2009) [doi: 10.1117/3.769214.ch6a].
16. M. Wedowski, S. Bajt, J. A. Folta, E. M. Gullikson, U. Kleinberg, L. E. Klebanoff, M. E. Malinowski, and W. M. Clift, "Lifetime studies of Mo/Si and Mo/Be multilayer coatings for extreme ultraviolet lithography," *Proc. SPIE* **3767**, 217–224 (1999) [doi: 10.1117/12.371120].
17. J. Hollenshead and L. Klebanoff, "Modeling radiation induced carbon contamination of extreme ultraviolet optics," *J. Vac. Sci. Tech. B* **24**, 64 (2006).
18. J. Hollenshead and L. Klebanoff, "Modeling extreme ultraviolet/H2O oxidation of ruthenium optic coatings," *J. Vac. Sci. Tech. B* **24**, 118 (2006).

Downloaded From: https://www.spiedigitallibrary.org/ebooks/ on 09 Mar 2022
Terms of Use: https://www.spiedigitallibrary.org/terms-of-use

19. F. Liu, J. M. Sturm, C. J. Lee, and F. Bijkerk, "Extreme UV induced dissociation of amorphous solid water and crystalline water bilayers on Ru(0001)," Surf. Sci. **646**, 101–107 (2015).
20. A. F. G. Leontowich and A. P. Hitchcock, "Secondary electron deposition mechanism of carbon contamination," *J. Vac. Sci. Tech. B* **30**, 030601 (2012).
21. A. F. G. Leontowich and A. P. Hitchcock, "Secondary electron deposition mechanism of carbon contamination," presented at 11th International Conference on Synchrotron Radiation Instrumentation, Saint-Aubin, France, 16 July, 2012.
22. S. Bajt, J. B. Alameda, T. W. Barbee, Jr., W. M. Clift, J. A. Folta, B. Kaufmann, and E. A. Spiller, "Improved reflectance and stability of Mo-Si multilayers," *Opt. Eng.* **41**, 1797–1804 (2002) [doi: 10.1117/1.1489426].
23. S. Bajt, N. V. Edwards, and T. E. Madey, "Properties of ultrathin films appropriate for optics capping layers exposed to high energy photon irradiation," *Surf. Sci. Rep.* **63**, 73–99 (2008).
24. D. L. Windt, "IMD: Software for modeling the optical properties of multilayer films," *Computer in Physics* **12**, 360–371 (1998).
25. http://www-cxro.lbl.gov/optical_constants/ web page maintained by E. M. Gullikson.
26. T. Tsarfati, E. Zoethout, R. W. E. van de Kruijs, and F. Bijkerk, "Atomic O and H exposure of C-covered and oxidized d-metal surfaces," *Surf. Sci.* **603**, 2594–2599 (2009).
27. S. Bajt, H. N. Chapman, N. Nguyen, J. Alameda, J. C. Robinson, M. Malinowski, E. Gullikson, A. Aquila, C. Tarrio, and S. Grantham, "Design and performance of capping layers for extreme-ultraviolet multilayer mirrors," *Appl. Opt.* **42**, 5750–5758 (2003).
28. S. Bajt et al., "Lifetime Benchmarking of EUV Multilayer Optics: Report on Screening Tests of Multilayer 2," Project Report for LITH160, 2004.
29. K.-H. Ro, W. Park, G. Choe, and J.-C. Ahn, "The microstructure and optical properties of TiO_2 thin film by rf magnetron reactive sputtering," *Korean J. Mater. Res.* **7**(1), 21–26 (1997).
30. S.-H. Kim, Y.-L. Choi, Y.-S. Song, D. Y. Lee, and S.-E. Lee, "Influence of sputtering parameters on microstructure and morphology of TiO_2 thin films," *Mat. Lett.* **57**, 343 (2002).
31. S. Bajt, S. Hau-Riege, Z. R. Dai, J. Alameda, E. Nelson, C. Evans, J. S. Taylor, F. Dollar, S. Hill, M. Chandhok, and M. Fang, "Protective capping layer for EUVL optics using TiO_2," 2015 EUVL Symposium, 7–9 Nov., San Diego, California.
32. S. Yulin, N. Benoit, T. Feigl, N. Kaiser, M. Fang, and M. Chandhok, "Mo/Si multilayers with enhanced TiO_2 and RuO_2 capping layers," *Proc. SPIE* **6921**, 692118 (2008) [doi: 10.1117/12.772653].

Downloaded From: https://www.spiedigitallibrary.org/ebooks/ on 09 Mar 2022
Terms of Use: https://www.spiedigitallibrary.org/terms-of-use

33. M. Kriese, Yu. Platonov, J. Rodriguez, G. Fournier, S. Grantham, C. Tarrio, J. Curry, S. B. Hill, and T. B. Lucatorto, "Development and evaluation of interface-stabilized and reactive-sputtered oxide-capped multilayers for EUV lithography," *Proc. SPIE* **9422**, 94220K (2015) [doi: 10.1117/12.2085934].
34. M. Malinowski, P. Grunow, C. Steinhaus, M. Clift, and L. Klebanoff, "Use of molecular oxygen to reduce EUV-induced carbon contamination of optics," *Proc. SPIE* **4343**, 347–356 (2001) [doi: 10.1117/12.436677].
35. M. E. Malinowski, C. A. Steinhaus, D. E. Meeker, W. M. Clift, L. E. Klebanoff, and S. Bajt, "Relation between electron- and photon-caused oxidation in EUVL optics," *Proc. SPIE* 5037 429–438 (2003) [doi: 10.1117/12.499360].
36. Y. Kakutani, M. Niibe, K. Kakiuchi, H. Takase, S. Terashima, H. Kondo, S. Matsunari, T. Aoki, Y. Gomei, and Y. Fukuda, "A reflectance measurement system for investigating radiation damage to EUVL mirrors in New-SUBARU," *Proc. SPIE* **5533**, 47–57 (2004) [doi: 10.1117/12.559395].
37. M. Weiss, M. Wedowski, H. Trenkler, B. Mertens, B. Wolschrijn, R. Jansen, A. vd Runstraat, K. Spee, R. Klein, S. Ploger, E. Louis, R. vd Kruijs, R. Kurt, H. Meiling, and R. Moors, "The optics contamination/lifetime program: an overview of supporting facilities," *presented at The Second International EUVL Symposium*, 30 September to 2 October, 2003, Antwerp, Belgium.
38. R. Klein, A. Gottwald, F. Scholze, R. Thornagel, J. Tümmler, G. Ulm, M. Wedowski, F. Stietz, B. Mertens, N. Koster, and J. van Elp, "Lifetime testing of EUV optics using intense synchrotron radiation at the PTB radiometry laboratory," *Proc. SPIE* **4506**, 105–112 (2001) [doi: 10.1117/12.450950].
39. S. Oestreich, R. Klein, F. Scholze, J. Jonkers, E. Louis, A. Yakshin, P. Gorts, G. Ulm, M. Haidl, and F. Bijkerk, "Multilayer reflectance during exposure to EUV radiation," *Proc. SPIE* **4146**, 64–71 (2000) [doi: 10.1117/12.406677].
40. N. Koster, B. Mertens, R. Jansen, A. vd Runstraat, F. Stietz, M. Wedowski, H. Meiling, R. Klein, A. Gottwald, F. Scholze, M. Visser, R. Kurt, P. Zalm, E. Louis, and A. Yakshin, "Molecular contamination mitigation in EUVL by environmental control," *Microelectron. Eng.* **61–62**, 65–76 (2002).
41. C. Tarrio and S. Grantham, "Synchrotron beamline for extreme-ultraviolet multilayer mirror endurance testing," *Rev. Sci. Instrum.* **76**, 056101 (2005).
42. C. Tarrio, S. Grantham, S. B. Hill, N. S. Faradzhev, L. J. Richter, and T. B. Lucatorto, "A synchrotron beamline for extreme-ultraviolet photoresist testing," *Rev. Sci. Instrum.* **82**, 073102 (2011).

Downloaded From: https://www.spiedigitallibrary.org/ebooks/ on 09 Mar 2022
Terms of Use: https://www.spiedigitallibrary.org/terms-of-use

43. S. B. Hill, N. S. Faradzhev, L. J. Richter, S. Grantham, C. Tarrio, T. B. Lucatorto, S. Yulin, M. Schürmann, V. Nesterenko, and T. Feigl, "Optics contamination studies in support of high-throughput EUV lithography tools," *Proc. SPIE* **7969**, 79690M (2011) [doi: 10.1117/12.879852].
44. Y. Gomei, Y. Kakutani, H. Takase, M. Niibe, S. Terashima, T. Aoki, and S. Matsunari, "The role of ambient hydrocarbon species to reduce oxidation in Ru capping layers for EUVL optics mirrors," *Microelectron. Eng.* **83**, 676–679 (2006).
45. S. B. Hill, I. Ermanoski, S. Grantham, C. Tarrio, T. B. Lucatorto, T. E. Madey, S. Bajt, M. Chandhok, P. Yan, O. Wood, S. Wurm, and N. V. Edwards, "EUV testing of multilayer mirrors: critical issues," *Proc. SPIE* **6151**, 61510F (2006) [doi: 10.1117/12.656502].
46. T. E. Madey, N. S. Faradzhev, B. Y. Yakshinskiy, and N. V. Edwards, "Surface phenomena related to mirror degradation in extreme ultraviolet (EUV) lithography," *Appl. Surf. Sci.* **253**, 1691–1708 (2006).
47. K. R. Dean, I. Nishiyama, H. Oizumi, A. Keen, H. Cao, W. Yueh, T. Watanabe, P. Lacovig, L. Rumiz, G. Denbeaux, and J. Sion, "An analysis of EUV resist outgassing measurements," *Proc. SPIE* **6519**, 65191P (2007) [doi: 10.1117/12.712379].
48. C. Tarrio, R. E. Vest, T. B. Lucatorto, and R. Caudillo, "Tracking down sources of carbon contamination in EUVL exposure tools," *Proc. SPIE* **7271**, 727112 (2009) [doi: 10.1117/12.813684].
49. B. Wolschrijn, R. Jansen, A. Storm, R. van Vliet, B. Mertens, D. Ehm, M. Wedowski, T. Stein, R. Moors, and V. Banine, "Progress in optics lifetime program for ASML for EUV lithographic tools," presented at the 2005 EUVL Symposium, San Diego, California, 7–9 November, 2005.
50. S. B. Hill, N. S. Faradzhev, C. Tarrio, T. B. Lucatorto, R. A. Bartynski, B. Yakshinskiy, and T. E. Madey, "Measuring the EUV-induced contamination rates of TiO_2-capped multilayer optics by anticipated production-environment hydrocarbons," *Proc. SPIE* **7271**, 727113 (2009) [doi: 10.1117/12.814111].
51. B. V. Yakshinskiy, S. Zalkind, R. A. Bartynski, R. Caudillo, and T. E. Madey, "Carbon film growth on model electron-irradiated MLM cap layer: interaction of benzene and MMA vapor with TiO_2 surface," *Proc. SPIE* **7271**, 727110 (2009) [doi: 10.1117/12.814385].
52. S. Zalkind, B. V. Yakshinskiy, and T. E. Madey, "Interaction of benzene with TiO_2 surfaces: Relevance to contamination of extreme ultraviolet lithography mirror capping layers," *J. Vac. Sci. Technol. B* **26**, 2241 (2008).
53. M. I. Temkin and V. Pyzhov, "Recent modifications to Langmuir isotherms," *Acta Physicochimica U.R.S.S.* **12**, 217–222 (1940).
54. I. Langmuir, "The adsorption of gases on plane surfaces of glass, mica, and platinum," *J. Am. Chem. Sci.* **40**, 1361–1403 (1918).

Downloaded From: https://www.spiedigitallibrary.org/ebooks/ on 09 Mar 2022
Terms of Use: https://www.spiedigitallibrary.org/terms-of-use

55. S. B. Hill, N. S. Faradzhev, L. J. Richter, and T. B. Lucatorto, "Complex species and pressure dependence of intensity scaling laws for contamination rates of EUV optics determined by XPS and ellipsometry," *Proc. SPIE* **7636**, 76360E (2010) [doi: 10.1117/12.846849].
56. P. Thomas, L. Yankulin, Y. Khopkar, R. Garg, C. Mbanaso, A. Antohe, Y.-J. Fan, G. Denbeaux, S. Aouadi, V. Jindal, and A. Wuest, "Wavelength dependence of carbon contamination on mirrors with different capping layers," *Proc. SPIE* **7636**, 76361X (2010) [doi: 10.1117/12.847015].
57. B. Lesiak, A. Jablonski, Z. Prussak, and P. Mrozek, "Experimental determination of the inelastic mean free path of electrons in solids," *Surf. Sci.* **223**, 213–232 (1989).
58. T. Matsuura, S. Okubo, K. Oda, and T. Ushiro, "Development of refractive-index modulated diffractive optical element using a-C:H film," *SEI Technical Review* **65**, p. 31 (2007).
59. Y. Nishiyama, T. Anazawa, H. Oizumi, I. Nishiyama, O. Suga, K. Abe, S. Kagata, and A. Izumi, "Carbon contamination of EUV mask: film characterization, impact on lithographic performance, and cleaning," *Proc. SPIE* **7921**, 792116 (2008) [doi: 10.1117/12.771978].
60. S. Kobayashi, J. J. Santillan, H. Oizumi, and T. Itani, "EUV resist outgassing quantification and application," *Proc. SPIE* **7273**, 72731P (2009) [doi: 10.1117/12.813362].
61. H. Hada, T. Watanabe, K. Hamamoto, H. Kinoshita, and H. Komano, "Evaluation of resists outgassing by EUV radiation," *Proc. SPIE* **5374**, 686–694 (2004) [doi: 10.1117/12.534972].
62. G. Denbeaux, R. Garg, J. Waterman, C. Mbanaso, J. Netten, R. Brainard, Y.-J. Fan, L. Yankulin, A. Antohe, K. DeMarco, M. Jaffe, M. Waldrom, and K. Dean, "Quantitative measurement of EUV resist outgassing," *Proc. SPIE* **6533**, 653318 (2007) [doi: 10.1117/12.737192].
63. W. Yueh, H. B. Cao, V. Thirumala, and H. Choi, "Quantification of EUV resist outgassing," *Proc. SPIE* **5753**, 765–770 (2005) [doi: 10.1117/12.600540].
64. K. R. Dean, K. E. Gonsalves, and M. Thiyagarajan, "Effects of material design on EUV resist outgassing," *Proc. SPIE* **6153**, 61531E (2006) [doi: 10.1117/12.657163].
65. C. Tarrio, "Method for the characterization of extreme-ultraviolet photoresist outgassing," *J. Res. NIST* **114**, 179–183 (2009).
66. C. Tarrio, I. Pollentier, C. Mbanaso, G. Denbeaux, and A. Antohe, "Summary of OS1 outgassing results by NIST, IMEC, and CNSE," *presented at EUVI Resist* TWG (2009).
67. C. Tarrio, R. E. Vest, T. B. Lucatorto, and R. Caudillo, "Tracking down sources of carbon contamination in EUVL exposure tools," *Proc. SPIE* **7271**, 727112 (2009) [doi: 10.1117/12.813684].

Downloaded From: https://www.spiedigitallibrary.org/ebooks/ on 09 Mar 2022
Terms of Use: https://www.spiedigitallibrary.org/terms-of-use

68. B. Wolschrijn, R. Moors, and D. Elm, "New method for resist outgassing qualification," *IEUVI Resist TWG*, Barcelona, Spain, 20 October, 2006.
69. I. Pollentier, R. Lokasani, R. Gronheid, S. Hill, C. Tarrio, and T. Lucatorto, "Relationship between resist-related outgassing and witness-sample contamination in the NXE outgas qualification using electrons and photons," *Proc. SPIE* **8679**, 8679K (2013) [doi: 10.1117/12.2011541].
70. I. Takagi, T. Toshiya, and S. Norihiko, "Comparison of resist family outgassing characterization between EUV and EB," *J. Photopolymer Sci. Tech.* **26**, 673–678 (2013).
71. S.-H. Chang, S.-F. Chen, Y.-Y. Chen, M.-C. Chien, S.-C. Chien, T.-L. Lee, J. J. H. Chen, and A. Yen, "Balancing lithographic performance and resist outgassing in EUV resists," *Proc. SPIE* **8679**, 86790O (2013) [doi: 10.1117/12.2010794].
72. Y.-J. Fan, K. Maruyama, R. Ayothi, T. Naruoka, T. Chakraborty, D. Ashworth, J. S. Chun, C. Montgomery, S.-H. Jen, M. Neisser, and K. Cummings, "First results of outgas resist family test and correlation between outgas specifications and EUV resist development," *Proc. SPIE* **9422**, 942211 (2015) [doi: 10.1117/12.2087424].
73. N. Harned, "NXE resist outgas testing update," *IEUVI Resist TWG*, Miami, Florida, 20 October, 2011.
74. N. Harned, "ASML Update," *IEUVI Resist TWG*, San Jose, California, 23 February, 2014.
75. N. Harned, "Resist outgassing spec relaxation," *IEUVI Resist TWG*, San Jose, California, 22 February, 2015.
76. L. Li, S. Chakrabarty, K. Spyrou, C. K. Ober, and E. P. Giannelis, "Studying the mechanism of hybrid nanoparticle photoresists: Effect of particle size on photopatterning," *Chem. Materials* **27**, 5027–5031 (2015).
77. A. Grenville, J. T. Anderson, B. L. Clark, P. De Schepper, J. Edson, M. Greer, K. Jiang, M. Kocsis, S. T. Meyers, J. K. Stowers, A. J. Telecky, D. De Simone, and G. Vandenberghe, "Integrated fab process for metal oxide EUV photoresist," *Proc. SPIE* **9425**, 94250S (2015) [doi: 10.1117/12.2086006].
78. J. Passarelli, M. Murphy, R. Del Re, M. Sortland, J. Hotalen, L. Dousharm, R. Fallica, Y. Ekinci, M. Neisser, D. A. Freedman, and R. L. Brainard, "Organometallic carboxylate resists for extreme ultraviolet with high sensitivity," *J. Micro-Nanolith., MEMS, and MOEMS* **14**, 043503 (2015) [doi: 10.1117/1.JMM.14.4.043503].
79. D. H. Ehm, J. H. J. Moors, B. T. Wolschrijn, V. Banine, and V. V. Ivanov, "Method for removing contamination of optical surfaces and optical arrangement," U.S. Patent 8,279,397 B2 (2012).
80. D. H. Ehm, J. H. J. Moors, B. T. Wolschrijn, and T. Stein, and E. te Sligte, "Method for removing a contamination layer from an optical

Downloaded From: https://www.spiedigitallibrary.org/ebooks/ on 09 Mar 2022
Terms of Use: https://www.spiedigitallibrary.org/terms-of-use

surfaces and arrangement therefor as well as a method for generating a cleaning gas and arrangement therfor," U.S. Patent 8,419,862 B2 (2013).
81. H.-K. Nienhuys, P. G. Jonkers, and A. M. A. Huijberts, "Lithographic apparatus configured to suppress contamination from passing into the projection system and method," U.S. Patent 8,625,068 B2 (2014).
82. ASML presentation at the Resist TWG, San Jose, California, February 2015.
83. E. Shiobara, S. Mikami, and S. Tanaka, "The recent study of resist outgassing in the hydrogen environment," 2006 EUVL Symposium, Hiroshima, Japan, October 2016.
84. Y.-J. Fan, SEMATECH presentation at the Resist TWG, EUVL Symposium, Hiroshima, Japan, October 2016.
85. J. Chen, E. Louis, C. J. Lee, H. Wormeester, R. Kunze, H. Schmidt, D. Schneider, R. Moors, W. van Schaik, M. Lubomska, and F. Bijkerk, "Detection and characterization of carbon contamination on EUV multilayer mirrors," *Optics Express* **17**, 16969–16979 (2009).
86. A. Dolgov, D. Lopaev, C. J. Lee, E. Zoethout, V. Medvedev, O. Yakushev, and F. Bijkerk, "Characterization of carbon contamination under ion and hot atom bombardment in a tin plasma extreme ultraviolet light source," *Appl. Surf. Sci.* **353**, 708 (2015).
87. J. Chen, E. Louis, R. Harmsen, T. Tsarfati, H. Wormeester, M. van Kampen, W. van Schaik, R. van de Kruijs, and F. Bijkerk, "In situ ellipsometry study of atomic hydrogen etching of extreme ultraviolet induced carbon layers," *Appl. Surf. Sci.* **258**, 7 (2011).
88. N. S. Faradzhev, M. McEntee, J. T. Yates, Jr., S. B. Hill, and T. B. Lucatorto, "EUV-driven carbonaceous film deposition and its photo-oxidation on a TiO_2 film surface," *J. Phys. Chem.* **117**, 23072–23081 (2013).
89. I. Nishiyama, H. Oizumi, K. Motai, A. Izumi, T. Ueno, H. Akiyama, and A. Namiki, "Reduction of oxide layer on Ru surface by atomic-hydrogen treatment," *J. Vac. Sci. Technol. B* **23**, 3129–3131 (2005).
90. J. T. Yates, Jr., *Experimental Innovations in Surface Science*, Springer-Verlag, New York, Chapter 201, pp. 682–687 (1997).
91. S. Graham, C. Steinhaus, M. Clift, L. Klebanoff, and S. Bajt, "Atomic hydrogen cleaning of EUV multilayer optics," *Proc. SPIE* **5037**, 460–469 (2003) [doi: 10.1117/12.499373].
92. B. Mertens, B. van der Zwan, P. W. H. de Jager, M. Leenders, H. G. C. Werij, J. P. H. Benschop, and A. J. J. van Dijsseeldonk, "Mitigation of surface contamination from resist outgassing in EUV lithography," *Microelectron. Eng.* **53**, 659–662 (2000).
93. R. M. van der Horst, J. Beckers, E. A. Osorio, D. I. Astakhov, W. J. Goedheer, C. J. Lee, V. V. Ivanov, V. K. Krivtsum, K. N. Koshelev, and D. V. Lopaev, "Exploring the electron density in plasma induced by EUV

Downloaded From: https://www.spiedigitallibrary.org/ebooks/ on 09 Mar 2022
Terms of Use: https://www.spiedigitallibrary.org/terms-of-use

radiation: I. Experimental study in hydrogen," *J. Phys. D: Appl. Phys.* **49**, 145203 (2016).
94. TNO presentation "New developments in cleaning of EUVL mirrors and reticles," at the 2009 EUVL Symposium, Prague, Czech Republic, 18–21 October, 2009.
95. R. C. Wieggers, W. J. Goedheer, M. R. Akdim, F. Bijkerk, and P. A. Zegeling, "A particle-in-a-cell plus Monte Carlo study of plasma-induced damage of normal incidence collector optics used in extreme ultraviolet lithography," *J. Appl. Phys.* **103**, 013308 (2008).
96. M. M. J. W. van Herpen, D. J. W. Klunder, W. A. Soer, R. Moors, and V. Banine, "Sn etching with hydrogen radicals to clean EUV optics," *Chem. Phys. Lett.* **484**, 197–199 (2010).
97. D. Ugur, A. J. Storm, R. Verberk, J. C. Brouwer, and W. G. Sloof, "Decomposition of SnH_4 molecules on metal and metal oxide surfaces," *Appl. Surf. Science* **288**, 673–676 (2014).
98. M. Pachecka, J. M. Sturm, R. W. E. van de Kruijs, C. J. Lee, and F. Bijkerk, "Electronegativity-dependent tin etching from thin films," *API Advances* **6**, 075222 (2016).

Charles S. Tarrio received his B.S. from Bates College in Lewiston, Maine and Ph.D. in physics from the University of Virginia. He has been at NIST since 1991 studying at-wavelength EUV metrology and properties and contamination of EUV optics.

Shannon B. Hill is a staff physicist at NIST, where he works on the synchrotron ultraviolet radiation facility. He has over a decade of experience developing instruments and methods to study the degradation of optic surfaces induced by exposure to extreme-ultraviolet (EUV) radiation. Dr. Hill received his Ph.D. in atomic and molecular physics from Rice University in 1998.

Robert F. Berg belongs to the Ultraviolet Radiation Group at NIST. He received his Ph.D. in physics from the University of Florida in 1983. His interests include contamination of solar-observing spacecraft and standards for ultraviolet LEDs. His previous work includes measurements of vapor pressure, standards for gas flow and vacuum, and two experiments on the Space Shuttle.

Downloaded From: https://www.spiedigitallibrary.org/ebooks/ on 09 Mar 2022
Terms of Use: https://www.spiedigitallibrary.org/terms-of-use

Saša Bajt received her Ph.D. in physics at the University of Heidelberg. She worked at the National Synchrotron Light Source and at LLNL, where she led a team that developed high-reflectivity and high-stability MLMs for EUVL. Her optics enabled the first coherent x-ray diffraction experiments as well as the first warm dense matter experiments. Since 2008 she has been at Deutsches-Elektronen Synchrotron (DESY) in Hamburg, where she is currently working on the next generation of x-ray optics for future x-ray microscopes using novel coherent x-ray sources.

Downloaded From: https://www.spiedigitallibrary.org/ebooks/ on 09 Mar 2022
Terms of Use: https://www.spiedigitallibrary.org/terms-of-use

Chapter 6B
Collector Contamination: Normal-Incidence (Multilayer) Collectors

Daniel T. Elg
University of California, Berkeley, USA

Shailendra N. Srivastava and David N. Ruzic
University of Illinois at Urbana-Champaign, USA

6B.1 Introduction
6B.2 Overview of Normal-Incidence Collector Mirrors
6B.3 Collector Performance
6B.3.1 Debris mitigation and contamination
6B.3.2 Atomic hydrogen cleaning
6B.3.3 Hydrogen plasma cleaning
6B.3.4 Compatibility of multilayer mirrors with H_2 plasma
6B.4 Summary
Acknowledgments
References

6B.1 Introduction

Throughout the 1980s and 1990s, as the semiconductor industry upheld Moore's law and continuously shrank device feature sizes, the wavelength of the lithography source remained at or below the resolution limit of the minimum feature size. Since 2001, however, the light source has been the 193-nm ArF excimer laser.[1] While the industry has managed to keep up with Moore's law, shrinking feature sizes without reducing the lithographic wavelength has required extra innovations and steps that increase fabrication time, cost, and complexity. These innovations include immersion lithography and double patterning. Currently, the industry is at the 14-nm technology node. Thus, the minimum feature size is almost an order of magnitude below the exposure wavelength. For the 10-nm node, quadruple patterning has

Downloaded From: https://www.spiedigitallibrary.org/ebooks/ on 09 Mar 2022
Terms of Use: https://www.spiedigitallibrary.org/terms-of-use

been proposed, causing potentially even more cost, fabrication time, and complexity.

Such a trend cannot continue indefinitely in an economic fashion, and it is desirable to decrease the wavelength of the lithography sources to improve the resolution of the scanner. Thus, much research has been invested in EUVL, which uses 13.5-nm light. While much progress has been made in recent years, some challenges must still be solved in order to yield a throughput high enough for EUVL to be commercially viable for high-volume manufacturing (HVM). One of these problems is collector contamination. Additionally, even once EUVL reaches HVM insertion, source power will need to be continually increased as feature sizes continue to shrink; this increase in source power may potentially come at a cost of increased debris. Thus, debris mitigation solutions that work for the initial generation of commercial EUVL systems may not be adequate for future generations, which will require an *in situ* technology to clean collector optics.

Collector contamination is caused by the interaction between the EUV light source and the first piece in the optical chain: the collector optic. Currently, due to the 92-eV energy of a 13.5-nm photon, EUV light must be made by a plasma rather than produced by a laser. Specifically, the industrially favored EUV source topology is to irradiate a droplet of molten Sn with a laser, creating a dense, hot laser-produced plasma (LPP)[2,3] and ionizing the Sn to (on average) the +10 state[4,5] and higher. In the past, different fuels, such as Xe, were considered, allowing for gas discharge-produced plasmas (DPPs).[2] However, the high-power requirements for EUV sources, coupled with the low conversion efficiency of non-Sn fuels, rendered these sources inadequate for EUV power production. While DPPs can still be used for low-power metrology applications, the EUV power market has been captured exclusively by Sn-based LPPs. Thus, the discussion in this chapter will mostly be confined to collector optics for such sources.

The collector optics for such sources are normal-incidence multilayer mirrors (MLMs). To overcome the high EUV absorption of all known solid materials, MLMs employ synthetic Bragg reflection to reflect EUV light. This requires stacks of alternating Mo and Si layers, with each layer being less than 5 nm thick.[6] An overview of MLMs will be given in Section 6B.2. The collector optic, which collects the EUV light from the source and sends it to the rest of the optical chain, is exposed directly to the Sn plasma. However, this plasma produces not only EUV photons but also Sn ion and neutral debris. Collector contamination is caused by the interaction of this debris flux with the collector. This contamination can take three different forms: sputtering, implantation, and deposition. The first two forms of damage are irreversible, while the third can be reversed by cleaning.

Due to the nanoscale size of the MLM layers, contamination on the same small scale can significantly reduce the EUV reflectivity of the collector optic.[7]

Downloaded From: https://www.spiedigitallibrary.org/ebooks/ on 09 Mar 2022
Terms of Use: https://www.spiedigitallibrary.org/terms-of-use

This reduces the total EUV throughput of the system, leading to a longer processing time for each wafer and hindering the economic efficiency of the EUV tool. A solution to such a problem is necessary in order to allow for HVM implementation of EUVL.

Accordingly, a great deal of effort has been put into debris mitigation and cleaning. Debris mitigation is the process of either slowing down debris (which prevents sputtering and implantation by high-energy particles) and/or moving the debris away from the collector (which can prevent sputtering, implantation, and deposition). The most common types of debris mitigation are magnetic fields (to deflect ions) and buffer gas (to slow down and deflect ions and neutrals by means of collisions between the Sn particles and the buffer gas molecules). These are discussed in Section 6B.3.1. Debris mitigation has achieved much success in recent years, slowing high-energy ions enough to prevent most sputtering and implantation. Additionally, the Sn deposition rate has been greatly decreased.[3]

However, deposition can take place at all ion and neutral energies, and no mitigation method can deterministically deflect all neutrals away from the collector. Thus, deposition still takes place, lowering the collector reflectivity and increasing the time needed to deliver enough EUV power to pattern a wafer. Luckily, deposition is a reversible process. However, a suitable cleaning technique must be employed. Externally cleaning the collector requires both cost and significant source downtime; therefore, it is desirable to clean the collector *in situ*, or inside the EUV source chamber. Thus, the portion of this chapter following Section 6B.3.1 will be dedicated to *in situ* collector cleaning methods. While studies involving Cl etching have previously been performed,[8] the current accepted method of *in situ* cleaning involves etching by H radicals. Research concerning etching by an atomic hydrogen source is covered in Section 6B.3.2. Research on plasma-based hydrogen etching is covered in Section 6B.3.3. For both methods, the goal of hydrogen-based cleaning is to supplement debris mitigation methods and eliminate the effect of Sn deposition on the collector while allowing the EUV system to remain at vacuum (and, ideally, in operation with no cleaning-related downtime).

The collector lifetime is a leading challenge to the successful implementation of HVM EUVL. This chapter addresses the contamination of normal-incidence collectors and solutions to collector contamination.

6B.2 Overview of Normal-Incidence Collector Mirrors

EUVL technology, which is based on reflective optics for 13.5 nm, is currently being developed using Mo/Si reflective coatings as EUV reflectors.[9] Mo/Si MLMs also have been used for other spectroscopy applications.[10–15] Mo/Si MLMs are usually deposited as a periodic stack of alternating Mo and Si layers. In spite of the small reflection through individual layers, the

Downloaded From: https://www.spiedigitallibrary.org/ebooks/ on 09 Mar 2022
Terms of Use: https://www.spiedigitallibrary.org/terms-of-use

reflections from all of the interfaces in a MLM can interfere constructively to yield a total reflectivity close to 70% at the 13.5 ± 0.2 wavelengths.[16,17] To achieve the highest reflectivity from such interference-based mirrors, the bilayer period must be tuned to a particular wavelength.[18] To achieve near-normal-incidence reflectivity in the EUV range, the bilayer period must be approximately 6.9 nm. The highest reflectivity occurs when the Mo layer thickness is approximately 40% of the bilayer period. Bragg's law is then the necessary condition to achieve the maximum reflection efficiency in a MLM.[19,20] Multilayer mirrors with a highly reflective quality have been made using several sputtering and deposition techniques.[16,17,21–24] The most common are ion beam deposition and magnetron sputtering.

The materials selection for 13.5-nm MLMs was performed with the goal of maximizing reflection and minimizing absorption. Qualitatively, reflection depends on the difference between the real permittivities of the materials, while absorption depends on the imaginary permittivities. Thus, it is desirable to select one material with a minimum imaginary permittivity. For 13.5 nm, the material with the minimum imaginary permittivity is Si. Thus, Si was chosen as one of the materials (the spacer) in order to minimize EUV absorption. In fact, it was the low absorption of Si at 13.5 nm that originally made 13.5 nm a contender for next-generation lithography. Mo was then chosen as the other material (the reflector) due to the difference between its real permittivity and that of Si. Quantitatively, assuming an optimized thickness ratio between the two layers, maximum reflectivity is achieved by maximizing f and minimizing g, where f and g are given below, and 1 and 2 denote the different materials:

$$f = \frac{\mathrm{Re}(\varepsilon_1 - \varepsilon_2)}{\mathrm{Im}(\varepsilon_1 - \varepsilon_2)}; \tag{6B.1}$$

$$g = \frac{\mathrm{Im}(\varepsilon_2)}{\mathrm{Im}(\varepsilon_1 - \varepsilon_2)}. \tag{6B.2}$$

Thus, to minimize g, the imaginary permittivity (and, therefore, absorption) of material 2 must be minimized, and the difference between the real permittivities of the materials must be maximized. A plot of the effect of f and g is shown in Fig. 6B.1. Each solid line represents a different value of peak reflectivity. Thus, as g is lowered and f is raised, the (f, g) coordinate will lie on a line of higher reflectivity. Region 1 outlines the region of interference reflection mirrors, where EUV MLMs reside. Region 2 outlines a region dominated by a phenomenon called the Borrmann effect,[25,26] which is caused by very low values of g (implying that, even with a suboptimal reflector, some reflectance can still be achieved if the spacer absorption is kept at a minimum). For more information on the theory of MLMs, the reader is referred to the work by Kozhevnikov.[26]

Downloaded From: https://www.spiedigitallibrary.org/ebooks/ on 09 Mar 2022
Terms of Use: https://www.spiedigitallibrary.org/terms-of-use

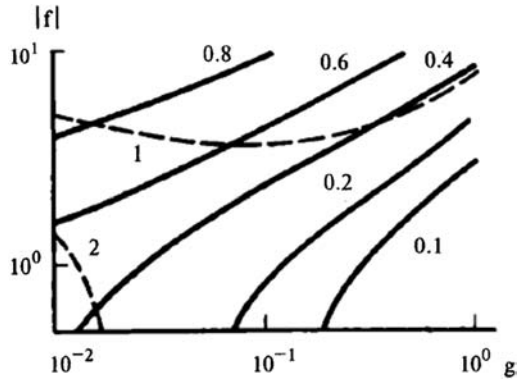

Figure 6B.1 Maximum theoretical reflectivity of an MLM. Solid lines indicate different peak reflectivities. The *x* coordinate is proportional to the absorption of the spacer material (Si for EUV MLMs), while the *y* coordinate is proportional to the difference in real permittivities between the two materials. Thus, by minimizing absorption of the spacer and maximizing the difference in real permittivities, a high theoretical reflectivity is achieved (reprinted from Ref. 26 with permission from Springer).

An optical path through the stacks of Mo and Si layers is schematically represented in Fig. 6B.2. The large number of periods will result in higher reflectivity because there is more constructive interference. However, since absorption is also present in the layers, the reflectivity will not increase continuously with the number of periods. Due to increasing absorption as more layers are penetrated, EUV reflectivity saturates at approximately 50 bilayers; the reader is referred to Fig. 6B.6 for a graphical visualization of this phenomenon.

Reflectivity variation is shown versus the wavelength for an ideal MLM in Fig. 6B.3. Reflectivity is typically quoted as peak reflectivity, which is approximately 73% for a 13.5-nm Mo/Si mirror. It is difficult to replicate this theoretical maximum with real fabrication techniques. Thermal stability and layer intermixing have been studied in depth,[27–46] and mirrors with peak reflectivities of about 70% have been experimentally deposited.[47]

The lifetime of a MLM depends greatly on the efficiency of the debris mitigation and cleaning. EUV sources differ in which debris mitigation techniques they can use.

In a DPP source (Fig. 6B.4), the debris mitigation approaches have some advantages. Since the light needs to traverse only the space between the source and the collector optics in one direction, there is room for items that can extend the lifetime of the mirrors. In addition, grazing-angle collectors can be used, as shown in Fig. 6B.4. These mirrors are not MLMs and have a lower reflectivity as the angle of incidence becomes steeper. LPP EUV sources use normal-incidence MLMs (Fig. 6B.5) and cannot use collimating debris filters because the light traverses the same region in multiple directions. However, the collectors for LPP sources, due to their larger solid angle of collection, allow a higher collection efficiency of EUV light than from the grazing-angle

Downloaded From: https://www.spiedigitallibrary.org/ebooks/ on 09 Mar 2022
Terms of Use: https://www.spiedigitallibrary.org/terms-of-use

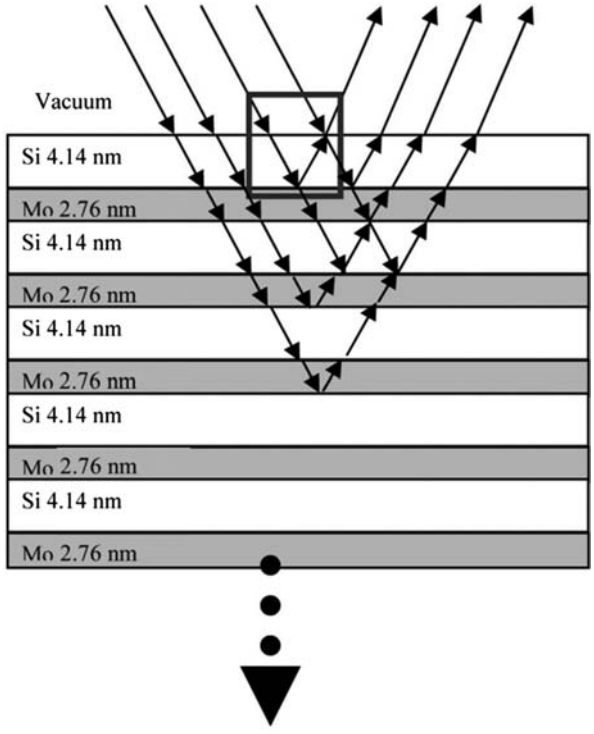

Figure 6B.2 Reflection from a MLM.

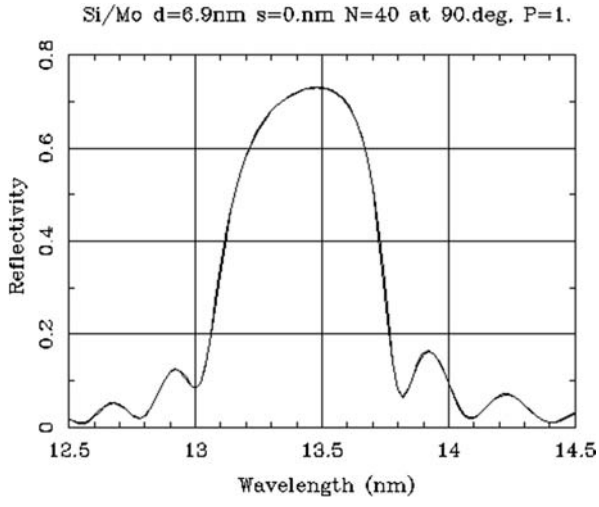

Figure 6B.3 Reflectivity variation as a function of wavelength for a Si/Mo ML [reprinted from the website of the Center for X-Ray Optics (CXRO)[48]].

Downloaded From: https://www.spiedigitallibrary.org/ebooks/ on 09 Mar 2022
Terms of Use: https://www.spiedigitallibrary.org/terms-of-use

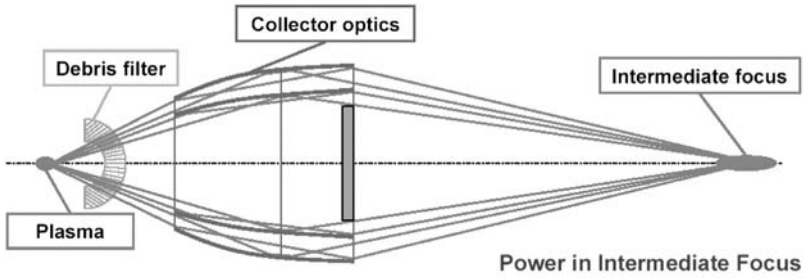

Figure 6B.4 DPP source-collector system with a grazing-incidence collector.

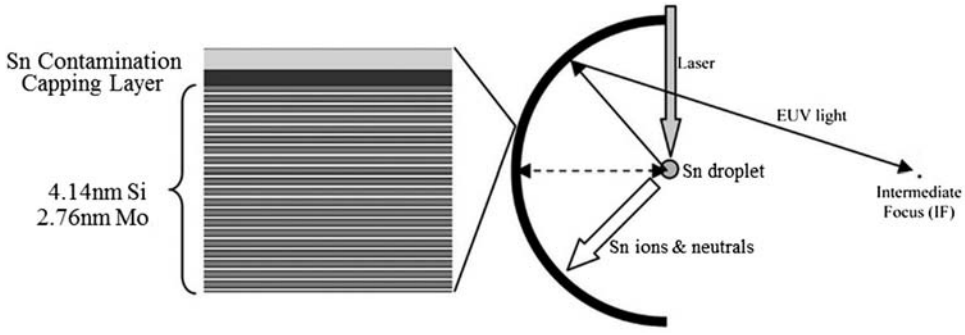

Figure 6B.5 LPP source-collector system with a normal-incidence collector.

collectors used in DPP EUV sources. Due to the usage of such collectors in today's LPP EUV power sources, most of this chapter will be confined to normal-incidence MLMs.

6B.3 Collector Performance

Given the challenges of using MLM reflective optics in EUVL, the remainder of this chapter will focus on the specific problems and solutions concerning fast-ion damage, mirror surface contamination, and optics cleaning.

6B.3.1 Debris mitigation and contamination

Reflectivity degradation of the collector optics is an effect of debris interaction with the collector optics. For grazing-incidence mirrors, sputter-induced roughness and contamination are the main causes of reflectivity loss. For normal-incidence mirrors, sputter-induced roughness, sputter-induced erosion, energetic ion implantation, and Sn deposition cause reflectivity degradation. The optimum number of bilayers for high reflectivity is about 50. In the absence of any debris mitigation, erosion is the most harmful; it destroys the MLM and cannot be reversed. To mitigate the erosion due to plasma debris in LPP sources, additional bilayers can be used on the MLM

Downloaded From: https://www.spiedigitallibrary.org/ebooks/ on 09 Mar 2022
Terms of Use: https://www.spiedigitallibrary.org/terms-of-use

collector optics to extend lifetime. The thicker stacks of MLMs have enough bilayers to keep the reflectivity constant as layers are eroded away. However, more bilayers lead to an increased manufacturing cost. A calculation in Fig. 6B.6 shows how the reflectivity changes with the number of bilayers left in a MLM.[49] The highest theoretical reflectivity of a MLM is around 73% (Fig. 6B.6), although this reflectivity has yet to be achieved experimentally.

The plasmas used to produce EUV photons have temperatures of approximately 20–30 eV.[4] However, energies of ions expelled from these plasmas can be orders of magnitude higher in the keV range.[50] This is most likely due to Coulombic acceleration; as the plasma expands, electrons travel outwards much more quickly than ions, setting up an electric field. This, in turn, accelerates ions to keV-level energies. Ions with such energies can very easily cause extreme erosion and implantation.

To provide an example of an ion energy distribution, results are shown from experiments using a spherical energy sector analyzer (ESA) developed at the Center for Plasma-Material Interactions (CPMI) at the University of Illinois.[51] The ESA measures ions based on their charge-to-mass ratio, according to

$$\frac{E}{q} = \frac{\Delta V}{\frac{r_2}{r_1} - \frac{r_1}{r_2}}, \tag{6B.3}$$

where E is the ion energy, q is the ion charge, r_1 is the inner radius of the instrument, r_2 is the outer radius of the instrument, and ΔV is the voltage difference applied across the two concentric spherical sectors, as shown in Fig 6B.7. An ion that satisfies Eq. (6B.3) travels through the ESA along the dotted path and reaches the detector. Ions of other energy-to-charge ratios hit

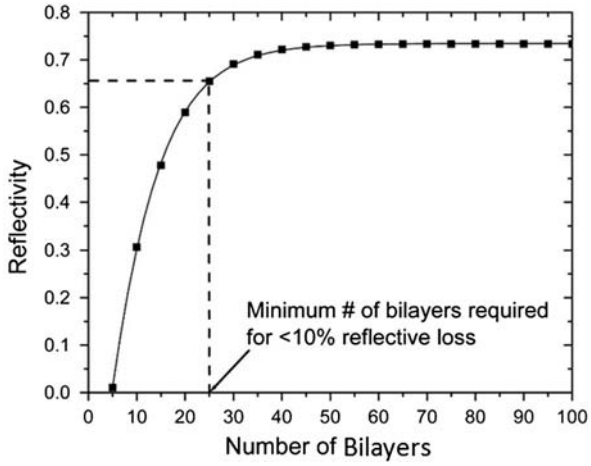

Figure 6B.6 Calculation showing the reflectivity from a MLM versus the number of bilayers.

Downloaded From: https://www.spiedigitallibrary.org/ebooks/ on 09 Mar 2022
Terms of Use: https://www.spiedigitallibrary.org/terms-of-use

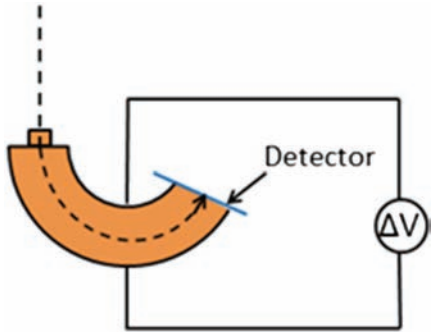

Figure 6B.7 Diagram showing the path of an ion [that satisfies Eq. (6B.3)] through the ESA.

either the inner spherical sector of the instrument or the outer spherical sector and do not reach the detector. Further information about this apparatus can be found in Ref. 51.

Figure 6B.8 shows the experimental setup used at CPMI. The plasma source was XTREME Technologies' XTS 13-35 DPP source.[1] This plasma source uses Xe gas to create 35 W of EUV light (2% bandwidth) in 2π steradians with a conversion efficiency of 0.55%. The self-compression of the Xe gas column results in heating sufficient to generate Xe^{8+} to Xe^{12+} ions, which are necessary for the emission of EUV light at 13.5 nm. Though this

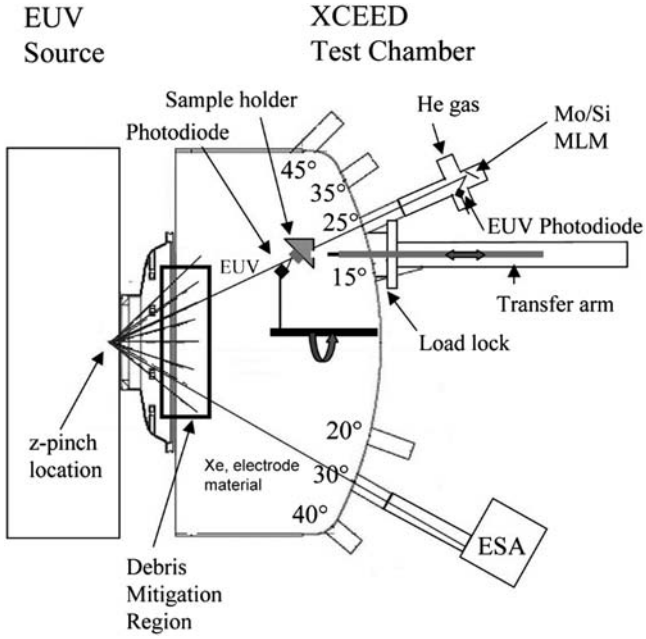

Figure 6B.8 Diagram of XTREME Technologies' XTS 13-35 DPP EUV source at CPMI, University of Illinois.

Downloaded From: https://www.spiedigitallibrary.org/ebooks/ on 09 Mar 2022
Terms of Use: https://www.spiedigitallibrary.org/terms-of-use

source is a DPP rather than an LPP, the plasmas are fully ionized, have similar ionization states (average +10), have similar electron densities (10^{19}–10^{20} cm^{-3}), and have similar electron temperatures (20–30 eV). Thus, the results from this source should be at least indicative of the expected range of incident ions from an LPP, as well. Additionally, the source was modified to use an erodible Sn electrode that was ablated by a laser; thus, ion energy measurements from a Sn-fueled EUV plasma are available as well. Results from the Xe-fueled pinch are shown in Fig. 6B.9, while results from the Sn-fueled pinch are shown in Fig. 6B.10. Both figures show Xe and Sn ions with similar kinetic energies.

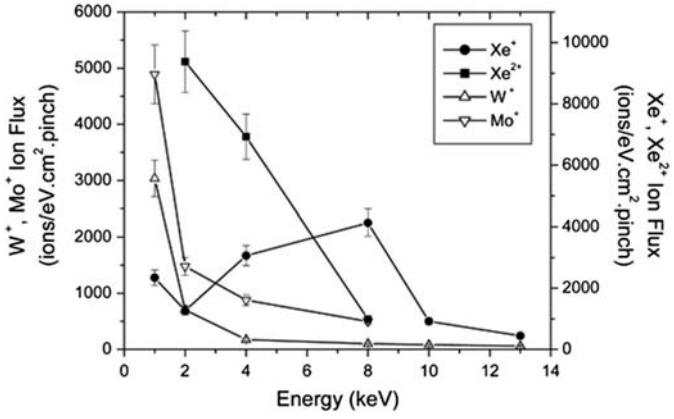

Figure 6B.9 Ion spectra of a Xe-fueled XTS source in absolute fluxes versus the ion energies in keV measured at 157 cm. Individual error bars are shown; however, day-to-day reproducibility of a given spectrum can vary from 10 to 20%.

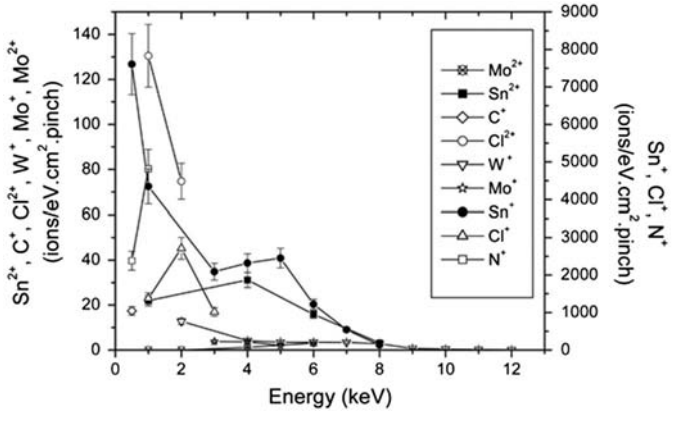

Figure 6B.10 Ion spectra of a Sn-fueled XTS source in absolute fluxes versus the ion energies in keV measured at 157 cm. Individual error bars are shown; however, day-to-day reproducibility of a given spectrum can vary from 10 to 20%.

Downloaded From: https://www.spiedigitallibrary.org/ebooks/ on 09 Mar 2022
Terms of Use: https://www.spiedigitallibrary.org/terms-of-use

With ions of such high energies, sputtering and erosion can easily be achieved. Thus, the ions must be either slowed down or deflected. One way of deflecting ionic debris is by means of magnetic fields.

Academic experiments have been performed on the use of magnetic fields for ion debris mitigation. In one such work by Roy et al., a 0.5-T magnetic field was shown to deflect ions produced by ablating a solid Sn target with a laser for 10- and 15-ns pulse durations.[52] The average ion energy was 1.2 keV. The ion flux measured with a Faraday cup (FC) was shown to be approximately 5 times smaller with the field present than without the field (Fig. 6B.11). The FC was positioned 15 cm away from the source, at an angle of 66 deg.

Another set of experiments performed at CPMI showed the ability to predict and measure deflected ion distributions.[53] In these experiments, the apparatus from Figs. 6B.7 and 6B.8 was used, and a 1-T Halbach array[54,55] was placed 5 cm in front of the plasma source. The ESA was used to analyze ion energies at 0, 35, and 45 deg from the pinch with and without the magnet present. First, ions were measured at the 0-deg port without the magnet; these were then used to generate a simulated ion energy probability distribution. Ions were then measured at 0 deg without the magnet present and were shown to be almost completely removed. These results are presented in Fig. 6B.12.

The simulated energy distribution generated in Fig. 6B.12 was then used to generate computational ions, which were flown through a simulated magnetic field identical to that of the Halbach array. In this way, deflected distributions were also measured experimentally and confirmed to be in agreement with simulation;

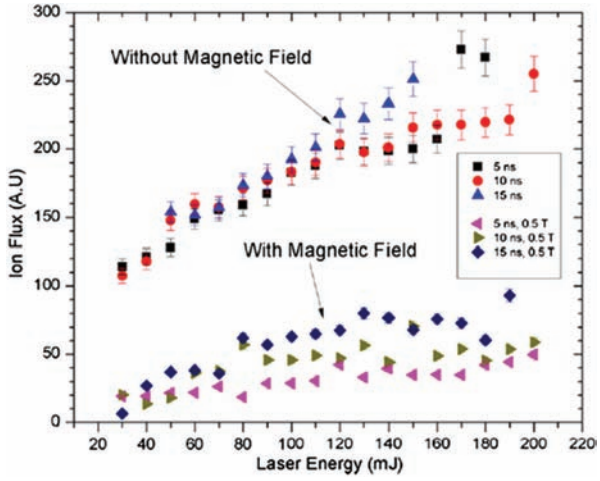

Figure 6B.11 Ions produced by laser ablation of a solid Sn target measured by a Faraday cup at 66 deg from the source. A 0.5-T field is used to deflect the ions. The ion flux measured with the field present is approximately 5 times lower than without the field present (reprinted from Ref. 52 with permission from AIP Publishing LLC).

Downloaded From: https://www.spiedigitallibrary.org/ebooks/ on 09 Mar 2022
Terms of Use: https://www.spiedigitallibrary.org/terms-of-use

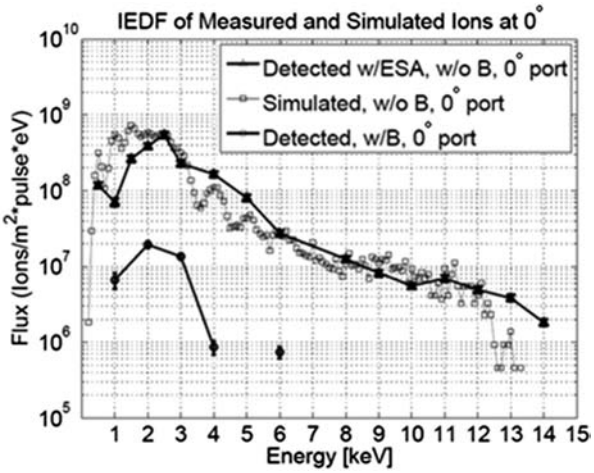

Figure 6B.12 Ions produced by the XTS 13-35 EUV source at CPMI are measured at 0 deg from the source with and without magnetic debris mitigation. With the magnet present, most ions are deflected away (IEDF stands for ion energy distribution function) (reprinted from Ref. 53).

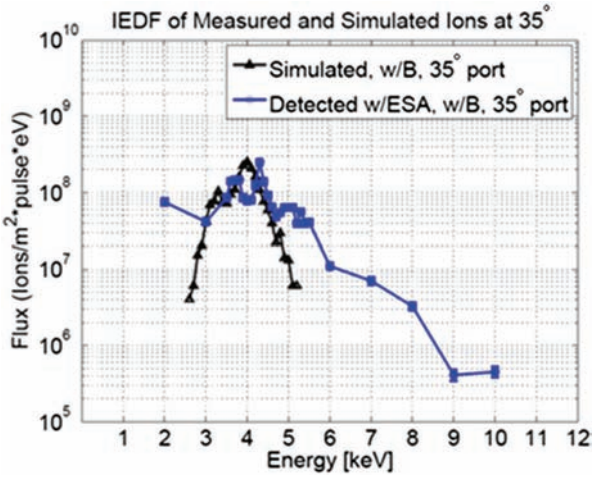

Figure 6B.13 The distribution of ions deflected 35 deg by the 1-T magnet. The peak is at approximately 4 keV. Experimental results are in good agreement with simulation. At energies far from 4 keV, some ions are still present experimentally due to scattering (reprinted from Ref. 53).

an example at the 35-deg port is shown in Fig. 6B.13. Thus, given a magnetic field and initial ion energy distribution, final destinations of deflected ions can be predicted. Alternatively, given the size of a collector optic and its position relative to the EUV-producing plasma, a magnetic field topology can be designed to deflect ions in a desired energy range away from the collector.

Downloaded From: https://www.spiedigitallibrary.org/ebooks/ on 09 Mar 2022
Terms of Use: https://www.spiedigitallibrary.org/terms-of-use

Some industrial magnetic debris mitigation results have also been published. In one such publication, Endo reported an FC ion current signal that was reduced to the noise floor after installing a 1-T magnetic field (Fig. 6B.14).[56] This experiment was performed on a Sn-fueled LPP source.

Magnetic debris mitigation is currently part of the industrial LPP EUV power source produced by Gigaphoton.[57,60] A diagram of the relevant portion of the source is shown in Fig. 6B.15. Surrounding the collector are two superconducting electromagnets, which create a strong field that deflects Sn ions away from the collector.

However, magnetic debris mitigation addresses only part of the picture, since the laser vaporizes the Sn droplet. While fast ions may be responsible for sputtering, most Sn debris takes the form of neutral vapor, which is not at all affected by magnetic fields. Although their initial energies are lower than those of ions (due to the lack of electrostatic acceleration), neutrals of all energies can still cause deposition. In addition, the high temperature of the EUV plasma (20–30 eV) still allows some expelled Sn neutrals to cause sputtering. Finally, charge-exchange collisions can transfer charge from a high-energy ion to a slow neutral, yielding a high-energy neutral that can cause the same damage as an ion but cannot be mitigated by magnetic fields.[59]

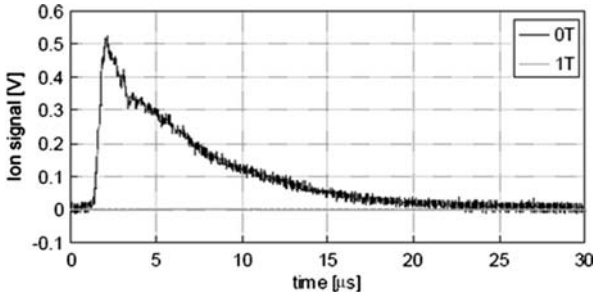

Figure 6B.14 Ions from a Sn-fueled LPP source are deflected by a 1-T magnetic field. The ion current signal on the Faraday cup is reduced to the noise floor when the field is applied and is compared to the ion current signal without the field (reprinted from Ref. 56).

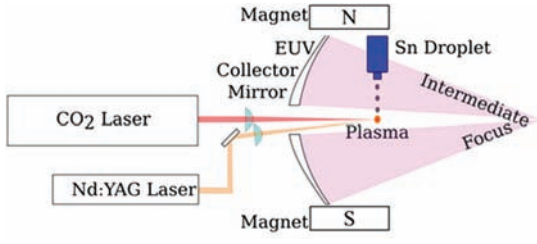

Figure 6B.15 A magnetic debris mitigation system used in an industrial EUV source. The system consists of superconducting coils surrounding the collector (adapted from Ref. 58 with permission from IOP Publishing Ltd).

Downloaded From: https://www.spiedigitallibrary.org/ebooks/ on 09 Mar 2022
Terms of Use: https://www.spiedigitallibrary.org/terms-of-use

In Sn LPP sources at Gigaphoton (such as the one shown in Fig. 6B.15), the droplet size (20 μm) is optimized to maximize the ionization fraction of the droplet, allowing magnetic debris mitigation to deflect as much debris as possible.[51,53] However, some Sn remains neutral and deposits on the collector; deposition rates of 0.1 nm/MPulse have been reported.[57]

Accordingly, neutrals must be dealt with by either a debris mitigation technique, which both slows them down and deflects them away from the collector, a collector cleaning technique, or both. One such debris mitigation technique is a foil trap, which consists of many thin pieces of foil located between the source and the collector, radiating outwards from the axis of the EUV source. The foil both provides a physical buffer for many Sn ions and neutrals, and reduces the ability of gas to flow between the source and the collector. By thus lowering the conductance, the foil trap causes pressure to rise on the source side; this increased pressure leads to an increase in the number of collisions between Sn and gas atoms, slowing down fast atoms. Some foil trap designs include both a rotating section and a static section in order to further reduce conductance.[61] However, the foil trap can also impede the trajectory of EUV photons. This makes it best suited to a source in which EUV photons will only pass through it once, such as the DPP source with a grazing-incidence collector diagrammed in Fig. 6B.4. Currently, foil traps are used in the laser-assisted DPP sources manufactured by Ushio for metrology applications.[61] These sources utilize an electrical discharge through an ablated Sn vapor cloud to produce EUV from Sn. However, in an LPP source with a normal-incidence collector, such as those shown in Figs. 6B.5 and 6B.15, photons must traverse the region between the plasma and the collector twice. Thus, foil traps are seen mainly in DPP sources, which are no longer considered for high-power EUV source applications. Since this chapter is focused on normal-incidence collectors for power sources, the remainder of this chapter will be devoted to such systems.

A different debris mitigation technique that makes use of collision-based slowing and deflection without the need for a physical foil is buffer gas mitigation. In such a technique, background gas is injected into the chamber, raising the pressure in the entire chamber. This gas collides with both ions and neutrals, slowing them down and altering their trajectories. This technique is present in most LPP sources in the field today.

However, in addition to neutral vapor, Sn may also take the form of larger particles, especially in cases where the Sn droplet is not fully converted into plasma. These particles are very difficult to control with buffer gas collisions. Therefore, it first becomes necessary to design the EUV system in such a way as to minimize particle creation and maximize vapor creation. This may be done by ensuring that the entire Sn droplet is converted into plasma when irradiated by the laser. Vapor maximization generally requires three components. First, the Sn droplet must be small (on the order of tens of

Downloaded From: https://www.spiedigitallibrary.org/ebooks/ on 09 Mar 2022
Terms of Use: https://www.spiedigitallibrary.org/terms-of-use

microns[3]), so that no unused Sn is left over after a laser pulse. Secondly, the droplet is irradiated by a pre-pulse prior to the main plasma-producing laser pulse. The pre-pulse causes the spherical droplet to deform into a flat 2D disk. This 2D structure maximizes the amount of Sn surface area that is directly exposed to the main laser. Additionally, the droplet size and pre-pulse intensity are correlated to cause the size of the flattened Sn disk to correspond to the cross-sectional area of the focused main laser beam. If the droplet area were larger than the laser irradiation area, additional Sn debris would be generated; if the droplet area were smaller than the laser irradiation area, laser energy would be wasted, resulting in reduced conversion efficiency (CE). Setting the areas equal to each other avoids both of these situations. Finally, CE is optimized by means of a laser timing control system that uses the droplet position and velocity to control the timing of the pre-pulse and main laser. This not only ensures maximum EUV power production but also minimizes the chances of a droplet being only partially irradiated or not irradiated at all. In this manner, droplet utilization is maximized, and large particle creation is minimized.

Once the Sn droplet has been vaporized, the vapor must be mitigated by means of buffer gas. The importance of mitigation cannot be underestimated. Current industrial sources use approximately 2 kg of Sn per week; a deposition of only 5 nm on the collector surface can remove 70% of the collector's EUV reflectivity. If it is assumed that the collector occupies 10% of the EUV vessel surface area and the Sn were to be spread homogeneously throughout the EUV vessel, this thickness could be deposited on the collector in less than 30 s in the absence of debris mitigation at an operating frequency of 50 kHz. If the collector occupies more than 10% of the chamber surface area, this time could be decreased even further.

Some studies have been performed on buffer gas mitigation. In one, Antonsen et al. show that buffer gas flow can lower the ion flux below the noise threshold of the ESA from Fig. 6B.7.[51] Sizyuk, Hassanein, and Bakshi computationally showed that lighter buffer gas elements (such as He) transmit EUV much more easily than heavier elements (such as Ar)[62] at the same partial pressures. This result is important because, while buffer gas mitigation must provide enough gas to mitigate the Sn debris, it must not provide so much gas that EUV transmission is significantly hampered. For this reason, the lightest gas (H_2) is used in commercial EUV sources today.[63] Ion energy losses due to buffer gas collisions were also modeled by these researchers.

Few studies, however, have been performed on the transport of neutrals (as opposed to ions) in the presence of buffer gas. One exception is the work by Sporre, who experimentally and computationally analyzed the debris flux transported to the intermediate focus of a DPP source.[64] However, his results are also relevant to debris transport to the collector of an LPP source. Sporre found that the buffer gas pressure must be carefully chosen to avoid simply

Downloaded From: https://www.spiedigitallibrary.org/ebooks/ on 09 Mar 2022
Terms of Use: https://www.spiedigitallibrary.org/terms-of-use

energizing the buffer gas. At certain pressures, energetic buffer gas debris was detected, due to momentum transfer collisions that energized the buffer gas; at higher pressures, this effect was suppressed by increased collisionality. A sample of these results (with 0.3 mTorr being the operating pressure with no buffer gas) is shown in Fig. 6B.16. For this research, the experimental diagnostic was a set of microchannel plates (with an electrostatic ion deflector) to detect energetic neutrals, while the computational work was carried out by means of a collision-based Monte Carlo model. The buffer gas used for this work was Ar.

Sporre also used witness plates to analyze Sn deposition at the intermediate focus (IF), which is the focal point of the collector optic.[65] Sn was introduced by means of a Sn electrode, as described earlier. It should be noted that the direct path from the EUV plasma to the measurement location was obscured; thus, the Sn deposition seen is due to scattering of the Sn around the obscuration (hence the low deposition rate with no buffer gas at 0.3 mTorr). Similarly to Fig. 6B.16, Fig. 6B.17 shows that buffer gas at very low pressures fails to perform its purpose. Instead, it simply scatters Sn to the IF, rather than inhibiting transport. Higher pressures are necessary to inhibit transport. It should also be noted that the simulation only accounted for energetic Sn; the discrepancy between experiment and simulation is due to deposition by low-energy Sn, since even low-energy Sn causes deposition.

As shown by the investigations above, one concern must be the need to balance an appropriately high buffer gas pressure with EUV absorption by the buffer gas. As previously mentioned, the current industrial choice for buffer

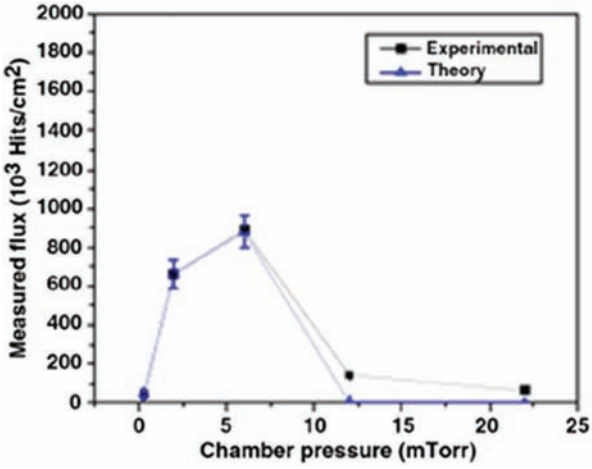

Figure 6B.16 At 2 mTorr and 6 mTorr, the energetic debris from an EUV plasma transfers its energy to the buffer gas, creating energetic buffer gas species that can harm the collector. This effect must be suppressed by the use of increased collisionality at higher pressures. The base pressure with no buffer gas was 0.3 mTorr in these experiments (reprinted from Ref. 64).

Downloaded From: https://www.spiedigitallibrary.org/ebooks/ on 09 Mar 2022
Terms of Use: https://www.spiedigitallibrary.org/terms-of-use

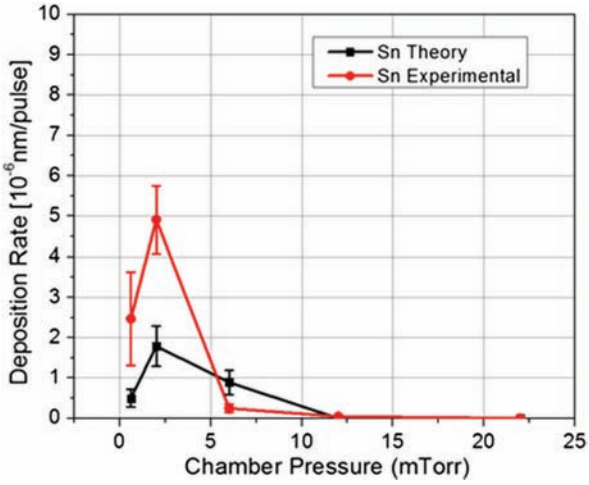

Figure 6B.17 Sn deposition at the intermediate focus of a DPP source with a Sn electrode. For these experiments, the direct line of sight from plasma to IF was obscured (hence the low deposition rate at 0.3 mTorr, where no buffer gas is present). At 2 mTorr and 6 mTorr, buffer gas fails to inhibit the transport of Sn debris. Instead, it simply scatters the Sn around the obscuration and to the IF. This indicates that similar failure of buffer gas could occur in an LPP, allowing Sn deposition on the collector. Higher pressures are necessary to prevent Sn transport. The difference between experiment and theory at low pressures is caused by low-energy Sn debris; Sn atoms below 100 eV were not accounted for in the simulation of energetic debris (reprinted from Ref. 64).

gas is H_2, due to its low EUV absorption; this allows commercial systems to utilize high buffer gas pressures without absorbing too much EUV. It should be noted, however, that this does not necessarily make H_2 the ideal buffer gas for all applications. The model by Sporre also showed that, at the same pressure, higher-mass buffer gas species (such as Ar) are more effective than lower-mass buffer gas species at extracting energy from the Sn atoms, due to increases in the collision cross-section and energy transfer coefficient.[63] Thus, higher pressures are necessary in order to provide sufficient deflection when using H_2 as the buffer gas; higher pressures can decrease the photon mean free path and reduce some of the transmittance advantage gained by using a light buffer gas.

Current industrial EUV scanner systems use a pressure on the order of 1 Torr, which allows for both EUV transmission and stopping of energetic Sn. Stopping and range tables from the Stopping and Range of Ions in Matter (SRIM) program[66] show a projected range of only 10–30 cm for Sn ions in the 1- to 10-keV range. However, other concerns also guide the design of today's modern industrial buffer gas mitigation systems. A diagram of the EUV source currently manufactured by Cymer, LLC is provided in Fig. 6B.18.

Within this system, H_2 pressure and flow must be optimized to protect both the collector and the IF. At the higher pressures used in current industry systems, diffusion is no longer as large as at lower pressures, and the vessel

Downloaded From: https://www.spiedigitallibrary.org/ebooks/ on 09 Mar 2022
Terms of Use: https://www.spiedigitallibrary.org/terms-of-use

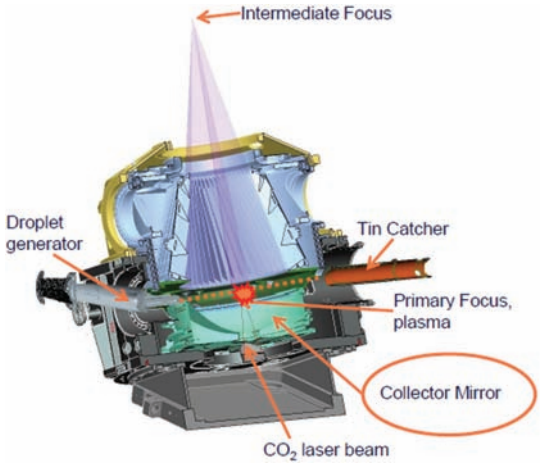

Figure 6B.18 Diagram of the current Sn LPP EUV source produced by Cymer, LLC. Sn is ejected from the droplet generator and irradiated by the CO_2 laser beam. Buffer gas must protect both the collector mirror and the intermediate focus. Any droplets missed by the laser are captured by the tin catcher (source: Cymer document, used by permission).

enters a regime where Sn transport can be at least partially controlled by advection and H_2 flow profiles. Thus, two different flow designs are employed simultaneously: a collector flow that protects the collector and a dynamic gas lock that prevents debris from reaching the IF and traveling to the downstream optics. The flow rates and flow profile designs are limited by instabilities and the need for the collector flow and the dynamic gas lock to not interfere with each other. Sn deflected by the mitigation system is captured by the vessel walls and by the pumping system. A scrubber in the pumping system prevents Sn from clogging the exhaust.

Results from this buffer gas mitigation technique have been very promising. As mentioned earlier, the collector lifetime without any debris mitigation would be less than 30 s, or 1.5 MPulses. However, using the same metric of collector lifetime (50% of initial reflectivity), 80-W sources in the field have achieved lifetimes that approach 100 GPulses, as shown in Fig. 6B.19.

The results presented in Fig. 6B.19 are certainly very promising. However, for HVM implementation, plans have been made to work toward a lifetime of 1 TPulse with a relative reflectivity of 90%. While more progress can be made on debris mitigation, the technique described in this section has been very successful in preventing contamination caused directly by the Sn plasma (also known as "fast" contamination). Currently, much of the reflectivity-reducing contamination takes the form of "slow" contamination. Slow contamination is due to Sn from other sources; mostly, this is due to Sn particles that are ejected from buildup on the walls of the chamber. These particles are too large to easily be stopped and deflected with buffer gas. Thus, in order to further extend collector lifetimes, it will be necessary to supplement buffer gas

Downloaded From: https://www.spiedigitallibrary.org/ebooks/ on 09 Mar 2022
Terms of Use: https://www.spiedigitallibrary.org/terms-of-use

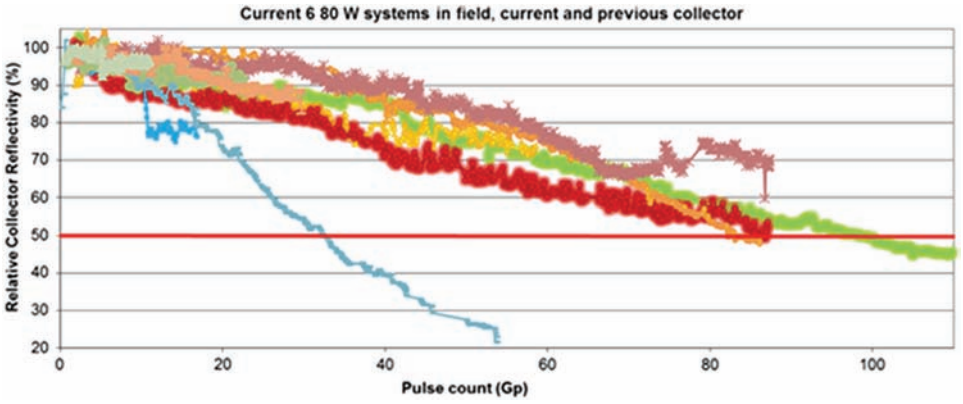

Figure 6B.19 Using the H_2 buffer gas debris mitigation system, 80-W EUV sources at various chip manufacturers have shown collector lifetimes (defined as the time until 50% EUV reflectivity degradation) that approach 100 GPulses. This figure is in comparison to the expected lifetime of less than 1.5 MPulses without debris mitigation (source: Cymer document, used by permission).

mitigation with collector cleaning. The next section is dedicated to H_2 radical cleaning, while Section 6B3.3 covers H_2 plasma cleaning.

6B.3.2 Atomic hydrogen cleaning

Originally, collector cleaning was performed by removing the collector and cleaning it with liquid chemicals. However, this method creates an unacceptable amount of source downtime. Thus, research in recent years has focused on how to clean the collector without removing it from the chamber. Ideally, this method would be truly *in situ*, which means that it would be able to be carried out without venting the system and without stopping the EUV source.

The most widely researched potentially *in situ* cleaning method involves the use of hydrogen radicals. When Sn is exposed to H radicals, it can react to form volatile stannane (SnH_4), which can then be pumped away according to the following reaction:

$$\mathrm{Sn(s) + 4H(g) \rightarrow SnH_4(g).} \tag{6B.4}$$

In this way, hydrogen can chemically etch Sn. SnH_4 is an unstable gas with a melting point of –146 °C and a boiling point of –52 °C.[67] The average bond energy is approximately 226 kJ/mol, although the individual Sn-H bonds are not of equal energies.[68] When gaseous, SnH_4 decomposes by dissociative adsorption upon surface-impact collision.[69] The rate of decomposition depends on both the surface temperature and the surface material.[70] For example, oxides have been shown to yield slower decomposition rates than metals.[61,62] This raises concerns about potential redeposition of Sn.

Downloaded From: https://www.spiedigitallibrary.org/ebooks/ on 09 Mar 2022
Terms of Use: https://www.spiedigitallibrary.org/terms-of-use

H radicals can potentially be used while running an EUV source, since H_2 is already present during normal source operation. Different methods of producing H radicals exist. On a broad scale, they can be grouped into two categories: atomic hydrogen sources and hydrogen plasma sources. Atomic hydrogen sources provide only radicals. In the case of a hydrogen plasma etching source, H_2 plasma is created in the EUV chamber itself, and plasma ions as well as radicals are incident on the collector. This section will cover atomic hydrogen etching techniques.

Atomic hydrogen sources are usually realized by means of a hot filament (which provides enough heat to dissociate H_2) or an external plasma source (which creates a H_2 plasma and then blows the radicals into the chamber). In the case of the external plasma source, the charged plasma species recombine on the walls of the external source and the radical delivery system connecting the generator to the chamber. The wall material is chosen to have a low radical recombination coefficient and maximize the delivery of radicals as much as possible; thus, radical fluxes are delivered without charged species.

Hydrogen etching of Sn was reported by van Herpen et al. in 2009.[72] This work utilized a hot filament atomic hydrogen source positioned 2 cm away from a Sn-coated sample. The pressure was approximately 15 Torr; however, the radical density was not measured, and the cracking efficiency of the hot filament was not known. Thus, it is unclear how many radicals were actually produced. Etching was carried out for 10-s intervals on both Sn-coated Si samples and Sn-coated Ru samples. The highest etch rate was on the order of 50 nm/min for the Sn-coated Si sample. Cracking efficiencies for hot filament hydrogen radical sources can easily run all the way from 1% to 100%.[73,74] If a 1% cracking efficiency is assumed, a partial pressure of 150 mTorr of radicals results. At room temperature, the ideal gas law yields a radical density of 4.9×10^{15} cm^{-3} for a radical pressure of 150 mTorr. The radical flux Γ may then be calculated by

$$\Gamma_H = \frac{1}{4} n_H v_{th}, \tag{6B.5}$$

where n_H is the radical density, and v_{th} is the thermal velocity. At room temperature, this yields a radical flux of approximately 3.1×10^{20} cm^{-2}s^{-1}. If n_{Sn} is the solid density of Sn (approximately 3.7×10^{22} cm^{-3}), the etched flux of SnH_4 may be calculated by

$$\Gamma_{SnH_4} = (Etch\ Rate)(n_{Sn}), \tag{6B.6}$$

yielding an SnH_4 flux of 3.1×10^{15} cm^{-2}s^{-1}. Dividing the fluxes yields a reaction efficiency of about 10^{-5}; alternatively, approximately 10^5 H atoms were required to etch a single Sn atom. If a higher cracking efficiency is

Downloaded From: https://www.spiedigitallibrary.org/ebooks/ on 09 Mar 2022
Terms of Use: https://www.spiedigitallibrary.org/terms-of-use

assumed, the reaction efficiency will be lower (and the number of H atoms required to etch a single Sn atom will be higher).

Additionally, the etch rate was observed to be lower for the Sn-coated Ru samples. These etches were undertaken for very thin films of Sn (approximately 10 nm). Since Sn is known to form islands[75] and the film is very thin, it is likely that parts of the underlying substrate were exposed for part or most of the etches. Thus, the very thin nature of the films, along with the tendency of Sn to form islands, may indicate either a substrate-dependent effect on the etch rate of the last few nanometers or a higher rate of dissociation and re-deposition for SnH_4 on Ru than for SnH_4 on Si. Redeposition is the phenomenon by which SnH_4 dissociates upon collision with a wall, yielding two H_2 molecules and depositing a Sn atom.[71] These results are shown in Fig. 6B.20.

Atomic hydrogen etching of Sn was also investigated by Ugur et al.[70,76] In these studies, hydrogen radicals were used to etch Sn from the surface of Sn-coated quartz crystal microbalances (QCMs). These studies were performed at a lower pressure (approximately 75 mTorr). In one set of experiments, radicals were incident on a Sn-coated QCM, yielding SnH_4; Sn redeposition was then measured on a clean Au-coated QCM. This study also made use of a hot filament source. A catalytic radical probe was used to measure the radical density. A diagram of Ugur's setup is shown in Fig. 6B.21.

In one set of experiments, Ugur measured an incident hydrogen radical flux of 3.2×10^{17} $cm^{-2}s^{-1}$ and an etched SnH_4 flux of 3.4×10^{12} $cm^{-2}s^{-1}$. Dividing the SnH_4 flux by the radical flux yields an etching probability of just

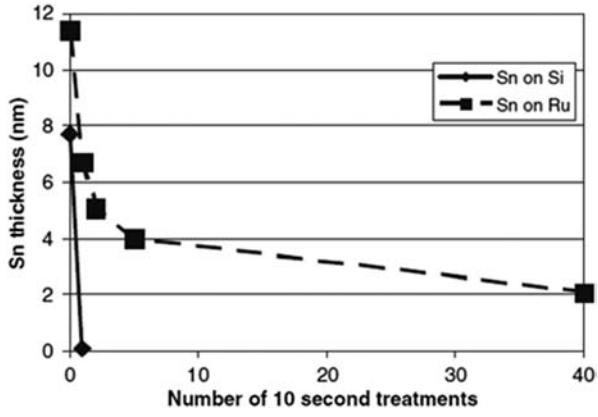

Figure 6B.20 Si and Ru samples coated with approximately 10 nm of Sn were exposed to atomic hydrogen by turning on a hot filament radical source for pulses of 10 s each. Sn was etched more quickly from the Si substrate. This indicates a possible substrate-dependent etching effect for the last few nanometers or a higher redeposition probability for Sn on Ru than for Sn on Si. The etch rate for Sn on Si was approximately 50 nm/min, and the pressure was approximately 15 Torr. Depending on the cracking efficiency of the radical source, this yields an etching reaction efficiency of approximately 10^{-5} or lower (reprinted from Ref. 72 with permission from Elsevier).

Downloaded From: https://www.spiedigitallibrary.org/ebooks/ on 09 Mar 2022
Terms of Use: https://www.spiedigitallibrary.org/terms-of-use

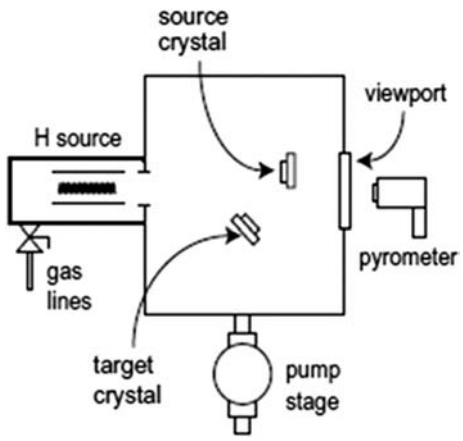

Figure 6B.21 The setup used by Ugur. H_2 passes by a hot filament, which produces H radicals. The radicals etch Sn from the source crystal, which measures the etch rate. Some of the etched SnH_4 deposits on the target crystal (reprinted from Ref. 76 with permission from Elsevier).

under 1.1×10^{-5}, or 94,000 H radicals per Sn. It should be noted that, unlike van Herpen's experiments, this experiment used a thicker film of approximately 450 nm. Deposition of Sn on the exposed Au target crystal was observed by SEM.

In another set of experiments, the target crystal was replaced by a series of different samples, and the thickness of Sn films grown by redeposition was measured.[70] It was observed that Ni, Ru, Rh, and Au saw deposition rates one to two orders of magnitude higher than deposition rates on TiO_2 and ZrO_2.

Cleaning by atomic hydrogen was also studied by Braginsky.[77] Braginsky used a plasma source to dissociate H_2; however, the ions incident on the sample were of low energy (10–20 eV). Additionally, Braginsky measured the same etching probability per radical when the plasma source was located in a remote chamber, confining the charged species while allowing radicals to be blown at the sample. Thus, it was deduced that, at the ion energies present in Braginsky's setup, no ion-driven plasma effect was seen, and the source was equivalent to a pure hydrogen radical source. As expected, the etching probability measured by Braginsky was on the same order as that of Ugur.

Atomic hydrogen cleaning has also been explored in industry.[78] So far, experiments have been performed utilizing an external microwave generator. This system uses a microwave source to break down a H_2 plasma in an external chamber; radicals from the plasma (with a minimal amount of ions) are blown into the main chamber through a delivery system. Two implementations of this system have been achieved. The first utilizes a glass tube placed in front of the collector to deliver the radicals. A before/after comparison of etching on an industrial collector (650-mm diameter) is shown in Fig. 6B.22.

Downloaded From: https://www.spiedigitallibrary.org/ebooks/ on 09 Mar 2022
Terms of Use: https://www.spiedigitallibrary.org/terms-of-use

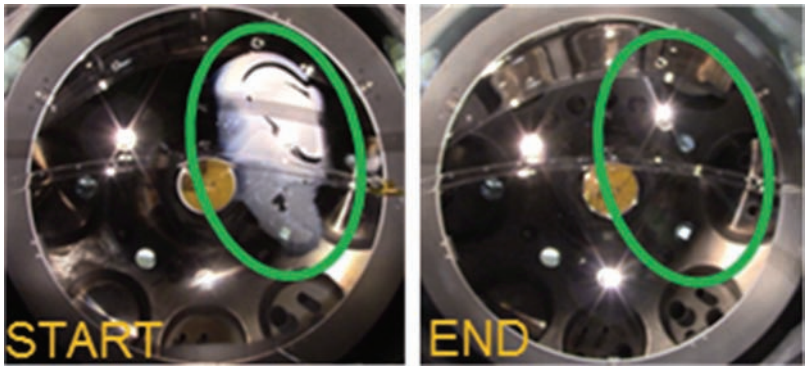

Figure 6B.22 An industrial demonstration of hydrogen radical cleaning. Radicals are created outside the chamber and then blown in through a clear tube in front of the collector. Sn contamination that is present before radical exposure is removed by radicals (courtesy of Cymer[79]).

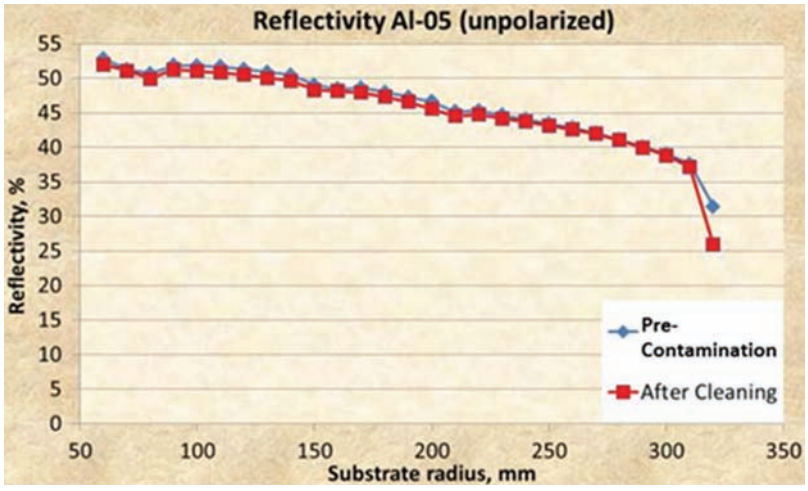

Figure 6B.23 EUV reflectivity measured for the collector shown in Fig. 6B.22. The reflectivity after cleaning is identical to the pre-contamination reflectivity at almost every point on the collector (courtesy of Cymer[79]).

EUV reflectivity has been compared before contamination and after cleaning. These results, presented in Fig. 6B.23, show that over most of the collector, reflectivity is completely restored to its pre-contamination values.

Unfortunately, placing a delivery system for radicals in front of the collector requires EUV source downtime while the delivery tube is inserted, used, and removed. Therefore, another implementation of this technique has been tested using a delivery system located around the perimeter of the collector. A before/after comparison of etching using this system is shown in Fig. 6B.24, and EUV reflectivity results are shown in Fig. 6B.25.

Downloaded From: https://www.spiedigitallibrary.org/ebooks/ on 09 Mar 2022
Terms of Use: https://www.spiedigitallibrary.org/terms-of-use

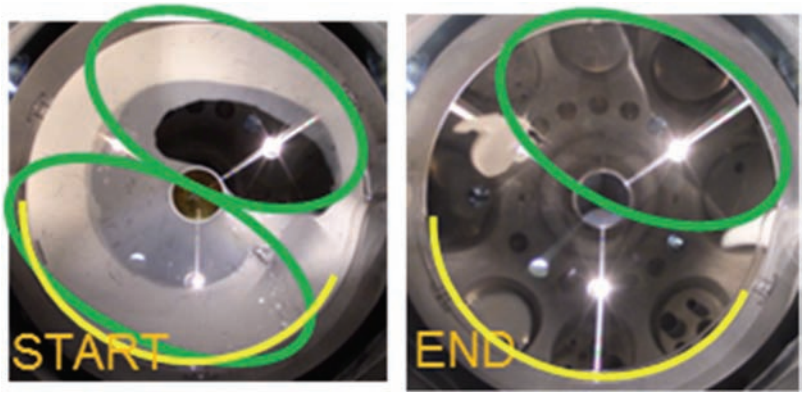

Figure 6B.24 Industrial demonstration of hydrogen radical cleaning. Radicals are created outside the chamber and then blown in through a tube encircling the perimeter of the collector. Sn contamination that is present before radical exposure is removed by radicals (courtesy of Cymer[79]).

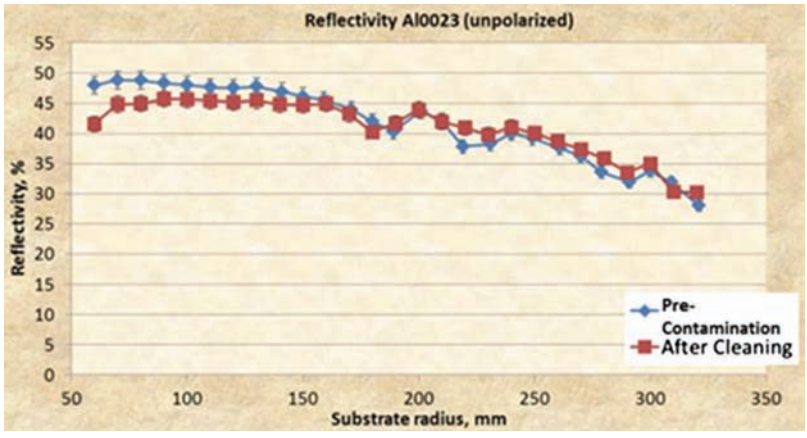

Figure 6B.25 EUV reflectivity measured for the collector shown in Fig. 6B.24. The reflectivity after cleaning nearly equals the reflectivity before contamination (courtesy of Cymer[79]).

While the reflectivity results from this cleaning system are slightly lower than those from the previous system, this system has the advantage of not requiring a tube in front of the collector. Thus, while *in situ* implementation has not yet occurred, this system could theoretically be used in a running EUV source without requiring downtime for cleaning. Etch rates with both of these systems have been measured at <4 nm/min.

It is also possible to etch Sn without an external radical source and delivery system. This will be explored in the next section, which will cover plasma-based etching of Sn. Additionally, it will be shown that ions from plasma can cause a very beneficial etch rate enhancement.

Downloaded From: https://www.spiedigitallibrary.org/ebooks/ on 09 Mar 2022
Terms of Use: https://www.spiedigitallibrary.org/terms-of-use

6B.3.3 Hydrogen plasma cleaning

Hydrogen plasma etching involves creating a plasma in the EUV chamber, allowing both the radicals and the ionized plasma species to be incident on the Sn contamination. Hydrogen plasma etching has been explored at CPMI and also observed through an accidental yet beneficial effect in industry. This section will detail these investigations.

Plasma-etching experiments at CPMI have centered around using the collector itself as a plasma electrode.[80] In the XCEED chamber, a 300-mm-diameter stainless steel dummy collector is mounted, isolated from ground, and connected to a 13.56-MHz RF supply in the presence of H_2 gas, as shown in the setup in Fig. 6B.26. This technique creates radicals immediately at the collector surface without any delivery system.

Initial experiments were carried out at 65 mTorr and 500 sccm of H_2 flow. As shown in the previous section, other work concentrated on etching Sn only from small samples. Thus, for these experiments, the entire collector was coated with Sn via magnetron sputtering; the Sn was then etched by H_2 plasma at 300 W for 2 h. To quantify etch rates, Si samples were placed radially along the collector, with 3 cm being the inner radius and 15 cm being the outer radius. Sn removal rates measured with a surface profilometer are shown in Fig. 6B.27. These rates were measured for an initial deposition of 200 nm. Error is caused by noise and leveling in the profilometer.

The restoration of EUV reflectivity has also been measured. For these experiments, Si samples were replaced by ZrN-capped MLM samples, which were exposed to various conditions. The Control sample was never removed from its case. The Bare sample was removed from its case and handled, to show if any reflectivity was removed by atmospheric contaminants and handling. The Etched sample was left bare but exposed to the etching plasma for 45 min.

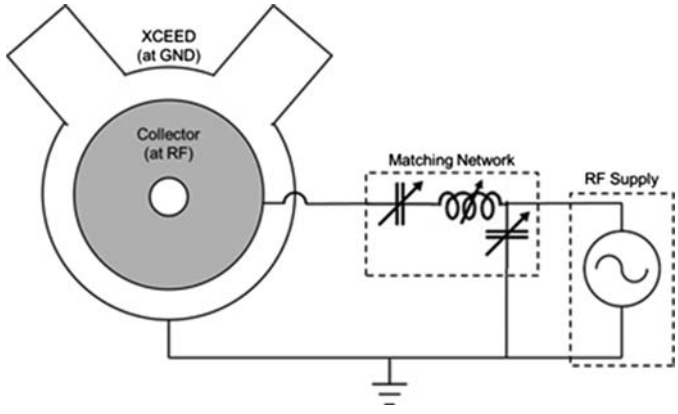

Figure 6B.26 A circuit diagram of the plasma source setup. The collector is isolated inside XCEED and is attached to a 300-W 13.56-MHz RF supply. A matching network serves to minimize reflected power (reprinted from Ref. 80 with permission from AIP Publishing).

Downloaded From: https://www.spiedigitallibrary.org/ebooks/ on 09 Mar 2022
Terms of Use: https://www.spiedigitallibrary.org/terms-of-use

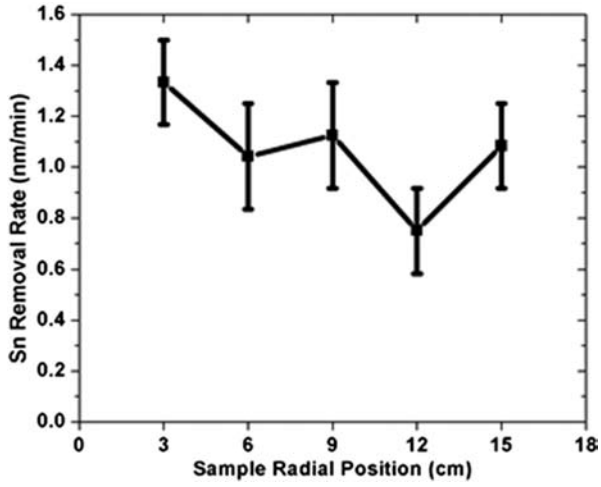

Figure 6B.27 Removal rates across the collector for full-collector cleaning at 65 mTorr, 500 sccm, and 300 W. Sample 1 is located at the inner radius; sample 5 is located at the outer radius.

The Deposited sample was coated with Sn, and the Deposited and Etched sample was (along with the whole collector) coated with Sn and then cleaned over a period of 45 min. Samples were then sent to Lawrence Berkeley National Laboratory for EUV reflectivity measurements. Results are shown in Fig. 6B.28. Error levels were determined by comparing EUV reflectivity measurements from two identical samples.

No difference is seen between the Control (unhandled) sample and the Bare (handled) sample, indicating that sample handling does not affect reflectivity measurements. The uncoated sample that was exposed to the plasma (Etched) indicates that the plasma species do not damage the reflectivity of the MLM (more details on this will be provided in Section 6B.3.4). Sn deposition predictably reduces reflectivity; the final sample shows that this reflectivity is restored by plasma cleaning. The slight difference between the Bare/Control value and the Deposited & Etched value is due to non-Sn contamination from the deposition experiment. More information on this setup and these experiments may be found in Ref. 80.

Parameter variations and the fundamental processes underlying plasma etching of Sn have also been explored. Raising the pressure to 325 mTorr resulted in decreased removal rates of approximately 0.1–0.2 nm/min, measured with the profilometer. H radical densities have been measured by a catalytic radical probe and validated by a zero-dimensional plasma chemistry model. The catalytic probe consists of a thermocouple attached to a small piece of material with a high recombination coefficient for the radical of interest; in this case, Au is used to catalyze recombination of H radicals to H_2. Energy released by recombination reactions heats the probe,

Downloaded From: https://www.spiedigitallibrary.org/ebooks/ on 09 Mar 2022
Terms of Use: https://www.spiedigitallibrary.org/terms-of-use

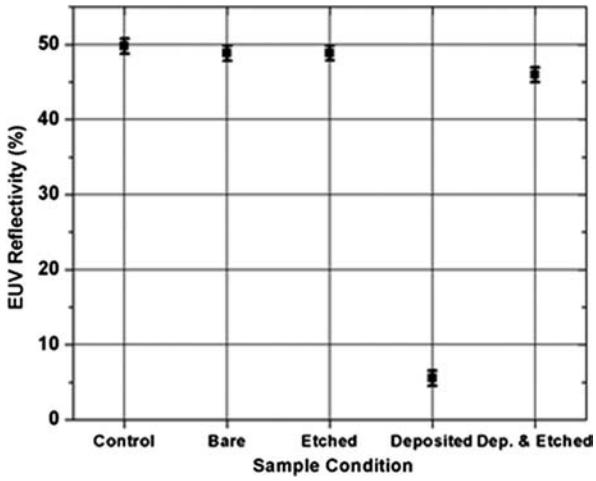

Figure 6B.28 EUV reflectivitity measurements for various ZrN-capped MLM samples. The negligible difference between Control and Bare indicates no reflectivity loss due to atmospheric contaminants and handling. The Etched sample was left uncoated and was exposed to the plasma for 45 min; the lack of reflectivity loss indicates no damage to the MLM by the plasma (see Section 6B.3.4 for more details). The difference between the Deposited sample and the Deposited and Etched sample indicates that H_2 plasma cleaning restores EUV reflectivity to Sn-coated MLMs. The small difference between the Deposited and Etched value and the original value is due to non-Sn contamination from the deposition experiment.

allowing for calculation of the power delivered by radicals; this number is then used to calculate the radical density. For more information on catalytic probes and their operation, the reader is referred to Refs. 81–83.

As shown in Fig. 6B.29, the radical density is higher at 325 mTorr than at 65 mTorr (though within error bars). Radical densities do not rise linearly with pressure. This is due to the fact that radicals are made primarily by electron-impact dissociation of H_2. Pressure increases cause an increase in H_2 density but a decrease in electron density; thus, the increase in radical density within the given pressure range is not linear. Error is caused by assumptions in the probe theory and slope smoothing applied to the catalytic probe temperature curves.

The fact that the etch rate decreases by an order of magnitude while the radical density increases suggests that something other than radical density is controlling the etch rate. One potential hypothesis was redeposition. At a high pressure, the mean free path is low; thus, it would be more difficult for SnH_4 to leave the vicinity of the collector before hitting the surface and potentially redepositing. Redeposition could have lowered the total net removal rate.

However, the redeposition coefficient of Sn was measured in 1956 by Tamaru to obey an Arrhenius form and to be very low.[71] For example, at 77 °C, the redeposition coefficient can be calculated as 1.35×10^{-7}. Experiments have been performed at the University of Illinois to verify this. SnH_4 was prepared according to a procedure similar to that described by Norman et al.[85]

Downloaded From: https://www.spiedigitallibrary.org/ebooks/ on 09 Mar 2022
Terms of Use: https://www.spiedigitallibrary.org/terms-of-use

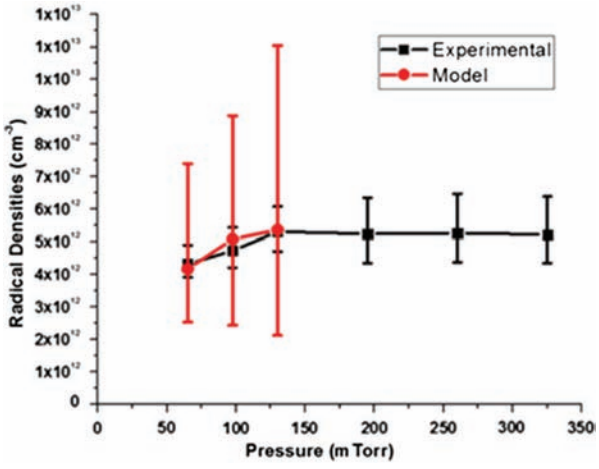

Figure 6B.29 The radical density is higher at 325 mTorr than at 65 mTorr. However, the Sn etch rate decreases by an order of magnitude when moving from 65 mTorr to 325 mTorr, suggesting that radicals are not the limiting factor in plasma etching of Sn (reprinted from Ref. 84).

and inserted into a glass chamber in the presence of a Sn-coated QCM. Over 20 minutes, no measurable deposition was observed above the noise floor at a SnH_4 pressure of 10 Torr. This is consistent with such a small redeposition coefficient.

Additionally, instantaneous etch rates for a bare collector were measured by placing a Sn-coated QCM on the collector. These were measured to be approximately 1.9 nm/min at 65 mTorr and 0.2 nm/min at 325 mTorr. These are in reasonable agreement with the etch rates reported earlier for a fully coated collector. Since the QCM diameter is only 8 mm, the source of Sn in the QCM experiments was much smaller than in the fully coated collector experiments; a large redeposition coefficient would produce significantly lower etch rates with a large source of Sn. COMSOL Multiphysics® simulations were also carried out to verify that, for an etching flux of SnH_4 derived from these removal rates, the redeposition rate would be negligibly low given Tamaru's redeposition coefficient.[71,86]

It was observed, however, that etch rates appeared to scale with the ion energy flux, which is the product of the ion flux (measured from the ion current of a Langmuir Probe) and the average ion energy (measured with a high-voltage probe near the collector on the RF power line). This is shown in Fig. 6B.30, along with a comparison to radical densities. Quantities are normalized to their value at 65 mTorr in order to print all of them on one graph. Error is caused by positioning of the high-voltage probe and error in the measurement of the area of the Langmuir probe.

The results in Fig. 6B.30 are indicative of reactive ion etching (RIE). In RIE, energetic ions aid in breaking Sn-Sn bonds (allowing H radicals to bond to the Sn) and desorbing SnH_4 molecules.

Downloaded From: https://www.spiedigitallibrary.org/ebooks/ on 09 Mar 2022
Terms of Use: https://www.spiedigitallibrary.org/terms-of-use

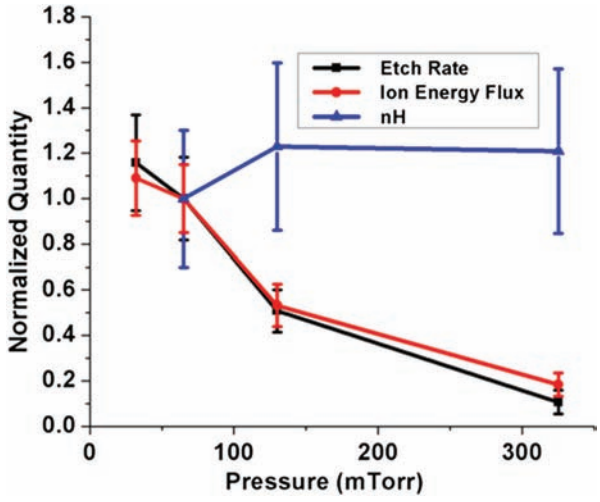

Figure 6B.30 While the etch rate does not follow the radical flux, it does follow the ion energy flux. This is indicative of a reactive-ion-etching regime, where ion bombardment is responsible for Sn-Sn bond breaking and SnH_4 desorption. This shows that the ion species in a plasma can help increase etching. Quantities are normalized to their value at 65 mTorr to allow for plotting on one graph.

RIE can explain how this plasma system has achieved higher radical-per-Sn efficiency numbers than the atomic hydrogen systems in the previous section. If Eqs. (6B.3) and (6B.4) are carried out on the data presented at 65 mTorr, they yield an efficiency of approximately 4.3×10^{-4}, or 2300 radicals per Sn. This is more than an order of magnitude more efficient than the values reported in Section 6B.3.2 with atomic hydrogen sources. These results show that cleaning rates in EUV sources could potentially be raised by the use of plasma.

While H_2 plasma etching has not been industrially implemented in a dedicated process, it has already been observed as a beneficial side effect. As discussed in Section 6B.3.1, the EUV source operates in an H_2 environment. While most EUV photons are transmitted, some cause inelastic collisions with H_2, creating a diffuse hydrogen plasma. This plasma, which is present during source operation, has been observed to clean Sn.

The cleaning rate due to this plasma has been estimated as follows. First, the buffer gas flow is reduced, hampering debris mitigation and allowing some Sn to deposit on the collector. Second, the film thickness is measured. Third, debris mitigation is restored, reducing the deposition rate to nearly zero. At this point, the Sn will begin to be etched away by the plasma. Finally, the time required to complete etching is recorded. In this manner, the cleaning rate due to this photon-created plasma has been estimated at approximately 1 nm/min.

The use of plasmas raises a question about surface damage. While ions can accelerate etching, they also have the potential to sputter and implant,

Downloaded From: https://www.spiedigitallibrary.org/ebooks/ on 09 Mar 2022
Terms of Use: https://www.spiedigitallibrary.org/terms-of-use

damaging the MLM. The next section will briefly summarize a set of experiments used to determine MLM compatibility with plasma.

6B.3.4 Compatibility of multilayer mirrors with H_2 plasma

Regardless of any dedicated cleaning technique, the collector optic is going to be exposed to a H_2 plasma, due to the photo-ionization caused by the EUV plasma and described at the end of the previous section. Thus, it is relevant to understand the ability of MLMs to tolerate exposure to an H_2 plasma, as ions can cause sputtering and implantation.

Research has been carried out to determine what effect, if any, a H_2 plasma has on MLMs with ZrN and SiN capping layers. As a preliminary investigation, a bare Si sample was exposed to the cleaning plasma from the previous section (65 mTorr, 300 W) for 2 h. An AFM scan, shown in Fig. 6B.31, confirms that the surface remains smooth with an RMS roughness of 0.32 nm. This is very close to the value for a polished Si wafer (0.15 nm), and this small discrepancy can easily be explained by the fact that the sample was cut and handled outside of a cleanroom. Handling appeared to induce an error bar of around 1 nm. Thus, no sputtering-induced roughness was observed.

A more thorough investigation was begun by carrying out sputtering simulations of common materials in MLMs. Thus, sputtering of Si and Mo, as well as Zr and Ru, was considered (since capping layers are often made of Ru or ZrN). Simulations were carried out with the Stopping and Range of Ions in Matter (SRIM) code. In order to simulate ion-surface interactions, the ion

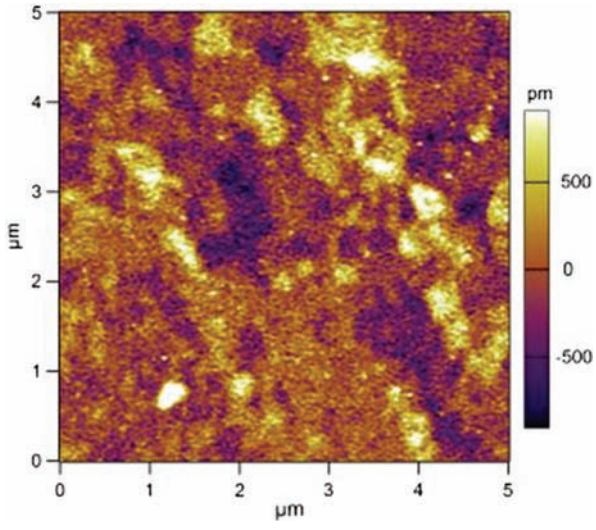

Figure 6B.31 A bare Si sample exposed to H_2 plasma at 65 mTorr and 300 W for 2 h shows a very smooth surface with a RMS roughness of 0.32 nm, indicating an absence of sputtering-induced roughness.

Downloaded From: https://www.spiedigitallibrary.org/ebooks/ on 09 Mar 2022
Terms of Use: https://www.spiedigitallibrary.org/terms-of-use

energy must be known. The average ion energy is given by the addition of the plasma potential and the electrode voltage. Voltage on the collector was measured by a high-voltage probe, while plasma potential was measured with a Langmuir probe. These measurements yielded an average ion energy of approximately 250 eV. SRIM results for H+ atoms at 250 eV are shown in Table 6B.1.

Only a small yield is shown for Si, and no sputtering is expected for the other materials. It should also be noted that, since these simulations were performed for H^+, they represent a worst-case scenario. In reality, most plasma ions in the pressure range considered in the previous section (65–325 mTorr) will be H_3^+.[87] The sputtering effect of a H_3^+ ion is identical to dividing the energy equally amongst three H^+ ions. If the simulations are undertaken once again but for H_3^+ by simulating H^+ at 83 eV, all of the sputtering yields go to 0.

Experimental investigations were carried out for MLM samples with two different capping layers (ZrN and SiN). Secondary-ion mass spectroscopy (SIMS) was used to generate depth profiles of the samples' first few tens of nanometers by bombarding the samples with high-energy ions and analyzing the mass of ionized sputtered species. SIMS results indicate no difference between bare samples and samples exposed to the etching plasma for 45 min. As an example, SIMS profiles of a bare ZrN-capped sample and an etched ZrN-capped sample are shown in Fig. 6B.32. The Zr feature is the same size in both profiles, indicating that it was not sputtered away at all.

Additionally, EUV reflectivity was compared between bare samples and plasma-exposed samples. The results presented in Figs. 6B.28 and 6B.32 confirm that exposure to the H_2 plasma does not reduce the EUV reflectivity of ZrN-capped samples. However, as shown in Fig. 6B.33, the same cannot be said for SiN-capped samples, which experience a reflectivity degradation after plasma exposure. The same experimental conditions were used for each of the three sets of samples; they are identical to the conditions of the same names described in the caption for Fig. 6B.28.

The reason for this can be seen in Fig. 6B.34, which compares SEM images of an etched SiN-capped sample and an etched ZrN-capped sample. The reflectivity drop for SiN-capped samples is due not to sputtering but to implantation-induced blistering.

Table 6B.1 Sputtering yields for common MLM materials bombarded by 250 eV H^+ ions.

	Si	Mo	Ru	Zr
Sputtering yield	0.017 at/ion	0	0	0
Sputtering rate	0.029 nm/min	0	0	0
Thickness sputtered after 45 min.	1.3 nm	0	0	0

Downloaded From: https://www.spiedigitallibrary.org/ebooks/ on 09 Mar 2022
Terms of Use: https://www.spiedigitallibrary.org/terms-of-use

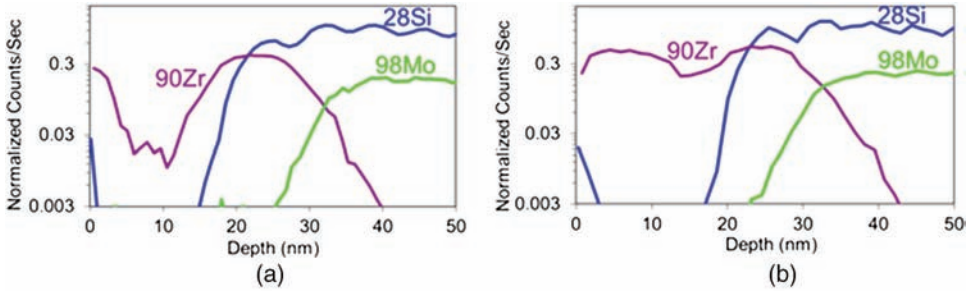

Figure 6B.32 SIMS depth profiles of (a) a bare ZrN-capped MLM sample and (b) a ZrN-capped MLM sample exposed to an H_2 etching plasma at 65 mTorr and 300 W for 45 min. No difference is seen between the Zr features in the two profiles, indicating that the capping layer was not sputtered by the plasma. This is in agreement with the SRIM simulations. It should be noted that the apparent difference between the Si and Mo levels is due to the materials' different ionization yields; for this reason, SIMS cannot be used to quantitatively compare concentrations of different materials (reprinted from Ref. 80 with permission from AIP Publishing).

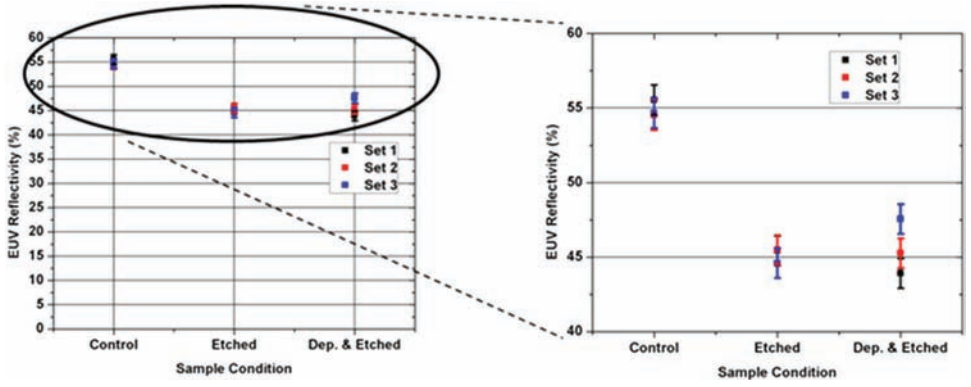

Figure 6B.33 EUV reflectivity analysis was undertaken for SiN-capped samples. Samples exposed to a H_2 plasma saw a significant decrease in reflectivity compared to the original control values. This effect was also observed for Sn-coated samples that were cleaned by the plasma. Thus, even though the plasma can clean Sn, it can affect the reflectivity of SiN-capped samples in a negative way.

Though hydrogen ions do not sputter the SiN-capped MLM, they implant into it. After implantation, they can recombine and form H_2 bubbles. However, it is known that the native oxide of SiN inhibits hydrogen diffusion. This traps implanted hydrogen, preventing them from diffusing out; instead, it nucleates and forms bubbles, which cause blisters and eventually burst. This effect is not seen on the ZrN-capped sample. Additionally, reactions of H radicals with Si can form gaseous SiH_x, while ZrH_x is a solid.

It is known that ZrN has also been observed industrially to be more stable than SiN in the H_2 plasma environment produced by the EUV plasma.[88] This fact, along with the results presented above, highlight the importance for

Downloaded From: https://www.spiedigitallibrary.org/ebooks/ on 09 Mar 2022
Terms of Use: https://www.spiedigitallibrary.org/terms-of-use

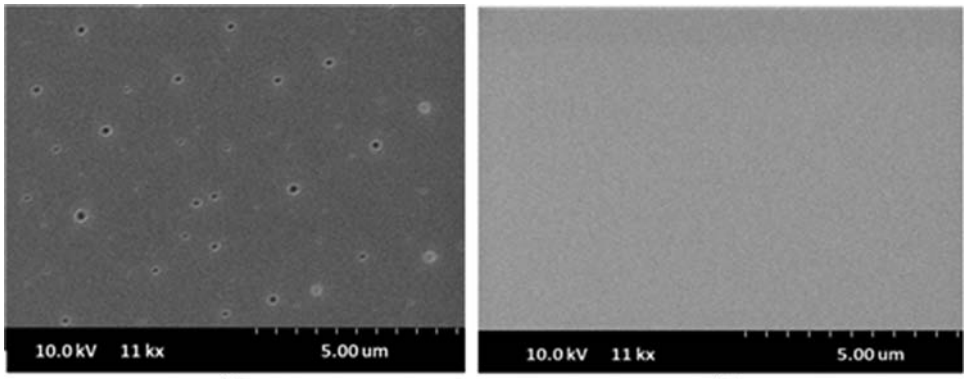

Figure 6B.34 (a) In an SiN-capped sample, hydrogen implants into the MLM and becomes trapped, forming bubbles that blister and burst. This causes an EUV reflectivity reduction due to plasma exposure. (b) A ZrN-capped sample exposed to the same plasma is not damaged at all, and the EUV reflectivity is not reduced. Thus, the ZrN capping layer is compatible with a H_2 plasma (reprinted from Ref. 80 with permission from AIP Publishing).

industry to choose a capping layer material, such as ZrN, that is compatible with a H_2 plasma environment. With this in mind, a collector that is compatible with the photon-induced H_2 plasma should also be compatible with a dedicated H_2 cleaning plasma, as long as that plasma's ions are not allowed to reach energies high enough for significant sputtering.

6B.4 Summary

EUVL is the leading next-generation lithography candidate for producing feature sizes 7 nm and smaller in HVM of chips. One main difference between EUVL and other lithography techniques is that EUVL requires reflective optics because sufficient transmission at the EUV wavelength does not exist. For normal-incidence collector optics, a Mo-Si MLM is designed to reflect light at 13.5 nm. This normal-incidence collector mirror is exposed to a Sn plasma, which produces harsh debris in the form of Sn ions and neutrals that can cause sputtering, implantation, and Sn deposition, resulting in reflectivity loss.

Ion energies from an EUV source have been quantified to be in the keV range. Strong debris mitigation is necessary to prevent these ions from causing irreversible damage. Magnetic debris mitigation and buffer gas mitigation have been explored as a means of preventing ion-induced damage. Industrial buffer gas techniques have been very successful at extending collector lifetime, leading to a current lifetime of 100 GPulses. Buffer gas not only slows down and deflects ions, but also deflects most Sn neutrals, which can deposit at any energy. Source operation has been optimized to reduce production of large Sn particles and maximize production of Sn vapor, which can be controlled more easily by buffer gas than particles can.

Downloaded From: https://www.spiedigitallibrary.org/ebooks/ on 09 Mar 2022
Terms of Use: https://www.spiedigitallibrary.org/terms-of-use

However, debris mitigation cannot deterministically control the path of every single neutral, and some particles are still formed, especially from Sn buildup on the chamber walls. Thus, some Sn deposition still occurs on the collector, and cleaning is required. Currently, the preferred method of cleaning is to use hydrogen radicals to react with Sn and form the etch product SnH_4. Since H_2 is currently used as the buffer gas, hydrogen cleaning could potentially be carried out *in situ* while running the EUV source. In academia, atomic hydrogen radical sources have been explored and have shown etching efficiencies of 1 etched Sn atom per approximately 10^5 incident radicals for Sn-coated samples. Industrially, external hydrogen radical sources have been shown to be capable of cleaning contamination from a collector and restoring EUV reflectivity. Different delivery systems have been tested, including one that does not block the collector and offers a pathway toward cleaning during source operation. However, these systems have not yet been implemented in a running EUV source.

Etching by means of a H_2 plasma has also been explored. In a plasma system, the radical-producing plasma is created inside the EUV chamber, allowing the collector to be exposed to both radicals and plasma ions. A particular plasma topology has been extensively tested; this topology involves using the collector itself as a plasma electrode and requires no delivery system. Plasma cleaning has been shown to clean a Sn-coated collector and restore EUV reflectivity. Additionally, cleaning efficiencies much higher than those achieved without energetic ion bombardment have been observed, up to 1 etched Sn atom per 2300 incident H atoms. Experimental studies have correlated this increased etching efficiency with ion energy flux. This suggests a reactive ion etching regime and indicates that charged plasma species can maximize cleaning beyond that provided by radicals alone. Industrially, plasma-induced cleaning has been observed because of a secondary effect. Photons from the EUV-producing plasma break down some of the H_2 buffer gas and form some H_2 plasma, which has been observed to clean Sn at approximately 1 nm/min.

Finally, compatibility of ZrN- and SiN-capped MLMs with H_2 plasma has been explored. Simulations and SIMS depth profiles have shown no plasma-induced sputtering with H_2 ions up to an average energy of 250 eV. Implantation was shown to lead to H_2 nucleation and blistering on SiN-capped samples, damaging the EUV reflectivity. This phenomenon does not occur on ZrN-capped samples, and plasma exposure does not damage their reflectivity at all. This is similar to effects seen in industry caused by the photon-induced H_2 plasma; for this reason, it is important, regardless of the cleaning method, to use a capping layer that is compatible with H_2 plasma.

While more work must be done to reduce contamination to levels acceptable for HVM, the success achieved so for with Sn management and contamination control cannot be understated. Without debris mitigation, the

Downloaded From: https://www.spiedigitallibrary.org/ebooks/ on 09 Mar 2022
Terms of Use: https://www.spiedigitallibrary.org/terms-of-use

expected collector lifetime is less than 2 MPulses; with debris mitigation, the lifetime has been raised to approximately 100 GPulses. Future work on debris mitigation optimization, minimization of Sn particles from vessel walls, and implementation of a cleaning system should help bring this number even higher and ensure HVM-compatible contamination management.

Acknowledgments

We would like to express special thanks to graduate students Gianluca Panici and Sumeng Liu, undergraduate students Shanna Bobbins, Sean Piper, Shubhang Goswami, and Luke Gasparich, and former undergraduate students Louis Chapdelaine, Pawel Piotrowicz, and Valentin Castro for their work on the plasma etching system at the Center for Plasma-Material Interactions (CPMI). We would also like to thank Dr. Erik Gullikson of Lawrence Berkeley National Lab for performing EUV reflectivity measurements. Additionally, we thank Cymer, LLC for research funding and for providing insights about the state of current industrial sources. EUV efforts at CPMI are also funded in part by NSF GOALI Grant #14-36081.

References

1. M. Rothschild, T. M. Bloomstein, T. H. Fedynyshyn, R. R. Kunz, V. Lierman, M. Switkes, N. N. Efremow, Jr., S. T. Palmacci, J. H. C. Sedlacek, D. E. Hardy, and A. Grenville, "Recent trends in optical lithography," *Lincoln Laboratory Journal* **14**(2), 221–236 (2003).
2. U. Stamm, J. Kleinschmidt, K. Gabel et al. "EUV source power and lifetime: the most critical issues for EUV lithography," *Proc. SPIE* **5374**, 133–144 (2004) [doi: 10.1117/12.535410].
3. D. C. Brandt, I. V. Fomenkov, N. R. Farrar et al., "LPP source readiness for NXE 3300B," *Proc. SPIE* **9048**, 90480C (2014) [doi: 10.1117/12.2048184].
4. R. A. Burdt, Y. Tao, M. S. Tillack, S. Yuspeh, N. M. Shaikh, E. Flaxer, and F. Najmabadi, "Laser wavelength effects on the charge state resolved ion energy distributions from laser-produced Sn plasma," *J. Appl. Phys.* **107**, 043303 (2010).
5. T. Kagawa, H. Tanuma, H. Ohashi, and K. Nishihara, "RCI Simulation for EUV spectra from Sn ions," *J. Physics: Conference Series* **58** (2007).
6. C. Hecquet, M.-F. Ravete-Krill, F. Delmotte et al., "Design, conception and metrology of EUV mirrors for aggressive environments," *Proc. SPIE* **6586**, 65860X (2007) [doi: 10.1117/12.723483].
7. J. P. Allain, M. Nieto, M. Hendricks, A. Hassanein, C. Tarrio, S. Granthan, and V. Bakshi, "Energetic and thermal Sn interactions and their effect on EUVL source collector mirror lifetime at high temperatures," *Proc. SPIE* **6517**, 65171V (2007) [doi: 10.1117/12.711270].

Downloaded From: https://www.spiedigitallibrary.org/ebooks/ on 09 Mar 2022
Terms of Use: https://www.spiedigitallibrary.org/terms-of-use

8. H. Shin, S. N. Srivastava, and D. N. Ruzic, "Tin removal from extreme ultraviolet collector optics by inductively coupled plasma reactive ion etching," *J. Vac. Sci. Technol. A Vacuum, Surfaces Film* **26** (3), 389–398 (2008).
9. W. Gwyn, R. Stulen, D. Sweeney, and D. Attwood, "Extreme ultraviolet lithography," *J. Vac. Sci. Technol. B* **16**, 3142 (1998).
10. R. B. Hoover, D. L. Shealy, B. R. Brinkley, P. C. Baker, T. W. Barbee, and A. B. C. Walker, "Development of the water window imaging x-ray microscope utilizing normal incidence multilayer optics," *Opt. Eng.* **30**, 1086 (1991) [doi: 10.1117/12.55924].
11. N. M. Ceglio, D. G. Stearns, D. P. Gaines, A. W. Hawryluk, and J. E. Trebes, "Multipass amplification of soft x rays in a laser cavity," *Opt. Lett.* **13**, 108 (1988).
12. M. Finkenthal, A. P. Zwicker, S. P. Regan, H. W. Moos, and D. Stutman, "Near normal incidence spectroscopy of a penning ionization discharge in the 110–180 Å range with flat multilayer mirrors," *Appl. Opt.* **29**, 3467 (1990).
13. T. W. Barbee, J. W. Weed, R. B. Hoover et al., "Multi-spectral solar telescope array II. Soft x-ray/EUV reflectivity of the multilayer mirrors," *Opt. Eng.* **30**, 1067–1075 (1991) [doi: 10.1117/12.55917].
14. D. S. Martinez-Galarce, A. B. C. Walker, D. B. Gore et al., "High resolution imaging with multilayer telescopes: resolution performance of the MSSTA II telescopes," *Opt. Eng.* **39**(4), 1063 (2000) [doi: 10.1117/1.602468].
15. M. Toyoda, Y. Shitami, M. Yanagihara, T. Ejima, M. Yamamoto, and M. Watanabe, "A soft-x-ray imaging microscope with a multilayer-coated Schwarzschild objective: Imaging tests," *Jpn. J. Appl. Phys.* **39**(1), 4A (2000).
16. E. Louis, A. E. Yakshin, P. C. Görts et al., "Progress in Mo/Si multilayer coating technology for EUVL optics," *Proc. SPIE* **3997**, 406–411 (2000) [doi: 10.1117/12.390077].
17. J. A. Folta, S. Bajt, T. W. Barbee et al., "Advances in multilayer reflective coatings for extreme-ultraviolet lithography," *Proc. SPIE* **3676**, 702–709 (1999) [doi: 10.1117/12.351156].
18. E. Spiller, *Soft X-ray Optics*, SPIE Press, Bellingham, Washington (1994) [doi: 10.1117/3.176482].
19. J. R. Meyer-Arendt, *Introduction to Classical and Modern Optics* **xv**, 4314th ed., Prentice Hall, Englewood Cliffs, New Jersey (1995).
20. D. T. Attwood, *Soft X-Rays and Extreme Ultraviolet Radiation: Principles and Applications*, Vol. **xvi**, Cambridge University Press, Cambridge, p. 470 (2000).
21. M. Putero-Vuaroqueaux and B. Vidal, "Extreme-ultraviolet multilayer mirrors deposited using radio-frequency magnetron sputtering: the

Downloaded From: https://www.spiedigitallibrary.org/ebooks/ on 09 Mar 2022
Terms of Use: https://www.spiedigitallibrary.org/terms-of-use

influence of self-bias voltage on reflectivity and roughness," *J. Phys. Condens. Matter* **13**, 3969–3976 (2001).
22. E. Spiller, S. Baker, P. A. Mirkarimi et al., "High performance Mo-Si multilayer coatings for EUV lithography using ion beam deposition," *Appl. Opt.* **42**, 4049–4058 (2003).
23. S. Braun, R. Dietsch, M. Haidl et al., "Mo/Si multilayers for EUV applications prepared by pulsed laser deposition (PLD)," *Microelectron. Eng.* **57–58**, 9–15 (2001).
24. M. Shiraishi, N. Kandaka, and K. Murakami, "Mo/Si multilayers deposited by low-pressure rotary magnet cathode sputtering for extreme ultraviolet lithography," *Proc. SPIE* **5037**, 249–256 (2003) [doi: 10.1117/12.484436].
25. A. K. Hagenlocher, "Progress in extreme ultraviolet and soft x-ray multilayer coatings," *Proc. SPIE* **315**, pp. 118–122 (1981) [doi: 10.1117/12.932977].
26. I. V. Kozhevnikov and A. V. Vinogradov, "Multilayer x-ray mirrors," *J. Russian Laser Research* **16**(4), 343–385 (1995).
27. H. Takenaka and T. Lawamura, "Thermal stability of Mo/C/Si/C multilayer soft x-ray mirrors," *J. of Elec. Spec. and Rel. Phenom.* **80**, 381–384 (1996).
28. S. Bajt, J. B. Alameda, T. W. Barbee, Jr. et al., "Improved reflectance and stability of Mo-Si multilayers," *Opt. Eng.* **41**, 1797 (2002) [doi: 10.1117/1.489426].
29. R. R. Kola, D. L. Windt, W. K. Waskiewicz et al., "Stress relaxation in Mo/Si multilayer structures," *Appl. Phys. Lett.* **60**, 3120–3122 (1992).
30. H. Azuma, A. Takeichi, I. Konomi, Y. Watanabe, and S. Noda, "Thermally induced structural modification of nanometer-order Mo/Si multilayers by the spectral reflectance of laser-plasma soft X-rays," *Jpn. J. Appl. Phys.* **43**, 2078–2082 (1993).
31. D. L. Windt, M. Ave, and M. Hill, "Stress, microstructure, and stability of Mo/Si, W/Si, and Mo/C multilayer films," *J. Vac. Sci. Technol. A* **18**, 980–991 (2000).
32. Z. Jiang, X. Jiang, W. Liu, and Z. Wu, "Thermal stability of multilayer films Pt/Si, Mo/Si, and W/Si," *J. Appl. Phys.* **65**, 196–200 (1989).
33. R. S. Rosen, D. G. Stearns, M. A. Villiardos, M. E. Kassner, S. P. Vernon, and Y. Cheng, "Silicide layer growth rates in Mo/Si multilayers," *Appl. Opt.* **32**, 6975–6980 (1993).
34. Kloidt, K. Nolting, U. Kleineberg et al., "Enhancement of the reflectivity of Mo/Si multilayer mirrors by thermal treatment," *Appl. Phys.* **58**, 2601–2603 (1991).
35. C. Montcalm, "Reduction of residual stress in extreme ultraviolet Mo/Si multilayer mirrors with post deposition thermal treatments," *Opt. Eng.* **40**, 469–477 (2001) [doi: 10.1117/1.1346584].

Downloaded From: https://www.spiedigitallibrary.org/ebooks/ on 09 Mar 2022
Terms of Use: https://www.spiedigitallibrary.org/terms-of-use

36. L. Windt, S. Donguy, J. Seely, and B. Kjornrattanawanich, "Experimental comparison of extreme-ultraviolet multilayers for solar physics," *Appl. Opt.* **43**, 1835–1848 (2004).
37. J. M. Liang and L. J. Chen, "Interfacial reactions and thermal stability of ultrahigh vacuum deposited multilayered Mo/Si structures," *J. Appl. Phys.* **79**, 4072–4077 (1996).
38. T. Feigl, S. Yulin, T. Kuhlmann, and N. Kaiser, "Damage resistant and low stress EUV multilayer mirrors," *Japanese J. Applied Physics* **41**, 4082–4085 (2002).
39. Y. Ijdiyaou, M. Azizan, E. L. Ameziane, M. Brunel, and T. A. N. Tan, "On the formation of molybdenum silicides in Mo-Si multilayers: The effect of Mo thickness and annealing temperature," *Appl. Surf. Scien.* **55**, 165–171 (1992).
40. V. V. Kontradenko, Yu. P. Pershin, O. V. Poltseva et al., "Thermal stability of soft x-ray Mo-Si and $MoSi_2$-Si multilayer mirrors," *Appl. Opt.* **32**, 1811–1816 (1993).
41. H.-J. Voorma, E. Louis, N. B. Koster, and F. Bijkerk, "Temperature induced diffusion in Mo/Si multilayer mirrors," *J. Appl. Phys.* **83**, 4700–4708 (1998).
42. T. Leisegang, D. C. Meyer, A. A. Levin, S. Braun, and P. Paufler, "On the interplay of internal/external stress and thermal stability of Mo/Si multilayers," *Appl. Phys. A* **77**, 965–972 (2003).
43. T. Feigel, H. Lauth, S. Yulin, and N. Kaiser, "Heat resistance of EUV multilayer mirrors for long-time applications," *Microelectr. Eng.* **57-58**, 3–8 (2001).
44. E. Ziegler, "Multilayers for high heat load synchrotron applications," *Opt. Eng.* **34**, 445–452 (1995) [doi: 10.1117/12.194837].
45. T. Böttger, D. C. Meyer, P. Paufler et al., "Thermal stability of Mo/Si multilayers with boron carbide interlayers," *Thin Solid Films* **444**, 165–173 (2003).
46. H. Takenaka, H. Io, T. Haga, and T. Kawamura, "Design and fabrication of highly heat resistant Mo/Si multilayer soft x-ray mirrors with interleaved barrier layers," *J. Synchrotron Rad.* **5**, 708–710 (1998).
47. S. Yulin, N. Benoit, T. Feigl, and N. Kaiser, "Interface-engineered EUV multilayer mirrors," *Microelectronic Engineering* **83**(4–9), 692–694 (2006).
48. "Mirror Reflectivity," Center for X-Ray Optics. [Online]. Available: http://henke.lbl.gov/optical_constants/mirror2.html. [Accessed: 10-Aug-2017].
49. S. N. Srivastava, K. C. Thompson, E. L. Antonsen, H. Qiu, J. B. Spencer, D. Papke, and D. N. Ruzic, "Lifetime measurements on collector optics from Xe and Sn extreme ultraviolet sources," *J. Appl. Phys.* **102**, 023301 (2007).
50. T. Tomie, "Tin laser-produced plasma as the light source for extreme ultraviolet lithography high-volume manufacturing: history, ideal plasma,

Downloaded From: https://www.spiedigitallibrary.org/ebooks/ on 09 Mar 2022
Terms of Use: https://www.spiedigitallibrary.org/terms-of-use

present status, and prospects," *J. Micro/Nanolithography, MEMS, and MOEMS* **11**(2), 21109 (2012) [doi: 10.1117/1.JMM.11.2.021109].
51. E. L. Antonsen, K. C. Thompson, M. R. Hendricks, D. A. Alman, B. E. Jurczyk, and D. N. Ruzik, "Ion debris characterization from a z-pinch extreme ultraviolet light source," *J. Appl. Phys.* **99**, 066301 (2006).
52. A. Roy, S. M. Hassan, S. S. Harilal, A. Endo, T. Mocek, and A. Hassanein, "Extreme ultraviolet emission and confinement of tin plasmas in the presence of a magnetic field," *Physics of Plasmas* **21**(5), 053106 (2014).
53. D. T. Elg, J. R. Sporre, D. Curreli et al., "Magnetic debris mitigation system for extreme ultraviolet sources," *J. Micro/Nanolith., MEMS, and MOEMS* **14**(1), 013506 (2015) [doi: 10.1117/1.JMM.14.1.013506].
54. K. Halbach, "Design of permanent multipole magnets with oriented rare earth cobalt material," *Nucl. Instruments Methods* **169**, pp. 1–10 (1980).
55. R. Ravaud and G. Lemarquand, "Predicting the Exact Shape of the Magnetic Field Produced by Halbach Structures," in *Computer Field Models of Electromagnetic Devices*, S. Wiak and E. Napieralska-Juszczak, Eds., IOS Press, Amsterdam, pp. 880–886 (2010).
56. A. Endo, H. Hoshino, T. Suganama et al., "Laser produced EUV light source development for HVM," *Proc. SPIE* **6517**, 65170O (2007) [doi: 10.1117/12.711097].
57. H. Mizoguchi, H. Nakarai, T. Abe et al., "Sub-hundred Watt operation demonstration of HVM LPP-EUV source," *Proc. SPIE* **9048**, 90480D (2014) [doi: 10.1117/12.2046776].
58. G. O'sullivan, B. Li, R. D'Arcy et al., "Spectroscopy of highly charged ions and its relevance to EUV and soft x-ray source development," *J. Phys. B At.: Mol. Opt. Phys.* **48**(14), 144025 (2015).
59. J. R. Sporre, "Diagnosis of the flux emanating from the intermediate focus of an extreme ultraviolet light lithography source," Ph.D. dissertation, University of Illinois at Urbana-Champaign (2013).
60. H. Mizoguchi, H. Nakarai, T. Abe et al., "Performance of 250W high-power HVM LPP-EUV source," *Proc. SPIE* **9776**, 101431J (2016) [doi: 10.1117/12.2256652].
61. C. Metzmacher, H. Giese, A. Weber et al., "Foil trap and light source device using such foil trap," U.S. Patent US 20160195714 A1 (2016).
62. V. Sizyuk, A. Hassanein, and V. Bakshi, "Modeling and optimization of debris mitigation systems for laser and discharge-produced plasma in extreme ultraviolet lithography devices," *J. Micro/Nanolith. MEMS MOEMS* **6**(4), 043303 (2007) [doi: 10.1117/1.2804128].
63. A. Pirati, R. Peeters, D. Smith et al., "Performance overview and outlook of EUV lithography systems," *Proc. SPIE* **9422**, 94221P (2015) [doi: 10.1117/12.2085912].

Downloaded From: https://www.spiedigitallibrary.org/ebooks/ on 09 Mar 2022
Terms of Use: https://www.spiedigitallibrary.org/terms-of-use

64. J. R. Sporre, D. T. Elg, K. K. Kalathiparambil, and D. N. Ruzic, "Modeling and measuring the transport and scattering of energetic debris in an extreme ultraviolet plasma source," *J. Micro/Nanolith. MEMS MOEMS* **15**(1), 013503 (2016) [doi: 10.1117/1.JMM.15.1.013503].
65. V. Bakshi, "EUV Source Technology," Chapter 3 in *EUV Lithography*, V. Bakshi, Ed., SPIE Press, Bellingham, Washington pp. 104–131 (2009) [doi: 10.1117/3.769213.ch3].
66. J. F. Ziegler, M. D. Ziegler, and J. P. Biersack, "SRIM – The stopping and range of ions in matter (2010)," *Nucl. Instruments Methods Phys. Res. Sect. B Beam Interact. with Mater. Atoms* **268** (11–12), 1818–1823 (2010).
67. E. Wiberg, N. Wiberg, and A. F. Hoffman, *Inorganic Chemistry*, Academic Press, San Diego, p. 907 (2001).
68. N. D. Epiotis, "Beyond symmetry: from organic to main group to organometallic stereochemistry and back," *J. Molecular Structure* **153**, 1–53 (1987).
69. N. Faradzhev and V. Sidorkin, "Hydrogen mediated transport of Sn to Ru film surface," *J. Vac. Sci. Technol. A* **27**(2), 306–314 (2009).
70. D. Ugur, A. J. Storm, R. Verberk, J. C. Bower, and W. G. Sloof, "Decomposition of SnH_4 molecules on metal and metal–oxide surfaces," *Applied Surface Science* **288**(1), 673–676 (2014).
71. K. Tamaru, "The thermal decomposition of tin hydride," *J. Phys. Chem.* **60**(5), 610–612 (1956).
72. M. M. J. W. van Herpen, D. J. W. Klunder, W. A. Soer, R. Moors, and V. Babine, "Sn etching with hydrogen radicals to clean EUV optics," *Chemical Physics Letters* **484**(4–6), 197–199 (2010).
73. A. Sutoh, Y. Okada, S. Ohta, and M. Kawabe, "Cracking efficiency of hydrogen with tungsten filament in molecular beam epitaxy," *Japanese J. Applied Physics* **34**(2), 10B (1995).
74. G. W. Wicks, E. R. Rueckwald, and M. W. Koch, "Analysis of cracking efficiency of an atomic hydrogen source, and its effect on desorption of $Al_xGa_{1-x}As$ native oxides," *J. Vac. Sci. Technol. B* **14**, 2184 (1996).
75. M. Yoshimura, B. An, K. Yokogawa, and K. Ueda, "Atomic hydrogen induced surface restructuring on the tin-covered Si(111) observed by scanning tunneling microscopy," *Japanese J. Applied Physics* **36**, 7805–7808 (1997).
76. D. Ugur, A. J. Storm, R. Verberk, J. C. Brouwer, and W. G. Sloof, "Generation and decomposition of volatile tin hydrides monitored by *in situ* quartz crystal microbalances," *Chemical Physics Letters* **552**, 122–125 (2012).
77. O. V. Braginsky, A. S. Kovalev, D. V. Lopaev et al., "Removal of amorphous C and Sn on Mo:Si multilayer mirror surface in kydrogen plasma and afterglow," *J. Appl. Phys.* **111**(9), 093304 (2012).
78. F. T. Molkenboer, J. Burke, W. Claussen et al., "Cleaning apparatus and associated low pressure chamber apparatus," U.S. Patent WO 2015165705 A1 (2015).

Downloaded From: https://www.spiedigitallibrary.org/ebooks/ on 09 Mar 2022
Terms of Use: https://www.spiedigitallibrary.org/terms-of-use

79. K. Hoffmann, "Verbal communication," Cymer, an ASML Company, 2016.
80. D. T. Elg, J. R. Sporre, G. A. Panici, S. N. Srivastava, and D. N. Ruzic, "*In situ* collector cleaning and extreme ultraviolet reflectivity restoration by hydrogen plasma for extreme ultraviolet sources," *J. Vac. Sci. Technol. A* **34**(2), 021305 (2016).
81. M. Mozetič, M. Drobnič, A. Pregelj, and K. Zupan, "Determination of density of hydrogen atoms in the ground state," *Vacuum* **47**(6–8), 943–945 (1996).
82. M. Mozetic, A. Vesel, U. Cvelbar, and A. Ricard, "An iron catalytic probe for determination of the O-atom density in an Ar/O_2 afterglow," *Plasma Chem. Plasma Process.* **26**, 103 (2006).
83. M. Mozetic, A. Vesel, A. Drenik, I. Poberaj, and D. Babic, "Catalytic probes for measuring H distribution in remote parts of hydrogen plasma reactors," *J. Nucl. Mater.* **363–365**, 1457–1460 (2007).
84. D. T. Elg, G. A. Panici, J. A. Peck, S. N. Srivastava, and D. N. Ruzic, "Modeling and measurement of hydrogen radical densities of *in situ* plasma-based Sn cleaning source," *J. Micro/Nanolithography, MEMS, MOEMS*, **16**(2), 23501 (2017) [doi: 10.1117/1.JMM.16.2.023501].
85. A. Norman, J. R. Webster, W. L. Jolly et al., "Silane, Stannane, Silane-d_4, Germane-d_4, and Stannane-d_4," Chapter 36 in *Inorganic Syntheses* **11**, McGraw-Hill, New York, pp. 170–181 (1968).
86. D. T. Elg, "Removal of tin from extreme ultraviolet collector optics by an in-situ hydrogen plasma," Ph.D. dissertation, University of Illinois at Urbana-Champaign, 2016.
87. I. Mendez, F. J. Gordillo-Vasquez, V. J. Herrero, and I. Tanarro, "Atom and ion chemistry in low pressure hydrogen dc plasmas." *J. Phys. Chem. A* **110**(18), 6060–6066 (2006).
88. A. I. Ershov, N. R. Bowering, B. La Fontaine, and S. De Dea, "Harsh environment optical element protection," U.S. Patent WO 2014055308 A1 (2014).

Daniel T. Elg obtained his Ph.D. in 2016 from the Department of Nuclear, Plasma, and Radiological Engineering at the University of Illinois at Urbana-Champaign. His M.S. and Ph.D. research focused on debris management strategies for EUV systems. He is currently performing postdoctoral work researching atmospheric pressure plasmas for medical applications at the University of California, Berkeley. His research interests include low-temperature plasma science, plasma processing applications, and plasma–material interactions.

Downloaded From: https://www.spiedigitallibrary.org/ebooks/ on 09 Mar 2022
Terms of Use: https://www.spiedigitallibrary.org/terms-of-use

Shailendra N. Srivastava worked as a post-doctoral fellow in the Department of Nuclear, Plasma and Radiological Engineering at the University of Illinois at Urbana-Champaign. Dr. Srivastava obtained his Ph.D. from Technische Universität Kaiserslautern, Germany, in experimental physics, where he worked extensively on laser-produced plasmas. He has been working in the semiconductor industry for many years, focusing on EUV source technology development and the study of EUV collector contamination and mitigation. His research interests are plasma–material interactions, laser–material interactions, and metrology development.

David N. Ruzic is a professor in the Department of Nuclear, Plasma and Radiological Engineering at the University of Illinois at Urbana-Champaign. He joined the faculty in 1984 after receiving his Ph.D. in physics from Princeton University and doing post-doctoral work at Princeton Plasma Physics Laboratory. His research centers on the interaction of plasmas with materials; and applications include magnetic fusion energy as well as microelectronic processing. Professor Ruzic has a passion for teaching, particularly about energy sources, because he gets to blow something up in almost every class.

Downloaded From: https://www.spiedigitallibrary.org/ebooks/ on 09 Mar 2022
Terms of Use: https://www.spiedigitallibrary.org/terms-of-use

Chapter 7
EUV Mask and EUV Mask Metrology

Jinho Ahn
Hanyang University, South Korea

Chan-Uk Jeon
Samsung Electronics, South Korea

7.1 Introduction
7.2 EUVL Mask Structure and Process Flow
7.3 Mask Substrate
- 7.3.1 Thermal Expansion Coefficient
- 7.3.2 Surface figure requirements
- 7.3.3 Defect requirements

7.4 Multilayer and Backside Conductive Coating
- 7.4.1 Multilayer deposition process
- 7.4.2 Multilayer characterization
- 7.4.3 Multilayer performance improvement techniques and defect mitigation
- 7.4.4 Capping layer
- 7.4.5 Backside conductive coating and mask handling

7.5 Absorber Stack and Pattern Fabrication
- 7.5.1 Absorber layer
- 7.5.2 Antireflection coating
- 7.5.3 E-beam patterning
- 7.5.4 Absorber stack etch

7.6 Mask Inspection, Metrology and Repair
- 7.6.1 Multilayer defect inspection
- 7.6.2 Absorber pattern inspection
- 7.6.3 Multilayer defect repair
- 7.6.4 Multilayer defect compensation
- 7.6.5 Absorber defect repair
- 7.6.6 Next-generation repair
- 7.6.7 Aerial image metrology

7.7 Mask Contamination Protection and Cleaning
- 7.7.1 Pellicle
- 7.7.2 Mask cleaning

Downloaded From: https://www.spiedigitallibrary.org/ebooks/ on 09 Mar 2022
Terms of Use: https://www.spiedigitallibrary.org/terms-of-use

7.8 Advanced Mask Structure for Better Imaging
7.8.1 Shadowing effect
7.8.2 Bossung curve asymmetry and focus shift
7.8.3 Alternative mask structures
7.8.4 Etched ML binary mask
7.8.5 Attenuated phase shift mask
7.8.6 Alternating phase shift mask
7.8.7 Black border
7.8.8 Mask design for high-NA
7.9 Summary and Future Outlook

7.1 Introduction

EUV mask technology is considered to be one of the most critical issues for the successful implementation of EUVL in the semiconductor fabrication process. Since EUV light is strongly absorbed by most materials, reflective optics is applied to all of the optical components, including the mask structure. As a result, the EUV mask structure, based on the multilayer mirror (MLM), is radically different from that of conventional optical lithography. All of the mask films must be prepared with great care, which requires nanoscale thin-film technologies. The target technology node for EUVL implementation is 7 nm and below; today, mask defects are one of the leading challenges associated with EUV mask fabrication.[1]

A ML structure consisting of many alternating layers of materials showing dissimilar EUV optical constants is essential for reflecting 13.5-nm wavelength light. Bragg reflection—constructive interference of the partially reflected beam at several interfaces—is necessary to maximize EUV reflection at near–normal incidence, and its efficiency is determined by the structure (e.g., thickness of each layer and their ratios) as well as optical properties (refractive index and extinction coefficient). To produce optical contrast for imaging, the patterns with high EUV absorbance are formed on the top of this MLM. However, an oblique incident light angle, which is required for image transfer with a reflective system, causes various mask 3D effects, as will be discussed in detail later in the chapter.

The mask format specified by SEMI P37-0613 is 152 ± 0.1 mm with a thickness of 6.35 ± 0.1 mm, which is the same as the current optical mask format. This common form factor allows the use of current mask fabrication infrastructure with minimum modification. However, special considerations are required for the tools in order to meet the mask requirements for small pattern transfer. One consideration is defect mitigation to minimize fabrication-induced mask defects. Another consideration is a mask inspection issue caused by wavelength-dependent defectivities. EUV-specific inspection and metrology tools will be discussed in the following sections.

Table 7.1 shows EUV mask requirements obtained from SEMI P37-0613 and 2013 ITRS for an 18-nm half-pitch pattern. During the past few years, a

Downloaded From: https://www.spiedigitallibrary.org/ebooks/ on 09 Mar 2022
Terms of Use: https://www.spiedigitallibrary.org/terms-of-use

Table 7.1 Substrate material and EUV blank ML requirements from SEMI P37-0613 and 2013 ITRS for EUVL mask requirements.[2,3]

	Parameter	Requirements
Substrate Material	Temperature range for CTE requirement	19 °C to 25 °C
	Mean CTE (±ppb/K)	±5
	CTE spatial variation (±ppb/K)	6
	Flatness front (nm) (PV)	30
	Flatness back (nm) (PV)	30
	Minimum defect size ($\Delta CD < \pm 10\%$, nm)	20
Blank Defects	Minimum size ($\Delta CD < \pm 10\%$, nm)	15
Multilayer Performance	Peak reflectivity (%)	>65
	Peak reflectivity uniformity (%, 3σ, Abs.)	0.19
	Reflected centroid λ uniformity (nm, 3σ)	0.03
	Multilayer roughness (nm, rms)	0.05

lot of progress has been made in EUV mask fabrication processes. However, to meet all of the requirements for application to sub-7-nm technology nodes, further improvements in a wide range of mask components are required. The following sections will address the status of the mask fabrication processes and their future prospects.

7.2 EUVL Mask Structure and Process Flow

An EUV mask fabrication process consists of two phases: mask blank fabrication and mask patterning.[4] A high-precision EUV mask requires low-thermal-expansion material (LTEM) as a starting substrate. This substrate is coated with an EUV-reflective ML and is covered using a capping layer to prevent any unwanted oxidation. An absorber layer coating followed by an antireflective coating (ARC) as well as a backside conductive layer coating will complete the mask blank fabrication process. The mask patterning, which consists of e-beam writing and dry etching, is similar to the current optical mask process. A typical EUV mask fabrication process flow is shown in Fig. 7.1.

An EUV mask consists of several layers that have unique mechanical, chemical, and optical functions. The mask substrate maintains the rigidity of the mask with minimum distortion. It should have a flat and smooth surface with zero defect as well as a low coefficient of thermal expansion (CTE). The ML is one of the key components to determine mask efficiency; lower reflectivity of the ML causes more loss of optical power by the mask. One of the greatest risks for EUV mask viability is maintaining ML performance over a reasonably long operation time. The ML's capping layer protects masks from degradation. The absorber layer in an EUV mask has a similar purpose to the chrome layer of a DUV binary mask in terms of the pattern-forming function. Due to the reflective nature of the EUV mask structure, the absorber material

Downloaded From: https://www.spiedigitallibrary.org/ebooks/ on 09 Mar 2022
Terms of Use: https://www.spiedigitallibrary.org/terms-of-use

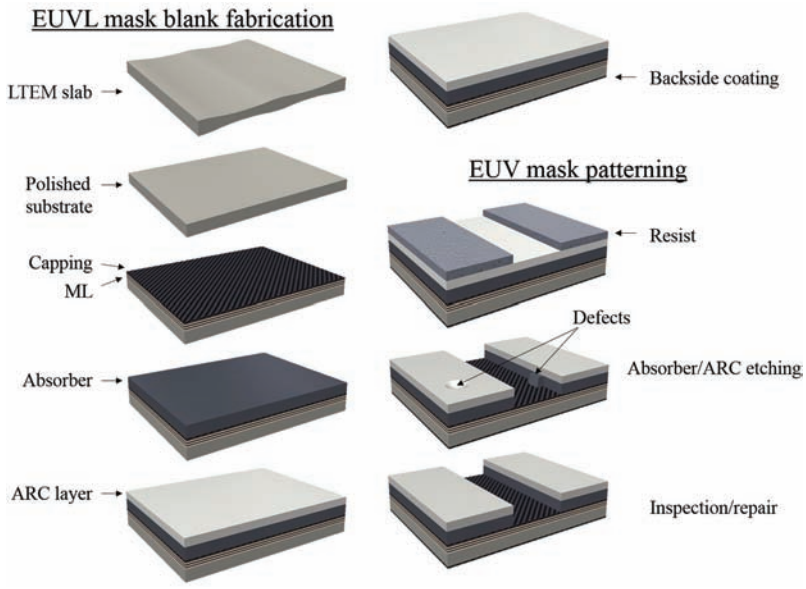

Figure 7.1 Schematics of the EUV mask fabrication process flow.

can secure the pattern image contrast against the ML through absorption with minimum reflection. However, most of the metallic absorber materials show high DUV reflectivity, which can cause a problem in mask inspection efficiency using a DUV wavelength. To attain sufficient DUV contrast, an ARC can be applied on top of the absorber layer. The backside conductive layer is for electrostatic chucking, which might be required in various process tools as well as in the exposure tool. The key properties of an EUV mask are the peak wavelength (or centroid wavelength), which will be discussed in Section 7.4.1, and the peak reflectivity.

7.3 Mask Substrate

The substrate is the starting material for EUV mask fabrication, and its quality assurance is necessary even though it is not a condition for successful mask fabrication. The SEMI P37-1102 standard specifies substrate requirements: average and spatial variation in thermal expansion, surface flatness, and defect level (Fig. 7.2). These requirements stem from EUV-specific issues as well as general nanoscale patterning applications.

7.3.1 Thermal expansion coefficient

Since the inplane distortion of the mask caused by the temperature difference during exposure and mask manufacturing contributes to the image placement error at the wafer, a LTEM is required as a mask substrate. Mask distortion is influenced by the spatial variation as well as the average value of the CTE. The

Downloaded From: https://www.spiedigitallibrary.org/ebooks/ on 09 Mar 2022
Terms of Use: https://www.spiedigitallibrary.org/terms-of-use

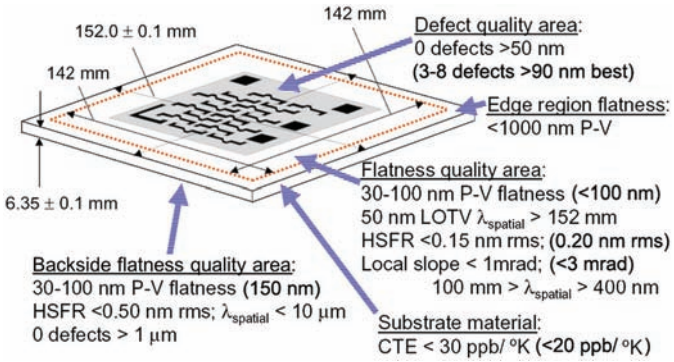

Figure 7.2 SEMI P37-1102 substrate requirements (reprinted from Ref. 5).

mask substrate standard SEMI P37-0613 requires a CTE in the range from 0 ± 5 ppb/K with a 6 ppb/K total spatial variation to 0 ± 30 ppb/K with a 10 ppb/K total spatial variation. Since there is no commercial dilatometer that meets EUVL requirements (measurement resolution of 1 ppb/K), a technique to measure the absolute CTE with high accuracy and reproducibility is required. Interferometric dilatometers using different lasers have been proposed, and the results show the reproducibility to be less than 1 ppb/K with a handling capability of a wide variety of materials with CTEs ranging from ppm/K to ppb/K.[6,7]

7.3.2 Surface figure requirements

The ML is coated onto the substrate of an EUV mask to attain high reflectivity at the 13.5-nm wavelength. The EUV reflectivity is degraded by the roughness of the substrate surface, especially by high-spatial-frequency roughness (HSFR).[8] As can be seen in Fig. 7.3(a), HSFR causes large-angle scattering and loss of EUV light from the projection lens. Mid-spatial-frequency roughness (MSFR), causing wavefront error and speckle through small-angle scattering, is shown in Fig. 7.3(b).

Mask MSFR (also referred to as slope error) is not a source of flare as it is in mirrors, but rather leads to intensity variation in the image plane and becomes a source of line-edge roughness (LER) or image placement error.[9] It was proposed that the frequency f range for MSFR and HSFR should be $10^{-6}/\text{nm} < f < 0.004/\text{nm}$ and $0.004/\text{nm} < f < 0.02/\text{nm}$, respectively. The ML smoothing deposition technique can reduce the mask HSFR, but it is not effective for MSFR. The SEMI P37 standard specifies a HSFR of <0.15 nm rms and a local slope angle of the front surface of <1.0 mrad.

The mask flatness issue stems from the unique EUVL imaging system design, which is a nontelecentric illumination system. Any height variation of the patterned mask surface (e.g., the nonflatness) causes an image placement error (or overlay error) on the wafer.[10] The image placement error Δx on the

Downloaded From: https://www.spiedigitallibrary.org/ebooks/ on 09 Mar 2022
Terms of Use: https://www.spiedigitallibrary.org/terms-of-use

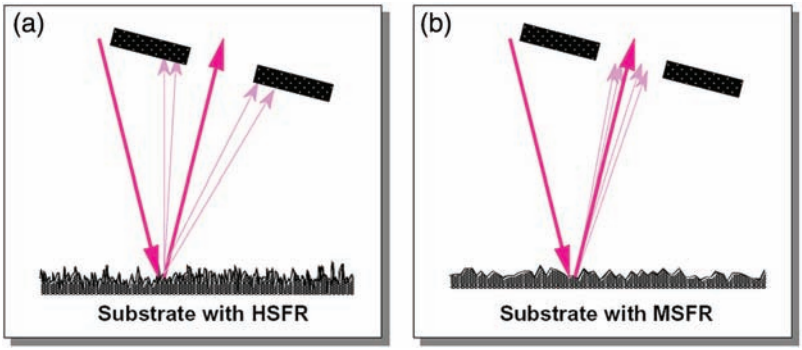

Figure 7.3 Schematics of (a) HSFR and (b) MSFR. HSFR leads to scattering outside the exit pupil, which causes loss of light throughput. MSFR leads to small-angle scattering, which causes wavefront error and speckle (adapted from Ref. 8).

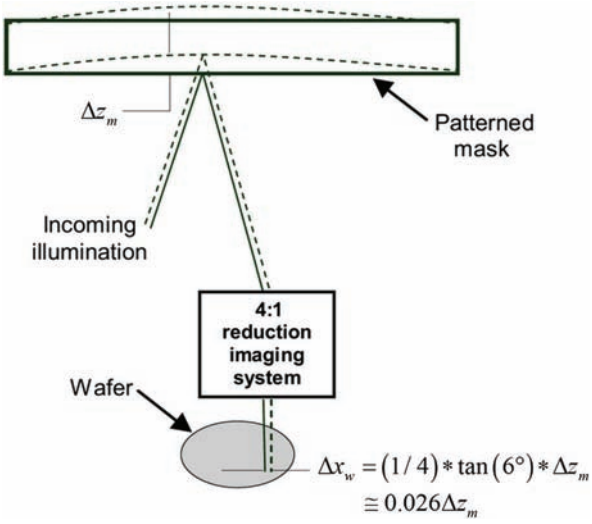

Figure 7.4 Image placement error at the wafer resulting from mask nonflatness in a nontelecentric illumination system (adapted from Ref. 11).

wafer is about 1/38 of the nonflatness Δz of the mounted mask at the nominal 6-deg illumination angle θ (see also Fig. 7.4):

$$\Delta x = \frac{\Delta z \times \tan(\theta)}{M}. \tag{7.1}$$

The front surface flatness of an as-mounted mask is influenced by the freestanding flatness of the substrate surfaces and by how parallel they are to each other. The backside flatness of the mask also contributes to front side flatness since a flat-faced electrostatic chuck is the designated method of

Downloaded From: https://www.spiedigitallibrary.org/ebooks/ on 09 Mar 2022
Terms of Use: https://www.spiedigitallibrary.org/terms-of-use

mounting a mask in an exposure tool. The SEMI P37 standard specifies the front (freestanding) and backside flatness values at less than 30 nm PV.

7.3.3 Defect requirements

A substrate surface defect tends to propagate through the ML coating. It was reported that ~80% of the defects detected on a ML blank originate from the substrate; this study implies the importance of substrate defect control.[12] Depending on the deposition process and condition, the substrate defect can be magnified or demagnified.[13] If the propagated mask surface defect is greater than a threshold value (diameter and height), it can be printed as a defect at the wafer.[14] This causes perturbation of the reflected wavefront (Fig. 7.5); this propagated mask surface defect is called a phase defect.[15] Since it is not possible to describe a 3D particle on the substrate with one unique number, the spherical equivalent volume diameter (SEVD) is used. There should be a sphere that has a volume equivalent to that of the particle, and we can use the SEVD to define the substrate defect size. One useful

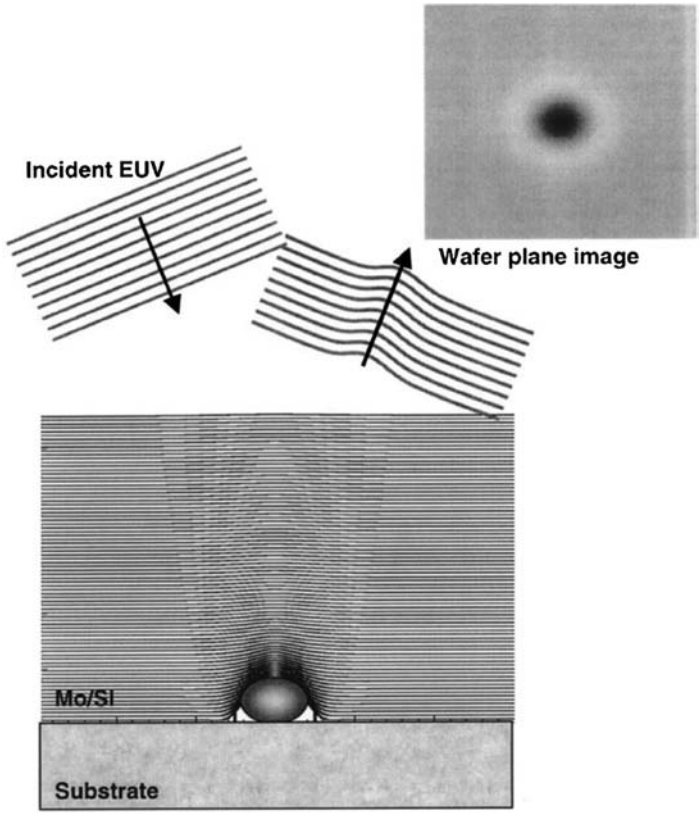

Figure 7.5 Schematic illustration of defect propagation due to a substrate particle during ML deposition (reprinted from Ref. 15).

Downloaded From: https://www.spiedigitallibrary.org/ebooks/ on 09 Mar 2022
Terms of Use: https://www.spiedigitallibrary.org/terms-of-use

example is the SEVD size of a Gaussian defect, which is related to the defect height h_0 and the FWHM by the following relation:

$$(SEVD)_G = 2\left(\frac{3h_0(FWHM)^2}{16\ \ln(2)}\right)^{\frac{1}{3}}. \tag{7.2}$$

If we have information about the defect decoration effect by a ML deposition process and printability of the propagated mask surface defect, we can predict the critical defect size on the substrate. Abbas et al. reported that defects <2 nm deep with a FWHM <20 nm (equivalent to 12 nm SEVD) on the substrate were completely smoothed by their ML deposition processes (Fig. 7.6).[12] Megasonic cleaning can be used to remove surface particles on the mask substrate.[16,17] Even though most particles are removed after the first cleaning, pit defects created by megasonic cavitation collapse are observed after repeated cleaning.

7.4 Multilayer and Backside Conductive Coating

7.4.1 Multilayer deposition process

At the EUV wavelength, every material has a refractive index close to 1 and the transmittance and reflectivity are almost zero. Thus, all EUVL optics are required to be reflective, and a ML-coated mirror consisting of a large number of alternating material layers having dissimilar EUV optical constants is the solution to achieving high reflectance by interfering EUV light. According to the Fresnel equation, the reflectivity at the boundary is proportional to the square of the difference in the indices of refraction. Typically, two different layers in the ML each have a high and a low atomic number, respectively, to maximize the difference in electron density. These materials also should have

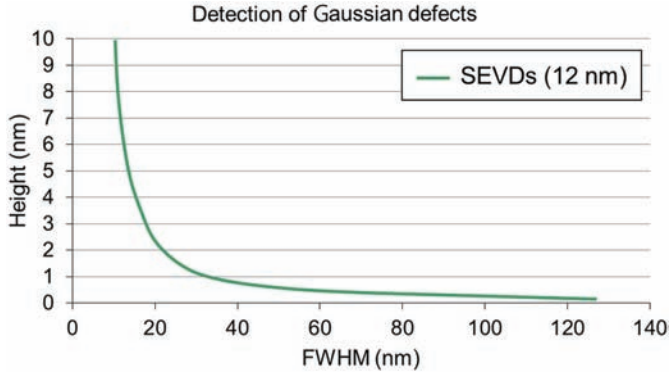

Figure 7.6 Critical defect size for the 22-nm half-pitch (HP) node with 10% CD change criteria is 12 nm SEVD. The line shows a constant volume curve of a Gaussian defect with 12 nm SEVD with different heights and FWHM values (adapted from Ref. 12).

Downloaded From: https://www.spiedigitallibrary.org/ebooks/ on 09 Mar 2022
Terms of Use: https://www.spiedigitallibrary.org/terms-of-use

low EUV light absorption, which is determined by the imaginary part of the refractive index (extinction coefficient). Considering process capability as well as optical performance, Mo/Si MLs are known to be among the best choices from the several material combinations for high reflectivity at a wavelength around 13.5 nm, and are essential components for EUV exposure optics as well as for EUV masks.[18,19] The Si layer has a low EUV absorption and works as a spacer for the periodic structure, while the Mo layer scatters the light even though it shows a high absorption characteristic. The thickness of the Mo/Si pair (d-spacing) and the ratio of the Mo thickness to the bilayer period (γ ratio) are designed to exhibit maximum reflection but minimum absorption. The period of the ML pairs should satisfy a modified version of Bragg's law to produce maximum reflectance at the EUV wavelength:

$$n\lambda = 2d \cos\theta\sqrt{1 - \frac{2\delta}{1 - \cos^2\theta}}, \tag{7.3}$$

where n is an integer, d is the period of the ML pairs (d-spacing), λ is the EUV wavelength, θ is the light incident angle to the mask normal (currently 6 deg), and δ is the bilayer-weighted δn. δn is defined as $1 - n$, where n is the real part of the refractive index.

A Mo/Si ML stack for an EUV mask blank typically consists of 80 thin-film layers, or 40 pairs of Mo/Si bilayers.[20] The d-spacing (thickness of one period of bilayer) is ~6.9 nm, with a Mo thickness of ~2.8 nm and a Si thickness of ~4.1 nm (Fig. 7.7). The theoretical value of the peak reflectivity is about 75%, but the practical value is several percentage points lower (Fig. 7.8).[21,22] The primary factor for the reflectivity loss is the intermixing of Mo and Si at the interface. The extent of interdiffusion is more serious at the

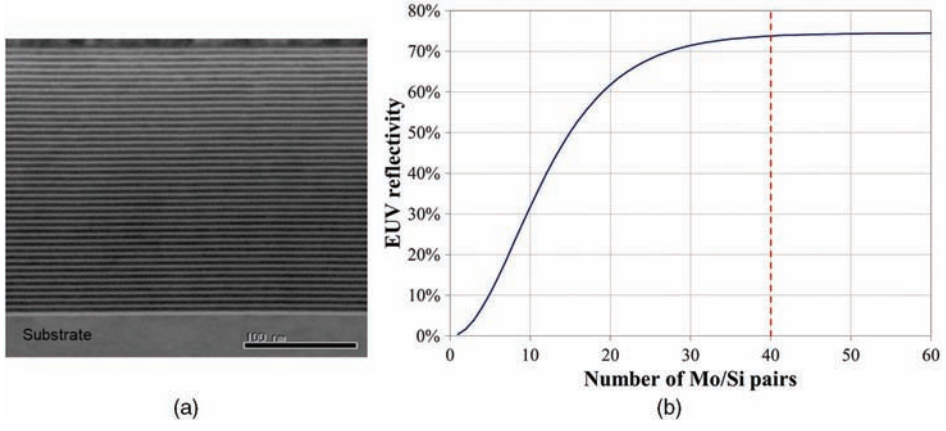

Figure 7.7 (a) Cross-sectional TEM image of the Mo/Si ML stack. (b) Calculated peak reflectivity of the Mo/Si ML coating at normal incidence as a function of the number of periods.

Downloaded From: https://www.spiedigitallibrary.org/ebooks/ on 09 Mar 2022
Terms of Use: https://www.spiedigitallibrary.org/terms-of-use

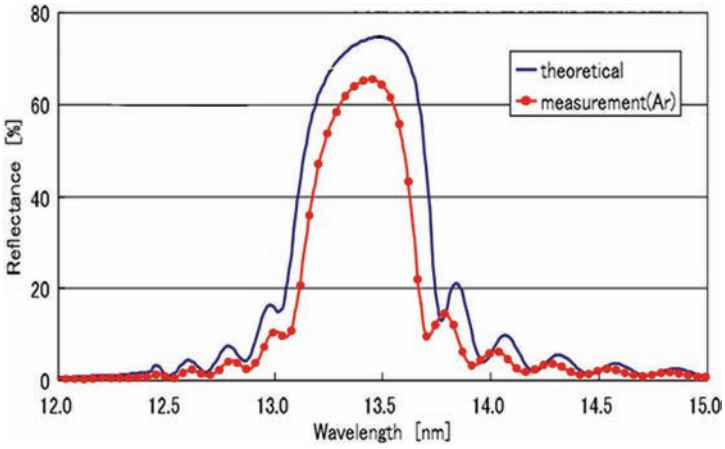

Figure 7.8 Theoretical and experimental EUV reflectance spectra of a 40-pair Mo/Si ML (adapted from Ref. 21).

Mo-on-Si interface compared to the Si-on-Mo interface. Interface engineering by a third layer (see Section 7.4.3) inserted at the Mo/Si interfaces improves reflectance by realizing sharper and smoother interfaces.[23–25] The currently available peak reflectance at 13.5 nm is about 70%.[26]

The biggest challenge to EUV mask blank fabrication is defect reduction. Defects on the substrate before ML deposition or defects generated inside the ML during the deposition process have the potential to cause printable defects during the lithography process. Printability is determined by the defect location in the ML stack and its size.

The ion-beam sputter deposition (IBD) tool equipped with a full standard mechanical interface (SMIF) has been developed for defect-free ML deposition (Fig. 7.9).[15,27–30] Major system improvements have been made to the

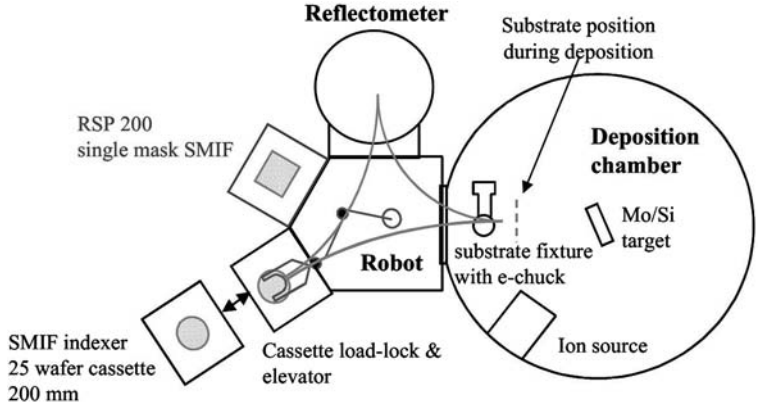

Figure 7.9 Plane view of a low-defect IBD system with reticle SMIF pod (RSP 200) robotics for coating standard-format mask blanks (reprinted from Ref. 28).

Downloaded From: https://www.spiedigitallibrary.org/ebooks/ on 09 Mar 2022
Terms of Use: https://www.spiedigitallibrary.org/terms-of-use

following components: a substrate robotic handling system, a low-particulate ion source, and clean deposition-chamber shielding, which resists flaking and particle generation.

Research on defect mitigation for EUV blank MLs has been ongoing since the early 2000s, and the total number of EUV blank defects of 25 nm in size (SEVD) is in the low single digits.[31] With the development of an actinic blank inspection (ABI) tool, the detection capability has been improved to detect 30-nm defects and pit/bump defects. In order to detect defects $\leq$30 nm in size, light sources and optics for the ABI tool were developed.[32] Further improvements in blank defect levels require much more sensitive inspection platforms. Greater defect reduction will be possible by moving toward tools with greater inspection sensitivity. Another parameter of interest is the centroid wavelength at which a ML's reflectivity is measured. The centroid wavelength is the median wavelength of the reflectance after fitting to the centroid; it is usually very close to but slightly deviating from the reflectance peak. The centroid wavelength of interest is 13.5 nm. During the IBD process, uniformity is a strong function of the substrate angle normal to the direction of the deposition flux and a weaker function of the target's angular orientation. A high substrate angle close to 55 deg results in good uniformity but a high defect density. Normal-incidence deposition results in poor uniformity. A deposition flux angle of 26 deg has been reported to yield good uniformity as well as a low defect density.[33]

7.4.2 Multilayer characterization

Cross-sectional TEM (Fig. 7.10) is a powerful tool for confirming the layered structure of the ML. The specimens for TEM are prepared following the procedure described by Bravman and Sinclair.[34] Careful calibration of the image scale is needed to obtain precise thickness values of the nanometer-scale layers. If the specimen is thin enough and the defocus is small, the

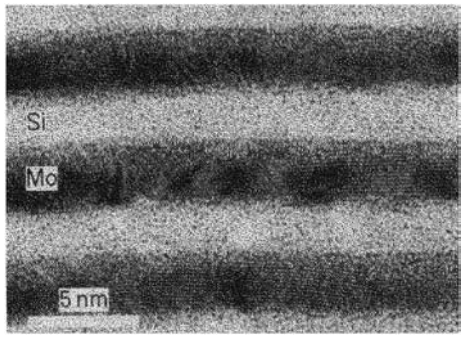

Figure 7.10 High-resolution TEM image of a Mo/Si ML. Layer thickness as well as microcrystalline structure (amorphous Si and polycrystalline Mo) can be clearly observed (reprinted from Ref. 35 with permission from AIP Publishing).

Downloaded From: https://www.spiedigitallibrary.org/ebooks/ on 09 Mar 2022
Terms of Use: https://www.spiedigitallibrary.org/terms-of-use

appearance of the resulting images is almost entirely due to amplitude contrast, with Si layers appearing light and Mo layers dark. Micrographs convey detailed structural information of each layer as well as the general quality of the ML. The general optical behavior of the ML (e.g., peak wavelength) can be deduced from the geometrical data.

However, cross-sectional TEM is a destructive technology requiring long sample-preparation time. Low-angle x-ray diffraction (XRD) is a nondestructive analytical technique that can extract structural information about the ML.[19,36] The ML period can be calculated from the low-angle peak positions by applying the Bragg equation, modified for refraction:

$$\sin^2 \theta \cong \left(\frac{m\lambda}{2d}\right) + 2\delta, \tag{7.4}$$

where d is the period, m is the integer reflection order number, and δ is the average deviation of the index from unity. When the experimentally determined peak positions are fitted to Eq. (7.4), the equation yields δ with moderate accuracy and d to an accuracy of approximately $\pm 0.1\%$. To obtain more structural information from the low-angle spectra, the peak positions can be fitted using a Fresnel-type optical model.[37] These fits can be used to extract layer thickness and interface roughness parameters. Careful modeling for the practical layered structure considering interdiffusion can result in an accurate analysis (Fig. 7.11).

EUV reflectometry is an important tool for mask quality assurance. A synchrotron is a high-quality EUV source that is ideal for scientific research but is not suitable for in-house applications. Well-stabilized high-accuracy EUV reflectometers are available at several synchrotron facilities around the world. In-house at-wavelength metrology requires compact and easy-to-operate systems, and they are based on laser- or discharge-produced plasma. Table-top EUV reflectometers with precise computer-controlled positioning units are available that allow complex surface scan and angle variation.[38–40]

7.4.3 Multilayer performance improvement techniques and defect mitigation

Much effort has been given to optimizing the deposition condition to maximize the reflectance of Mo/Si MLs. By optimizing the γ ratio and increasing the number of bilayers to more than 40, reflectance can be improved by up to $\sim 69\%$. However, further improvement requires a major change in the ML design.

One of the imperfections in MLs that reduces reflectance is the formation of surface oxide. Typical Mo/Si MLs are terminated with Si, but their reflectance tends to decrease in the presence of EUV light and water vapor due to growth of the silicon oxide layer. It is believed that EUV irradiation

Downloaded From: https://www.spiedigitallibrary.org/ebooks/ on 09 Mar 2022
Terms of Use: https://www.spiedigitallibrary.org/terms-of-use

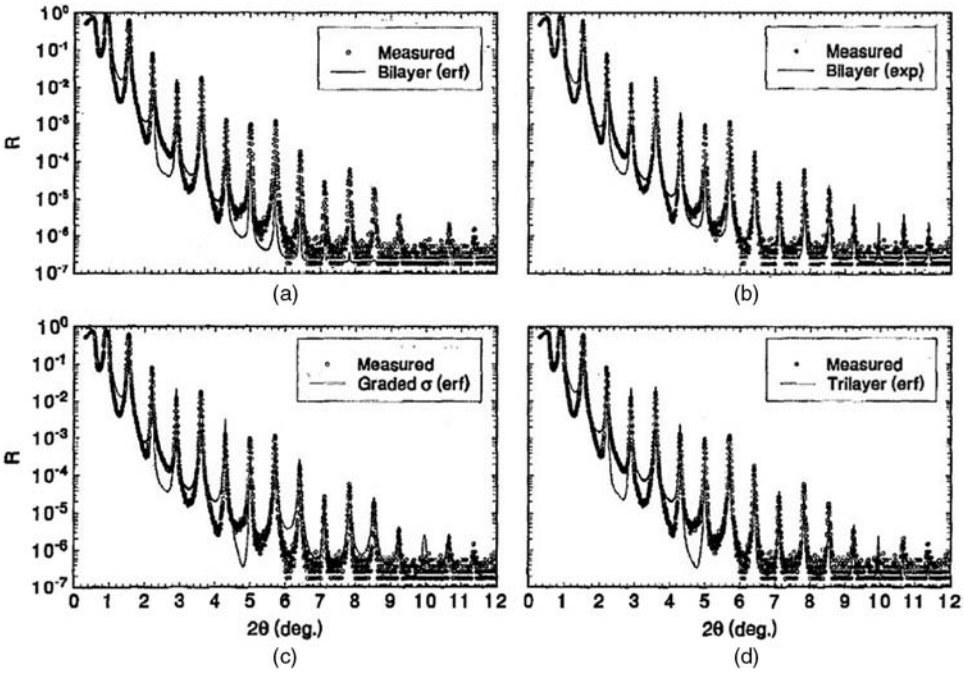

Figure 7.11 Example of low-angle XRD data and the fit for a Mo/Si ML (reprinted from Ref. 19 with permission from AIP Publishing).

creates low-energy secondary electrons that promote surface oxidation.[26] Thus, a capping layer material that acts as an effective oxidation barrier is required. Ruthenium (Ru) is one of the strongest candidates for the capping layer due to its oxidation resistance as well as high initial reflectance.[41,42] Some studies have pointed out the long-term lifetime of Ru capping in projection optics mirrors,[43–46] and Ru's high etch selectivity against absorber material is an additional benefit.[42] Another capping layer, iridium (Ir), has been proposed to capitalize on its inertness in a harsh environment of oxygen and acids.[47] Since the capping layer has extra roles in the EUV mask structure, more detailed discussion will be given in Section 7.4.4.

Another source of imperfection is silicide formation between the Mo and Si layers. Silicide formation results in reflectance degradation as well as ML period contraction. Interestingly, the silicide layer thickness is interface-dependent; the silicide thickness of the Mo-on-Si layer is about two times thicker than that of the Si-on-Mo interface. A reduction of interdiffusion can be accomplished by introducing thin diffusion barriers between the Mo and Si layers, which leads to a transition from the traditional Mo/Si bilayer structure to an interface-engineered triple or quadruple structure (Fig. 7.12). Some examples of diffusion barrier material are boron carbide (B_4C), carbon (C), silicon carbide (SiC), and Ru; peak reflectivity as high as 70% has been obtained using these materials.[25,26] Another benefit from this interface

Downloaded From: https://www.spiedigitallibrary.org/ebooks/ on 09 Mar 2022
Terms of Use: https://www.spiedigitallibrary.org/terms-of-use

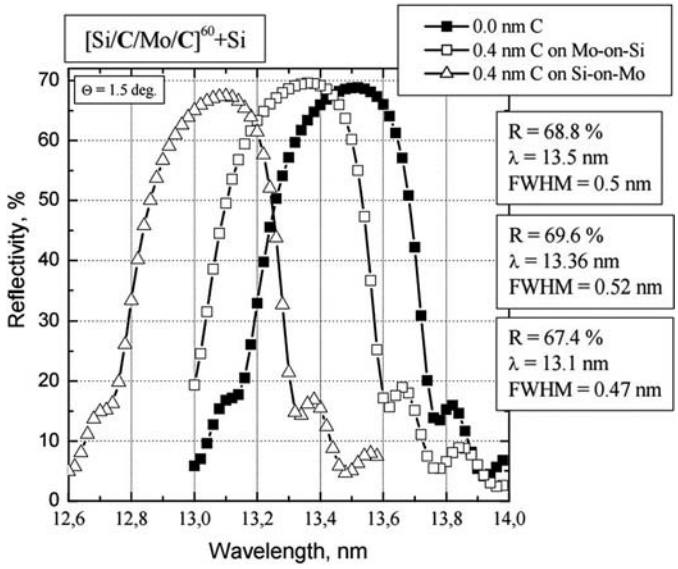

Figure 7.12 Measured reflectivity of standard Mo/Si, interface-engineered Mo/C/SI, and Mo/Si/C MLMs (reprinted from Ref. 25).

engineering is long-term thermal stability.[48] Thermal instability can cause two problems: (1) reflectivity loss and (2) a centroid wavelength shift toward the shorter wavelength. Volume contraction occurs when the Mo and Si react with each other and form molybdenum silicide ($MoSi_2$), causing a decrease in d-spacing and a centroid shift. The centroid shift is a more serious problem than the peak reflectivity loss, since the drop in reflectivity at the desired wavelength (13.5 nm) can become drastic with the spectral band shift. In the case of the Mo/Si ML, silicide formation can occur at temperatures as low as 150 °C, and the silicidation becomes more active at higher temperatures. At temperatures as high as 400 °C, complete silicidation of the ML can occur within a short period of heating time.[49]

Roughness of interfaces is another imperfection that lowers ML reflectance. A previous study identified a critical Mo thickness where the roughness increases dramatically due to the amorphous-to-crystalline transition.[50] Fortunately, in an optimized ML for an EUV mask, the typical Mo thickness is well below that critical value. Using ML smoothing techniques during the deposition process can effectively reduce roughness problems caused by small substrate surface defects and substrate surface roughness. The propagation of substrate imperfections is strongly dependent on the substrate imperfection type, the deposition tool, and the deposition process conditions.

In a typical IBD process, the ion-beam energy and incident angle of deposition are the main process variations. Higher ion-beam energy can enhance the smoothing by increasing the mobility of adatoms on the surface so the atoms can move around after attachment to the substrate. However,

Downloaded From: https://www.spiedigitallibrary.org/ebooks/ on 09 Mar 2022
Terms of Use: https://www.spiedigitallibrary.org/terms-of-use

higher ion energy promotes the intermixing of Mo and Si layers during ML deposition, resulting in a reflectivity loss. The ion beam incident angle also results in conflicting effects on reflectivity uniformity and defect smoothing. Deposition with a non-normal angle usually produces better deposition uniformity. However, the shadowing at the defect results in a less effective substrate bump smoothing.

Ion polishing using a secondary step has been proposed for defect smoothing. Ion polishing is most effective if it is performed only on the Si layers after the deposition of each Si layer (Fig. 7.13). This planarization process for smoothing substrate particles using a secondary ion source has been reported to smooth ~45-nm-height particles on the substrate to a residual height of ~0.2 nm, which would render them noncritical in an EUVL printing process (Fig. 7.14).[14] It has been reported that approximately 50-nm-diameter particles can be planarized to a height of 0.2 nm.[51] However, a small peak reflectivity loss associated with the smoothing process has been found. EUV absorption by implanted argon (Ar) atoms or interfacial layer mixing due to a secondary ion source is speculated to be the source of reflectivity loss.[30] Another concern is pits, which is another type of defect in the EUV substrate.[52] Pits can be smoothed by using more glancing angles for etch flux, while substrate particles can be flattened using normal angle etching.[53–56] To smooth particles and pits simultaneously, a multistep process uses two different etch angles, the first focusing on pits, the second on particles, since the optimal etch angle of each is different. A 600-eV ion energy (Ar) and a medium incident angle of 30 deg is suggested for IBD as an optimum process condition combined with secondary ion-beam polishing of 250-eV Ar.

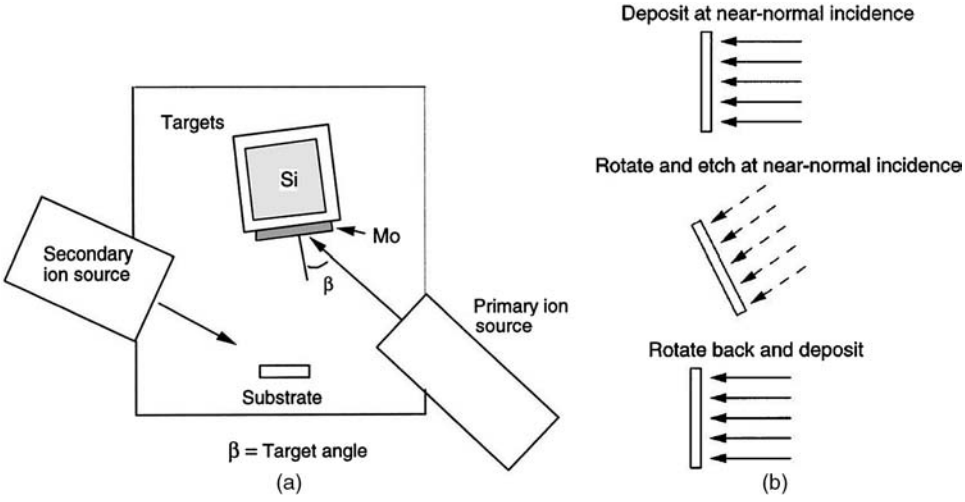

Figure 7.13 (a) Schematic diagram of the IBD tool. (b) Illustration of the ion-assisted procedure using a secondary ion source (reprinted from Ref. 15).

Downloaded From: https://www.spiedigitallibrary.org/ebooks/ on 09 Mar 2022
Terms of Use: https://www.spiedigitallibrary.org/terms-of-use

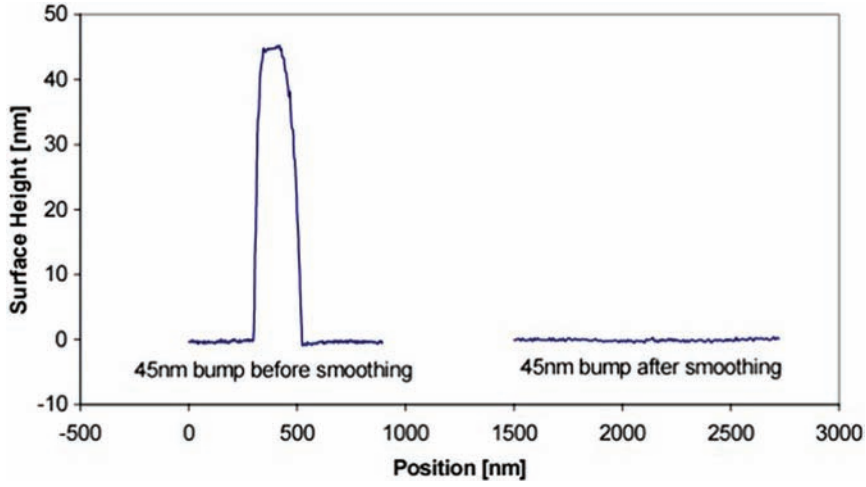

Figure 7.14 Cross-sectional surface profile as measured by atomic force microscopy (AFM) of a programmed bump on a Si surface before and after 20 smoothing cycles (reprinted from Ref. 14).

Figure 7.15 shows the defect reduction trend for EUV mask blanks since 2012.[31] Defect size is defined in terms of SEVD—the diameter of a sphere having equivalent volume to native defects. EUV blank MLs with defect counts ≤10 at below 25 nm in size became commercially available from a mask blank supplier in 2015. The industry goal is to fabricate EUV blank MLs with defect counts ≤10 at 16 nm in size by 2018. A significant amount of work still must be done to achieve the specification of zero added defects for particles ≥23 nm SEVD.

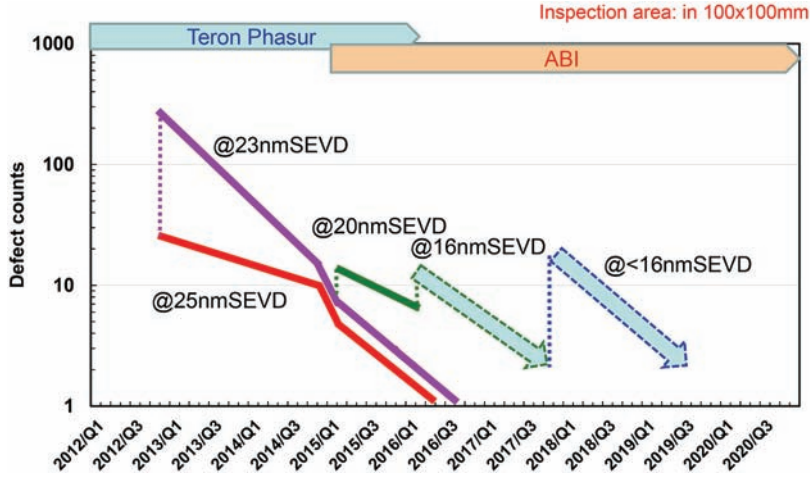

Figure 7.15 Defect reduction trend of EUV mask blanks from 2012 (reprinted from Ref. 31).

Downloaded From: https://www.spiedigitallibrary.org/ebooks/ on 09 Mar 2022
Terms of Use: https://www.spiedigitallibrary.org/terms-of-use

The flatness requirement of the mask brings up a stress issue that concerns all of the layers used in EUV mask fabrication, which include the ML, capping layer, absorber, and backside conductive layers. Out-of-plane distortion (OPD) caused by the film stress eventually induces a pattern placement error of the patterned mask. A typical high-reflectance Mo/Si ML exhibits residual stress close to −400 MPa (compressive), which results from the combined effect of tensile (∼300 MPa) Mo layers and compressive (∼ −1300 MPa) Si layers.[57] Most of the stress reduction approaches such as layer thickness adjustment, deposition condition variation, post-deposition annealing, and spacer layer compensation result in a loss of reflectivity. Since many other layers besides the ML are involved in the mask structure and some of them are locally etched away, the best approach for mask flatness is to attain near-zero stress in each and every layer of the mask structure. By doing so, nonuniform stress release that causes local mask distortion can be minimized.

7.4.4 Capping layer

The capping layer protects the ML from oxidation because reflectivity loss due to surface oxidation is expected for a Si-terminated ML. A study showed that the lifetime of a Ru-capped ML is more than 40 times longer than that of a Si-capped ML (Fig. 7.16).[41] Among the several candidate materials, Ru is widely used as a capping layer for EUV masks due to its suitability for EUV mask manufacturing.[42–46,58] A thin (∼2 nm) Ru capping layer shows a high etch selectivity to the absorber layer[51] and high chemical stability under mask wet cleaning condition in addition to the minimum reflectivity loss when added on top of a ML. The capping layer should also be able to protect the ML surface during the pattern repair process using a focused ion beam (FIB) or an e-beam,[59] as well as during cleaning process. A typical cleaning process comprises multiple steps.[60] The first step is to reduce the contact angle so that the surface becomes wet in subsequent cleaning steps. Then organics and particles are removed using a sulfuric acid / hydrogen

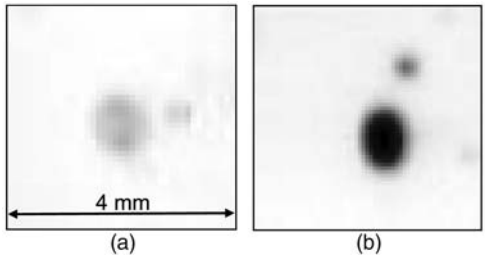

Figure 7.16 Reflectance change maps of (a) a Ru-capped ML and (b) a Si-capped ML after ∼60 hours of EUV beam exposure in a water vapor environment. The grayscale is the same for both maps and ranges on a linear scale from –16.5% (black) to 0% (white) (reprinted from Ref. 41).

Downloaded From: https://www.spiedigitallibrary.org/ebooks/ on 09 Mar 2022
Terms of Use: https://www.spiedigitallibrary.org/terms-of-use

peroxide mixture followed by an ammonium hydroxide / hydrogen peroxide and deionized water mixture. Finally, the surface is rinsed and dried. The Ru layer easily oxidizes when exposed to cleaning chemistries, thereby increasing its surface roughness.[16] Greater roughness promotes EUV light scattering, causing speckle in lithography. Another issue is the loss of EUV reflectivity due to absorption of the EUV by Ru oxides. Cleaning using a 1-MHz megasonic nozzle creates pits on the Ru-capped ML blank, just as it does on a LTEM substrate.

7.4.5 Backside conductive coating and mask handling

Since the EUV mask is a reflective mask, it is possible to chuck the mask from its backside to flatten it. A traditional vacuum chuck will not work in an EUV exposure tool since the wafer exposure is performed in high vacuum. One possible alternative is to use an electrostatic chuck (e-chuck), in which case a conductive mask backside coating is required. As a result, the SEMI P38-1103 standard requires a backside conductive coating for the EUV mask blank, and the SEMI P40-1109 standard sets stringent flatness requirements for the EUV mask chuck. Mask distortion—both inplane distortion (IPD) and out-of-plane distortion (OPD)—will occur due to the residual stress of the ML, absorber layer, and ARC. However, consistency in mask mounting during e-beam writing and wafer exposure will minimize IPD and OPD as long as the substrate flatness meets the requirements.

Another critical issue in the EUVL process is mask protection from particle contamination during storage, handling, and exposure. A specially designed mask carrier is utilized for mask handing and transportation. A dual-pod approach led to nearly particle-free use during a simulated life cycle at ~50-nm inspection sensitivity.[61] The dual-pod mask carrier consists of two parts. An inner pod protects the mask surface from particle contamination until the mask is inserted into the EUV scanner. The inner pod should be housed outside the vacuum environment on an outer carrier called the outer pod.[62,63] A pellicle placed in front of the masks plays the most important role in protecting the masks from particle contamination. However, organic film, which has been used for the DUV pellicle membrane, cannot be used for the EUV pellicle due to the extreme absorption at the EUV wavelength. A new concept for EUV pellicles is under development and will be discussed in Section 7.7.1.

7.5 Absorber Stack and Pattern Fabrication

An EUV mask requires a two- or three-layer film, called the absorber stack, on top of the ML. A thinner absorber stack is desirable to achieve minimal shadowing effect due to absorber pattern topography. A phase shift layer and an ARC can be added in the absorber stack if needed.

Downloaded From: https://www.spiedigitallibrary.org/ebooks/ on 09 Mar 2022
Terms of Use: https://www.spiedigitallibrary.org/terms-of-use

7.5.1 Absorber layer

The absorber layer must exhibit several characteristics, including high EUV absorption, stability under EUV radiation, conductivity, high etch selectivity to the capping layer (the buffer is no longer used, at least not widely), and proper DUV reflectivity (in some cases, high reflectivity is actually good for patterns near or below optical resolution) to afford optical surface defect inspection. Several candidate materials, including compounds of tantalum (Ta), titanium (Ti), and nickel (Ni) have been proposed.[64–68] Among them, Ta-based materials have been widely studied. Ta-based materials, which have been developed for x-ray masks, can be easily etched with Cl_2 and F-based chemistry, and yield very little etch bias. These materials have also been found to be suitable for EUV mask fabrication and printing.[69] Aerial image contrast depends on the absorber material (higher with TaN and Cr) as well as the absorber thickness (higher with a thicker absorber). However, a low-refractive-index material such as TaN can be used for an attenuated phase shift mask (PSM), resulting in even higher contrast at low thickness (~45 nm in the case of TaN) (see Fig. 7.17).[70] Chemical cleaning compatibility as well as the defect level of the TaN absorber layer is comparable with high-end Cr material.[71] Recently, studies of using thinner absorber layer with high extinction coefficient for the EUV wavelength have been reported. The material candidates are transition metals such as Ni and Pd.[72–74] A thinner absorber layer becomes more important with a high-NA system for resolution extension because the higher chief ray angle of incidence increases the mask 3D effect. A very low refractive index can provide a 180-deg phase shift at very small thicknesses (e.g., PdO with $n = 0.8634$ at 20 nm), and this can exhibit even better performance in combination with its high extinction coefficient.[74]

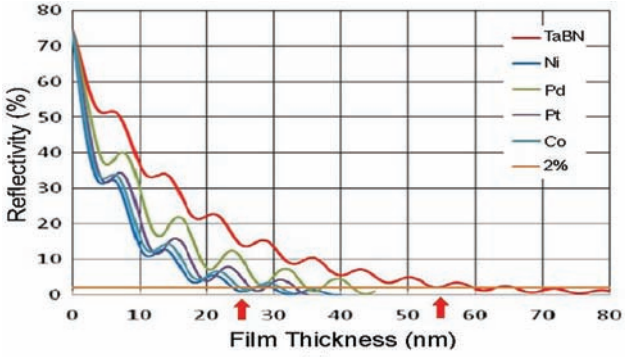

(a)

Film	R (%)	T (nm)
TaBN	2.10	54.2
Ni	0.94	25.4
Pd	1.00	36.0
Pt	1.10	27.6
Co	1.26	26.0

(b)

Figure 7.17 (a) Calculated net reflectivity of a Ru-capped Mo/Si ML with 40 bilayers at 13.5-nm wavelength and 6-deg angle of incidence overcoated with various absorbing films as a function of film thickness. (b) Table of candidate absorber materials with thickness values *T* at which the net reflectivity *R* falls below 2% (reprinted from Ref. 73).

Downloaded From: https://www.spiedigitallibrary.org/ebooks/ on 09 Mar 2022
Terms of Use: https://www.spiedigitallibrary.org/terms-of-use

7.5.2 Antireflection coating

A traditional optical mask can be inspected using transmission, reflection, or a combination of the two methods. However, EUV masks can only be inspected using the reflection mode. The image contrast depends on the reflectivity difference between the ML region and the absorber region. The image contrast is defined as

$$\text{Image contrast} = \frac{R_{ml} - R_{abs}}{R_{ml} + R_{abs}} \times 100\%, \tag{7.5}$$

where R_{ml} and R_{abs} are reflectivities measured on the ML and the absorber, respectively, as shown in Fig. 7.18. Note that when "ML" is used in equations and figures, it usually represents a ML with a capping layer deposited on top of it.

Since any metal layer (with Ta-based films being the strongest candidates for the absorber layer) would reflect too much of the DUV light, an ARC is needed for DUV inspection to reduce this reflection as much as possible. The EUV light reflection at the absorber can be decreased by adjusting the thickness as well as by selecting a material such that an ARC is not needed for actinic inspection. Coupled with the typical ML reflectivity of 55% to 60% at the DUV wavelength, a considerable reflection on top of the absorber layer requires the antireflection function of the ARC layer to reduce the light reflection from the top of the absorber. Image contrasts of 75% and 88% were reported with 33-nm SiON-ARC on TaSiN and 20-nm Al_2O_3-ARC on TaN, respectively.[75,76] In addition to the low reflectivity at the inspection wavelength, the ARC should be easy to etch with zero etch bias and should be stable under mask cleaning chemistry.

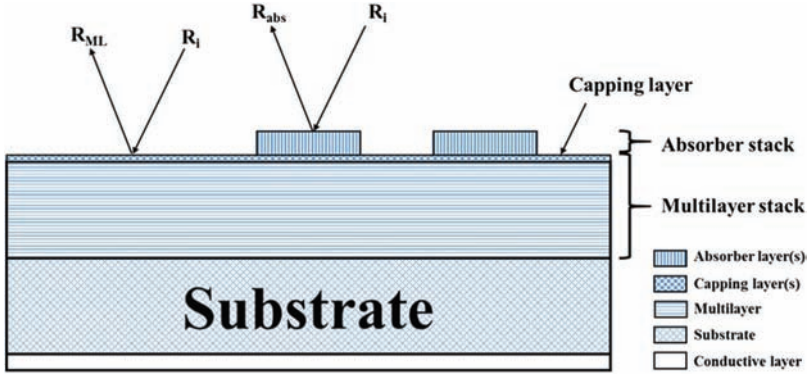

Figure 7.18 Reflectivity of the patterned and unpatterned areas used to determine the inspection image contrast (adapted from Ref. 76).

Downloaded From: https://www.spiedigitallibrary.org/ebooks/ on 09 Mar 2022
Terms of Use: https://www.spiedigitallibrary.org/terms-of-use

7.5.3 E-beam patterning

EUV mask e-beam patterning is similar to that of the conventional optical mask. However, the temperature (post-exposure bake, dry etch, and repair) should be maintained below 150 °C due to ML thermal instability and mask distortion.[77] One of the continuing challenges in e-beam lithography is the proximity effect, which can severely degrade pattern fidelity and CD control. The proximity effect is due to electron scattering in the resist and electron backscattering from the substrate materials. The range of proximity effects depends on the energy of incident electrons, the substrate material, and the thickness of the resist and substrate. A high-energy e-beam results in high-resolution resist patterns due to the minimized exposure by forward scattering, as well as dispersed backscattered electrons. Materials with a high atomic number have high electron backscattering cross-sections and are expected to have larger proximity effects than those of materials with a lower atomic number. Since EUV masks generally contain high-atomic-number elements for the absorber, the proximity effects are expected to be higher for these substrates than for low-atomic-number materials such as Si. Experimental results on the proximity effect during e-beam writing have been reported for some absorber stacks.[78] As shown in Fig. 7.19, a structure with a TaSiN top layer results in a larger proximity effect due to a larger number of backscattered electrons from the high-atomic-number TaSiN layer exposing the resist.

7.5.4 Absorber stack etch

The absorber etch process must stop with a sufficient selectivity to the capping layer. For TaN absorber etching with hexafluoric (SF_6) chemistry, a high etch

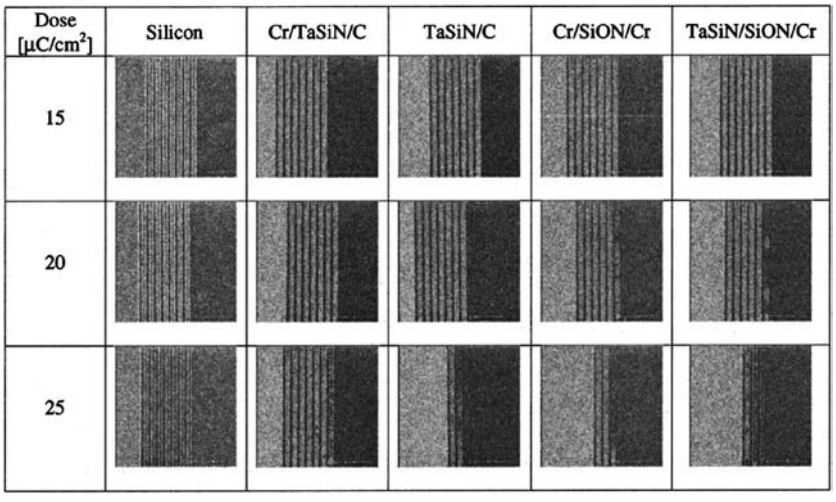

Figure 7.19 Proximity effect test patterns of a 200-nm line/space pattern on the selected absorber stack for different exposure doses (reprinted from Ref. 78 with permission from AIP Publishing).

Downloaded From: https://www.spiedigitallibrary.org/ebooks/ on 09 Mar 2022
Terms of Use: https://www.spiedigitallibrary.org/terms-of-use

selectivity of 60:1 was reported against a Ru capping layer.[79] An etch bias of less than 5 nm was obtained and was independent of both structure and size, which contrasts with the results of the Cr absorber. Other important issues in the absorber etch process are the sidewall angle and line edge roughness (LER). Also, the absorber etch process should have a minimal effect on the EUV reflectivity of the ML. Possible contributing factors for reflectivity loss are surface oxidation or surface morphology change. Sufficient uniformity with only a small loss of reflectance has been reported with a Ta-based absorber etch process.[77] Durability of the ARC during etch is an important issue as well because any reduction of the ARC thickness can impact the DUV inspection contrast. Ru is a good capping material due to its high etch selectivity against TaN absorber.[44,79]

7.6 Mask Inspection, Metrology, and Repair

7.6.1 Multilayer defect inspection

In order to ensure a reliable supply of defect-free mask blanks, it is necessary to develop techniques to reliably and accurately detect mask blank defects prior to patterning. The ML defect can be generated from a substrate defect or from a particle during ML deposition. Multilayer defects can be classified into two types: one is an amplitude defect and the other is a phase defect.[80] Amplitude defects directly absorb EUV light, and phase defects disrupt the constructive interference of the reflections from each of the ML interfaces due to phase difference (Fig. 7.20). Amplitude defects are either particles near the top of the ML stack or flaws in the ML. On the other hand, phase defects are swellings or depressions on the surface of the ML.

High-throughput DUV (e.g., 199 nm, 248 nm, 257 nm, and 266 nm) inspection tools are currently used for blank inspections.[81–84] However, in order to have confidence in the DUV light inspection strategy, it is necessary to confirm whether any defects visible by EUV are not being detected by the DUV inspection tool. The mask inspection system should be able to capture all classes of printable mask defects. But discrepancies still exist between actinic (at-wavelength) and nonactinic inspection results, and their correlation is under study. One particular challenge is to detect small buried defects by nonactinic defect inspection tools.

Actinic inspection using dark-field microscopy has been studied and resulted in high sensitivity.[85–88] Some inspection methods can detect a bright-field signal and a dark-field signal simultaneously.[89,90] The highest sensitivity for EUV defect detection has been obtained in the dark-field scanning mode, where only the light scattered out of the entrance pupil is detected. In this mode it is also possible to observe a bright-field image from the mask with a zone plate. This inspection system is operated in two modes; one is the EUV dark-field scanning mode and the other is the aerial image monitoring mode

Downloaded From: https://www.spiedigitallibrary.org/ebooks/ on 09 Mar 2022
Terms of Use: https://www.spiedigitallibrary.org/terms-of-use

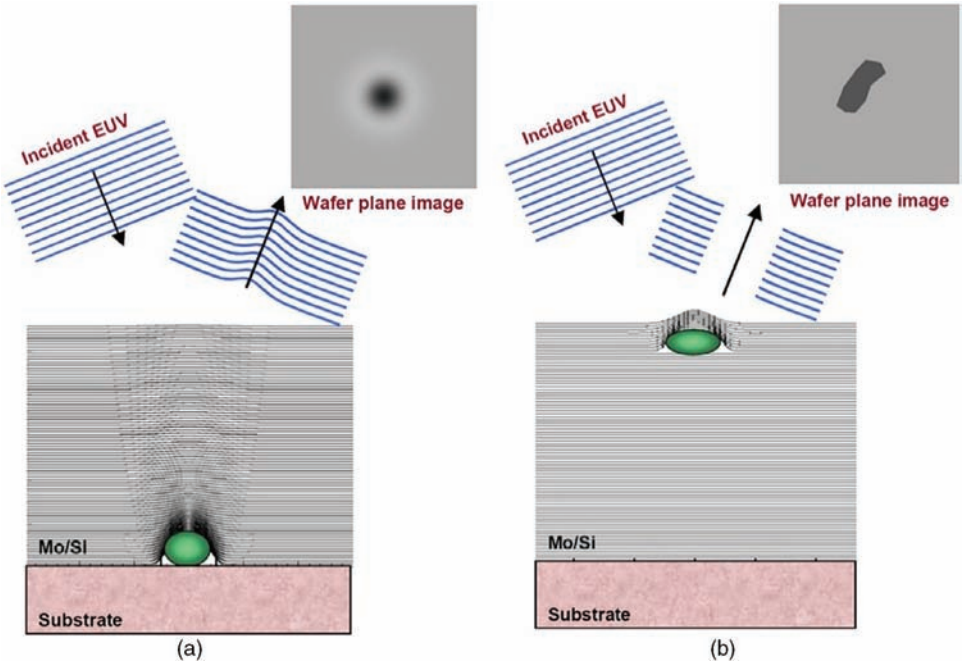

Figure 7.20 Classification of ML defects: (a) phase defect and (b) amplitude defect (reprinted from Ref. 80).

(Fig. 7.21).[90] First, all of the mask blanks are scanned in high-speed inspection (scanning) mode to identify and map all locations on the mask that scatter significant amounts of EUV light. In the imaging mode (defect review mode), a zone plate is placed in the reflected beam path to image a region of interest onto a CCD detector with an effective resolution.

The recent development of a high-volume-manufacturing (HVM) dark-field actinic ABI tool is based on a concept advanced by AIST and MIRAI-ASET.[91,92] Lasertec Corp. simultaneously began to develop a HVM tool with support from EIDEC.[93–95] The HVM ABI tool (Fig. 7.22) consists of an EUV source module, illumination optics containing two ellipsoidal mirrors and a fold mirror, Schwarzschild optics for imaging, and an EUV-sensitive back-illuminated CCD camera. A full-field HVM ABI prototype has been successfully developed to achieve a target line of printable phase defects for the 16-nm HP node.[96–102]

To verify the detection capability of the HVM ABI prototype, native phase defects measured with AFM were tested for various cases. The minimum detectable size range is expected to be 1.0 nm (height) by 36 nm (width) (~14-nm SEVD range) with 100% capture rate (Fig. 7.23).[95]

Consequently, the HVM ABI prototype could verify wafer-printable phase defects by using the relationship between defect signal intensity (DSI) and wafer-printability on an EUV scanner.[103,104] EIDEC and IMEC jointly

Downloaded From: https://www.spiedigitallibrary.org/ebooks/ on 09 Mar 2022
Terms of Use: https://www.spiedigitallibrary.org/terms-of-use

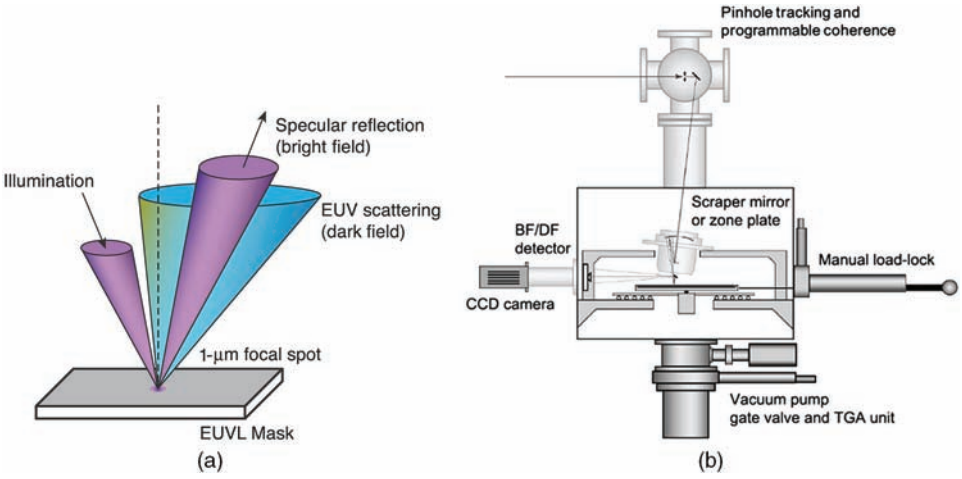

Figure 7.21 (a) Bright-field (BF) and dark-field (DF) signal from the mask used for defect inspection and (b) conceptual layout of a dual-mode actinic defect inspection system (TGA is thermogravimetric analysis). The scraper mirror is used for the scanning mode, and the reflective zone plate lens is used for the high-resolution imaging mode (reprinted from Ref. 89).

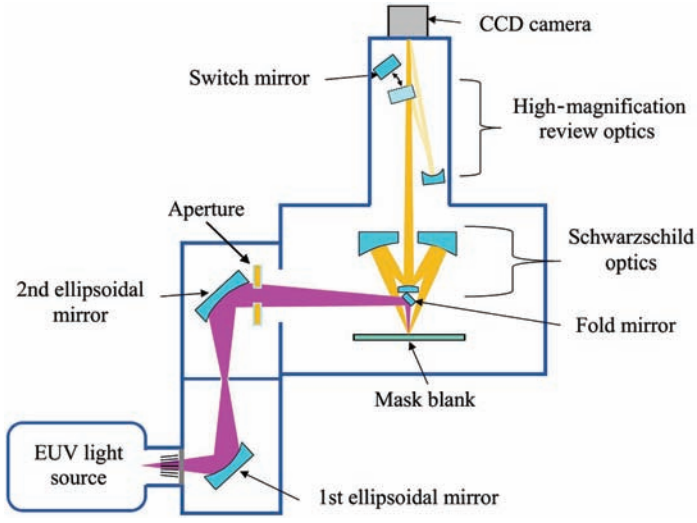

Figure 7.22 Schematic diagram of a HVM ABI prototype (reprinted from Ref. 102).

correlated defect detection by the HVM ABI prototype and defect impact on wafer printing by an IMEC EUV scanner.[105,106] The DSI can be defined as the volume of the peak signal intensity after subtracting the background level of its surroundings (Fig. 7.24).[102] Since lower-aspect-ratio phase defects result in a lower scattered light angle, enlargement of the illumination NA can

Downloaded From: https://www.spiedigitallibrary.org/ebooks/ on 09 Mar 2022
Terms of Use: https://www.spiedigitallibrary.org/terms-of-use

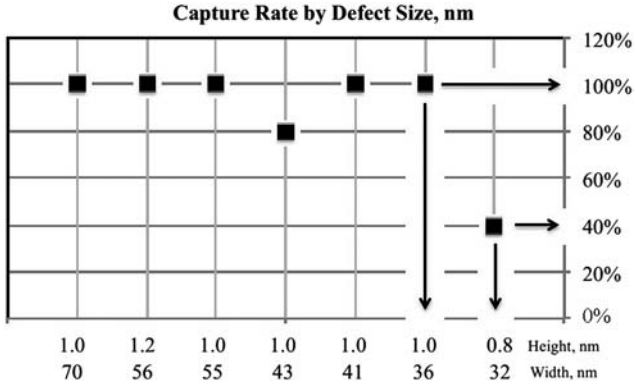

Figure 7.23 Detection capability based on native phase defects detected by the ABI HVM prototype (reprinted from Ref. 95).

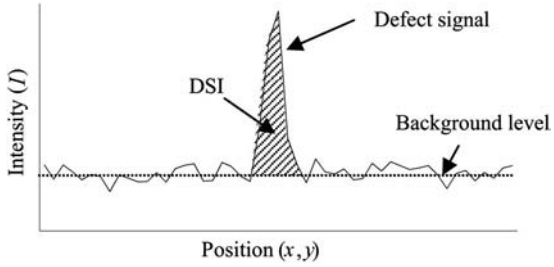

Figure 7.24 Graphical representation of defect signal intensity (DSI) (reprinted from Ref. 102).

increase the dark-field signal intensity (Fig. 7.25). Yamane et al. claimed that a NA of 0.1 can be used to detect all the printable phase defects.[102]

7.6.2 Absorber pattern inspection

Both actinic and nonactinic inspection techniques are usable for absorber defect inspection. Nonactinic inspection tools (DUV or e-beam) have limitations in meeting the requirements of pattern inspections for EUVL (Fig. 7.26).[107] E-beam may be adopted for high-resolution inspection tools, but it has low throughput and is incompatible with EUV pellicles.[107,108]

It is highly likely that the high-throughput inspection tool will be operated at the DUV wavelength where the resolution can be improved by reducing the inspection wavelength.[83] In order to overcome the optical resolution limit of the DUV inspection tool, defect signal enhancement is also attempted not only by utilizing various resolution enhancement technologies and noise control techniques,[109] but also by optimizing the EUV absorber stack.[110] Obtaining high contrast for mask inspection is important because the interference effects obtained in the reflection inspection image can complicate

Downloaded From: https://www.spiedigitallibrary.org/ebooks/ on 09 Mar 2022
Terms of Use: https://www.spiedigitallibrary.org/terms-of-use

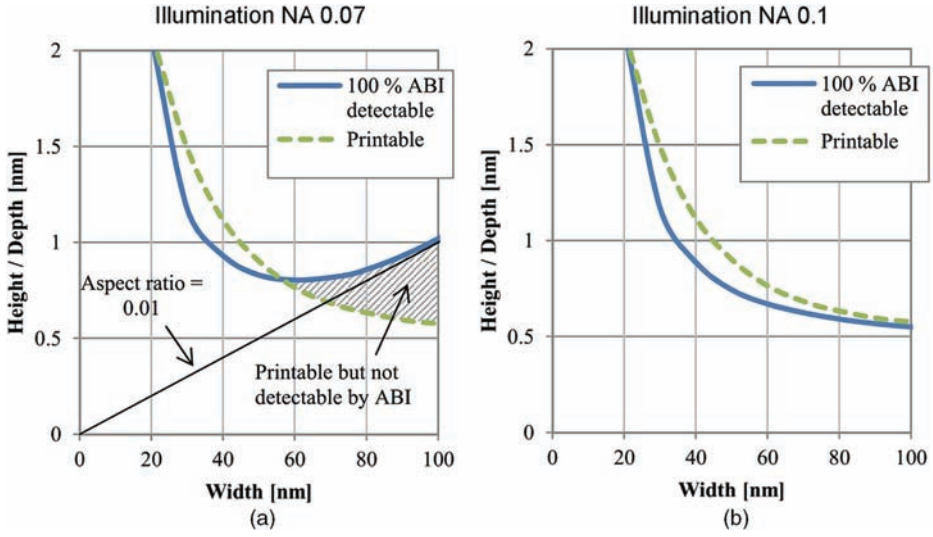

Figure 7.25 Dimensions of phase defects printable for a 16-nm node and detectable by ABI with an illumination NA of (a) 0.07 and (b) 0.1 (reprinted from Ref. 102).

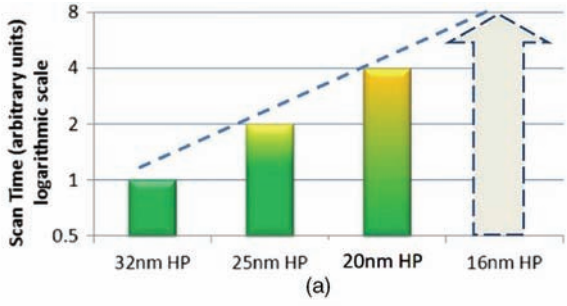

Technology Node [nm]	28	22	16	11	8
Defect size [nm]	40	30	20	<10	7
193nm inspection					
E-Beam inspection					

(b)

Figure 7.26 (a) Increasing inspection time according to design node shrinkage. (b) Mask inspection performance using 193-nm and e-beam inspection (green – positive, yellow – needs development, red – negative) (reprinted from Ref. 107).

the edge profiles between the ML and the absorber. This is especially troublesome when the step height of the absorber is on the order of one-quarter of the inspection wavelength, which yields significant destructive interference between the light reflected from the absorber and the ML at the edges unless the

Downloaded From: https://www.spiedigitallibrary.org/ebooks/ on 09 Mar 2022
Terms of Use: https://www.spiedigitallibrary.org/terms-of-use

reflectivity of the absorber is very low. An absorber reflectivity range between 5% and 10% has been suggested from the standpoint of mask inspectability without using significantly tight constraints on EUV absorber reflectivity.[83] Inspection setting using double focal planes, one on the ML surface and the other on the absorber surface, with flexible illumination and polarization shows improved defect sensitivity [Fig. 7.27(a)].[109] Conventional or annular illumination and circular polarization are employed for hole layers, while dipole illumination and linear polarization are used for line/space layers. A thick absorber in combination with a thin ARC results in better inspectability [Fig. 7.27(b)].

7.6.3 Multilayer defect repair

Some exploratory research on repairing ML defects has been done, but it has not been easy to implement the resulting techniques in mask fabrication. The ML defect compensation approach seems more practical than defect repair if the number of ML defects is very limited. Descriptions of the studies on ML defect repair are presented here.

The basic principle of amplitude defect repair is to restore the local reflectivity by removing the particle. Focus ion beam is widely used in nanotechnology for local deposition and etching due to its high spatial resolution. Multilayer repair also can be done by physically removing the particle using FIB [Fig. 7.28(a)]. The reflectivity drop due to layer removal can be controlled because the ML reflectivity is a direct function of the number of bilayers in the ML stack. It has been shown that removing 20 pairs from the original ML consisting of 50 to 60 bilayers will result in a reflectivity drop of about 1%.[80] To prevent oxidation after repair, *in situ* local IBD of a capping layer has been proposed [Fig. 7.28(b)].[80]

Since the phase defects originate from the bottom of the ML stack, standard mask repair technology is incompatible. High-resolution electron-beam repair technology has been proposed to heat the ML and activate silicide formation and then local contraction of the layer structure (Fig. 7.29). Another consideration is the shift in the centroid wavelength, which is expected according to the following equation using a simplifying assumption:

$$\Delta\lambda = 0.874\,(2\Delta d), \tag{7.6}$$

where Δd is the contraction of a single period. An interferometer surface scan and cross-sectional TEM micrograph confirmed the feasibility of this technique (Fig. 7.30).[111,112] However, there is a limitation to the height of a defect that can be repaired with this technique. It is apparent that if the defect is too large, then after repair, the ML Bragg peak will be shifted outside the bandpass of the optical system and the phase defect will become an amplitude defect. This limitation is expected to be a Gaussian defect of several nanometers in height.

Downloaded From: https://www.spiedigitallibrary.org/ebooks/ on 09 Mar 2022
Terms of Use: https://www.spiedigitallibrary.org/terms-of-use

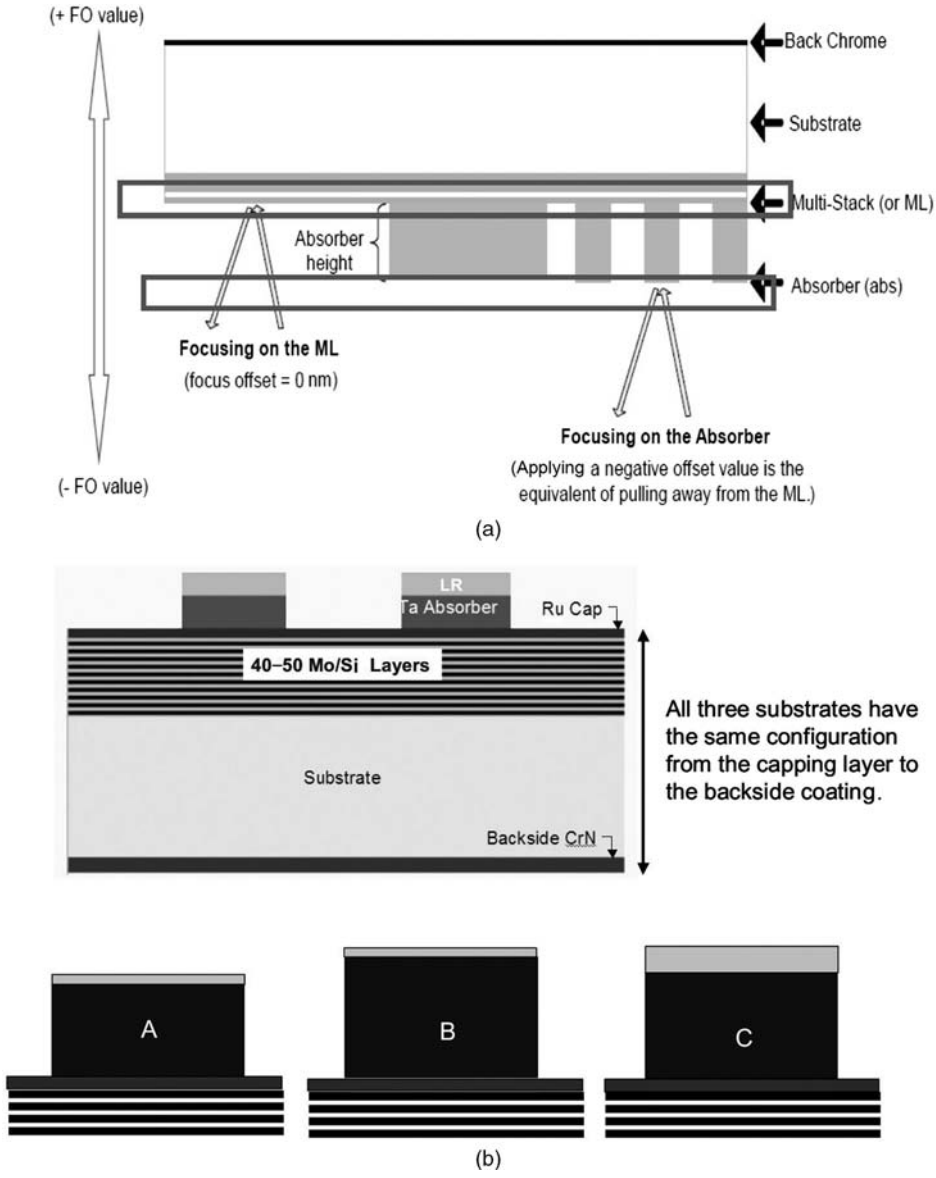

Figure 7.27 (a) Focus offset optimization for defect signal enhancement. (b) Comparison of the structures of three EUV absorbers. Sample B (thin ARC with thick absorber) shows the highest sensitivity (reprinted from Ref. 109).

Furthermore, to realize phase defect repair for an EUV mask blank, the depression diameter must to be considered. Hau-Riege et al. reported that deformations were primarily due to the compaction of the substrate and not the ML, and inevitably led to large depression diameters that were greater than 20 times the electron-beam diameters of 20 nm or less.[113] In order to achieve

Downloaded From: https://www.spiedigitallibrary.org/ebooks/ on 09 Mar 2022
Terms of Use: https://www.spiedigitallibrary.org/terms-of-use

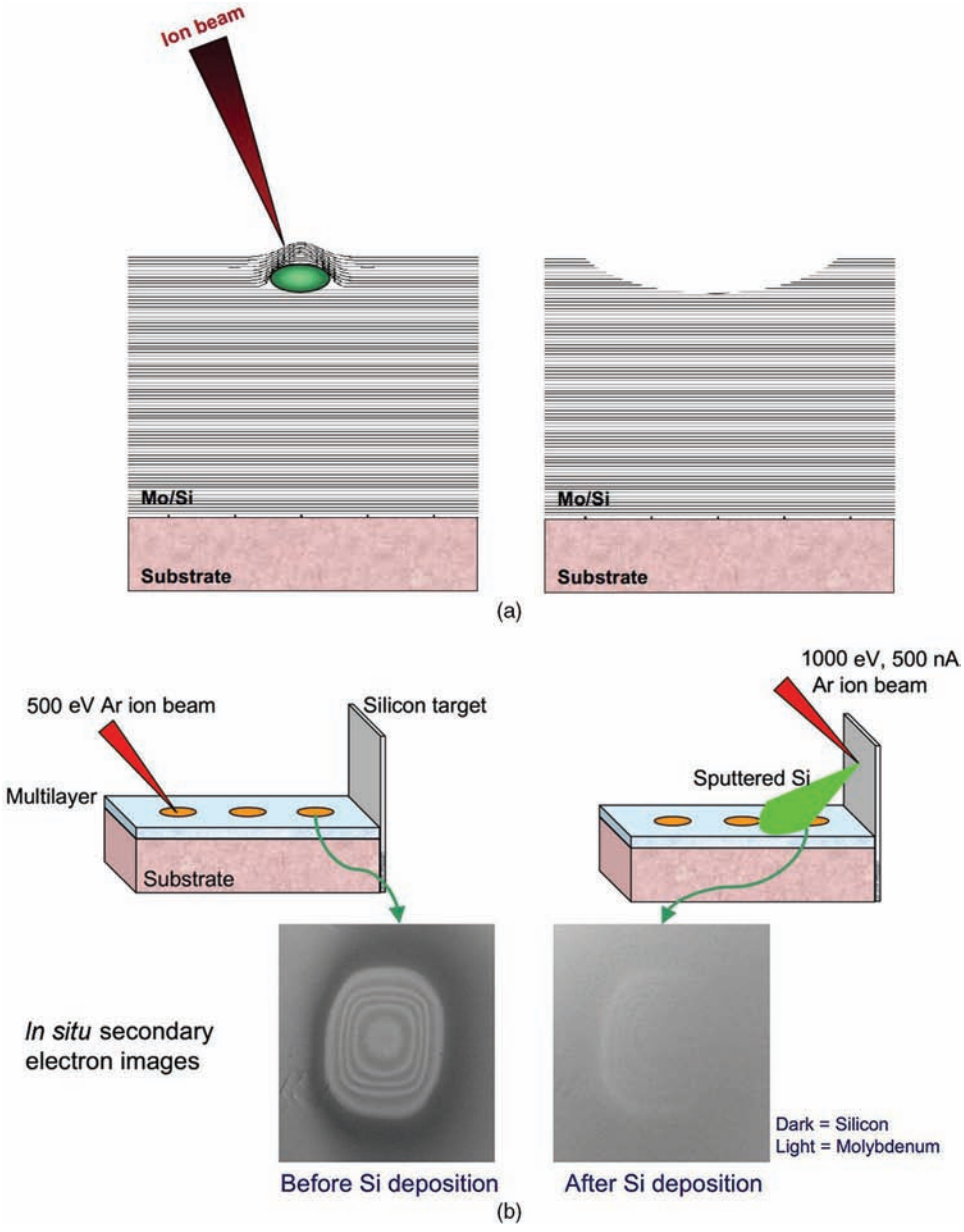

Figure 7.28 (a) Schematics showing the concept of amplitude defect repair using FIB and (b) *in situ* IBD for localized capping of the repaired region (reprinted from Ref. 80).

surface depressions of smaller diameters, substrate compaction must be prevented by using a lower-energy e-beam, a thicker ML, an underlayer between the ML and substrate that absorbs the beam spillover, or else by using a different substrate material.

Downloaded From: https://www.spiedigitallibrary.org/ebooks/ on 09 Mar 2022
Terms of Use: https://www.spiedigitallibrary.org/terms-of-use

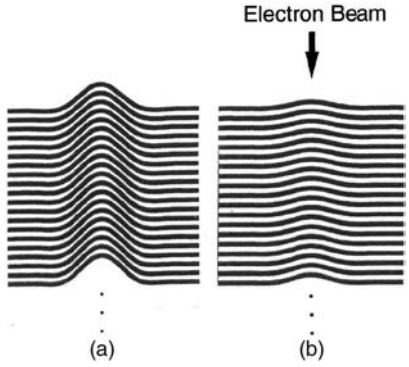

Figure 7.29 Schematic illustration of (a) a phase defect and (b) the defect after repair (reprinted from Ref. 111 with permission from AIP Publishing).

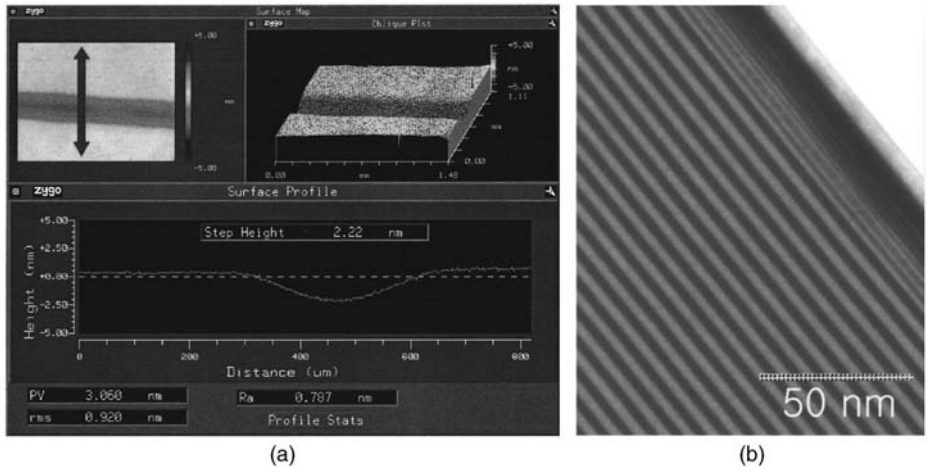

Figure 7.30 (a) Interferometer scan of a depression in the ML induced by an electron beam and (b) a cross-sectional TEM micrograph of the top portion of the ML after e-beam heating (reprinted from Refs. 111 and 112 with permission from AIP Publishing).

7.6.4 Multilayer defect compensation

The ML defect compensation scheme can be divided into two approaches: optical proximity correction (OPC) and ML defect avoidance (MDA). The efficiency of these two methods depends on the location of the defects and the type of the mask (clear field or dark field). OPC on an EUV mask is similar to that on an optical mask. When a defect causes a printed pattern distortion, the absorber pattern near the defect is trimmed (Figs. 7.31–7.33). By doing so, the final printed image will be compensated with the proximity effect between the trimmed pattern and the defect, yielding the original designed pattern.[114] The reflectivity loss from ML defects can be compensated in the EUV scanner

Downloaded From: https://www.spiedigitallibrary.org/ebooks/ on 09 Mar 2022
Terms of Use: https://www.spiedigitallibrary.org/terms-of-use

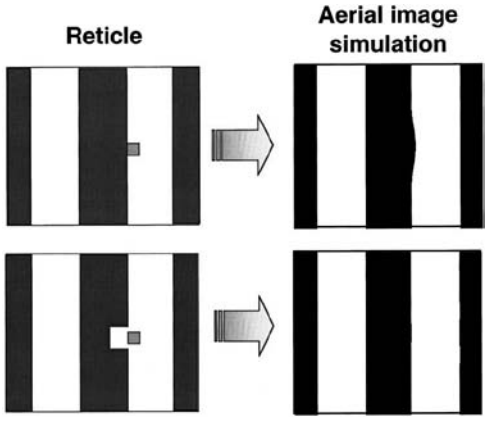

Figure 7.31 Aerial image simulation of a 80 × 80 nm π-phase edge defect without and with compensation (reprinted from Ref. 114 with permission from AIP Publishing).

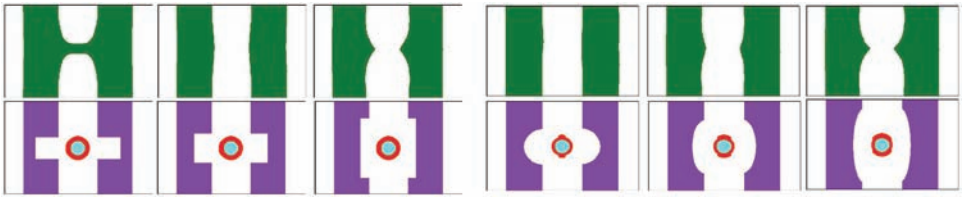

Figure 7.32 Simulated resist image in top view (top row) for varying area distributions of the compensation repair: rectangular (left half of the figure) and elliptical (right half of the figure). Too much concentrated or sparse distribution causes insufficient compensation. Repair performed on a 6-nm-high bump with 56 nm FWHM, at best focus minus 100 nm (reprinted from Ref. 115).

by removing absorber around the defective area. The accurate repair shape and the area can be determined by simulations.[115] A ML pit and a ML bump, both previously printing with a strong dependency on the focus setting during wafer printing, were successfully compensated over a 200-nm focus range.[116]

Also, the absorber pattern can directly cover the ML defect (Fig. 7.34). This is especially attractive in the case of a dark-field mask, such as a contact layer mask, where most of the mask areas are covered by the absorber patterns. To implement the MDA techniques, several steps are required; (1) fiducial alignment marking on the ML, (2) defect identification (size and location) from the ML inspection tool, (3) mask pattern data matching with ML defect locations so that a maximum number of ML defects are covered by the absorber with an appropriate corrective mask pattern translation and rotation, and (4) e-beam writing with compensated data. Ultimately, the effectiveness of the pattern shift depends on the defect size, the number of defects and location accuracy in the inspection, and the alignment overlay of the e-beam writing.[117,118]

Downloaded From: https://www.spiedigitallibrary.org/ebooks/ on 09 Mar 2022
Terms of Use: https://www.spiedigitallibrary.org/terms-of-use

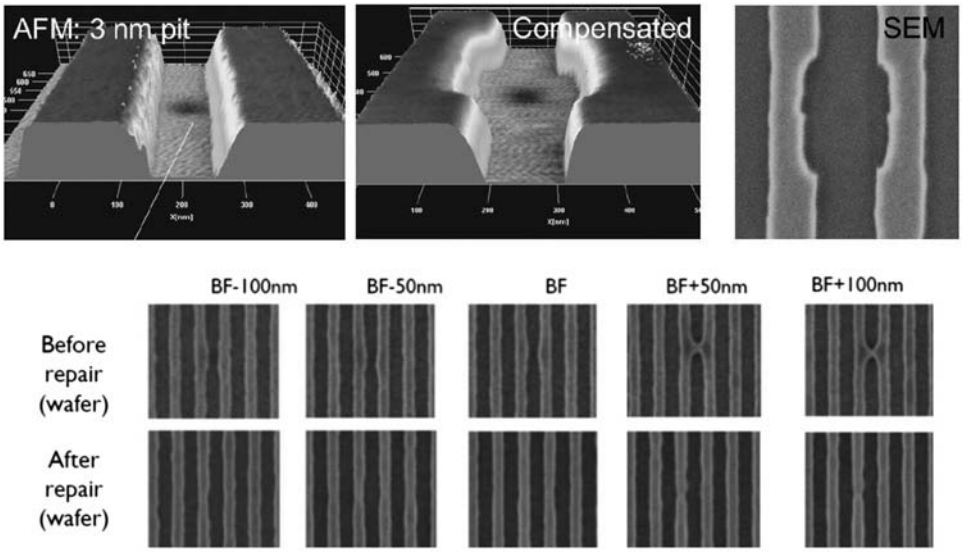

Figure 7.33 Demonstration of successful through-focus compensation repair on a real ML pit in 40-nm line/space. (Top) Reticle AFM imaging of the defect before (left) and after (middle) repair (performed with two different AFM tips yielding different cross-sectional edge profiles). (Top right) MeRiT® top-view SEM imaging after repair. Notice that the ML pit is almost invisible. (Bottom) SEM views of the ADT-printed wafers before and after repair, at different focus positions around best focus (BF) (reprinted from Ref. 116).

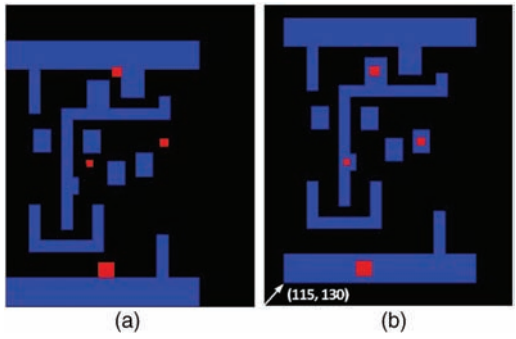

Figure 7.34 (a) Before layout shift, all four defects impact printing. (b) After shifting the layout by (115, 130), all of the defect impact is completely mitigated by absorber pattern coverage (reprinted from Ref. 118).

7.6.5 Absorber defect repair

Several techniques can be used for repairing opaque defects on an EUV mask. These techniques include e-beam repair, FIB,[119] and scanning probe-based mechanical nanomachining.[115,120,121] Among these, e-beam repair is the primarly solution for removing absorber defects in EUV masks.[122–126]

Downloaded From: https://www.spiedigitallibrary.org/ebooks/ on 09 Mar 2022
Terms of Use: https://www.spiedigitallibrary.org/terms-of-use

Ta-based EUV absorber materials can easily react with e-beam etch chemistry. Once the absorber material is etched with etch chemistry established for 193-nm photomasks, parasitic degradation may be induced. The absorber dissolves between the capping layer and the antireflective layer, forming a cavity [Fig. 7.35(a)]. It can be observed clearly in the SEM image [Fig. 7.35(b)] that the first contact hole has a big "aura," which is also visible in the middle contact hole. This aura is due to a growing cavity below the antireflective layer. Carl Zeiss SMT GmbH developed a new etch process that has no spontaneous etching, as shown in the bottom row of Fig. 7.35(b).[120]

Several types of opaque defects were successfully repaired with the single-process recipe shown in Fig. 7.36. For the partial-height defects, no AFM information was necessary since the process stops on the Ru-cap—the shorter process duration, which was 50% to 75% of that needed for full-height

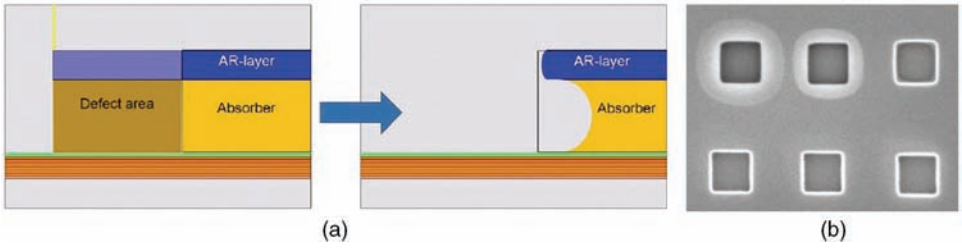

Figure 7.35 (a) Basically all EUV absorber materials show parasitic degradation if etched with established etch chemistry for a 193-nm photomask. (b) SEM image on the top left corner shows undercut. On the lower part, the same experiment was repeated with the new etch chemistry, and no absorber degradation could be observed (reprinted from Ref. 120 with permission from AIP Publishing).

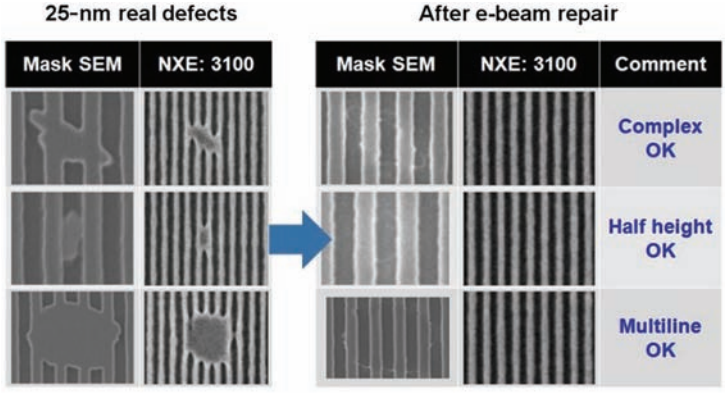

Figure 7.36 Example repair results for 25-nm natural opaque absorber defects on a multinode EUV reticle. MeRiT® SEM top views of the defects and SEM views of NXE: 3100 wafer prints from the defect areas. The mask patterns and wafer prints on the right demonstrate successful repair (reprinted from Ref. 122).

Downloaded From: https://www.spiedigitallibrary.org/ebooks/ on 09 Mar 2022
Terms of Use: https://www.spiedigitallibrary.org/terms-of-use

defects—reflected the reduced absorber thickness. All single-space defects were successfully repaired, with no measurable CD variation remaining on the printed image.[120]

The AFM-technology-based technique of nanomachining has been well proven in the area of photomask repair.[127] In nanomachining repair, the hardness of the mask material is the important factor to consider because tip wear reduces repair accuracy. Since the EUV absorber layer is much harder than the opaque layer of the optical mask, the tip wears out much faster in Ta-based EUV mask repair than in Cr- or MoSi-based optical mask repair, which results in a large tip deflection.[121] A nanomachining repair tool from RAVE LLC was applied for EUV mask repair, and the sidewall angle and tip lifetime were improved, as shown in Fig. 7.37.[121,127,128] The z control of the currently available nanomachining tool is ±3 nm, and the next generation of the tool has been developed with a target of ±0.5 nm.[121]

For clear defects, e-beam-induced deposition is performed. The upper left picture in Fig. 7.38 shows a SEM image of an absorber defect. This defect appears to be not very critical, but with AFM (upper middle picture) it can be seen that the absorber is thinned. The lower left picture is a SEM image of the area as printed on the wafer. From this image it can be seen that the defect is printed during the exposure process possibly because the absorber material is too thin to sufficiently absorb the EUV light. This defect is repaired using an e-beam deposition process (upper right image). After repair, the corresponding wafer print shows that this defect is no longer printable to the wafer. Again, no negative interference of the repair process can be observed in the area surrounding the repaired area.[116]

7.6.6 Next-generation repair

In the case of an e-beam repair system, the primary spot size is typically on the order of 1 nm and does not limit the size of the obtained repairs. However, if the beam energy is considerably reduced, the spot size increases due to chromatic aberrations, requiring design modifications of the electron optical system. Depending on their energy and the depth at which these electrons are created, they can reach the surface at a certain distance from the primary impact. If a precursor molecule is adsorbed at this emission site, a chemical reaction can be induced. When focused electrons are used, backscattered primary electrons (BSEs) also contribute to the induced reactions. The radius around the focal spot from which secondary and backscattered electrons are emitted can be reduced by decreasing the electron energy. A simulation of the trajectories of the scattered primary electrons is shown in Fig. 7.39. For a 1000-eV beam, the beam radius of the area where backscattered electrons are emitted is around 18 nm. This radius decreases to 7 nm for a 500-eV beam and decreases to 2 nm for a 200-eV beam.[129]

Downloaded From: https://www.spiedigitallibrary.org/ebooks/ on 09 Mar 2022
Terms of Use: https://www.spiedigitallibrary.org/terms-of-use

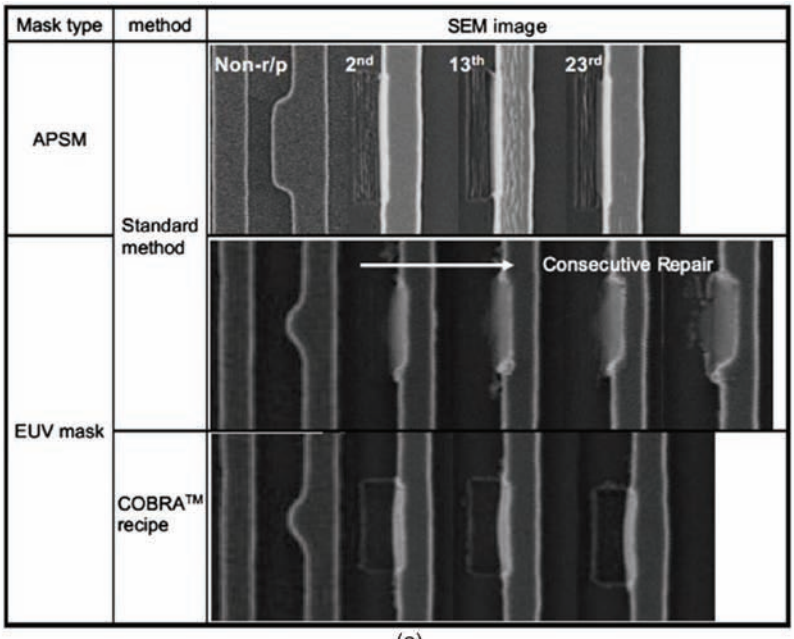

(a)

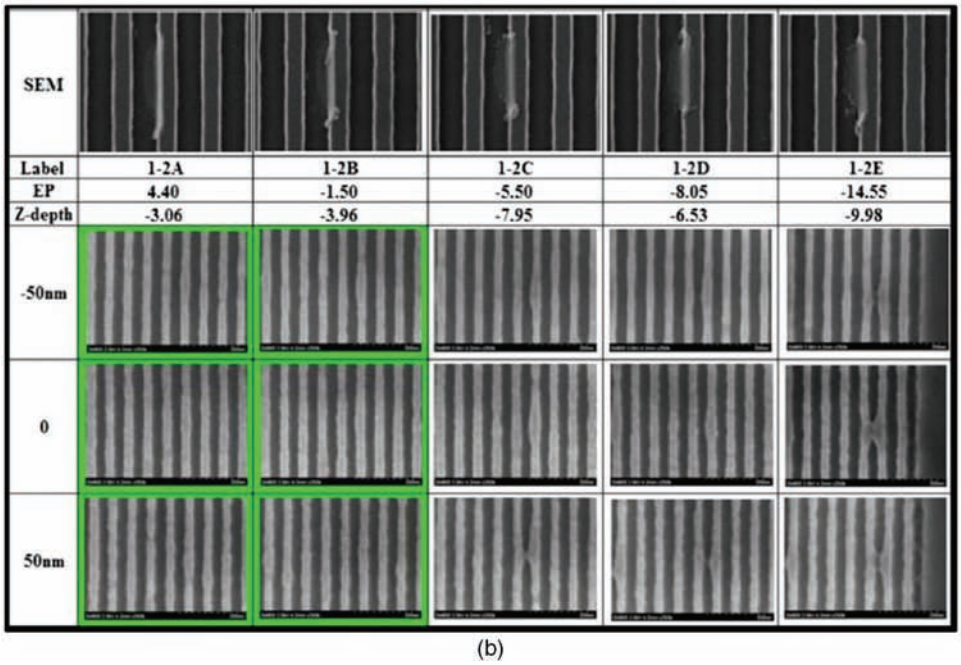

(b)

Figure 7.37 (a) SEM image profiles using various mask types and repair methods. (b) SEM image and EUV exposure results of repair points with a target *z* depth of –5 nm for a 2× extension defect (reprinted from Ref. 121).

Downloaded From: https://www.spiedigitallibrary.org/ebooks/ on 09 Mar 2022
Terms of Use: https://www.spiedigitallibrary.org/terms-of-use

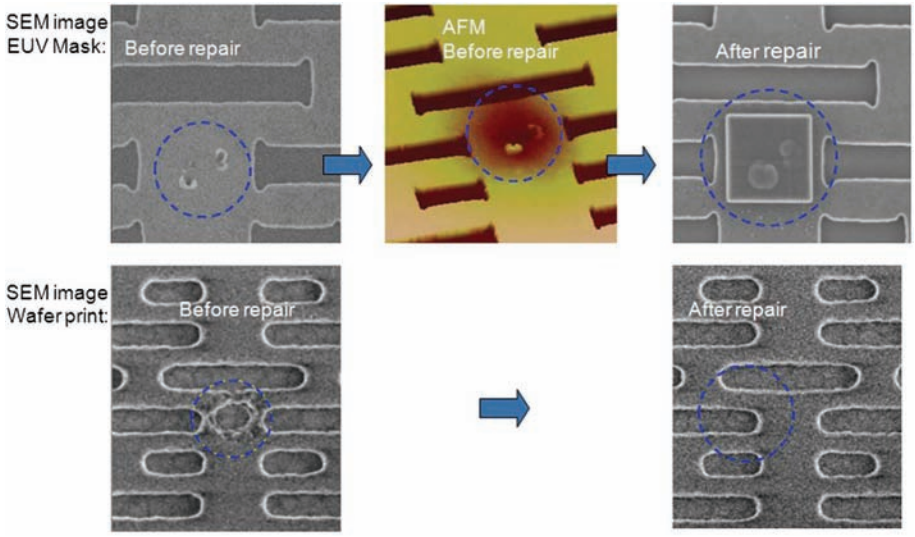

Figure 7.38 Example of e-beam deposition repair. Where the defect is almost invisible in SEM, AFM shows that the absorber is too thin, a fact that is confirmed in the wafer print. After deposition, the defect is no longer transferred to the wafer (reprinted from Ref. 120 with permission from AIP Publishing).

Using a current, commercial e-beam repair tool with 1-keV acceleration voltage, the minimum repairable size is ~25–30 nm. However, as shown in Fig. 7.40(a), a 10-nm line can be achieved, and a 10 nm × 500 nm thin defect was successfully repaired by applying a low-energy e-beam-based repair process.[130]

Another next-generation repair technology is a modified FIB repair. Conventional FIB uses gallium ions (Ga^+) generated by a liquid metal ion source (LMIS), but the modified FIB repair uses hydrogen ions (H_2^+) generated by a gas field ion source (GFIS). The minimum reaction area of H_2^+ FIB is theoretically much smaller than that of e-beam repair, as shown in Fig. 7.41.[131]

Fig. 7.42 shows a typical structure of a GFIS. The GFIS emits ions through field ionization process at the apex of the sharpened needle which is refrigerated to very low temperature, for example about 40 K. The beam diameter in FIB is generally expressed by the equation in Fig. 7.42. Since ions of a GFIS are generated in a field of a few atoms, the source size R_s of the GFIS is much smaller than that of a LMIS. Since gas molecules are ionized in an electric field of a particular intensity, the energy spread ΔE of the GFIS is much smaller than that of the LMIS. Thus, the beam diameter D of a GFIS is much smaller than that of a LMIS.[131]

A He^+ scan with high acceleration voltage (30 keV) causes the ML shrinkage on the TEM image (Fig. 7.43). However, a H_2^+ scan with the

Downloaded From: https://www.spiedigitallibrary.org/ebooks/ on 09 Mar 2022
Terms of Use: https://www.spiedigitallibrary.org/terms-of-use

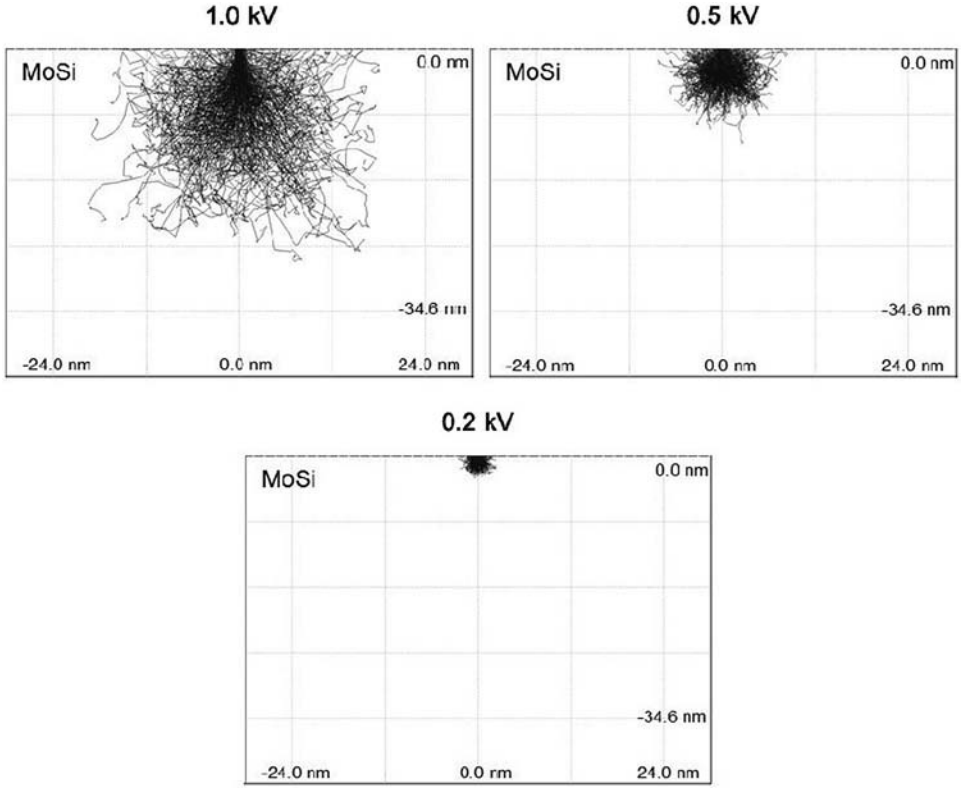

Figure 7.39 Comparison of electron/solid interaction volumes at different primary beam energies as simulated by Monte Carlo calculations (software: CASINO). The solid is a MoSi absorber material, and the beam radius is set to 1 nm (reprinted from Ref. 129).

equivalent acceleration voltage (25 keV) causes neither an EUV reflection peak shift nor a reflectivity loss.[131] The minimum etching width using a N_2 GFIS is 8.9 nm, as shown in Fig. 7.44. The sidewall of the groove is almost perpendicular. However, the beam stability of the GFIS needs to be further improved.[132] In addition, more investigation is required regarding the EUV mask durability of implanted H_2 ions under accumulated exposure.

7.6.7 Aerial image metrology

An aerial imaging system is used in the mask manufacturing flow as a printability verification tool. The basic structure is the same as a microscope, and it emulates the same wavelength, NA, and σ found on the exposure tool to predict the defect printability on the wafer. The main difference between the aerial imaging system and the exposure tool is the magnification of the mask pattern on a CCD or wafer. While this can lead to a difference in the vector effect in the imaging of the mask pattern, very little effect is expected in an optical system of 0.33 NA.[133]

Downloaded From: https://www.spiedigitallibrary.org/ebooks/ on 09 Mar 2022
Terms of Use: https://www.spiedigitallibrary.org/terms-of-use

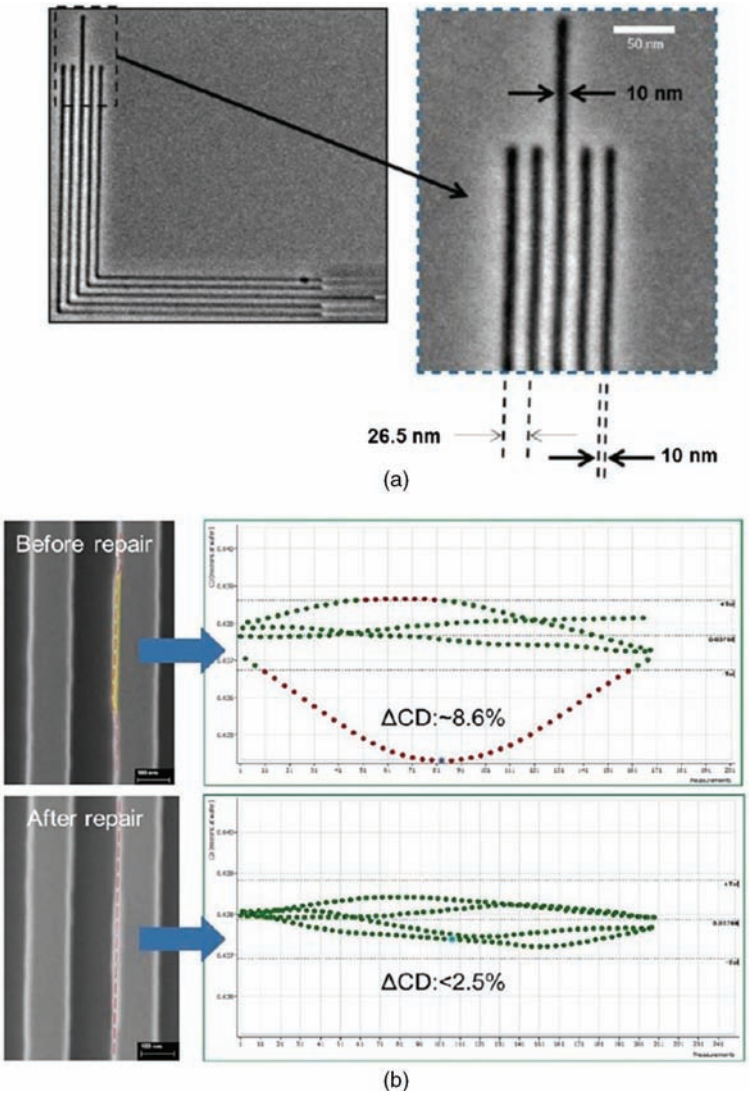

Figure 7.40 (a) A dense line/space pattern etched into quartz material by e-beam-induced processing produces an etching resolution of 10 nm. (b) Example of complicated 10 nm × 500 nm defect on the mask. Upper left: SEM image before repair. Upper right: AIMS measurement predicting ΔCD of –8.6%. Lower left: Post-repair SEM image. Lower right: The same AIMS measurement is performed, and the measured ΔCD is below 2.5%, indicating a successful repair (reprinted from Ref. 130).

There are two types of imaging systems: full-field systems and scanning systems. Schematic diagrams of each imaging system type are shown in Fig. 7.45. Carl Zeiss SMT GmbH has been developing a full-field-type aerial image measurement system (AIMS).[134] AIMS consists of an incoherent EUV light from a DPP source, three illumination mirrors, and three mirrors for

Downloaded From: https://www.spiedigitallibrary.org/ebooks/ on 09 Mar 2022
Terms of Use: https://www.spiedigitallibrary.org/terms-of-use

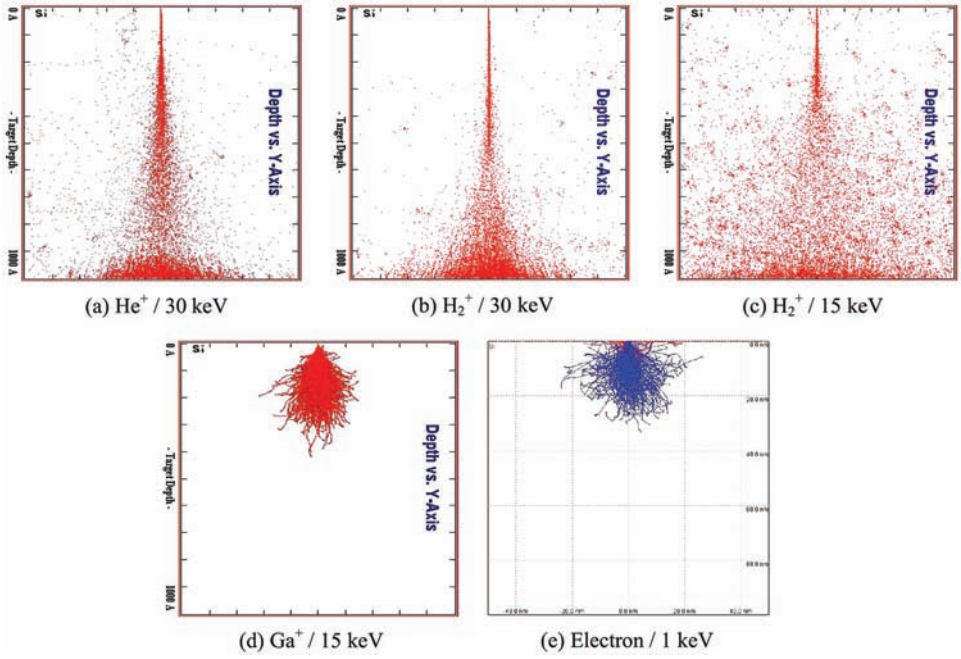

Figure 7.41 Trajectories of ions and electrons in the case where the ions and electrons are implanted into Si bulk (reprinted from Ref. 131).

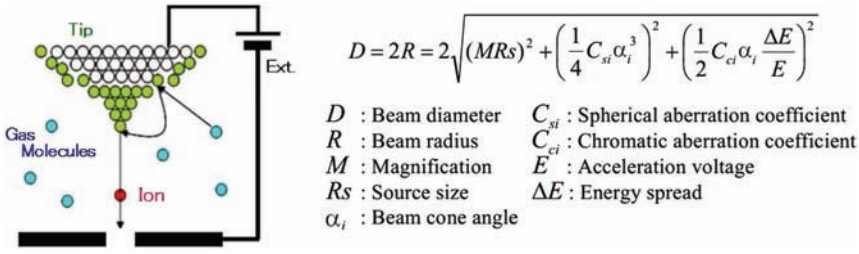

Figure 7.42 Typical structure of a GFIS and the FIB beam diameter equation (reprinted from Ref. 131).

imaging the mask pattern on the CCD. On the other hand, Samsung has developed a scanning EUV reflective microscope (SERM) in order to reduce the system development time and cost.[135] A simple scanning system using a coherent source and the diffractive optics of a zone plate lens was applied. Aerial images obtained by these two methods are theoretically equivalent.[136]

An aerial image from the SERM system at Samsung is shown in Fig. 7.46(b),[137] where the phase defect printability on the wafer is well reproduced. A diffraction-limited spot in the scanning system was formed by focusing the coherent EUV source generated by high-order harmonic generation, using a zone plate lens designed and fabricated by CXRO.[137] This tool was designed

Downloaded From: https://www.spiedigitallibrary.org/ebooks/ on 09 Mar 2022
Terms of Use: https://www.spiedigitallibrary.org/terms-of-use

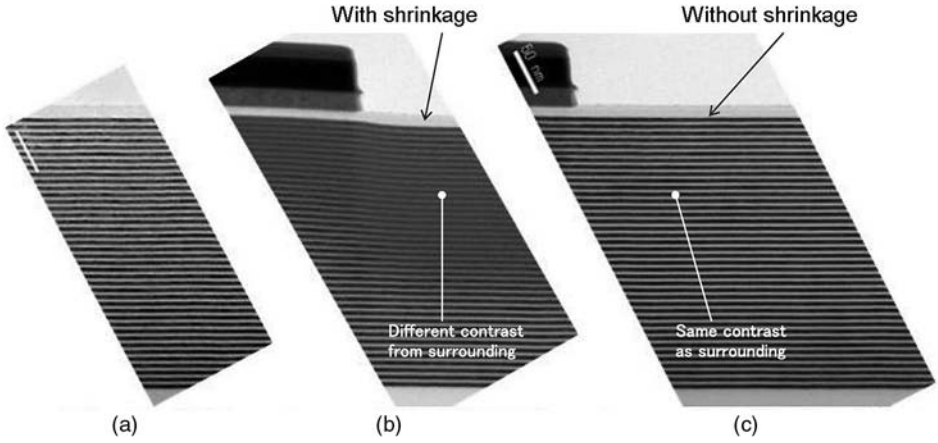

Figure 7.43 TEM cross-sections of EUVL masks after ion implantation: (a) He^+/30 keV/2×10^{15} ions/cm^2; (b) He^+/30 keV/2×10^{16} ions/cm^2; (c) H_2^+/30 keV/2×10^{16} ions/cm^2 (reprinted from Ref. 131).

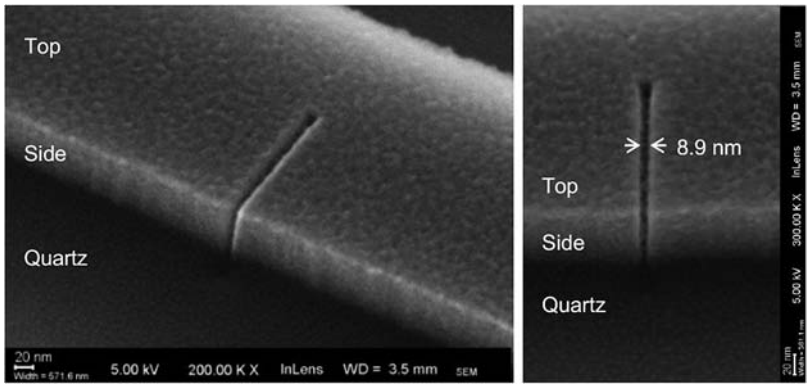

Figure 7.44 SEM images of a MoSi film after one-line etching with the GFIS system (N_2^+ beam, acceleration voltage = 25 kV, probe current = 0.1 pA) (reprinted from Ref. 132).

in 2012 to be used for reviewing defect printability at the 22-nm HP node and can now be upgraded to use with a high-NA system, which is possible by simply changing the zone plate and improving the EUV source power. Aerial images from AIMS are shown in Fig. 7.47. The phase defect printability on the wafer was confirmed by an aerial image with a sub-100-nm-size pattern.[138]

7.7 Mask Contamination Protection and Cleaning

7.7.1 Pellicle

Contamination during the lithography process is one of the critical issues to be solved for the application of EUVL technology to HVM.[139] A pellicle is a physical particle shield and protective film mounted above the patterned surface

Downloaded From: https://www.spiedigitallibrary.org/ebooks/ on 09 Mar 2022
Terms of Use: https://www.spiedigitallibrary.org/terms-of-use

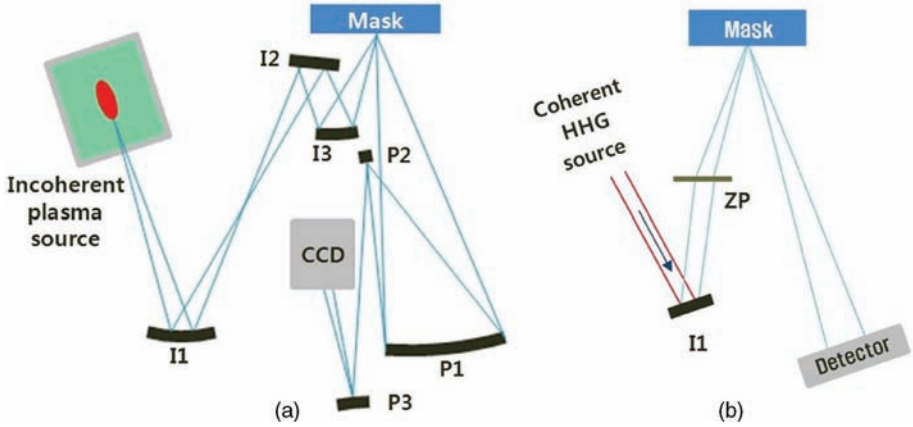

Figure 7.45 (a) Schematic diagram of the optical layout of the full-field imaging system with a plasma source and mirror optics; I1, I2, and I3 are illumination optics, and P1, P2, and P3 are imaging optics. (b) Scanning-type imaging system using a coherent source and a zone plate (ZP) lens; I1 is a bending mirror, and HHG is high-order harmonic generation. [Part (a) adapted from Ref. 135 and part (b) adapted from Ref. 137 with permission from OSA.]

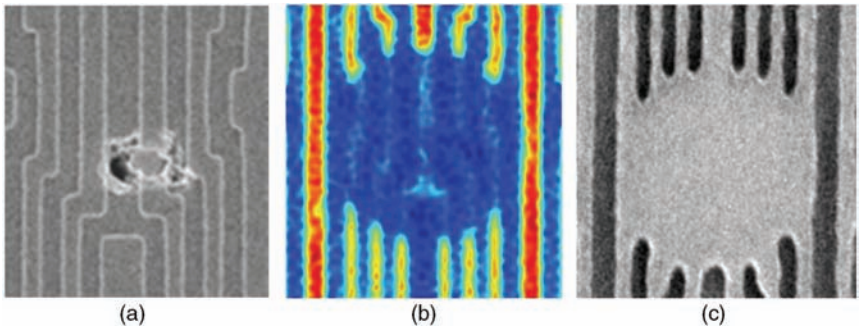

Figure 7.46 (a) SEM image of an EUV mask with a defect. (b) Aerial image taken with scanning EUV reflective microscopy. (c) SEM image of a defect printed on a wafer (reprinted from Ref. 137 with permission from OSA).

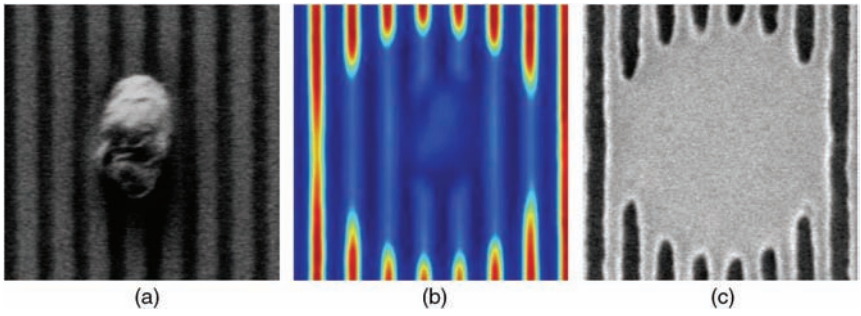

Figure 7.47 (a) SEM image of an EUV mask with a defect. (b) Aerial image taken with the AIMS. (c) SEM image of a defect printed on a wafer (reprinted from Ref. 134).

Downloaded From: https://www.spiedigitallibrary.org/ebooks/ on 09 Mar 2022
Terms of Use: https://www.spiedigitallibrary.org/terms-of-use

of the mask.[140] The critical size of printable particle is much larger on the pellicle above the imaging surface compared to that on the mask surface. Figure 7.48 shows the path of light diffracted by contamination without a pellicle and with a pellicle. It should be noted that the double pass of EUV light through the EUV pellicle is dictated by the reflective mask. If the EUV pellicle has 90% transmittance, the exposure dose will be reduced to 81% of incident. This means a productivity loss of ~20%, and this lost energy will heat the pellicle membrane, potentially inducing thermo-mechanical challenges.

Because it is difficult to select a proper material and design for the EUV pellicle as a result of the high extinction coefficient of materials at EUV wavelengths, development of the EUV pellicle has been challenging. However, the possibility of an EUV pellicle was demonstrated by fabricating Si-based membranes with a thickness on the order of 10 nm.[141,142] According to the published EUVL pellicle requirements, a top priority requirement for the EUV pellicle is to meet more than 90% single-pass transmittance, as shown in Table 7.2.[143]

Silicon, with a low extinction coefficient for the EUV wavelength (as can be seen in Fig. 7.49), was suggested for the main component of the EUV pellicle membrane to secure more than 90% single-pass transmittance.[144] However, the EUV pellicle membrane must be thinner than several tens of nanometers in order to achieve high EUV transmittance, and this structure results in thermo-mechanical instability.[145] In the early stages of pellicle development, a mesh-support-type pellicle was suggested to supplement the mechanical property of the pellicle membrane.[146] Considering better mechanical property enhancement effects and a larger open space for high EUV transmittance, a honeycomb-type mesh structure was chosen, as shown in Fig. 7.50. However, a transmittance nonuniformity problem due to the mesh structure was observed.[147] Also, recent research shows that the mesh structure can lead to mechanical and thermal nonuniformity, inducing a short lifetime for the EUV pellicle.[148] Due to these

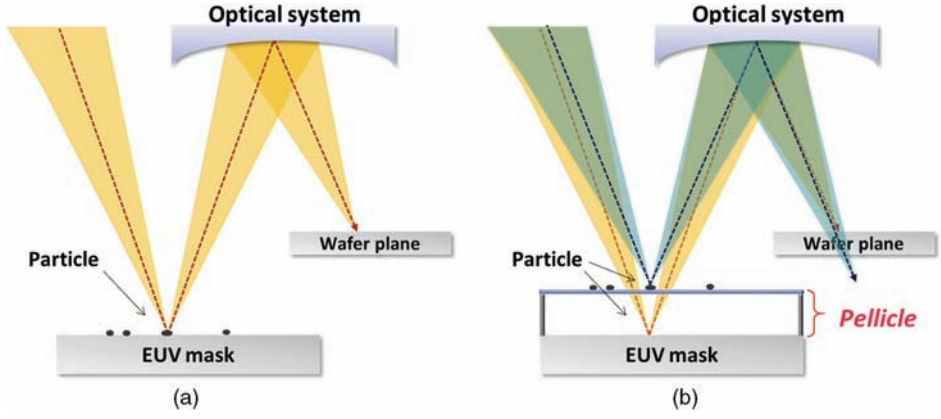

Figure 7.48 Schematic diagram of the EUV light path (a) without a pellicle and (b) with a pellicle.

Downloaded From: https://www.spiedigitallibrary.org/ebooks/ on 09 Mar 2022
Terms of Use: https://www.spiedigitallibrary.org/terms-of-use

Table 7.2 Preliminary EUV pellicle guidelines and requirements for HVM (data from Ref. 143).

	Item	Requirements and guidelines
Pellicle material requirements	Pellicle film EUV transmission	90% single pass (81% double pass)
	EUV transmission spatial nonuniformity	<0.2%
	EUV transmission angular nonuniformity	<300-mrad maximum local pellicle angle
	EUV intensity in scanning slit at pellicle position	5 W/cm^2 (250-W EUV source equivalent)
	Lifetime	~315 hrs (production hours in an EUV + H_2 environment)
Pellicle + frame requirement	Standoff distance	2 ± 0.5 mm
	Maximum acceleration	100 m/s^2
	Maximum ambient pressure rate of change	<3.5 mbar/s (peak during pump down in the load lock)
	Reticle reserved area for pellicle assembly (centered on substrate)	110.7 mm × 144.1 mm : inner 118.0 mm × 150.7 mm : outer
Pellicle impact on imaging performance: <0.1 nm CDU impact on wafer		

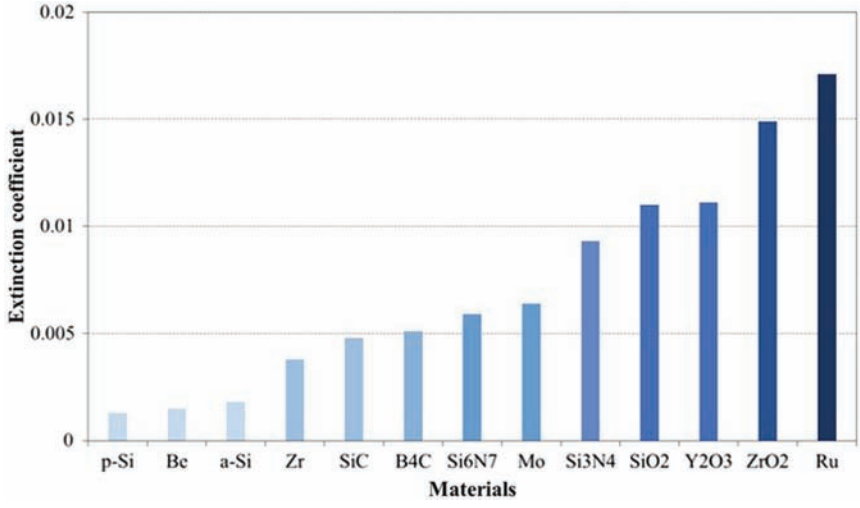

Figure 7.49 Extinction coefficients of various materials at the 13.5-nm wavelength.

technical challenges, research on the mesh-supported type of pellicle was discontinued.

Currently, most of the research focuses on the freestanding pellicle, a membrane without a support structure.[149] Figure 7.51 shows the latest prototype of the freestanding EUV pellicle design, which consists of a polysilicon membrane capped with silicon nitride.[149] Although this prototype pellicle meets transmittance requirements, its mechanical and thermal stabilities, which are directly related to the lifetime, are insufficient for HVM power levels.[150] A maximum temperature for 40-nm poly-Si (emissivity ~0.02) is expected to reach as high as ~944 °C for EUV scanners operating with a 250-W EUV

Downloaded From: https://www.spiedigitallibrary.org/ebooks/ on 09 Mar 2022
Terms of Use: https://www.spiedigitallibrary.org/terms-of-use

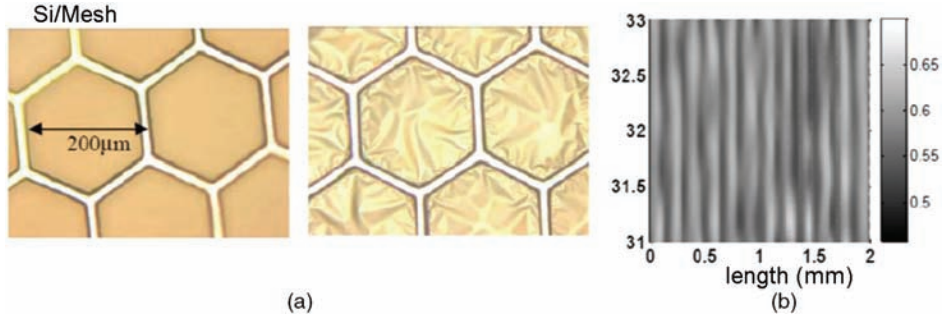

Figure 7.50 (a) Image of the honeycomb mesh structure and (b) the resulting interference pattern caused by the mesh structure (reprinted from Ref. 147).

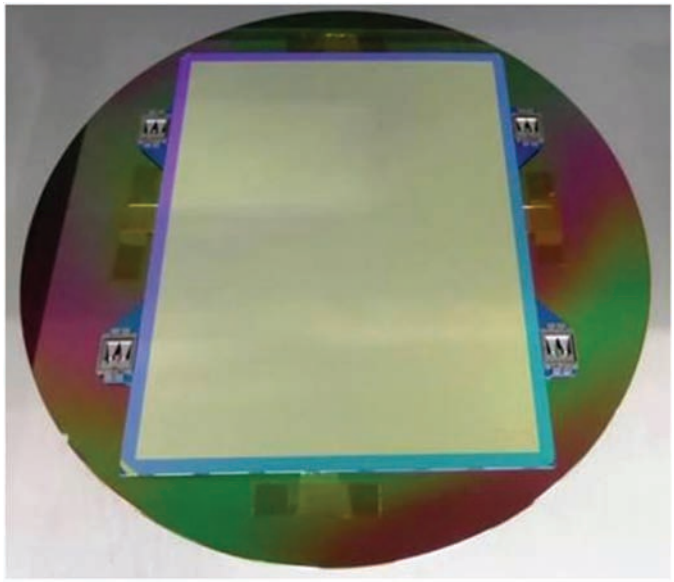

Figure 7.51 Photograph of the recently developed prototype EUV pellicle (polysilicon membrane capped with silicon nitride) (reprinted from Ref. 149).

source, as shown in Fig. 7.52.[151] It should be noted that the only cooling mechanism for the EUV pellicle during exposure is radiation because of the thin-film structure (negligible conduction) in a high-vacuum environment (negligible convection). The amount of radiation is determined by emissivity, which is defined as the ratio of the energy radiated by a body to the energy radiated by a blackbody; most materials have emissivities of less than 1. The surface radiation efficiency depends on many factors, including temperature, surface composition and thickness, surface roughness, and wavelength of the radiation. Because of these many contributing factors, a large range of emissivity values is reported in the literature.

Downloaded From: https://www.spiedigitallibrary.org/ebooks/ on 09 Mar 2022
Terms of Use: https://www.spiedigitallibrary.org/terms-of-use

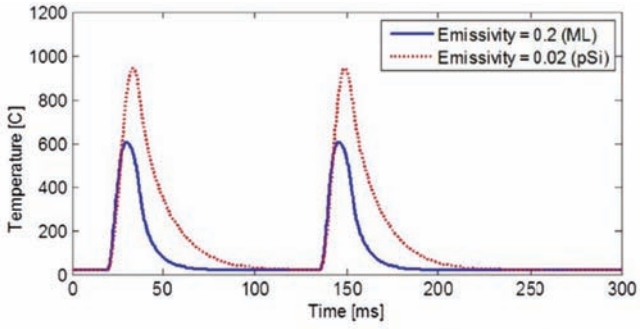

		ML	pSi
EUV transmission	%	90	90
Thickness	nm	25	40
Absorbed power	W/cm^2	~0.65	~0.56
Emissivity	-	~0.2	~0.02
Max temperature	°C	608	944

Figure 7.52 Temperature profiles of EUV pellicles assuming NXE parameters (250-W source) at a dose of 15 mJ/cm^2. The dotted line in the graph represents the pSi film (emissivity ~0.02), and the solid line represents the high-emissivity (~0.2) ML (Si/Mo/Nb) film (reprinted from Ref. 151).

Improving the mechanical properties by inserting carbon-based materials and enhancing thermal properties by capping with higher-thermal-emissivity materials are two of the more recent approaches.[150–154] Coating with a highly emissive thin film (e.g., Ru or B_4C) on the pellicle side has been reported to improve the total emissivity and thus decrease the peak temperature during the exposure process (Fig. 7.53).[150,155] Carbon nanotube (CNT) is one of the film candidates due to the low extinction coefficient value of carbon as well as its low density, which can provide very high EUV transmittance. A pellicle with metal- (Ru or Mo) capped CNT has been reported to have improved mechanical strength with high and uniform EUV transmittance (Fig. 7.54).[156,157] Another option is graphene, which is also an allotrope of carbon in the form of a 2D, atomic-scale, honeycomb lattice in which one atom forms each vertex. Perfect graphene is known to be about 100 times stronger than the strongest steel.[158] It is thermally and electrically conductive, and is highly transparent to EUV.[145] However, graphene is not compatible with the silicon process (it does not grow on Si), and it is very difficult to obtain a graphene layer without defects and to scale up to full-pellicle sizes.[159,160]

ASML has proposed a pellicle-mounting scheme that adopts a removable design, where the pellicle assembly can be removed for intermediate reticle inspection and then replaced without particle generation (Fig. 7.55) After the patterned reticle is finished, the studs that will later accommodate the

Downloaded From: https://www.spiedigitallibrary.org/ebooks/ on 09 Mar 2022
Terms of Use: https://www.spiedigitallibrary.org/terms-of-use

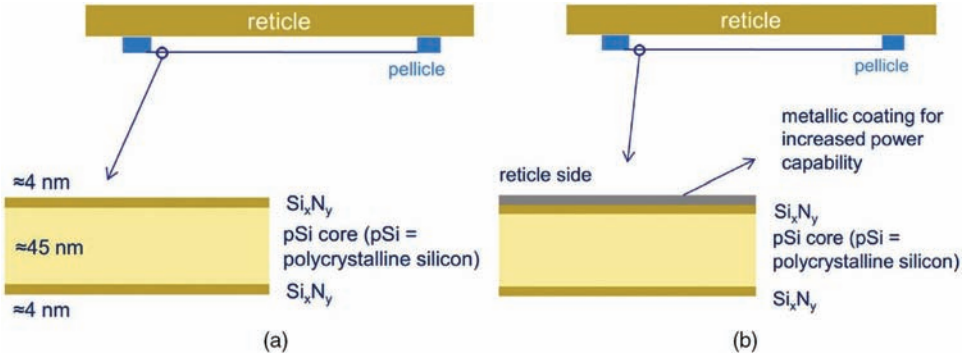

Figure 7.53 (a) A pSi core membrane capped with silicon nitride. (b) A thin metallic coating is applied to improve emissivity (reprinted from Ref. 161).

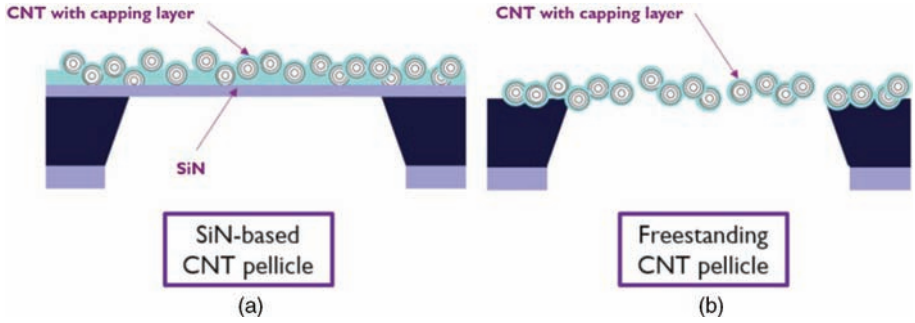

Figure 7.54 CNT-based pellicles: (a) CNT on a SiN membrane and (b) a freestanding CNT pellicle (reprinted from Ref. 156).

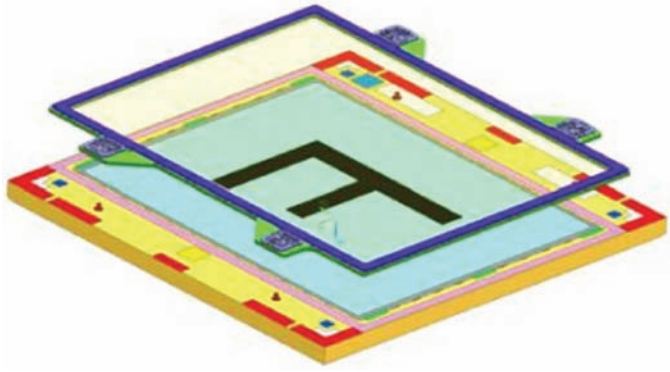

Figure 7.55 NXE pellicle-mounting structure (reprinted from Ref. 161).

pellicle are installed. The studs need to be glued onto the substrate of the pellicle, for which a zone of the mask blank ML needs to be etched away. With a specially designed tool, the pellicle can be mounted and demounted from a reticle with studs.[155]

Downloaded From: https://www.spiedigitallibrary.org/ebooks/ on 09 Mar 2022
Terms of Use: https://www.spiedigitallibrary.org/terms-of-use

7.7.2 Mask cleaning

To provide clear pattern transfer during exposure, it is important to maintain the mask surface free from contamination. For this purpose, a cleaning process is utilized during mask fabrication and between lithography process steps. The cleaning process must remove particles from the surface yet avoid damaging any of the films. If an EUV pellicle is not available, the EUV mask will need to be cleaned more frequently than a pelliclized mask to remove residue and particles. However, mask damage such as pinhole generation, reflectivity degradation, and mask CD changes should be avoided during the cleaning process.[162] Megasonic cleaning can be used to remove particles from the pattern mask without cleaning-induced pattern damage. However, particle removal efficiency decreases when patterns become smaller, especially in contact holes.[16] If carbon contamination is to be removed by a cleaning process, oxidizing chemistries are used, but this will oxidize the Ru capping layer.

The following alternative cleaning technologies have been suggested for EUV mask cleaning: UV cleaning, supersonic hydrocleaning (SHC), plasma-assisted cleaning by electrostatics (PACE), and laser shock-wave cleaning (LSC).

UV cleaning of carbon contamination has been demonstrated by irradiation with a 172-nm excimer lamp (Fig. 7.56).[163] A high density of active oxygen was generated directly from molecular oxygen by 172-nm light irradiation (where the absorption coefficient of molecular oxygen is very high), which enabled efficient mask cleaning. The contamination removal rate was 2 nm/min in the low-pressure (2×10^{-3} Pa) O_2 environment.

Figure 7.57 shows the concept of SHC, where a supersonic flow is created by the ejection of a carrier gas from a nozzle under high pressure. A cleaning liquid is mixed with the carrier gas in the nozzle, and the droplets ejected from the nozzle strike the substrate to physically remove particles. Since the organic contaminants on the mask surface reduce the particle removal efficiency, they must be removed by UV irradiation prior to particle removal by SHC.[164,165]

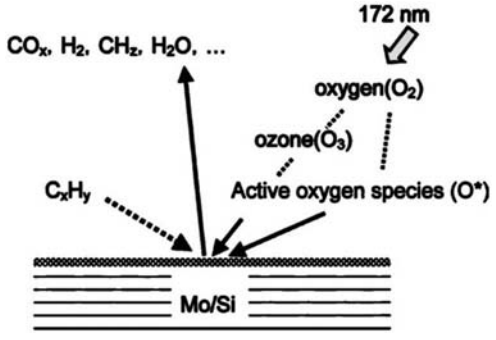

Figure 7.56 Mechanism for removing contamination by UV irradiation (reprinted from Ref. 163 with permission from AIP Publishing).

Downloaded From: https://www.spiedigitallibrary.org/ebooks/ on 09 Mar 2022
Terms of Use: https://www.spiedigitallibrary.org/terms-of-use

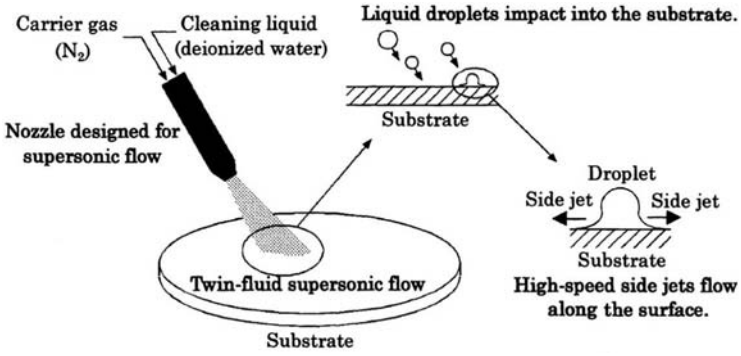

Figure 7.57 Schematic illustration of the supersonic hydrocleaning (SHC) technique (reprinted from Ref. 164).

PACE technology utilizes the potential drop in a plasma sheath electric field and the charge imbalance between the particle and the mask to propel the particles off the surface.[166] By applying a positive bias to the substrate and using weak local plasma to charge the particles, the contamination is removed from the surface. As the particle size decreases, the amount of time needed to charge the particle becomes longer, leading to a longer cleaning process.

LSC technology, which uses a dry laser shock wave generated by a Nd:YAG laser, has been studied.[167] To avoid any possible surface damage, the UV energy and the gap distance between the laser shock-wave focal point and the surface need to be optimized.[95] The organic particles cannot be effectively removed from the surface by LSC, but the particle removal efficiency can be significantly improved by combining this technology with UV cleaning. Enhanced particle removal by UV irradiation may be attributed to photothermal and photochemical effects, by which the former effect explosively evaporates any remaining water molecules from the surface, and the latter effect breaks any possible chemical bonds between the surface and particles. A more than 95% removal efficiency of 63-nm fluorescent polystyrene latex (PSL) particles was achieved by UV irradiation followed by a laser shock-wave exposure. The biggest advantage of this technique is that targeted local cleaning is possible when combined with defect inspection tools.

7.8 Advanced Mask Structure for Better Imaging

7.8.1 Shadowing effect

The mask shadowing effect is a problem caused by the combination of oblique illumination and mask topography. Due to this effect, a printed CD bias and position shift occur.[168] The shadowing effect is schematically shown in Fig. 7.58. Compared to the designed mask CD, the space features will print

Downloaded From: https://www.spiedigitallibrary.org/ebooks/ on 09 Mar 2022
Terms of Use: https://www.spiedigitallibrary.org/terms-of-use

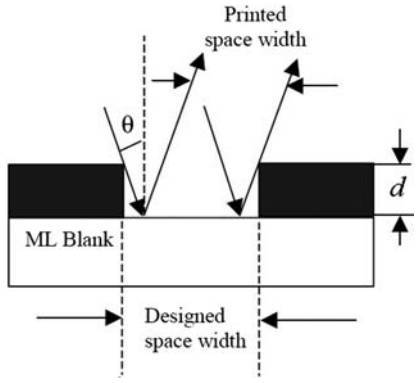

Figure 7.58 Geometrical optics illustration of the EUV mask shadowing effect (reprinted from Ref. 70).

smaller and the line features will print larger. This geometrical effect is amplified with increasing thickness of the absorber stack according to

$$\text{Space CD (printed)} = \text{CD (designed)} - (2d \times \tan\theta) \times M, \qquad (7.7)$$

and

$$\text{Line CD (printed)} = \text{CD (designed)} + (2d \times \tan\theta) \times M, \qquad (7.8)$$

where CD (printed) is measured at the wafer plane, M is the EUV scanner reduction factor, and θ is the light incident angle to the mask.

When the effect of near-field diffraction is considered, the electrical field in the dark region near the absorber edge is no longer completely dark.[169] The light extends to the dark region at the edge and gradually attains zero intensity at a distance extended to the inside of the absorber (Fig. 7.59). The electrical field that is diffracted at the mask edge will also interfere with the light reflected back from the ML. As a result, the light diffraction depends on both the geometrical structure and the optical properties (index of refraction) of the material.

According to the simulation, the use of TaN and Cr, which have a larger Δn (the difference between the real part of the refractive index and that of vacuum), results in a larger shadowing effect compared to other materials such as Al and germanium (Ge).[70] As the absorber thickness increases, the difference in CD for different materials decreases (Fig. 7.60). However, the additional effect of an ARC should be considered if adopted in the mask structure. Studies have been performed on reducing the shadowing effect by using thin absorber materials such as Ni, Pd, Pt, and Co, which have high extinction coefficients for the EUV wavelength.[74,170,171] It should be noted that the difference caused by the shadowing effect can be compensated via mask biasing but ultimately limits the minimum feature possible.[171,172] To

Downloaded From: https://www.spiedigitallibrary.org/ebooks/ on 09 Mar 2022
Terms of Use: https://www.spiedigitallibrary.org/terms-of-use

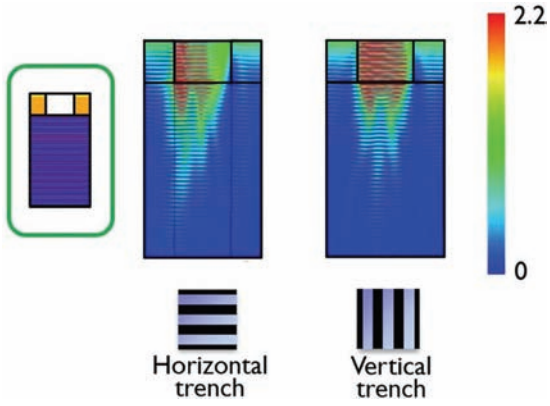

Figure 7.59 Simulation results of a near-field image in horizontal and vertical L/S patterns (reprinted from Ref. 169).

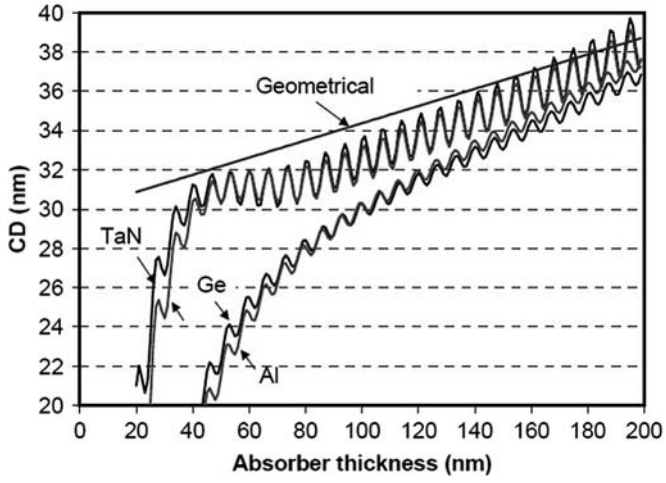

Figure 7.60 Printed CD as a function of absorber height based on geometrical optics calculations for a 4× reduction exposure system (reprinted from Ref. 70).

obtain the highest image contrast, the absorber thickness must be sufficient so that the leakage light is as low as possible.

7.8.2 Bossung curve assymetry and focus shift

When an EUV mask with a given topography is considered, the Bossung curve of a line at a large pitch is tilted and the best focus is shifted.[172,173] This best-focus shift is pitch dependent. From the periodic lines to the isolated lines, the best-focus shift increases as the pitch increases. Figure 7.61 shows plots of Bossung curves for dense and isolated 30-nm lines for a 100-nm-thick TaN absorber. A small best-focus shift exists, even for the periodic lines. The

Downloaded From: https://www.spiedigitallibrary.org/ebooks/ on 09 Mar 2022
Terms of Use: https://www.spiedigitallibrary.org/terms-of-use

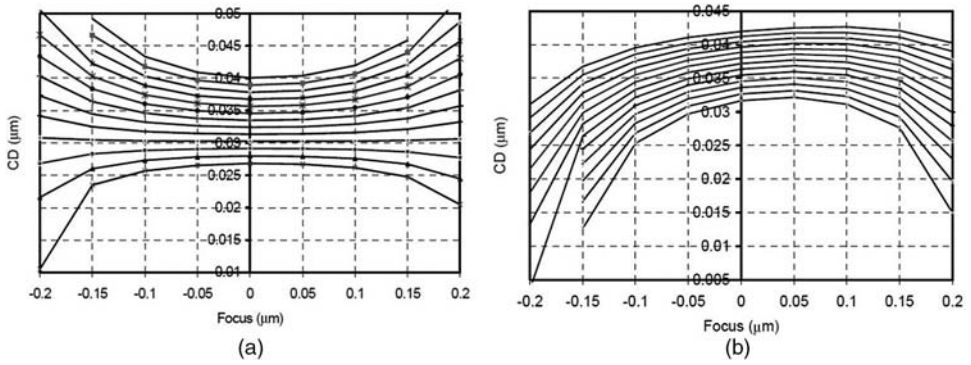

Figure 7.61 Bossung curves of (a) 30-nm dense lines and (b) 30-nm lines at a 200-nm pitch. The mask has a 100-nm TaN absorber with no buffer (reprinted from Ref. 70).

maximum best-focus-shift difference between dense and isolated lines for the TaN case is as large as 40 nm. When the best-focus shifts are different between different pitches, the scanner focus adjustment cannot compensate for the best-focus shift of all of the lines with different pitches. Since the total depth of focus (DOF) is only about 100 nm in EUVL, a 40-nm best-focus mismatch between the dense and isolated lines has a big impact on the total lithographic process window. Like the shadowing effect, this best-focus shift depends on the n and k values of the absorber material. But the thickness of the absorber material, as long as it allows sufficient EUV light absorption (residual reflectivity <1%), plays a relatively small role in the best-focus shift effect. If an additional layer is applied (e.g., a phase shift layer), the best-focus shift and the Bossung curve tilt effect will be modulated by the optical properties of this additional layer material. When a third layer with a relatively large Δn is used, the best-focus shift and the Bossung curve tilt effect will increase, regardless of the optical properties of the absorber material.[172]

7.8.3 Alternative mask structures

Alternative mask structures can alleviate the mask 3D effect and eventually extend the resolution limit of EUV lithography. Various kinds of advanced EUV masks have been proposed, including the phase shift concept shown in Fig. 7.62. Other types include an etched ML binary mask, an attenuated PSM (embedded or etched ML), an alternating PSM (substrate or ML etched), and a modified alternating PSM (double etched or with an absorber stack).[174–178] Most of the studies on these structures have been based on simulation, but some of the experimental results have revealed the possibility of practical implementation.

One such achievement is the etched ML binary mask. A low-reflectivity Mo/Si ML (20 pairs instead of 40 pairs) was locally etched to form dark trenches, and its optical properties were investigated. Horizontal–vertical

Downloaded From: https://www.spiedigitallibrary.org/ebooks/ on 09 Mar 2022
Terms of Use: https://www.spiedigitallibrary.org/terms-of-use

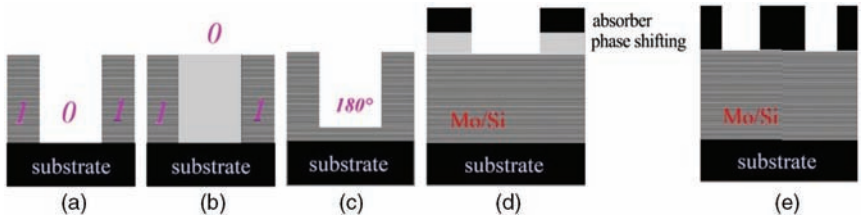

Figure 7.62 Advanced EUV masks: (a) etched ML binary mask, (b) refilled ML binary mask, (c) etched ML attenuated PSM, (d) embedded attenuated PSM, and (e) substrate-etched alternating PSM (reprinted from Ref. 177).

(H-V) CD bias and best-focus shift through the pitch were improved compared to the standard mask, but some optical properties were degraded (e.g., higher mask error enhancement factor). The most critical challenges of this structure are the manufacturability and cleanability. Also, the printability of the unattenuated PSM has been demonstrated using etched ML masks (etch depth ~100 nm, sidewall slope ~60 deg), and the phase shift edge on the mask was printed at 13.5 nm.[179] The results show an improved exposure and focus latitude with good agreement between the simulation and experiments compared to the binary masks; however, the reflectivity degradation (~2%) of the etched ML mask without a capping layer was pointed out as a problem. A more detailed practical methodology has been proposed based on the experimental results.[180] Direct measurement of the phase shift on a reflected wavefront at 13.5 nm was performed with a Fresnel bi-mirror interferometer using a phase shift sample based on the theoretical design. The measured phase shift was found to be close to the expected value. Based on previously presented research,[176] the etched ML mask generally shows larger DOF, higher contrast, no linewidth variation due to interference phenomenon, and reduced H-V bias and image placement error (IPE) due to the shadow effect.

7.8.4 Etched ML binary mask

In addition to the mask-patterning method that defines layout patterns in the absorber stack, it is possible to etch into the ML to leave the pattern trenches on the mask where the EUV light is either not reflected or less reflected such that the etched region appears dark. The remaining bilayers in the etched region contribute to attenuated reflectivity, and the depth of the etched trench contributes to the phase shift due to the round-trip optical path difference. The resultant reflectivity and phase shift can be designed to achieve different types of masks with different imaging functionalities. If all of the MLs are removed in the trench region, a much higher aerial image contrast of 99.96% can be obtained since only 0.09% of EUV light reflects off of the substrate surface in the etched trench.[176] The reflected near-field intensities show no edge streamer and fewer shadow effects at the edges compared with those

Downloaded From: https://www.spiedigitallibrary.org/ebooks/ on 09 Mar 2022
Terms of Use: https://www.spiedigitallibrary.org/terms-of-use

from the conventional mask with an absorber stack. The other difference is that photon attenuation (the dark region) is created at the bottom of the trench (lower in position) for an etched ML mask architecture, while it is created at the top of the ML stack (higher in position) for a conventional mask architecture with an absorber layer on top. As a result, the shadow effects are in opposite tones in these two cases of mask patterns. Figure 7.63 clearly shows less asymmetry and more similarity between the near fields reflected from the etched bilayer mask and that from a Kirchhoff mask

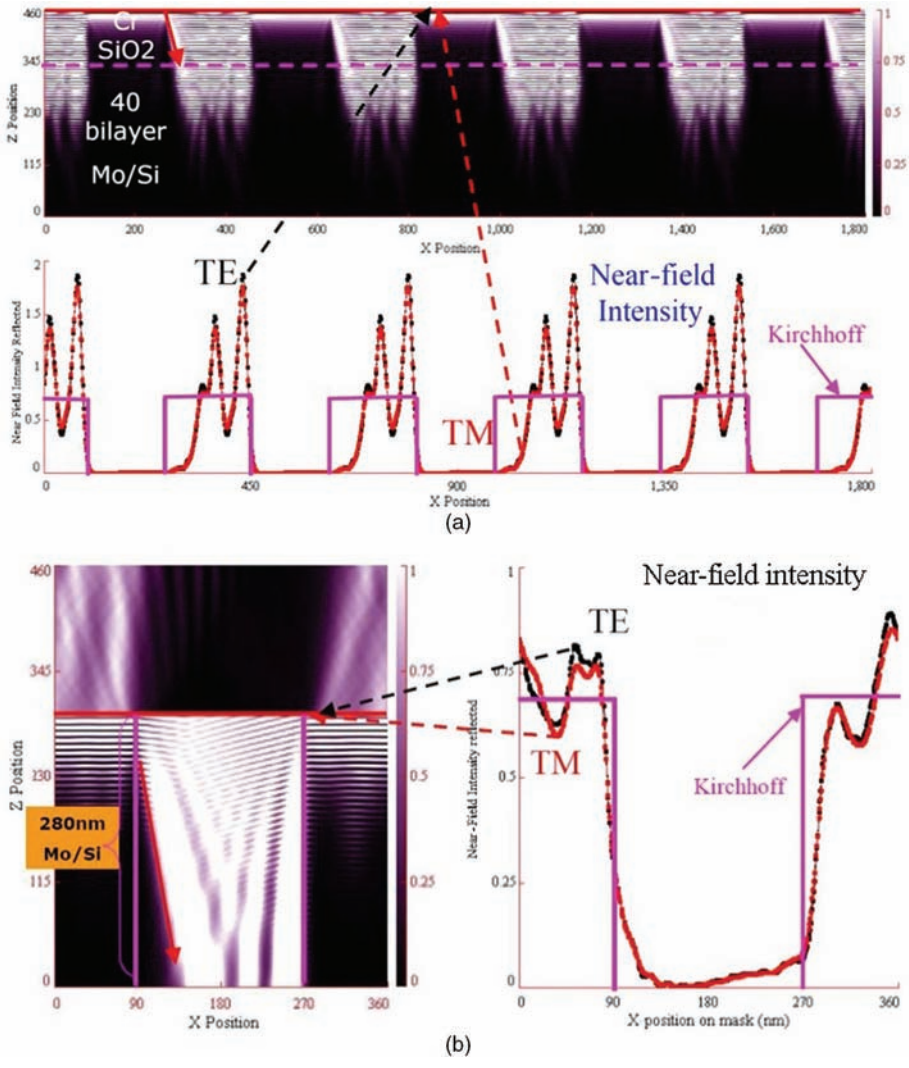

Figure 7.63 Near-field intensities reflected at the top with the oblique light incidence from the left for (a) a binary mask with absorber stacks and (b) an etched binary ML mask (reprinted from Ref. 176).

Downloaded From: https://www.spiedigitallibrary.org/ebooks/ on 09 Mar 2022
Terms of Use: https://www.spiedigitallibrary.org/terms-of-use

(thin mask model). Also, the DOF can be improved with an etched ML structure, especially with the bias-etched binary ML mask (Fig. 7.64). However, as the pitch decreases, mask cleaning of etched binary masks causes serious pattern collapse (Fig. 7.65).[181]

One suggested modification of the etched ML binary mask involves refilling the trench with a material having a high absorbing coefficient; 70-nm chrome is reported to be enough to provide good contrast (99.3%) and a small CD variation with the etching depth. The planar geometry of refilled masks prevents a large shadowing effect. Both refilled and etched near fields show much less

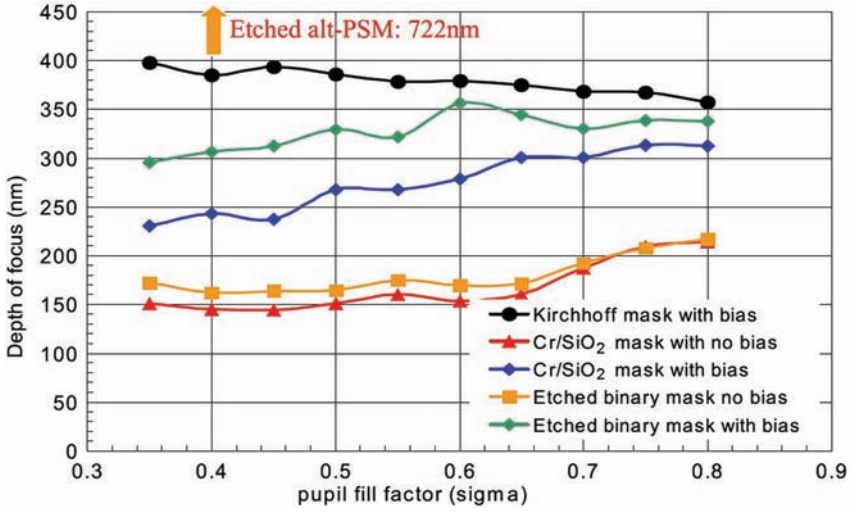

Figure 7.64 DOF for different mask-patterning schemes with and without mask CD bias (reprinted from Ref. 176).

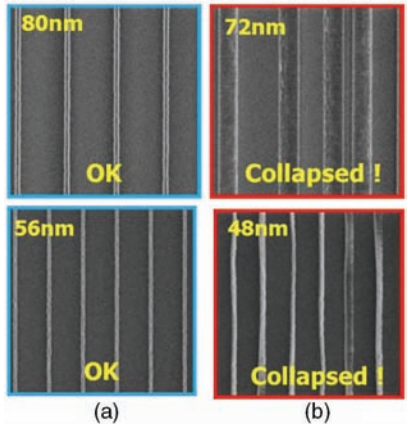

Figure 7.65 Top-view SEM images of the isolated line pattern of an etched binary mask after the wet cleaning process with (a) 40 pair of bilayers and (b) 20 pair of bilayers (reprinted from Ref. 181).

Downloaded From: https://www.spiedigitallibrary.org/ebooks/ on 09 Mar 2022
Terms of Use: https://www.spiedigitallibrary.org/terms-of-use

shadowing effect at the right edge (light incidence from the left) compared to the same in an absorber binary mask, so they will produce better images in terms of H-V bias and IPE (Fig. 7.66). IPE is defined as the maximum component deviation (X or Y) error of the array of centerline images relative to a defined reference grid after removal of the isotropic magnification error.

7.8.5 Attenuated phase shift mask

An attenuated PSM can be fabricated in two ways. One is by etching the ML to a defined depth without an absorber stack (etched ML attenuated PSM), and the other is by implementing a phase shifter on top, as in the PSM in optical masks (embedded attenuated PSM).

In the etched ML attenuated PSM, the remaining bilayers in the etched region contribute to attenuated reflectivity, and the depth of the etched trench contributes the phase shift with the round-trip optical path difference. If the ML stack is etched with only four bilayers remaining, the etched region has about a 6% attenuated field intensity. By removing a partial number of bilayers, a 180-deg phase shift can be obtained between the near field reflected from the etched region and that from the unetched region (Fig. 7.67).

This process can be implemented by precisely controlling the etch depth or by adopting an etch stop layer (ESL). An ESL allows good control of the etch process, but the material and thickness need to be chosen carefully so that it does not decrease the total reflectivity of the ML and yet provides good etch selectivity for processing (Fig. 7.68). Silicon dioxide is one of the ESL candidates due to its high etch selectivity (Mo/SiO_2 ~90 with $Cl_2/HBr/He/O_2$

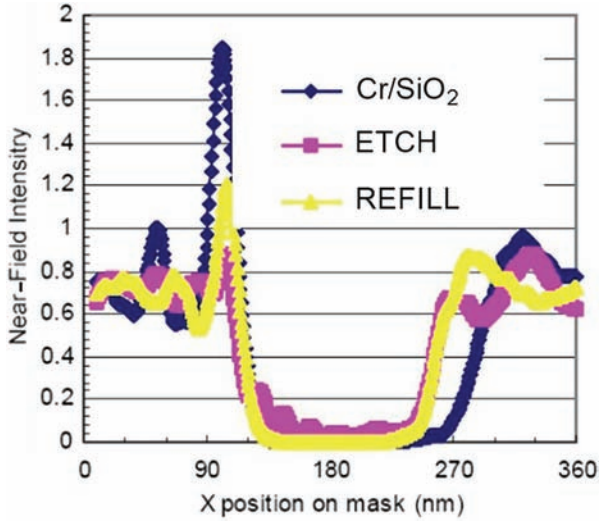

Figure 7.66 Comparison of the near-field intensities reflected at the top for a refilled ML binary mask to those of conventional and etched ML masks (reprinted from Ref. 177).

Downloaded From: https://www.spiedigitallibrary.org/ebooks/ on 09 Mar 2022
Terms of Use: https://www.spiedigitallibrary.org/terms-of-use

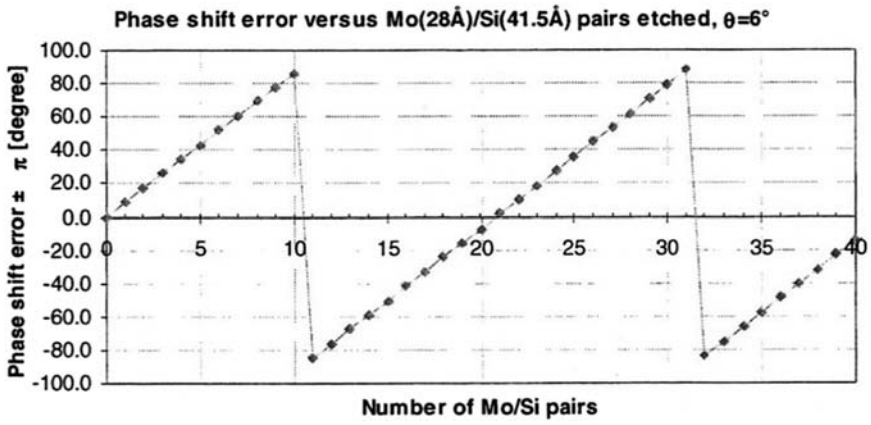

Figure 7.67 Phase shift error versus number of Mo/Si etched pairs (reprinted from Ref. 180).

plasma chemistry) and wet etchability.[182] The low EUV absorption of SiO_2 may allow a PSM without removing the ESL, which can act as a capping layer in the etched region. This phase shift of the near fields is mainly due to the optical path difference of light propagation down to and up from the trench, which can be calculated by $2 \times (2\pi/\lambda) \times \text{etch depth} \times [n_{air} - (0.6n_{Si} + 0.4n_{Mo})]$ for a normal incident angle. The simulation results show a linear relationship with a slope of 2.43-deg phase shift per nm of the etched depth, which gives a tolerance of 2.47 nm in the etched depth for a ±3 deg phase variation at a 180-deg phase shift point (Fig. 7.69).[176,183]

Another attenuated PSM is the embedded PSM, which is similar to an optical PSM.[184,185] In the case of the embedded PSM, some studies show that a 180-deg phase shift effect can be obtained by the single absorber layer, resulting in effects similar to those of the attenuated PSM (Fig. 7.70).[74,186] However, the absorber stack for EUV should satisfy both the phase and the desired absorption, and the most plausible approach is a two-layer structure. One layer mainly functions as an absorber, and the other layer functions as a phase shifter. The optimization methodology is depicted in detail in Fig. 7.71.[187] Among the several material variations for the two-material attenuated PSM, four optical parameters and two thicknesses must be optimized. The EUV attenuation is governed by the absorption coefficient k and the film thickness, and the attenuated EUV intensity in the absorber region after a round-trip reflection from the ML is given by

$$I \cong I_0 \left| \left[-\left(\frac{2\pi}{\lambda}\right)\left(\frac{2k_1 d_1}{\cos\theta} + \frac{2k_2 d_2}{\cos\theta}\right)\right]\right|^2, \tag{7.9}$$

where I is the EUV light intensity reflected from the absorber region (round trip), I_0 is the incident EUV light intensity, λ is the EUV light wavelength,

Downloaded From: https://www.spiedigitallibrary.org/ebooks/ on 09 Mar 2022
Terms of Use: https://www.spiedigitallibrary.org/terms-of-use

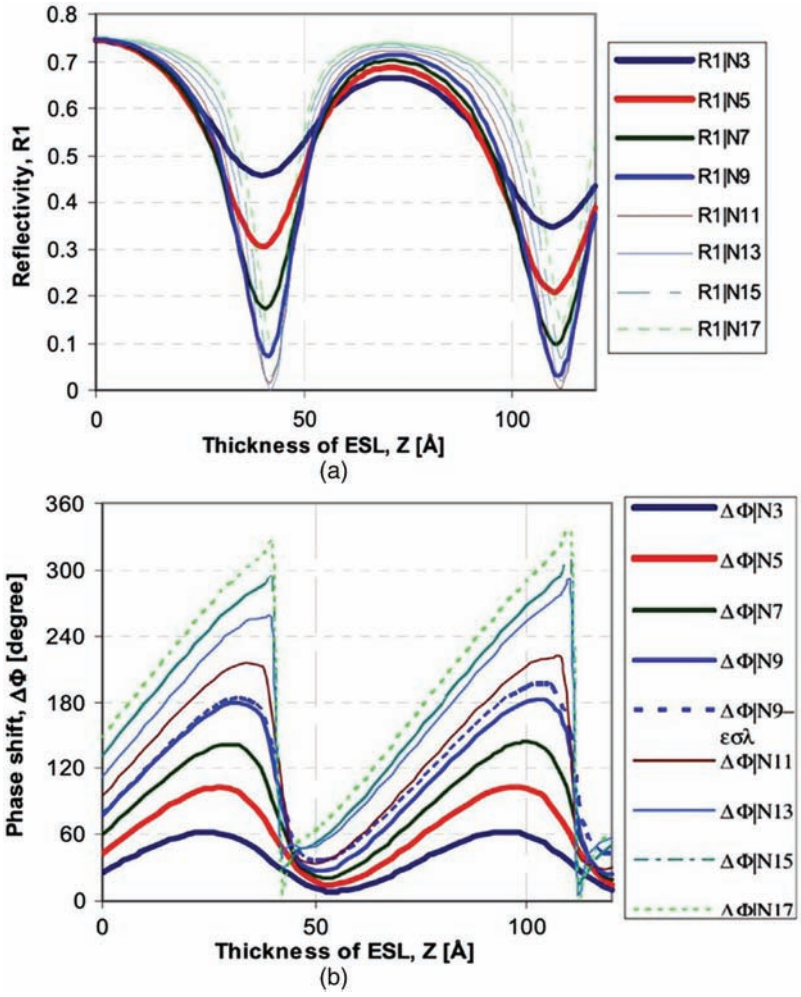

Figure 7.68 (a) Reflectivity R_1 for the unetched region versus the thickness of the SiO_2 ESL coated on a 40-Mo/Si ML for different numbers of MLs covering the ESL (N3 to N17 pairs by a step of 2). (b) Phase shift Φ versus SiO_2 ESL thickness. The dotted curve for N9 shows Φ if the ESL is removed from the etched region (reprinted from Ref. 180).

k_1 and k_2 are the imaginary parts of the refractive index of films 1 and 2, respectively, d_1 and d_2 are the thicknesses of films 1 and 2, respectively, and θ is the light incident angle to the mask normal.

The phase shift is determined by the film thickness as well as by the real part of the refractive index. An attenuated PSM with a 180-deg phase shift should satisfy the following condition:

$$\left| \frac{2\pi}{\lambda} \left(\frac{2\Delta n_1 d_1}{\cos\theta} + \frac{2\Delta n_2 d_2}{\cos\theta} \right) \right| = \pi, \tag{7.10}$$

Downloaded From: https://www.spiedigitallibrary.org/ebooks/ on 09 Mar 2022
Terms of Use: https://www.spiedigitallibrary.org/terms-of-use

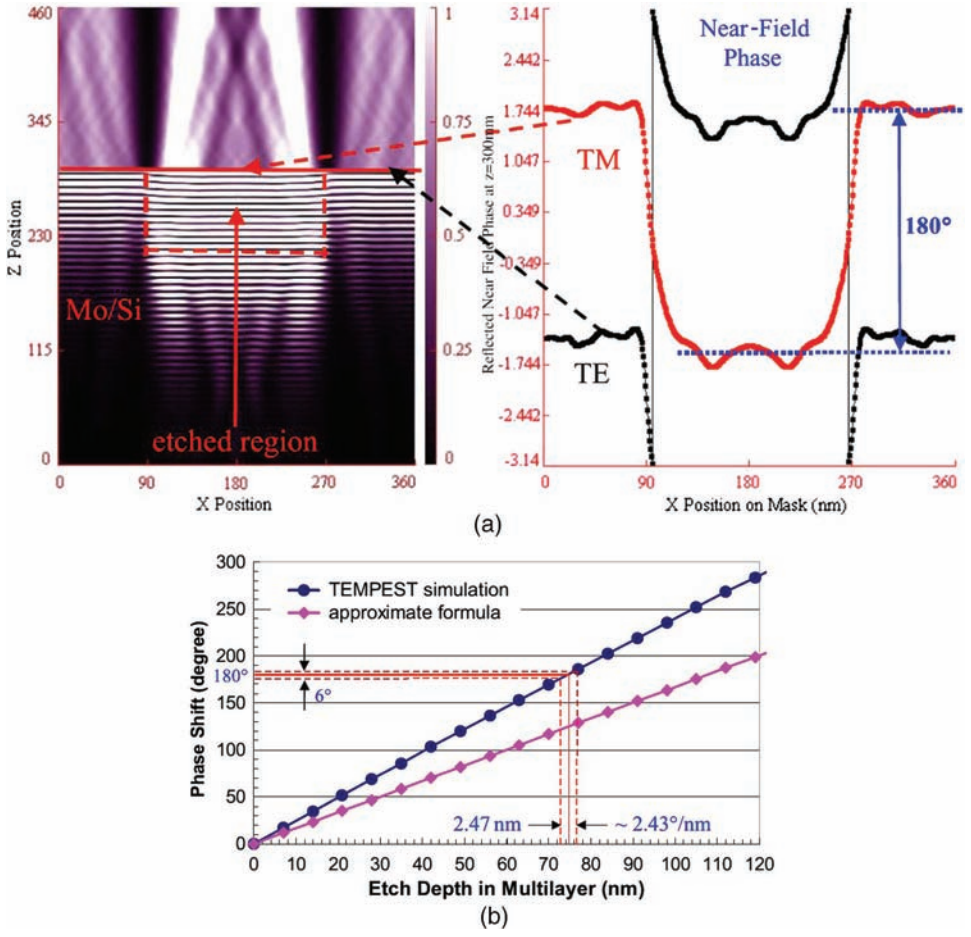

Figure 7.69 (a) Near-field phase reflected from the etched PSM. (b) Phase shift as a function of etched depth (reprinted from Ref. 176).

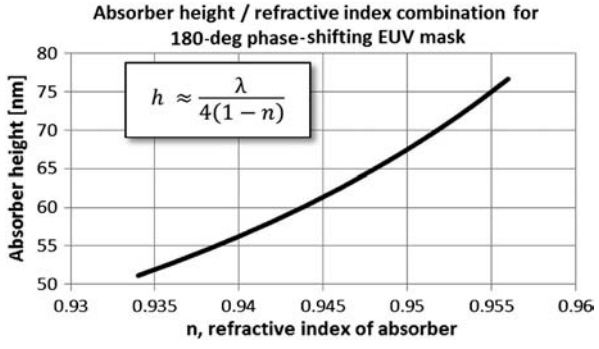

Figure 7.70 Absorber thickness with a 180-deg phase shift depending on the refractive index of a single-layer absorber (reprinted from Ref. 186).

Downloaded From: https://www.spiedigitallibrary.org/ebooks/ on 09 Mar 2022
Terms of Use: https://www.spiedigitallibrary.org/terms-of-use

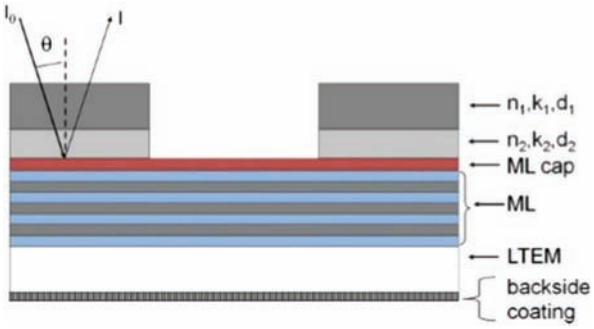

Figure 7.71 Schematic of the two-material EUVL embedded PSM structure (reprinted from Ref. 188).

where $\Delta n_1 = 1 - n_1$ (n_1 is the real part of the refractive index of film 1), and $\Delta n_2 = 1 - n_2$ (n_2 is the real part of the refractive index of film 2). In Eqs. (7.9) and (7.10), the reflected light from the thin film to the thin-film interface, and the thin film to the vacuum interface, are ignored due to the closely matched real parts of the refractive indices. By solving these two equations, we get d_1 and d_2 values using the following equations:

$$d_1 = \cos\,\theta\left(\frac{-\lambda\Delta n_1\,\ln\,\frac{I}{I_0}}{8\pi} + \frac{\lambda\alpha_1}{4}\right) \div (\Delta n_1\alpha_2 - \Delta n_2\alpha_1), \tag{7.11}$$

and

$$d_2 = \cos\,\theta\left(\frac{-\lambda\Delta n_2\,\ln\,\frac{I}{I_0}}{8\pi} + \frac{\lambda\alpha_2}{4}\right) \div (\Delta n_2\alpha_1 - \Delta n_1\alpha_2). \tag{7.12}$$

For a given attenuation I/I_0, any combination of two films can be used if the mask thickness d has a reasonable value. The appropriate combination of two films can improve the imaging performance as well as reduce the mask shadowing effect.[185,188] This two-layer approach is consistent with the absorber/buffer structure of a conventional EUV mask. However, several considerations should be made for etch selectivity and compatibility with other processes.

All of these complicated optimization processes can be simplified when the absorber and phase shifter have very similar refractive indices.[185] The out-of-phase condition (180-deg phase shift) was achieved with a ~40.5 nm-thick total absorber stack (TaN absorber + Mo phase shift layer), irrespective of the thickness ratio (Fig. 7.72). Using this valuable characteristic, the reflectivity can be controlled by adjusting the thickness of the Mo phase shifter while maintaining the out-of-phase condition when the total thickness of the absorber stack is fixed at 40.5 nm. This is possible due to the Mo phase shifter, which has a refractive index similar to that of the TaN absorber. Experimental

Downloaded From: https://www.spiedigitallibrary.org/ebooks/ on 09 Mar 2022
Terms of Use: https://www.spiedigitallibrary.org/terms-of-use

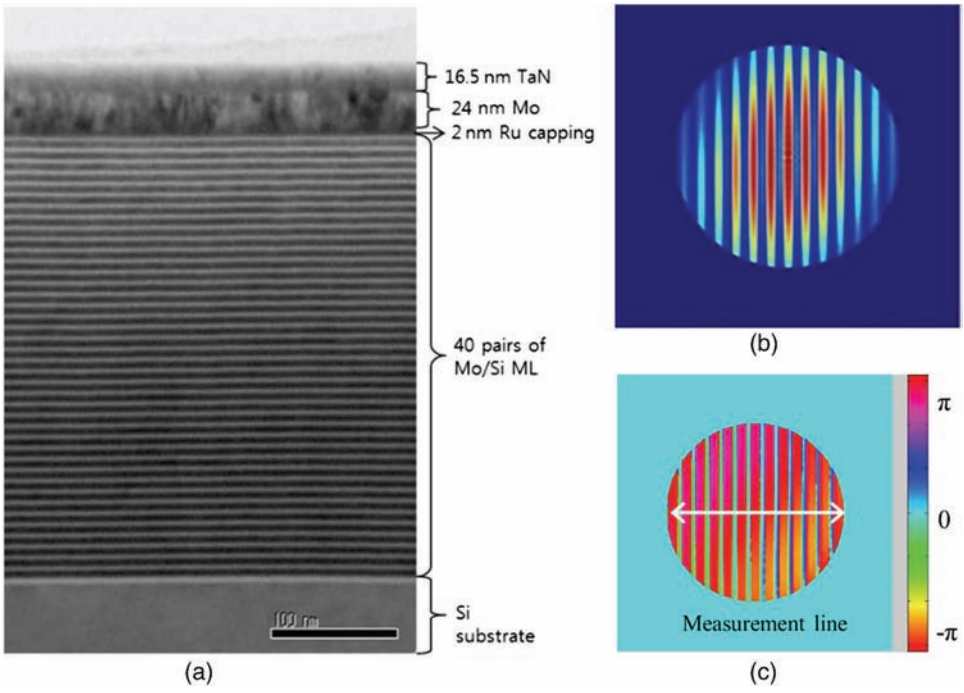

Figure 7.72 (a) Cross-section TEM photograph of a TaN/Mo-embedded PSM, (b) amplitude map, and (c) phase map measured by CSM. [Part (a) reprinted from Ref. 189; parts (b) and (c) reprinted from Ref. 190 with permission from OSA.]

results investigated using coherent scattering microscopy (CSM) showed improvements in optical performance parameters such as H-V CD bias and mask error enhancement factor (MEEF). The coherent scattering microscope could observe a 180-deg phase difference at the pattern edge and measure the improved diffraction efficiency of the PSM over a standard binary mask.[189,190]

7.8.6 Alternating phase shift mask

The phase difference due to mismatching of the ML in the two regions (0- and 180-deg phase regions) can be created by a phase step in the substrate before the ML coating to make what is known as an alternating PSM (APSM) (see Fig. 7.73). The step height that induces a 180-deg phase mismatch in the ML is determined by $[\lambda/(4\cos\theta)](2m+1)$, where m is an integer (0, 1, 2, ...).[175,191] With an exposure wavelength of 13.5 nm, the first few allowed step heights are 3.39, 10.18, 16.97 nm, etc. In the normal deposition process, the surface roughness changes with ML deposition and the minimum step may not be easily controllable. One well-known issue with the APSM is the image imbalance effect, which shifts the line positions. The image imbalance phenomenon in EUVL strongly depends on the interference between the reflected light in the reflector and the reflected light on the top of the absorber,

Downloaded From: https://www.spiedigitallibrary.org/ebooks/ on 09 Mar 2022
Terms of Use: https://www.spiedigitallibrary.org/terms-of-use

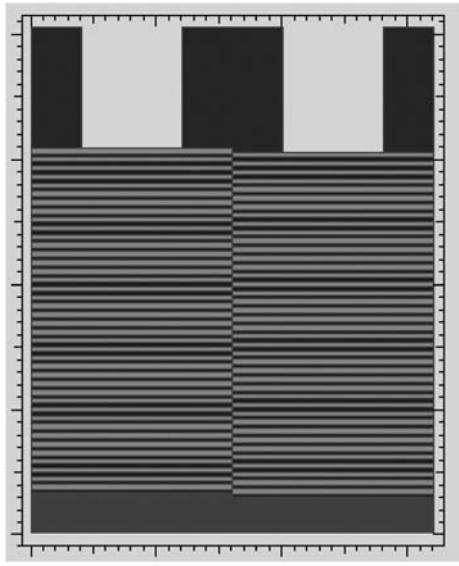

Figure 7.73 An APSM with the minimum step height ($m = 0$). The light that is reflected in the two reflector regions and is separated by the step is out of phase by 180 deg (reprinted from Ref. 175).

and this effect increases with a step height increase. As the pattern pitch increases, the image imbalance effect diminishes, even with more highly etched phase steps. Compared to the conventional binary mask, a larger exposure and focus latitude can be observed for 15-nm mask lines at a 50-nm pitch and a targeted CD of 10 nm for the 22-nm technology node with an APSM (Fig. 7.74). However, in order to make an EUVL APSM, more research is needed on the phase layer etch step height and uniformity control, ML step coverage spread control, and absorber layer alignment control.[191]

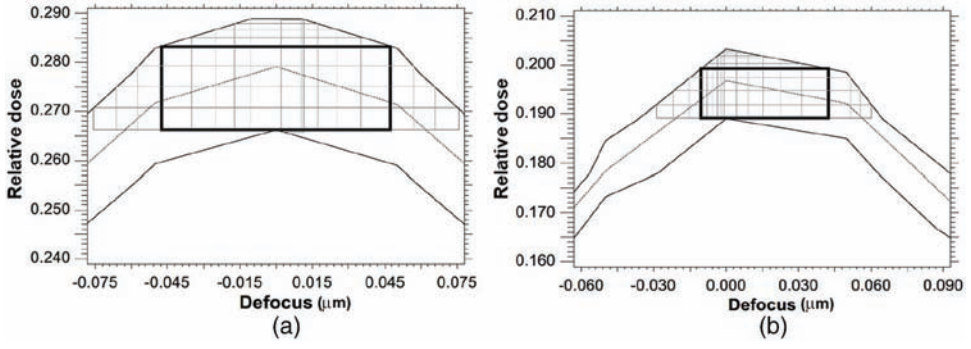

Figure 7.74 Process windows of (a) an APSM and (b) a conventional binary mask for 15-nm mask lines at a 50-nm pitch and a targeted CD of 10 nm. The allowable CD variation is ±1 nm (1×). The bold-faced window process is the largest one for a 10-nm target CD (adapted from Ref. 175).

Downloaded From: https://www.spiedigitallibrary.org/ebooks/ on 09 Mar 2022
Terms of Use: https://www.spiedigitallibrary.org/terms-of-use

An APSM can be fabricated with an etched ML structure similar to that of the attenuated PSM. If the etched region has enough bilayers remaining for high reflectivity, i.e., it is similar to the unetched region (e.g., 77-nm etching depth starting with 60-period bilayers), this etched region can work as a 180-deg phase shift region in an APSM.[175]

Modification of the APSM can be made by etching once again down to the substrate, by depositing absorber stacks on the unetched region, or by partially refilling the etched APSM (Fig. 7.75). It was reported that the double-etched APSM has a larger DOF compared to those of the binary mask and the APSM with an absorber.

7.8.7 Black border

EUV reflectivity of the absorber image border is 1–3%, depending on the absorber height. Therefore, as illustrated in Figure 7.76, structures at the edge of the die receive 1.5–5% extra background light, while in the corners this can

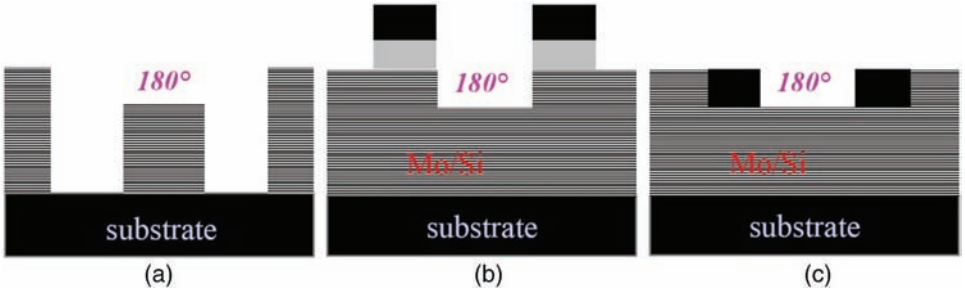

Figure 7.75 (a) A double-etched APSM, (b) an APSM with an absorber stack, and (c) a refilled APSM (reprinted from Ref. 176).

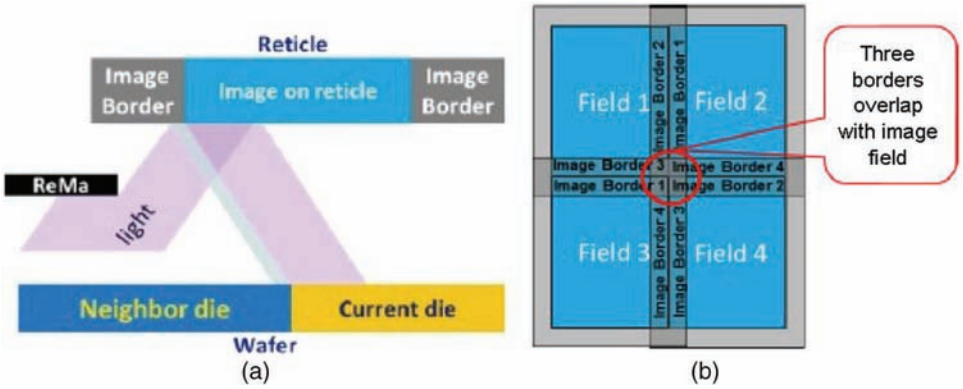

Figure 7.76 (a) Die-to-die interaction on the wafer. EUV light is reflected at the image border and impacts the imaging in the neighboring die. (b) At the corners of the dies, reflections from the three neighboring image borders overlap the die area (reprinted from Ref. 192).

Downloaded From: https://www.spiedigitallibrary.org/ebooks/ on 09 Mar 2022
Terms of Use: https://www.spiedigitallibrary.org/terms-of-use

be as much as 4.5–15%. Such high levels of extra background light will result in an unacceptable CD drop at the edges of the adjacent dies and deterioration of imaging in the corners. The contrast and process window of structures at the edges is also very poor because of this parasitic exposure.[192]

A solution to this problem is to reduce EUV reflectivity at the image border. Because of the presence of DUV out-of-band light in current EUV exposure tools, the DUV reflectivity of the image border should also be controlled. One method to reduce the reflectivity in this region involves removal of the absorber and MLM by etching down to the glass substrate and creating a low-reflection trench around the image field.[193] It was shown that the resulting EUV reflectivity was below 0.05% and DUV reflectivity was less than 6%.[194]

7.8.8 Mask design for high-NA

Increasing the NA of the projection optics to collect more diffracted light from the mask has been one of the most effective resolution enhancement technologies in lithography. Therefore, it is necessary to adopt optics with a NA higher than 0.33 to extend resolution below 8 nm in EUVL.[195] A chief ray angle (CRA) of 6 deg and 4× demagnification cannot be maintained with a NA of 0.45 because the incident and reflecting light cones overlap. To separate the light cones, an increase of the CRA or the demagnification factor is needed. With a demagnification factor higher than 4, the size of the mask should be enlarged to prevent a reduced exposure field size that occurs with a higher demagnification factor, which results in a throughput decrease.[196] However, it is difficult to change the size of the mask because this requires a big change in the mask fabrication infrastructure. If the CRA is increased instead to separate two light cones, the mask 3D effect due to the absorber thickness and oblique incident light is intensified.[197] Moreover, an imbalance in zeroth-order diffractions, which is due to a reflectivity variation according to the angle of incidence, results in a telecentricity error that causes a pattern shift on the wafer.[198] Since pattern shifts and mask 3D effects become more significant with finer pattern pitch, modified designs of the absorber stack and MLMs are required to alleviate the above-mentioned problems.

The MLM consisting of a periodic Mo/Si bilayer should be re-designed by adjusting the d-spacing and gamma ratio to be applied to the high-NA system with CRA of 9 deg. The range of the incidence angle α for the incident light cone, which depends on the NA and demagnification factor M, can be expressed as

$$\alpha = 2\sin^{-1}\frac{NA}{M}. \tag{7.13}$$

Thus, in accordance with Eq. (7.13), by increasing the NA, a wider range of incidence angles is expected. For a NA of 0.33 and 4× demagnification, the

Downloaded From: https://www.spiedigitallibrary.org/ebooks/ on 09 Mar 2022
Terms of Use: https://www.spiedigitallibrary.org/terms-of-use

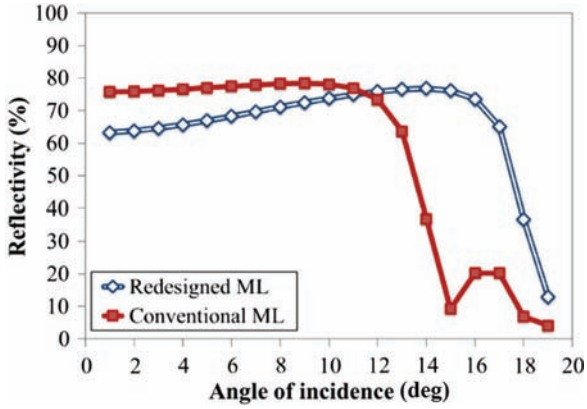

Figure 7.77 Comparison of reflectivity depending on the angle of incidence between the conventional ML with a 6-deg CRA and the redesigned ML optimized for a 9-deg CRA (reprinted from Ref. 199 with permission; © 2016 American Scientific Publishers).

range of incidence angles α is 9.5 deg and the reflectivity variation over this range of incidence angles is less than 3% with a conventional MLM. However, for a NA of 0.45 and a CRA of 9 deg, the incidence angle ranges are 2.5–15.5 deg and 4.3–13.7 deg for 4× and 6× demagnifications, respectively. Therefore, as shown in Fig. 7.77, the variation in reflectivity increased up to 65% when using the conventional MLM.[199] In order to reduce the imbalance of the reflectivity, the MLM was modified.

The mask shadowing effect becomes even more serious due to higher-angle-of-incident light. This effect results in the size of the printed space on the wafer being smaller than the designed space on the mask. This, in turn, results in H-V CD bias and eventually a limitation in resolution. A high-NA EUV mask absorber requires a thinner layer, but this can result in a deterioration in the imaging properties due to decreased mask contrast. Thin absorber material with a high extinction coefficient or phase shift absorber stack will help to alleviate the mask 3D effect with a high incident angle of a high-NA system.

7.9 Summary and Future Outlook

EUVL is an extension of optical lithography that uses 13.5-nm light. The characteristics of this wavelength require major modifications from standard optical lithography techniques, primarily due to the very strong absorption of EUV light by most materials. Refractive optics can no longer be used, necessitating the use of a MLM based mask as well as an oblique incident angle of light. The imaging performance of the mask strongly depends on the mask structure and materials. The key challenge of an EUV mask is to meet all of the requirements simultaneously. Although the basic technologies related to

Downloaded From: https://www.spiedigitallibrary.org/ebooks/ on 09 Mar 2022
Terms of Use: https://www.spiedigitallibrary.org/terms-of-use

the LTEM substrate, ML, absorber stack, mask patterning, cleaning, and metrology have recently shown significant improvements, further systematic studies are needed to meet the requirements of 7-nm technology node applications. Resolution enhancement technology such as PSMs might be a solution for the technology's extension, but this will require collaborative studies related to the simulation, metrology, and fabrication processes. The robust EUV pellicle with high transmittance is one of the imminent challenges that must be solved before the insertion of EUVL into mass production can occur. Additional challenges currently being addressed are the mask infrastructure (e.g., EUV mask fabrication), inspection, repair, pellicle integration, and handling of pelliclized masks.[33]

Acknowledgments

We would like to thank all of the authors of technical papers referenced in this chapter. The authors would also like to thank Vivek Bakshi, the editor of this book, for providing the opportunity to participate in this meaningful work. We are indebted to Dr. Chang Young Jeong, Dr. Seongchul Hong, Jung Sik Kim, Jung Hwan Kim, Yong Ju Jang, and Dong Gon Woo for their dedicated assistance.

References

1. ITRS, 2014 *International Technology Roadmap for Semiconductors*.
2. ITRS, 2013 *International Technology Roadmap for Semiconductors*.
3. SEMI, P37-0613 – Specification for Extreme Ultraviolet Lithography Substrates and Blanks (2013).
4. P.-Y. Yan, "Masks for Extreme Ultraviolet Lithography," Chapter 11 in *Handbook of Photomask Manufacturing Technology*, S. Rizvi, Ed., CRC Press/Taylor & Francis Informa Group, Boca Raton, Florida, p. 234 (2005).
5. S. Hector, "Standards for EUV mask," presented at SEMI EUV Mask Standards Meeting, San Francisco, California (2005).
6. Y. Takeichi, I. Nishiyama, and N. Yamada, "High-precision (<1 ppb/°C) optical heterodyne interferometric dilatometer for determining absolute CTE of EUVL materials," *Proc. SPIE* **6151**, 61511Z (2006) [doi: 10.1117/12.656368].
7. R. Schödel, "Ultra-high accuracy thermal expansion measurements with PTB's precision interferometer," *Meas. Sci. Tech.* **19**(8), 084003 (2008).
8. S. Hector, "Update on SEMI standards for EUV masks," presented at EUV Mask Workshop, Miyazaki, Japan (2004).
9. E. Gullikson, K. Blaedel, C. Larson, S. L. Baker, and J. S. Taylor, "EUV scattering from mask substrate roughness," presented at the First International Symposium on EUVL, 15–17 Oct., Dallas, Texas (2002).

Downloaded From: https://www.spiedigitallibrary.org/ebooks/ on 09 Mar 2022
Terms of Use: https://www.spiedigitallibrary.org/terms-of-use

10. K. Ballman, C. Lee, T. Dunn, and A. Bean, "Error analysis of overlay compensation methodologies and proposed functional tolerances for EUV photomask flatness," *Proc. SPIE* **9984**, 99840S (2016) [doi: 10.1117/12.2242282].
11. K. L. Blaedel, J. S. Taylor, S. D. Hector, P. Yan, A. Ramamoorthy, and P. D. Brooker, "Vendor capability for low thermal expansion mask substrates for EUV lithography," *Proc. SPIE* **4688**, 767 (2002) [doi: 10.1117/12.472273].
12. A. Rastegar and V. Jindal, "EUV mask defects and their removal," *Proc. SPIE* **8352**, 83520W (2012) [doi: 10.1117/12.923882].
13. P. B. Mirkarimi and D. G. Stearns, "Investigation the growth of localized defects in thin fiand using gold nanospheres," *Appl. Phys. Lett.* **77**(14), 2243 (2000).
14. R. Randive, A. Ma, I. Reiss, P. Mirkarimi, E. Spiller, B. Beier, T. Uno, P. Kearney, and C.-U. Jeon, "Defect mitigation and reduction in EUVL mask blanks, *Proc. SPIE* **6517**, 651726 (2007) [doi: 10.1117/12.712103].
15. P. B. Mirkarimi, E. A. Spiller, S. L. Baker, V. L. Sperry, D. G. Stearns, and E. M. Gullikson, "Developing a viable multilayer coating process for extreme ultraviolet lithography reticles," *J. Microlith., Microfab., Microsyst.* **3**(1), 139–145 (2004) [doi: 10.1117/1.1631006].
16. A. Rastegar, M. House, and A. J. Kadaksham, "Cleaning challenges of EUV mask substrates, blanks, and patterned mask," *ECS Trans.* **41**(5), 139 (2011).
17. A. Rastegar, B. Lee, and A. J. Kadaksham, "Mechanisms of EUV reflectivity loss from the multiple cleanings," 2011 EUVL Symposium, 17–19 October, Miami, Florida.
18. T. W. Barbee, Jr., S. Mrowka, and M. C. Hettrick, "Molybdenum-silicon multilayer mirrors for the extreme ultraviolet," *App. Opt.* **24**(6), 883 (1985).
19. J. M. Slaughter, D. W. Schulze, C. R. Hills, A. Mirone, R. Stalio, R. N. Watts, C. Tarrio, T. B. Lucatorto, M. Krumrey, P. Mueller, and C. M. Falco, "Structure and performance of Si/Mo multilayer mirrors for the extreme ultraviolet," *J. Appl. Phys.* **76**(4), 2144 (1994).
20. P.-Y. Yan, in *Handbook of Photomask Manufacturing Technology*, ed. S. Rizvi, CRC Press/Taylor & Francis Informa Group, Boca Raton, Florida, p. 239 (2005).
21. T. Tomofuji, N. Kandaka, T. Komiya, M. Shiraishi, and K. Murakami, "Mo/Si multilayer(ML) mirror deposited with ion beam sputtering using Kr gas," 2004 EUVL Symposium, 1–4 Nov., Miyazaki, Japan (2004).
22. S. Y. Lee, S. M. Hur, H. J. Kim, C. S. Yoon, Y. T. Lee, I. Y. Kang, Y.-C. Chung, M. Yi, C. K. Bok, O. Kim, and J. Ahn, "Analysis of multilayer structure for reflection of extreme-ultraviolet wavelength," *Jpn. J. Appl. Phys.* **41**, 4086 (2002).

Downloaded From: https://www.spiedigitallibrary.org/ebooks/ on 09 Mar 2022
Terms of Use: https://www.spiedigitallibrary.org/terms-of-use

23. S. Bajt, J. B. Alameda, T. W. Barbee, W. M. Clift, J. A. Folta, B. B. Kaufmann, and E. A. Spiller, "Improved reflectance and stability of Mo/Si multilayers," *Proc. SPIE* **4506**, 65 (2001) [doi: 10.1117/12.450946].
24. S. Braun, H. Mai, M. Moss, R. Scholz, and A. Leson, "Mo/Si multilayers with different barrier layers for applications as extreme ultraviolet mirrors," *Jpn. J. Appl. Phys.* **41**, 4074–4081 (2002).
25. S. Yulin, N. Benoit, T. Feigl, and N. Kaiser, "Interface-engineered multilayer mirrors," *Proc. SPIE* **5963**, 59630U (2005) [doi: 10.1117/12.624861].
26. S. Bajt, J. B. Alameda, T. W. Barbee, Jr., W. M. Clift, J. A. Folta, B. Kaufmann, and E. A. Spiller, "Improved reflectance and stability of Mo-Si multilayers," *Opt. Eng.* **41**(8), 1797 (2002) [doi: 10.1117/1.1489426].
27. P. A. Kearney, C. E. Moore, S. I. Tan, S. P. Vernon, and R. A. Levesque, "Mask blanks for extreme ultraviolet lithography: ion beam sputter deposition of low defect density Mo/Si multilayers," *J. Vac. Sci. Technol. B* **15**(6), 2452 (1997).
28. J. A. Folta, J. C. Davidson, C. C. Larson, C. C. Walton, and P. A. Kearney, "Advances in low-defect multilayers for EUVL mask blanks," *Proc. SPIE* **4688**, 173 (2002) [doi: 10.1117/12.472287].
29. P. B. Mirkarimi, E. A. Spiller, D. G. Stearns, V. Sperry, and S. L. Baker, "An ion-assisted Mo-Si deposition process for planarizing reticle substrates for extreme ultraviolet lithography," *IEEE J. Quantum Electron.* **37**(12), 1514 (2001).
30. E. A. Spiller, S. L. Baker, P. B. Mirkarimi, V. Sperry, E. M. Gullikson, and D. G. Stearns, "High-performance Mo-Si multilayer coatings for extreme-ultraviolet lithography by ion-beam deposition," *App. Opt.* **42**(12), 4049 (2003).
31. T. Onoue, T. Shoki, and J. Horikawa, "Progress of EUV mask blanks development," 2016 EUVL Symposium, 24–26 Oct., Hiroshima, Japan.
32. T. Yamane, T. Amano, N. Takagi, H. Watanabe, I. Mori, T. Ino, T. Suzuki, K. Takehisa, H. Miyai, and H. Kusunose, "Advances in the detection capability on actinic blank inspection," *Proc. SPIE* **9776**, 97761G (2016) [doi: 10.1117/12.2222747].
33. A. Ma, P. Kearney, D. Krick, R. Randive, I. Reiss, P. Mirkarimi, and E. Spiller, "Progress towards the development of a commercial tool and process for EUVL mask blanks," *Proc. SPIE* **5751**, 168 (2005) [doi: 10.1117/12.599936].
34. J. C. Bravman and R. Sinclair, "The preparation of cross-section specimens for transmission elec-tron microscopy," *Microsc. Res. Tech.* **1**, 53 (1984).
35. D. G. Stearns, R. S. Rosen, and S .P. Vernon, "Fabrication of high-reflectance Mo-Si multilayer mirrors by planar-magnetron sputtering," *J. Vac. Sci. Technol. A* **9**(5), 2662 (1991).

Downloaded From: https://www.spiedigitallibrary.org/ebooks/ on 09 Mar 2022
Terms of Use: https://www.spiedigitallibrary.org/terms-of-use

36. D. E. Kim, D. H. Cha, and S. W. Lee, "Structural characterization of a Mo/Si multilayer reflector by means of x-ray diffraction measurements," *J. Vac. Sci. Technol. A* **15**(4), 2291 (1997).
37. B. Vidal and P. Vincent, "Metallic multilayers for x rays using classical thin film theory," *Appl. Phys. Lett.* **23**, 1794 (1894).
38. U. Hinze and B. Chichkov, "Table-top EUV reflectometer," *Proc. SPIE* **6151**, 615136 (2006) [doi: 10.1117/12.656060].
39. A. Egbert and S. Becker, "Advanced at-wavelength reflectometry with the EUV tube," *Proc. SPIE* **6151**, 61512X (2006) [doi: 10.1117/12.648839].
40. H. Iguchi, H. Hashimoto, M. Kuki, T. Harada, T. Watanabe, and H. Kinoshita, "Development of a reflectometer for a large EUV mirror in NewSUBARU," *Proc. SPIE* **9658**, 965819 (2015) [doi: 10.1117/12.2199014].
41. S. Bajt, H. N. Chapman, N. Nguyen, J. B. Alameda, J. C. Robinson, M. E. Malinowski, E. Gullikson, A. Aquila, C. Tarrio, and S. Grantham, "Design and performance of capping layers for EUV multilayer mirrors," *Proc. SPIE* **5037**, 236 (2003) [doi: 10.1117/12.484966].
42. P.-Y. Yan, G. Zhang, S. Chegwidden, E. A. Spiller, and P. B. Mirkarimi, "EUVL mask with Ru ML capping," *Proc. SPIE* **5256**, 1281 (2003) [doi: 10.1117/12.520024].
43. S. Bajt, Z. R. Dai, E. J. Nelson, Mark A. Walla, J. Alameda, N. Nguyen, S. Baker, J. C. Robinson, J. S. Taylor, M. Clift, A. Aquila, E. M. Gullikson, and N. V. G. Edwards, "Oxidation resistance of Ru-capped EUV multilayers," *Proc. SPIE* **5751**, 118 (2005) [doi: 10.1117/12.597433].
44. H. Takase, S. Terashima, Y. Gomei, M. Tanabea, Y. Watanabe, T. Aoki, K. Murakami, S. Matsunari, M. Niibe, and Y. Kakutani, "Study of ruthenium-capped multilayer mirror for EUV irradiation durability," *Proc. SPIE* **6151**, 615135 (2006) [doi: 10.1117/12.657089].
45. I. Nishiyama, "Model of Ru surface oxidation for the lifetime scaling of EUVL projection optics mirror," *Proc. SPIE* **6151**, 61510G (2006) [doi: 10.1117/12.655499].
46. J. Hollenshead and L. Klebanoff, "Modeling extreme ultraviolet/H_2O oxidation of ruthenium optic coatings," *J. Vac. Sci. Technol. B* **24**(1), 118 (2006).
47. S. T. Prisbrey, S. P. Vernon, and W. M. Clift, "Iridium/silicon capping layer for soft x-ray and extreme ultraviolet mirrors," *J. Vac. Sci. Technol. B* **23**(6), 2378 (2005).
48. M. Kriese, Y. Platonov, J. Rodriguez, G. Fournier, S. Grantham, C. Tarrio, J. Curry, S. Hill, and T. Lucatorto, "Development and evaluation of interface-stabilized and reactive-sputtered oxide-capped multilayers for EUV lithography," *Proc. SPIE* **9422**, 94220K (2015) [doi: 10.1117/12.2085934].

Downloaded From: https://www.spiedigitallibrary.org/ebooks/ on 09 Mar 2022
Terms of Use: https://www.spiedigitallibrary.org/terms-of-use

49. P.-Y. Yan, "Masks for Extreme Ultraviolet Lithography," Chapter 11 in *Handbook of Photomask Manufacturing Technology*, S. Rizvi, Ed., CRC Press/Taylor & Francis Informa Group, Boca Raton, Florida, p. 241 (2005).
50. S. Bajt, D. G. Stearns, and P. A. Kearney, "Investigation of the amorphous-to-crystalline transition in Mo/Si multilayers," *J. Appl. Phys.* **90**, 1017 (2001).
51. P. Kearney, A. Ma, C. U. Jeon, T. Uno, and B. Beier, "Defect mitigation and reduction in EUVL mask blanks," EUVL Symposium 2006, 16–18 October, Barcelona, Spain.
52. A. Rastegar, S. Eichenlaub, V. Kapila, A. J. Kadaksham, and P. Marmillion, "New requirements for the cleaning of EUV blanks," *Proc. SPIE* **6517**, 65171D (2007) [doi: 10.1117/12.712105].
53. R. Randive, A. Ma, I. Reiss, P. Mirkarimi, E. Spiller, B. Beier, T. Uno, P. Kearney, and C.-U. Jeon, "Defect mitigation and reduction in EUVL mask blank," *Proc. SPIE* **6517**, 651726 (2007) [doi: 10.1117/12.712103].
54. A. Rastergar, S. Eichenlaub, H. Popp, K. Goncher, and P. Marmillion, "Removing sub-50 nm particles during blank substrate cleaning," *Solid State Technol.* **49**, 47 (2006).
55. E. Gullikson, C. Cerjan, D. Stearns, P. Mirkarimi, and D. Sweeney, "Practical approach for modeling extreme ultraviolet lithography mask defects," *J. Vac. Sci. Technol. B* **20**(1), 81 (2002).
56. P. B. Mirkarimi, E. Spiller, S. L. Baker, D. G. Stearns, J. C. Robinson, D. L. Olynick, F. Salmassi, J. A. Liddle, T. Liang, and A. R. Stivers, "A silicon-based, sequential coat-and-etch process to fabricate nearly perfect substrate surfaces," *J. Nanosci., Nanotech.* **6**, 28 (2006).
57. P. B. Mirkarimi, "Stress, reflectance, and temporal stability of sputter deposited Mo/Si and Mo/Be multilayer films for extreme ultraviolet lithography," *Opt. Eng.* **38**, 1246 (1999) [doi: 10.1117/1.602170].
58. T. G. Kim, S. Y. Lee, C. Y. Kim, I. S. Park, I. Y. Kang, N. E. Lee, Y. C. Chung, and J. Ahn, "Characterization of Ru layer for capping/buffer application in EUVL mask," *Microelec. Eng.* **83**, 688 (2006).
59. B. T. Lee, E. Hoshino, M. Takahashi, T. Yoneda, H. Yamanashi, H. Hoko, A. Chiba, M. Ito, M. Ryoo, T. Ogawa, and S. Okazaki, "Characteristics of Ru buffer layer for EUVL mask patterning," *Proc. SPIE* **4343**, 746 (2001) [doi: 10.1117/12.436699].
60. A. Rastegar, S. Eichenlaub, A. John, B. Lee, M. House, S. Huh, B. Cha, H. Yun, I. Mochi, and K. Goldberg, "Particle removal challenges of EUV patterned masks for the sub-22nm HP node," *Proc. SPIE* **7636**, 76360N (2010) [doi: 10.1117/12.847056].
61. L. He, K. Orvek, P. Seidel, S. Wurm, J. Underwood, and E. Betancourt, "Status and path to a final EUVL reticle-handling solution," *Proc. SPIE* **6517**, 375 (2007) [doi: 10.1117/12.712872].

Downloaded From: https://www.spiedigitallibrary.org/ebooks/ on 09 Mar 2022
Terms of Use: https://www.spiedigitallibrary.org/terms-of-use

62. L. He, S. Wurm, P. Seidel, K. Orvek, E. Betancourt, and J. Underwood, "Status of EUV reticle handling solution in meeting 32 nm hp EUV lithography," *Proc. SPIE* **6921**, 69211Z (2008) [doi: 10.1117/12.773278].
63. N. Hayashi, "EUV mask handling," 2011 IEUVI Mask TWG Meeting, 18 Sept., Monterey, California (2011).
64. P.-Y. Yan, G. Zhang, P. Kofron, J. E. Powers, M. Tran, T. Liang, A. R. Stivers, and F.-C. Lo, "EUV mask absorber characterization and selection," *Proc. SPIE* **4066**, 116 (2000) [doi: 10.1117/12.392025].
65. M. Niibe, T. Watanabe, H. Nii, T. Tanaka, and H. Kinoshita, "Contrast measurement of reflection masks fabrication from Cr and Ta absorbers for extreme ultraviolet lithography," *Jpn. J. Appl. Phys.* **39**, 6815 (2000).
66. P. J. S. Mangat, S. D. Hector, S. Rose, G. F. Cardinale, E. Tejnil, and A. R. Stivers, "EUV mask fabrication with Cr absorber," *Proc. SPIE* **3997**, 76 (2000) [doi: 10.1117/12.390099].
67. E. Hoshino, T. Ogawa, N. Hirano, H. Hoko, M. Takahashi, H. Yamanashi, A. Chiba, M. Ito, and S. Okazaki, "Dry etching of Ta absorber for EUVL masks," *Proc. SPIE* **4186**, 749 (2000) [doi: 10.1117/12.410755].
68. H.-J. Voorma, E. Louis, N. B. Koster, F. Bijkerk, T. Zijlstra, L. E. M. de Groot, B. A. C. Rousseeuw, J. Romijn, E. W. J. M. van der Drift, and J. Friedrich, "Fabrication and analysis of extreme ultraviolet reflection masks with patterned W/C absorber bilayers," *J. Vac. Sci. Technol. B* **15**(2), 293 (1997).
69. P.-Y. Yan, G. Zhang, A. Ma, and T. Liang, "TaN EUVL mask fabrication and characterization," *Proc. SPIE* **4343**, 409 (2001) [doi: 10.1117/12.436668].
70. P.-Y. Yan, "Impact of EUVL mask buffer and absorber material properties on mask quality and performance," *Proc. SPIE* **4688**, 150 (2002) [doi: 10.1117/12.472285].
71. F. Sobel, L. Aschke, M. Renno, H. Seitz, H. W. Becker, N. Olschewski, T. Reichardt, G. Heß, U. Buttgereit, K. Knapp, F. Letzkus, J. Butschke, and C. Koepernik, "Absorber stack optimization towards EUV lithography mask blank pilot production," *Proc. SPIE* **5567**, 781 (2004) [doi: 10.1117/12.568787].
72. A. Rastegar, M. House, R. Tian, T. Laursen, A. Antohe, and P. Kearney, "Study of alternative capping and absorber layers for extreme ultraviolet (EUV) masks for sub-16 nm half-pitch nodes," *Proc. SPIE* **9048**, 90480L (2014) [doi: 10.1117/12.2048074].
73. E. O. Wood, S. Raghunathan, P. Mangat, V. Philipsen, V. Luong, P. Kearney, E. Verduijn, A. Kumar, S. Patil, C. Laubis, V. Soltwisch, and F. Scholze, "Alternative materials for high numerical aperture extreme ultraviolet lithography mask stacks," *Proc. SPIE* **9422**, 94220I (2015) [doi: 10.1117/12.2085022].

Downloaded From: https://www.spiedigitallibrary.org/ebooks/ on 09 Mar 2022
Terms of Use: https://www.spiedigitallibrary.org/terms-of-use

74. J. U. Lee, S. Hong, and J. Ahn, "Very thin extreme ultraviolet mask absorber material for extremely fine pitch patterning," *Appl. Phys. Express* **6**, 076502 (2013).
75. S. Y. Lee, T. G. Kim, C. Y. Kim, I.-Y. Kang, Y.-C. Chung, and J. Ahn, "Combined absorber stack for optimization of the EUVL mask," *Proc. SPIE* **6151**, 61511Y (2006) [doi: 10.1117/12.656928].
76. J. R. Wasson, S.-I. Han, N. V. Edwards, E. Weisbrod, W. J. Dauksher, P. J. S. Mangat, and D. W. Pettibone, "Integration of anti-reflection coating on EUV absorber stacks," *Proc. SPIE* **4889**, 382 (2002) [doi: 10.1117/12.468104].
77. P. J. S. Mangat, S. D. Hector, M. A. Thompson, W. J. Dauksher, J. Cobb, K. D. Cummings, D. P. Mancini, D. J. Resnick, G. Cardinale, C. Henderson, P. Kearney, and M. Wedowski, "Extreme ultraviolet lithography mask patterning and printability studies with a Ta-based absorber," *J. Vac. Sci. Technol. B* **17**(6), 3029 (1999).
78. J. R. Wasson, B. Lu, P. J. S. Mangat, K. Nordquist, and D. J. Resnick, "Writing, repairing and inspecting of extreme ultraviolet lithography reticles considering the impact of the materials," *J. Vac. Sci. Technol. B* **19**(6), 2635 (2001).
79. W. Park, O. Kwon, J. Lee, and K. W. Whang, "Dry etching characteristics of TaN absorber for extreme ultraviolet mask with Ru buffer layer," *J. Vac. Sci. Technol. A* **30**(4), 041301 (2012).
80. A. Barty, P. B. Mirkarimi, D. G. Stearns, D. W. Sweeney, H. N. Chapman, W. M. Clift, S. D. Hector, and M. Yi, "EUVL mask blank repair," *Proc. SPIE* **4688**, 385 (2002) [doi: 10.1117/12.472313].
81. N. Kikuiri, S. Murakami, H. Tsuchiya, M. Tateno, K. Takahara, S. Imai, R. Hirano, I. Isomura, Y. Tsuji, Y. Tamura, K. Matsumura, K. Usuda, M. Otaki, O. Suga, and K. Ohira, "Development of advanced reticle inspection apparatus for hp 65 nm node device and beyond," *Proc. SPIE* **6283**, 62830Y (2006) [doi: 10.1117/12.683579].
82. K. Lim, J. Park, D. Chung, S. Choi, W. Han, H. Takizawa, and K. Miyazaki, "Novel mask inspection flow for better defect review and analysis," *Proc. SPIE* **6283**, 62830Z (2006) [doi: 10.1117/12.681858].
83. D. W. Pettibone, A. V. Veldman, T. Liang, A. R. Stivers, P. J. S. Mangat, B. Lu, S. D. Hector, J. R. Wasson, K. L. Blaedel, E. Fisch, and D. M. Walker, "Inspection of EUV reticles," *Proc. SPIE* **4688**, 363 (2002) [doi: 10.1117/12.472311].
84. E. Golan, D. Meshulach, N. Raccah, J. H. Yeo, O. Dassa, S. Brandl, C. Schwarz, B. Pierson, and W. Montgomery, "Immersion lithography defectivity analysis at DUV inspection wavelength," *Proc. SPIE* **6518**, 65180S (2007) [doi: 10.1117/12.712400].

Downloaded From: https://www.spiedigitallibrary.org/ebooks/ on 09 Mar 2022
Terms of Use: https://www.spiedigitallibrary.org/terms-of-use

85. M. Yi, T. Haga, C. Walton, and J. Bokor, "High sensitivity actinic detection of native defects on extreme ultraviolet lithography mask blanks," *J. Vac. Sci. Technol. B* **19**(6), 2401 (2001).
86. T. Terasawa, T. Yamane, T. Tanaka, T. Iwasaki, O. Suga, and T. Tomie, "Actinic mask blank inspection and signal analysis for detecting phase defects down to 1.5 nm in height," *Jpn. J. Appl. Phys.* **48**(6S), 06FAO4 (2009).
87. Y. Tezuka, M. Ito, T. Terasawa, and T. Tomie, "Actinic detection and signal characterization of multilayer defect on EUV mask blanks," *Proc. SPIE* **5567**, 791 (2004) doi: 10.1117/12.557773].
88. T. Terasawa, T. Yamane, T. Tanaka, and O. Suga, "Actinic dark-field mask blank inspection and defect printability analysis for detecting critical phase defects," 2010 EUVL Symposium, 17–20 Oct., Kobe, Japan.
89. A. Barty, Y. Liu, E. Gullikson, J. S. Taylor, and O. Wood, "Actinic inspection of multilayer defects on EUV masks," *Proc. SPIE* **5751**, 651 (2005) [doi: 10.1117/12.598488].
90. Y. Liu, A. Barty, E. Gullikson, J. S. Taylor, J. A. Liddle, and O. Wood, "A dual-mode actinic EUV mask inspection tool," *Proc. SPIE* **5751**, 660 (2005) [doi: 10.1117/12.598559].
91. T. Tomie, T. Terasawa, Y. Tezuka, and M. Ito, "Concept of ultra-fast at-wavelength inspection of defects on multilayer mask blanks using a laser-produced plasma source," *Proc. SPIE* **5038**, 41 (2003) [doi: 10.1117/12.482811].
92. T. Murachi, T. Amano, T. Suzuki, and H. Miyai, "Improvement of defect mitigation with EUV actinic blank inspection prototype for 16 nm hp," *Proc. SPIE* **9048**, 904820 (2014) [doi: 10.1117/12.2046130].
93. T. Murachi, T. Amano, T. Suzuki, and H. Miyai, "Effectiveness of extreme ultraviolet actinic blank inspection prototype for 16-nm half-pitch for mitigation of multilayered defects," *J. Micro/Nanolith. MEMS MOEMS* **13** (1), 013011 (2014) [doi: 10.1117/1.JMM.13.1.013011].
94. H. Miyai, T. Suzuki, K. Takehisa, H. Kusunose, T. Yamane, T. Terasawa, H. Watanabe, and I. Mori, "The capability of high magnification review function for EUV actinic blank inspection tool," *Proc. SPIE* **8701**, 870118 (2013) [doi: 10.1117/12.2030712].
95. A. Tchikoulaeva, H. Miyai, T. Suzuki, K. Takehisa, H. Kusunose, T. Yamane, T. Terasawa, H. Watanabe, S. Inoue, and I. Mori, "EUV actinic blank inspection: from prototype to production," *Proc. SPIE* **8679**, 867901 (2013) [doi: 10.1117/12.2011776].
96. T. Amano, N. Takagi, and T. Abe, "Variations in programmed phase defect size and its impact on defect detection signal intensity using at-wavelength inspection system," *Proc. SPIE* **9635**, 963513 (2015) [doi: 10.1117/12.2197620].

Downloaded From: https://www.spiedigitallibrary.org/ebooks/ on 09 Mar 2022
Terms of Use: https://www.spiedigitallibrary.org/terms-of-use

97. T. Yamane, T. Ino, and H. Miyai, "Analysis of a low-aspect phase defect for actinic EUVL mask blank inspection," *Proc. SPIE* **9658**, 96580N (2015) [doi: 10.1117/12.2197502].
98. T. Suzuki, H. Miyai, K. Takehisa, H. Kusunose, H. Watanabe, and I. Mori, "Detection capability of actinic blank inspection tool," *Proc. SPIE* **9658**, 96580O (2015) [doi: 10.1117/12.2197309].
99. T. Suzuki, H. Miyai, K. Takehisa, H. Kusunose, T. Yamane, H. Watanabe, and I. Mori, "Defect analysis on actinic blank inspection tool," *Proc. SPIE* **9256**, 92560O (2014) [doi: 10.1117/12.2069197].
100. T. Suzuki, H. Miyai, K. Takehisa, H. Kusunose, T. Yamane, T. Terasawa, H. Watanabe, S. Inoue, and I. Mori, "EUV actinic blank inspection tool with a high magnification review mode," *Proc. SPIE* **8441**, 844115 (2012) [doi: 10.1117/12.964983].
101. R. Jonckheere, T. Yamane, N. Takagi, H. Watanabe, and C. Beral, "ABI tool performance confirmation by NXE3300 printing results for native EUV blank defects at 16nm half pitch," 2016 EUVL Symposium, 24–26 Oct., Hiroshima, Japan.
102. T. Yamane, T. Amano, N. Takagi, H. Watanabe, I. Mori, T. Ino, T. Suzuki, K. Takehisa, H. Miyai, and H. Kusunose, "Advances in the detection capability on actinic blank inspection," *Proc. SPIE* **9776**, 97761G (2016) [doi: 10.1117/12.2222747].
103. T. Amano, H. Watanabe, and T. Abe, "Phase defect detection signal analysis: dependence of defect size variation," *Proc. SPIE* **9235**, 92351H (2014) [doi: 10.1117/12.2068370].
104. T. Yamane, Y. Kim, N. Takagi, T. Terasawa, T. Ino, T. Suzuki, H. Miyai, K. Takehisa, and H. Kusunose, "Performance in practical use of actinic EUVL mask blank inspection," *Proc. SPIE* **9256**, 92560P (2014) [doi: 10.1117/12.2067566].
105. N. Takagi, H. Watanabe, D. van den Heuvel, R. Jonckheere, and E. Gallagher, "EUV scanner printability evaluation of natural blank defects detected by actinic blank inspection," *Proc. SPIE* **9658**, 96580F (2015) [doi: 10.1117/12.2197622].
106. R. Jonckheere, D. Van den Heuvel, N. Takagi, H. Watanabe, and E. Gallagher, "Correlation of actinic blank inspection and experimental phase defect printability on NXE3x00 EUV scanner," *Proc. SPIE* **9422**, 942216 (2015) [doi: 10.1117/12.2085801].
107. L. Shoval, S. Mangan, I. Schwarzband, S. Khristo, V. Balasubramanian, S. Goldstein, R. Brikman, and N. Shoshani, "Applicability of e-beam mask inspection to EUV mask production," *Proc. SPIE* **8322**, 832227 (2012) [doi: 10.1117/12.927634].
108. R. Bonam, H.-Y. Tien, C. Park, S. Halle, F. Wang, D. Corliss, W. Fang, and J. Jau, "E-beam inspection of EUV mask defects: To etch or not to etch?" *Proc. SPIE* **9048**, 904812 (2014) [doi: 10.1117/12.2048284].

Downloaded From: https://www.spiedigitallibrary.org/ebooks/ on 09 Mar 2022
Terms of Use: https://www.spiedigitallibrary.org/terms-of-use

109. K. Badger, E. Gallagher, K. Seki, G. McIntyre, T. Konishi, Y. Kodera, and V. Redding, "Evaluation of non-actinic EUV mask inspection and defect printability on multiple EUV mask absorbers," *Proc. SPIE* **8701**, 870114 (2013) [doi: 10.1117/12.2029882].
110. H. Inoue, N. Kikuiri, H. Tsuchiya, R. Ogawa, I. Isomura, T. Hirano, and R. Yoshikawa, "DUV inspection tool application for beyond optical resolution limit pattern," *Proc. SPIE* **9635**, 96350R (2015) [doi: 10.1117/12.2197890].
111. P. B. Mirkarimi, D. G. Stearns, S. L. Baker, J. W. Elmer, D. W. Sweeney, and E. M. Gullikson, "Method for repairing Mo/Si multilayer thin film phase defects in reticles for extreme ultraviolet lithography," *J. Appl. Phys.* **91**(1), 81 (2002).
112. S. Y. Lee, T. G. Kim, J. G. Park, J. K. Song, O. H. Kim, C.-W. Yong, and J. Ahn, "Investigation of multilayer structural changes in phase and amplitude-defects correction process," *J. Vac. Sci. Technol. B* **23**(6), 2866 (2005).
113. S. P. Hau-Riege, A. Barty, P. B. Mirkarimi, S. Baker, M. A. Coy, M. Mita, V. E. Robertson, T. Liang, and A. Stivers, "Repair of phase defects in extreme-ultraviolet lithography mask blanks," *J. Appl. Phys.* **96**(11), 6812 (2004).
114. A. K. Ray-Chaudhuri, G. Cardinale, A. Fisher, P.-Y. Yan, and D. W. Sweeney, "Method for compensation of extreme-ultraviolet multilayer defects," *J. Vac. Sci. Technol. B* **1**(6), 3024 (1999).
115. R. Jonckheere, T. Bret, D. Van den Heuvel, J. Magana, W. Gao, and M. Waiblinger, "Repair of natural EUV reticle defects" *Proc. SPIE* **8166**, 81661G (2011) [doi: 10.1117/12.898864].
116. T. Bret, R. Jonckheere, D. Van den Heuvel, C. Baur, M. Waiblinger, and G. Baralia, "Closing the gap for EUV mask repair," *Proc. SPIE* **8322** 83220C (2012) [doi: 10.1117/12.918322].
117. J. Burns and M. Abbas, "EUV mask defect mitigation through pattern placement," *Proc. SPIE* **7823**, 782340 (2010) [doi: 10.1117/12.865160].
118. Y. Du, H. Zhang, and M. D. F. Wong, "Linear time EUV blank defect mitigation algorithm considering tolerance to inspection inaccuracy," *Proc. SPIE* **8522**, 85221R (2012) [doi: 10.1117/12.964103].
119. T. Liang, A. Stivers, R. Livengood, P.-Y. Yan, G. Zhang, and F.-C. Lo, "Progress in extreme ultraviolet mask repair using a focused ion beam," *J. Vac. Sci. Technol. B* **18**(6), 3216 (2000).
120. M. Waiblinger, K. Kornilov, T. Hofmann, and K. Edinger, "E-beam induced EUV photomask repair: a perfect match," *Proc. SPIE* **7545**, 75450P (2010) [doi: 10.1117/12.863542].
121. S.-Y. Lee, G.-B. Kim, H.-S. Sim, S.-H. Lee, H.-S. Kim, J.-H. Lee, H.-S. Seo, H.-S. Han, S.-S. Kim, S.-Y. Moon, S.-G. Woo, R. Bozak, A. Dinsdale, T. Robinson, D. Lee, and H. K Cho, "Analysis of process

Downloaded From: https://www.spiedigitallibrary.org/ebooks/ on 09 Mar 2022
Terms of Use: https://www.spiedigitallibrary.org/terms-of-use

margin in EUV mask repair with nano-machining," *Proc. SPIE* **7122**, 71222I (2008) [doi: 10.1117/12.801415].
122. M. Waiblinger, T. Bret, R. Jonckheere, and D. Van den Heuvel, "E-beam based mask repair as door opener for defect free EUV masks," *Proc. SPIE* **8522**, 85221M (2012) [doi: 10.1117/12.966387].
123. T. Liang and A. Stivers, "Damage-free mask repair using electron beam induced chemical reactions," *Proc. SPIE* **4688**, 375–384 (2002) [doi: 10.1117/12.472312].
124. T. Liang, A. R. Stivers, M. Penn, D. Bald, C. Sethi, V. Boegli, M. Budach, K. Edinger, and P. Spies, "Demonstration of damage-free mask repair using electron beam-induced processes," *Proc. SPIE* **5466**, 291–300 (2004) [doi: 10.1117/12.557788].
125. T. Liang, E. Frendberg, D. J. Bald, M. Penn, and A. R. Stivers, "E-beam mask repair: fundamental capability and applications," *Proc. SPIE* **5567**, 456–466 (2004) [doi: 10.1117/12.569210].
126. T. Liang, E. Frendberg, B. Lieberman, and A. Stivers, "Advanced photolithographic mask repair using electron beams," *J. Vac. Sci. Technol. B* **23**(6), 3101 (2005).
127. T. Robinson, R. White, R. Bozak, K. Roessler, B. Arruza, D. Hogle, M. Archuletta, and D. Lee, "New tools to enable photomask repair to the 32 nm node," *Proc. SPIE* **7488**, 74880F (2009) [doi: 10.1117/12.847238].
128. G. McIntyre, E. Gallagher, T. Robinson, A. C. Smith, M. Lawliss, J. LeClaire, R. Bozak, R. White, and M. Archuletta, "Through-focus EUV multilayer defect repair with nanomachining," *Proc. SPIE* **8679**, 86791I (2013) [doi: 10.1117/12.2014935].
129. K. Edinger, K. Wolff, H. Steigerwald, N. Auth, P. Spies, J. Oster, H. Schneider, M. Budach, T. Hofmann, and M. Waiblinger, "Bringing mask repair to the next level," *Proc. SPIE* **9235**, 92350R (2014) [doi: 10.1117/12.2072474].
130. K. Edinger, K. Wolff, P. Spies, T. Luchs, H. Schneider, N. Auth, Ch. F. Hermanns, and M. Waiblinger, "Photomask repair using low energetic electrons," *Proc. SPIE* **9635**, 96351P (2015) [doi: 10.1117/12.2207755].
131. F. Aramaki, T. Ogawa, O. Matsuda, T. Kozakai, Y. Sugiyama, H. Oba, A. Yasaka, T. Amano, H. Shigemura, and O. Suga, "Development of new FIB technology for EUVL mask repair," *Proc. SPIE* **7969**, 79691C (2011) [doi: 10.1117/12.879609].
132. F. Aramaki, T. Kozakai, O. Matsuda, A. Yasaka, S. Yoshikawa, K. Kanno, H. Miyashita, and N. Hayashi, "Performance of GFIS mask repair system for various mask materials," *Proc. SPIE* **9235**, 92350F (2014) [doi: 10.1117/12.2069435].
133. A. Zibold, U. Stroessner, A. Ridley, T. Scherübl, N. Rosenkranz, W. Harnisch, E. Poortinga, R. Schmid, J. Bekaert, V. Philipsen, L. Van Look, and P. Leunissen, "Printability study with polarisation capable

Downloaded From: https://www.spiedigitallibrary.org/ebooks/ on 09 Mar 2022
Terms of Use: https://www.spiedigitallibrary.org/terms-of-use

AIMS fab 193i to study polarisation effects," *Proc. SPIE* **6152**, 61522F (2006) [doi: 10.1117/12.656235].
134. E. Verduijn, E. Hosler, P. Mangat, O. Wood, R. Capelli, S. Perlitz, K. Magnusson, M. Weiss, D. Hellweg, V. Jindal, M. P. Benk, A. Wojdyla, and K. A. Goldberg, "Assessment of AIMS EUV and SHARP actinic wavelength mask defect review tools for the evaluation of blank defect printability," 2015 EUVL Symposium, 4–7 Oct., Maastricht, The Netherlands.
135. S. S. Kim, D. Lee, J. Park, E. Kim, C. U. Jeon, H. Cho, B. Jeon, C. Choi, C. Anderson, R. Myakawa, and P. Naulleau, "EUV mask imaging system based on the scanning reflective microscopy," 2013 EUVL Symposium, 6–10 Oct., Toyama, Japan.
136. C. J. R. Sheppard and T. Wilson, "Reciprocity and equivalence in scanning microscopes," *J. Opt. Soc. Am.* **3**, 755 (1986).
137. P. P. Naulleau, C. N. Anderson, E. H. Anderson, N. Andreson, W. Chao, C. Choi, K. A. Goldberg, E. M. Gullikson, S. S. Kim, D. Lee, R. Miyakawa, J. Park, S. Rekawa, and F. Salmassi, "Electro-optical system for scanning microscopy of extreme ultraviolet masks with a high harmonic generation source," *Opt. Express* **22**(17), 20144 (2014).
138. D. Hellweg, S. Perlitz, K. Magnusson, R. Capelli, M. Koch, and M. Malloy, "Actinic review of EUV masks: performance data and status of the AIMS EUV system," *Proc. SPIE* **9776**, 97761A (2016) [doi: 10.1117/12.2219247].
139. J. Benschop and P. Kurz, "Extreme ultraviolet lithography: challenges and progress," *Microlithography World* **10**, 4 (2001).
140. P.-Y. Yan, M. S. Yeung, and H. T. Gaw, "Printability of pellicle defects in 0.5 μm lithography," *Proc. SPIE* **1604**, 106117 (1991) [doi: 10.1117/12.56939].
141. D. L. Goldfarb, "Fabrication of a full-size EUV pellicle based on silicon nitride," *Proc. SPIE* **9635**, 96350A (2015) [doi: 10.1117/12.2196901].
142. D. G. Woo, S. Hong, H. K. Cho, and J. Ahn, "Impact of EUV pellicle transmittance on imaging performance analyzed by coherent scattering microscopy," *Nanosci. Nanotech. Lett.* **8**, 1 (2016).
143. D. Brouns, "Pellicle HVM specifications," 2016 IEUVI Pellicle TWG, 21 Feb., San Jose, California.
144. The Center for X-ray Optics, http://www.cxro.lbl.gov.
145. M. Nasalevich, P. J. van Zwol, E. Abegg, P. Voorthuijzen, D. Vles, M. Péter, W. van der Zande, and H. Vermeulen, "Researching new EUV pellicle films for source powers beyond 250 watts," *Proc. SPIE* **10032**, 100320L (2016) [doi: 10.1117/12.2255040].
146. Y. A. Shroff, M. Goldstein, B. Rice, S. H. Lee, K. V. Ravi, and D. Tanzil, "EUV pellicle development for mask defect control," *Proc. SPIE* **6151**, 615104 (2006) [doi: 10.1117/12.656551].

Downloaded From: https://www.spiedigitallibrary.org/ebooks/ on 09 Mar 2022
Terms of Use: https://www.spiedigitallibrary.org/terms-of-use

147. K. Ko, E.-J. Kim, J.-W. Kim, J.-T. Park, C.-M. Lim, and H. Oh, "Effect of extreme ultraviolet pellicle support to patterned mask," *Proc. SPIE* **8322**, 832230 (2012) [doi: 10.1117/12.918019].
148. Y. A. Shroff, P.-Y. Yan, F. Salamassi, and E. Gullikson, "High transmission EUVL pellicle development," 2008 EUVL Symposium, 21 Sept. to 1 Oct., Lake Tahoe, California.
149. D. Smith, "NXE pellicle progress update," EUV Mask Pellicle TWG, 2015 EUVL Symposium, 4–7 Oct., Maastricht, The Netherlands.
150. S. Kwon, Y. Jung, H. Jeon, J. Kim, J. Choi, B. G. Kim, and C. U. Jeon, "EUV pellicle TWG (Samsung)," EUV Mask Pellicle TWG, 2015 EUVL Symposium, 4–7 Oct., Maastricht, The Netherlands.
151. L. Scaccaborozzi, D. Smith, P. R. Diago, E. Casimiri, N. Dziomkina, and H. Meijer, "Investigation of EUV pellicle feasibility," *Proc. SPIE* **8679**, 867904 (2013) [doi: 10.1117/12.2015833].
152. J. H. Kim, S. Hong, S. M. Lee, J. S. Kim, H. Cho, and J. Ahn, "Feasibility study on inserting graphene layers into EUV pellicle structure," 2015 EUVL Symposium, 4–7 Oct., Maastricht, Netherlands.
153. M. J. Kim, H. C. Jeon, R. Chalykh, E. Kim, J. Na, B.-G. Kim, H. Kim, C. Jeon, S.-G. Kim, D.-W. Shin, T. Kim, S. Kim, J. H. Lee, and J.-B. Yoo, "Study of nanometer-thick graphite film for high-power EUVL pellicle," *Proc. SPIE* **9776**, 97761Z (2016) [doi: 10.1117/12.2218228].
154. I. Pollentier, J. Vanpaemel, J. U. Lee, C. Adelmann, H. Zahedmanesh, C. Huyghebaert, and E. E. Gallagher, "EUV lithography imaging using novel pellicle membranes," *Proc. SPIE* **9776**, 977620 (2016) [doi: 10.1117/12.2220031].
155. D. Brouns, A. Bendiksen, P. Broman, E. Casimiri, P. Colsters, P. Delmastro, D. de Graaf, P. Janssen, M. van de Kerkhof, R. Kramer, M. Kruizinga, H. Kuntzel, F. van der Meulen, D. Ockwell, M. Peter, D. Smith, B. Verbrugge, D. van de Weg, J. Wiley, N. Wojewoda, C. Zoldesi, and P. van Zwol, "NXE pellicle: offering an EUV pellicle solution to the industry," *Proc. SPIE* **9776**, 97761Y (2016) [doi: 10.1117/12.2221909].
156. J. U. Lee, J. Vanpaemel, I. Pollentier, C. Adelmann, H. Zahedmanesh, C. Huyghebaert, M. Timmermans, M. De Volder, and E. Gallagher, "Introducing the EUV CNT pellicle," *Proc. SPIE* **9985**, 99850C (2016) [doi: 10.1117/12.2243019].
157. E. E. Gallagher, J. Vanpaemel, I. Pollentier, H. Zagedmanesh, C. Adelmann, C. Huyghebaert, R. Jonckheere, and J. U. Lee, "Properties and performance of EUVL pellilce membranes," *Proc. SPIE* **9635**, 96350X (2015) [doi: 10.1117/12.2199076].
158. C. Lee, X. Wei, J. W. Kysar, and J. Hone, "Measurement of the elastic properties and intrinsic strength of monolayer graphene," *Science* **321**, 385 (2008).

Downloaded From: https://www.spiedigitallibrary.org/ebooks/ on 09 Mar 2022
Terms of Use: https://www.spiedigitallibrary.org/terms-of-use

159. F. Banhart, J. Kotakoski, and A. V. Krasheninnikov, "Structural defects in graphene," *ACS Nano* **5**(1), 26–41 (2011).
160. M. Her, R. Beams, and L. Novotny, "Graphene transfer with reduced residue," *Physics Letters A* **377** (2013).
161. D. Smith, "ASML NXE Pellicle progress update," 2016 EUV Mask Pellicle TWG, 21 Feb., San Jose, California.
162. P. Nesládek, T. Schedel, and M. Bender, "Clean induced feature CD shift of EUV mask," *Proc. SPIE* **9984**, 99840N (2016) [doi: 10.1117/12.2240308].
163. K. Hamamoto, Y. Tanaka, T. Watanabe, N. Sakaya, M. Hosoya, T. Shoki, H. Hada, N. Hishinuma, H. Sugahara, and H. Kinoshita, "Cleaning of extreme ultraviolet lithography optics and mask using 13.5 nm and 172 nm radiation," *J. Vac. Sci. Technol. B* **23**(1), 247 (2005).
164. N. Hirano, H. Hoko, E. Hoshino, T. Ogawa, A. Chiba, H. Yamanashi, M. Takahashi, and S. Okazaki, "Surface preparation of EUVL-mask substrate for multi-layer coating by supersonic hydrocleaning technique," *Proc. SPIE* **4066**, 430 (2000) [doi: 10.1117/12.392046].
165. T. Yoneda, H. Hoko, E. Hoshino, T. Ogawa, S. Okazaki, Y. Isobe, T. Matsumoto, and T. Mizoguchi, "Evaluation of cleaning techniques for EUVL mask by using a highly sensitive particle detection system," *Microelec. Eng.* **61–62**, 213–218 (2002).
166. W. M. Lytle, M. J. Neumann, and D. N. Ruzic, "Plasma-assisted cleaning by electrostatics (PACE)," *Proc. SPIE* **6151**, 61511B (2006) [doi: 10.1117/12.656645].
167. S. H. Lee, Y. J. Kang, J. G. Park, A. Busnaina, J. M. Lee, T. H. Kim, G. Zhang, F. Eschbach, and A. Ramamoorthy, "Laser shock removal of nanoparticles from Si capping layer of extreme ultraviolet lithography masks," *Jpn. J. Appl. Phys.* **44**(7B), 5560 (2005).
168. D. Civay, E. Hosler, V. Chauhan, T. G. Neogi, L. Smith, and D. Pritchard, "EUV telecentricity and shadowing errors impact on process margins," *Proc. SPIE* **9422**, 94220Z (2015) [doi: 10.1117/12.2087639].
169. L. Van Look, V. Phillipsen, E. Hendrickx, G. Vandenberghe, N. Davydova, F. Wittebrood, R. de Kruif, A. van Oosten, J. Miyazaki, T. Filervoet, J. van Schoot, and J. T. Neumann, "Alternative EUV mask technology to compensate for mask 3D effects," *Proc. SPIE* **9658**, 96580I (2015) [doi: 10.1117/12.2197213].
170. A. Erdmann and P. Evanschitzky, "Imaging characteristics of binary and phase shift masks for EUV projection lithography," *Proc. SPIE* **8550**, 85503K (2012) [doi: 10.1117/12.981444].
171. V. Philipsen, V. Luong, E. Hendrickx, A. Erdmann, D. Xu, P. Evanschitzky, R. W. Kruijs, A. Edrisi, F. Scholze, C. Laubis, M. Irmscher, S. Naasz, and C. Reuter, "Mitigating EUV mask 3D effects by

Downloaded From: https://www.spiedigitallibrary.org/ebooks/ on 09 Mar 2022
Terms of Use: https://www.spiedigitallibrary.org/terms-of-use

alternative metal absorbers," 2016 EUVL Symposium, 24–26 Oct., Hiroshima, Japan.
172. C. G. Krautschik, M. Ito, I. Nishiyama, and K. Otaki, "Impact of the EUV mask phase response on the asymmetry of Bossung curves as predicted by rigorous EUV mask simulations," *Proc. SPIE* **4343**, 392 (2001) [doi: 10.1117/12.436666].
173. M. Burkhardt and A. Raghunathan, "Best focus shift mechanism for thick masks," *Proc. SPIE* **9442**, 94420X (2015) [doi: 10.1117/12.2085948].
174. R. Wood, II, D. L. White, J. E. Bjorkholm, L. E. Fetter, D. M. Tennant, A. A. MacDowell, B. LaFontaine, and G. D. Kubiak, "Use of attenuated phase masks in extreme ultraviolet lithography," *J. Vac. Sci. Technol. B* **15**(6), 2448 (1997).
175. P.-Y. Yan, "EUVL alternating phase shift mask imaging evaluation," *Proc. SPIE* **4889**, 1099 (2002) [doi: 10.1117/12.468103].
176. Y. Deng, B. L. Fontaine, H. J. Levinson, and A. R. Neureuther, "Rigorous EM simulation of the influence of the structure of mask patterns on EUVL imaging," *Proc. SPIE* **503**, 302 (2003) [doi: 10.1117/12.484986].
177. Y. Deng, B. L. Fontaine, A. R. Pawloski, and A. R. Neureuther, "Simulation of fine structures and defects in EUV etchted multilayer masks," *Proc. SPIE* **5374**, 760 (2004) [doi: 10.1117/12.537229].
178. K. Takai, T. Motokawa, K. Murano, T. Kamo, and N. Hayashi, "Patterning of EUVL binary etched multilayer mask," *Proc. SPIE* **8880**, 88802M (2013) [doi: 10.1117/12.2033258].
179. B. L. Fontaine, A. R. Pawloski, O. Wood, Y. Deng, H. J. Levinson, P. Naulleau, P. E. Denham, E. Gullikson, B. Hoef, C. Holfeld, C. Chovino, and F. Letzkus, "Demonstration of phase shift masks for extreme-ultraviolet lithography," *Proc. SPIE* **6151**, 61510A (2006) [doi: 10.1117/12.652212].
180. C. Constancias, M. Richard, D. Joyeux, J. Chiaroni, R. Blanc, J. Y. Robic, E. Quesnel, and V. Muffato, "Phase shift mask for EUV lithography," *Proc. SPIE* **6151**, 61511W (2006) [doi: 10.1117/12.655583].
181. K. Takai, K. Murano, T. Kamo, Y. Morikawa, and N. Hayashi, "Capability of etched multilayer EUV mask fabrication," *Proc. SPIE* **9235**, 923515 (2014) [doi: 10.1117/12.2067892].
182. L. Dreeskornfeld, G. Haindl, U. Kleineberg, U. Heinzmann, F. Shi, B. Volland, I. W. Rangelow, E. Majkova, S. Luby, Kostic, L. Matay, P. Hrkut, P. Hudek, and H.-Y. Lee, "Nanostructuring of Mo/Si multilayer by means of reactive ion etching using a three-level mask," *Thin Solid Films* **458**, 227 (2004).
183. P. Naulleau, C. N. Anderson, W. Chao, K. A. Goldberg, E. Gullikson, F. Salmassi, and A. Wojdyla, "Ultrahigh efficiency EUV contact-hole

Downloaded From: https://www.spiedigitallibrary.org/ebooks/ on 09 Mar 2022
Terms of Use: https://www.spiedigitallibrary.org/terms-of-use

printing with chromeless phase shift mask," *Proc. SPIE* **9984**, 99840P (2016) [doi: 10.1117/12.2243321].
184. P. Y. Yan, I. Mochi, and K. A. Goldberg, "EUV actinic imaging tool aerial image evaluation of EUVL embedded phase shift mask performance," *Proc. SPIE* **8322**, 83221P (2012) [doi: 10.1117/12.919710].
185. S. Lee, I. Lee, J. Ahn, J. Doh, J. Lee, and S. Hong, "Improved imaging properties of thin attenuated phase shift masks for extreme ultraviolet lithography," *J. Vac. Sci. Technol. B* **31**(2), 021606 (2013).
186. N. Davydova, R. de Kruif, H. Roff, B. Connolly, E. van Setten, A. Lammers, D. Oorschot, N. Fukugami, and Y. Kodera, "Experimental approach to EUV imaging enhancement by mask absorber height optimization," *Proc. SPIE* **8886**, 88860A (2013) [doi: 10.2227/12.2030806].
187. P.-Y. Yan, "Masks for Extreme Ultraviolet Lithography," Chapter 11 in *Handbook of Photomask Manufacturing Technology*, S. Rizvi, Ed., CRC Press/Taylor & Francis Informa Group, Boca Raton, Florida, p. 265 (2005).
188. P.-Y. Yan, M. J. Leeson, S. Lee, G. Zhang, E. M. Gullikson, and F. H. Salmassi, "Extreme ultraviolet-embedded phase-shift mask," *J. Micro/Nanolith. MEMS MOEMS* **10**(3), 033011 (2011) [doi: 10.1117/1.3616060].
189. J. U. Lee, S. J. Jeong, S. Hong, S. M. Lee, and J. Ahn, "Imaging performance of attenuated phase-shift mask using coherent scattering microscope," *Proc. SPIE* **9048**, 90481X (2014) doi: 10.1117/12.2045877].
190. D. G. Woo, J. U. Lee, S. Hong, J. S. Kim, and J. Ahn, "Coherent scattering microscopy as an effective inspection tool for analyzing performance of phase shift mask," *Opt. Express* **24**(11) 12055–12062 (2016).
191. P.-Y. Yan, A. Myers, Y. Shroff, M. Chandhok, G. Zhang, E. Gullikson, and F. Salmassi, "EUVL alternating phase shift mask," *Proc. SPIE* **7969**, 79690G (2011) [doi: 10.1117/12.884790].
192. N. Davydova, R. de Kruif, N. Fukugami, S. Kondo, V. Philipsen, E. van Setten, B. Connolly, A. Lammers, V. Vaenkatesan, J. Zimmerman, and N. Harned, "Impact of an etched EUV mask black border on imaging and overlay," *Proc. SPIE* **8522**, 852206 (2012) [doi: 10.1117/12.964547].
193. T. Kamo, H. Aoyama, T. Tanaka, O. Suga, T. Abe, T. Takikawa, N. Hayashi, T. Shoki, Y. Usui, and M. Hosoya, "EUVL practical mask structure with light shield area for 32nm half pitch and beyond," *Proc. SPIE* **7122**, 712227 (2008) [doi: 10.1117/12.801576].
194. N. Fukugami, K. Matsui, G. Watanabe, T. Isogawa, S. Kondo, Y. Kodera, Y. Sakata, S. Akima, J. Kotani, H. Morimoto, and T. Tanaka, "Black border with etched multilayer on EUV mask," *Proc. SPIE* **8441**, 84411K (2012) [doi: 10.1117/12.965536].

Downloaded From: https://www.spiedigitallibrary.org/ebooks/ on 09 Mar 2022
Terms of Use: https://www.spiedigitallibrary.org/terms-of-use

195. K. van Ingen Schenau, G. Bottiglieri, J. van Schoot, J.-T. Neumann, and M. Roesch, "Imaging performance of the EUV high NA anamorphic system," *Proc. SPIE* **9661**, 96610S (2015) [doi: 10.1117/12.2195476].
196. H. J. Levinson, P. Mangat, T. Wallow, L. Sun, P. Ackmann, and S. Meyers, "Considerations for high-numerical aperture EUV lithography," *Proc. SPIE* **8679**, 867916 (2013) [doi: 10.1117/12.2015829].
197. J. Ruoff, "Impact of mask topography and multilayer stack on high NA imaging of EIV masks," *Proc. SPIE* **7823**, 78231N (2010) [doi: 10.1117/12.864120].
198. V. Philipsen, E. Hendrickx, E. Verduijn, S. Raghunathan, O. Wood, V. Soltwisch, F. Scholze, N. Davydova, and P. Mangat, "Imaging impact of multilayer tuning in EUV masks, experimental validation," *Proc. SPIE* **9235**, 92350J (2014) [doi: 10.1117/12.2066222].
199. Y. J. Jang, J. S. Kim, S. Hong, and J. Ahn, "Phase shift mask to compensate for mask 3D effect at high-NA extreme ultraviolet lithography," *Nanosci. Nanotechnol. Lett.* **8**(9), 729–733 (2016).

Jinho Ahn received his B.S. (1986) and M.S. (1988) degrees from Seoul National University, and his Ph.D. (1992) from the University of Texas at Austin; all three degrees were in materials science and engineering. He worked for Microelectronics Research Laboratory at NEC, Tsukuba, Japan (1993–1995) and joined Hanyang University in 1995 as a Professor of Materials Science and Engineering. He has been a leader of several national projects on advanced lithography. He has authored more than 160 technical papers and invented more than 45 patents. He is currently a member of the National Academy of Engineering of Korea and a board member of the National Nano Infrastructure Association and the National R&D Information Management Committee.

Chan-Uk Jeon received his B.S. degree in electrical engineering (1990) from Yonsei University and was granted an honorary doctorate degree (2013) from Samsung. He joined the semiconductor division in 1989 and has been contributing to the mask technology for 28 years. In 2006, he was dispatched to SEMATECH, where he led the commercialization of the EUV mask, and in 2012, he became the head of the Mask Development Team at Samsung Electronics. Currently, he is in charge of both R&D and mass production of flat panel display and semiconductor masks.

Downloaded From: https://www.spiedigitallibrary.org/ebooks/ on 09 Mar 2022
Terms of Use: https://www.spiedigitallibrary.org/terms-of-use

Chapter 8
Photoresists for EUV Lithography

Robert L. Brainard
SUNY Polytechnic Institute, Albany, New York, USA

Mark Neisser
Kempur Microelectronics Inc., Beijing, China

Gregg Gallatin
Applied Math Solutions, LLC, Newtown, Connecticut, USA

Amrit Narasimhan
GLOBALFOUNDRIES Inc., Albany, New York, USA

8.1 Introduction
8.2 Earliest EUV Resist Imaging
8.3 Absorption Coefficients of EUV Photoresists
- 8.3.1 Definitions of transmission and absorption
- 8.3.2 Early absorption goals
- 8.3.3 A change in absorption goals: from light to dark
- 8.3.4 Measuring absorption of actual resist films

8.4 Mechanisms of Resist Exposure to EUV Light
- 8.4.1 Introduction
- 8.4.2 The physics of EUV exposure mechanisms
- 8.4.3 The chemistry of EUV exposure mechanisms
- 8.4.4 Maximum quantum yield in chemically amplified photoresists
- 8.4.5 Total electron yield in EUV photoresists
- 8.4.6 Mechanisms of acid generation in CARs
- 8.4.7 Electron travel distance in photoresists
- 8.4.8 Conclusions

8.5 Organic Photoresists
- 8.5.1 Polymethylmethacrylate (PMMA) resists
- 8.5.2 Environmentally stable chemically amplified photoresists
- 8.5.3 Low-activation-energy, acetal, or ketal resists
- 8.5.4 Chain-scission resists
- 8.5.5 ArF polymer platforms

Downloaded From: https://www.spiedigitallibrary.org/ebooks/ on 09 Mar 2022
Terms of Use: https://www.spiedigitallibrary.org/terms-of-use

8.5.6 Sulfonium-based resists
8.5.7 High-fluorine resists
8.5.8 Non-polymer-based organic EUV resists
8.6 Characterization of Development Using AFM
8.7 Strategies for Improving Resist Sensitivity: Acid Amplifiers and Photosensitized CARs
8.7.1 Introduction to acid amplifiers
8.7.2 Lithographic capabilities of acid amplifiers in EUV photoresists
8.7.3 Fluorine-stabilized AAs and olefin triggers
8.7.4 Synthesis and preliminary lithographic performance of fluorine-stabilized polymers
8.7.5 Photosensitized chemically amplified resists (PSCAR)
8.7.6 Conclusions
8.8 Metal-Containing Resists
8.8.1 Metal oxide resists from Oregon State University and Inpria
8.8.2 Tin oxide cluster resists from CNSE
8.8.3 Mononuclear metal resists
8.9 LER and Modeling
8.9.1 Background: continuous and stochastic models
8.9.2 Modeling steps
8.9.3 Specific resist models
8.10 Benchmarking Studies: Tool Dependence and Resist Performance
8.10.1 Introduction
8.10.2 Interference lithography
8.10.3 MET imaging
8.10.4 Beta tool and production scanner imaging
8.10.5 Comparison to ArF
8.10.6 Comparison of organic and metal-based resists
8.11 Summary
8.11.1 Background
8.11.2 Mechanism of EUV exposure
8.11.3 Types of resists
8.11.4 Acid amplifiers and PSCAR
8.11.5 LER and modeling
8.11.6 Benchmarking of resists
Notes and References

8.1 Introduction

Extreme ultraviolet lithography (EUVL) has advanced dramatically since its inception in 1986. Progress in EUV research has required an interdisciplinary approach involving partnerships of scientists and engineers within both industry and academics. Contributions from the fields of physics, optics, computer science, business, materials science, and chemistry have been critical to all phases of EUV technical advances.

One of the most important components of EUVL is the technological advancement of photoresists. Although EUV photoresist performance has made dramatic advances over the years, resist requirements are extremely demanding. Since the first edition of this book came out in 2008,[1] several technical challenges have been met in all areas of technology to advance EUVL for use in high-volume manufacturing (HVM) fabs. Most notable have

Downloaded From: https://www.spiedigitallibrary.org/ebooks/ on 09 Mar 2022
Terms of Use: https://www.spiedigitallibrary.org/terms-of-use

been the improvements in source power, reliability and uptime of sources, defect-free masks, and the development and sale of full-field exposure tools. For details, readers are referred to other chapters in this edition of the book that cover these developments. Equally remarkable has been the development of photoresists for use in EUVL.

This review starts by describing the history of the first resists imaged by EUV light, skips several of the important resist accomplishments from 1995 to 2008 since they are well covered in the first edition of this book,[1] and focuses on the accomplishments of resist chemists from 2008 to 2017. The development of photoresists has occurred through the successful collaboration of industry and academia. Typically, the best-performing resists come from industry; however, most industrial research is proprietary, so technical details are generally not publicly disclosed. Fortunately, the role played by academics lends balance to the industry by advancing and evaluating new chemical approaches and publishing the results. This review will cover contributions from both industry and academia, but will primarily emphasize publications that reveal the most information available during each period of research.

8.2 Earliest EUV Resist Imaging

This section reviews the work of several pioneers in the field from 1986 to 1995. This was a time when there were few researchers and many critical problems to solve. The decisions made by these researchers set the foundation upon which today's technology has been built. Perhaps the most critical decision was which wavelength to use. Wavelengths from 5 to 40 nm were considered. The determination of what wavelength to use (~13.5-nm) was made by analysis of the work described in this section.

The earliest published EUV imaging is that of Kinoshita et al. in Japan in 1986[2] and a few years later in the U.S. in 1989.[3] In Kinoshita et al.'s work, the developed depth of poly(methyl methacrylate) (PMMA) was plotted against the incident absorbed dose for 5- and 11.8-nm light (Fig. 8.1). The 11.8-nm light leveled off at a depth of ~90-nm film thickness, whereas the 5-nm light easily penetrated to 300 nm of PMMA. These results led Kinoshita and coworkers to conclude that bilayer processes would need to be developed for imaging wavelengths of 10 nm or greater.

Kinoshita et al. built a Schwarzschild 1/8 reduction optic with two spherical mirrors for use at 5- and 12.4-nm wavelengths. The spherical mirrors were coated with carbon and tungsten multilayers (MLs), but no reflectivity values were reported for these mirrors.[2,3] They printed 500-nm lines in PMMA using 12.4-nm light and a reflection mask. The NA was estimated to be >0.032. Similarly, they printed 1.0-μm trenches using a positive-tone bilayer resist—silicone-based positive photoresist (SPP) and the OFPR-Novolak resist (developed by TOK).[6] The top SPP layer was 50-nm thick and

Downloaded From: https://www.spiedigitallibrary.org/ebooks/ on 09 Mar 2022
Terms of Use: https://www.spiedigitallibrary.org/terms-of-use

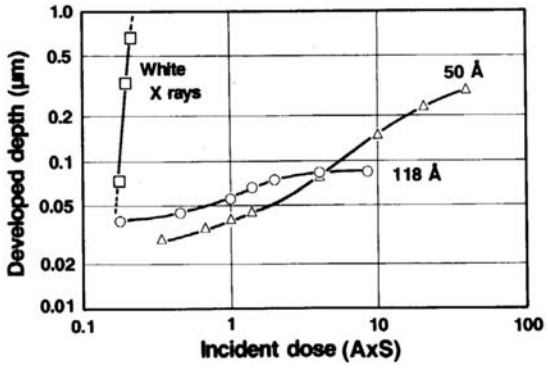

Figure 8.1 Spectral characteristics of a PMMA resist using 5 nm, 11.8 nm, and white x rays (reprinted from Ref. 3 with permission; © 1989 American Vacuum Society).

was exposed using the stencil mask and 12.4-nm light, followed by O_2 reactive ion etching (RIE), producing fairly vertical profiles (Fig. 8.2).[3–5]

In 1990, Bjorkholm et al. first published their work about printing images into PMMA films using 14-nm light.[7] They used a Schwarzschild objective with a molybdenum-silicon (Mo/Si) ML coating to provide ~40% reflectivity at 14 nm. They printed 50-nm lines in a 60-nm film of PMMA on primed Si (Fig. 8.3). They also printed 100- and 150-nm dense lines using a trilayer resist composed of PMMA/germanium/hard-baked photoresist. They successfully transferred the pattern in PMMA (60-nm thick) to the germanium (Ge) and a hard-baked resist using RIE with CF_3Br, then oxygen. The resulting patterns showed excellent line-edge roughness (LER).[8–10]

In 1991, Mansfield et al. measured the lithographic parameters of PMMA at 37.5- and 14-nm and used them to simulate resist profiles.[11] They

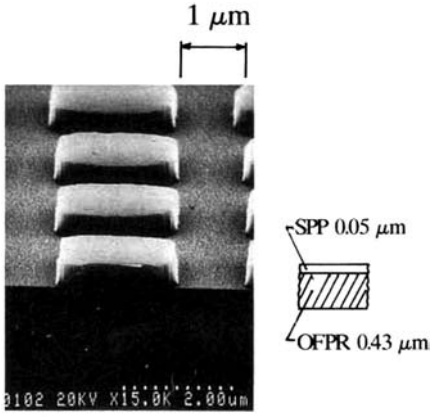

Figure 8.2 Scanning electron microscopy (SEM) micrograph of a 1.0-μm line pattern in a Si-based negative resist/over PMMA (OFPR) as a planarizing layer (reprinted from Ref. 3 with permission; © 1989 American Vacuum Society).

Downloaded From: https://www.spiedigitallibrary.org/ebooks/ on 09 Mar 2022
Terms of Use: https://www.spiedigitallibrary.org/terms-of-use

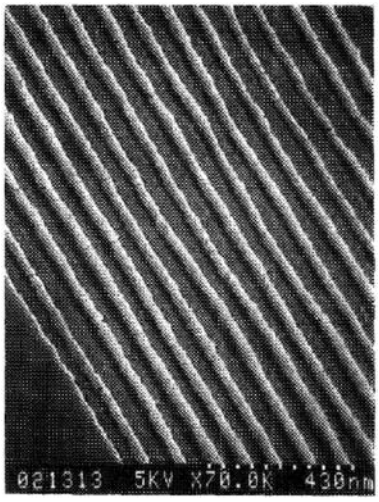

Figure 8.3 SEM micrograph showing 50-nm lines and spaces printed in 60 nm of PMMA on Si using 14-nm EUV light (reprinted from Ref. 7 with permission; © 1990 American Vacuum Society).

determined the resist thickness removed as a function of dose at 37.5 nm and 14 nm. They also determined the clearing dose E_0 for 60-nm films of PMMA to be 23 and 55 mJ/cm^2 for 37.5- and 14-nm light, respectively. Similarly, they also determined the volumetric sensitivity to be 3000 J/cm^3 for both wavelengths using

$$\text{Volume sensitivity} \equiv (E_0 \times \text{absorbance})/\text{film thickness}. \tag{8.1}$$

The identical values of PMMA volumetric sensitivity for these two wavelengths indicate that the exposure mechanism[12,13] depends only on the amount of energy absorbed, not on the number of photons absorbed. This further indicates that the film quantum yield[14] for the PMMA imaging mechanism is higher with higher energy photons, since 37.5-nm light has 2.7× more photons/mJ than 14-nm light. According to this result, the 14-nm light would have 2.7× higher film quantum yield. Mansfield et al. determined the Dill B and C parameters (absorption and optical sensitivity, respectively)[15] using 37.5- and 14-nm light by a combination of fitting their experimental data and by using Henke's data (Table 8.1).[16,17] The modeling predicted that the sidewall angle in 200-nm dense lines printed with 37.5-nm light in 60-nm-thick films of PMMA would be much shallower than when using 14-nm light as verified by cross-sectional SEM.

In 1992, Early et al.[19,20] evaluated a series of variables in pursuit of high-resolution imaging: radiation type (14-nm EUV light, 50-keV e-beam); resist type (negative chemically amplified resist AZ PN114[21] and PMMA); film thickness (50–200 nm); substrate (Si and trilayer); developer (NaOH,

Downloaded From: https://www.spiedigitallibrary.org/ebooks/ on 09 Mar 2022
Terms of Use: https://www.spiedigitallibrary.org/terms-of-use

Table 8.1 PMMA B and C parameters determined by Mansfield et al.[11] using their experimental data and by using the Website for the Center for X-ray Optics (CXRO) at Lawrence Berkeley National Laboratory (LBNL).[16–18]

	B Parameter (base e Absorbance)		C Parameter
Wavelength	**Mansfield**	**CXRO-LBL**	**Optical Sensitivity**
14 nm	6.2/μm	5.6/μm	0.01 cm^2/mJ
37.5 nm	26/μm	35/μm	0.042 cm^2/mJ

TMAH); and post-exposure bake (PEB) temperature (105–115 °C). This work demonstrated three interesting aspects:

- the first 75-nm dense lines using a chemically amplified resist (PN114);
- studies of pinhole density versus film thickness studies; and
- early investigations into LER and discussions of shot-noise effects.

The AZ PN114 resist was coated in a 50-nm film over primed Si, and exposed with 14-nm light using a 20X Schwarzschild camera ($NA = 0.08$). These conditions allowed the resist to print 75-, 100-, and 150-nm lines at 10 mJ/cm^2, but it did not resolve 50-nm dense lines. The pinhole density was studied using a defect magnification technique[19] and was found to increase dramatically with decreasing film thickness of AZ PN114 (Table 8.2). This pinhole data raised important questions about the possibility of single-layer resist films to remedy the imaging issues encountered with higher absorbance. Lastly, this group compared the LER of PMMA and PN114 in 100- and 200-nm dense lines. Unfortunately, this LER study was performed using e-beam (50 keV) rather than EUV light.

Kubiak et al.[22] compared the imaging and modeling of PMMA and SAL601 using a 20X Schwarzschild optic with 13.9-nm EUV light. They experimentally measured the absorbance of PMMA at 13.9 to be 5.95 1/μm (nearly identical to calculations)[16,17] and a C-parameter of 0.42 cm^2/mJ. They calculated the absorbance of SAL601 making assumptions about composition and density (~1.14 g/cm^3). They also determined the C-parameters from the contrast curves shown in Fig. 8.4.

Dense lines (100 nm) were printed from 100-nm-thick films of PMMA, and 150-nm dense lines from 120-nm-thick films of the negative resist

Table 8.2 Pinhole densities found in spin-cast films of AZ PN114.

Thickness (nm)	Pinholes (1/cm^2)
380	0.2
250	1
100	4
50	15

Downloaded From: https://www.spiedigitallibrary.org/ebooks/ on 09 Mar 2022
Terms of Use: https://www.spiedigitallibrary.org/terms-of-use

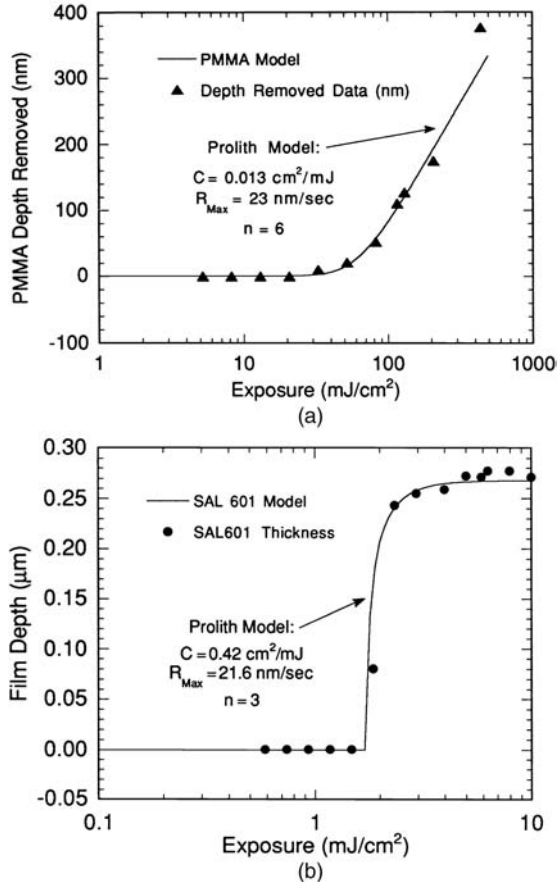

Figure 8.4 (a) Exposure sensitivity curves of PMMA. (b) SAL 601 at 13.9 nm (points) and best-fit model sensitivity curves (solid lines) (reprinted from Ref. 22).

SAL601. Optical modeling predicted that PMMA would print 135-nm lines with a sidewall angle of ~79 deg, whereas the negative resist SAL601 would print lines with re-entrant wall angles of ~85 deg.

In 1994, Wood et al.[23,24] performed a series of experiments to fully investigate the wavelength options for EUVL. They assembled three Schwarzschild cameras that used 37.5-, 13.9-, and 6.8-nm light. Characteristics for each camera and some resist results are summarized in Table 8.3. The 37.5 wavelength was evaluated because it is the shortest wavelength that can be used without resorting to ML technology for reflective surfaces in the optic. The 37.5-nm camera was fabricated using spherical mirrors coated with iridium (Ir) since these coatings can attain reflectivities as high as 20%.[25,26] Molybdenum-silicon MLs were used in the 13.9-nm camera and are available today near the theoretical reflectivity of 68%. Carbon-based MLs were used in the 6.8-nm camera and provided only poor reflectivity.

Downloaded From: https://www.spiedigitallibrary.org/ebooks/ on 09 Mar 2022
Terms of Use: https://www.spiedigitallibrary.org/terms-of-use

Table 8.3 Summary of characteristics for three Schwarzschild cameras and resist results.

	Optic		PMMA Resist			PN114 Resist	
Wavelength (nm)	Reflective Surface	NA	Absorbance* (1/μm)	E size (mJ/cm^2)	Sidewall Angle	Absorbance* (1/μm)	Sidewall Angle
37.5	Iridium	0.113	37	80	19 deg	–	–
13.9	Mo/Si Multilayer	0.0835	5.95	66	65 deg	4.4	Undercut ~75 deg
6.8	Ru/B4C Multilayer	0.07	1.2	–	87 deg		Nearly Vertical

*Absorbance values taken from Kubiak et al.,[27] except PMMA at 37.5 and 6.8 nm, which were calculated.[16,17]

Table 8.3 shows the results of printing 500-nm dense lines in 60-nm-thick PMMA. Sidewall angles were measured using scanning tunneling microscopy (STM) and by measurement of cross-section SEMs. PMMA optical density was determined experimentally by Kubiak[22,27] or through calculation.[16,17] The PMMA absorption coefficient increases dramatically with increasing wavelength; consequently, the sidewall angle decreases at longer wavelengths. Wood et al. concluded that wavelengths shorter than 13.9 should be pursued for increased transparency and steeper sidewall angles, and they also concluded that bilayer or trilayer resist schemes may be necessary for EUVL to remedy problems such as pinholes and low etch resistance.

8.3 Absorption Coefficients of EUV Photoresists

The absorption of imaging light is one of the most important resist properties.[28] Photoresist absorption of EUV light is just as important as in the previous four lithography wavelengths; however, the mechanism by which EUV photons are absorbed is very different from the mechanisms for absorbance of longer wavelengths (157 to 365 nm). At longer wavelengths, the light interacts with the molecules in the resist by exciting an electron from a filled molecular orbital to an empty orbital (Fig. 8.5). In EUVL, however, the 92-eV photons remove electrons from the molecule, creating high-energy electrons (~80 eV) and holes. One important consequence of these mechanistic differences is that the EUV absorption is primarily determined by the elemental composition and mass densities of the resist—not the precise arrangement of these elements within the molecule (its structure) as it is at longer wavelengths.

8.3.1 Definitions of transmission and absorption

The absorption by the film depends both on the resist thickness t and the absorbance A, also referred to as the absorption coefficient, of the resist material. The absorbance A is a per-unit distance, and t must be in the same distance units. For resist films, t is usually in microns and A is per micron.

Downloaded From: https://www.spiedigitallibrary.org/ebooks/ on 09 Mar 2022
Terms of Use: https://www.spiedigitallibrary.org/terms-of-use

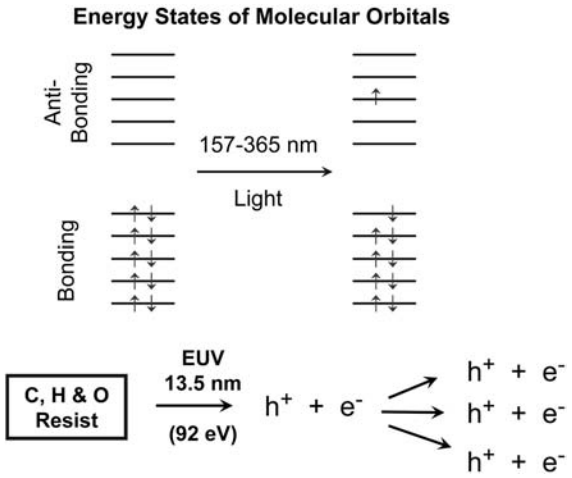

Figure 8.5 Comparison of exposure mechanisms at EUV and longer wavelengths (reprinted from Ref. 1).

A source of great confusion is the fact that absorbance using both the base e and the base 10 definitions are in common practice. Care must be exercised in comparing literature values for absorbance since the base e value will always be 2.303 times larger than the value reported at base 10. Whenever possible, base e values will be used in this chapter. The transmission and absorption of a resist film are defined as

$$\text{Transmission} \equiv I/I_o = e^{At}, \tag{8.2}$$

$$\ln(I_o/I) = At = 2.303\log(I_o/I), \tag{8.3}$$

$$\text{Absorption} = 1 - \text{Transmission}. \tag{8.4}$$

In Eqs. (8.2)–(8.4), I_o is the incident light intensity, and I is the intensity after the light has passed through the resist film. A is the absorbance per unit thickness, and t is the thickness of the film, so At is a dimensionless number specific to a particular film thickness. The absorbance A is equivalent to the sum of the Dill A and Dill B parameters. For EUV absorption there is no bleaching of the resist film, so the Dill A parameter is 0. Thus, the absorbance A is the same as the Dill B parameter.

8.3.2 Early absorption goals

The atomic absorption cross-section tables published by Henke, Gullikson, and Davis[16,17] have been the cornerstone for many of the absorption values determined in EUVL. A qualitative representation of absorption coefficients of many of the elements in the periodic table provides insight into the relationship between absorption and chemical composition (Fig. 8.6).[29]

Downloaded From: https://www.spiedigitallibrary.org/ebooks/ on 09 Mar 2022
Terms of Use: https://www.spiedigitallibrary.org/terms-of-use

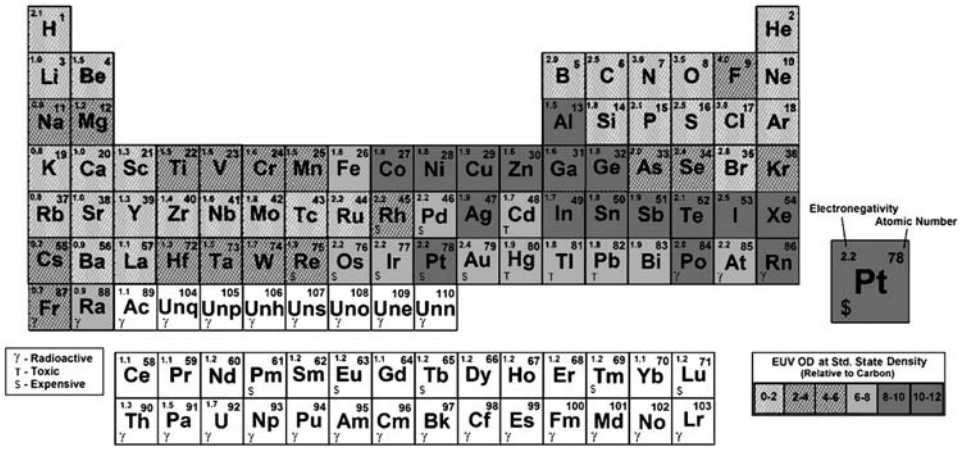

Figure 8.6 The periodic table with respect to EUV optical density (reprinted from Ref. 29).

Heavy elements tend to be darker than light elements. Historically, developing resists for new imaging wavelengths has always involved a struggle to find resist materials that were transparent enough to provide straight sidewalls in printed features. For example, transparency has been an important principle driving the development of new polymers for i-line (365 nm, novolaks), deep ultraviolet (DUV) (248-nm, polyhydroxystyrene), 193-nm (aliphatic esters), and 157-nm (fluoropolymers) lithographies. Similarly, during the first years of EUVL, when resist films were 100–300 nm thick, resist chemists made a number of efforts to increase the transparency of the resists. In 2004, Dai and Ober developed a boron-containing photoresist with the idea that its high transparency at EUV wavelengths was desirable.[30] In 2006, Kwark et al.[31] measured absorbance of resist films and suggested not only that low absorbance was desirable, but that lowering the density of resist films might be a good way to achieve this.

8.3.3 A Change in absorption goals: from light to dark

Three key papers in 2008 caused the resist community to reconsider their efforts to make more-transparent resists and to instead make darker resists. Kozawa et al. did a study of 22-nm line-and-space (L/S) imaging using EUV light, focusing on the tradeoff between sensitivity, resolution, and line edge roughness.[32] The researchers found that for resist systems formulated for low doses, there was not enough contrast in the latent image and unacceptable line edge roughness would be expected, assuming imaging was still feasible. They recommended increasing resist absorption and/or acid generation efficiency per photon. Sasaki et al. investigated EUV resists made with main-chain fluorinated polymers with the idea that this would increase EUV absorbance and thus increase EUV photospeed.[33] These author found that the fluorinated

Downloaded From: https://www.spiedigitallibrary.org/ebooks/ on 09 Mar 2022
Terms of Use: https://www.spiedigitallibrary.org/terms-of-use

polymers gave up to 10X better photospeed than nonfluorinated polymers. Additionally, they detected small amounts of HF in the fluorinated polymers after exposure to EUV light, but did not determine the extent to which this contributed to the improvements in photosensitivity.

In 2008, Gronheid, Van Roey, and Van Steenwinckel investigated EUV resist performance as a function of resist thickness.[34] They found that linewidth roughness (LWR) increased as films got thinner and attributed this to reduced absorption of EUV light by the thinner films. Gronheid et al. continued this work in 2009[35] and suggested that the best optical density for printing 22-nm dense lines in 50-nm resist films is 10/μm. This recommended absorbance was much larger than the absorbance of the commercial EUV resist (3.88/μm) they were using at the time.

In 2011, Thackeray discussed absorbance of EUV resists and proposed using fluorine to increase absorbance.[36] However, he noted that for the resist thicknesses needed for sub-20-nm imaging, even perfluorotetraethylene would not have as much EUV absorption as is desirable. He noted that non–chemically amplified resists could reduce noise in imaging and thus reduce LWR, but that they typically had slow photospeeds. In this time frame, many other papers also proposed increasing EUV resist absorbance. For example, in 2011 Yamashita used fluorine to do this,[37,38] in 2012 Ongayi reported using polymer-bound fluorine containing chromophores to increase absorption,[39] and in 2013 Christianson also used fluorinated materials with the goal of increasing absorbance.[40]

Despite the high absorptivity of metals (Fig. 8.6), and published demonstrations of EUV-sensitive, metal-based resists, no one proposed metal-based resists as a solution for getting enough EUV absorption until Neisser, Cho, and Petrillo suggested it in 2012.[41] Metal-based EUV resists have proved to be a promising and active area of research and are discussed in Section 8.8.

8.3.4 Measuring absorption of actual resist films

The measurement of resist film absorption can be done by several methods. One way is to do a straightforward absorption measurement. One of the first measurements of this kind was done in 1992 by Kubiak et al.,[27] who determined the absorbance of several thicknesses (75 to 500 nm) of PMMA coated on 360-nm thick membranes of Si_3N_4. Another example is the 2007 work by Garg, Antohe, and Denbeaux.[42] In 1999, Matsuzawa et al.[43–45] combined Bicerano's graph-theoretical[46] method for calculating polymer density with the Henke elemental absorption coefficients[16,17] to predict the absorption coefficients of 150 polymers using EUV light (13.5 nm). The researchers found that polymers used in i-line, DUV, and 193-nm photoresists all had roughly similar transmission of ~30% for 300-nm films, and ~65% for 100-nm films, respectively. As expected, they found that low density made

Downloaded From: https://www.spiedigitallibrary.org/ebooks/ on 09 Mar 2022
Terms of Use: https://www.spiedigitallibrary.org/terms-of-use

polymers more transparent. They found that silane polymers had exceptionally low absorbances and fluoropolymers give high absorption values.

One can also measure absorbance by using reflectivity methods. In 2002, Irie et al.[47,48] experimentally measured the EUV transmittance of thin films prepared from 8 polymers and 11 photoresists by coating these materials onto Mo-Si MLs and measuring their reflectivity over a range of reflection angles. The authors concluded that polymers high in carbon and silicon would be relatively transparent, whereas polymers containing fluorine would have low transparency. They also concluded that the addition of ~10% photo-acid generator (PAG) would not make the resist absorption significantly different from that of the polymer. In 2006, Kwark et al.[31] measured the absorbance of various polymer films by using grazing-incidence synchrotron-generated EUV light. They found that the absorbance of various polymers ranged from 2/μm to 7/μm, with the highest absorbance being for a fluorinated polymer. They also found a good correlation between experimental and calculated EUV absorbance. They suggested adding silicon to improve transparency, provided not too much oxygen was added at the same time.

A third method is to combine the measured resist density and the resist atomic composition, determined either from measurement or calculation, with the tabulated absorption coefficients of individual atomic species to predict the film absorbance. This method is sensitive to errors in film density measurement, which are relatively large given the thickness of films used in lithography and the possible presence of solvents or other impurities in actual resist films.

Some papers have compared different methods of determining film absorbance of EUV light. In 2003, Chandhok et al.[49,50] examined four methods for evaluating the absorption of the EUV tool test resist, EUV-2D.[51] The first two methods experimentally determined the density followed by the absorption calculation.[16,17] The first method uses the ratio of the weight of the resist film divided by its volume determined by thickness measurements. The weight divided by the volume is the density. The second method measured the density using specular x-ray reflection at a grazing angle of incidence. For both of these methods, the known atomic composition was then used to calculate an EUV absorbance using the measured density. The third method measured the s-polarization reflectivity as a function of incident angle on a 120-nm film of EUV-2D. The fourth method involved coating EUV-2D resist onto an EUV mirror and measuring reflectivity. The first method gave an absorbance estimate of 4.6/μm. The other three methods roughly agreed and gave absorbance measurements of 4.07/μm to 4.2/μm. Unlike the first method, the last three methods all require an EUV light source. In this case, the values reliant on calculation are higher than the measured values. But this is not always the case. The work by Kwark et al. discussed above[31] compared calculated absorbances with absorbances measured by grazing reflectivity and

Downloaded From: https://www.spiedigitallibrary.org/ebooks/ on 09 Mar 2022
Terms of Use: https://www.spiedigitallibrary.org/terms-of-use

found generally good agreement. In 2015, Sekiguchi et al. reported comparisons between calculated and measured values. They found that the calculated values were higher than the measured ones for a number of materials.[52] In 2016, Fallica et al. did measurements of a number of different types of resists, including metal-based resists, and compared them to calculated values and also found reasonable agreement between calculated and measured absorbance. They also defined a resist parameter they called *chemical sensitivity*, which is the inverse of the *volume* sensitivity parameter defined in Eq. (8.1).[53]

8.4 Mechanisms of Resist Exposure to EUV Light

8.4.1 Introduction

The large change in wavelength between 193-nm and 13.5-nm (EUV) light produces an enormous improvement in resolution, yet it also creates new challenges for resist chemists since the mechanism of EUV exposure is completely different from the mechanisms previously encountered using 193- or 248-nm light. In particular, the absorbance of 193-nm photons causes molecular electrons to be excited from ground state to an excited state *within the same molecule* (Fig. 8.6). In contrast, the absorption of EUV photons causes molecular electrons to be ejected from the molecules with ~75–82 eV energy, leaving a radical-cation "hole" in the molecule.[54–58] These liberated electrons have sufficient energy to induce further ionization or other reactions. It is these electrons and their holes that provide the chemical transformations needed to produce solubility changes in photoresists. Therefore, understanding the reactivity of electrons and holes is key to optimizing the performance of future EUV photoresists.

The exposure mechanisms that occur in chemically amplified resists (CARs) during exposure to 193- or 248-nm light are well understood.[59,60] For example, either the photon is absorbed by a PAG, creating an excited state in the PAG, or the photon is absorbed by the polymer, which can then sensitize a PAG molecule. At these wavelengths, the resist components can be tailored to minimize photon absorption in the polymer and maximize photon absorption by the PAG.[59] Because the concentration of reacting species is known, the quantum yields of these reactions are also known. Furthermore, at these longer wavelengths the quantum yields of PAG exposure do not exceed 100%.[61]

However, in EUVL, the underlying physical and chemical mechanisms of EUV exposure are areas of active research, and many of the fundamental questions remain unanswered. This section aims to address some of these topics and provide an overview of research that attempts to answer specific questions, namely:

1. What are the elementary physical and chemical mechanisms in EUV photochemistry? (Sections 8.4.2 and 8.4.3)

Downloaded From: https://www.spiedigitallibrary.org/ebooks/ on 09 Mar 2022
Terms of Use: https://www.spiedigitallibrary.org/terms-of-use

2. What is the total number of electrons generated (total electron yield) during EUV exposure? (Sections 8.4.4 and 8.4.5)
3. How does total electron yield impact our mechanistic understanding of EUV chemistry, specifically in CARs? (Section 8.4.6)
4. How far do electrons generated in EUV exposure travel in resists? (Section 8.4.7)

8.4.2 The physics of EUV exposure mechanisms

In EUVL, photons can interact strongly with any resist components, generating electrons through photo-ionization. An initial photoelectron with an energy range of about 75–82 eV may cause further ionization in the resist, generating additional electrons that contribute to the chemical reactions during exposure. In this section, we describe the physics of the interactions of these electrons as they interact with molecules from their initial creation with energies of ~80 eV until they decay to energies of ~2 eV.

There are four underlying elementary interactions between these ~2–80 eV photo- and secondary electrons[62] (Fig. 8.7):

1. **Photo-ionization**: a photon is absorbed by an atom and liberates an electron with enough kinetic energy to interact further. The ionized resist component may yield further electrons or charged ion fragments through electronic and atomic relaxation proceses.[58]
2. **Electron ionization**: a ballistic electron scatters off an atom and produces another electron such that the total kinetic energy of the two electrons equals the energy of the incident electron less the binding energy of the "daughter" electron.
3. **Plasmon generation**: an incident electron scatters off an atom, losing energy and causing a coherent displacement wave in the bound electrons. It is currently unclear if plasmons can be an additional source of electron–hole pairs.

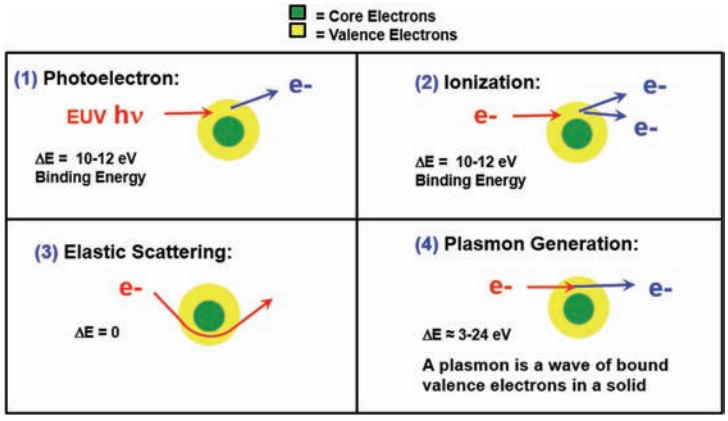

Figure 8.7 A schematic drawing of the four elementary physical electron–matter interactions described above (adapted from text in Ref. 62).

Downloaded From: https://www.spiedigitallibrary.org/ebooks/ on 09 Mar 2022
Terms of Use: https://www.spiedigitallibrary.org/terms-of-use

4. **Elastic scattering**: the trajectory of an incident electron is altered by the Coulombic potential of an atom with no associated energy loss. In CARs, ionization and plasmon generation of PAG or polymer may directly produce acid.[55]

In order to understand the interactions of electrons with molecules in resist films, we must learn from the excellent research being conducted in the gas phase by atmospheric scientists. These gas-phase experiments can provide precise and useful data to help the EUV community understand EUV resist mechanisms. However, these experiments do not account for phenomena such as molecular dampening or cage recombination that are present in condensed-phase interactions, and thus must be interpreted with care. An excellent review of electron-induced chemistry by W. F. van Dorp[54] provides a summary of this work and suggests applications to EUV resist exposure mechanisms. This work divides these eight interactions (Fig. 8.8) into three broad categories: (1) electron impact ionization, (2) electron attachment, and (3) electron excitation. In electron impact ionization (Fig. 8.8, Eqs. 1–3), following the interaction of a molecule with the initial electron, charged species are generated either as a charged molecule and additional electrons, or as at least one charged molecular component (i.e., a bond is broken) sometimes accompanied by an additional electron. (2) In electron attachment (Fig. 8.8, Eqs. 5 and 6), an electron can attach to a molecule, thereby occupying a higher energy orbital and creating a charged molecule, which may ultimately lead to the dissociation of the molecule (known as dissociative electron attachment, or internal excitation). (3) In electron excitation, (Fig. 8.8, Eqs. 4, 7, and 8) an energetic electron may donate some energy to a nearby molecule, elevating a bound electron to a higher energy, and thus exciting the molecule. This excited molecule may then dissociate into neutral species.

$$AB + e^- \rightarrow AB^{n+} + e^-_{scattered} + ne^-_{emitted} \quad \text{(ionization, single, or multiple)} \quad (1)$$

$$\rightarrow A + B^+ + e^-_{scattered} + e^-_{emitted} \quad \text{(dissociative ionization)} \quad (2)$$

$$\rightarrow A^+ + B^- + e^-_{scattered} \quad \text{(ion pair formation)} \quad (3)$$

$$\rightarrow AB^* + e^-_{scattered} \quad \text{(excitation)} \quad (4)$$

$$\rightarrow AB^{-*} \quad \text{(attachment)} \quad (5)$$

$$\rightarrow A + B^- \quad \text{(dissociative attachment)} \quad (6)$$

$$\rightarrow A + B + e^-_{scattered} \quad \text{(dissociation into neutrals)} \quad (7)$$

$$\rightarrow A^* + B + e^-_{scattered} \quad \text{(dissociation into excited neutrals)} \quad (8)$$

Figure 8.8 The physical interactions of electrons with molecular species as chemical equations (adapted from Ref. 54).

Downloaded From: https://www.spiedigitallibrary.org/ebooks/ on 09 Mar 2022
Terms of Use: https://www.spiedigitallibrary.org/terms-of-use

8.4.3 The chemistry of EUV exposure mechanisms

Researchers[55,56,60,63–68] have proposed that the dominant chemical mechanisms involved in EUV CARs include: (1) electron trapping (or dissociative electron attachment), (2) hole-initiated chemistry, or (3) internal excitation (or dissociative electron excitation), as illustrated in Fig. 8.9. In electron trapping, a low-energy electron (perhaps 0–5 eV[54]) may be trapped by a PAG molecule, thereby occupying an antibonding orbital in the PAG. This leads to a change in the electronic structure of the PAG, causing the molecule to fall apart.[55,62,63] (2) Holes left in ionized atomic species within the resist may also contribute to resist chemistry.[55,63] A hole on a polymer may lead to a disproportionation reaction with other polymer side-chains, ultimately producing acid on its own. Additionally, (3) electrons of higher energy (10–80 eV) in resists may deposit energy by exciting electrons from bonding to antibonding states in PAG molecules. This excited PAG molecule may then dissociate to produce acid.[64]

Electrons also interact with polymers directly.[65,69,70] Enomoto et al. exposed different polymers to increasing doses of e-beam (90 keV) and analyzed the resulting resist through gel permeation chromatography.[65] They observed that PHS-type chemically amplified photoresists exhibited cross-linking, while poly-2-methyladamantane-2-methacrylate underwent chain scission upon exposure, similar to PMMA. High-dose e-beam exposure of polystyrene was also posited by Narasimhan et al. to cause a high degree of backbone conjugation that ultimately lead to e-beam-induced fluorescence.[64] Fedynyshyn et al. have demonstrated the relationship between resist polymer composition and clearing dose E_0,[69] and calculated chain scission and crosslinking reaction quantum yields in polymers due to EUV exposure.[70]

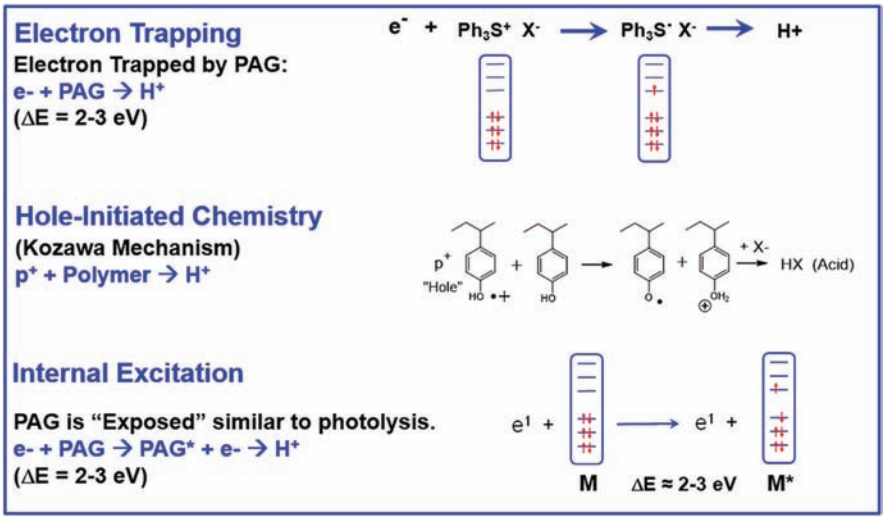

Figure 8.9 Chemical mechanisms of EUV exposure (reprinted from Ref. 71).

Downloaded From: https://www.spiedigitallibrary.org/ebooks/ on 09 Mar 2022
Terms of Use: https://www.spiedigitallibrary.org/terms-of-use

8.4.4 Maximum quantum yield in chemically amplified photoresists

Research by Higgins et al.[72,73] and Hirose, Kozawa, and Tagawa[74] determined film quantum yields (FQYs) of acid production during EUV exposure by formulating CARs with an acid-sensitive dye (Coumarin-6) to measure the concentration of acid in a film with UV/Vis absorbance spectroscopy. These researchers determined FQYs for resists containing three different PAGs at concentrations ranging from 0–1000 mM. Ultimately, the FQYs of these resists were shown (Fig. 8.10) to plateau at PAG concentrations greater than 600 mM, with iodonium PAGs producing more acid than sulfonium or nonionic PAGs at all concentrations. More importantly, this work demonstrated a maximum FQY of 4.9–5.9 acids per photon for the iodonium PAGs.[72,74]

8.4.5 Total electron yield in EUV photoresists

In EUVL, FQYs for PAGs have been shown to exceed 100%. In a single initial ionization process, one EUV photon is absorbed, so greater-than-unity quantum yields indicate that the number of electrons generated plays a large role in resist sensitivity. Work carried out by several groups[55–57] suggests that the total electron yield (TEY) from EUV absorption is ~2–4 electrons per absorbed photon ($e^-/h\nu$). The exact TEY value is not important, but these greater-than-unity numbers influence the mechanistic understanding of the EUV exposure process. In general, these studies are approached through either experimentation or modeling. In either case, studies may build upon assumptions that are carried over from research that may or may not be directly applicable to EUVL (e.g., gas phase, or exposure with keV electrons or photons).

Quantum yield measurements of acid produced in EUV exposure carried out by the groups of Brainard, Kozawa, and Tagawa have shown film quantum yields up to ~6 acids per absorbed EUV photon. Typical photochemical

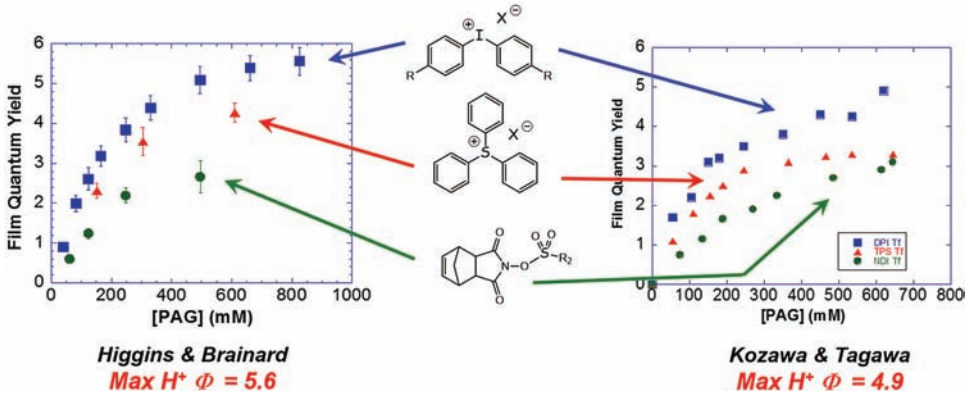

Figure 8.10 Film quantum yields for an iodonium, sulfonium, and non-ionic PAG measured by two groups using absorbance measurements of protonated Coumarin-6 (data from Refs. 72 and 74 used with permission from SPIE and The Japan Society of Applied Physics, respectively).

Downloaded From: https://www.spiedigitallibrary.org/ebooks/ on 09 Mar 2022
Terms of Use: https://www.spiedigitallibrary.org/terms-of-use

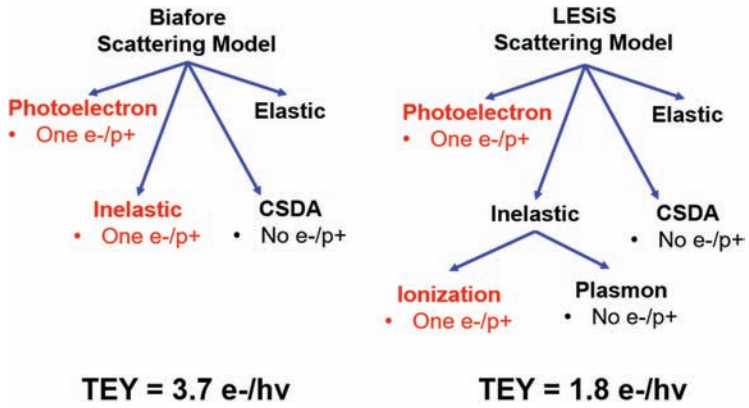

Figure 8.11 Similar electron scattering models developed by two different groups predict different TEYs based on different handling of input parameters such as ionization (or inelastic) cross-sections. The continuous slowing-down approximation (CSDA) handles residual energy loss to the stopping power of the material [adapted from the text in Refs. 75 (left) and 62 (right)].

reactions have yields of 60–100%, so it may seem that 6–10 electrons are required to yield 6 H^+. To investigate this claim, several groups have used Monte Carlo modeling (Fig. 8.11) to simulate EUV exposures. LESiS (low-energy electron scattering in solids), developed by Ocola and Brainard, predicted 1.8 ± 0.8 electron per absorbed photon ($e^-/h\nu$).[56] Similar modeling, developed by Biafore et al. and used with PROLITH by De Schepper et al. predicts 3.69 ± 0.08 $e^-/h\nu$.[57,75] Additionally, Kozawa and Tagawa predict 4.2 $e^-/h\nu$, using assumptions from higher energy radiation physics.[55]

Experiments by De Schepper et al. estimate 4.2 ± 0.3 $e^-/h\nu$ for a standard EUV resist.[57] These researchers contacted the back of a conductive substrate to ground through an ammeter, and then coated a 50-nm resist on top. They then measured the current flowing into the substrate while exposing the resist to 5- to 500-nm light. In this experiment, the charge imbalance created by electrons scattering out of the film is compensated by a current into the substrate. By measuring the compensating current and adjusting for the resist absorption at the exposure wavelengths, the group then calculated the TEY. Further experimentation should be carried out to validate these results.

8.4.6 Mechanisms of acid generation in CARs

Kozawa and Tagawa of Osaka University have conducted excellent work in understanding the photo- and radio-chemistry of photoresists. Of particular importance to EUVL is their work in pulse radiolysis to understand electron–polymer and electron–PAG interactions. Their review of this work in 2010 summarizes many of their findings.[55]

Due to the difficulty of studying thin polymer films, and especially of generating EUV photons, many early pulse radiolysis experiments were

Downloaded From: https://www.spiedigitallibrary.org/ebooks/ on 09 Mar 2022
Terms of Use: https://www.spiedigitallibrary.org/terms-of-use

conducted with model resist solutions and 75-keV electrons. In these pulse radiolysis experiments,[55,76–78] a quartz cell is loaded with a chosen solution, in many cases a polymer, PAG, and sometimes Coumarin-6, all dissolved in tetrahydrofuran. High-energy electrons are injected into the system, and the transient UV-Vis-IR absorbance is measured. The reaction of the high-energy electron, now solvated, with solution components can be monitored via the absorbance of the solution (at a particular wavelength) over a short period, usually several picoseconds. This is referred to as a kinetic trace in these experiments (Fig. 8.12).

These kinetic traces are useful for monitoring the rate of reactions of thermalized (<1 eV) electrons in the presence of different polymers or PAGs. Through this work, as well as measurements of acid yield through acid-sensitive dye experiments (Section 8.4.3), Kozawa and Tagawa have arrived at a proposed mechanism for acid production in chemically amplified EUV resists. Their proposal is best summarized by Thackeray et al. (Fig. 8.13).[63]

Hole-initiated chemistry. In this mechanism (Fig. 8.13), (1) an EUV photon is directly absorbed by the polymer matrix, liberating a photoelectron and leaving a charged radical on the polymer side group. (2) The radical cation polymer undergoes a disproportionation reaction with a nearby unexposed polymer unit, creating a neutral radical and a cationic polymer group. (3) The primary electron, or any other secondary electron, interacts with a PAG through electron trapping (dissociative electron attachment) to release the acid anion. (4) The acid anion reacts with the radical polymer group created in step 2, and the acid is "released."

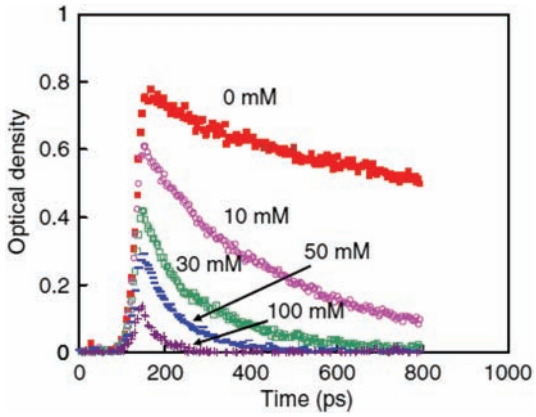

Figure 8.12 Kinetic traces (absorbance at 1300 nm versus time) for several concentrations of the PAG triphenylsulfonium tris(trifluoromethansulfonyl)methane. High-energy electrons are injected at $t = 100$ s and are thermalized (i.e., their energies are <1–2 eV) by approximately 100 ps. It can be observed that these thermalized electrons react (and thus their signal decays) faster with increasing concentrations of PAG in solution [reprinted from Ref. 55 with permission; © (2010) The Japan Society of Applied Physics].

Downloaded From: https://www.spiedigitallibrary.org/ebooks/ on 09 Mar 2022
Terms of Use: https://www.spiedigitallibrary.org/terms-of-use

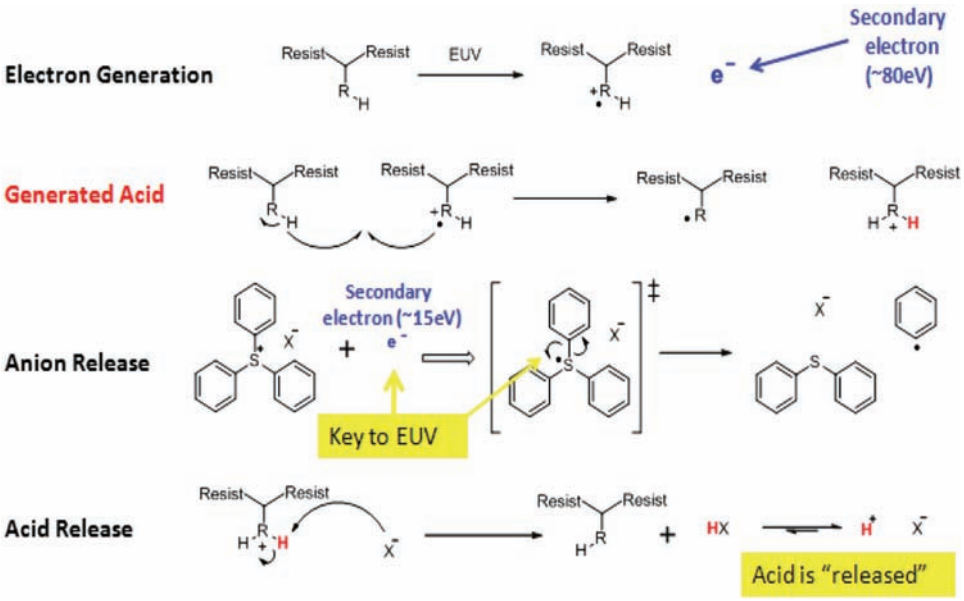

Figure 8.13 A mechanism for the generation of acid in CARs, proposed by Kozawa and Tagawa, and summarized by Thackeray et al. (reprinted from Ref. 63).

This mechanism is built on several assumptions—principally, that direct acid generation due to the absorption of EUV photons by PAG molecules is rare and only becomes appreciable at high PAG concentrations. Traditional PAGs and EUV resist polymers have similar EUV optical densities, so this assumption seems reasonable.[70,79] A second assumption, implicit in the proposed mechanism, is that hole-initiated chemistry and electron trapping are both required in order to produce acid. In other words, acid production is a function of *co-dependent* electron trapping and hole-initiated chemistry. However, there is some evidence that these mechanisms may be able to operate independently in EUV resists.

Acid quantum yield measurements were made by Nakano et al.[78] using Coumarin-6 in two different polymers with the same PAG. Two resists consisting of poly-4-hydroxystyrene (PHS) polymer and of poly-4-methoxystyrene (PMS) were exposed to 75-keV electrons followed by the determination of the amount of acid generated using the acid-sensitive dye, Coumarin-6, and absorbance spectroscopy. They observed almost double the acid quantum yield in the PHS resist compared to the PMS resist and attributed this difference to the relative ease of deprotonation in PHS versus PMS (Fig. 8.14). This was further supported by molecular dynamics calculations made by Endo et al.,[79] which calculated that a smaller activation energy was required for the deprotection of PHS than was required for PMS. However, the key piece of data is that a PMS resist *does* produce acid.

Downloaded From: https://www.spiedigitallibrary.org/ebooks/ on 09 Mar 2022
Terms of Use: https://www.spiedigitallibrary.org/terms-of-use

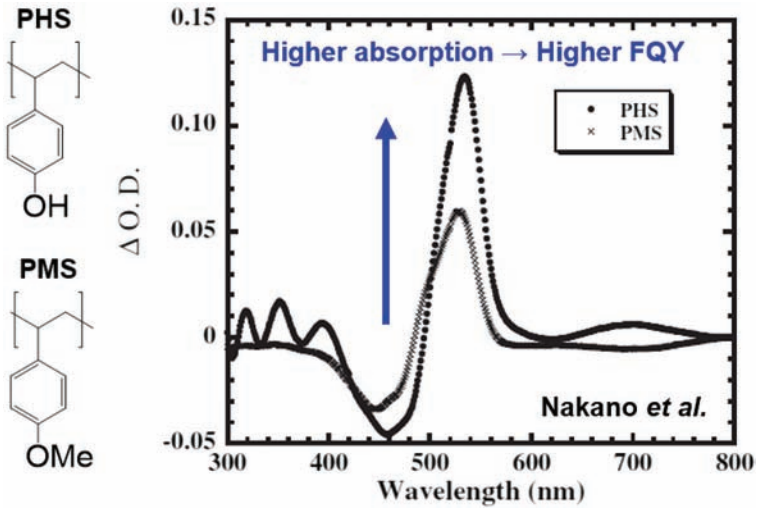

Figure 8.14 Film quantum yields for resists composed of poly-4-hydroxystyrene (PHS) and poly-4-methoxystyrene (PMS) containing the same PAGs at the same concentrations. The higher absorption of the PHS resist at $\lambda = 530$ nm indicates a higher acid quantum yield [reprinted and adapted from Ref. 78 with permission; © (2006) The Japan Society of Applied Physics].

Electron trapping. The production of acid in a PMS-based film lends support to the independent operation of electron–PAG reactions to produce acid. PMS has been shown, through pulse radiolysis[55] and calculation,[78] to have a higher energetic barrier to deprotonation than phenolic resists. This high energetic barrier effectively "knocks out" the hole-induced chemistry pathway for the PMS resist, and yet acid is still produced, presumably entirely from the PAG. In addition, Thackeray et al.,[63] Goldfarb et al.,[67] and Tarutani et al.[68] have shown that PAG reduction potential correlates well with EUV clearing dose E_0 and acid yield, indicating that PAG electron affinity directly relates to acid production in EUV exposure (Fig. 8.15). Further research is needed to determine if direct electrolysis of PAGs can produce acid, or if hole-initiated chemistry alone can operate independently as well.

Furthermore, co-dependent electron trapping and hole-initiated chemistries would require a full 6–10 electron–hole pairs to produce the 5–6 H^+ observed by acid quantum yield measurements (Section 8.4.4). Fully independent operation of these mechanisms may instead push the number of required e^-/p^+ pairs down to 3–5, more in line with TEY predictions and measurements. There is yet a third assumption built into the proposed mechanism of Kozawa and Tagawa—their mechanism requires that an acid anion be released near the polymer-bound proton. Generally, the bound proton is thought to be immobile, so electrons must be confined to short distances from their ionization sites in order to provide the anion release needed for efficient acid production. If acid production mechanisms can

Downloaded From: https://www.spiedigitallibrary.org/ebooks/ on 09 Mar 2022
Terms of Use: https://www.spiedigitallibrary.org/terms-of-use

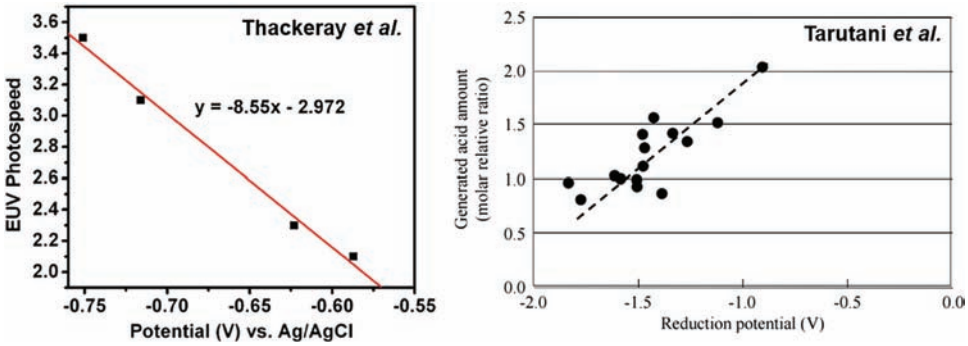

Figure 8.15 Thackeray et al. and Tarutani et al. have shown that PAG reduction potential correlates well with EUV photospeed E_0 and acid yield (reprinted from Refs. 63 and 68).

instead operate independently, this confinement of electron range is no longer required. Therefore, it is important to investigate how far electrons can travel in resists (Section 8.4.7).

Internal excitation. The discrepancy between the analysis of acid and TEY poses a challenge in understanding EUV photochemistry. If six acids can be produced by up to four electrons, then either electrons can produce multiple acids (perhaps via internal excitation), or holes left behind by ionization can independently generate acid, or else some other mechanism(s) must account for this discrepancy. Internal excitation (Fig. 8.9) provides a potential avenue for many acids to be generated without the consumption of an electron. An electron may donate the relatively small amount of energy (2–3 eV) required to promote a bound electron to an excited state,[64] and then continue on to the next interaction.

However, investigating internal excitation in thin polymer films is difficult. Researchers at the Colleges of Nanoscale Science and Engineering (CNSE) of SUNY Polytechnic Institute instead studied an analogous system to gain insight. Rather than attempting to monitor specific reaction pathways of PAGs and electrons, Narasimhan et al. exposed polymer films containing fluorescent dyes to 80- to 5000-eV electrons and observed electron-induced fluorescence.[63] A PAG that reacts via internal excitation produces acid, just as it would through other reaction pathways. Fluorescent dyes, on the other hand, generally relax to a lower energy state by emitting a photon, which is more easily measured.

The results, in terms of number of photons emitted per incident electron, were reported for 10 fluorophores in up to 4 different polymer environments (Fig. 8.16). It was observed that the film quantum yields of emitted photons per each incident 80-eV electron were all less than 1%. This, combined with additional kinetic data demonstrating the rate of decay of the fluorescent signal versus e-beam dose, indicates that internal excitation is not a very efficient excitation mechanism for producing acid. Therefore, even if we

Downloaded From: https://www.spiedigitallibrary.org/ebooks/ on 09 Mar 2022
Terms of Use: https://www.spiedigitallibrary.org/terms-of-use

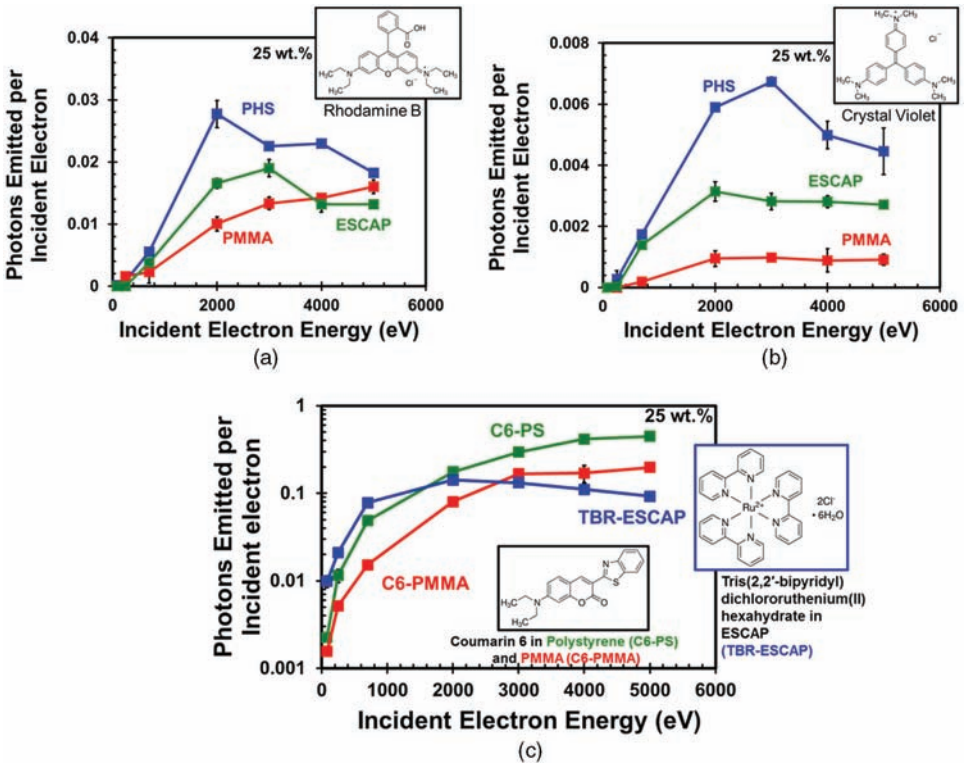

Figure 8.16 Experimental data showing emitted photon yield per incident electron versus incident electron energy for (a) Rhodamine B and (b) Crystal Violet in the polymers PHS, environmentally stable chemically amplified photoresist (ESCAP), and PMMA. Additionally, (c) data for Coumarin-6 and tris(2,2'-bipyridyl)dichlororuthenium hexahydrate showing <1% of incident electron result in an emitted photon, indicating that internal excitation is not an efficient mechanism for the reaction of PAGs to produce acid (reprinted and adapted from Ref. 64).

assume a 100% reaction efficiency of electrons (i.e., every electron or electron–hole pair produces an acid), internal excitation cannot explain the discrepancy between the predicted yield of 2–4 electrons and the measured 5–6 H^+ per absorbed EUV photon. These results lead to the necessary reexamining of the exact relationship between electron trapping and hole-initiated chemistry in EUV resist chemistry.

8.4.7 Electron travel distance in photoresists

The distance travelled by an electron from the site of ionization to where it can no longer cause reactions due to a loss in energy is called the electron travel. This distance has been estimated by a couple of groups to be on the order of 2–4 nm.[57,75] This distance is consistent with the electron travel range for the

Downloaded From: https://www.spiedigitallibrary.org/ebooks/ on 09 Mar 2022
Terms of Use: https://www.spiedigitallibrary.org/terms-of-use

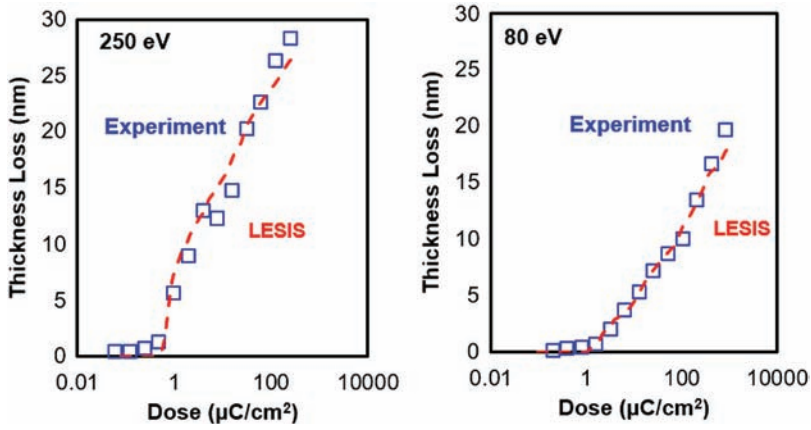

Figure 8.17 Thickness loss in an open-source chemically amplified positive-tone resist due to e-beam exposure at CNSE (experimental data in squares) compared with LESiS simulation (dashed lines). 80-eV electrons are shown to penetrate up to 20 nm at high doses, in agreement with simulation (adapted from Ref. 81).

linked mechanism proposed by Kozawa and Tagawa. However, experiments conducted at CNSE (Fig. 8.17) and at the Center for X-ray Optics (CXRO) of LBNL (Fig. 8.18), have shown that low-energy electrons (15–250 eV) can penetrate up to 10+ nm in resists.[62,80] In both studies, thickness loss due to low-energy e-beam exposure was measured with ellipsometry. Additionally, models based on dielectric response theory[80] and simulations in LESiS[81] have shown agreement between electron penetration depth calculations and experimentation.

The results by CNSE and CXRO show that electrons can travel up to 20 nm in EUV resists, potentially outside the reaction-accessible range of a polymer-bound proton, suggesting that electron trapping and hole-initiated chemistry need not occur near each other to generate acid. Further investigation is needed to characterize electron travel distances in different resists platforms. Such studies may aid in determining the mechanisms of EUV exposure, in CARs or other more exotic platforms. In either case, however, this work may be important in determining the ultimate resolution capabilities for EUV resists.

8.4.8 Conclusions

The basic physical interactions involved in EUV photochemistry are well known, but their impact on EUV photochemistry remains an active area of research. The TEY has been narrowed to a range of 2–4 $e^-/h\nu$ through modeling, and the acid yield in chemically amplified photoresists has been determined to be a maximum of six acids/absorbed photon through a few measurements. Experimentation is needed to make final conclusions about the

Downloaded From: https://www.spiedigitallibrary.org/ebooks/ on 09 Mar 2022
Terms of Use: https://www.spiedigitallibrary.org/terms-of-use

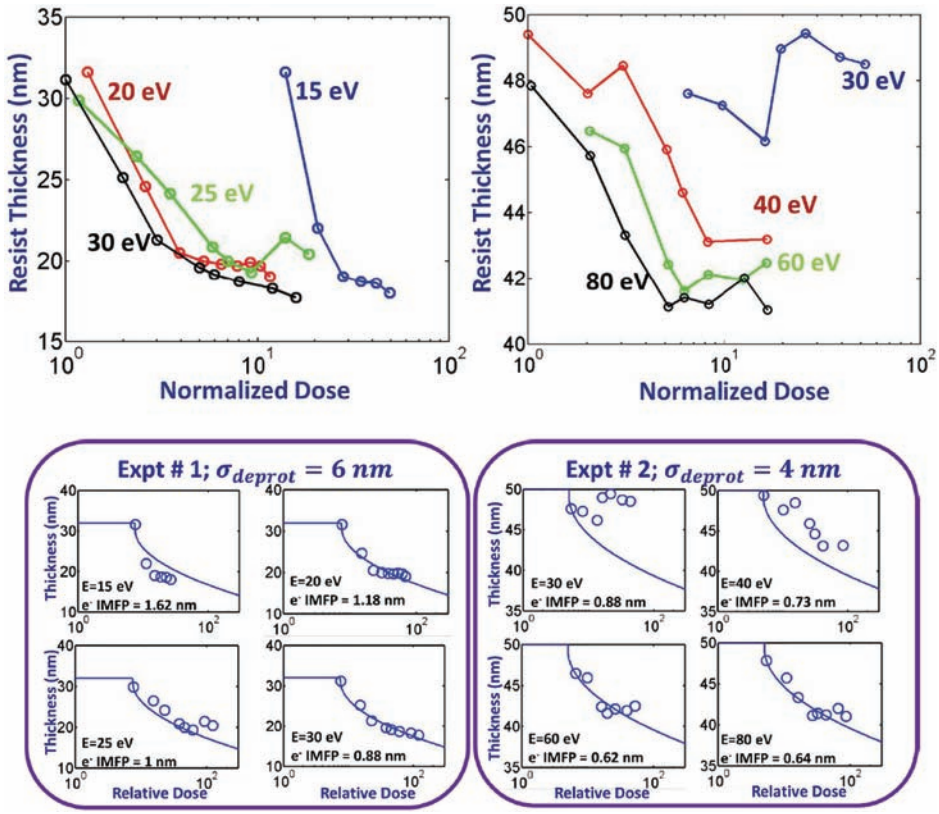

Figure 8.18 (Top) Thickness loss data in a chemically amplified positive-tone EUV resist due to e-beam exposures with electron energies of 15–80 eV, showing electron penetration of up to 10+ nm. (Bottom) Fitting the experimental data with a model generated from electron inelastic mean free paths calculated from electron energy loss spectroscopy data with a dielectric model for scattering (IMFP – inelastic mean free path) (reprinted from Ref. 80).

number of electrons generated or the amount of acid generated upon exposure to EUV light. Further work is needed to determine if the TEY or acid yield can be improved, especially in other resist platforms, to produce better resists for manufacturing. However, some of the underlying chemical mechanisms involved in EUV exposure are still not well understood. Experimental evidence supports a mechanism in which direct electron-trapping by PAGs can produce acid, and indicates that polymers are also involved in acid production mechanisms; however, further research is required to determine if electron trapping and hole-initiated chemistry operate co-dependently or independently. Future work should also be directed to applying mechanistic analysis and experimentation to the development of more-exotic metal-based or nanoparticle resist systems.

Downloaded From: https://www.spiedigitallibrary.org/ebooks/ on 09 Mar 2022
Terms of Use: https://www.spiedigitallibrary.org/terms-of-use

8.5 Organic Photoresists

8.5.1 Polymethylmethacrylate (PMMA) resists

As described in Section 8.2, the first EUV imaging experiments were done with PMMA. PMMA is a readily available material with sensitivity to many imaging wavelengths, so it was a good choice for initial imaging work. Since it operates by chain scission, there is very little blur in the imaging, and it can give excellent resolution. However, it has limited etch resistance, poor SEM stability, is known to outgas, and has poor photospeed. A good example of PMMA's imaging capability using EUVL was reported in 2007 by Solak et al., who printed 15-nm dense lines and spaces in 25-nm films of PMMA (Fig. 8.19).[82]

Both of these results used the interference lithography (IL) exposure tool at the Paul Scherrer Institute. It took several years before these early PMMA results could be surpassed using a conventional resist on a conventional (non-IL) exposure tool.

This resolution was not matched without using an interference tool and with a more conventional resist until 2015. A. Pirati et al. reported that a conventional CARs had resolved 13.5-nm lines and spaces using a 0.33-NA NXE3300 EUV scanner.[83] This was better than the 16-nm L/S minimum resolution reported for the available commercial tools in 2013.

8.5.2 Environmentally stable chemically amplified photoresists

The first generally useful EUV resists were based on chemically amplified photoresist or environmentally stable chemically amplified photoresist

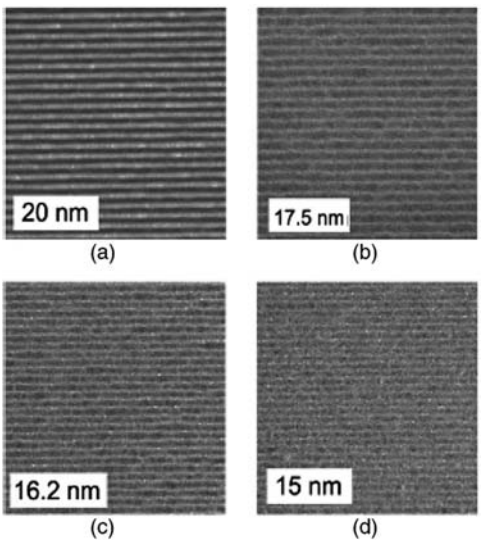

Figure 8.19 Top-down SEM micrographs of L/S patterns in PMMA with half-pitches of (a) 20 nm, (b) 17.5 nm, (c) 16.25 nm, and (d) 15 nm. The thickness of the PMMA film is 25 nm (reprinted from Ref. 82 with permission; © 2007 American Vacuum Society).

Downloaded From: https://www.spiedigitallibrary.org/ebooks/ on 09 Mar 2022
Terms of Use: https://www.spiedigitallibrary.org/terms-of-use

(ESCAP) platforms derived from existing KrF and ArF resist chemistries.[59] In CARs, the photochemistry of absorption results in the creation of acid. During the post-exposure bake step, the photogenerated acid catalyzes chemical reactions that result in changes in solubility within the exposed areas in the resist. Since the acid reaction can catalyze many reactions, this amplification increases resist photospeed. In practice, this mechanism has proven to give not only fast resists, but also high-resolution resists.

In CARs, most of the EUV photons are absorbed by the polymer. For these resists to be reasonably sensitive, the energy absorbed by the polymer must be transferred to the PAG and, thereby, create acid. In the early days of EUVL, it was not obvious that exposures would occur by this mechanism. Brainard et al. compared the imaging dose of 19 resist materials at EUV and DUV wavelengths (Fig. 8.20).[51] Excellent correlations were observed among resists prepared from the same polymer ($r^2 = 0.91$, 0.91, and 0.97), whereas a very poor correlation was observed between the resists prepared from the same PAGs ($r^2 = 0.75$ and 0.02). The polymer correlations afford excellent predictability of EUV photospeed performance within a single polymer family, but they are independent of PAG type. This result emphasizes the importance of the polymer in the mechanism of acid generation by EUV and DUV wavelengths.

One of the earliest demonstrations of applying chemically amplified technology to EUVL was in 1999. Rao[84] and Brainard et al.[51] explored the use of ESCAP platforms in EUVL. EUV imaging was performed using 85-nm films and the 0.088-NA, 10X1 EUV camera and was compared with DUV (248 nm) imaging (100-nm films) using a GCA 0.53-NA stepper. This work led to the development of the EUV-2D resist that served the EUV community as a tool-test resist from 1998 to 2005.[85]

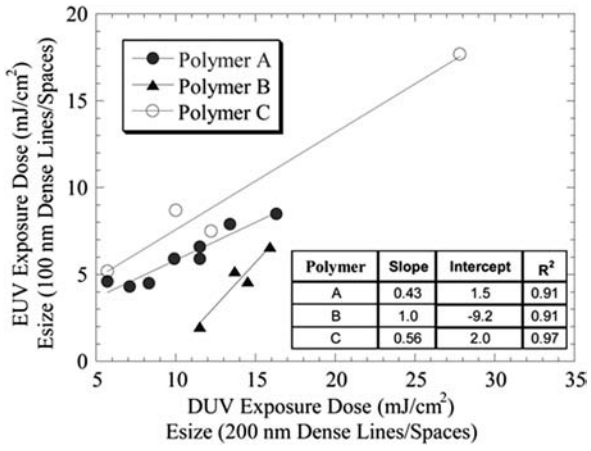

Figure 8.20 Comparison of EUV and DUV exposure energies as a function of polymer type (reprinted from Ref. 51 with permission; © 1999 American Vacuum Society).

Downloaded From: https://www.spiedigitallibrary.org/ebooks/ on 09 Mar 2022
Terms of Use: https://www.spiedigitallibrary.org/terms-of-use

ESCAP-based resists have been a popular class of resists for EUVL. In 2004, Kohler et al.[86] and Steenwinckel et al.[87] reported on improved ESCAP materials and developed the MET-1K resist, which replaced EUV-2D resist as a baseline material for micro-exposure tool (MET) imaging. The two resists had similar minimum resolutions, but the process windows for MET-1K were much better. The best resolution of this material was 40-nm lines and spaces on the LBNL microstepper. In their work, they found that small acids along with high base loading gave the best results. The high base loading result was consistent with previous studies in that it gave better process windows but slower photospeed.[88,89]

Other notable examples of ESCAP EUV resists are those of Golovinka et al.[90] and Jouve et al.[91] These two groups achieved very good resolution, particularly Golovinka et al., who reported 26-nm lines and spaces; but these exposures were done on interference tools. Interference tools have much higher contrast aerial images than do ministeppers or scanners, so the resolutions and LER reported from experiments with them are not easily comparable with other results. Nonetheless, these results indicated the potential of EUV resists to resolve very small feature sizes.

Recently, Pirati et al. reported that a CAR had resolved 13.5-nm lines and spaces using a 0.33-NA NXE3300 EUV scanner.[83] This was the leading L/S resolution using CARs on a commercial EUVL exposure tool in 2015. Production use of the tool was suggested to be for 16-nm lines and spaces. In the same publication it was reported that a non–chemically amplified metal-based resist had a slightly better resolution, achieving 13-nm lines and spaces.

8.5.3 Low-activation-energy acetal or ketal resists

Because EUV absorption is independent of the types of functional groups in a resist (unlike previous imaging wavelengths), many different types of chemistries have been explored for EUV resists. KRS resists are another variety of CARs. They also have PAGs, but the polymer contains acetal groups that protect acid functionality. The acetal groups are very sensitive to acid and can often be deprotected at room temperature, resulting in a material that doesn't need a post-exposure bake to function. Their ability to deprotect at low temperatures keeps acid diffusion to a minimum and gives a potential for high resolution.[92] In 2005, Naulleau showed that resists with this chemistry could resolve 25-nm lines and spaces on the LBNL MET. This was the highest resolution achieved on that exposure tool in 2005 (Fig. 8.21).[93]

The acid-catalyzed deblocking of acetal blocking groups proceed by reactions that are considered to have low activation energy E_a, whereas the acid-catalyzed deblocking of ESCAP resists proceed by reactions that are considered to have high E_a. In 2006, Thackeray et al. reported a comparison of high- and low-activation energy polymers using exposures conducted mostly on microstepper tools.[94] The researchers found that their

Downloaded From: https://www.spiedigitallibrary.org/ebooks/ on 09 Mar 2022
Terms of Use: https://www.spiedigitallibrary.org/terms-of-use

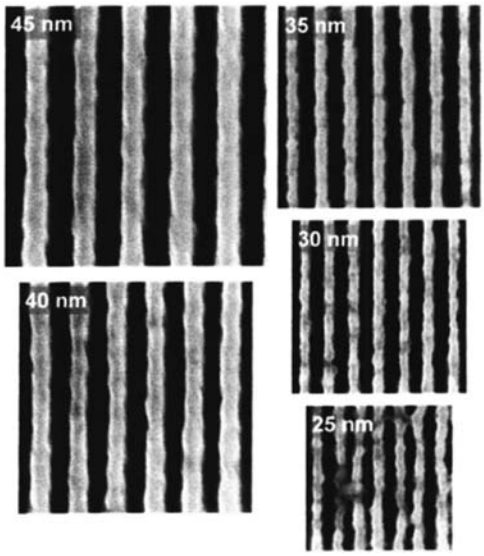

Figure 8.21 Equal-L/S images ranging from 25- to 45-nm printed in experimental KRS resist provided by IBM (reprinted from Ref. 93 with permission; © 2005 American Vacuum Society).

low-activation-energy system had better exposure latitude and slightly better resolution than their high-activation-energy system. However, the high-activation-energy system gave slightly better LER. They concluded that a blend of the two gave the best performance and reported a resolution of 35-nm lines and spaces using the Berkeley MET. The LER of 40-nm lines and spaces was 3 nm at an exposure dose of roughly 30 mJ/cm^2.

In 2007, Kim et al. also reported a comparison of high- and low-activation-energy EUV resist systems.[95] These researchers used both polyvinyl phenol polymers and acrylate polymer, and had three different types of protecting groups for each backbone. They changed the activation energy by changing the ease of deprotection of the ester using slightly different protecting groups. They found that low-activation-energy materials had somewhat better resolution and LER. The low-activation-energy systems did not use acetal protecting groups.

8.5.4 Chain-scission resists

In 2010, Cardineau et al. demonstrated that linear polymers with tertiary ester functionality built into the main chain could undergo chain scission under acid catalysis and function as a chemically amplified chain-scission resist for EUVL.[96] Resolution down to 36 nm was achieved using the Berkeley MET. In 2013, Cardineau et al. reported the continuation of this work, where they made additional polymers using improved synthetic methods.[97] They found clean imaging using the Berkeley MET down to 40-nm lines and spaces, and

Downloaded From: https://www.spiedigitallibrary.org/ebooks/ on 09 Mar 2022
Terms of Use: https://www.spiedigitallibrary.org/terms-of-use

signs of modulation down to 14-nm lines and spaces. But the smaller features showed line wiggling and bridging, which the authors attributed to the low glass transition temperature T_g of these materials.

In 2015, Kudo et al. also demonstrated chain-scission-type resists.[98] Their materials were complicated polymers based on acetal-linked cyclodextrins. Resists made with these polymers and the PAG triphenylsulfonium nonaflate were tested for clearing dose and showed very high sensitivity with clearing doses ranging from 0.25 to 1 mJ/cm^2.

8.5.5 ArF polymer platforms

ArF-type polymer chemistry, which is commonly based on acrylate polymers, can also be used as a basis for chemically amplified EUV resists. In 2010 Furakawa et al. reported EUV resists based on acrylate polymers made from methacrylate esters of a variety of adamantyl alcohol.[99] EUV sensitivities were measured by E_0 and E_{size} of lines and spaces was demonstrated by e-beam exposure. The work of Kim et al. also shows EUV sensitivity with mostly acrylate ArF-resist-like polymers.[95]

8.5.6 Sulfonium-based resists

In 2014, Satyanarayana et al. reported polymer-bound PAG systems di(methyl)hydroxyphenolsulfonium triflate esterified to methacrylic acid as a polymer-bound PAG functionality.[100] Even though the polymer's structure includes a PAG, this was not a CAR. In this system, EUVL exposure converts the sulfonium group into a sulfide after exposure. The polymer-bound sulfide is not soluble in standard developer (0.26 N tetramethylammonium hydroxide, TMAH), but the original sulfonium-containing polymer is. Development in TMAH then dissolves the unexposed regions of the resist, providing negative-tone imaging. These materials resolved 20-nm lines and spaces, both in e-beam and EUVL imaging.

8.5.7 High-fluorine resists

As the need for higher EUV absorbance in EUV resists became better understood, researchers started adding fluorine to polymers to enhance absorbance. Much of this work is discussed in the previous section on optical density. In addition, in 2008, Sasaki et al. reported on two methods of increasing absorbance by adding fluorine to the resist polymer.[33] One method involved having trifluoro-vinyl styrene as one of the monomers. The other approach used an acyclic-fluorine-containing monomer. Both approaches showed 2× to 10× improvements in dose to clear compared to unfluorinated analogues.

In 2013 Christianson et al. reported the preparation of free-radical polymers using *t*-butyl trifluoromethacrylate as one of the monomers.[40] They screened different polymers using EUV flood exposures and found that all of

Downloaded From: https://www.spiedigitallibrary.org/ebooks/ on 09 Mar 2022
Terms of Use: https://www.spiedigitallibrary.org/terms-of-use

the initial formulations had dose to clear of 3.4 mJ/cm^2 or less. After optimizing the materials for coating and adhesion, several materials were tested on the Berkeley MET. These reseachers achieved a resolution of 35-nm lines and spaces with an exposure dose of only 10.3 mJ/cm^2.

8.5.8 Non-polymer-based organic EUV resists

Molecular glasses are materials that have a defined molecular structure and molecular weight, but are big enough to form good films and thus can be used for making photoresist. In theory, they can produce better control of resist properties due to their clearly defined resist structure. In 2006, Oizumi et al. demonstrated CARs based on polyphenols.[101] This group achieved a resolution of 30-nm lines and spaces on a 0.3-NA MET. They had to reduce the film thickness to 40 nm in order to get this resolution. They achieved what they considered good LER of 6.3 nm at an exposure dose of 10 mJ/cm^2.

The work by Satyanarayana et al. cited above is not the only approach to negative-tone imaging for EUVL.[102] For example, in 2007 Shimizu et al. reported crosslinking resists made with partially protected poly vinyl phenol and on a resist made with protected noria. Noria is a poly-phenolic compound with a circular shape. It is high enough in molecular weight that it forms good films. Both materials made good-quality resists. The two material sets showed comparable resolution of 26-nm lines and spaces on the Berkeley MET.

Other groups have also reported noria-based resists. Niina et al.[103] reported positive-tone materials made by adding protecting groups to noria and got a 10 mJ/cm^2 resist with clean imaging of 32-nm lines and spaces on a ministepper. Nishikubo et al.[104] reported similar work using a different protecting group. Seki et al. also reported noria-based materials for which they used attached oxetanyl groups to provide acid-catalyzed crosslinking[105] and an approach with acid-sensitive protecting groups to provide positive-tone resists.[106] These results both gave resolution of roughly 40-nm lines and spaces on a ministepper.

Green et al. reported EUV resists based on calixeranes, which are another polyphenolic molecule with a defined circular structure.[107] They got a positive-acting resist by protecting the phenolic functionality with acetals. These resists were imaged using EUVL but showed bridging and pinching of lines. The authors attributed this to the low T_g of the materials and developed some additional materials with higher T_g. These new materials have not yet been imaged.

Henderson's group at Georgia Tech has published extensively on negative-tone, nonpolymeric-based EUV resists. Most of their EUV work relates to molecules with three or four phenol groups functionalized with epoxides that are crosslinked using chemically amplified chemistry. In 2014 the group reported EUV results using such molecules combined with a photodecomposable nucleophile (PDN).[108,109] They reported that the PDN functions to

Downloaded From: https://www.spiedigitallibrary.org/ebooks/ on 09 Mar 2022
Terms of Use: https://www.spiedigitallibrary.org/terms-of-use

quench the epoxide chain reaction in the same way a base quenches an acid-catalyzed protection in a typical CAR. They achieved 18-nm line-space resolution using a ministepper at an exposure dose of 39 mJ/cm^2. These materials were solvent developed. In 2015 the group reported extending this chemistry to a TMAH-developable system, although with somewhat lower resolution.[110]

Research was reported by researchers at the University of Birmingham in 2013 on negative-tone resists based on a fullerene derivative that can be crosslinked using photo-generated acid. However, no chemical details of the material were reported and the exposures were done on an interference imaging tool, so it is hard to judge the potential of this resist system.[111]

Another small-molecule-based approach uses a molecular component called xMT, which contains 2 tert-butoxycarbonyl (tBOC)-protected functional groups along with a multiple-epoxy-containing crosslinker, PAG, and base. The authors reported that the interference imaging performance improved from 14-nm lines and spaces to 11-nm lines and spaces when xMT was added compared with a resist based only on epoxy crosslinking.[112] The authors suggest that the high resolution of their system is due to what they call a multi-trigger mechanism, where two different acid-catalyzed events are needed in the same area of a resist.[113] However, the specific mechanism of each of the two proposed triggers is not described.

8.6 Characterization of Development Using AFM

Characterization of a resist development process has typically been done by measuring the development rate as a function of exposure dose. Generally, a step function result is desired. That is, for a positive-tone resist, there is an exposure threshold below which there is very slow dissolution, and for doses above that threshold, the dissolution rate is very high. A resist with such properties is considered a high-contrast resist. Usually, these studies are conducted using a development rate monitor that measures the thickness of the resist film when immersed in developer as a function of time, resulting in a contrast curve. The contrast curve provides the resist contrast along with other parameters.[114,115] By determining the deprotection level of the polymer as a function of the exposure dose, one can turn a contrast curve into a graph of dissolution rate versus polymer blocking level. This information is useful in understanding if a resist has an effective chemical switch for changing solubility as well as in making a mathematical model of the resist.

These measurements, and the mathematical models usually used with them, treat the resist as a continuous material. However, as the size of the printed features decreases, understanding the behavior of a resist as a mixture of individual molecules becomes more important. One instrument that has provided insight into dissolution on the molecular scale is a high-speed atomic force microscope (AFM). This instrument continuously scans a resist as it is

Downloaded From: https://www.spiedigitallibrary.org/ebooks/ on 09 Mar 2022
Terms of Use: https://www.spiedigitallibrary.org/terms-of-use

developed. Such characterization is very challenging as resist development is typically much faster than normal AFM scans; however, one research group at EIDEC has developed tooling and a technique for this sort of measurement and applied it to EUV resist development.[116–123] The group has published a series of papers describing their technique and applying it to characterizing EUV resists. A diagram of their resist apparatus is shown in Fig. 8.22.

A small piece of silicon wafer is mounted face-down on a sample assembly and the height is adjusted so that when the assembly moves downward the chip is immersed in a liquid and the AFM tip is at the right height to scan it. For positive-tone resists, the liquid is water,[116] and for negative-tone resists, the liquid is decane.[117] The wafer chip is continually scanned as the liquid is replaced by developer. Scans are repeated every two seconds until development is complete. In some cases, resist profiles during rinse are characterized by then replacing the developer by a rinse liquid.

The first experiments were done using twenty-fold diluted aqueous developer so that the development was slow enough to fully characterize by AFM.[118] However, the technique was improved to the point where full-strength developer can be used.[119] Even with the improved, high-speed AFM, the size of EUV lines and spaces pushes the resolution and speed of the AFM. The improved equipment can scan 1000 × 750 nm at 0.5 frames per second, giving a field composed of 400 × 300 2.5 nm × 2.5 nm pixels. This is barely fast enough to give reasonable time resolution for a modern develop process, and the pixel size is maybe 10% of the dimension of the smallest lines and

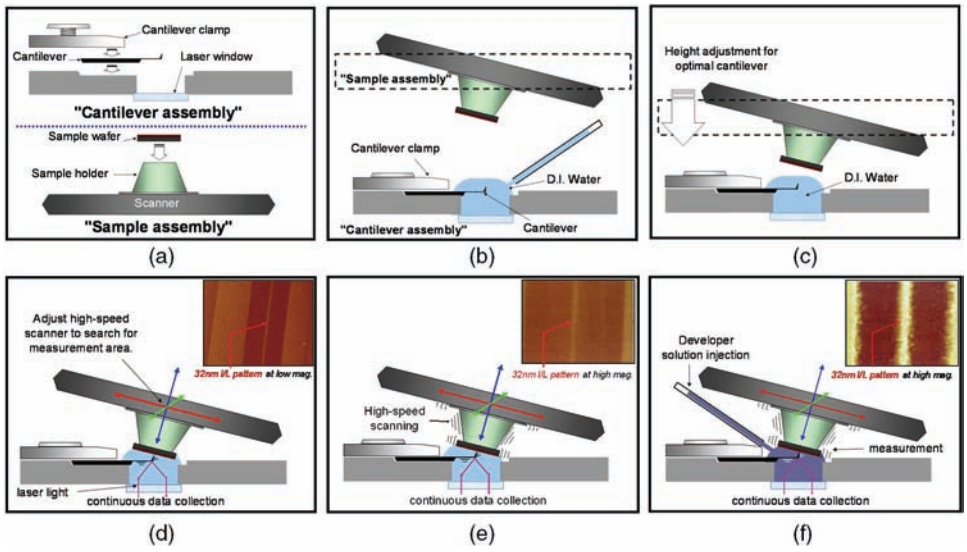

Figure 8.22 Apparatus used to perform AFM measurements during resist development (reprinted from Ref. 116 with permission; © 2010 The Japan Society of Applied Physics).

Downloaded From: https://www.spiedigitallibrary.org/ebooks/ on 09 Mar 2022
Terms of Use: https://www.spiedigitallibrary.org/terms-of-use

spaces tested. Using an AFM tip with a radius of 10 nm, the probe could not reach the bottom of 26-nm lines and spaces. Nonetheless, the AFM provides very interesting data. EUV resist development can be far from a relatively featureless and continuous process. The AFM work showed that dramatic swelling can occur in development or during rinse, that the resist can develop in chunks of different sizes, and that there are considerable differences in development between different resist chemistries. Figure 8.23 shows an example of the differences in development for three different resist chemistries.

For more details on the results of this AFM work, please consult the references for AFM measurement of negative-tone development,[117] linewidth LWR during development,[117] thickness of resist versus development process,[120] comparison of different developers,[121] and comparison of different types of PAGs.[122]

8.7 Strategies for Improving Resist Sensitivity: Acid Amplifiers and Photosensitized CARs

Two chemical strategies have been developed to increase the sensitivity of chemically amplified EUV resists: acid amplifiers and photosensitized chemically amplified resists (PSCAR™). This chapter will more fully describe the acid amplifiers because this work has been completed, whereas the PSCAR work is currently an area of active research.

8.7.1 Introduction to acid amplifiers

One challenge facing the developers of EUV resists is the need to simultaneously improve the resolution, LER, and sensitivity (RLS) tradeoff.[124] Brainard and coworkers have predicted that the best way to beat the RLS tradeoff is to create more acid molecules per absorbed photon,[88] and that one method for achieving this goal may be through the use of acid amplifiers (AAs). Acid amplifiers are compounds that decompose in the presence of catalytic acid to create more acid [Fig. 8.24(a)]. In a CAR, therefore, they

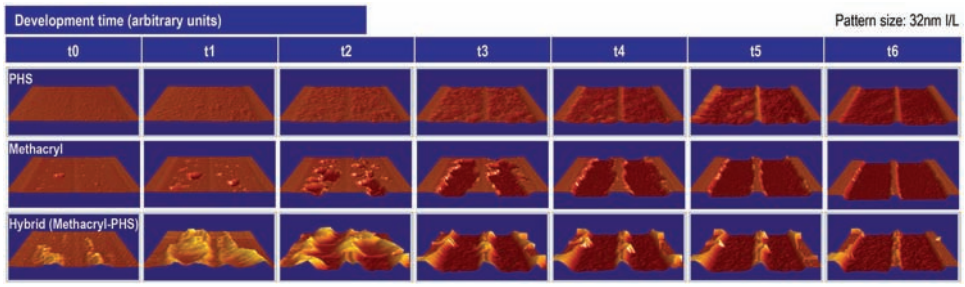

Figure 8.23 Comparison of the development processes of three different resist chemistries by high-speed AFM (reprinted from Ref. 123 with permission from The Society of Photopolymer Science and Technology).

Downloaded From: https://www.spiedigitallibrary.org/ebooks/ on 09 Mar 2022
Terms of Use: https://www.spiedigitallibrary.org/terms-of-use

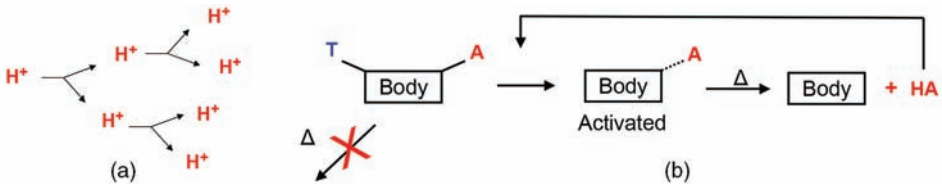

Figure 8.24 (a) Autocatalytic generation of acid. (b) Generic AA design featuring a body, trigger (T), and an acid precursor (A). (Reprinted from Ref. 133 with permission; © 2010 The Japan Society of Applied Physics.)

can be used to amplify the amount of acid generated by PAGs during exposure.

Acid amplifiers have been known since the 1990s, and 26 were described in the literature[125–130] prior to their first use in EUVL.[131] For the most part, the AAs presented in the early work almost always generated weak sulfonic acids, typically, toluene sulfonic acid. Only two AAs generated fluorinated sulfonic acids.[130] However, the AAs designed for use in EUV resists were specifically designed to create very strong fluorinated acids since they give the best lithographic performance.[132] This section describes the use of AAs in EUV photoresists and shows how specific structural features within the AAs affect the lithographic performance of the resists and the stability of the AAs.

The basic design of AAs for use in EUV resists is shown schematically in Fig. 8.24(b).[131,133] Acid amplifiers contain three parts: a body, an acid labile trigger (T), and an acid precursor (A). In the presence of catalytic acid, the trigger is "pulled," generating an intermediate that has a weak bond between the body and the acid precursor. The acid is released from the body and can then catalyze further decomposition of the AA.

A possible mechanism for catalyzed and uncatalyzed decomposition of acid amplifier 3HB is shown in Fig. 8.25. When the decomposition is autocatalytic, the trigger is first protonated and then cleaved (T) to produce an allylic sulfonic ester, which then decomposes thermally to yield a second double bond and a sulfonic acid (A). The sulfonic acid produced by the AA should be strong enough to cause autocatalytic decomposition. In the absence of acid, the sulfonic ester can still decompose to generate a sulfonic acid via an uncatalyzed mechanism (U). The strategy for designing new acid amplifiers is to maximize the rate of the acid-catalyzed decomposition while suppressing the rate of the uncatalyzed decomposition.

8.7.2 Lithographic capabilities of acid amplifiers in EUV photoresists

In an early study, a control open-source resist (OS1)[228] was prepared with and without 70 mM of added acid amplifier.[133] The addition of AA 6AB improves resolution, LER, and sensitivity versus the control resist [Fig. 8.26(a)]. A 2D Z-parameter plot shows how the addition of two AAs can improve Z from

Downloaded From: https://www.spiedigitallibrary.org/ebooks/ on 09 Mar 2022
Terms of Use: https://www.spiedigitallibrary.org/terms-of-use

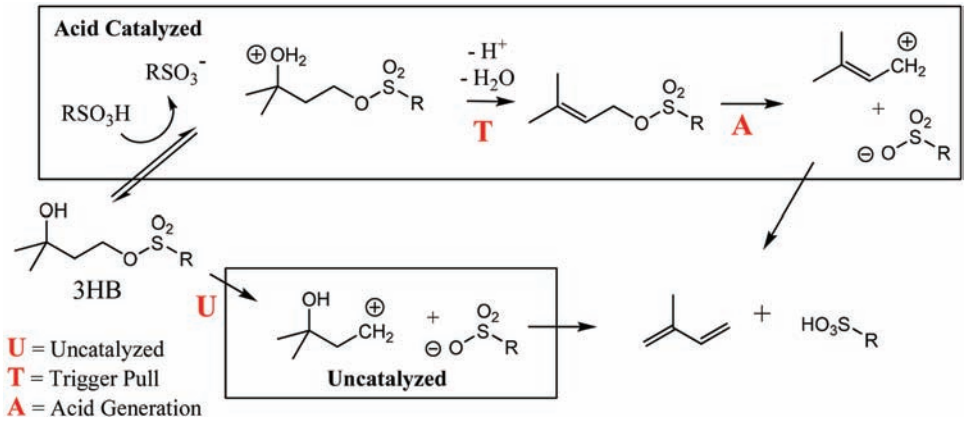

Figure 8.25 Proposed mechanism for catalyzed and uncatalyzed AA-3HB; R represents p-$C_6H_4CF_3$ (reprinted from Ref. 131 with permission; © 2009 American Chemical Society).

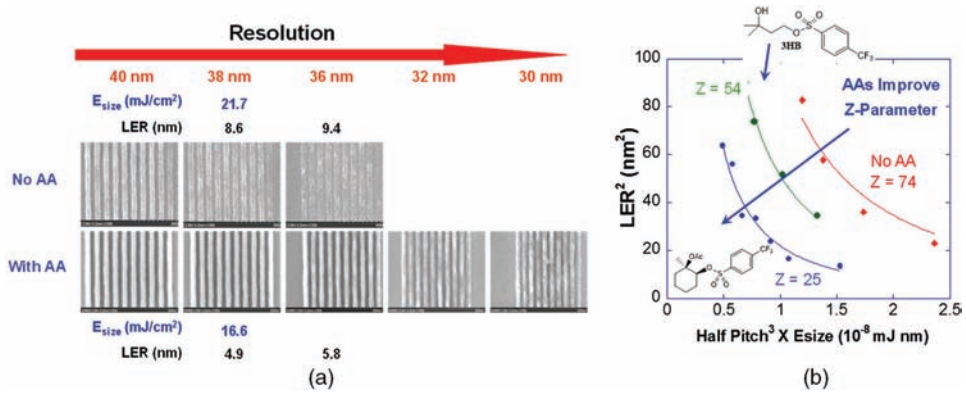

Figure 8.26 (a) Comparison of EUV L/S images (Berkeley MET) of the OS1 control resist + 70 mM 6AB, SB = 90 °C/60 s, PEB = 90 °C/90 s. (b) *Z*-parameter plot for a resist without AA and with 70 mM of 3HB or 6AB, SB = 90 °C/60 s, PEB = 90 °C/90 s (SB – soft bake; PEB – post-exposure bake) (reprinted from Ref. 133 with permission; © 2010 The Japan Society of Applied Physics).

74×10^{-8} mJ·nm^3 to 54×10^{-8} mJ·nm^3 (for 3HB) and 25×10^{-8} mJ·nm^3 (for 6AB) [Fig. 8.26(b)].[134]

To study the importance of the acid strength on the performance of AAs, Brainard and coworkers[132] prepared and evaluated four acid amplifiers with the same body, but two types of triggers and two types of acid precursors. They found that AAs that produce fluorinated acids (3AB and 3HB) yield resists with higher sensitivity, better LER, and a better *Z*-parameter relative to AAs that produce nonfluorinated toluene sulfonic acid (Fig. 8.27). These results show fairly clear evidence that AAs that produce fluorinated acids give the best combination of sensitivity, LER, and exposure latitude.

Downloaded From: https://www.spiedigitallibrary.org/ebooks/ on 09 Mar 2022
Terms of Use: https://www.spiedigitallibrary.org/terms-of-use

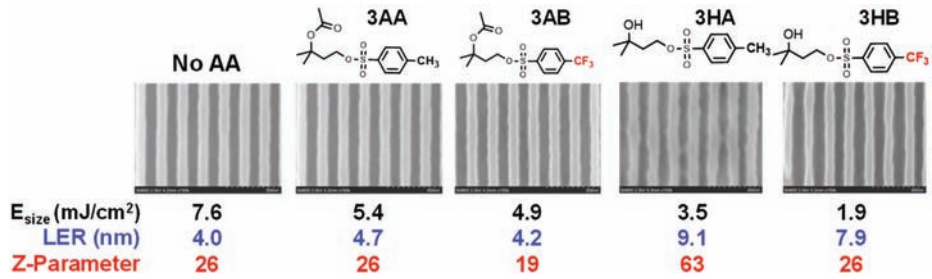

Figure 8.27 Comparison of EUV images (Berkeley MET) using 60-nm lines and spaces using the OS1 control resist + 70 mM concentrations of AAs: 3AA, 3AB, 3HA, and 3HB (reprinted from Ref. 132 with permission from The Society of Photopolymer Science and Technology).

In another study, Kruger et al. systematically varied the chemical structure of 12 AAs and studied their reaction kinetics by using the *Z*-parameter to compare the lithographic performance of EUV resists prepared with and without 70 mM concentration of AA (Fig. 8.28).[132,135] Seven of the AAs were capable of showing improved lithographic performance (lower *Z*-parameter) versus the control resist. The *Z*-parameter improved three-fold with the addition of 3MA. For the most part, resists prepared with perfluorobenzenesulfonate esters (3HC, 3MC or 2MC) gave poor lithographic performance versus the control. The authors demonstrated that these AAs have the poorest thermal stabilities and explained that the poor lithographic performance of these highly fluorinated sulfonates was due to their poor thermal stability in the resist.

A study by Maruyama et al.[136] compared the lithographic performance of a commercial resist with and without an undisclosed acid amplifier. They found improvements in resolution (from 26 to 24 nm) and sensitivity (from 30.6 to 14.9 mJ/cm^2), but with a degradation in LWR (from 4.7 to 5.5 nm). Overall, the *Z*-parameter improved from 9.1 to 6.1 10^{-8}.

8.7.3 Fluorine-stabilized AAs and olefin triggers

One of the biggest challenges in designing AAs for use in CARs is that the AAs that generate fluorinated acids tend to be unstable. Product analysis experiments[137] showed that the pathways for the unwanted, noncatalytic decomposition reactions involved either S_N2 or S_N1 reactions between phenolic nucleophiles in polymer films or in solution and the primary sulfonic ester bonds [Fig. 8.29(a)]. Therefore, a strategy was devised for blocking both decomposition pathways by preparing AAs with a trifluoromethyl (-CF_3) group alpha to the sulfonic ester. The authors proposed that the CF_3 would reduce the rate of the S_N2 pathway by increasing steric hindrance, and would reduce the rate of the S_N1 pathway by preventing the buildup of positive charge. Another strategy for creating stable AAs that can release highly

Downloaded From: https://www.spiedigitallibrary.org/ebooks/ on 09 Mar 2022
Terms of Use: https://www.spiedigitallibrary.org/terms-of-use

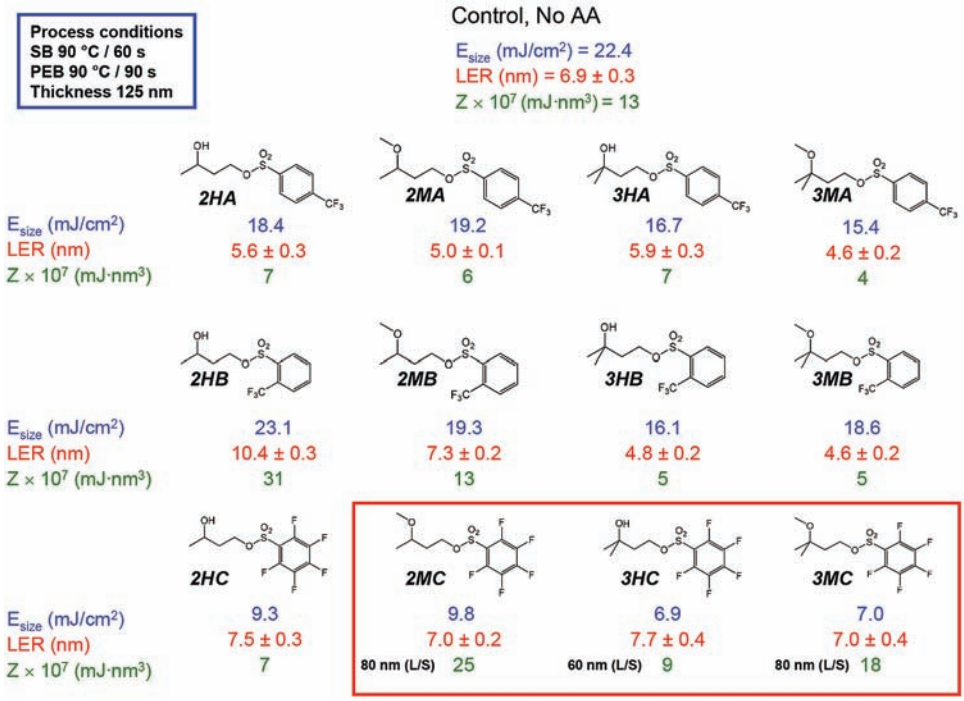

Figure 8.28 1 control resist without AA and 12 resists with 70 mM AA exposed to EUV light. The sensitivity E_{size}, LER, and *Z*-parameter of these resists are reported for 50-nm equal lines and spaces or at best resolution (reprinted from Ref. 135 with permission; © 2010 American Chemical Society).

fluorinated acids is to use olefins as triggers instead of leaving groups.[138] Previous to the work of Kruger et al., all AAs used triggers that were leaving groups.[125–132]

Combining both the olefin trigger and the α-CF_3 concept into one trigger-body design, Kruger et al. produced acid amplifiers AA4 and AA5 [Fig. 8.29(b)], which produce pentafluorobenzene-sulfonic acid ($C_6F_5SO_3H$, PFBS) and triflic acid (CF_3SO_3H, TfOH), respectively. Using earlier body-trigger designs,[132,133,135] the authors were able to prepare AAs that generate PFBS; however, without the α-CF_3 concept, they were never able to prepare stable AAs that make acids any stronger than PFBS acid. As described above, it was possible to prepare AAs that generate PFBS, but these AAs did not provide good lithographic performance due to problems with thermal stability. The olefin trigger and α-CF_3 concept provides AAs that can generate PFBS that is stable for 29 days at 145 °C. Triflic acid is a superacid that is 50× stronger than perfluorooctane sulfonic acid (PFOS),[138,139] yet its AA is stable for days at 140 °C. In addition to the enhanced stability of these new AAs (AA4 and AA5), they also work well as acid amplifiers, as demonstrated using ^{19}F NMR (nuclear magnetic resonance) kinetics [Fig. 8.29(b)].

Downloaded From: https://www.spiedigitallibrary.org/ebooks/ on 09 Mar 2022
Terms of Use: https://www.spiedigitallibrary.org/terms-of-use

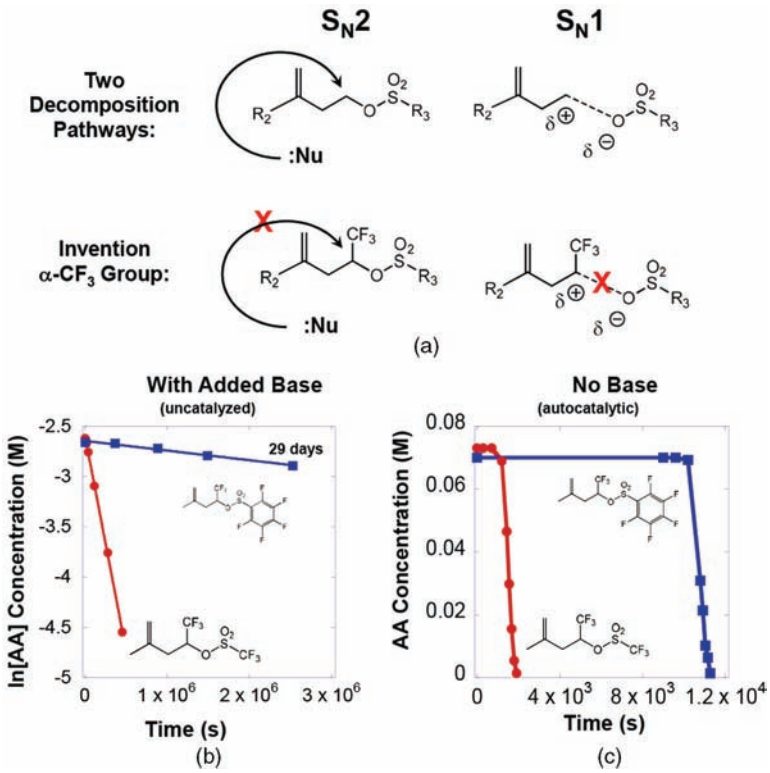

Figure 8.29 (a) Addition of the α-CF_3 to the sulfonic ester inhibits S_N2 and S_N1 reactions. (b) Thermal decomposition of AA4 and AA5 with added base and (c) in the absence of base (reprinted from Ref. 138).

8.7.4 Synthesis and preliminary lithographic performance of fluorine-stabilized polymers

Hosoi et al. prepared three monomers based on the α-CF_3 stabilization and ketal triggers that have a *para*-amide-styrene functionality capable of participating in polymerization reactions (Fig. 8.30).[138,140] The lithographic performance of resists prepared with blended and polymer-bound, fluorine-stabilized AAs against AA-free controls were evaluated using EUV interference lithography (Fig. 8.30). The control resist prepared with 1% base produced an LER of 5.6 ± 0.4 nm. Blending 70 mM of AA10 provided an improvement in LER to 3.1 ± 0.1 nm. The polymer bound AA (PBAA11) also showed an improvement in LER to 3.8 ± 0.4 nm. Overall, this work demonstrated the first-known polymer-bound AAs that show good LER.[141]

8.7.5 Photosensitized chemically amplified resists (PSCAR)

PSCAR is a clever and elegant approach for improving sensitivity of chemically amplified photoresists and may have the potential for making

Downloaded From: https://www.spiedigitallibrary.org/ebooks/ on 09 Mar 2022
Terms of Use: https://www.spiedigitallibrary.org/terms-of-use

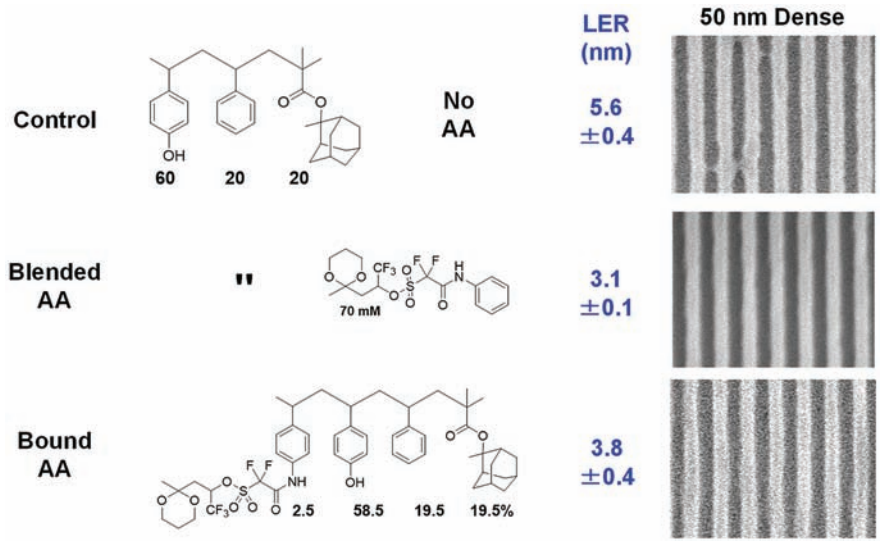

Figure 8.30 Lithographic properties of the new acid amplifiers (base loading = 1.0%) (reprinted from Ref. 138).

advances against the RLS tradeoff.[124,142–146] Researchers from around the world have contributed to the research, but much of it has been presented by members of the Tagawa group at Osaka University.

The primary difference a between standard CAR and PSCAR process is that the PSCAR process utilizes an additional flood exposure step to enhance sensitivity (Fig. 8.31). The key to making this platform work is the use of a photosensitizer precursor (PP). During the pattern exposure using EUV light, an EUV-active PAG creates acid in the exposed areas. The PP has a ketal protecting group that can be converted to a ketone in the presence of catalytic

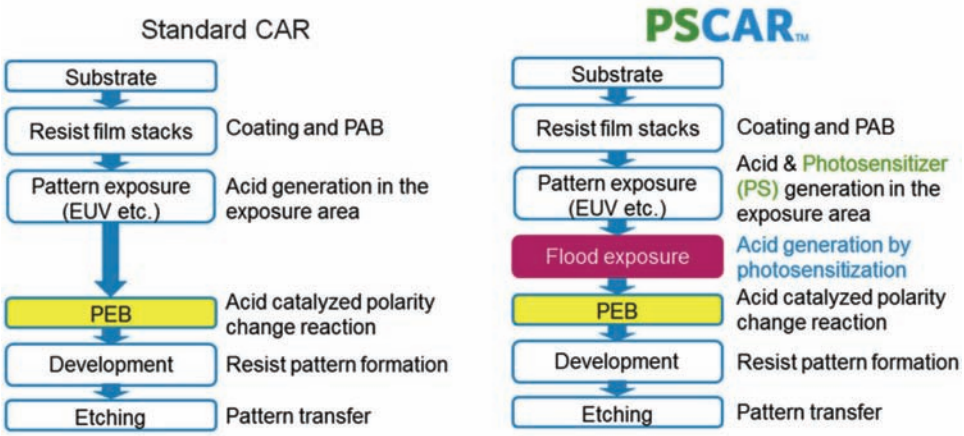

Figure 8.31 A comparison between CAR and PSCAR processes (reprinted from Ref. 143).

Downloaded From: https://www.spiedigitallibrary.org/ebooks/ on 09 Mar 2022
Terms of Use: https://www.spiedigitallibrary.org/terms-of-use

acid and water. The ketone compound is called the photosensitizer (PS). The formation of the ketone changes the chromophore of the PP, thereby producing a redshift in one of its absorption bands from 300 to 360 nm in the PS (Fig. 8.32). Prior to the redshift, the PP does not absorb 365-nm light; thereafter, however, the PS *can* absorb 365-nm light. In summary, the EUV imaging dose creates acid, the acid converts the PP to PS (at room temperature since the protecting group is a ketal), then the flood exposure at 365 nm causes the PS to sensitize the PAG to create more acid in the areas originally exposed with the EUV patterning exposure.

The flood exposure using 365-nm light increases the sensitivity of patterning 18-nm lines by 1.8X (Fig. 8.33), but in this example, the speed increase is accompanied by a degradation in LWR from 3.9 to 6.1 nm.[142] Researchers have tried a number of approaches for optimizing the PSCAR platform. One such example compares PSCAR at low base and without UV flood exposure to another PSCAR formulation with high base and with 1.0 J/cm^2 UV flood exposure. In this case, the LWR is about the same (4.0 to 3.9 nm), and the sensitivity improvement is modest (33.1 to 31.8 mJ/cm^2; see Fig. 8.34).

Figure 8.32 (a) Deprotection strategy for converting PP to PS. (b) UV–Vis spectra demonstrating the redshift as a result of the deprotection reaction (reprinted from Ref. 146).

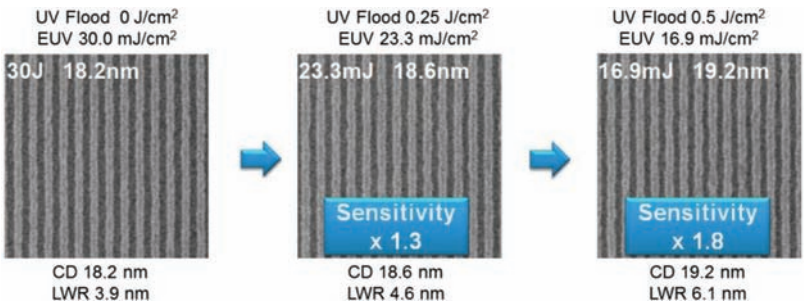

Figure 8.33 Sensitivity as a function of UV flood exposure for 18-nm dense line patterns. Original patterning exposures were conducted using interference lithography at Paul Scherrer Institute (reprinted from Ref. 142).

Downloaded From: https://www.spiedigitallibrary.org/ebooks/ on 09 Mar 2022
Terms of Use: https://www.spiedigitallibrary.org/terms-of-use

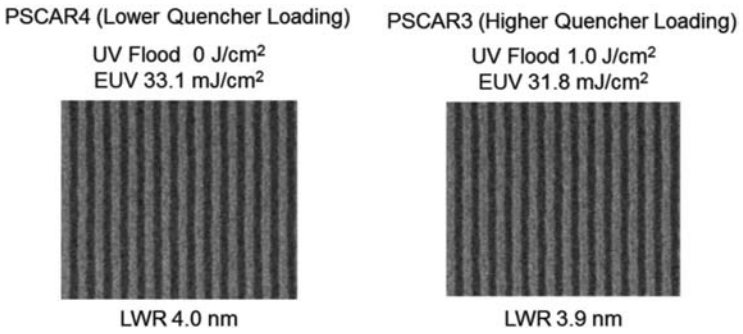

Figure 8.34 Comparison of printing 15 nm L/S patterns between a low-base PSCAR without flood exposure and a high-base PSCAR with flood exposure dose (reprinted from Ref. 142).

8.7.6 Conclusions

Acid amplifiers. Acid amplifiers have been developed in an effort to help make progress against the RLS tradeoff by creating more acids per absorbed photon. Although AAs existed prior to their use in EUVL,[131] this section describes the creation of new AAs specifically designed to work in chemically amplified EUV photoresists. A number of design strategies have been used to create stable AAs that create strong, fluorinated acids that can be added to existing resists, or can be bound to polymers.

PSCAR. The PSCAR platform is much newer than the AA platform; therefore, it is currently an area of active research. Overall, it is an elegant and creative approach to solving the RLS tradeoff using an acid-deprotectable photosensitizer precursor that has clearly demonstrated a capacity for improving photosensitivity.

Summary. A number of lithographic experiments have shown that AAs can improve the overall RLS (*Z*-parameter) performance of resists versus control resists, and the PSCAR platform has shown dramatic improvements in sensitivity. However, two questions remain: (1) Neither approach improves the photon statistics of absorption; therefore, are they capable of beating the RLS tradeoff? (2) Are AAs and PPs only capable of making bad resists better, or are they also capable of making good resists great?

8.8 Metal-Containing Resists

Since 2009, the photoresist community has shown a great deal of interest in EUV photoresists containing metallic elements. This recent interest in metal-containing resists was most likely initiated by three circumstances:

1. Key, high-profile papers by Doug Keszler at Oregon State University (OSU)[147,148,227] and Chris Ober at Cornell University[149–158]

Downloaded From: https://www.spiedigitallibrary.org/ebooks/ on 09 Mar 2022
Terms of Use: https://www.spiedigitallibrary.org/terms-of-use

demonstrated that hafnium oxide (films or nanoparticles, respectively) could act as good EUV photoresists.
2. The realization that capturing more EUV photons (higher OD as discussed in Section 8.31) will be essential to provide manufacturing capabilities with the necessary photon statistics.[36,159] Additionally, since second-row elements (e.g., C, O, N, F) are relatively transparent to EUV light, other elements must be used.
3. The maturation of EUVL has convinced resist companies around the world to assign more chemists to invent better EUV resists, prompting the investigation into more exotic resist designs.

This section will describe multinuclear (two or more metal atoms/molecule) materials followed by mononuclear (one metal atom/molecule) resist systems. Due to space limitations, resists containing less than 1 atomic % metal and/or resists for which the photochemistry does not involve the metal center will not be included.[160–162]

8.8.1 Metal oxide resists from Oregon-State University and Inpria

The e-beam imaging capability of metal-oxide resists developed by Keszler and coworkers at OSU was first published in 2009.[227] These researchers described metal-oxide films (not nanoparticles) composed of peroxo-modified forms of hafnium oxide sulfate (HafSOx) or zirconium oxide sulfate (ZircSOx) that showed e-beam sensitivity ($D_{0.8}$ = dose to 80% thickness using 30 keV e-beams) as low as 21 and 7.6 $\mu C/cm^2$, respectively. These relatively fast resists had molar metal-to-sulfate ratios of ~2:1. The ZircSOx resist printed 16-nm isolated lines and 28-nm dense lines with LWRs of 3.4 and 6.4 nm, and with doses of 112 and 50 $\mu C/cm^2$, respectively, using the same 2:1 of metal to sulfate ratio [Figs. 8.35(a) and (b)]. When the metal-to-sulfate ratio is reduced to 1.4:1, the LWR improves but at a cost to sensitivity. These resists printed 15-nm isolated lines and 32-nm dense lines with LWRs of 1.9 and 2.1 nm, and with doses of 999 and 810 $\mu C/cm^2$, respectively. Additionally, the HafSOx and ZircSOx resists were evaluated for etch resistance versus that of thermally grown SiO_2. The authors found that these metal oxide resists etch 9× and 7× slower than the SiO_2 control, respectively. Commercial work on these metal-oxide resists has been done by the Inpria Corporation.

The key to the photoreactivity of the HafSOx resists appears to be controlling the dehydration reaction [Fig. 8.36(a)], which crosslinks and thereby reduces the solubility of these metal oxo-films.[147] This dehydration reaction is inhibited by binding peroxide to Hf. Fortunately, the metal peroxide decomposition can be induced by high-energy light or electrons [Fig. 8.36(b)], thereby creating metal hydroxides that can condense and become insoluble. In brief, the metal peroxides allow the resists to dissolve in the unexposed regions,

Downloaded From: https://www.spiedigitallibrary.org/ebooks/ on 09 Mar 2022
Terms of Use: https://www.spiedigitallibrary.org/terms-of-use

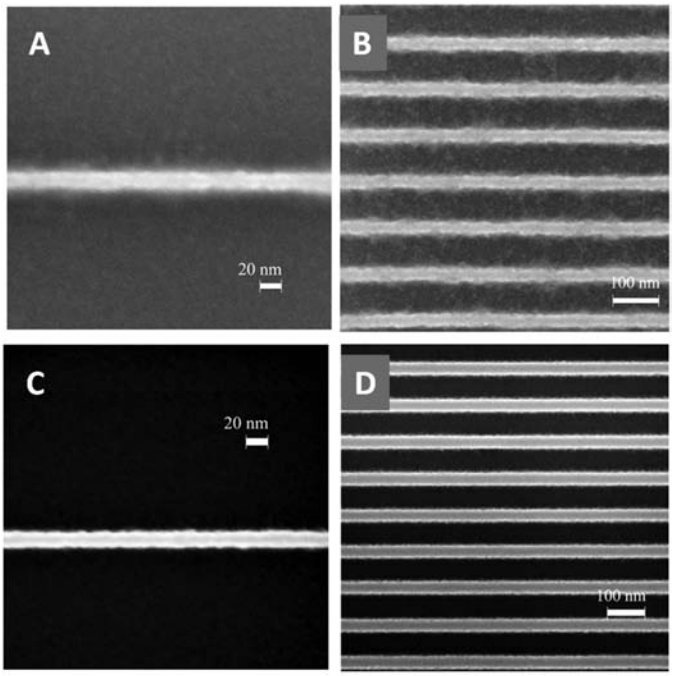

Figure 8.35 SEM images of ZircSOx resist films exposed with 30-keV electron beams: (a) metal/sulfate = 2.0, 16-nm isolated line, dose = 112 μC/cm^2; (b): metal/sulfate = 2.0, 28/72-nm lines and spaces, dose = 50 μC/cm; (c) metal/sulfate = 1.4, 15-nm isolated line, dose = 999 μC/cm^2; (d) metal/sulfate = 1.4, 36/64-nm lines and spaces, dose = 810 μC/cm^2 (reprinted from Ref. 227 with permission; © 2009 Elsevier).

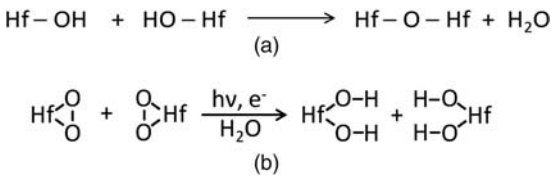

Figure 8.36 Proposed mechanisms for OSU/Inpria resists: (a) dehydration mechanism and (b) photomechanism (reprinted from Ref. 147).

and upon photolysis the metal peroxides become metal hydroxides and condense to become insoluble features of the negative-tone resists.

The first manuscript to describe EUV imaging of these OSU/Inpria metal-oxo resists on the Berkeley MET showed 22-nm posts and 22-nm lines with modulation down to 15 nm (Fig. 8.37).[148] Later, Ekinci and coworkers from the Paul Scherrer Institut (PSI) demonstrated the remarkable imaging capabilities of Inpria XE151JB and XE151IB using EUV interference lithography. These resists printed dense lines from 22–16 nm with doses of 75–80 and 160–200 mJ/cm^2, respectively (Fig. 8.38). The LER of XE151JB

Downloaded From: https://www.spiedigitallibrary.org/ebooks/ on 09 Mar 2022
Terms of Use: https://www.spiedigitallibrary.org/terms-of-use

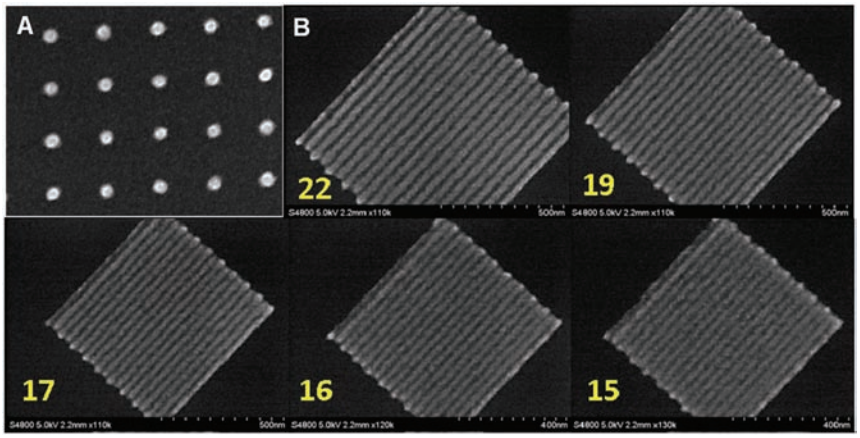

Figure 8.37 SEM images of patterns printed using the Inpria metal-oxide resist: (a) 22-nm posts printed using conventional annular illumination; (b) 22- to 15-nm dense lines printed using pseudo–phase shift mode on the 0.3-NA Berkeley MET (reprinted from Ref. 148).

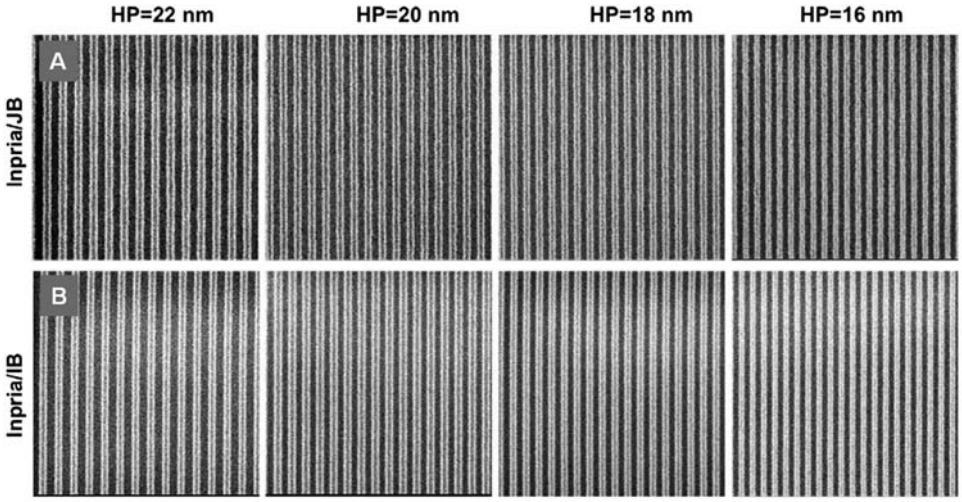

Figure 8.38 SEM images printed using Inpria/OSU resists as imaged by interference lithography at the PSI: (a) Inpria/JB resist and (b) Inpria/IB resist (reprinted from Ref. 163).

was determined to be 2 ± 0.5 nm. Furthermore, XE151JB and XE151IB could resolve 12- and 8-nm dense lines at doses estimated to be $\geq$80 and $\geq$200 mJ/cm^2, respectively (Fig. 8.39).

Hafnium oxide and zirconium oxide nanoparticle resists. Research by C. Ober, E. Giannelis, and coworkers at Cornell University demonstrated several unique resist systems based on HfO_2 or ZrO_2 nanoparticles with carboxylate ligands (Fig. 8.40).[149–158] These interesting and unique resists exhibit negative-tone imaging upon exposure to DUV, 193-nm, EUV, and

Downloaded From: https://www.spiedigitallibrary.org/ebooks/ on 09 Mar 2022
Terms of Use: https://www.spiedigitallibrary.org/terms-of-use

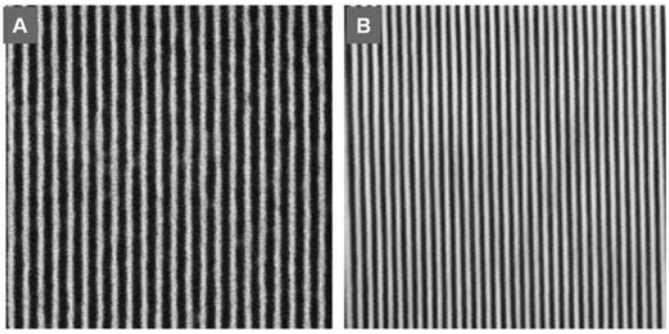

Figure 8.39 SEM images of (a) 12-nm half-pitch dense lines printed using the Inpria/JB resist and (b) 80-nm half-pitch dense lines printed using the Inpria/IB resist (reprinted from Ref. 163).

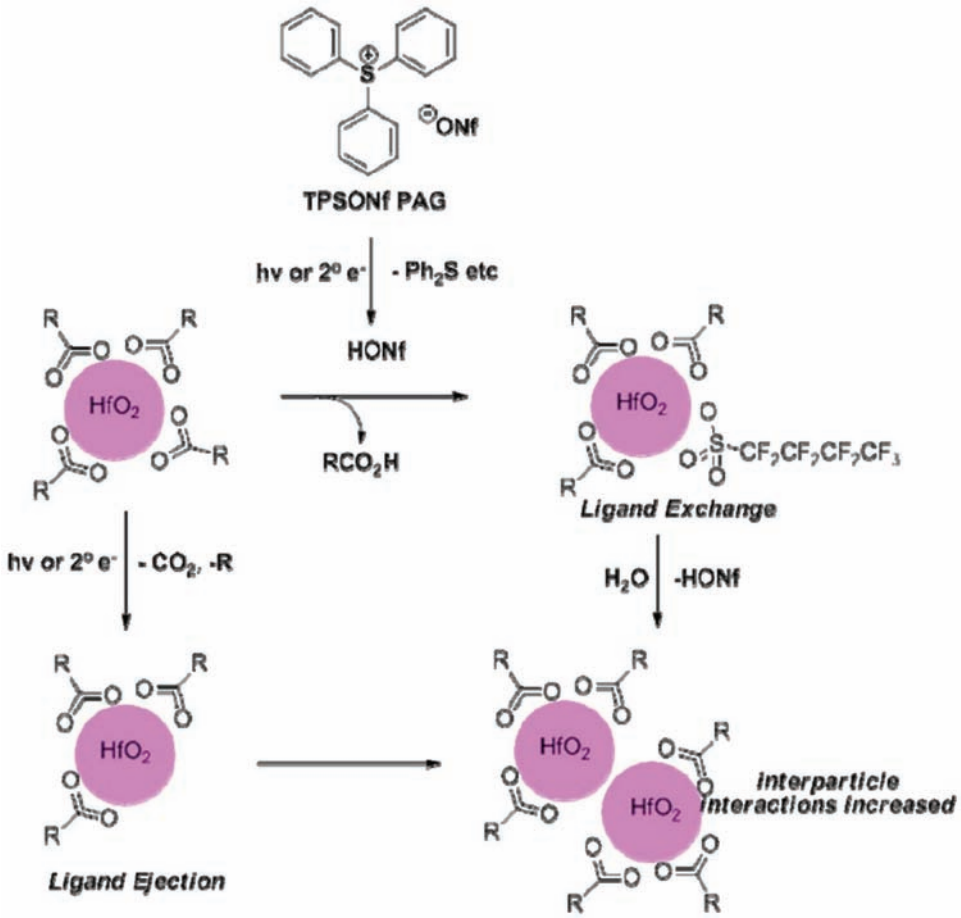

Figure 8.40 Photomechanism of negative-tone HfO_2 nanoparticle resists (reprinted from Ref. 155).

Downloaded From: https://www.spiedigitallibrary.org/ebooks/ on 09 Mar 2022
Terms of Use: https://www.spiedigitallibrary.org/terms-of-use

e-beam radiation. Furthermore, these resists can also produce positive-tone imaging using wavelengths of 193-nm and DUV when processed using post-exposure bakes.

The earliest versions of these resists were prepared using methacrylate [$-O_2CC(CH_3)=CH_2$)] as a ligand and formulated with either PAGs or free-radical initiators. Although the use of methacrylate ligands suggest that the negative-tone imaging mechanisms might involve free-radical crosslinking, careful spectroscopic, thermodynamic, and mechanistic studies reveal that the negative-tone solubility switches do not involve free-radical crosslinking, but instead involve a ligand exchange mechanism that can proceed without PAGs [Fig. 8.40 (left)] or with the assistance of PAGs [Fig. 8.40 (right)].[153,155–158,164]

These nanoparticle resists have good EUV patterning capability at extremely fast photospeeds. Recently, Ober and coworkers demonstrated the imaging capabilities of HfO_2 and ZrO_2 nanoparticle resists prepared with trans-dimethylacrylic acid as a solubilizing ligand and containing 3 wt % non-ionic PAG (Fig. 8.41).[156] 20- and 30-nm isolated lines were printed using doses of 2.4 and 1.6 mJ/cm^2, for HfO_2 and ZrO_2, respectively. Although the LER values of these resists are modest (5–7 nm), the LER is not too poor, considering that the resists are extremely sensitive and are composed of nanoparticles that are 1–2 nm in diameter.[149]

8.8.2 Tin oxide cluster resists from CNSE

Cardineau, Brainard, and coworkers described the synthesis and lithographic evaluation of thin films of tin-oxo clusters ($[(RSn)_{12}O_{14}(OH)_6]X_2$ [Fig. 8.42(a)]), using EUV light (13.5 nm).[165,166] These tin clusters consist of spherical tin-oxo cages in which each tin atom is covalently bound to one

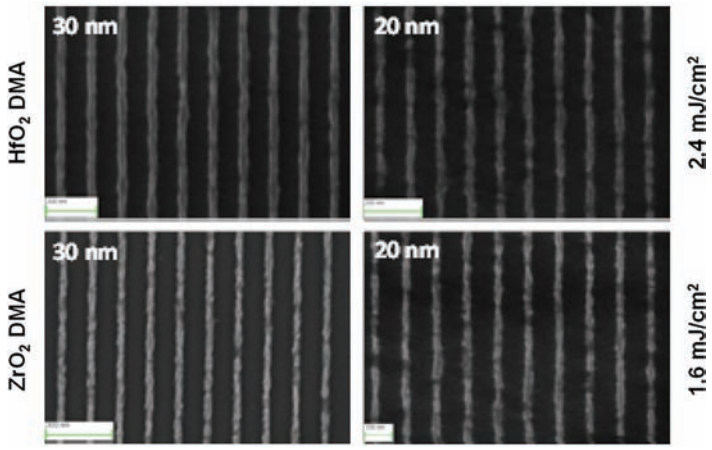

Figure 8.41 Imaging capability of HfO_2 and ZrO_2 nanoparticle resists (reprinted from Ref. 156 with permission from The Society of Photopolymer Science and Technology).

Downloaded From: https://www.spiedigitallibrary.org/ebooks/ on 09 Mar 2022
Terms of Use: https://www.spiedigitallibrary.org/terms-of-use

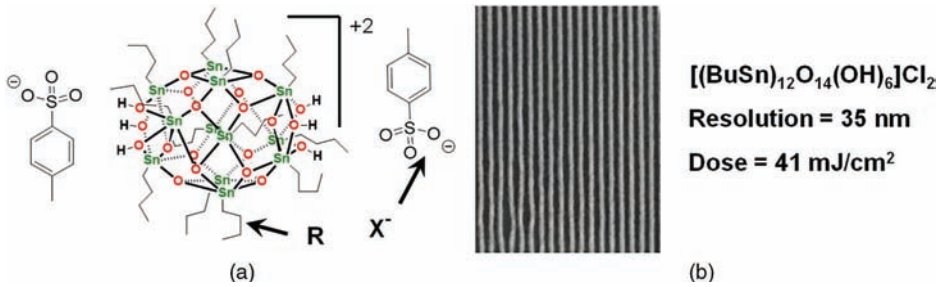

Figure 8.42 The mechanism of photolysis for tin clusters of the type $[(RSn)_{12}O_{14}(OH)_6]X_2$ was explored through structural variation. (a) Clusters were made varying the bond energies of both the counter-ions (X) and the organic ligands (R), and tested for EUV lithographic performance. (b) 35-nm dense lines printed using $[(BuSn)_{12}O_{14}(OH)_6]Cl_2$ (reprinted from Ref. 166).

organic (R) group. The clusters have a +2 charge and are typically precipitated with pairs of anions (X). Furthermore, these new resists should be relatively dark since both tin and oxygen readily absorb EUV photons with optical densities that are 10.5× and 1.7× greater than carbon (Fig. 8.6).[16,17]

Lithographic results. In an initial study, the tin-oxo cluster $[(n\text{-}BuSn)_{12}O_{14}(OH)_6](p\text{-}CH_3C_6H_4SO_3)_2$ was dissolved in 2-butanone and spin-coated into a thin film. The film was exposed to EUV light in an open-field pattern using the Berkeley direct contrast tool[167] (DCT) and developed in 66% aqueous isopropanol solvent for 30 s. This film exhibits negative-tone sensitivity of 20 mJ/cm^2. The authors also printed 35-nm dense lines by exposing a film of $[(n\text{-}BuSn)_{12}O_{14}(OH)_6]Cl_2$ using the interference lithographic tool at PSI, albeit with a dose of 41 mJ/cm^2 [Fig. 8.42(b)].

Correlation between sensitivity and C-Sn bond strength. The authors evaluated sensitivities of resists prepared with three organic groups bonded to tin: benzyl, butyl and phenyl. One possible reaction that could occur during exposure is homolytic cleavage of the tin–carbon bond. Tin–carbon bonds are relatively weak (~50 kcal/mol), and tin forms extremely stable radicals; therefore, the authors reasoned that EUV exposure could cause homolysis of the Sn-C bond.[168] Figure 8.43(a) shows the C-H bond dissociation energies of the three hydrocarbons. These C-H bond energies predict the relative stabilization of their radical fragments.

Clusters 8 through 10 were coated on wafers and tested lithographically [Fig. 8.43(a)]. Figure 8.43(b) shows the C-H bond energy versus dose to E_{size} curve for the tin-oxo cluster.[169] In general, the clusters with the weaker C-H bonds show the best sensitivity. By analogy, the authors conclude that the reactivity of the clusters is correlated to the strength of the tin–carbon bonds. This correlation supports a photolysis mechanism in which the homolysis of the tin–carbon bond is involved in the observed change in film dissolution rate.

Downloaded From: https://www.spiedigitallibrary.org/ebooks/ on 09 Mar 2022
Terms of Use: https://www.spiedigitallibrary.org/terms-of-use

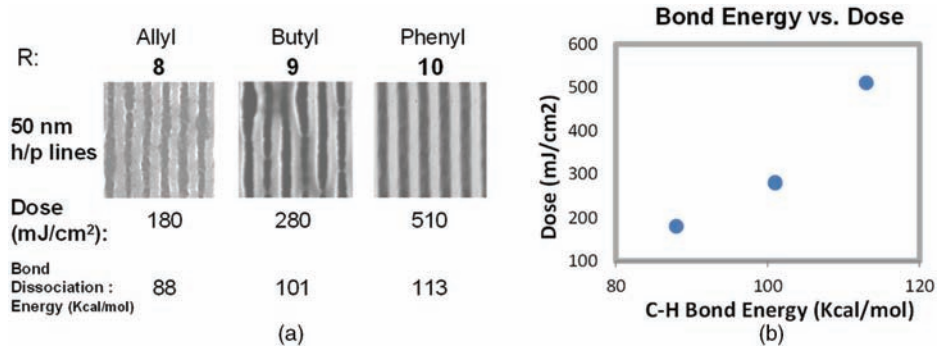

Figure 8.43 (a) The bond dissociation energies for three organic groups and lithographic results. By incorporating these groups into the tin clusters, a broad distribution of Sn-C bond energies should be achieved. (b) For the three clusters tested, there appears to be a direct correlation between the radical stability of the organic group and the sensitivity of the cluster, suggesting that homolysis is occurring (reprinted from Ref. 166).

8.8.2.1 Organo-bismuth oligomers

Passarelli and coworkers developed resists based on bismuth oligomers.[170,171] Figure 8.44 shows the lithographic capabilities of four of these oligomers. The best resolution was obtained from the dichloride variant (21 nm) and the best

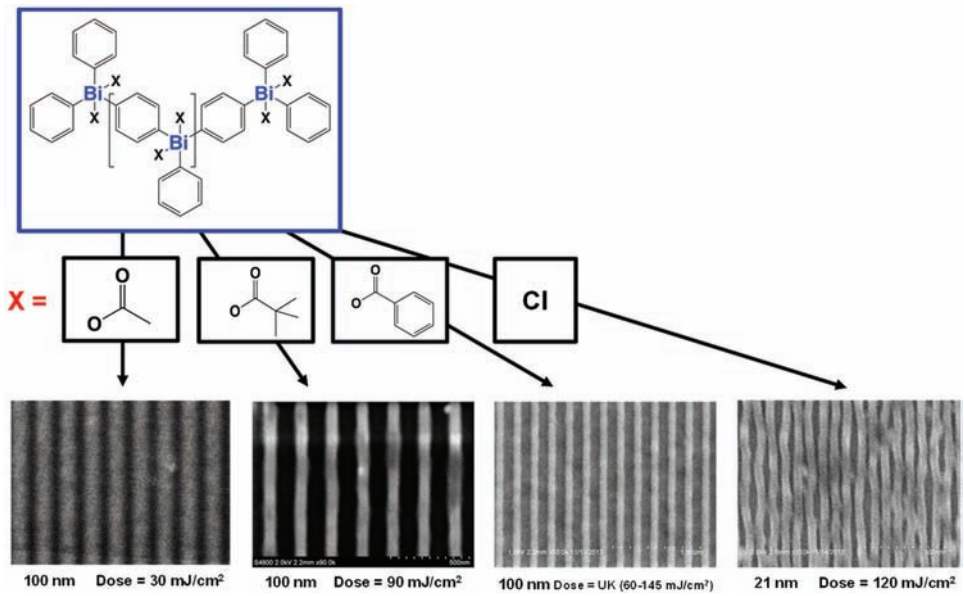

Figure 8.44 Lithographic results for oxidized bismuth oligomer with various X group substituents. Exposures were performed using the LBNL 0.3-NA MET. Dose of 30 mJ/cm^2 is achieved for X = O_2CCH_3, and a resolution of 21 nm is achieved for X = Cl. The dose for the resist in which X = benzoate was between 60 and 145 mJ/cm^2 (reprinted from Ref. 170).

Downloaded From: https://www.spiedigitallibrary.org/ebooks/ on 09 Mar 2022
Terms of Use: https://www.spiedigitallibrary.org/terms-of-use

sensitivity from the diacetate variant (30 mJ/cm^2). All of the SEM images displayed are of negative-tone development. The authors propose that the negative-tone imaging may result from homolytic cleavage of the Bi-X bond (Fig. 8.44) followed by covalent bond formation between the metal center and aromatic ligand.

8.8.3 Mononuclear-metal resists

Researchers at CNSE and SUNY New Paltz have conducted a broad exploration of resists containing metals with high EUV cross-sections (excluding Hf and Zr studied by OSU, Inpria, and Cornell). The name of this program is Molecular Organometallic Resists for EUV (MORE). Two *multinuclear* resists developed by this program are described in Sections 8.8.2 and 8.8.2.1. This section reviews four resist approaches based on *mononuclear* organometallic complexes. Although these resists have lower concentrations of metal atoms, important photochemical transformations occur at the metal centers and, therefore, provide insight into the kinds of reactions that can occur in metal-containing EUV resists.

Transition-metal oxalates. Freedman and coworkers developed a series of transition-metal oxalates that produce negative-tone resists. One study showed the importance of oxalate loading [versus bipyridine (bpy)] in cobalt complexes.[172] The negative-tone sensitivity of these resists increases dramatically with the number of oxalate ligands (Fig. 8.45). As the number of oxalate ligands increases, so does the negative charge on the transition-metal complex. Authors were not sure which effect was more important for giving good sensitivity: numbers of oxalate ligands or the negative charge.

Another study showed that E_{size} improves as the identity of the central transition-metal changes from chromium to iron to cobalt (Fig. 8.46). Although the ligands are all the same and the oxidation states of the central metal are all the same (+3), as both the number of d-electrons (4, 5, 6) and the optical density of the transition metal (16, 21, 27) increase, the sensitivity improves.

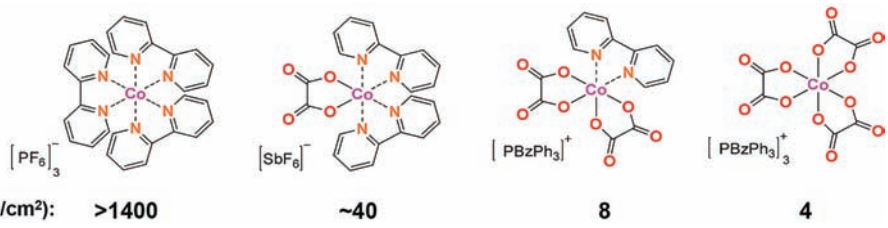

Figure 8.45 Cobalt complexes using bipyridine and oxalate ligands were exposed using an open-frame technique at PSI. The resists improve in EUV photosensitivity when the number of oxalate ligands increases and when the charge on the cobalt complex becomes more negative (reprinted from Ref. 172).

Downloaded From: https://www.spiedigitallibrary.org/ebooks/ on 09 Mar 2022
Terms of Use: https://www.spiedigitallibrary.org/terms-of-use

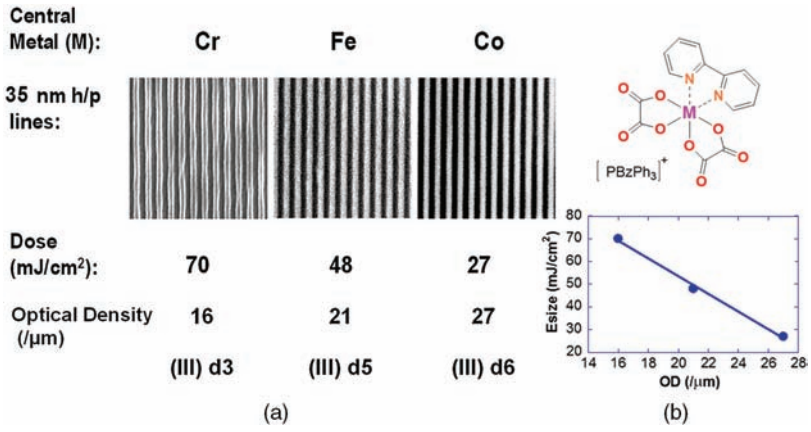

Figure 8.46 (a) EUV imaging capability of resists prepared from three complexes of the type $PBzPh_3$ bpy(ox)$_2$*M*, where *M* = Cr, Fe, and Co, versus optical density and number of d-electrons of the central metal. (c) A plot of E_{size} versus optical density of the central metal (reprinted from Ref. 172).

Positive-tone palladium oxalates. Sortland and coworkers developed the first mononuclear positive-tone organometallic resists for EUVL [Fig. 8.47(a)].[173,174] Positive-tone photoresists are attractive as they allow for dark-field masks in contact hole manufacturing. Dark-field masks are preferred as they minimize flare and are easier to correct for mask defects than bright-field masks. Researchers found that bis-phosphine palladium or platinum oxalates give resists that produce positive-tone images when developed in nonpolar solvents [Fig. 8.47(b)].

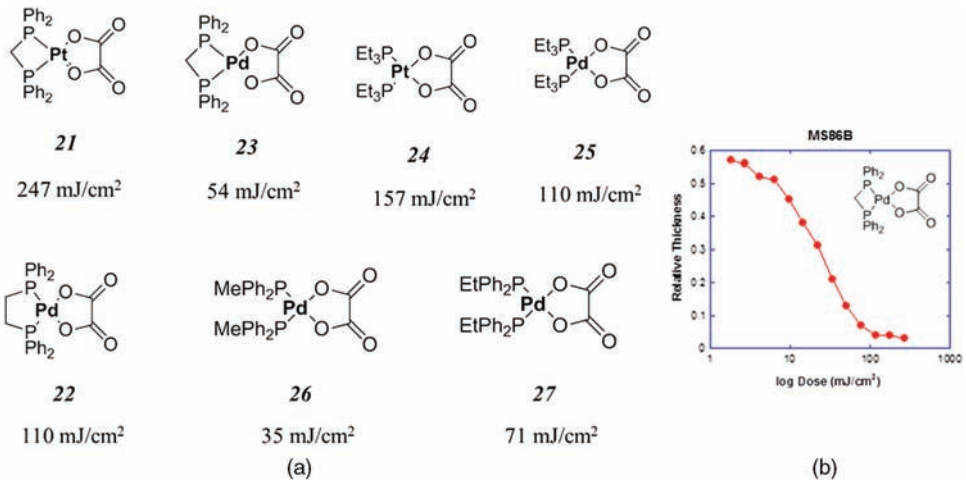

Figure 8.47 (a) E_0 for different platinum and palladium-phosphine oxalates when exposed using the open-frame technique at PSI. (b) Contrast curve of one palladium oxalate resist (reprinted from Ref. 173).

Downloaded From: https://www.spiedigitallibrary.org/ebooks/ on 09 Mar 2022
Terms of Use: https://www.spiedigitallibrary.org/terms-of-use

Comparison with solution-phase photochemistry in the literature[175–177] and exposure of crystals to i-line light by the authors led the authors to propose the exposure mechanism shown in Fig. 8.48, in which metal oxalates create CO_2 as well as zero-valent palladium-phosphine complexes and palladium metal. This photoreaction is consistent with all experimental data, and similar results are found in the literature.[175,178] The L_4Pd complex is more soluble than the starting material, explaining the positive-tone behavior of this resist system. Unfortunately, palladium metal is insoluble, and the authors were unable to get complete clearing in the exposed regions.

Low-LER dibenzyl tin complexes. Del Re and coworkers developed a series of organometallic tin dicarboxylates $[R_2Sn(O_2CR')_2]$ that print dense L/S patterns with very low LER.[169,179] Although the sensitivity of many of these compounds is poor (E_{size} = 50–600 mJ/cm^2), they were capable of good resolution and excellent LER when exposed using interference lithography at PSI. In particular, dibenzyl tin dibenzoate [Fig. 8.49(a)] prints 50- and 35-nm dense lines with LWR of 1.7 nm, and dibenzyltin dipivalate resolves 16-nm half-pitch dense lines with 2.1-nm LER and resolves 22-nm half-pitch dense lines with 1.4-nm LER [Fig. 8.49(b)].

Interestingly, these resists seem to show better sensitivity with lower molecular weights, perhaps indicating that higher metal content is important for achieving better sensitivity. We also see a linear trend when we compare molecular weights with E_{max} within a particular compound family (Fig. 8.50).

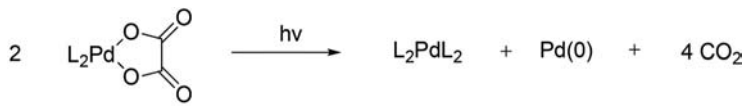

Figure 8.48 Proposed photoreaction for (dppm)Pd(C_2O_4) and $(Ph_2EtP)_2PdC_2O_4$. The photoreaction is consistent with all experimental data (reprinted from Ref. 173).

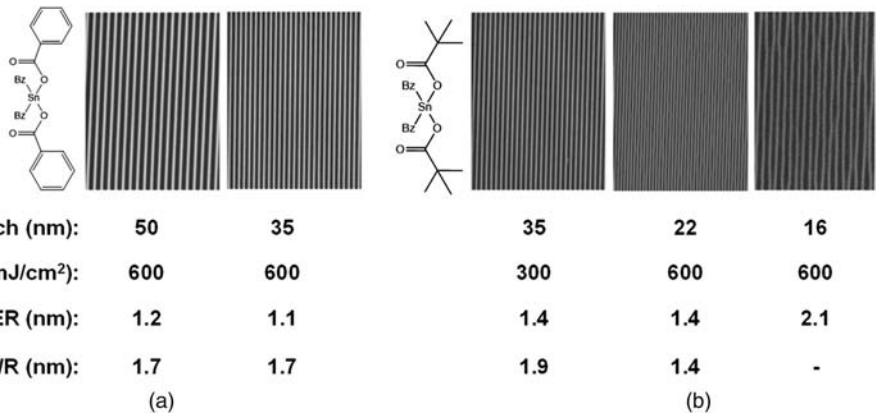

Figure 8.49 EUV imaging capabilities of (a) dibenzyl tin dibenzoate and (b) dibenzyltin dipivalate (reprinted from Ref. 179).

Downloaded From: https://www.spiedigitallibrary.org/ebooks/ on 09 Mar 2022
Terms of Use: https://www.spiedigitallibrary.org/terms-of-use

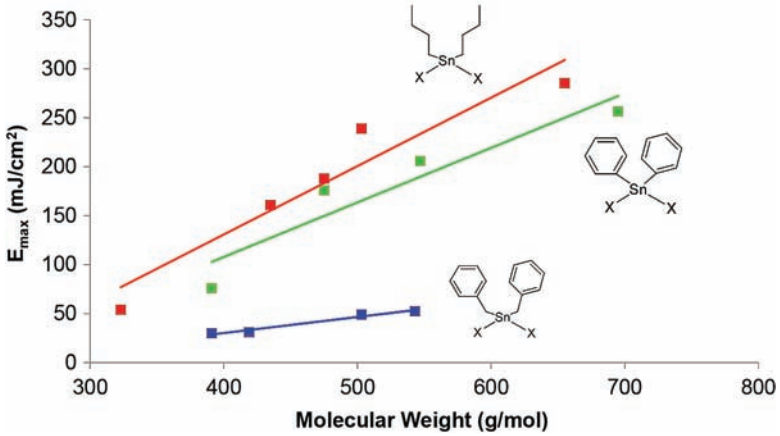

Figure 8.50 Strong correlations exist between sensitivity and molecular weight for $R_2Sn(O_2CR)_2$ complexes when the hydrocarbon moiety (i.e., butyl, phenyl, or benzyl) bonded to tin is the same (reprinted from Ref. 179).

8.8.3.1 High-speed resists using antimony, tin, tellurium, and bismuth

Passarelli and coworkers have presented a series of high-speed, negative-tone resists of the general form $R_nM(O_2CR')_2$ where M is the main-group metal antimony, tin, tellurium or bismuth, and the carboxylate group is capable of undergoing free-radical polymerization (acrylate, methacrylate, or styrene carboxylate). The authors explored the systematic variations of the metal (M), the aliphatic or aromatic R group, and the polymerizable carboxylate group (O_2CR') by preparing and lithographically evaluating more than 35 compounds.[180,181]

One resist, tri(phenyl)antimony diacrylate (JP-20), prints 35-nm lines with modulation down to 16 nm, with sensitivities of 5.6 and 9.2 mJ/cm^2 when developed in hexanes or water, respectively (Fig. 8.51). This resist exhibits negative-tone imaging in both developers. It has also passed witness plate-based outgassing tests and has excellent shelf-life.

Four resists of the type $Ph_nM(acrylate)_2$ and containing antimony, tin, tellurium, or bismuth were synthesized, coated, and evaluated for contrast-curve performance (Fig. 8.52). The relative sensitivities are: antimony produces the fastest resist, then bismuth = tin, and tellurium is the slowest. This sensitivity trend cannot be explained by optical density differences since tin and tellurium are about the same and darkest, then antimony, followed by bismuth. The sensitivity of these resists is, therefore, not merely due to their ability to absorb photons, but also due to other factors explored by the authors.

The authors proposed that these main-group olefin complexes undergo photolysis and solubility changes through a mechanism that involves free-radical polymerization of double bonds (Fig. 8.53). They propose that the initiation involves homolytic cleavage of the M-carboxylate bond followed by

Downloaded From: https://www.spiedigitallibrary.org/ebooks/ on 09 Mar 2022
Terms of Use: https://www.spiedigitallibrary.org/terms-of-use

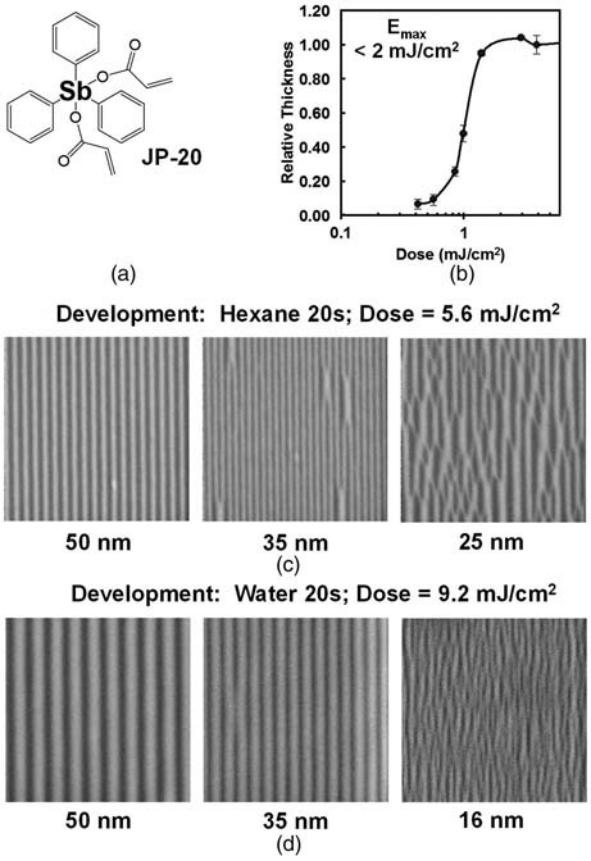

Figure 8.51 Lithographic performance of (a) $Ph_3Sb(O_2CCH{=}CH_2)_2$ (JP-20). (b) High-contrast and high-sensitivity are achieved. (c) JP-20 can be developed in either hexane or (d) water. Both developers produce negative-tone imaging (reprinted from Ref. 180).

polymerization to create linear or branched oligomers within the exposed region. This mechanism is supported by three additional studies: (1) $Ph_3Sb(O_2CH{=}CH_2)_2$ is ~15× faster than $Ph_3Sb(O_2CH_3)_2$. (2) $Ph_3Sb(O_2CH{=}CH_2)_2$ and $(cyclohexyl)_3Sb(O_2CH{=}CH_2)_2$ have exactly the same photospeed, suggesting that M-C bond cleavage is not involved in the mechanism. (3) The sensitivity of the resist directly correlates to the concentration of olefins in the resist (discussed below).

The authors tested the hypothesis that the greatest contributor to the sensitivity of molecules of the type $R_nSb(O_2CR')_2$ is the concentration of polymerizable olefins in the resist. They reasoned that in order for the propagation of free-radical polymerization to proceed, the olefins must be in contact with other olefins, and that higher concentrations of olefins would lead to higher turnover numbers. Larger turnover number should lead to greater sensitivity because more molecules are reacted per initiation event, and

Downloaded From: https://www.spiedigitallibrary.org/ebooks/ on 09 Mar 2022
Terms of Use: https://www.spiedigitallibrary.org/terms-of-use

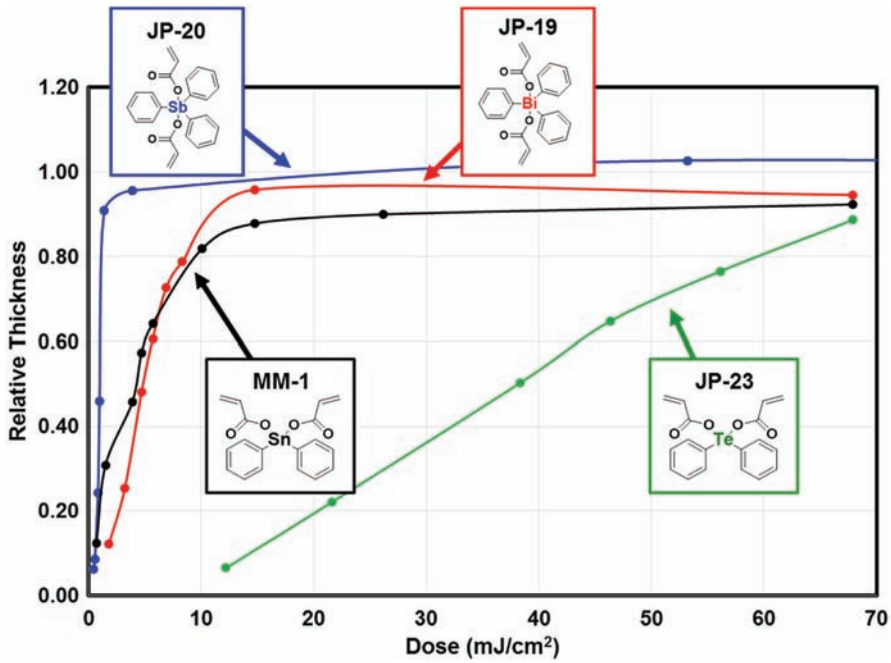

Figure 8.52 Comparison of $Ph_nM(Acrylate)_2$ where M = antimony, bismuth, tin, or tellurium. Antimony is the most sensitive (reprinted from Ref. 180).

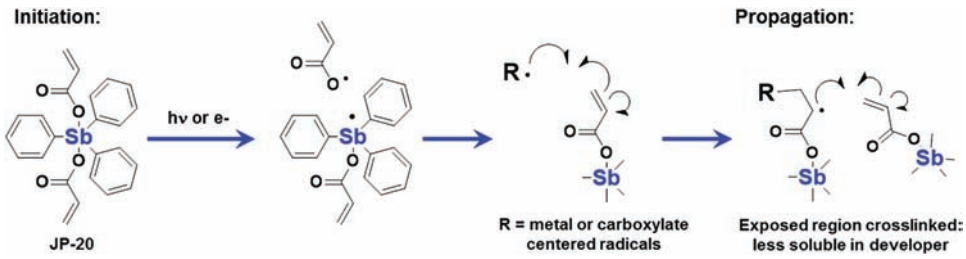

Figure 8.53 Proposed mechanism of an antimony organometallic carboxylate resist system. The authors propose that good sensitivity is achieved through one photochemical homolysis event leading to a cascade of subsequent solubility-changing polymerization reactions (reprinted from Ref. 180).

because higher-molecular-weight molecules have lower solubility. To test this hypothesis, the authors defined a parameter called polymerization olefin loading (POL) as the number of olefins/number of all atoms (excluding hydrogen). A semi-log plot of E_{max} versus POL is shown for 15 resist materials in Fig. 8.54. There is a linear relationship between $\text{Log}E_{max}$ versus POL, whereas as POL increases, E_{max} decreases (the resist becomes more sensitive). The authors conclude that this correlation is further evidence in support of the imaging mechanism shown in Fig. 8.53.[180]

Downloaded From: https://www.spiedigitallibrary.org/ebooks/ on 09 Mar 2022
Terms of Use: https://www.spiedigitallibrary.org/terms-of-use

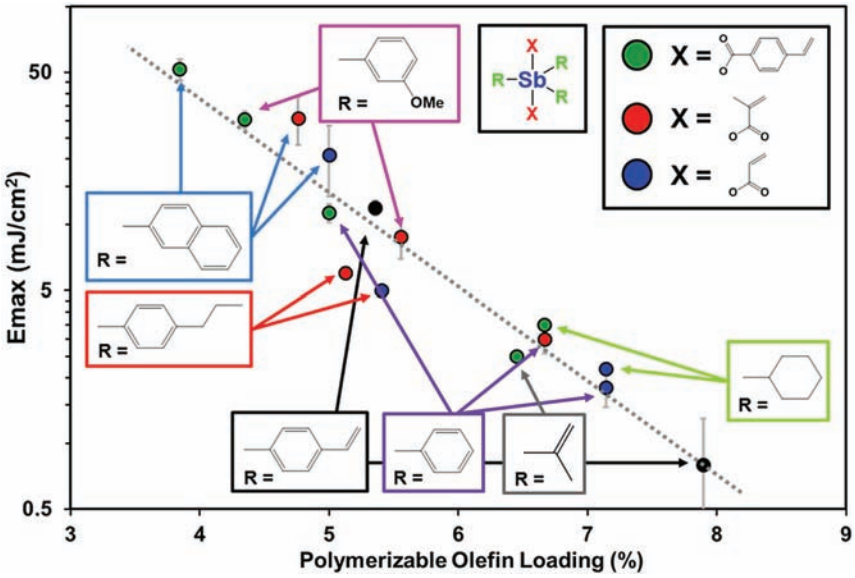

Figure 8.54 Plot of E_{max} versus polymerizable olefin loading (POL). A linear trend is demonstrated in LogE_{max} versus POL for multiple antimony organometallic carboxylates (reprinted from Ref. 180).

8.9 LER and Modeling

8.9.1 Background: continuous and stochastic models

There are three generic approaches to modeling the exposure and development of photoresist: nonstochastic continuum models, stochastic continuum models, and discrete stochastic models. The nonstochastic continuum approach treats all relevant quantities (e.g., absorbed dose, PAG distribution, latent image) as smooth continuous functions of position. Stochastic continuum models allow for statistical fluctuations of continuously varying functions. Discrete stochastic models, in one way or other, treat the resist as a lattice of discrete pixels in 2D or voxels in 3D that are on the order of a few nanometers on a side and compute what happens individually in each pixel or voxel at discrete time steps.

Figure 8.55 schematically shows the difference between continuum and stochastic models. In Fig. 8.55(a), the absorbed dose distribution is plotted as a continuous function in terms of the number of absorbed photons per unit area in the resist. Figure 8.55(b) is generated by using the value in Fig. 8.55(a) in each 1-nm-square pixel as the average value in a Poisson distribution and then generating a statistical value for the number of absorbed photons in that pixel based on that Poisson distribution. In both graphs, the grayscale indicates the numerical value in each pixel. This physics is the same for any wavelength and any feature size or shape. In reality, the effect of dose on the

Downloaded From: https://www.spiedigitallibrary.org/ebooks/ on 09 Mar 2022
Terms of Use: https://www.spiedigitallibrary.org/terms-of-use

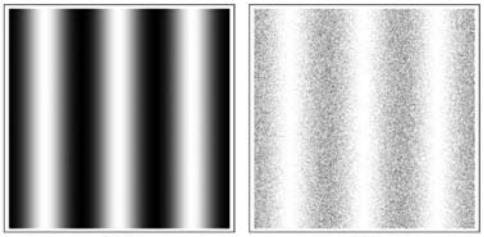

Figure 8.55 Schematic illustration of the difference between (a) a continuum model of absorption and (b) a discrete or stochastic model.

photoresist is discrete [Fig. 8.55(b)] and not continuous [Fig. 8.55(a)]. This is because, following the rules of quantum mechanics, single photons are absorbed by single atoms or molecules. This discreteness, along with the randomness of photoresist chemistry, and the statistics or stochastics it engenders, is the dominant cause of LER.

As a second example, the solution to the diffusion equation yields a smooth function that can be interpreted as the smooth nonstochastic local density of some molecular species. But the same solution can be re-interpreted as the probability of finding a given number of molecules of that species in a given volume. With this probabilistic interpretation, statistical fluctuations in the local density can be accounted for using a Poisson distribution. A full discrete stochastic model directly keeps track of the number of the molecular species in each pixel or voxel.

It is clear from Fig. 8.55(b) that the stochastic nature of the exposure process will lead to statistical effects in the developed resist features, effects that are referred to generically as shot noise. As briefly discussed below and more completely in Chapter 10, this shot noise effect coming from the discreteness of released acids during exposure is the dominant cause of LER and can be used to predict the dependence of LER on dose, image resolution, and other parameters as well as the frequency content of the LER.[182] It should be noted that, although photon or acid shot noise may be the dominant cause of LER, stochastic chemical effects occurring during PEB and development can also be significant contributors. In fact, the purpose of stochastic resist simulation as discussed below is precisely to be able to simulate all possible stochastic effects in order to precisely predict their impact on resist features.

In contrast to 248- and 193-nm optical lithography, where the exposure mechanism predominantly proceeds via direct absorption of photons by PAG molecules, the exposure mechanism for EUVL proceeds dominantly via a cascade of electrons generated by the absorption of an EUV photon by any molecular species in the resist. (For a detailed discussion see Section 8.4). However, the electrons themselves, directly or indirectly, cause PAGs to create acid molecules. The reason this is the predominant mechanism is that a

Downloaded From: https://www.spiedigitallibrary.org/ebooks/ on 09 Mar 2022
Terms of Use: https://www.spiedigitallibrary.org/terms-of-use

13.5-nm EUV photon carries ~92 eV of energy as opposed to the 6.4 eV of energy carried by a 193-nm photon, and so is highly absorbed by many atomic species (Fig. 8.56). It is essentially identical to electron beam exposure where the primary or incident electron, which generally has energy in the keV range, is replaced with an EUV-generated electron with ~75 to 82 eV. However, it should be noted that due to the combination of (1) the finite temperature of the resist, (2) the multiple different energy levels in each resist molecule, and (3) the spreading or blurring of energy levels due to interactions between molecules, it follows from quantum mechanics that electrons can be generated with energies over the full range from 0 to 92 eV, but with nominally significantly lower probability than the ~75 to 82 eV range. Defining quantum efficiency as the average number of acids released per absorbed photon we see that for EUV wavelengths the quantum efficiency can easily be greater than one (Section 8.4).

Also, because an EUV photon carries a little over 14× more energy than a 193-nm photon, the *number of photons* absorbed to generate a given exposure dose in the resist is *14 times smaller*; hence, the shot noise effect coming from the number of absorbed photons is roughly $\sqrt{14}$ or ~3.8× larger. This difference is illustrated in Fig. 8.57, which shows the number of 193-nm photons absorbed in a given resist volume [Fig. 8.57(a)] and the number of EUV photons absorbed in the same volume needed to yield the same absorbed dose [Fig. 8.57 (b)].

8.9.2 Modeling steps

Independent of the type of model used, the following steps must be accounted for in more or less detail when modeling a CAR.

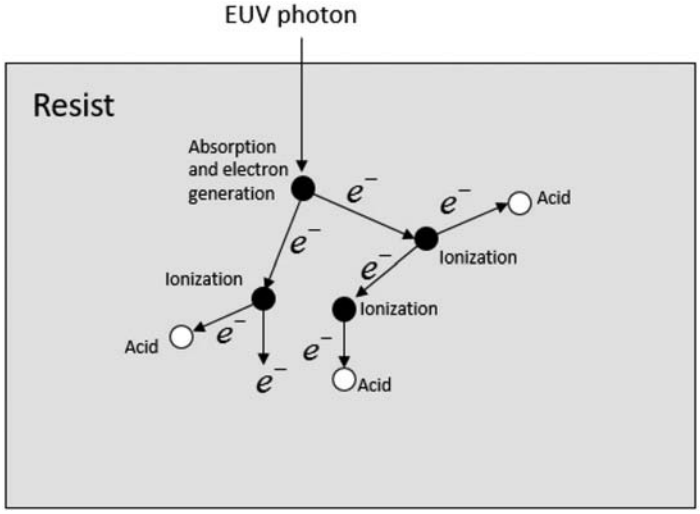

Figure 8.56 13.5-nm EUV photons are absorbed by essentially every atom or molecule in the photoresist and not just by the PAG molecules.

Downloaded From: https://www.spiedigitallibrary.org/ebooks/ on 09 Mar 2022
Terms of Use: https://www.spiedigitallibrary.org/terms-of-use

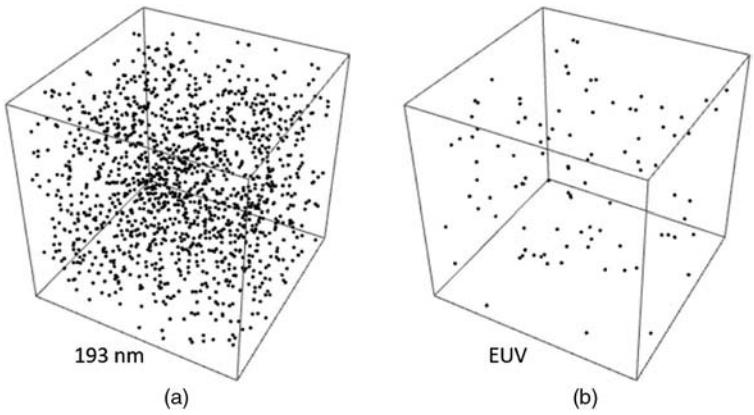

Figure 8.57 Volumetric illustration of the difference between (a) the number of 193-nm photons absorbed for a given dose and (b) the number of 13.5-nm EUV photons absorbed to produce the same dose in terms of mJ/cm^2.

1. Initial resist state. In many continuum models, only the thickness and index of refraction need to be defined. In models that account for more-detailed resist properties, either continuum or stochastic, the distribution of PAG and base quencher molecules is included either as a continuous density distribution or as a statistical distribution.

2. Image intensity distribution. The intensity distribution is determined either as an aerial image or as the image in the resist. Ideally, the image in the resist is volumetric. Depending on the level of detail required, the effect of absorption in terms of decreasing the image intensity going from the top to the bottom of the resist may be included. In low-NA imaging, where the mask is illuminated at normal and/or near–normal incidence over a small range of angles, the diffraction from a transmitting mask can be adequately represented using the thin mask approximation, which treats the mask as an amplitude and phase sheet. That is, the electric field transmitted through the mask is simply the incident field multiplied by a position-dependent amplitude and phase, and the diffraction pattern is the Fourier transform of this result. This is a valid approach as long as both the wavelength of the light and the mask topography are much smaller than the feature sizes on the mask, in which case boundary condition effects on the electromagnetic field caused by the edges of the mask features can be ignored. When the feature sizes are close to or even less than the wavelength, and/or the topography is large compared to the mask features, Maxwell's equations with the relevant boundary conditions must be solved within the mask structure to determine the diffraction. For EUV wavelengths, the mask is reflecting, topographic, and illuminated at an angle, nominally on the order of 6 deg. Even though the range of illumination angles is small, the 3D structure of the mask leads to shadowing and other effects. To a first approximation, shadowing can be

Downloaded From: https://www.spiedigitallibrary.org/ebooks/ on 09 Mar 2022
Terms of Use: https://www.spiedigitallibrary.org/terms-of-use

accounted for by geometrically determining the position-dependent amplitude and phase distribution of the reflected field, and again Fourier transforming. However, accurate values of the reflected field distribution require solving Maxwell's equations.

3. Exposure. This step accounts for the changes in the resist due to the absorption of photons. In a CAR, the relevant effect is the release of acid molecules from the PAG molecules. In 193-nm lithography, PAGs release acids by direct absorption of the 193-nm photons. In EUVL, any molecule can absorb an EUV photon to create a primary photoelectron with ~75- to 82-eV energy. The energy of this primary electron is lower than the energy of the photon because the ionization event has to overcome the binding energy of the electron to the molecule. This primary electron moves around in the resist, repeatedly scattering off molecules in the resist, and with some probability generates extra or secondary electrons. As discussed in Section 8.4, the precise mechanism of the interactions of the generated electrons with PAG molecules—the mechanism that leads to acid generation—is not understood in complete detail and is currently an active area of research.

Based on the fact that 248-nm (5-eV) photons are able to photolyze PAG molecules, it is generally believed that an electron interacting with the PAG molecule must also have at least several electron volts of energy to cause acid release. But it should be noted that some researchers (see the Tagawa/Kozawa discussion in the Section 8.9.3 and in Section 8.4) believe that acid release can occur even when a thermalized electron with as little as 1/40 eV of energy attaches to a PAG molecule. They refer to this process as dissociative electron attachment. For the purpose of this discussion on modeling, we will assume that an electron can cause the release of acid from a PAG when the electron has energy of ~2–5 eV.

4. Post exposure bake (PEB). During this step, the wafer with the exposed resist is placed on a hot plate at a given temperature for a given amount of time. Common values of time and temperature are on the order of 1 min at 100 °C. Because of the elevated temperature, the acid and base molecules diffuse through the resist volume, performing essentially a random walk in the resist. In a positive-tone resist, the acid molecules deprotect the resist polymer. In a negative-tone resist, they crosslink the polymer. When acid and base (also called quencher) molecules meet, they neutralize each other, and the acid no longer causes deprotection (or protection in a negative-tone resist).

5. Development. During this step, the soluble molecules are dissolved by the developer, leaving the final insoluble resist topography. In continuum models, the local density of deprotected resist molecules determines the dissolution rate. This position-dependent rate is used to propagate the initially flat resist surface to the final resist topography using a propagation rate that depends on the local density of blocking groups in positive-tone resists and

Downloaded From: https://www.spiedigitallibrary.org/ebooks/ on 09 Mar 2022
Terms of Use: https://www.spiedigitallibrary.org/terms-of-use

crosslinking in negative-tone resists. In lattice statistical models, a common approach is to remove voxels from the lattice based on their level of deprotection and on the state of their neighboring voxels (i.e., how many neighboring voxels remain at each time step).

8.9.3 Specific resist models

As might be expected, accounting computationally for all of the above steps in detail, even with present day computing power, is time consuming for large resist volumes. Hence, approximations and shortcuts are often used. For example, optical proximity correction (OPC) requires adjusting the mask features across many microns of the mask in order to yield the desired resist pattern. Given the fact that this is an iterative process, it is essentially impossible to do it using all the simulation steps listed above. It turns out that with sufficient calibration data for a given resist exposure and development process, a threshold resist model—wherein the aerial or in-resist image is thresholded at a certain level to determine the positions of the developed resist edges—can be accurate to better than a nanometer and so can be used for OPC. Of course, this requires a great deal of calibration data, and any change in the exposure and/or development process requires re-collecting the calibration data to maintain accuracy. On the other hand, people often focus on only one of the above steps to model in detail and treat the other steps as approximations. For example, to model the PEB and deprotection step, one can sidestep the imaging calculation by assuming a sinusoidal intensity profile and also sidestep the development step by assuming that thresholding the deprotection density will yield an accurate enough result for the resist edge placement and edge roughness for the stochastic case.[183,184]

We now discuss specific models that have been developed and provide some of the results obtained. We will concentrate on stochastic simulations and models. For discussion of continuum nonstochastic simulation, refer to Mack[185] and Wong.[186]

Han and Hinsberg stochastic models. Two early stochastic models were developed by Han et al.[187] and Hinsberg et al.[188] The Han model uses Monte Carlo modeling to calculate the transfer of energy from electrons to molecules in the photoresist. It accounts for four types of scattering events: elastic, ionization, excitation, and plasmon. In an elastic event, only the direction of the incident electron is changed. In an ionization event, the incident electron is scattered and a secondary electron is produced. In an excitation event, the electron loses energy to the molecule it scatters from, but no extra electron is generated. Finally, in a plasmon event, the electron loses energy and changes direction, but the energy in this case generates a plasmon that is a collective oscillation of outer-shell electrons of groups of molecules caused by Coulomb repulsion with the incident electron. Since plasmons are nonlocalized, generically longitudinal charge oscillations, they do not readily couple to

Downloaded From: https://www.spiedigitallibrary.org/ebooks/ on 09 Mar 2022
Terms of Use: https://www.spiedigitallibrary.org/terms-of-use

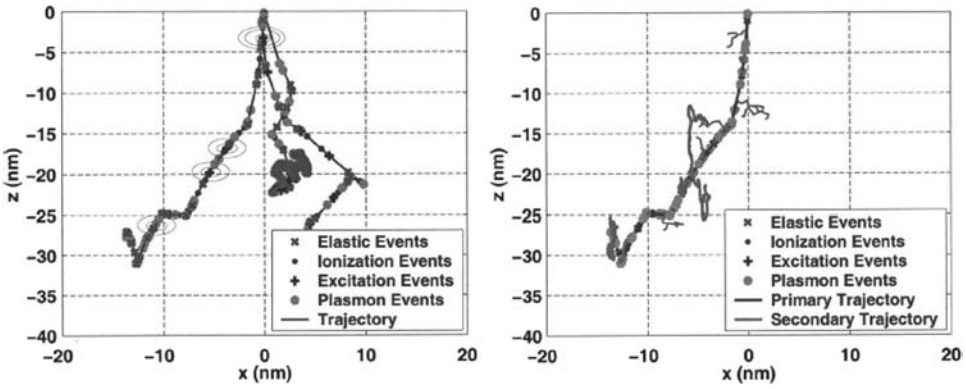

Figure 8.58 From Han's group, plots illustrating specific electron trajectories calculated with their code and the various processes that occur along each trajectory (reprinted from Ref. 187 with permission; © 2002 American Vacuum Society).

molecular transitions, and their energy ends up as heat in the resist material. Example electron trajectories with associated event types are shown in Fig. 8.58.

The model developed by Hinsberg, et al.[188] is a discrete volume and time step, chemical kinetics model. The simulation volume is treated as a lattice of voxels on the order of 1 nm squared for 2D or 1 nm cubed for 3D. In each time step, the chemical processes that occur in each cell are statistically evaluated. The critical ionization model (i.e., the assumption that a threshold level of ionization of a polymer chain is necessary before it dissolves) is used to determine the threshold of where the resist switches to being soluble.[189] Latent images (i.e., the distribution of acids released during exposure) are thus converted into the final resist topographic profile. Since the model is stochastic, it can also predict LER as well as contact hole ellipticity and contact hole edge roughness. Figure 8.59 shows an example result that converts the latent image in terms of the acid distribution after exposure into the developed resist profile. Figure 8.60 shows an example of a contact hole with and without photon shot noise, but in both cases the chemical kinetics are treated statistically. Since the statistics of each step— exposure, PEB, and chemical reaction kinetics—can be treated either deterministically or statistically, the model can be used to determine the source of the dominant contribution to contact hole edge roughness. Results from the model show that, although photon statistics are the dominant contributor, chemical stochastics also make a major contribution, as can be seen in Fig. 8.60.[190] Detailed computations show that even though stochastic effects coming from the chemical kinetics during PEB and development make significant contributions to the LER, the dominant contribution—in an RSS (square-root of the sum of the squares) sense—to contact hole roughness is coming from the absorbed photon shot noise.

Downloaded From: https://www.spiedigitallibrary.org/ebooks/ on 09 Mar 2022
Terms of Use: https://www.spiedigitallibrary.org/terms-of-use

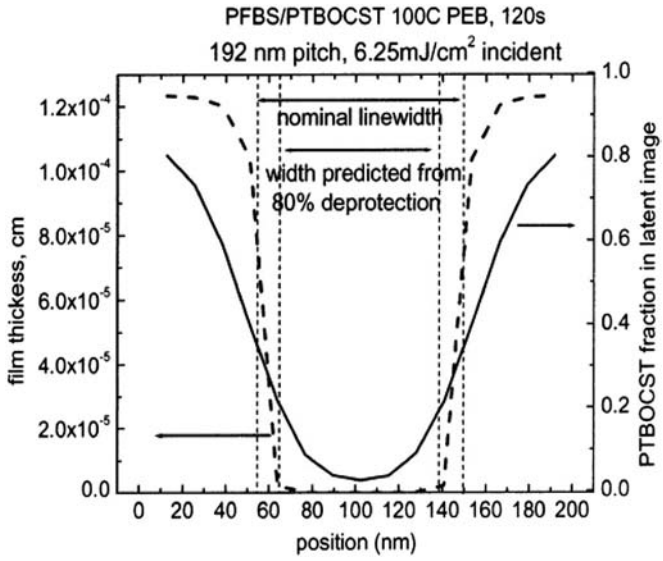

Figure 8.59 From Hinsberg, plot illustrating results from their code, showing the difference between developed linewidth (dashed curve) and the level of deprotection (solid curve) as indicated by the volumetric fraction of remaining PTBOCST after a 120-s PEB at 100 °C (reprinted from Ref. 188 with permission from American Chemical Society).

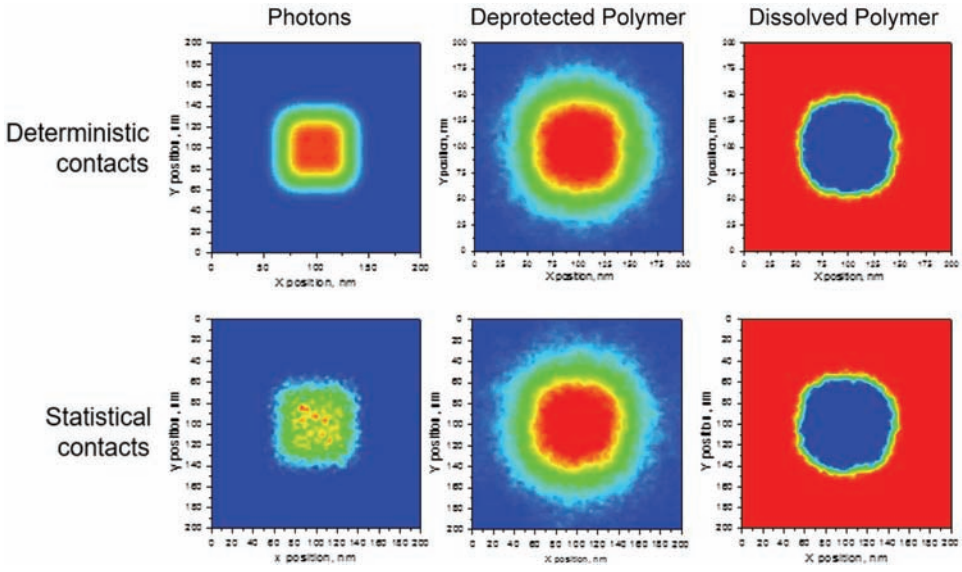

Figure 8.60 Computationally determined difference between deterministic exposure (absorbed photon positions are deterministic based on image intensity and statistically calculated absorbed photon positions based on Poisson statistics) and the resulting contact-hole shape. The horizontal and vertical scale in the images is 200 nm (reprinted from Ref. 190).

Downloaded From: https://www.spiedigitallibrary.org/ebooks/ on 09 Mar 2022
Terms of Use: https://www.spiedigitallibrary.org/terms-of-use

Biafore full stochastic model. Biafore et al.[191] created a full stochastic model that includes: photon shot noise, acid shot noise, exposure reaction quantum efficiency, distances between reactants, PAG loading, quencher loading, diffusion, reaction kinetics, neutralization kinetics, and fluctuations in the placement of the resist edge. The model results in Fig. 8.61 show that acids appear in clumps around photon-absorption sites for the case in which quantum efficiency is greater than one. Because the photo- and secondary electrons (not direct photon absorption by the PAG molecules) are the dominant acid release mechanism, and the electrons have inelastic mean free paths (the distance they travel between inelastic scattering events) on the order of a few nanometers, the acids are generated in "clumps" centered on the sites where photons are absorbed. Also, since the absorption of a single 92-eV EUV photon can generate multiple free electrons, the number of acid molecules released is generally greater than the number of photons absorbed. This ratio is commonly referred to as the quantum efficiency and for EUVL is generally understood to have a value roughly around two.

Line-edge roughness results are shown in Fig. 8.62. The left and right images have the same LWR value, which is defined as 3× the RMS variation in the width of each line. The results show that the same LWR can be obtained with very different doses, indicating that although dose stochastics, in terms of the shot noise of absorbed photons, is, on average, a primary driver of LWR, there can be other significant contributors that can enhance or mitigate the shot noise effect.

The LWR results in Fig. 8.62 indicate that more than just shot noise, i.e., statistical fluctuations in the number of photons absorbed per unit volume,

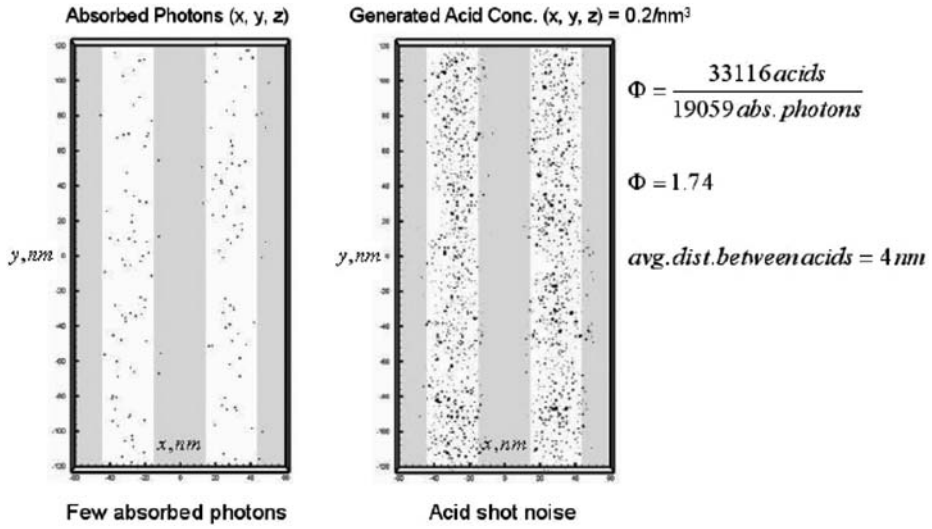

Figure 8.61 From Biafore et al., showing the difference between absorbed photons (left image) and the acids generated (right image) (reprinted from Ref. 191).

Downloaded From: https://www.spiedigitallibrary.org/ebooks/ on 09 Mar 2022
Terms of Use: https://www.spiedigitallibrary.org/terms-of-use

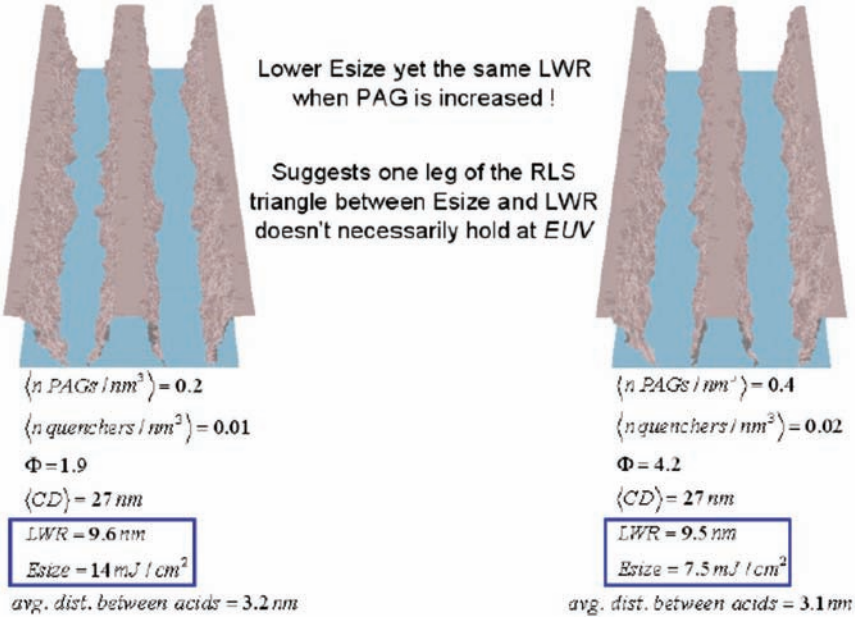

Figure 8.62 From Biafore et al., showing computationally determined resist profiles. The left and right images have the same LWR value, which is defined as 3× the RMS variation in the width of each line (reprinted from Ref. 191).

contributes to LER. One example of these other effects is image resolution. At the same dose, in general, a low-resolution image will produce more LER than a high-resolution image. Also, the stochastic chemistry that occurs during PEB and resist development can make a larger or smaller contribution to LER, depending on the details of the resist chemistry and processing.

On the other hand, experimental data of LER versus dose as shown in Fig. 8.63 (diamonds) does show a distinct, on-average $1/\sqrt{dose}$ trend, as expected for shot noise.[192] The solid line (with squares) below the data comes from a prediction based solely on shot noise, which indicates that, at least for standard CARs, shot noise is the limiting factor for LER. The fact that all of the data lies above the solid line indicates that LER depends on factors in addition to shot noise, such as resist chemistry, processing, and saturation effects.

Modeling by the Tagawa/Kozawa group. Using a combination of reaction–diffusion and rate equations, Kozawa and Hirayama studied the relationship between quencher diffusion and reaction radius for contact hole imaging.[193] They found that the effect on the gradient of the deprotection density differed depending on the dose level. Below 20 mJ/cm^2 the gradient didn't vary with quencher diffusion, but above 20 mJ/cm^2 the chemical gradient increased with quencher diffusion. Both through modeling and experiment, Kozawa et al.[194] studied the effect of having the anion of a PAG molecule covalently bonded

Downloaded From: https://www.spiedigitallibrary.org/ebooks/ on 09 Mar 2022
Terms of Use: https://www.spiedigitallibrary.org/terms-of-use

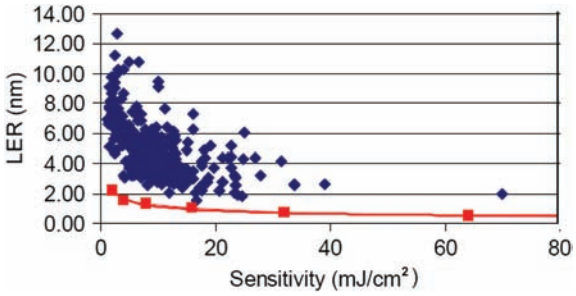

Figure 8.63 The diamonds are experimental results for LER which, by definition, is 3× the RMS variation in edge position after subtracting a best-fit straight line from the edge position data. The curve with the squares is based solely on shot noise and indicates, at least for standard CARs, that shot noise is the limiting factor (reprinted from Ref. 192).

to the polymer. The authors found that accounting for the effect of the electric field generated by the bound anions on proton diffusion produced latent images that "corresponded well" to the measured linewidths and chemical gradient estimated from the experimental results. They also used the chemical gradient simulation results to predict the LER range by taking LER to scale as the reciprocal of the deprotection gradient. Polymer structure effects on dissolution kinetics were studied experimentally by Yamamoto et al.[195] This group found that, probably due to steric hindrance, for bulky protecting groups, the activation energy is significantly influenced by the protecting ratio.

Finally, the general belief is that at least several electron volts of energy are required to release an acid molecule from a PAG molecule. This belief comes, justifiably, from the fact that 248-nm photons, which cause acid release, carry only 5 eV of energy; whereas, light with longer wavelengths and hence lower energy, e.g., 365 nm i-line with only 3.4 eV of energy, generally cannot. (This is not an absolute. At the atomic level, quantum mechanics rules, and there are usually only larger or smaller probabilities for certain processes to happen. Hence, depending on the resist, the probability of acid release using 365-nm photons is only *much less* probable than acid release via 193- or 248-nm photons. It is not absolutely forbidden.) The point of view of the Tagawa and Kozawa group on the other hand, is that acid release can actually be caused by thermalized electrons (electrons with <1 eV, even down to 1/40 eV) via a process they call dissociative electron attachment. The details of this idea are discussed in Section 8.4.

Molecular dynamic simulations. Most stochastic simulators work at a resolution on the order of 1 nm and so are not directly sensitive to the distribution or evolution of the resist on the atomic scale. To overcome this limitation and "see" what is happening at the atomic scale, molecular dynamics simulations can be performed.[196] But given the computational cost of such simulations, the cases that can be considered in such simulations

Downloaded From: https://www.spiedigitallibrary.org/ebooks/ on 09 Mar 2022
Terms of Use: https://www.spiedigitallibrary.org/terms-of-use

are generally restricted to nanometer-scale volumes of resist and several-nanosecond time scales. For example, Toriumi, et al.[197] studied the inhomogeneous distribution and diffusion, at room temperature, of PAG molecules in a cubic volume 3.36 nm on a side of an EUV-type methacrylate resist. The simulation time scale in this case was 5 ns. Other molecular dynamics simulations of various properties of resists have been performed. For example, the adhesion of resists to a substrate was studied by Zhang et al.,[198] and the development process of PMMA was studied by Mohammad et al.[199]

Stochastic models. While stochastic simulation can be directly used to study various properties and processes in photoresist, it can also be used to estimate, in a more or less exact way, the numerical values of the various parameters and their statistical fluctuations as well as the relations used in mesoscale continuum-type models. For example Mack et al.[159] use the Monte Carlo–based PROLITH stochastic resist model (available from KLA-Tencor Corp.) to evaluate both the mean and statistical fluctuation of the Dill C parameter,[200] which has units of 1/dose = area/energy. The exponential of minus C times the dose is the probability of unexposed PAG molecules remaining. This follows from the rate equation, where the rate at which the number of unexposed PAG molecules decreases with time equals minus C times the image intensity times the current number of unexposed PAG molecules.

It is not surprising that experimental results can also be used to calibrate stochastic resist models. Gao et al.[201] used several hundred values of both CD and LWR data for L/S patterns obtained through dose and focus to calibrate their model and several hundred points for validation. They achieved 1.1-nm rms error between measured and predicted CDs and 0.7 nm between measured and predicted LWR values.

The model was also tested against contact hole patterns, resulting in a 1.8-nm rms error between measured and simulated contact hole CDs. Figure 8.64 shows results through focus for contact hole patterns.

Metal-oxide model. A promising alternative to CARs for EUVL are metal-containing resist systems such as metal-oxides (MOx), which are discussed in Section 8.8. Recently, Hinsberg and Meyers[202] developed a numerical stochastic model of the exposure, condensation (metal-oxygen-metal network formation) and development of MOx resists. They use a "minimalist description of the resist structure, chemistry and physics"[202] with a set of user-definable parameters so that the model can be tailored to specific cases. The exposure and condensation processes contained in the model are illustrated in Fig. 8.65. Ligands (L) surround a highly polar metal-oxide center (core). EUV exposure causes fragmentation of the ligands, which leave active sites (A) on the core. The exposure mechanism is via the stochastic or random generation of photoelectrons from the absorption of EUV photons, as

Downloaded From: https://www.spiedigitallibrary.org/ebooks/ on 09 Mar 2022
Terms of Use: https://www.spiedigitallibrary.org/terms-of-use

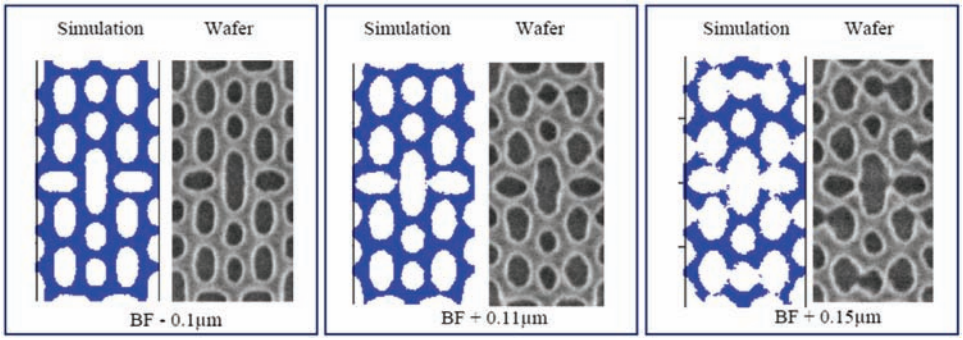

Figure 8.64 Gao et al. computed results showing the match between printed resist patterns through focus and simulated patterns computed using a stochastic resist model calibrated with experimental data (reprinted from Ref. 201).

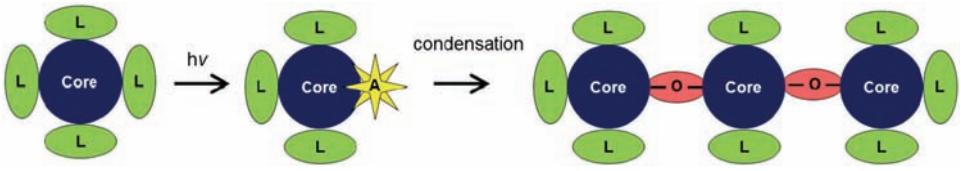

Figure 8.65 Hinsberg and Meyers' model of MOx exposure and condensation (metal-oxide-metal network formation) (reprinted from Ref. 202).

in a standard CAR. The number of ligands/core as well as the size of the ligand–core structure are settable parameters. The ligand–core structures are taken to be arrayed in a simple cubic packing format. Once the active sites have been generated, condensation, which is the formation of a 3D metal-oxide-metal network (. . .-core-O-core-O-. . .) via random attachment via oxide bonding is computed. The model also includes blur by specifying the average photoelectron diffusion range and quantum yield by specifying the average number of active sites generated per absorbed EUV photon. The MOx network is insoluble, so these resists are negative tone.

Example MOx network structures generated at different exposure doses are shown in Fig. 8.66 for a 16-nm L/S pattern in Inpria YA-BA MOx resist. Since the MOx network is generated stochastically in the model, the number of connected cores in any given network is also stochastic. The notation #-mer in the figure indicates the number of connected cores (indicated by different colors) in each specific network structure. Networks that are not in contact with the substrate are assumed to be removed during the development step. Note in Fig. 8.66 that at the lower doses the structures are formed predominantly at the top of the resist. Also, note that at the higher doses the maximum number of connected cores in a network has risen dramatically. The cyan curve indicates the shape of the aerial image.

Downloaded From: https://www.spiedigitallibrary.org/ebooks/ on 09 Mar 2022
Terms of Use: https://www.spiedigitallibrary.org/terms-of-use

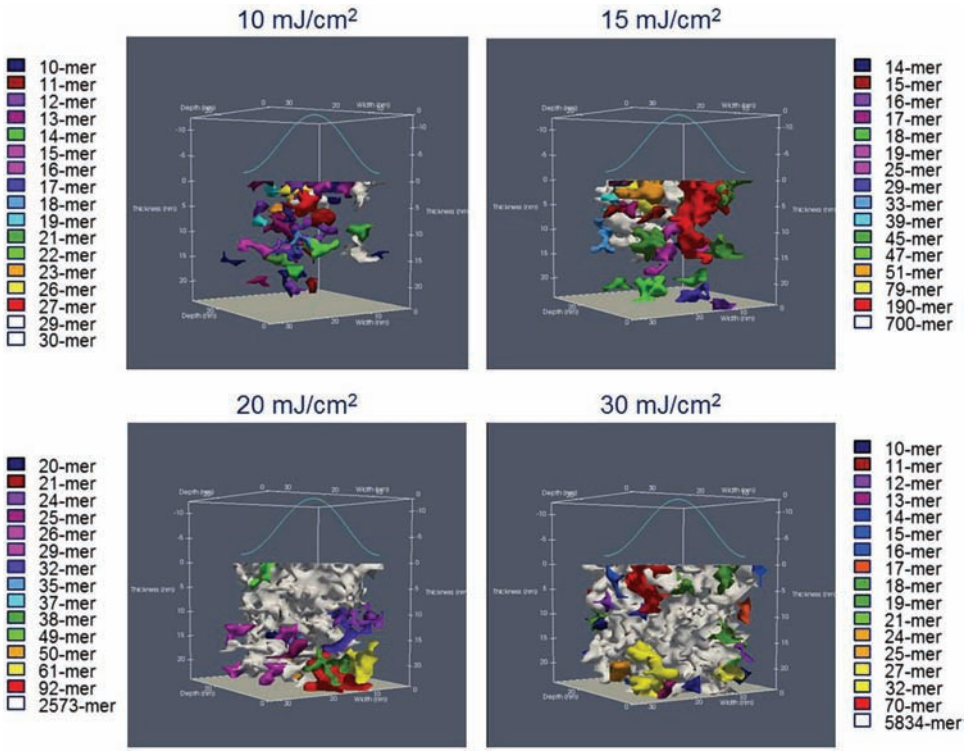

Figure 8.66 Example connected-core networks at different exposure doses for the Inpria YA-BA MOx resist for a 16-nm L/S pattern. The color coding indicates the number of connected cores in each MOx network structure. Note that the number of connected cores rises significantly with exposure dose. The cyan curve indicates the shape of the aerial image (reprinted from Ref. 202).

8.10 Benchmarking Studies: Tool Dependence and Resist Performance

8.10.1 Introduction

EUV lithography technology has been under development for many years, with the earliest imaging occurring in 1986.[203] As technology development proceeded, benchmarking studies were conducted to assess the state-of-the-art of EUV resists, exposure tools, and EUVL as a whole. Benchmarking of EUV resists is tool dependent. Before commercial EUV exposure tools were available, most benchmarking was conducted on small-field exposure tools. These tools were developed to enable development of resist and mask technology before full-scale EUV scanners were available. Tools were located at LBNL in California, at SEMATECH in Albany, and at SELETE in Japan. The groups at these facilities published regular benchmarking studies at leading lithography conferences. In addition, researchers at various semiconductor companies sometimes used these tools for resist benchmarking.

Downloaded From: https://www.spiedigitallibrary.org/ebooks/ on 09 Mar 2022
Terms of Use: https://www.spiedigitallibrary.org/terms-of-use

As commercial scanners became available, other groups started doing benchmarking. Most notably, IMEC has published a series of papers showing resist progress and benchmarking,[204,205] but benchmarking has also been reported from SUNY Polytechnic Institute[220] and from corporate researchers.[206]

Exposure tools using interference lithography have also been reported. These tools have very good resolution capability and can do better than a commercial scanner, but do not match the aerial image expected in production use of EUV resists.

When EUV scanners were first introduced, there was concern about resist outgassing affecting the scanner optics,[207] and some test procedures for resist outgassing were developed.[208,209] The worry was that the high energy of EUV photons would eject atoms or small molecules from a resist film undergoing exposure, and the outgassed materials would redeposit on the EUV mirrors that make up EUV lenses and degrade their imaging quality. Many resists were tested for outgassing. Having low outgassing was a constraint on resist formulation, and the necessary testing required special equipment and a slow cycle time to send a resist formulation out for testing. However, as practical experience was gained, outgassing became less of a worry. In October of 2015 ASML waived the need for any outgas test for chemically amplified formulations and waived tests for any material used in small-wafer-count testing;[210] in April of 2017 ASML stated that "EUV scanners now include a membrane that protects the optics from photoresist out-gassing; this could open new material options."[211]

8.10.2 Interference lithography

In IL, the aerial image is of high quality, the brightest point in an image is the same, or almost the same, intensity as an open frame image, and the darkest points are zero light intensity or close to it, no matter what pitch is being imaged. This is in contrast to stepper imaging, where, typically, smaller pitches have lower contrast, and the image for them alternates between light gray and dark gray in intensity. Thus, for interference imaging the image log slope is independent of pitch, but for scanner imaging the image log slope gets worse for smaller pitch features. This pitch independence makes IL a good way to assess intrinsic resist capability. For pitches above the imaging limit of the interference tool, one can determine which pitches the resist chemistry supports. Also, since the aerial image quality is independent of pitch, the LWR is independent of pitch, and the measured LWR is a characteristic of the resist system being tested. A good description of this technique is in a 2016 paper by Fan and Ekinci, who report on new interference mask preparation that enables imaging of 1:1 lines and spaces down to a half-pitch of 6 nm.[212]

A recent resist study by interference imaging appeared in 2016. Fallica et al. reported on studies of different types of resist systems using interference imaging.[213] They compared PMMA, hydrogen silsesquioxane (HSQ), three

Downloaded From: https://www.spiedigitallibrary.org/ebooks/ on 09 Mar 2022
Terms of Use: https://www.spiedigitallibrary.org/terms-of-use

different CARs, and two metal-oxide-based resists for their LWR characteristics. Pitches ranging from 100 to 36 nm were tested. The small molecule resists (HSQ and the metal-oxide resists) showed low LWR, and the PMMA showed quite high LWR, while the CARs showed variable LWR with one formulation approaching the small-molecule resists in LWR capability. A clear difference in the LWR correlation length ξ was seen between the polymer-based resists and the small-molecule ones. The polymer-based resists had 2 to 3 times the correlation length compared to the small-molecule resists. This was attributed to the intrinsically larger molecular size of polymer-based resists. Despite the varied chemical structures of the resists tested, the familiar tradeoff of photospeed to LWR was present in the data and roughly followed the expected dose-to-LWR mathematical relationship.

8.10.3 MET imaging

Micro-exposure tools (METs) were the first tools used for regular evaluation of EUV resists. One of the first reported ministepper studies of EUV resist capability was reported in 2006.[214] A new, small-field exposure tool was used and demonstrated resolution of 27-nm lines and spaces in non–chemically amplified resist and 28-nm lines and spaces in CAR. Other studies with small-field tools reported in this time frame gave similar results, with 32-nm half-pitch resolution reported in 2007[215] and 28-nm half-pitch resolution reported in 2008 (Table 8.4).[200] Linewidth roughness was noted to be high. For example, the 2007 study reported a LWR of 6 nm for 32-nm lines and spaces, and this was a comparatively good result. Because LWR and LER were often high, especially for minimum resolution features, many papers report LWR and LER for larger features than the minimum resolution and/or report LER instead of LWR (for EUV imaging, LER is typically significantly smaller than LWR).

Reported resolution improved over time. In 2009 it was reported that improved illumination options on a small-field system that used a synchrotron EUV source gave resolution down to 20-nm lines and spaces,[216] and in 2011 another study showed 24-nm L/S resolution using annular-type illumination.[217]

Even with considerable advances in resist formulation, there was a clear tradeoff between LWR and photospeed. In 2014 it was reported that the best resists had LWR of roughly 4 nm 3σ, even with slow photospeed, and fast resists had LWR of 5 nm or more.[218] This represents considerable progress over the results cited above, but is still far from the ITRS target of sub-2-nm LWR.[219] The team at SEMATECH and the SUNY Polytechnic Institute tracked the *Z*-parameter of benchmarked resists and found that, despite individual improvements in resolution or speed, the actual photospeed, resolution, and LWR tradeoff had not improved much over a three-year period, suggesting that LWR will continue to be a challenge.[220]

Downloaded From: https://www.spiedigitallibrary.org/ebooks/ on 09 Mar 2022
Terms of Use: https://www.spiedigitallibrary.org/terms-of-use

Downloaded From: https://www.spiedigitallibrary.org/ebooks/ on 09 Mar 2022
Terms of Use: https://www.spiedigitallibrary.org/terms-of-use

Table 8.4 Selected benchmarking studies.

Exposure Tool	Mini-Stepper at SELETE NA = 0.30	Mini-Stepper at SELETE NA = 0.30	Mini-Stepper Intel NA = 0.30	LBL Mini-Stepper Synchrotron Source NA = 0.30	LBL Mini-Stepper Synchrotron Source NA = 0.30	Mini-Stepper at SELETE NA = 0.30	Mini-Stepper at SEMATECH NA = 0.30	NXE:3100 Scanner IMEC NA = 0.25	NXE:3100 Scanner IMEC NA = 0.25	NXE:3300B NA = 0.33	NXE:3300B NA = 0.33
Resist Type	Non-CAMP	CAMP			CAMP					CAMP	Solgel Metal Resist
Year	2006	2006	2007	2008	2009	2011	2014	2012	2012	2015	2015
Resolution (nm)	27	28	32	28	20	24		18	22	13.5	13
LER (nm)									3.2		
LWR (nm)			6				4				
Sensitivity (mJ/cm2)			19 mJ/cm^2				Slow Resists		18.4 mJ/cm^2		30-35 mJ/cm^2

8.10.4 Beta tool and production scanner imaging

As exposure tool technology progressed, beta versions of production scanners became available, and resist benchmarking started being done on these tools. These tools were superseded by the ASML NXE:3100, NXE:3300B, and further models of EUV scanners. The availability of production-like tools has enabled improved imaging and better resist performance. In 2014, Goethals et al. and DeSimone et al. reported benchmarking of EUV resists on production-type tools.[205,221] They used a preproduction test scanner called the Alpha Demo Tool (ADT) to screen resists and then tested promising resists on an ASML 0.25-NA NXE:3100. The ADT was used for imaging down to 27-nm L/S imaging, and the NXE:3100 was used for imaging down to 18-nm lines and spaces. They tested over two-dozen commercial resists and selected one that showed an LER of 3.2 nm at a photospeed of 18.4 mJ/cm^2 and had a wide process latitude as their plan-of-record resist for 22-nm lines and spaces. They also evaluated resists for 18-nm lines and spaces. No resist met the LWR target, and high exposure doses were needed just to resolve this dimension. Both papers reported that process modifications such as an anti-collapse rinse were needed to prevent line collapse from being an issue.

8.10.5 Comparison to ArF

Some work has been reported comparing EUV resist capability to ArF resist capability. In 2007 Wei et al. reported a comparison of resists at both EUV and ArF wavelengths.[222] They used an ArF immersion scanner and a 0.3-NA EUV mini–exposure tool. When the half-pitch of the pattern exposed at the two wavelengths was similar, the process window was also similar. Since the EUV aerial image is significantly better than the ArF one at the same pattern size, the authors concluded that the EUV resist was not as advanced as the ArF resist. The authors also noted that the performance of the ArF resist was limited by the aerial image, while that of the EUV resist seemed to be resist limited. In 2010, Kim et al. reported a performance comparison of ArF and EUV resists.[223] Even with a higher contrast aerial image, the EUV resist had substantially worse LWR than the ArF resist. The authors attributed this to shot noise effects. From these two studies it is apparent that EUV resists can still improve a lot; but, even if they do, there will probably still be issues with noise in the imaging that are worse than those issues in ArF.

8.10.6 Comparison of organic and metal-based resists

Some work has been reported comparing organic and metal-based resists. Metal resists were compared to organic ones for dose-to-clear and absorbance.[53] Metal-based resists have more absorbance, but less volume of resist was exposed for each mJ/cm^2. As of this writing, metal-based resists have demonstrated slightly better resolution and slightly slower photospeed

Downloaded From: https://www.spiedigitallibrary.org/ebooks/ on 09 Mar 2022
Terms of Use: https://www.spiedigitallibrary.org/terms-of-use

on a commercial scanner. A recent report shows that the scanner was able to print 13.5-nm half-pitch lines and spaces with a CAR, and was able to print 13-nm lines and spaces using metal-based resists at doses between 30 and 35 mJ/cm^2.[83] Metal-based resists require a process integration that differs from that used by organic resists. In 2015, DeSimone and coworkers reported using metal-based resist to patterns composed of pillars and of block layers.[224] The metal resist was applied directly on a spin-on carbon layer, eliminating two etch steps compared to the baseline trilayer process. Good-resolution and high-fidelity pattern transfer was achieved. It should be noted that these layers were chosen because they work well with a negative-resist process. Positive-tone metal-based resists have not achieved results comparable to state-of-the-art organic resists.

8.11 Summary

8.11.1 Background

EUV resist work started in the 1980s at a time when the specific wavelength for EUVL had yet to be selected. This early work showed successful imaging at several wavelengths (5 to 40 nm), demonstrated successful pattern transfer from EUV resist to substrate, and demonstrated that CARs could be used for EUV imaging. This exploratory work used much thicker resist films and printed larger features than are now being used for EUVL, but it helped to identify EUV lithography as a fruitful area for continued development.

Historically, as the lithographic technologies shifted to shorter wavelengths, resist chemists sought ways to increase transparency of photoresist materials. Partly due to historical practices and partly because initial resist films were quite thick (~300 nm), early researchers pursued strategies that would increase the transparency of EUV resists. As work proceeded and resist resolution improved, the thickness of EUV resist films decreased. Thinner resist films absorb less light. In the mid-2000s, researchers realized that it is a challenge to get enough EUV absorbance in thin resist films and recommended that resist absorbance be increased first by adding fluorine, then by adding other heteroatoms such as metals.

8.11.2 Mechanism of EUV exposure

The mechanism by which EUV light exposes photoresists is significantly different from the mechanisms by which 193-nm light exposes resists. At longer wavelengths (e.g., 193 or 248 nm), photon absorption excites an electron that stays within the molecule, whereas, the absorption of an EUV photon causes an electron to exit the molecule with energies in the range of 75–82 eV. This primary electron can cause additional ionization reactions, creating secondary electrons. These electrons (and the radical-cation holes they leave behind) cause the chemical reactions that provide the solubility

Downloaded From: https://www.spiedigitallibrary.org/ebooks/ on 09 Mar 2022
Terms of Use: https://www.spiedigitallibrary.org/terms-of-use

changes in EUV resists. Experiments show that electrons can travel more than 10 nm in resists. This has implications for understanding noise, LER, and CDU variations in EUV resists.

Measurements of the amount of acids generated from CARs show maximum quantum yields of five to six acids per absorbed EUV photon, indicating that one photon can produce up to six chemical reactions in CARs. Measurements and simulations of the number of electrons generated by one EUV photon predict that two to four electrons are generated per absorbed photon. Simulation models of the trajectories of electrons in solids such as resist films predict photon absorption, ionization, and secondary electron generation, but they don't have explicit terms for interactions that chemically change functional groups.

The mechanism by which the primary and secondary electrons interact with compounds in the resist is still poorly understood and is the subject of much research. Three types of mechanisms have been proposed. (1) Internal excitation is a mechanism in which a passing electron excites a molecule. Experiments testing the interaction of dyes with electrons suggest that the internal excitation of a molecule by a passing electron is relatively unlikely and, therefore, does not make a significant contribution to the reactions caused by EUV exposure. (2) Electron trapping is a mechanism in which a molecule traps an electron, causing further reactions. (3) Hole-initiated mechanisms include reactions in which the radical cation initiates reactions. There is evidence for all of these mechanisms occurring. It is not yet clear which mechanisms predominate or how chemical properties will influence the mechanistic pathways.

To date, nearly all mechanistic studies have been conducted for organic CARs. Metal resists are the subject of much resist development, and their imaging mechanism may prove to be different. Some elegant work has been done using high-speed AFM to characterize the EUV resist development process. These studies show significant differences in the way different sorts of EUV resists develop.

8.11.3 Types of resists

Many of the first imaging experiments were done with PMMA as the resist. This material has excellent resolution but poor etch resistance, outgassing performance, SEM stability, and sensitivity. It is, therefore, not suitable for use in production. Since CARs were already developed for the i-line, KrF, and ArF lithography, they were adapted for EUVL. Many different types of CARs, such as ESCAP and acetal materials were used. Other types of organic materials and imaging mechanisms have also been used, e.g., polyphenol-based resists, chain-scission resists, noria-based resists, cyclodextrin-based resists, calixarene-based resists, and polysulfonium salt-based resists.

Line edge roughness is a significant issue for EUVL. Faster resists give worse LER, and all reported resist systems with manufacturable photospeed

Downloaded From: https://www.spiedigitallibrary.org/ebooks/ on 09 Mar 2022
Terms of Use: https://www.spiedigitallibrary.org/terms-of-use

have significant LER. LER was already an issue for ArF resists, but since LER does not scale with feature size, the smaller CDs pursued in EUVL makes LER an even greater issue in EUVL. Additionally, the much lower numbers of photons (14× fewer in EUVL than in 193-nm lithography at equal energy) makes shot noise a significant problem. Shot noise contributes to LER and worsens CDU.

Higher absorption. One of the strategies for achieving good LER despite the shot noise issue with EUVL is to increase the optical density of resists (Section 8.3). One approach for achieving higher OD has been to use high levels of fluorine; another approach is to incorporate metal atoms into the resists.

Metal-containing resists. One of the primary drivers for exploring the use of resists containing metals is to increase absorption. This enables thinner imaging films, which is important for printing smaller CDs. Metal resists also have excellent etch resistance. However, new process integration schemes are required to use them in chip production, there are concerns about metal contamination of silicon leading to worse device electrical performance, and they do not solve the issue of stochastic noise leading to LWR. Yet, they currently are some of the best resolving resists in the world. When ASML reported the imaging performance of its production scanner in 2015, they reported the imaging performance of both organic resists and of metal-based resists.[83] They reported that the best resolution using an ASML NXE:3300B scanner was 13.5-nm lines and spaces at a dose of 31.5 mJ/cm^2 using an organic CAR, and 13-nm lines and spaces at 35 mJ/cm^2 using a metal-based resist from Inpria.

There are several different types of metal-based resists. Peroxo-modified forms of metal oxides such as hafnium oxide can be spun-on from solution and operate in negative tone. These are notable for their excellent resolution. Hafnium and zirconium nanoparticles with carboxylate ligands can be made into resists that function in negative tone and can produce extremely fast photospeeds. Tin oxide nanoclusters have produced good photospeed for 35-nm lines and spaces. Organobismuth oligomers have been demonstrated as EUV resists. Monomolecular-metal-containing compounds also function as EUV resists; examples include cobalt oxalates, palladium oxalates, dibenzyl tin complexes, and carboxylate compounds of antimony, tin tellurium, and bismuth. The palladium result is notable because it works in positive tone, unlike the other metal resists described here.

8.11.4 Acid amplifiers and PSCAR

A key issue in developing EUV resists is the need for high photospeed together with good LER and resolution. There is a tradeoff between these three properties, and much work has been done to try to improve the tradeoff. One approach many researchers have tried is to use acid amplifiers. An acid

Downloaded From: https://www.spiedigitallibrary.org/ebooks/ on 09 Mar 2022
Terms of Use: https://www.spiedigitallibrary.org/terms-of-use

amplifier is a chemical compound that reacts catalytically with acid to generate more acid. Researchers have shown improved resist performance by the addition of these sorts of compounds to EUV resists.

PSCAR is a newer approach to improving resist photospeed by an amplification process. For PSCARs, the EUV exposure generates acid that deprotects a photosensitizer precursor. Then a 365-nm-wavelength flood exposure is used. This second exposure converts more PAG to acid in the areas where the photosensitizer was deprotected, i.e., is in the areas exposed by EUV light. Thus, when the PEB is done, there is more acid in the exposed areas than was present right after EUV exposure. The photospeed enhancements of this technique are clear, but its potential for beating the RLS tradeoff is still an open question.

8.11.5 LER and modeling

There are three generic approaches to modeling the exposure and development of photoresists: non-stochastic continuum models, stochastic continuum models, and discrete stochastic models. All of these modeling types have to take an initial resist state and simulate the image intensity distribution, the exposure process, and the chemical changes directly resulting from exposure, the PEB process, and the development process. Which type of model is used depends on what sort of information is needed. In EUV imaging, some modeling of primary and secondary electron behavior is also needed if a detailed simulation model is to be used.

The nonstochastic models have many uses but cannot model LWR or CDU because the source of those effects is stochastic. Stochastic resist chemistry effects are due to the random nature of the distribution in space of photoresist protecting groups, PAGs, and quencher molecules, as well as the actual conformations and positions of the polymer molecules. The other source of stochastic variation is shot noise, the random variation in the actual number of photons absorbed for a nominal exposure dose. Because the EUV wavelength is 14× shorter than that of ArF, the shot noise is the square root of 14 (3.8) times larger for EUV than ArF, all other things being equal. But all other things are not equal. The smaller feature size of resists printed with EUVL means that there are fewer photons per printed feature in EUV imaging than in ArF imaging. The size of the shot noise is determined by the square root of the number of absorbed photons, so shot noise, as a percentage of the nominal CD, is worse for smaller features. These two effects, fewer photons and smaller CDs, combine to make noise a larger issue in EUV imaging than in ArF. EUV photons are expensive, and scanner throughput is important for EUV cost, so making the resist slower in photospeed to increase the number of photons used is not desirable. An alternative is to increase resist absorption to increase the number of absorbed photons and, thus, reduce the shot noise.

Downloaded From: https://www.spiedigitallibrary.org/ebooks/ on 09 Mar 2022
Terms of Use: https://www.spiedigitallibrary.org/terms-of-use

The results of calibrated models can match experimental behavior quite well. One set of researchers found that simulated CDs matched experimental values within one nanometer for lines and spaces and within two nanometers for contact holes. Linewidth roughness was predicted with an error of less than one nanometer. The stochastic models show the experimentally observed photospeed to LWR/LER tradeoff quite well and suggest that a lower bound to the LWR and LER is achievable with CARs.

8.11.6 Benchmarking of resists

Many groups have done benchmarking of commercial and experimental EUV resists. Interference imaging gives a much better aerial image than scanner lenses do and is useful for exploring the ultimate resolution of resists. Scanner benchmarking is better for selecting a resist for actual use. While much progress has been made in resists, the benchmarking has consistently shown more LWR and CDU than is desired and a clear tradeoff of photospeed and LWR. The results do show that improved tools and resists optimized for them have improved EUV resist imaging. Given that EUV tools are continuing to improve in many aspects, we can expect better EUV imaging in the future. However, it is clear from all of the benchmarking and science discussed in this chapter that improving EUV noise is much more of an issue than improving EUV resolution. Recent work reported just as this chapter was written suggests that this issue will be worse than might be expected from simple extrapolations of CD variation using the normal distribution,[225,226] and future EUV imaging is expected to be done with smaller feature sizes, which will also make imaging noise more of a concern. The future of EUVL will be determined by the ability of equipment providers, materials providers, and EUV users to minimize, manage, and accommodate all of the stochastic effects in EUV imaging.

Notes and References

1. R. Brainard, "Photoresists for Extreme Ultraviolet Lithography," Chapter 8 in *EUV Lithography*, SPIE Press, Bellingham, Washington (2008) [doi: 10.1117/3.769214.ch8].
2. T. Namioka, "Current research activities in the field of multilayers for soft X-rays in Japan," paper No. 28-AF-15 presented at the 47th Autumn Meeting of the Japan Society of Applied Physics (1986). [Published in *Revue Phys. Appl.* **23**, 1711–1726 (1988).]
3. H. Kinoshita, K. Kurihara, Y. Ishii, and Y. Torii, "Soft x-ray reduction lithography using multilayer mirrors," *J. Vac. Sci. Tech. B* **7**(6), 1648–1651 (1989).
4. Tungsten-carbon MLs were used previously. Attempts to print images using 5-nm light were unsuccessful. [Rau, F. Stratton, C. Fields et al.,

Downloaded From: https://www.spiedigitallibrary.org/ebooks/ on 09 Mar 2022
Terms of Use: https://www.spiedigitallibrary.org/terms-of-use

"Shot-noise and edge roughness effects in resists patterned at 10nm exposure," *J. Vac. Sci. Tech. B* **16**(6), 3784–3788 (1998).]

5. T. W. Barbee, S. Mrowka, and M. C. Hettrick, "Molybdenum-silicon multilayer mirrors for the extreme ultraviolet," *Appl. Opt.* **24**(6), 883–886 (1985).
6. Personal communication with Rick Uchida (TOK): The two resists supplied by TOK were SPP (silicone-based positive photoresist) and OFPR (Ohka fine-pattern resist); personal communication with Hiroo Kinoshita: SPP is a Si-containing resist developed by Dr. A. Tanaka of NTT that exhibits negative-tone behavior at EUV wavelengths; H. Ban, A. Tanaka, Y. Kawai, and S. Imamura, "Synthesis of alkaline-soluble silicone resin suitable for resist material in microlithography," *Polymer* **31**(3), 564–568 (1990); A. Tanaka, H. Ban, and S. Imamura, "Preparation of novel silicone-based positive photoresist and its application to an image reversal process," *Polym. Mater. Sci. Eng*. **60**, 366–370 (1989); A. Tanaka, H. Ban, S. Imamura, and K. Onose, "Resolution characteristics of novel silicone-based positive photoresist," *J. Vac. Sci. Tech*. **7**(3), 572–575 (1989); H. Ban, A. Tanaka, and S. Imamura, "Alkaline-developable silicone-based positive photoresist for electron beam lithography," *Japan J. Appl. Phys*. **27**(11), L2137–L2138 (1988).
7. J. E. Bjorkholm, J. Bokor, L. Eichner et al., "Reduction imaging at 14 nm using multilayer-coated optics: printing of features smaller than 0.1 mm," *J. Vac. Sci. Tech. B* **8**(6), 1509–1513 (1990).
8. D. He and F. Cerrina, "Process dependence of roughness in a positive-tone chemically amplified resist," *J. Vac. Sci. Tech. B* **16**(6), 3748–3751 (1998).
9. If the roughness between two edges of a line are uncorrelated, the values of line edge roughness (LER) and linewidth roughness (LWR) are related by $\sqrt{2}$, or LWR $\cong 1.41 \times$ LER.
10. H. B. Cao, Y. Wang, B. J. Rice et al., "Sources of line-width roughness for EUV resists," *Proc. SPIE* **5376**, 757–764 (2004) [doi: 10.1117/12.536041].
11. W. M. Mansfield et al., "Effects of absorption on resist performance in soft x-ray projection lithography," in *Soft X-Ray Projection Lithography*, Vol. **12**, J. Bokor, Ed., Optical Society of America, Washington D.C., pp. 129–131 (1991).
12. A. Gupta, R. Liang, F. D. Tsay, and J. Moacanin, "Characterization of a dissociative excited state in the solid state: photochemistry of poly(methyl methacrylate). Photochemical processes in polymeric systems. 5," *Macromolecules* **13**(6), 1696–1700 (1980).
13. A. Uhl, J. Bendig, J. Leistner, U. Jagdhold, and J. J. Bauer, "E-beam and deep-UV exposure of PMMA based resists - identical or different chemical behavior?" *Proc. SPIE* **3333**, 1452–1457 (1998); A. Uhl,

Downloaded From: https://www.spiedigitallibrary.org/ebooks/ on 09 Mar 2022
Terms of Use: https://www.spiedigitallibrary.org/terms-of-use

J. Bendig, U. A. Jagdhold, and J. J. Bauer, "DUV and e-beam chemistry of high-sensitivity positive PMMA-based resist," *Proc. SPIE* **3678**, 1381–1387 (1999); A. Uhl, J. Bendig, and J. Leistner et al., "Nonstatistical degradation and development characteristics of poly(methylmethacrylate) based resists during electron beam exposure," *J. Vac. Sci. Tech. B* **16**(6), 2968–2973 (1998); R. B. Fox, L. G. Isaacs, and S. Stokes, "Photolytic degradation of poly(methyl methacrylate)," *J. Polymer Sci.* **1**(Pt. A), 1079–1086 (1963).

14. R. L. Brainard, P. Trefonas, J. H. Lammers et al., "Shot noise, LER, and quantum efficiency of EUV photoresists," *Proc. SPIE* **5374**, 74–85 (2004) [doi: 10.1117/12.536411].
15. C. M.Berger and C. L. Henderson, "Chemically amplified photoresist characterization using interdigitated electrodes: an improved method for determining the Dill C parameter," *Proc. SPIE* **5376**, 995–1006 (2004) [doi: 10.1117/12.536243].
16. B. L. Henke, E. M. Gullikson, and J. C. Davis, "X-ray interactions: photoabsorption, scattering, transmission, and reflection at $E = 50$–30,000 eV, $Z = 1$–92" *Atomic Data & Nucl. Data Tables* **54**, 181–342 (1993).
17. The website "X-Ray Interaction with Matter" http://henke.lbl.gov/optical_constants/filter2.html has an algorithm for calculating the absorption of EUV by thin films.
18. Mansfield et al. did not specifically name the absorption value (B parameter) determined at 37.5-nm light for PMMA, but did state that the C parameter at this wavelength was determined as a ratio of the B/C constants because the volumetric sensitivity was a constant.
19. K. Early, D. M. Tennant, and D. Y. Jeon et al., "Characterization of AZ PN114 resist for a soft-x-ray projection lithography," *Appl. Opt.* **32**(34), 7044–7049 (1993).
20. K. Early, D. M. Tennant, D. Y. Jeon et al., "Characterization of AZ PN114 resist for high resolution using electron-beam and soft-x-ray projection lithographies," *J. Vac. Sci. Tech. B* **10**(6), 2600–2605 (1992).
21. J. Grimm, J. Chlebek, T. Schulz, and H. L. Huber, "The influence of post-exposure bake on linewidth control for the resist system RAY-PN (AZ PN 100) in x-ray mask fabrication," *J. Vac. Sci. Tech. B* **9**(6), 3392–3398 (1991); R. Dammel, K. F. Doessel, J. Lingnau et al., "Negative-tone high-resolution photocatalytic resist for x-ray lithography," *Microelec. Eng.* **9**(1–4), 575–578 (1989); S. Pongratz, R. Demmeler, and C. Ehrlich et al., "Electron-beam application of highly sensitive positive and negative-tone resists for x-ray mask making," *Proc. SPIE* **1089**, 303–316 (1989) [doi: 10.1117/12.968538]; C. Eckes, G. Pawlowski, K. Przybilla et al., "Process latitude for the chemical amplification resists AZ PF514 and AZ PN114," *Proc. SPIE* **1466**, 394–407 (1991) [doi: 10.1117/12.46388].

Downloaded From: https://www.spiedigitallibrary.org/ebooks/ on 09 Mar 2022
Terms of Use: https://www.spiedigitallibrary.org/terms-of-use

22. G. D. Kubiak, D. A. Tichenor, W. W. Chow, W. C. Sweatt, and M. D. Himel, "Resist performance in soft x-ray projection lithography," *Proc. SPIE* **1924**, 18–29 (1993) [doi: 10.1117/12.146504].
23. O. R. Wood, II, J. E. Bjorkholm, K. F. Dreyer et al., "Experiments and simulations of EUV lithographic resist patterning at wavelengths from 7 to 40 nm," in *OSA Proc. Extreme Ultraviolet Lithogr., Proc. Top. Meet*. 1994, pp. 83–88 (1995).
24. O. R. Wood, II, J. E. Bjorkholm, L. Fetter et al., "Wavelength dependence of the resist sidewall angle in extreme ultraviolet lithography," *J. Vac. Sci. Tech. B* **12**(6), 3841–3845 (1994).
25. O. R. Wood, II, W. T. Silfvast, and T. E. Jewell, "Short-wavelength annular-field optical system for imaging tenth-micron features," *J. Vac. Sci. Tech. B* **7**(6), 1613–1615 (1989).
26. W. R. Hunter, "Design criteria for reflection polarizers and analyzers in the vacuum ultraviolet," *Applied Optics* **17**(8), 1259–1270 (1978).
27. G. D. Kubiak, E. M. Kneedler, R. Q. Hwang et al., "Characterization of chemically amplified resists for soft x-ray projection lithography," *J. Vac. Sci. Tech. B* **10**(6), 2593–2599 (1992).
28. R. L. Brainard, G. G. Barclay, E. H. Anderson, and L. E. Ocola, "Resists for next generation lithography," *Microelec. Eng.* **61–62**, 707–715 (2002).
29. B. Cardineau, R. Del Re, H. Al-Mashat, M. Marnell, M. Vockenhuber, Y. Ekinci, C. Sarma, M. Neisser, D. A. Freedman, and R. L. Brainard, "EUV resists based on tin-oxo clusters," *Proc. SPIE* **9051**, 9051B (2014) [doi: 10.1117/12.2046536].
30. J. Dai and C. K. Ober, "Novel resists with non-traditional compositions for EUV lithography," *Proc. SPIE* **5376**, 508–516 (2004) [doi: 10.1117/12.534319].
31. Y. Kwark, J. Bravo-Vasquez, M. Chandhok, H. Cao, H. Deng, E. Gullikson, and C. K. Ober, "Absorbance measurement of polymers at extreme ultraviolet wavelength: Correlation between experimental and theoretical calculations," *J. Vac. Sci. Technol. B* **24**, 1822–1826 (2006).
32. T. Kozawa, S. Tagawa, J. J. Santillan et al., "Feasibililty study of chemically amplified extreme ultraviolet resists for 22 nm fabrication," *Jpn. J. Appl. Phys.* **47**(6), 4465–4468 (2008).
33. T. Sasaki, O. Yokokoji, T. Watanabe, and H. Kinoshita, "Development of partially fluorinated EUV-resist polymers for LER and sensitivity improvement," *Proc. SPIE* **6923**, 692347 (2008) [doi: 10.1117/12.772542].
34. R. Gronheid, F. Van Roey, and D. Van Steenwinckel, "Using K_{LUP} for understanding trends in EUV resist performance," *J. Photopolym. Sci. Technol.* **21**, 429–434 (2008).
35. R. Gronheid, C. Fonseca, M. J. Leeson, J. R. Adams, J. R. Strahan, C. G. Willson, and B. W. Smith, "EUV resist requirements: absorbance and acid yield," *Proc. SPIE* **7273**, 727332 (2009) [doi: 10.1117/12.814716].

Downloaded From: https://www.spiedigitallibrary.org/ebooks/ on 09 Mar 2022
Terms of Use: https://www.spiedigitallibrary.org/terms-of-use

36. J. W. Thackeray, "Materials challenges for sub-20-nm lithography," *J. Micro/Nanolithogr. MEMS MOEMS* **10**(3), 033009 (2011) [doi: 10.1117/1.3616067].
37. T. Yamashita, M. Morita, Y. Tanaka, J. J. Santillan, and T. Itani, "High-sensitivity EUV resists based on tetrafluoroethylene contained fluoropolymers," *J. Photopolym. Sci. Technol.* **24**, 165–172 (2011).
38. T. Yamashita, M. Morita, Y. Tanaka, J. J. Santillan, and T. Itani, "High-sensitivity EUV resists based on fluorinated polymers," *Proc. SPIE* **7972**, 79721G (2011) [doi: 10.1117/12.879568].
39. O. Ongayi, M. Christianson, M. Meyer, S. Coley, D. Valeri, A. Kwok, M. Wagner, J. Cameron, and J. Thackeray, "High sensitivity chemically amplified EUV resists through enhanced EUV absorption," *Proc. SPIE* **8322**, 83220T (2012) [doi: 10.1117/12.916482].
40. M. D. Christianson, M. M. Meyer, O. Ongayi, D. Valeri, and M. Wagner, "High absorbing resists based on trifluoromethacrylate-vinyl ether copolymers for EUV lithography," *Proc. SPIE* **8682**, 868216 (2013) [doi: 10.1117/12.2014385].
41. M. Neisser, K. Cho, and K. Petrillo, "The physics of EUV photoresist and how it drives strategies for improvement," *J. Photopolym. Sci. Technol.* **25**, 87–94 (2012).
42. R. Garg, A. Antohe, and G. Denbeaux, "Absorption measurements of extreme ultraviolet radiation in photoresists," *Proc. SPIE* **6517**, 65172O (2007) [doi: 10.1117/12.712427].
43. N. N. Matsuzawa, H. Oizumi, and S. Mori et al., "Theoretical calculation of photoabsorption of various polymers in an extreme ultraviolet region," *Japan. J. Appl. Phys. Pt. 1* **38**(12B), 7109–7113 (1999).
44. N. N. Matsuzawa, H. Oizumi, S. Mori et al., "Theoretical estimation of absorption coefficients of various polymers at 13 nm," *Microelec. Eng.* **53** (1–4), 671–674 (2000).
45. N. N. Matsuzawa, S. Irie, E. Yano, S. Okazaki, and A. Ishitani, "Theoretical calculations of photoabsorption of polymers in the EUV (extreme ultraviolet) region," *Proc. SPIE* **4343**, 278–284 (2001) [doi: 10.1117/12.436657].
46. J. Bicerano, *Predictions of the Properties of Polymers from Their Structures*, Marcel Dekker, New York (1993).
47. S. Irie, M. Endo, M. Sasago et al., "Study of transmittance of polymers and influence of photoacid generator on resist transmittance at extreme ultraviolet wavelength," *Japan. J. Appl. Phys. Pt. 1* **41**(9), 5864–5867 (2002).
48. S. Irie, M. Endo, M. Sasago et al., "Measurement of resist transmittance at extreme ultraviolet wavelength using the extreme ultraviolet reflectometer," *Japan. J. Appl. Phys. Pt. 1* **41**(6A), 4027–4030 (2002).

Downloaded From: https://www.spiedigitallibrary.org/ebooks/ on 09 Mar 2022
Terms of Use: https://www.spiedigitallibrary.org/terms-of-use

49. M. Chandhok, H. Cao, Y. Wang et al., "Techniques for directly measuring the absorbance of photoresists at EUV wavelengths," *Proc. SPIE* **5374**, 861–868 (2004) [doi: 10.1117/12.535959].
50. M. Chandrock and R. L. Brainard, "EUV-2D absorption," poster presented at the 2003 EUVL Symposium, 30 Sept. to 2 Oct., Antwerp, Belgium.
51. R. L. Brainard, C. Henderson, J. Cobb et al., "Comparison of the lithographic properties of positive resists upon exposure to deep- and extreme-ultraviolet radiation," *J. Vac. Sci. Tech. B* **17**(6), 3384–3389 (1999).
52. A. Sekiguchi, Y. Matsumoto, T. Harada, T. Watanabe, and H. Kinoshita, "Study of Dill's B parameter measurement of EUV resist," *Proc. SPIE* **9422**, 94222L (2015) [doi: 10.1117/12.2082883].
53. R. Fallica, J. K. Stowers, A. Grenville, A. Frommhold, A. P. G. Robinson, and Y. Ekinci, "Dynamic absorption coefficients of chemically amplified resists and nonchemically amplified resists at extreme ultraviolet," *J. Micro/Nanolith. MEMS MOEMS* **15**(3), 033506 (2016) [doi: 10.1117/1.JMM.15.3.033506].
54. W. F. Van Dorp, "Theory: Electron-induced Chemistry," in *Materials and Processes for Next Generation Lithography* Vol. **11**, A. P. G. Robinson and R. A. Lawson, Eds., Elsevier, London, pp. 115–134 (2016).
55. T. Kozawa and S. Tagawa, "Radiation chemistry in chemically amplified resists," *Jpn. J. Appl. Phys.* **49**(3R), 030001 (2010).
56. J. Torok, R. Del Re, H. Herbol, S. Das, I. Bocharova, A. Paolucci, L. E. Ocola, C. Ventrice, Jr., E. Lifshin, G. Denbeaux, and R. L. Brainard, "Secondary electrons in EUV lithography," *J. Photopolym. Sci. Tech.* **26**(5), 625–634 (2013).
57. P. De Schepper, A. V. Pret, T. Hansen, A. Giglia, K. Hoshiko, A. Mani, and J. J Biafore, "XAS photoresists electron/quantum yields study with synchrotron light," *Proc. SPIE* **9425**, 942507 (2015) [doi: 10.1117/12.2085951].
58. D. F. Ogletree, "Molecular Excitation and Relaxation of Extreme Ultraviolet Lithography Photoresists, in *Materials and Processes for Next Generation Lithography*, A. P. G. Robinson, and R. A. Lawson, Eds., Elsevier, London, pp. 91–114 (2016).
59. H. Ito, G. Breyta, D. Hofer et al., "Environmentally stable chemical amplification positive resist: principle, chemistry, contamination resistance and lithographic feasibility," *J. Photopolymer Sci. Tech.* **7**(3), 433–447 (1994).
60. R. A. Lawson and A. P. G. Robinson, "Overview of Materials and Processes for Lithography," in *Materials and Processes for Next Generation*

Downloaded From: https://www.spiedigitallibrary.org/ebooks/ on 09 Mar 2022
Terms of Use: https://www.spiedigitallibrary.org/terms-of-use

Lithography, Vol. **11**, A. P. G. Robinson and R. A. Lawson, Eds., Elsevier, London, pp. 1–90 (2016).
61. R. Brainard, E. Hassanein, J. Li et al., "Photons, electrons, and acid yields in EUV photoresists: a progress report," *Proc. SPIE* **6923**, 692325 (2008) [doi: 10.1117/12.773869].
62. A. Narasimhan, S. Grzeskowiak, B. Srivats et al., "Studying thickness loss in extreme ultraviolet resists due to electron beam exposure using experiment and modeling," *J. Micro/Nanolithogr. MEMS MOEMS* **14**(4), 043502 (2015) [doi: 10.1117/1.JMM.14.4.043502].
63. J. Thackeray, J. Cameron, V. Jain, P. LaBeaume, S. Coley, O. Ongayi, M. Wagner, A. Rachford, and J. Biafore, "Progress in resolution, sensitivity, and critical dimensional uniformity of EUV chemically amplified resists," *Proc. SPIE* **8682**, 868213 (2013) [doi: 10.1117/12.2011565].
64. A. Narasimhan, S. Grzeskowiak, J. Ostrander, J. Schad, E. Rebeyev, M. Neisser, L. E. Ocola, G. Denbeaux, and R. L. Brainard, "Studying electron-PAG interactions using electron-induced fluorescence," *Proc. SPIE* **9779**, 97790F (2016) [doi: 10.1117/12.2219850].
65. S. Enomoto, A. Oshima, and S. Tagawa, "Reaction mechanisms of various chemically amplified EUV and EB resist," *Proc. SPIE* **8679**, 86792C (2013) [doi: 10.1117/12.2011634].
66. S. Ptasińska, D. Gschliesser, P. Bartl, I. Janik, P. Scheier, and S. Denifl, "Dissociative electron attachment to triflates," *J. Chem. Phys.* **135**(21), 214309 (2011).
67. D. L. Goldfarb, A. Afzali-Ardakani, and M. Glodde, "Acid generation efficiency: EUV photons versus photoelectrons," *Proc. SPIE* **9779**, 97790A (2016) [doi: 10.1117/12.2218457].
68. S. Tarutani, H. Tsubaki, H. Tamaoki, H. Takahashi, and T. Itou, "Study on approaches for improvement of EUV-resist sensitivity," *Proc. SPIE* **7639**, 763909 (2010) [doi: 10.1117/12.846031].
69. T. H. Fedynyshyn, R. B. Goodman, and J. Roberts, "Polymer matrix effects on acid generation," *Proc. SPIE* **6923**, 692319 (2008) [doi: 10.1117/12.7716692].
70. T. H. Fedynyshyn, R. B. Goodman, A. Cabral, C. Tarrio, and T. B. Lucatorto, "Polymer photochemistry at the EUV wavelength," *Proc. SPIE* **7639**, 76390A (2010) [doi: 10.1117/12.845997].
71. A. Narasimhan, S. Grzeskowiak, C. Ackerman, T. Flynn, G. Denbeaux, and R. L. Brainard, "Mechanisms of EUV exposure: electrons and holes," *Proc. SPIE* **10143**, 101430W (2017) [doi: 10.1117/12.2258321].
72. E. Hassanein, C. Higgins, P. Naulleau, R. Matyi, G. Gallatin, G. Denbeaux, A. Antohe, J. Thackeray, K. Spear, C. Szmanda, and C. N. Anderson, "Film quantum yields of EUV and ultra-high PAG photoresists" *Proc. SPIE* **6921**, 69211I (2008) doi: 10.1117/12.774009].

Downloaded From: https://www.spiedigitallibrary.org/ebooks/ on 09 Mar 2022
Terms of Use: https://www.spiedigitallibrary.org/terms-of-use

73. C. Higgins, A. Antohe, G. Denbeaux, S. Kruger, J. Georger, and R. L. Brainard, "RLS tradeoff vs. quantum yield of high PAG EUV resists," *Proc. SPIE* **7271**, 727147 (2009) [doi: 10.1117/12.814307].
74. R. Hirose, T. Kozawa, S. Tagawa, T. Kai, and T. Shimokawa, "Dependence of acid generation efficiency on molecular structures of acid generators upon exposure to extreme ultraviolet radiation," *Appl. Phys. Express* **1**(2), 027004 (2008).
75. J. J. Biafore, M. D. Smith, E. van Setten, T. Wallow, P. Naulleau, D. Blankenship, S. A. Robertson, and Y. Deng, "Resist pattern prediction at EUV," *Proc. SPIE* **7636**, 76360R (2010) [doi: 10.1117/12.846535].
76. T. Kozawa, Y. Mizutani, M. Miki, T. Yamamoto, S. Suemine, Y. Yoshida, and S. Tagawa, "Development of subpicosecond pulse radiolysis system," *Nucl. Instru. Meth. Phys. Res. Sect. A: Acceler. Spectrom. Detect. Assoc. Equip.* **440**(1), 251–253 (2000).
77. T. Kozawa, T. Shigaki, K. Okamoto, A. Saeki, S. Tagawa, T. Kai, and T. Shimokawa, "Analysis of acid yield generated in chemically amplified electron beam resist," *J. Vac. Sci. & Technol. B: Microelectron. Nanometer Struct. Process. Meas. Phenom.* **24**(6), 3055–3060 (2006).
78. A. Nakano, T. Kozawa, K. Okamoto, S. Tagawa, T. Kai, and T. Shimokawa, "Acid generation mechanism of poly (4-hydroxystyrene)-based chemically amplified resists for post-optical lithography: acid yield and deprotonation behavior of poly (4-hydroxystyrene) and poly (4-methoxystyrene)," *Jpn. J. Appl. Phys.* **45**(9R), 6866 (2006).
79. M. Endo and S. Tagawa, "Theoretical study of ionization of polymers for EUV resist," *J. Photopolym. Sci. Technol.* **25**, 101–108 (2012).
80. S. Bhattarai, A. R. Neureuther, and P. P. Naulleau, "Study of energy delivery and mean free path of low energy electrons in EUV resists," *Proc. SPIE* **9779**, 97790B (2016) [doi: 10.1117/12.2220390].
81. A. Narasimhan, S. Grzeskowiak, C. Ackerman, L. E. Ocola, G. Denbeaux, and R. L. Brainard, "EUV exposure mechanisms: photons, electrons and holes," Presented at Low-Energy Electrons: Lithography, Imaging, and Soft Matter (LEELIS-II), Amsterdam, The Netherlands (2016).
82. H. H. Solak, Y. Ekinci, P. Kaser, and S. Park, "Photon-beam lithography reaches 12.5 nm half-pitch resolution," *J. Vac. Sci. Tech. B.* **25**(1), 91–95 (2007).
83. A. Pirati, R. Peeters, D. Smith, S. Lok, A. Minnaert, M. van Noordenburg, J. Mallmann, N. Harned, J. Stoeldraijer, C. Wagner, C. Zoldesi, E. van Setten, J. Finders, K. de Peuter, C. de Ruijter, M. Popadic, R. Huang, M. Lin, F. Chuang, R. van Es, M. Beckers, D. Brandt, N. Farrar, A. Schafgans, D. Brown, H. Boom, H. Meiling, and R. Kool, "Performance overview and outlook of EUV lithography systems," *Proc. SPIE* **9422**, 94221P (2015) [doi: 10.1117/12.2085912].

Downloaded From: https://www.spiedigitallibrary.org/ebooks/ on 09 Mar 2022
Terms of Use: https://www.spiedigitallibrary.org/terms-of-use

84. V. Rao, J. L. Cobb, C. C. Henderson et al., "Ultrathin photoresists for EUV lithography," *Proc. SPIE* **3676**, 615–626 (1999) [doi: 10.1117/12.351135].
85. Dose calibration for several tools were defined based on printing 100-nm dense line sizing dose (E_{size} = 6.8 mJ/cm^2) of EUV-2D (XP98248B) using 125-nm-thick films coated over primed silicon wafers, soft bake = 130 °C/60 s, PEB = 130 °C/90 s, and 45 s development in CD-26 developer at room temperature.
86. T. Koehler, R. L. Brainard, P. P. Naulleau et al., "Performance of EUV photoresists on the ALS micro exposure tool," *Proc. SPIE* **5753**, 754–764 (2005) [doi: 10.1117/12.600511].
87. D. van Steenwinckel, J. H. Lammers, T. Koehler, R. L. Brainard, and P. Trefonas, "Resist effects at small pitches," *J. Vac. Sci. Tech. B* **24**(1), 316–320 (2006).
88. R. L. Brainard, P. Trefonas, J. H. Lammers et al., "Shot noise, LER, and quantum efficiency of EUV photoresists," *Proc. SPIE* **5374**, 74–85 (2004) [doi: 10.1117/12.536411].
89. C. A. Cutler, J. F. Mackevich, J. Li et al., "Effect of polymer molecular weight on AFM polymer aggregate size and LER of EUV resists," *Proc. SPIE* **5037**, 406–417 (2003) [doi: 10.1117/12.482370].
90. V. N. Golovkina, P. F. Nealey, F. Cerrina et al., "Exploring the ultimate resolution of positive-tone chemically amplified resists: 26 nm dense lines using extreme ultraviolet interference lithography," *J. Vac. Sci. Tech. B* **22** (1), 99–103 (2004).
91. A. Jouve, J. Simon, J. Foucher et al., "Overcoming pattern collapse of ultra high resolution dense lines obtained with EUV resists," *Proc. SPIE* **5753**, 720–731 (2005) [doi: 10.1117/12.598763].
92. G. M. Wallraff, D. R. Medeiros, M. Sanchez et al., "Sub-50 nm half-pitch imaging with a low activation energy chemically amplified photoresist," *J. Vac. Sci. Tech. B* **22**(6), 3479–1023 (2004).
93. P. Naulleau, J. P. Cain, E. Anderson et al., "Characterization of the synchrotron-based 0.3 numerical aperture extreme ultraviolet micro-exposure tool at the advanced light source," *J. Vac. Sci. Tech. B* **23**(6), 2840–2843 (2005).
94. J. W. Thackeray, R. A. Nassar, K. Spear-Alfonso, T. Wallow, and B. LaFontaine, "Evaluation of high and low activation resists for EUV lithography," *J. Photopolym. Sci. Technol.* **19**, 525–531 (2006).
95. S. Kim, G. Yu, J. Lee, H. Kim, J. Lee, D. Kim, Y. Kang, and J. Kim, "Effect of deprotection activation energy on lithographic performance of EUVL resist," *Proc. SPIE* **6519**, 651947 (2007) [doi: 10.1117/12.711951].
96. B. Cardineau, S. Kruger, W. Earley, C. Higgins, S. Revuru, J. Georger, and R. Brainard, "Chain-scission polyesters for EUV lithography," *J. Photopolym. Sci. Technol.* **23**, 665–671 (2010).

Downloaded From: https://www.spiedigitallibrary.org/ebooks/ on 09 Mar 2022
Terms of Use: https://www.spiedigitallibrary.org/terms-of-use

97. B. Cardineau, P. Garczynski, W. Earley, and R. L. Brainard, "Chain-scission polyethers for EUV lithography," *J. Photopolym. Sci. Technol.* **26**, 665–671 (2013).
98. H. Kudo, S. Matsubara, H. Yamamoto, and T. Kozawa, "Synthesis of hyperbranched polyacetals via $a_n + b_2$-type polyaddition ($n = 3$, 8, 18, and 21): Candidate resists for extreme ultraviolet lithograph," *J. Polym. Sci. Part A: Polym. Chem.* **53**, 2343–2350 (2015).
99. K. Furukawa, Y. Arai, H. Yamamoto, T. Kozawa, and S. Tagawa, "Evaluation of hydroxyl derivatives for chemically amplified extreme ultraviolet resist," *Proc. SPIE* **7639**, 76391L (2010) [doi: 10.1117/12.846460].
100. V. S. V. Satyanarayana, F. Kessler, V. Singh, F. R. Scheffer, D. E. Weibel, S. Ghosh, and K. E. Gonsalves, "Radiation-sensitive novel polymeric resist materials: iterative synthesis and their EUV fragmentation studies," *ACS Appl. Mater. Interfaces* **6**, 4223–4232 (2014).
101. H. Oizumi, F. Kumasaka, Y. Tanaka, T. Hirayama, D. Shiono, H. Hada, J. Onodera, A. Yamaguchi, and I. Nishiyama, "Performance of molecular resist based on polyphenol in EUV lithography," *Microelectron. Eng.* **83**, 1107–1110 (2006).
102. D. Shimizu, K. Maruyama, A. Saitou, T. Kai, T. Shimokawa, K. Fujiwara, Y. Kikuchi, and I. Nishiyama, "Progress in EUV resist development," *J. Photopolym. Sci. Technol.* **20**, 423–428 (2007).
103. N. Niina, H. Kudo, H. Oizumi, T. Itani, and T. Nishikubo, "Synthesis and property of noria (water-wheel like macrocycle) derivatives with pendant alkoxyl and adamantyl ester groups, and their application for extreme ultraviolet resist," *Thin Solid Films* **534**, 459–464 (2013).
104. T. Nishikubo, H. Kudo, Y. Suyama, H. Oizumi, and T. Itani, "Novel noria (water wheel-like cyclic oligomer) derivative as a chemically amplified extreme ultraviolet (EUV)-resist material," *J. Photopolym. Sci. Technol.* **22**, 73–76 (2009).
105. H. Seki, Y. Kato, H. Kudo, H. Oizumi, T. Itani, and T. Nishikubo, "Negative-type extreme ultraviolet resist materials based on water-wheel-like cyclic oligomer (noria)," *Jpn. J. Appl. Phys.* **49**, 06GF06 (2010).
106. H. Seki, H. Kudo, H. Oizumi, T. Itani, and T. Nishikubo, "Extreme ultraviolet resist fabricated using water wheel-like cyclic oligomer with pendant adamantyl ester groups," *Jpn. J. Appl. Phys.* **50**, 121602 (2011).
107. D. P. Green, V. Jain, B. Bailey, M. Wagner, M. Clark, D. Valeri, and S. Lakso, "Development of molecular resist derivatives for EUV lithography," *Proc. SPIE* **8679**, 867912 (2013) [doi: 10.1117/12.2011805].
108. R. Lawson, J. Chun, M. Neisser, L. Tolbert, and C. L. Henderson, "Methods of controlling cross-linking in negative-tone resists," *Proc. SPIE* **9051**, 90510Q (2014) [doi: 10.1117/12.2046616].

Downloaded From: https://www.spiedigitallibrary.org/ebooks/ on 09 Mar 2022
Terms of Use: https://www.spiedigitallibrary.org/terms-of-use

109. R. Lawson, J. Chun, M. Neisser, L. Tolbert, and C. L. Henderson, "Methods of controlling cross-linking in negative-tone resists," *Proc. SPIE* **9051**, 90510Q (2014) [doi: 10.1117/12.2046616].
110. R. Lawson, H. Norcross, B. Sharp, J. Chun, M. Neisser, L. Tolbert, and C. Henderson, "Optimizing performance in cross-linking negative-tone molecular resists," *Proc. SPIE* **9425**, 94250A (2015) [doi: 10.1117/12.2086007]; B. Sharp, R. Lawson, A. Fralick, H. Norcross, J. Chun, M. Neisser, L. Tolbert, and C. Henderson, "Base developable negative-tone molecular resist based on epoxide cross-linking," *Proc. SPIE* **9425**, **94251S** (2015) [doi: 10.1117/12.2086039].
111. A. Frommhold, D. Yang, A. McClelland, X. Xue, R. Palmer, and A. Robinson, "EUV lithography performance of negative-tone chemically amplified fullerene resist," *Proc. SPIE* **8682**, 86820Q (2013) [doi: 10.1117/12.2011464].
112. A. Frommhold, A. McClelland, D. Yang, R. Palmer, J. Roth, Y. Ekinci, M. Rosamund, and A. Robinson, "Towards 11 nm half-pitch resolution for a negative-tone chemically amplified molecular resist platform for EUV lithography," *Proc. SPIE* **9425**, 942504 (2015) [doi: 10.1117/12.2085672].
113. C. Popescu, A. Frommhold, A. McClelland, J. Roth, Y. Ekinci, and A. Robinson, "Sensitivity enhancement of the high-resolution xMT multi-trigger resist for EUV lithography," *Proc. SPIE* **10143**, 101430V [doi: 10.1117/12.2258098].
114. http://www.lithoguru.com/scientist/litho_tutor/TUTOR08(Autumn 94).pdf.
115. T. Brunner, "Relationship between the slope of the HD curve and the fundamental resist process contrast," *J. Vac. Sci. Technol. B* **17**(6), 3362 (1999) [and references therein].
116. T. Itani, and J. J. Santillan, "*In situ* characterization of photoresist dissolution," *Appl. Phys. Express* **3**(6), 0616013 (2010).
117. J. Santillan, M. Shichiri, and T. Itani "An *in situ* analysis of resist dissolution in alkali-based and organic solvent-based developers using high speed atomic force microscopy," *Proc. SPIE* **9051**, 90510O (2014) [doi: 10.1117/12.2045886]
118. J. J. Santillan and T. Itani, "Dissolution characteristics of EUV resist by high speed AFM," *J. Photopolym. Sci. Technol.* **25**, 95–100 (2012).
119. J. J. Santillan and T. Itani, "*In situ* analysis of the EUV resist pattern formation during the resist dissolution process," *J. Photopolym. Sci. Technol.* **26**, 611–616 (2013).
120. J. J. Santillan and T. Itani, "*In situ* dissolution analysis of ultrathin extreme ultraviolet resists," *Jpn. J. Appl. Phys*. **51**, 06FC06 (2012).
121. T. Itani and J. J. Santillan, "Alternative developer solutions for extreme ultraviolet resist," *J. Vac. Sci. Technol. B* **27**, 2986–2989 (2009).

Downloaded From: https://www.spiedigitallibrary.org/ebooks/ on 09 Mar 2022
Terms of Use: https://www.spiedigitallibrary.org/terms-of-use

122. T. Itani and J. J. Santillan, "*In situ* dissolution analysis of EUV resists," *Proc. SPIE* **7972**, 79720H (2011) [doi: 10.1117/12.878670].
123. J. J. Santillan and T. Itani, "Dissolution characteristics of EUV resist by high speed AFM," *J. Photopolym. Sci. Technol.* **25**, 95–100 (2012).
124. G. M. Gallatin, P. Naulleau, and R. L. Brainard, "Fundamental limits to EUV photoresist," *Proc. SPIE* **6519**, 651911 (2007) [doi: 10.1117/12.712346].
125. K. Ichimura, "Nonlinear organic reactions to proliferate acidic and basic molecules and their applications," *The Chemical Record* **2**(1), 46–55 (2002).
126. K. Arimitsu, K. Kudo, and K. Ichimura, "Autocatalytic fragmentation of acetoacetate derivatives as acid amplifiers to proliferate acid molecules," *J. Am. Chem. Soc.* **120**(1), 37–45 (1998).
127. S. Noguchi, K. Arimitsu, K. Ichimura, K. Kudo, T. Ohfuji, and M. Sasago, "Novel resist materials using acid amplifiers. Part II," *J. Photopoly. Sci. and Tech.* **10**(2), 315–316 (1997).
128. O. T. Naito, M. Endo, H. Morimoto, K. Arimitsu, and K. Ichimura, "193 nm lithography with novel highly transparent acid amplifier for chemically amplified resists," *J. Photopoly. Sci. and Tech.* **12**(3), 509–514 (1999).
129. S.-W. Park, K. Arimitsu, K. Ichimura, and T. Ohfuji, "Synthesis and characteristics of a novel acid amplifier with a low absorbance at 193 nm," *J. Photopoly. Sci. and Tech.* **12**(2), 293–296 (1999).
130. S. Lee, K. Arimitsu, S.-W. Park, and K. Ichimura, "Synthesis and evaluation of novel acid amplifiers liberating fluoroalkanesulfonic acids," *J. Photopoly. Sci. and Tech.* **13**(2), 215–216 (2000).
131. S. Kruger, S. Revuru, C. Higgins, S. Gibbons, D. A. Freedman, W. Yueh, T. R. Younkin, and R. L. Brainard, "Fluorinated acid amplifiers for EUV lithography," *J. Am. Chem. Soc.* **131**(29), 9862–9863 (2009).
132. R. Brainard, S. Kruger, C. Higgins, S. Revuru, S. Gibbons, D. Freedman, Y. Wang, and T. Younkin, "Kinetics, chemical modeling and lithography of novel acid amplifiers for use in EUV photoresists," *J. Photopolym. Sci. Technol.* **22**, 43–50 (2009).
133. S. A. Kruger, C. Higgins, S. Revuru, S. Gibbons, D. Freedman, and R. L. Brainard, "Can acid amplifiers help beat the resolution, line edge roughness and sensitivity trade-off?" *Jap. J. App. Phys.* **49**(4), 041602 (2010).
134. The Z-Parameter can be calculated from a single SEM as $Z = CD^3 \times LER^2 \times E_{size}$, where a smaller value is better.
135. S. A. Kruger, C. Higgins, B. Cardineau, T. R. Younkin, and R. L. Brainard, "Catalytic and autocatalytic mechanisms of acid amplifiers for use in EUV photoresists," *Chem. Mat.* **22**(19), 5609–5616 (2010).

Downloaded From: https://www.spiedigitallibrary.org/ebooks/ on 09 Mar 2022
Terms of Use: https://www.spiedigitallibrary.org/terms-of-use

136. K. Maruyama, M. Shimizu, Y. Hirai, K. Nishino, T. Kimura, T. Kai, K. Goto, and S. Sharma, "Development of EUV resist for 22nm half pitch and beyond," *Proc. SPIE* **7636**, 76360T (2010) [doi: 10.1117/12.846332].
137. S. A. Kruger, "Fluorinated acid amplifiers for extreme ultraviolet lithography," Ph.D. Thesis, University at Albany, Albany, New York, 2011.
138. S. Kruger, K. Hosoi, B. Cardineau, K. Miyauchi, and R. Brainard, "Stable, fluorinated acid amplifiers for use in EUV lithography," *Proc. SPIE* **8325**, 832514 (2012) [doi: 10.1117/12.917015].
139. pKa values were calculated using Advanced Chemistry Development software V11.02.
140. K. Hosoi, B. Cardineau, S. Kruger, K. Miyauchi, and R. Brainard, "Fluorine-stabilized acid amplifiers for use in EUV lithography," *J. Photopolym. Sci. Technol.* **25**, 575–581 (2012).
141. Typically, the synchrotron at PSI is extremely stable. Unfortunately, during the week of these experiments, the intensity of the EUV source was variable, so we were unable to provide the doses of these preliminary experiments.
142. S. Nagahara, M. Carcasi, H. Nakagawa, E. Buitrago, O. Yildirim, G. Shiraishi, Y. Terashita, Y. Minekawa, K. Yoshihara, M. Tomono, H. Mizoguchi, J. Estrella, T. Nagai, T. Naruoka, S. Dei, M. Hori, A. Oshima, M. Vockenhuber, Y. Ekinci, M. Meeuwissen, C. Verspaget, R. Hoefnagels, G. Rispens, R. Maas, H. Nakashima, and S. Tagawa, "Challenge toward breakage of RLS trade-off for EUV lithography by photosensitized "chemically amplified resist (PSCAR) with flood exposure," *Proc. SPIE* **9776**, 977607 (2016) [doi: 10.1117/12.2219433].
143. M. Carcasi, S. Nagahara, G. Shiraishi, T. Iseki, Y. Minekawa, K. Yoshihara, H. Nakagawa, T. Naruoka, T. Nagai, A. Oshima, and S. Tagawa, "Simulation and experimentation of PSCAR chemistry for complex structures," *Proc. SPIE* **10143**, 1014329 (2017) [doi: 10.1117/12.2258166].
144. S. Tagawa, S. Enomoto, and A. Oshima, "Super high sensitivity enhancement by photo-sensitized chemically amplified resist (PS-CAR) process," *J. Photopolymer Science and Technology* **26**(6), 825 (2013).
145. S. Tagawa, A. Oshima, S. Enomoto, and C. Q. Dinh, "High-resist sensitization by pattern and flood combination lithography," *Proc. SPIE* **9048**, 90481S (2014) [doi: 10.1117/12.2046790].
146. T. Nagai, H. Nakagawa, T. Naruoka, S. Tagawa, A. Oshima, S. Nagahara, G. Shiraishi, K. Yoshihara, Y. Terashita, Y. Minekawa, E. Buitrago, Y. Ekinci, O. Yildirim, M. Meeuwissen, R. Hoefnagels, G. Rispens, C. Verspaget, and R. Maas, "Novel high sensitivity EUV photoresist for sub-7nm node," *Proc. SPIE* **9779**, 977908 (2016) [doi: 10.1117/12.2218936].

Downloaded From: https://www.spiedigitallibrary.org/ebooks/ on 09 Mar 2022
Terms of Use: https://www.spiedigitallibrary.org/terms-of-use

147. J. M. Amador, S. R. Decker, S. E. Lucchini, R. E. Ruther, and D. A. Keszler, "Patterning chemistry of HafSOx photoresist," *Proc. SPIE* **9051**, 90511A (2014) [doi: 10.1117/12.2046606].
148. P. Naulleau, C. N. Anderson, L.-M. Baclea-an et al., "The SEMATECH Berkeley MET pushing EUV development beyond 22nm half pitch," *Proc. SPIE* **7636**, 76361J (2010) [doi: 10.1117/12.848438].
149. M. Trikeriotis, W. J. Bae, E. Schwartz, M. Krysak, N. Lafferty, P. Xie, B. Smith, P. A. Zimmerman, C. K. Ober, and E. P. Giannelis, "Development of an inorganic photoresist for DUV, EUV, and electron beam imaging," *Proc. SPIE* **7639**, 76390E (2010) [doi: 10.1117/12.846672].
150. M. Krysak, M. Trikeriotis, E. Schwartz, N. Lafferty, P. Xie, B. Smith, P. Zimmerman, W. Montgomery, E. Giannelis, and C. K. Ober, "Development of an inorganic nanoparticle photoresist for EUV, e-beam, and 193 nm lithography," *Proc. SPIE* **7972**, 79721C (2011) [doi: 10.1117/12.879385].
151. M. Trikeriotis, M. Krysak, Y. S. Chung, C. Ouyang, B. Cardineau, R. Brainard, C. K. Ober, E. P. Giannelis, and K. Cho, "Nanoparticle photoresists from HfO_2 and ZrO_2 for EUV patterning," *J. Photopolym. Sci. Technol.* **25**, 583–586 (2012).
152. M. Kryask, M. Trikeriotis, C. Ouyang, A. Chakrabarty, E. P. Giannelis, and C. K. Ober, "Nanoparticle photoresists: ligand exchange as a new and sensitive EUV patterning mechanism," *J. Photopolym. Sci. Technol.* **26**, 659–664 (2013).
153. S. Chakrabarty, C. Ouyang, M. Krysak, M. Trikeriotis, K. Cho, E. P. Giannelis, and C. K. Ober, "Oxide nanoparticle EUV resists: toward understanding the mechanism of positive and negative tone patterning," *Proc. SPIE* **8679**, 867906 (2013) [doi: 10.1117/12.2011490].
154. C. Y. Ouyang, Y. S. Chung, L. Li, M. Neisser, K. Cho, E. P. Giannelis, and C. K. Ober, "Non-aqueous negative-tone development of inorganic metal oxide nanoparticle photoresists for next generation lithography," *Proc. SPIE* **8682**, 86820R (2013) [doi: 10.1117/12.2011282].
155. M. E. Krysak, J. M. Blackwell, S. E. Putna, M. J. Leeson, T. R. Younkin, S. Harlson, K. Frasure, and F. Gstrein, "Investigation of novel inorganic resists materials for EUV lithography," *Proc. SPIE* **9048**, 904805 (2014) [doi: 10.1117/12.2046677].
156. J. Jiang, S. Chakrabarty, M. Yu, and C. K. Ober, "Metal oxide nanoparticle photoresists for EUV patterning," *J. Photopolym. Sci. Technol.* **27**(5), 663–666 (2014).
157. J. Jiang, B. Zhang, M. Yu, L. Li, M. Neisser, J. S. Chun, E. P. Giannelis, and C. K. Ober, "Oxide nanoparticle EUV (ONE) photoresists: current understanding of the unusual patterning mechanism," *J. Photopolym. Sci. Technol.* **28**, 515–518 (2015).

Downloaded From: https://www.spiedigitallibrary.org/ebooks/ on 09 Mar 2022
Terms of Use: https://www.spiedigitallibrary.org/terms-of-use

158. L. Li, S. Chakrabarty, J. Jiang, B. Zhang, C. Ober, and E. P. Giannelis, "Solubility studies of inorganic-organic hybrid nanoparticle photoresists with different surface functional groups," *Nanoscale* **8**, 1338–1343 (2016).
159. C. A. Mack, J. W. Thackeray, J. J. Biafore, and M. D. Smith, "Stochastic exposure kinetics of extreme ultraviolet photoresists: simulation study," *J. Micro/Nanolithogr. MEMS MOEMS* **10**(3), 033019 (2011) [doi: 10.1117/1.3631753].
160. V. Singh, V. Kalyani, V. S. V. Satyanarayana, C. P. Pradeep, S. Ghosh, S. Sharma, and K. E. Gonsalves, "Organic-inorganic hybrid resists for EUVL," *Proc. SPIE* **9051**, 90511W (2014) [doi: 10.1117/12.2041907].
161. V. S. V. Satyanarayana, V. Singh, V. Kalyani, C. P. Pradeep, S. Sharma, S. Ghosh, and K. E. Gonsalves, "A hybrid polymeric material bearing a ferrocene-based pendant organometallic functionality: synthesis and applications in nanopatterning using EUV lithography," *RSC Advances* **4**, 59817–59820 (2014).
162. V. Kalyani, V. S. V. Satyanarayana, V. Singh, C. P. Pradeep, S. Ghosh, S. K. Sharma, and K. E. Gonsalves, "New polyoxometalates containing hybrid polymers and theirpPotential for nano-patterning," *Chem. - Eur. J.* **21**, 2250–2258 (2015).
163. Y. Ekinci, M. Vockenhuber, L. Wang, and N. Mojarad, "Evaluation of EUV resist performance with interference lithography towards 11 nm half-pitch and beyond," *Proc. SPIE* **8679**, 867910 (2013) [doi: 10.1117/12.2011533].
164. B. Cardineau, M. Krysak, M. Trikeriotis, R. L. Brainard et al., "Tightly bound ligands for hafnium nanoparticle EUV resists," *Proc. SPIE* **8322**, 83220V (2012) [doi: 10.1117/12.917014].
165. B. Cardineau, R. Del Re, M. Marnell, H. Al-Mashat, M. Vockenhuber, Y. Ekinci, C. Sarma, D. A. Freedman, and R. L. Brainard, "Photolithographic properties of tin-oxo clusters using extreme ultraviolet light (13.5 nm)," *Microelectron. Eng.* **127**, 44–50 (2014).
166. B. Cardineau, R. Del Re, H. Al-Mashat, M. Marnell, M. Vockenhuber, Y. Ekinci, C. Sarma, M. Neisser, D. A. Freedman, and R. L. Brainard, "EUV resists based on tin-oxo clusters," *Proc. SPIE* **9051**, 90511B (2014) [doi: 10.1117/12.2046536].
167. Dose calibration tool (DCT): A tool designed and used at LBNL in the dose calibration of a resist. The resist-coated wafer is placed in the tool and is exposed with 50 separate exposures, with each exposure at a different dose. The wafer is then processed and the film-thickness-versus-dose curves are typically measured.
168. E. W. Abel, G. A. Stone, and G. Wilkinson, Eds., *Comprehensive Organometallic Chemistry* II, Pergamon Press, Oxford (1982).
169. R. Del Re, J. Passarelli, M. Sortland, B. Cardineau, Y. Ekinci, E. Buitrago, M. Neisser, D. A. Freedman, and R. L. Brainard, "Low-line

Downloaded From: https://www.spiedigitallibrary.org/ebooks/ on 09 Mar 2022
Terms of Use: https://www.spiedigitallibrary.org/terms-of-use

edge roughness extreme ultraviolet photoresists of organotin carboxylates," *J. Micro/Nanolith. MEMS MOEMS* **14**(4), 043506 (2015) [doi: 10.1117/JMM.14.4.043506].
170. J. Passarelli, B. Cardineau, R. Del Re, M. Sortland, M. Vockenhuber, Y. Ekinci, C. Sarma, M. Neisser, D. A. Freedman, and R. L. Brainard, "EUV resists comprised of main group organometallic oligomeric materials," *Proc. SPIE* **9051**, 90512A (2014) [doi: 10.1117/12.2046537].
171. J. Passarelli, M. Sortland, R. Del Re, B. Cardineau, C. Sarma, D. A. Freedman, and R. L. Brainard, "Bismuth resists for EUV lithography," *J. Photopolym. Sci. Technol.* **27**, 661–667 (2014).
172. M. Marnell, B. Cardineau, H. Al-Mashat, K. Heard, A. Aslam, J. Pavlich, R. Del Re, M. Vockenhuber, Y. Ekinci, C. Sarma, M. Neissar, R. Brainard, and D. Freedman, "A molecular inorganic approach to EUV photoresists," presented at the SPIE Advanced Lithography Symposium, Feb. 2014, San Jose, California.
173. M. Sortland, J. Hotalen, R. Del Re, J. Passarelli, M. Murphy, T. S. Kulmala, Y. Ekinci, M. Neisser, D. A. Freedman, and R. L. Brainard, "Platinum and palladium oxalates: positive-tone extreme ultraviolet resists," *J. Micro/Nanolith. MEMS MOEMS* **14**(4), 043511 (2015) [doi: 10.1117/1.JMM.14.4.043511].
174. M. Sortland, R. Del Re, J. Passarelli, J. Hotalen, M. Vockenhuber, Y. Ekinci, M. Neisser, D. A. Freedman, and R. L. Brainard, "Positive-tone EUV resists: complexes of platinum and palladium," *Proc. SPIE* **9422**, 942227 (2015) [doi: 10.1117/12.2086598].
175. R. S Paonessa, A. L. Prignano, and W. C. Trogler, "Photochemical generation of bis(phosphine)palladium and bis(phosphine)platinum equivalents," *Organometallics* **4**(4), 647–657 (1985).
176. D. M. Blake and C. J. Nyman, "Photochemical reactions of oxalatobis (triphenylphosphine)platinum(II) and related compounds," *J. Am. Chem. Soc.* **92**(18), 5359–5364 (1970).
177. Y. J. Pan, J. T. Mague, and M. J. Fink, "Synthesis, structure, and unusual reactivity of a d10-d10 palladium(0) dimer," *J. Am. Chem. Soc.* **115**(9), 3842–3843 (1993).
178. G. K. Anderson, G. J. Lumetta, and J. W. Siria, "Photochemical reactions of diphosphineplatinum(II) oxalate complexes," *J. Organometallic Chemistry* **434**(2), 253–259 (1992).
179. R. Del Re, M. Sortland, J. Pasarelli, B. Cardineau, Y. Ekinci, M. Vockenhuber, M. Neisser, D. Freedman, and R. L. Brainard, "Low-LER tin carboxylate photoresists using EUV," *Proc. SPIE* **9422**, 942221 (2015) [doi: 10.1117/12.2086597].
180. J. Passarelli, M. Murphy, R. Del Re, M. Sortland, J. Hotalen, L. Dousharm, Y. Ekinci, M. Neisser, D. Freedman, R. Fallica, D. A.

Downloaded From: https://www.spiedigitallibrary.org/ebooks/ on 09 Mar 2022
Terms of Use: https://www.spiedigitallibrary.org/terms-of-use

Freedman, and R. L. Brainard, "Organometallic carboxylate resists for extreme ultraviolet with high sensitivity," *J. Micro/Nanolith. MEMS MOEMS* **14**(4), 043503 (2015) [doi: 10.1117/1.JMM.14.4.043503].
181. J. Passarelli, M. Murphy, R. Del Re, M. Sortland, L. Dousharm, M. Vockenhuber, Y. Ekinci, M. Neisser, D. A. Freedman, and R. L. Brainard, "High-sensitivity molecular organometallic resist for EUV (MORE)," *Proc. SPIE* **9425**, 94250T (2015) [doi: 10.1117/12.2086599].
182. G. M. Gallatin, "Resist blur and line edge roughness," *Proc. SPIE* **5754**, 38 (2005) [doi: 10.1117/12.607233].
183. T. Kozawa, H. Yamamoto, and S. Tagawa, "Effect of inhomogeneous acid distribution on line edge roughness: relationship to line edge roughness originating from chemical gradient," *J. Photopolym. Sci. Technol.* **23**, 625–630 (2010).
184. T. Kozawa, "Effects of dose shift on line width, line edge roughness, and stochastic defect generation in chemically amplified extreme ultraviolet resist with photodecomposable quencher," *Jpn. J. Appl. Phys.* **54**, 16503 (2015).
185. C. Mack, *Fundamental Principles of Optical Lithography: The Science of Microfabrication*, John Wiley & Sons, Ltd, Chichester (2007).
186. A. K. Wong, *Optical Imaging in Projection Microlithography*, SPIE Press, Bellingham, Washington (2005) [doi: 10.1117/3.612961].
187. G. Han, M. Khan, Y. Fang, and F. Cerrina, "Comprehensive model of electron energy deposition," *J. Vacuum Sci. Tech. B* **20**, 2666 (2002).
188. F. A. Houle, W. D. Hinsberg, and M. I. Sanchez, "Kinetic model for positive tone resist dissolution and roughening," *Macromolecules* **35**, 8591–8600 (2002).
189. P. C. Tsiartis, L. W. Flanagin, C. L. Henderson, W. D. Hinsberg, I. C. Sanchez, R. T. Bonnecaze, and C. G. Willson, "The mechanism of phenolic polymer dissolution: A new perspective," *Macromolecules* **30**(16), 4656 (1997).
190. J. L. Cobb, F. A. Houle, and G. M. Gallatin, "Estimated impact of shot noise in extreme ultraviolet lithography," *Proc. SPIE* **5037**, 397–405 (2003) [doi: 10.1117/12.484730].
191. J. J. Biafore, M. D. Smith, C. A. Mack, J. W. Thackeray, R. Gronheid, S. A. Robertson, T. Graves, and D. Blankenship, "Statistical simulation of photoresists at EUV and ArF," *Proc. SPIE* **7273**, 727343 (2009) [doi: 10.1117/12.813551].
192. P. P. Naulleau, C. N. Anderson, L. Baclea-an, P. Denham, S. George, K. A. Goldberg, G. Jones, B. McClinton, R. Miyakawa, S. Rekawa, and N. Smith, "Critical challenges for EUV resist materials," *Proc. SPIE* **7972**, 797202 (2011) [doi: 10.1117/12.882955].
193. T. Kozawa and T. Hirayama, "Theoretical relationship between quencher diffusion constant and effective reaction radius for

Downloaded From: https://www.spiedigitallibrary.org/ebooks/ on 09 Mar 2022
Terms of Use: https://www.spiedigitallibrary.org/terms-of-use

neutralization in contact hole imaging using chemically amplified extreme ultraviolet resists," *Jpn. J. Appl. Phys.* **53**, 066502 (2014).
194. T. Kozawa, J. J. Santilian, and T. Itani, "Modeling and simulation of acid diffusion in chemically amplified resists with polymer-bound acid generator," *Appl. Phys. Express* **5**, 074301 (2012).
195. H. Yamamoto, T. Kozawa, S. Tagawa, T. Mimura, T. Iwai, and J. Onodera, "Dissolution kinetics in chemically amplified EUV resist," *J. Photopolym. Sci. Technol.* **24**(4), 405–410 (2011).
196. D. C. Rapaport, *The Art of Molecular Dynamics Simulation*, Cambridge University Press, New York (1995).
197. M. Toriumi and T. Itani, "Inhomogeneity of photoacid generators in methacrylate-type EUV resist film studied by molecular dynamics simulations," *Jpn. J. Appl. Phys.* **54**, 1–7 (2015).
198. X. Zhang, L. Du, and Z. Xu, "The effect of soft bake on adhesion property between SU-8 photoresist and Ni substrate by molecylar dynamic simulation," *J. Appl. Polym. Sci.* **127**(6), 4456–4462 (2013).
199. M. A. Mohammad, K. P. Santo, S. K. Dew, and M. Stepanova, "Study of the interaction of polymethylmethcrylate fragments with methyl isobutyl ketone and isopropyl alcohol," *J. Vac. Sci. Technol. B* **30**(6), 06FF11 (2012).
200. F. H. Dill, W. P. Hornberger, P. S. Hauge, and J. M. Shaw, "Characterization of positive photoresist," *IEEE Trans. Electron Devices* **22**(7), 445–452 (1975).
201. W. Gao, A. Philippou, U. Klostermann, J. Siebert, V. Philipsen, E. Hendrickx, T. Vandeweyer, and G. Lorusso, "Calibration and verification of a stochastic model for EUV resist," *Proc. SPIE* **8322**, 83221D (2012) [doi: 10.1117/12.917804].
202. W. D. Hinsberg and S. Meyers, "A numeric model for the imaging mechanism of metal oxide EUV resists," *Proc. SPIE* **10146**, 1014604 (2017) [doi: 10.1117/12.2260265].
203. See Section 8.2 Earliest EUV Resist Imaging.
204. A. M. Goethals, R. Gronheid, F. Van Roey, H. H. Solak, and Y. Ekinci, "Progress in EUV resist performance," *J. Photopolym. Sci. Technol.* **19**, 501–506 (2006).
205. A.-M. M. F. Goethals, P. Foubert, K. Hosokawa, F. Van Roey, A. Niroomand, D. Van den Heuvel, and I. Pollentier, "EUV resist process performance investigations on the NXE3100 full field scanner," *J. Photopolym. Sci. Technol.* **25**, 559–567 (2012).
206. T. I. Wallow, R. Kim, B. LaFontaine, P. P. Naulleau, C. N. Anderson, and R. L. Sandberg, "Progress in EUV photoresist technology," *Proc. SPIE* **6533**, 653317 (2007) [doi: 10.1117/12.737189].
207. K. Dean, I. Nishiyama, H. Oizumi, A. Keen, H. Cao, W. Yueh, T. Watanabe, P. Lacovig, L. Rumiz, G. Denbeaux, and J. Simon, "An

Downloaded From: https://www.spiedigitallibrary.org/ebooks/ on 09 Mar 2022
Terms of Use: https://www.spiedigitallibrary.org/terms-of-use

analysis of EUV resist outgassing measurements," *Proc. SPIE* **6519**, 6519P1 (2007) [doi: 10.1117/12.712379].
208. S. Grantham, C. Tarrio, S. Hill, L. Richter, T. Lucatorto, J. van Dijk, C. Kaya, N. Harned, R. Hoefnagels, M. Silova, and J. Steinhoff, "The NIST EUV facility for advanced photoresist qualification using the witness-sample test," *Proc. SPIE* **7969**, 79690K (2011) [doi: 10.1117/12.879519].
209. I. Pollentier, I. Neira, and R. Gronheid, "Assessment of resist outgassing related EUV optics contamination for CAR and non-CAR material chemistries," *Proc. SPIE* **7972**, 797208 (2011) [doi: 10.1117/12.881215].
210. G. Rispens, "Outgassing of CAR and alternative resists: The way forward," presented at EUVL Resist TWG, 4 Oct. 2015.
211. https://www.semiwiki.com/forum/content/6723-spie-2017-asml-interview-presentations.html?s=1e0cda6a178006ff81ff46dc270028cd.
212. D. Fan and Y. Ekinci, "Photolithography reaches 6 nm half-pitch using extreme ultraviolet light," *J. Micro/Nanolith. MEMS MOEMS* **15**(3), 033505 (2016) [doi: 10.1117/1.JMM.15.3.033505].
213. R. Fallica, E. Buitrago, and Y. Ekinci, "Comparative study of line roughness metrics of chemically amplified and inorganic resists for extreme ultraviolet," *J. Micro/Nanolith. MEMS MOEMS* **15**(3), 034003 (2016) [doi: 10.1117/1.JMM.15.3.034003].
214. H. Oizumi, Y. Tanaka, T. Kumise, D. Shiono, T. Hirayama, H. Hada, J. Onodera, A. Yamaguchi, and I. Nishiyama, "Evaluation of new molecular resist for EUV lithography," *J. Photopolym. Sci. Technol.* **20**, 403–410 (2007).
215. S. Wurm, "Extreme ultraviolet lithography development in the United States," *Jpn. J. Appl. Phys., Part 1* **46**, 6105–6112 (2007).
216. P. P. Naulleau, C. N. Anderson, J. Chiu, P. Denham, S. George, K. A. Goldberg, M. Goldstein, B. Hoef, R. Hudyma, G. Jones, C. Koh, B. La Fontaine, A. Ma, W. Montgomery, D. Niakoula, J. Park, T. Wallow, and S. Wurm, "22-nm half-pitch extreme ultraviolet node development at the SEMATECH Berkeley microfield exposure tool," *Microelectron. Eng.* **86**, 448–455 (2009).
217. T. Itani, "A comprehensive review of EUV resist materials and processing at Selete," *J. Photopolym. Sci. Technol.* **24**, 111–118 (2011).
218. M. Neisser, S. Jen, J. S. Chun, A. Antohe, L. He, P. Kearney, and F. Goodwin, "EUV research activity at SEMATECH," *J. Photopolym. Sci. Technol.* **27**, 600 (2014).
219. www.itrs.net and www.itrs2.net.
220. Y.-J. Fan, M. Mellish, J. S. Chun, S. McWilliams, C. A. Montgomery, and W. Montgomery, "Benchmarking study of EUV resists for NXE:3300B," *Proc. SPIE* **9776**, 97760W (2016) [doi:10.1117/12.2222065].

Downloaded From: https://www.spiedigitallibrary.org/ebooks/ on 09 Mar 2022
Terms of Use: https://www.spiedigitallibrary.org/terms-of-use

221. D. De Simone, A. Goethals, F. Van Roey, T. Zheng, P. Foubert, E. Hendrickx, G. Vandenberghe, and K. Ronse, "Progresses and challenges of EUV lithography materials," *J. Photopolym. Sci. Technol.* **27**, 610 (2014).
222. Y. Wei, M. Bender, W. Domke, A. Laessig, M. Sebald, S. Trogisch, and D. Back, "Performance of chemically amplified resists at half-pitch of 45 nm and below," *Proc. SPIE* **6519**, 65190R (2007) [doi: 10.1117/12.706887].
223. H. Kim, H. Na, K. Cho, C. Park, T. Yasue, S. Mayya, H. Cho, and B. M. La Fontaine, "Patterning with EUVL: the road to 22nm node," *Proc. SPIE* **7636**, 76360Q (2010) [doi: 10.1117/12.846474].
224. D. De Simone, M. Mao, M. Kocsis, P. De Schepper, F. Lazzarino, G. Vandenberghe, J. Stowers, S. Meyers, B. Clark, A. Grenville, V. Luong, F. Yamashita, and D. Parnell, "Demonstration of an N7 integrated fab process for metal oxide EUV photoresist," *Proc. SPIE* **9776**, 97760B (2015) [doi: 10.1117/12.2220051].
225. T. A. Brunner, X. Chen, A. Gabor, C. Higgins, L. Sun, and C. A. Mack, "Line-edge roughness performance targets for EUV lithography," *Proc. SPIE* **10143**, 101430E (2017) [doi: 10.1117/12.2258660].
226. R. L. Bristol and M. E. Krysak, "Lithographic stochastics: beyond 3σ," *Proc. SPIE* **10143**, 101430Z (2017) [doi: 10.1117/12.2264046].
227. J. Stowers and D. A. Keszler, "High resolution, high sensitivity inorganic resists," *Micro. Eng.* **86**, 730–733 (2009).
228. C. D. Higgins, C. R. Szmanda, A. Antohe, G. Denbeaux, J. Georger, and R. L. Brainard, "Resolution, line-edge roughness, sensitivity tradeoff, and quantum yield of high photo acid generator resists for extreme ultraviolet lithography," *Jpn. J. Appl. Phys.* **50**(3), 036504 (2011).

Robert Brainard received his B.S. in chemistry from University of California Berkeley in 1979. He studied the reaction mechanisms of organoplatinum compounds during his graduate studies with Professor Whitesides at MIT and Harvard University. After receiving his Ph.D. in 1985, he studied the reaction mechanisms on copper and silver surfaces under ultrahigh-vacuum conditions as a post-doctoral student with Professor Madix at Stanford University.

Robert worked for Polaroid (1987–1990) and at Shipley/Rohm & Haas (1990–2005), where he did product development research in the areas of electrodeposited, dielectric, color filter, DUV, EUV, x-ray, and e-beam photoresists. Robert was the first chemist in the world to design resists for EUVL, starting in 1998 while working at Shipley Co. and in collaboration with the EUV LLC.

Robert is now a tenured Professor at the College of Nanoscale Science and Engineering within SUNY Polytechnic Institute investigating new

Downloaded From: https://www.spiedigitallibrary.org/ebooks/ on 09 Mar 2022
Terms of Use: https://www.spiedigitallibrary.org/terms-of-use

materials for use in EUVL and biological applications. His specific research interests include:

- EUV photoresist exposure mechanisms
- High-quantum-efficiency EUV photoresists
- Design and synthesis of photoacid generators
- Acid amplifiers for use in EUVL
- Design and synthesis of photoimagable hydrogels for cell growth
- Molecular organometallic resists for EUV (MORE)

Mark Neisser is the Technology Director at Kempur Microelectronics Inc., where he directs the development of photoresist and other new products. Previously, he worked in the Lithography Program at SEMATECH, where he led a team that did research into expanding current EUV resist material platforms and researching new solutions such as metal-based resists. He earned his Bachelor's degree at Cornell University and his Master's and Ph.D. degrees at the University of Michigan, Ann Arbor, all in Chemistry. Dr. Neisser worked at IBM for 16 years, where he focused on packaging materials and semiconductor lithography research, followed by positions managing research and development of photoresists and of ancillary materials for lithography at Arch and at AZ Electronic Materials, respectively. He is the author of over three-dozen patents and 100 technical publications, and is the inventor of double exposure as a resolution enhancement for lithography. Dr. Neisser is the current chair of the International Roadmap for Devices and Systems (IRDS) Lithography Technical Working Group.

Gregg Gallatin received his Ph.D. in theoretical physics from Penn State in 1981 and worked in academia until 1984 when he went to industry. He has worked for Perkin-Elmer, SVG Lithography, Bell Labs, IBM Watson, and the Center for Nanoscale Science and Technology (CNST) at NIST in Gaithersburg, Maryland. Currently, he is consulting full time. The name of his consulting company is Applied Math Solutions, LLC. He has done modeling, simulation, and analysis covering a broad range of topics, including essentially everything from signal processing to quantum field theory, but with an emphasis on lithography for semiconductor manufacturing. At the CNST he worked on modeling, simulation, and analysis covering a range nanofabrication processes and nanometrology systems, including DNA origami, block copolymer self-assembly, roll-to-roll imprint, and the quantum mechanics of electron beams carrying axial orbital angular momentum.

Downloaded From: https://www.spiedigitallibrary.org/ebooks/ on 09 Mar 2022
Terms of Use: https://www.spiedigitallibrary.org/terms-of-use

Amrit Narasimhan is a materials engineer at GLOBALFOUNDRIES Inc., where he evaluates EUV photoresists for process research and development for insertion into high-volume manufacturing. He received B.S. degrees in Materials Science & Engineering, and in Physics, and a M.S. degree in materials science from Carnegie Mellon University. He received his Ph.D. degree in Nanoscale Engineering from the University at Albany, State University of New York.

Downloaded From: https://www.spiedigitallibrary.org/ebooks/ on 09 Mar 2022
Terms of Use: https://www.spiedigitallibrary.org/terms-of-use

Chapter 9
Fundamentals of EUVL Scanners

Jan B. P. van Schoot and Johannes (Hans) C. M. Jasper
ASML Netherlands B.V., Veldhoven, The Netherlands

9.1 Introduction
- 9.1.1 EUVL scanner outline
- 9.1.2 Business drivers

9.2 EUVL Projection Tool Overview: History and Future
- 9.2.1 Small-field tools
- 9.2.2 Full-field tools: past 0.25 NA
- 9.2.3 Full-field tools: current 0.33 NA
- 9.2.4 Full-field tools: future 0.55 NA
- 9.2.5 Solutions and throughput impact

9.3 EUVL Scanner Architecture
- 9.3.1 Introduction: architecture overview
- 9.3.2 The optical system
- 9.3.3 Mechatronic architecture
- 9.3.4 Wafer and mask stage
- 9.3.5 Optics and contamination control
- 9.3.6 Metrology
- 9.3.7 Material handling systems and clamps
- 9.3.8 EUV pellicles

9.4 Outlook
- 9.4.1 Future prospects

Acknowledgments
References

9.1 Introduction

9.1.1 EUVL scanner outline

The main task of a step-and-scan system is to transfer an image as present on a mask into a pattern on a wafer. The mask holds a magnified version (typical 4×) of the desired pattern.[1] Figure 9.1 illustrates the principle of such a system. A source generates EUV light. This light is radiated into a so-called

Downloaded From: https://www.spiedigitallibrary.org/ebooks/ on 09 Mar 2022
Terms of Use: https://www.spiedigitallibrary.org/terms-of-use

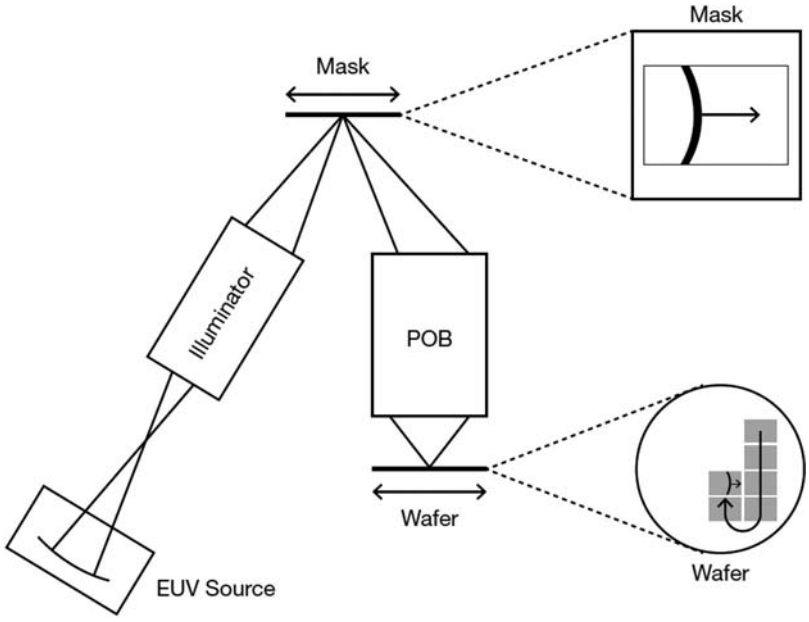

Figure 9.1 Principle of an EUV step-and-scan lithography system (source: ASML).

illuminator and reshaped to illuminate the pattern on the mask. Note that the illuminator is projected in a curved shape in order to match the shape of the entrance slit shape of the projection optics box (POB). The reason for this shape is explained in Chapter 5. The light reflected from the mask is collected by the POB, and a demagnified image is projected on the wafer. Note that current high-end commercial lithography tools scan the mask while the wafer moves synchronously with the mask. This way, relatively small projection optics can be used to expose a large area on the wafer.[2–5]

Because of the strong absorption of EUV light in air, the core parts of the system are enclosed in a vacuum* vessel. This puts several constraints on the system design. The component on the lower left in Fig. 9.1 is the 13.5nm EUV light source. More details on these topics will be given in section 5.3.

9.1.2 Business drivers

Figure 9.2 shows a typical layout of a part of an integrated circuit. In Fig. 9.3, one can see that such a device consists of several layers. There are layers with conducting lines and layers with plugs [so-called contact holes (CH)

*Note that the term vacuum can be misleading here. Although the used components are specified to maintain an ultrahigh vacuum, mainly for reasons of cleanliness, the vessel is actually filled with H_2 at a pressure of 0.03 mBar. More details can be found in Section 9.3.5.

Downloaded From: https://www.spiedigitallibrary.org/ebooks/ on 09 Mar 2022
Terms of Use: https://www.spiedigitallibrary.org/terms-of-use

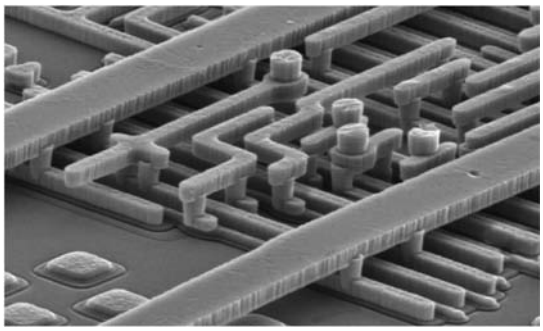

Figure 9.2 A 3D view of a part of an integrated circuit. The isolation material is etched away to get a clear view of the metal wires and the connecting contacts (courtesy of W. Kaiser and P. Kürz).

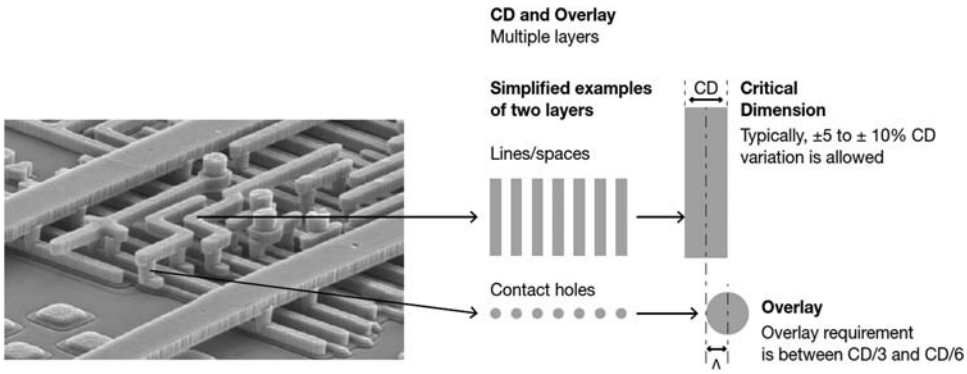

Figure 9.3 In a simplified way the properties of the several pattern layers can be expressed in terms of lines and contacts. To ensure proper electrical contact between a wire and a contact, the overlay error (typically referred to simply as overlay) should be small, typically on the order of 1/3 to 1/6 of the linewidth (CD) (courtesy of W. Kaiser and P. Kürz).

connecting the conducing lines vertically. Each layer is imaged in a separate exposure step on a lithography tool. From this picture it is clear that a step-and-scan system should fulfill the following main tasks:

- **Imaging:** Print any individual layer at a resolution supporting the design of the layer.
- **Overlay:** Put the next layer very accurately on top of the previous layer. In other words, the lines and the contacts in Fig. 9.3 should be well aligned over the entire chip area. An illustration of the tremendous challenge chipmakers are facing is shown in Fig. 9.4.

Apart from these two requirements, a third business driver is also important:

- **Productivity:** These layers have to be printed in an economical way, so the exposure tool must have a sufficiently large throughput.

Downloaded From: https://www.spiedigitallibrary.org/ebooks/ on 09 Mar 2022
Terms of Use: https://www.spiedigitallibrary.org/terms-of-use

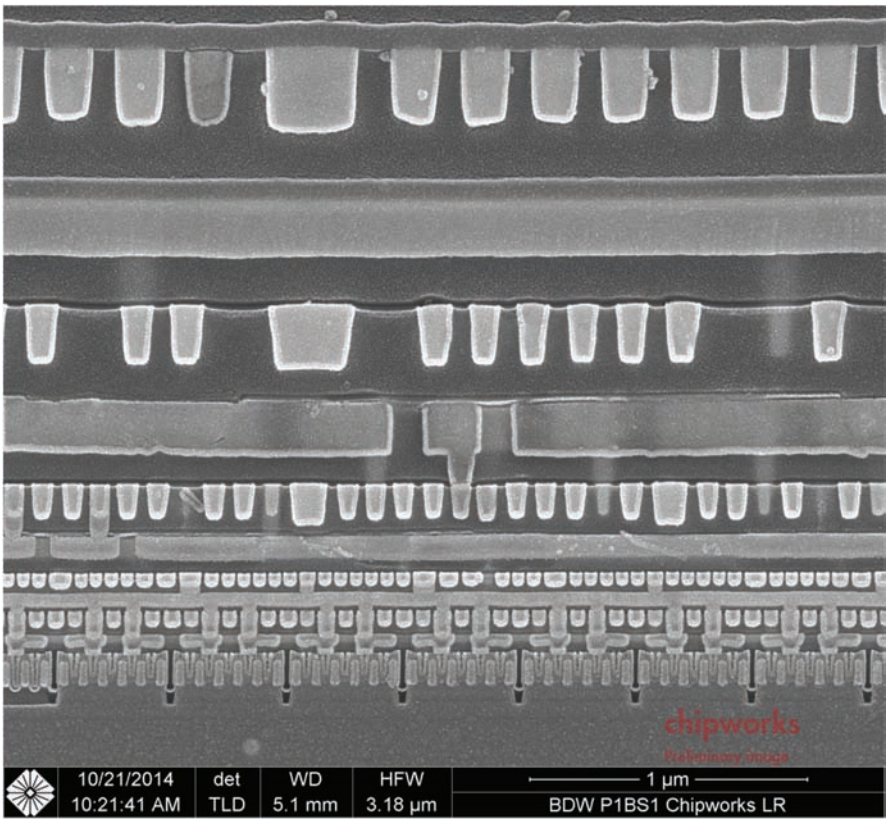

Figure 9.4 The importance of tight CD and overlay control becomes very clear in this cross section of a chip produced with a CMOS process with FINFETs as transistors, local interconnects on top of the transistors to create the basic logic components. There are 5 metal layers connected with 5 contact layers to make the connections between the basic components [courtesy of TechInsights (formerly Chipworks), Ottawa, Ontario, Canada, used with permission].

9.1.2.1 Imaging

Imaging is all about how well a template on the mask is reproduced as an image in the resist on the wafer. As an example, a standard 10-nm-node logic cell is studied, the results of which are given in Fig. 9.5.[6] The image was made with an ArF-immersion scanner;[1,3,5] three consecutive lithography steps were required to achieve the desired resolution of 44 nm. The right-hand image was obtained in a single exposure on an EUV scanner. The higher resolution is a clear advantage of the EUV exposure tool, as it prevents complex multiple exposures. Also, the pattern fidelity is much better, although this is difficult to express in a single number. Usually, some simplified metrics are used to express the imaging quality of an exposure system.

Downloaded From: https://www.spiedigitallibrary.org/ebooks/ on 09 Mar 2022
Terms of Use: https://www.spiedigitallibrary.org/terms-of-use

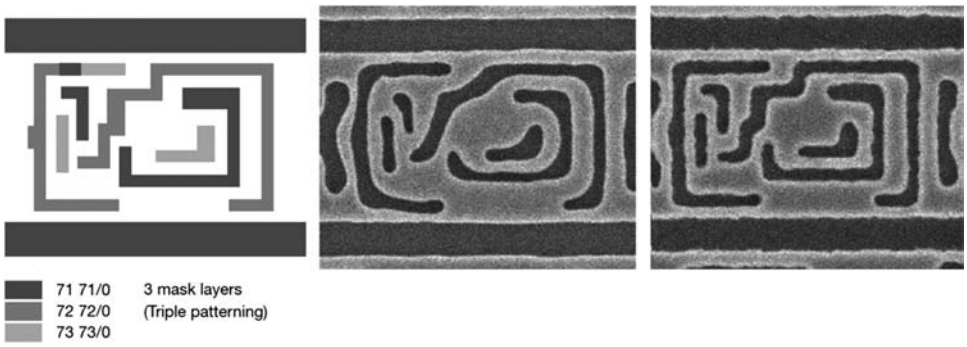

Figure 9.5 (left) The mask template and (right) two SEM images of 44-nm structures of a 10-nm-node standard logic cell exposed in different ways. The SEM image on the left was exposed using 193-nm immersion, triple exposure. An EUV singly exposed image is shown on the right. Note also that the EUV exposure results in a better defined image[6] (source: IMEC, Leuven, Belgium, used with permission).

An often-used metric is the width of a line or critical dimension (CD). The minimum CD of dense lines is given by the first Rayleigh equation:[1]

$$CD = k_1 \cdot \frac{\lambda}{NA}. \tag{9.1}$$

This equation was formulated by Lord Rayleigh in the 19th century. CD in this case represents the theoretical minimum half-pitch of a regular line-and-space pattern. In this formula, λ is the wavelength of the radiation used for the exposure, and NA is the numerical aperture of the projection optics system. The free parameter here is k_1. At a value of $k_1 > 0.25$, the diffracted light from the patterns at the mask are partly captured by the projection optics. If k_1 is below 0.25, none of the diffracted light is captured by the lens, so no imaging is possible. At the value of $k_1 = 0.25$, the projection lens very nearly captures first-order light, so this is the resolution limit of such a projection system. At larger values for k_1, the contrast of the aerial image generally increases, making it easier to reproduce an image in the photoresist. The practical limit for k_1 is around 0.3. See also Fig. 9.6 for an illustration of these situations. A frequently used way to express contrast is the normalized image log slope (NILS):

$$NILS = CD \cdot \frac{d \cdot \ln[I(x)]}{dx}, \tag{9.2}$$

where $I(x)$ is the intensity as a function of the location x. The NILS is a very useful metric for contrast since it is a contrast metric independent of the linewidth. For proper imaging, a certain NILS value is required. In EUV a

Downloaded From: https://www.spiedigitallibrary.org/ebooks/ on 09 Mar 2022
Terms of Use: https://www.spiedigitallibrary.org/terms-of-use

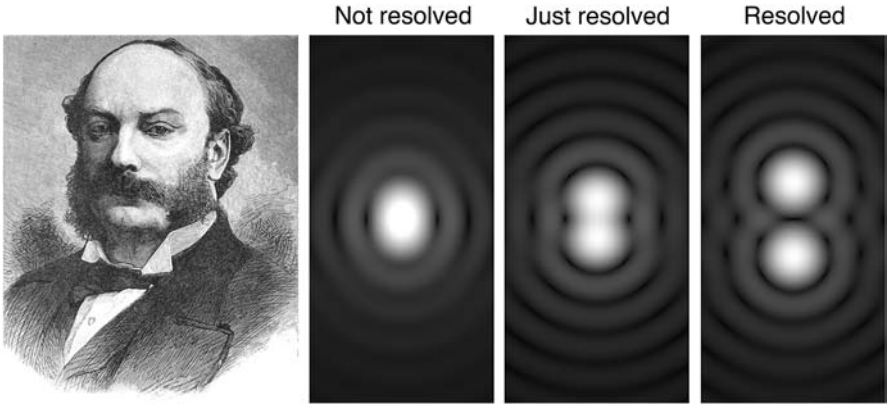

Figure 9.6 (left) John William Strutt or Lord Rayleigh†. (right) Three images of light spots demonstrating the concept of resolved patterns: $k_1 < 0.25$ not resolved, k_1 just above 0.25 will just resolve the spots, and k_1 significantly above 0.25 corresponds to clearly resolved patterns (source: Wikimedia commons, under public domain).

minimum value of 2 is usually taken as a boundary condition, although specific situations can require larger values.[7]

Good contrast leads to a well-defined aerial image—a fact that is also important in controlling the CD distribution over the field, wafer, and lot. High image contrast also reduces the so-called mask error factor, resulting in smaller CD errors on the wafer due to mask writing errors.[8] The CD distribution on the wafer is called CD uniformity (CDU).

The CDU consists of two parts: a so-called global (i.e., relatively slowly varying over the wafer area) part that is due to, e.g., focus and dose errors, and a local part, generally referred to as local CDU (LCDU). This is a consequence of the stochastic behavior of photons and will show a very localized behavior: each individual feature has its own size. On every location of the wafer, the number of photons that arrive is partially determined by this stochastic behavior. This stochastic, local dose will translate through the contrast into a local CD.[9–11] The number of photons determining the local CD at a certain exposure dose scales with the size of the feature to be printed and inversely to the energy per photon. With the introduction of EUV, the energy per photon increased from 6.42 eV (193 nm) to 91.84 eV. In other words, the number of photons at a given dose decreased by a factor of 14. Additionally, the features to be printed are also decreasing. As an example, consider a contact hole with a diameter of 10 nm to be printed with EUV at a

†In lithography, Eq. (9.1) is traditionally called the Rayleigh equation, after Lord Rayleigh. Others were also defining similar equations for the resolution limit at around the same time, including, e.g., Ernst Abbe. Sometimes these equations are attributed to Abbe in the literature.[90]

Downloaded From: https://www.spiedigitallibrary.org/ebooks/ on 09 Mar 2022
Terms of Use: https://www.spiedigitallibrary.org/terms-of-use

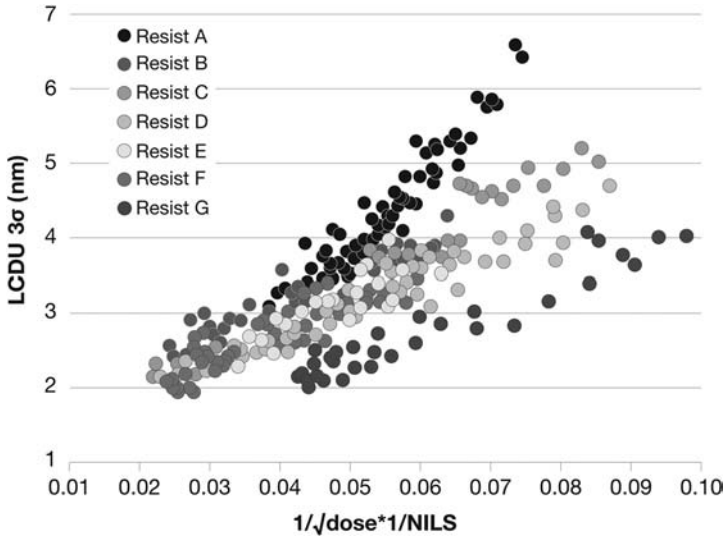

Figure 9.7 $LCDU \sim 1/\sqrt{dose}$*1/*NILS* for multiple resists.

dose of 20 mJ/cm^2. The number of photons passing through this area is ~1000. A reasonable assumption is that 30% of these photons will be absorbed in the photoresist. Finally, only half of the photons actually define the edge of the contact hole (the highest concentration of photons is in the center of the contact hole and well above the resist threshold, so they do not determine the edge). As a consequence, only ~150 photons, a rather small number, define the actual CD of a single contact hole.

From the above information, it follows that the LCDU is a function of image contrast and dose. Experiments on the NXE:3350B confirm that LCDU is lowered by the contrast of the patterning and is approximately linearly dependent on 1/*NILS*.[12] LCDU depends on the exposure dose as 1/sqrt(dose), representing the shot noise character of dose uncertainty in a certain feature size.[13] A combination of these to effects lead to

$$LCDU \sim \frac{1}{\sqrt{Dose}} \cdot \frac{1}{NILS}. \tag{9.3}$$

Figure 9.7 shows experimental results with 0.33 NA, confirming this relation for various EUV resists. In Section 9.2.4, the consequences of increasing the NA and its effect on dose and throughput will be further discussed.

9.1.2.2 Focus and dose control

For a given imaging system, the CD is, in general, very sensitive to how well-focused the printed image is, as well as the applied dose. A general way to represent this behavior is the so-called process window, two examples of which are given in Fig. 9.8.

Downloaded From: https://www.spiedigitallibrary.org/ebooks/ on 09 Mar 2022
Terms of Use: https://www.spiedigitallibrary.org/terms-of-use

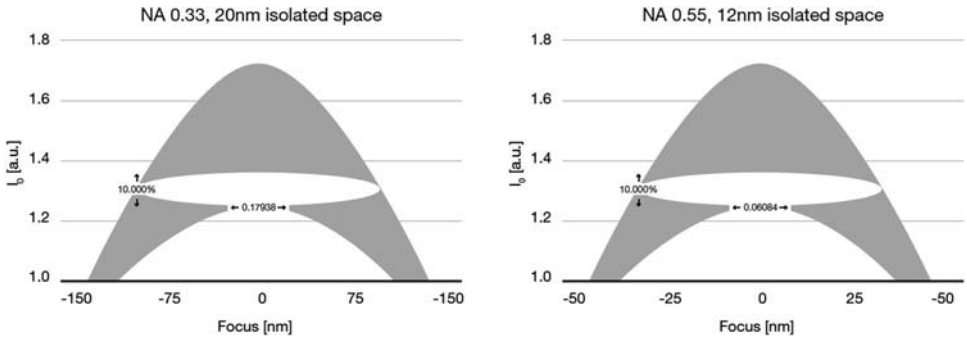

Figure 9.8 Simulations of the process windows of isolated spaces for $NA = 0.33$ and $NA = 0.55$. The target space size has been scaled with the NA (source: J. T. Neumann, Carl Zeiss SMT).

In its basic form, a process window consists of two curves, one determining at which focus and dose values the feature prints 10% too large, the other determining at which focus and dose values the feature prints 10% too small. Hence, the area between the two curves represents all focus and dose combinations at which the feature CD prints within ±10%. Usually, one fits an ellipse inside this area to represent the case where dose and focus are considered normally distributed. The acceptable focus range is usually called depth of focus (DOF) and is expressed in nanometers. The acceptable dose range is called exposure latitude and is expressed as a relative number. Note that many ellipses can be fitted; in Fig. 9.8, only one example is given in which the exposure latitude is kept at 10%. An ellipse with a larger exposure latitude would result in a smaller DOF.

In Fig. 9.8 the process window of two situations is given: a 20-nm isolated space printed with a 0.33-NA system, and a similar feature printed with a 0.55-NA system, where the feature size is scaled with the NA. Comparing the two figures shows that the required dose control is comparable for the two situations; the 0.55-NA case requires a much tighter focus control. From this example, it is clear that focus control is one of the main driving parameters in the design of a lithographic scanner system when the NA is increased.

A larger NA results in a smaller DOF according to the second Rayleigh equation:[1,7]

$$DOF = k_2 \cdot \frac{\lambda}{(NA)^2}, \tag{9.4}$$

where k_2 is usually taken to be 1. The evaluation of this equation is depicted in Fig. 9.9. Going from $NA = 0.33$ toward $NA = 0.55$ results in a reduction in DOF of approximately a factor of 3, as can be seen in Fig. 9.8. Therefore, additionally, the required focus control capability of an EUVL scanner will need to scale with this number. The next-generation EUVL scanner (the so-called high-NA scanner—see Section 9.2.4) will have a NA of 0.55. The targeted

Downloaded From: https://www.spiedigitallibrary.org/ebooks/ on 09 Mar 2022
Terms of Use: https://www.spiedigitallibrary.org/terms-of-use

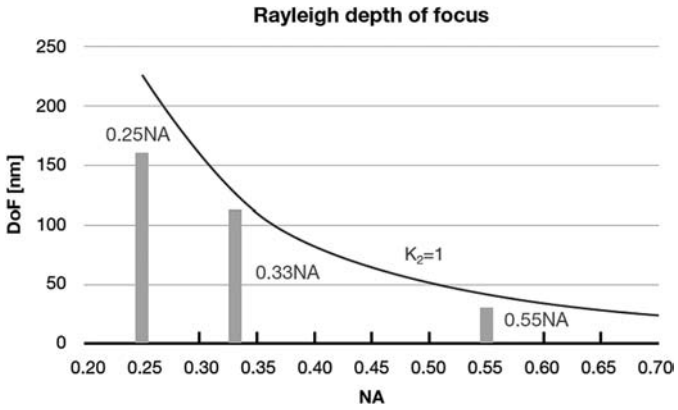

Figure 9.9 The evaluation of the Rayleigh equation for DOF. The bars represent the focus budget of the exposure tool at introduction (source: ASML).

focus control of this high-NA tool will be 30 nm. Note that the constant k_2 in Eq. (9.4) depends on many factors, such as the type of structure being used and the criterion used to judge whether a structure is in or out of specification. $k_2 = 1$ describes a focus-critical structure such as an isolated line, with a DOF criterion of CD ±10%. See, for example, Ref. 7 for more information on this topic.

Simulations have been carried out in which we compare two NAs (0.33 and 0.55) together with a series of spaces through pitch. The target space width has been scaled with the NA. As can be seen in Fig. 9.8, the process windows also scale by a factor of 3. It should also be noted that in this case the target focus control of 30 nm seems to be sufficient to achieve the overlapping DOF of ∼50 nm.

Figure 9.10 shows how to achieve the required focus control. Apart from improvements in the scanner (better leveling performance) and optics

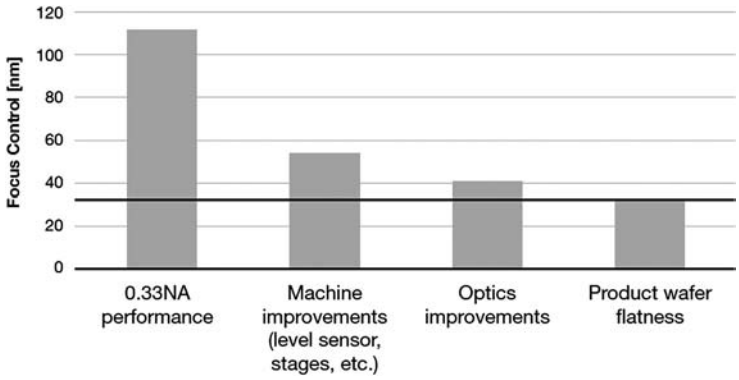

Figure 9.10 Overview of measures to be taken to achieve 30-nm focus control (source: ASML).

Downloaded From: https://www.spiedigitallibrary.org/ebooks/ on 09 Mar 2022
Terms of Use: https://www.spiedigitallibrary.org/terms-of-use

(focal plane deviation), product wafers are expected to follow the wafer flatness requirements over time, as described in the ITRS.[14]

9.1.2.3 Overlay

How well the individual layers in a chip line up with each other is called overlay. The overlay metric that is most relevant for the lithography process is called on-product overlay (OPO). OPO expresses the overlay error as measured on product wafers with customer structures in resist and hence also includes—in addition to lithography terms—process effects.

Many disturbance sources can lead to overlay errors in the lithography process. These errors can be classified into four categories related to the nature of the errors. The first three types of errors have their origin in the exposure tools, and the fourth type has error sources outside the tool.

1. Dedicated chuck overlay errors. These are the errors that show when two layers are exposed using the same scanner and chuck, the same mask, and the same exposure settings. This category expresses the basic reproducibility of the exposure tool. Examples of error sources are system dynamics, servo performance, and position measurement noise.

2. Matched machine overlay errors. These are the errors that show when exposing two identical layers (same mask and exposure settings) on different exposure tools. This category expresses how well different tools resemble each other. Examples of error sources are lens distortion variation and system calibration accuracy.

3. Application-specific overlay errors. These errors show when exposing two layers on the same exposure tool, but using different exposure settings and different masks for each layer. This category expresses how well the exposure tool performs in multiple operation points. Although the errors are related to the application of the tool, they have their origin inside the tool. Examples are lens aberration, and mask and wafer heating effects.

4. Overlay errors related to the customer process. These errors have their source outside the exposure tool. They are the result of imperfections in the advanced process control (APC) loops that run between exposure tools and metrology tools. These control loops are used to correct for process-induced overlay errors, e.g., inplane wafer deformations. This also shows the robustness of the system for a large variation in process parameters. Examples are inplane wafer deformation, mask write errors, alignment mark deformation, and metrology tool measurement noise.

Each of the error sources are stochastic in nature and are mutually uncorrelated. Adding all stochastic errors will result in a Gaussian-distributed average of the overlay error over many wafers exposed on a large population of machines and applications. The OPO number is three times the standard

Downloaded From: https://www.spiedigitallibrary.org/ebooks/ on 09 Mar 2022
Terms of Use: https://www.spiedigitallibrary.org/terms-of-use

deviation of the distribution. In order to determine the total OPO, the quadratic Gaussian sum is taken of each of the overlay contributors. Note that most of the errors occur twice when exposing two layers. Consequently, they appear twice in the quadratic Gaussian sum. It is common practice for a well-balanced design (cost, effort, and complexity) to have an equal contribution from each of the four categories to the OPO. Example OPO budgets for several exposure tool generations are given in Table 9.1.

During machine qualification the overlay performance is measured. This is done by exposing two consecutive exposures of the same layer on 12 wafers. Each layer holds a large number of alignment marks. The offset between two corresponding alignment marks in the two layers determines the overlay. Typical results for a dedicated-chuck overlay and a machine-to-machine overlay measurement are depicted in Fig. 9.11.

Table 9.1 Overview of a typical OPO budget. The total OPO value is the quadratic sum of the 4 individual error contributions.

Top-level specifications [nm]		**0.25 NA**	**0.33 NA**	**0.55 NA**
Inside scanner	Dedicated-chuck overlay (DCO)	4	1.5	0.5
	Machine-to-machine overlay (MMO)	6	2	0.5
	Application-specific overlay	4	2.5	0.5
Outside scanner	Metrology errors, mask writing errors, etc.	4	2	0.5
Total OPO target		**9**	**4**	**1**

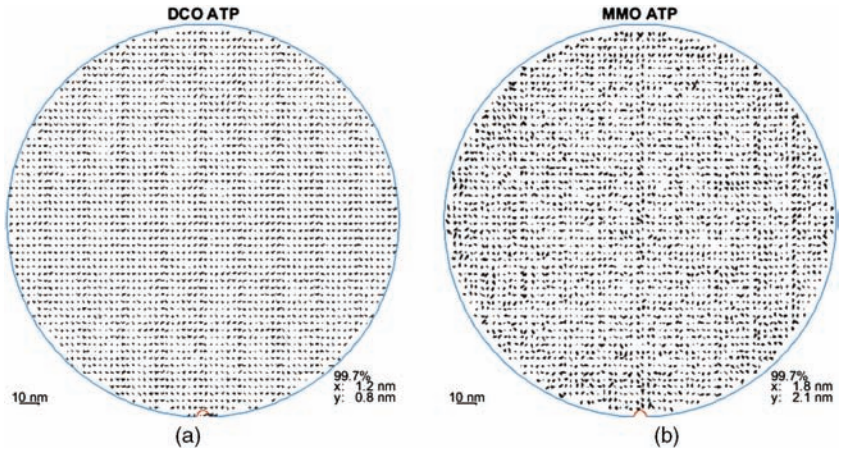

Figure 9.11 Typical overlay test result of a 0.33-NA machine:[15] (a) dedicated-chuck overlay and (b) machine-to-machine overlay (ATP – acceptance testing procedure) (source: ASML).

Downloaded From: https://www.spiedigitallibrary.org/ebooks/ on 09 Mar 2022
Terms of Use: https://www.spiedigitallibrary.org/terms-of-use

9.1.2.4 Edge placement errors

The edge placement error (EPE) is a metric combining all overlay and CD errors. The maximum EPE is a sum of systematic errors (OPC, tool-to-tool), local stochastic errors, and global errors; these errors together with the resolution of the exposure determine the pattern density that can be printed. This approach is frequently followed, especially in logic applications.[16–18] The EPE requirements drive the overlay, CDU, and LCDU and/or linewidth roughness (LWR) needed. While overlay and CDU are mostly independent of dose, the achievable LCDU is mainly driven by photon shot noise and thus strongly dependends on the absolute dose, as already described in subsection 9.1.2.1.[11,19] Assuming that systematic and global contributions are known and dose independent, LCDU determines the achievable EPE at a given dose, or *vice versa*.

In the example in Fig. 9.12, the critical layer is made in three steps: first, a mandrel layer is deposited and developed. Then, with a so-called spacer technique, the spatial frequency of this pattern is doubled (sidewall-assisted double patterning).[20–24] In a third step, the lines are cut into pieces with a so-called cut mask. The end result is a layer with unidirectional line pieces. In order to print such a layer without errors, the cuts should completely cut the lines and not leave a part of the line behind. Whether this is the case is determined by the linewidth of the spacer, the dimension of the cut, and the relative positioning of the two features. Note that the dimension of the features is determined by the global CDU as well as the local CDU.

The total EPE is given in Eq. (9.5), which, together with the resolution of the exposure, determines the pattern density that can be printed:

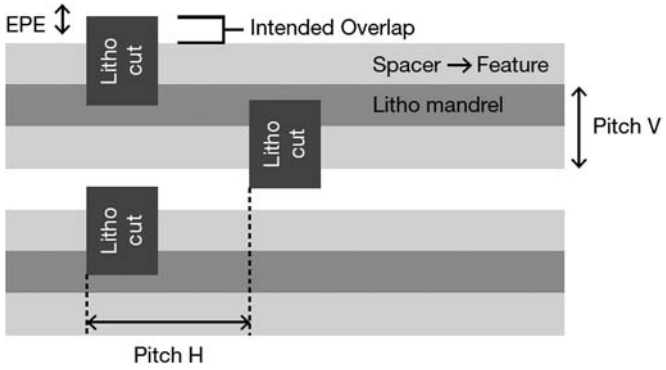

Figure 9.12 EPE defined as tolerance of the relative placement of two edges (litho cut and spacer feature) (source: ASML).

Downloaded From: https://www.spiedigitallibrary.org/ebooks/ on 09 Mar 2022
Terms of Use: https://www.spiedigitallibrary.org/terms-of-use

$$\boldsymbol{EPE_{max} = systematics + local + global},$$

$$EPE_{max} = \frac{HR_{OPC}}{2} + \frac{3\sigma_{PBA}}{2} + \frac{6\sigma_{LWR}}{\sqrt{2}} + \sqrt{(3\sigma_{OVL})^2 + \left(\frac{3\sigma_{CDU}}{2}\right)^2},$$

$$\text{where} \quad \sigma_{LWR} = \sqrt{\sigma^2_{LWR_line} + \sigma^2_{LCDU_cuts}},$$

$$\text{and} \quad \sigma_{CDU} = \sqrt{\sigma^2_{CDU_lines} + \sigma^2_{CDU_cuts}}. \tag{9.5}$$

9.2 EUVL Projection Tool Overview: History and Future

The history of EUVL dates back to 1986 with the first exposures on a small-field tool with a NA of 0.10 and a field size below 1 mm. Since then, many generations of research and production tools have been built, of which the most advanced realized tool has a NA of 0.33 and a field size of 26 mm × 33 mm—the standard size of current lithographic exposure equipment.

9.2.1 Small-field tools

The first application of soft-x-ray radiation in lithography was through proximity printing.[25] To overcome problems associated with the 1× mask, and to position soft-x-ray radiation as the successor of the DUV technology, a reduction printer was pursued. This was first demonstrated in 1986 by Hiroo Kinoshita and coworkers (Fig. 9.13). Since then, many small-field tools have been developed in order to demonstrate the potential of this technology and to develop the key components needed to make it a commercial success: very smooth mirrors, multilayer coatings, masks, a source, a resist, etc. In 1986, the wavelength was still a variable; the combination of Sn as a source material and MoSi as a multilayer eventually led researchers toward the 13.5-nm wavelength, which is used in current EUVL.

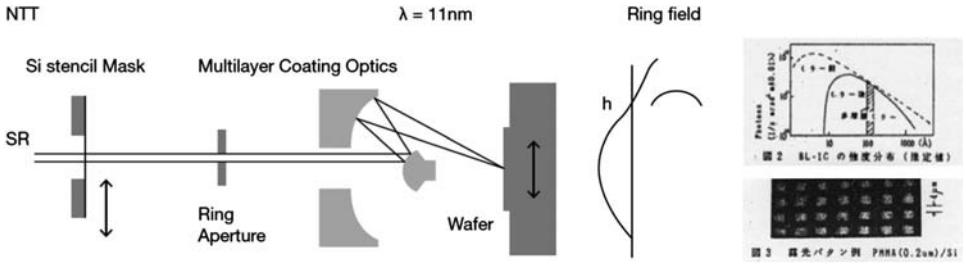

Figure 9.13 Sketch of the first EUV projection system build by H. Kinoshita.[1] Note that the wavelength was not fixed at that time, several experiments were performed at wavelengths between 4.5 and 17nm, which was later changed to 13.5nm due to multi-layer and source considerations[26] (reprinted from Ref. 26 with permission from the American Vacuum Society).

Downloaded From: https://www.spiedigitallibrary.org/ebooks/ on 09 Mar 2022
Terms of Use: https://www.spiedigitallibrary.org/terms-of-use

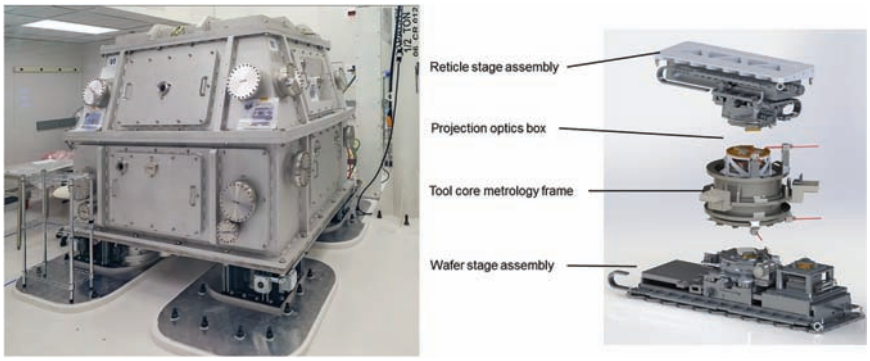

Figure 9.14 Small-field exposure tool MET5 by LBNL and EIDEC. $NA = 0.5$.[36] The illuminator is not installed yet, and the POB is ready for installation. The system is expected to be operational at the end of 2017 (right image courtesy of P. Naulleau).

All small-field tools have a similar projection optics layout consisting of two mirrors, as shown in Table 9.2. The illuminators of these systems came in various implementations. The modern small-field systems have a scanning illuminator: a narrow beam of EUV light is projected on a set of scanning mirrors in order to make a 2D scan of the pupil. With this shaped pupil, the light is then projected onto the mask. By modulating the intensity of the incoming beam, it is possible to create a variety of pupil shapes, making these small-field tools very powerful in predicting the imaging behavior of the full-field tools that also have extended capabilities to shape the pupil to optimize the imaging. In order to prepare for imaging with an even higher NA, a 0.5-NA MET optics has been developed. The system is installed at EIDEC and is under installation at LBNL, as shown in Fig. 9.14.[36,37]

9.2.2 Full-field tools: past 0.25 NA

The first full-field EUVL system was introduced in 2006 and had a NA of 0.25.[38] It was the so-called Alpha Demo Tool (ADT) (Fig. 9.15). The

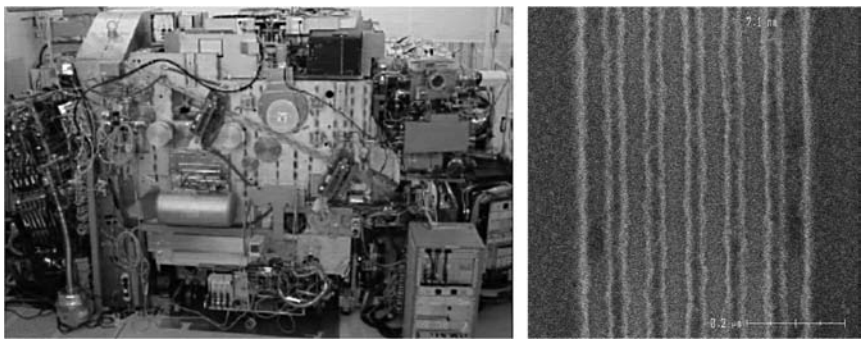

Figure 9.15 2006: Full-field exposure tool ADT by ASML. The SEM image shows 32-nm dense lines, $NA = 0.25$[38,44] (source: ASML).

Downloaded From: https://www.spiedigitallibrary.org/ebooks/ on 09 Mar 2022
Terms of Use: https://www.spiedigitallibrary.org/terms-of-use

Downloaded From: https://www.spiedigitallibrary.org/ebooks/ on 09 Mar 2022
Terms of Use: https://www.spiedigitallibrary.org/terms-of-use

Table 9.2 Overview of small-field tools.

Tool	**Ref. 26**	**SFET[27,28]**	**SFET[29,30]**	**SFET[31]**	**HiNA[97,98]**	**MET3[32]**	**SFET[33,34]**	**HSFET[35]**	**MET5[36]**
Group	**NTT**	**FOM**	**Bell Labs**	**Sandia (SNL)**	**Nikon**	**LBNL**	**SELETE**	**EIDEC**	**LBNL**
First exposure	**1985**	**1992**	**1990**	**1994**	**2001**	**2003**	**2006**	**2016**	**2018 (planned)**
wavelength	**11 nm**	**10.5 nm**	**36/13.9 nm**	**13.5 nm**	**13.5 nm**	**13.5 nm**	**13.5 nm**	**13.5 nm**	**13.5 nm**
POB									
NA	0.10	0.15	0.08	0.10	0.3	0.3	0.3	0.51	$0.03 \times 0.15\,mm^2$
Field size		4 mm Ø	0.5 mm	$0.5 \times 0.5\,mm^2$	$0.3 \times 0.5\,mm^2$	$0.2 \times 0.6\,mm^2$	$0.2 \times 0.6\,mm^2$	$0.03 \times 0.2\,mm^2$	8 nm
Resolution	4 μm	80 nm	100 nm	100 nm	30 nm	13 nm		14 nm	
Demag	8×	10×	20×	10×	5×	5×	5×	5×	5×
Illuminator									
Type	Condenser	Condenser	Collimated beam	Condenser	Switchable fly's eye	Scanning	Koehler		Scanning
Sigma				0.5	0.8	0.0–1.0/flex	0.7/0.3	1.0/6 apertures	0.01–1.0/flex
Source									
Type	Synchrotron	LPP	Synchrotron	LPP/Sn tape	Synchrotron	Synchrotron	DPP/LPP	Xe-DPP	Synchrotron

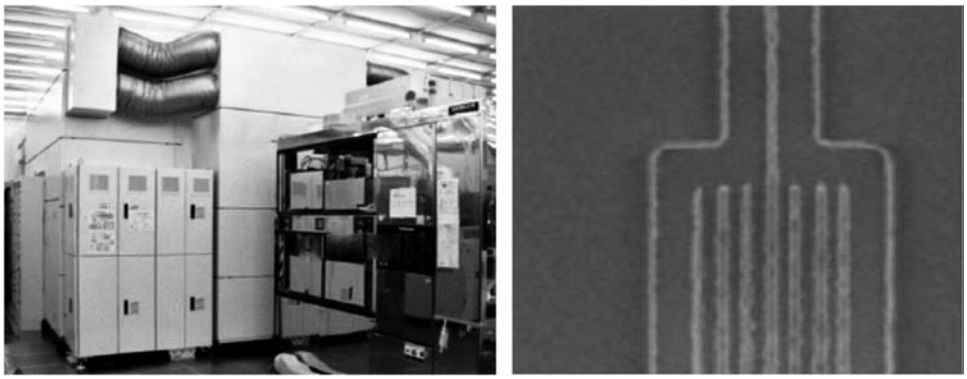

Figure 9.16 2009: Full-field exposure tool EUV1 by SELETE. The SEM image shows 30-nm dense and isolated lines. $NA = 0.25$[39] (source: SELETE).

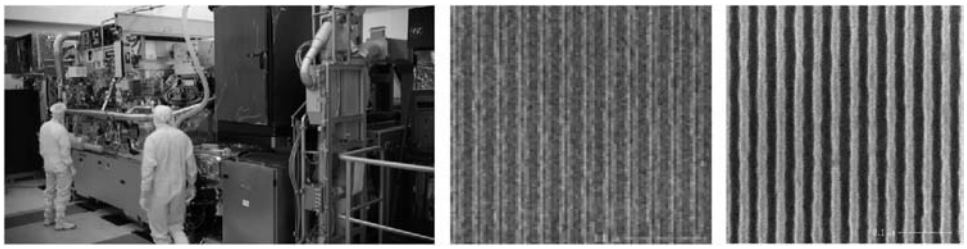

Figure 9.17 2010: Full-field exposure tool NXE:3100 by ASML. $NA = 0.25$.[40] The SEM images show from left to right 27 nm L/S at 11 mJ/cm^2 and 16 nm L/S at 33 mJ/cm^2 (source: ASML).

two realized systems were installed at the research institutes IMEC and SEMATECH and used for early process and resist development. The system supported the 32-nm node. One year later, Nikon introduced their EUV1 exposure tool.[39] This system was installed at SELETE (Fig. 9.16).

In 2010 ASML introduced the NXE:3100 (Fig. 9.17),[40] a twin stage system with a NA of 0.25 targeted for early production. In total, six of these systems were built. The next generation was targeted for the 16-nm node and has a NA of 0.33. With advanced off-axis illumination, the resolutions of these systems can be extended down to 13 nm. Going farther in resolution requires a larger NA. Figure 9.18 shows possible POB designs for the different NAs. Table 9.3 provides an overview of the early full-field tools.

Table 9.3 Overview of the early full-field tools.

Tool	ETS[41–43]	ASML ADT	Nikon	ASML NXE:3100
NA	0.1	0.25	0.25	0.25
Sigma	0.7	0.5	0.8	0.8
Field size	24×32	26×33	26×33	26×33
Resolution	70 nm	32 nm	30 nm	22 nm

Downloaded From: https://www.spiedigitallibrary.org/ebooks/ on 09 Mar 2022
Terms of Use: https://www.spiedigitallibrary.org/terms-of-use

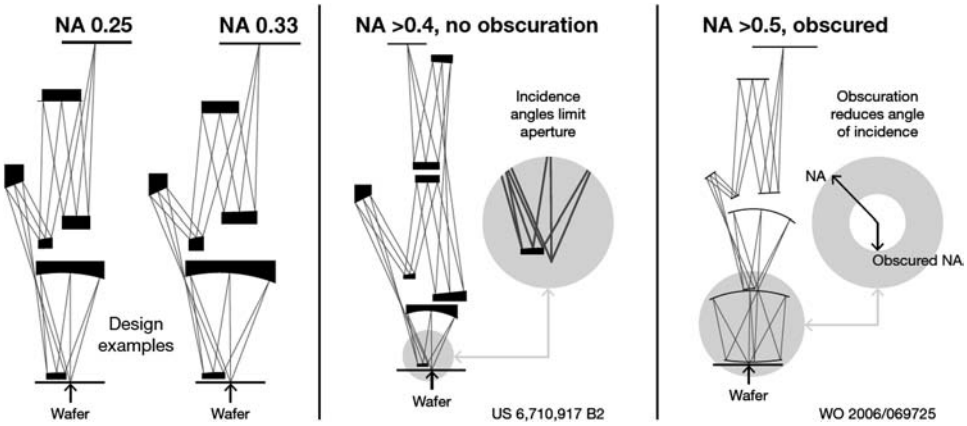

Figure 9.18 Possible POB designs for different NAs (source: ASML).

9.2.3 Full-field tools: current 0.33 NA

The current-generation EUV tools (Table 9.4) are intended for use in mass production. With a NA of 0.33, they are capable of printing lines and spaces down to 13 nm (Fig. 9.19). The most recent system, the NXE:3400B (Fig. 9.20), has an improved, loss-free highly flexible illuminator. More details are given in Section 9.3.2.2.

Table 9.4 Overview of the current full-field production tools. The pupil fill ratio (PFR) describes the minimum relative area of the pupil that can be used without light loss.

Tool	ASML NXE:3300B	ASML NXE:3350B	ASML NXE:3400B
NA	0.33	0.33	0.33
Sigma	0.2–0.9/flexible	0.2–0.9/flexible	0.06–1/highly flexible
PFR	40%	40%	20%
Field size	26×33 mm^2	26×33 mm^2	26×33 mm^2
Resolution	18 nm	16 nm	13 nm
Throughput		125 wph	145 wph

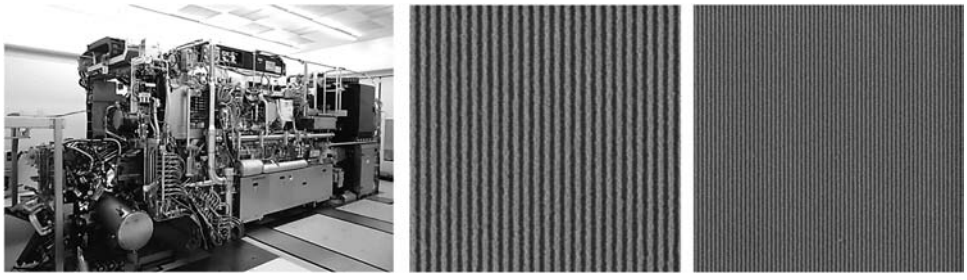

Figure 9.19 2013: Full-field exposure tool NXE:3350B by ASML. $NA = 0.33$.[45] The exposures are carried out with a nanoparticle resist.[46] The SEM images show from left to right 16 nm L/S at 18.5 mJ/cm^2 and 13 nm L/S at 31 mJ/cm^2 (source ASML).

Downloaded From: https://www.spiedigitallibrary.org/ebooks/ on 09 Mar 2022
Terms of Use: https://www.spiedigitallibrary.org/terms-of-use

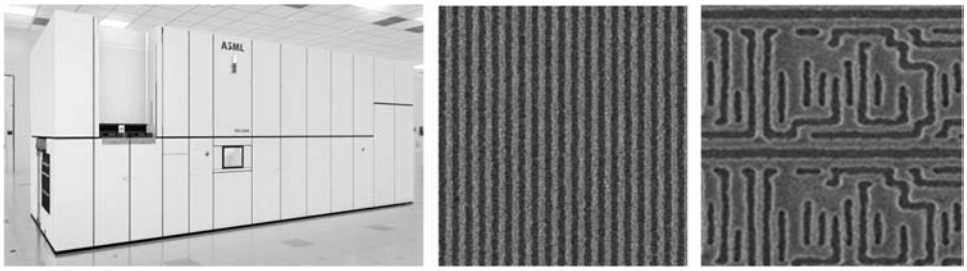

Figure 9.20 2017: Full-field exposure tool NXE:3400B by ASML.[45] $NA = 0.33$. The illuminator has a smaller pupil fill ratio (PFR) to increase aerial image contrast (see Section 9.3.2.2). The exposures are carried out with a nanoparticle resist[46] (source ASML).

9.2.4 Full-field tools: future 0.55 NA

To further improve the resolution, the NA of future-generation EUV tools (Table 9.5) will be 0.55.[47–51] This allows for a resolution of 8-nm lines and spaces. A further increase in the NA would result in large mask shadowing effects. In order to circumvent this, the printable field size can be reduced to 26 mm $\times$16.5 mm. The reason for this will be explained below.

For any projection system with a given NA at the image plane (wafer), there is also a NA at the object plane (mask), where the relation between these two NAs is given as

$$NA_{mask} = \frac{NA_{wafer}}{MAG}, \tag{9.6}$$

where MAG is the demagnification of the projection system. In all modern lithography scanners, $MAG = 4\times$, meaning that the image is a $4\times$ reduced copy of the image at the mask. Figure 9.21 a schematic overview of such a system.

In order to increase the NA, the NA at the mask will need to increase, absent a change in magnification. Given the so-called chief ray angle at object (CRAO) of 6 deg, the incoming and outgoing cones of light will overlap if the

Table 9.5 The projected high-NA half-field production.

Tool	ASML High-NA
NA	0.55
Sigma	~0–1/highly flexible
Field size	26×16.5 mm^2
Resolution	8 nm
Throughput	185 wph

Downloaded From: https://www.spiedigitallibrary.org/ebooks/ on 09 Mar 2022
Terms of Use: https://www.spiedigitallibrary.org/terms-of-use

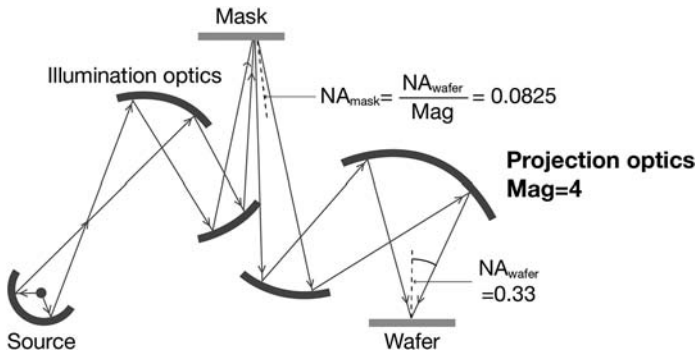

Figure 9.21 Schematic overview of the optical column of an EUV lithography scanner system. Note that the NA of the light cone at the mask equals the NA at the mask divided by the (de)magnification of the system, typically 4. In this example, the highest NA available for an HVM system is used[45] (source: ASML).

NA at the wafer is increased to values above ~0.4 NA. This volume conflict can be solved by increasing the CRAO as indicated in Fig. 9.22.

A consequence of the increased angles on the mask is the variation of the multilayer reflectivity of the mask and a larger mask 3D effect,[52–55] sometimes referred to as 'shadowing.' An intuitive illustration is shown in Fig. 9.23. The consequence of the increased mask 3D effect is a reduced contrast, an increased telecentricity error, and a lower reflection of the light at the mask. Apart from adding significant complexity to the mask by burying the absorber in the multilayer,[56,57] one way to mitigate these effects is to reduce the angles at the mask by increasing the magnification of the projection optics.

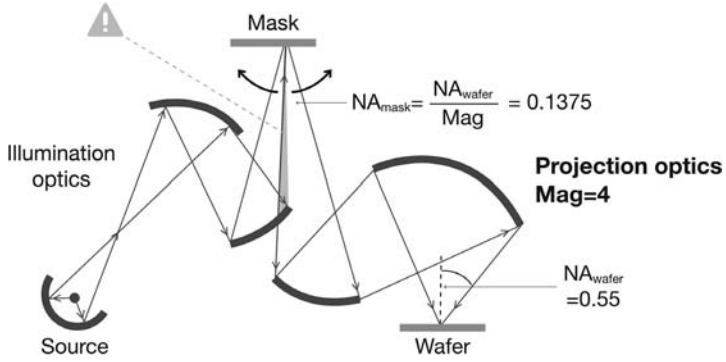

Figure 9.22 Increasing the system NA also increases the NA at the mask for a fixed magnification. If the light arrives at the mask at a shallower angle, the incoming and outgoing beams at the mask can be separated more easily (source: ASML).

Downloaded From: https://www.spiedigitallibrary.org/ebooks/ on 09 Mar 2022
Terms of Use: https://www.spiedigitallibrary.org/terms-of-use

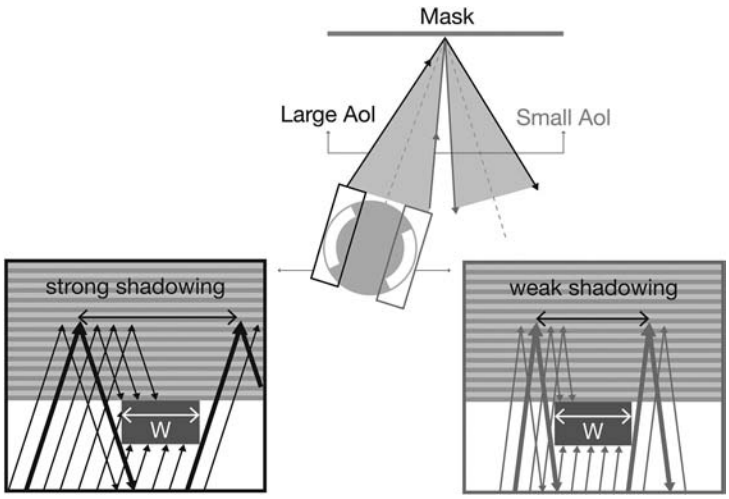

Figure 9.23 Increasing the system NA also increases the NA at the mask and thus the angles at the mask. Increased angles lead to more rays of light being absorbed due to shadowing. This negatively influences contrast, telecentricity, and the required source power (AoI – angle of incidence) (source: ASML).

One approach, therefore, is to change the magnification of the projection optics. The left graph of Fig. 9.24 shows that the contrast (NILS) is increased by increasing the magnification; together with this, the CRAO is decreased. For a sufficient contrast ($NILS > 2$), a magnification above $\sim 7\times$ is sufficient.

The right graph of Fig. 9.24 shows that increasing angles in the x direction also reduces the contrast—however, to a much smaller extent. Also, increasing the magnification does not significantly increase the contrast for vertical lines

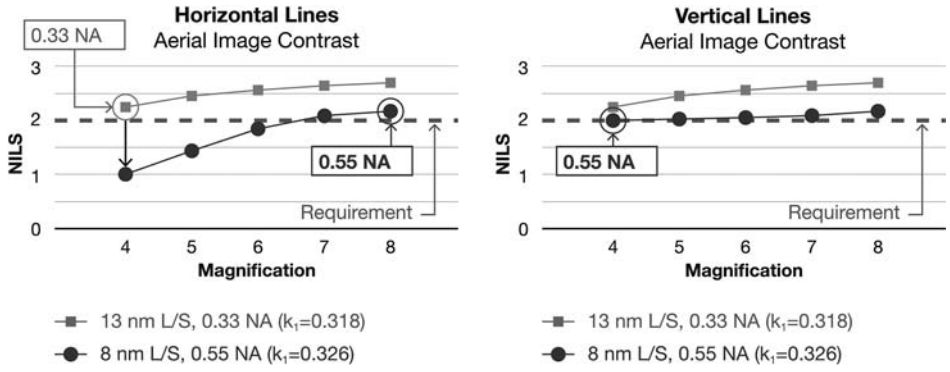

Figure 9.24 Aerial image contrast for horizontal and vertical lines. The k_1 for the 0.33-NA tool and the high-NA tool are equal; the difference at the $4\times$ magnification of the horizontal lines is mainly caused by shadowing. Because the nonzero CRAO is only needed in one direction, the angles at the mask are significantly smaller in the other direction. As a result, the increased magnification has an almost negligible impact on the vertical lines (source: ASML).

Downloaded From: https://www.spiedigitallibrary.org/ebooks/ on 09 Mar 2022
Terms of Use: https://www.spiedigitallibrary.org/terms-of-use

because the angles on the mask are much smaller for the vertical lines. The reason for this is the absence of the CRAO in the direction perpendicular to the plane depicted in Fig. 9.22.

Looking at the reflection as just a function of the angle at the mask gives us the same conclusion, as seen in Fig. 9.25. Only in the *y* direction is the angular range of high reflection of the multilayer exceeded. Therefore, increasing the magnification in only the *y* direction is enough to restore the beneficial reflection capabilities. Using different magnifications for two orthogonal directions is called anamorphic imaging.

Following this approach, the magnification of the projection lens for horizontal lines should be around 8, where the magnification in the other direction can be chosen arbitrarily between 4 and 8. Based on this insight, two concepts are studied further: an isomorphic 8× magnification system and an anamorphic 4×/8× system.

In the case of the isomorphic 8× system, and given the same 6-inch mask size as today, the resulting field on the wafer is a quarter-field, as shown in Fig. 9.26(b). In Fig. 9.27(a), the system throughput is given as a function of source power/exposure dose. This figure shows that the throughput of this 8× system (labeled high-NA QF) is limited to around 110 wph, even after significantly increasing the stage accelerations, and regardless of what source power is available. The reason for this is that the turnaround time of the stages dominates the actual scan time. The total turnaround time is the time needed to accelerate and de-accelerate the stages × the number of fields on the wafer. Compared to the full-field situation, there are 4× more fields. Due to the smaller slit width (13 mm versus 26 mm), the light is concentrated on a smaller area, so the wafer has to move at double the speed to expose the same dose at

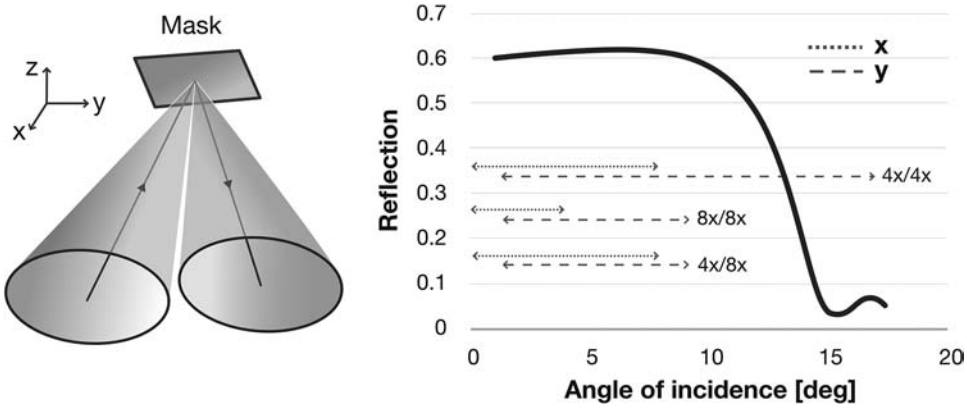

Figure 9.25 The angular range present on the mask for *x* and *y* as indicated by the arrows. It is clear that 4× isomorphic exceeds the potential of the multilayer in the *y* direction. This is solved by going to 8× isomorphic; however, in the 4×/8× anamorphic case the angular range is also within the capabilities of the multilayer (source: ASML).

Downloaded From: https://www.spiedigitallibrary.org/ebooks/ on 09 Mar 2022
Terms of Use: https://www.spiedigitallibrary.org/terms-of-use

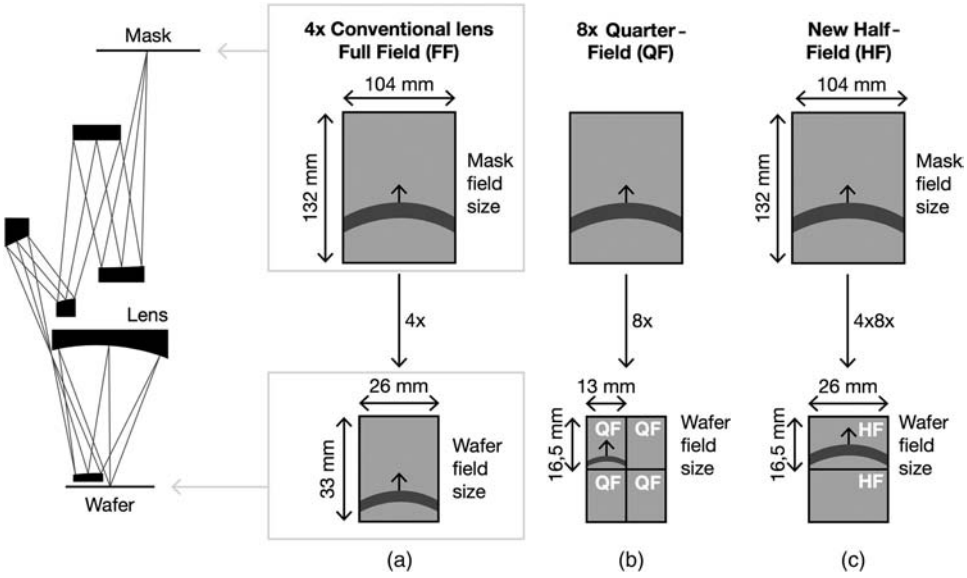

Figure 9.26 Field dimension at the mask and wafer. (a) Today's isomorphic 4× mag. (b) 8× isomorphic. (c) 4×/8× anamorphic (source: ASML).

the wafer. The mask has to move at 4× the original speed: 2× because of the faster wafer, and 2× because of the 8× magnification. Therefore, in total, the overhead time is 16× more than in the full-field situation.

In the case of the anamorphic 4×/8× system, the resulting field on the wafer is a half-field, as shown in Fig. 9.26(c). Note that in this case the slit width equals that in the full-field case: 26 mm. As a result, the wafer stage does move at the same speed as in the full-field situation to deliver the same dose at the wafer. Furthermore, only twice as many fields need to be exposed, so the overhead time at the wafer is now 2× as large as in the full-field situation; this is 4× for the mask because of the double magnification in the y direction. By adjusting the accelerations of the wafer stage by 2 and of the mask stage by 4, the increase in overhead time can be compensated, as shown in Fig. 9.27(a).

Figure 9.27(b) shows what happens if the transmission of the optical column is approximately doubled. It can be seen that the throughput of this system now saturates at ∼180 wph for a power/dose around 20 W/(mJ/cm^2). And a still very workable throughput of 125 wph is reached at a power/dose of 8.3. In other words, with a dose of 60 mJ/cm^2, a source power of ∼500 W is needed. Reference 50 shows how to achieve the double transmission of the optical column. Throughput values well above 100 wph are generally accepted values to be used in HVM.

It is becoming clear that mask 3D effects are increasingly impacting the imaging performance of EUV tools.[12,58,91,92] Figure 9.28 provides a closer

Downloaded From: https://www.spiedigitallibrary.org/ebooks/ on 09 Mar 2022
Terms of Use: https://www.spiedigitallibrary.org/terms-of-use

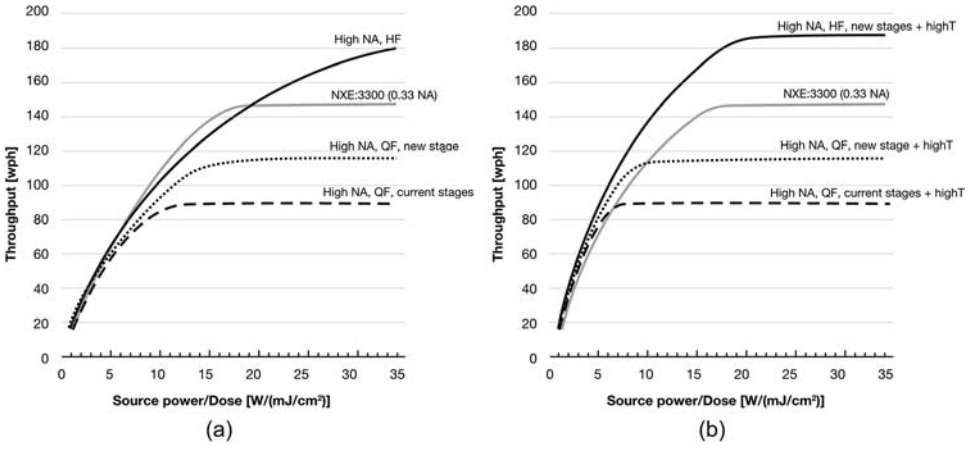

Figure 9.27 Throughput for the studied systems as compared to the NXE:3300B. (a) The throughput for an optical column transmission equal to today's NXE:3300B. (b) The same graph but with an increased transmission. The horizontal axis (Source Power/Dose) is used to enable handling a large range of dose and power values. 250 W source power and 20 mJ/cm^2 is equivalent to, e.g., 500 W and 40 mJ/cm^2; the stages will run at the same speed.‡ New stages have double the acceleration for the wafer stage, and quadruple for the mask stage (source ASML).

look at this effect. In fact, the reflection is a rather complex phenomenon that can be described by solving the electromagnetic field equations. In a rather simplified way, this can be described by three simultaneous effects: a reflection from the MoSi multilayer, a geometric shadowing effect, and a phase effect. The shadowing effect is depicted in Fig. 9.28(a). Light is lost due to the geometrical shadowing. Relatively more light will be lost by increasing the angle α or by decreasing the pitch at the mask. The amount of light lost is depicted in Fig. 9.28(b). As can be seen in the left part of Fig. 9.25, different parts of the pupil will reflect at different angles at the mask and therefore will reflect with different efficiencies. This imbalance causes a focus shift of the aerial images of the two individual trenches of a two-bar trench structure, as depicted in the upper graph of Fig. 9.29. This figure compares the mask 3D effects of the 0.33-NA and 0.55-NA systems when printing horizontal lines.[59] Due to the smaller angles that occur at the mask of the anamorphic high-NA system, the effect is significantly smaller in the larger-NA situation. The situation is different for vertical lines; however, the maximum angle at the mask as observed by the vertical lines is still smaller than as observed by the horizontal lines (see Fig. 9.25).

‡Note that all of the lines in this figure consists of three regimes: (1) At the left, a more or less linear regime. Due to a low source power of a high requested dose, the stages run at a low speed. The scan time dominates the throughput, and the impact of the turnaround time or overhead is small. (2) At the right, the stages limit the throughput. More source power of a requested lower dose will no longer increase the throughput. (3) A transition region between these two extreme regimes.

Downloaded From: https://www.spiedigitallibrary.org/ebooks/ on 09 Mar 2022
Terms of Use: https://www.spiedigitallibrary.org/terms-of-use

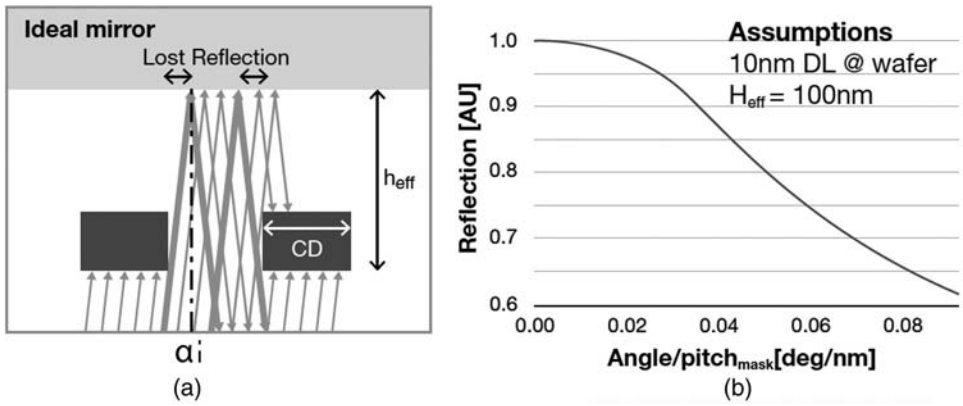

Figure 9.28 Reflection against an absorber pattern on a MoSi multilayer (as depicted in Fig. 9.23) can be regarded as a pure multilayer reflection plus a shadowing effect that depends on the angle/pitch ratio. The reflection is an EM simulation taking the material properties of the absorber into account. The mirror is assumed to be ideal[61,62] (source: ASML).

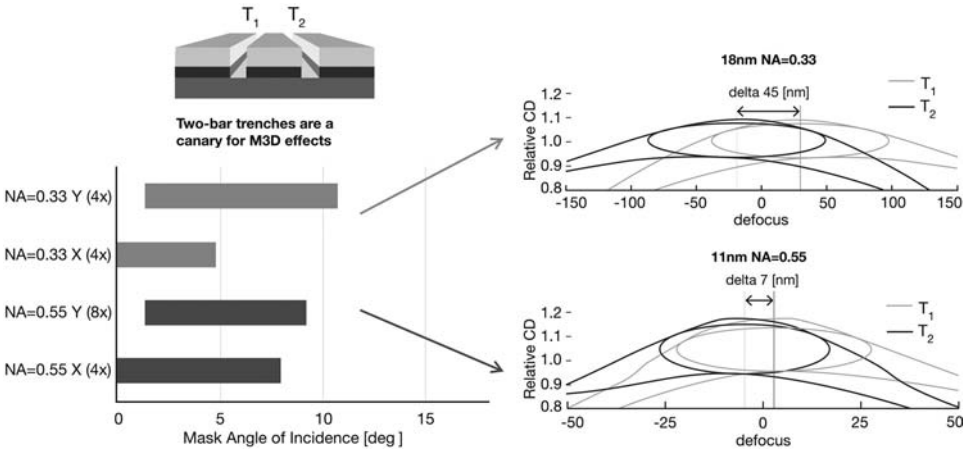

Figure 9.29 Simulation of the process windows of two-bar trenches at $NA = 0.33$ and $NA = 0.55$. Due to the smaller angles at the mask in the high-NA situation, less focus shift in the process windows of the individual trenches is observed. The target space size has been scaled accordingly. Note that the two-bar trenches are by nature very sensitive to mask 3D effects. Placement of, e.g., assist features will partly mitigate the observed effects in real-life situations (source: ASML).

Because the increase in y magnification (2×, from 4× to 8×) is larger than the increase in NA (1.67×, from 0.33 to 0.55), the cones at the mask level are actually smaller in the y direction. This provided an opportunity to fold the light cones closer together, hence, reducing the CRAO from 6 deg in the previous EUV systems to 5.355 deg in the high-NA system. Because in the case of the anamorphic high-NA lens the maximum angles at the mask are reduced, the mask 3D effects and therefore the focus shifts are reduced, as

Downloaded From: https://www.spiedigitallibrary.org/ebooks/ on 09 Mar 2022
Terms of Use: https://www.spiedigitallibrary.org/terms-of-use

can be seen in the lower graph of Fig. 9.29. This effect is observed for horizontal lines since there the angles do decrease. For vertical lines, the angles increase, however to a smaller maximum value compared to the horizontal lines, as depicted in the bar chart of Fig. 9.29. This helps, e.g., to drive the focus control toward the required 30 nm. A more in-depth explanation of this effect is given in Refs. 12 and 60.

The main reason for moving to high-NA is to increase the resolution or, in other words, to reduce the amount of patterning steps needed to achieve a certain resolution. As an example, in Fig. 9.30, a regular contact hole pattern is printed to match an underlying grid of lines and spaces. This can be seen as an example of a cut mask (compare to Fig. 9.12) or via application. The NA of the projection optics allows for a minimum distance between the contact holes

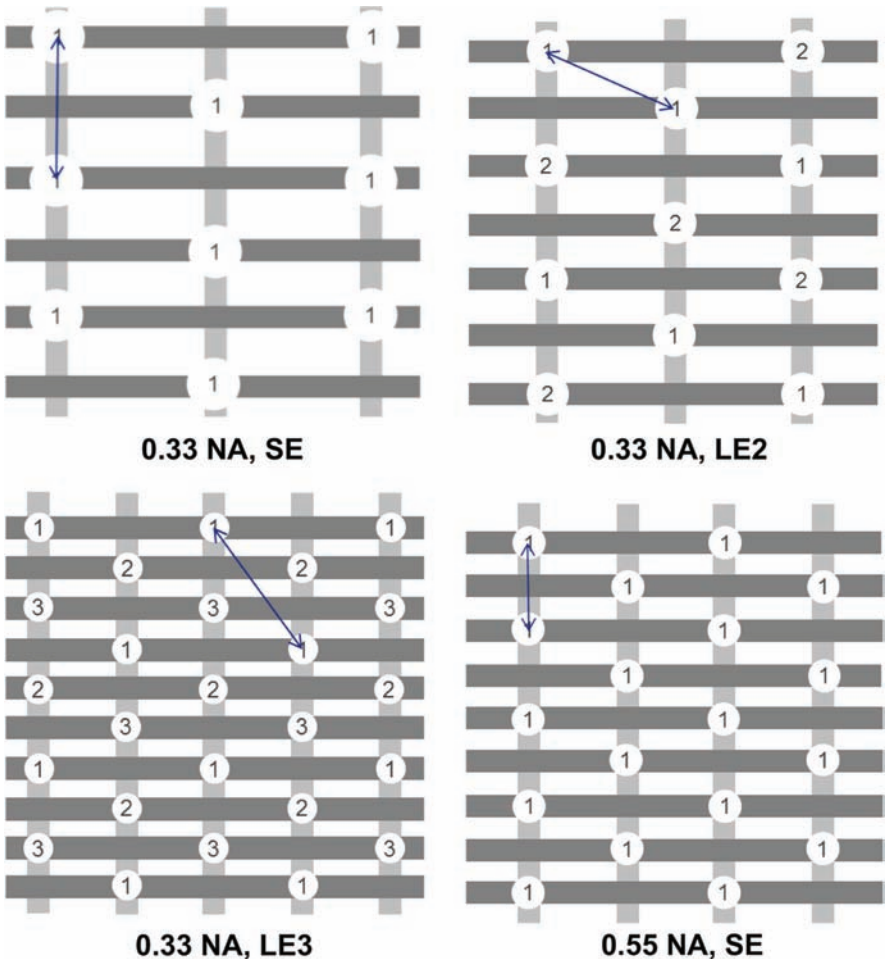

Figure 9.30 Effect of multiple patterning on the minimum printable pitch of contact holes (SE – single exposure, LE2 – double exposure, LE3 – triple exposure). The arrows show the minimum printable pitch, which scales with the NA^{63} (source: ASML).

Downloaded From: https://www.spiedigitallibrary.org/ebooks/ on 09 Mar 2022
Terms of Use: https://www.spiedigitallibrary.org/terms-of-use

in a single exposure, indicated by the arrows in the figure. Going from single exposure to double patterning allows the entire pattern to be shrunk by reducing the minimum distance between the contact holes. Note that the distance between two contact holes in each exposure (the litho pitch) is equal in all situations. Going to triple exposure allows for even more shrinkage of the pattern. Consequently, increasing the number of exposures to define a pattern allows this pattern to be shrunk further, although this comes at a cost penalty. By using a NA of 0.55 instead of 0.33, the contact hole pitch in a single layer can be reduced. This results in a finer resolution by just one exposure.

To compare the overall effective throughput of these situations, one should take into account three quantities: (1) the dose needed to achieve the required LCDU, (2) the resulting throughput (see Fig. 9.27), and (3) the number of patterning steps needed.

The higher contrast of the 0.55-NA scanner should lead to significantly lower LCDU (Fig. 9.31). Alternatively, the dose required for a certain LCDU can be written as $Dose \sim 1/(NILS)^2$ [see also Eq. (9.3)]. This means that the dose needed to achieve a LCDU of, e.g., 15% of the critical feature CD after development and inspection is much smaller for $NA = 0.55$ than for $NA = 0.33$ by virtue of the higher imaging contrast for 0.55 NA, as shown in Fig. 9.32. A LCDU of 15% after development and inspection is targeted to result in ~50% reduction in LCDU (~7.5% of CD) after etch and inspection by virtue of smoothing by the etch process.[64–66]

For an equal feature size, e.g., the 18-nm dense holes in Fig. 9.31, the high-NA systems meets the LCDU target (15% assumed in this figure) at a significantly lower dose than the system with $NA = 0.33$. Assuming equal source power and a higher optical column transmission for the high-NA system, and assuming that the stages for 0.55 NA compensate for the stage

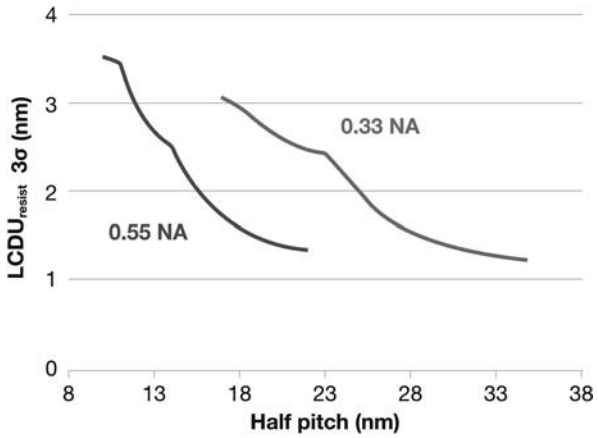

Figure 9.31 Higher contrast leads to lower LCDU for 0.55 NA as compared to 0.33 NA as modeled for regular contact holes with Quasar illumination and a 20-mJ/cm^2 non-CAR resist (source: ASML).

Downloaded From: https://www.spiedigitallibrary.org/ebooks/ on 09 Mar 2022
Terms of Use: https://www.spiedigitallibrary.org/terms-of-use

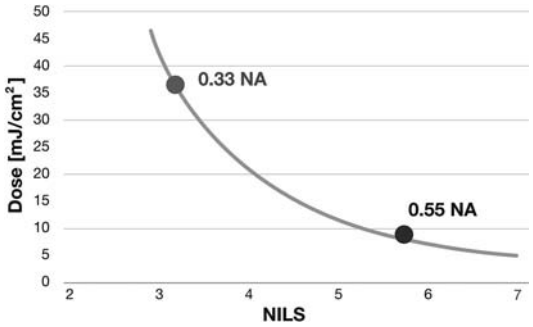

Figure 9.32 Lower exposure dose required to meet *LCDU* = 15% of CD for 0.55 NA versus 0.33 NA as modeled for regular 18-nm contact holes with Quasar illumination and a CAR resist (source: ASML).

overhead associated with the half-field, a much higher throughput can be achieved with the high-NA scanner by virtue of this lower dose. This allows for cost reduction per exposure pass by high-NA, even when assuming a higher high-NA scanner price accounting for the increased cost for the high-NA optics and the scanner platform.

Alternatively, a scanner with 0.55 NA can print a feature size (at an equal process factor k_1) that is proportionally smaller by the NA ratio 0.33/0.55 and thereby increases the number of critical features per unit area proportionally with $(0.55/0.33)^2$, in line with the historic lithographic shrink by NA increase (or a wavelength reduction) over time.

Hence, the NA 0.55 allows for a smaller number of exposure steps and a reduction of the dose required for an acceptable LCDU. The combined effect of these two advantages on the effective exposure throughput (TPT) of the high-NA EUV scanner for the case of the regular contact holes of Fig. 9.30 is shown in Fig. 9.33. The up to 4× higher effective throughput at a pattern

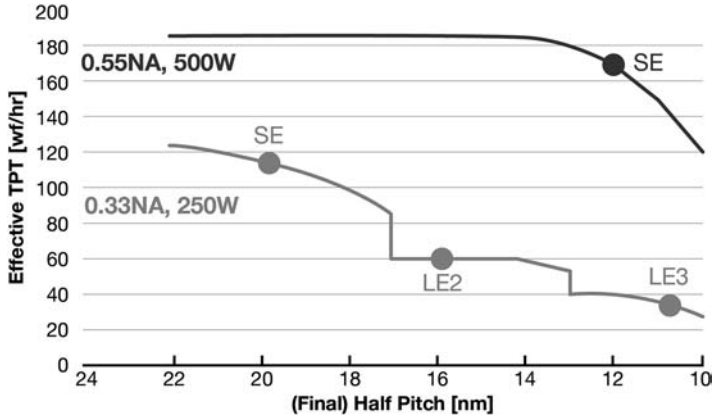

Figure 9.33 Simulation of contact hole printability taking photon shot noise into account. Dose is taken such that the resulting *LCDU* = 2 nm. The dots refer to the four situations depicted in Fig. 9.30[63] (source: ASML).

Downloaded From: https://www.spiedigitallibrary.org/ebooks/ on 09 Mar 2022
Terms of Use: https://www.spiedigitallibrary.org/terms-of-use

half-pitch of ~12 nm substantially improves economics when assuming a substantially higher high-NA scanner price accounting for increased scanner complexity.

9.3 EUVL Scanner Architecture

9.3.1 Introduction: architecture overview

The EUV scanner architecture is basically the same as the architecture for the DUV scanner system.[3,5,67] Existing modules such as sensor systems and stages have, however, to be made vacuum compatible. For wafer and mask handling, dedicated modifications are required in order to address a particle-free transfer of mask and wafers to the vacuum environment. The vacuum environment is unique for EUV systems and requires a modification of the DUV scanner architecture.

Figure 9.34 shows a schematic overview of an EUV scanner system. The main components in vacuum are the source, the optics, and the mask and wafer stages. The mask and wafer handler has both an ambient and a vacuum component. In the following subsections, the main modules will be discussed.

9.3.2 The optical system

The major optical components of the optical system are the light source illumination system and the projection system. A general layout showing these systems is given in Fig. 9.1. The light source is an integral part of the EUV tool; a short overview of the light source is provided in this chapter. A more detailed description of the EUV source is given in Chapter 3A. Masks in EUV exposure tools are reflective; as a result, the illumination of the mask is

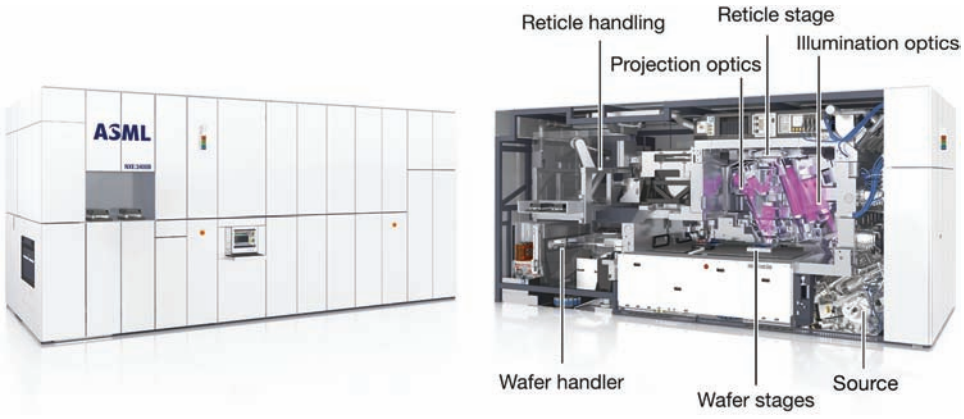

Figure 9.34 EUVL exposure tool overview (source: ASML).

Downloaded From: https://www.spiedigitallibrary.org/ebooks/ on 09 Mar 2022
Terms of Use: https://www.spiedigitallibrary.org/terms-of-use

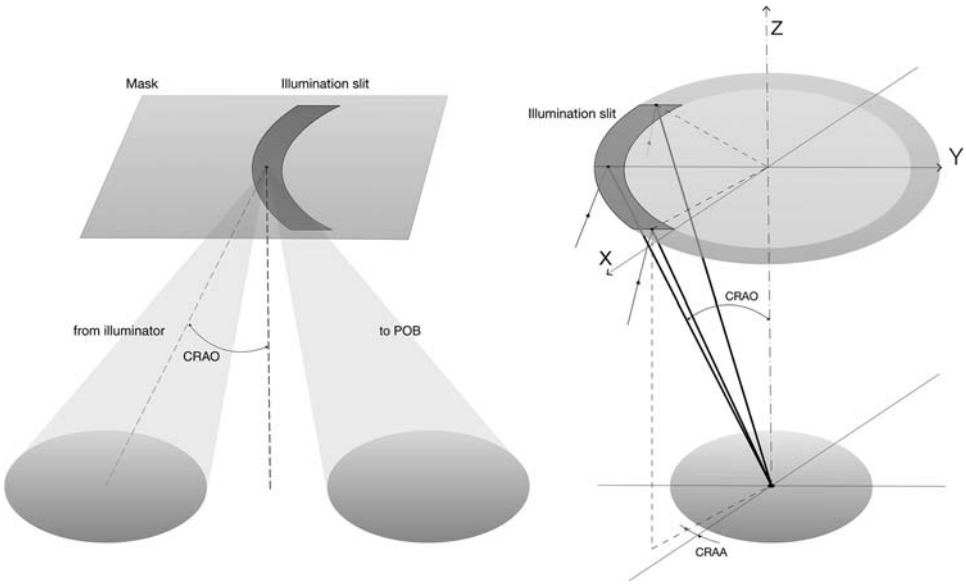

Figure 9.35 Illustrations defining the chief ray at object side (CRAO) and the chief ray azimuthal angle (CRAA) (source: ASML).

nontelecentric, as shown in Fig. 9.35. The angle of incidence is called the chief ray angle at object side (CRAO).

Figure 9.35 shows that the chief ray angle depends on the position in the illuminated field. The angle of incidence on the mask has a strong impact on the mask 3D effect. In order to fully understand the mask 3D effect, all incident angles of the mask must be known. For the compensation of mask 3D effects in computational lithography, this angle of incidence must be known. This means that not only the illumination mode, but also the CRAO as well as the chief ray azimuthal angle (CRAA) as a function of the field position must be known.

9.3.2.1 The EUV light source

The light source has been one of the biggest challenges for EUV lithography. Two Sn-based technologies have been investigated for generating a plasma that can produce the 13.5-nm EUV light. A schematic layout of both technologies is shown in Fig. 9.36. In a DPP system, the plasma is formed as a pulsed high-current discharge. The EUV light emitting from the plasma is directed to the illuminator by a grazing collector. A foil trap is added to collect the Sn particles coming from the plasma.

In a LPP system, a high-power pulsed infrared laser is focused on a Sn droplet, creating the plasma. The light generated by the plasma is collected with an elliptical mirror and focused on the entrance plane of the illuminator, called the intermediate focus (IF). Early EUV tools (ADT, NXE:3100) were

Downloaded From: https://www.spiedigitallibrary.org/ebooks/ on 09 Mar 2022
Terms of Use: https://www.spiedigitallibrary.org/terms-of-use

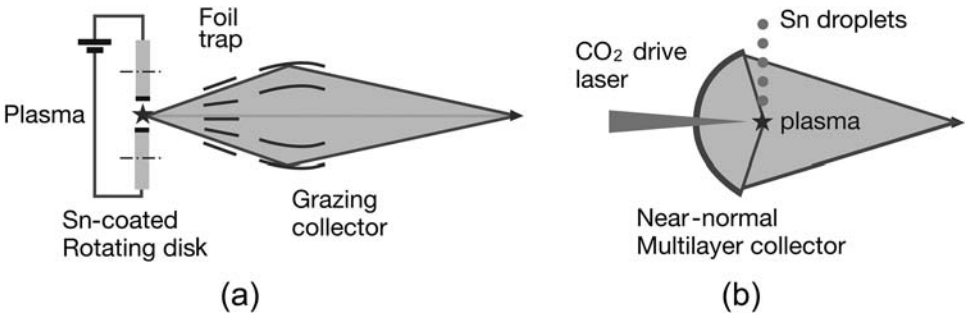

Figure 9.36 Schematic layouts of two Sn-based EUV sources: (a) DPP system and (b) LPP system (source: ASML).

equipped with a DPP source. For today's tools, an LPP source is also an option. With the availability of high-power CO_2 lasers, these tools can operate at a source power of 200–250 W. Future extensions above 300 W appear to be possible. For future power requirements, alternative sources have been considered. The free-electron laser is potentially a promising technique, but compared to the LPP source, it will be very complex and expensive.

9.3.2.2 The illumination system

The illumination system projects the light from the source onto the mask. The refracted orders from the patterns on the mask are captured by the projection optics box (POB) and create an aerial image of the mask pattern at the wafer level. The purpose of the illumination system is to illuminate the mask with a uniform intensity profile. Apart from this, the system must have the flexibility to offer a variable angular distribution of the light (pupil shape) in order to optimize the aerial image.

Key elements in the design of an EUV illuminator are the field facet module and the pupil facet mirror. Figure 9.37 shows a schematic presentation of such an illuminator.

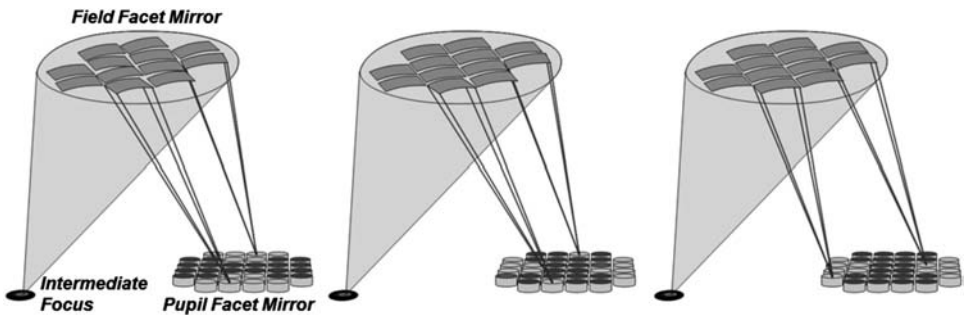

Figure 9.37 Schematic representation of an EUV illumination system (source: ASML).

Downloaded From: https://www.spiedigitallibrary.org/ebooks/ on 09 Mar 2022
Terms of Use: https://www.spiedigitallibrary.org/terms-of-use

The pupil facets image the individual field facets on top of each other onto the mask. The illuminated field at the mask and wafer is ring shaped to fit the POB requirements (see Chapter 5). The pupil facets are individually tilted such that at the mask level the images of the field facets overlap as far as possible. The intensity profile at the mask level is the sum of the individual channels in the illuminator. This greatly enhances the uniformity at the mask level when comparing it to the uniformity of the far field of the source at the field facets. Each field facet mirror is associated with more than one pupil facet mirror and can be switched between them. This way, flexible illumination modes can be supported without losing optical efficiency. Examples of some pupils are shown in Fig. 9.38.

The optical design of the illuminator is not bound to the geometrical shapes shown in Fig. 9.38; other more-complex shapes can be created, which is especially useful to support the so-called source mask optimization (SMO). The flexibility of the illumination system can be used to optimize the system performance for imaging parameters such as overlay and exposure latitude.[68] Relevant design parameters for an illuminator design are the σ range and the PFR. To enable the maximum flexibility for SMO, the supported σ range should cover the complete pupil. The PFR is a parameter that is used to optimize the contrast of the aerial image. To illustrate this we can look at the imaging contrast for dense lines. Dense line imaging near the resolution limit is normally done in a dipole illumination mode. The image is formed by the interference of the first and zero orders. Optimal imaging behavior in terms of contrast and DOF is obtained when the first and zero orders fully overlap, as shown in Fig. 9.39. The figure shows that with increasing resolution, the size of the illumination source and therefore the PFR must reduce. In this specific case (0.33 NA and 13-nm dense lines), optimal contrast is reached at a maximum PFR of 25%.

The uniformity requirements for the system are driven by the CD uniformity budget. A typical specification for the slit nonuniformity is better

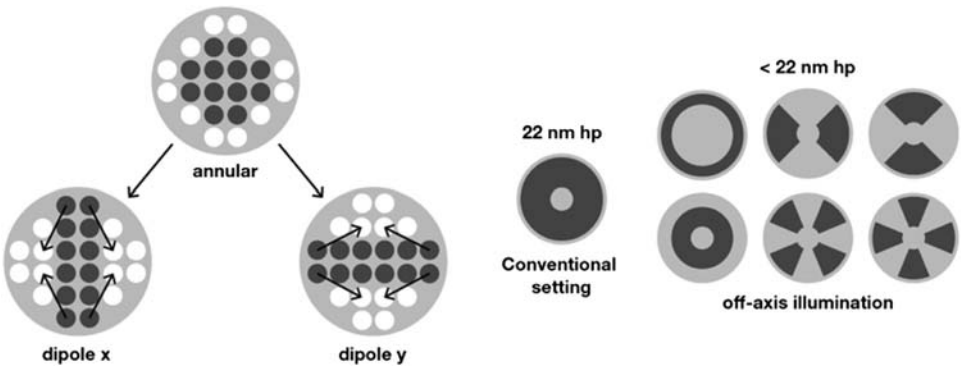

Figure 9.38 Flexible illumination modes in an EUV illumination system (source: ASML).

Downloaded From: https://www.spiedigitallibrary.org/ebooks/ on 09 Mar 2022
Terms of Use: https://www.spiedigitallibrary.org/terms-of-use

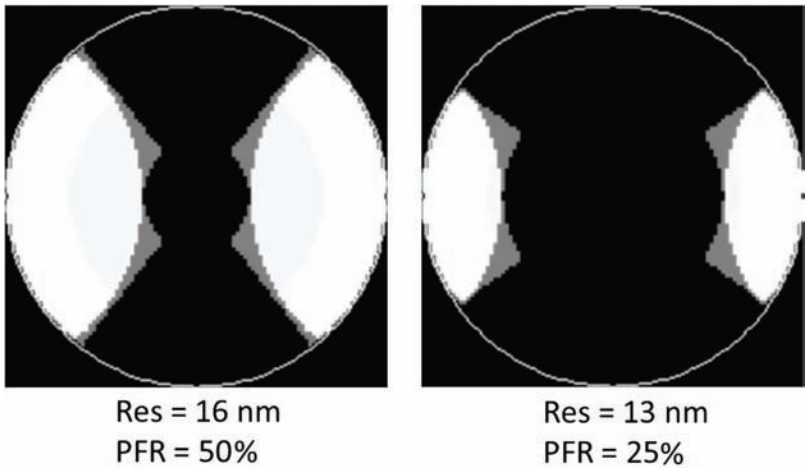

Figure 9.39 Illumination pupil for 16- and 13-nm dense lines with dipole illumination (source: ASML).

than 0.5%. In order to guarantee this requirement under all circumstances, an additional uniformity correction module—a so-called Unicom—is added to the illumination system (Fig. 9.40). The Unicom modifies the integrated slit uniformity by inserting multiple opaque fingers into the slit. Before a wafer is exposed, the uniformity can be measured at the wafer level and subsequently corrected. As in ArF(i) systems, the slit uniformity, eventually in conjunction with the dose profile, can also be distorted to correct for, e.g., mask or etch fingerprints.[69]

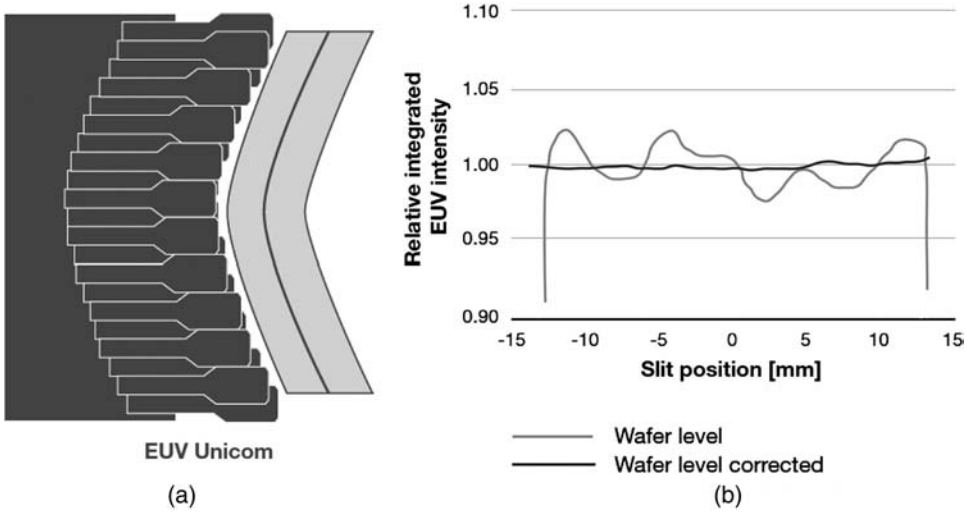

Figure 9.40 (a) Schematic layout of the Unicom. (b) Uncorrected and corrected intensity versus slit position at the wafer level (source: ASML).

Downloaded From: https://www.spiedigitallibrary.org/ebooks/ on 09 Mar 2022
Terms of Use: https://www.spiedigitallibrary.org/terms-of-use

9.3.2.3 The projection system

The EUV development for the projection system is described in Sections 9.2.2–9.2.4. The most prominent design parameters are the NA and the wavefront error.

The aberrations can be divided based on their impact as follows:

- The total wavefront error degrades the aerial image and results in contrast loss.
- The odd aberrations cause a pattern shift (overlay) and imaging asymmetry (left/right differences).
- The even aberrations impact focus performance.

The first-generation EUV systems were characterized by a RMS value less than 1 nm, while current systems have a RMS value below 0.3 nm. The requirement for the high-NA systems should match the ultimate resolution requirement and will need to be around 0.15 nm. Figure 9.41 shows the evolution of the wavefront requirements for the different NAs. The requirements for the even and odd wavefronts are derived from the overlay and focus specification, as discussed in Section 9.1.2.

Wavefront improvement is basically achieved by improving the manufacturing processes for polishing and metrology. Inline wavefront metrology at the actinic wavelength is essential for system setup and maintaining system stability in a production environment. For this purpose, the EUVL systems have an inline wavefront sensor incorporated into the wafer stage.[70] This sensor is capable of measuring individual Zernike polynomials with an accuracy better than 0.1 nm.

In the initial setup of the system, the wavefront sensor data in combination with data from resist measurements can be used to optimize the system for imaging and overlay performance. The measured wavefront can be optimized by adjusting the position of the mirrors in the POB. Figure 9.42 shows the basic sequence used to set up the projection optics.

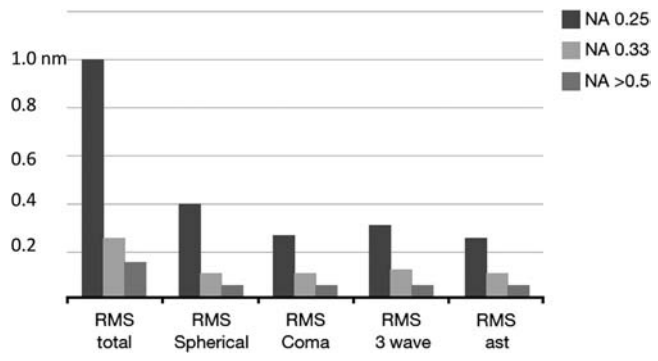

Figure 9.41 RMS [nanometer] roadmap for EUV systems (source: ASML).

Downloaded From: https://www.spiedigitallibrary.org/ebooks/ on 09 Mar 2022
Terms of Use: https://www.spiedigitallibrary.org/terms-of-use

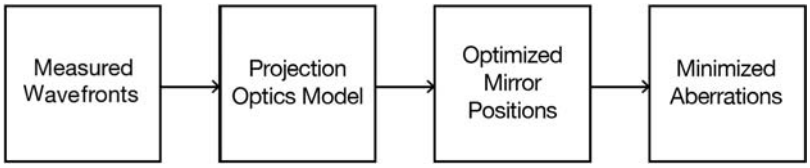

Figure 9.42 Schematic overview of the setup sequence of the projection optics (source: ASML).

When wafers are exposed, ~40% of EUV light is absorbed on every mirror. This causes global and local heating of the mirrors, which may cause changes in aberrations, overlay, and focus. The average temperature of the POB is kept constant with a passive cooling system. Local temperature effects can be minimized by using a mirror material with a very low thermal expansion coefficient. The thermal expansion coefficient of the mirror material depends on the temperature, as shown in Fig. 9.43. The thermal expansion coefficient is zero at a certain temperature: the zero-crossing temperature (ZCT). Mirrors operating around the ZCT show minimal temperature deformations.

Residual effects of mirror heating are monitored by scanner metrology and corrected by adjustment of the mirror positions. The time constants for POB heating are long compared to the wafer exposure time, so no corrections are needed during the exposure of a single dose. Long-term aberration drifts are measured with the inline wavefront sensor and fed back to the mirror positions.

9.3.3 Mechatronic architecture

In EUV systems, the mirrors in the projection optics are typically position-controlled using actuators and high-resolution encoder sensors.[71,72] The encoders are mounted on a metrology frame, which must be dynamically stable since any deformation will lead to positioning errors.[73] Also, high-frequency movements of the POB frame cannot be accurately tracked by

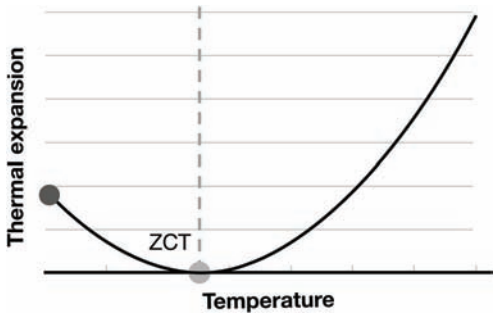

Figure 9.43 Thermal expansion coefficient as a function of mirror temperature (source: ASML).

Downloaded From: https://www.spiedigitallibrary.org/ebooks/ on 09 Mar 2022
Terms of Use: https://www.spiedigitallibrary.org/terms-of-use

the mirror control loops. For these reasons, the metrology frame must be dynamically isolated from the supporting base frame, which itself is disturbed by floor motion and stage reaction forces. Other dynamical requirements on the optics structure include the dynamical reaction path of the mirrors, and mirror disturbance forces propagating through the POB frame, which absorbs the mirror reaction forces (Fig. 9.44).

Since the EUV system operates in vacuum, the stages cannot use air bearings. Therefore, magnetically levitating long-stroke movers may be combined with six-degrees-of-freedom short-stroke actuators and flexure-suspended balance masses. Interferometer systems can be used for position measurement of the stage with respect to the projection optics. No atmospheric disturbances of the interferometer-based measurement systems are present as the system operates in vacuum.

9.3.4 Wafer and mask stage

Existing wafer and mask stage technology have to be adapted for the vacuum environment. Wafers and masks in DUV systems are held in position with vacuum forces. For EUV systems, clamps based on electrostatic force have been developed.[74] The air bearing used in the stages of current state-of-the-art lithographic systems are replaced by a magnetic plate that allows the stages to move with high scan speed and acceleration.[75,76] The concept of an EUV wafer stage is shown in Fig. 9.45.

The first full-field EUVL systems were single-stage systems, as they were meant to demonstrate the capability of EUV lithography; throughput was not the key performance parameter. For systems in high-volume production, the

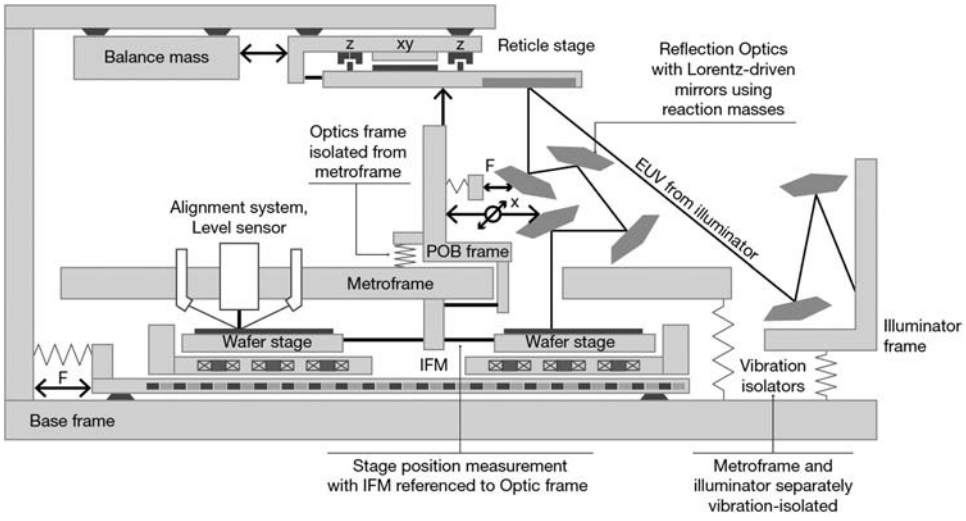

Figure 9.44 Example schematic diagram of the dynamical architecture (IFM – interferometer) (source: ASML).

Downloaded From: https://www.spiedigitallibrary.org/ebooks/ on 09 Mar 2022
Terms of Use: https://www.spiedigitallibrary.org/terms-of-use

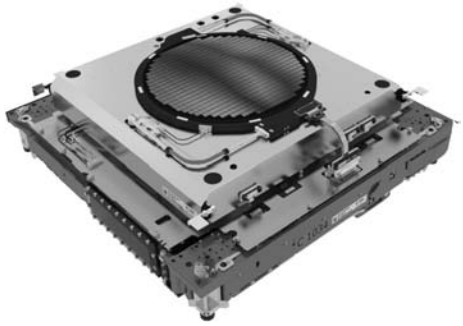

Figure 9.45 EUV wafer stage concept (source: ASML).

throughput is becoming important. The dual-stage concept significantly reduces the metrology overhead.

The design of the stages is critical for overlay and imaging.[73] For productivity, the stages must support high acceleration parameters in order to minimize the step overhead time between fields. The stages have to support the single machine and on-product overlay requirements, leading to low-frequency (moving-average filtered) position error specifications. For smaller nodes, the high frequency stage position accuracy requirement becomes important because high frequent position variations affect the contrast of the aerial image. The requirements scale linearly in a first approximation with the resolution. The mask stage design must support the wafer stage parameters. Due to the magnification ratio of 4:1, the velocity and acceleration requirements are higher by a factor of 4.

The maximum scan velocity for EUV is limited by the relatively low transmission of the optical system and by the EUV dose requirements. The scan velocity V_{scan} is a function of the source power, optical transmission n, slit height H (26 mm) at the wafer level, and the dose:

$$V_{scan} = n \cdot \frac{P_{source}}{H \cdot dose}. \tag{9.7}$$

The reflectivity of the optical elements is relatively low; the total reflection efficiency averaged over all angles of incidence on the mirrors is around 60%. In combination with the high number of reflecting surfaces, this results in a low overall transmission. As an example an optical design with 11 reflecting surfaces (including the mask) the total transmission would be around 0.5%. For the 16-nm node, the expected dose is 15 mJ/cm^2, and given a source with a power of 250 W, the wafer stage will move at 0.3 m/s.

9.3.5 Optics and contamination control

The optics within the illuminator and the POB are contained within a vacuum vessel. Wafers and masks are transported from atmospheric pressure to

Downloaded From: https://www.spiedigitallibrary.org/ebooks/ on 09 Mar 2022
Terms of Use: https://www.spiedigitallibrary.org/terms-of-use

vacuum within the wafer and mask load locks, the wafer handler and mask handler transport them towards the wafer stage and the mask stage. In order to reduce the number of mask moves between ambient and vacuum, the mask handler may contain an in-vacuum mask library.

The multilayer mirrors are very sensitive to contamination, especially in combination with EUV light. Contamination reduces the reflectivity and lifetime of the mirrors. In order to enhance optics lifetime, cleanliness requirements are very strict near the optics. In order to shield the optics from the rest of the (dirtier) system, they can be contained in a so-called mini-environment that is actively purged with clean gas in order to flush the environment and create a suppression of contaminants originating from neighboring compartments (wafer stage, reticle stage, and source). This allows for less strict contamination requirements in other parts of the system. A dynamic gas lock is at the interface between the wafer stage compartment and the POB. In the dynamic gas lock, contamination of the optics by resist outgassing is reduced by a gas flow directed towards the wafer.[77] Figure 9.46 shows a possible architecture for the vacuum system.

To achieve the highest transmission, the pressure in the light path should be minimized. The transmission of EUV light is governed by the Beer–Lambert law:

$$T = \exp[-\alpha(\lambda) l p], \tag{9.8}$$

where T is the transmission coefficient, l is the length of the light path [m], p is the pressure of the medium [mbar], and $\alpha(\lambda)$ is the absorptivity coefficient, which depends on medium and wavelength. Table 9.6 lists absorptivity

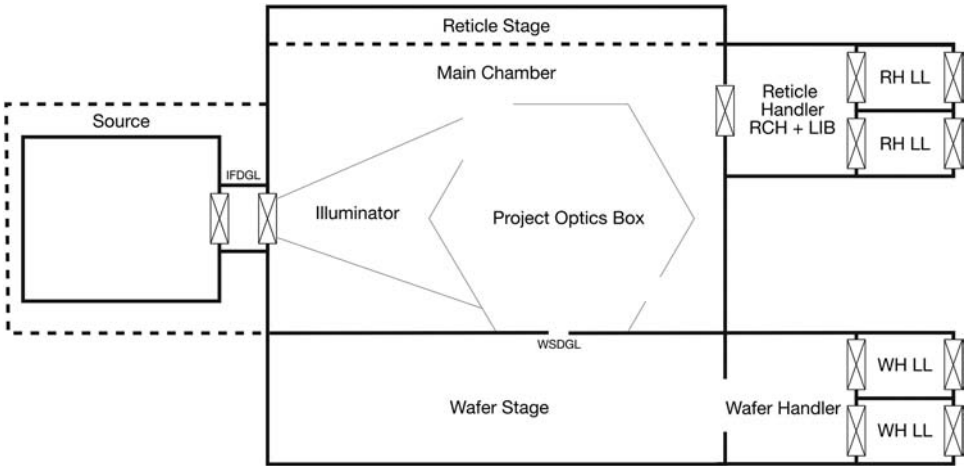

Figure 9.46 Principal layout of the vacuum architecture of an EUV scanner (RH – reticle handler, LL – load lock, WH – wafer handler, RCH – robot chamber, LIB – reticle library) (source: ASML).

Downloaded From: https://www.spiedigitallibrary.org/ebooks/ on 09 Mar 2022
Terms of Use: https://www.spiedigitallibrary.org/terms-of-use

Table 9.6 Example of maximum pressure for several gases.

Gas	α [mbar^{-1}m^{-1}]	P_{max} [mbar]
Hydrogen (H_2)	0.1550	$3.2 \cdot 10^{-2}$
Helium (He)	1.291	$3.8 \cdot 10^{-3}$
Nitrogen (N_2)	5.961	$8.3 \cdot 10^{-4}$
Argon (Ar)	3.403	$1.5 \cdot 10^{-3}$
Air	6.859	$7.2 \cdot 10^{-4}$

coefficients of several components at a wavelength of 13.5 nm. A budget of 4% of transmission loss (from the IF to the wafer) is reserved for EUV absorption by gas molecules (transmission is thus 96%). This budget restricts the maximum pressure as well as the partial pressures of the main gas components in vacuum.

Table 9.6 gives an example of the maximum pressure (averaged over a typical light path of ~1 m) for several gases, assuming that gas is the only component in the system. The gas transmission in EUV exposure tools is dominated by H_2. Hydrogen is added to the vacuum environment to enable carbon cleaning of the mirrors. A partial pressure in the range of 3–5 Pa is needed to enable an effective cleaning.

9.3.6 Metrology

The metrology of EUV scanners is in principle the same as that used for ArF(i) systems. The sensors needed for wavefront metrology and for alignment of the wafer to the mask must operate in vacuum. EUVL scanners can make use of the same software and metrology sequence. An example is the 'measure wafer' metrology step, which results in the optimum leveling of the chucked wafer (left part of Fig. 9.47). As in an ArF(i) tool, first a wafer is aligned to the wafer stage. Then the topology of the complete wafer is measured using the positioning system and focus sensor system (left side of Fig. 9.47). On the exposure side, the wafer stage is aligned to the reticle and reticle stage. By combining information on the measurement and the exposure position, the wafer is aligned to the reticle in the horizontal plane (right side of Fig. 9.47). The entire sequence is fully automated under software control.

Section 9.2.1 explains that the Rayleigh depth of focus is strongly reduced for high-NA systems, and hence improvements of the focus control systems are required. The topology of the wafer is measured based on the principle of optical triangulation. The light entering the sensor light is reflected by the wafer surface, and the height is measured by the displacement of the reflected beam. The incoming beam is not only reflected by the top surface, but also by the underlying layer stack, as shown in Fig. 9.48. This so-called process-dependent effect can result in an error in the measured wafer height. The process dependency of the sensor can be reduced by optimizing the angle of

Downloaded From: https://www.spiedigitallibrary.org/ebooks/ on 09 Mar 2022
Terms of Use: https://www.spiedigitallibrary.org/terms-of-use

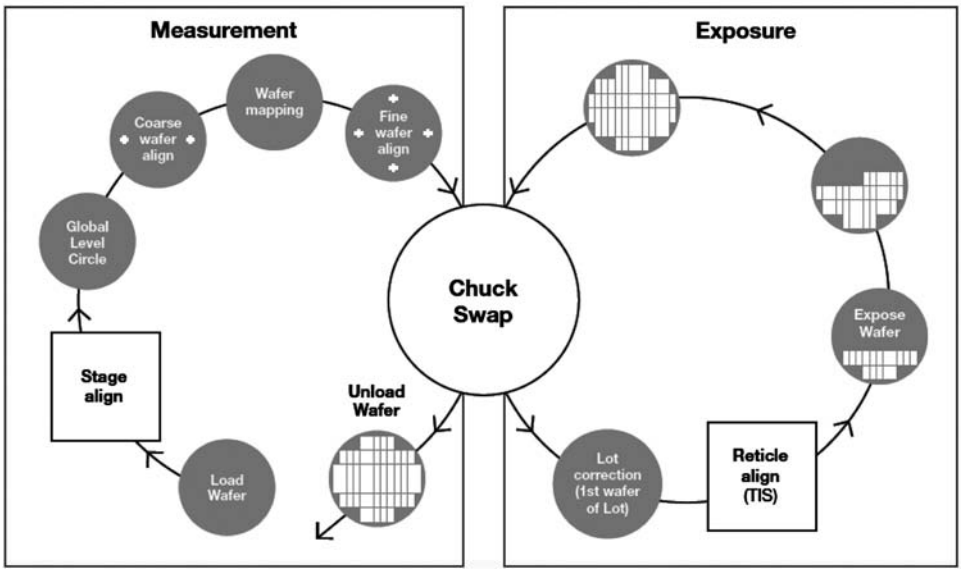

Figure 9.47 Schematic view of EUVL metrology (TIS – transmission image sensor) (source: ASML).

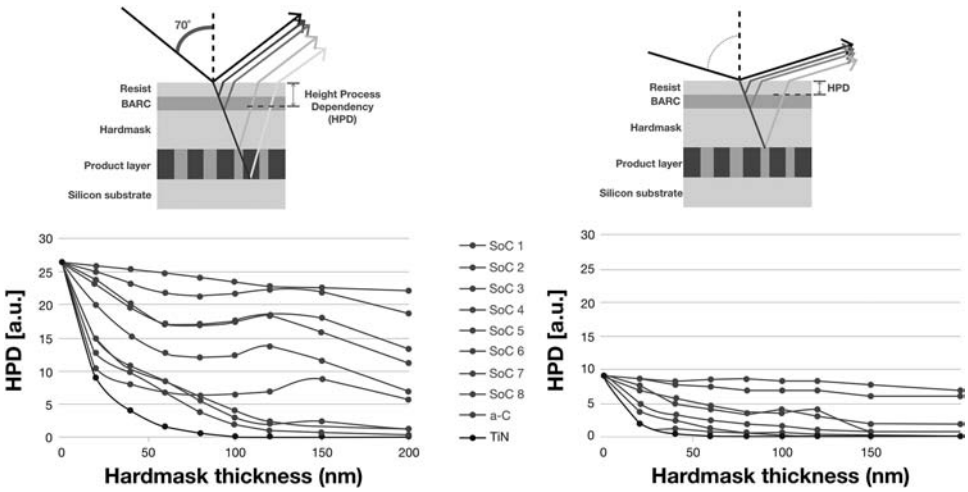

Figure 9.48 Principle of the level sensor in scanners (source: ASML).

incidence of the light and/or optimizing the spectrum of the light. Figure 9.48 shows the simulated process dependency for a number of different layer stacks and two different level-sensor configurations. On the left, the process dependency for different layer stacks is shown for a sensor with a 70-deg

Downloaded From: https://www.spiedigitallibrary.org/ebooks/ on 09 Mar 2022
Terms of Use: https://www.spiedigitallibrary.org/terms-of-use

angle of incidence and a certain light spectrum. On the right, the angle of incidence is increased, and the spectrum is shifted to a shorter DUV wavelength. By doing this, a reduction of more than a factor of 2 in the process dependency has been demonstrated.

New challenges are corrections for wafer, mask, and POB heating. POB heating is minimized by selection of a lens material with a low thermal expansion and by inline metrology. The mask is made from the same material as the POB mirrors, but the thermal load can be significantly larger. The heat absorption in the mask partly depends on the patterned area. The most dominant heating effect is magnification; this effect is measured and corrected during the so-called mask alignment. Higher-order mask heating deformations become relevant when the source power increases and the overlay requirement is more stringent. In this case, more-advanced correction strategies are needed. Observer-based control strategies, using real-time input of the heat load and temperature measurements on the system, will be applied.[78] Figure 9.49 is an example of such a control strategy.

The performance of mask heating has been investigated for the different correction strategies.[79] The results are presented in Fig. 9.50, which shows that the mask alignment based on the wafer stage sensor system TIS significantly reduces the effect. Furthermore, an observer-based model further reduces the effect.

A similar method can be applied for wafer heating. The wafer and wafer clamp temperature increase significantly due to absorption of EUV and infrared light. The infrared light results from the way EUV light is produced in the EUV source. Wafer heating causes thermo-mechanical deformations of

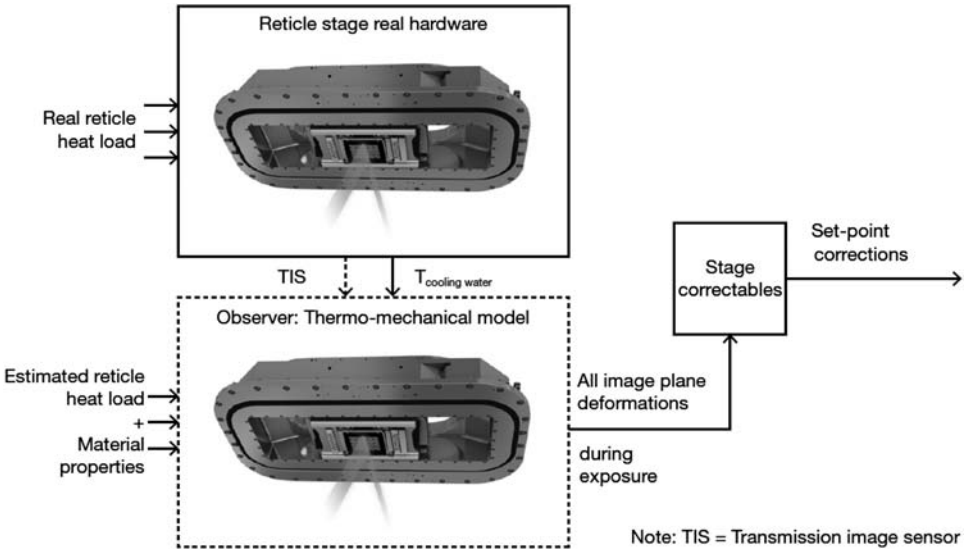

Figure 9.49 Observer-based control model for mask heating correction (source: ASML).

Downloaded From: https://www.spiedigitallibrary.org/ebooks/ on 09 Mar 2022
Terms of Use: https://www.spiedigitallibrary.org/terms-of-use

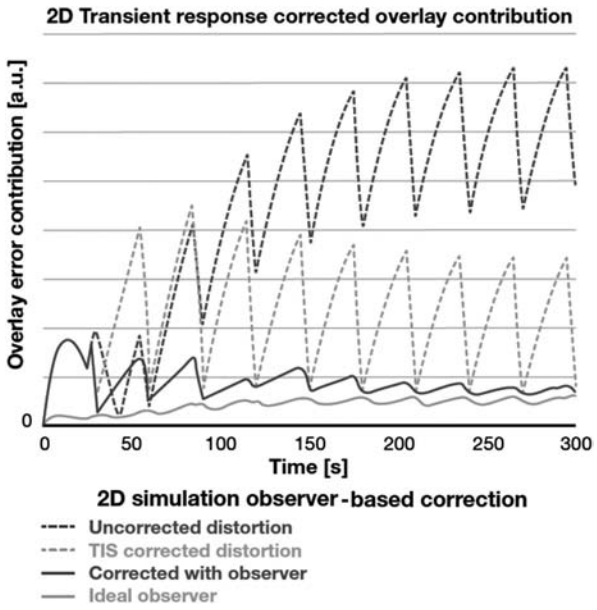

Figure 9.50 Overlay performance for different control strategies (source: ASML).

both the clamp and the wafer. The design of the system is such that the wafer and clamp temperature are as stable as possible, but the resulting deformations are larger than allowed by the overlay budget. Therefore, a correction model is needed. The correction model is calibrated by measuring the heating-induced overlay effects. The calibration and expose flow is given in Fig. 9.51.

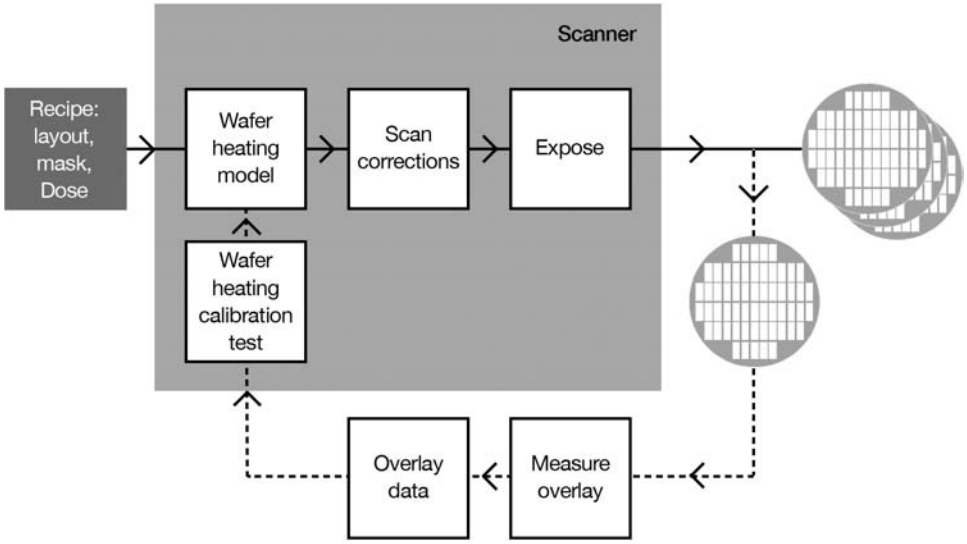

Figure 9.51 Correction model for wafer heating (source: ASML).

Downloaded From: https://www.spiedigitallibrary.org/ebooks/ on 09 Mar 2022
Terms of Use: https://www.spiedigitallibrary.org/terms-of-use

9.3.7 Material handling systems and clamps

The wafer and mask handling subsystems in EUV scanner systems form the interface between the atmospheric environment and the vacuum main chamber of the scanner. The main difference compared to non-EUV systems is that masks and wafers cannot be fixed with vacuum forces, so electrical forces are needed. This means that the mask and wafer stages are equipped with an electrostatic clamp.[80] Figure 9.52 shows the principle of an electrostatic clamp. Between the mask and the electrode is a dielectric layer. The clamp force depends on the applied voltage, the dielectrical properties, and the distance between the mask/wafer and the electrode (see Fig. 9.52). Both the wafer and the mask are clamped over the full surface, meaning that special attention must be paid to prevent contamination; a particle on the back side can introduce wafer or mask deformation.

The wafer handler forms the interface between the track (equipment for coating and development of the wafers) or a front-opening unified pod (FOUP) and the scanner system. Figure 9.53 shows the wafer flow. The wafer is pre-aligned in the atmospheric part, brought to the vacuum environment, and loaded to the measurement stage. After completion of the measure and exposure sequence, the wafer is unloaded and handed to the track or FOUP for the next process steps.

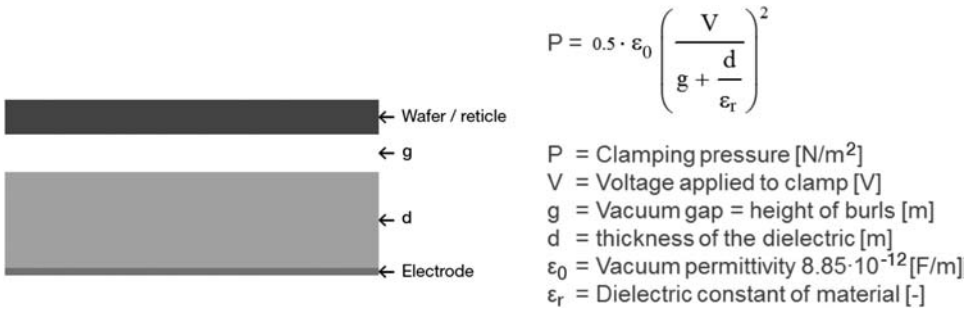

Figure 9.52 Electrostatic clamp principle for EUVL systems (source: ASML).

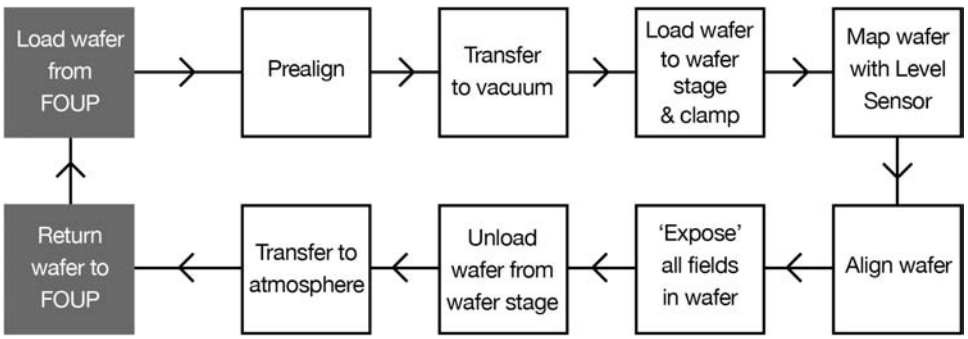

Figure 9.53 Wafer load sequence (source: ASML).

Downloaded From: https://www.spiedigitallibrary.org/ebooks/ on 09 Mar 2022
Terms of Use: https://www.spiedigitallibrary.org/terms-of-use

Cleanliness is extremely important during mask handling. Particles on the back side introduce mask deformation, which can give overlay and focus errors. Particles on the front side can be imaged and have a direct impact on yield. Recent developments have led to the introduction of an EUV pellicle, effectively eliminating the frontside contamination risk (Section 9.3.9).

For future systems with a higher resolution, pellicles are considered to be essential. If the mask back side gets contaminated with particles that are large in height (>3 μm), there can be an impact on overlay; however, given the nature of the scanner mask chuck design, many tens of adders can be tolerated without impacting performance, particularly since most contamination found is organic and is compressed when the mask is clamped.

To minimize the potential for added contamination to the front side or back side of the mask, special precautions are needed for the mask management design. EUV dual pods—a type of mini environment—are used outside of the scanner and in presenting masks to the scanner for loading. Materials used in the dual pods and in the scanner must be specially selected to avoid shedding, and the locations of moving parts and materials in contact with the mask are controlled. In an EUV scanner, the mask is never directly handled when it is transported in the EUV inner pod. The only direct contact to the mask is at the back side when the mask is clamped to the mask stage for exposure (Fig. 9.54).

9.3.8 EUV pellicles

A pellicle is a thin membrane that prevents particles from landing on the mask front surface. A particle on the membrane will not be imaged because the membrane will be out of the focal plane, while a particle on the mask will have a sharp image on the wafer and therefore can lead to a defect. The existing organic thin-film technology as used in DUV lithography is not applicable to EUVL due to the low transmission. Because the EUV mask is reflective, the light has to pass the membrane twice: first when the EUV light comes from the illuminator and again when the EUV light is reflected from the mask toward the POB. The principle of the pellicle is shown in Fig. 9.55.

In order to obtain an acceptable transmission for EUV pellicles, they have to be made from extremely thin solid materials.[81] With a typical thickness of approximately 50 nm or thinner, a single-pass transmission of 10% is possible.[82] The membrane film will absorb part of the incoming and reflecting light. This will increase the temperature of the pellicle, which can reduce the lifetime and reduce the maximum acceptable power that hits the pellicle. Current EUV pellicles have proven to support source powers well above 125 W,[83] and development is underway to support higher powers. Note that in the high-NA system, due to the larger magnification in the scan direction, the intensity at the pellicle will be smaller, allowing for even larger

Downloaded From: https://www.spiedigitallibrary.org/ebooks/ on 09 Mar 2022
Terms of Use: https://www.spiedigitallibrary.org/terms-of-use

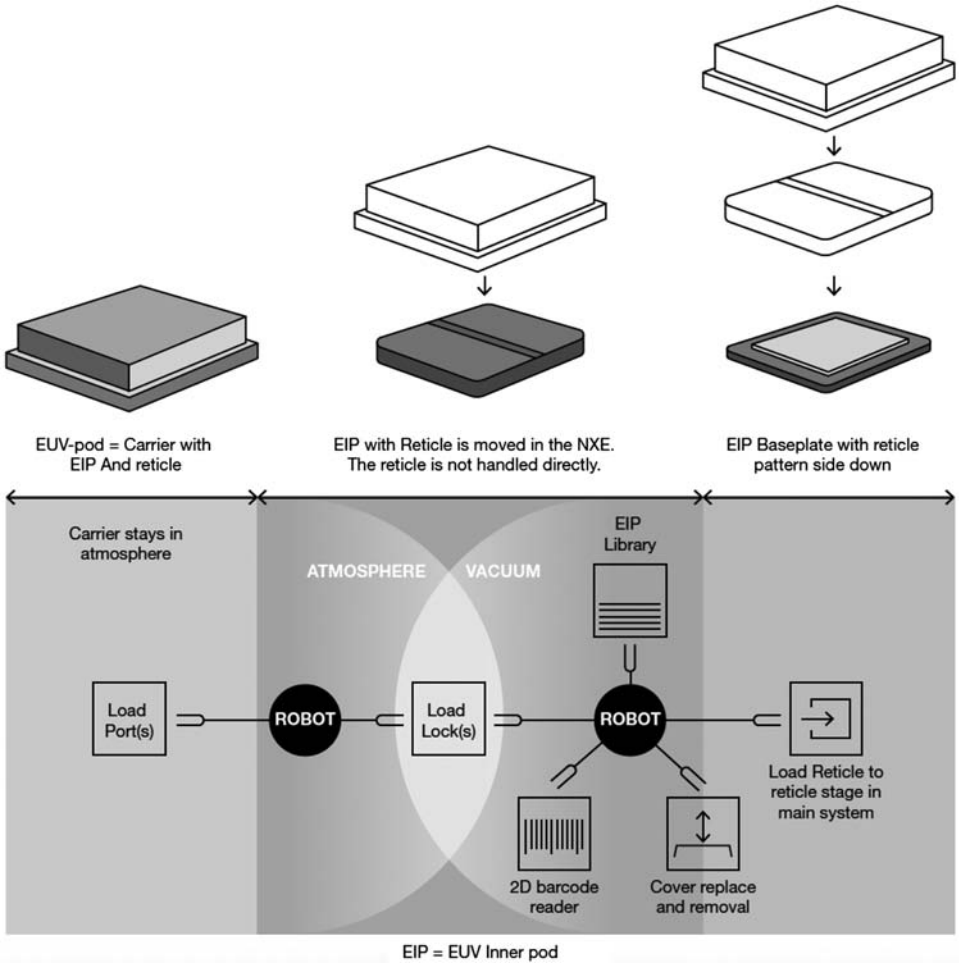

Figure 9.54 Mask (also called reticle) handling from the EUV inner pod into the scanner (source: ASML).

source powers.[84] The pellicle design for the NXE systems is shown in Fig. 9.56. The pellicle is mounted on a frame that can be removed for mask inspection.

9.4 Outlook

It has been more than 30 years since the first experiments on an EUVL reduction system were conducted in 1986.[26] EUVL has been on the roadmap of scanner manufacturers, with its initial introduction in 2005.[86,87] Since then, many technological hurdles have been overcome, especially in source technology and optics fabrication. While initially source power development was slow, steady progress has been made since 2013 after the merger of

Downloaded From: https://www.spiedigitallibrary.org/ebooks/ on 09 Mar 2022
Terms of Use: https://www.spiedigitallibrary.org/terms-of-use

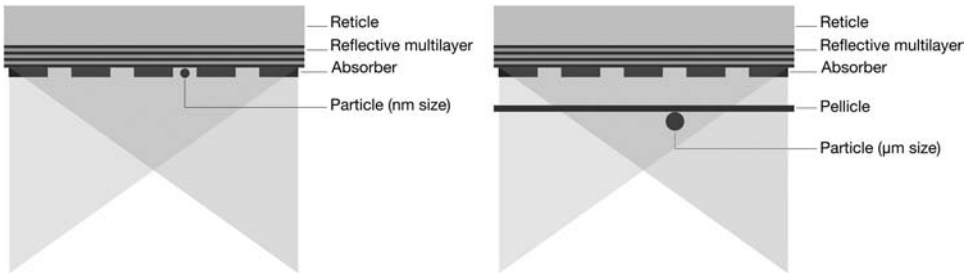

Figure 9.55 EUV pellicle principle: the particle is kept out of focus and as a result will not image (source: ASML).

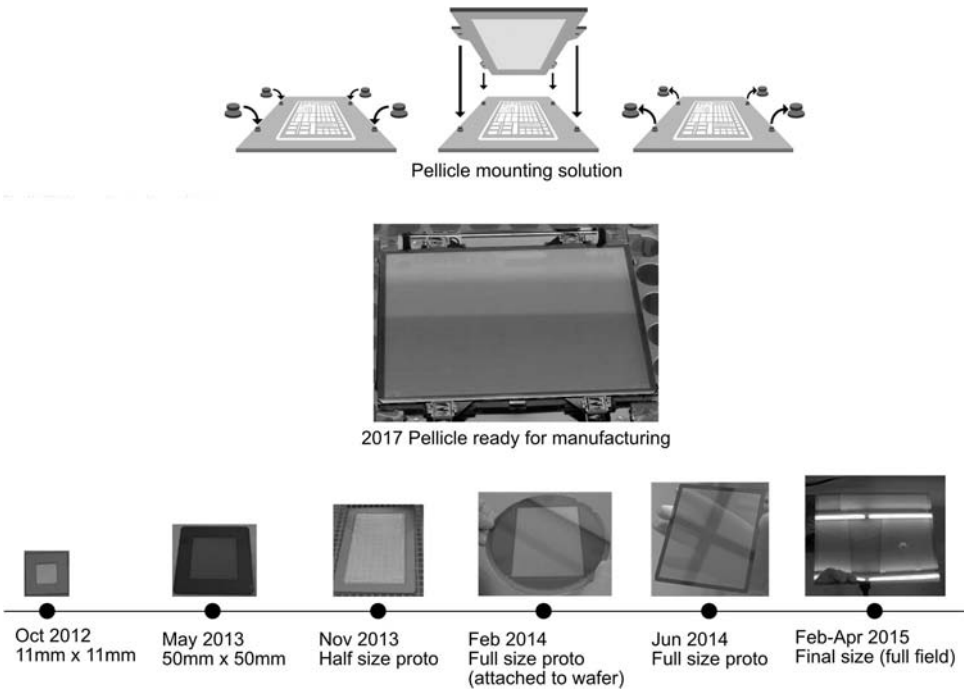

Figure 9.56 (top) Diagrams showing a pellicle and pellicle mounting. (bottom) Photographs showing the development of the pellicle over time as well as one of the first full-size pellicles produced (source: ASML).

ASML and Cymer, which effectively tripled the development efforts, as can be seen from the overview of achieved source power shown in Fig. 9.57.

At the moment of this writing, NXE:3400B systems with a 125-W source achieving a throughput of 85 wph have been shipped, while at the same time in the lab more than 125 wph has been demonstrated with a 250-W source. This is approaching the HVM requirements and ultimately led to statements

Downloaded From: https://www.spiedigitallibrary.org/ebooks/ on 09 Mar 2022
Terms of Use: https://www.spiedigitallibrary.org/terms-of-use

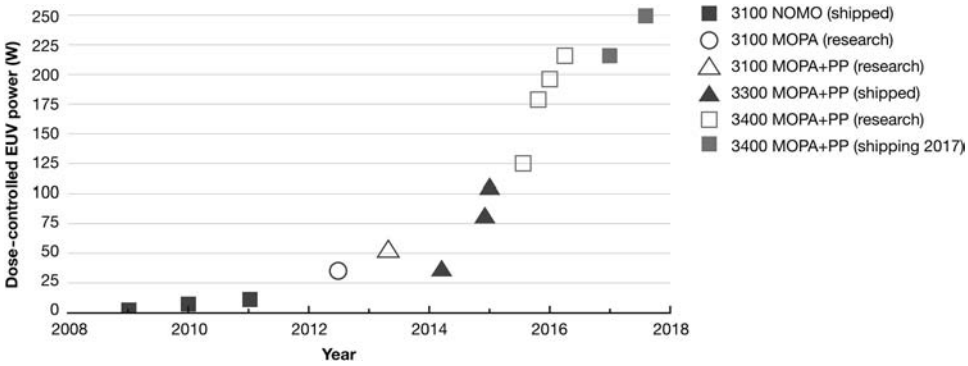

Figure 9.57 EUV LPP source power developments over time[87] (see Chapter 3A) (source: ASML).

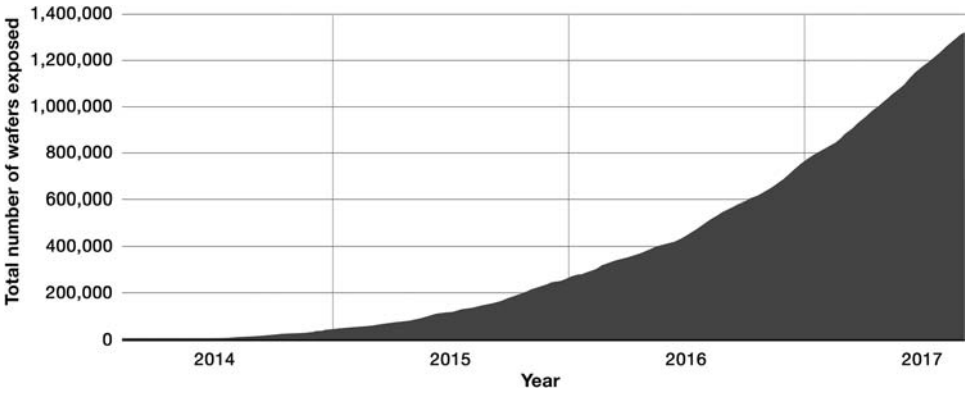

Figure 9.58 Cumulative number of exposed wafers on 0.33-NA systems. At the right end of the graph, eight systems were installed at customer sites[83] (source: ASML).

by major semiconductor manufacturers that they intend to introduce EUVL in mass production around 2018.[88,89] The graphs shown in Figs. 9.57 and 9.58 show steady progress supporting the statement that EUVL will be the next mainstream technology to print integrated circuits.

9.4.1 Future prospects

Now we can ask ourselves, what are the potential next steps to continue to follow Moore's law? Starting with the first Rayleigh equation [Eq. (9.1)], there are basically three possibilities:

– Continue to improve the 13.5-nm 0.55-NA system in a manner similar to ArF immersion development: Improve the imaging and overlay

Downloaded From: https://www.spiedigitallibrary.org/ebooks/ on 09 Mar 2022
Terms of Use: https://www.spiedigitallibrary.org/terms-of-use

performance, and increase throughput. This approach allows for further shrinkage by operation at a lower k_1 and/or by multiple patterning.
– Increase the NA to beyond 0.55.
– Take the next step toward a shorter wavelength.

All three approaches have their own advantages and technological challenges.

High-NA multiple-patterning extension

This is the logical extension of an existing platform, with implications smaller than changing the NA and/or the wavelength. Much experience is gained in extending the ArF immersion tools. This method certainly has its limitations. Following Moore's law means producing more components at a comparable price. Double patterning means twice the number of components at double the exposure price; on top of this, additional processing costs need to be included. Furthermore, multiple patterning brings considerable process complexity, leading to a lower yield and/or longer time to yield. Yield can be increased by a smaller pupil fill ratio, leading to better contrast at smaller resolutions or allowing for operation at a smaller k_1. Cost reduction has to be realized, e.g., by a higher throughput. In immersion lithography, this approach has been successful for a long time; at some point an intrinsic better resolution is desired by increasing the NA or reducing the wavelength.

Further increase of the NA

A higher NA is attractive for improving the resolution because it leaves the wavelength unchanged. This approach requires no new source technology nor a dramatic change in resist infrastructure. The first limitation that needs to be addressed is mask shadowing. The anamorphic 0.55-NA lens exploited some unused headroom in the mask angles; an even larger NA will need a larger demagnification, leading to a reduced throughput. An alternative might be the intrinsic reduction of the shadowing by embedding the absorber in the multilayer of the mask.[56,57] Although very promising from a theoretical point of view, many practical hurdles have to be overcome in order to make such a technology feasible. Especially issues such as defectivity and reparability of the mask are very challenging.

Reduction in wavelength

This would be the next step if all other possibilities are exhausted. Wavelength reduction would require many new technologies, such as a new source, new photoresists, and new optical coatings.[93–96] A shorter wavelength results in tighter surface roughness requirements to keep both aberrations and the stray light level of the projection optical system within acceptable limits. On top of this, higher energy per photon decreases the number of photons at the same optical power,

Downloaded From: https://www.spiedigitallibrary.org/ebooks/ on 09 Mar 2022
Terms of Use: https://www.spiedigitallibrary.org/terms-of-use

resulting in increased impact of photon shot noise, or *vice versa*: higher powers are needed to keep the photon shot noise within acceptable limits. The larger penetration depth in the multilayer will also increase the mask 3D effect, calling for additional solutions in the mask technology as well.

EUV lithography has come a very long way since the first EUV exposures were carried out in 1986.[26] Now that the greatest hurdles in source power are mostly behind us, EUV is on its way to production. With the extendibility of the NA to a value of 0.55 and maybe even beyond, EUV has the promise to become the lithography workhorse for many years to come. What's next is still in the fog: a lot of research work is underway today to explore the path to further extend Moore's law.

Acknowledgments

The authors would like to express their thanks to Jos Benschop, Jos de Klerk, Jo Finders, Tony Yen, Anton van Dijsseldonk, Peter Schaap, Kars Troost, Hans Meiling, Jens Timo Neumann, Bernhard Kneer, and Sascha Migura for reviewing this document and giving valuable comments. Special thanks are expressed to Hiroo Kinoshita for supplying me additional information for the historic part of this chapter. Finally, we would like to thank Jeannot Driedonkx for his effort in creating the figures.

We thank the Dutch Ministry of Economic Affairs, the German Federal Ministry of Education and Research, and the European ENIAC and ECSEL Joint Undertakings for funding of the projects "E450LMDAP" (NL: ENIA142001 / DE: 16ES0255K / EU: 621280), "SeNaTe" (NL: ECSEL152002 / DE: 16ESE0036K / EU: 662338), "TAKE5" (NL: ECSL162004 / DE: 16ESE 0072K / EU: 692522), and "TAKEMI5" (NL: ECSL172001 / EU: 737479). Additionally, we thank the Federal Ministry of Education and Research (Germany) for funding of the BMBF project "ETIK" (DE: 16N12256K).

References

1. H. Levinson, *Principles of Lithography*, Third Edition, SPIE Press, Bellingham, Washington (2011) [doi: 10.1117/12.3.865363].
2. J. D. Buckley and C. Karatzas, "Step and scan: A systems overview of a new lithography tool," *Proc. SPIE* **1088** (1989) [doi: 10.1117/12.953171].
3. M. van den Brink, H. Jasper, S. Slonaker, P. Wijnhoven, and F. Klaassen, "Step-and-scan and step-and-repeat: a technology comparison," *Proc. SPIE* **2762** (1996) [doi: 10.1117/12.240936].
4. D. A. Markle, "The future and potential of optical scanning systems," *Solid State Technology* **27**(9), 159–166 (1984).
5. G. de Zwart, M. van den Brink, R. George, D. Satriasaputra, J. Baselmans, H. Butler, J. van Schoot, and J. de Klerk, "Performance of a step-and-scan

Downloaded From: https://www.spiedigitallibrary.org/ebooks/ on 09 Mar 2022
Terms of Use: https://www.spiedigitallibrary.org/terms-of-use

system for DUV lithography," *Proc. SPIE* **3026** (1997) [doi: 10.1117/12.276002].
6. B. Vandewalle, B. Chava, S. Sakhare, J. Ryckaert, and M. Dusa, "Design technology co-optimization for a robust 10nm metal solution for logic design and SRAM," *Proc. SPIE* **9053**, 90530Q (2014) [doi: 10.1117/12.2048079].
7. C. A. Mack, "Optimizing numerical aperture and partial coherence," *The Lithography Tutor* **12** (Winter 1996).
8. J. B. P. van Schoot, J. Finders, K. van Ingen Schenau, M. Klaassen, and C. Buijk, "The mask error factor: causes and implications for process latitude," *Proc. SPIE* 3679 (1999) [doi: 10.1117/12.354338].
9. G. F. Lorusso, M. Mao, L. Reijnen, K. Viatkina, R. Knops, G. Rispens, and T. Fliervoet, "Influence of etch process on contact hole local critical dimension uniformity in extreme-ultraviolet lithography," *Proc. SPIE* **9425**, 94250K (2015) [doi: 10.1117/12.2085722].
10. J. Jiang, D. De Simone, O. Yildirim, M. Meeuwissen, R. Hoefnagels, G. Rispens, P. Derks, and R. Custers, "Impact of acid statistics on EUV local critical dimension uniformity," *Proc. SPIE* **10143**, 1014323 (2017) [doi: 10.1117/12.2257903].
11. O. Yildirim, E. Buitrago, R. Hoefnagels, M. Meeuwissen, S. Wuister, G. Rispens, A. van Oosten, P. Derks, J. Finders, M. Vockenhuber, and Y. Ekinci, "Improvements in resist performance towards EUV HVM," *Proc. SPIE* **10143**, 101430Q (2017) [doi: 10.1117/12.2257415].
12. J. Finders, S. Wuister, T. Last, G. Rispens, E. Psara, J. Lubkoll, E. van Setten, and F. Wittebrood, "Contrast optimization for 0.33NA EUV Lithography," *Proc. SPIE* **9776**, 97761P (2016) [doi: 10.1117/12.2220036].
13. J. van Schoot, A. Pirati, K. Troost, R. van Ballegoij, P. Krabbendam, J. Stoeldraijer, E. Loopstra, H. Meiling, B. Kneer, B. Thuering, W. Kaiser, T. Heil, and S. Migura, "EUV roadmap extension by higher numerical aperture," 2016 International Symposium on Extreme Ultraviolet Lithography, 24–26 Oct., Hiroshima, Japan.
14. ITRS roadmap, www.itrs2.net.
15. A. Pirati, R. Peeters, D. Smith et al., "Performance overview and outlook of EUV lithography systems," *Proc. SPIE* **9422**, 94221P (2015) [doi: 10.1117/12.2085912].
16. J. Mulkens, M. Hanna, H. Wei, V. Vaenkatesan, H. Megens, and D. Slotboom, "Overlay and edge placement control strategies for the 7nm node using EUV and ArF lithography," *Proc. SPIE* **9422**, 94221Q (2015) [doi: 10.1117/12.2085761].
17. I. Bouchoms, M. Leenders, J. Jaap Kuit et al., "Extending 1.35 NA immersion lithography down to 1x nm production nodes," *Proc. SPIE* **8326**, 83260L (2012) [doi: 10.1117/12.915807].

Downloaded From: https://www.spiedigitallibrary.org/ebooks/ on 09 Mar 2022
Terms of Use: https://www.spiedigitallibrary.org/terms-of-use

18. Y. Borodovsky, "EUV lithography at insertion and beyond," 2012 International Workshop on EUV Lithography, 4–8 June, Maui, Hawaii.
19. G. M. Gallatin, "Resist blur and line edge roughness," *Proc. SPIE* **5754** (2005) [doi: 10.1117/12.607233].
20. H. J. Levinson, "The lithographer's dilemma: Shrinking without breaking the bank," *Proc. SPIE* **8886**, 888602 (2013) [doi: 10.1117/12.2030193].
21. S. Sayan, T. Marzook, B. T. Chan, N. Vandenbroeck, A. Singh, D. Laidler, E. A. Sanchez, P. Leray, P. R. Delgadillo, R. Gronheid, G. Vandenberghe, W. Clark, and A. Juncker, "Toward sub-20nm pitch Fin patterning and integration with DSA," *Proc. SPIE* **9779**, 97790R (2016) [doi: 10.1117/12.2220120].
22. J. Finders, M. Dusa, B. Vleeming, B. Hepp, M. Maenhoudt, S. Cheng, and T. Vandeweyer, "Double patterning lithography for 32 nm: critical dimensions uniformity and overlay control considerations," *J. Micro/Nanolith. MEMS MOEMS* **8**(1), 011002 (2009) [doi: 10.1117/1.3079349].
23. K. Xu, L. Souriau, D. Hellin, J. Versluijs, P. Wong, D. Vangoidsenhoven, N. Vandenbroeck, H. Dekkers, X. Shi, J. Albert, C. L. Tan, J. Vertommen, B. Coenegrachts, I. Orain, Y. Kimura, V. Wiaux, and W. Boullart, "Key contributors for improvement of line width roughness, line edge roughness, and critical dimension, uniformity: 15 nm half-pitch patterning with extreme ultraviolet and self-aligned double patterning," *J. Micro/Nanolith. MEMS MOEMS* **12**(4), 041302 (2013) [doi: 10.1117/1.JMM.12.4.041302].
24. H. J. Levinson, "Technological innovations for a sustainable business model in the semiconductor industry," *Proc. SPIE* **9189**, 91890E (2014) [doi: 10.1117/12.2060976].
25. H. Kinoshita, *Extreme Ultraviolet Lithography: Principles and Basic Technologies*, Lambert Academic Publishing, Saarbrücken, Germany (2016).
26. H. Kinoshita, K. Kurihara, Y. Ishii, and Y. Torii, "Soft x-ray reduction lithography using multilayer mirrors," *J. Vac. Sci. Technol. B* **7**(6), 1648–1651 (1989).
27. H.-J. Voorma and F. Bijkerk, "Design of an extended image field soft-x-ray projection system," *Microelectronic Engineering* **17**(14), 145–148 (1992).
28. E. Louis, "Physics and Technology Development of Multilayer EUV Reflective Optics," Ph.D. thesis, University of Twente, The Netherlands (2012).
29. J. E. Bjorkholm, J. Bokor, L. Eichner et al., "Reduction imaging at 14 nm using multilayer-coated optics: Printing of features smaller than 0.1 μm," *J. Vacuum Science and Technology B* **8**(6), 1509–1503 (1990).
30. T. E. Jewell, M. M. Becker, J. E. Bjorkholm, J. Bokor, L. Eichner, R. R. Freeman, W. M. Mansfield, A. A. MacDowell, M. L. O'Malley, E. L. Raab, W. T. Silfvast, L. H. Szeto, D. M. Tennant, W. K. Waskiewicz,

Downloaded From: https://www.spiedigitallibrary.org/ebooks/ on 09 Mar 2022
Terms of Use: https://www.spiedigitallibrary.org/terms-of-use

D. L. White, D. L. Windt, O. R. Wood, and J. H. Bruning, "20:1 projection soft x-ray lithography using Tn-level resist," *Proc. SPIE* **1263** (1990) [doi: 10.1117/12.20173].
31. D. A. Tichenor, G. D. Kubiak, M. E. Malinowski et al., " Development of a laboratory extreme ultraviolet lithography tool" *Proc. SPIE* **2194** (1994) [doi: 10.1117/12.175834].
32. P. Naulleau, K. A. Goldberg, E. Anderson et al., "EUV microexposures at the ALS using the 0.3-NA MET projection optics," *Proc. SPIE* **5751** (2005) [doi: 10.1117/12.600388].
33. Y. Tanaka, Y. Kikuchi, D. H. Goo, and I. Nishiyama, "Fidelity of rectangular patterns printed with 0.3-NA MET optics," *Proc. SPIE* **6517**, 65172L (2007) [doi: 10.1117/12.711900].
34. H. Tanaka, K. Tawarayama, S. Magoshi, and Y. Tanaka, "Current status of EUV exposure tools in Selete," http://www.sematech.org/meetings/archives/litho/8059/pres/ET-03-Tanaka.pdf (2007).
35. S. Tanaka, S. Magoshi, H. Kawai, S. Inoue, W. Rosenthal, L. Girard, L. Marchetti, B. Kestner, and J. Kincade, "Current development status of HSFET (High NA Small Field Exposure Tool) in EIDEC," *Proc. SPIE* **9776**, 97761N (2016) [doi: 10.1117/12.2219368].
36. P. Naulleau, A. Allezy, C. Anderson, C. Cork, P. Denham, M. Dickinson, G. Gaines, K. Goldberg, R. Miyakawa, S. Rekawa, W. Thur, D. Zehm, R. Soufli, R. Hudyma, M. Bremer, L. Girard, B. Kestner, J. Kincade, D. Ashworth, and K. Cummings, "Development of the SEMATECH Berkeley MET5 platform," 2014 International Symposium on Extreme Ultraviolet Lithography, 27–29 October, Washington, D.C.
37. H. Kinoshita, T. Watanabe, Y. Li, A. Miyafuji, T. Oshino, K. Sugisaki, K. Murakami, S. Irie, S. Shirayone, and S. Okazaki, "Recent advances of three-aspherical-mirror system for EUVL," *Proc. SPIE* **3997** (2000) [doi: 10.1117/12.390091].
38. H. Meiling, H. Meijer, V. Banine, R. Moors, R. Groeneveld, H.-J. Voorma, U. Mickan, B. Wolschrijn, B. Mertens, G. van Baars, P. Kürz, and N. Harned, "First performance results of the ASML alpha demo tool," *Proc. SPIE* **6151**, 615108 (2006) [doi: 10.1117/12.657348].
39. I. Mori, O. Suga, H. Tanaka, I. Nishiyama, T. Terasawa, H. Shigemura, T. Taguchi, T. Tanaka, and T. Itani, "Selete's EUV program: progress and challenges," *Proc. SPIE* **6921**, 692102 (2008) [doi: 10.1117/12.77625].
40. C. Wagner, J. Bacelar, N. Harned et al., "EUV Lithography at chipmakers has started: performance validation of ASML's NXE:3100," *Proc. SPIE* **7969**, 79691F (2011) [doi: 10.1117/12.878603].
41. H. N. Chapman, A. K. Ray-Chaudhuri, D. A. Tichenor, W. C. Replogle, R. H. Stulen, G. D. Kubiak, P. D. Rockett, L. E. Klebanoff, D. O'Connell, A. H. Leung, K. L. Jefferson, J. B. Wronosky, J. S. Taylor, L. C. Hale, K. Blaedel, E. A. Spiller, G. E. Sommargren, J. A. Folta, D. W. Sweeney,

Downloaded From: https://www.spiedigitallibrary.org/ebooks/ on 09 Mar 2022
Terms of Use: https://www.spiedigitallibrary.org/terms-of-use

E. M. Gullikson, P. Naulleau, K. A. Goldberg, J. Bokor, D. T. Attwood, U. Mickan, R. Hanzen, E. Panning, P.-Y. Yan, C. W. Gwyn, and S. H. Lee, "First lithographic results from the extreme ultraviolet engineering test stand," *J. Vac. Sci. Technol. B* **19**, 2389 (2001).

42. D. A. Tichenor, A. K. Ray-Chaudhuri, S. H. Lee et al. "Initial results from the EUV engineering test stand," *Proc. SPIE* **4506** (2001) [doi: 10.1117/12.450953].
43. D. A. Tichenor, A. K. Ray-Chaudhuri, W. C. Replogle, R. H. Stulen, G. D. Kubiak, P. D. Rockett, L. E. Klebanoff, K. J. Jefferson, A. H. Leung, J. B. Wronosky, L. C. Hale, H. N. Chapman, J. S. Taylor, J. A. Folta, C. Montcalm, R. Soufli, E. A. Spiller, K. L. Blaedel, G. E. Sommargren, D. W. Sweeney, P. P. Naulleau, K. A. Goldberg, E. M. Gullikson, J. Bokor, P. J. Batson, D. T. Attwood, Jr., K. H. Jackson, S. D. Hector, C. W. Gwyn, and P.-y. Yan, "System integration and performance of the EUV engineering test stand," *Proc. SPIE* **4343** (2001) [doi: 10.1117/12.436665].
44. N. Harned, M. Goethals, R. Groeneveld et al., "EUV lithography with the Alpha Demo Tools: status and challenges," *Proc. SPIE* **6517**, 651706 (2007) [doi: 10.1117/12.712065].
45. R. Peeters, S. Lok, J. Mallman, M. van Noordenburg, N. Harned, P. Kuerz, M. Lowisch, E. van Setten, G. Schiffelers, A. Pirati, J. Stoeldraijer, D. Brandt, N. Farrar, I. Fomenkov, H. Boom, H. Meiling, and R. Kool, "EUV lithography: NXE platform performance overview," *Proc. SPIE* **9048**, 90481J (2014) [doi: 10.1117/12.2046909].
46. D. De Simone, Y. Vesters, and G. Vandenberghe, "Photoresists in extreme ultraviolet lithography (EUVL)," *Advanced Optical Technologies* **6**(3/4), 159 (2017).
47. J. B. P. van Schoot, C. Valentin, K. van Ingen-Schenau, and S. Migura, "EUVL lithography scanner for sub 9 nm resolution," 2014 International Symposium on Extreme Ultraviolet Lithography, 27–29 October, Washington, D.C.
48. S. Migura, B. Kneer, J. T. Neumann, W. Kaiser, and J. van Schoot, "EUV lithography optics for sub 9 nm resolution," 2014 International Symposium on Extreme Ultraviolet Lithography, 27–29 October, Washington, D.C.
49. J. van Schoot, K. van Ingen Schenau, C. Valentin, and S. Migura, "EUV lithography scanner for sub 8 nm resolution," *Proc. SPIE* **9422**, 94221F (2015) [doi: 10.1117/12.2087502].
50. B. Kneer, S. Migura, J. T. Neumann, W. Kaiser, and J. van Schoot, "EUV lithography optics for sub-9nm resolution," *Proc. SPIE* **9422**, 94221G (2015) [doi: 10.1117/12.2175488].
51. J. van Schoot, E. van Setten, G. Rispens, K. Troost, B. Kneer, S. Migura, J. T. Neumann, and W. Kaiser, "High-numerical aperture extreme

Downloaded From: https://www.spiedigitallibrary.org/ebooks/ on 09 Mar 2022
Terms of Use: https://www.spiedigitallibrary.org/terms-of-use

ultraviolet scanner for 8-nm lithography and beyond," *J. Micro/Nanolith. MEMS MOEMS* **16**(4), 041010(2017) [doi: 10.1117/1.JMM.16.4.1010].
52. T. Neumann, P. Gräupner, W. Kaiser, R. Garreis, and B. Geh, "Interaction of 3D mask effects and NA in EUV lithography," *Proc. SPIE* **8522**, 852211 (2012) [doi: 10.1117/12.2009117].
53. J. T. Neumann, P. Gräupner, J. Ruoff, W. Kaiser, R. Garreis, and B. Geh, "3D reticle effects for high NA EUV lithography," 2012 International Symposium on Extreme Ultraviolet Lithography, 30 Sept. to 4 Oct., Brussels, Belgium.
54. J. T. Neumann, P. Gräupner, W. Kaiser, R. Garreis, and B. Geh, "Mask effects for high-NA EUV: impact of NA, chief-ray-angle, and reduction ratio," *Proc. SPIE* **8679**, 867915 (2013) [doi: 10.1117/12.2011455].
55. P. A. Kearney, O. Wood, E. Hendrickx, G. McIntyre, S. Inoue, F. Goodwin, S. Wurm, J. van Schoot, and W. Kaiser, "Driving the industry towards a consensus on high numerical aperture (high-NA) extreme ultraviolet (EUV)," *Proc. SPIE* **9048**, 90481O (2014) [doi: 10.1117/12.2048397].
56. L. Van Look, V. Philipsen, E. Hendrickx, N. Davydova, F. Wittebrood, R. de Kruif, A. van Oosten, T. Fliervoet, J. van Schoot, and J. T. Neumann, "Alternative EUV mask technology for mask 3D effect compensation," 2014 International Symposium on Extreme Ultraviolet Lithography, 27–29 October, Washington, D.C.
57. T. Kamo, K. Takai, K. Murano, Y. Morikawa, and N. Hayashi, "Status and outlook for etched multilayer EUV mask," 2014 International Symposium on Extreme Ultraviolet Lithography, 27–29 October, Washington, D.C.
58. J. T. Neumann, M. Rösch, P. Gräupner, S. Migura, B. Kneer, W. Kaiser, and K. van Ingen Schenau, "Imaging performance of EUV lithography optics configuration for sub-9nm resolution," *Proc. SPIE* **9422**, 94221F (2015) [doi: 10.1117/12.2175658].
59. L. de Winter, T. Last, N. Davydova, and J. Finders, "Understanding the litho-impact of phase due to 3D mask-effects when using off-axis illumination," *Proc. SPIE* **9661**, 96610A (2015) [doi: 10.1117/12.2195469].
60. T. Last, Z. Wang, P. van Adrichem, L. de Winter, and J. Finders, "Experimental verification of AI decomposition-based source optimization for M1 two-bar building blocks in 0.33NA EUVL," *Proc. SPIE* **9985**, 99850W (2016) [doi: 10.1117/12.2240862].
61. J. van Schoot, K. van Ingen-Schenau, G. Bottiglieri, K. Troost, J. Zimmerman, S. Migura, B. Kneer, J. T. Neumann, and W. Kaiser, "EUV high-NA scanner and mask optimization for sub 8 nm resolution," *Proc. SPIE* **9635**, 963503 (2015) [doi: 10.1117/12.2202258].
62. J. van Schoot, K. van Ingen-Schenau, G. Bottiglieri, K. Troost, J. Zimmerman, S. Migura, B. Kneer, J. T. Neumann, and W. Kaiser, "EUV high-NA scanner and mask optimization for sub 8 nm resolution,"

Downloaded From: https://www.spiedigitallibrary.org/ebooks/ on 09 Mar 2022
Terms of Use: https://www.spiedigitallibrary.org/terms-of-use

2015 International Symposium on Extreme Ultraviolet Lithography, Maastricht, The Netherlands.
63. J. van Schoot, E. van Setten, G. Bottiglieri, K. Troost, S. Migura, J.-T. Neumann, B. Kneer, and W. Kaiser, "EUV lithography high-NA scanner for sub 8 nm resolution," 2016 EUVL Workshop, Berkeley, California.
64. Y. Feurprier, K. Lutker-Lee, V. Rastogi, H. Matsumoto, Y. Chiba, A. Metz, K. Kumar, G. Beique, A. Lebonte, C. Labelle, Y. Mignot, B. Hamieh, and J. Arnold, "Trench and hole patterning with EUV resists using dual frequency capacitively coupled plasma (CCP)," *Proc. SPIE*. **9428**, 94280F (2015) [doi: 10.1117/12.2086519].
65. K. Petrillo, K. Cho, A. Fritz, C. Montgomery, D. Ashworth, M. Neisser, S. Wurm, T. Sato, L. Huli, A. Ko, and A. Metz, "Resist process applications to improve EUV patterning," *Proc. SPIE* **8679**, 867911 (2013) [doi: 10.1117/12.2011566].
66. C. Mack, "Reducing roughness in extreme ultraviolet lithography," 2017 International Symposium on Extreme Ultraviolet Lithography, 11–14 Sept. Monterey, California.
67. J. de Klerk, C. Wagner, R. Droste, L. Levasier, L. Jorritsma, E. van Setten, H. Kattouw, J. Jacobs, and T. Heil, "Performance of a 1.35NA ArF immersion lithography system for 40-nm applications," *Proc. SPIE* **6520**, 65201Y (2007) [doi: 10.1117/12.712094].
68. X. Liu, R. Howell, S. Hsu, K. Yang, K. Gronlund, F. Driessen, H.-Y. Liu, S. Hansen, K. van Ingen Schenau, T. Hollink, P. van Adrichem, K. Troost, J. Zimmermann, O. Schumann, C. Hennerkes, and P. Gräupner, "EUV source-mask optimization for 7nm node and beyond," *Proc. SPIE* **9048**, 90480Q (2014) [doi: 10.1117/12.2047584].
69. J. B. van Schoot, O. Noordman, P. Vanoppen, F. Blok, D. Yim, Ch.-H. Park, B.-H. Cho, T. Theeuwes, and Y.-H. Min, "CD uniformity improvement by active scanner corrections," *Proc. SPIE* **4691**, 304 (2002) [doi: 10.1117/12.474579].
70. M. A. van de Kerkhof, W. de Boeij, H. Kok, M. Silova, J. Baselmans, and M. Hemerik, "Full optical column characterization of DUV lithographic projection tools," *Proc. SPIE* **5377** (2004) [doi: 10.1117/12.536331].
71. M. J. M. Renkens, R. Tabor, G. van Baars, P. C. M. Frissen, H. Meiling, E. R. Loopstra, and H. Meijer, "Design of vacuum mechatronics for the ASML EUL Alpha," ASPE Proceedings, *Challenges at the Intersection of Precision Engineering and Vacuum Technology* (2006).
72. M. Renkens, R. Tabor, and T. Ruijl, "Providing precision mechatronic solutions for the challenges in EUV lithography," *Proc. ASPE, Precision Mechanical Design and Mechatronics for Sub-50nm Semiconductor Equipment* (2008).

Downloaded From: https://www.spiedigitallibrary.org/ebooks/ on 09 Mar 2022
Terms of Use: https://www.spiedigitallibrary.org/terms-of-use

73. H. Butler, "Position control in lithographic equipment: an enabler for current day chip manufacturing," *IEEE Control Systems* **31**(5), 28–47 (2011).
74. M. R. Sogard, A. R. Mikkelson, V. Ramaswamy, and R. L. Engelstad, "Analysis of Coulomb and Johnsen–Rahbek electrostatic chuck performance in the presence of particles for EUV lithography," *J. Micro/Nanolith. MEMS MOEMS* **8**(4), 041506 (2009) [doi: 10.1117/1.3238518].
75. A. Katalenic, "Control of Reluctance Actuators for High-Precision Positioning," Ph.D. thesis, Technische Universiteit Eindhoven, The Netherlands (2013).
76. I. J. C. Compter and P. C. M. Frissen, "Electro-dynamic planar motor," *Precision Engineering* **28**(2), 171–180 (2004).
77. B. M. Mertens, B. van der Zwan, P. W. H. de Jager, M. Leenders, H. G. C. Werij, J. P. H. Benschop, and A. J. J. van Dijsseldonk, "Mitigation of surface contamination from resist outgassing in EUV lithography," *Microelectronic Eng*. **53**(1–4), 659–662 (2000).
78. H. Vermeulen, " Thermal challenges for next generation EUV lithography systems," Paper presented at Euspen Conference Prague (March 18, 2016).
79. C. J. Martin, R. L. Engelstad, and E. G. Lovell, "Thermomechanical modeling of EUV reticle during exposure," *Proc. SPIE* **4343** (2001) [doi: 10.1117/12.436683].
80. L. Hartsough, "Electrostatic wafer holding," *Solid State Technology* **35**, 87–89 (1993).
81. L. Scaccabarozzi, D. Smith, P. Rizo Diago, E. Casimiri, N. Dziomkina, and H. Meijer, "Investigation of EUV pellicle feasibility," *Proc. SPIE* **8679**, 867904 (2013) [doi: 10.1117/12.2015833].
82. D. Brouns, "Development and performance of EUV Pellicles," *Advanced Optical Technologies* **6**(3–4) (2017).
83. R. van Es, M. van de Kerkhof, J. Jasper, L. Levasier, and R. Peeters, "EUV lithography industrialization progress NXE:3400B scanner for (sub) 7 nm single patterning," 2017 International Symposium on Extreme Ultraviolet Lithography, 11–14 Sept., Monterey, California.
84. J. van Schoot, K. Troost, F. Bornebroek, R. van Ballegoij, S. Lok, P. Krabbendam, J. Stoeldraijer, E. Loopstra, J. Benschop, J. Finders, H. Meiling, E. van Setten, B. Kneer, P. Kuerz, W. Kaiser, T. Heil, S. Migura, and J. T. Neumann, "High-NA EUV lithography enabling Moore's law in the next decade," 2017 International Symposium on Extreme Ultraviolet Lithography, 11–14 Sept., Monterey, California.
85. C. Gwyn and S. Wurm, "EUV LLC: An Historical Perspective," Chapter 2 in *EUV Lithography*, V. Bakshi, Ed., SPIE Press, Bellingham, Washington (2009) [doi: 10.1117/3.769214].

Downloaded From: https://www.spiedigitallibrary.org/ebooks/ on 09 Mar 2022
Terms of Use: https://www.spiedigitallibrary.org/terms-of-use

86. H. Meiling, P. Kuerz, B. D. Blum, G. J. Heerens, and N. Harmed, "The EUV program at ASML: an update," *Proc. SPIE* **5037** (2003) [doi: 10.1117/12.483706].
87. I. Fomenkov, A. Schafgans, S. Rokitski et al. "Industrialization of a laser produced plasma EUV light source for lithography," Conference on Lasers and Electro-Optics (CLEO), paper ATu4C.4, *OSA Technical Digest* (online) (2017).
88. B. Turkot, S. Carson, A. Lio, T. Liang, M. Phillips, B. McCool, E. Stenehjem, T. Crimmins, G. Zhan, and S. Sivakumar, "EUV progress toward HVM readiness," *Proc. SPIE* **9776**, 977602 (2016) [doi: 10.1117/12.2225014].
89. B. Turkot, "EUV lithography readiness for high volume manufacturing," presented at the SPIE 2017 Advanced Lithography conference Extreme Ultraviolet (EUV) Lithography VIII.
90. E. Abbe "Beiträge zur Theorie des Mikroskops und der mikroskopischen Wahrnehmung. In: Archiv für mikroskopische Anatomie," **9**(1), 413–468 (1873).
91. H. Kang, S. Hansen, J. van Schoot, and K. van Ingen Schenau, "EUV simulation extension study for mask shadowing effect and its correction," *Proc. SPIE* **6921**, 69213I (2008) [doi: 10.1117/12.772487].
92. A. Erdmann, P. Evanschitzky, J. T. Neumann, and P. Graeupner, "Mask-induced best-focus shifts in deep ultraviolet and extreme ultraviolet lithography," *J. Micro/Nanolith. MEMS MOEMS* **15**(2), 021205 (2016) [doi: 10.1117/1.JMM.15.2.021205].
93. Y. Ekincia, M. Vockenhuber, B. Terhalle, M. Hojeij, L. Wang, and T. R. Younkin, "Evaluation of resist performance with EUV interference lithography for sub-22 nm patterning," *Proc. SPIE* **8322**, 83220W (2012) [doi: 10.1117/12.916541].
94. I. A. Makhotkin, "Structural and Reflective Characteristics of Multilayers for 6.x nm wavelength," Ph.D thesis, University of Twente, The Netherlands (2013).
95. V. Banine, A. Yakunin, and D. Glushkov, "Next generation of EUV lithography: Challenges and opportunities," 2010 International Workshop on Extreme Ultraviolet Sources, 13–15 Nov., Dublin, Ireland.
96. K. Koshelev, V. Banin, V. Ivanov, G. Zukakishvili, V. Krivtsun, V. Koloshnikov, E. Korop, R. Gayazov, Yu. Sidelnikov, and V. Gomozov, "Some physical aspects of EUV source problem," SeMaTech EUV Source Workshop, Dallas, Oct. 2002.
97. T. Asami, "EUV exposure system development plan in Nikon," 2004 EUVL Symposium, 1–4 November, Miyazaki, Japan.
98. T. Oshino, M. Shiraishi, N. Kandaka, K. Sugisaki, H. Kondo, K. Ota, K. Mashima, K. Murakami, H. Oizumi, I. Nishiyama, and S. Okazaki, "Development of illumination optics and projection optics for high-NA EUV exposure tool (HiNA)," *Proc. SPIE* **5037**, 75–82 (2003) [doi: 10.1117/12.484936].

Downloaded From: https://www.spiedigitallibrary.org/ebooks/ on 09 Mar 2022
Terms of Use: https://www.spiedigitallibrary.org/terms-of-use

Jan B. P. van Schoot received his Ph.D. in physics at the University of Twente, the Netherlands in the field of non-linear optics. He joined ASML in 1996 and worked on the first 5500/500 scanner and Imaging Products (DoseMapper, Customized Illumination). In 2007 he became Senior Principle Architect in the department of System Engineering and was responsible for the optical columns of the NXE:3100 and NXE:3300B EUV systems. After this he worked on the design of the EUV source. Currently, he is study leader of the high-NA EUV system.

Hans C. M. Jasper joined ASML in 1985. From 1985 until 2006 he was system engineer for the different ASML platforms, Pas2500, Pas5500, and Twinscan. He was the product system engineer of the first catadioptric system, the XT:1700. Recently, he has been working as a system engineer on EUV systems. Hans Jasper studied phsics at the Eindhoven University of Technology. His thesis was on ionization phenomena in an argon plasma generated by shock waves. Before he joined ASML, he worked for the Netherlands Organization for Applied Scientific Research (TNO).

Downloaded From: https://www.spiedigitallibrary.org/ebooks/ on 09 Mar 2022
Terms of Use: https://www.spiedigitallibrary.org/terms-of-use

Chapter 10
EUVL System Patterning Performance

Patrick Naulleau
Center for X-ray Optics, Lawrence Berkeley National Laboratory, Berkeley, California, USA

Gregg Gallatin
Applied Math Solutions, LLC, Newtown, Connecticut, USA

10.1 Introduction: The Benefits of EUV Imaging
10.2 Parameters Affecting EUV Patterning Performance
10.2.1 Partial coherence
10.2.2 Aberrations and contrast
10.2.3 Flare and contrast
10.2.4 Chromeless phase-shift-mask printing in the EUV range
10.3 EUV and Aerial Image Variability
10.3.1 LER transfer from the mask to the wafer
10.3.2 Mask roughness effects on LER
10.3.3 Mask roughness effects on printed contact size variations
10.4 Stochastics in Patterning
10.4.1 Introduction
10.4.2 Photon stochastics: an analytic description
10.4.3 A stochastic model
10.4.4 Photon and material effects
10.4.5 Contact CDU limits
References

10.1 Introduction: The Benefits of EUV Imaging

The great promise of EUVL comes from its tremendous reduction in wavelength, it being a photon-based technology and thus free of charged-particle limitations, and it being a projection-based demagnifying system, avoiding the problems of 1X and contact masks. The latter two characteristics make it clear that EUVL is simply an extension of

Downloaded From: https://www.spiedigitallibrary.org/ebooks/ on 09 Mar 2022
Terms of Use: https://www.spiedigitallibrary.org/terms-of-use

conventional optical projection lithography, allowing us to leverage half a century of learning.

The standard lithographic resolution equation holds that

$$R = \left(\frac{k_1 \lambda}{NA}\right), \tag{10.1}$$

where λ is the imaging wavelength, NA is the numerical aperture, and k_1 is the Rayleigh constant. The Rayleigh constant is affected by several variables, including illumination conditions and mask architecture. Assuming a conservative k_1 factor of 0.5, which can be achieved readily with conventional illumination and a binary amplitude mask, the half-pitch resolution of a 0.3-NA EUV (13.5-nm wavelength) system would be 22.5 nm. Using resolution enhancement techniques such as off-axis illumination and/or phase shift masks, the ultimate resolution k_1 factor can be decreased to 0.25, corresponding to a 0.3-NA resolution limit of 11.25 nm.

Even further extendibility can be obtained by pushing the NA to 0.5 and beyond. At this NA, the resolution limits become 13.5 and 6.75 nm for $k_1 = 0.5$ and $k_1 = 0.25$, respectively. It is illustrative to view the simulated aerial images to understand the significance of the larger k_1 factor compared to that which we have grown accustomed to with 248- and 193-nm lithography. Figure 10.1 shows calculated aerial images for 0.35-NA and 0.50-NA EUVL systems with conventional disk illumination (partial coherence of 0.7) and a conventional binary mask with no optical proximity or bias correction. At 0.35 NA, strong image modulation is clearly observed even at the 16-nm half-pitch level, and increasing the NA to 0.5 readily takes us to 13-nm half-pitch.

As noted above, even better imaging performance can be achieved when we consider the use of techniques such as modified illumination and/or phase shift masks. One such technique is dipole illumination, which if applied to the 0.5-NA case, can achieve 8-nm half-pitch (Fig. 10.2). For dipole illumination, we assume a pole radius of 0.2 and a pole offset of 0.8 in the horizontal direction, providing resolution enhancement for vertical lines.

Another significant benefit of the lower NA of EUVL systems is the relatively large focus latitude it affords. The depth of focus (DOF) can be expressed in terms of the wavelength and the NA as

$$DOF = \frac{k_2 \lambda}{(NA)^2}, \tag{10.2}$$

where k_2 is a constant representative of the lithographic process conditions. A typical value for k_2 for a conventional illumination process is 0.5. For a

Downloaded From: https://www.spiedigitallibrary.org/ebooks/ on 09 Mar 2022
Terms of Use: https://www.spiedigitallibrary.org/terms-of-use

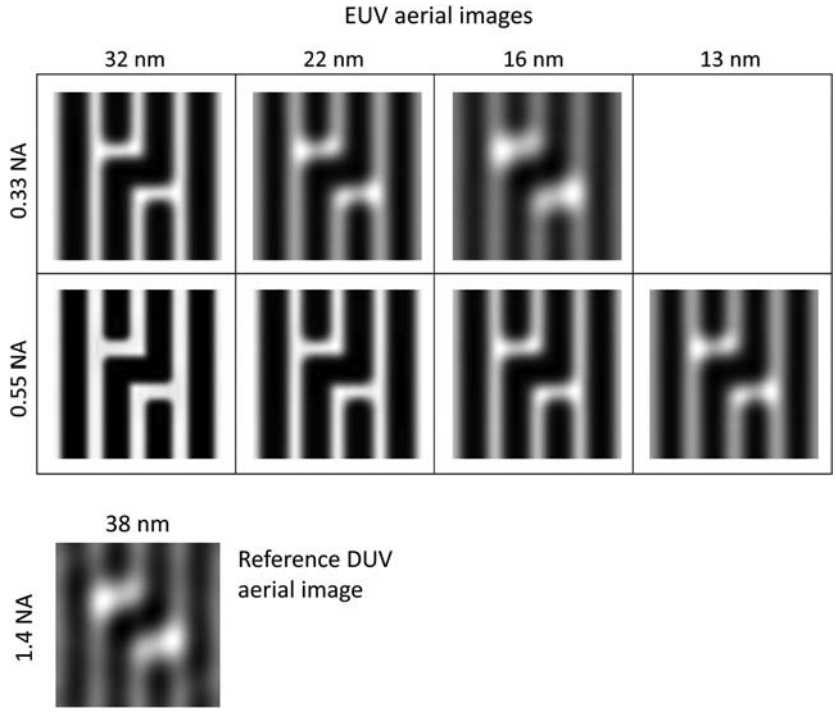

Figure 10.1 Aerial image modeling results for 0.33-NA and 0.55-NA EUV printing under general disk illumination with a partial coherence of 0.7 as compared to the reference DUV image of 38-nm half-pitch features, assuming a wavelength of 193 nm, a NA of 1.4, and optimized crosspole illumination.

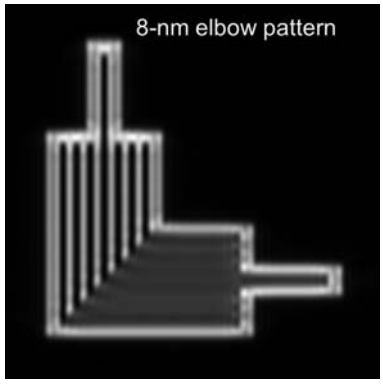

Figure 10.2 Aerial image modeling results for a 0.5-NA system with dipole illumination (pole radius = 0.2 and pole offset = 0.8) (reprinted from Ref. 49 with permission from McGraw-Hill).

0.3-NA system operating at its on-axis illumination diffraction limit (~22-nm half-pitch resolution), the DOF would be 75 nm. Using an optimized process, the DOF could be increased to 150 nm ($k_2 = 1$).

Downloaded From: https://www.spiedigitallibrary.org/ebooks/ on 09 Mar 2022
Terms of Use: https://www.spiedigitallibrary.org/terms-of-use

10.2 Parameters Affecting EUV Patterning Performance

10.2.1 Partial coherence

As described above, partial coherence (i.e., illumination settings) can impact the imaging performance of the system. The power of this approach is further demonstrated with the plot in Fig. 10.3, which shows the aerial image contrast $[(I_{max} - I_{min})/(I_{max} + I_{min})]$ as a function of half-pitch for a 0.32-NA EUV system under four different illumination conditions. For this example, we assume an ideal, aberration-free imaging system and an ideal binary mask.

10.2.2 Aberrations and contrast

The results presented in the previous subsection assume ideal optical systems with zero aberration. In practice, this is extremely difficult to achieve, especially in the EUV regime, where the short wavelength and reflective optics place extremely tight constraints on mirror shape errors. To quickly illustrate this effect, we consider aerial image contrast as a function of half-pitch for a 0.32-NA system with varying levels of aberration ranging from 0.25 nm to 1 nm rms (Fig. 10.4). Using the criterion of <1 nm impact on resolution, we find the aberration limit to be 0.25 nm or ~λ/50. Assuming a 6-mirror system and the errors on each of the mirrors to be uncorrelated, this yields a wavefront error limit of 100 pm for each mirror (a surface error limit of 50 pm).

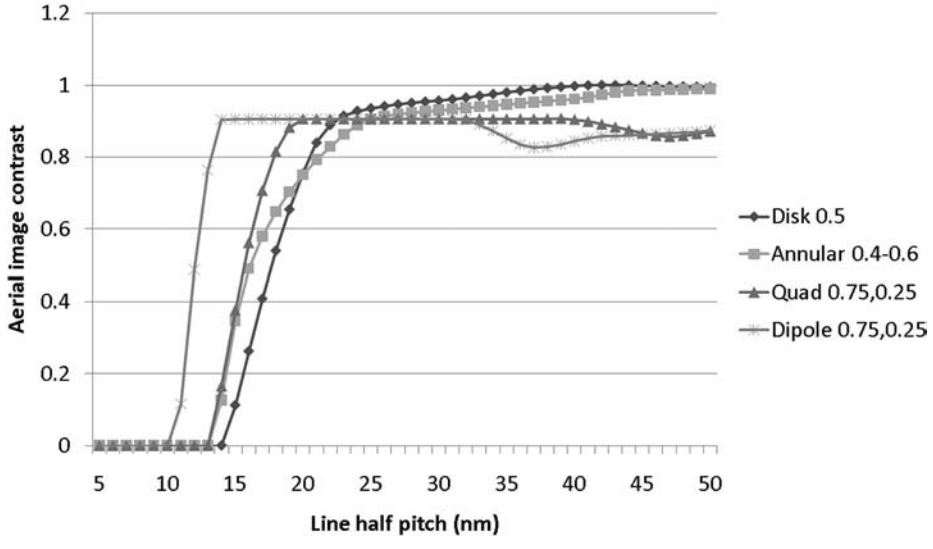

Figure 10.3 Aerial image contrast as a function of half-pitch for a 0.32-NA EUV system under four different illumination conditions (reprinted from Ref. 49 with permission from McGraw-Hill).

Downloaded From: https://www.spiedigitallibrary.org/ebooks/ on 09 Mar 2022
Terms of Use: https://www.spiedigitallibrary.org/terms-of-use

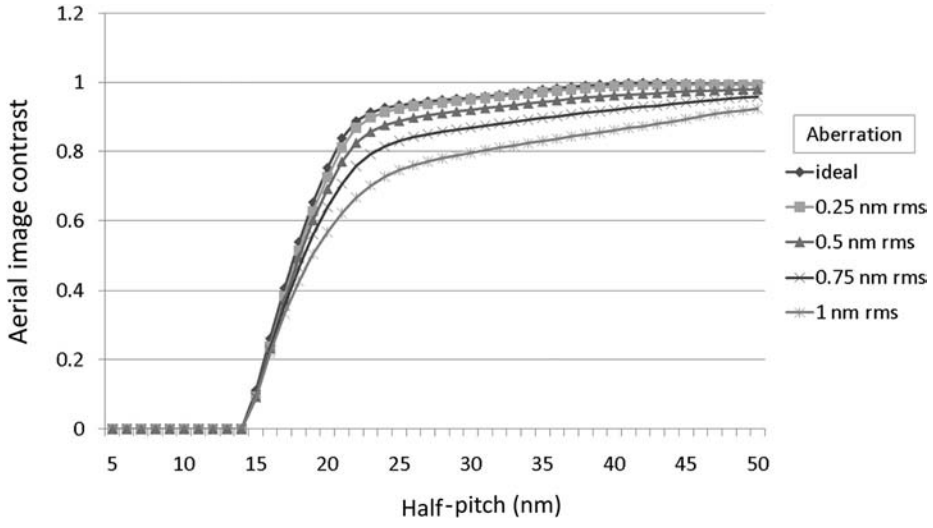

Figure 10.4 Aerial image contrast as a function of half-pitch for a 0.32-NA system with varying levels of aberration ranging from 0.25 nm to 1 nm (reprinted from Ref. 49 with permission from McGraw-Hill).

10.2.3 Flare and contrast

Mirror surface errors, which contribute to what we refer to as aberrations, are low-spatial-frequency errors. These errors are typically 10 cycles or less across the pupil and tend to affect the shape of the optical system point spread function. Finer spatial period errors on the mirrors (mid-spatial-frequency roughness), however, also play an important role in the imaging performance. Figure 10.5 shows how such errors in the pupil tend to scatter light (light purple rays) out of the point spread function (labeled 'Img' in the figure), creating a background halo of illumination into a large area surrounding the image point.

For high-quality (low roughness) optics, the total amount of light scattering into the halo, or total integrated scatter (TIS), can be expressed as

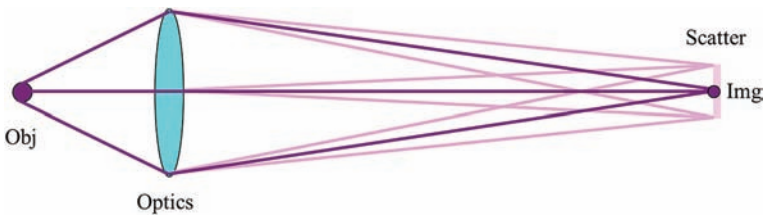

Figure 10.5 Mid-spatial-frequency roughness on the imaging optics causes light to be scattered out of the imaging cone, creating a background halo of illumination.

Downloaded From: https://www.spiedigitallibrary.org/ebooks/ on 09 Mar 2022
Terms of Use: https://www.spiedigitallibrary.org/terms-of-use

$$TIS \approx \left(\frac{4\pi\sigma_s}{\lambda}\right)^2, \tag{10.3}$$

where σ_s is the rms roughness of the surface, and λ is the imaging wavelength. The impact of this scattered light is to reduce the contrast through an effect called flare. Flare is defined as the amount of light seen at the center of an ideally dark feature that is significantly larger than the diffraction limit of the optic, ensuring that diffraction is not substantially contributing to the light seen at the center of the feature. This definition is depicted in Fig. 10.6. Flare will reduce the contrast of all feature sizes, and its total magnitude depends on the local feature density.

10.2.4 Chromeless phase-shift-mask printing in the EUV range

A significant benefit of EUVL is that it is simply an extension of optical lithography, which means that the toolbox of resolution enhancement techniques developed for optical lithography can also be applied to EUVL. One such example is modified illumination, as discussed Section 10.2.1. Another example is phase-shift-mask technology. Phase shift masks have played a crucial role in the extension of optical lithography and could also be used in the future to push EUVL to its ultimate limits. Another benefit of phase shift masks is their utility in print-based aberration measurement techniques.[1–3]

One method to generate a phase shift mask in the EUV range is to fabricate a relief pattern in the substrate and then overcoat with a multilayer (ML). This method is nearly identical to the method used to generate high-efficiency phase gratings in the EUV.[4–9] The method is illustrated schematically in Fig. 10.7, and a cross-section of a fabricated mask with

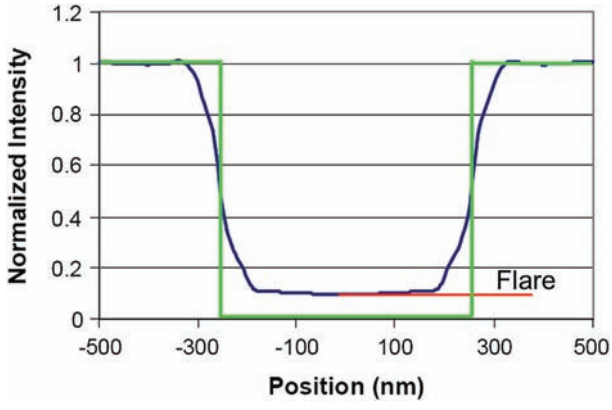

Figure 10.6 Light scattered out of the bright regions of the image and into ideally dark features is referred to as flare and reduces the contrast of the aerial image for all feature sizes.

Downloaded From: https://www.spiedigitallibrary.org/ebooks/ on 09 Mar 2022
Terms of Use: https://www.spiedigitallibrary.org/terms-of-use

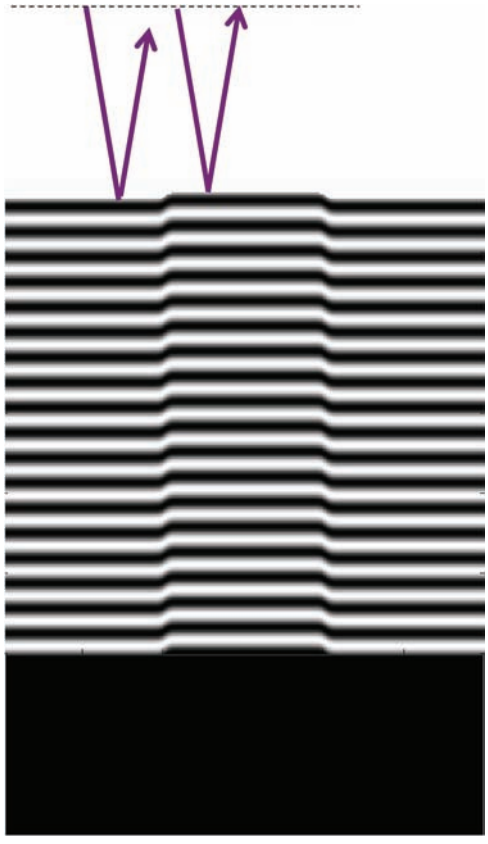

Figure 10.7 Diagram of relief-substrate phase-shift-mask method.

200-nm-pitch lines and spaces is shown in Fig. 10.8. Figure 10.9 shows through-focus printing of subresolution, isolated lines on a relief phase shift mask printed in a 0.1-NA EUV lithography tool. We define subresolution as structures on the mask with lateral dimensions smaller than the absolute diffraction limit of the optics [$0.25\lambda/(NA)$]. The printed feature size is on the order of 70 to 80 nm, near the resolution limit of the optic. Another demonstration of phase shift printing is shown in Fig. 10.10, where a large phase object is placed adjacent to an absorber feature (the mask layout is shown in Fig. 10.11). As expected from phase shift printing, only the outline of the large phase structure is printed.

The crucial problem with this method is the fact that the ML-coating process significantly limits the resolution of the phase features one can obtain on the mask. Since the time when this early work was done, a more sophisticated implementation of phase shift masks (including attenuated phase shift masks) based on ML etching has been developed and was demonstrated in a 0.3-NA exposure tool.[10] Another major benefit of using a

Downloaded From: https://www.spiedigitallibrary.org/ebooks/ on 09 Mar 2022
Terms of Use: https://www.spiedigitallibrary.org/terms-of-use

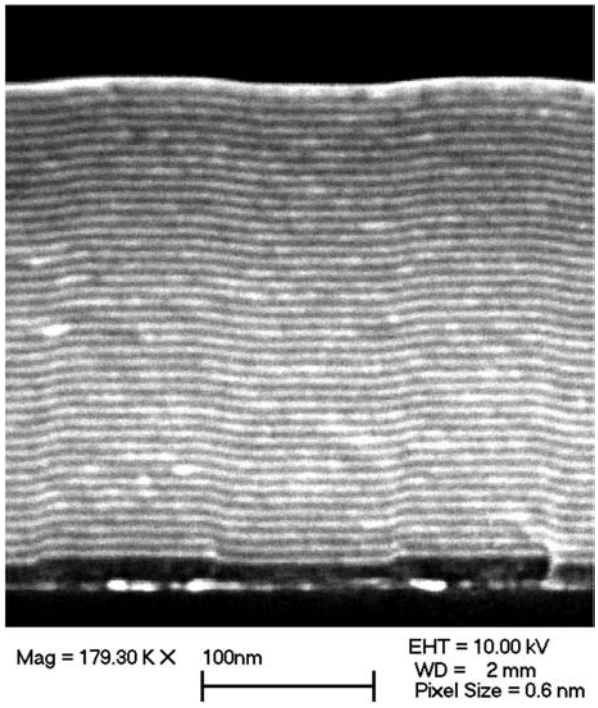

Figure 10.8 Cross-section of a fabricated mask with 200-nm pitch lines and spaces.

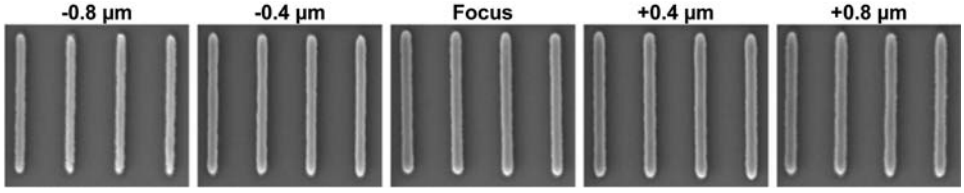

Figure 10.9 Through-focus printing of subresolution phase lines on the mask at 0.1 NA.

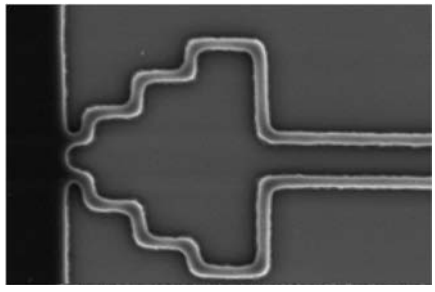

Figure 10.10 Printing of the large phase-shift structure in Fig. 10.11.

Downloaded From: https://www.spiedigitallibrary.org/ebooks/ on 09 Mar 2022
Terms of Use: https://www.spiedigitallibrary.org/terms-of-use

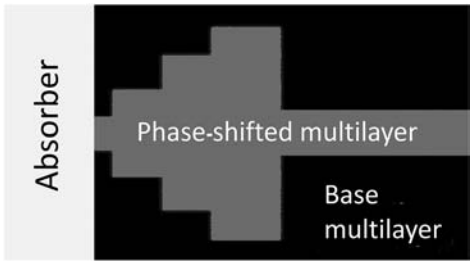

Figure 10.11 Mask layout corresponding to the printing in Fig. 10.10.

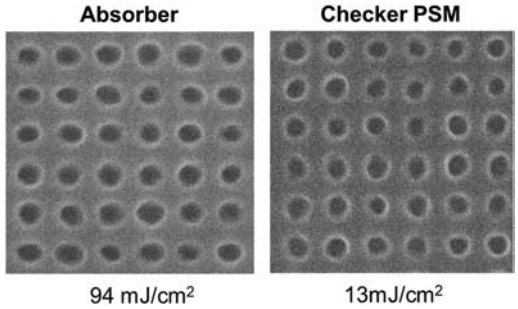

Figure 10.12 Direct lithographic patterning comparison of the conventional and the checker phase-shift mask (PSM) in the Berkeley 0.3-NA micro-exposure tool. Patterning of 25-nm contacts shows that the checker PSM provides a 7× efficiency gain relative to the conventional absorber mask (reprinted from Ref. 11).

phase shift mask is that removal of the absorber greatly improves the total optical throughput of the mask and thus the patterning tool.[11] This is especially valuable when considering contact hole features. Figure 10.12 shows patterning results for 25-nm dense contacts printed in a 0.3-NA lithography tool, directly comparing a conventional absorber mask to a chromeless phase shift mask. Note that the dose at the wafer is not actually changed, as must be the case since we are using the same resist. What is changed is the optical efficiency of the mask. This is important because if the resist were truly being patterned with 7× fewer photons at the resist, the stochastics would certainly suffer.

10.3 EUV and Aerial Image Variability

Pattern variability in the form of contact hole critical dimension uniformity (CDU) and line-edge/width roughness (LER/LWR) remains a significant challenge for EUVL. EUVL suffers from two primary EUV-specific challenges from this perspective: sub-nanometer phase roughness on the reflective mask and photon shot noise concerns arising from the high energy per photon. An additional mask source of patterning variability is mask

Downloaded From: https://www.spiedigitallibrary.org/ebooks/ on 09 Mar 2022
Terms of Use: https://www.spiedigitallibrary.org/terms-of-use

pattern roughness, which is very effectively coupled to the wafer as a result of the high resolution of EUV. Moreover, as we approach feature sizes in the single-digit nanometer regime, resist material stochastics also begin to play a crucial role.

10.3.1 LER transfer from the mask to the wafer

It is evident that roughness on the mask will, to some extent, transfer to roughness in the printed feature. In this section, we explicitly study this coupling using computer simulation methods. For an analytical description of this coupling, see Ref. 12, which presents the concept of the LER transfer function (LTF). This new transfer function differs fundamentally from both the conventional optical transfer function (OTF) and the modulation transfer function (MTF). Moreover, the experimental results in this section demonstrate the impact of current EUV masks on projection-lithography-based LER experiments.

The LTF concept can be readily studied through computer simulation. In addition to providing physical insight into the LTF, this method also facilitates the incorporation of parameters such as aberrations in the optical system and unconventional illumination conditions. One method for computer-based modeling of the LTF involves generating a mask pattern containing a white LER spectrum [Fig. 10.13(a)] and calculating the LER spectrum from the resulting aerial image [Fig. 10.13(b)]. Figure 10.14 shows the resulting input and output LER power spectral densities (PSDs). In this case, the 0.1-NA EUV Engineering Test Stand (ETS) Set-2 optic[13,14] is modeled. The aerial-image modeling includes the measured wavefront aberrations from the optic[15] and assumes partially coherent disk illumination with a coherence factor σ of 0.7. The mask is modeled as a simple thin binary mask.

The PSDs shown in Fig. 10.15 are actually averages from four separate simulations with four statistically independent white-noise LER masks. This averaging is performed to avoid gaps in the characterization frequencies,

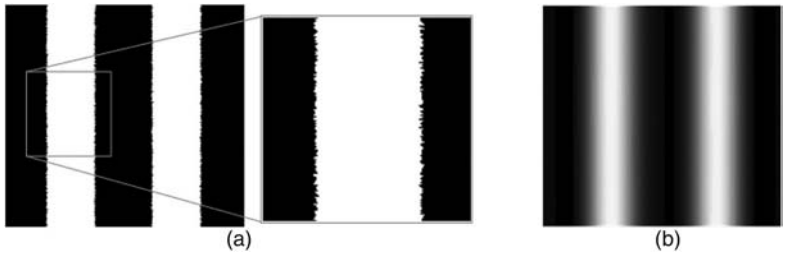

Figure 10.13 (a) LTF simulation input mask with a white LER spectrum and 100-nm features. (b) Computer-calculated aerial image assuming the 0.1-NA ETS Set-2 optic, including EUV-measured wavefront aberrations and assuming partially coherent illumination ($\sigma = 0.7$) (reprinted from Ref. 12).

Downloaded From: https://www.spiedigitallibrary.org/ebooks/ on 09 Mar 2022
Terms of Use: https://www.spiedigitallibrary.org/terms-of-use

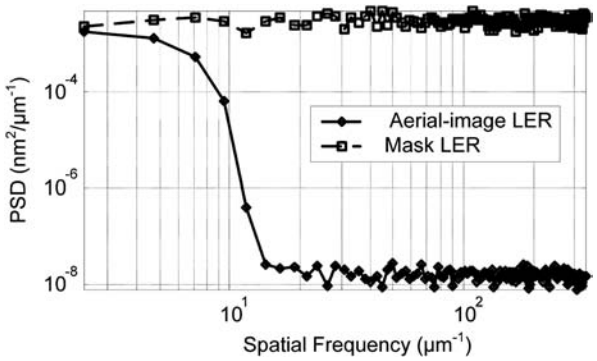

Figure 10.14 LER PSDs for the input mask (upper trace) and output aerial image (lower trace). The PSDs are averages of calculations from four independent realizations of the process described in Fig. 10.13 (reprinted from Ref. 12).

which occur when a single white-noise mask is used. The noise floor observed in the PSD is due to the pixilation limits in the various simulation and processing steps. We define the LTF as the square root of the aerial-image PSD divided by the white-noise mask PSD (Fig. 10.15). In the limit of infinite averaging, the white-noise mask PSD will, by definition, be uniform, and the aerial-image PSD equals the white-noise mask PSD at a spatial frequency of 0. Thus, the LTF can be taken simply as the square root of the normalized aerial-image LER PSD in the infinite averaging limit.

Next we consider the alternative calculation approach that uses a series of mask patterns, each with a unique LER frequency, then determining the LER from the resulting aerial images. This method provides a discrete sampling of the LTF. Figure 10.16(a) shows an example of a sinusoidal LER mask with an LER period of 210 nm and a feature CD of 100 nm; Fig. 10.16(b) shows the calculated aerial image. This serves as a single-frequency probe of the LTF. By generating a variety of these single-frequency probes, the LTF can be

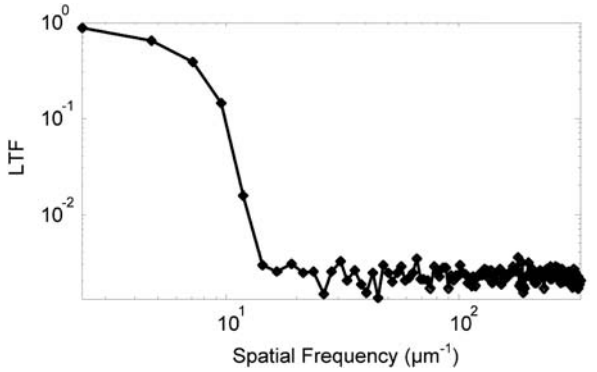

Figure 10.15 LTF derived by taking the square root of the aerial-image LER PSD divided by the white-noise mask PSD from Fig. 10.13 (reprinted from Ref. 12).

Downloaded From: https://www.spiedigitallibrary.org/ebooks/ on 09 Mar 2022
Terms of Use: https://www.spiedigitallibrary.org/terms-of-use

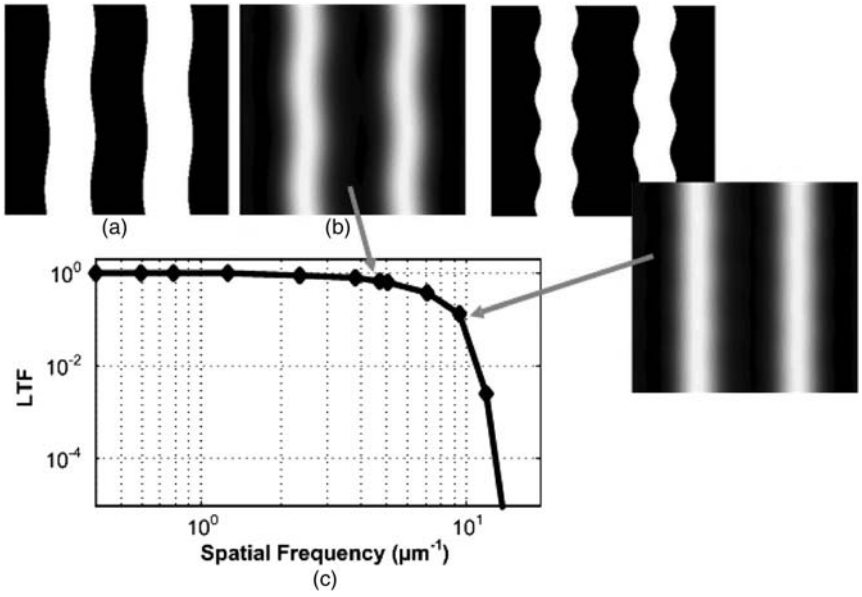

Figure 10.16 (a) Example of a probe mask. (b) Aerial image resulting from the probe mask. (c) LTF generated by calculating the system response to a series of single-frequency LER probes (reprinted from Ref. 12).

constructed as shown in Fig. 10.16(c). The linearity of this process was verified by considering a single spatial frequency at three different amplitudes covering an order of magnitude. As required for linearity, the ratio of the output LER magnitude to input LER magnitude was found to be independent of the input LER magnitude.

Figure 10.17 shows a direct comparison of the two LTF modeling methods presented above as well as the analytical LTF from Ref. 12. The analytical LTF is depicted by the solid trace, the white-noise-calculated LTF is depicted by the diamond symbols, and the single-frequency-probe-calculated LTF is depicted by the square symbols. The various LTF calculation methods agree extremely well. The small differences between the modeling methods and the analytical method can be attributed to the incorporation of the wavefront error in the modeling methods, which causes the modulation to drop slightly relative to the diffraction-limited case.

Finally, it is also interesting to directly compare the LTF to the more conventional MTF. Figure 10.18 shows the MTF (solid trace), the white-noise-calculated LTF (diamond symbols), and the single-frequency-probe-calculated LTF (square symbols). What is referred to here as the MTF is actually the square wave transfer function under partially coherent illumination, where the illumination conditions are identical to those described above for the LTF modeling. The LTF has a sharper roll-off than that of the MTF. The faster roll-off is due to the 2D nature of the LER and its interaction with

Downloaded From: https://www.spiedigitallibrary.org/ebooks/ on 09 Mar 2022
Terms of Use: https://www.spiedigitallibrary.org/terms-of-use

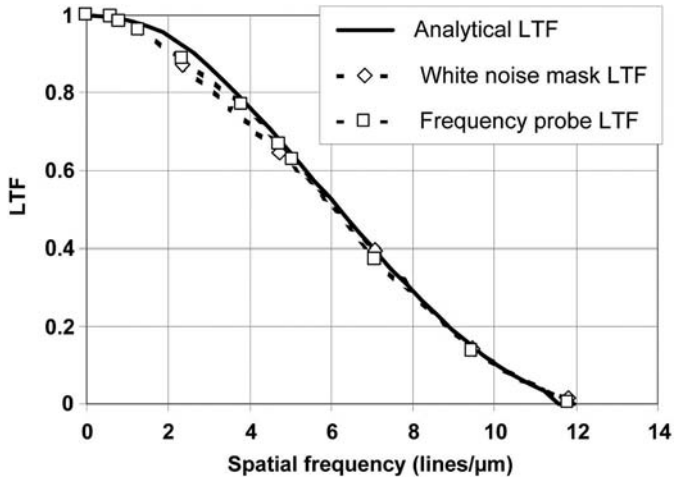

Figure 10.17 Direct comparison of the two LTF modeling methods and the analytical LTF calculation. The analytical LTF is depicted by the solid trace, the white-noise-calculated LTF is depicted by the diamond symbols, and the single-frequency-probe-calculated LTF is depicted by the square symbols (reprinted from Ref. 12).

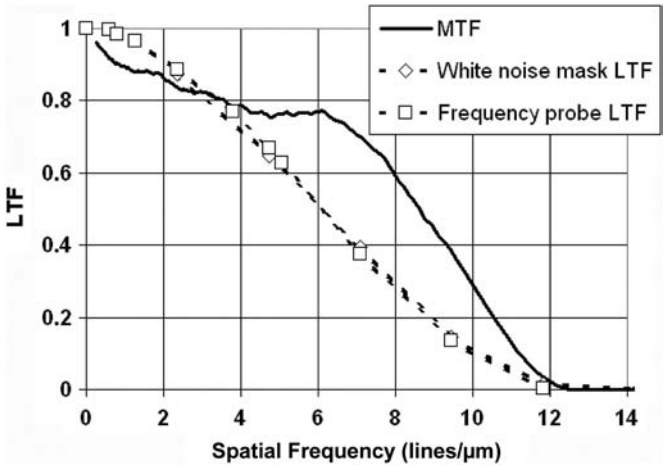

Figure 10.18 Direct comparison of LTF and MTF. What is referred to here as the MTF is actually the square wave transfer function under partially coherent illumination, where the illumination conditions are identical to those described for LTF modeling (reprinted from Ref. 12).

the point spread function (PSF) compared to a pure 1D line situation treated by the MTF. The LER coupling is stronger than predicted by the MTF at very low frequencies because the low end of the MTF reduction is dominated by flare (effectively a DC background), which does not affect LER coupling. In the case of low-frequency structures affected by flare, the pattern will be faithfully reproduced with a simple DC offset since the LER

Downloaded From: https://www.spiedigitallibrary.org/ebooks/ on 09 Mar 2022
Terms of Use: https://www.spiedigitallibrary.org/terms-of-use

is quantified, assuming an ideal threshold resist model for which flare has little effect on the LER. This may not be the case for actual resist LER, in which case the reduced line-edge slope could increase the LER, yet this effect is fundamentally different from the mask-LER-coupling issue of concern here.

10.3.2 Mask roughness effects on LER

10.3.2.1 Influence of partial coherence

Independent of intensity fluctuations in the image plane, which are due to mask roughness and can cause LER, as discussed in the following sections, the partial coherence itself has residual intensity fluctuations that depend on the exposure time and the bandwidth of the light, and can contribute to LER. Classically speaking, all light is perfectly coherent, and so the intensity distribution produced by a combination of sources with uncorrelated (but fixed) phases and precisely the same wavelength will always produce a fully developed speckle pattern. However, if the sources have a finite distribution of wavelengths, i.e., a finite bandwidth, then the relative phases of the sources change with time, as does the speckle pattern. Hence, if the exposure time is sufficiently long compared to the rate at which the speckle pattern changes, then the net or integrated intensity will be effectively uniform. It is this fact that allows various source pupil fills—top hat, annular, quadrupole, dipole, etc.—to produce an essentially uniform illumination dose distribution instead of the intensity distribution associated with the Fourier transform of the source pupil geometry.[40,41]

A single monochromatic speckle pattern is stationary in time and has 100% contrast; i.e., it has at least one, but usually many, points where the intensity is exactly zero. The sum or net intensity of N uncorrelated speckle patterns has an average contrast of [100/sqrt(N)]%, so the net intensity of say 10,000 uncorrelated speckle patterns has a contrast (at the rms or 1σ level) of 1%. This is illustrated in Fig. 10.19 for a random-phase, top-hat fill geometry with the net or residual speckle contrast shown in Fig. 10.20.

To estimate the contrast or, equivalently, the nonuniformity of the residual speckle in a lithographic illumination system, we thus need to estimate the number of spatially uncorrelated speckle patterns. This is given by the total exposure or dose time T divided by the coherence time τ of the illumination. The coherence time in terms of the bandwidth is given by

$$\tau \simeq \frac{1}{2\pi\Delta\nu} \simeq \frac{1}{2\pi c}\frac{\lambda^2}{\Delta\lambda}, \tag{10.4}$$

where c is the speed of light, $\Delta\nu$ is the bandwidth in hertz, λ is the center wavelength, and $\Delta\lambda$ is the bandwidth in nanometers. For pulsed illumination systems, the total exposure or dose time is the number of pulses times the

Downloaded From: https://www.spiedigitallibrary.org/ebooks/ on 09 Mar 2022
Terms of Use: https://www.spiedigitallibrary.org/terms-of-use

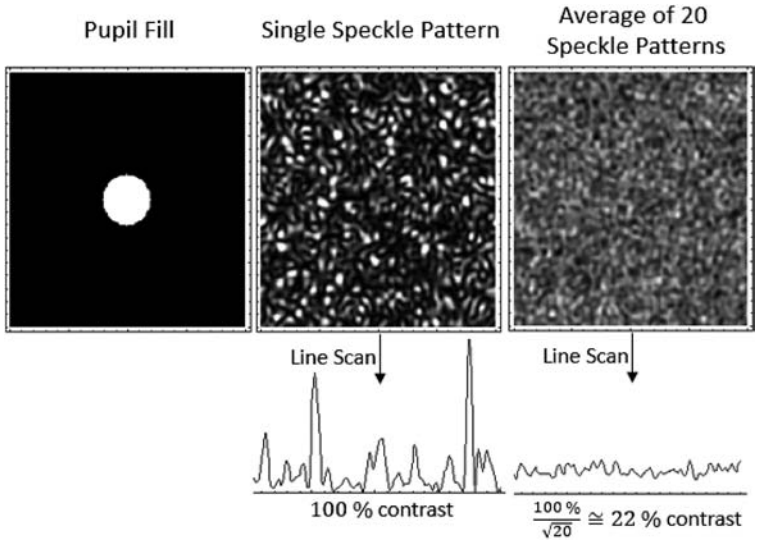

Figure 10.19 A strictly monochromatic random-phase, top-hat pupil fill (left) generates a 100% contrast speckle pattern (middle). The average of 20 uncorrelated speckle patterns produced by the same top-hat pupil fill (right) yields a final speckle contrast of approximately 22%.

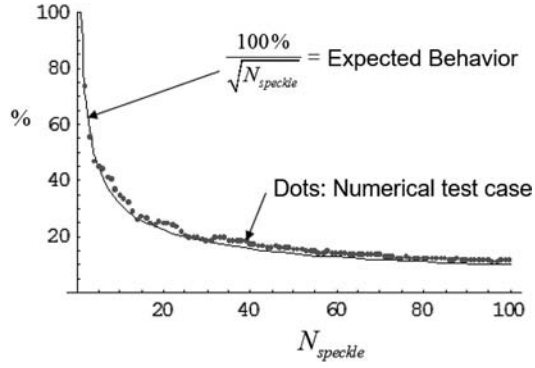

Figure 10.20 Numerical evaluation of the decrease in contrast with the number of uncorrelated speckle patterns that contribute to the total dose. At 10,000 uncorrelated speckle patterns contributing to the total dose, the residual illumination nonuniformity at the 1σ level will be on the order of 1%.

temporal length of each pulse. The bandwidth of EUVL is nominally determined by the passband of the ML optics, which is approximately 2% of 13.5 nm, or $\Delta\lambda/\lambda = 0.02$, yielding a coherence time of approximately 1.4×10^{-19} s. Pulse lengths for EUV illumination sources are expected to be on the order of tens of nanoseconds, and the number of pulses per dose is expected to be on the order of a few tens of pulses. Thus, assuming a total exposure time of only 100 ns, we still have more than 10^{10} independent speckle patterns to

Downloaded From: https://www.spiedigitallibrary.org/ebooks/ on 09 Mar 2022
Terms of Use: https://www.spiedigitallibrary.org/terms-of-use

average over and thus a temporal-coherence-limited speckle contrast of less than 0.001%. Clearly, temporal coherence is not a concern for EUVL. It should be remembered that this conclusion assumes that the 10^{10} speckle patterns are independent or uncorrelated. Depending on the illuminator design and/or the illumination settings, this condition may not be satisfied, in which case, the speckle patterns may not average to a uniform illumination.

10.3.2.2 Mask-roughness-induced LER

Another potentially important contributor to aerial-image variability from the mask is ML roughness coupling to speckle in the aerial image and, consequently, LER in the printed pattern.[16,17] Because EUVL relies on reflective masks, it is particularly vulnerable to this problem. Mask roughness is geometrically coupled to phase roughness, scaled by a factor of 2 due to the reflection. Given the 13.5-nm wavelength, very small levels of roughness on the ML-coated mask can contribute to significant modulation of the phase. Although the lithographic process involves re-imaging the mask surface to the wafer, the process remains sensitive to phase errors at the mask by virtue of the band-limited imaging process. Moreover, as defocus is introduced into the system, the imaging condition no longer strictly holds, and phase errors at the mask directly couple to intensity variation or speckle. The problem becomes increasingly severe as the illumination coherence is increased,[18] which is often done for resolution-enhancing pupil fills.

In principle, the question of mask surface roughness coupling to LER can be understood analytically using partially coherent image formation theory coupled with the statistical representation of the mask as a random phase object.[17] However, the problem quickly becomes intractable even under the small-phase-perturbation approximation. Moreover, the analytic solution becomes even more complex as defocus or other aberrations are considered.

An alternative analytical approach could use geometric optics while describing the rough mask in terms of local slope error. Although this simple approach provides a convenient mechanism for visualizing defocus effects, it completely fails to account for the impact of partial coherence on the process. Given that the mask-roughness-induced LER is fundamentally a speckle issue,[18] coherence plays a crucial role. Moreover, the extent to which speckle (small spatial scale intensity variation) couples to LER depends on the aerial-image line-edge slope. Given a fixed speckle contrast, the LER would be worse with a smaller line-edge slope. This factor, however, is not captured by the geometric analysis.

Given the difficulties with the analytic approaches described above, numeric modeling of the partially coherent imaging process remains the most viable method for studying relevant cases of mask-roughness-induced LER. This approach has previously been used to study the in-focus dependence of LER on mask roughness and illumination partial coherence.[19] The numeric

Downloaded From: https://www.spiedigitallibrary.org/ebooks/ on 09 Mar 2022
Terms of Use: https://www.spiedigitallibrary.org/terms-of-use

modeling approach can also be readily extended to study arbitrary imaging conditions, including defocus as well as any other wavefront aberration.

The modeling described below relies on a numeric implementation of partial-coherence image-formation equations[18] coupled with a random-phase object description of the mask. Defocus as well as other aberrations can be accounted for by modifying the pupil function of the modeled imaging system.

Of significant concern for analyzing meaningful situations of mask-roughness-induced LER is the roughness description in the model. Masks used in EUVL are reflective and are rendered so through the deposition of a ML coating typically comprising 40 or more bilayers.[20] If one starts with knowledge of the uncoated substrate surface, ML growth models can be used to predict the coating properties throughout the stack.[21,22] From the calculated coating properties, rigorous electromagnetic field modeling could be used to calculate the electric field reflected from the mask.[46–48] However, such an approach would be extremely time consuming. In most cases relevant to the moderate roughness of interest here, the effect of the rough mask can be readily modeled as a pure phase distribution, where the phase is determined from the geometric path-length differences imparted by assuming the EUV light to be reflected from the top surface of the mask.[23] In practice, this simplification works because the vast majority of the non-conformal ML growth occurs within a small number of layers closest to the substrate. Within the EUV penetration region of a typical 40-or-more-bilayer ML coating, the layer growth tends to be conformal for the roughness range of interest here. Using this simplified approach, one only needs to measure the topographic profile of the final ML-coated mask.

To consider the importance that mask surface roughness may have on LER, we performed a numeric study using the modeling methods described above in combination with the simplified representation of the mask roughness. The parameters we chose were selected to coincide with EUV print tests performed using a 4×-reduction optical system with a NA of 0.1. The roughness of the mask used in those tests was measured after final patterning using AFM (Fig. 10.21). The measured 0.54-nm rms roughness of that mask was approximately a factor of 5 worse than typical high-quality masks available today. To generate the input mask used in the simulations presented here, the mask surface PSD was calculated (Fig. 10.22) from the AFMs and was used to generate a statistical surface of the proper size. Assuming a wavelength of 13.4 nm, the topographic surface was converted to a phase perturbation. This phase distribution was then overlain (multiplied) by an ideal binary amplitude line/space pattern. Figure 10.23 shows the resulting 4× input mask for features designed to print as 100-nm lines and spaces. The completely black areas represent the absorber regions, and the grayscale areas represent the wrapped phase of the clear regions on the mask. Although the mask rms surface roughness was only 0.54 nm, upon reflection, the induced peak-to-valley phase modulation was greater than 1 wave (2π) based on an illumination wavelength of 13.4 nm.

Downloaded From: https://www.spiedigitallibrary.org/ebooks/ on 09 Mar 2022
Terms of Use: https://www.spiedigitallibrary.org/terms-of-use

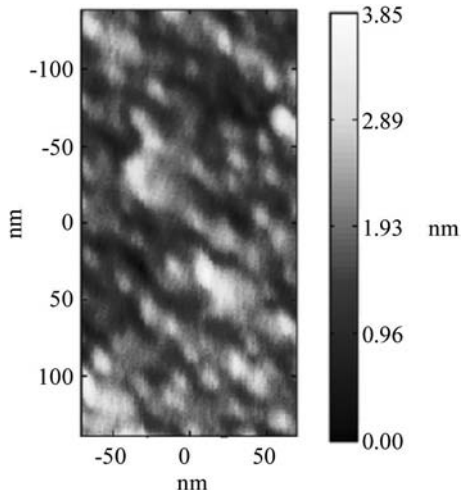

Figure 10.21 AFM image from a clear area on an EUV mask fabricated for printing with a 0.1-NA optic. The rms roughness is 0.54 nm (reprinted from Ref. 19).

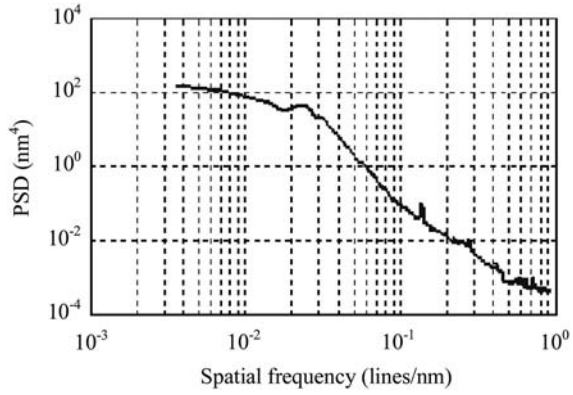

Figure 10.22 Isotropic PSD based on the AFM in Fig. 10.21 (reprinted from Ref. 19).

Figure 10.24 shows simulation results for three different printed linewidths as a function of focus and the coherence factor σ. An ideal 0.1-NA EUV optical system has been assumed. The small NA assumed in this case allows the aerial-image modeling to be performed under the thin mask and scalar approximations. An ideal binary resist model is used, and the threshold is set separately for each σ value to provide proper sizing of the 100-nm lines at best focus. The single-sided 3σ LER is then calculated from the resulting binary image as the deviation of the measured line edge from a straight line. Interpolation of the line edge allows the actual threshold position to be determined to subpixel resolution. For the results presented in this section, an image-space pixel spacing of 1.57 nm was used. In practice, this interpolation is crucial because it allows the aerial-image simulations to be performed over a grid size amenable to current memory

Downloaded From: https://www.spiedigitallibrary.org/ebooks/ on 09 Mar 2022
Terms of Use: https://www.spiedigitallibrary.org/terms-of-use

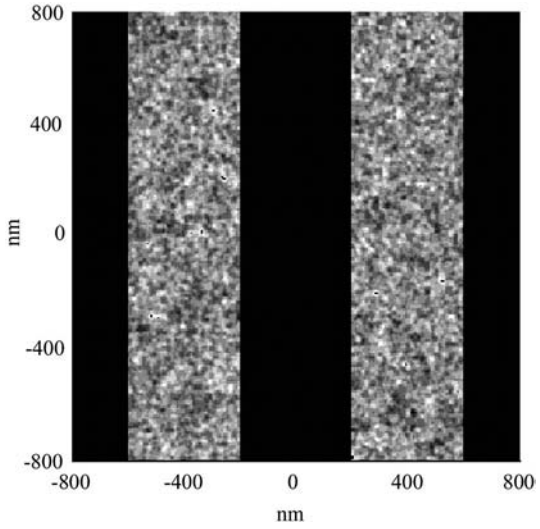

Figure 10.23 Representative input 4× mask for aerial-image simulations. Phase roughness is generated based on the PSD in Fig. 10.22. This particular mask is designed to model 100-nm printed line/space patterns. The solid black regions represent the chrome absorber, and the grayscale regions represent the wrapped phase, where black is 0 and white is 2π (reprinted from Ref. 19).

and processing limitations. This is especially important if compute-intensive 3D modeling is used to determine the aerial image. In general, the LER gets worse at smaller linewidths, presumably due to the decreased aerial-image line-edge slope. Defocus also plays a crucial role in the mask-roughness-to-LER coupling, with increased coherence enhancing the effect. The increased coherence effect appears to saturate at approximately $\sigma = 0.4$, with LER trends even reversing in some cases. It is interesting to note that at best focus, we see very little dependence of LER on the coherence factor and consistently observe the LER to increase with σ (decreasing coherence).

A more detailed analysis, including a discussion of the importance of statistical variation in the simulation results, can be found in Ref. 19. The statistical analysis results validate the trends shown in Fig. 10.24, including reduced LER with increasing coherence at best focus. These results also indicate that the coherence effect saturates at approximately $\sigma = 0.4$ and suggest that the trend reversals with coherence shown in Fig. 10.24 are not systematic but rather a manifestation of statistical uncertainty.

Given the strong influence of defocus and the fact that defocus can be thought of simply as an aberration, it is also interesting to consider the effects that lens aberrations may produce in the process. A study of these effects can also be found in Ref. 19. For the $\lambda/20$ wavefront error case considered, the results show no significant difference compared to the aberration-free case.

Downloaded From: https://www.spiedigitallibrary.org/ebooks/ on 09 Mar 2022
Terms of Use: https://www.spiedigitallibrary.org/terms-of-use

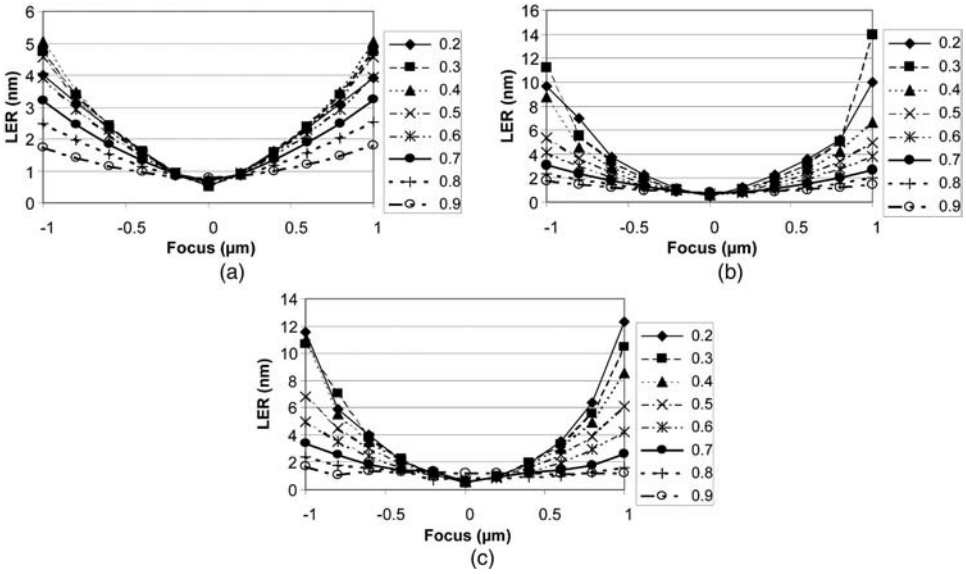

Figure 10.24 Simulation results for three different printed linewidths as a function of focus and the coherence factor σ: (a) 100-nm lines and spaces, (b) 90-nm lines and spaces, and (c) 80-nm lines and spaces. An ideal 0.1-NA EUV optical system has been assumed. A binary resist model is used with the threshold set separately for each σ value to provide proper sizing of the 100-nm lines at best focus. The single-sided 3σ LER is then calculated from the resulting binary image (reprinted from Ref. 19).

Given the importance of the LER issue for resist development, it is also crucial to consider the expected importance of mask roughness on recent LER studies. Again, this has been considered in detail in Ref. 19. The results indicate that for a 0.1-NA system with a 0.5-nm rms roughness assumed, the mask contribution to LER is negligible provided that focus is adequately controlled.

Next we consider the impact of the NA by studying the mask phase roughness effect on LER for the 0.3-NA micro-exposure-tool (MET) case. To this end, we generated a new set of simulation masks that correspond to printed linewidths ranging from 25 to 50 nm. To generate the roughness on the masks, we used the same PSD as described in Fig. 10.22 while decreasing its magnitude by a factor of 2 to more accurately represent slightly more recent mask-fabrication capabilities.[24–26] In all cases, annular illumination with an inner σ of 0.3 is assumed, while the outer σ is allowed to vary from 0.4 to 0.8. The simulated focus range is ±150 nm, with ±100 nm being the nominal design DOF for 30-nm features.

Figure 10.25 shows the modeled LER results through focus for feature sizes from 50 to 40 nm, and Fig. 10.26 for feature sizes from 35 to 25 nm. The major trends are similar to those observed with the 0.1-NA case in that the LER tends to worsen as the coherence is increased, the feature size is reduced, and the defocus is increased. The trend of LER improving with increased

Downloaded From: https://www.spiedigitallibrary.org/ebooks/ on 09 Mar 2022
Terms of Use: https://www.spiedigitallibrary.org/terms-of-use

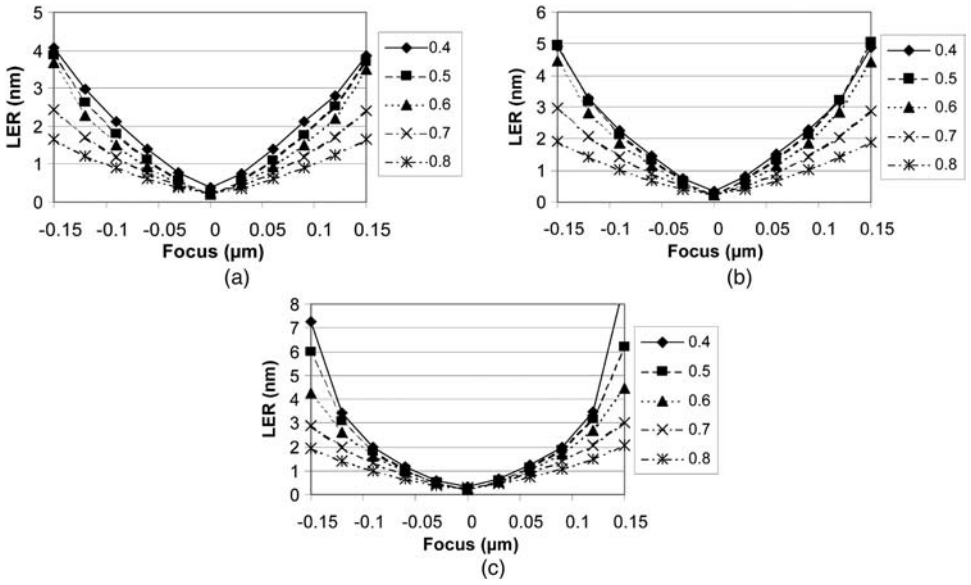

Figure 10.25 LER modeling results for the 0.3-NA MET optic design. Each plot represents a different nested-feature size: (a) 50 nm, (b) 45 nm, and (c) 40 nm. In all cases the illumination is annular with an inner σ of 0.3, and the individual traces represent different outer σ values.

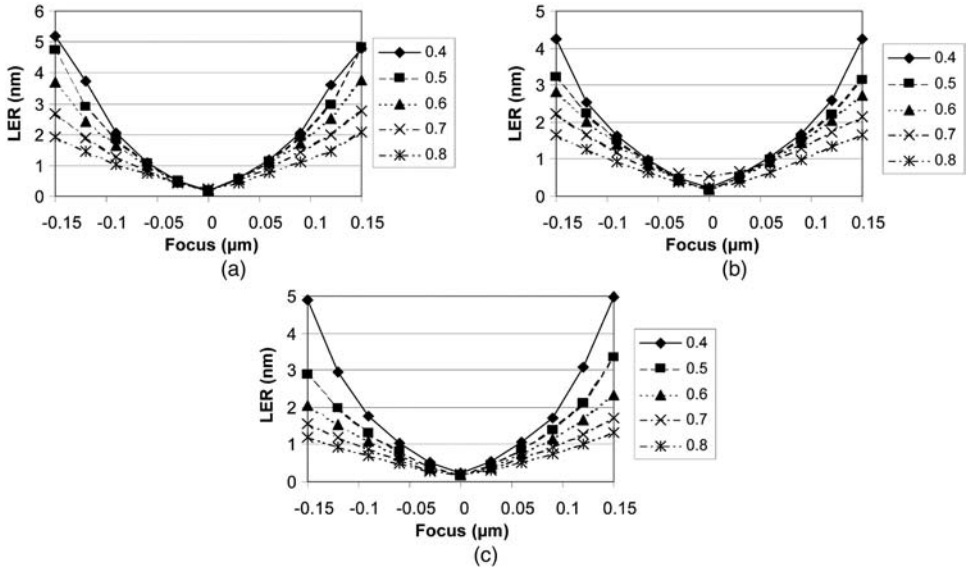

Figure 10.26 LER modeling results for the 0.3-NA MET optic design. Each plot represents a different nested-feature size: (a) 35 nm, (b) 30 nm, and (c) 25 nm. In all cases the illumination is annular with an inner σ of 0.3, and the individual traces represent different outer σ values.

Downloaded From: https://www.spiedigitallibrary.org/ebooks/ on 09 Mar 2022
Terms of Use: https://www.spiedigitallibrary.org/terms-of-use

coherence at best focus is not evident in this case, which is most likely due to the inner annulus of the illumination being so close to the edge of the central obscuration that it yields significant filtering effects from the pupil. Other anomalies are also observed, such as decreasing LER with decreasing feature size at some coherence settings. An example of this is the LER trend from 40 to 30 nm for an outer σ of 0.5 and smaller. This may be caused by an interaction between the diffracted orders from the object pattern and the central obscuration. Finally, these simulations show that at the edge of focus, the mask-roughness-induced LER accounts for the entire specified resist LER budget for the 45-nm node unless very low coherence is used. This means that extreme care must be taken when using such a system for LER screening of a resist. Assuming subsequent nodes to have even tighter LER specifications, the problem becomes even more acute.

10.3.3 Mask roughness effects on printed contact size variations

Next we consider the contact equivalent to LER—contact size variation—and the importance mask phase roughness plays in its determination. As shown above, mask roughness leads to LER through the concept of speckle. When considering the printing of contacts, in the case of most interest where the contact size is close to the diffraction limit, the size of the contact in the image plane will be equivalent to the speckle size. Under these conditions, speckle will cause a global intensity change in the contact aerial image. This intensity change will be random from contact to contact, so a field of contacts would suffer printed-size variations.

As discussed above, solving the general problem of partially coherent image formation in the presence of object-plane phase roughness quickly becomes intractable even under the small-phase-perturbation approximation.[17] The more specific case of contact printing, however, lends itself well to several simplifications and an analytical solution.[27] Considering only contact sizes close to the diffraction limit or smaller, and assuming illumination partial coherence of 0.9 and smaller, the image formation problem can be simplified to the coherent imaging case. Coherent imaging analysis holds because under the aforementioned restrictions, the illumination coherence area will be larger than the entire contact. Moreover, because we are dealing with structures that are close to the diffraction limit, the morphology of the imaged structure can be assumed to be approximately equivalent to the optical system PSF, so we need to concern ourselves only with the global intensity of the structure.

Because the contacts of interest here are near the diffraction limit, any structure within the contact, phase or otherwise, will not be resolved. Thus, every point within the contact in object space can be assumed to contribute to all points in the imaged contact, and the intensity of the imaged contact can be treated as a coherent summation of all of the points in the contact in object space. Assuming mask roughness, or random phase, this summation will take

Downloaded From: https://www.spiedigitallibrary.org/ebooks/ on 09 Mar 2022
Terms of Use: https://www.spiedigitallibrary.org/terms-of-use

the form of a random walk whose statistics can be analytically determined. The statistics of this random walk will be equivalent to the statistics of contact-to-contact intensity variations within a field of contacts and thus provides insight into printed contact size variations. Following this methodology, the standard deviation of the normalized intensity can be shown to be

$$\sigma_{\hat{I}} = \frac{2\sqrt{\left[\frac{1}{2}1 + \exp(-2\sigma^2)\right] - \exp(-\sigma^2)}}{\sqrt{\frac{A_c}{A_r}}\exp\left(-\frac{\sigma^2}{2}\right)}, \tag{10.5}$$

where A_c is the area of a single contact on the mask, A_r is the correlation area of the intracontact mask roughness, and σ^2 is the phase variance of the field reflected from the mask (i.e., directly proportional to the mask roughness). The actual printed-contact-size variation can be determined by taking into account the slope of the aerial image:

$$\sigma_W = \sigma_{\hat{I}} \frac{dW}{d\hat{I}}, \tag{10.6}$$

where W is the printed contact width. For a more detailed derivation and explanation of the results, see Ref. 27.

Mask yield and, in turn, the minimization of mask defects are crucial issues for EUVL. Mask roughness coupling to printed-contact-size variation will have an impact on mask yield similar to that of more conventional defects. For example, using the analysis presented above, one can determine the maximum allowable mask roughness in order to achieve a desired mask yield for a mask containing a given number of contacts. For the analysis below, the following parameters are chosen:

- a lithographic system utilizing a 0.25-NA, 13.5-nm wavelength optic;
- a 4× mask with 120-nm nominally square contacts on the mask (30 nm as printed);
- an intracontact mask roughness correlation area of approximately 5000 nm^2 (this corresponds to a coherence diameter of 80 nm, a typical value for a current state-of-the-art EUV mask);
- a desired mask yield of 99%, with each mask containing 109 contacts; and
- contact failure defined as a greater than ±10% width change within a single-sided focal range of 100 nm.

It is important to note that focus can be assumed to affect only the image slope while not impacting the contact-to-contact intensity variation because, under the constraints described above, the effect of the roughness is simply to modulate the overall intensity of each contact and not the morphology of the

Downloaded From: https://www.spiedigitallibrary.org/ebooks/ on 09 Mar 2022
Terms of Use: https://www.spiedigitallibrary.org/terms-of-use

imaged contact. In the defocused case, the normalization used to determine the normalized aerial image is with respect to the in-focus image, thereby accounting for the reduced image slope with defocus. Following Ref. 27, the rms mask-roughness limit within the frequency-range limit set by the contact size is 0.15 nm. This compares favorably with current substrate manufacturing capabilities combined with ion-assisted ML deposition techniques,[25,26] where recent results have yielded rms roughness values of approximately 0.084 nm within a frequency band covering periods of 120 nm and smaller.

Another potential area of concern for mask roughness is the impact it might have on the printed-contact process window. Given all of the other process-window constraints—focus, dose, mask defects, mask CD errors, shot noise, etc.—it would be preferable for the mask roughness term to be essentially negligible. Because the mask-roughness-induced CD error cannot be assumed to be uncorrelated from some significant full-field error sources such as defocus and dose, a safe limit for the mask roughness term might be 5% of the total error budget. Given a 10% 3σ process-window tolerance, the total error budget for 30-nm contacts is 3 nm. Thus, the total acceptable mask-roughness-induced 3σ printed size variation would be 0.15 nm. This corresponds to σ_W less than or equal to 0.05 nm. Using the system parameters described in the previous example, the rms mask-roughness limit within the low-frequency limit set by the contact size becomes 0.045 nm, approximately a factor of 2 better than current fabrication limits. At current fabrication limits (approximately 0.084-nm intracontact rms roughness for the CD and reduction factor considered here), the mask roughness would account for a total of 0.53-nm 3σ printed-contact size variation, which represents a significant fraction of the total error budget. Modeling-based verification of these results can be found in Ref. 27.

10.4 Stochastics in Patterning

10.4.1 Introduction

The problem of stochastics in photoresist patterning is becoming increasingly important as we push to critical dimensions in the single-digit nanometer regime. Historically, this has been viewed primarily from the photon perspective, where Poisson statistics allow us to draw a clear relationship between localized average exposure dose and variability. The problem becomes especially acute at EUV relative to DUV wavelengths owing to the fact that EUV photons are approximately 15× more energetic than DUV photons. Thus, for the same dose conditions, an EUV exposure will nominally have 15× fewer photons than a DUV exposure. Because dose variability is actually dependent on the mean photon count rather than the mean dose, under identical dose conditions, an EUV exposure will suffer from significantly higher variability. As a rule of thumb, Poisson statistics tells us

Downloaded From: https://www.spiedigitallibrary.org/ebooks/ on 09 Mar 2022
Terms of Use: https://www.spiedigitallibrary.org/terms-of-use

that the variability in the number of photons exposing a given feature will equal the square root of the average number of photons in that feature. Let us take for example a contact hole; if one were to use a photoresist that required only 100 photons on average to expose that contact, we could expect the rms variation in actual delivered photons to be 10, or 10% of the average. This would translate to a 10% rms dose variation, which clearly would not be acceptable. In practice, the situation is certainly more complicated and nuanced, but the limitations of Poisson photon statistics are unavoidable.

The stochastic challenges, however, do not end here. The photon image can be thought of as the best case, but in reality this photon image must still be captured in a physical material, which itself may suffer from stochastic limits. Noting that resist can be thought of as a blend of chemical components with finite densities such that counting statistics come into play when considering the number of relevant chemical components within a given target-patterning feature volume, the material components themselves can be treated as Poisson random variables. For example, consider a typical chemically amplified resist consisting of photo-acid generator, quencher, and polymer with protecting groups. If we go back to our example of a 10-nm contact and ask the question of how many photo-acid generators, quenchers, and protecting groups there are in the given volume, we will get a mean number and a standard deviation that will approximately equal the square root of the mean value, as we saw in the case for the photons. This localized materials variability thus also plays an important role in the final pattern variability.

Although the presence and trends of these stochastic effects can be readily described heuristically as above, a quantitative understanding of the limitations requires the use of stochastic modeling methods.[28–34] One such method is the Multivariate Poisson Propagation Model (MPPM),[29,31,34] which enables the study of the relative importance of a variety of stochastic terms in both chemically amplified (CA) and non–chemically amplified resists both in terms of LWR and CDU.

10.4.2 Photon stochastics: an analytic description

As discussed above, many parameters contribute to the net overall stochastic behavior of LER, LWR, and CDU. In this section we analytically consider the contribution to LER from the absorbed photons. The analysis follows the approach used in Ref. 28. But as noted above, there are many other contributors, and photons are not always the dominant ones.[29]

Classically speaking, the electromagnetic energy absorbed by a material with conductivity σ is given by $\sigma\vec{E}^2$, where $\vec{E}$ is the electric field. In terms of quantum mechanics, the probability of absorbing a photon—in the electric dipole approximation, which is the dominant mechanism for photon

Downloaded From: https://www.spiedigitallibrary.org/ebooks/ on 09 Mar 2022
Terms of Use: https://www.spiedigitallibrary.org/terms-of-use

absorption—is also proportional to $\vec{E}^2$. Hence, we can take the probability of absorption of a photon in an incremental volume dV located at position $\vec{r}$ in the resist as being proportional to $\vec{E}(\vec{r})^2 dV$. Normalizing the total probability to unity in the entire exposed resist volume, the probability density for a photon to be absorbed at position $\vec{r}$ is given by

$$p(\vec{r}) = \frac{\vec{E}(\vec{r})^2}{\int_V d^3 r \vec{E}(\vec{r})^2}. \tag{10.7}$$

Note that since we have normalized the probability to unity in the exposed resist volume V, we are by definition automatically considering only the statistics of the absorbed photons, which are precisely the photons of interest. We note, however, that there is a finite possibility that a photon not absorbed in the resist is absorbed somewhere else, e.g., in the substrate, underlayer, etc., and generates a secondary electron, or some other energy-transferring mechanism, which then causes an exposure event in the resist. Although this probability is not zero, it is extremely small compared to the direct exposure mechanism and so can be ignored. By comparison, this is not the case in e-beam systems, where secondary-electron–substrate interactions do contribute nontrivially to exposure.

As discussed in detail in Chapter 8 on photoresists, the EUV exposure mechanism differs from the exposure mechanism at the DUV wavelengths of 248 nm and 193 nm. For DUV wavelengths, predominantly only the PAG molecules themselves directly absorb the photons, with the non-PAG molecules in the resist being for the most part nonabsorbing. For EUV wavelengths, on the other hand, every molecule in the resist is absorbing. Absorptions in this case predominantly cause the ejection of secondary electrons from the absorbing molecule. Depending on binding energy, these secondary electrons can have energies approaching the full 92 eV of the incident photon. As these electrons move through the resist and interact with the PAG molecules, they cause acid release, i.e., exposure; in this sense, EUV exposure is more similar to e-beam exposure than DUV exposure.

The probability of absorption in any particular subvolume v of V centered at position $\vec{r}$ is given by

$$q(\vec{r}) = \int_v d^3 r' p(\vec{r}'). \tag{10.8}$$

It is straightforward[28] to show that if there are N total absorptions throughout the entire exposed resist volume V, then the probability Q_n of having n of those absorptions take place in a subvolume v centered at position $\vec{r}$ is given by the binomial distribution

Downloaded From: https://www.spiedigitallibrary.org/ebooks/ on 09 Mar 2022
Terms of Use: https://www.spiedigitallibrary.org/terms-of-use

$$Q_n(\vec{r}) = \frac{N!}{n!(N-n)!} q(\vec{r})^n [1 - q(\vec{r})]^{N-n}. \tag{10.9}$$

Note that $N!/[n!(N-n)!]$ is the number of ways of independently selecting n out of N objects, with the probability of selection being $q(\vec{r})$ and the probability of nonselection being $[1 - q(\vec{r})]$.

The exposed resist volume equals $A \times T$, where A is the exposure area, and T is the resist thickness. The exposure area is on the order of mm^2, and the thickness is on the order of 100 nm, so $V \sim \text{mm}^2 \times 100 \text{ nm} \sim 10^{14} \text{ nm}^3$, whereas for stochastic analysis, ν is on the order of 1 nm^3, so $\nu \ll V$. Thus, we have

$$q(\vec{r}) \ll 1, n \ll N, \tag{10.10}$$

in which case

$$[1 - q(\vec{r})]^{N-n} \cong \exp[-Nq(\vec{r})] \text{ and } \frac{N!}{(N-n)!} \cong N^n, \tag{10.11}$$

so

$$Q_n(\vec{r}) \cong \frac{[Nq(\vec{r})]^n}{n!} \exp[-Nq(\vec{r})]. \tag{10.12}$$

This is a Poisson distribution; therefore, even if the total number of absorptions N throughout the exposed resist volume V is precisely fixed, the number of absorptions in any tiny volume ν follows a Poisson distribution.

There are several ways to proceed from here. We can assume that on average in ν there are N_{acid} acid molecules released per absorbed photon. Then the probability for the acid latent image distribution $A_n(\vec{r})$ in terms of the number of acids released during exposure in a volume ν centered at position $\vec{r}$ is given by

$$A_n(\vec{r}) = N_{acid} Q_n(\vec{r}) = N_{acid} \frac{[Nq(\vec{r})]^n}{n!} \exp[-Nq(\vec{r})]. \tag{10.13}$$

During post-exposure bake (PEB), each released acid diffuses, causing (in a positive tone resist) deprotection of resist polymer molecules. The average deprotection PSF or "blur" caused by an acid molecule has been both measured[42] and calculated from the diffusion equation.[28] Convolving $A_n(\vec{r})$ with this blur function then gives the statistics of the deprotection,[30] and from that the statistics of the printed features including LER, LWR, CDU, etc., are obtained. This convolution also directly predicts a frequency distribution of LER that very well matches the experimentally determined frequency distribution.[28]

Downloaded From: https://www.spiedigitallibrary.org/ebooks/ on 09 Mar 2022
Terms of Use: https://www.spiedigitallibrary.org/terms-of-use

But this approach ignores many other statistics that enter into the determination of the net or total statistics for feature edges. Even though photon statistics are often the dominant cause, other statistics do enter, and depending on the details, these other statistics can themselves be dominant, or at least significant contributors, to the total or net statistics.[29,30,43] For example, the PAG and base quencher molecules are discrete entities and, up to interactions between molecules such as steric repulsion, if randomly and independently distributed, should follow the binomial distribution described above, which again reduces to a Poisson distribution in a volume $v \ll V$. Also, the interactions between acid molecules and resist polymer molecules and base quencher molecules are statistical. For example, if during PEB an acid and a base quencher molecule meet in the same volume v, it is not automatically guaranteed that they will neutralize each other, or that, if an acid molecule comes into contact with a resist polymer molecule, the acid molecule will cause a deprotection reaction. Including reaction probability effects leads to a set of reaction-diffusion equations that link the time evolution of the acid, base quencher, and deprotection probability densities, as are considered in Ref. 44 and 45, and as described in the next section.

10.4.3 A stochastic model

In the MPPM, all relevant counting terms are treated as Poisson random variables instead of average values. Note that this is not the same as a Monte Carlo model and, in principle, can be treated as an analytic model. In the implementation used here,[35] however, the model is implemented numerically. The modeling process begins with an arbitrary aerial image representing the time-averaged photon density as a function of position (pixel). The first random variable represents the absorbed photons per pixel, thus capturing the photon noise effect. The next random variable represents the number of chemical events per absorbed photon. This is a function of both the chemical yield, or quantum efficiency (QE), and the random variable, as well as the local photo-active chemical density random variable. For the rest of the description below, we consider the case of a CA resist. In this case, the local photo-active chemical density is the photo-acid generator (PAG) density. The outcome of this step is a random variable representing the number of acids. The next step includes a reaction-diffusion process where there is an interaction with the local quencher concentration (also a random variable), as well as with the protecting group concentration (yet another random variable). The end result is a random variable representing the deprotection ratio. Finally, a threshold development model is used to yield the stochastic pattern that can be analyzed using conventional LWR or CDU analysis software.[36]

Each of the input random variables described above can be viewed as a counting problem. In each case, the relevant value is the number of events or

Downloaded From: https://www.spiedigitallibrary.org/ebooks/ on 09 Mar 2022
Terms of Use: https://www.spiedigitallibrary.org/terms-of-use

particles per unit volume. From the stochastic perspective, these cases are conveniently represented as Poisson random variables. The model then consists of a series of Poisson random variables acted upon and combined through a series of functions. Thus, the problem can be viewed as a classical error-propagation problem. Note that since the MPPM is implemented numerically, one is not restricted to using Poisson distributions; any desired distribution can be used for each of the random variables.

Although described above in terms of a CA resist, the model can also be applied to non-CA resists. In this case, the PAG concentration is replaced by the relevant photo-active element, and the quencher is set to zero.

Examples of deterministic variables used in the MPPM include the aerial image, absorptivity, electron mean free path, chemical diffusion range, quencher diffusion range, and chemical reaction rates. Also, not being a Monte Carlo model, each random variable can readily be substituted in the model, with its mean value allowing the impact of individual stochastic terms to be assessed. Note that since the MPPM is essentially an error propagation model, deterministic variables will still have an impact on the stochastic output, given that those variables affect the functions acting on the input and propagated random variables.

10.4.4 Photon and material effects

In this section we consider the relative importance of the various stochastic terms described above. In the first example, we explore a conventional polymer CA resist with a dose to size for 16-nm line/space features of 33 mJ/cm^2. The patterning performance of this resist in the Berkeley MET tool[37] is shown in Fig. 10.27.

Using supplier-provided estimates for the material parameters (a resist thickness of 35 nm), and estimating the acid diffusion based on the measured LWR correlation length,[34] Table 10.1 shows the model-predicted LWR and CDU (both 3σ values) for 16-nm dense features. For computation of the line/space aerial image, we use optimized dipole illumination, and for the contacts,

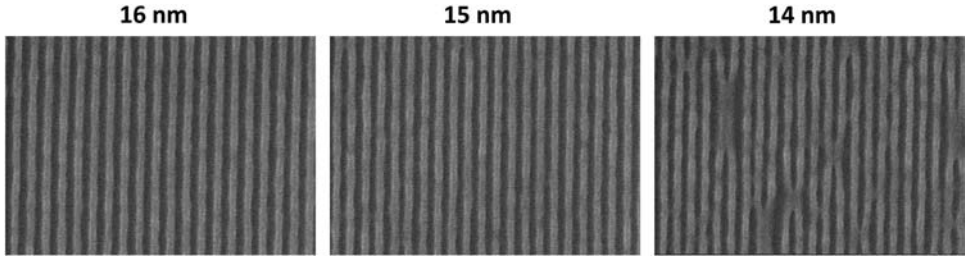

Figure 10.27 Line/space patterning results for a leading-performance CA resist in the Berkeley MET tool (reprinted from Ref. 50).

Downloaded From: https://www.spiedigitallibrary.org/ebooks/ on 09 Mar 2022
Terms of Use: https://www.spiedigitallibrary.org/terms-of-use

Table 10.1 MPPM predicted LWR and CDU terms for 16-nm dense features.

Stochastic terms	LWR (nm)	CDU (nm)
Photon	2.0 ± 2%	3.0 ± 8%
Acid	1.2 ± 2%	1.9 ± 8%
PAG	0.6 ± 2%	1.1 ± 8%
Quencher	1.9 ± 2%	2.6 ± 8%
Protecting groups	0.1 ± 2%	0.1 ± 8%
All combined	3.0 ± 2%	4.1 ± 8%

we use optimized quadrupole illumination. The error bars are a result of the finite sample size used in the simulation.

The model shows that, for this resist, the total material term (the root sum square of all of the terms except for the photon term) is greater than the photon term. Moreover, of the material terms, the quencher dominates. The quencher dominating is simply a result of that being the term of the smallest mean count, therefore suffering from the largest relative stochastic variation.

Fundamentally, the output variability, be it LWR or CDU, is determined by the input noise (stochastic terms), and the functional coupling is determined by the deterministic or mean-field terms. This means, for example, that the photon-noise-induced LWR as shown in Table 10.1 should not be viewed as an absolute limit of the counting terms; rather, it can also be modified by deterministic parameters in the model, including both resist and system parameters. A simple example of this is to consider the aerial image contrast. For the line/space analysis above, which had assumed dipole illumination, the aerial image contrast was 85%. If instead this contrast is reduced to 55%, we get the results in Table 10.2, which shows a very significant increase in the coupling of all of the input noise terms and an increase in the total LWR by 66%.

The results in Table 10.2 show absorbed photon and quencher counts to be the dominant input noise contributors to LWR and CDU for a conventional CA resist. Both of these terms, however, can be mitigated by considering inorganic, non-CA resists. The ability to include metal in significant quantities

Table 10.2 MPPM-predicted LWR for 16-nm lines and spaces using resist parameters identical to those in Table 10.1, but reducing the aerial image contrast from 85% to 55%.

Stochastic terms	LWR (nm)
Photon	3.2 ± 2%
Acid	1.9 ± 2%
PAG	0.9 ± 2%
Quencher	3.1 ± 2%
Protecting groups	0.1 ± 2%
All combined	4.9 ± 2%

Downloaded From: https://www.spiedigitallibrary.org/ebooks/ on 09 Mar 2022
Terms of Use: https://www.spiedigitallibrary.org/terms-of-use

allows absorption to be increased substantially; thus, for the same exposure dose, many more photons contribute to the pattern, thereby reducing the photon noise. A typical polymer resist will have an absorptivity of approximately 4 μm^{-1}, whereas metal oxide resists have been shown to achieve values as high as 20 μm^{-1}.[38] Note, however, that there are limits to the acceptable absorptivity since making it too high could cause exposure problems through thickness and thus sidewall slope issues. At a value of 20 μm^{-1}, a 20-nm thick resist will have 33% less dose at the bottom of the resist compared to the top.

Another benefit of the non-CA resist is that by eliminating reliance on quencher, the non-CA resist can improve chemical/material stochastics as well. Table 10.3 shows the model-predicted LWR and CDU terms for 16-nm dense features for an assumed non-CA resist. The aerial image parameters used in Table 10.1 are again used here. The model parameters include: absorptivity = 20 μm^{-1}, thickness = 20 nm, sensitivity = 60 mJ/cm^2, quantum efficiency (radiation chemistry events per absorbed photon) = 2, chemical blur = 12 nm, and the active chemical component density = 2/nm^3. The patterning performance of a non-CA resist that is expected to have properties similar to those described above is shown in Fig. 10.28.

10.4.5 Contact CDU limits

Assuming a contact CDU requirement of 10% of CD, we see that even the model non-CA resist from Table 10.3 does not meet the requirements. If we instead assume a sensitivity of 80 mJ/cm^2 and a chemical blur of 7 nm

Table 10.3 MPPM predicted LWR and CDU terms for 16-nm dense features in an assumed non-CA resist.

Stochastic terms	LWR (nm)	CDU (nm)
Photon	1.2 ± 2%	1.5 ± 8%
Photochemistry	0.9 ± 2%	1.0 ± 8%
Active components	0.2 ± 2%	0.3 ± 8%
All combined	1.6 ± 2%	1.8 ± 8%

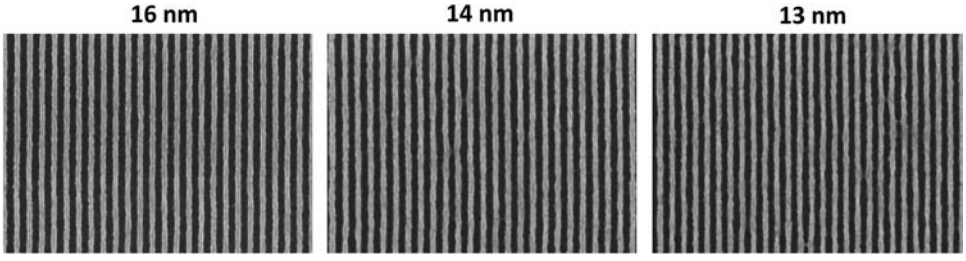

Figure 10.28 Patterning results for a leading-performance non-CA resist in the Berkeley MET tool (reprinted from Ref. 50).

Downloaded From: https://www.spiedigitallibrary.org/ebooks/ on 09 Mar 2022
Terms of Use: https://www.spiedigitallibrary.org/terms-of-use

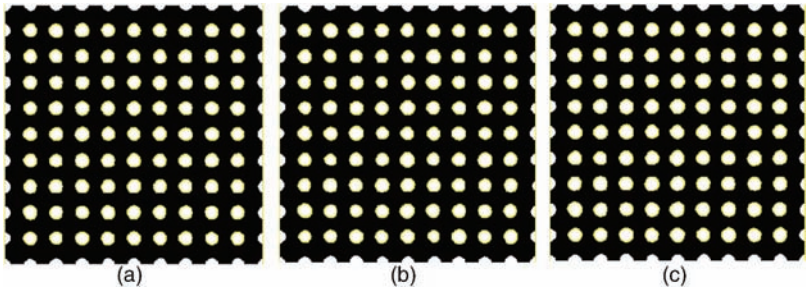

Figure 10.29 MPPM output for a non-CA resist patterning: (a) 16-nm dense contacts yielding a CDU of 1.2 nm; (b) 10-nm dense contacts yielding a CDU of 1.7 nm; and (c) 10-nm contacts after increasing QE to 4 and decreasing resist blur to 4 nm, yielding a CDU of 1 nm (reprinted from Ref. 50).

(a parameter that has been demonstrated experimentally[39]), while keeping the other parameters as described for Table 10.3, the MPPM shows that a CDU of 1.2 nm can be achieved. Figure 10.29 shows the MPPM output.

The result in Fig. 10.29(a) outperforms the 10% requirement and thus provides headroom for considering even smaller contacts. Table 10.4 shows the MPPM-predicted contact CDU as a function of half-pitch while keeping all of the resist parameters identical to those described for Fig. 10.29(a) and directly scaling the aerial image, thereby assuming that the optical performance is improving (i.e., NA is increasing). Note that although some of the relative changes appear to be on the order of the reported error bars, the model's ability to predict relative performance is much superior to the reported precision, which is a function of the dataset size (81 contacts in this case). The model, however, has the ability to use a predefined random-number generator seed, allowing the stochastic distributions to be replicated from run to run. For example, Fig. 10.29(b) shows the MPPM results for 10-nm contacts, where one can observe the same relative distribution of contact sizes as compared to the 16-nm case in Fig. 10.29(a). Therefore, the relative performance will not suffer from the same dataset-size-limited uncertainty as do the individual datasets.

The results in Table 10.4 show that once the CD drops to below 14 nm, the 10% CDU requirement can no longer be met for the assumed resist and

Table 10.4 MPPM-predicted contact CDU as a function of contact half-pitch.

Half-pitch (nm)	CDU (nm)
16	1.2 ± 8%
14	1.3 ± 8%
12	1.5 ± 8%
10	1.7 ± 8%

Downloaded From: https://www.spiedigitallibrary.org/ebooks/ on 09 Mar 2022
Terms of Use: https://www.spiedigitallibrary.org/terms-of-use

aerial image parameters. We thus next consider which parameters would allow the 10% CDU requirement to be met even at 10-nm half-pitch without increasing the dose. Noting that the QE plays a key role in the chemical noise term and that the resist blur is important to the coupling of stochastic noise to the final CDU, we consider increasing the QE from 2 to 4 and decreasing the blur from 7 nm to 4 nm. Doing so, we can achieve a CDU of 1 nm on 10-nm contacts, as shown in Fig. 10.29(c).

Although Fig. 10.29(c) shows that 10% CDU is achieved at 10 nm with the assumed resist parameters, the dose in this case is still 80 mJ/cm^2. Ideally, one would like to reduce this dose. If we make the further assumption of increasing the absorptivity to 30 μm^{-1} and further decreasing the blur to 3 nm, we can achieve a CDU of 1 nm at a dose of 50 mJ/cm^2. Note, however, that at this level of absorptivity, we will have nearly 50% less dose at the bottom of the 20-nm resist film as compared to the top.

References

1. P. Dirksen, C. Juffermans, R. Pellens, M. Maenhoudt, and P. Debisschop, "Novel aberration monitor for optical lithography," *Proc. SPIE* **3679**, 77–86 (1999) [doi: 10.1117/12.354385].
2. H. Fukuda, K. Hayano, and S. Shirai, "Determination of high-order lens aberration using phase/amplitude linear algebra," *J. Vac. Sci. Technol. B* **17**, 3318–3321 (1999).
3. G. Robins, K. Adam, and A. Neureuther, "Measuring optical image aberrations with pattern and probe based targets," *J. Vac. Sci. Technol. B* **20**, 338–343 (2002).
4. E. Spiller, "Evaporated multilayer dispersion elements for soft X-rays," *AIP Conf. Proc.* **75**, 124–130 (1981).
5. W. Jark, "Enhancement of diffraction grating efficiencies in the soft X-ray region by a multilayer coating," *Opt. Comm.* **60**, 201–205 (1986).
6. J. C. Rife, W. R. Hunter, T. W. Barbee, Jr., and R. G. Cruddace, "Multilayer-coated blazed grating performance in the soft x-ray region," *Appl. Opt.* **28**, 2984–2986 (1989).
7. R. A. M. Keski-Kuha, R. J. Thomas, J, S. Gum, and C. E. Condor, "Performance of multilayer coated diffraction gratings in the EUV," *Appl. Opt.* **31**, 4529–4531 (1990).
8. J. F. Seely, M. P. Kowalski, W. R. Hunter et al., "On-blaze operation of a Mo/Si multilayer-coated concave diffraction grating in the 136–142 Å wavelength region and near normal incidence," *Appl. Opt.* **32**, 4890–4897 (1993).
9. P. P. Naulleau, J. A. Liddle, E. H. Anderson, E. M. Gullikson, P. Mirakarimi, F. Salmassi, and E. Spiller, "Fabrication of high-efficiency

Downloaded From: https://www.spiedigitallibrary.org/ebooks/ on 09 Mar 2022
Terms of Use: https://www.spiedigitallibrary.org/terms-of-use

multilayer-coated gratings for the EUV regime using e-beam patterned substrates," *Opt. Comm.* **229**, 109–116 (2003).
10. B. La Fontaine, A. Pawloski, O. Wood, Y. Deng, H. J. Levinson, P. Naulleau, P. E. Denham, E. Gullikson, B. Hoef, C. Holfeld, C. Chovino, and F. Letzkus, "Demonstration of phase-shift masks for extreme-ultraviolet lithography," *Proc. SPIE* **6151**, 61510A (2006) [doi: 10.1117/12.652212].
11. P. Naulleau, C. N. Anderson, W. Chao, K. A. Goldberg, E. Gullikson, F. Salmassi, and A. Wojdyla, "Ultrahigh efficiency EUV contact-hole printing with chromeless phase shift mask," *Proc. SPIE* **9984**, 99840P (2016) [doi: 10.1117/12.2243321].
12. P. Naulleau and G. Gallatin, "The line-edge roughness transfer function and its application to determining mask effects in EUV resist characterization," *Appl. Opt.* **42**, 3390–3397 (2003).
13. D. Tichenor, W. Replogle, S. Lee, W. P. Ballard, A. H. Leung, G. D. Kubiak, L. E. Klebanoff, S. Graham, Jr., J. E. M. Goldsmith, K. L. Jefferson, J. B. Wronosky, T. G. Smith, T. A. Johnson, H. Shields, L. C. Hale, H. N. Chapman, J. S. Taylor, D. W. Sweeney, J. A. Folta, G. E. Sommargren, K. A. Goldberg, P. P. Naulleau, D. T. Attwood, and E. M. Gullikson, "Performance upgrades in the EUV Engineering Test Stand," *Proc. SPIE* **4688**, 72 (2002) [doi: 10.1117/12.472328].
14. D. W. Sweeney, R. Hudyma, H. N. Chapman, and D. Shafer, "EUV optical design for a 100 nm CD imaging system," *Proc. SPIE* **3331**, 2–10 (1998) [doi: 10.1117/12.309559].
15. K. Goldberg, P. Naulleau, J. Bokor, and H. Chapman, "Testing EUV optics with visible-light and EUV interferometry," *J. Vac. Sci. Technol. B* **20**, 2834–2839 (2002).
16. N. Beaudry and T. Milster, "Effects of object roughness on partially coherent image formation," *Opt. Lett.* **25**, 454–456 (2000).
17. N. Beaudry and T. Milster, "Effects of mask roughness and condenser scattering in EUVL systems," *Proc. SPIE* **3676**, 653–662 (1999) [doi: 10.1117/12.351140].
18. J. W. Goodman, *Statistical Optics*, John Wiley & Sons, New York, Chapter 7, pp. 286–360 (1985).
19. P. Naulleau, "The relevance of mask-roughness-induced printed line-edge roughness in recent and future EUV lithography tests," *Appl. Opt.* **43**, 4025–4032 (2004).
20. J. H Underwood and T. W. Barbee, Jr., "Layered synthetic microstructures as Bragg diffractors for X rays and extreme ultraviolet: theory and predicted performance," *Appl. Opt.* **20**, 3027–3034 (1981).
21. D. Stearns, "Stochastic model for thin film growth and erosion," *Appl. Phys. Lett.* **62**, 1745–1747 (1993).
22. D. Stearns and E. Gullikson, "Nonspecular scattering from extreme ultraviolet multilayer coatings," *Physica B* **283**, 84–91 (2000).

Downloaded From: https://www.spiedigitallibrary.org/ebooks/ on 09 Mar 2022
Terms of Use: https://www.spiedigitallibrary.org/terms-of-use

23. E. Gullikson, C. Cerjan, D. Stearns, P. Mirkarimi, and D. Sweeney, "Practical approach for modeling extreme ultraviolet lithography mask defects," *J. Vac. Sci. Technol. B* **20**, 81–86 (2002).
24. S. D. Hector, "EUVL masks: requirements and potential solutions," *Proc. SPIE* **4688**, 134–149 (2002) [doi: 10.1117/12.472284].
25. P. Mirkarimi, E. Spiller, D. Stearns, V. Sperry, and S. Baker, "An ion-assisted Mo-Si deposition process for planarizing reticle substrates for extreme ultraviolet lithography," *IEEE J. Quantum Electron.* **37**, 1514–1516 (2001).
26. T. Ogawa, M. Ito, H. Yamanashi, H. Hoko, E. Hoshino, and S. Okazaki, "Simulation studies of roughness-smoothing effect of molybdenum/silicon multilayer coating based on resputtering model," *Proc. SPIE* **4688**, 716–724 (2002) [doi: 10.1117/12.472346].
27. P. Naulleau, "The effect of mask-roughness on printed contact size variation in EUV lithography," *Appl. Opt.* **44**, 183–189 (2004).
28. G. M. Gallatin, "Resist blur and line edge roughness," *Proc. SPIE* **5754**, 38 (2005) [doi: 10.1117/12.607233].
29. C. Anderson and P. Naulleau, "Do not always blame the photons: Relationships between deprotection blur, line-edge roughness, and shot noise in extreme ultraviolet photoresists," *J. Vac. Sci. Technol. B* **27**(2), 665 (2009).
30. C. Mack, "Stochastic approach to modeling photoresist development," *J. Vac. Sci. Technol. B* **27**, 1122 (2009).
31. P. Naulleau and G. Gallatin, "The effect of resist on the transfer of line-edge roughness spatial metrics from mask to wafer," *J. Vac. Sci. Technol. B* **28**, 1259 (2010).
32. J. Biafore and M. Smith, "Application of stochastic modeling to resist optimization problems," *Proc. SPIE* **8325**, 83250H (2012) [doi: 10.1117/12.916518].
33. T. Kozawa, J. Santillan, and T. Itani, "Analysis of stochastic effect in line-and-space resist patterns fabricated by extreme ultraviolet lithography," *Appl. Phys. Express* **6**, 026502 (2013).
34. P. Naulleau, C. Anderson, W. Chao, S. Bhattarai, and A. Neureuther "Studying resist stochastics with the Multivariate Poisson Propagation Model," *J. Photopolym. Sci. Technol.* **27**, 747–750 (2014).
35. Stochastic modeling performed using SuMMIT software (www.lithometrix.com).
36. LWR and CDU analysis performed using SuMMIT software (www.lithometrix.com).
37. P. Naulleau, K. A. Godlberg, E. Anderson, J. P. Cain, P. Denham, B. Hoef, K. Jackson, A.-S. Morlens, S. Rekawa, and K. Dean, "Status of EUV microexposure capabilities at the ALS using the 0.3-NA MET optic," *Proc. SPIE* **5374**, 881–891 (2004) [doi: 10.1117/12.600388].

Downloaded From: https://www.spiedigitallibrary.org/ebooks/ on 09 Mar 2022
Terms of Use: https://www.spiedigitallibrary.org/terms-of-use

38. R. Fallica, J. Stowers, A. Grenville, A. Frommhold, A. Robinson, and Y. Ekinci, "Dynamic absorption coefficients of CAR and non-CAR resists at EUV," *Proc. SPIE* **9776**, 977612 (2016) [doi: 10.1117/12.2219193].
39. P. Naulleau, C. Anderson, W. Chao, K. Goldberg, A. Wojdyla, S. Bhattarai, A. Neureuther, F. Goodwin, and M. Neisser, "Enabling EUV resist research at the 1x and smaller regime," *J. Photopolym. Sci. Technol.* **28**, 777–782 (2015).
40. C. Rydberg, J. Bengtsson, and T. Sandstrom, "Dynamic laser speckle as a detrimental phenomenon in optical projection lithography," *J. Microlith., Microfab., Microsyst.* **5**, 033004 (2006) [doi: 10.1117/1.2242524].
41. G. Gallatin, N. Kita, T. Ujike, and W. Partlo, "Residual speckle in a lithographic illumination system," *J. Micro/Nanolith. MEMS MOEMS* **8**(4), 043003 (2009) [doi: 10.1117/1.3256007].
42. J. A. Hoffnagle, W. D. Hinsberg, M. I. Sanchez, and F. A. Houle, "Method of measuring the spatial resolution of a photoresist," *Opt. Lett.* **27**(20), 1776–1778 (2002).
43. G. Gallatin, F. Houle, and J. Cobb, "Statistical limitations of printing 50 and 80 nm contact holes by EUV lithography," *J. Vac. Sci. Technol. B* **21**, 3172 (2003).
44. A. Erdmann, W. Henke, S. Robertson, E. Richter, B. Tollkühn, and W. Hoppe, "Comparison of simulation approaches for chemically amplified resists," *Proc. SPIE* **4404**, 99 (2001) [doi: 10.1117/12.425196].
45. G. M. Gallatin, P. P. Naulleau, and R. Brainard, "Modeling the effects of acid amplifiers on photoresist stochastics," *Proc. SPIE* **8322**, 83221C (2012) [doi: 10.1117/12.917006].
46. Z. Zhu, K. Lucas, J. Cobb, S. D. Hector, and A. Strojwas, "Rigorous EUV mask simulator using 2D and 3D waveguide methods," *Proc. SPIE* **5037**, 494–503 (2003) [doi: 10.1117/12.484963].
47. A. Erdmann, C. K. Kalus, T. Schmoller, and A. Wolter, "Efficient simulation of light diffraction from three-dimensional EUV masks using field decomposition techniques," *Proc. SPIE* **5037**, 482–493 (2003) [doi: 10.1117/12.482744].
48. T. Pistor, T. Y. Deng, and A. Neureuther, "Extreme ultraviolet mask defect simulation: Low-profile defects," *J. Vac. Sci. Technol. B* **18**, 2926–2929 (2000).
49. B. Wu and A. Kumar, "Exposure System," Chapter 2 in *Extreme Ultraviolet Lithography*, McGraw-Hill, New York, pp. 31–120 (2009).
50. P. Naulleau, C. Anderson, W. Chao, S. Bhattarai, and A. Neureuther, "Stochastics and EUV patterning in the 1x-nm regime," *J. Photopolym. Sci. Technol.* **29**, 797–802 (2016).

Downloaded From: https://www.spiedigitallibrary.org/ebooks/ on 09 Mar 2022
Terms of Use: https://www.spiedigitallibrary.org/terms-of-use

Patrick Naulleau received his B.S. and M.S. degrees in electrical engineering from the Rochester Institute of Technology, Rochester, New York, in 1991 and 1993, respectively. He received his Ph.D. in electrical engineering from the University of Michigan, Ann Arbor in 1997, specializing in optical signal processing and coherence theory. In 1997 Dr. Naulleau joined Lawrence Berkeley National Laboratory as a staff scientist, where he has focused his research on advanced EUV lithography and metrology. From June 2005 through March 2008, Dr. Naulleau additionally joined the faculty at the University at Albany, SUNY as Associate Professor, also concentrating in the area of EUV lithography. In April 2010 Dr. Naulleau took the position of Director of the Center for X-ray Optics at Lawrence Berkeley National Laboratory. Dr. Naulleau has more than 300 publications as well as 19 patents, and is a Fellow of OSA and SPIE.

Gregg Gallatin currently runs Applied Math Solutions, LLC, a consulting company focused on modeling simulation and analysis of problems in the areas of optics, lithography, nanofabrication, nanotechnology, materials research, and data analysis. He received his Ph.D. in theoretical physics from Penn State in 1981 and worked in academia until 1984, when he joined the Optical Group Research Division of Perkin Elmer. In 1990 he joined SVG Lithography as Systems Engineer/Senior Staff Physicist; in 2000 he joined Bell Labs in Murray Hill as a Member of Technical Staff working on the SCAPEL e-beam lithography tool; and from 2001 to 2005 he was Research Staff Member in the TCAD group at IBM Watson. In 2005 he founded Applied Math Solutions, LLC and worked full-time as a consultant until May 2009, when he became employed full time as a Physicist/Physical Scientist at the Center for Nanoscale Science and Technology (CNST) at the National Institute of Standards and Technology (NIST) in Gaithersberg, Maryland. At the end of 2012, he returned to Applied Math Solutions, LLC, where he currently does simulation, analysis, and modeling, including design and development, of systems and processes covering areas from signal processing to quantum physics. He has expertise in electromagnetics, optics, lasers, lithography, semiconductor fabrication, nanofabrication, self-assembly, nanometrology, signal processing, materials science, data science (avoiding the pitfalls of Ramsey's theorem), and data analysis.

Downloaded From: https://www.spiedigitallibrary.org/ebooks/ on 09 Mar 2022
Terms of Use: https://www.spiedigitallibrary.org/terms-of-use

Appendix
Reference Data for the EUV Spectral Region*

Eric M. Gullikson and David Attwood
Lawrence Berkeley National Laboratory, Berkeley, California, USA

A.1 Introduction
References

A.1 Introduction

Basic equations and data for the interaction of EUV radiation with materials is presented. The complex refractive index and penetration of EUV radiation into materials is presented in terms of the real and imaginary parts of the atomic scattering factors for various atoms of common interest. These scattering factors are presented graphically as a function of photon energy, with sample tabulated values. Full access for all elements, and sample calculation routines for compound materials, are referred to the CXRO website. Basic physical constants from the NIST website are also given. Tabulations of electron binding energies and characteristically emitted photon energies are presented in tables for all natural elements.

* This Appendix has not be updated from the first edition of this book (2009).

Downloaded From: https://www.spiedigitallibrary.org/ebooks/ on 09 Mar 2022
Terms of Use: https://www.spiedigitallibrary.org/terms-of-use

Table A.1 Optical constants and absorption data for extreme ultraviolet wavelengths.[1,2]

$n(\omega) = 1 - \delta + i\beta \quad \frac{I}{I_0} = e^{-\rho\mu x}$

$\delta = \frac{n_a r_e \lambda^2}{2\pi} f_1^0(\omega) \qquad \mu = \frac{2 r_e \lambda}{A m_u} f_1^0(\omega)$

$\beta = \frac{n_a r_e \lambda^2}{2\pi} f_2^0(\omega)$

$\sigma_a(\text{barns/atom}) = \mu(\text{cm}^2/\text{g}) \times 14.97$

$E(\text{keV})\mu(\text{cm}^2/\text{g}) = f_2^0 \times 4669.04$

Beryllium (Be)
Z = 4
Atomic weight = 9.012

Energy (eV)	f_1^0	f_2^0	$\mu(\text{cm}^2/\text{g})$
30	1.787	4.396E–01	6.841E+04
70	1.669	2.497E–01	1.666E+04
100	0.647	1.591E–01	7.431E+03
300	4.333	1.150E+00	1.790E+04
700	4.217	2.571E–01	1.715E+03
1000	4.140	1.282E–01	5.986E+02
3000	4.026	1.360E–02	2.117E+01
7000	4.005	2.106E–03	1.405E+00
10000	4.003	9.384E–04	4.381E–01
30000	4.000	7.379E–05	1.148E–02

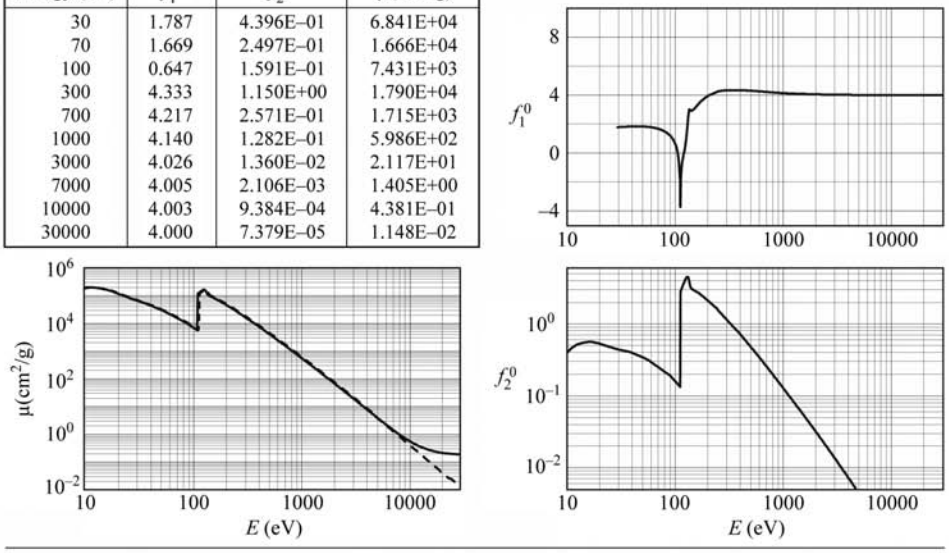

Edge Energies: K 111.5 eV

$\sigma_a(\text{barns/atom}) = \mu(\text{cm}^2/\text{g}) \times 19.95$

$E(\text{keV})\mu(\text{cm}^2/\text{g}) = f_2^0 \times 3503.31$

Carbon (C)
Z = 6
Atomic weight = 12.011

Energy (eV)	f_1^0	f_2^0	$\mu(\text{cm}^2/\text{g})$
30	3.692	2.664E+00	3.111E+05
70	4.249	1.039E+00	5.201E+04
100	4.253	6.960E-01	2.438E+04
300	2.703	3.923E+00	4.581E+04
700	6.316	1.174E+00	5.878E+03
1000	6.332	6.328E–01	2.217E+03
3000	6.097	7.745E–02	9.044E+01
7000	6.025	1.306E–02	6.536E+00
10000	6.013	5.892E–03	2.064E+00
30000	6.000	4.425E–04	5.168E–02

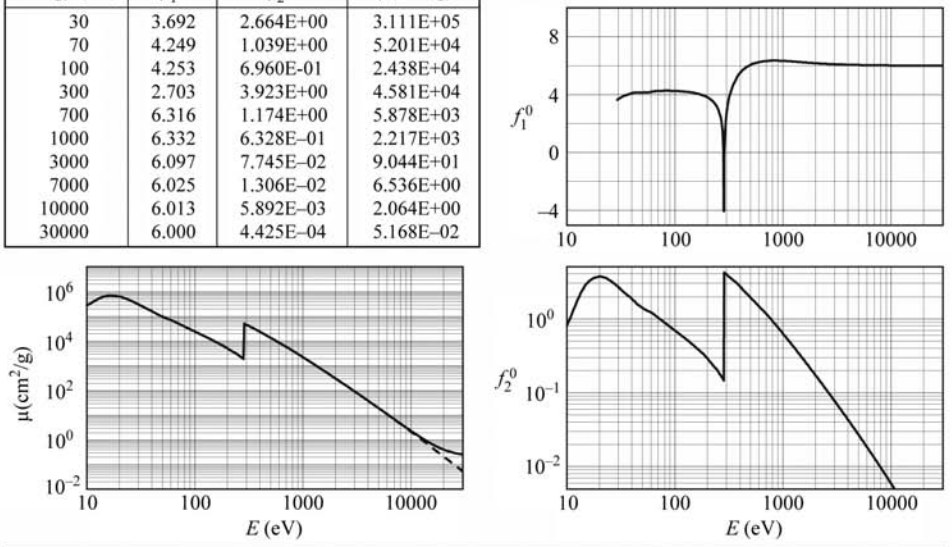

Edge Energies: K 284.2 eV

(*continued*)

Downloaded From: https://www.spiedigitallibrary.org/ebooks/ on 09 Mar 2022
Terms of Use: https://www.spiedigitallibrary.org/terms-of-use

Table A.1 (*Continued*)

σ_a(barns/atom) = μ(cm^2/g) × 23.26
E(keV)μ(cm^2/g) = f_2^0 × 3004.14

Nitrogen (N)
Z = 7
Atomic weight = 14.007

Energy (eV)	f_1^0	f_2^0	μ(cm^2/g)
30	3.225	4.373E+00	4.379E+05
70	5.158	2.123E+00	9.110E+04
100	5.421	1.449E+00	4.354E+04
300	4.887	3.056E–01	3.060E+03
700	7.088	1.971E+00	8.459E+03
1000	7.353	1.100E+00	3.306E+03
3000	7.152	1.434E–01	1.436E+02
7000	7.041	2.481E–02	1.065E+01
10000	7.022	1.140E–02	3.424E+00
30000	7.001	9.389E–04	9.402E–02

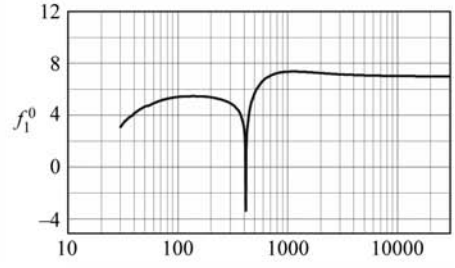

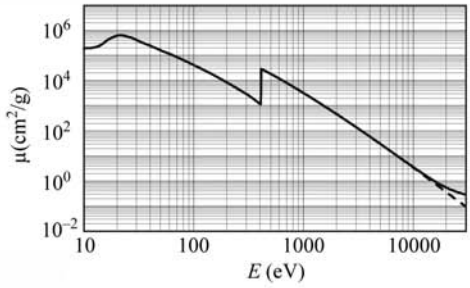

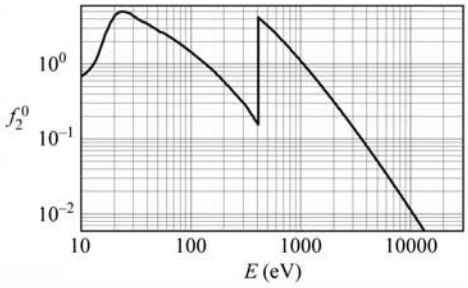

Edge Energies: K 409.9 eV L_1 37.3 eV

σ_a(barns/atom) = μ(cm^2/g) × 26.57
E(keV)μ(cm^2/g) = f_2^0 × 2629.99

Oxygen (O)
Z = 8
Atomic weight = 15.999

Energy (eV)	f_1^0	f_2^0	μ(cm^2/g)
30	1.415	4.661E+00	4.086E+05
70	5.433	3.381E+00	1.270E+05
100	6.158	2.582E+00	6.791E+04
300	6.312	5.645E–01	4.948E+03
700	7.246	3.054E+00	1.148E+03
1000	8.226	1.755E+00	4.615E+03
3000	8.216	2.516E–01	2.205E+02
7000	8.066	4.533E–02	1.703E+01
10000	8.036	2.110E–02	5.548E+00
30000	8.002	1.808E–03	1.585E–01

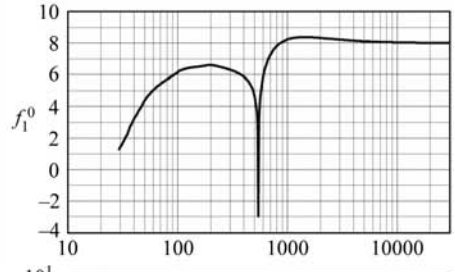

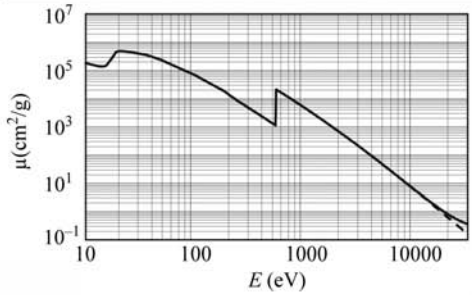

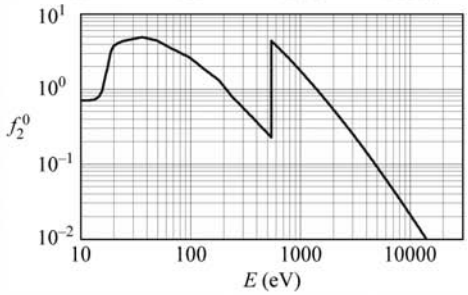

Edge Energies: K 543.1 eV L_1 41.6 eV

(*continued*)

Downloaded From: https://www.spiedigitallibrary.org/ebooks/ on 09 Mar 2022
Terms of Use: https://www.spiedigitallibrary.org/terms-of-use

Table A.1 (*Continued*)

σ_a(barns/atom) = μ(cm^2/g) × 44.80
E(keV)μ(cm^2/g) = f_2^0 × 1559.52

Aluminum (Al)
Z = 13
Atomic weight = 26.982

Energy (eV)	f_1^0	f_2^0	μ(cm^2/g)
30	2.32	0.1737	9.0300E+03
70	-1.449	0.2495	5.5590E+03
100	0.0591	6.908	1.0773E+05
300	12.01	5.017	2.6082E+04
700	12.1	1.406	3.1330E+03
1000	11.65	0.7626	1.1890E+03
3000	13.36	1.501	7.8050E+02
7000	13.25	0.3161	7.8050E+02
10000	13.16	0.1581	2.4660E+01
30000	13.02	0.0165	8.5700E-01

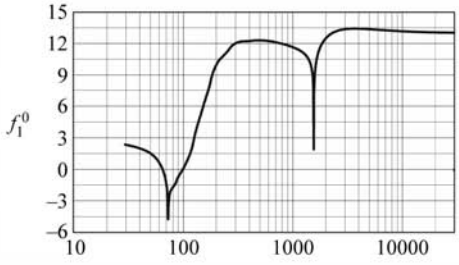

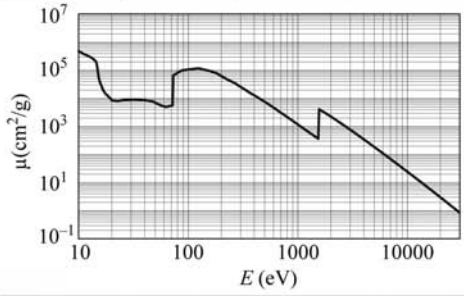

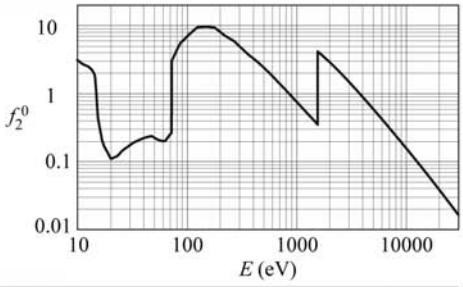

Edge Energies: K 1559.6 eV L$_1$ 117.8 eV
L$_2$ 72.9 eV
L$_3$ 72.5 eV

σ_a(barns/atom) = μ(cm^2/g) × 46.64
E(keV)μ(cm^2/g) = f_2^0 × 1498.22

Silicon (Si)
Z = 14
Atomic weight = 28.086

Energy (eV)	f_1^0	f_2^0	μ(cm^2/g)
30	3.795	0.3734	1.8646E+04
70	2.459	0.5701	1.2202E+04
100	-4.674	2.133	3.1959E+04
300	11.98	6.439	3.2155E+04
700	13.29	1.951	4.1750E+03
1000	12.98	1.07	1.6020E+03
3000	14.21	1.961	9.7920E+02
7000	14.3	0.424	9.0750E+01
10000	14.19	0.2135	3.1990E+01
30000	14.03	0.0228	1.1410E+00

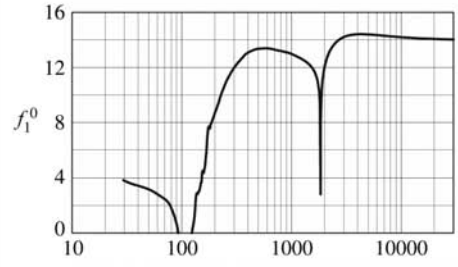

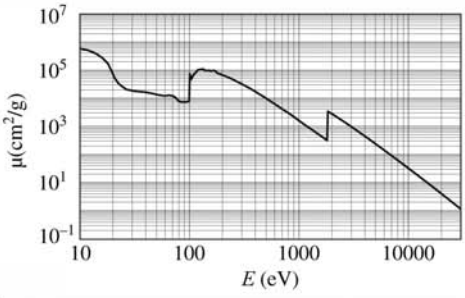

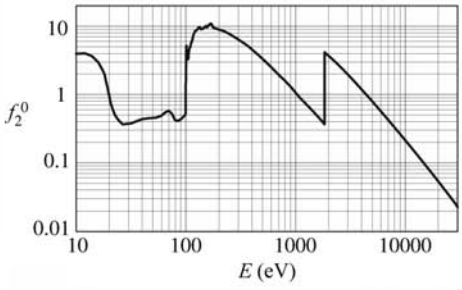

Edge Energies: K 1838.9 eV L$_1$ 149.7 eV
L$_2$ 99.8 eV
L$_3$ 99.2 eV

(*continued*)

Downloaded From: https://www.spiedigitallibrary.org/ebooks/ on 09 Mar 2022
Terms of Use: https://www.spiedigitallibrary.org/terms-of-use

Table A.1 (*Continued*)

σ_a(barns/atom) = μ(cm^2/g) × 58.87
E(keV)μ(cm^2/g) = f_2^0 × 1186.88

Chlorine (Cl)
Z = 17
Atomic weight = 35.453

Energy (eV)	f_1^0	f_2^0	μ(cm^2/g)
30	10.00	4.697E+00	1.858E+05
70	5.637	1.299E+00	2.203E+04
100	5.632	1.489E+00	1.768E+04
300	10.42	1.118E+01	4.421E+04
700	16.53	4.118E+00	6.982E+03
1000	16.50	2.374E+00	2.818E+03
3000	14.71	3.764E+00	1.489E+03
7000	17.40	9.014E–01	1.528E+02
10000	17.31	4.663E–01	5.535E+01
30000	17.06	5.358E–02	2.120E+00

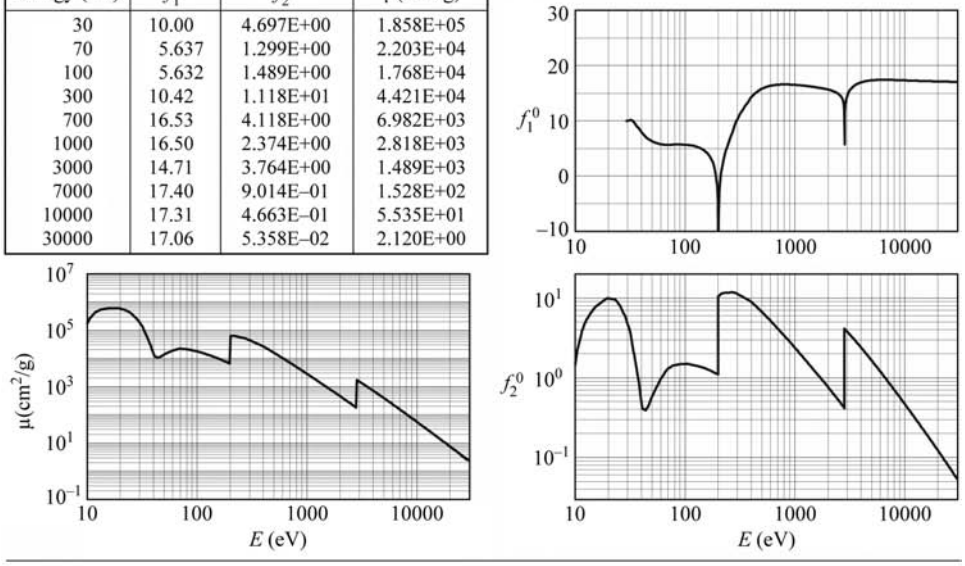

Edge Energies: K 2822.4 eV L_1 270.2 eV
L_2 201.6 eV
L_3 200.0 eV

σ_a(barns/atom) = μ(cm^2/g) × 92.74
E(keV)μ(cm^2/g) = f_2^0 × 753.46

Iron (Fe)
Z = 26
Atomic weight = 55.847

Energy (eV)	f_1^0	f_2^0	μ(cm^2/g)
30	4.775	3.219	8.0848E+04
70	7.831	7.727	8.3176E+04
100	9.212	7.668	5.7775E+04
300	16.18	5.584	1.4024E+04
700	6.551	2.022	2.1770E+03
1000	22.09	11.96	9.0140E+03
3000	25.73	2.159	5.4230E+02
7000	22.00	0.4952	5.3310E+01
10000	25.97	2.267	1.7080E+02
30000	26.20	0.3038	7.6310E+00

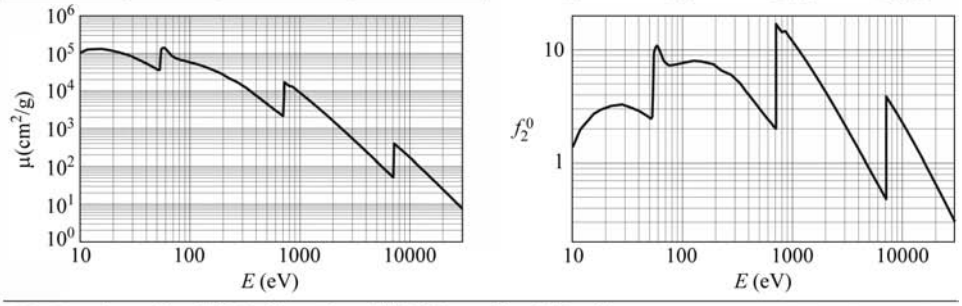

Edge Energies: K 7112.0 eV L_1 844.6 eV M_1 91.3 eV
L_2 719.9 eV M_2 52.7 eV
L_3 706.8 eV M_3 52.7 eV

(*continued*)

Downloaded From: https://www.spiedigitallibrary.org/ebooks/ on 09 Mar 2022
Terms of Use: https://www.spiedigitallibrary.org/terms-of-use

Table A.1 (*Continued*)

σ_a(barns/atom) = μ(cm^2/g) × 97.46
E(keV)μ(cm^2/g) = f_2^0 × 716.92

Nickel (Ni)
Z = 28
Atomic weight = 58.693

Energy (eV)	f_1^0	f_2^0	μ(cm^2/g)
30	4.136	3.658E+00	8.742E+04
70	1.899	8.582E+00	8.789E+04
100	7.746	9.790E+00	7.018E+04
300	17.75	7.698E+00	1.840E+04
700	16.38	2.810E+00	2.878E+03
1000	18.14	1.456E+01	1.044E+04
3000	27.92	2.890E+00	6.907E+02
7000	26.40	6.775E–01	6.939E+01
10000	27.33	2.911E+00	2.087E+02
30000	28.23	4.090E–01	9.774E+00

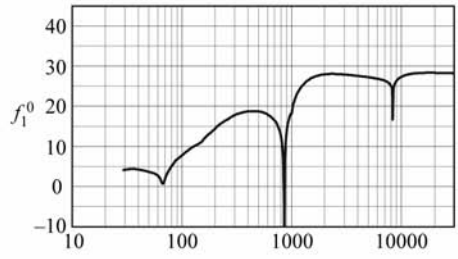

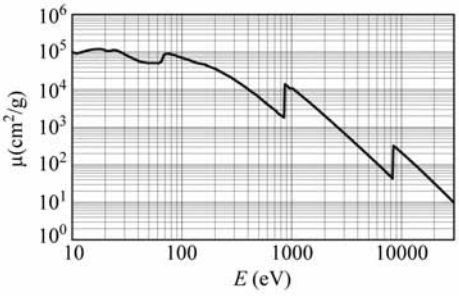

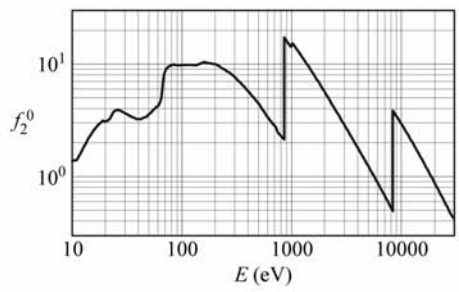

Edge Energies: K 8332.8 eV L_1 1008.6 eV M_1 110.8 eV
L_2 870.0 eV M_2 68.0 eV
L_3 852.7 eV M_3 66.2 eV

σ_a(barns/atom) = μ(cm^2/g) × 105.52
E(keV)μ(cm^2/g) = f_2^0 × 662.17

Copper (Cu)
Z = 29
Atomic weight = 63.546

Energy (eV)	f_1^0	f_2^0	μ(cm^2/g)
30	1.701	4.838E+00	1.068E+05
70	4.223	7.469E+00	7.066E+04
100	5.891	9.478E+00	6.276E+04
300	18.21	8.434E+00	1.862E+04
700	18.37	3.439E+00	3.253E+03
1000	16.61	1.620E+01	1.073E+04
3000	29.03	3.356E+00	7.408E+02
7000	27.68	7.828E–01	7.405E+01
10000	27.71	3.281E+00	2.173E+02
30000	29.26	4.727E–01	1.043E+01

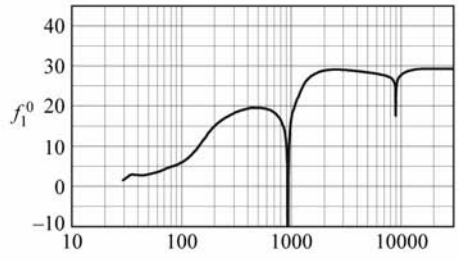

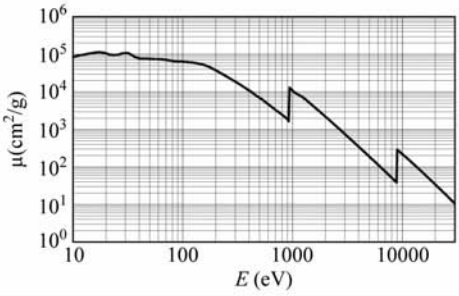

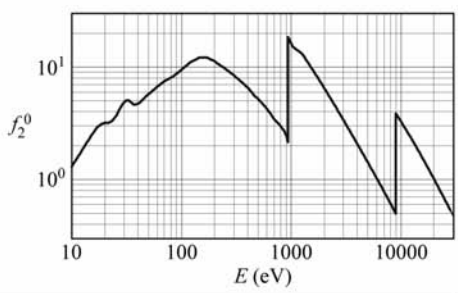

Edge Energies: K 8978.9 eV L_1 1096.7 eV M_1 122.5 eV
L_2 952.3 eV M_2 77.3 eV
L_3 932.5 eV M_3 75.1 eV

(*continued*)

Downloaded From: https://www.spiedigitallibrary.org/ebooks/ on 09 Mar 2022
Terms of Use: https://www.spiedigitallibrary.org/terms-of-use

Table A.1 (*Continued*)

σ_a(barns/atom) = μ(cm^2/g) × 159.31
E(keV)μ(cm^2/g) = f_2^0 × 438.59

Molybdenum (Mo)
Z = 42
Atomic weight = 95.940

Energy (eV)	f_1^0	f_2^0	μ(cm^2/g)
30	7.697	2.949	4.3114E+04
70	18.26	4.732	2.9649E+04
100	13.6	1.124	4.9310E+03
300	4.57	15.68	2.2917E+04
700	31.41	18.19	1.1397E+04
1000	35.13	11.88	5.2120E+03
3000	35.91	13.66	1.9970E+03
7000	42.12	3.494	2.1890E+02
10000	41.67	1.881	8.2490E+01
30000	42.04	1.894	2.7690E+01

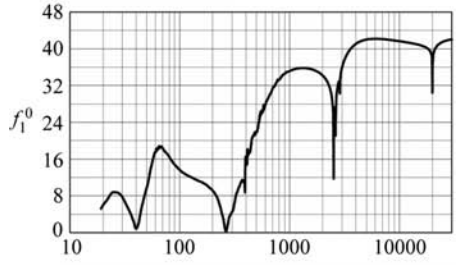

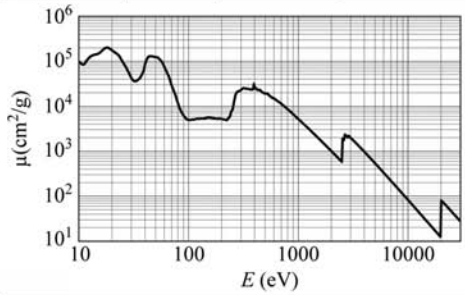

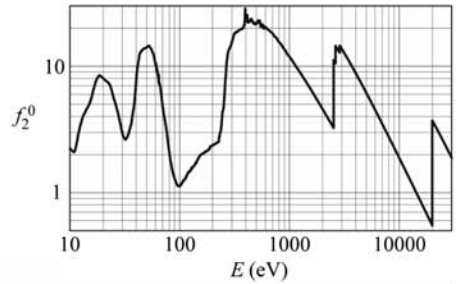

Edge Energies: K 19999.5 eV
L_1 2865.5 eV
L_2 2625.1 eV
L_3 2520.2 eV
M_1 506.3 eV
M_2 411.6 eV
M_3 394.0 eV
M_4 231.1 eV
M_5 227.9 eV
N_1 63.2 eV
N_2 37.6 eV
N_3 35.5 eV

σ_a(barns/atom) = μ(cm^2/g) × 167.83
E(keV)μ(cm^2/g) = f_2^0 × 416.33

Ruthenium (Ru)
Z = 44
Atomic weight = 101.070

Energy (eV)	f_1^0	f_2^0	μ(cm^2/g)
30	7.202	6.852	9.5090E+04
70	19.53	11.07	6.5823E+04
100	17.29	1.841	7.6630E+03
300	2.263	8.156	1.1319E+04
700	31.96	19.49	1.1591E+04
1000	36.64	13.81	5.7480E+03
3000	31.46	13.8	1.9150E+03
7000	44.15	4.147	2.4660E+02
10000	43.82	2.235	9.3060E+01
30000	43.8	2.2	3.0530E+01

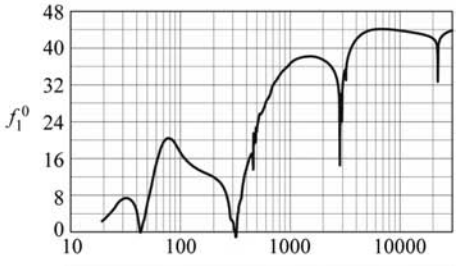

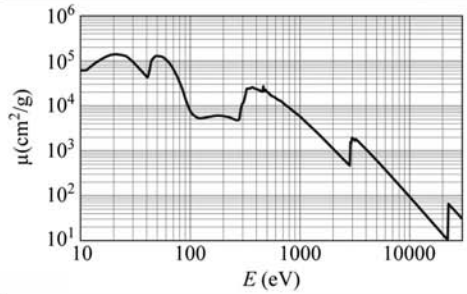

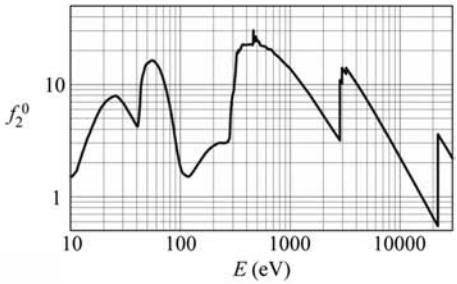

Edge Energies: K 22117.2 eV
L_1 3224.0 eV
L_2 2966.9 eV
L_3 2837.9 eV
M_1 586.2 eV
M_2 483.5 eV
M_3 461.4 eV
M_4 284.2 eV
M_5 280.0 eV
N_1 75.0 eV
N_2 46.5 eV
N_3 43.2 eV

(*continued*)

Downloaded From: https://www.spiedigitallibrary.org/ebooks/ on 09 Mar 2022
Terms of Use: https://www.spiedigitallibrary.org/terms-of-use

Table A.1 (*Continued*)

σ_a(barns/atom) = μ(cm^2/g) × 179.12
E(keV)μ(cm^2/g) = f_2^0 × 390.09

Silver (Ag)
Z = 47
Atomic weight = 107.868

Energy (eV)	f_1^0	f_2^0	μ(cm^2/g)
30	–1.680	1.051E+01	1.366E+05
70	11.74	1.929E+01	1.075E+05
100	26.63	1.109E+01	4.326E+04
300	13.18	4.821E+00	6.269E+03
700	29.04	2.594E+01	1.446E+04
1000	38.90	1.821E+01	7.103E+03
3000	38.15	3.900E+00	5.072E+02
7000	47.12	5.407E+00	3.013E+02
10000	47.02	2.928E+00	1.142E+02
30000	46.19	2.752E+00	3.579E+01

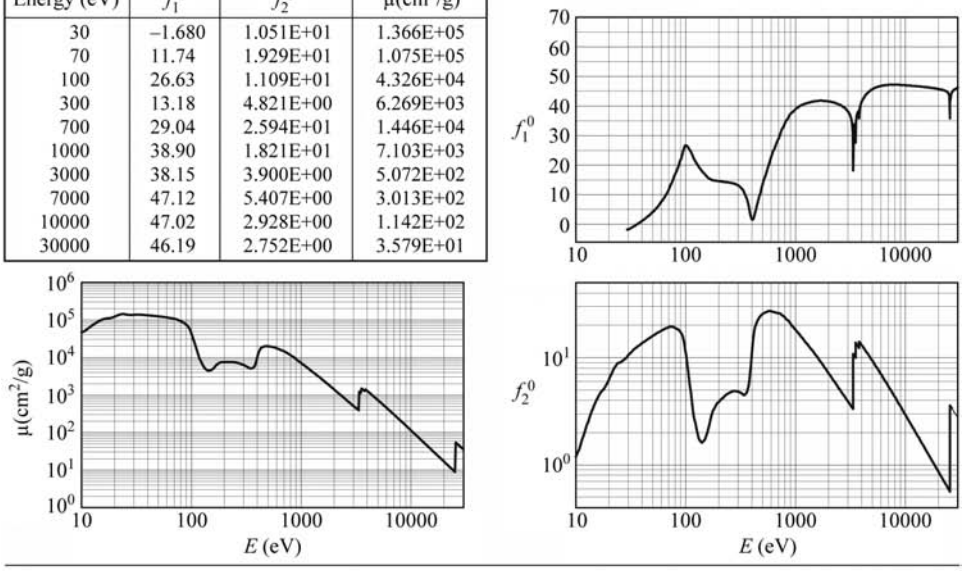

Edge Energies: K 25514.0 eV; L_1 3805.8 eV; L_2 3523.7 eV; L_3 3351.1 eV; M_1 719.0 eV; M_2 603.8 eV; M_3 573.0 eV; M_4 374.0 eV; M_3 368.0 eV; N_1 97.0 eV; N_2 63.7 eV; N_3 58.3 eV

σ_a(barns/atom) = μ(cm^2/g) × 305.29
E(keV)μ(cm^2/g) = f_2^0 × 228.87

Tungsten (W)
Z = 74
Atomic weight = 183.850

Energy (eV)	f_1^0	f_2^0	μ(cm^2/g)
30	4.668	4.227E+00	3.225E+04
70	15.03	1.090E+01	3.564E+04
100	12.64	8.017E+00	1.835E+04
300	21.17	2.282E+01	1.741E+04
700	41.46	2.303E+01	7.531E+03
1000	46.38	1.727E+01	3.953E+03
3000	65.29	2.549E+01	1.944E+03
7000	69.85	7.186E+00	2.350E+02
10000	64.09	4.074E+00	9.325E+01
30000	73.51	2.714E+00	2.070E+01

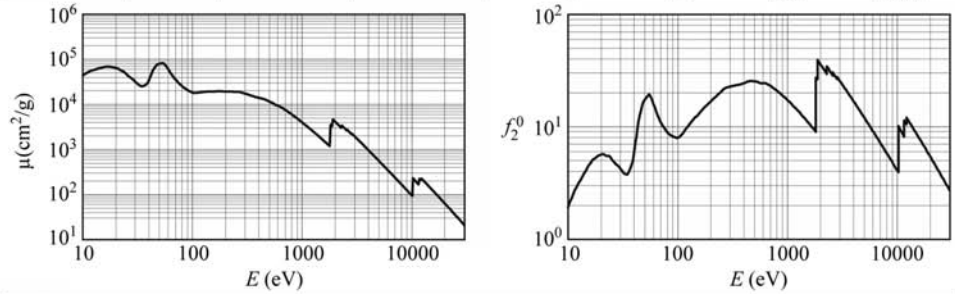

Edge Energies: L_1 12099.8 eV; L_2 11544.0 eV; L_3 10206.8 eV; M_1 2819.6 eV; M_2 2574.9 eV; M_3 2281.0 eV; M_4 1871.6 eV; M_5 1809.2 eV; N_1 594.1 eV; N_2 490.4 eV; N_3 423.6 eV; N_4 255.9 eV; N_5 243.5 eV; N_6 33.6 eV; N_7 31.4 eV; O_1 75.6 eV; O_2 45.3 eV; O_3 36.8 eV

Downloaded From: https://www.spiedigitallibrary.org/ebooks/ on 09 Mar 2022
Terms of Use: https://www.spiedigitallibrary.org/terms-of-use

(*continued*)

Table A.1 (*Continued*)

σ_a(barns/atom) = μ(cm^2/g) × 327.08
E(keV)μ(cm^2/g) = f_2^0 × 213.63

Gold (Au)
Z = 79
Atomic weight = 196.967

Energy (eV)	f_1^0	f_2^0	μ(cm^2/g)
30	3.399	12.15	8.6500E+04
70	16.58	13.41	4.0925E+04
100	21.00	8.642	1.8462E+04
300	14.89	21.55	1.5344E+04
700	40.71	29.8	9.0930E+03
1000	51.72	25.31	5.4060E+03
3000	61.30	29.78	2.1210E+03
7000	75.42	9.68	2.9540E+02
10000	73.45	5.42	1.1580E+02
30000	78.58	3.626	2.5820E+01

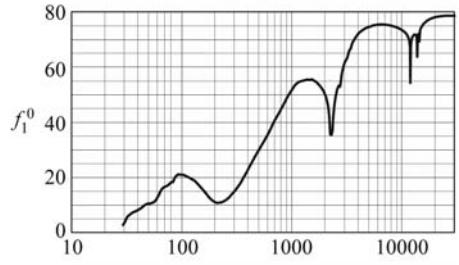

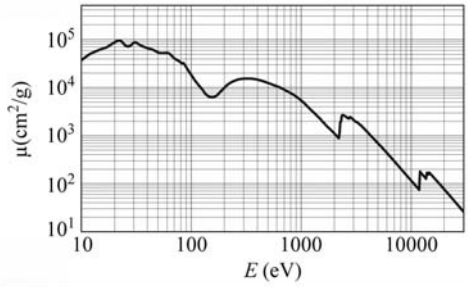

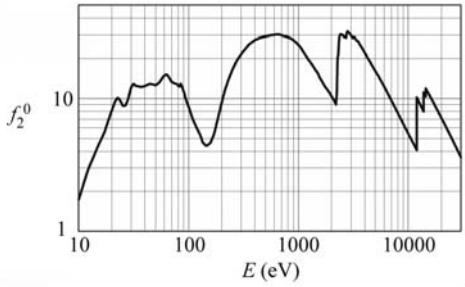

Edge Energies:										
	L_1	14352.8 eV	M_1	3424.9 eV	N_1	762.1 eV	N_6	87.6 eV	O_1	107.2 eV
	L_2	13733.6 eV	M_2	3147.8 eV	N_2	642.7 eV	N_7	83.9 eV	O_2	74.2 eV
	L_3	11918.7 eV	M_3	2743.0 eV	N_3	546.3 eV			O_3	57.2 eV
			M_4	2291.1 eV	N_4	353.2 eV				
			M_5	2205.7 eV	N_5	335.1 eV				

Downloaded From: https://www.spiedigitallibrary.org/ebooks/ on 09 Mar 2022
Terms of Use: https://www.spiedigitallibrary.org/terms-of-use

Table A.2 Physical constants.[3,4]

Quantity	Symbol	Value*	Units
Speed of light in vacuum	c	299,792,458 (exactly)	$m \cdot s^{-1}$
Permeability of vacuum	μ_0	$4\pi \times 10^{-7}$ (exactly)	$N \cdot A^{-2}$
Permittivity of vacuum	$\in_0$	$1/(\mu_0 c^2) = 8.854,187,817...$	10^{-12} F · m^{-1}
Planck's constant	h	4.135,667,33(10)	10^{-15} eV · s
Planck's constant/2π	$\hbar$	6.582,118,99(16)	10^{-15} eV · s
Electron charge	e	1.602,176,487(40)	10^{-19} C
Electron mass	m	9.109,382,15(45)	10^{-31} kg
Electron rest energy	mc^2	0.510,998,910(13)	MeV
Proton mass	m_p	1.672,621,637(83)	10^{-27} kg
Neutron mass	m_n	1.674,927,211(84)	10^{-27} kg
Atomic mass unit $[m(^{12}C)/12]$	m_u	1.660,538,782(83)	10^{-27} kg
Rydberg constant $(me^4/32\pi^2 \in_0^2 \hbar^2)$	$R_\infty hc$	13.605,691,93(34)	eV
Bohr radius $(4\pi \in_0 \hbar/me^2)$	a_0	0.529,177,208,59(36)	10^{-10} m
Classical electron radius $(e^2/4\pi \in_0 mc^2)$	r_e	2.817,940,2894(58)	10^{-15} m
Thomson cross-section $(8\pi r_e^2/3)$	σ_e	0.665,245,8558(27)	10^{-28} m^2
Fine-structure constant $(e^2/4\pi \in_0 \hbar c)$	α	7.297,352,5376(50)	10^{-3}
Compton wavelength (h/mc)	λ_C	2.426,310,2175(33)	10^{-12} m
Bohr magneton $(e\hbar/2m)$	μ_B	5.788,381,7555(79)	10^{-5} eV · T^{-1}
Nuclear magneton $(e\hbar/2m_p)$	μ_N	3.152,451,2326(45)	10^{-8} eV · T^{-1}
Avogadro's number	N_A	6.022,141,79(30)	10^{23} mol^{-1}
Boltzmann constant (R/N_A)	κ	8.617,343(15)	10^{-5} eV · K^{-1}
Stefan–Boltzmann constant $[(\pi^2/60)\kappa^4/\hbar^3 c^2]$	σ	5.670,400(40)	10^{-8} W · m^{-2} · K^{-4}
Universal (molar) gas constant	R	8.314,472(15)	J · mol^{-1} · K^{-1}
Molar volume (ideal gas) (RT/P) (at 273.15 K, 101,325 Pa)	V_m	22.413,996(39)	10^{-3} m^3 · mol^{-1}
Loschmidt's number (N_A/V_m)	nL	2.686,777,4(47)	10^{25} m^{-3}
Photon energy–wavelength product	hc	1239.8418(04)	eV · nm

*The numbers in parentheses indicate the uncertainties in the last digits. For example, $h = 4.1356692(12)$ is equivalent to $h = 4.1356692 \pm 0.0000012$.

Downloaded From: https://www.spiedigitallibrary.org/ebooks/ on 09 Mar 2022
Terms of Use: https://www.spiedigitallibrary.org/terms-of-use

Downloaded From: https://www.spiedigitallibrary.org/ebooks/ on 09 Mar 2022
Terms of Use: https://www.spiedigitallibrary.org/terms-of-use

Table A.3 Electron binding energies in electron volts for the elements in their natural forms.[5]

Element	K 1s	$L_1$2s	L_2 2$p_{1/2}$	L_3 2$p_{3/2}$	$M_1$3s	M_2 3$p_{1/2}$	M_3 3$p_{3/2}$	M_4 3$d_{3/2}$	M_5 3$d_{5/2}$	$N_1$4s	N_2 4$p_{1/2}$	N_3 4$p_{3/2}$
1 H	13.6											
2 He	24.6[b]											
3 Li	54.7[b]											
4 Be	111.5[b]											
5 B	188[b]											
6 C	284.2[b]											
7 N	409.9[b]	37.3[b]										
8 O	543.1[b]	41.6[b]										
9 F	696.7[b]											
10 Ne	870.2[b]	48.5[b]	21.7[b]	21.6[b]								
11 Na	1070.8[c]	63.5[c]	30.4[c]	30.5[b]								
12 Mg	1303.0[c]	88.6[b]	49.6[c]	49.2[c]								
13 Al	1559.6	117.8[b]	72.9[b]	72.5[b]								
14 Si	1838.9	149.7[b]	99.8[b]	99.2[b]								
15 P	2145.5	189[b]	136[b]	135[b]								
16 S	2472	230.9[b]	163.6[b]	162.5[b]								
17 Cl	2822.4	270.2[b]	202[b]	200[b]								
18 Ar	3205.9[b]	326.3[b]	250.6[b]	248.4[b]	29.3[b]	15.9[b]	15.7[b]					
19 K	3608.4[b]	378.6[b]	297.3[b]	294.6[b]	34.8[b]	18.3[b]	18.3[b]					
20 Ca	4038.5[b]	438.4[c]	349.7[c]	346.2[c]	44.3[c]	25.4[c]	25.4[c]					
21 Sc	4492.8	498.0[b]	403.6[b]	398.7[b]	51.1[b]	28.3[b]	28.3[b]					
22 Ti	4966.4	560.9[c]	461.2[c]	453.8[c]	58.7[c]	32.6[c]	32.6[c]					
23 V	5465.1	626.7[c]	519.8[c]	512.1[c]	66.3[c]	37.2[c]	37.2[c]					
24 Cr	5989.2	695.7[c]	583.8[c]	574.1[c]	74.1[c]	42.2[c]	42.2[c]					
25 Mn	6539.0	769.1[c]	649.9[c]	638.7[c]	82.3[c]	47.2[c]	47.2[c]					
26 Fe	7112.0	844.6[c]	719.9[c]	706.8[c]	91.3[c]	52.7[c]	52.7[c]					
27 Co	7708.9	925.1[c]	793.3[c]	778.1[c]	101.0[c]	58.9[c]	58.9[c]					
28 Ni	8332.8	1008.6[c]	870.0[c]	852.7[c]	110.8[c]	68.0[c]	66.2[c]					

(*continued*)

Table A.3 (*Continued*)

Element	K 1s	$L_1$2s	L_2 2$p_{1/2}$	L_3 2$p_{3/2}$	$M_1$3s	M_2 3$p_{1/2}$	M_3 3$p_{3/2}$	M_4 3$d_{3/2}$	M_5 3$d_{5/2}$	$N_1$4s	N_2 4$p_{1/2}$	N_3 4$p_{3/2}$
29 Cu	8978.9	1096.7[c]	952.3[c]	932.5[c]	122.5[c]	77.3[c]	75.1[c]					
30 Zn	9658.6	1196.2[b]	1044.9[b]	1021.8[b]	139.8[b]	91.4[b]	88.6[b]	10.2[b]	10.1[b]			
31 Ga	10367.1	1299.0[b]	1143.2[c]	1116.4[c]	159.5[c]	103.5[c]	103.5[c]	18.7[c]	18.7[c]			
32 Ge	11103.1	1414.6[b]	1248.1[b]	1217.0[b]	180.1[b]	124.9[b]	120.8[b]	29.0[b]	29.0[b]			
33 As	11866.7	1527.0[b]	1359.1[b]	1323.6[b]	204.7[b]	146.2[b]	141.2[b]	41.7[b]	41.7[b]			
34 Se	12657.8	1652.0[b]	1474.3[b]	1433.9[b]	229.6[b]	166.5[b]	160.7[b]	55.5[b]	54.6[b]			
35 Br	13473.7	1782.0[b]	1596.0[b]	1549.9[b]	257[b]	189[b]	182[b]	70[b]	69[b]			
36 Kr	14325.6	1921.0	1730.9[b]	1678.4[b]	292.8[b]	222.2[b]	214.4	95.0[b]	93.8[b]	27.5[b]	14.1[b]	14.1[b]
37 Rb	15199.7	2065.1	1863.9	1804.4	326.7[b]	248.7[b]	239.1[b]	113.0[b]	112[b]	30.5[b]	16.3[b]	15.3[b]
38 Sr	16104.6	2216.3	2006.8	1939.6	358.7[c]	280 3[c]	270.0[c]	136.0[c]	134.2[c]	38.9[c]	20.3[c]	20.3[c]
39 Y	17038.4	2372.5	2155.5	2080.0	392.0[b]	310.6[b]	298.8[b]	157.7[c]	155.8[c]	43.8[b]	24.4[b]	23.1[b]
40 Zr	17997.6	2531.6	2306.7	2222.3	430.3[c]	343.5[c]	329.8[c]	181.1[c]	178.8[c]	50.6[c]	28.5[c]	27.7[c]
41 Nb	18985.6	2697.7	2464.7	2370.5	466.6[c]	376.1[c]	360.6[c]	205.0[c]	202.3[c]	56.4[c]	32.6[c]	30.8[c]
42 Mo	19999.5	2865.5	2625.1	2520.2	506.3[c]	411.6[c]	394.0[c]	231.1[c]	227.9[c]	63.2[c]	37.6[c]	35.5[c]
43 Tc	21044.0	3042.5	2793.2	2676.9	544[b]	445[b]	425[b]	257[b]	253[b]	68[b]	39[c]	39[b]
44 Ru	22117.2	3224.0	2966.9	2837.9	586.2[c]	483.5[c]	461.4[c]	284.2[c]	280.0[c]	75.0[c]	46.5[c]	43.2[c]
45 Rh	23219.9	3411.9	3146.1	3003.8	628.1[c]	521.3[c]	496.5[c]	311.9[c]	307.2[c]	81.4[b]	50.5[c]	47.3[c]
46 Pd	24350.3	3604.3	3330.3	3173.3	671.6[c]	559.9[c]	532.3[c]	340.5[c]	335.2[c]	87.6[b]	55.7[c]	50.9[c]
47 Ag	25514.0	3805.8	3523.7	3351.1	719.0[c]	603.8[c]	573.0[c]	374.0[c]	368.0[c]	97.0[c]	63.7[c]	58.3[c]
48 Cd	26711.2	4018.0	3727.0	3537.5	772.0[c]	652.6[c]	618.4[c]	411.9[c]	405.2[c]	109.8[c]	63.9[c]	63.9[c]
49 In	27939.9	4237.5	3938.0	3730.1	827.2[c]	703.2[c]	665.3[c]	451.4[c]	443.9[c]	122.7[c]	73.5[c]	73.5[c]
50 Sn	29200.1	4464.7	4156.1	3928.8	884.7[c]	756.5[c]	714.6[c]	493.2[c]	484.9[c]	137.1[c]	83.6[c]	83.6[c]
51 Sb	30491.2	4698.3	4380.4	4132.2	946[c]	812.7[c]	766.4[c]	537.5[c]	528.2[c]	153.2[c]	95.6[c]	95.6[c]
S2 Te	31813.8	4939.2	4612.0	4341.4	1006[c]	870.8[c]	820.8[c]	583.4[c]	573.0[c]	169.4[c]	103.3[c]	103.3[c]
53 I	33169.4	5188.1	4852.1	4557.1	1072[b]	931[b]	875[b]	631[b]	620[b]	186[b]	123[b]	123[b]
54 Xe	34561.4	5452.8	5103.7	4782.2	1148.7[b]	1002.1[b]	940.6[b]	689.0[b]	676.4[b]	213.2[b]	146.7	145.5[b]
55 Cs	35984.6	5714.3	5359.4	5011.9	1211[b]	1071[b]	1003[b]	740.5[b]	726.6[b]	232.3[b]	172.4[b]	161.3[b]
56 Ba	37440.6	5988.8	5623.6	5247.0	1293[b]	1137[b]	1063[b]	795.7[b]	780.5[b]	253.5[c]	192	178.6[c]
57 La	38924.6	6266.3	5890.6	5482.7	1362[b]	1209[b]	1128[b]	853[b]	836[b]	247.7[b]	205.8	196.0[b]

Downloaded From: https://www.spiedigitallibrary.org/ebooks/ on 09 Mar 2022
Terms of Use: https://www.spiedigitallibrary.org/terms-of-use

58	Ce	40443.0	6548.8	6164.2	5723.4	1436[b]	1274[b]	1187[b]	902.4[b]	883.8[b]	291.0[b]	223.2	206.5[b]
59	Pr	41990.6	6834.8	6440.4	5964.3	1511.0	1337.4	1242.2	948.3[b]	928.8[b]	304.5	236.3	217.6
60	Nd	43568.9	7126.0	6721.5	6207.9	1575.3	1402.8	1297.4	1003.3[b]	980.4[b]	319.2[b]	243.3	224.6
61	Pm	45184.0	7427.9	7012.8	6459.3	—	1471.4	1356.9	1051.5	1026.9	—	242	242
62	Sm	46834.2	7736.8	7311.8	6716.2	1722.8	1540.7	1419.8	1110.9[b]	1083.4[b]	347.2[b]	265.6	247.4
63	Eu	48519.0	8052.0	7617.1	6976.9	1800.0	1613.9	1480.6	1158.6[b]	1127.5[b]	360	284	257
64	Gd	50239.1	8375.6	7930.3	7242.8	1880.8	1688.3	1544.0	1221.9[b]	1189.6[b]	378.6[b]	286	270.9
65	Tb	51995.7	8708.0	8251.6	7514.0	1967.5	1767.7	1611.3	1276.9[b]	1241.1[b]	396.0[b]	322.4[b]	284.1[b]
66	Dy	53788.5	9045.8	8580.6	7790.1	2046.8	1841.8	1675.6	1332.5	1292.6[b]	414.2[b]	333.5[b]	293.2[b]
67	Ho	55617.7	9394.2	8917.8	8071.1	2128.3	1922.8	1741.2	1391.5	1351.4	432.4[b]	343.5	308.2[b]
68	Er	57485.5	9751.3	9264.3	8357.9	2206.5	2005.8	1811.8	1453.3	1409.3	449.8[b]	366.2	320.2[b]
69	Tm	59398.6	10115.7	9616.9	8648.0	2306.8	2089.8	1884.5	1514.6	1467.7	470.9[b]	385.9[b]	332.6[b]
70	Yb	61332.3	10486.4	9978.2	8943.6	2398.1	2173.0	1949.8	1576.3	1527.8	480.5[b]	388.7[b]	339.7[b]
71	Lu	63313.8	10870.4	10348.6	9244.1	2491.2	2263.5	2023.6	1639.4	1588.5	506.8[b]	412.4[b]	359.2[b]
72	Hf	65350.8	11270.7	10739.4	9560.7	2600.9	2365.4	2107.6	1716.4	1661.7	538[b]	438.2[c]	380.7[c]
73	Ta	67416.4	11681.5	11136.1	9881.1	2708.0	2468.7	2194.0	1793.2	1735.1	563.4[c]	463.4[c]	400.9[c]
74	W	69525.0	12099.8	11544.0	10206.8	2819.6	2574.9	2281.0	1871.6	1809.2	594.1[c]	490.4[c]	423.6[c]
75	Re	71676.4	12526.7	11958.7	10535.3	2931.7	2681.6	2367.3	1948.9	1882.9	625.4	518.7[c]	446.8[c]
76	Os	73870.8	12968.0	12385.0	10870.9	3048.5	2792.2	2457.2	2030.8	1960.1	658.2[c]	549.1[c]	470.7[c]
77	Ir	76111.0	13418.5	12824.1	11215.2	3173.7	2908.7	2550.7	2116.1	2040.4	691.1[c]	577.8[c]	495.8[c]
78	Pt	78394.8	13879.9	13272.6	11563.7	3296.0	3026.5	2645.4	2201.9	2121.6	725.4[c]	609.1[c]	519.4[c]
79	Au	80724.9	14352.8	13733.6	11918.7	3424.9	3147.8	2743.0	2291.1	2205.7	762.1[c]	642.7[c]	546.3[c]
80	Hg	83102.3	14839.3	14208.7	12283.9	3561.6	3278.5	2847.1	2384.9	2294.9	802.2[c]	680.2[c]	576.6[c]
81	Tl	85530.4	15346.7	14697.9	12657.5	3704.1	3415.7	2956.6	2485.1	2389.3	846.2[c]	720.5[c]	609.5[c]
82	Pb	88004.5	15860.8	15200.0	13035.2	3850.7	3554.2	3066.4	2585.6	2484.0	891.8[c]	761.9[c]	643.5[c]
83	Bi	90525.9	16387.5	15711.1	13418.6	3999.1	3696.3	3176.9	2687.6	2579.6	939[c]	805.2[c]	678.8[c]
84	Po	93105.0	16939.3	16244.3	13813.8	4149.4	3854.1	3301.9	2798.0	2683.0	995[b]	851[b]	705[b]
85	At	95729.9	17493	16784.7	14213.5	4317	4008	3426	2908.7	2786.7	1042[b]	886[b]	740[b]
86	Rn	98404	18049	17337.1	14619.4	4482	4159	3538	3021.5	2892.4	1097[b]	929[b]	768[b]
87	Fr	101137	18639	17906.5	15031.2	4652	4327	3663	3136.2	2999.9	1153[b]	980[b]	810[b]

(*continued*)

Downloaded From: https://www.spiedigitallibrary.org/ebooks/ on 09 Mar 2022
Terms of Use: https://www.spiedigitallibrary.org/terms-of-use

Table A.3 (*Continued*)

Element	K 1s	$L_1$2s	L_2 2$p_{1/2}$	L_3 2$p_{3/2}$	$M_1$3s	M_2 3$p_{1/2}$	M_3 3$p_{3/2}$	M_4 3$d_{3/2}$	M_5 3$d_{5/2}$	$N_1$4s	N_2 4$p_{1/2}$	N_3 4$p_{3/2}$
88 Ra	103921.9	19236.7	18484.3	15444.4	4822.0	4489.5	3791.8	3248.4	3104.9	1208[b]	1057.6[b]	879.1[b]
89 Ac	106755.3	19840	19083.2	15871.0	5002	4656	3909	3370.2	3219.0	1269[b]	1080[b]	890[b]
90 Th	109650.9	20472.1	19693.2	16300.3	5182.3	4830.4	4046.1	3490.8	3332.0	1330[b]	1168[b]	966.4[c]
91 Pa	112601.4	21104.6	20313.7	16733.1	5366.9	5000.9	4173.8	3611.2	3441.8	1387[b]	1224[b]	1007[b]
92 U	115606.1	21757.4	20947.6	17166.3	5548.0	5182.2	4303.4	3727.6	3551.7	1439[b]	1271[b]	1043.0[c]

Element	$N_4$4$d_{3/2}$	$N_5$4$d_{5/2}$	$N_6$4$f_{5/2}$	$N_7$4$f_{7/2}$	$O_1$5s	$O_2$5$p_{1/2}$	$O_3$5$p_{3/2}$	$O_4$5$d_{3/2}$	$O_5$5$d_{5/2}$
48 Cd	11.7[c]	10.7[c]							
49 In	17.7[c]	16.9[c]							
50 Sn	24.9[c]	23.9[c]							
51 Sb	33.3[c]	32.1[c]							
52 Te	41.9[c]	40.4[c]							
53 I	50[b]	50[b]							
54 Xe	69.5[b]	67.5[b]	—	—	23.3[b]	13.4[b]	12.1[b]		
55 Cs	79.8[b]	77.5[b]	—	—	22.7	14.2[b]	12.1[b]		
56 Ba	92.6[c]	89.9[c]	—	—	30.3[c]	17.0[c]	14.8		
57 La	105.3[b]	102.5[b]	—	—	34.3[b]	19.3[b]	16.8[b]		
58 Ce	109[b]	—	—	—	37.8	19.8[b]	17.0[b]		
59 Pr	115.1[b]	115.1[b]	—	—	37.4	22.3	22.3		
60 Nd	120.5[b]	120.5[b]	—	—	37.5	21.1	21.1		
61 Pm	120	120	—	—	—	—	—		
62 Sm	129	129	—	—	37.4	21.3	21.3		
63 Eu	133	127.7[b]	—	—	31.8	22.0	22.0		
64 Gd	140.5	142.6[b]	—	—	43.5[b]	20	20		
65 Tb	150.5[b]	150.5[b]	—	—	45.6[b]	28.7[b]	22.6[b]		
66 Dy	153.6[b]	153.6[b]	—	—	49.9[b]	29.5	23.1		
67 Ho	160[b]	160[b]	—	—	49.3[b]	30.8[b]	24.1[b]		
68 Er	167.6[b]	167.6[b]	—	—	50.6[b]	31.4[b]	24.7[b]		

Downloaded From: https://www.spiedigitallibrary.org/ebooks/ on 09 Mar 2022
Terms of Use: https://www.spiedigitallibrary.org/terms-of-use

69 Tm	175.5[b]	175.5[b]	—	—	54.7[b]	31.8[b]	25.0[b]		
70 Yb	191.2[b]	182.4[b]	—	—	52.0[b]	30.3[b]	24.1[b]		
71 Lu	206.1[b]	196.3[c]	8.9[b]	7.5[b]	57.3[b]	33.6[b]	26.7[b]		
72 Hf	220.0[c]	211.5[c]	15.9[c]	14.2[c]	64.2[c]	38[b]	29.9[b]		
73 Ta	237.9[c]	226.4[c]	23.5[c]	21.6[c]	69.7[c]	42.2[b]	32.7[b]		
74 W	255.9[c]	243.5[c]	33.6[b]	31.4[c]	75.6[c]	45.3[b]	36.8[b]		
75 Re	273.9[c]	260.5[c]	42.9[b]	40.5[c]	83[c]	45.6[b]	34.6[b]		
76 Os	293.1[c]	278.5[c]	53.4[c]	50.7[c]	84[c]	58[b]	44.5[c]		
77 Ir	311.9[c]	296.3[c]	63.8[c]	60.8[c]	95.2[b]	63.0[b]	48.0[c]		
78 Pt	331.6[c]	314.6[c]	74.5[c]	71.2[c]	101[c]	65.3[b]	51.7[c]		
79 Au	353.2[c]	335.1[c]	87.6[c]	83.9[c]	107.2[b]	74.2[c]	57.2[c]		
80 Hg	378.2[c]	358.8[c]	104.0[c]	99.9[c]	127[c]	83.1[c]	64.5[c]	9.6[c]	7.8[c]
81 Tl	405.7[c]	385.0[c]	122.2[c]	117.8[c]	136[b]	94.6[c]	73.5[c]	14.7[c]	12.5[c]
82 Pb	434.3[c]	412.2[c]	141.7[c]	136.9[c]	147[b]	106.4[c]	83.3[c]	20.7[c]	18.1[c]
83 Bi	464.0[c]	440.1[c]	162.3[c]	157.0[c]	159.3[b]	119.0[c]	92.6[c]	26.9[c]	23.8[c]
84 Po	500[b]	473[b]	184[b]	184[b]	177[b]	132[b]	104[b]	31[b]	31[b]
85 At	533[b]	507[b]	210[b]	210[b]	195[b]	148[b]	115[b]	40[b]	40[b]
86 Rn	567[b]	541[b]	238[b]	238[b]	214[b]	164[b]	127[b]	48[b]	48[b]
87 Fr	603[b]	577[b]	268[b]	268[b]	234[b]	182[b]	140[b]	58[b]	58[b]
88 Ra	635.9[b]	602.7[b]	299[b]	299[b]	254[b]	200[b]	153[b]	68[b]	68[b]
89 Ac	675[b]	639[b]	319[b]	319[b]	272[b]	215[b]	167[b]	80[b]	80[b]
90 Th	712.1[c]	675.2[c]	342.4[c]	333.1	290[b]	229[b]	182[b]	92.5[c]	85.4[c]
91 Pa	743[b]	708[b]	371[b]	360[b]	310[b]	232[b]	232[b]	94[b]	94[b]
92 U	778.3[c]	736.2[c]	388.2[b]	377.4[c]	321[b]	257[b]	192[b]	102.8[c]	94.2[c]

[b]From M. Cardona and L. Lay, Eds., *Photoemission in Solids I: General Principles*, Springer-Verlag, Berlin (1978).
[c]From J. C. Fuggle and N. Mårtensson, "Core-level binding energies in metals," *J. Electron. Spectrosc. Relat. Phenom.* **21**, 275 (1980).

Downloaded From: https://www.spiedigitallibrary.org/ebooks/ on 09 Mar 2022
Terms of Use: https://www.spiedigitallibrary.org/terms-of-use

Table A.4 Photon energies in electron volts of principal K- and L-shell emission lines.[6]

Element	Ka_1	Ka_2	Kb_1	La_1	La_2	Lb_1	Lb_2	Lg_1
3 Li	54.3							
4 Be	108.5							
5 B	183.3							
6 C	277							
7 N	392.4							
8 O	524.9							
9 F	676.8							
10 Ne	848.6	848.6						
11 Na	1,040.98	1,040.98	1,071.1					
12 Mg	1,253.60	1,253.60	1,302.2					
13 Al	1,486.70	1,486.27	1,557.45					
14 Si	1,739.98	1,739.38	1,835.94					
15 P	2,013.7	2,012.7	2,139.1					
16 S	2,307.84	2,306.64	2,464.04					
17 Cl	2,622.39	2,620.78	2,815.6					
18 Ar	2,957.70	2,955.63	3,190.5					
19 K	3,313.8	3,311.1	3,589.6					
20 Ca	3,691.68	3,688.09	4,012.7	341.3	341.3	344.9		
21 Sc	4,090.6	4,086.1	4,460.5	395.4	395.4	399.6		
22 Ti	4,510.84	4,504.86	4,931.81	452.2	452.2	458.4		
23 V	4,952.20	4,944.64	5,427.29	511.3	511.3	519.2		
24 Cr	5,414.72	5,405.509	5,946.71	572.8	572.8	582.8		
25 Mn	5,898.75	5,887.65	6,490.45	637.4	637.4	648.8		
26 Fe	6,403.84	6,390.84	7,057.98	705.0	705.0	718.5		
27 Co	6,930.32	6,915.30	7,649.43	776.2	776.2	791.4		
28 Ni	7,478.15	7,460.89	8,264.66	851.5	851.5	868.8		
29 Cu	8,047.78	8,027.83	8,905.29	929.7	929.7	949.8		
30 Zn	8,638.86	8,615.78	9,572.0	1,011.7	1,011.7	1,034.7		
31 Ga	9,251.74	9,224.82	10,264.2	1,097.92	1,097.92	1,124.8		
32 Ge	9,886.42	9,855.32	10,982.1	1,188.00	1,188.00	1,218.5		
33 As	10,543.72	10,507.99	11,726.2	1,282.0	1,282.0	1,317.0		
34 Se	11,222.4	11,181.4	12,495.9	1,379.10	1,379.10	1,419.23		

Downloaded From: https://www.spiedigitallibrary.org/ebooks/ on 09 Mar 2022
Terms of Use: https://www.spiedigitallibrary.org/terms-of-use

35 Br	11,924.2	11,877.6	13,291.4	1,480.43	1,480.43	1,525.90		
36 Kr	12,649	12,598	14,112	1,586.0	1,586.0	1,636.6		
37 Rb	13,395.3	13,335.8	14,961.3	1,694.13	1,692.56	1,752.17		
38 Sr	14,165	14,097.9	15,835.7	1,806.56	1,804.74	1,871.72		
39 Y	14,958.4	14,882.9	16,737.8	1,922.56	1,920.47	1,995.84		
40 Zr	15,775.1	15,690.9	17,667.8	2,042.36	2,039.9	2,124.4	2,219.4	2,302.7
41 Nb	16,615.1	16,521.0	18,622.5	2,165.89	2,163.0	2,257.4	2,367.0	2,461.8
42 Mo	17,479.34	17,374.3	19,608.3	2,293.16	2,289.85	2,394.81	2,518.3	2,623.5
43 Tc	18,367.1	18,250.8	20,619	2,424.0	—	2,536.8	—	—
44 Ru	19,279.2	19,150.4	21,656.8	2,558.55	2,554.31	2,683.23	2,836.0	2,964.5
45 Rh	20,216.1	20,073.7	22,723.6	2,696.74	2,692.05	2,834.41	3,001.3	3,143.8
46 Pd	21,177.1	21,020.1	23,818.7	2,838.61	2,833.29	2,990.22	3,171.79	3,328.7
47 Ag	22,162.92	21,990.3	24,942.4	2,984.31	2,978.21	3,150.94	3,347.81	3,519.59
48 Cd	23,173.6	22,984.1	26,095.5	3,133.73	3,126.91	3,316.57	3,528.12	3,716.86
49 In	24,209.7	24,002.0	27,275.9	3,286.94	3,279.29	3,487.21	3,713.81	3,920.81
50 Sn	25,271.3	25,044.0	28,486.0	3,443.98	3,435.42	3,662.80	3,904.86	4,131.12
51 Sb	26,359.1	26,110.8	29,725.6	3,604.72	3,595.32	3,843.57	4,100.78	4,347.79
52 Te	27,472.3	27,201.7	30,995.7	3,769.33	3,758.8	4,029.58	4,301.7	4,570.9
53 I	28,612.0	28,317.2	32,294.7	3,937.65	3,926.04	4,220.72	4,507.5	4,800.9
54 Xe	29,779	29,458	33,624	4,109.9	—	—	—	—
55 Cs	30,972.8	30,625.1	34,986.9	4,286.5	4,272.2	4,619.8	4,935.9	5,280.4
56 Ba	32,193.6	31,817.1	36,378.2	4,466.26	4,450.90	4,827.53	5,156.5	5,531.1
57 La	33,441.8	33,034.1	37,801.0	4,650.97	4,634.23	5,042.1	5,383.5	5,788.5
58 Ce	34,719.7	34,278.9	39,257.3	4,840.2	4,823.0	5,262.2	5,613.4	6,052
59 Pr	36,026.3	35,550.2	40,748.2	5,033.7	5,013.5	5,488.9	5,850	6,322.1
60 Nd	37,361.0	36,847.4	42,271.3	5,230.4	5,207.7	5,721.6	6,089.4	6,602.1
61 Pm	38,724.7	38,171.2	43,826	5,432.5	5,407.8	5,961	6,339	6,892
62 Sm	40,118.1	39,522.4	45,413	5,636.1	5,609.0	6,205.1	6,586	7,178
63 Eu	41,542.2	40,901.9	47,037.9	5,845.7	5,816.6	6,456.4	6,843.2	7,480.3
64 Gd	42,996.2	42,308.9	48,697	6,057.2	6,025.0	6,713.2	7,102.8	7,785.8
65 Tb	44,481.6	43,744.1	50,382	6,272.8	6,238.0	6,978	7,366.7	8,102
66 Dy	45,998.4	45,207.8	52,119	6,495.2	6,457.7	7,247.7	7,635.7	8,418.8
67 Ho	47,546.7	46,699.7	53,877	6,719.8	6,679.5	7,525.3	7,911	8,747
68 Er	49,127.7	48,221.1	55,681	6,948.7	6,905.0	7,810.9	8,189.0	9,089

(*continued*)

Downloaded From: https://www.spiedigitallibrary.org/ebooks/ on 09 Mar 2022
Terms of Use: https://www.spiedigitallibrary.org/terms-of-use

Table A.4 (*Continued*)

Element	Ka_1	Ka_2	Kb_1	La_1	La_2	Lb_1	Lb_2	Lg_1
69 Tm	50,741.6	49,772.6	57,517	7,179.9	7,133.1	8,101	8,468	9,426
70 Yb	52,388.9	51,354.0	59,370	7,415.6	7,367.3	8,401.8	8,758.8	9,780.1
71 Lu	54,069.8	52,965.0	61,283	7,655.5	7,604.9	8,709.0	9,048.9	10,143.4
72 Hf	55,790.2	54,611.4	63,234	7,899.0	7,844.6	9,022.7	9,347.3	10,515.8
73 Ta	57,532	56,277	65,223	8,146.1	8,087.9	9,343.1	9,651.8	10,895.2
74 W	59,318.24	57,981.7	67,244	8,397.6	8,335.2	9,672.35	9,961.5	11,285.9
75 Re	61,140.3	59,717.9	69,310	8,652.5	8,586.2	10,010.0	10,275.2	11,685.4
76 Os	63,000.5	61,486.7	71,413	8,911.7	8,841.0	10,355.3	10,598.5	12,095.3
77 Ir	64,895.6	63,286.7	73,560.8	9,175.1	9,099.5	10,708.3	10,920.3	12,512.6
78 Pt	66,832	65,112	75,748	9,442.3	9,361.8	11,070.7	11,250.5	12,942.0
79 Au	68,803.7	66,989.5	77,984	9,713.3	9,628.0	11,442.3	11,584.7	13,381.7
80 Hg	70,819	68,895	80,253	9,988.8	9,897.6	11,822.6	11,924.1	13,830.1
81 Tl	72,871.5	70,831.9	82,576	10,268.5	10,172.8	12,213.3	12,271.5	14,291.5
82 Pb	74,969.4	72,804.2	84,936	10,551.5	10,449.5	12,613.7	12,622.6	14,764.4
83 Bi	77,107.9	74,814.8	87,343	10,838.8	10,730.91	13,023.5	12,979.9	15,247.7
84 Po	79,290	76,862	89,800	11,130.8	11,015.8	13,447	13,340.4	15,744
85 At	81,520	78,950	92,300	11,426.8	11,304.8	13,876	—	16,251
86 Rn	83,780	81,070	94,870	11,727.0	11,597.9	14,316	—	16,770
87 Fr	86,100	83,230	97,470	12,031.3	11,895.0	14,770	14,450	17,303
88 Ra	88,470	85,430	100,130	12,339.7	12,196.2	15,235.8	14,841.4	17,849
89 Ac	90,884	87,670	102,850	12,652.0	12,500.8	15,713	—	18,408
90 Th	93,350	89,953	105,609	12,968.7	12,809.6	16,202.2	15,623.7	18,982.5
91 Pa	95,868	92,287	108,427	13,290.7	13,122.2	16,702	16,024	19,568
92 U	98,439	94,665	111,300	13,614.7	13,438.8	17,220.0	16,428.3	20,167.1
93 Np	—	—	—	13,944.1	13,759.7	17,750.2	16,840.0	20,784.8
94 Pu	—	—	—	14,278.6	14,084.2	18,293.7	17,255.3	21,417.3
95 Am	—	—	—	14,617.2	14,411.9	18,852.0	17,676.5	22,065.2

Downloaded From: https://www.spiedigitallibrary.org/ebooks/ on 09 Mar 2022
Terms of Use: https://www.spiedigitallibrary.org/terms-of-use

References

1. D. Attwood, *Soft X-Rays and Extreme Ultraviolet Radiation, Principles and Applications*, Cambridge Univ. Press, Cambridge, UK (2000).
2. E. Gullikson, www.cxro.LBL.gov.
3. E. R. Cohen and B. N. Taylor, "The fundamental physical constants," *Phys. Today*, p. BG9 (August 1995).
4. http://physics.nist.gov/constants. 2006 update to original source: P. J. Mohr and B. N. Taylor, "CODATA recommended values of the fundamental physical constants: 2002," *Rev. Mod. Phys.* **77**(1), 1–107 (2005).
5. A compilation by G. P. Williams of Brookhaven National Laboratory, "Electron binding energies," in *X-Ray Data Booklet*, Lawrence Berkeley National Laboratory Pub-490 Rev. 2 (2001), based largely on values given by J. A. Bearden and A. F. Barr, "Reevaluation of x-ray atomic energy levels," *Rev. Mod. Phys*. **39**, 125 (1967); corrected in 1998 by E. Gullikson (LBNL, unpublished). For further updates, consult http://www-cxro.lbl.gov. The energies are given in electron volts relative to the vacuum level for the rare gases and for H_2, N_2, O_2, F_2, and Cl_2; relative to the Fermi level for the metals; and relative to the top of the valence bands for semiconductors.
6. Photon energies in electron volts of some characteristic emission lines of the elements of atomic number $3 \leq Z \leq 95$, as compiled by J. B. Kortright, "Characteristic x-ray energies," in *X-Ray Data Booklet*, Lawrence Berkeley National Laboratory Pub-490 Rev. 2 (1999). Values are largely based on those given by J. A. Bearden, "X-ray wavelengths," *Rev. Mod. Phys*. **39**, 78 (1967), which should be consulted for a more complete listing. Updates may also be noted at http:/www-cxro.lbl.gov/data-booklet/.

Eric M. Gullikson received his B.A. in physics from the University of Hawaii in 1977 and a Ph.D. in physics from the University of California, San Diego in 1984. After a post-doc at AT&T Bell Labs, he joined the Center for X-Ray Optics at Lawrence Berkeley National Laboratory in 1987. He has worked on the development of high-accuracy reflectometry and scattering measurement techniques for EUV and soft x-ray radiation. He is author or coauthor of over 200 publications.

Downloaded From: https://www.spiedigitallibrary.org/ebooks/ on 09 Mar 2022
Terms of Use: https://www.spiedigitallibrary.org/terms-of-use

David Attwood received his Ph.D. in applied physics from New York University in 1972. He has been a Professor in Residence at UC Berkeley since 1989. He was co-founder of the Applied Science and Technology Ph.D. program and serves on its Executive Committee. He has been faculty advisor for the undergraduate Engineering Physics program for 15 years. His research interests center on the use of short-wavelength electromagnetic radiation, soft x-rays, and extreme ultraviolet radiation in the 1–50 nm range. Applications of particular interest include element-specific soft-x-ray microscopy and EUV lithography. He and his students are also active in the use of novel Fourier optics, image contrast techniques, and the development and use of coherent sources at these short wavelengths. At the contiguous Lawrence Berkeley National Laboratory, he is the founding Director of the Center for X-Ray Optics (CXRO) and was the first (1985–1988) Scientific Director of the Advanced Light Source (ALS). He is a Fellow of the American Physical Society and the OSA. He is author of *Soft X-Rays and Extreme Ultraviolet Radiation: Principles and Applications* (Cambridge University Press, 2000). His lectures are regularly broadcast live over the Internet and electronically archived, such as at http://www.coe.berkeley.edu/AST/sxreuv and http://www.coe.berkeley.edu/AST/srms.

Downloaded From: https://www.spiedigitallibrary.org/ebooks/ on 09 Mar 2022
Terms of Use: https://www.spiedigitallibrary.org/terms-of-use

Index

0.07-NA EUV imaging system, 29
0.08-NA Schwarzschild imaging, 15
0.0825 NA_{mask}, 241
0.25 NA, 2, 25, 603
0.33 NA, 229, 237, 242, 248–253, 295, 447, 599–600, 603, 605, 609–610, 616
0.45 NA, 2, 242, 248, 266, 473
0.5-NA six-aspherical-mirror imaging system, 27
0.50-NA ring-field imaging system, 28
0.5 NA MET, 232
0.5 σ, 232
0.55 σ, 266
0.55 NA, 251–253, 600, 603, 610, 616, 618–619, 655
0.7 σ, 652
2-butanone, 540
2 tert-butoxycarbonyl (tBOC)-protected functional groups, 524
2,2,2-trifluoroethyl a-chloro-acrylate (EBR-9), 37
2D disk, 383
2D PSD of the surface topography (PSD_{2D}), 31, 274, 282, 285, 288, 293
3D EUV mask effects, 314, 412, 429, 461, 473, 611, 614, 615, 621
3D spherical target, 135
4X reduction, 241
5X reduction, 16
10X-II Schwarzschild, 15
10X reduction microstepper, 67
20X reduction Schwarzschild optics, 19

A

Abbe, Ernst, 26, 598
aberration correction, 25–26
ABRIXAS mission, 259
absolute figure uncertainty, 28
absorbance *A*, 500–501
absorbed power density, 270
absorber-over-layer reflection masks, 19
absorber patterning 35, 91, 102
absorber shadowing, 247, 249
absorber thickness, 247, 429, 444, 459, 468
absorption coefficient, 37
—of PMMA, 24
absorption data, 690
absorption edge of C, 7, 351
absorption edge of Si, 5, 33, 37
acceptance testing procedure (ATP), 316
acetal blocking groups, 520
acetal protecting groups, 521
acid amplifier (AA), 526
—3BH, 527
acid-catalyzed deblocking, 520
acid-catalyzed crosslinking, 523
acid quantum yield, 512, 513
acid-sensitive dye (Coumarin-6), 509, 511
acrylate polymer, 521

Downloaded From: https://www.spiedigitallibrary.org/ebooks/ on 09 Mar 2022
Terms of Use: https://www.spiedigitallibrary.org/terms-of-use

actinic blank inspection (ABI), 421, 433–435
actinic wavefront metrology, 39, 625
action requirement (AR), 66
actuators, 105, 131, 626, 627
acyclic-fluorine-containing monomer, 522
aerial image 112, 246, 249, 449, 661
—contrast, 35, 429, 462, 520, 597, 610, 612, 628, 654, 645, 680
—LER PSD, 661
—metrology, 230, 233
—microscope, 311
—modeling, 653, 660, 669
—PSD, 661
—scanner, 309, 310
—shape, 561
—simulation, 441, 669
—slope, 673
Aerial Image Measurement System (AIMS™), 227, 308
—typical use, 310
AES, 68
Airy disk, 289
Airy function $PSF_0(r)$, 289
aliphatic esters, 502
Alpha Demo Tool (ADT), 228, 232
—metrology, 233, 565, 606, 608
alternating phase shift mask, 461, 470
—modified, 461
ambient hydrocarbons, 345
AMD Typhoon, 233
amorphous-titanium–doped fused silica, 275
amplified spontaneous emission (ASE), 177
amplified spontaneous emission (ASE), back-propagating, 176
amplitude defect, 433
—repair, 439
anamorphic imaging, 249, 253, 614
anamorphic system, 614
—high-NA, 615
angle-resolved scattering (ARS), 281
annulus (or ring field), 271
antireflective coating (ARC), 413
a-periodic multilayer coatings, 300
aplanatic design, 255
ArF resist polymers, 522
Arrhenius law, 302
asphere, 17, 27, 227, 272
—fabrication, 19, 28
aspheric departure, 26
aspheric surfaces, 2
Association for Super-Advanced Electronics Technologies (ASET), 20
astigmatic errors, 273
astigmatism, 25
at-wavelength inspection, 35, 37
atomic force microscopy (AFM), 10, 275, 525
atomic hydrogen cleaning, 390
atomic scatter factors, 689
attenuated phase shift mask, 461, 466
Au-drum target, 39
AZ PN114, 38

B

backscattered primary electron (BSE), 444
backside conduction layer, 413
barrier layers, 301
beam transport system (BTS), 114
Beer–Lambert law, 629
Berkeley direct contrast tool (DCT), 540
Bessel function of the first kind, 289
BESSY, 230
Biafore full stochastic model, 556
Bicerano's graph-theoretical method, 503
bidirectional scattering distribution function (BSDF), 281–283, 285
bipyridine ligands, 542
bismuth oligomers, 541

Downloaded From: https://www.spiedigitallibrary.org/ebooks/ on 09 Mar 2022
Terms of Use: https://www.spiedigitallibrary.org/terms-of-use

bis-phosphine palladium oxalates, 543
BL1b, beamline, 346
BL8, beamline, 350
blazed-grating filter, 259
bore geometry, EQ-10195
Boremann effect, 372
boron carbide (B_4C), 302, 423, 455, 500
Bossung curve, 460, 461
bright-field image, 432
bright-field masks, 281, 543
bright-field signals, 434
Bragg reflection, 370, 412
Bragg wavelength, 23
Bragg's law, 419
broadband coatings, 301
broadband mirrors, 300
buffer gas, 401
—specific heat capacity, 147
—alternatives, EUV transmission, 148
—alternatives, heat conductivity, 148
—mitigation, 385–387

C

CaF_2 birefringence, 74
capping layer, 185, 305, 340, 341, 413, 423, 427, 431, 437, 443, 466
—carbon, 338
—ruthenium, 342, 345, 432, 457
—SiN, 398
—standard benchmark, 341
—TiO_2, 342, 343
—ZrN, 398, 399, 401
carbon (C), 3, 34, 302, 423
carbon-based resists, 24
carbon contamination, 37, 337
carbon deposition, 336
carbon growth rate, 350
—for several wavelength bands, 350
carbon K x-rays, 5
carbon layer, 305, 336
carbon nanotube (CNT), 455
carbon removal, 336
carbonaceous film, 351
carbonaceous layer, 339
carbonization, 336, 338, 339, 345
carboxylate ligands, 537
Cassegrain multilayer telescope, 33
Cassegrain reflector, 256
catalytic probes, 395
Center for Plasma-Material Interactions (CMPI), 376
centroid wavelength shift, 437
charge-and-deflect concept, 132
charge exchange collision, 381
chemical mechanisms of EUV exposure, 505, 508, 517
chemical sensitivity, 505
chemically amplified resist (CAR), 356, 497, 505
—non-CAR, 503, 563,
chief ray angle (CRA), 473
chief ray angle at object side (CRAO), 241–243, 246–248, 271–272, 610, 621
chipmakers, leading-edge, 82
chirp rate, 177
chromatic vignetting, 24
CLEARCERAM®, 275
clearing dose E_0, 497
CO_2 laser, 166, 178–179
—amplifier, 120
—beam diameter, 169
—high-power, 114, 120
coating influence on the PSD, 305
coefficient of thermal expansion (CTE), 256, 626
coherence time, 664
coherent scattering microscopy (CSM), 472
collector contamination, 370
collector lifetime, 40, 142, 146, 219, 371, 386, 401

Downloaded From: https://www.spiedigitallibrary.org/ebooks/ on 09 Mar 2022
Terms of Use: https://www.spiedigitallibrary.org/terms-of-use

colloidal graphite-coated target, 4
computer-controlled optical surfacing, 17, 28
computer-controlled polishing (CCP), 274
computer-generated holographic nulls, 17, 29
COMSOL Multiphysics®, 396
concave spherical mask, 7
condenser mirror, 39
—lifetime, 41
contact hole (CH), 240, 443, 457, 543, 554, 557, 559, 594
contact hole printability, simulation, 619
contamination growth, 349, 355
contamination rates, 345, 347, 349
continuous slowing-down approximation (CSDA), 510
continuous-wave source, 346
continuum model of absorption, 549
conversion efficiency (CE), 10, 38, 116, 120, 123, 136, 166, 182, 198, 213, 383
cooperative research and development agreement (CRADA), 13, 59
COSTAR correction optics, 28
Coulombic acceleration, 376
cracking efficiencies, 388
critical dimension (CD), 22, 112, 597
critical dimension uniformity (CDU), 271, 281, 598, 604, 659
critical illumination, 13, 265
cryogenic pellet targets, 41
$(cyclohexyl)_3Sb(O_2CH{=}CH_2)_2$, 546
CXRO, 197
—website, 689

D

dawn of EUVL, 8
dark-field masks, 543
dark-field microscopy, 432
dark-field scanning mode, 432
dark-field signal, 434
debris mitigation, 38, 40, 142
—magnetic, 150, 166, 381
debris shields, 209
decadic TISD, 289
defect reduction trend of EUV mask blanks, 426
defect signal enhancement, 438
defect signal intensity (DSI), 433–435
defect smoothing, 425
Defense Advanced Research Projects Agency (DARPA), 67
Department of Commerce (DOC), 67, 88
Department of Defense (DOD), 67
Department of Energy (DOE), 67
deprotection strategy, 533
depth-graded multilayer coatings, 300
depth of focus (DOF), 22, 240, 461, 600, 652
diamond grinding wheel, 28
dibenzyl tin dibenzoate, 544
—imaging capabilities, 544
diffraction-limited imaging, 8
dilatometer, 415
Dill A parameters, 501
Dill B parameters, 497, 501
Dill C parameters, 497
Director of Defense Research & Engineering (DDR&E), Office of the, 67
discharge-produced plasma (DPP), 75, 113, 193, 207, 214, 254, 370, 422
discrete model of absorption, 549
discrete stochastic models, 548
disk-shaped electrodes, 207
disk target, 135, 170, 171
dome target, 171
dose-controlled EUV power, 129

Downloaded From: https://www.spiedigitallibrary.org/ebooks/ on 09 Mar 2022
Terms of Use: https://www.spiedigitallibrary.org/terms-of-use

dose error, 118, 281, 598
dose stability and control, 118, 155, 183, 215, 221
dose tolerance, 240
double-logarithmic PSD curve, 286
drive laser, 110, 118, 119, 121, 123, 124
—high-power, 126
droplet generator (DLG), 114, 131
—parameters, 131
—steering system (DGSS), 154
droplet steering, 154
dual stage, 628
duty cycle, 116, 119, 136, 183, 212
DUV binary mask, 413
DUV plasma spectra, 140
DUV ZEISS AIMS, 309
dynamic gas lock, 357

E

E_{size}, 542
economic downturn, 85
edge placement error (EPE), 604
effective attenuation length (EAL), 351
eight-mirror shell collector, 257
elastic scattering, 507
electro-optical modulation, 175
electron-beam deposition repair, 446
electron-beam evaporation, 304
electron-beam-induced deposition of carbon, 337
electron-beam projection lithography (EPL), 68, 84
electron-beam repair, 442
electron binding energies, 689, 699
electron density, 97, 171, 395, 418
electron ionization, 506
electron temperature, 114, 171, 378
electron trapping, 513
electron travel range, 515
electrostatic clamp, 634
electrostatic repeller field, 40
electrostatic wafer chuck, 15
ellipsoid collector, 260
ellipsoid mirror, 256, 260
embedded phase shift mask structure, 469
energy extraction efficiency, 178
energy overhead, 155
energy sector analyzer (ESA), 376–377
EMF, 195
Engineering Test Stand (ETS), 17, 58, 110, 308, 660
environmentally stable chemically amplified resist (ESCAR), 518–519
EQ-10, 193
ESA's XMM-Newton x-ray observatory, 259
ESPRIT, 229
etch selectivity, 465
etch stop layer (ESL), 465–467
etched binary mask, 464
etched flux, 388
étendue, 116, 118, 196, 198, 212, 255, 265, 312
EUCLIDES, 20, 229
EUREKA, 299
EUV-2D, 504
EUV beam analyzer, 210
EUV blank multilayer requirements, 413
EUV camera, 211
EUV chemically amplified resist (CAR), 508
—electron trapping, 508
—hole-initiated, 508
—internal excitation, 508
EUV dual pods, 314
EUV emission
—position stability, 216
—volume, 208
EUV illuminator, 622
EUV-induced cracking, 351
EUV interferometry, 32

Downloaded From: https://www.spiedigitallibrary.org/ebooks/ on 09 Mar 2022
Terms of Use: https://www.spiedigitallibrary.org/terms-of-use

EUV light
—film absorbance, 504
—incoherent sources, 113
EUV LLC, 2
—risk-level definitions, 70
EUV mask
—defects on, 311
—fabrication process flow, 414
—shadowing effect, 459
EUV Mask Infrastructure (EMI) consortium, 308
EUV multilayer, TEM image, 337
EUV multilayer, microstructure, 342
EUV optical density, 502
EUV optical system, 227, 241
—resolution, 241
EUV pellicle, 428, 454, 635
—guidelines and requirements, 453
—mounting, 637
—principle, 637
—temperature profiles, 455
EUV penetration region, 667
EUV polarimeter, 299
EUV power at IF, 120, 129
EUV projection system, first, 605
EUV reflectance spectra, theoretical and experimental, 420
EUV reflectivity, 300
—measurement, 395
EUV reflectometers, 422
EUV resist absorbance, 503
EUV scanner, optical column, 611, 614–615
EUV scanner, optical train, 228
EUV scanner ring field, 313
—emulation, 313
EUV source, Sn-based, 622
EUV source requirements, 116
—cleanliness, 116
—EUV power (inband), 116
—integrated energy stability, 116
—size, 117
—output, étendue, 116
—max. solid angle input to illuminator (sr), 116
—repetition frequency, 116
—spectral purity, 116
EUV source–scanner interface, 153
EUV source tin consumption, 152
EUV source vessel, 113, 115
EUV spectrometer, 201
EUV step-and-scan system, 595
—principle, 594
—productivity, 595
EUV–visible scintillator, 211
EUVL exposure tool overview, 620
even aberrations, 625
Evolving nano-process Infrastructure Development Center (EIDEC), 355
Exitech Ltd, 232, 311
exposure latitude, 118, 240, 521, 528, 600, 623
exposure wavelength, 22, 227, 233, 369
extinction coefficients of materials at 13.5-nm wavelength, 453
extracavity modulation, 175
extreme-ultraviolet lithography (EUVL), 2, 3, 11, 21, 22
Extreme Ultraviolet Lithography System Development Association (EUVA), 20
EXULT project, 20, 299

F
f, 120
fabrication tolerance, 276
far-field test tool (FFTT), 138
Faraday cup (FC), 379
fast axial flow (FAF)
fast electrical pulse, 194
figure, 28, 230, 271, 272, 279, 305,
—control, 277–278
—correction, 274

Downloaded From: https://www.spiedigitallibrary.org/ebooks/ on 09 Mar 2022
Terms of Use: https://www.spiedigitallibrary.org/terms-of-use

—errors, 29, 34, 273, 275, 280, 289, 293, 305, 307
—metrology, 276
fast transverse flow (FTF), 121, 178
field facet module, 622
field of view (FOV), 309
film quantum yield (FQY), 509
Fizeau interferometer, 11, 19, 277
flare, 16, 32, 236, 239, 291, 297
—density $FD^{(n)}$, 296
—efficiency function, 295–296
—sources, 279
flexible illumination, 237, 268, 609
—modes, 623
flexure-suspended balance masses, 627
fluoropolymers, 502, 504
fly's eye integrator unit, 266
focus offset optimization, 438
focused ion beam (FIB), 429, 437, 446
footprint, 209, 221
Foucault testing, 32
four-aspherical-mirror reflective imaging system, 26
four-mirror EUV imaging system, 17
fractal, 31
fragments, number of, 173
Fraunhofer Institute for Laser Technology (ILT), 207
free-radical polymers, 522
frequency-doubled Nd:YAG laser, 39
Fresnel number, 179
front-opening unified pod (FOUP), 634
full-aperture interferometer, 275
full-field production tools, 609
full-field tools, 228, 606, 608–609
—EUV1, 228, 234, 608
full scanner emulation, 312
full-time equivalent (FTE), 83

G

g-line of mercury (Hg), 5
gain switching, 174
gallium ions (Ga^+), 446
gas chromatograph with a mass spectrometer (GC-MS), 354
gas field ion source (GFIS), 446
gas jet, 40
gas puff targets, 41
GC-MS with cryofocusing, 354
glass ceramics, 275
glass transition temperature T_g, 522, 523
grazing-incidence collector, 255, 375
—Wolter type, 255, 256
grazing-incidence optical system, 15
grazing-incidence Ru collector, nested, 219
grazing-incidence Ru collector lifetime, 219
grazing-incidence Ru mirror, 220

H

H_2 bubbles, 147, 400
hafnium oxide, 535
hafnium oxide sulfate (HafSOx), 535
Halbach array, 379
Han stochastic model, 553
Henke elemental absorption coefficients, 503
Henke tables, 37
hexafluorine (SF_6), 431
Hidaka Kougaku, 11
high-density gas clusters, 41
High Energy Physics Laboratory, 5, 19
high NA, 232, 241, 244, 246, 249
—DUV ZEISS AIMS tool, 309
—multiple-patterning extension, 639
—QF, 613
—scanner, 600, 619

Downloaded From: https://www.spiedigitallibrary.org/ebooks/ on 09 Mar 2022
Terms of Use: https://www.spiedigitallibrary.org/terms-of-use

High Power EUV Irradiation Tool, 357
high-power seed system (HPSS), 126
high-precision metal replica process, 258
high-pupil-frequency aberration, 291
high-resolution encoder sensor, 626
high-spatial-frequency roughness (HSFR), 17, 31, 273, 279, 305, 415
high-volume manufacturing (HVM), 79, 94, 109, 165–167, 227, 370, 433–435
Himeji Institute of Technology (HIT), 20
HiNA, 232
Hinsberg stochastic model, 553
hole-initiated chemistry, 511
homolysis of tin–carbon bonds, 540
homolytic cleavage of the M-carboxylate bond, 545
honeycomb mesh structure, 454
horizontal/vertical (H-V) bias, 234
hot filament hydrogen radical source, 388
hydrogen-based cleaning, 373
hydrogen buffer gas pressure, 144
hydrogen etching of Sn, 388
hydrogen implants, 401
hydrogen penetration, 185
hydrogen radical, 336, 358
—cleaning, 391
hydrogen silsesquioxane (HSQ), 562
hyperboloid reflector, 256

I

ideal PSF (Airy disk), 289–293
illumination channel, 267
illuminator, 228, 263, 594
illuminator pupil tuning, 269
image contrast, 250, 430
image optimization, 269
image placement error (IPE), 415–416, 462, 465
image quality, 250
IMEC—Interuniversity Microelectronics Centre, 228
in situ cleaning, 40, 102, 105, 156, 371, 387
inband EUV brightness, 198, 213
inband EUV output power, 213
inband EUV spectrum, 117
inplane distortion (IPD), 430
intensity dependence, 345–349
intensity uniformity, 263
interdiffusion, 301, 338
interface roughness, 301, 424
interferogram, 231
interferometry-based metrology, 231
intermediate focus (IF), 112, 153, 219, 228, 621
internal excitation, 514
inverse Cassegrain, 25
ion average charge state, 171
ion-beam figuring (IBF), 274
ion-beam projection lithography (IPL), 68, 84
ion-beam sputter deposition (IBD), 36, 304, 420
ion polishing, 425
ion spectra, 378
ion wind, 134
ionization rate of Sn, 173
IR drive laser, 262
IR-suppression grating, 262
iridium (Ir)-coated Schwarzschild optic, 8
isomorphic system, 614
ITRS, 42, 60, 602

J

joint development agreement (JPA), 68
joint development program (JDP), 61

Downloaded From: https://www.spiedigitallibrary.org/ebooks/ on 09 Mar 2022
Terms of Use: https://www.spiedigitallibrary.org/terms-of-use

K
k_1, k_2, 22, 226, 597, 600
ketal protecting group, 532
ketone, 532
kinetic traces, 511
Kirchhoff mask, 463
Köhler critical-illumination system, 20, 265–267
Köhler design, 10
KrF excimer laser, 10
KrF laser-induced soft-x-ray source, 20

L
L_4Pd complex, 544
large-scale integration, 42
Larmor movement, 166
laser amplifier, 120
laser-assisted discharge-produced plasma (LDP), 207
laser-induced fluorescence, 172
laser plasma source, 10
laser power, 120
laser-produced plasma (LPP), 38, 40, 109, 112, 113
—sources, 113, 115, 126, 166
laser shockwave cleaning (LSC), 457
laser-to-droplet targeting, 155
laser-to-droplet timing, 154–155
layered synthetic microstructure (LSM), 4
lifetime, 118
lifetime studies, 338
line-edge roughness (LER), 38, 43, 415, 539, 549, 556–557
—modeling, 671
line-edge roughness transfer function (LTF), 660–663
linewidth roughness (LWR), 503, 526, 529, 533, 563, 569, 604
liquid-droplet target system, 20, 41
liquid metal ion source (LMIS), 446
liquid tin, 208
—bath, 207–208
—thermal conductivity, 209
lithium salt of ethylenediamine (LiEDA), 37
lithographic resolution, 652
load mismatch, 201
local-oxidation-of-silicon (LOCOS), 17
local critical dimension uniformity (LCDU), 598–599, 604, 618
long-term aberration drifts, 626
longwave surface figure errors, 275
low-activation-energy system, 521
low-departure aspheric reflectors, 16
low-energy electron scattering in solids (LESiS), 510, 516
low-étendue source, 265
low-LER dibenzyl tin complexes, 544
low-spatial-frequency roughness (LSFR), 280
low-thermal-expansion material (LTEM), 34, 413

M
magnetic debris mitigation, 150, 166, 381
magnetic plate, 627
magnetically levitated wafer stage, 15
magnetorheological figuring (MRF), 274
magnetron sputtering, 304
magnification (MAG), 230, 241–243, 251
mandrels, 258
Maréchal criterion, 32, 276
Marshall Space Flight Center, 3
mask effect on high-NA imaging, 247
mask efficiency, 250
mask error enhancement factor (MEEF), 470
mask (reticle) handling, 636

Downloaded From: https://www.spiedigitallibrary.org/ebooks/ on 09 Mar 2022
Terms of Use: https://www.spiedigitallibrary.org/terms-of-use

mask heating, 632
mask MSFR (slope error), 415
mask stage, 628
mask writing errors, 598
mass-limited target, 40, 114
master oscillator power amplifier (MOPA), 110, 114, 121, 175
—architecture, 123
—with pre-pulse, 121
mechanism for the generation of acid in CARs, 512
MEDEA+ Extreme UV Alpha Tools Integration Consortium (EXTATIC), 21
Media Lario Technologies, 259
megasonic cleaning, 418
MET5, 232, 606
metal-containing resists, 568
metal-oxide films, 535
metal-oxide model, 559–560
metal–oxide semiconductor (MOS), 12
methacrylate [-$O_2CC(CH_3)=CH_2$)], 539
metrology source requirements, 198
Microelectronics Development for European Applications+ (MEDEA+), 21
micro-exposure tool (MET), 67, 228, 230, 563, 670
—image field, 228
micro-interferometers, 274
microscope, resolution limit, 226
mid-spatial-frequency roughness (MSFR), 16, 17, 32, 273, 279, 305, 415, 655
Mie scattering, 172
mirror surface errors, 655
mitigating gas, 357
Mo/Si coating at normal incidence,
—peak reflectivity, 419
Mo/Si mirror reflectivity, 118, 227
Mo/Si multilayer, TEM image, 423
Mo/Si multilayer mirror
—long-term stability, 338
—planar, 211
—spherical, 211
Mo/Si stack, cross-sectional TEM image, 419
$MoSi_2$, 342
mode-locking, passive or active, 174
modeling of resist
—development, 552
—exposure, 552
—image intensity distribution, 551
—initial resist rate, 551
—post-exposure bake, 552
modulation transfer function (MTF), 660, 662–663
moiré alignment system, 15
molar metal-to-sulfate ratios, 535
molecular dynamic simulation, 558–559
Molecular Organometallic Resists for EUV (MORE), 542
mononuclear organometallic complexes, 542
Monte Carlo modeling, 510, 533
multilayer defect avoidance (MDA), 440
multilayer mirror lifetime, 373
multilayer mirror reflectivity, 374
—theoretical, 373
multilayers as Bragg reflectors, 227
multiple-epoxy-containing crosslinker, 524
multiple patterning, 226
Multivariate Poisson Propagation Model (MPPM), 675, 678
—predicted LWR and CDU terms, 680

N

nanomachining, 444
nanoradian, 272

Downloaded From: https://www.spiedigitallibrary.org/ebooks/ on 09 Mar 2022
Terms of Use: https://www.spiedigitallibrary.org/terms-of-use

NaOH, 497
National Institute for Standards and Technology (NIST), 67, 344
Nd:YAG lasers, 208
negative chemically amplified resist AZ PN114, 497
negative-tone sensitivity of resists, 542
New Energy and Industrial Technology Development Organization (NEDO) Japan, 179, 185
next-generation lithography (NGL), 64, 230
niobium oxide, 305
no master oscillator (NOMO), 121
nonlinear coupled oscillator, driven, 195
non-null Fizeau interferometer, 29
nonstochastic continuum models, 548, 553, 569
normal-incidence
—design, 136
—collector, 375
—ellipsoid collector, 261
—EUV collector, 111, 114, 137, 255
—reflective optics, 3
—reflectivity, 6
normalized image log slope (NILS), 246, 264, 597, 612
Northrop Grumman, 87
novolaks, 502
NTT superconducting storage ring in Atsugi (Super ALIS), 13
nuclear magnetic resonance (NMR), 530
NuFlare Technology, Inc., 235
null corrector, 277
numerical aperture (NA), 2, 226
—further increase, 639
NXE:3100, 608
NXE:3300B, 109, 229
—illumination settings, 238
NXE:3350B, 109, 229, 237, 240, 599, 609
NXE:3400B, 109, 229, 609–610
—illumination settings, 238

O

obscuration impact on imaging, 246
odd aberrations, 625
off-axis illumination, 117, 226
off-axis Schwarzschild system, 25
Offner ring-field imaging system, 8, 16
on-product overlay (OPO), 602–603
—typical budget, 603
open-frame exposure, 248
open-loop power, 129
optical constants, 690
optical proximity correction (OPC), 234, 267, 553
optical transfer function (OTF), 660
optical triangulation, principle, 630
optics contamination, 335
—summary and outlook, 358
organometallic tin dicarboxylates $[R_2Sn(O_2CR')_2]$, 544
organosilane monolayer film, 37
out-of-band (OOB) energy monitor, 210
out-of-band (OOB) light, 173
out-of-band (OOB) radiation, 138
—power measurements, 215, 140
out-of-band (OOB) spectrum from EUV plasma, 174
out-of-plane distortion, 427, 428
overhead, 120
—time, 119
overlay errors
—application-specific, 602
—dedicated chuck, 602
—matched machine, 602
—related to customer process, 602

Downloaded From: https://www.spiedigitallibrary.org/ebooks/ on 09 Mar 2022
Terms of Use: https://www.spiedigitallibrary.org/terms-of-use

oxalate ligands, 545
oxalate loading, 542
oxidization, 338

P
PAG triphenylsulfonium tris (trifluoromethansulfonyl) methane, 511
palladium (Pd), 258, 342, 544
para-amide-styrene, 531
paraboloid mirror, 256
parasitic reflections, 122
parasitic seeding, 175
partial coherence (σ), 228, 229, 232, 264, 623, 653, 654, 664, 666
patents
—environment, 102
—ETS and illuminator, 103–104
—lithography, 104
—mask, 103
—metrology, 100
—miscellaneous, 105
—multilayer, 101–102
—optics, 100–101
—source, 104
Paul Scherrer Institut (PSI), 536
PdAu, 342
PdO, 429
peak brightness, 221
pedestal, 175
pedestal energy, 124–125
pellicle-mounting structure, 456
pellicles, 115, 450
—CNT-based, 456
—membrane, 452
pentafluorobenzene-sulfonic acid ($C_6F_5SO_3H$, PFBS), 530
perfluorobenzenesulfonate esters (3HC, 3MC, 2MC), 529
perfluorooctane sulfonic acid (PFOS), 530
periodic change relationship to figure change, 307
phase defects, 35, 417, 433
—printable, 436
phase-measuring interferometer (PMI), 28
phase shift error, 466
phase shift mask (PSM), 429
—relief-substrate, 657
phase-shifting point-diffraction interferometer (PSPDI), 22, 30
$Ph_3Sb(O_2CH{=}CH_2)_2$, 546
$Ph_3Sb(O_2CH_3)_2$, 546
$Ph_nM(acrylate)_2$, 545
photo-acid generator (PAG), 355, 504, 511, 678
—reduction potential, 514
photodecomposable nucleophile (PDN), 523
photo-electrons, 506
photo-ionization, 506
photolysis mechanism, 540
photon energies, 704
photosensitized chemically amplified resist (PSCAR™), 526, 532, 569
photosensitizer (PS), 533
photosensitizer precursor (PP), 532
PHS-type CAR, 508
physical constants, 698
physical interactions of electrons with molecular species, 507
Physikalisch-Technische Bundesanstalt (PTB), 298
plasma-assisted cleaning by electrostatics (PACE), 457
plasmon generation, 506
platinum oxalates, 543
point spread function (PSF), 288, 663
Poisson distribution, 548
Poisson number, 305
poly-4-hydroxystyrene (PHS), 512

Downloaded From: https://www.spiedigitallibrary.org/ebooks/ on 09 Mar 2022
Terms of Use: https://www.spiedigitallibrary.org/terms-of-use

poly-4-methoxystyrene (PMS), 512
polybutene-1 sulfone (PBS), 37
polyhydrostyrene, 502
polymer backbone, 355
polymer-bound AAs, 531
polymerization of organic molecules, 337
polymerization olefin loading (POL), 547
poly(methyl methacrylate) (PMMA), 10, 37, 495–498
—B and C parameters, 498
—exposure sensitivity curves, 499
—spectral characteristics, 496
polyphenolic molecule, 523
polystyrene latex (PSL), 458
polyvinyl phenol polymers, 521
positive-tone palladium oxalates, 543
post-exposure bake (PEB), 498, 677
power requirement, source, 116
power spectral density (PSD), 31, 270, 284, 660–661
precision aspheres, fabrication, 22
precision-to-tolerance ratio (P/T), 276
pre-pulse (PP), 110, 154
—laser, 167
—technology, 166
pre-pulse, picosecond, 168
pre-pulse-conditioned target, 110
pressure dependence, 347–350
primary growth mechanism due to secondary electrons, 340
process window, 252–253, 270, 599
—simulation, 616
Programme Extreme UV (PREUVE), 21
projection optics, 228
projection optics box (POB), 67, 594, 606–609, 622
—heating, 632
PROLITH, 510, 559
proximity effect test patterns, 431
proximity x-ray lithography, 68, 84
PSF_{flare}, 292
pulse count modulation (PCM), 155
pulse-forming system, 194
pulse radiolysis, 510–511
pulse-shaping switch, 124
pulsed-laser deposition, 304
pulsed source, 346
pupil facet mirror, 622
pupil fill ratio, 226, 237, 264, 269, 599, 609–610, 623

Q

Q-switching, 175
—intracavity, 174
quantum cascade laser (QCL)
—seeder, 177
quantum cascade laser (QCL), mid-IR emitting, 176
quantum efficiency (QE), 678
quarter-wave stack, 23
quartz crystal microbalance (QCM), 388
quasi-critical illumination, 256
quasi-conventional illumination, 313
quencher, 356

R

radiation hardness, 338
radiation hydrodynamics simulation, 171
radiation-induced processes related to carbon contamination, 338
radical-cation hole, 505
radical flux, 388
RAVE LLC, 444
Rayleigh breakup mechanism, 133
Rayleigh criterion, 32
Rayleigh equation, 597
Rayleigh–Rice vector perturbation theory, 281, 295
Rayleigh theory of jet breakup, 132

Downloaded From: https://www.spiedigitallibrary.org/ebooks/ on 09 Mar 2022
Terms of Use: https://www.spiedigitallibrary.org/terms-of-use

reactive ion etching (RIE), 396, 496
reflection against an absorber pattern, 616
reflective Cook triplet, 26
reflective masks, 8
reflective multilayer coatings, 2
reflective triplet, 16
reflectivity from a MLM versus the number of bilayers, 376
refractive index, 226, 273, 280, 299, 302, 418, 429, 459, 467, 689
refractive null, 29
reliability tests, long-term, 217
repetition rate, 118
residual gas analyzer, 344, 353
residual hydrocarbons, cracking, 34
resists
—bilayer, 38
—chain-scission, 521–532
—electron-beam, 37
—EUV-2D, 519
—hafnium oxide nanoparticle, 537–539
—high-speed negative-tone, 545
—Inpria XE151JB and XE151IB, 536
—KRS, 520
—MET-1K, 520
—metal-based, 503
—multinuclear, 542
—negative-tone hafnium oxide nanoparticle, photomechanism, 538
—negative-tone nonpolymeric-based EUV, 523
—noria-based, 523
—OFPR Novolak, 495
—open-source (OS1), 527
—organo-metallic
—OSU/Inpria dehydration mechanism and photomechanism, 536
—outgas test, 336
—penetration depth, 7
—sidewall profile, 24
—soft-x-ray, 8
—surface-imaging, 37
—trilayer, 38
—tri(phenyl)antimony diacrylate (JP-20), 545
—zirconium oxide nanoparticle, 537–539
resist film absorption, 501
resist film transmission, 501
resist–silicon-based positive photoresist (SPP), 495
resolution, 22, 226
resolution, LER, and sensitivity (RLS) tradeoff, 526, 534
rhenium-tungsten (Re-W) alloy, 3
rhodium (Rh), 258, 305
right of first refusal (ROFR), 61, 62
ring field, 27
ring-shaped field, 13
RMS^2 of the roughness, 283–284
RMS values of PSDs, 290
RMS density (RMSD), 286
$R_nM(O_2CR')_2$, 545
Ronchi testing, 32
ROSAT, 259
rotating mechanical chopper, 40
Ru-capped multilayers, 343
Ru sputter rate, 218
ruthenium (Ru), 258, 305, 423
ruthenium oxide, 305

S

SAL601, 498, 499
scan velocity, 628
scanning electron microscopy (SEM), 308
scanning EUV reflective microscope (SERM), 449
scanning transmission electron microscopy (STEM), 343

Downloaded From: https://www.spiedigitallibrary.org/ebooks/ on 09 Mar 2022
Terms of Use: https://www.spiedigitallibrary.org/terms-of-use

scanning tunneling microscopy (STM), 500
Schwarzschild camera, 10, 498, 500
Schwarzschild imaging system, 8, 15
Schwarzschild optics, 2, 10, 25, 311, 495
scraper mirror, 434
second-row elements (e.g., C, O, N, F), 535
second-to-last mirror, 245
secondary debris, 152
secondary electrons, 506
secondary-ion mass spectroscopy (SIMS), 399
seed wavelength, 177
SEMATECH, 67, 228
—EUV Resist Center, 90
—Mask Blank Development Center, 90
—MET, 90
—NGL Task Force, 230
SEMI P37-0613, 412
—substrate requirements, 415
SEMI P38-1103, 428
SEMI P40-1109, 428
Semiconductor Equipment and Materials International (SEMI) standards, 96
Semiconductor Industry Association (SIA), 67
Semiconductor Research Corporation (SRC), 67
SHARP, 312
—microscope, 249
shadowing, 610–612
Si-capped multilayers, 343
SiC, 342
SiH_x, 400
Si/Mo ML reflectivity variation as a function of wavelength, 374
sidewall angle, 38
silane polymers, 504
silicide formation, 423
silicon carbide (SiC), 423
simulated resist image, 441
six-degrees-of-freedom short-stroke actuator, 627
six-mirror optical design, 272
slab-waveguide diffusion-cooled geometry, 178–179
small-field tools, 607
Sn deposition at the intermediate focus (IF), 384
S_N2 and S_N1 reactions, 531
SnH_4, 358
soft-x-ray projection lithography (SXPL), 7, 11
soft-x-ray reduction lithography, 8
Solar and Heliospheric Observatory (SOHO), 337
solid-state laser (SSL), 169
solid-state laser, picosecond, 168
SORTEC, 19
source head module, 207
source mask optimization (SMO), 237, 269, 623
source requirements
—ABI, 198, 212
—AIMS, 198, 212
—APMI, 198, 212
—high-power source for scanner, 116
spatial stability, 200
speckle pattern, 664–665
spectral content, 117
spectral purity filter (SPF), 259
spectroscopic ellipsometry (SE), 346
spherical equivalent volume diameter (SEVD), 417–418
sputtering yields for common MLM materials, 399
standard-mechanical-interface (SMIF), 420
—pods, 314
stannane (SnH_4), 144, 149, 387
Starlith®3100, 228, 236, 267

Downloaded From: https://www.spiedigitallibrary.org/ebooks/ on 09 Mar 2022
Terms of Use: https://www.spiedigitallibrary.org/terms-of-use

Starlith®3300 wavefronts, 239
Starlith®3300/3400, 236
statement of work (SOW), 98
static random-access memory (SRAM) cell, 233
stochastic continuum models, 548
stochastic effects, 112, 549, 554, 675
stochastic model of absorption, 549
stochastic models, 559
stochastic resist chemistry, 569
Stoney equation, 305–307
Stopping of Range of Ions in Matter (SRIM) program, 385, 389
striae, 275
subaperture polishing, 28
substrate material requirements, 413
substrate phase defects, 37
supermirrors, 300
surface chemistry, 341
surface defect, 417
surface figure, 28
surface finish, 28
surface interferometry, 230
surface topography, 292
supersonic gas cluster targets, 41
supersonic hydrocleaning (SHC), 457, 458
SVG Lithography, 13, 63
synchrotron light source, 10, 39
Synchrotron Ultraviolet Radiation Facility (SURF), 197

T

t-butyl trifluoromethacrylate, 522
T configuration, 110
Tagawa/Kowaza modeling, 557–558
Tamaru's redeposition coefficient, 396
TaN absorber layer, 429
target density, 136
target shape, 136
TaSiN, 431
telecentricity, 10, 25, 249, 265, 473, 612
temporal stability, 200
tetrahydrofuron, 511
thermal instability, 424
thermal load, 116, 254, 262, 303, 632
thermal stability of EUV multilayers, 302
Thomson scattering, 171
three-aspherical-mirror ring-field imaging system, 16, 20
through-focus compensation repair, 442
throughput, 22, 43, 115, 116, 595, 609–610, 614–615
tin (Sn)
—circulation modules, 208
—cleaning rate, 149
—cleaning technique, 142
—clusters, mechanism of photolysis, 540
—deposition rate, 184
—droplets, 130
—management inside the vessel, 151
—removal from the vessel, 152–153
tin-ion stopping power, 143
tin jet breakup, 132
tin-oxo cages, 539
tin-oxo cluster $[(n\text{-}BuSn)_{12}O_{14}(OH)_6]$ $(p\text{-}CH_3C_6H_4SO_3)_2$, 540
tin-oxo cluster $([(RSn)_{12}O_{14}(OH)_6]$ X_2, 539
tin plasma, optimum ion density, 169
Tinsley Laboratories, 11, 68
TiO_2, 342
TIS density (TISD), 286, 294

Downloaded From: https://www.spiedigitallibrary.org/ebooks/ on 09 Mar 2022
Terms of Use: https://www.spiedigitallibrary.org/terms-of-use

TIS values of PSDs, 290
titanium dioxide, 305
TMAH (0.26 N tetramethylammonium hydroxide), 498, 522
TMAH-developable system, 524
toroidal mirrors, 10
total electron yield (TEY), 509–510, 513
total integrated scatter (TIS), 280, 285, 303, 655
total wavefront error, 625
transition-metal oxalates, 542
transmission image sensor, 631
transmission of 10-nm-thick Sn layer, 145
transmission mask, 10, 231
transverse flow of CO_2 gas, fast, 121
triflic acid (CF_3SO_3H or TfOH), 530
trifluoromethyl (-CF_3) group, 529
trigger-body design, 530
Trumpf TruFlow laser series, 178
—amplifiers, 121
TRW Inc., 68
tungsten-carbon ML, 5
turning mirrors, 119
turnover numbers, 546
two-aspherical-mirror imaging system, 10, 12, 13, 19
two-mirror illumination system, 10

U
ULE®, 275
Ultratech, 68
ultraviolet cleaning, 459
uniformity correction module (Unicom), 624
United States Advanced Lithography (USAL), 63
U.S. National EUV Lithography Program, 13, 18
UV-Vis-IR absorbance, 511

V
vacuum vessel, 114
Veeco Instruments, 68
—low-defect-deposition ML tool, 37
Virtual National Laboratory (VNL), 61
—Resource Development Center (RDC), 87
volume sensitivity, 497
—parameter, 505

W
wafer heating, 632
wafer load sequence, 634
wafer stage, 627
wafer throughput model, 115
wafer-to-wafer heat exchange, 119
wafer topology, 630
wafers, cumulative number of exposed, 638
wall angles, 499
wavefront aberration, 271
wavefront error, 14, 273, 669
—aberration-driven, 273
—total system, 32
wavefront metrology, 20, 630
wavelength dependence, 350–351
wavelength reduction, 639
wet etchability, 466
white-light interferometry, 17
white papers, 72
witness sample, 355
Wolter, Hans, 255
Wolter collector, 255, 266
Wolter type-1 system, 256–257
Wolter–Schwarzschild design, 256

X
xMT, 524
x-ray diffraction (XRD), 422
x-ray fluorescence, 218

Downloaded From: https://www.spiedigitallibrary.org/ebooks/ on 09 Mar 2022
Terms of Use: https://www.spiedigitallibrary.org/terms-of-use

x-ray photoelectron spectroscopy (XPS), 343
x-ray proximity lithography (XPL), 5, 12
x-ray reduction lithography, 5
xenon plasma, 195

Y
YAG-laser-driven LPP, 214
ytttria-stabilized zirconia, 342

Z
Z-parameter, 527–528, 563
Z-pinch, 193
Zernike, Fritz, Jr., 13
Zernike coefficients, 236
Zernike polynomials, 236, 625
zero-crossing temperature (ZCT), 275, 626
ZERODUR®, 3, 230, 275
zero-valent palladium-phosphine complexes, 544
zirconium (Zr) foils, 196
zirconium dioxide, 305
zirconium oxide sulfate (ZircSOx), 535
zone plate, 8, 311, 434, 449
Zr-coated Si photodiode, 210
ZrH_x, 400
ZrN, 400
Zr/Si_3N_4 filter, 211

Downloaded From: https://www.spiedigitallibrary.org/ebooks/ on 09 Mar 2022
Terms of Use: https://www.spiedigitallibrary.org/terms-of-use